AD-A209 469

# Laboratory Plasma Studies

Final Report

SAIC-89/1435

Contract No. N00014-86-C-2499

May 23, 1989

Science Applications International Corporation

An Employee-Owned Company

DTIC
ELECTE
JUN 27 1989
S D
D

DISTRIBUTION STATEMENT A
Approved for public release
Distribution Unlimited

89 6 01 006

# Laboratory Plasma Studies

Final Report

SAIC-89/1435

Contract No. N00014-86-C-2499

May 23, 1989

SAIC

Science Applications International Corporation

DTIC
ELECTE
JUN 27 1989
S D
D

DISTRIBUTION STATEMENT A
Approved for public release;
Distribution Unlimited

Post Office Box 1303, 1710 Goodridge Drive, McLean, Virginia 22102, (703) 821-4300

# Laboratory Plasma Studies

Final Report

SAIC-89/1435

May 23, 1989

Submitted to:

Dr. Max Rhinewine

High Power Electromagnetic Radiation Branch

Plasma Physics Division

Naval Research Laboratory

Washington, DC 20375-5000

Prepared by:

Ellis Hyman, Principal Investigator, with

David Bacon, Paul Boris, Alban Deniz, Demosthenes Dialetis,

William Grossmann, Bahman Hafizi, Douglas Kirkpatrick,

Jonathan Krall, Thomas Peyser, Spilios Riyopoulos,

Carol Sullivan, Thomas Antonsen, John Finn, Victor Granatstein,

Nicholas Krall, and Dennis Papadopoulos

DTIC COPY INSPECTED 6

Accesion For

NTIS CRA&I

DTIC TAB

Unannounced

Justification

By per ltr

Distribution/

Availability Codes

Dist | Avail and/or Special

A-1

Prepared Under:

Contract No. N00014-86-C-2499

Dr. Max Rhinewine explains that page 24fig.6.not included and that page 27 has various extraction schemes are given in appendix VV.

Per Max Rhinewine 8-9-89 hp.

## TABLE OF CONTENTS


I. Technical Discussion . . . . . 1

A. Plasma Filled Gyrotron . . . . . 1

B. Cyclotron Autoresonance Maser . . . . . 4

C. Quasi-Optical Gyrotron . . . . . 6

D. Support for Experimental Microwave Program . . . . . 6

E. Advanced Topics in Electrophysics . . . . . 10

F. Analysis of High Power Gyrotron Operation . . . . . 11

G. Externally Modulated Intense Relativistic Electron Beams . . . . . 12

H. Relativistic Klystron Amplifier . . . . . 13

I. NRL Two-Beam Accelerator . . . . . 13

J. Electron Beam Propagation in the Ion-Focussed Regime . . . . . 14

K. FEL Studies . . . . . 15

L. X-Ray Source for Lithography . . . . . 17

M. Studies of Coherent Radiation Sources . . . . . 17

N. Support to the NRL Charged Particle Beam Program . . . . . 20

O. Modified Betatron Theory and Experiment . . . . . 24

P. Studies of the NRL Dense Z-Pinch Experiment . . . . . 29

Q. Experimental Studies of the Effects of Induced Spatial Incoherence (ISI) on Laser-Plasma Instabilities . . . . . 31

R. Electron Beam Energy Deposition in a KrF Laser . . . . . 32

S. Experimental Study of Laser-Plasma Expansions in Magnetic Fields: Laboratory Simulations of Space Plasmas . . . . . 33

T. MHD Solar Coronal Plasma Code . . . . . 34

References . . . . . 36

II. Appendices

A. Megavolt, Multi-Kiloamp $K_a$-Band Gyrotron Oscillator Experiment

B. Experimental Investigation of the Effects of a Neutralizing Background Plasma on the Operation of a High Current Gyrotron

C. The Design of a 100 GHz CARM Oscillator Experiment

D. Design of a Waveguide Resonator with Rapid Wall Reflectors for a 100 GHz CARM Oscillator Experiment

E. Development of High Power CARM Oscillators

F. Design and Operating Characteristics of a CW Relevant Quasi-Optical Gyrotron with Variable Mirror Separation

G. Experimental Study of a 115 GHz Quasi-Optical Gyrotron with a Large Cavity

H. High Peak Power $K_a$-band Gyrotron Oscillator Experiments with Slotted and Unslotted Cavities

I. Review of the Tenth International Free Electron Laser Conference (Jerusalem, August 29-September 2, 1988)

J. The Effect of the Time-Dependent Self-Consistent Electrostatic Field on Gyrotron Operation

K. Mode Stability in a Quasi-Optical Gyrotron

L. Modulation of an Intense Beam by an External Microwave Source: Theory and Simulation

M. Nonlinear Space-Charge Waves on an Intense Relativistic Electron Beam

N. Externally Modulated Intense Relativistic Electron Beams

O. Relativistic Klystron Amplifier

P. Operation of a Multigigawatt Relativistic Klystron Amplifier

Q. On Certain Theoretical Aspects of Relativistic Klystron Amplifiers

R. Simulation Studies of Particle Acceleration Powered by Modulated Intense Relativistic Electron Beams

S. A Compact Accelerator Powered by the Relativistic Klystron Amplifier

T. Numerical and Experimental Studies of Particle Acceleration

U. IFR Conditioning and Transport

V. Numerical Simulations of Asymmetric Erosion Processes in Ion Focused Regime-Transported Beams

W. Analysis of the NSWC Beam Erosion Experiment

X. Delphi Theory-Axisymmetric Erosion and Wake Field Effects

Y. Numerical Studies of Erosion and Transport of Chopped and Unchopped Beams

Z. Relativistic Beam Propagation Through Diffuse Plasmas

AA. Diamagnetic Effects in Endoatmospheric Electron Beam Propagation

BB. Diamagnetic Cavity Formed During the Formation of a Laser Channel in the Ionosphere

CC. Guided Radiation Beams in Free Electron Lasers

DD. Optical Gain, Phase Shift, and Profile in Free-Electron Lasers

EE. Comparison of Sideband Growth in Tapered and Untapered Free Electron Lasers

FF. Development of Sidebands in Tapered and Untapered Free-Electron Lasers

GG. An X-Ray Source for Lithography Based on A Quasi-Optical Maser Undulator

HH. Small Signal Analysis of the Induced Resonance Electron Cyclotron Maser

II. Higher Harmonic Generation in the Induced Resonance Electron Cyclotron Maser

JJ. The Structure of the Sideband Spectrum in Free Electron Lasers

KK. Chaotic Electron Motion Caused by Sidebands in Free Electron Lasers

LL. Transformations of Gaussian Light Beams Caused by Reflection in FEL Resonators

MM. Reflection Matrix for Optical Resonators in FEL Oscillators

NN. Cavity Eigenmodes for the NIST/NRL Free Electron Laser

OO. Beam Conditioning Using Resistive Wires

PP. Resistive Wire Conditioning

QQ. SARLAC Hose and Tracking Simulations: The Movie

RR. Improving the Current-Carrying Capability of the Modified Betatron (Presentation)

SS. Improving the Current Carrying Capability of the Modified Betatron

TT. Beam "Self-Trapping" in the NRL Modified Betatron Accelerator

UU. A Novel Trapping Scheme in the Modified Betatron Accelerator

VV. Beam Extraction from the Modified Betatron
Development of a Beam Extraction Scheme for the NRL Modified Betatron
Beam Extraction Scheme from the NRL Modified Betatron Accelerator

WW. Beam Extraction Scheme from the Modified Betatron Accelerator

XX. Studies of a Multi-Kiloampere Electron Ring Confined in a Modified Betatron Accelerator

YY. On the Relationship Between Neutron Yield and Plasma Current in the Dense Z-Pinch

ZZ. Laser-Plasma Experiments and Laser Development at the Naval Research Laboratory

AAA. Nanosecond Framing Photography for Laser-Produced Interstreaming Plasmas

BBB. Large-Larmor-Radius Interchange Instability

CCC. Structuring Processes in Expanding Laser-Produced Plasmas

DDD. Laboratory Laser-Produced Astrophysical-Like Plasmas

EEE. Jets in Laser-Produced Plasmas

FFF. Equilibrium of Solar Coronal Arcades

# I. TECHNICAL DISCUSSION

The work performed by Science Applications International Corporation (SAIC) on this contract, "Laboratory Plasma Studies," Contract Number N00014-86-C-2499, SAIC Project Number 1-157-13-290, encompasses a wide range of topics in experimental, computational, and analytical laboratory plasma physics. The accomplishments described in this report were in support of the programs of the High Power Electromagnetic Radiation Branch of the Naval Research Laboratory (NRL) and cover the period 12 September 1986 to 24 March 1989. In the following subsections we will describe each of the topics investigated and the results obtained. Much of the research work has resulted in journal publications and NRL Memorandum Reports in which the investigation is described in detail. These reports are included as Appendices to this Final Report. A portion of this effort was conducted under subcontracts to Physical Sciences Inc. and to Mission Research Corporation. The Principal Investigators for these studies were respectively Dr. M.E. Read and Dr. T. A. Hargreaves.

## A. Plasma Filled Gyrotron

Recently, there has been much interest in developing means of circumventing the space-charge current limit in high-power microwave devices, notably the gyrotron. The space-charge current limit is most severe in the gyrotron due to the nature of the instability, which is most favorable when the beam alpha ($\alpha = \beta_\perp/\beta_\parallel$, the ratio of perpendicular to parallel velocity) is in the range 1 - 2, corresponding to low parallel velocity and therefore low limiting currents. The concept of injecting a neutral background plasma into the region of the electron beam has been investigated extensively in the Soviet Union, and has recently been the focus of some investigation at the University of Maryland with regard to Backward-Wave-Oscillators. The plasma is introduced to short out the self-electric field of the electron beam and effectively remove the space-charge of the electron beam as a current limiting obstacle. In order for this to be accomplished, the density of the neutral plasma must be greater than the density of the beam electrons, so that sufficient background electrons may be expelled from the region of the transiting electron beam to provide for

neutralization. The other element of importance is for the interaction to be based on a relativistic electron beam interaction; non-relativistic beams generate oscillations with non-relativistic phase velocities, which in the background plasma are highly electrostatic and trapped.

During the last year of the contract, an experiment to investigate the effects of a neutralizing background plasma on a relativistic gyrotron device has been designed and constructed, and is presently in place on the VEBA accelerator. The experiment is designed to be an extension of an earlier, relativistic gyrotron in vacuum and uses the results of that earlier experiment as a vacuum experiment baseline. The earlier vacuum experiment involved a collaboration among researchers from NRL, SAIC, JAYCOR, and the University of Maryland and has been documented in NRL Memorandum Report 6419, entitled "Megavolt, Multi-Kiloamp $K_a$-Band Gyrotron Oscillator Experiment." It is included in this report in Appendix A and a paper on this work has been submitted to Physics of Fluids. A previous Soviet result observed an increase in radiated power from 7 MW to 60 MW when a neutral plasma was introduced, corresponding to a factor of 2 increase in the injected current and a factor of 4 increase in efficiency. Similar benefits applied to our vacuum gyrotron baseline experiment would result in output powers P > 1 GW. The results are summarized in the following Proceedings article from a talk on the subject given at the Thirteenth International Conference on Infrared and Millimeter Waves in Honolulu, Hawaii, during December of 1988 (see 1988 Conference Digest, Volume 1039, p. 364):

## EXPERIMENTAL INVESTIGATION OFTHE EFFECTS OF A NEUTRALIZINGBACKGROUND PLASMA ON THE OPERATION OF A HIGHCURRENT GYROTRON*

D.A. Kirkpatrick†, S.H. Gold, A.K. Kinkead, W.M. Manheimer,
C.A. Sullivan†, T.M. Antonsen‡, and B. Levush‡

High Power Electromagnetic Radiation Branch
Plasma Physics Division
Naval Research Laboratory

### ABSTRACT

We present plans for an experiment to investigate the effects of a neutralizing background plasma on the operation of a high current gyrotron. A neutral plasma filling

the electron beam transport and gyrotron cavity regions allows for the propagation of super-vacuum currents and for tuning of the interaction frequency through the neutralizing plasma density $\omega_p^0$. The background plasma is completely ionized before the passage of the high current electron beam, and the plasma density (in the absence of the electron beam) is a known, measured quantity.

## INTRODUCTION

Recent developments in high current electron beams have led to substantial increases in the output powers of devices based on the electron-cyclotron-maser[1] such as the gyrotron. The electron beam current propagated in these devices is approaching the vacuum limit, where the space-charge field of the beam depresses the electron beam energy and prohibits any further increase in the current transmitted. Well before this strict limit is reached, the space charge field interacts with the beam electrons to increase their velocity spread, reducing the device efficiency and limiting the output power.

Several experiments have already been carried out which use a neutralizing background plasma as a means to transcend these difficulties[2,3]. The background plasma which fills the beam transport and radiation interaction regions must be dense enough to neutralize and screen the charge in the high current electron beam, while at the same time it must be tenuous enough to allow for the free propagation of the output radiation and not have a deleterious effect on the desired beam interaction. An earlier experiment[3] with a 320 keV, 1.2 kA electron beam noted an increase in the output 10 GHz gyrotron power from 7 MW to 60 MW when the neutral plasma density was increased from $n_p \sim 10^9$ cm$^{-3}$ to $n_p \sim 2 \times 10^{11}$ cm$^{-3}$. Increasing the plasma density further to $n_p \sim 5 \times 10^{11}$ cm$^{-3}$ resulted in a rapid reduction in the output power to about 10 MW. The beam current of 1.2 kA was greater than the vacuum current limit $I_{vac} = 640$ A by slightly less than a factor of two. The plasma in this experiment was produced by a secondary, low voltage electron gun which was used to pre-ionize a background gas. Residual neutral gas which might be ionized by the passage of the high voltage electron beam would contribute to an uncertainty in $n_p^0$.

## EXPERIMENT

We are presently modifying a 35 GHz gyrotron oscillator experiment[4] to operate in the presence of a neutralizing background plasma. A 1 - 10 kA, $\sim$ 1 MeV electron beam is generated by a masked, cylindrical diode. The electron beam is spun up by means of a rapid drop in the axial magnetic field caused by a small field-reversed coil placed well after the cathode-anode gap. The beam is compressed into the gyrotron interaction region and then dumped on the downstream side by the fringing magnetic fields. Recent experiments in the absence of a neutralizing background plasma have produced 200 MW of RF power at a frequency of 35 GHz. The maximum intracavity beam current was approximately 2 kA.

A neutralizing background plasma is added to this system by plasma guns[5] situated after the anode mask and before the field-reversed coil. The plasma guns are ideal for this application in that they are compact and produce a highly directional, almost completely ionized neutral plasma. Different plasma densities can be realized by firing the VEBA accelerator ($\tau \sim 40$ ns) at different times after firing the plasma guns. The plasma inventory

as a function of time after the firing of the plasma guns is measured in situ by pairs of electrostatic probes. The plasma density available from four plasma guns situated symmetrically in the azimuth is then variable between $n_p \sim 10^{11}$ -$10^{13}$ cm$^{-3}$ corresponding to $\omega_p^0/2\pi \sim 3$ - 30 GHz. The number density of the high energy electron beam is n$-beam \sim 6 \times 10^{11}$ cm$^{-3}$ for J $\sim 3$ kA/cm$^2$, and the available range in neutral plasma density should be able to scan through shielding the beam self-fields and approach cutting off the desired 35 GHz gyrotron interaction.


1. P. Sprangle and A.T. Drobot, IEEE Trans.Microwave Theory Tech., MTT-25 (6):528 (1977).
2. V.I. Krementsov, M.S. Rabinovich, A.A. Rukhadze, P.S. Strelkov, and A.G. Shkvarunets, Sov. Phys.-JETP, 4(4):622 (1976).
3. V.I. Krementsov, M.I. Petelin, M.S. Rabinovich, A.A. Rukhadze, P.S. Strelkov, and A.G. Shkvarunets, Sov. Phys.-JETP, 48 (6):1084 (1978).
4. W.M. Manheimer, S.H. Gold, J. Burke, A.W. Fliflet,and W.M. Black, Microwave and Particle Beam Sources and Propagation, N. Rostoker Ed., Proc. SPIE 873, p. 2 (1988).
5. R.J. Commisso, D.D. Hinshelwood, J.M. Neri, W.F. Oliphant, and B.V. Weber, NRL Memo Report 6057 (1987).



*Work supported by the Office of Naval Research.



Permanent address: Science Applications International Corporation, McLean, VA 22102.

Permanent address: University of Maryland, Plasma Physics Laboratory, College Park, MD 20742.


The viewgraphs from this presentation are included as Appendix B. The plasma gun system, interferometry system, and experimental apparatus are assembled and in the process of being integrated with the VEBA accelerator.

### B. Cyclotron Autoresonance Maser

Cyclotron Autoresonance masers (CARMs) involve the interaction of an electron beam and an electromagnetic wave. They are characterized by the Doppler shifted cyclotron frequency, providing a higher operating frequency than that of a gyrotron operating at the same magnetic field. The dispersion relation for the CARM is

$$\omega - kv_o - n\Omega_c = 0,$$

where $\omega$ is the operating frequency, k is the wave number, $v_o$ is the electron beam velocity,

n is the harmonic number, and $\Omega_c$ is the relativistic cyclotron frequency.

SAIC and NRL scientists jointly designed a 100 GHz CARM oscillator experiment operating with a 600 kV, 200 A electron beam. The resonant cavity is a Bragg reflector cavity with a Q of 1500. The projected output power of the oscillator is greater than 10 MW at an efficiency greater than 20%. The electron beam for the CARM experiment is generated using the TRITON accelerator. Modifications have been made to the accelerator in order to match the impedance of the accelerator to that of the electron gun and to keep the voltage ripple below the 3% design criterion. The magnets for the CARM have been designed, fabricated, and installed on the experiment. We redesigned the electron gun because the original gun was emitting off the anodized aluminum surface and the velvet emitter was not well-behaved when immersed in a magnetic field. The redesigned gun is a graphite emitter on a stainless steel shank. The anode is also made of graphite with annular pin holes to scrape the beam to reduce the current to approximately 200 A and to improve the beam axial-velocity spread. We have transported a well-aligned, 200 A electron beam through the system. Preliminary studies have been initiated on the CARM experiment. We have detected radiation over 90 GHz and are continuing the experiment with newly installed microwave diagnostics.

The design of the experiment is documented in NRL Memorandum Report 6273 entitled "The Design of a 100 GHz CARM Oscillator Experiment," while the cavity design was presented in the paper "Design of a Waveguide Resonator with Rippled Wall Reflectors for a 100 GHz CARM Oscillator Experiment," *Int. J. Electronics* **65**, 463-475 (1988). These papers are included here as Appendices C and D respectively.

A 280 GHz CARM Oscillator experiment is currently in the design and procurement stage. This experiment was designed by NRL and SAIC scientists. The 280 GHz experiment will operate with a beam voltage of 500 kV, a current of 100A for 1 $\mu$sec, and a magnetic field of 60 kG. The resonator for the 280 GHz CARM is a quasi-optical design, capitalizing on SAIC's expertise in quasi-optical gyrotron research. Contracts for fabrication of long-lead-time major hardware components of this experiment have been awarded. The preliminary design of this experiment is documented in NRL Memorandum Report

6388, 1989 "Development of High Power CARM Oscillators," and appears in this report as Appendix E.

### C. Quasi-Optical Gyrotron

A 150 kW quasi-optical gyrotron experiment has been designed, assembled and tested at NRL. Measured efficiencies were as high as 12%. This experiment incorporated many new features including several that set the quasi-optical gyrotron apart from standard cavity gyrotrons. The resonant cavity mirrors were individually adjustable, allowing the mirrors to be aligned with each other as well as with the electron beam, and permitting the mirror separation to vary from 20 - 28 cm. This resulted in the output coupling from the cavity varying from 0.4 - 3%. Changing the output coupling allowed the electric field strength in the interaction region to be held constant at the value for optimum efficiency over a large range of operating currents. Single-mode operation at powers up to 125 kW and multimode operation have been characterized. The operating frequency of the device could be varied from 95-130 GHz by adjusting the applied magnetic field and/or the electron gun voltage. Details of the experimental design, numerical modeling and the data gathered are described in NRL Memorandum Report 6459 (1989), included here as Appendix F. This work, supported in part by a subcontract with Mission Research Corporation, is entitled "Design and Operating Characteristics of a CW Relevant Quasi-Optical Gyrotron with Variable Mirror Separation."

In addition, the results of an experiment on the NRL large cavity quasi-optical gyroton have been analyzed and compared with theory. These results were presented at a symposium on gyrotrons and free electron lasers in Chengdu, China and were published in a special issue of the International Journal of Electronics (Volume **65**, 3, 309-325 (1988)) entitled, "Experimental Study of a 115 GHz Quasi-Optical Gyrotron with a Large Cavity." The report is included here in Appendix G. This effort was supported in part by a subcontract with Physical Sciences Inc.

### D. Support for Experimental Microwave Program

As part of this contract, SAIC provided support to two additional projects. These

projects were (1) the development of a high power repetitively pulsed 10 GHz gyrotron for the U.S. Army Walter Reed Medical Center ("Army gyrotron") and (2) the high-frequency quasi-optical gyrotron (Q.O.). The former project was canceled prematurely due to a failure of the funding agency to make their third annual installment on the project; the SAIC support of the latter project ended when the existing hardware was dismantled in order to make room for a new superconducting magnet. Nevertheless, the remainder of this section will describe the SAIC involvement in each project.

1. Army Gyrotron

The purpose of this project was to deliver to Walter Reed Medical Center a turn-key system capable of producing 10 MW pulses with 10 microsecond duration of 10 GHz microwaves with a pulse repetition rate of 10 Hz. At the commencement of the SAIC support, the electron gun and the gyrotron tube had been designed and parts were either in house or on order. While a 1 microsecond modulator existed at NRL, a new modulator sufficient to meet the specifications of the project had to be designed and built; this was the initial SAIC support.

The design of the overall system consisted of an electron gun which was capable of emitting 250 A of electrons with an energy of 250 keV. This implies a power requirement on the gun of 62.5 MW with a gun impedance of 1000 ohm. The pulse transformer which feeds the gun was designed to be a 16:1 step-up transformer with a 1 microhenry primary inductance. This implied that the input to the transformer would necessarily be 4.0 kA of current at 15.6 kV and that the matched load impedance of the transformer would be 3.9 ohms.

Given the above parameters, SAIC began the design of the modulator. Assuming a matched load, a transmission line capable of powering the transformer described above would require an impedance of 3.9 ohms and a voltage of 31.2 kV (2 $\times$ the output voltage required). Transmission line theory can be used to immediately determine the total capacitance and inductance of the line for any desired pulse length:

$$C\ (nf) = 128.2 \text{ tau (microseconds)}$$

$$L \text{ (microhenry)} = 1.95 \text{ tau (microseconds)}$$

Given a desire on the part of the staff of Walter Reed to have the potential for pulse lengths of 1, 3, or 10 microseconds, the determination of the overall design then had to be made compatible with this desire. Three different lines were initially considered – 1, 3, and 10 microseconds long respectively. Each one of these lines, however, required different capacitors and inductors. As a result, an alternative was developed which consisted of a 1 microsecond line and a 10 microsecond line, each of which was not built to optimum specifications (which would have required many different sizes of capacitors and inductors), but rather built in a modular fashion (for simplicity and ease of maintenance). This alternative consisted of:

| Nc | $C(nf)$ | $L(nh)$ | Tau (microseconds) |
|---|---|---|---|
| 13 | 10 | 152 | 1.01 |
| 43 | 30 | 460 | 10.06 |

with the potential for tapping off the 10 microsecond line at multiple points to yield shorter pulses (e.g. 3 microseconds).

Once the transmission line design was complete, the method of charging the line was considered. The initial alternatives were: (1) inductively isolate the power supply from the line; (2) resistively isolate the power supply from the line; (3) resonant charging; and (4) actively control the power supply voltage. Assuming a 1 A power supply, inductive charging would require a charging inductor which was unreasonably large ($>$ 300 h) and resistive or resonant charging would take too long ($>$ 200 milliseconds). Only active control was capable of achieving a charging time within the required specifications. Such a power supply, however, was not readily at hand which led to the consideration of a fifth alternative - a varactor circuit. A 0.5 A/50 kV varactor capable of a constant 15.6 kW output at 31.2 kV charging voltage would result in a charging time of approximately 40 ms for the 10 microsecond pulse forming line. This is well within the required specifications.

Having made the first guess at the electrical design, SAIC then proceeded to ana-

lyze the proposed modulator design using the simple transmission line code BERTHA. BERTHA is the latest in a string of transmission line models developed at NRL all based on the original Transmission Line Code (TLC) of John Shipman. BERTHA was a modification of the Standard Transmission Line Code (STLC), both of which were written by David Hinshelwood. For this effort, SAIC modified BERTHA to run on an IBM PC by converting it to MicroSoft Fortran. The modified program was then used to determine the modulator output voltage time history for the various configurations. The results of the BERTHA simulations for the 1 microsecond modulator, the 10 microsecond modulator tapped at the 13th element to create a 3 microsecond pulse, and the 10 microsecond modulator are shown in figures D.1 a-c. The key point to note in any design of a discrete element transmission line is that the number of elements does matter; the 1 and, to a lesser extent, 3 microsecond pulses are not as flat as the 10 microsecond pulse due to the limited (13) number of capacitors (as opposed to the 43 capacitors in the 10 microsecond line). Nevertheless, a flat-topped region is available which should be adequate for the design considerations.

Once the electrical design was complete, the mechanical design commenced. This led to the design of the cabinet shown in Figure D.2. This cabinet is constructed of angle bracket with light aluminum walls. The top row is designed to hold the 1 microsecond line with the lower three rows holding the 10 microsecond line. The modular design is both simple and allows easy maintenance and repairs – both important considerations in a turn-key system to be operated by researchers in other fields.

The final support to this program from the design viewpoint was the preliminary costing of the power supply/modulator/transformer system. These efforts are not documented here as this data is out of date.

Other SAIC support on this program consisted of aiding in the fabrication of the gyrotron tube once all of the pieces had arrived and in preparation for initial measurements. As mentioned above, this work was stopped in mid-effort due to a failure on the part of the funding agency to provide funds.

Ok

1ML.O
2.500E-07 s/div

| NODE | PLOT | FULL SCALE |
|---|---|---|
| 50 | 1 | 9.996E-01 |

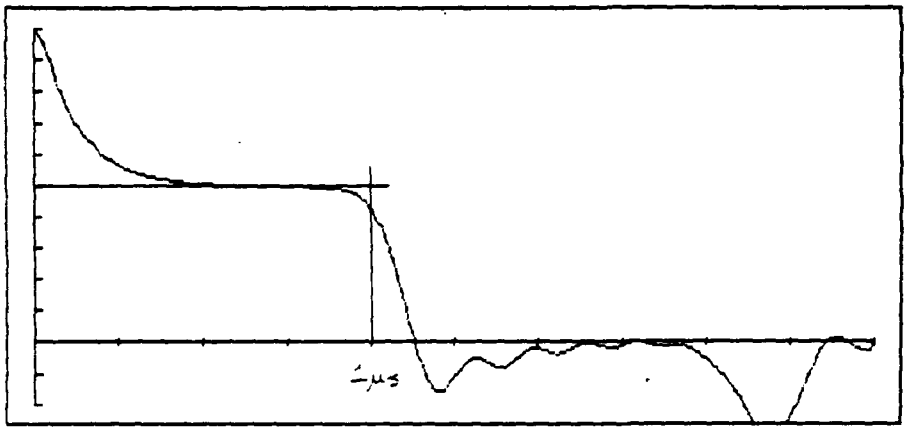



Figure D.1.a

Ok

3ML.O
5.000E-07 s/div

| NODE | PLOT | FULL SCALE |
|---|---|---|
| 50 | 1 | 9.994E-01 |

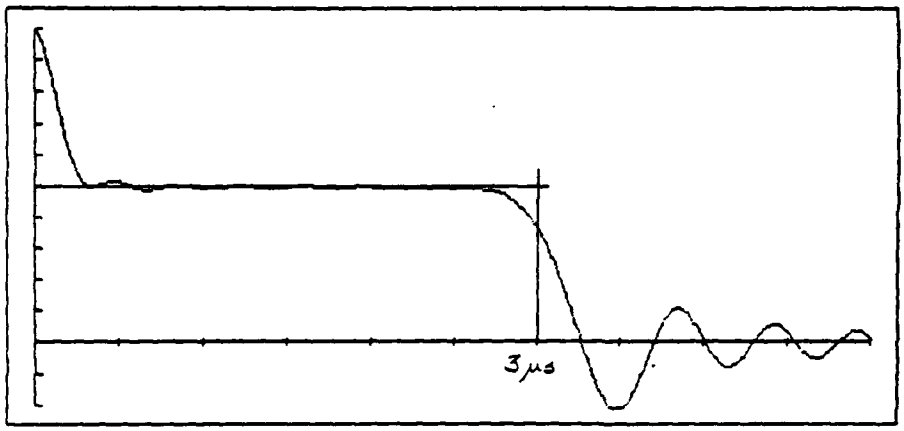



Figure D.1.b

Ok

10MLA.O
1.250E-06 s/div

| NODE | PLOT | FULL SCALE |
|---|---|---|
| 170 | 1 | 9.978E-01 |

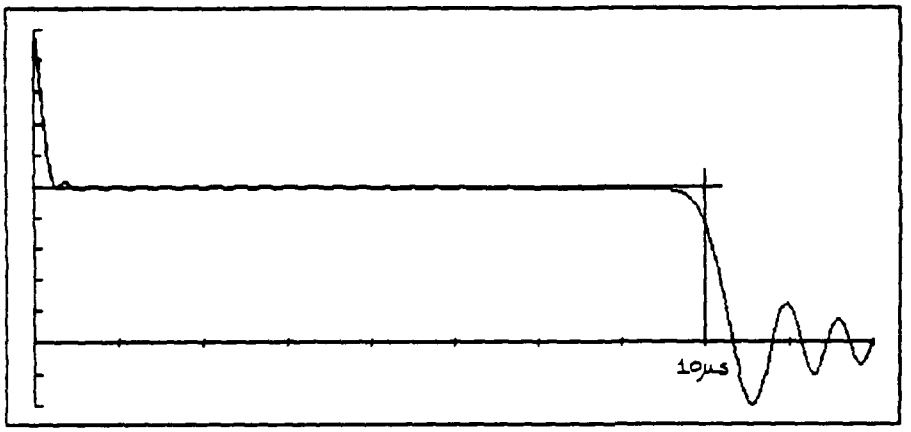


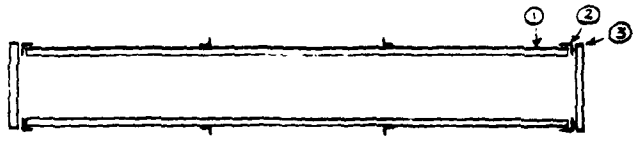

Figure D.1.c

MODULATOR - MECHANICAL DESIGN

BOX - OUTSIDE DIMENSIONS : 96" long × 60" high × 32" deep

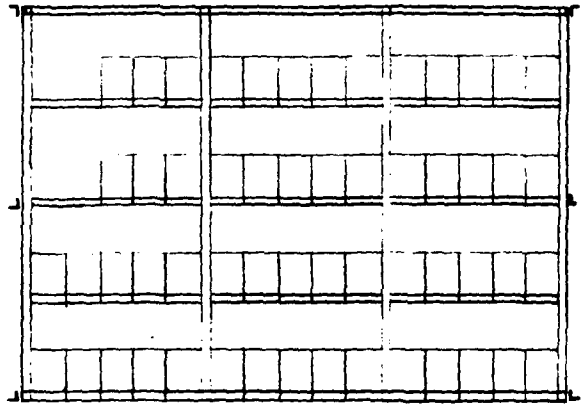
FRAMING -

TOP VIEW:

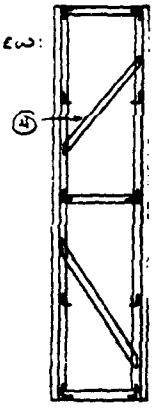



① 10 pcs 1½" ANGLE BRACKET 28" LONG
② 8 pcs 1½" ANGLE BRACKET 49½" LONG
③ 6 pcs 1½" ANGLE BRACKET 73¾" LONG
④ 4 pcs 1½" × ⅛" FLAT STOCK ~36" LONG

FRONT VIEW:



SIDE VIEW:




OVERALL DIMENSIONS : 71 5/16" LONG × 49½" HIGH × 13 5/8" DEEP

Figure D.2.

2. Quasi-Optical Gyrotron

At the time of the commencement of the SAIC experimental support, the Q.O. project was in a state of dis-assembly. The trim magnet had failed and had to be reconstructed. This was accomplished and the cooling of the superconducting magnet commenced. Unfortunately, during the down time, some moisture must have condensed inside the magnet because the cooling was not successful. The magnet was then allowed to come to room temperature, pumped down, and the cooling process was re-commenced. The Q.O. was then fired up only to discover that the wavemeter/BFO system was not functioning correctly. Considerable effort was then spent in trying to calibrate and automate the wavemeter/BFO and data collection system. This process was ongoing at the time the decision was made to dis-assemble the existing hardware due to the arrival of a new superconducting magnet.

## E. Advanced Topics in Electrophysics

Investigations in the following areas were carried out: (1) to establish the requirements for high peak power sources of rf radiation to drive linear supercolliders, especially with relevance to Soviet progress in developing x-band girocons and oppportunities for NRL to extend this work, (2) to design broadband output windows (eg., moth-eye windows) for millimeter wave generators, (3) to design Bragg reflectors for use in defining a cavity for a 100 GHz CARM oscillator (Appendix D), (4) to optimize performance of Ka-band gyrotron oscillators driven by intense relativistic electron beams. This work has been described in the IEEE Transactions of Plasma Science **16**, 142-148 (1988), entitled "High Peak Power Ka-band Gyrotron Oscillator Experiment with Slotted and Unslotted Cavities," and appears here as Appendix H (see, also, Appendix A), (5) to determine the state-of-the-art in free electron laser research, especially regarding the controversy over single mode or multi-mode operation of FEL's intended for spectroscopic studies. Details of this effort have been given in Comments in Plasma Physics XII, 217 (1989) entitled "Review of the Tenth International Free Electron Laser Conference" and appear here as Appendix I.

## F. Analysis of High Power Gyrotron Operation

During the contract period three projects concerning the operation of high power gyrotrons were completed. The work was performed by Professor T. Antonsen of the University of Maryland, consulting for SAIC on this contract, in collaboration with colleagues at the University of Maryland and at NRL. The following is a brief summary of the research.

1) Self field effects in gyrotrons. A study was completed to determine the effect of AC space charge on the operation of high power gyrotrons. The model used was one developed during the previous reporting period. It was found that at high beam densities the nonlinear efficiency of a gyrotron is modified significantly by the AC space charge associated with the bunched electron beam. The currents at which this modification occurs are higher than the typical currents in experiments carried out at NRL. Thus, we concluded that AC space charge was not a significant factor in these experiments. In Appendix J we present further details on this effect from a paper entitled "The Effect of the Time-Dependent Self-Consistent *Electrostatic* Field on Gyrotron Operation," Phys. Fluids **31**, 375 (1988).

2) Effects of a background plasma on High Current Gyrotrons. Calculations were made to determine the effect of a background plasma on the dispersion characteristics of waveguide modes in the interaction region of a high power gyrotron. The effect of plasma density and magnetic field strength on the cut off frequency of TE modes was analyzed to determine the extent by which the plasma could be used to tune the cavity over a range of frequencies. Further, the possibility of using plasma to suppress the fundamental cyclotron mode to allow for operation at the first harmonic was investigated. (See Proceedings article in this report, Section I.A.).

3) Mode stability in quasioptical gyrotrons. An analysis of the stability of single mode operation in a quasioptical gyrotron was made. The results indicate that over a range of operating parameters single mode operation is stable independent of the separation of the mirrors which define the quasioptical cavity. Various mechanisms for controlling the operating mode, including prebunching for the beam and direct injection of RF into the

cavity were investigated. A manuscript describing this work is still in the process of being written. Appendix K gives further details from the Conference Proceedings of the Thirteenth International Conference on Infrared and Millimeter Waves (Volume 1039, p. 281, 1988) from a paper entitled "Mode Stability in a Quasi-Optical Gyrotron."

### G. Externally Modulated Intense Relativistic Electron Beams

The experimental demonstration[1] of deep current modulation of an intense relativistic annular electron beam ($\sim$ 5 kA, 500 keV, $r_b$ = 1.9 cm) by a moderate external microwave source ($\sim$ 50 kW) suggested a strong potential for amplification of RF power to gigawatts at frequencies between 1 and 10 GHz. This prompted the initiation of a theoretical effort to understand this deep current modulation and to support the ongoing experiments at NRL.

Several unusual properties were seen in the experiments, namely, the high degree of phase and amplitude stability in the output signal and the ease with which the current modulation was achieved and could be manipulated by the introduction of additional undriven cavities downstream from the initial externally driven cavity.

Many aspects of these experiments are now understood as a result of theoretical and numerical efforts. The modulation in the linear regime has now been verified via particle simulation, with excellent agreement with theory and experiment. Here the device acts largely like a classical klystron, with a velocity modulation causing ballistic bunching as the particles move in a drift tube. Many nonlinear aspects of the problem have also been explored and verified in the simulations. Among these are the strong current modulation immediately following a modulating gap in the case where the gap voltage is greater than a threshold voltage which has been calculated analytically. In this regime, unlike the linear case, a drift tube is not required for bunching, and modulation levels as high as 80% can be achieved. Other aspects of the problem, such as the amplitude stability, the phase locking between the external RF input and the output signal, and the generation of harmonics have also been explored.

The chief numerical tool for the simulations has been CONDOR,[2] a two-dimensional,

fully relativistic, fully electromagnetic, particle code. CONDOR is able to handle complicated structures and boundaries, such as those existing in the experiments. Details of these studies can be found in Appendices L-N: "Modulation of an Intense Beam by an External Microwave Source: Theory and Simulation," *Appl. Phys. Lett.* **52**, 431 (1988), "Nonlinear Space-Charge Waves on an Intense Relativistic Electron Beam," *IEEE Trans. Plas. Sci.* **16-2**, 249 (1988), and "Externally Modulated Intense Relativistic Electron Beams," *J. Appl. Phys.* **64**, 3353 (1988).

### H. Relativistic Klystron Amplifier

The success of the experimental and theoretical efforts to produce highly modulated intense electron beams has encouraged experimentalists at NRL to pursue several extensions of this work. One of these is the relativistic klystron amplifier, which is designed to produce very high power radiation amplification in the 1-10 GHz range. Theoretical and numerical efforts by SAIC have supported the relativistic klystron amplifier experiment at NRL, which resulted in the generation of 1.3 GHz microwaves at a power of 3 GW with an efficiency of approximately 25%. Details of this research can be found in Appendices O-Q: "Relativistic Klystron Amplifier," *Proc. Soc. Photo-Optical Instr. Eng.* **873**, 92 (1988), "Operation of a Multigigawatt Relativistic Klystron Amplifier," to appear in *Proc. Soc. Photo-Optical Instr. Eng.* (1989), and "On Certain Theoretical Aspects of Relativistic Klystron Amplifiers," to appear in *Proc. Soc. Photo-Optical Instr. Eng.* (1989).

### I. NRL Two-Beam Accelerator

The research into modulated intense relativistic electron beams discussed above has shown that high electric fields can be established in RF structures by such beams. Such a beam, which has power greater than $10^9$ W, may be used as an RF source to power an accelerator in which this low energy, high current beam interacts via a metallic structure with a low current beam to obtain very high voltage gradients. This accelerator is the subject of an ongoing experimental effort at NRL.

SAIC theoretical and numerical support has resulted in a series of computer simulations in which the efficiency and transformer ratio (related to the maximum possible

accelerating gradient) were characterized for this device. Preliminary experimental results have verified these predictions. Details of this research can be found in Appendices R-T: "Simulation Studies of Particle Acceleration Powered by Modulated Intense Relativistic Electron Beams," NRL Memo Report 6409, (1989), "A Compact Accelerator Powered by the Relativistic Klystron Amplifier," to appear in *Proc. Soc. Photo-Optical Instr. Eng.* (1989), and "Numerical and Experimental Studies of Particle Acceleration Powered by Modulated Intense Relativistic Electron Beams," to appear in *Proc. IEEE Particle Accelerator Conf.* (1989).

### J. Electron Beam Propagation in the Ion-Focussed Regime

SAIC efforts have contributed to the recently developed FRIEZR simulation code. FRIEZR has been used for studies of IFR (ion focussed regime) and magnetic transport of electron beams, as well as transitions between these two schemes, as in the Advanced Test Accelerator (ATA) at LLNL (see Appendix U), "IFR Conditioning and Transport," LLNL Report CONF 8709146, 357 (1987)). FRIEZR is a two-dimensional, fully relativistic, electromagnetic particle code that performs simulations in a coordinate system that moves with the electron beam.

In IFR transport, the beam is injected along a plasma channel, with $n_p \leq n_b$, so that the highly relativistic beam electrons electrostatically force the plasma electrons from the vicinity of the beam, forming an ion channel which focuses the beam electrons.

Several issues of importance to this transport scheme have been addressed. Of primary importance for transport over long distances is the issue of beam head erosion, wherein the physics at the beam head, which can be quite complicated, results in the loss of some portion of the beam. An extensive numerical and theoretical study of this process in the axisymmetric limit resulted in an improved analytical model of inductive erosion (losses due to the inductive electric field at the head of the beam), and an improved understanding of emittance-driven erosion, in which our numerical studies were used to discover and explain erosion rates that tend toward zero over long distances, in contrast to previous theoretical models. These erosion processes were confirmed by experiments carried out at NSWC.

Details of the FRIEZR code, the erosion studies, and the NSWC experiment are given in Appendices V and W "Numerical Simulations of Axisymmetric Erosion Processes in Ion Focused Regime-Transported Beams," to appear in *Phys. Fluids*, and "Analysis of the NSWC Beam Erosion Experiment," *Proc. of the Annual Propagation Phys. Rev.* Vol. I, 85 (1988).

Further studies of electron beam propagation were carried out for the case where a diffuse background plasma is present in addition to the plasma channel discussed above. These simulations resulted in the discovery of wake field effects, wherein plasma waves excited at the beam head copropagate with the beam. In regions where the field from the plasma wave was decelerating, the beam was disrupted. Further studies showed that the severity of this problem was affected by such parameters as the rise length of the beam and that the plasma waves could be suppressed to some degree by chopping the beam at a frequency higher than the plasma frequency of the diffuse background plasma. These studies are detailed in Appendices X-Z: "Delphi Theory-Axisymmetric Erosion and Wake Field Effects," LLNL Report CONF 8709146, 361 (1987), "Numerical Studies of Erosion and Transport in Chopped and Unchopped Beams," *Proc. of the Annual Propagation Phys. Rev.* Vol. I, 381 (1988), and "Relativistic Beam Propagation Through Diffuse Plasmas," *Proc. of the Annual Propagation Phys. Rev.* Vol. I, 377 (1988).

Finally, several theoretical studies of diamagnetic effects associated with relativistic electron beam (REB) propagation were performed during 1986. Some of the work was classified. However, Appendices AA and BB describe unclassified aspects of the REB effort. The titles are respectively "Diamagnetic Effects in Endoatmospheric Electron Beam Propagation" and "Diamagnetic Cavity Formed During the Formation of a Laser Channel in the Ionosphere."

### K. FEL Studies

In vacuo, diffraction causes a beam of radiation of finite transverse extent to spread out on a scale length referred to as the Rayleigh range, $Z_R$. Over the past several years it has become clear that in a free-electron laser (FEL) the emitted radiation tends to be

guided and focused by the electron beam, thus permitting interaction lengths considerably greater than $Z_R$. This can lead to a significant improvement in the extraction efficiency of the FEL.

Sprangle *et al.*[4] have developed a technique for efficient numerical study of the development of the radiation field in FEL's. Details of this work are given in Reference 4 and in "Guided Radiation Beams in Free Electron Lasers," *Nucl. Instr. and Meth. in Phys. Res.* **A272**, 536 (1988), Appendix CC of this report. Using this technique, we have examined in detail the phenomenon of optical guiding in the small signal, exponential regime of operation. The most significant result of this study is that the radiation may be perfectly guided by the electron beam. That is, the width of the radiation beam maintains a constant, and unique, value throughout the exponential regime. This work is presented in detail in Appendix DD, entitled "Optical gains, phase shift, and profile in free electron lasers," Phys. Rev. **A36**, 1739 (1987).

In an FEL the synchrotron oscillation of electrons trapped in the ponderomotive potential well may couple energy into sideband frequencies. The ensuing instability leads to the modulation of the output signal and to an increase in its spectral width. In a number of applications this is a serious drawback.

We have developed a multi-dimensional, time-dependent code to study FELs. This code has been used to examine the development of sidebands in a FEL operating as an amplifier. The most significant outcome of this study is that upon tapering the wiggler magnetic field – which is the usual method of enhancing the efficiency – the growth rate of the sidebands may be drastically reduced, the output radiation beam displaying very little modulation. This work has been reported in detail in Nuclear Instruments and Methods in Physics Research **A272**, 392 (1988) entitled "Comparison of Sideband Growth in Tapered and Untapered Free Electron Lasers," and in Physical Review **A38**, 197 (1988), "Development of Sidebands in Tapered and Untapered Free-Electron Lasers." These reports are included in Appendices EE and FF.

## L. X-Ray Source for Lithography

Miniaturization of semi-conductor devices lies at the heart of the tremendous developments taking place in the electronics industry. Current state-of-the-art requirements by the integrated-circuits industry call for the ability to pattern submission-size circuit-dimensions on silicon wafers. This is presently achieved by lithography using UV radiation ($\sim$ 200 $\mu$m). However, for mass-production of critical, leading-edge circuits for computers, memories, signal processors and other devices, circuit dimensions less than 0.1 $\mu$m are envisaged. It appears that radiation in the x-ray band will have to be used to achieve this improvement in resolution.[5] At present synchrotron radiation from storage rings is the only viable source for this purpose. However storage rings are extremely costly ($\sim$ \$10M) and not very efficient. We have considered the possibility of employing the spontaneous x-radiation from the interaction of an electron beam with microwaves in a quasi-optical maser for the purposes of lithography. Preliminary results indicate that this scheme may provide a commercially viable source for mass-production of integrated circuits on silicon wafers. (Patent application has been made.) A paper describing these techniques has been submitted for publication in *Electronics Letters* "An X-ray Source for Lithography Based on a Quasi-Optical Maser Undulator." It is included here as Appendix GG.

## M. Studies of Coherent Radiation Sources

In the area of coherent radiation sources, the SAIC theoretical effort covered support of both existing and planned experiments, and the pursuit of advanced concepts. The analytic work was about equally divided between two areas of interest: gyrotrons and FELs.

The tasks performed in support of the gyrotron program are summarized as follows:

(1) Small signal analysis, for the Quasi-optical CARM, or induced resonance electron cyclotron maser (IREC). This is a promising source of submillimeter microwaves, combining the frequency upshifting of the CARM, with the low wall loading and improved mode separation of the open (quasi-optical) resonators. The linear growth rate and the current to start-up oscillations in the cavity were derived. The sensitivity of

the device to thermal spreads of the electron beam was also addressed, and an optimization condition was found. This has been reported in NRL Memorandum Report 5986 (1987), "Small Signal Analysis of the Induced Resonance Electron Cyclotron Maser," included here in Appendix HH.

(2) Operation of the Q.O. CARM in higher harmonics of the upshifted cyclotron period. The slow-time equations describing the resonant interaction with a given harmonic were derived. The small signal electronic efficiency was obtained, yielding the start-up current. Small amplitude results were confirmed by simulations, which showed considerable electronic efficiencies for high amplitude operation. This work has been published in *Phys. Fluids* **31**, 924 (1988) entitled "Higher Harmonic Generation in the Induced Resonance Electron Cyclotron Maser," and appears in Appendix II.

(3) Modeling of the mode competition in the Quasi-optical Gyrotron. Non-linear effects become very important at high power operation, as shown by experimental results. Several modes are excited and interact in the cavity. Whether a final steady state exists at all, how many modes participate in it, and whether a given steady state is accessible, are inherently non-linear issues. A set of mode-coupling equations describing the mode interaction has been derived. The particle dynamics have been absorbed in the mode-coupling coefficients, of known analytic dependence, that mediate the interactions among the cavity modes. Particle simulations can then be replaced by a set of ODEs, cutting the computation time considerably. More substantially, the final steady state can be found analytically from these equations, as a function of the control parameters.

The issues addressed in the field of FELs are summarized as follows:

(1) Study of the excitation of parasitic frequencies (sidebands). Using dynamic equations in action-angle formalism, it was possible to include the thermal spreads in the synchrotron frequencies of particles trapped in the ponderomotive fields. Novel results were found for the structure of the sideband spectrum. For example symmetric upper and lower sidebands have opposite growth rates (complementary stability). Also the growth rate, determined by the distribution of particles according to their synchrotron periods, is much slower than predicted by previous results, which ignored

thermal spreads. This is described in more detail in Appendix JJ, "The Structure of the Sideband Spectrum in Free Electron Lasers," *Phys. Fluids* **31**, 1708 (1988).

(2) Efficiency deterioration caused by sidebands. It is well known that particle motion in a multi-frequency field may easily become chaotic. Therefore, excitation of sidebands in FELs may cause particle detrapping and loss of amplification. The threshold in sideband amplitude for the onset of stochastic motion was computed. The rate of particle diffusion was studied and found to depend on the total sideband power. It was also shown to depend on the kind of sideband spectrum, falling into one of the following general categories: a narrow, a broad discrete and a broad continuous spectrum. The length (in wiggler periods) required for the average particle to get detrapped was found to be independent of the beam energy. This work, described in Appendix KK, is entitled "Chaotic Electron Motion Caused by Sidebands in Free Electron Lasers," NRL Memorandum Report 6365 (1988).

(3) Study of the reflection for Gaussian light beams in FEL resonators. An incident light beam of a pure Gaussian mode will in general be reflected into other modes, as a result of the finite mirror size, the deflection of the light beam, and spherical aberration effects. It was shown that the shape of the appropriate mirror surface is connected to the deflection angle for the light beam. The reflection process was modeled by a reflection matrix that includes all the above effects. This work is described in Appendices LL and MM respectively entitled, "Transformation of Gaussian Light Beams Caused by Reflection in FEL Resonators," and "Reflection Matrix for Optical Resonators in FEL Oscillators," NRL Memorandum Reports 6347 and 6285 (1988).

(4) Study of the cavity eigenmodes for the NBS FEL oscillator. The optical performance of the racetrack microtron powered FEL was analyzed using a vacuum eigenmode expansion. The cavity eigenmodes were obtained by solving the eigenvalue problem for the cavity transfer matrix. The latter includes the effects of multiple reflections on the resonator mirrors as well as the transmission through the vacuum vessel aperture. It was shown that the cavity has a very good optical performance (high Q) and model

purity in the operation regime from 0.2$\mu$m to 10$\mu$m. This is described in Appendix NN entitled, "Cavity Eigenmodes for the NIST/NRL Free Electron Laser," to be submitted for publication in *J. Appl. Phys.*

## N. Support to the NRL Charged Particle Beam Program

During this contract period SAIC performed several tasks in support of the NRL research program to investigate the propagation of charged particle beams. These tasks included creating and modifying graphical systems to analyze simulation data; developing better ways of presenting results to the scientific community and, most importantly, participating directly in the research effort by developing several computer programs which use numerical methods and techniques to evaluate analytical solutions and theoretical expressions. To facilitate these tasks and the research of NRL scientists, it was necessary to bring up and bebug a number of computer systems and software packages. This computer knowledge has become valuable to NRL's Plasma Theory Branch as the basis for important decisions concerning graphical hardware and software.

The most significant numerical project carried out during this period was the development of an envelope equation model of a wire guiding cell for a particle beam. SAIC worked with a model developed by Dr. R. Fernsler of NRL to solve a form of Maxwell's equations numerically. The backbone of this code was the dynamic solution of the circuit equations that determine the force felt by the particle beam due to the wire. The paper presented at Beams '88, entitled "Beam Conditioning Using Resistive Wires," here in Appendix OO, has an in depth discussion of the equations solved. Plotting routines developed under this project, as described below, were used to display the solutions in graphical form. Such quantities as the evolution of the beam radius and of the beam emittance were measured. This code indicated that a wire cell could be used to emittance condition a particle beam.

The success of the aforementioned wire guide code, led to the development of a more sophisticated model using a particle-pushing code to more thoroughly evaluate the effect of the wire cell on important beam evolution characteristics. The particle-pusher was implemented by Dr. S. Slinker of NRL. The paper, presented at DARPA 88, "Resistive Wire Conditioning," in Appendix PP, more fully describes this code. As predicted, the particle-pusher more accurately handled the emittance evolution of the beam and demonstrated that the emittance conditioning was not as dramatic as predicted from the envelope code, though still significant. The code did, however, demonstrate that the beam centering could

be achieved using a wire cell.

SAIC devised several graphics analysis programs and routines to analyze data for the Plasma Theory Branch's simulations and the data sets from NRL's experimental branch. In addition to analysis, it proved necessary to make the graphical output more professional and more efficient. SAIC created a Point Plotter package in the graphical language IDL, for example. This plotter made it possible to use the VAXs to graph arrays of data, either gathered by hand or output from simulation codes, and combine them on single graphs. This freedom to blend different sets of data made such tasks as comparing simulation results to theoretical results much simpler. The IDL plotter also provided the project scientists with an alternative to the much slower process of hand plotting results and then sending them to NRL's TID to have them redrawn.

SAIC modified NRL's major particle codes to take advantage of the NCAR Autograph plotting package and the improvements in character manipulation developed by Horace Mitchell of SAIC. Using this combination of graphical enhancements, SAIC modified the existing post-processors to output presentation quality graphics. With the increase in quality, the need to touch up individual frames was eliminated, causing a marked increase in efficient use of the scientists time and making the plots easier to interpret. Using a version of NCAR that would allow slightly modified code to work on the VAX and the CRAY, SAIC created an AUTOPLOT program that could be linked to post-processors on both machines. AUTOPLOT eliminated the necessity for having separate versions for the VAX and the CRAY and helped to standardize output from the various beam simulation models. It was also necessary to reprogram the post-processors themselves to take full advantage of the SAIC character improvements. While working on updating these codes, a fault in the NCAR contour routines became apparent. Using the contour-smoothing routine developed in NRL's Laboratory for Computational Physics to alleviate this fault, SAIC subsequently installed this routine, SCROOB, in the new post-processor codes.

To view scientific phenomena that evolve in a complicated and nonobvious manner, SAIC developed applications packages to exploit our scientific animation software. This software made extensive use of the ATARI 1040ST's graphics abilities and of ANTIC's excellent line of animation software. With the addition of motion to previously still pictures, dynamics effects such as wake-field accelerations in particle beams and channel tracking in experimental simulations were more easily interpreted. In Appendix QQ, "SARLAC, The Movie," an NRL-SAIC collaborative effort, the animation process is explained. This

report also contains black and white reduced pictures from one of the animations.

To complement the graphical support SAIC provided to the Plasma Theory Branch, we also solved a number of analytical problems and theoretical models numerically. The solutions generated from these programs were used to test new ideas for simulation codes, to check existing codes to determine if they agreed with theoretical answers, and to determine input values for the various simulation codes. A list of these codes includes:

PRANGEB – Determines when the beam radius has expanded out of the IFR regime for the PURE propagation mode. Used to prove that PURE mode is a viable propagation mode.

PLREQA – Calculates $R_{eq}$ for magnetic and IFR transport and plots these quantities against propagation distance. Used as a diagnostic for particle simulation codes.

XENON – Calculates the ionization and excitation rates for xenon gas when it is used in a IFR cell and is exposed to a laser pulse of a specific length, energy, and radius. Used to determine input curves for particle simulation codes.

XENDIS – An extension of the XENON code which uses the DRGEARS integration package to accurately determine the density of xenon ions at various times after a laser beam has passed through an IFR cell. Used to refine the pressure ramp function for the xenon density in the particle simulation model of an IFR cell.

MAGNET – Calculates the magnetic field strength felt by a beam in the ATA beam line, based on tables of actual magnet settings used in ATA experiments. Used to determine correct forces for simulations of ATA beam propagation.

RADLEE1 – Calculates beam radius in an IFR channel given channel size, radius, and initial channel temperature as inputs. Used to compare simulation code results with theory.

TRKPLOT – Evaluates and plots Fernsler's tracking force equation for a Bennett profile beam in a square channel. Used to determine values of this force for entry into particle simulation models of the tracking experiment.

FOIL1 – Calculates the momentum kick given to a flat-topped particle beam when it passes through a thin foil, using Bessel functions. Used to model foils as tools for focusing particle beams and as impulses for particle codes.

FOIL2 – Same as above code, but evaluates a Bessel profile beam.

FOCFOIL1 – Determines and graphs the focal length and the emittance degradation for a flat-topped beam passing through a foil. Used to determine the spacing between foils. It proved that this focusing scheme degrades too much to be used by the NRL experimentalists.

FOCFOIL 2 – Same as above code, but evaluates Bessel profile beam.

FBERN – Models the momentum kick a particle receives as it interacts with two coupled foils. Used to determine that coupled foil models give more realistic results than do isolated foil simulations.

To maintain a knowledge of the current state-of-the-art in presentation graphics for the SAIC contract with the Plasma Theory Branch, SAIC tested numerous software packages on many computer systems. Among these systems are: (CRAY) NCAR; (VAX) SAIC's Animation Software, NCAR, IDL; (ATARI 1040ST) Cyber Animation Software, Degas Elite, Spectrum 512; (MAC II) Pixel Paint, Mac Draft, Power Point, (IBM) Mass11 Draw; (VAX Station) Interleaf. We determined which of these programs were best suited to specific analysis tasks. We also became proficient at TEX, the typesetting language, to assist in displaying the results of programming projects. A list of some of the reports containing graphical or presentation materials developed under this aspect of the project follows:

1. "Simulation of Stability, Tracking and Range Extension in WIPS Channels (U)," by R.F. Hubbard, S.P. Slinker, W.M. Fawley, and G. Joyce.
2. "Experimental Program Options to Demonstrate Weapons-Scalable Propagation (U)," by Martin Lampe, and Richard F. Hubbard.
3. "A New Laser Hybrid Scheme for WIPS-Mode Propagation (U)," by R.F. Hubbard, R.F. Fernsler, A.W. Ali, S.P. Slinker, M. Lampe, and A. Prakash.
4. "SARLAC Hose and Tracking Simulations: The Movie," by R.F. Hubbard, P. Boris, S.P. Slinker, W.M. Fawley, and G. Joyce.
5. "Simulation and Analysis of the ATA Transport Experiment," by R.F. Hubbard, G. Joyce, S.O. Slinker, and M. Lampe.
6. "Resistive Wire Conditioning," by R.F. Fernsler and S.P. Slinker.
7. "Simulation of IFR and Magnetic Transport in Accelerators," by S. Slinker, R. Hubbard, G. Joyce, M. Lampe, and R. Fernsler.

In addition, SAIC has been assisting the experimental branch evaluate data from earlier

tracking experiments. This project requires the use of data manipulation programs on both the IBM and the MAC II including the IBM spreadsheet, Quattro, and the graphically oriented MAC spreadsheet, WINGZ. In preparation for the arrival of the IRIS workstation, an SAIC staff member has taken courses through the NRL training facility, the C programming language and the UNIX operating system. These subjects will also be useful for future numerical projects involving the IRIS and the Connection Machine.

## O. Modified Betatron Theory and Experiment

1. Theory

High energy physics experiments require electron beams with energy in the TeV range at relatively low average current. In contrast most industrial and defense related applications demand high average beam current in the energy range from a few MeV to approximately 1 GeV. In addition, while the compactness of the accelerator is critical in most commercial and defense applications, it plays only a secondary role in the high energy physics experiments.

The development of the modified betatron accelerator at NRL is motivated by its compact size and its potential to generate high current beams of several hundred MeV energy. Extensive theoretical studies over the last few years have shown that the modified betatron accelerator has current carrying capability substantially higher than the conventional betatron. The improved current carrying capability of the modified betatron is due to the toroidal magnetic field that controls the minor radius of the circulating electron ring.

The current carrying capability of the modified betatron can be further improved by adding a strong focusing field. Details of this technique have been presented at the Conference on the Application of Accelerators in Research and Industry at North Texas State University, November, 1986. Appendix RR contains the viewgraphs from this presentation and Appendix SS includes a resulting publication in *Nucl. Inst. and Meth. in Phys. Res.* **B24/25**, 805 (1987) entitled "Improving the Current Carrying Capability of the Modified Betatron."

Following the successful experiments with multikiloampere electron beams injected into the NRL modified betatron, the research effort has focused on efficient trapping and confinement of the ring as a prelude to acceleration. In these studies, a 0.5-1.0 MeV, 1-4

kA beam is injected along the 1-3 kG applied toroidal magnetic field $B_\theta$ in controlling the minor radius of the beam and are in agreement with the theoretical predictions concerning high current equilibria in the modified betatron.

The dynamics of high current equilibria in the modified betatron are dominated by the forces due to the self-field images of the beam. At the matching value of the betatron magnetic field $B_z$, the forces due to the images, the Lorentz force $ev_\theta \times B_z$ (where $e$ is the charge on the electron and $v_\theta$ is the toroidal velocity) and the centrifugal force are in balance, and the beam does not drift poloidally. After one revolution around the major axis, the beam returns to the injector and strikes the back of the cathode. However, in the high current regime, if the betatron field is less than the matching value, the equilibrium position $r_{eq}$ shifts radially inward, and the beam drifts poloidally about the equilibrium position. The poloidal displacement can easily be adjusted to be sufficient so that the beam does not strike the injector after one turn. For a wide range of parameters, the poloidal drift trajectory is closed, and the beam returns to the injector after a poloidal oscillation (bounce) period. This drift motion has been observed and confirmed with several different diagnostic techniques and is in very good agreement with theory. To achieve trapping, the equilibrium position must be shifted radially inward during the poloidal bounce period so that the beam does not strike the injector.

Within a narrow range of parameters, 'self-trapping' is observed with $\approx 80\%$ efficiency. Self-trapping is discussed in detail in the book "High Brightness Accelerators," Ed. A. Hyder, M. Rose and A. Guenther, p. 773, Plenum Publishing Corporation (1988) and is included in this report in Appendix TT. 'Self-trapped' rings with circulating current of 2-3 kA remain for $\approx 4\mu$sec ($\approx 200$ revolutions around the major axis). Confinement for 10 $\mu$sec is observed at 1 kA.

'Self-trapping' results from the localized magnetic field associated with current flowing in the cathode stalk during a second pulse that follows $\approx 200$ nsec after the main injection pulse. This afterpulse occurs because the diode is not matched to the pulse forming line of the injector. Because plasma closure has reduced the diode impedance at the afterpulse, a 1-4 kA current may flow although the applied potential is only $\approx 150$ kV. Thus, the magnetic forces are larger than the electron forces and the net component produces a radial inward shift of the beam.

This explanation is supported by experiments with a current carrying conductor, i.e.,

a kicker coil, that is oriented along $B_\theta$. When a short cathode stalk is used and the kicker is not energized, the afterpulse does not significantly affect the beam. However, when the kicker is energized, the shift is similar to that produced by a long cathode stalk with afterpulse. The observed poloidal drift trajectories agree well with calculated orbits.

The use of a kicker coil for trapping avoids the disadvantage of 'self-trapping', namely that the conditions for trapping cannot be adjusted independently from the injection conditions. However, such a coil is unattractive. It must be driven with a sufficiently long pulse so that the radius of the poloidal drift trajectory can be reduced by acceleration, and the coil represents another obstacle that the beam must avoid. Therefore, a new trapping scheme is being developed. In this scheme, an induction field is applied to a gap in the torus. During the poloidal bounce following injection, the beam is accelerated by this applied field and $r_{eq}$ is shifted. A preliminary experiment to test this scheme has been performed. This is explained in detail in "A Novel Trapping Scheme in the Modified Betatron Accelerator," published in the *Proceedings of the IEEE Particle Accelerator Conference*, Vol. 2, March, 1987 and contained in Appendix UU of this report.

Devising a scheme for extraction of the beam from the modified betatron turned out to be a formidable problem. A preliminary study showed that when the energy mismatch of the beam increases slowly in time in relation to the bounce period, the ring follows the radially outward motion of its equilibrium position while its radius of rotation around the equilibrium position (i.e. the fast motion) remains very small. Analytic expressions were derived which provided radially symmetric magnetic fields for any given radial dependence of the field index. Based on these expressions, computer runs were made for the beam dynamics for various radial configurations for the field index, such that the beam would be shifted radially outward and eventually be captured by the extractor. These runs were not successful since the radial velocity of the beam became prohibitively large and the beam would hit the walls of the extractor. Another extraction scheme was studied in which the extractor was made of a ferromagnetic material. In the region surrounded by the ferromagnetic material, the magnetic fields are zero and the electron ring, as it shifts into this region, by intentionally mismatching the magnetic flux and the betatron magnetic fields, unwinds into a straight beam. Extensive use was made of the Poisson code to compute the magnetic fields for various configurations of the ferromagnetic material. External coils were also added to eliminate the distortion of the fields in the vicinity of the ferromagnetic material due to the presence of the external fields. The computed fields

were used in computer runs to study the beam dynamics. Again, the beam extractions proved to be not feasible, since the amplitude of the cyclotron motion due to the toroidal magnetic field increased to prohibitively large values as the beam reached the extractor.

Finally, an extraction scheme was devised that is easily realizable and has the potential to lead to a very high extraction efficiency. The proposed extraction scheme is based on the transformation stationary helix, in the toroidal direction, by exciting the resonance that naturally exists for some specific values of the ratio of the vertical to toroidal magnetic field. Transformation of the ring into a helix is achieved with a localized vertical magnetic field disturbance that is generated by an agitator coil. As the minor radius of the helix increases with each passage through the gap of the agitator coil, the electrons eventually reach the extractor, which has the property that all the magnetic field components transverse to its axis are equal to zero. Thus, the electron ring unwinds into a straight beam. Analytic expressions were derived for the agitator and were used in computer runs to study the proposed extraction scheme. As expected, the electrons of the ring performed a coherent motion and a stationary helix formed in the toroidal direction. With successive passes through the disturbance of the agitator, the radial excursion of the orbit increases until the electrons reach the extractor, which is located at a slightly greater radial distance than the agitator coil. The extractor is a completely enclosed conducting structure so that fringing fields are absent. Special consideration was given in its design so that the effects of the unwanted component of the toroidal magnetic field, which is normal to the direction of the extraction pipe, are minimized. Computer runs that were made with the agitator and the extractor present, demonstrated that this is a workable scheme for extraction of the beam in the modified betatron. Viewgraphs from presentations from three meetings of the APS-PPD (1986, 1987, 1988) describing the various extraction schemes are given in Appendix VV. Appendix WW gives details of the latter scheme "Beam Extraction Scheme from the Modified Betatron Accelerator," *Phys. Rev. Lett.* **61**, 86 (1988) as does Appendix XX, "Studies of a Multi-Kiloampere Electron Ring Confined in a Modified Betatron Accelerator," Proceedings of *'Beams 88'*.

2. Experiment

The NRL Modified Betatron Accelerator is a toroidal high-current induction accelerator. Like the conventional betatron, it has a vertical field which keeps the electrons in equilibrium and accelerates them. As of 10 December 1989, studies have been done on the beam dynamics without any acceleration. Data on the betatron bounce period and

equilibrium position had been taken. The vacuum chamber in these experiments was made of stainless steel, and had a magnetic field diffusion time of hundreds of microseconds.

One of the problems associated with a pulsed experiment is that there is a great deal of electrical noise on the data cables. In order to reduce this problem, the feasibility of using intensity-modulated fiber-optic links was investigated. A commercial product was located, and tests indicated that it would eliminate most of the noise. The data-taking and display software system in use was judged to be inefficient and inadequate. A new system was designed and implemented. Another problem is that there was not time-resolved information on the beam position. Accordingly, probes to measure the poloidal field of the beam were constructed, along with the necessary electronics. In addition, a modified rogowski coil to measure the beam displacement above the midplane was constructed. The poloidal field probes, along with other diagnostics, were used to document a discrepancy between the observed and predicted beam bounce period.

Several hypotheses to account for this discrepancy were formulated. The first assumed that no image currents flowed in the chamber, but this was disproved by measurement. The second assumed perpendicular electron velocity, but it was found that even a 50% velocity did not account entirely for the discrepancy. The presently accepted hypothesis, suggested by J. Golden of NRL, is that there are low-energy electrons in the chamber. A very simple model was formulated, and a software system to solve it and display the results was implemented. It was found that the presence of low-energy electrons could greatly affect the bounce period.

For beam equilibrium in the low-current regime (i.e. for high energy), the field index must be between 0 and 1. In order to check this, a magnetic probe and gradiometer was developed jointly with NRL. Since the index must be measured at many points inside the chamber, a software system to map and display the index and field was developed. This system was used to study the magnetic field penetration in the stainless steel chamber, and the new fiberglass-epoxy chamber. The field index was found to be outside the stated limits in some regions (e.g. near the ports). This problem was corrected.

In addition to the requirement of the index, the vertical field flux must satisfy a condition for the beam equilibrium to remain inside the chamber. This was measured in collaboration with FM Technologies. The flux was adjusted to satisfy the requirements.

In order to accelerate the beam, it must be prevented from hitting the diode after one

bounce period (trapped). To do this, a set of external current-carrying coils was designed and constructed, with the help of personnel from SFA. Beam trapping in the stellatron (a modified betatron with stellarator windings) was numerically investigated. Both internal and external current-carrying coils were considered.

After the beam is accelerated, its energy must be measured. At the suggestion of C. Kapetanakos of NRL, detection of photoneutrons from the threshold of the giant resonance was investigated. Various targets, with thresholds from 1.7 MeV to 10 MeV were considered. Yields from both the target and the surrounding structure were calculated. Suitable detectors were located. Various methods to move the beam to hit the target were considered.

### P. Studies of the NRL Dense Z-Pinch Experiment

The primary focus of the research carried out on the physics of the NRL dense Z-pinch (DZP) has been on the neutron generation. The experimental observation of some $10^9$ neutrons per pulse and observed scaling of total neutrons varying with current at $N \sim I^{10}$ has, until recently, not been understood. It is now believed that the neutrons are produced through a beam target interaction with the beam arising from the strong electric fields associated with the $m = 0$ instability ultimately responsible for the plasma column disruption. An analysis of the electric fields accompanying the column collapse has been carried out and is described in detail in Appendix YY. This report, entitled "On the Relationship Between Neutron Yield and Plasma Current in the Dense Z-Pinch," will be submitted to *Physics of Fluids*. It was shown that the maximum amplitude of the z-component of the electric field occurs late in the fibre collapse. Acceleration of a high energy deuteron beam would then occur late in pinch collapse and hence any beam-target interaction would also occur late in the collapse. According to the analysis, the acceleration and beam-target neutron production would occur in a time on the order of one to two nanoseconds, consistent with experimental observation. Assuming that a beam of deuterons does form with a background temperature equal to the Bennett temperature, it has been shown that, depending on the mean beam energy, the total neutron yield scales as $I^\alpha$, $8.6 < \alpha < 11.6$. The value of $\alpha$ represents the mean beam energy in KeV relative to the deuterium-deuterium cross-section. The details of the beam-target analysis are given in Appendix YY.

In order to determine if a high energy deuteron beam forms during the fibre collapse,

a particle simulation of the collapse dynamics has been carried out. Although the work is currently in progress, sufficient evidence exists to support the early analysis leading to the generation of large electric fields and accelerated deuterons. The simulations are being performed with a hybrid model, particle ion and fluid electrons, due to Hewett.[6] The hybrid model treats a plasma-vacuum interface thus allowing reasonably realistic edge conditions to be simulated. The density of the plasma varies from $10^{20}$ particles/cm$^3$ at the column center to a few percent of this value at the column edge. The axial plasma current is assumed to be uniform across the plasma column initially. The total value of axial current is held fixed by specifying a value of the $B_\theta$ component of the magnetic field at some outer boundary to be constant in time. At subsequent times, the plasma current distribution is determined.

Simulations to date have shown the column to collapse on the expected time scale of one to two nanoseconds with large electric fields being generated. The initial simulations have been carried out using a much reduced particle number than the code is capable of treating. Typical results are shown in the following figures. Figure P.1. shows the initial distribution to 4000 particles in "r" and "z", the axial averaged radial density distribution and the radial averaged axial density distribution. The electrons have a uniform temperature of 100 ev, the ions are cold and the total axial current is 500 kiloamperes resulting in the $B_\theta$ profile shown in Figure P.2. Figure P.3. shows that the unstable pinch has already collapsed to 1/2 the original radius. More detail on the $m = 0$ nature of the instability is shown in Figure P.4. The maximum value of the $B_\theta$ field is seen to occur where the $m = 0$ perturbation is expected, namely, in the middle of the column's length. Figure P.5. shows the radial and axial electric fields building up to a value of roughly $10^5$ volts per meter.

The investigations have shown that particle simulation techniques can model the key features of the DZP unstable collapse. The work is continuing and will be directed toward resolving the final phase of the pinch collapse, the generation of fast deuterons and eventually an understanding of the deuteron-target interaction responsible for the neutron production in the dense z-pinch.

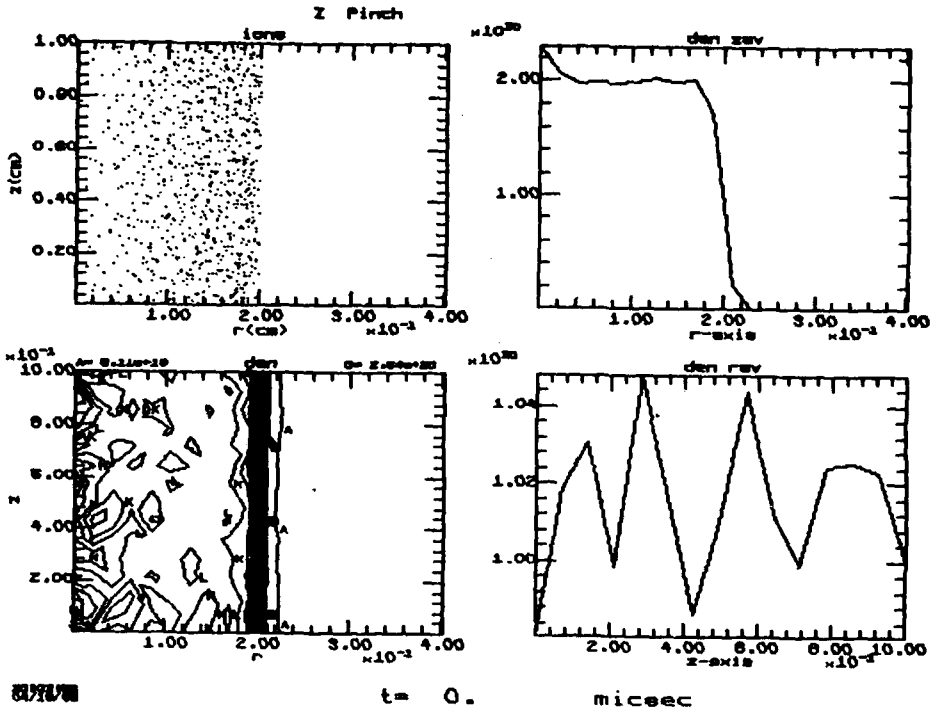

Z Pinch
ions
z(cm)
r(cm)
den zav
r-axis
den
z
den rav
z-axis
t= 0.
micsec

Figure P.1.

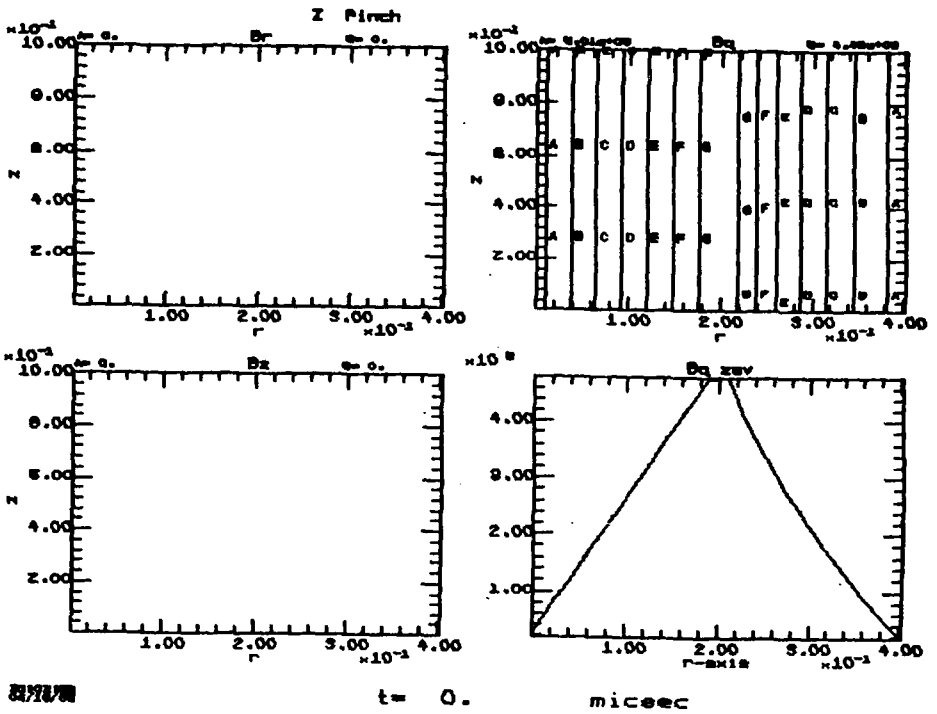



Figure P.2.

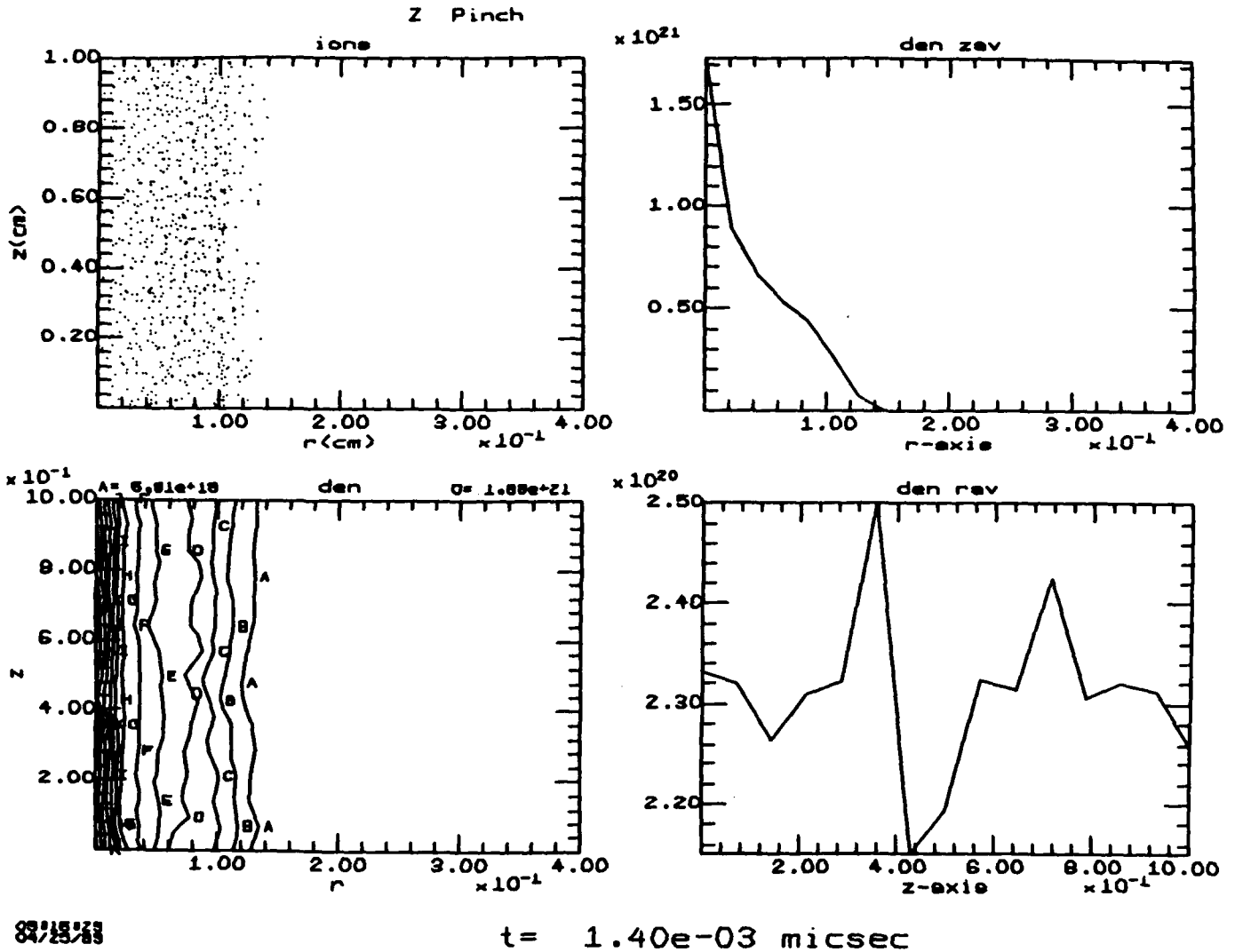

Z Pinch
ions
z(cm)
r(cm)
x10⁻¹
x10²¹
den zav
r-axis
x10⁻¹
x10⁻¹
A= 5.81e+18
den
D= 1.88e+21
z
r
x10⁻¹
x10²⁰
den rav
z-axis
x10⁻¹
t= 1.40e-03 micsec

Figure P.3.

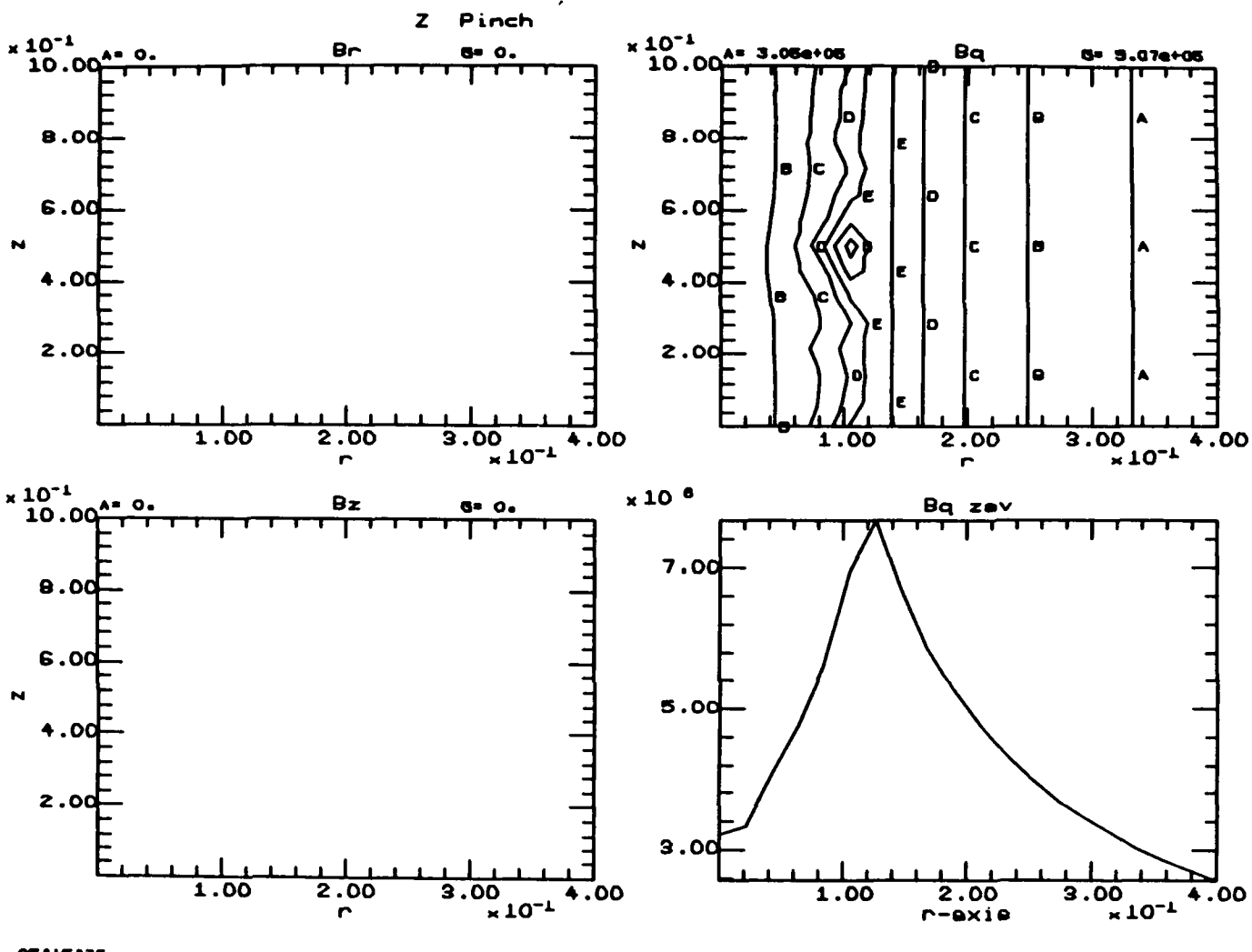
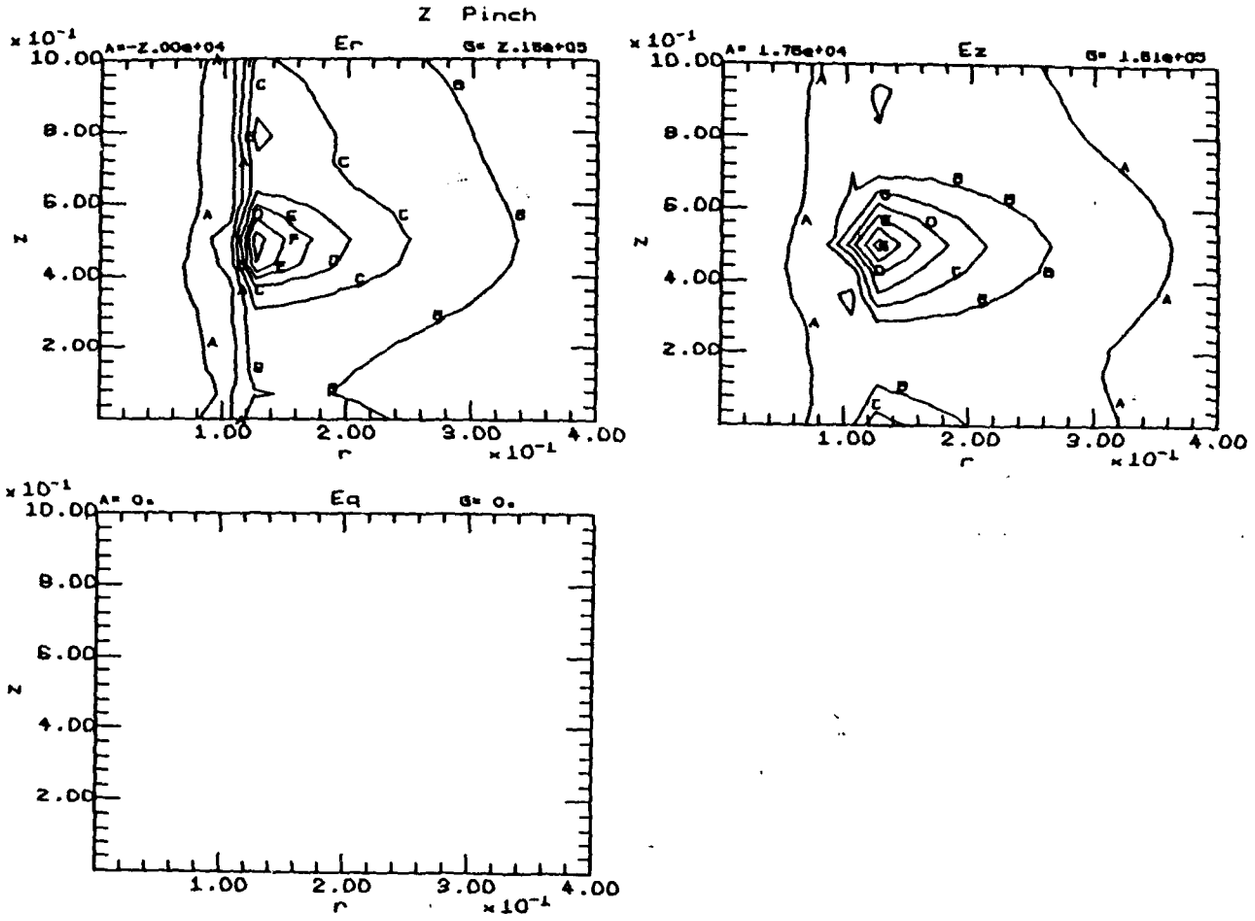



Figure P.4.




t= 1.40e-03 micsec

Figure P.5.

## Q. Experimental Studies of the Effects of Induced Spatial Incoherence (ISI) on Laser-Plasma Instabilities

The direct drive approach to laser fusion requires a high degree of illumination uniformity in order to reduce the probability of catastrophic break-up of the fusion target before reaching the thermonuclear regime. NRL has pioneered the use of Induced Spatial Incoherence (ISI) as a beam-smoothing technique. ISI has been found, however, not only to provide a high level of uniform illumination but also to suppress a number of important instabilities associated with the reflection and absorption of the incident laser energy such as stimulated Raman scattering (SRS) and stimulated Brillouin scattering (SBS). The effect of ISI on SRS and SBS as well as plans for extending the technique of ISI beam smoothing to 0.25 $\mu$m KrF gas lasers is discussed in an article entitled "Laser-Plasma Experiments at the Naval Research Laboratory," in the *Proceedings of the Twelfth International Conference on Plasma Physics and Controlled Nuclear Fusion Research* (1988). This report is included here as Appendix ZZ.

The effect of ISI on other laser-plasma instabilities, most notably the two plasmon decay instability, had not been studied either theoretically or experimentally. Two plasmon decay is important to laser fusion because electrons can be accelerated to high energies by electron plasma waves (plasmons), thus preventing efficient pellet compression. A detailed experiment was performed comparing the effects of laser bandwidth and ISI beam smoothing on the two plasmon decay instability as inferred from $3\omega_o/2$ harmonic emission obtained with the use of ISI or other beam smoothing techniques. It appears possible that the two plasmon decay instability and the concomittant energetic electron and preheat phenomena observed in many earlier experiments may be less important than previously thought for laser drivers with ISI beam smoothing. This work was presented at the 30th Annual Meeting of the American Physical Society Division of Plasma Physics. A detailed article is in preparation for submission to *Physical Review Letters*. An abstract of the APS presentation follows.

The Effect of Bandwidth and ISI on $3\omega/2$ Emission at 0.53 $\mu$m, T.A. PEYSER*, C.K. MANKA, S.P. OBENSCHAIN, J.A. STAMPER, A. MOSTOVYCH, and K.J. KEARNEY, Naval Research Laboratory, Plasma Physics Division, Washington, DC 20375-5000
– Plasma waves produced by quarter-critical density instabilities can excite energetic electrons leading to preheat of ICF targets and poor compression. $3\omega/2$ emission is a signature of such quarter-critical instabilities.

Time-integrated spectrally- and spatially-resolved measurements were made of $3\omega/2$ emission from planar CH targets irradiated at 0.53 $\mu$m with the Pharos III laser. Mea-

surements were taken over a wide range of incident laser energies (25J < E < 250J) and over a wide range of laser bandwidths (0.01 A < $\delta\lambda$ < 10 A). $3\omega/2$ emission was found to decrease by an order of magnitude at the 10 A broad bandwidth compared with the 0.01 A narrow bandwidth. An additional reduction in the $3\omega/2$ emission was observed with the use of induced spatial incoherence (ISI).[1]

* SAIC, McLean, VA 22102.

[1] R.H. Lehmberg and S.P. Obenschain, *Opt. Commun.* **46**, 27 (1983).

### R. Electron Beam Energy Deposition in a KrF Laser

This project examines the techniques presently used to calculate energy deposition by e-beams in a KrF laser, to determine whether these calculations will continue to be valid for higher power systems.

The successful scaling of KrF lasers to higher energy output is an important part of the program plan for direct-drive laser fusion. The new NRL KrF laser, Nike, is designed to demonstrate the practicability of scaling KrF lasers to high power, as well as to test the use of the laser in accelerating thin targets. A central feature of the Nike system will be the use of energy deposition by electron beams to pump the amplifier. The ability to scale this pumping scheme to higher powered systems is clearly one of the central elements in the KrF program plan.

To determine the range of parameters within which present calculations of e-beam deposition are valid, we carried out a systematic discussion with physicists active in this field, and obtained the original papers on which these calculations are based. We then analyzed the physics elements both included and omitted in various versions of the Monte Carlo codes, and also analyzed the physics base for calculating e-beam deposition, ranging from the seminal work of Bethe, Rose, and Smith in 1938 to the work of J. Jacob and his colleagues in 1973-1982. To test the sensitivity of deposition calculations to physics input, we constructed a simple computer model of electron slowing and diffusion in a KrF gas (simple means that the code runs in less than a second on an 80286/287 personal computer). We compared the results with output from Monte Carlo calculations, for several beam energies and other parameters. In the present phase of the project, we are carrying out the same process of survey-identification of physics elements – analysis and calculations to delineate the parameters for which the existing Monte Carlo techniques might fail. A report of the first phase of this work is in preparation.

## S. Experimental Study of Laser-Plasma Expansions in Magnetic Fields: Laboratory Simulations of Space Plasmas

Laser-produced plasmas are similar in many important respects to plasmas encountered in our solar system and beyond. Laser plasma expansions into ambient magnetic fields can provide laboratory scientists a rare opportunity to study plasma processes and instabilities usually encountered only in space or astrophysical contexts. Over the past two years, SAIC personnel developed new diagnostic techniques for the study of laser-produced plasmas and were directly involved in detailed experiments on these phenomena.

A fast-framing camera developed by Kentech Instruments, Ltd. of Great Britain was used to obtain two-dimensional images of the laser produced plasmas with time resolution between 120 picoseconds and 5 nanoseconds. This was the first use of this new technology in plasma physics and was reported at the SPIE 32nd Annual International Technical Symposium on Optical and Optoelectronic Applied Science and Engineering in 1988. It was published in the Proceedings of the Conference and appears here as Appendix AAA, entitled "Nanosecond Framing Photography for Laser-Produced Interstreaming Plasmas." The use of this diagnostic permitted NRL scientists to make the first laboratory study of a large-larmor radius interchange instability that had been previously observed only in barium release space experiments. These experiments were reported at numerous scientific meetings and were the subject of several publications including a *Physical Review Letter*, **59**, 2299 (1987), "Large-Larmor Radius Interchange Instability" (Appendix BBB) and an NRL Memorandum Report 6154 (1988), "Structuring Processes in Expanding Laser-Produced Plasmas" (Appendix CCC).

A second series experiments with hollow cylindrical targets studied the formation of plasma jets, the propagation of plasmas across magnetic fields and various structuring instabilities in addition to the large larmor radius instability mentioned above. Two papers were presented at the 19th European Conference on Laser Interaction with Matter held in Madrid in 1988 entitled respectively "Laboratory Laser-Produced Astrophysical-Like Plasmas" (Appendix DDD), and "Jets in Laser-Produced Plasmas" (Appendix EEE). Two additional detailed papers on the velocity shear instability observed in these experiments were presented first at the American Physical Society Topical Conference on Plasma Astrophysics held in Santa Fe in 1988 and then at the 30th Annual Meeting of the American Physical Society Division of Plasma Physics. A lengthy article summarizing the work on the cylindrical jets is currently in preparation and will be submitted to *The Physics of*

*Fluids.* Abstracts of the presentations at the above two meetings respectively follow.

Jets in Laboratory Laser Produced Plasmas,[+] T.A PEYSER,[*], C.K. MANKA, B.H. RIPIN, E.A. MCLEAN, J.A. STAMPER, K. KEARNEY, A.N. MOSTOVYCH, J. GRUN, and J. CRAWFORD,[**] Plasma Physics Division, Naval Research Laboratory, Washington, D.C. 20375-5000. Laboratory, laser-produced plasmas have many properties similar or scalable to astrophysical plasmas. We describe several such experiments performed with the NRL Pharos III laser facility. Laser-produced plasma jets with propagation perpendicular to the magnetic field have been studied with a variety of diagnostics, including fast-framing camera photography and dark-field shadowgraphy. Large well-defined jets are observed to persist over long distances and for surprisingly long times after plasma production. Collimation of the expanding plasma into a jet occurs in the presence of strong magnetic fields (up to 10 kG).[1] In addition, we will examine the effect of magnetic fields on the Kelvin-Helmholtz instability.

[+] Supported by DNA.

*SAIC McLean, VA 22102.

** Southwest Texas State U. San Marcos, TX 78666.

[1] C.K. Manka, T.A. Peyser, B.H. Ripin to be published.

Late-Time Large-Scale Structures In Laser-Produced Plasmas,* C.K. MANKA, T.A. PEYSER,** B.H. RIPIN, E.A. MCLEAN, J.A. STAMPER, A.N. MOSTOVYCH, J. GRUN, and J. CRAWFORD,[+] Naval Research Laboratory, Plasma Physics Division, Washington, D.C. 20357-5000–Recent NRL experiments have produced cross-field plasma jets and other centimeter scale plasma structures which persist to several microseconds. Laser energies were 30-300 J at 1.05 $\mu$m wavelength with FWHM $\simeq$ 4 ns. Targets were of various geometrical shapes, and an external magnetic field of up to 10 kG was applied. The development of these structures has been studied using emitted light fast framing photography, laser probing shadowgraphy and other diagnostics. The plasma structures are compared to those predicted from various plasma instabilities (such as Rayleigh-Taylor, Kelvin-Holmholtz, etc.) which may be applicable in this parameter regime. Scaling to atmospheric and astrophysical plasmas is discussed.

* Supported by the US DNA.

** SAIC, McLean, Virginia 22102.

[+]Southwest Texas State University, San Marcos, TX.

## T. MHD Solar Coronal Plasma Code

During this period, SAIC wrote a numerical code to compute MHD equilibria in solar coronal arcade geometries, i.e. geometries symmetric in z. This code allows the footpoint displacement and the entropy to be specified, rather than the z-component of the magnetic field and the pressure. The latter approach, which has been used by other authors in the past, leads to bifurcations that have been suggested as the cause of solar flares, coronal mass ejections, and other coronal activity. In collaboration with Dr. Chen of NRL, SAIC used the above code, and found that the former, more physically relevant, specification of

equilibrium quantities does not lead to bifurcations, and that, indeed, equilibria exist for arbitrarily large values of footpoint displacement $d$ and entropy $s$. For very large values of $d$ and $s$ the configuration opens up, but does not develop the singular, sheet current, configurations suggested by Sturrock and co-workers. This work was reported in NRL Memorandum Report 6402 (1988), entitled "Equilibrium of Solar Coronal Arcades," and appears here as Appendix FFF.

## References


1. M. Friedman and V. Serlin, *Phys. Rev. Lett.* **55**, 2860 (1985).
2. CONDOR is an extension of the MASK particle code, discussed in A. Palevsky and A. Drobot, in *Proceedings of the 9th Conference on Numerical Simulation of Plasmas*, July 1980 (Northwestern University, Evanston, IL) (unpublished).
3. M. Friedman and V. Serlin, *Appl. Phys. Lett.* **49**, 596 (1986).
4. P. Sprangle, A. Ting, and C.M. Tang, *Phys. Rev. Lett.* **59**, 202 (1987).
5. A.D. Wilson, *Solid State Technology* **29**, 249 (1986).
6. D.W. Hewett, *J. Comp. Phys.* **38**, 378 (1980).

# APPENDIX A

## Megavolt, Multi-Kiloamp $K_a$-Band Gyrotron Oscillator Experiment

**Naval Research Laboratory**

Washington, DC 20375-5000

NRL Memorandum Report 6419

# Megavolt, Multi-Kiloamp $K_a$-Band Gyrotron Oscillator Experiment

W. M. BLACK,* S. H. GOLD, A. W. FLIFLET, D. A. KIRKPATRICK,**
W. M. MANHEIMER, R. C. LEE,† V. L. GRANATSTEIN,††
D. L. HARDESTY, A. K. KINKEAD AND M. SUCY†

*High Power Electromagnetic Radiation Branch*
*Plasma Physics Division*

**Electrical and Computer Engineering Department*
*George Mason University, VA 22021*

***Science Applications International Corporation*
*McLean, VA 22102*

†*JAYCOR, Inc.*
*Vienna, VA 22180*

††*Electrical Engineering Department*
*University of Maryland*
*College Park, MD 20742*

March 15, 1989

Approved for public release; distribution unlimited.

## CONTENTS


I. INTRODUCTION ..... 1

II. EXPERIMENTAL SETUP ..... 5

III. EXPERIMENTAL RESULTS AND DISCUSSION ..... 8

ACKNOWLEDGMENTS ..... 14

REFERENCES ..... 15

DISTRIBUTION LIST ..... 21

# MEGAVOLT, MULTI-KILOAMP
# $K_a$-BAND GYROTRON OSCILLATOR EXPERIMENT

## I. Introduction

Gyrotron oscillators have proved to be efficient sources of very high-power radiation in the microwave and millimeter wave regimes. Conventional gyrotrons use thermionic cathodes, with typical operating currents of $\lesssim$50 A at voltages of $\lesssim$100 keV, and have demonstrated hundreds of kW of average power at efficiencies approaching 50%. However, some future applications of millimeter-wave radiation, such as radars and high energy linear electron (and positron) accelerators, may require substantially higher peak power levels than have been produced using conventional thermionic microwave tube technologies. The pursuit of higher microwave powers inevitably requires the application of higher beam powers, implying operation at higher currents and/or voltages. Gyrotron scaling to high current, high voltage operation is relatively favorable,[1] and a number of high voltage (>250 kV) gyrotron experiments have been reported in recent years that take advantage of the substantially higher currents and voltages available for short pulses (typically, $\lesssim$100 nsec) from high voltage pulseline accelerators driving plasma-induced field emission cathodes. Among these are a set of experiments from the P.N. Lebedev Physics Institute of the Soviet Union that demonstrated 23 MW at 40 GHz in a linearly-polarized (i.e., non-rotating) $TE_{13}$ mode with 5% efficiency, using a 350 keV electron beam.[2] Studies of gyrotrons driven by pulseline accelerators or Marx generators have also been carried out at the University of Michigan[3] and at the University of Strathclyde in the United Kingdom.[4]

Manuscript approved January 24, 1989.

In 1984, a program was initiated at the Naval Research Laboratory to investigate very high power gyrotron oscillators driven by intense relativistic electron beams. These experiments were designed to operate in $K_a$-band, with the principal interest at 35 GHz. The early experiments were carried out on a compact Febetron pulser capable of producing a 600 kV, 6 kA, 55 nsec pulse into a 100 Ω matched load.

A key requirement for intense beam gyrotrons, unlike most other high power microwave devices driven by intense relativistic electron beams, is to produce an electron beam with a large amount of momentum transverse to the applied axial magnetic field prior to injection into the interaction region. The first series of experiments attempted to produce the required beam α, where α is the ratio of transverse to parallel momentum, by emitting electrons across magnetic field lines at the cathode to produce some initial nonzero value of α, and then adiabatically compressing the beam into the gyrotron cavity to increase α while positioning the beam to couple strongly to the desired waveguide mode. These experiments operated at approximately 350 kV and 800 A, and produced approximately 20 MW of output power at 35 GHz with 8% efficiency in a "whispering-gallery" $TE_{62}$ mode.[5]

When this approach was found to lack flexibility, a new approach was implemented, in which the diode was designed to emit primarily along the direction of the axial magnetic field, i.e. to produce a very low initial beam α, and the α was then sharply increased by transit through a localized nonadiabatic dip in the axial field, produced by a "pump" magnet, before being adiabatically compressed into the gyrotron cavity. This allowed the use of a very simple diode geometry, and provided a separate experimental control for beam α that greatly increased the experimental flexibility.

For this second series of experiments, the Febetron pulser was operated at its full rated charge voltage and mismatched upward at the diode to produce voltages higher than 600 kV (up to 900 kV) at lower currents. Due to the high impedance of the pulser, it was impossible to employ relatively low impedance diodes, such as diodes with beam-scraper anodes, without substantially reducing the operating voltages. The experiments were therefore carried out in a foilless geometry employing a magnetic-field-immersed, cylindrical graphite cathode with a sharpened edge, in which the cylindrical vacuum vessel served as the anode. In this geometry, the diode produces a beam current determined by the space-charge limited flow of the annular beam within the cylindrical vacuum enclosure in the vicinity of the cathode. In general, this was more current than could be effectively employed in the experiment, and the use of a "pump" magnet to increase the average beam $\alpha$ to a level sufficient to drive the gyrotron interaction invariably resulted in the loss of a sizable fraction of the beam current. Current loss occurred due to electron mirroring during the adiabatic compression stage, due in part to the effects of beam space charge on the electron beam kinetic energy, and in part to the effects of pitch-angle spread in the beam. It was not clear exactly where the reflexing electrons were collected, or whether they caused a space-charge build-up that effected the performance of the diode.

Based on single particle simulations of the effects of the pump magnet on electrons entering with a small initial value of $\alpha$ and random gyrophase, it is apparent that the pump magnet has the effect of greatly magnifying any initial spread in pitch angle. Fortunately, gyrotron oscillators are not very sensitive to such pitch angle spreads. However, one result of a large electron beam pitch angle spread is to limit the average beam $\alpha$ achievable by this

technique, since as the strength of the pump magnet is increased, the highest $\alpha$ portion of the particle distribution function will be reflected during the subsequent adiabatic compression phase. Optimum high power operation generally occurred with pump strengths resulting in the loss of half or more of the total beam current between the diode and the gyrotron cavity. In addition, the diode voltage waveform was highly transient, with no true steady-state conditions of current and voltage obtainable anywhere within the pulse.

The second series of experiments was carried out in both whispering-gallery $TE_{m2}$ modes and linearly-polarized $TE_{1n}$ modes.[6,7] Results included a peak power of 100 MW at 35 GHz at 8% efficiency in a rotating $TE_{62}$ mode, a peak power of 35 MW at 35 GHz in a linearly-polarized $TE_{13}$ mode through use of a slotted gyrotron cavity. The gyrotron signal frequency could be step-tuned over the range 28 to 49 GHz in a sequence of $TE_{m2}$ modes by variation of the axial magnetic field. Results were in general agreement with the predictions of steady-state gyrotron theory, with theoretical values of power and efficiency typically being larger than experimental values by about a factor of two. However, due to the nonideal voltage waveform provided by the Febetron pulser, the typical microwave pulse length was only 15 nsec.

In order to extend these experiments to higher microwave powers and longer pulses, as well as to gain some flexibility in the diode design in order to permit the production of a better quality electron beam, these experiments were moved to the VEBA pulseline accelerator, which can operate at voltages exceeding 1.5 MV and has a 20 $\Omega$ output impedance and a 55 nsec FWHM pulse, of which approximately 40 nsec is relatively flat ($\pm$3-5%). These new experiments initially employed a very similar experimental setup to that

utilized previously in the Febetron experiments, except that the Q=250, $TE_{62}$ cavity of the 100 MW experiments was replaced by a slightly shorter cavity with a cold-cavity Q of 180. However, the best results have been achieved by replacing the foilless diode geometry with a beam scraper diode. By varying the cathode-anode gap, the new diode geometry has permitted control of the total current injected into the drift tube, and in addition, the more planar cathode-anode geometry is believed to produce a lower spread in the initial beam pitch angle, with the potential to produce a higher average value of $\alpha$ in the gyrotron cavity. Furthermore, in the new geometry, any reflexing electrons are likely to be collected on the downstream side of the beam scraper anode, thus eliminating a possible space-charge build-up problem present in the foilless experiment.

As a result of the higher beam power and improved beam quality, the output power has been increased to approximately 250 MW at 35 GHz in a $TE_{62}$ mode with an efficiency of approximately 10%.

## II. Experimental Setup

The 1.5 MeV VEBA pulseline accelerator with 20 $\Omega$ output impedance and 55 nsec voltage pulse was used to generate a multi-kiloamp annular electron beam by explosive plasma formation from a graphite cathode. Two diode geometries were employed. In the first, the electron beam was produced by emission from the sharpened edge of a cylindrical graphite anode in a simple foilless diode geometry. In the second, a more conventional planar anode-cathode gap was used, in which emission takes place from the rounded edge of a hollow cathode, and a small fraction of the total current is extracted from the diode through an

annular slot in the graphite anode. In either case, the beam is created in a uniform axial field provided by the main solenoidal magnet.

Figure 1 illustrates the overall experimental setup employing the second of these diode geometries. The initial transverse momentum is low, because the emission is predominantly along the direction of the applied magnetic field. Downstream, the transverse momentum is induced by transit through a localized depression in the axial field, which is produced by the "pump" magnet. Finally, the beam is adiabatically compressed to its final radius by the cavity solenoid. A Rogowski coil positioned between the pump magnet and the gyrotron cavity measures the net current into the gyrotron. In order to achieve separate adjustment of the electron transverse momentum, the magnetic compression ratio, and the final magnetic field in the gyrotron cavity, each of the three magnets (i.e., the pump magnet, the cavity solenoid, and the main magnet) is powered by a separate capacitor bank discharge.[6] By a proper selection of pump magnet strength and compression ratio, the beam diameter can be adjusted to couple to the desired $TE_{62}$ mode in the cavity while the electron velocity pitch ratio $\alpha$ is increased to a value near unity. The cavity itself is cylindrically symmetric with a diameter of 3.2 cm and has a calculated cold-cavity Q of 180 for the $TE_{62}$ mode. Beyond the cavity there is a 5° output taper transition to a 120 cm long drift tube with diameter of 14 cm. Finally, a one-meter-long output horn is terminated with a 32-cm-diam. output window.

In the foilless diode configuration, used in the earlier experiments, the beam current is space-charge limited with a typical value of 10 kA; however, under the usual operating conditions that maximize gyrotron microwave emission as a function of the strength of the pump magnet, only one-third of this current actually reaches the gyrotron cavity. Due to

emission from the edge of the cathode, the beam from this foilless diode possesses a relatively large spread in pitch angle, which is greatly magnified by the pump magnet. This results in a large uncontrolled loss of half or more of the beam current during the adiabatic compression, as measured by the Rogowski coil, thereby limiting the achievable pitch ratio and potentially causing space charge problems due to the reflexing electrons.

To improve the beam quality, the foilless diode was replaced by an apertured diode configuration, in which a hollow ring-like cathode is placed from 1 to 2.2 cm from an anode plate with an annulus cut in it to match the cathode ring. The mean diameter of the annulus was 3.34 cm, and its radial extent was 1.5 mm. The anode functions in part as an emittance filter, since it scrapes off the inner and outer edges of the annular electron beam produced by the cathode, and in part as a control grid, since changes in the cathode-anode gap are a reliable means to control the beam current, which is space-charge limited. A consequence of the use of an apertured anode, rather than a foilless geometry, is the emission of a large amount of cathode current (25-35 kA), with roughly 90% being scraped off before leaving the diode. However, the more planar emission geometry and the controlled beam scraping provides the beam with a lower initial $\alpha$ and a smaller velocity spread before it enters the pump magnet and beam compression regions. As a result, the beam quality is improved and the current loss from the diode to the cavity can be reduced to approximately 10 to 15% under typical conditions of gyrotron operation. This small fraction of reflected electrons is most likely to be collected on the downstream side of the anode scraper plate, thereby preventing a build-up of space charge anywhere in the system.

The microwave measurement system consists of two separate detection channels, each composed of calibrated "in-band" WR-28 components, including filters, attenuators and directional couplers, and beginning with a small microwave aperture antenna positioned within 1 cm of the output window. One aperture is maintained at a fixed position on the output window, while the second is scanned. A band-pass filter limits the detected signal to a narrow frequency band (1.6 GHz FWHM) centered at 35 GHz. These diagnostics as well as the overall experimental setup are described in greater detail in Ref. 6. The changes affecting the present work are in the diode region, the cavity Q, and the currents, voltages, and magnetic fields employed in the experiment.

## III. Experimental Results and Discussion

The waveforms for the diode voltage, diode current, cavity current, and 35 GHz microwave pulses for a "typical" shot are shown in Fig. 2. The improved voltage waveform and beam quality, compared to that described in Ref. 6, have generally permitted high power microwave pulses with a duration of up to 40 nsec, nearly matching the duration of the flat portion of the high voltage pulse applied to the diode. However, the microwave pulse is subject to large shot-to-shot variation in amplitude and pulse shape. A set of measurements were conducted as a function of beam energy, magnetic field, magnetic compression ratio, and pump field amplitude, in order to find the optimum operating parameters.

Figure 3 shows a scan of the output mode of the device as a function of radius in both $|E_r|^2$ and $|E_\theta|^2$ with a cavity magnetic field of $B_0$=32 kG, a current of 2.5 kA, and a peak diode voltage of 1.2 MV. The estimated experimental uncertainties are ±1.5 kG on the

magnetic field, ±0.1 kA on the instantaneous current measured by the Rogowski coil, and ±0.1 MV on the diode voltage, including the effect of voltage ripple during the voltage flat-top. (The net current will be lower if current interception takes place between the Rogowski coil and the gyrotron cavity. Fluorescent screen data taken subsequent to the microwave measurements suggests that up to 20% of the current may have been intercepted under these experimental conditions.) The peak beam kinetic energy should be corrected downward by approximately 50 keV because of space charge depression, assuming an average beam $\alpha$ of 1.

The normalized beam radius (i.e., the ratio of the beam guiding center radius $r_b$ to the cavity wall radius $r_w$) for this scan was approximately 0.725. However, there was some spread in the electron guiding centers due to beam thickness (reflecting the 1.5 mm width of the anode annulus) and finite decentering of the beam in the gyrotron cavity. This radius is close to optimum for coupling to the circularly-polarized $TE_{62}$ mode counterrotating to the sense of electron gyration in the axial magnetic field. However, in the vicinity of 35 GHz, the beam will also couple to the $TE_{10,1}$ and $TE_{14}$ modes, and more weakly to the $TM_{23}$ and $TM_{04}$ modes. The general shape of the measured profile in Fig. 3 fits reasonably well to the $TE_{62}$ mode for both the radial and azimuthal polarizations of the rf electric field, and is similar to that of Ref. 6. The peaks at small values of the radii may be due to parasitic excitation of the $TM_{04}$ mode. Mode purity at the output window may also be reduced by mode conversion in the 5° output taper and horn. For instance, mode conversion to the $TE_{61}$ mode might explain the higher than expected peak in $|E_r|^2$ near the wall. A scan under

similar experimental conditions with the foilless diode with its resulting poorer quality beam revealed a higher content of undesired modes.

For the data of Fig. 3, the measured mode pattern can be used to calculate the total gyrotron power by integrating over the output window, and correcting for the measured losses in the detection system. This procedure has been described in detail elsewhere.[6] The power estimate, which is based on the average of several shots per position in the scan, is 160 MW. Subsequent data taken at a fixed position has shown the total equivalent output power to reach a single-shot peak value of 275 MW, with 250 MW being measured on several occasions. The single shot efficiencies, based on the Rogowski coil measurements of beam current, varied from 9 to 14%. Based on error bars in the averaging process and in the calibration of the various multiplicative factors, the overall uncertainty of the power values is estimated to be less than 3 dB.

Figure 4 shows starting current and output isopower curves for the gyrotron interaction with the counterrotating $TE_{62}$ mode, calculated from a steady-state model[8] for $B_0$=32 kG. The beam current is assumed to scale as $V^{1.5}$ with a maximum value of 2.5 kA at 1.15 MV, and the beam $\alpha$ is assumed to scale linearly with V, with a maximum value of $\alpha$=1 at 1.15 MV. The starting current and isopower curves are calculated assuming a half-sinusoidal rf-field profile along the cavity axis with a length of 3.5 cm and a hollow beam with a radius, normalized to the cavity wall radius, of 0.725. The dotted line models the behavior of the electron beam current during the rise of the voltage waveform. The effect of increasing voltage on the coupling to this mode may be inferred from this figure. As the voltage (and current) rise to their flat-top values, the interaction will begin at the left of the figure, where

the beam line crosses the starting current line labelled $I_{thr}$, and then progressively tune to higher powers as the voltage and current continue to rise. The line ends at 2.5 kA and 1.15 MeV, and corresponds to predicted operation outside of the starting current curve, i.e. in the "hard excitation" regime, with a peak power of approximately 400 MW. Aside from the peak power predictions, this simulation is in reasonable agreement with the experimental observations.

In order to better understand the time-dependent nature of the gyrotron operation, as illustrated in Fig. 2, we have carried out a set of slow-time-scale single-mode time-dependent simulations of gyrotron operation for the approximate experimental conditions corresponding to the measurements shown in Fig. 3. Figure 5 shows a series of time-dependent simulations of the gyrotron operation,[9] employing a simulated VEBA voltage waveform that models the leading edge of the pulse, the duration of the approximately flat portion of the voltage waveform, and a "typical" short-duration voltage "spike" during the "flat-top." These simulations employ the same sinusoidal rf-field profile used for the steady-state simulations, and assume the same dependence of current and beam $\alpha$ on voltage. For the four runs shown, only the magnetic field was varied. At the lowest magnetic field, $B_0$=31 kG (Fig. 5a), the microwave signal occurs only during the rise and fall of the voltage waveform, and there is no interaction at the voltage flat-top. The next case (Fig. 5b), for $B_0$=32 kG, corresponds to the steady-state simulations of Fig. 4. In this case, the microwave signal grows substantially during the leading edge of the voltage pulse, and persists up to the voltage flat-top. Figure 5b demonstrates that the full voltage of the flat-top, corresponding to the upper end point of the beam line in Fig. 4, results in a highly detuned state of the gyrotron interaction, corresponding

to "hard excitation." This is evident because the short-duration voltage spike modeled at approximately 45 nsec detunes the interaction further, causing the output power to fall off dramatically, and the power does not begin to recover until the voltage falls below the flat-top voltage. This case agrees well with the steady-state simulation of Fig. 4, and the peak power predicted by this simulation exceeds the best experimental value by approximately a factor of two, as in Fig. 4. At $B_0$=33 kG (Fig. 5c), the voltage flat-top no longer corresponds to hard excitation, since the microwave signal falls off during the voltage spike, but then recovers during the remainder of the flat-top. Finally, at $B_0$=34 kG (Fig. 5d), the simulation shows the microwave power to follow the voltage signal for the duration of its flat portion including the voltage spike, and the power actually increases during the voltage spike.

For the assumed voltage waveform, the best agreement between the experimental microwave signals and the predictions of the single-mode time-dependent code, as a function of magnetic field, occurs at the experimental value of $B_0$=32 kG. However, the experimental values have error bars, as noted previously. In addition, the predictions of the time-dependent simulation depend in part on the exact shape of the axial rf-field profile assumed for the interaction, and small variations in the assumed length of the sinusoidal profile, or in substituting an approximately equivalent gaussian profile for the sinusoid, will change the required values of the externally-applied axial magnetic field by one to two kG. The time-dependent simulations of Fig. 5 suggest that the microwave signal should last longer and reach higher power as the magnetic field is increased beyond the best experimental value of $B_0$=32 kG. In general, this is not observed in the laboratory. A possible explanation for this experimental observation lies in the area of mode competition. Specifically, as the magnetic

field is increased, it becomes increasingly probable that a higher frequency mode will start oscillation during the rise of the voltage waveform, and will interfere with the start-up of the $TE_{62}$ mode at 35 GHz. The most likely competing mode in this situation is the counterrotating $TE_{72}$ mode. Time-dependent simulations carried out for the $TE_{72}$ mode indicate that it should begin to compete with the start-up of the $TE_{62}$ mode at approximately 34 kG. A thorough analysis of the effects of mode competition and other transient phenomena on the operation of a high voltage gyrotron would require the use of true multimode simulations, such as the fast-time-scale particle-in-cell simulations carried out by A.T. Lin et al. for the parameters of Ref. 6.[10]

In summary, a 35 GHz gyrotron oscillator has successfully operated at voltages exceeding 1 MeV and currents of several kiloamps to produce peak power levels of up to a quarter of a GW in a $TE_{62}$ mode at peak efficiencies exceeding 10%. Its interaction efficiency has been improved compared to earlier experiments by the use of an apertured diode, in piace of the foilless diode configuration used previously, which has allowed better control of the current injected into the gyrotron and better beam quality. By comparison, an earlier $TE_{62}$ experiment operating at approximately 800 keV and 1.6 kA at the same frequency in the same $TE_{62}$ mode achieved 100 MW at 8% efficiency. Overall experimental operation is in general agreement with the predictions of theory, with the best experimental powers within a factor of two of the theoretical predictions.

## Acknowledgments

This work was supported in part by the Office of Naval Research. This work was also supported in part by the Office of Innovative Science and Technology of the Strategic Defense Initiative Organization and managed by the Harry Diamond Laboratories.

## References


1. A.W. Fliflet, Naval Research Laboratory Memorandum Report 5598, 1985. Also available as National Technical Information Service Document No. ADA-157476.
2. S.N. Voronkov, V.I. Krementsov, P.S. Strelkov, and A.G. Shkvarunets, Zh. Tekh. Fiz. 52, 106 (1982) [Sov. Phys.-Tech. Phys. 27, 68 (1982)]. Also, V.V. Bogdanov, S.N. Voronkov, V.I. Krementsov, P.S. Strelkov, V.Yu. Shafer, and A.G. Shkvarunets, Zh. Tekh. Fiz. 53, 106 (1983) [Sov. Phys.-Tech. Phys. 28, 61 (1983)].
3. R.M. Gilgenbach, J.G. Wang, J.J. Choi, C.A. Outten, and T.A. Spencer, in Conference Digest of the Thirteenth International Conference on Infrared and Millimeter Waves, edited by R.J. Temkin (SPIE, Bellingham, WA, 1988), pp. 362-363.
4. A.D.R. Phelps, T. Garvey, and A.S. Hasaani, Int. J. Electron. 57, 1141 (1984).
5. S.H. Gold, A.W. Fliflet, W.M. Manheimer, W.M. Black, V.L. Granatstein, A.K. Kinkead, D.L. Hardesty, and M. Sucy, IEEE Trans. Plasma Sci. PS-13, 374 (1985).
6. S.H. Gold, A.W. Fliflet, W.M. Manheimer, R.B. McCowan, W.M. Black, R.C. Lee, V.L. Granatstein, A.K. Kinkead, D.L. Hardesty, and M. Sucy, Phys. Fluids 30, 2226 (1987).
7. S.H. Gold, A.W. Fliflet, W.M. Manheimer, R.B. McCowan, R.C. Lee, V.L. Granatstein, D.L. Hardesty, A.K. Kinkead, and M. Sucy, IEEE Trans. Plasma Sci. PS-16, 142 (1988).
8. A.W. Fliflet, M.E. Read, K.R. Chu, and R. Seeley, Int. J. Electron. 53, 505 (1982).
9. A.W. Fliflet and W.M. Manheimer, Phys. Rev. A, to be published.
10. A.T. Lin, C.-C. Lin, Z.H. Yang, K.R. Chu, A.W. Fliflet, and S.H. Gold, IEEE Trans. Plasma Sci. 16, 135 (1988).

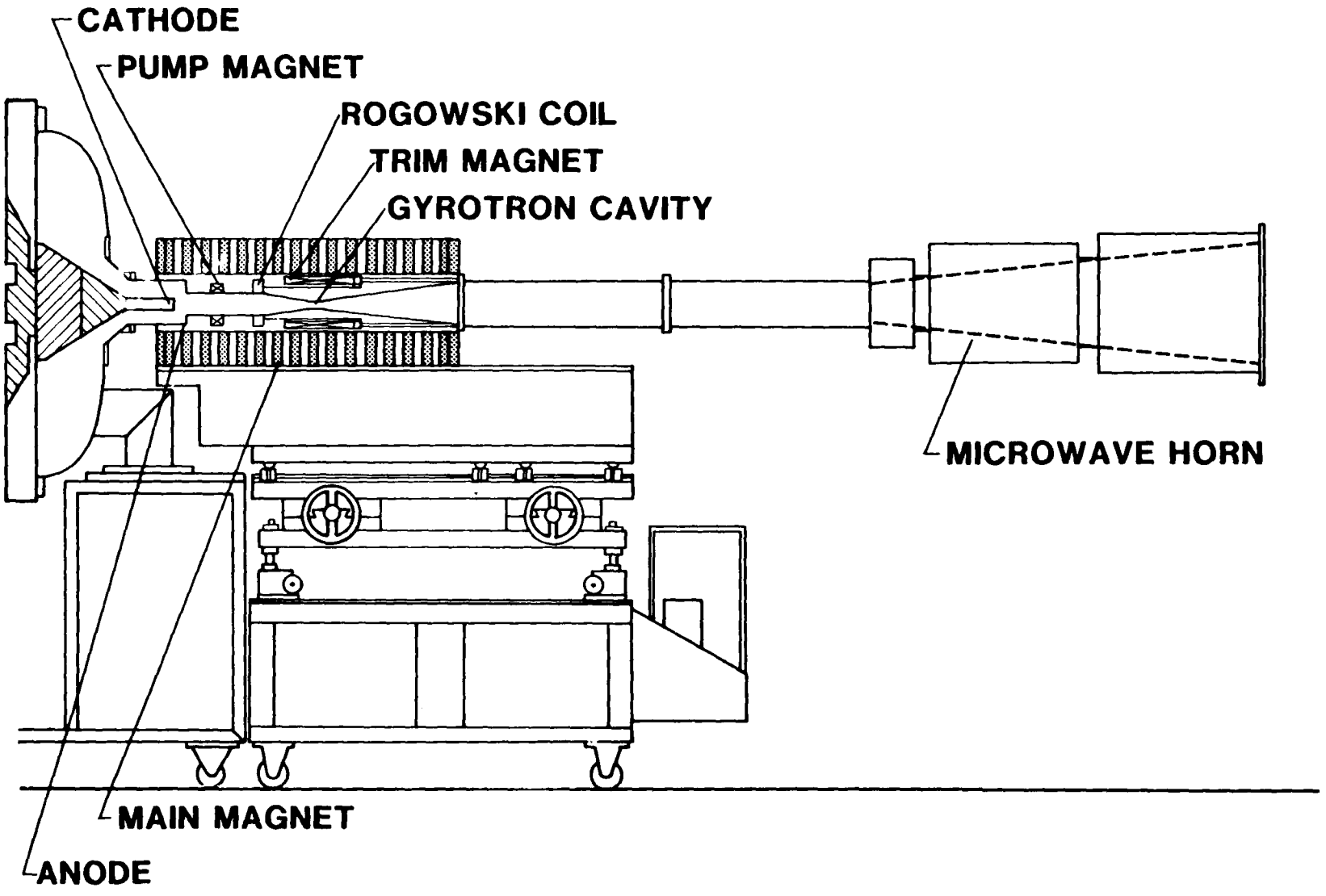



Fig. 1. Schematic diagram of the high voltage gyrotron experimental setup.

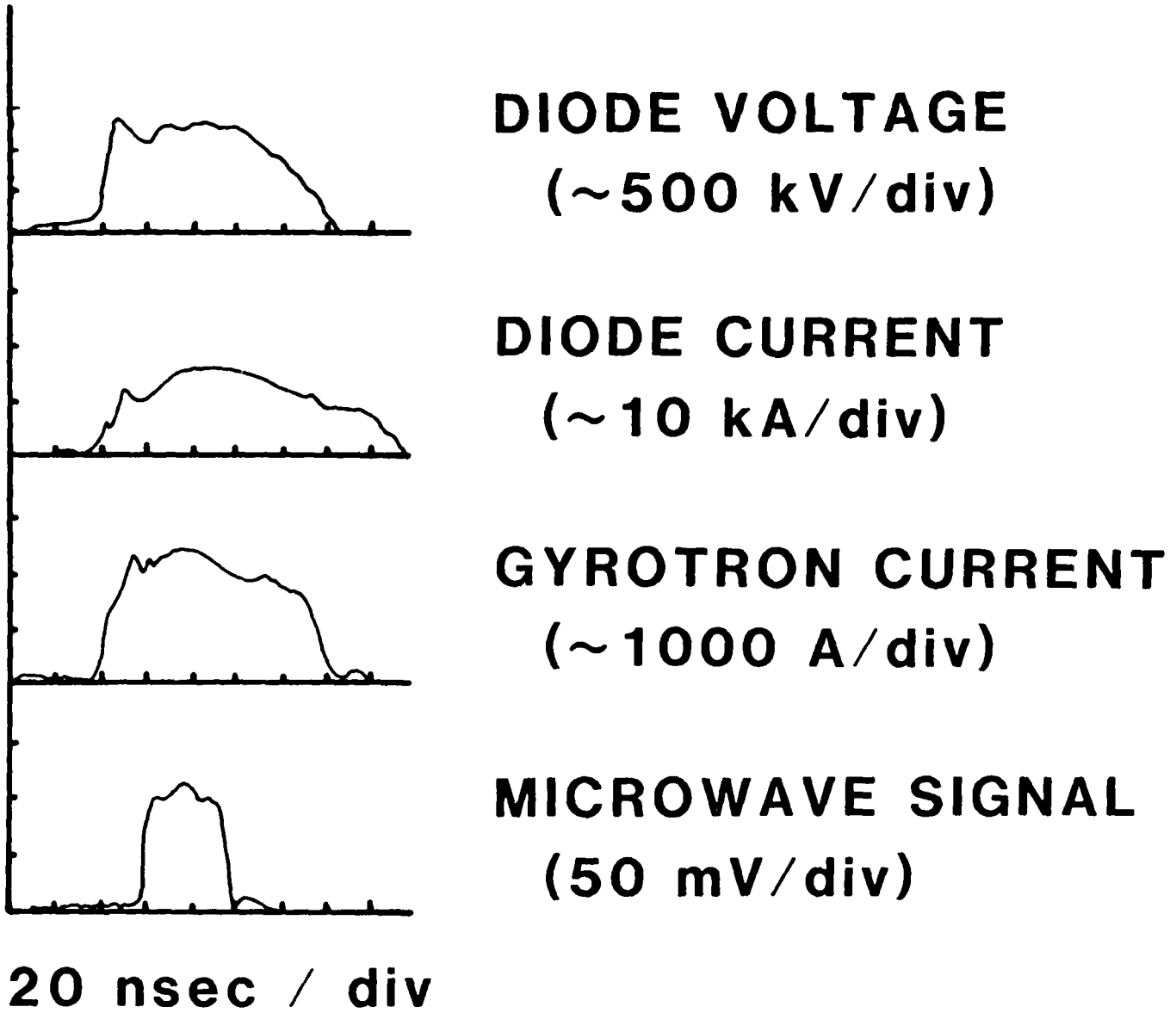



Fig. 2. Measured experimental waveforms as a function of time.

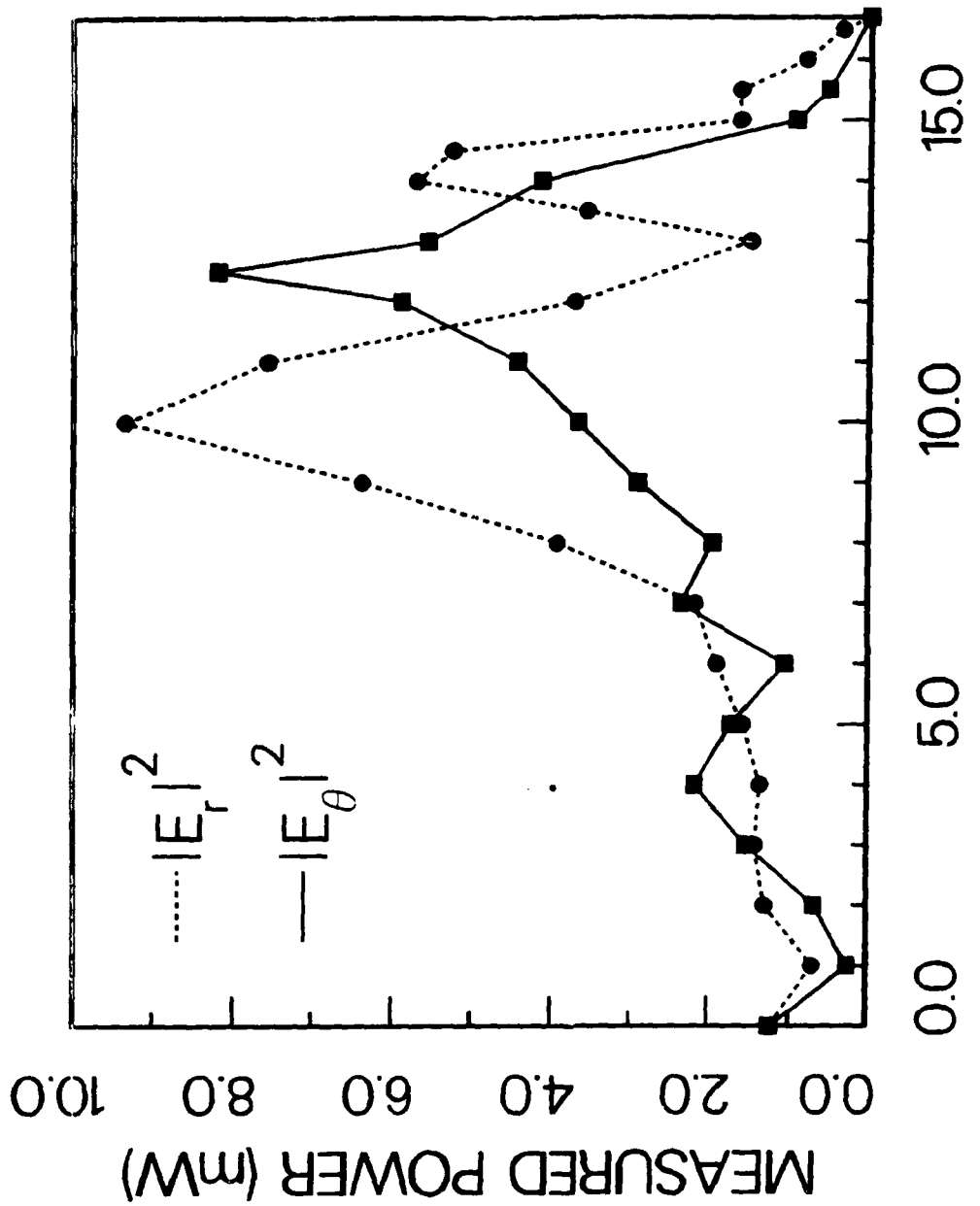



Fig. 3. Scan of output power versus radius, in both radial and azimuthal polarizations, across the output window.

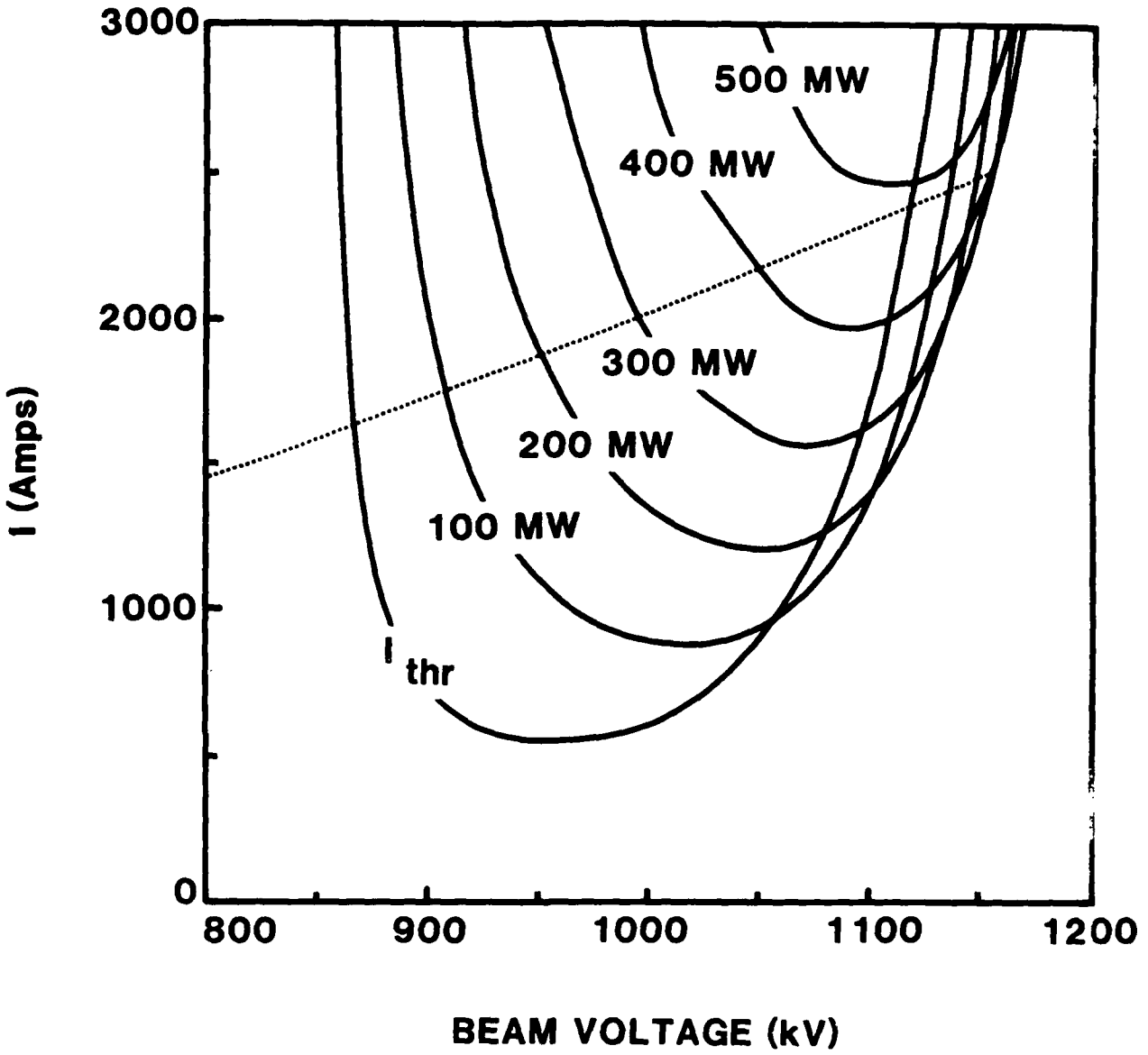



Fig. 4. Gyrotron starting current and isopower curves for the counterrotating $TE_{62}$ mode as a function of beam voltage, assuming $r_b/r_w=0.725$, $B_0=32$ kG, and that the beam $\alpha$ is proportional to V, with $\alpha=1$ at 1.15 MeV. A beam line is included, with the current assumed to scale as $V^{1.5}$, with a maximum value I=2.5 kA at 1.15 MeV.

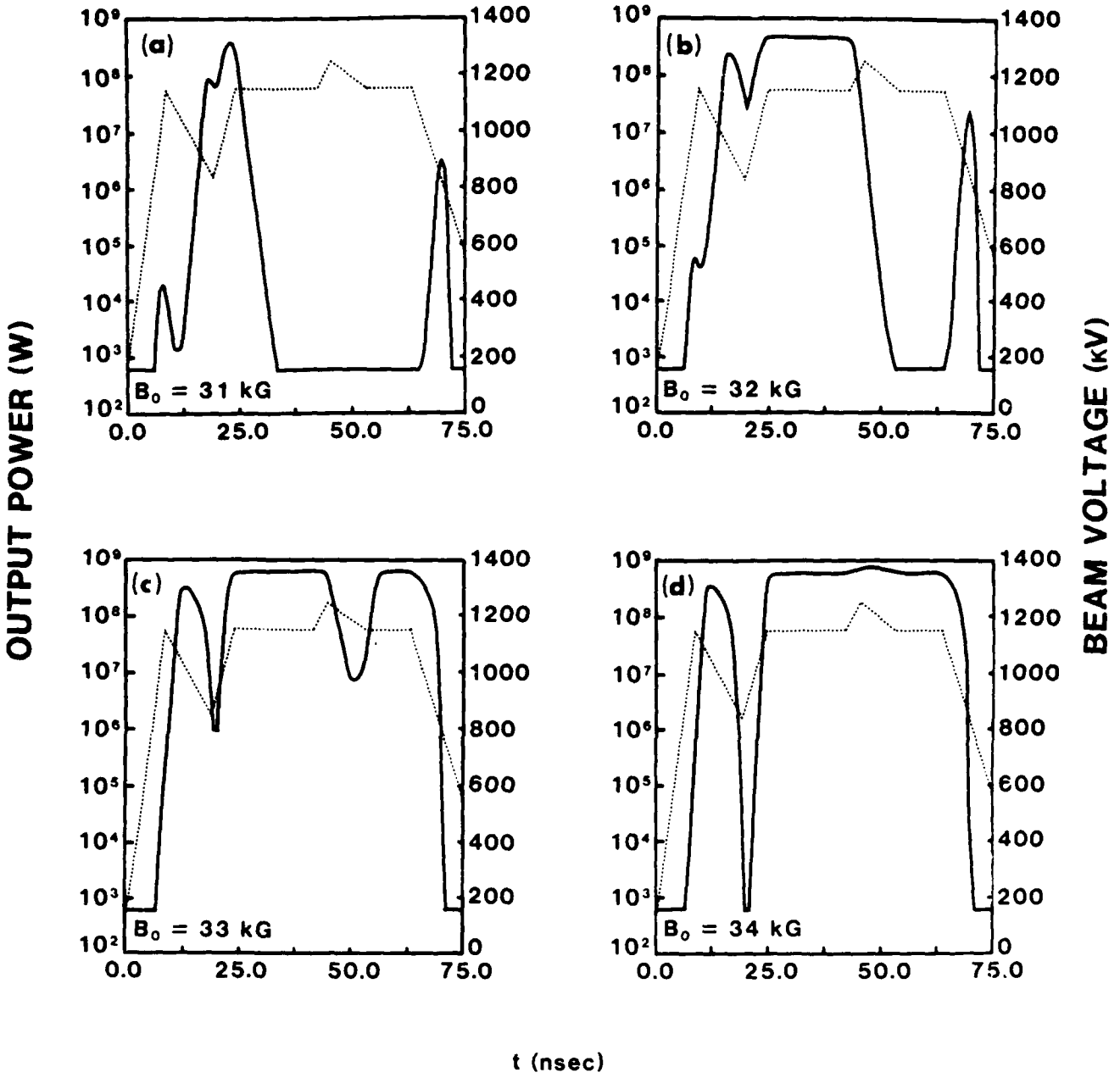



Fig. 5. Single-mode slow-time-scale time-dependent simulations of gyrotron operation in the counterrotating $TE_{62}$ mode for a simulated VEBA voltage waveform, assuming $r_b/r_w$=0.725, $\alpha \propto V$ with $\alpha$=1 at 1.15 MeV, and $I \propto V^{1.5}$ with I=2.5 kA at 1.15 MeV. Runs with four values of $B_0$ are shown: (a) 31 kG, (b) 32 kG, (c) 33 kG, and (d) 34 kG.

# APPENDIX B

## Experimental Investigation of the Effects of a Neutralizing Background Plasma on the Operation of a High Current Gyrotron

NRL | PLASMA LOADED GYROTRON

# EXPERIMENTAL INVESTIGATION OF THE EFFECTS OF A NEUTRALIZING BACKGROUND PLASMA ON THE OPERATION OF A HIGH CURRENT GYROTRON

# NRL | PLASMA LOADED GYROTRON


**INVESTIGATORS**

D.A. Kirkpatrick†

S.H. Gold

A.K. Kinkead

W.M. Manheimer

R. B. McCowan

C.A. Sullivan†

T.M. Antonsen‡

B. Levush‡

†Science Applications International Corporation, McLean VA 22102

‡Universitry of Maryland, Plasma Physics Laboratory, College Park MD 20742

# NRL | PLASMA LOADED GYROTRON

## MOTIVATION

TO ACHIEVE HIGHER OUTPUT POWERS OUT OF THE CONVENTIONAL GYROTRON

$$P_{OUT} = \eta \cdot I \cdot V$$

- $I$: LIMITED BY VACUUM LIMITING CURRENT
- $\eta$: LIMITED BY LARGE BEAM TEMPERATURES FOR CURRENTS NEAR THE VACUUM LIMITING CURRENT

BY INTRODUCING A PLASMA OF WEAK DENSITY INTO THE CAVITY, HOW FAR CAN WE GO UP IN CURRENT WITHOUT PERTURBING THE CAVITY MODE STRUCTURE?

# NRL | PLASMA LOADED GYROTRON

## PLASMA SOURCES

- FLASH LAMP (PARTIAL IONIZATION, REQUIRES PRESENCE OF BACKGROUND GAS)
- PROPAGATION THROUGH A BACKGROUND GAS (TEMPORALLY DEPENDENT DENSITY, NON-UNIFORM DENSITY)
- COUNTER-PROPAGATING ELECTRON BEAM (NON-UNIFORM DENSITY, PARTIAL IONIZATION)
- PLASMA GUNS

# NRL | PLASMA LOADED GYROTRON

## PLASMA GUNS

- PLASMA PRODUCED IS ALMOST COMPLETELY IONIZED - THE NEUTRAL COMPONENT REMAINS IN THE VICINITY OF THE PLASMA GUN.

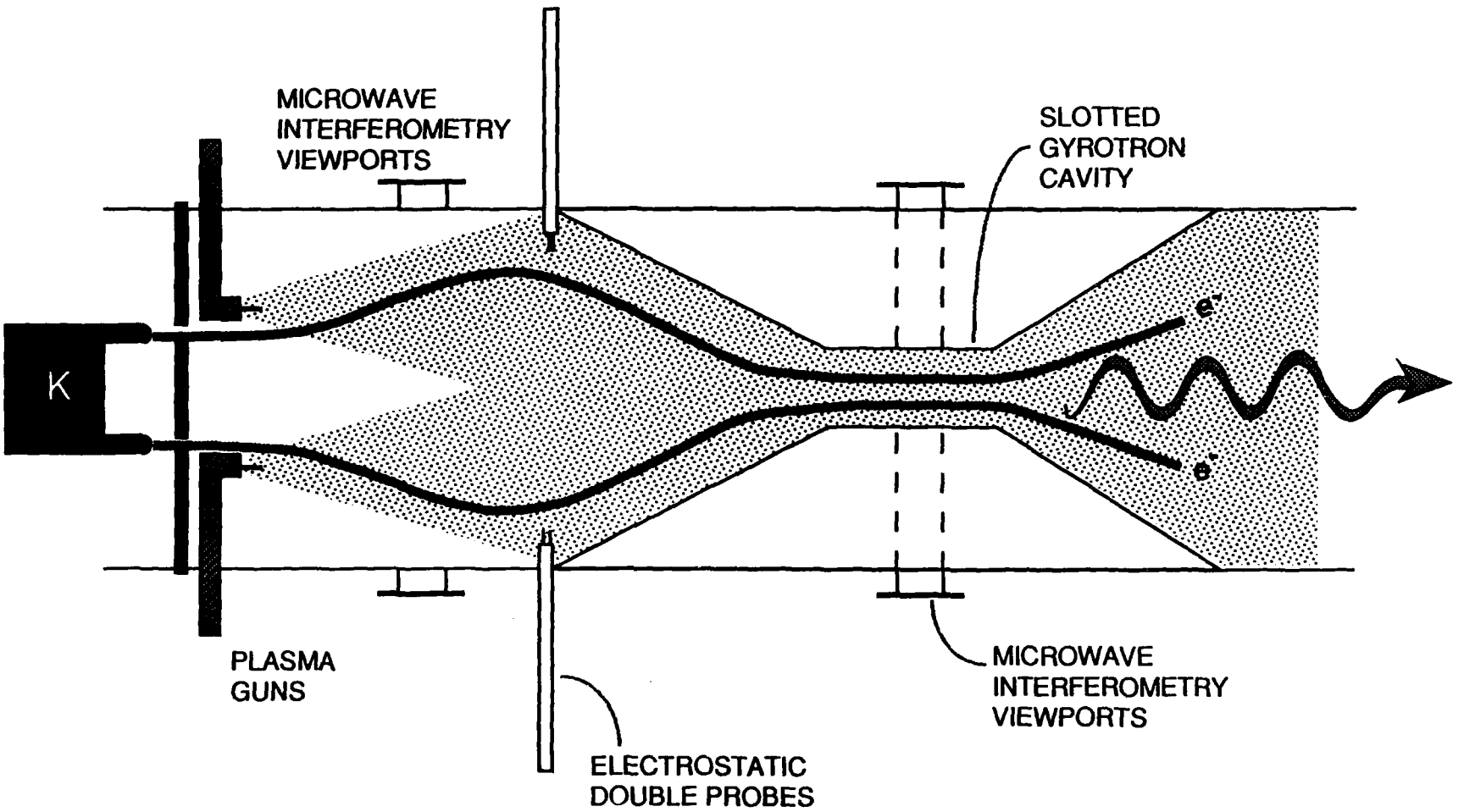
- DOWNSTREAM DENSITY IS A FUNCTION OF TIME, RISES IN ~10 μsec, THEN DECAYS WITH 1/e TIME ~20 μsec

- NO BACKGROUND GAS. PLASMA ORIGINATES FROM CARBON-BLACK COATING ON PLASMA GUN

- FOR THESE EXPERIMENTS, $\omega_{pi} > \omega_{ci}$ , SO THAT NEUTRAL PLASMA WILL FOLLOW PREDOMINANTLY BALLISTIC TRANSPORT ACROSS FIELD LINES (FOR $B_z = 20$ kG, $\omega_{pi} > \omega_{ci}$ FOR $n_i > 2 \times 10^{10}\ cm^{-3}$ )

# NRL | PLASMA LOADED GYROTRON

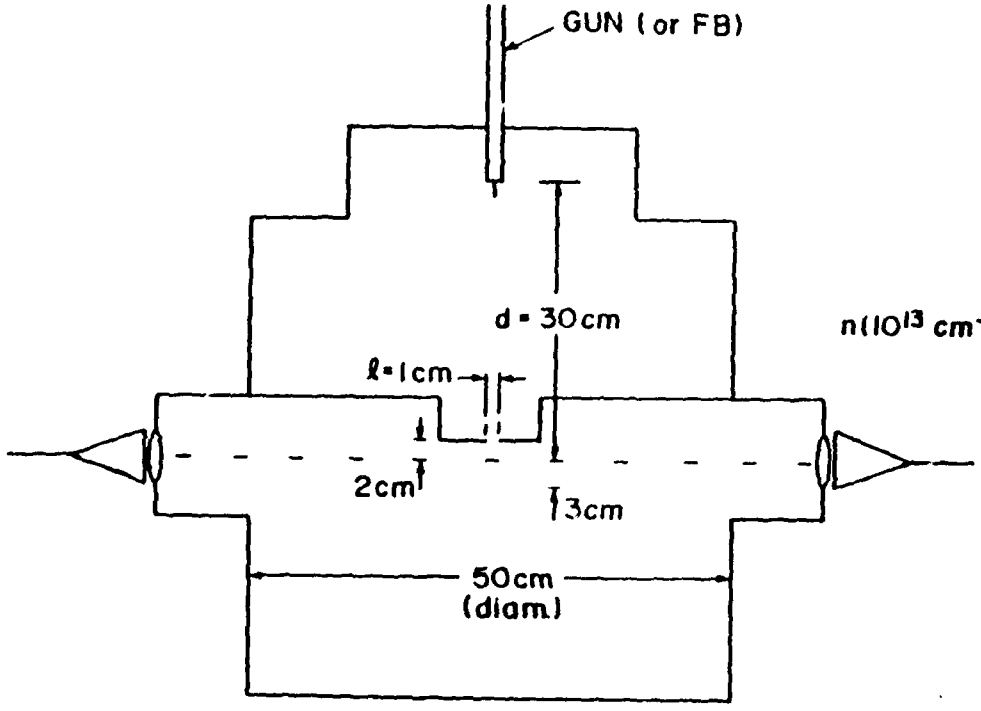
## TEST EXPERIMENT

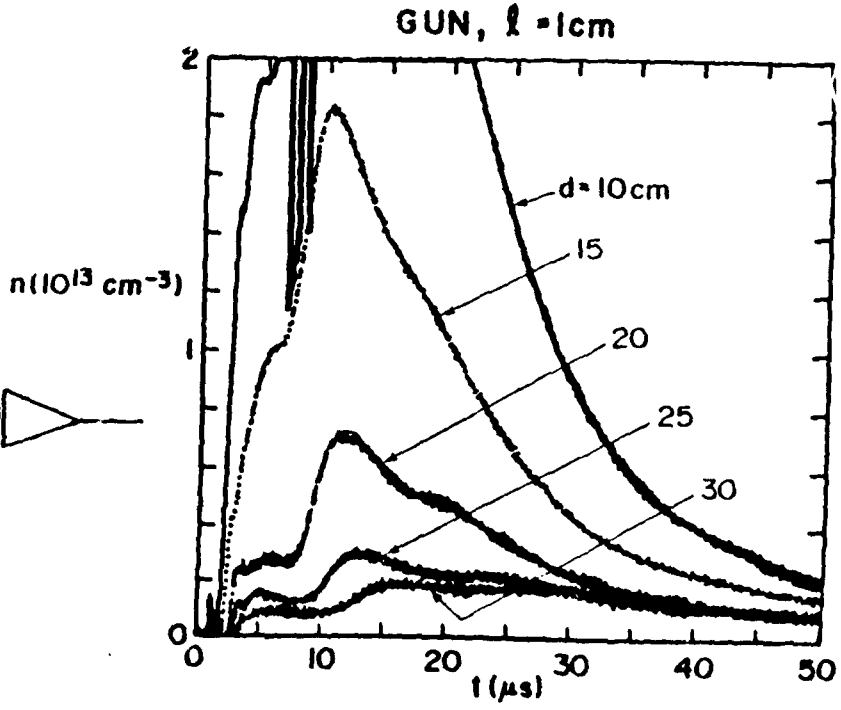


# NRL | PLASMA LOADED GYROTRON

## PLASMA GUN TESTS FOR PEOS

(COURTESY B.V. WEBER)



# NRL | PLASMA LOADED GYROTRON

## BASELINE EXPERIMENT: $TE_{62}$ VACUUM GYROTRON

- VEBA ACCELERATOR
  - BEAM VOLTAGE: 1.0 - 1.2 MV
  - BEAM CURRENT: 3 kA
- FREQUENCY: 35 GHz
- POWER : 200 MW ( = 6.7% EFFICIENCY)
- PULSE LENGTH: 40 ns
- OUTPUT MODE: $TE_{62}$

GOAL FOR PLASMA OPERATION: INCREASE BEAM CURRENT TO 10 kA WITH NO REDUCTION IN ELECTRONIC EFFICIENCY.

# NRL | PLASMA LOADED GYROTRON

## PREVIOUS EXPERIMENTS UTILIZING PLASMA NEUTRALIZATION

- Krementsov, et al., Lebedev Physics Institute, Moscow (1978).
  - $V = 320$ kV, $I = 1.2$ kA, $I_{vac} = 640$ A.
  - NEUTRAL PLASMA GENERATED BY COUNTER-PROPAGATING LOW ENERGY ELECTRON BEAM IN XENON.
  - DENSITY MEASURED BY 35 GHz INTERFEROMETRY.
  - $P(VAC) = 7$ MW, $P(n_p = 2 \times 10^{11}\ cm^{-3}) = 60$ MW.
  - PRESENCE OF BACKGROUND GAS DURRING THE HIGH-ENERGY ELECTRON BEAM PULSE RESULTS IN UNCERTAINTY IN $n_p$.
- Y. Carmel, et al., University of Md., College Park, MD (1988)
  - BWO
  - ARGON PLASMA GUN
  - PLASMA DENSITY NOT MEASURED
  - OUTPUT POWER INCREASED BY x 8.

# NRL | PLASMA LOADED GYROTRON

THE DISPERSION RELATION FOR MODES INA CYLINDRICAL, (MAGNETIZED) PLASMA-FILLED CAVITY IS

$$\frac{k_0 r_1}{k_{c1}^2}\left[D_m(Z_1) + \frac{\varepsilon_x}{\varepsilon_\perp} - \frac{\varepsilon_{||}}{\varepsilon_\perp}\frac{k_z}{k_0 r_1}\right] = \frac{k_0 r_2}{k_{c2}^2}\left[D_m(Z_2) + \frac{\varepsilon_x}{\varepsilon_\perp} - \frac{\varepsilon_{||}}{\varepsilon_\perp}\frac{k_z}{k_0 r_2}\right]$$

WHERE $D_m(Z) = Z J'_m(Z)/(m J_m(Z)$ AND $k_{c(1,2)}$ ARE SOLUTIONS OF

$$\varepsilon_\perp n_\perp^4 + n_\perp^2\left[n_z^2(\varepsilon_\perp + \varepsilon_{||}) - \varepsilon_\perp\varepsilon_{||} - (\varepsilon_x^2 - \varepsilon_\perp^2)\right] + \varepsilon_{||}\left[n_z^4 - 2n_z^2\varepsilon_\perp^2 + \varepsilon_\perp^2 - \varepsilon_x^2\right] = 0$$

$$n_\perp = k_{c(1,2)}/k_0 \quad ; \quad n_z = k_z/k_0 \quad ; \quad k_0 = \omega/c \quad ;$$

$$r_{(1,2)} = -\frac{k_z k_0 \varepsilon_x \varepsilon_{||}}{\varepsilon_\perp}\left[k_0^2(\varepsilon_\perp - \frac{\varepsilon_x^2}{\varepsilon_\perp}) - k_c^2 - k_0^2\right]^{-1}$$

$$\varepsilon_\perp = 1 - \frac{\omega_p^2}{\omega^2 - \Omega^2} \quad ; \quad \varepsilon_x = -\frac{\Omega}{\omega}\frac{\omega_p^2}{\omega^2 - \Omega^2} \quad ; \quad \varepsilon_{||} = 1 - \frac{\omega_p^2}{\omega^2}$$

# NRL | PLASMA LOADED GYROTRON

## FREQUENCY TUNABILITY: DISPERSION RELATION NEAR CUTOFF

IN THE LIMIT $k_z \rightarrow 0$ THE DISPERSION RELATION DECOUPLES INTO TE-MODES (X-MODE) AND TM-MODES (O-MODE). FOR GYROTRON APPLICATIONS THE TE-MODE IS ASSUMED TO BE THE MODE OF INTEREST.

TE-MODE:

$$D_m(k_c r_w) + \frac{\varepsilon_x}{\varepsilon_\perp} = 0 \qquad k_c^2 = k_0^2 \frac{\varepsilon_\perp^2 - \varepsilon_x^2}{\varepsilon_\perp}$$

WHERE

$$D_m(k_c r_w) = \frac{k_c r_w J'_m(k_c r_w)}{m J_m(k_c r_w)} \quad ; \quad k_0 = \omega/c$$

SOLUTION: SPECIFY $k_c r_w$ AND $(\Omega r_w/c)$; SOLVE FOR $\omega = \omega(\omega_p)$.

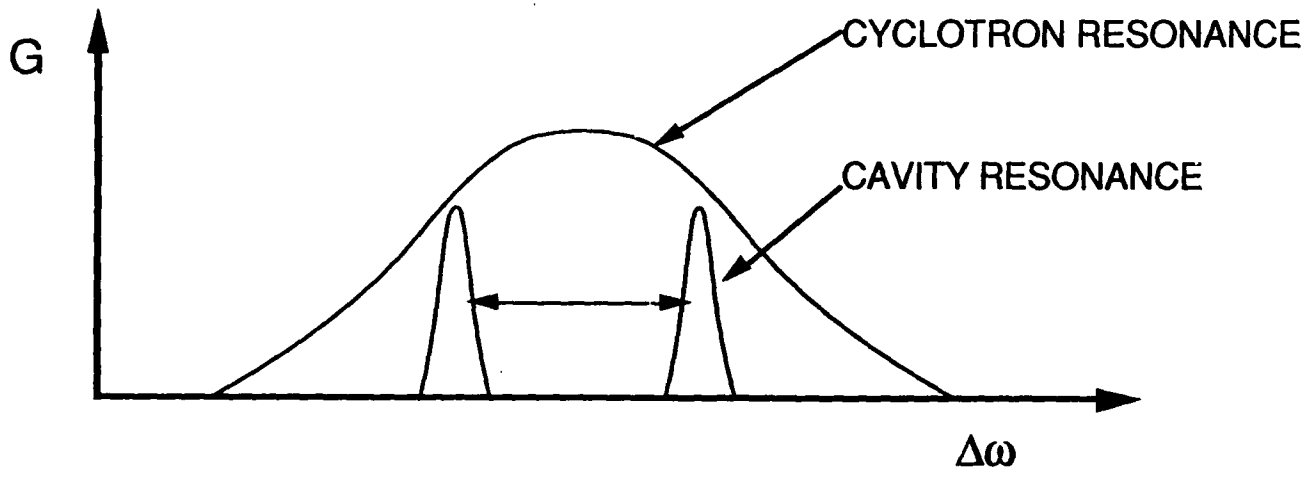
# NRL | PLASMA LOADED GYROTRON

## FREQUENCY TUNABILITY

THE CYCLOTRON RESONANCE IS TYPICALLY BROAD, $(\Delta\omega/\omega)\sim 5\%$

THE CAVITY RESONANCE IS NARROWER, $(\Delta\omega/\omega)\sim(1/Q) < 1\%$

TUNING WITH PLASMA DENSITY IS ACHIEVED BY SHIFTING THE NARROWER CAVITY RESONANCE WITHIN THE BROADER CYCLOTRON RESONANCE.

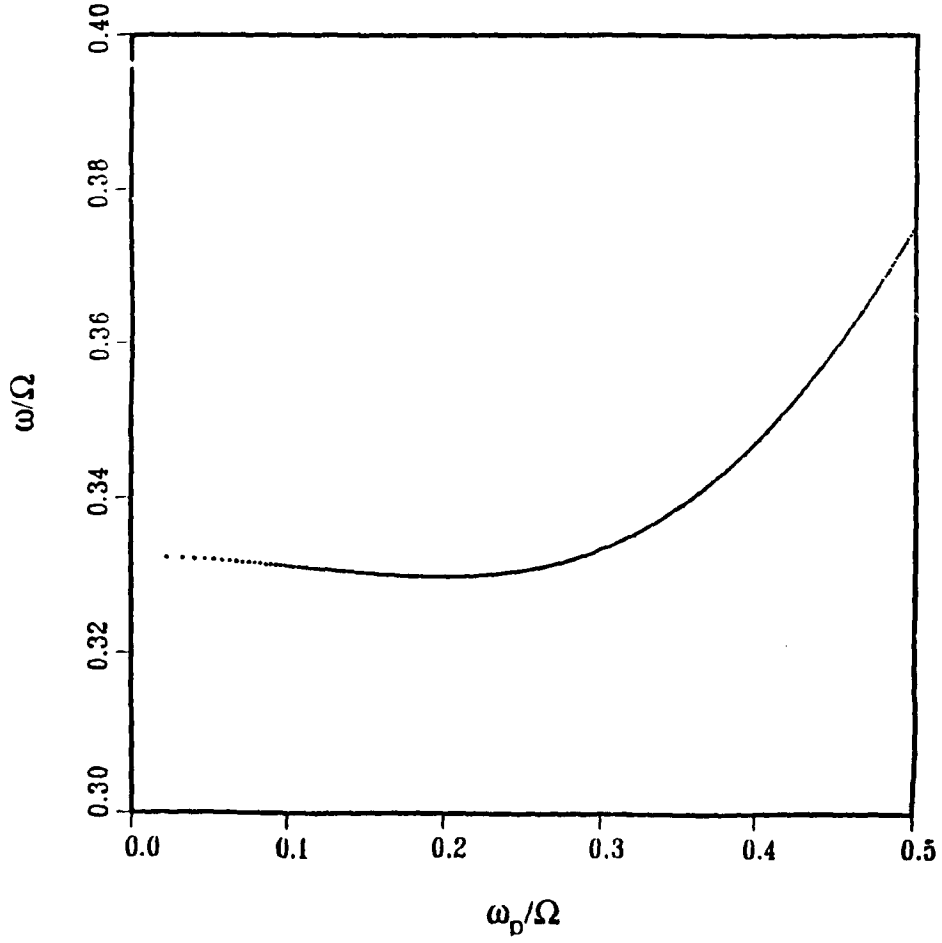


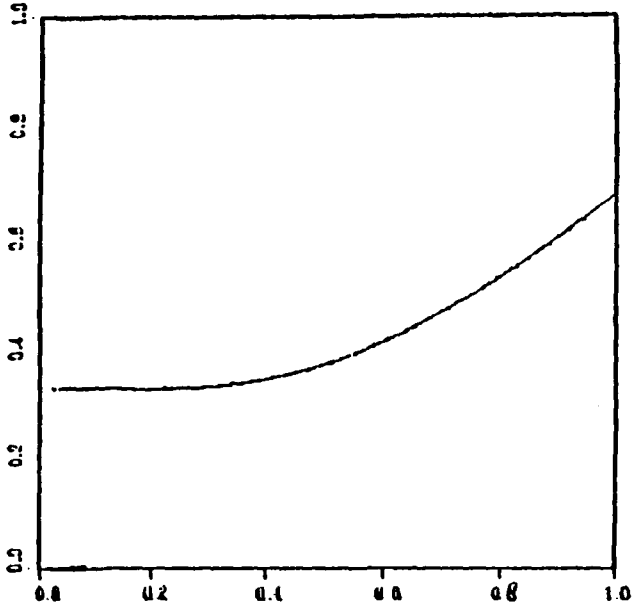

FOR OUR PARAMETERS $n_p \sim 1.6 \times 10^{13} \rightarrow (\Delta f/f)\sim 5\%$ (INCREASE)

# NRL | PLASMA LOADED GYROTRON

## FREQUENCY TUNABILITY, $f(\omega_p)$

$\gamma$=3, $f$(vac) = 35 GHz, $TE_{6,2}$ MODE



# NRL | PLASMA LOADED GYROTRON

## SUMMARY

- 70 GHz INTERFEROMETRY OPERATIONAL FOR PLASMA GUN TEST STAND( INCLUDES ELECTRIC LANGMUIR PROBES)

- PLASMA LOADED, SUPER-VACUUM CURRENT, TEST CAVITY IS IN FABRICATION. IT WILL USE 4 PLASMA GUNS, WITH INTRA-"CAVITY" 70 GHz INTERFEROMETRY AND INTRA-"CAVITY" ROGOWSKI COIL.

- SUPER-VACUUM CURRENT PROPAGATION EXPERIMENTS START MARCH 1, 1989.

# APPENDIX C

## The Design of a 100 GHz CARM Oscillator Experiment

**Naval Research Laboratory**

Washington, DC 20375-5000

NRL Memorandum Report 6273

# The Design of a 100 GHz CARM Oscillator Experiment

R. B. McCowan

*SAIC*
*McLean, VA*

A. W. Fliflet, S. H. Gold and A. K. Kinkead

*High Power Electromagnetic Radiation Branch*
*Plasma Physics Division*

W. M. Black

*High Power Electromagnetic Radiation Branch*
*Plasma Physics Division*
*and*
*Department of Electrical and Computer Engineering*
*George Mason University*
*Fairfax, VA*

V. L. Granatstein

*Department of Electrical Engineering*
*University of Maryland*
*College Park, MD*

M. Sucy

*JAYCOR, Inc.*
*Vienna, VA*

September 14, 1988

Approved for public release; distribution unlimited.

## CONTENTS


INTRODUCTION ..... 1

DESIGN OF THE BRAGG CAVITY ..... 2

THE CARM ELECTRON BEAM REQUIREMENTS ..... 5

DESIGN PROCEDURE FOR THE ANNULAR GUN ..... 6

SUMMARY ..... 7

ACKNOWLEDGEMENT ..... 7

REFERENCES ..... 7

DISTRIBUTION LIST ..... 19

# THE DESIGN OF A 100 GHZ CARM OSCILLATOR EXPERIMENT

## I. Introduction

High-power millimeter waves have many important applications. For example, millimeter-wave radar systems will yield higher target resolution than lower-frequency systems for a particular antenna aperture. Communications systems may benefit from a more strongly-focused radiation beam and from the larger information bandwidth available as the frequency is increased. Electron-cyclotron-resonance heating of fusion plasmas will require high-frequency radiation when strong magnetic fields are used to confine the plasma.[1]

The cyclotron auto-resonance maser (CARM) is a promising source of high-power radiation in the 100 GHz to 500 GHz frequency range that may impact the requirements of advanced systems for applications such as those mentioned above. The requirements for guide magnetic-field strength and electron energy in a CARM may be advantageous when compared with competing devices. Compared with a gyrotron, the required magnetic field strength requirement is substantially reduced. The CARM can provide mm and sub-mm radiation in the first electron-cyclotron harmonic using currently available magnet technology. For example, the experiment at the Naval Research Laboratory is designed to produce powers in excess of 10 MW at 100 GHz with a 600 kV beam and a magnetic field of only 25 kG, while a first-harmonic gyrotron operating at 100 GHz with the same beam voltage requires a magnetic field of over 70 kG. Compared with a conventional magnetostatic-wiggler FEL, the CARM can reach sub-mm wavelengths with a lower electron-beam voltage. For example, a 500 kV CARM oscillator has the potential for efficient multi-MW operation at wavelengths down to 0.75 mm with a 100 kG superconducting magnet; a 500 kV FEL oscillator with a 3 cm period magnetic-wiggler will produce radiation at 4.5 mm.[2]

The CARM can be either an amplifier or an oscillator. An oscillator design removes the need for an input source and input couplers. In addition, amplifier operation requires suppression of backward-wave instabilities.

The CARM oscillator, like the gyrotron oscillator, is a cyclotron maser. In contrast to the gyrotron, which requires an electron beam with a large momentum pitch angle (typically $p_\perp/p_z > 1$), the CARM has an electron beam with a low to moderate pitch angle ($p_\perp/p_z < 0.7$) and a substantial amount of axial momentum. The CARM benefits from the doppler upshift provided by the axial velocity of the beam: the operating frequency of the CARM is approximately $\gamma^2 f_c$, where $f_c$ is the relativistic cyclotron frequency associated

Manuscript approved June 21, 1988.

with the axial magnetic field, and $\gamma$ is the usual relativistic factor. The dispersion relation for the NRL CARM is shown in Fig. 1. The CARM interaction corresponds to the upper intersection of the beam cyclotron mode and the waveguide mode.

There is a fairly extensive literature on the theory and simulation of CARMs and other doppler-shifted cyclotron maser configurations [3]-[10]. The only experimental studies reported to date, however, have been the experiments of Botvinnik et al [11],[12], who achieved 6 MW at a wavelength of 4.3 mm and 4% efficiency, and 10 MW at a wavelength of 2.4 mm and 2% efficiency. A major objective of the present experiment is the achievement of higher efficiency, ~20%, which is predicted by theory for the CARM.

Fig. 2 shows the important components of the experiment. The electron beam is launched from the velvet emitter surface into a uniform magnetic field provided by the gun solenoid. A magnetic kicker supplies transverse momentum. Adiabatic compression in the input taper region increases the momentum pitch ratio to 0.6 in a magnetic field of 24 kG. The beam generates microwaves in a Bragg cavity[13], and is collected on the wall of the output taper.

Competition between the desired mode and other available modes can lead to unstable operation; the density of modes which can be excited by the CARM interaction is generally high. In addition, gyrotron modes, which are nearly cut-off and operate near the cyclotron frequency, also present significant competition. Electron beam velocity spread, which leads to lowered efficiency, is also a critical factor in the design of a CARM oscillator. This paper presents the design of an electron gun and a microwave resonator to achieve a highly efficient CARM.

## II. Design of the Bragg cavity

In order that the CARM oscillate in the correct mode at the Doppler-shifted frequency, the oscillation-threshold current of the CARM mode should be lower than the threshold currents of competing modes. The cavity and beam parameters chosen for this experiment are based on the theoretical study of the CARM interaction given in Ref. 14. As shown in that paper, the efficiency of the CARM is optimized by choosing a normalized interaction length $\mu = 8$, and a normalized wave amplitude $F = 0.2$, where $\mu$ and F are defined below.

$$\mu \equiv \frac{\beta_{\perp o}^2}{2} \frac{1 - \beta_{ph}^{-2}}{1 - \beta_z/\beta_{ph}} \frac{\omega L}{c}, \tag{1}$$

and,

$$F \equiv \frac{4k_z}{\gamma_o m_o c^2} \frac{C_{mn} J_{m-s}(k_{mn} r_o) \times \left(1 - \beta_z/\beta_{ph}\right)}{2\beta_{\perp o}^3 \left(1 - \beta_{ph}^{-2}\right)} \Pi, \tag{2}$$

where $\Pi$ is the mode-equivalent-voltage amplitude[12], $\beta_z$ is the axial velocity of the electrons, $\beta_{ph}$ is the phase velocity of the radiation, $k_{mn}$ is the wave number of the radiation, $r_o$ is the mean radius of the electron beam, $\beta_{\perp o}$ is the transverse velocity of the electrons, L is the length of the cavity, $\omega$ is the angular frequency of the radiation, and $C_{mn}$ is a beam-wave coupling coefficient that depends on the mode indices.[15]

Gyrotron modes are the most dangerous competing modes because the gyrotron interaction is the strongest cyclotron-maser interaction; the cavity must be kept short to raise the threshold currents of the gyrotron modes. The Q of the resonator is 1500 for the design mode, which makes the oscillation threshold current for the CARM approximately 50 Amp; the gyrotron interaction must have a higher start current. In order to minimize the total cavity length, the reflectors must be short.

A cavity design that satisfies the criteria for a CARM oscillator is the Bragg cavity. The Bragg cavity is a section of smooth waveguide connecting two rippled-waveguide reflectors[13]. For the proper mode, for which the guide wavelength is twice the ripple period, constructive interference of the small reflections from the ripples can provide a strong reflection. Whispering-gallery ($TE_{m1}$) modes couple most strongly to the corrugations[16], and therefore have the highest reflectivities. Other modes can have low reflectivity. The Q of the resonator can be increased either by lengthening the uncorrugated section, or by increasing the reflectivity of the corrugated sections. Since each reflector provides a 90° phase shift, the length of the smooth section must be such that the total path length of the radiation in one round trip of the resonator is an odd integral number of half wavelengths.

If the corrugated sections are highly reflective, the Q of the Bragg resonator is

$$Q = \frac{k^2 L_{eff}}{k_z(1 - R_1 R_2)} \tag{3}$$

where k is the free-space wave number, $k_z$ is the waveguide axial wave number, and $R_1$ and $R_2$ are the reflectivities of the corrugated sections which are given by

$$R = \mathrm{Tanh}^2\, GL. \tag{4}$$

$L_{eff}$ is the effective length of the cavity, which is larger than the length of the smooth-waveguide section because of the energy stored in the rippled-waveguide sections.

$$L_{eff} = L_0 + \frac{1}{G_1}\left(1 - e^{-G_1 L_1}\right) + \frac{1}{G_2}\left(1 - e^{-G_2 L_2}\right), \tag{5}$$

where $L_1$ and $L_2$ are the lengths of the reflectors; $G_1$ and $G_2$, are the coupling coefficients of the reflectors and are

$$G = \frac{l_0}{2}\left\{\frac{x'^4_{mn} - m^2a^2\left(\omega^2/c^2 + \beta^2\right)}{\beta a^3\left(x'^2_{mn} - m^2\right)}\right\} \tag{6}$$

for the TE modes, and

$$G = \frac{l_0}{2a}\frac{\omega^2/c^2 + \beta^2}{\beta} \tag{7}$$

for the TM modes[3],[16]. $l_0$ is the length of the rippled section, $x'_{mn}$ is the zero of the derivative of the Bessel function with respect to its argument, m as the azimuthal index, a is the waveguide wall radius, $\omega$ is the angular frequency, $\beta$ is the wave number of the radiation, and c is the speed of light.

In order for the device to work successfully as a CARM, the threshold currents of gyrotron modes must be greater than the threshold current of the desired CARM mode. The CARM has a beam with a low to moderate ratio ($\alpha$) of transverse momentum to axial momentum, which raises the threshold current of the gyrotron modes. Even so, the Q of the gyrotron modes must be kept as low as possible, which means the cavity must be kept as short as possible. The smallest possible Q of a gyrotron mode in a straight cavity of length $L_0$ is the minimum diffraction Q:

$$Q_{min} = \frac{4\pi}{p}\left(\frac{L_0}{\lambda_{fs}}\right)^2, \tag{8}$$

where $\lambda_{fs}$ is the free-space wavelength of the near-cutoff mode, and p is the number of half wavelengths in the cavity. The shorter the cavity, the less dangerous the gyrotron modes.

Table I summarizes the design of the cavity for the NRL 100 GHz experiment, and Fig 3 shows the relationship between the cavity geometry and the radiation envelope. The Q of the resonator for the CARM must be high enough to ensure that that competing gyrotron modes will not start before the CARM mode starts. For the parameters of the NRL experiment,the highest Q gyrotron mode has a Q of approximately 500. In order to satisfy the requirement that the CARM mode oscillates at a lower current than any competing gyrotron mode, the Q of the CARM operating mode must exceed 1400. Since a reflectivity of 90% was chosen for the downstream reflector and a reflectivity of 98% was chosen for the upstream reflector, the smooth section of the resonator must be 2.5 cm long. The upstream reflector is the shallower of the two corrugated sections, and hence has the longer radiation e-folding length. The upstream and downstream reflectors are 3 cm and 1.5 cm long respectively.

The time dependence of the CARM oscillator driven by a pulsed-power system must be considered. A model of the voltage pulse that consists of a linear voltage rise from zero to the operating voltage, followed by a constant voltage for the rest of the pulse was chosen to be used in a single-mode, time-dependent, fixed-field CARM oscillator code.

The results of this code, shown in fig 4, indicate that a 70 nsec pulse is more than adequate to drive the CARM mode to saturation. In addition, the start-up of the various cavity modes during the rise of the pulse must be considered. Fig 5 shows a plot of the start current for the modes in the Bragg cavity for a beam with the parameters outlined in the next section. The starting currents are calculated for a fixed field profile and for voltages ranging from 0 to 700 kV, while the magnetic field is kept constant. $\alpha$ is assumed proportional to V. The current in the beginning of the pulse is assumed to vary as the voltage to the 3/2 power in order to model space-charge limited flow from a relativistic diode.. As the current rises in the pulse, the $TE_{81}$ mode is expected to start first, followed by the $TE_{71}$, which is followed by the $TE_{61}$ mode. The major competing gyrotron modes are also plotted; they are denoted by the dashed line.

The ohmic Q of the cavity is approximately 16000[16]. For a 10 MW output power, approximately 1 MW is dissipated by wall currents. Since the cavity wall has an effective area of 20 $cm^2$, the power density dissipated by wall currents is 50 $kW/cm^2$, acceptable only for short-pulse, low-duty-factor operation.

## III. The CARM electron beam requirements

For the NRL 100 GHz, 10 MW CARM design, the requirements for the electron beam are unique. A 600 kV, 200 A. electron beam is needed for optimum efficiency with the present cavity design. The beam requires transverse velocity $v_\perp/c \cong 1/\gamma$ to achieve high efficiency with significant Doppler upshift. Thus, for the current design, $\alpha \equiv v_\perp/v_\parallel \cong 0.6$. The waveguide mode is the $TE_{61}$ whispering gallery mode, and has a group velocity of 0.89c. Although this group velocity is less than optimum for autoresonance, it leads to a short interaction length (approximately 8 cyclotron orbits) and reduced sensitivity to beam spread.

The constraint on beam axial-velocity spread can be estimated by a simple coherence argument, which leads to the condition $\Delta v_z/v_z < \lambda/2L$. The constraint on energy spread for a beam with no pitch angle spread is

$$\Delta\gamma/\gamma < \frac{1 - \gamma_o^{-2}}{\left(1 + \alpha^2\right)\left(\Omega/\omega - \gamma_o^{-2}\right)} \tag{10}$$

Nonlinear efficiency calculations indicate that if the velocity spread is within these constraints, the efficiency of the interaction will be degraded only slightly. According to Fig. 6, which plots the beam quality constraints, the interaction will be unaffected if the axial velocity spread is kept less than 3%. These curves also show that there is greater sensitivity to pitch-angle spread than to energy spread, a feature related to the auto-resonant character of the interaction.

Fig. 7, which shows the coupling strength[15] of the $TE_{61}$ mode as a function of radial beam position, demonstrates that the beam must have most of the current concentrated near the wall in order that it interact strongly with the operating mode.

The electron gun is designed to produce a high-quality electron beam without requiring beam scraping. The electrode shapes are chosen to compensate for space-charge repulsion within the electron beam. The beam is launched parallel to the guide magnetic field. Downstream from the diode, a nonadiabatic magnetic region provides the required transverse momentum. Separation of the beam formation stage from the transverse momentum pump allows each stage to be analyzed independently.

## IV. Design procedure for the annular gun

The cold-cathode electron gun was designed in two steps: electrode synthesis, and validation of the synthesized electrodes with an electron trajectory code[17]. The approximate electrode shapes were determined using an electrode-synthesis technique[18]. The synthesis code calculates the charge distribution due to a space-charge-limited, laminar flow of electrons based on a one-dimensional, planar, relativistic model. From the charge distribution, the code determines the equipotentials by solving Laplace's equation in regions external to the beam. Electrodes are placed on these equipotentials. In order to predict the behavior of the electron beam in a realistic, two-dimensional cylindrical geometry, the electrode surfaces chosen for the gun were used in a number of electron trajectory code runs. The trajectory code is the best way to determine the velocity spread in the beam, as well as to determine the transverse momentum. Fig. 8 shows the shape of the cathode and anode.

The anode-cathode system designed by the above procedure produces a cold annular beam with negligible transverse momentum. In order to efficiently produce radiation, the present CARM oscillator requires an electron beam with $\alpha = 0.6$. Therefore it is necessary to impart transverse momentum to the beam. A magnetic kicker provides the required transverse momentum.

The magnetic kicker consists of a local depression of the axial magnetic field and is similar to the one used by Gold et. al[19] in the NRL high voltage gyrotron experiments. If the magnitude of the magnetic field changes on a length scale shorter than a cyclotron orbit, $(dB_z/dz)/B_z < 2\pi v_z/\omega_c$, beam axial momentum is converted to beam transverse momentum. A magnetic kicker is simple to construct: a coil is wound on a section of the vacuum vessel, and a current is driven through the coil to produce a field opposite in direction to the main axial field. The combination of the nearly cold beam followed by a magnetic kicker provides a flexible way to create an electron beam suitable for the CARM; proper choice of operating parameters will generate an electron beam with any $\alpha$ between 0.5 and 0.7, and an axial-velocity spread that shouldn't exceed 3%.

At the operating voltage of 600 kV, the electron emitter must provide uniform electron emission with an emitter surface field strength of 125 kV. At the same time, the focus electrodes, which are subjected to a field strength of 400 kV/cm, must withstand electrical breakdown. Therefore, the diode materials were carefully chosen. The emission surface is cotton velvet. The tufts of the velvet provide local enhancements to the electric field, and encourage electrical breakdown and plasma formation. Reliable emission at electric fields less than 100 kV/cm has been achieved using cotton velvet cathodes[20]. The velvet is attached to the aluminum cathode using silver-bearing epoxy.

The focus electrode is constructed of anodized aluminum. Hard coat anodization creates a corundum surface .002" thick. This surface will prevent emission at field strengths greater than 400 kV/cm, provided that the voltage pulse is less than 100 nsec long[21],[22]. Since the pulse length of the accelerator used for the CARM experiment is less than 70 nsec, the anodized surface will hold off all emission from the focus electrodes.

## V. Summary

The basic design for the 100 GHz, 10 MW NRL CARM oscillator has been presented. The basic components of the CARM are a pulseline accelerator, a novel 600 kV, 200 A field emission electron gun designed for $p_\perp/p_z = 0.6$ and $\Delta p_z/p_z < 3\%$, and a "whispering gallery" mode rippled wall cavity. The oscillator is designed to operate at an efficiency of over 20%. Construction of the experimental apparatus is completed and the electron gun is undergoing preliminary tests.

## VI. Acknowledgement

This work was supported by the Office of Naval Research

## REFERENCES

1) Granatstein, V. L., 1988, *Proc. of the 1987 Particle Accelerator Conf.*, (Washington, D. C. IEEE)

2) Sprangle, P., Smith, R. A., and Granatstein, V. L., 1979, in *Infrared and Millimeter waves*, (K. Button, ed.) Vol 1. Academic Press, New York.

3) Petelin, M. I., 1974, On the theory of ultrarelativistic cyclotron self-resonance masers. *Izv Vuzov Radiofizika*, **17**, 902-908. (*Radiophys. Quantum Electron.*, **17**, 686-690).

4) Kanavets, V. I., and Klimov, O. I., 1976, The electron efficiency of a monotron and klystron with a relativistic polyhelical electron beam. *Radiotekhnika i Electronika*, **21**, 2359-2364. (*Radio Engng. Electron. Phys.*, **21**, 78-73).

5) Ginzburg, N. S., Zarnitsyna, I. G., and Nusinovich, G. S., 1981, Theory of relativistic cyclotron-resonance maser amplifiers. *Izv. Vssh. Ucheb. Zaved., Radiofizika*, **24**, 481-490. (*Radiophys. Quant. Electron.*, **24**, 331-338).

6) Vomvoridis, J. L., 1982, An efficient Doppler-shifted electron-cyclotron maser oscillator. *Int J. Electron.*, **53**, 555-571.

7) Bratman, V. L., Ginzburg, N. S., Nusinovich, G. S., Petelin, M. I., and Strelkov, P. S., 1981, Relativistic gyrotrons and cyclotron autoresonance masers. *Int. J. Electron.*, **51**, 541-567.

8) Lin, A. T., 1984, Doppler shift dominated cyclotron masers. *Int. J. Electron.*, **57**, 1097-1107.

9) Lin, A. T., and Lin, C. C., 1985, Doppler shift dominated cyclotron maser amplifiers. *Int. J. Infrared Millimeter Waves*, **6**, 41-51.

10) Sprangle, P., Tang, C. M., and Serafim, P., 1985, Induced resonance electron cyclotron (IREC) masers. *Proc. 7th Int. FEL Conf.*, Tahoe City, California, U.S.A., 8-13 September.

11) Botvinnik, I. E., Bratman, V. L., Volkov, A. B., Denisov, G. G., Kol'chugin, B. D., and Ofitserov, M. M., 1982, Cyclotron-autoresonance maser with a wavelength of 2.4 mm. *Pis'ma Zh. Tekh. Fiz.*, **8**, 1386-1389. (*Sov. Tech. Phys. Lett.*, **8**, 596-597).

12) Botvinnik, I. E., Bratman, V. L., Volkov, A. B.,Ginzburg, N. S, Denisov, G. G., Kol'chugin, B. D., and Ofitserov, M. M., Petelin, M. I., 1982, *Pis'ma Zh. Eksp. Teor. Fiz.*, **35**, 418. (*JETP Lett.*, **35**, 516).

13) Bratman, V. L., Denisov, G. G., Ginzburg, N. S., and Petelin, M. I., 1983, FEL's with Bragg Reflection Resonators: Cyclotron Autoresonance Masers Versus Ubitrons. *I.E.E.E. J. Quant. Electron.*,**19** , 282.

14) Fliflet, A. W., 1986, Linear and non-linear theory of the Doppler-shifted cyclotron resonance maser based on TE and TM waveguide modes. *Int. J. Electronics*, VOL. **61**, NO 6, 1049-1080.

15) Gold, S. H., Fliflet, A. W., Manheimer, W. M., Black, W. M., Granatstein, V. L., Kinkead, A. K., Hardesty, D. L., and Sucy, M., 1985, High-voltage $K_a$-band gyrotron experiment. *IEEE Trans. on Plasma Science*, **PS-13**, No 6, 374-382.

16) McCowan, R. B., Fliflet, A. W., Gold, S. H., Granatstein, V. L., Wang, M. C., 1988, Design of a waveguide resonator with rippled-wall reflectors for a 100 GHz CARM oscillator experiment., *International Journal of Electronics*, To be published.

17) Herrmannsfeldt, W. B., 1979, SLAC Report *SLAC-226, UC-28 (A)*. Stanford University, Stanford, CA.

18) Finn, J. M., Fliflet, A. W., and Manheimer, W. M., 1986, One dimensional models for relativistic electron beam diode design. *Int. J. Electron.*, **61**, No 6, 985-1003.

19) Gold, S. H., Fliflet, A. W., Manheimer, W. M., McCowan, R. B., Black, W. M., Lee, R. C., Granatstein, V. L., Kinkead, A. K., Hardesty, D. L., and Sucy, M., 1987, High peak power $K_a$-band gyrotron oscillator experiment., *Phys. Fluids* ,**30**(7), p 2226-2238.

20) Adler, R. J., Kiuttu, G.F., Simpkins, B. E., Sullivan, D. J., and Voss, D. E., 1985, Improved electron emission by use of a cloth fiber cathode. *Rev. Sci. Instrumen.*, **56**, NO 5, 766-767.

21) Fink, J., Schilling, H. B., and Schumacher, U., 1980, Development and investigation of relativistic electron beams with finite energy spread and improved emittance. *J. Appl. Phys.*, **51**, NO 6, 2995-3000.

22) Kirkpatrick, D. A., Shefer, R. E., and Bekefi, G., 1985,High brightness electrostatically focused field emission gun for free electron laser applications. *J. Appl. Phys.*, **57**, NO 11, 5011-5016.

Table I: NRL 100 GHZ carm oscillator parameters

| | |
|---|---|
| Beam Voltage | 600 kV |
| Beam Current | 200 A |
| Pulse Length | 50 nsec |
| Magnetic Field | 25 kG |
| Phase Velocity | 1.17c |
| $\Omega_c$ | 32 GHz |
| $\alpha \equiv v_\perp/v_z$ | 0.6 |
| Efficiency | 20% |
| Power | 24 MW |
| Operating Mode | $TE_{61}$ |
| Cavity Parameters: | |
| Mean Wall Diameter | 1.59 cm |
| Upstream Reflector | |
| Length | ~3 cm (18 periods) |
| Ripple Depth | 0.25 mm |
| Ripple Period | 1.68 mm |
| Reflectivity | 99% |
| Downstream Reflector | |
| Length | ~1.5 cm (9 periods) |
| Ripple Depth | 0.31 mm |
| Ripple Period | 1.68 mm |
| Reflectivity | 90% |
| Center Section Length | 2.6 cm |
| Cavity Q | 1500 |

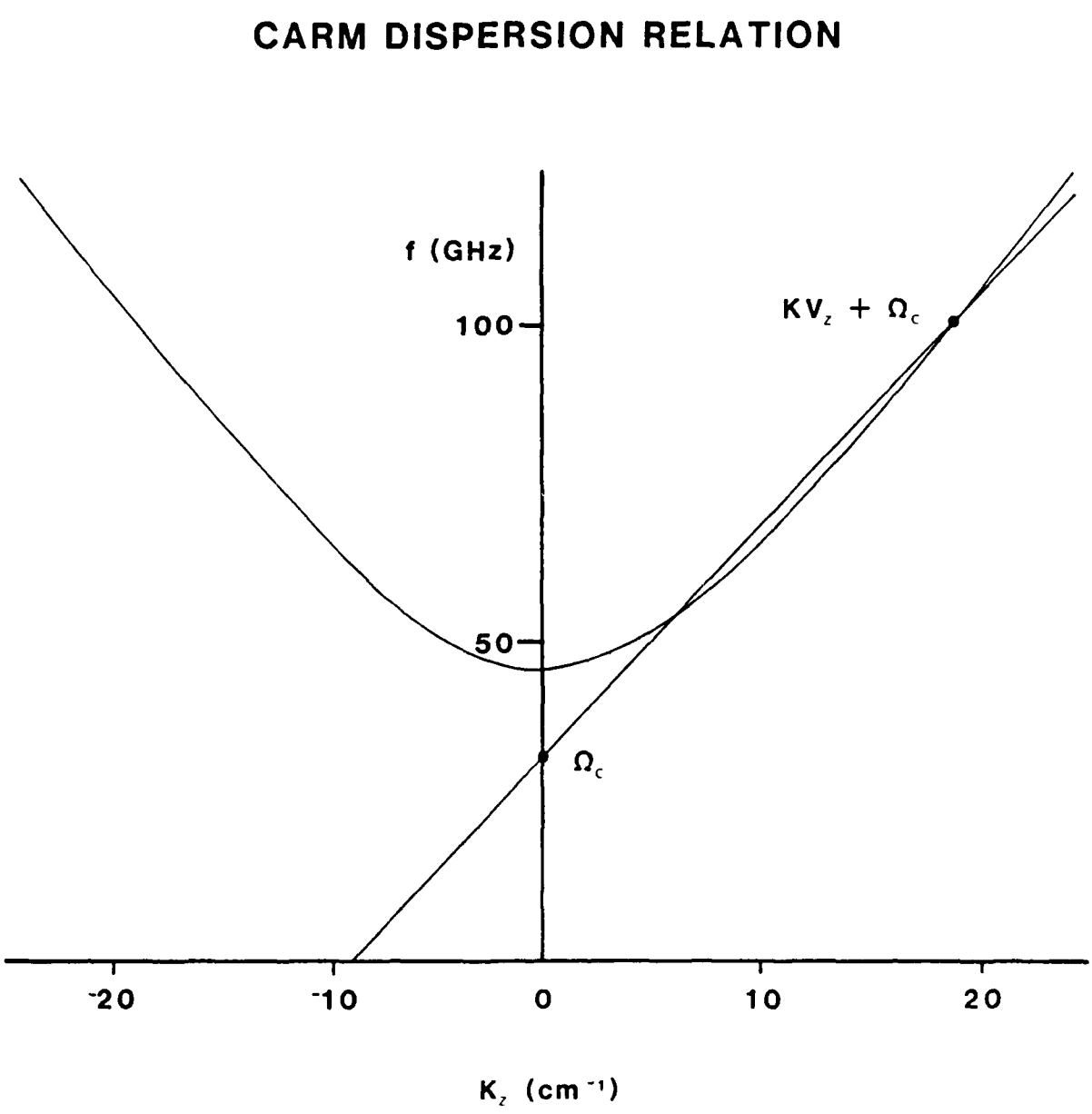



Fig. 1. The dispersion relation for the NRL 100 GHz. CARM experiment. The high frequency intersection of the electron beam line with the $TE_{61}$ waveguide dispersion relation is the CARM operating regime. The lower frequency intersection is a competing gyrotron mode.

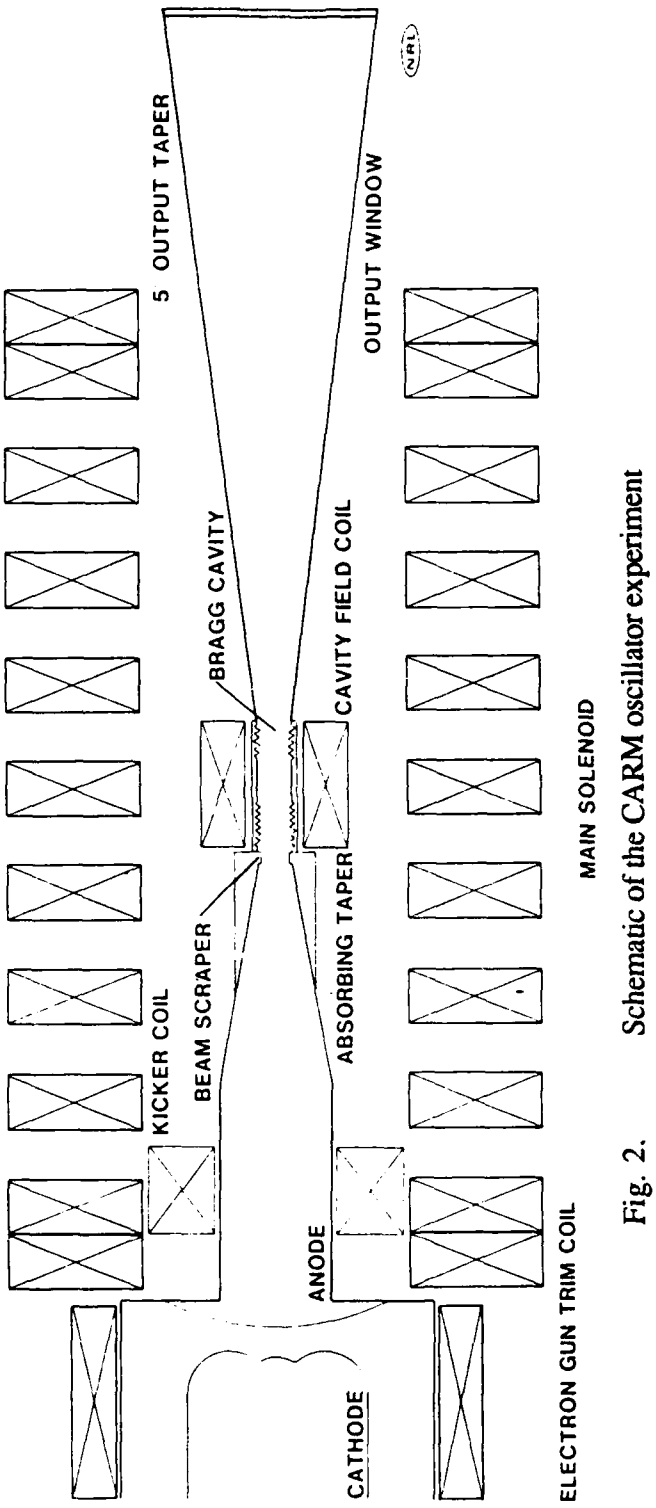



Fig. 2. Schematic of the CARM oscillator experiment

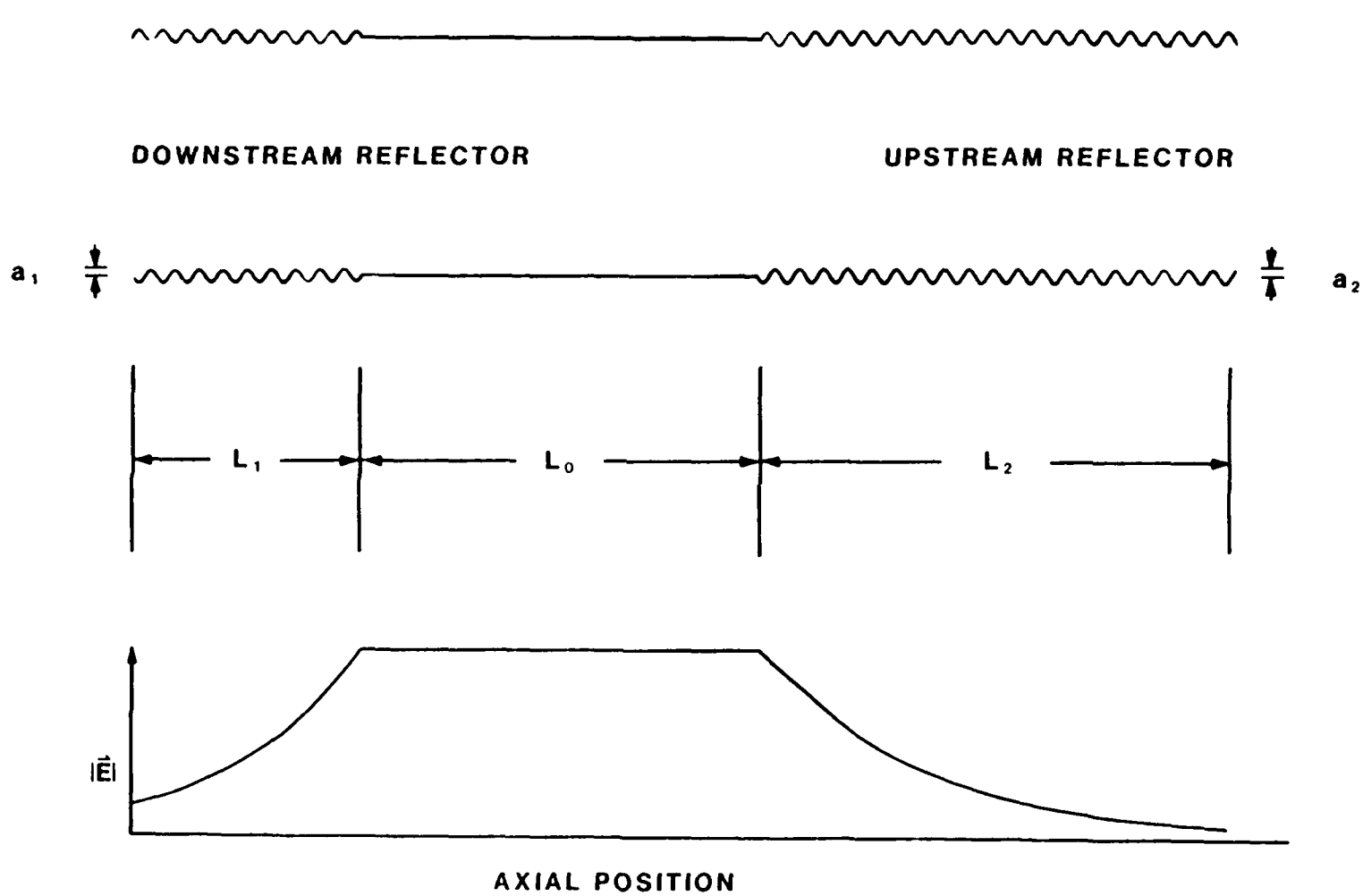



Fig. 3. The geometry of the CARM cavity with the electric field amplitude profile.

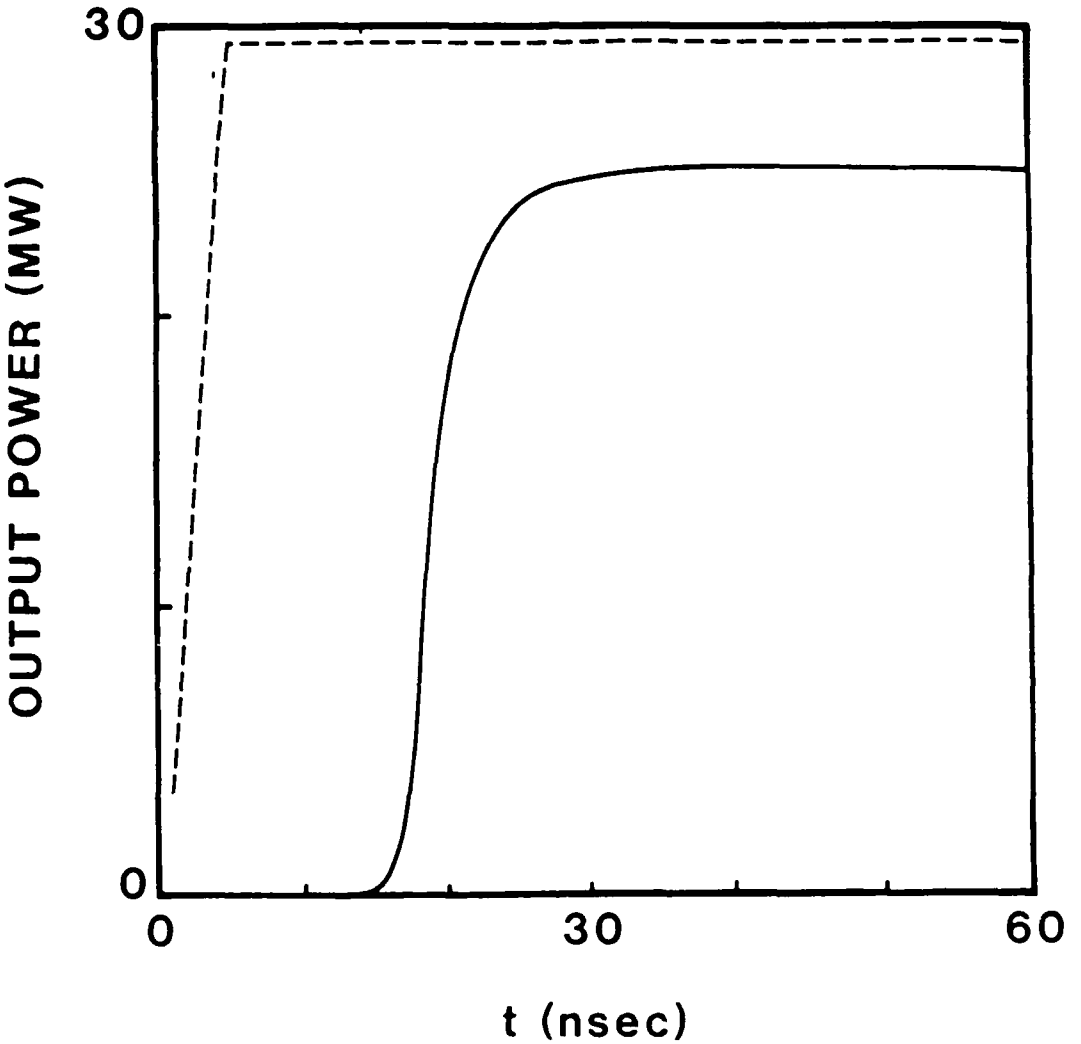



Fig. 4. Results of the time-dependent CARM oscillator code show that the 70 nsec pulse should be sufficient to drive the interaction to saturation. The dashed line represents the voltage waveform.

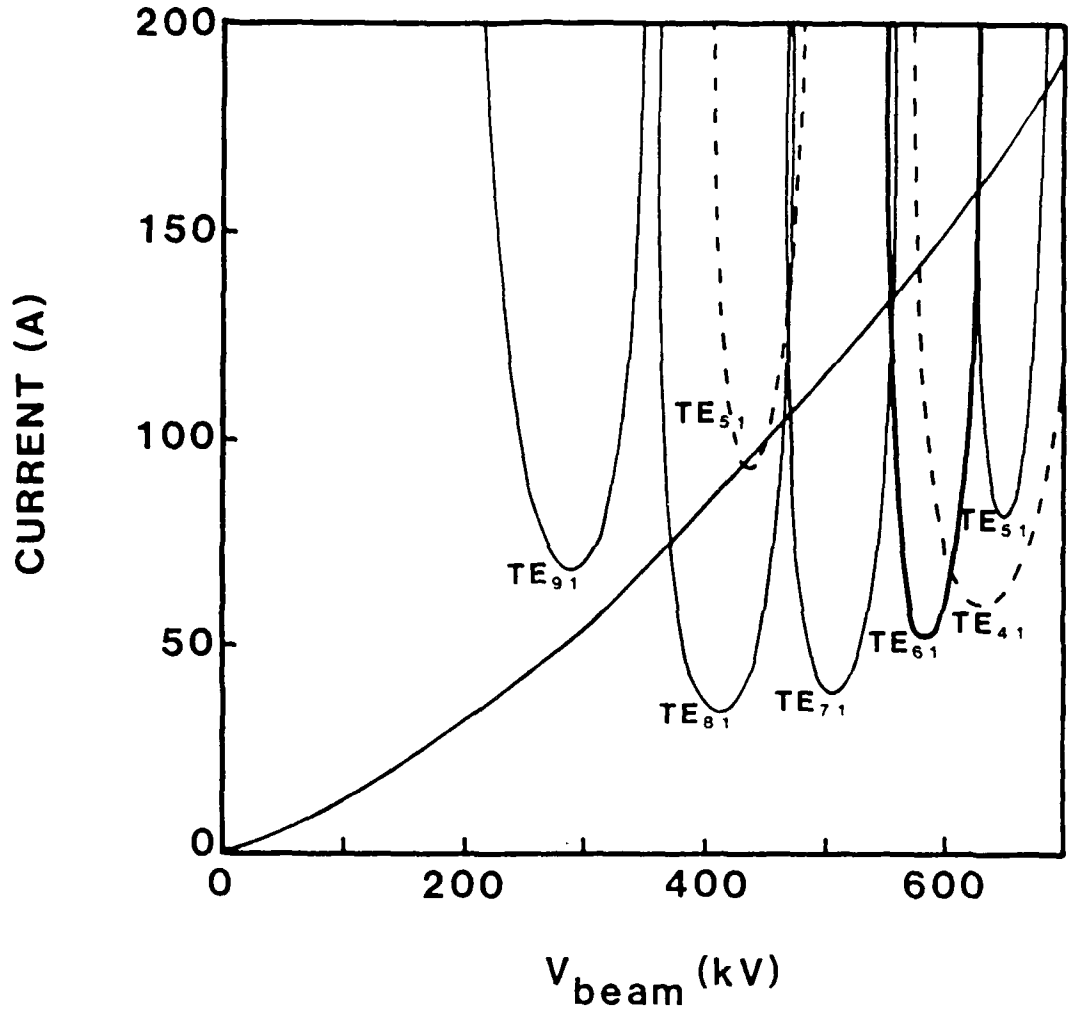



Fig. 5. Oscillation threshold currents for modes in the Bragg cavity for an electron beam with $\alpha$=0.6 and a Langmuir-Child current-voltage behavior of the electron beam.

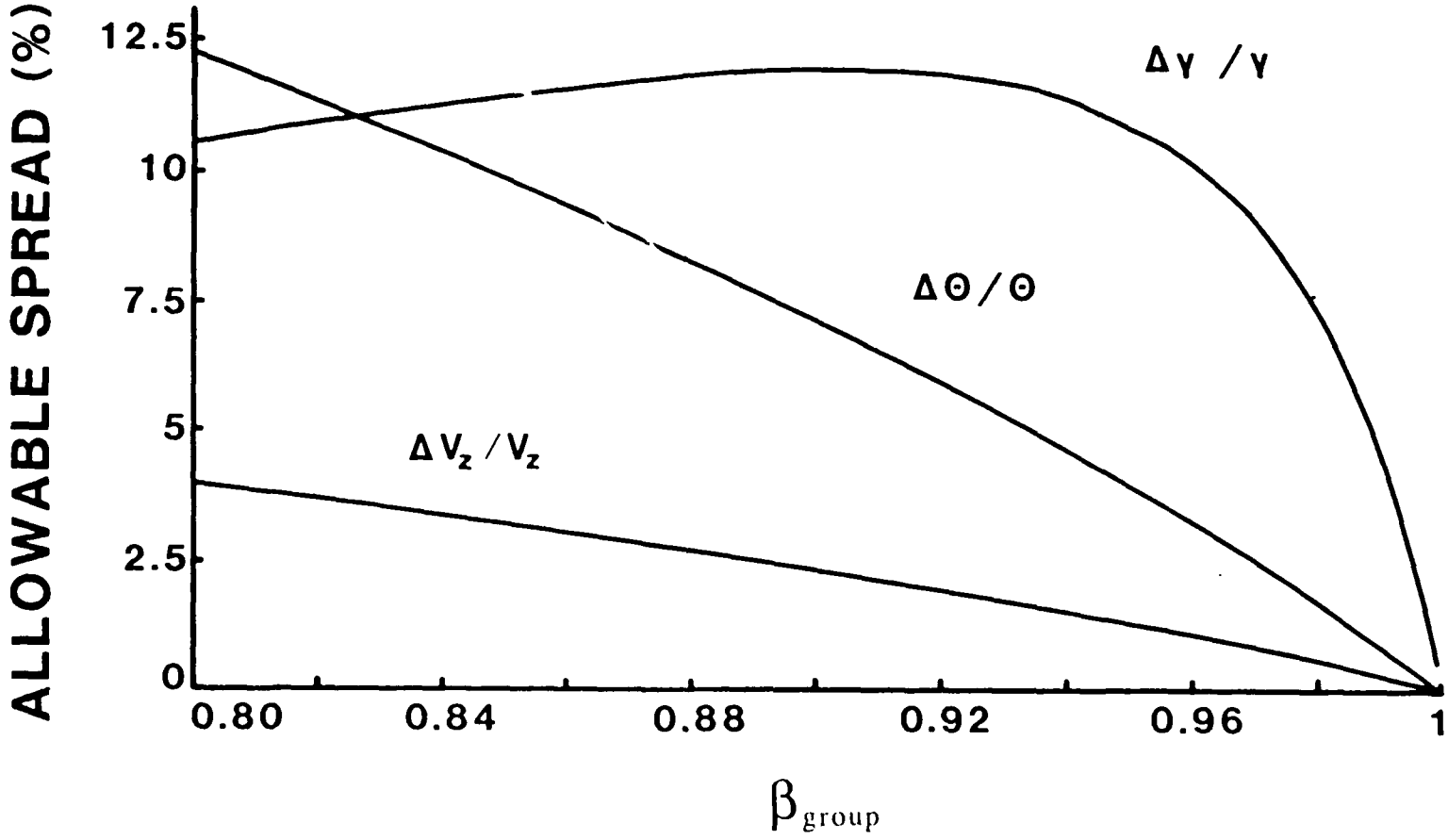



Fig. 6. The constraints on beam quality for high-efficiency CARM operation. If the beam quality is kept within these constraints the interaction will operate at nearly peak theoretical efficiency.

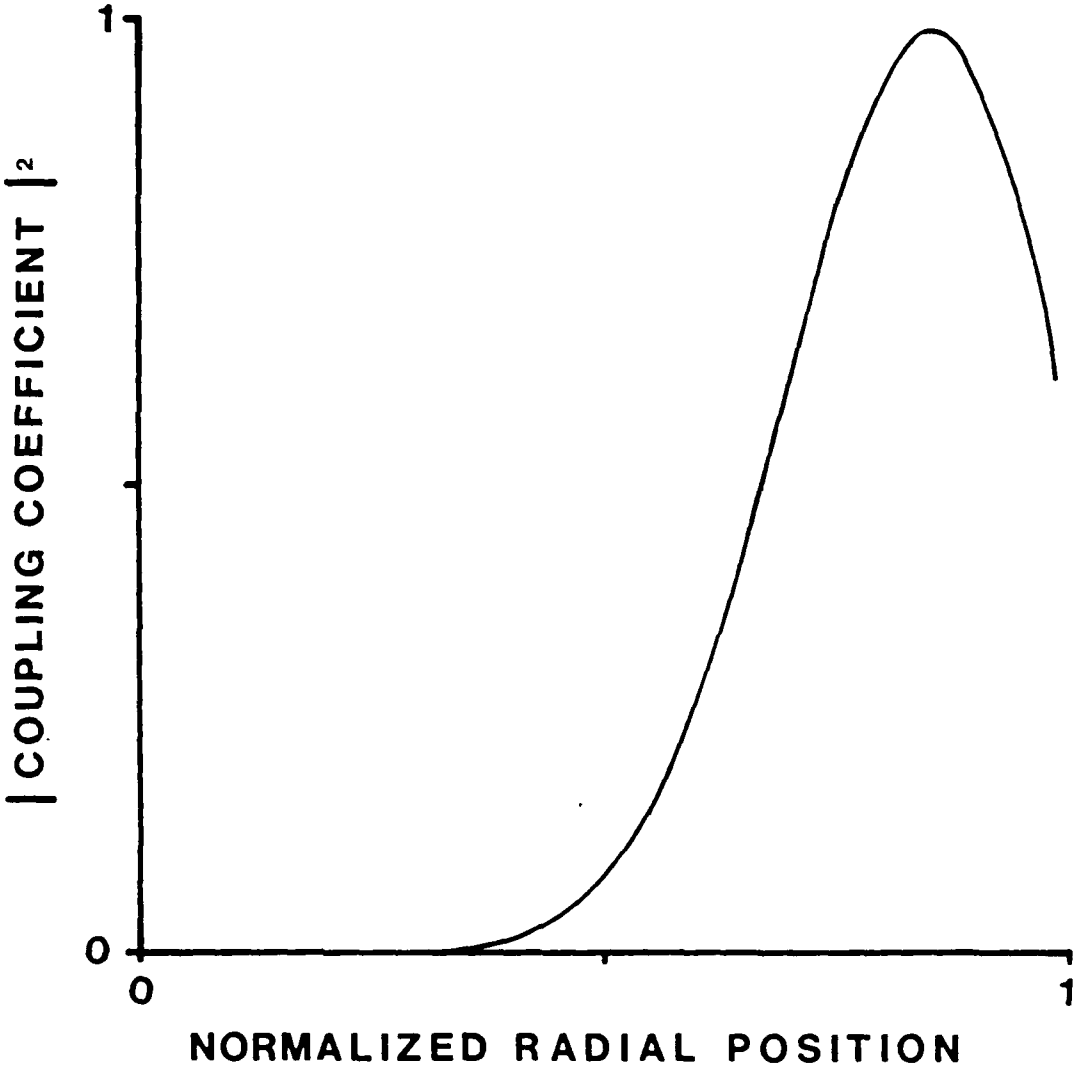



Fig. 7. The beam-wave coupling coefficient for the $TE_{61}$ mode as a function of radial beam position.

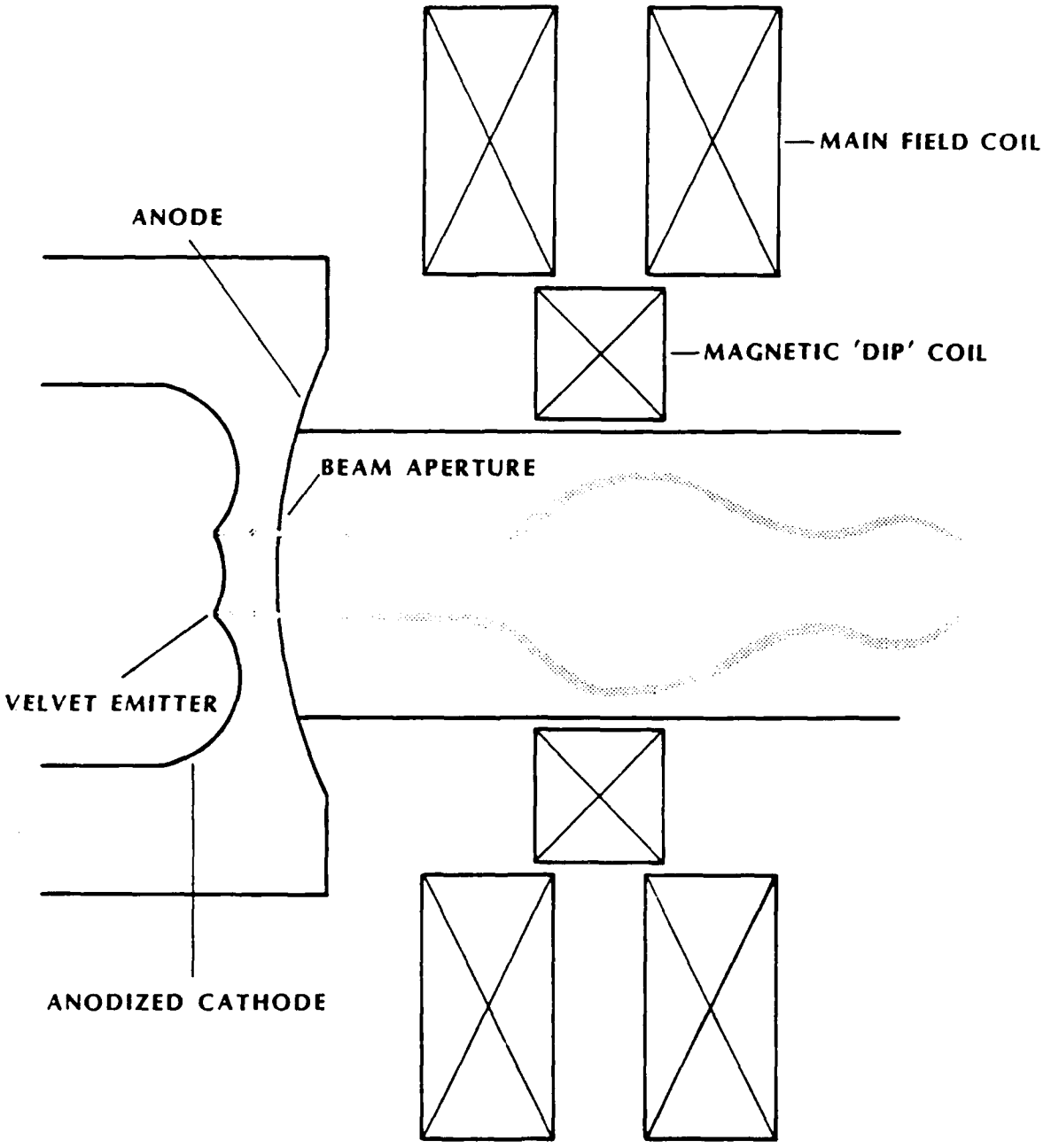



Fig. 8. Outline shape of the electron gun.

# APPENDIX D

## Design of a Waveguide Resonator with Rippled Wall Reflectors for a 100 GHz CARM Oscillator Experiment

INT. J. ELECTRONICS, 1988, VOL. 65, NO. 3, 463–475

# Design of a waveguide resonator with rippled wall reflectors for a 100 GHz CARM oscillator experiment†

R. B. McCOWAN§, A. W. FLIFLET‡, S. H. GOLD‡,
V. L. GRANATSTEIN‖ and M. C. WANG¶

High $Q$ Bragg resonators are studied for application to millimeter wave CARM oscillators driven by electron beams with power greater than 100 MW. 'Whispering-gallery' modes are shown to have the highest $Q$. The two effects that cause reflections, impedance mismatch owing to variations in the wall radius and currents driven in the walls of the reflector sections, are shown to compete, paving the way for anomalously low $Q$s for some of the other modes. The effect of wall resistance on the operation of the cavity is studied; as the frequency of the radiation is increased to near 250 GHz, wall heating severely limits the average power rating of whispering-gallery devices.

## 1. Introduction

High-power millimeter waves have many important applications. For example, millimeter-wave radar systems will yield higher target resolution than will lower frequency systems for a particular antenna aperture. Communications systems may benefit from a more strongly focussed radiation beam and larger information bandwidth available as the frequency is increased. Electron cyclotron heating of fusion plasmas will require high frequency radiation when strong magnetic fields are used to confine the plasma (Granatstein 1987).

The cyclotron autoresonance maser (CARM) is a promising source of high power radiation in the 100 GHz to 500 GHz frequency range, that may impact the requirements of advanced systems for applications such as those mentioned above. The requirements for guide magnetic field strength and electron energy in a CARM may be advantageous when compared with competing devices. Compared with a gyrotron, the required magnetic field strength requirement is substantially reduced. The CARM can provide millimeter and submillimeter radiation in the first electron cyclotron harmonic using currently available magnet technology. For example, a planned experiment at the U.S. Naval Research Laboratory (NRL) will produce powers in excess of 10 MW at 100 GHz with a 600 kV beam and a magnetic field of only 25 kG, while a fundamental harmonic gyrotron operating at 100 GHz with the same beam voltage requires a magnetic field of over 70 kG. Compared with a conventional magnetostatic wiggler FEL, the CARM can reach submillimeter wavelengths with a lower electron beam voltage. For example, a 0·5 MV CARM oscillator has the potential for efficient multimegawatt operation at wavelengths

Received 15 October 1987; accepted 15 November 1987.
† Work supported by the U.S. Office of Naval Research.
‡ Naval Research Laboratory, Washington, D.C. 20375, U.S.A.
§ SAIC, McLean, Virginia, U.S.A.
‖ University of Maryland, College Park, Maryland, U.S.A.
¶ Institute of Optics and Fine Mechanics, Shanghai, People's Republic of China.

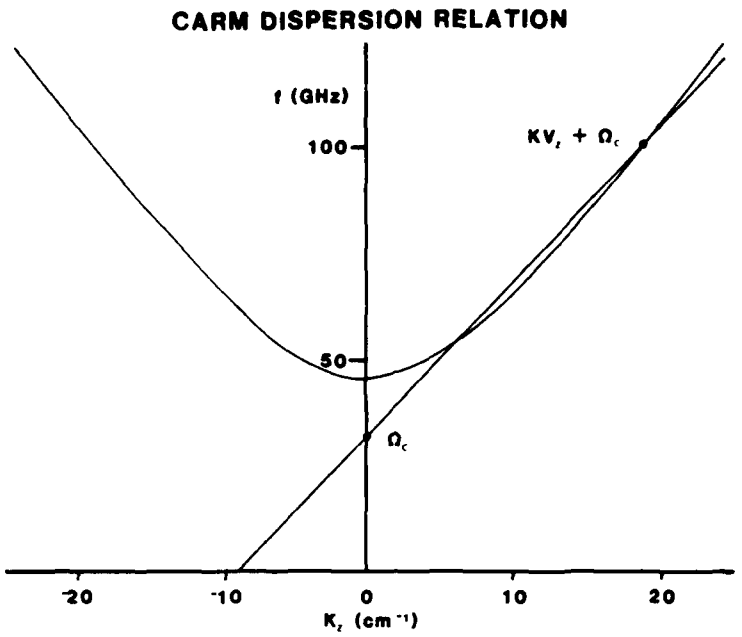



Figure 1. The dispersion relation for the NRL 100 GHz. CARM experiment. The high-frequency intersection of the electron beam line with the $TE_{61}$ waveguide dispersion relation is the CARM operating regime. The lower-frequency intersection is a competing gyrotron mode.

down to 0·75 mm with a 100 kG superconducting magnet; a 0·5 MV FEL oscillator with a 3 cm period magnetic wiggler will produce radiation at 4·5 mm.

The NRL experiment will use a 600 kV, 200 A electron beam. The NRL CARM operates near grazing incidence, where autoresonant effects are weak, but where the cyclotron maser interaction is strong. By keeping the interaction region short (less than ten cyclotron orbits), the effect of velocity spread is reduced and the efficiency can be quite high; computer simulations indicate that the device will operate at efficiencies greater than 20%.

The CARM oscillator, like the gyrotron oscillator, is a cyclotron maser. The dispersion relation for the NRL CARM is shown in Fig. 1. In contrast to the gyrotron, which requires an electron beam with a high pitch angle, the CARM has an electron beam with a moderate pitch angle and a substantial amount of axial momentum. The CARM benefits from the Doppler upshift provided by the axial velocity of the beam; the operating frequency of the CARM is approximately $\gamma f_c$, where $f_c$ is the nonrelativistic cyclotron frequency associated with the axial magnetic field, and $\gamma$ is the usual relativistic factor.

Because the CARM is a device that depends on a convective instability, the oscillator operation must take place in a cavity that provides feedback of the radiation onto the electron beam. For typical CARM operation, the resonator reflectors must provide high reflectivity for modes that are far from cutoff. Furthermore, mode selectivity is desirable, preferably with discrimination between modes differing in either transverse or axial structure. In addition, modes that are near cutoff must be suppressed in order to minimize competition from the gyrotron interaction. Finally,

the CARM cavity must allow unrestricted passage of an electron beam parallel to the axis.

A suitable realization of CARM resonator reflectors may be achieved by using a small periodic corrugation of the waveguide surface. Each ripple provides a small reflection of wave amplitude. If the corrugation period is such that the radiation reflected from each of the corrugations adds in phase, the corrugated section can be highly reflective and is known as a Bragg reflector (Bratman *et al.* 1983). This paper treats the reflection of rippled wall sections as a mode conversion from a forward wave to a backward wave, with an approach to the analysis that is similar to the analyses of other mode converters (Solymar 1959).

Previous work on Bragg reflectors has focussed on the design of cavities where the radiation modes are concentrated near the axis of the cavity (volume modes); whereas for the NRL CARM, the primary considerations are modes that are peaked near the wall (whispering-gallery modes). The results derived below have been presented without derivation by Bratman *et al.* (1983). Palmer (1987) derives results for Bragg cavities from a different starting point and examines the effects of multiple modes; however, he does not consider the effects of cavity wall resistance, and considers applications only to FELs.

The dominant mechanism for the reflections is different for whispering-gallery modes from that for volume modes; the physics of this difference is discussed below. In addition, the effects of energy dissipation by the walls of the cavity have been studied, and the ramifications of ohmic heating on frequency scaling for long-pulse devices are examined.

The general case of waveguides with cross sections that change along the axis has been treated by Solymar (1959), who formulated the equations governing the waveguide modes as a set of coupled differential equations for the wave amplitude, the 'generalized telegraphist's' equations. Each equation describes the amplitude of either the forward or the backward component of one waveguide mode.

$$\frac{dA_i^+}{dz} = j\beta_i A_i^+ - \frac{1}{2}\frac{d(\ln K_i)}{dz} A_i^- + \sum_p (S_{ip}^+ A_p^+ + S_{ip}^- A_p^-) \tag{1a}$$

$$\frac{dA_i^-}{dz} = -j\beta_i A_i^- + \frac{1}{2}\frac{d(\ln K_i)}{dz} A_i^+ + \sum_p (S_{ip}^+ A_p^- + S_{ip}^- A_p^+) \tag{1b}$$

where $A_i$ is the amplitude of the $i$th waveguide mode, $\beta$ is the wave number of the mode, $K$ is the wave impedance of the mode, and $S$ is a wave–wave coupling coefficient. The designations + and − signify forward-going and backward-going components, while the sum $p$ is over all waveguide modes.

The mode coupling arises from two sources. The second term of the right-hand side of the equations is the reflection owing to the impedance changes in the guide that arise from a changing wall radius, and converts a forward wave to a backward wave of the same transverse structure. The other source (the last term in the equations) is radiation by the wall current driven by the radiation in the guide. As indicated, this mechanism can couple any two modes.

The coupling coefficients $S_{ip}$ represent the mode coupling because of the wall currents in the waveguide, and can be expressed in terms of line integrals of the waveguide modes around the boundary of the waveguide. If the interaction is specialized to a single wave with forward-going and backward-going components, the subscripts $i$ can be dropped, the sum over $p$ vanishes and the coupling coefficient

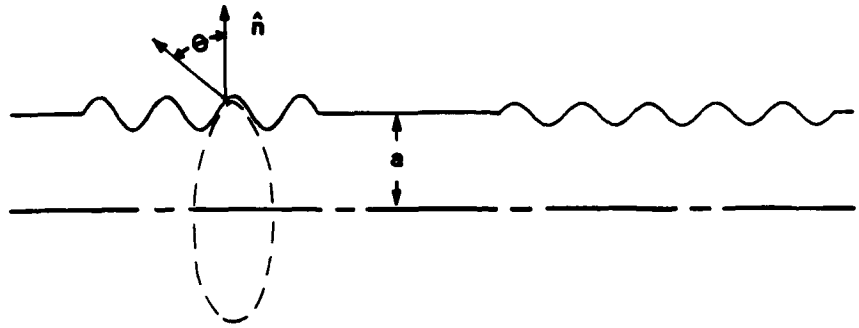



Figure 2. The relationship between $\hat{n}$ and $\theta$.

becomes

$$S^- = -\frac{1}{2}\int_c \tan\theta \frac{\partial \Psi}{\partial s}\, ds \tag{2}$$

for TE modes, and

$$S^- = -\frac{1}{2}\int_c \tan\theta \frac{\partial \Psi}{\partial n}\, ds \tag{3}$$

for TM modes. $S^+ = 0$ for both the TE and TM modes. The derivative $\partial/\partial s$ is with respect to the tangential path around the waveguide wall, and the derivative $\partial/\partial n$ is with respect to the normal to the unperturbed (straight) waveguide wall. The angle $\theta$ is the angle between the normal to the waveguide axis and the normal to the local waveguide wall. Figure 2 illustrates the relationship between $s$, $\hat{n}$ and $\theta$. The integral is performed around the perimeter of the waveguide.

For circular waveguide sections of radius $a$, the wave functions $\psi$ are:

$$\psi = \frac{J_m\left(\frac{x'_{mn} r}{a}\right) e^{jm\phi}}{(\pi(x'^2_{mn} - m^2)J_m)^{1/2}(x'_{mn})} \tag{4}$$

for TE modes, and

$$\psi = \frac{J_m\left(\frac{x_{mn} r}{a}\right) e^{jm\phi}}{\pi^{1/2} x_{mn} J'_m(x_{mn})} \tag{5}$$

for TM Modes. $J_m$ is the Bessel function of the first kind, $x_{mn}$ is the $n$th zero of $J_m$, $J'_m$ is the derivative of $J_m$ with respect to its argument $x'_{mn}$ is the $n$th zero of $J'_m$; $m$ and $n$ are the azimuthal and radial mode indices. The normal and tangential derivatives in the coupling coefficients can be written as derivatives with respect to the coordinates $r$ and $\phi$.

$$\frac{\partial \psi}{\partial n} = \frac{\partial \psi}{\partial r} \quad \text{and} \quad \frac{\partial \psi}{\partial s} = \frac{\partial \psi}{\partial (a\phi)}$$

For axisymmetric variations in wall radius, $\tan\theta$ can be taken outside the integral. The coupling coefficient becomes

$$S^- = \tan\theta \int_c \frac{\left(\frac{x'_{mn}}{a}\right)^2 J_m^2\left(\frac{x'_{mn} r}{a}\right)}{2\pi x'^2_{mn} J_m^2(x'_{mn})}\, ds \tag{6}$$

for TE modes, and

$$S^- = -\frac{\tan\theta}{2\pi a^2}\int_c ds \tag{7}$$

for TM modes.

Since the integrand is independent of the angular variable and the integration is around the circumference of the waveguide, the line integrals collapse to $2\pi a$, and eqns. (6) and (7) are easily evaluated as

$$S^- = \tan\theta \frac{m^2}{a(x'^2_{mn} - m^2)} \tag{8}$$

for TE modes, and $$S^- = -\frac{\tan\theta}{a} \tag{9}$$

for TM modes.

In order to complete the equations governing the waves in the cavity, we must evaluate the wave impedance in terms of the wall profile. The coefficient of the term caused by the impedance variation is the derivative of the logarithm of the wave impedance:

$$\frac{d}{dz}(\ln K) = \frac{d}{dz}\left(\ln\frac{\omega}{\beta}\right) = -\frac{1}{\beta}\frac{d\beta}{dz} \tag{10}$$

where $\omega$ is the angular frequency of the radiation. Substituting the waveguide dispersion relation into eqn. (10), we derive the following relation for the wave coupling due to impedance variations. For TE modes,

$$\frac{d}{dz}(\ln K) = -\frac{x'^2_{mn}}{\beta^2 a^3}\frac{da}{dz} \tag{11}$$

For TM modes, this differs only by an overall minus sign and by a change from $x'_{mn}$ to $x_{mn}$. By the definition of $\theta$, $da/dz = \tan\theta$.

Using eqns. (2), (3), (8), (9), and (11), the equations governing the spacial evolution of the forward-going and backward-going wave amplitudes may be written

$$\frac{dA^+}{dz} = j\beta A^+ - \frac{1}{2}\frac{x'^2_{mn}}{\beta^2 a^3}\tan\theta A^- + \tan\theta\frac{m^2}{a(x'^2_{mn} - m^2)}A^- \tag{12a}$$

$$\frac{dA^-}{dz} = -j\beta A^- + \frac{1}{2}\frac{x'^2_{mn}}{\beta^2 a^3}\tan\theta A^+ + \tan\theta\frac{m^2}{a(x'^2_{mn} - m^2)}A^+ \tag{12b}$$

for TE modes, and

$$\frac{dA^+}{dz} = j\beta A^+ - \frac{1}{2}\frac{x_{mn}^2}{\beta^2 a^3}\tan\theta A^- + \frac{\tan\theta}{a}A^- \tag{13a}$$

$$\frac{dA^-}{dz} = -j\beta A^- + \frac{1}{2}\frac{x_{mn}^2}{\beta^2 a^3}\tan\theta A^+ + \frac{\tan\theta}{a}A^+ \tag{13b}$$

for TM modes.

The equation pairs (12) and (13) can be expressed in the same form by combining the reflection terms caused by the impedance variation with the reflection terms owing to the wall currents.

$$\frac{dA^+}{dz} = j\beta A^+ - HA^- \tag{14a}$$

$$\frac{dA^-}{dz} = -j\beta A^- + HA^+ \tag{14b}$$

Here

$$H = \frac{\tan\theta}{2}\left\{\frac{x_{mn}'^4 - m^2a^2\left(\frac{\omega^2}{c^2} + \beta^2\right)}{\beta^2 a^3(x_{mn}'^2 - m^2)}\right\} \tag{15}$$

for the TE modes, and

$$H = \frac{\tan\theta}{2a}\left\{\frac{\frac{\omega^2}{c^2} + \beta^2}{\beta^2}\right. \tag{16}$$

for the TM modes.

For the remainder of this paper, we assume a weak sinusoidal ripple in the wall,

$$a(z) = a_0 + l_0\cos(k_b z + \phi_0) \tag{17}$$

where $a_0$ is the mean wall radius, $l_0$ is the ripple amplitude, $2\pi/k_b$ is the ripple period, and $\phi_0$ determines the corrugation phase. Equations (14) may then be simplified by assuming a solution of the form $A = f(z)e^{jkz}$. In this case, the reflected wave term is only important when the Bragg condition ($2k_z \approx k_b$) is satisfied, and the equations for the mode amplitude become

$$\frac{df^+}{dz} + j\Delta f^+ = -jGf^- \tag{18a}$$

$$\frac{df^-}{dz} - j\Delta f^- = jGf^+ \tag{18b}$$

where $G = H(\beta l_0/\tan\theta)$ and $\Delta = 2k_z - k_b$.

The strength of the coupling between the forward-going and backward-going waves is governed by the magnitude of the coupling coefficient $G$. Figure 3 summarizes the dependence of the coupling coefficient on mode; it is a plot of coupling coefficient for the specific configuration considered for the 100 GHz CARM. Figure 3 clearly shows that the coupling for the TM modes is independent of the mode indices, although it is a function of the frequency of the mode. The coupling of TM

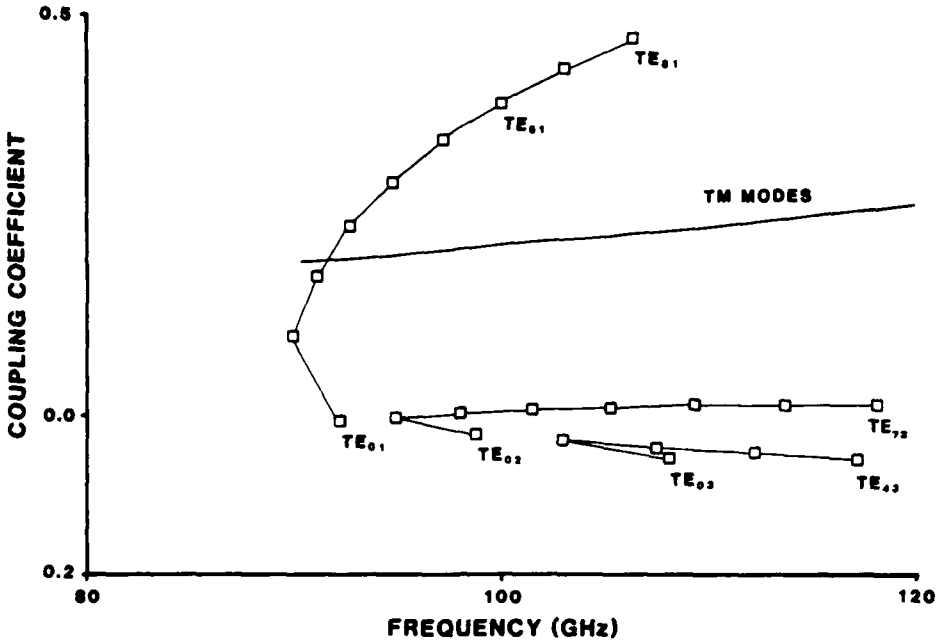



Figure 3. The coupling coefficient of rippled waveguide as a function of mode. The geometry is that of the 100 GHz, $TE_{61}$ CARM cavity. The whispering-gallery modes are dominant, while the TM modes are the strongest competing modes.

modes in this configuration is stronger than those of any of the TE modes with the exception of those of the whispering-gallery modes.

For TE modes, the situation is more complicated. The denominator of the expression for the coupling coefficient is minimized for the $TE_{m1}$ modes. Therefore, the coupling is expected to be strongest for these modes. Large wall currents driven by the electromagnetic fields, which are peaked near the walls, cause the strong coupling of these whispering-gallery modes. The reflection caused by the wall currents is 180° out of phase with that caused by the impedance mismatch. The reflections driven by wall currents dominate in the case of the whispering-gallery modes. Other modes will have reflectivities that are caused by a combination of both effects, except for the $TE_{0n}$ modes, which have reflectivities due entirely to impedance variations. The point where $G$ crosses through zero is a point of anomalously low reflectivity; the contributions of wall current reflections and impedance reflection cancel.

Equations (18) are a pair of first-order homogeneous linear differential equations, and may be solved using elementary techniques. The general solution of the equations is

$$f^{+}(z) = c_1(-jG)e^{\gamma z} + c_2(-jG)e^{-\gamma z} \tag{19a}$$

$$f^{-}(z) = c_1(j\Delta + \gamma)e^{\gamma z} + c_2(j\Delta - \gamma)e^{-\gamma z} \tag{19b}$$

where $\gamma^2 = G^2 - \Delta^2$, and $c_1$ and $c_2$ are determined by the boundary conditions. If $G > \Delta$, the solutions are exponential; for $G < \Delta$ the solutions are sinusoidal. The region of high reflectivity occurs mainly when $\gamma$ is real and the solution is exponentially damped.

If the waveguide sections attached to the reflector are matched in order to produce no reflections, the boundary conditions for a wave incident on the ripples are

$$f^{+}(0) = 1 + 0j$$

$$f^{-}(L) = 0 + 0j$$

The solution of eqns. (19) for these boundary conditions is

$$f^{+}(z) = \frac{j\Delta \sinh \gamma(L - z) + \gamma \cosh \gamma(L - z)}{j\Delta \sinh \gamma L + \gamma \cosh \gamma L} \tag{20a}$$

and

$$f^{-}(Z) = \frac{-jG \sinh \gamma(L - z)}{j\Delta \sinh \gamma L + \gamma \cosh \gamma L} \tag{20b}$$

For this case, the reflectivity is

$$R(\Delta) = |f^{-}(0)|^2 = \left| \frac{\gamma \sinh \gamma L}{j\Delta \sinh \gamma L + \gamma \cosh \gamma L} \right|^2$$

At the centre of the reflection band ($\Delta = 0$), $\gamma = G$ and the reflectivity is

$$R = \tanh^2 GL \tag{21}$$

The reflected wave is 90° out of phase with the incident wave. Equation 21 indicates that, for a given waveguide, the reflection coefficient depends only on the product of $G$ and $L$. Since $G$ is linearly proportional to the ripple depth, if the ripple depth is halved and the corrugation length is doubled, the reflectivity at the centre of the band will remain the same. As the ripple depth is decreased, however, the bandwidth of the reflected radiation becomes narrower. Therefore, the selectivity of a Bragg reflector can be increased by making the ripples shallower and the reflector longer. This effect is illustrated in Fig. 4, which is a plot of the reflectivity versus frequency in the $TE_{61}$ mode for the two reflectors that make up the CARM resonator. The upstream reflector has shallower ripples but a longer length than the downstream (output) reflector. Hence, the upstream reflector has a narrower reflection band and a higher reflectivity.

## 2. Making a resonator out of bragg reflectors

A high-$Q$ resonant cavity can be constructed by placing a section of straight, smooth-walled waveguide between two Bragg reflectors. $Q$ is defined as the ratio of the energy stored in the cavity to the energy lost per RF cycle. The $Q$ of the resonator is increased when the length of the straight section is increased or when the reflectivity of the corrugated sections is increased. The length of the resonator must be such that the total path length of the radiation in one round trip of the resonator is an integral number of wavelengths.

$$\phi_u + \phi_d + \Delta\phi_0 + \frac{2\pi L_0}{\lambda} = p\pi \tag{22}$$

where $\phi_u$ and $\phi_d$ are the phase shifts from the upstream and downstream reflectors, $\Delta\phi_0 = \phi_{0u} - \phi_{0d}$, the phase difference between the beginnings of the two rippled

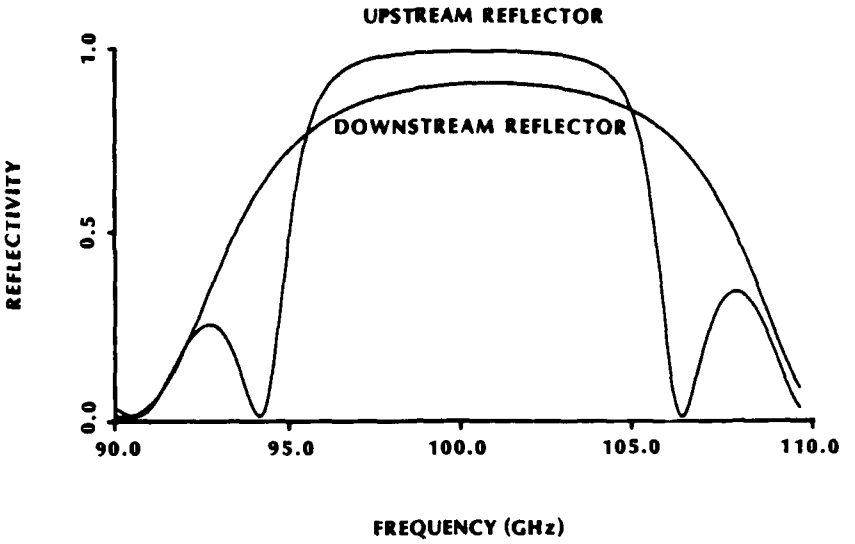



Figure 4. The variation of reflector bandwidth on ripple depth. The narrow bandwidth reflector has shallow ripples, while the broad bandwidth reflector has deeper ripples.

sections (see eqn. (17)), $L_0$ is the length of the smooth section between the rippled sections and $p$ is an even integer.

If the corrugated sections have high reflectivity, the $Q$ of the Bragg resonator is

$$Q = \frac{k^2 L_{\text{eff}}}{k_z(1 - R_1 R_2)} \tag{23}$$

where $k$ is the free space wave number, $k_z$ is the waveguide axial wave number, $R_1$ and $R_2$ are the reflectivities of the corrugated sections, and

$$L_{\text{eff}} = L_0 + \frac{1}{G_1}(1 - e^{-G_1 L_1}) + \frac{1}{G_2}(1 - e^{-G_2 L_2}) \tag{24}$$

$G_1$, $L_1$, $G_2$ and $L_2$ are the coupling coefficients and lengths of the reflectors.

In a long cavity, there may be more than one axial eigenmode for each transverse mode. If the modes are not close to cutoff, they are separated by approximately $\Delta f = v_{ph}/L_0$, where $v_{ph}$ is the phase velocity of the wave. If $\Delta f$ is too small ($L_0$ too large), the CARM may simultaneously oscillate in many axial modes of the same transverse mode. In addition, if the frequency difference between axial modes is nearly equal to the frequency difference between neighbouring transverse modes, the CARM may operate in more than one transverse mode as well. When the reflector bandwidth is chosen to be sufficiently narrow, however, the eigenmodes are reduced to one axial mode number per transverse mode, and the transverse modes of the resonator will not overlap. The decrease in bandwidth is achieved by decreasing the depth of the corrugations and increasing the length of the corrugated sections, thereby increasing the sensitivity of the reflector to wave number mismatch.

In order to design cavities for a high average power CARM, the ohmic heating of the cavity walls must be considered. For an open-ended cylindrical resonator where the field variations are small over a wavelength, the ohmic $Q$ of a cavity is

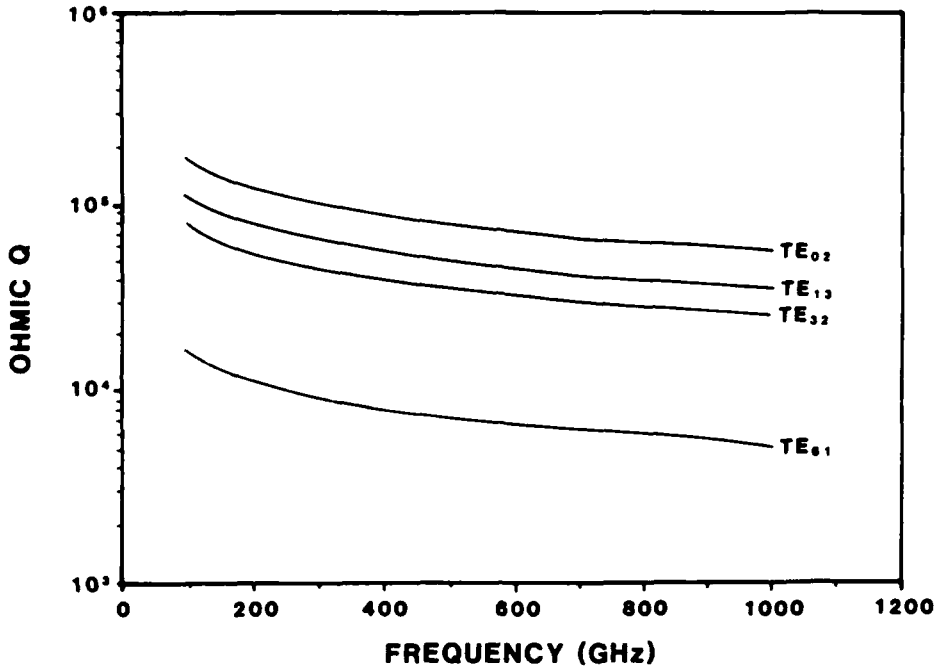



Figure 5. The ohmic $Q$ of an open ended cylindrical cavity as a function of frequency for various modes.

given by (Jackson 1975)

$$Q_l = \frac{a}{\delta} \frac{1 + \left(\frac{p\pi a}{x'_{mn} L_0}\right)^2}{1 + \left(\frac{p\pi a}{x'_{mn} L_0}\right)^2 \left(\frac{m}{x'_{mn}}\right)^2} \left[\frac{x'^2_{mn} - m^2}{x'^2_{mn}}\right] \tag{25}$$

where $\delta$ is the skin depth and $p$ is the axial mode index of the cavity mode ($p = 2L_0/\lambda_s$). Figure 5 shows the dependence of ohmic $Q$ on frequency as some prototype resonators are scaled to shorter wavelength. The highest ohmic losses occur with the whispering-gallery modes, because the fields of these modes are very strong near the walls of the cavity.

When designing a CARM oscillator, one must carefully consider possible competition from gyrotron oscillations. In order for the device to work successfully as a CARM, the starting currents of gyrotron modes must be greater than the starting currents of the desired CARM modes. The CARM has a beam with a low to moderate ratio of transverse momentum to axial momentum ($\alpha$). This raises the start current of the gyrotron modes somewhat. In addition, the $Q$ of the gyrotron modes must be kept as low as possible, which means the cavity must be kept as short as possible. The smallest possible $Q$ of a gyrotron mode in a straight cavity of length $L_0$ is the minimum diffraction $Q$,

$$Q_{\min} = \frac{4\pi}{p} \left(\frac{L_0}{\lambda_{rs}}\right)^2$$

| | |
|---|---|
| Beam energy | 600 kV |
| Beam current | 200 A |
| Pulse length | 50 ns |
| $\alpha \equiv v_t/v_z$ | 0·6 |
| Axial velocity spread $\equiv \Delta V_z/V_z$ | < 3% |
| Magnetic field | 25 kG |
| $\Omega_c$ | 32 GHz |
| Mode | $TE_{61}$ |
| Frequency | 100 GHz |
| Wavelength | 3·36 mm |
| Phase velocity | 1·17$c$ |
| Mean wall diameter | 1·59 cm |
| Upstream reflector | |
| length | 3·0 cm |
| ripple depth | 0·025 cm |
| ripple period | 1·68 mm |
| reflectivity | 99% |
| Downstream reflector | |
| length | 1·5 cm |
| ripple depth | 0·031 cm |
| ripple period | 1·68 mm |
| reflectivity | 90% |
| Centre section length | 2·6 cm |
| Cavity $Q$ | 1500 |

Table 1. 100 GHz CARM Bragg resonator parameters.

where $\lambda_{fs}$ is the free space wavelength of the near cutoff mode and $p$ is the number of half wavelengths in the cavity. The length of the cavity must be kept short in order to keep the $Q$ of gyrotron modes small. This consideration puts a lower limit on the bandwidth of the reflectors, because a narrow band reflector is the result of a long waveguide with many small ripples.

## 3. The 100 GHz CARM cavity

The $Q$ of the resonator for the CARM must be high enough so that competing gyrotron modes will not start before the CARM mode starts. For the parameters of the NRL experiment, the gyrotron modes have a $Q$ of approximately 500. In order to satisfy the requirement that the CARM modes start before the gyrotron modes, the $Q$ of the CARM operating mode must be more than 1400. Using a reflectivity of 90% on the downstream reflector and 98% on the upstream reflector, the required length of the straight section of resonator is 2·5 cm. In order to retain only one high $Q$ $TE_{61}$ axial mode, the ripple depth must be no greater than 0·025 cm. The ripple depth of the upstream reflector is the shallower of the two corrugations, and hence has the longer radiation e-folding length.

The ripple depth requirement, coupled with the stated 90% and 98% reflectivity requirements, forces the length of the rippled sections to be 1·5 cm and 3 cm long respectively. The total cavity length is 7 cm. Table 1 summarizes the design of the cavity for the NRL 100 GHz experiment and Fig. 6 shows the relationship between the cavity geometry and the radiation envelope.

For the 100 GHz CARM resonator design, the reflections owing to the impedance mismatch cancel the reflections caused by the wall currents for the $TE_{m2}$ modes; only the whispering-gallery modes have high $Q$s. The separation between

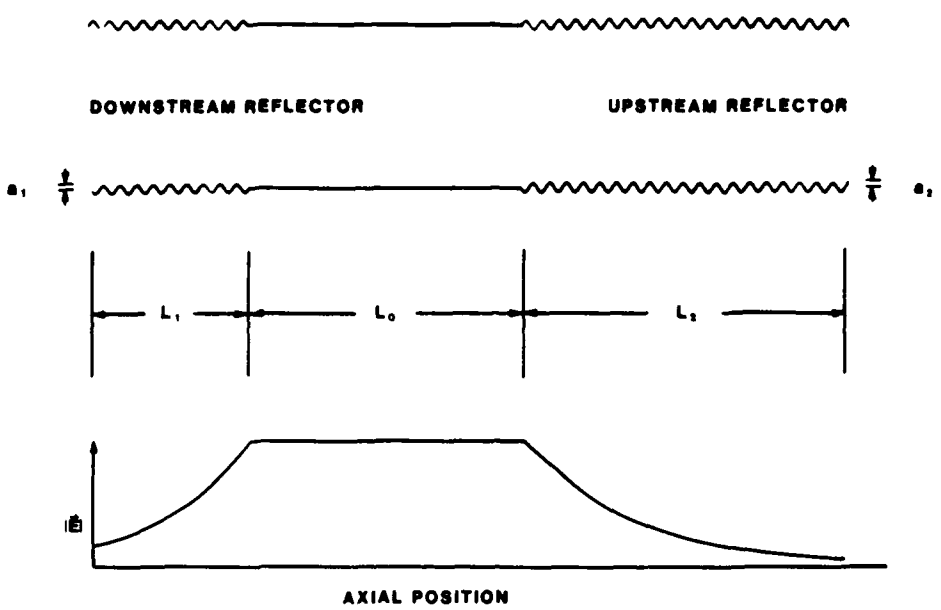



Figure 6. The geometry of the CARM cavity with the electric field amplitude profile.

the $TE_{m1}$ axial modes in the cavity is approximately 6 GHz. The bandwidth of the upstream reflector is narrow enough to exclude all but one axial mode for each transverse mode. The $TE_{51}$, $TE_{61}$, and $TE_{71}$ have frequencies of 97 GHz, 100 GHz and 103 GHz, respectively. The interaction can be tuned by varying the magnetic field to prevent simultaneous oscillations in more than one of these modes. Figure 7 shows the oscillating modes and frequencies of the CARM resonator. The $Q$ increases with frequency, so that the $TE_{71}$ mode has a higher $Q$ than the $TE_{61}$ mode.

The ohmic $Q$ of the cavity is approximately 16 000. For a 10 MW output power, approximately 1 MW is dissipated by wall currents. Since the cavity wall has an effective area of 20 $cm^2$, the wall loading is 50 kW $cm^{-2}$, which is acceptable for short-pulse, low-duty-factor operation.

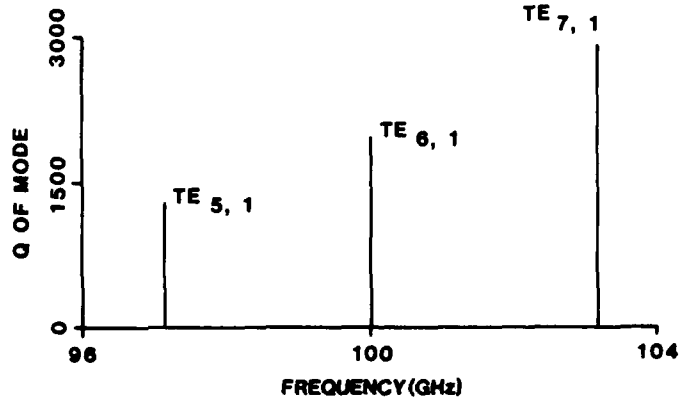



Figure 7. The important modes of the 100 GHz CARM cavity.

Because of the resonant nature of the Bragg reflector action, the CARM resonator must be fabricated to extremely high precision. For the 100 GHz design the machining accuracy must be 0·005 mm. These tolerances can be met using precision electroforming techniques.

## 4. High frequency resonators

As the frequency of microwave devices is increased to 250 GHz and beyond, the limitations of the Bragg resonators as presented here become apparent, especially if CW devices are planned.

The ohmic $Q$ of the resonator scales with the inverse square root of the frequency. The surface area of the resonator scales as the inverse square of the frequency. Therefore the power density dissipated in the walls scales with frequency to the 5/2 power. The wall loading on the whispering-gallery cavity, scaled to 250 GHz operation is 500 kW $cm^{-2}$. Safe operation of such a cavity could only be achieved with a duty factor of less than 0·5%.

Machining tolerances become more difficult as the frequency is increased. The ripple depth for the whispering-gallery cavity at 250 GHz is only 0·01 cm. In order to hold tolerance for structures of this size, careful temperature control is necessary; this is rather difficult to achieve with many kW $cm^{-2}$ of wall heating.

Clearly, in order to scale to high-duty-factor devices, cavities must be designed in modes other than the whispering-gallery modes. Volume-mode Bragg resonator designs will require much longer rippled sections and/or deeper corrugations than the whispering-gallery designs. CARM designs using long resonators will have problems with gyrotron mode competition that are not easy to overcome.

## 5. Conclusions

The basic design principles for Bragg resonators for short-pulse CARM operation have been presented, along with a design for the 100 GHz, 10 MW NRL CARM. The whispering-gallery modes are shown to provide a good combination of high reflectivity and mode selectivity, while the TM modes have moderate reflectivity but rather poor selectivity. Very selective cavities with $Q$s over 1000 are easily achieved using whispering-gallery mode resonators less than 10 cm in length. However, the resistive losses in the walls of the whispering-gallery cavities are shown to be prohibitively large for CW relevant devices. For high-duty-factor devices, either volume-mode Bragg resonators or quasi-optical cavities must be employed.

## References


BRATMAN, V. L., DENISOV, G. G., GINZBURG, N. S., and PETELIN, M. I., 1983, FELs with Bragg reflection resonators: Cyclotron autoresonance masers versus ubitrons. *I.E.E.E. Journal of Quantum Electronics*, **19**, 282.

GRANATSTEIN, V. L., 1987, *Proceedings of the 1987 Particle Accelerator Conference*, (Washington, D. C.: IEEE).

JACKSON, J. D., 1975, *Classical Electrodynamics*, 2nd ed. (New York: John Wiley) pp. 334–360.

PALMER, A. J., 1987, Coupled-mode theory of overmoded cylindrical metal Bragg-reflectors. *I.E.E.E. Journal of Quantum Electronics*, **23**, 65.

SOLYMAR, L., 1959, Spurious mode generation in nonuniform waveguide. *I.R.E. Transactions on Microwave Theory and Technology*, **MTT-7** (3) 379.

# APPENDIX E

## Development of High Power CARM Oscillators

**Naval Research Laboratory**

Washington, DC 20375-5000



**NRL Memorandum Report 6388**

# Development of High Power CARM Oscillators

A. W. FLIFLET, R. B. MCCOWAN, C. A. SULLIVAN,*
D. A. KIRKPATRICK,* S. H. GOLD AND W. M. MANHEIMER

*High Power Electromagnetic Radiation Branch*
*Plasma Physics Division*

**Science Applications International Corporation*
*McLean, Virginia*

March 14, 1989

Approved for public release; distribution unlimited.

SECURITY CLASSIFICATION OF THIS PAGE

## REPORT DOCUMENTATION PAGE

Form Approved
OMB No 0704 0188

| | |
|---|---|
| 1a REPORT SECURITY CLASSIFICATION<br>UNCLASSIFIED | 1b RESTRICTIVE MARKINGS |
| 2a SECURITY CLASSIFICATION AUTHORITY | 3 DISTRIBUTION AVAILABILITY OF REPORT<br>Approved for public release; distribution unlimited. |
| 2b DECLASSIFICATION / DOWNGRADING SCHEDULE | |
| 4 PERFORMING ORGANIZATION REPORT NUMBER(S)<br>NRL Memorandum Report 6388 | 5 MONITORING ORGANIZATION REPORT NUMBER(S) |
| 6a NAME OF PERFORMING ORGANIZATION<br>Naval Research Laboratory<br>6b OFFICE SYMBOL (If applicable)<br>Code 4740 | 7a NAME OF MONITORING ORGANIZATION |
| 6c ADDRESS (City, State, and ZIP Code)<br>Washington, DC 20375-5000 | 7b ADDRESS (City, State, and ZIP Code) |
| 8a NAME OF FUNDING / SPONSORING ORGANIZATION<br>ONR<br>8b OFFICE SYMBOL (If applicable) | 9 PROCUREMENT INSTRUMENT IDENTIFICATION NUMBER |
| 8c ADDRESS (City, State, and ZIP Code)<br>Washington, DC | 10 SOURCE OF FUNDING NUMBERS<br>PROGRAM ELEMENT NO / PROJECT NO / TASK NO RR-011-41 / WORK UNIT ACCESSION NO |
| 11 TITLE (Include Security Classification)<br>Development of High Power CARM Oscillators | |
| 12 PERSONAL AUTHOR(S) Fliflet, A.W., McCowan, R.B., Sullivan,* C.A., Kirkpatrick,* D.A., Gold, S.H. and Manheimer, W.M. | |
| 13a TYPE OF REPORT<br>13b TIME COVERED FROM 10/87 TO 10/88<br>14 DATE OF REPORT (Year, Month, Day) 1989 March 14<br>15 PAGE COUNT 28 | |
| 16 SUPPLEMENTARY NOTATION<br>*Science Application Corporation, McLean, VA | |
| 17 COSATI CODES<br>FIELD / GROUP / SUB-GROUP | 18 SUBJECT TERMS (Continue on reverse if necessary and identify by block number)<br>Electron cyclotron maser; Autoresonance; CARM; Oscillator; Doppler-shifted frequency; Magnetron-injection-gun |

19 ABSTRACT (Continue on reverse if necessary and identify by block number)

The Cyclotron Auto-Resonance Maser (CARM) is under investigation at the U.S. Naval Research Laboratory as an efficient source of high power millimeter-wave and submillimeter-wave radiation for applications such as plasma heating, advanced rf accelerators, and space-based radars. A short-pulse 100 GHz CARM oscillator experiment based on a 600 kV, 200 Amp, 50 nsec electron beam is under way. The mode selective, high-$Q$ waveguide cavity with rippled-wall Bragg reflectors is designed to operate in the $TE_{61}$ mode. A novel cold cathode diode is used to produce a high quality ($\Delta v_z/v_z \leq 3\%$) annular beam with a momentum pitch ratio of 0.6. The cathode features nonemitting focussing electrodes and an annular velvet emitter. The main objective of the experiment is to demonstrate high efficiency ~ 20% at a power of ap-

(Continues)

| | |
|---|---|
| 20 DISTRIBUTION AVAILABILITY OF ABSTRACT<br>☒ UNCLASSIFIED UNLIMITED ☐ SAME AS RPT ☐ DTIC USERS | 21 ABSTRACT SECURITY CLASSIFICATION<br>UNCLASSIFIED |
| 22a NAME OF RESPONSIBLE INDIVIDUAL<br>Arne W. Fliflet | 22b TELEPHONE (Include Area Code) (202) 767-2469<br>22c OFFICE SYMBOL Code 4740 |

DD Form 1473, JUN 86 *Previous editions are obsolete* SECURITY CLASSIFICATION OF THIS PAGE

S/N 0102-LF-014-6603

19. ABSTRACTS (Continued)

proximately 20 MW. In addition, a long pulse 250 GHz CARM oscillator experiment based on a 500 kV, 100 Amp, 1 $\mu$sec MIG-type thermionic cathode electron gun is planned. The design of these experiments and the optimization of CARM oscillator efficiency are discussed.

## CONTENTS


| | | |
|---|---|---|
| 1 | INTRODUCTION | 1 |
| 2 | CARM EFFICIENCY OPTIMIZATION | 3 |
| 3 | SHORT-PULSE 100 GHZ CARM OSCILLATOR | 5 |
| 4 | LONG-PULSE CARM OSCILLATOR | 7 |
| 5 | ACKNOWLEDGMENT | 8 |
| | REFERENCES | 9 |
| | DISTRIBUTION LIST | 17 |

# 1 Introduction

There is now a considerable research effort to develop high power, high frequency (millimeter wave to infrared) sources based on high voltage electron beams. These devices, the best known of which is the Free Electron Laser (FEL), are inherently high power and produce high frequencies by a doppler-shift effect which scales as the square of the relativistic mass ratio $\gamma$. The U.S. Naval Research Laboratory (NRL) has recently initiated an experimental program on a related device called the Cyclotron Auto-Resonance Maser (CARM) [1]. The frequency of this device is doppler-upshifted by $\sim \gamma^2$ from the relativistic cyclotron frequency (that is, upshifted by $\sim \gamma$ from the nonrelativistic cyclotron frequency). The efficiency potential of the CARM is similar to the gyrotron — of order 20–40% — but higher beam quality is required. Compared to gyrotrons, CARM's can have larger cavity structures for a given wavelength and have lower beam pitch angle. These properties simplify beam formation and reduce self-field effects as well as reducing cavity ohmic losses.

Because the interaction occurs with a forward propagating wave, electrons lose axial momentum—and axial velocity—during the interaction, and this leads high efficiency potential due to an "auto-resonance" effect. That is, the interaction resonance condition:

$$\omega = k_{||} v_{||} + \Omega_{nr}/\gamma \tag{1}$$

—where $\omega$ is the wave frequency, $k_{||}$ and $v_{||}$ are radiation wavenumber and electron beam velocity components in the beam drift direction, and $\Omega_{nr}$ is the nonrelativistic cyclotron frequency — is relatively insensitive to changes in beam energy. This is because the change in the relativistic cyclotron frequency $\Omega = \Omega_{nr}/\gamma$ during the interaction is compensated by a change in the the doppler shift $k_{||} v_{||}$. This effect reduces the detuning of the resonance condition during beam-wave energy exchange. A combination of high doppler upshift of the frequency and high efficiency occurs when $\beta_{\perp 0} = 1/\gamma_0$ provided that

$$1 - \beta_{ph}^{-2} \leq \gamma_0^{-2} \tag{2}$$

where $\beta_\perp = v_\perp/c$ and $\beta_{ph} = v_{ph}/c = \omega/(k_{||}c)$. The autoresonance effect leads to high efficiencies without the need for efficiency enhancement schemes based on tapering the

Manuscript approved December 14, 1988.

interaction parameters.

A 0.5 MV CARM has the potential for efficient, multi-MW operation at wavelengths of 1.1 mm (280 GHz) with a 63 kG superconducting magnet or 560 GHz with a 125 kG magnet. With a 1 MV beam or operation at harmonics there is a potential for THz frequencies. This potential makes the CARM an attractive candidate for development as a source for the Compact Ignition Tokamak (CIT).

The NRL development effort has chosen to conduct its first experiments on CARM oscillator configurations for several reasons. The CARM circuit generally involves a highly overmoded waveguide structure with the attendant probability of mode competition. Compared to the amplifier, the oscillator configuration appears to offer more alternatives for mode control. Waveguide cavities with rippled-wall Bragg reflectors can be highly selective with respect to frequency and axial mode index. On the other hand quasi-optical cavities have excellent transverse mode selectivity transverse mode selectivity. Because the radiation traverses an oscillator cavity many times instead of once as in an amplifier, the interaction length can be relatively short and this helps prevent the build-up of spurious oscillations which are a major issue for amplifiers, particularly at high frequencies. The short interaction length also helps reduce the sensitivity to beam velocity spread. Additionally, a free-running oscillator does not require a source of input power, an expensive and scarce commodity at submillimeter wavelengths. The amplifier also requires an overmoded but highly mode selective and nonbeam-intercepting input coupler, a difficult engineering problem. The efficiency potential of CARM oscillators and amplifiers appears to be similar, of order 20–40%. The circulating power in a high $Q$ oscillator is generally much greater than the output power. This leads to somewhat greater ohmic losses for a given output power for the oscillator compared to the amplifier; however, oscillators can be designed for megawatt CW powers.

NRL currently has an ongoing short pulse $\sim$ 50 nsec, 100 GHz CARM oscillator experiment based on a 600 kV, 200 Amp electron beam produced by a pulseline accelerator. The objectives of the experiment are to investigate CARM physics and to demonstrate the high efficiency potential of the CARM oscillator at multimegawatt power levels. A 200-300 GHz

CARM oscillator based on a 0.5 MV thermionic cathode electron gun is currently in the design and planning stage. The device would have a pulse length of 1 microsecond and be rep-rated. The goal of the "long pulse" experiment would be to achieve output powers of about 10 MW and efficiencies in the 20-40% range.

# 2 CARM Efficiency Optimization

Consider the interaction of the electron beam with the TE mode of a vacuum waveguide. The transverse electric field is the form:

$$\vec{E}_\perp(\vec{r},t) = \Re\left\{E_0\vec{z}\times\vec{\nabla}_\perp\psi(\vec{r})e^{-i\omega t}\right\} \tag{3}$$

where $E_0$ is the field amplitude, $\omega$ is the wave angular frequency, and $\psi$ is the mode scalar function. For a $TE_{mn}$ circular waveguide mode , the scalar function is given by:

$$\psi(\vec{r}) = C_{mn}J_m(k_{mn}r)e^{im\theta} \tag{4}$$

where $J_m$ is a Bessel function of the first kind, $m$ is the azimuthal index, $n$ is the radial index, and $x_{mn}$ is the $n^{th}$ zero of $J_m$. The mode normalization coefficient $C_{mn}$ is given by:

$$C_{mn} = \left\{\sqrt{\pi\left(x_{mn}^2 - m^2\right)}J_m(x_{mn})\right\}^{-1} \tag{5}$$

As shown by Fliflet [2], application of single particle theory to the CARM interaction for the $s^{th}$ harmonic leads to the following normalized equations of motion:

$$\frac{du}{d\zeta} = (1-u)^{s/2}\,\Re\left\{F_s e^{-i\Theta}\right\}/(1-bu) \tag{6}$$

$$\frac{d\Theta}{d\zeta} = \left[\Delta - u + \frac{s}{2}(1-u)^{s/2-1}\,\Re\left\{iF_s e^{-i\Theta}\right\}\right]/(1-bu) \tag{7}$$

where $u$ is the normalized electron energy:

$$u = \frac{2}{\beta_{\perp 0}^2}\left(1-\beta_{\|0}/\beta_{ph}\right)(1-\gamma/\gamma_0)\,, \tag{8}$$

$\Theta$ is a slowly varying phase, $F_s$ is the normalized wave amplitude function, which for the fundamental harmonic interaction is given by:

$$F_1 = \frac{2e}{\gamma_0 m_0 c^2}\frac{\left(1-\beta_{\|0}/\beta_{ph}\right)^2}{\beta_{\perp 0}^3\sqrt{1-\beta_{ph}^{-2}}}C_{mn}J_{m-1}(k_{mn}r_b)E_0, \tag{9}$$

$\zeta$ is the normalized axial coordinate:

$$\zeta = \frac{\beta_{\perp 0}^2}{2\beta_{\|0}} \frac{1-\beta_{ph}^{-2}}{1-\beta_{\|0}/\beta_{ph}} (\omega z/c), \tag{10}$$

$\Delta$ is the resonance detuning parameter:

$$\Delta = \frac{2\left(1-\beta_{\|0}/\beta_{ph}\right)}{\beta_{\perp 0}^2\left(1-\beta_{ph}^{-2}\right)} \left(1-\beta_{\|0}/\beta_{ph}-s\Omega/\omega\right) \tag{11}$$

and $b$ is the electron recoil parameter:

$$b = \frac{\beta_{\perp 0}^2}{2\beta_{\|0}\beta_{ph}\left(1-\beta_{\|0}/\beta_{ph}\right)} \tag{12}$$

In Equation (9), $e$ is the magnitude of the electron charge, and $m_0$ is the electron mass. The electron axial and transverse momenta are given by:

$$p_{\|} = \gamma_0 m_e c \beta_{\|0} (1-bu) \tag{13}$$

$$p_{\perp} = \gamma_0 m_e c \beta_{\perp 0} \sqrt{1-u} \tag{14}$$

The electron recoil parameter $b$ characterizes how the axial momentum varies with beam energy; as shown in Eq.(14), the larger $b$ is, the more rapidly the axial momentum decreases with decrease in $\gamma$. The CARM interaction is characterized by $b$ ~0.3–0.6, the gyrotron regime is obtained by setting $b = 0$.

The electronic efficiency can be written in the form: $\eta = \eta_{sp}\hat{\eta}$ where $\eta_{sp}$ is the is the single particle efficiency given by:

$$\eta_{sp} = \frac{\beta_{\perp 0}^2}{2\left(1-\beta_{\|0}/\beta_{ph}\right)\left(1-\gamma_0^{-1}\right)} \tag{15}$$

and $\hat{\eta}$ is the normalized efficiency given by:

$$\hat{\eta} = \int_0^{2\pi} u(\mu, \Theta_0)\, d\Theta_0 \tag{16}$$

where $\mu$ denotes the normalized interaction length and $\Theta_0$ is the initial value of the slowly varying phase parameter. For a given harmonic, recoil parameter, and axial profile for the wave field, the normalized efficiency for optimized $\Delta$ can be presented on an $F-\mu$ plot

similar to the plot used to characterize the gyrotron [3]. The parameter $F$ defined in this paper divided by two is equal to the amplitude parameter $F$ defined by Danly *et al* [3] in the limit: $b \rightarrow 0, \beta_{ph} \rightarrow \infty$. A plot of optimized constant normalized efficiency contours as a function of $F$ and $\mu$ is shown for the case of $b = 0.4$ and constant wave field amplitude in Figure 1. The corresponding iso-$\Delta$ values are shown in Figure 2. Figures 1 and 2 show that for a constant field profile, the maximum normalized efficiency is $\approx 36\%$ and the optimum parameters are $F = 0.2$, $\mu = 8$, and $\Delta = 0.6$. It is of interest to note that in the gyrotron limit ($b = 0$), the optimum normalized efficiency is 42%. In the case of the gyrotron the normalized efficiency can be increased to over 70% by suitably profiling the axial profile of the wave field and it is expected that a similar enhancement for the CARM can be achieved using this technique.

# 3 Short-Pulse 100 GHz CARM Oscillator

A Proof-of-Principle experiment based on a waveguide cavity with a Bragg reflectors has been set up to investigate the CARM configuration. The device is designed to operate at 100 GHz with a 600 KV, 200 Amp electron beam produced by a pulseline accelerator with a pulselength of $\sim$ 50 nsec. The choice of beam and cavity parameters is based on the theory outlined in Section 2. This theory, which assumes a cold beam, predicts an efficiency of 20% at a power of 24 MW. A schematic of the device configuration is shown in Figure 3. The annular electron beam propagates near the wall of the Bragg reflector waveguide cavity which has been optimized for the $TE_{61}$ circular waveguide mode.

The ability to produce a high quality beam is considered critical to the success of this experiment, a major objective of which is to demonstrate high efficiency for the CARM interaction. The beam quality requirement can be estimated by a simple coherence argument. The constraint on axial velocity spread is:

$$\Delta v_{\|}/v_{\|} < \lambda/(2L) \tag{17}$$

for no spread in beam energy. Equation (17) can readily be expressed as a constraint on pitch angle spread. The constraint on energy spread for a beam with no pitch angle spread

is

$$\frac{\Delta\gamma}{\gamma} < \frac{(1-\gamma_0^{-2})(\lambda/2L)}{(1+\alpha^2)(\Omega/\omega-\gamma_0^{-2})} \qquad (18)$$

where $\alpha$ is the average momentum pitch ratio of the beam. These relationships lead to the curves for axial momentum, pitch angle, and energy spread shown in Figure 4 for a 600 kV CARM with $\beta_\perp = 1/\gamma_0$. These curves show that there is greater sensitivity to pitch angle spread than to energy spread, a feature related to the auto-resonant character of the interaction. Note that the denominator of Eq.(18) can be small when $\gamma \gg 1$ since in this case for the CARM $\omega/\Omega \approx \gamma^2$. The required tolerances are considered achievable except for group velocities very close to the speed of light. To minimize sensitivity to beam velocity spread, a group velocity of 0.86c was chosen for the 100 GHz short pulse experiment.

The cold cathode diode is expected to produce a highly laminar space-charge-limited-flow beam via the use of nonemitting focussing electrodes. The cathode is anodized aluminum with a velvet or graphite emitting surface. The diode is expected to produce a high quality beam with only a few percent spread in axial momentum. This diode is based on a theory of relativistic laminar flow diodes recently developed at NRL by Finn, Fliflet and Manheimer [4]. The transverse momentum required for the CARM interaction is provided by a nonadiabatic dip in the applied magnetic field followed by adiabatic compression of the magnetic field [5]. Simulations of the beam formation system carried out using the Hermannsfeldt Electron Trajectory Code [6] indicate that an axial velocity spread of about 3% in the interaction region should be obtainable with this system.

An important feature of the Bragg reflector cavity is that it is has a high $Q$ factor for only a limited range of axial wavenumbers. Our design studies for the 100 GHz CARM experiment indicate that this type of cavity can be highly selective with respect to both transverse and longitudinal mode indices [7,8]. Other advantages of this type of resonator include compactness which facilitates beam transport and magnet design, and the possibility of profiling the cavity fields for efficiency enhancement similarly to what is done for gyrotrons. A Bragg cavity and associated radiation profile are shown in Figure 5. The depth of the Bragg ripples is considerably exaggerated. The $TE_{61}$ whispering gallery mode with $Q \approx 1500$ was chosen as the operating mode. This type of mode couples well to both the

electron beam and to the Bragg reflectors. Other whispering gallery modes with radial index $n = 1$ represent the principal CARM-type competing modes. The frequency separation of 3 GHz should prevent competition between these modes while allowing step-tunability. Another important feature of this cavity is that reflector bandwidth was chosen sufficienctly narrow that there is only a single axial mode per transverse mode. The CARM mode $Q$ factor must be chosen high enough to prevent competition from low frequency (gyrotron) modes.

# 4 Long-Pulse CARM Oscillator

The present 600 kV, 100 GHz CARM oscillator project is expected to provide important data on the potential of the CARM as an efficient high power source. However, a thermionic cathode experiment is essential for complete investigation of CARM issues. A preliminary design has been obtained at for a 500 kV, 250 GHz thermionic cathode device. A 55 kG magnetic field —produced by a superconducting magnet—is required for operation with $\beta_\perp = 1/\gamma$. A $TE_{14}$ mode has been chosen based on output power, e-beam size, and wall heating considerations. High power operation in a waveguide cavity at wavelengths $\leq$ 1 mm requires group velocities close to the speed of light with attendant sensitivity to beam quality. This results from the need for cavity dimensions large compared to the wavelength and the need to control ohmic heating. A group velocity of 0.97c was chosen for the preliminary design. An output power of 10 MW is obtained for 92% output reflectivity and the wall loading is about 3 kW/cm$^2$ for the optimum efficiency wave amplitude. The peak electric fields at the wall are less than 50 KV/cm for the $TE_{14}$ mode. Operation at 10% duty factor would result in an average power of 1 MW and an average wall loading of 0.3 kW/cm$^2$. The computed cold beam efficiency is $\sim$ 20% and the required beam current is 100 Amps. The cavity radius is 9.3 mm and the electron beam radius for a beam placed on the third E-field peak — this avoids coupling to whispering gallery modes which have high ohmic losses — is 5.6 mm. An annular electron beam is generated by a temperature-limited MIG type 500 kV electron gun. The cathode emission current density is $\sim$ 10 A/cm$^2$ at a current of 100 Amps, a cathode loading compatible with high duty factor operation.

The gun perveance is 0.28 $\mu$perv. For comparison, the gun for the SLAC klystron has a perveance of 2 $\mu$perv; thus space-charge defocussing effects should be controllable. Very low pitch angle spread (a critical CARM requirement) should be obtainable with this type of gun. The design goal is an axial momentum spread of a few percent. This experiment should provide highly a relevant technology base for a burst mode 280 GHz source for CIT or Alcator C-Mod.

A preliminary electrode design has been obtained for a 500 kV, 100 Amp, 1 $\mu$sec pulse-length MIG-type electron gun. Based on calculations using the Herrmannsfeldt Electron Trajectory Code, the electrodes produce a highly laminar, temperature-limited, annular electron beam with a final momentum pitch ratio $\alpha \sim 0.5$ and very low axial velocity spread, $\Delta v_{\|}/v_{\|} \sim 1\%$. A schematic of the gun is shown in Figure 6.

Volume TE modes such as $TE_{0n}$ or $TE_{1n}$ type modes have much lower wall losses due to ohmic heating and lower peak rf fields at the wall than whispering gallery ($TE_{m1}, m \gg 1$) modes and are therefore of interest for high duty factor applications. However, special cavity designs are required to select these modes. Possible approaches include the use of axial *slots to select* $TE_{1n}$ *modes or suppression of axial currents (wire-walled waveguide) for* $TE_{on}$ modes. Quasi-optical cavity configurations will also be investigated. The attractiveness of such cavities increases with increase in the radiation frequency since for high power it becomes necessary to increase cavity size relative to the wavelength. Open mirror quasi-optical cavities also allow the wave phase velocity to be controlled independently of the transverse mode or transverse dimensions of the cavity. As discussed by Sprangle *et al* [9], this control is obtained by varying the angle between the radiation and beam propagation directions. The phase velocity can also be chosen to minimize the effect of beam energy spread. Quasi-optical cavities have excellent transverse mode selectivity and should not support low frequency (gyrotron) modes.

# 5 Acknowledgment

This work was supported by the U.S. Office of Naval Research.

# References


[1] V. L. Bratman, N.S. Ginzburg, G.S. Nusinovich, M.I. Petelin, and P.S. Stelkov, Int. J. Electron. **51** (1981) 541

[2] A.W. Fliflet, Int. J. Electron. **61** (1986) 1049

[3] B.G. Danly and R.J. Temkin, Phys. Fluids **29** (1986) 561

[4] J.M. Finn, A.W. Fliflet and W.M. Manheimer, Int. J. Electron. **61** (1986) 985

[5] S.H. Gold, A.W. Fliflet, W.M. Manheimer, R.B. McCowan, W.M. Black, R.C. Lee, V.L. Granatstein, A.K. Kinkead, D.L. Hardesty and M. Sucy, Phys. Fluids **30** (1987) 2226

[6] W.B. Herrmannsfeldt, SLAC-Report-226, Stanford Linear Accelerator Center, Stanford, California, U.S.A. (1979)

[7] R.B. McCowan, A.W. Fliflet, S.H. Gold, V.L. Granatstein and M.C. Wang, Int. J. Electron. **65** (1988) 463

[8] R.B. McCowan, A.W. Fliflet, S.H. Gold, W.M. Black, A.K. Kinkead, V.L. Granatstein and M. Sucy, IEEE Trans. Electron Devices, Part II, to be published

[9] P. Sprangle, C.-M. Tang and P. Serafin, Nucl. Instrum. Methods Phys. Res. **250** (1986) 361

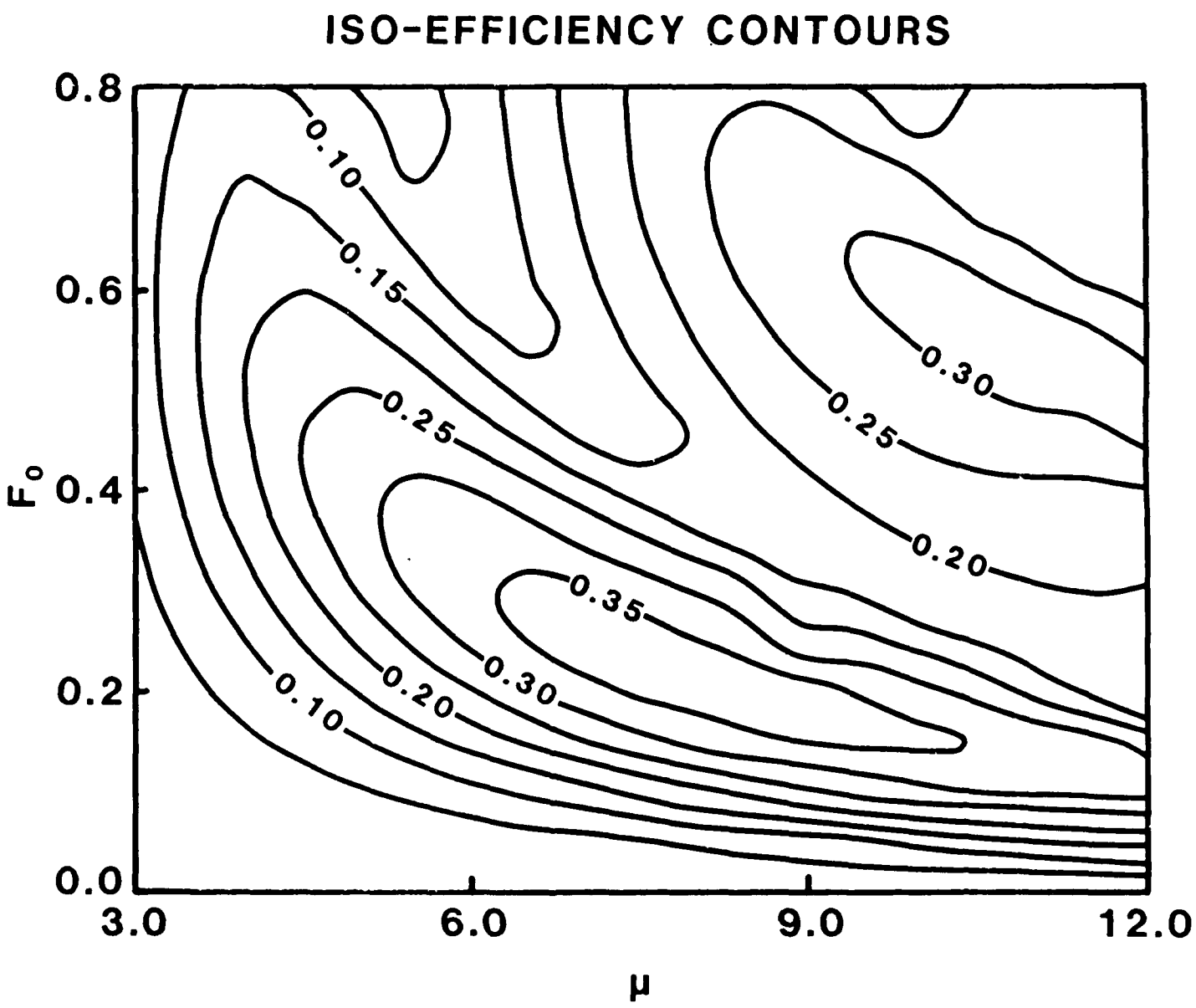



**Figure 1.** $F - \mu$ plot of optimum normalized efficiency for a constant amplitude wave and $b = 0.4$.

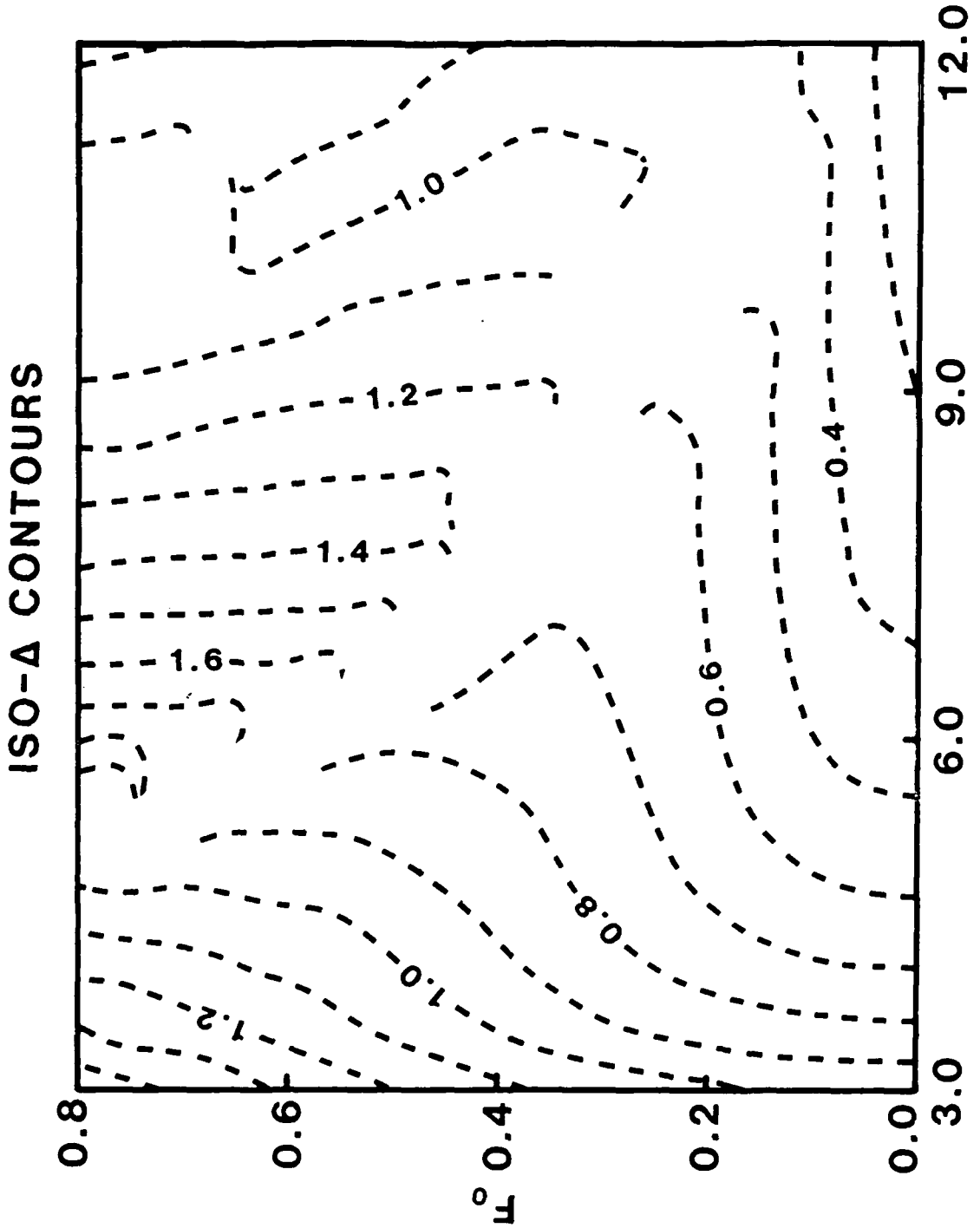



Figure 2. $F - \mu$ plot of $\Delta$ corresponding to optimum efficiency for a constant amplitude wave and$b = 0.4$.

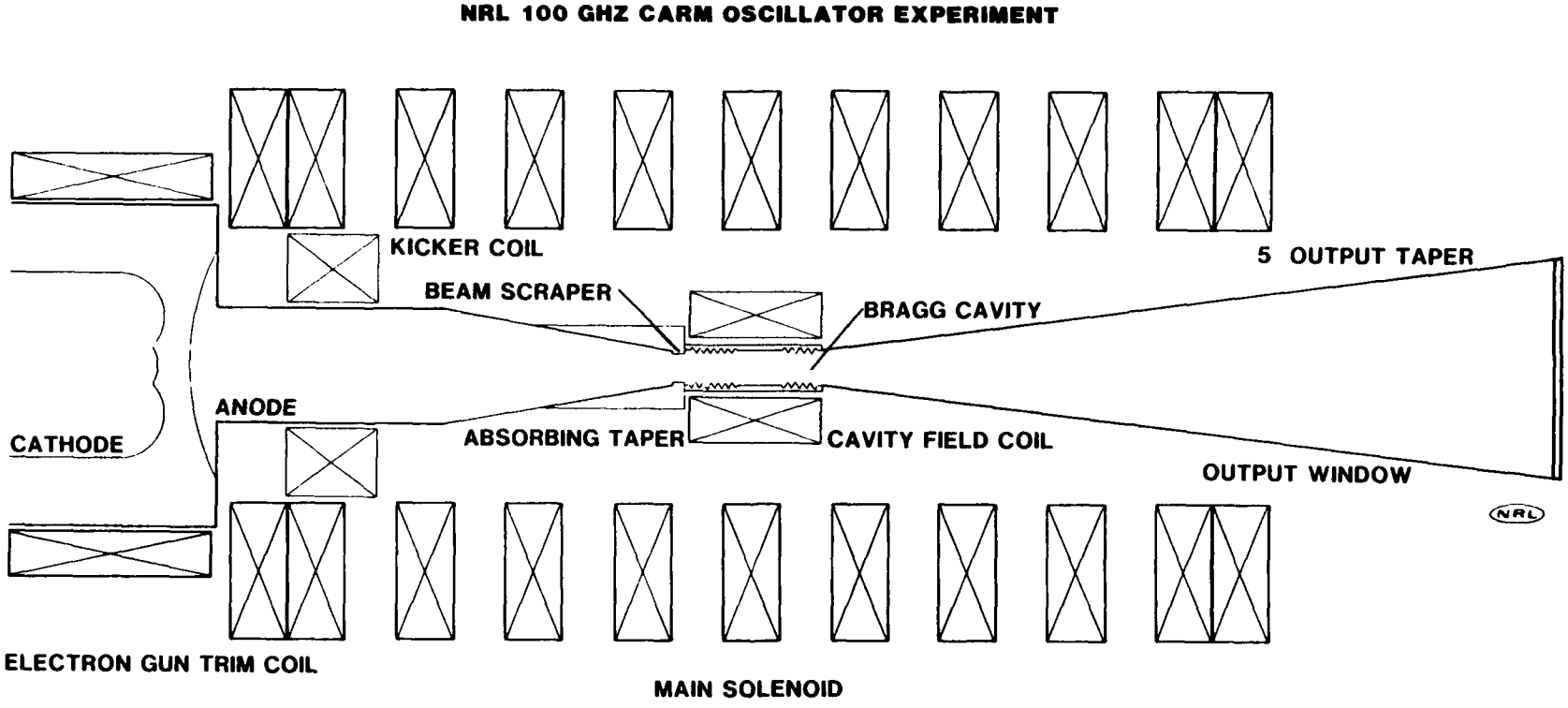



**Figure 3.** Schematic of 100 GHz short-pulse CARM Oscillator experiment.

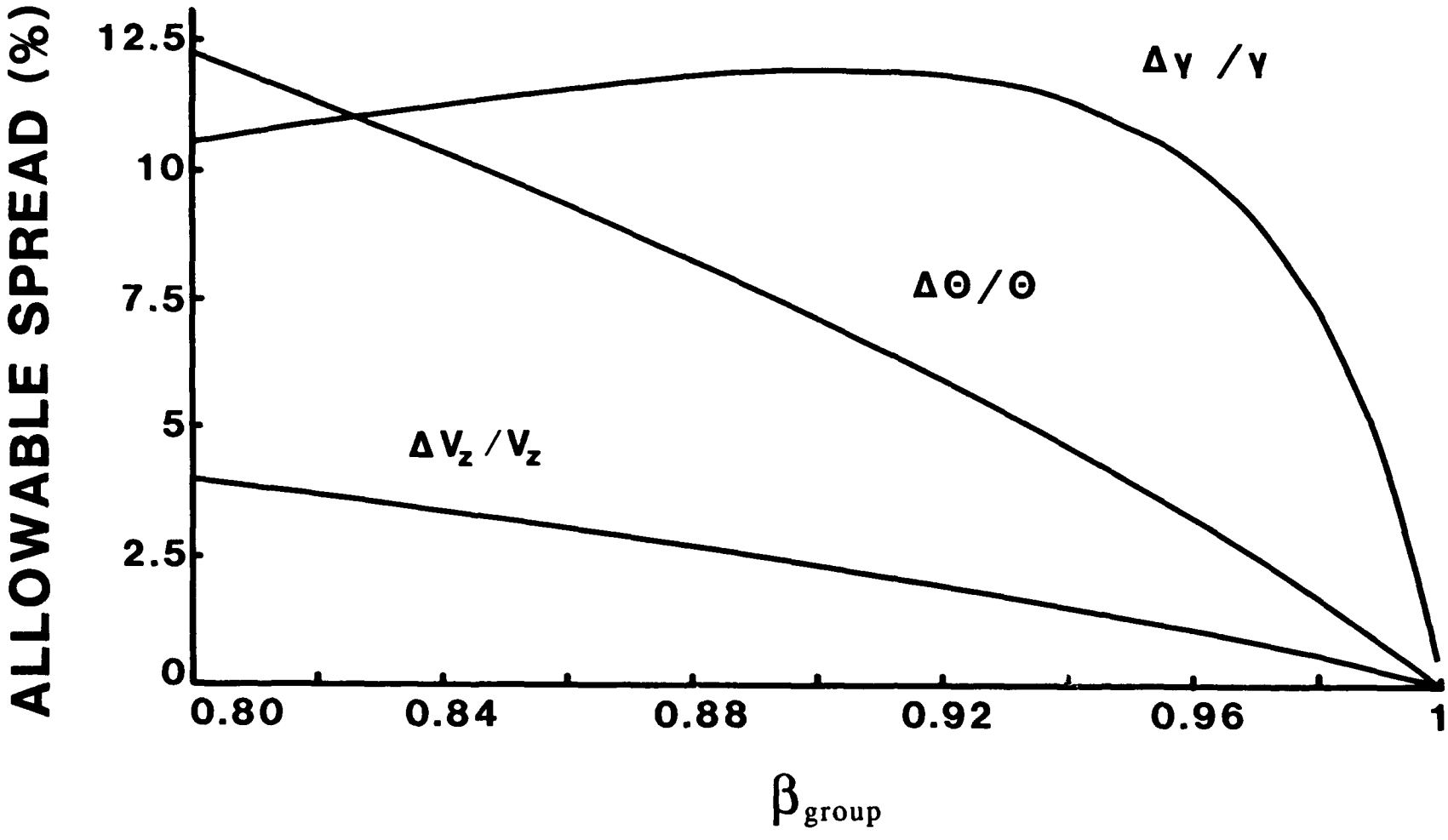



**Figure 4.** Electron beam quality requirements for a 600 kV CARM oscillator with $\beta_\perp = 1/\gamma_0$.

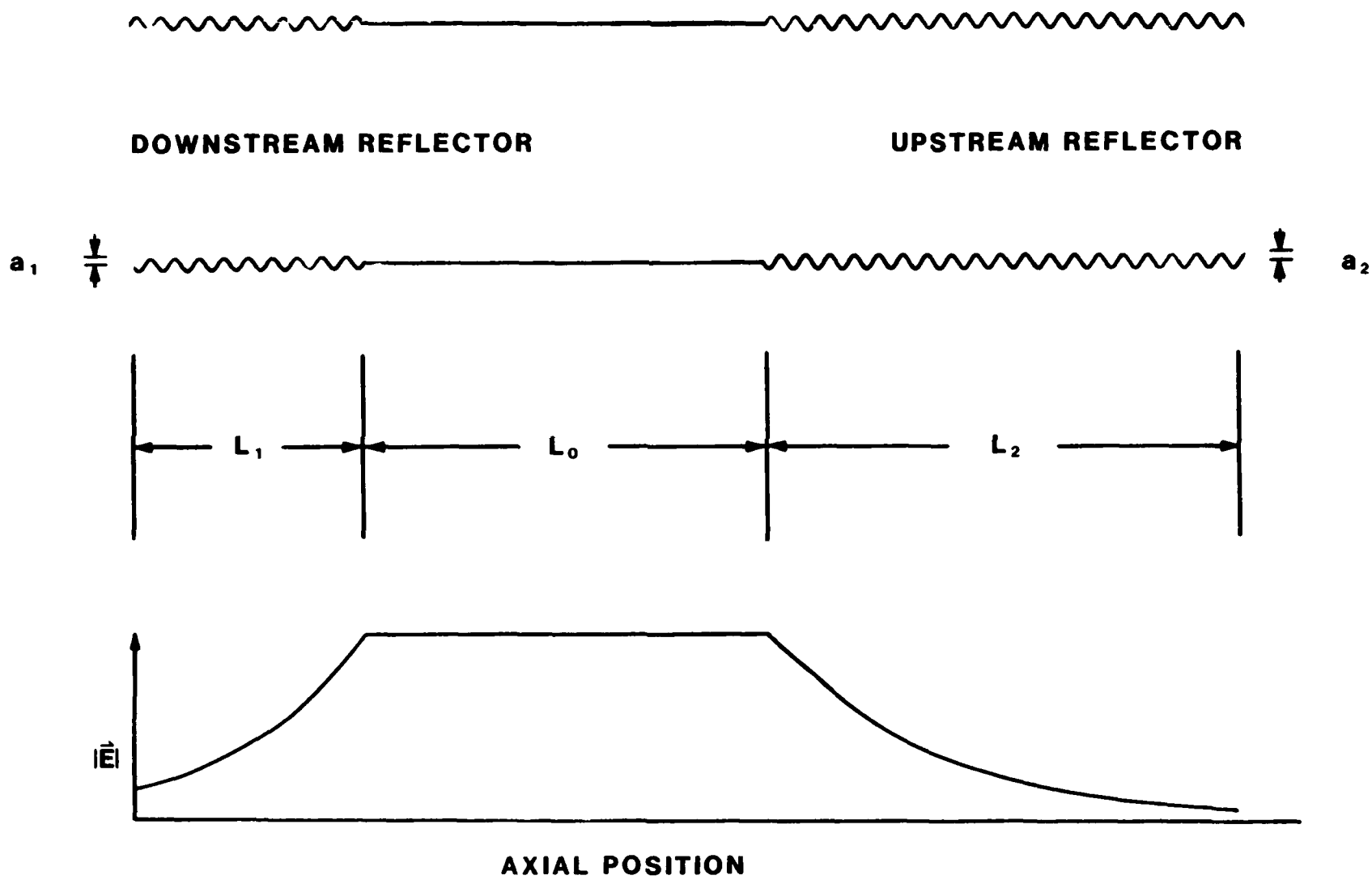



Figure 3. CARM waveguide cavity with Bragg reflectors and associated radiation profile.

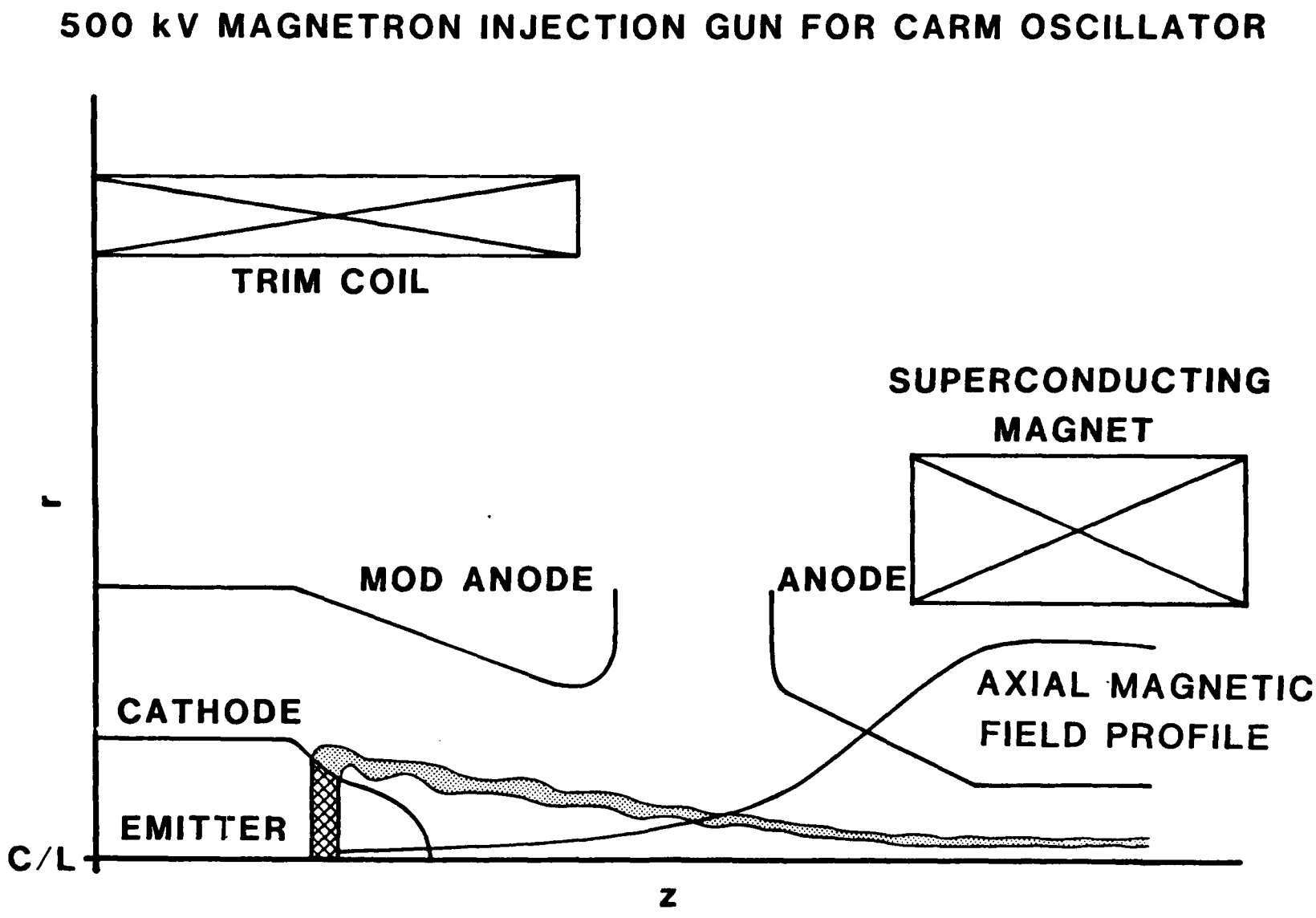



**Figure 6.** Schematic of a 500 kV, temperature-limited cathode, MIG-type electron gun for a 250 GHz CARM oscillator.

# APPENDIX F

## Design and Operating Characteristics of a CW Relevant Quasi-Optical Gyrotron with Variable Mirror Separation

# Design and Operating Characteristics of a CW Relevant Quasi-Optical Gyrotron with Variable Mirror Separation

A.W. Fliflet, T.A. Hargreaves,* W.M. Manheimer,
R.P. Fischer, M.L. Barsanti,†
B. Levush‡ and T. Antonsen§¶

High Power Electromagnetic Radiation Branch
Plasma Physics Division
U.S. Naval Research Laboratory
Washington, D.C. 20375-5000, U.S.A.

April 13, 1989

**Abstract**

Results from a quasi-optical gyrotron experiment with a 20–28 cm mirror separation will be presented showing operation at powers up to 150 kW and efficiencies up to 12%. The output coupling could be varied from 0.4–3% by changing the mirror separation and operating frequency. Operation was obtained over frequencies ranging from 95–130 GHz by changing the axial magnetic field, limited on the low end by waveguide cutoff in the diagnostics and at the high end by the maximum magnetic field achievable. The output power varied by approximately a factor of 2 over this range. Frequency variation of 4% was achieved by varying only the electron gun voltage; however, the output power also varied substantially due to the fact that the electron beam power was changing dramatically. Efficiency optimization by variation of output coupling and by tapering the magnetic field has been demonstrated. Regions of single-mode operation at powers up to 125 kW have been characterized and compared to recently developed theory. Details of the experimental design and its numerical modeling, along with the data obtained and its comparison to relevant theories are presented.

*Mission Reseach Corporation, Newington, VA
†Jaycor, Inc., Vienna, VA
‡University of Maryland, College Park, MD
§Science Applications International Corporation, McLean, VA
¶Permanent address: University of Maryland, College Park, MD

# I Introduction

There is currently a need for megawatt average power sources of 100–300 GHz radiation for electron cyclotron heating of fusion plasmas. The leading candidate for such a source, the waveguide cavity gyrotron [1], has produced output powers of 765 kW and efficiencies of 30% at 148 GHz in a CW-relevant configuration [2]. However, this gyrotron configuration is limited at high frequencies by high ohmic heating and problems with transverse mode competition, due to the highly overmoded configuration, and with beam collection, since the beam must be collected along a section of the output waveguide. The quasi-optical gyrotron (QOG), first proposed in 1980 by Sprangle, Vomvoridis and Manheimer [3], features an open resonator formed by a pair of spherical mirrors instead of a waveguide cavity and has the potential for overcoming each of these limitations. The resonator mirrors can be well removed from the beam-wave interaction region, allowing a large volume for the interaction and low ohmic heating densities at the mirrors. The beam direction is transverse to the cavity so that beam collection is separate from the output waveguide. This geometry is particularly well suited to the use of a depressed collector for electron beam energy recovery. The QOG operates in the lowest-order transverse ($TEM_{00l}$) Gaussian mode of the resonator, higher-order transverse modes being effectively suppressed by higher diffraction losses. Output coupling is via diffraction around the mirrors and can be controlled independently of other interaction parameters. The axial mode separation is small compared to the interaction bandwidth in CW-relevant configurations so that multimode effects are important.

The theory of multimode operation was developed by Bondeson, Manheimer and Ott [4]. The theory of quasi-optical gyro-klystrons and of operation at the harmonics of the electron cyclotron frequency has also been examined [5,6]. The first QOG experiment was carried out in 1984 by Hargreaves *et al.* [7] and used a resonator with a 4 cm mirror separation. Consistent with the relatively low axial mode density of this resonator, single-mode operation was observed at powers up to 80 kW at a frequency of 110 GHz and an efficiency of 11%. The first experiment with large mirror separation (81 cm) was conducted in 1986 by

Read *et al.* [8] and achieved an output power of 50 kW at a frequency of 115 GHz and an efficiency of 7%.

The QOG is currently under investigation by several different groups. Alternate resonator configurations have been proposed and analyzed by Zhonghai, Shenggang and Kongyi of the People's Republic of China [9,10] and an experimental study of different output structures has been performed by Morse and Pyle [11]. Itoh et al. have utilized yet another resonator design to produce 20 kW of RF power at an efficiency of 16% and a frequency of 120 GHz [12]. This experiment utilized a relatively low power electron beam ($V = 30$ kV, $I = 3.5$ A). Experiments similar to those described here are being performed by Tran et al. [13]. With limited experimental time, powers and efficiencies as high as 85 kW and 10% have been observed from a cavity with a mirror separation of 34 cm.

A resonator mirror separation of 81 cm is much larger than necessary for a CW device and therefore has many more cavity modes than necessary within the interaction bandwidth of the device. The limiting factor on reducing the mirror separation is the ohmic heating of the mirrors. To be relevant to a CW device, the ohmic losses must be kept below a few kW/cm$^2$. To investigate the operation of a QOG with a minimum mode density consistent with a CW device, experiments have been performed utilizing a resonant cavity with a mirror separation of 20–28 cm.

A consequence of the use of a spherical mirror cavity with diffraction output coupling is that the output coupling can be a sensitive function of the mirror separation while the gyrotron interaction length, which depends on the radiation beam waist, remains approximately constant. This feature has been exploited for the first time in this experiment by using mirror holders which are adjustable over a wide range. The ability to vary the separation of the resonator mirrors from 20 to 28 cm allowed the resonator output coupling to be optimized with respect to the electron beam power. It also allowed new tests of the gyrotron scaling theory. The coupling of the annular electron beam to the standing-wave radiation in the cavity could be varied by translating the cavity transversely to the electron beam. Finally, precise mirror alignment–needed for optimum cavity $Q$–was easily maintained.

Several other aspects of this experiment have been upgraded from past experiments as well. The vacuum window that the output radiation passes through which is used here is made of thin ($\sim \lambda/10$) mylar. Thus, the window is essentially completely transparent over the complete frequency range of the experiment, making the measurement of the relative amplitudes of the different modes possible. Also, the possibility of the RF being reflected from the window back into the resonant cavity and affecting the electron beam–RF interaction is minimized. The new superconducting magnet used in this experiment was much more reliable than the magnet used in the past and also produced a much more uniform axial magnetic field. Essentially the electrons now have a much lower magnetic field bump to pass over as they travel into and out of the resonant cavity.

This paper presents results from a thorough and extensive experimental study of the first QOG to operate at powers over 100 kW using a CW-relevant resonator. The QOG was tunable from 95–130 GHz and operated at powers up to 148 kW and output efficiencies up to 12%. The peak electronic efficiency is estimated to be $16 \pm 2\%$. The main effect responsible for the difference between the output and electronic efficiency is ohmic heating of the mirrors which can be a significant fraction of the total output at low output coupling. This effect becomes small at MW output power levels due to larger output coupling. Single-mode operation was observed at powers up to 125 kW. Conditions for single-mode operation in the highly overmoded system have been characterized and compared with theoretical predictions. Efficiency optimization by variation of output coupling and by tapering the magnetic field have been demonstrated. These results point the way to the realization of megawatt level devices with output efficiencies of $\sim 20\%$.

A detailed description of the experimental configuration and diagnostic systems is given in Section II. Section III describes an investigation of threshold current behavior. Section IV describes power and efficiency, and the frequency tuning measurements are discussed in Section V. Section VI describes an investigation of single-mode or nearly single-mode operation and the comparison of this data with new theoretical results. Section VII presents additional discussion and conclusions drawn from the experiment. The technique used for calibrating the calorimeter used in the power measurements is analyzed in the Appendix.

# II Description of Experiment

## II-A Experimental Setup

A schematic diagram of the experiment is shown in Figure 1. The gyrating electron beam is generated by the MIG-type electron gun at the bottom of the superconducting magnet and propogates up through the drift tube and cavity before being absorbed in the collector. The microwave fields interact with the electron beam between the collector and drift tube where electrostatic space charge depression can affect the beam electrons' energy. The microwave power diffracted around each mirror is collected as output and propogated through the thin mylar window out of the vacuum. Design details of each of the experimental components are given in the following sections.

## II-B Microwave Cavity

The microwave cavity utilized in these experiments consisted of the Fabry-Perot type open resonator shown in Figure 2. The spherical cavity mirrors formed an azimuthally symmetric cavity about the cavity axis. The mode structure and stability of this type of resonator is discussed by Yariv [14] who finds that the $x$-component of the electric field of the transverse electric and magnetic ($\mathrm{TEM}_{m,n}$) modes in the cavity is given by:

$$E_x^{m,n}(x,y,z) = E_0 \frac{w_0}{w(z)} H_m\left(\frac{\sqrt{2}x}{w(z)}\right) H_n\left(\frac{\sqrt{2}y}{w(z)}\right) \exp\left\{-\frac{(x^2+y^2)}{w^2(z)}\right\} \sin\{kz + \varphi(x,y,z)\} \cos\omega t \quad (1)$$

where $H_m$ is a Hermite polynomial of order $m$, $w_0$ is the radiation beam waist,

$$\varphi = \frac{k(x^2+y^2)}{2R_w(z)} - (m+n+1)\tan^{-1}(z/z_0) \quad (2)$$

is the wave phase shift,

$$w^2(z) = w_0^2\left(1 + z^2/z_0^2\right), \quad (3)$$

$$R_w(z) = z\left(1 + z_0^2/z^2\right), \quad (4)$$

$z_0 = \pi w_0^2/\lambda$ is the Rayleigh length, $k$ is the wave number, $\lambda$ is the wavelength and $\omega$ is the angular frequency of the radiation, and $R_w$ is the radius of curvature of the spherical

wavefront. As can be seen from Eq.(1), the electric field of the $TEM_{00}$ mode decreases more rapidly as a function of radius than that of the higher order modes. Therefore it may be expected that an appropriate choice of mirror diameter may yield a cavity where modes other than the $TEM_{00}$ are relatively unimportant due to their larger diffraction losses. For an electron beam located near the center of the cavity ($z \ll z_0$), and with dimensions small compared to the radiation beam waist, then $\wp \simeq 0$ and

$$E_x^{m,n}(x,y,z) = E_0 \exp\left\{-\frac{y^2}{w_0^2}\right\} \sin kz \cos \omega t. \tag{5}$$

The experimental cavity utilized 5 cm diameter mirrors with a 38.7 cm radius of curvature and were separated by 20–28 cm. These values place the cavity well into the stable region of parameter space as can be seen in Figure 3. A numerical code was used to calculate the electric field profiles at the surface of each mirror and thus the diffractive $Q$ factor of the cavity. The details of the scalar theory on which these calculations are based are discussed in Ref. [15]. The calculated diffraction losses are lowest for the $TEM_{00}$ mode, giving that mode the highest $Q$ value as expected. The diffractive output coupling for the $TEM_{00}$ mode calculated by the code is plotted as a function of mirror separation for frequencies of 110, 120, and 130 GHz in Figure 4. The corresponding calculated total $Q$ factors including ohmic losses for gold-coated mirrors (assumed conductivity: $\sigma = 4.5 \times 10^7$ siemens/m) are plotted in Figure 5. Other calculated parameters for the cavity are shown in Table I for various mirror separations.

The total ohmic losses in the cavity for a given electric field amplitude in the electron beam interaction region are independent of mirror separation for constant output coupling and are essentially independent of output coupling for constant mirror separation. Therefore, the fractional power lost to ohmic heating increases as the output coupling decreases. The ratio of power lost through ohmic heating of the mirrors ($P_o$) to the diffraction output power ($P_d$) is given by

$$\frac{P_o}{P_d} = \sqrt{\frac{32\omega}{Z_0 c \sigma}} \frac{1}{T}, \tag{6}$$

where c is the speed of light, $T$ is the total round trip cavity diffraction loss, and $Z_0 = 377$ is the free space impedance. The ratio of ohmic heating to radiated output power is plotted

as a function of mirror separation for frequencies of 110, 120, and 130 GHz in Figure 6. This figure shows that at 120 GHz and 20 cm mirror separation, the ohmic heating is over 40% of the radiated power. As shown in Eq. (6), this ratio would decrease to a much smaller value in a higher power device with several times larger output coupling. The peak heating density at the center of the mirrors can be expressed in the form

$$\rho\left(kW/cm^2\right) = 4.1 \times 10^{-22}\sigma^{-0.5}\omega^{2.5}\gamma^2\beta_\perp^6\left(1+g\right)F^2, \tag{7}$$

where $\gamma$ is the electron beam relativistic factor, $\beta_\perp$ is the transverse velocity normalized to the speed of light, $g = 1 - d/R$, where $d$ is the mirror separation and $R$ is the mirror radius of curvature, and $F$ is the peak normalized wave amplitude at the beam defined by

$$F = \frac{E_0}{B_0 c \beta_\perp^3}, \tag{8}$$

where $B_0$ is the applied axial magnetic field. The heating density can be controlled by allowing the parameter $g$ to approach $-1$, that is, by moving the mirrors further apart. Using the radius of the phase front, given by Eq. (4), it is readily verified that at $z = d/2$, $g > -1$, but approaches the unstable limit $g = -1$ as $d \to \infty$. As shown in Figure 3 the limit $g = -1$ corresponds to the concentric resonator which is on the boundary between stable and unstable configurations. In the present configuration $0.3 < g < 0.5$, which is well within the stable region. To a good approximation, the average heating density on the mirrors for a Gaussian resonator mode is obtained by dividing the peak heating density by $\ln T_m^{-1}$, where $T_m$ is the output coupling per mirror.

A final value calculated by the mirror cavity code is the amount of the diffracted power that is actually collected as output compared to that diffracted around the outside of the output collecting waveguide. In general, this fraction is highest for high output coupling and when the output is collected off of both mirrors. A second reason for collecting output from both mirrors is that it makes possible a completely symmetric system and simplifies the analysis.

## II-C Cavity Mirror Holders

It is well known with cavity gyrotrons that the cavity alignment with the electron beam is critical for optimum performance of the gyrotron. In the QOG, the cavity fields at the electron beam form essentially a standing plane wave. The position of the the annular electron beam (diameter: 3.2 mm) is not as critical, although there is a loss in coupling efficiency with single-mode theory predicting a reduction of approximately 30% in the output efficiency of the device relative to the case of a pencil beam. An overlay of the electron beam with the cavity electric field for the case of the beam axis on the field maximum is shown in Figure 7. On the other hand, alignment of the two cavity mirrors with each other is critically important. For this reason, the cavity mirror holders were designed so that each mirror could be individually aligned with the other mirror. The mirror holders are shown in Figure 8. Each mirror can move 4 cm axially, allowing the cavity to be translated as a unit relative to the electron beam as well as allowing for as much as an 8 cm variation in mirror separation.

## II-D Microwave Transmission System

The output waveguide system is an integral part of the mirror holder design shown in Figure 8. The fact that each mirror must be able to move relative to its mounting flange forces the output waveguide to be discontinuous, a less than desirable trait. The result of this discontinuity may be some reflection of the output microwave power back toward the resonant cavity, although the reflected power is expected to be relatively small due to the large diameter of the waveguide compared to the operating wavelength.

The output waveguide has a diameter of 10 cm at the surface of the cavity mirror, maximized to collect as much of the output radiation as possible, and limited only by the size of the magnet cross-bore. A cone is attached to the back of the mirror, so that the output system which begins as coaxial waveguide slowly tapers down to cylindrical waveguide. The cylindrical waveguide then undergoes a seri· of gradual tapers and two discontinuities as shown in the figure, with the final discontinuity occuring at the vacuum window. The tapers and discontinuities in the output waveguide are not expected to cause

large reflections since the waveguide diameter is always large compared to the radiation wavelength ($d \approx 20\lambda$). The vacuum window used in these experiments was 0.013 cm thick mylar. Its dielectric constant is estimated to be approximately 3.2, making the window thickness $< 0.1\lambda$ at 120 GHz. Therefore the window possessed the admirable quality of being essentially transparent to any of the radiation produced in the experiment.

The two waveguide outputs were typically terminated in different diagnostics. The microwaves from one were allowed to radiate from the open end of the waveguide toward a modified laser calorimeter placed approximately 5 cm away. The microwaves from the other output waveguide were allowed to radiate into a box lined with microwave absorber. The open end of a piece of fundamental waveguide was inserted through the end of the box into the radiation pattern and used as a pickup to measure the characteristics of the microwave radiation.

## II-E Electron Gun

The electron gun used in this experiment was a Varian VUW-8010 magnetron injection gun originally designed for use at 35 GHz [16]. Two trim coils in the gun region augmented the superconducting magnet coils. These coils were operated with opposing currents and were used to vary the magnetic compression of the beam and to avoid beam interception in the gun region. The fact that the QOG is relatively insensitive to the size of the electron beam and its axial velocity spread eased the requirements on the gun, making the VUW-8010 gun usable.

The electron gun was modeled using the Hermannsfeldt electron trajectory code [17]. Modeling the electron trajectories from the gun into the cavity is a fairly time consuming computational task due to the relatively large dimensions of the gun and beam drift tube compared to the electron gyroradius. For this reason the electrons were followed into the microwave cavity in only a few cases. Instead, the parameter space was experimentally explored, essentially by optimization of the trim coil currents, with the electron trajectory code being used to model specific experimental settings. The geometry modeled is shown in Figure 9, and the results of the calculation are plotted in Figure 10. This run was stopped

slightly after the position of maximum magnetic field. If the electron trajectories are then adiabatically scaled down to the cavity field, the average alpha value is reduced from 1.4 to 1.3. The 37% spread in alpha calculated means that some of the electrons in the beam are close to being reflected by the compressing magnetic field. This yields a beam with the largest $\alpha$ and is consistent with the experiment, which tended to produce the best results when the electron gun was operated on the edge of stability.

## II-F Electron Beam Path

The electron beam is produced by the electron gun in a relatively low ($B = 0.29$ T) magnetic field. As the electrons travel toward the cavity, they are compressed by the strengthening magnetic field which peaks at 5.4 T (for a 5.0 T magnetic field in the microwave cavity). As the electron beam is compressed, the electron energy is essentially transferred from motion parallel to the magnetic field into motion perpendicular to the magnetic field. It is the perpendicular motion that mainly interacts with the microwave fields in the cavity to produce radiation.

As the electrons emerge from the electron gun, they enter the drift tube shown in Figure 11, the first section of which is a tapered piece of graphite. Since the magnetic field and hence the electron beam velocity pitch ratio $\alpha$ is low, the chance of exciting gyrotron modes in this section is minimal. This danger increases as the electron beam travels toward the cavity and is compressed by the magnetic field. For this reason, dielectric rings (with a large loss tangent) are used to heavily load any possible microwave cavity in the remainder of the drift tube. The dielectric rings are alternated with copper "scraper" rings designed both to prevent the electrons from hitting the dielectric and also to ensure that excessive charge is prevented from building up on the surface of the dielectric, reducing the potential and affecting the beam propogation. The second (inner) dielectric ring shown in this figure has an intermediate dielectric constant to minimize reflections of the microwaves from the surface of the lossy medium. The peak magnetic field experienced by the electrons (where the electrons have their largest perpendicular momentum and, hence, free energy) is actually inside the drift tube.

In the QOG the electron beam experiences space-charge effects in the drift tube between the gun and the cavity and in the open region between the end of the beam drift tube and the collector. An estimate for the space-charge depression of the beam voltage in the drift tube is [18,19]

$$\Delta V_{sc} = \frac{60I}{\beta_{||}} \ln\left(R_d/r_b,\right) \tag{9}$$

where $I$ is the beam current, $\beta_{||}$ is the axial velocity normalized to the speed of light, $r_b$ is the beam radius, and $R_d$ is the drift tube radius which is 0.5 cm in the present experiment. For typical parameters of 75 kV and $\alpha = 1$, this leads to a voltage depression in the drift tube of $\Delta V = 2$ kV at 10 A. An accurate calculation of space-charge depression in this region involves two-dimensional effects, but a simple estimate for the space-charge depression of the beam voltage in this region can be obtained by replacing drift tube wall radius in Eq. (9) by half the drift tube–collector separation $L$. Although this choice is somewhat arbitrary and should be considered a temporary replacement for more accurate calculations, the result depends only logarithmically on the ratio of beam radius to half the length of the open space. A length of 5 cm was used in the present experiment. Cold tests showed that at this separation the presence of the beam guiding structures had no measurable effect on the cavity $Q$. The voltage depression of the beam due to space charge is plotted up to the space-charge-limited current for several beam voltages in Figure 12. This figure suggests that the highest currents at which the experiment was operated (which corresponded to the highest output powers) were near the space-charge limit. This prescription leads to an estimated space-charge depression of the beam in the optical resonator of $\Delta V = 4.8$ kV at 10 A which is more than twice the space-charge depression occurring in the drift-tube.

As soon as the electrons have exited the cavity fields, they enter the collector. The second peak of the magnetic field is inside the collector, which also serves to diminish space charge effects. Once past the magnetic field peak, the electrons essentially follow the magnetic field lines as they expand. Eventually, the magnetic field lines intersect the collector wall and the electrons are absorbed by the collector.

## II-G Diagnostics

A schematic diagram of the experimental diagnostics is shown in Figure 13. Standard millimeter-wave wafer diodes were used to measure the RF pulse shape. The diodes were terminated in 50 ohms to keep the response time of the diodes short compared to the radiation pulse width. Diodes from both Baytron and Hughes were used during these experiments with no inconsistencies observed.

The harmonic heterodyne system shown in Figure 14 was used to measure the frequency of the output radiation. The gyrotron radiation was inserted into the RF port of a harmonic mixer, and the power-leveled output of a frequency-locked 12-18 GHz YIG-tuned oscillator was applied to the LO port. The radiation out of the IF port was then measured through one of several bandpass filters used to vary the resolution of the device. The three frequencies are related by

$$f_{RF} = n f_{LO} \pm f_{IF}, \tag{10}$$

where n is the number of the harmonic of the local oscillator (frequency $f_{LO}$) that is mixed with the RF frequency from the experiment. The different bandpass filters each have a center frequency of 160 MHz so that for a given RF frequency, IF signals (frequency $f_{IF}$) will be measured for two different LO frequencies. The harmonic number may be determined from the frequency difference between the two LO frequencies,

$$n = 320 \text{ MHz}/\Delta f_{LO}. \tag{11}$$

Once the harmonic number has been determined, it is straightforward to calculate the experimental operating frequency from Eq. (10) above. The accuracy of this instrument depends mainly on the accuracy of the LO frequency measurement and the bandpass filter accuracy. Relative measurements depend only on the bandpass filter chosen so that accuracies of approximately $\pm 10$ MHz were possible. This was more than sufficient to differentiate between longitudinal cavity modes which have a frequency spacing of $\Delta\nu = c/(2d)$ or approximately 500 MHz at the maximum separation of 28 cm. A second method of measuring the frequency was to use the Fabry-Perot interferometer shown in Figure 15. The core of this device is a mirror cavity similar to the resonant cavity used in the experiment. The

electric fields in the interferometer are again given by Eq. (1), with modes other than the $TEM_{00}$ modes being effectively suppressed by the application of absorbing material around one of the mirrors to decrease its effective diameter. The phase of the RF field at position $z$ in the cavity is given by

$$\phi = \frac{2\pi z}{\lambda} - \tan^{-1}\left(\frac{z}{z_0}\right) \tag{12}$$

where $z_0 = 40$ cm is the Rayleigh length for this cavity. As the mirror separation is increased, successive resonances occur as $\phi$ is increased by $\pi$. To a good approximation, this occurs as the separation is increased integral numbers of half (free space) wavelengths. Thus by carefully measuring the distance that the mirror separation changes between successive resonances, the radiation wavelength can be measured to approximately 0.1%.

The main power diagnostic was the laser calorimeter shown in Figure 16. The absorbing surface was coated with several extra layers of paint, with its absorbancy being measured between each coat at 120 GHz. The absorbancy is plotted in Figure 17 as a function of paint thickness. Figure 18 shows the measured absorption of the calorimeter as a function of microwave frequency after the additional paint had been added. The problem of a plane electromagnetic wave incident on a dielectric layer backed by a conductor can be solved analytically. The geometry relevant to the quasi-optical gyrotron (electric field parallel to the boundary surface) is shown in Figure 19. The details of the calculation are given in Appendix A, where it is shown that the power reflection coefficient is $R = |(1-D)/(1+D)|^2$. The quantity $D$ is given by

$$D = \frac{\cos\theta_t}{\cos\theta_i}\sqrt{\frac{\epsilon_2}{\epsilon_0}}\left[\frac{1+e^{-2ik_2\tau\cos\theta_t}}{1-e^{-2ik_2\tau\cos\theta_t}}\right], \tag{13}$$

where $\theta_i$ is the angle of incidence; $\theta_t$ is the angle of transmittance; $\epsilon_2 = \epsilon_{r2}\epsilon_0(1-i\tan\delta)$ is the dielectric constant of the paint; $\epsilon_{r2}$, $\tan\delta$ and $k_2$ are the associated real part of the dielectric constant relative to vacuum, loss tangent and complex wave number, respectively; and $\tau$ is the thickness of the paint. Plots of the experimental data and the analytic calculations are shown in Figures 17 and 18. For these calculations the real part of the dielectric constant ($\epsilon_{r2}$) was 5 and the loss tangent was 0.25. These values result in reasonably good agreement once one realizes that the actual thickness of each layer of paint is unknown and probably

varied. For the data plotted, however, each paint layer is assumed to be of equal thickness.

The voltages applied to both the cathode and the intermediate anode were measured by capacitive dividers. Sample traces of each waveform are shown in Figure 20. The peak-to-peak voltage ripple is approximately 4% over the 12 $\mu$sec flat top of the cathode voltage pulse. The 10–90% rise time of the cathode pulse was 3.5 $\mu$sec, and the 90–10% fall time was 4 $\mu$sec. The intermediate anode voltage waveform was adjustable in steps of 1% of the cathode voltage. The shape (flatness and rise time) of the intermediate anode voltage trace could be controlled within limits by varying the capacitance in parallel with the voltage divider.

The collector and body currents were separately monitored by Pearson probes. These probes had a rise time of 10 nsec and a low frequency cutoff of 140 Hz, making them suitable for our purposes. The current trace is typically much longer than the flat-top of the voltage trace, due to the use of a thermionic electron gun with a voltage pulse that rises and falls somewhat slowly.

## II-H Magnetic Fields

The magnetic field is produced by a pair of superconducting coils and modified in the region of the electron gun by a pair of normal trim coils. The separation of the two superconducting coils is set by the cross-bore diameter necessary for the microwave cavity and radiation output structure. The presence of the cross-bore results in a magnetic field axial profile that is less than ideal. To achieve the necessary magnetic field strength in the cavity together with an appropriate cross-bore diameter, the superconducting coils had to be separated slightly more than a Helmholtz pair. This extra separation resulted in the cavity magnetic field being approximately 6.5% lower than the peak magnetic field along the magnet axis. A plot of the axial magnetic field is shown in Figure 21.

The effect of the pair of trim coils is localized near the position of the electron gun. The coil furthest from the superconductors acts to lower the magnetic field near the cathode thus increasing the magnetic field compression ratio and the beam $\alpha$ in the cavity. The second trim coil increases the axial field locally to compress the electron beam in order to

prevent it from being intercepted by the electron gun electrodes. The superconductor and trim coil positions relative to the cathode position are shown in Figure 22.

## II-I High Voltage Modulator

The modulator used to supply the high voltage to the electron gun is a standard capacitive-discharge type followed by a pulse-forming network and a step-up transformer. The modulator is capable of producing 50 A at voltages up to 90 kV. Most of the current is dissipated in an oil-filled load box via a resistive shunt in parallel with the electron gun. This serves to maintain a constant load impedence for the modulator despite the fact that the electron gun impedence changes radically throughout the pulse. A straight resistive divider is used to supply the necessary voltage to the intermediate anode. A schematic diagram of the high-voltage source is shown in Figure 23.

# III Threshold Current Studies

The threshold current for single-mode oscillation at the fundamental harmonic can be derived using single particle theory in the small signal approximation. The result in MKS units is [20]

$$I_{thr} = \frac{2\pi^4 m_e c}{\mu_0 e} \frac{\gamma \beta_\perp^4}{Q} \frac{d}{\lambda} \left(\frac{w_0}{\lambda}\right)^2 \frac{2}{1 \pm J_0(2kr_b)} \hat{I}(\Delta, \mu), \tag{14}$$

where $m_e$ and $e$ are the mass and charge (magnitude) of an electron, $\mu_0$ is the free space permittivity, $Q$ is the resonator quality factor, and $J_0$ is a regular Bessel function. The beam waist for the $TEM_{00}$ Gaussian mode of the resonator is given by

$$w_0 = \sqrt{\frac{d\lambda}{2\pi}} \left(\frac{1+g}{1-g}\right)^{1/4}. \tag{15}$$

The normalized threshold current $\hat{I}$ is given by [21]

$$\hat{I}(\Delta, \mu) = \frac{8}{\pi \mu^2} \frac{e^{\Phi^2/2}}{\mu\Phi - 2}, \tag{16}$$

where $\Phi = \mu\Delta/2$ is the kinematic phase-slip angle of the electrons transiting the resonator,

$$\mu = 2\pi\alpha\beta_\perp w_0/\lambda \tag{17}$$

is the normalized interaction length, and

$$\Delta = \frac{2}{\beta_\perp^2}\left(1 - \frac{eB_0}{\gamma m_e \omega}\right) \tag{18}$$

is the resonance detuning parameter. The factor $2/\left(1 \pm J_0(2kr_b)\right)$ in Eq. (14) accounts for the annular beam geometry [22]. The $+$ $(-)$ sign corresponds to placing the electron beam axis on a maximum (null) of the wave field as illustrated in Figure 7.

A comparison between the theoretical and measured threshold oscillation currents as a function of magnetic field is shown in Figures 24–26 for mirror separations of 25 and 20 cm. The beam accelerating voltage is 57 kV, $r_b = 1.6$ mm, and the operating frequency is near 110 GHz in both cases. The data in these figures was obtained by varying the magnetic field trim coils near the gun to minimize the threshold oscillation current. The theoretical curves are based on a momentum pitch ratio $\alpha = 1.5$ which is considered achievable in the present experiment at currents up to a few amperes based on previous operating experience with the electron gun and simulations of the gun. At higher currents the best estimate is $\alpha \sim 1$ with some drop-off expected for currents above 15 A. Near the minimum threshold current only a single-mode was observed to be present. Multimode operation was observed when the current exceeded 2–3 times the minimum threshold current. Thus the single-mode theory is valid only near the minimum oscillation current.

Results for a mirror separation of 25 cm are shown in Figure 24. For frequencies near 110 GHz the calculated resonator $Q$ factor including ohmic losses and the diffraction output coupling is $Q = 38,000$. The transmission coefficient $T = 2.8\%$ for this separation and the separation between adjacent longitudinal modes is 600 MHz. The measured frequency of the data denoted by the solid dots is $109.8 \pm 0.1$ GHz. This data was obtained by translating the mirrors while holding the separation constant to minimize the threshold current and thus place the beam on the microwave electric field maximum for this mode as shown in Figure 7. This had the effect of raising the threshold current of adjacent modes as expected and, at currents below 1.5 A, the adjacent modes could not be excited. The data shown by the open circles corresponds to the next lower frequency mode–which should also have its E-field maximum at the beam axis. The measured frequency of this mode is $108.7 \pm 0.1$ GHz.

A frequency of 109.8 GHz was used in obtaining the theoretical result denoted by the solid curve which is closest to the solid dot data. The other solid curves correspond to other longitudinal modes of the resonator with frequencies shifted by multiples of 1200 MHz. Consistent with the data, the solid curves correspond to modes for which the beam axis falls on a field maximum. Theoretical results for the intermediate modes, for which the beam axis falls on a field null, are shown by the dashed curves. Given the experimental uncertainties, the agreement between theory and experiment near the minimum threshold current is remarkably good. Probably the least well-known parameter is the beam $\alpha$. The sensitivity of the theoretical results to varying $\alpha$ is shown in Figure 25 which shows the 109.8 GHz data from Figure 24 compared with the corresponding theoretical results for $\alpha = 1$, 1.5, and 2. The best fit is clearly obtained for $\alpha = 1.5$.

Figure 26 shows data obtained for a mirror separation of 20 cm. The resonator $Q$ factor and output coupling are calculated to be 82,000 and 0.9% for frequencies near 110 GHz. The measured oscillation frequencies are $109.8 \pm 0.1$ GHz (solid dot data) and $109.2 \pm 0.2$ GHz (open circle data). The expected frequency separation for this mirror separation is 750 MHz. This data was obtained without minimizing either mode threshold current with respect to electron beam position. The fact that these adjacent modes have essentially equal minimum threshold currents indicates that the electron beam axis does not coincide with an E-field maximum for either mode. To account for this, the theoretical threshold currents plotted in Figure 26 represent an average of the threshold current obtained for the beam axis at a field maximum and the threshold current obtained for the beam axis at a field null. The theoretical curve closest to the solid dot data corresponds to a frequency of 109.8 GHz, and the other curves represent the other nearby longitudinal modes for this mirror separation.

The threshold current dependence on the beam axis position is shown explicitly in Figure 27. The data was obtained by translating the mirrors perpendicularly to the beam, holding the separation fixed at 20 cm. This is equivalent to translating the beam relative to the standing-wave pattern in the resonator. The resonator magnetic field ($B = 43$ kG), the electron beam voltage ($V = 52.4$ kV), and the cathode magnetic field were held constant during these measurments. Operation was single-moded at a frequency of $111 \pm 0.1$ GHz.

The solid sinusoidal curve shown in Figure 27 is proportional to the standing-wave E-field pattern in the resonator. The first maximum of this curve has been adjusted to coincide with the beam position which gives the minimum threshold current. The positions of measured threshold current maxima are then found to fall on nulls of the wave field. The ratio of minimum to maximum measured threshold current is 0.6. This is in good agreement with the theoretical ratio of 0.57 for an annular beam with $r_b = 1.6$ mm and provides further evidence that the electron beam is interacting with the $TEM_{00q}$ modes of the resonator.

# IV Multimode Power and Efficiency Measurements

Output power measurements were carried out as a function of beam current and mirror separation. A preliminary investigation of output power and efficiency showed that for currents of less than 8 A, output power was a decreasing function of mirror separation. Power measurements for a gun voltage of 66.7 kV and a current of 8 A at three mirror separations are shown by the solid square data points in Figure 28. Consequently, initial power and efficiency measurements were taken at the minimum mirror separation of 20 cm. This minimizes the output coupling and so leads to the optimum saturated efficiency at the lowest current, where beam quality should be highest. Mirror alignment and translation were optimized by minimizing the threshold current for a magnetic field of 50 kG and a beam voltage of 66.7 kV. A minimum threshold current of 0.25 A at a frequency of 125.8 GHz was obtained. For these conditions the calculated total resonator $Q$ factor is 160,000 and the theoretical minimum threshold current for $\alpha = 1.5$ is 0.12 A, or about half the measured value. This discrepancy suggests that the experimental total $Q$ factor may be $\sim$ 80,000, i.e, only half the predicted value, however, the calculated minimum threshold current depends on $\alpha$ which is not well characterized in the experiment. Using the total $Q$ inferred from the threshold measurement and the theoretical ohmic $Q$ leads to an estimate of the diffraction $Q$ of 96,000. The calculated diffraction $Q$ is 250,000.

The output power was obtained by multiplying the calorimeter power measurement by two, dividing by the repetition rate and the pulse width, and correcting for the absorption efficiency of the calorimeter. The radiation pulsewidth was found to be equal to a good

approximation to the beam voltage flat-top pulse width of 13 $\mu$sec under most conditions and this pulse width was used in the peak power calculation. The power output through the two windows was checked and found to be equal within measurement accuracy. As shown in Figure 18, the calorimeter absorptivity was measured to be 94% at 120 GHz and to decrease with decreasing frequency to $\sim 60\%$ at 90 GHz.

The output power as a function of beam current is shown in Figure 29 for magnetic fields of 44, 47, and 50 kG and a constant gun voltage of 71.5 kV. Based on the calorimeter reflectivity measurements, a calorimeter efficiency of 95% was used used in the output power computations for the magnetic fields of 47 and 50 kG; an efficiency of 88% was used for the 44 kG results. The corresponding output efficiency is shown in Figure 30. The observed maximum output efficiencies for these magnetic fields and conditions was 12% at 50 kG, 11.9% at 47 kG, and 11% at 44 kG. In obtaining this data no attempt was made to promote single-mode operation and, consequently, operation was generally multimoded. Typical multimode frequency spectra are shown in Figures 31(a)–(c). The spectra correspond to magnetic fields of 44, 47, and 50 kG, respectively, and a gun voltage of 71.5 kV. The beam current in Figures 31(a) and (c) is 8 A and is 14 A in Figure 31(b).

To obtain the electronic efficiency for a given output efficiency, it is necessary to correct for ohmic heating losses according to

$$\eta_{el} = (1 + Q_d/Q_o)\eta_{out}, \tag{19}$$

where $\eta_{el}$ and $\eta_{out}$ are the electronic and output efficiencies, and $Q_d$ and $Q_o$ are the diffraction and ohmic quality factors.

As discussed above the ratio $Q_d/Q_o$ depends sensitively on the diffraction $Q$ factor, which has not been directly measured. For operation at 50 kG, $Q_d/Q_o = 0.2$ based on $Q_d$ inferred from the threshold current measurement, whereas $Q_d/Q_o = 0.55$ based on $Q_d$ calculated using scalar diffraction theory. The corresponding electronic efficiencies are plotted as functions of $IQ/d$ in Figure 32. Using the value of $Q_d$ inferred from the threshold current measurement leads to a maximum electronic efficiency of 14%; using the value of $Q_d$ calculated with scalar diffraction theory leads to a maximum electronic efficiency of 18%. The

figure also shows theoretical results based on a nonlinear, multimode simulation [4] using parameters corresponding to the 50 kG data and assuming $\alpha = 1$. These calculations yield a maximum efficiency of 17.7%. The theoretical optimum value of $QI/d \sim 2.0 \times 10^6$ which is in good agreement with the experimental results based on the $Q$ factor inferred from the threshold current measurement but not with the results obtained using the theoretical $Q$ factor.

The electronic efficiency was not corrected for the space-charge depression of the beam voltage, because the free energy for the interaction is associated mainly with the transverse momentum of the electrons which is not greatly affected by the presence of space charge. Space charge does limit the maximum beam power which can be propagated in the resonator and reduces the achievable velocity pitch ratio.

As shown in Figure 30, for a magnetic field of 50 kG and a mirror separation of 20 cm, the output efficiency decreases as the current is increased beyond 6 A. This effect of overdriving the resonator is well known from cavity gyrotrons. Increased power and efficiency at currents above 6 A can be obtained in the QOG by increasing the output coupling by increasing the mirror separation until the optimum RF field amplitude is re-established in the cavity. This effect is illustrated by the solid data in Figure 28 which shows output power optimization by variation of the mirror separation for a constant beam current of 13.5 A and a constant gun voltage of 71.5 kV.

The output power and efficiency as a function of beam current for a magnetic field of 50 kG, gun voltage in the range 71–75 kV, and beam currents up to 24 A are shown in Figure 33. Operation was generally multimoded with 4–6 modes being excited. The frequency of the strongest modes was $\sim$ 125 GHz. The data indicated by the squares corresponds to the minimum mirror separation of 20 cm and a gun voltage of 71.5 kV. The calculated diffractive output coupling at this separation is 0.4% for 125 GHz radiation. The data indicated by the triangles and dots correspond to a mirror separation of 23 cm and a calculated 0.8% diffraction output coupling. The highest measured power, shown by the solid dots, was 148 kW and was obtained at a mirror separation of 23 cm, a beam voltage and current of 78 kV and 24 A, and a negative taper in the magnetic field of 2%

across the interaction region. This current is estimated to be near the space-charge limit for this voltage and $\alpha = 1$. No evidence of oscillation in higher order transverse modes was observed from the frequency measurements at 50 kG or other magnetic fields.

# V Frequency Tuning Measurements

In the QOG the operating frequency is approximately $\Omega_c/\gamma$, where $\Omega_c$ is the nonrelativistic electron cyclotron frequency, so that the operating frequency can be tuned by varying either the magnetic field or the gun voltage. Figure 34 presents frequency and power measurements for magnetic fields from 38 to 50 kG with fixed gun voltage (66.7 kV) and current ($\sim$ 12 A). Operation was usually multimoded as indicated in the figure which shows frequency variation from 95 to 130 GHz. Significantly, the power varied by $< 3$ dB for this frequency variation. The QOG could have operated at still lower frequencies (at lower magnetic fields), but such frequencies were below the cutoff frequency of the waveguide used in the heterodyne frequency diagnostic.

Frequency variation with electron gun voltage was also investigated. Frequency measurements were obtained several voltages between 43 and 72 kV for a magnetic of 50 kG and a current of $\sim$ 10 A. As shown in Figure 35, a 4% frequency increase was measured for this variation in gun voltage. A disadvantage of this method of frequency tuning is that power scales strongly with voltage and decreased from 70 to 25 kW as the voltage was decreased.

# VI Studies of Near-Single-Mode Operation

Since the longitudinal mode density of the QOG resonator is high, it might be thought that the device is inherently multimoded, but this is not the case. The operating parameter space was characterized by regions of stable single-mode or near-single-mode operation. Single-mode operation was most common at lower powers but was also observed at powers up to 125 kW. At a current near threshold, a single-mode having the highest growth rate can be excited. It was found that if the current was then increased holding the magnetic

field and gun voltage fixed, the cavity would oscillate in a sequence of higher frequency modes as shown in Figure 36. The data plotted in this figure was obtained for a gun voltage of 71.5 kV, a mirror separation of 23 cm, and a magnetic field of 47 kG in the middle of the interaction region. The magnetic field had a negative 2% taper across the interaction region. Alternatively, it was possible to vary the voltage while increasing the current (keeping the magnetic field fixed) so as to maintain single-mode operation in the mode initially excited. Figure 37 shows a region of single-mode operation in $V - I$ space obtained using the latter procedure. An untapered magnetic field of 47 kG was used to obtain this data at an operating frequency of 119 GHz. The area of single-moded operation is denoted approximately by the line thickness; voltage changes of $\sim 0.5$ kV led to observable changes in the mode spectrum. The maximum power of the data in this figure is 55 kW. Figure 38 shows the output power obtained during single-mode or near-single-mode operation for mirror separations of 23, 25.5 and 28 cm. The magnetic field was 47 kG and the oscillation frequency was 119–120 GHz in all cases. Here, output powers as high as 125 kW were obtained while maintaining nearly single-mode operation. At least 90% of the output power was in a single-mode, with most of the remaining power in the two adjacent modes. Relative mode power was measured using the amplitude response of the heterodyne frequency diagnostic.

As the current was increased above threshold, it was found that single-moded operation corresponded to progressively higher resonance frequency mismatches ($\omega - \Omega_c/\gamma$). Figure 39(a) shows frequency mismatch uncorrected for the space-charge effect versus the beam current normalized to the oscillation threshold current for the data shown in Figure 38. Figure 39(b) illustrates the frequency mismatch obtained by correcting the electron cyclotron frequency for space-charge depression of the beam as discussed in Section II-F.

To compare the theoretically predicted stable, single-mode operating regime [23] with the experimental data, it is convenient to express the data in terms of the normalized RF electric field amplitude, $\hat{E}$, and the kinematic phase parameter for the interaction, $\Phi$, which

are given by

$$\Phi = \frac{2\pi}{\beta_{||}}\left(1-\frac{\Omega}{\omega}\right)\frac{w_0}{\lambda} \tag{20}$$

$$\hat{E} = \frac{8\pi}{B_0\lambda}\frac{1+\alpha^2}{(1-\gamma^{-2})\,\alpha}\sqrt{\frac{Z_0 P}{\pi c^2 T}}, \tag{21}$$

where $P$ is the diffraction output power. The parameter $\hat{E}$ can be expressed in terms of the normalized interaction parameters $F$ and $\mu$ according to $\hat{E} = F\mu$, and as discussed above, $\Phi = \mu\Delta/2$. An advantage of the new parameters is their relative insensitivity to $\alpha$ which is not well determined in the experiment. Theoretically, the stable operating regime for a fixed $\mu$ corresponds to an area in $\hat{E}$–$\Phi$ space. Uncertainty in the beam velocity pitch ratio $\alpha$ leads to a range of possible $\mu$ values from 5–10. The region of stable, single-mode operation predicted by theory corresponds to the area bounded by the solid curves in Figures 40(a) and (b) which were obtained assuming $\alpha = 0.65$ ($\mu = 5$) and $\alpha = 1$ ($\mu = 10$), respectively. These plots were made for an annular beam of radius 1.6 mm centered on the electric field maximum of the equilibrium mode. Equilibria with values of $\hat{E}$ , $\Phi$ outside the stable region are unstable with respect to the growth of neighboring modes (sidebands). The use of an annular beam configuration has an important effect on the size and shape of the stability boundary [23]. In particular, the stable region for an annular beam is much smaller than that for a pencil beam. This reduction occurs because, unlike the pencil beam, an annular beam couples to both the odd and even symmetry modes of the resonator. If beam–RF coupling is optimized for the desired operating mode, coupling to the two adjacent modes, which have opposite symmetry, will be weaker. The weaker coupling of the principal competing modes inhibits saturation of their gain by the main mode, an important factor in determining the region of stable operation. Comparison of the Figures 40(a) and (b) shows that the predicted stable area is smaller for $\mu = 10$ than for $\mu = 5$. The reduction in stable region with increase in $\mu$ is a general feature of the theory for both pencil and annular beams. The experimental single-mode data for mirror separations of 23, 25.5 and 28 cm, assuming either $\alpha = 0.65$ or 1, is also shown in Figures 40(a) and (b). The data indicates single-mode operation occurs for $\hat{E} \lesssim 2$. This is consistent with the theoretical results for $\mu = 5$ but not $\mu = 10$. However, nonlinear, time

dependent, multimode simulations for $\mu = 10$ show that the unstable sidebands saturate at a sufficiently low level that the resulting equilibrium appears single-moded within the resolution of the experimental data (90% of power in main mode). Thus, the theoretical results regarding single-mode operation are not inconsistent with $\mu = 10$ ($\alpha = 1$) in the experiment. The experimental data is primarily limited to the lower halves of the stable regions, whereas theory predicts that all points should be accessible. Simulations modeling the finite rise time of the voltage pulse indicate that this is not a factor which limits the accessible region. The inability to tune the gyrotron within the stable region without loss of single-modedness is not understood, but may be related to the 4% ripple of the voltage pulse which corresponds to a variation in the detuning parameter $\Phi$.

The measured electronic efficiency corrected for ohmic effects is compared in Figure 41(a) and (b) with the theoretical annular beam single-mode efficiency for $\mu = 5$ and 10 and using the measured detuning. The agreement is much better for $\mu = 5$ than 10. The calculated efficiency for $\mu = 10$ is about 60% greater than the measured efficiency. In addition, the calculated efficiency peaks at a value of $\hat{E}$ lower than that suggested by the data. The calculated efficiency for $\mu = 5$ ($\alpha = 0.65$) is in better agreement with the data both in maximum value and dependence on $\hat{E}$.

# VII Discussion and Conclusions

Extensive results have been obtained for a CW-relevant QOG which demonstrate for the first time many of the advantages of this configuration at output powers up to 148 kW. A peak output efficiency of 12% was obtained which is estimated to correspond to an electronic efficiency of 14–18%. The difference between output and electronic efficiency is due mainly to ohmic heating losses which can dominate at low output coupling but would not be a factor in a 1 MW device, which would typically have a much larger output coupling. Single-mode operation was observed at powers up to 125 kW, and the frequency was tunable from 95 to 130 GHz by varying the magnetic field. Frequency tuning of 4% was obtained by gun voltage variation. Efficiency optimization by variation of the output coupling and by tapering the magnetic field has been demonstrated. The region of single-

mode operation of a highly overmoded quasi-optical cavity has been characterized for the first time.

The use of resonator mirror holders allowing flexible and precise adjustment of mirror separation, translation, and alignment has enabled the investigation of many interesting features of the quasi-optical gyrotron, especially the ability to vary the output coupling independently of other parameters. This allowed the output efficiency of the device to be optimized over a range of beam currents and operating frequencies.

The theory of stable, single-mode QOG operation based on sideband suppression by the dominant mode has been compared to experimental data for the first time. The theory extends previous theoretical work on the stability of free electron lasers [24] to the QOG with an annular beam [23]. The data confirms the prediction of significant regions of single-mode operation in a highly overmoded system without the application of mode stabilization or selection techniques. The annular beam geometry was found to have a strong effect on the single-mode stability: the stable parameter region is reduced relative to the pencil beam case due to the less effective sideband suppression by the main mode. The mode density in the present configuration is moderate: the mode frequency separation of $\sim 0.6\%$ leads to about 5 modes within the interaction bandwidth. Nevertheless, the region of stable operation is not expected to be greatly affected for configurations with much greater mode density, as may be needed in higher-frequency, megawatt-average-power systems.

As is the case for many high-power millimeter-wave experiments, the greatest unknown here is the value of the electron beam velocity pitch ratio, $\alpha$, and its spread. Numerical modeling is difficult at best, and actual experimental measurements are even more so and have not been made. The achievable value of $\alpha$ is typically limited in this experiment by arcing in the electron gun circuit. This can be caused by magnetic mirroring of a portion of the electron beam, or by some of the beam electrons intercepting the focusing electrodes in the gun. Each of these causes may be controlled by varying the magnetic field (amplitude and shape) in the electron gun region which is accomplished by varying the currents in the two trim coils. When maximum power was desired, the trim coils were varied accordingly and operation was limited by arcing. Usually the spectrum obtained in this manner was not

single-moded, although occasionally at high beam current it was. To obtain single-mode operation it was frequently necessary to adjust the trim coil currents to a region of reduced operating power and presumably lower $\alpha$. Consistent with the threshold current data, $\alpha$ values of 1.5 are considered to be achievable at low currents. However, due to the spread in $\alpha$, the average $\alpha$ must be decreased as the current is increased to prevent arcing. The amount of this decrease in average $\alpha$ is certainly debatable; however $\alpha = 1$ seems to yield reasonably good agreement between theory and experiment at currents above 15 amps. For some of the single-mode operation at these high currents, $\alpha$ values as low as 0.65 yield consistency between theory and experiment.

The accuracy of the theoretical modeling of the experiment is limited by the uncertainty in the resonator $Q$ factor as well as the uncertainty in the beam $\alpha$. Cold tests are currently in progress which should yield accurate data for the resonator $Q$ as a function of mirror separation. This data should resolve the discrepancy, discussed in Section IV, between the $Q$ factor inferred from threshold current measurements and the scalar diffraction theory result.

Although the fraction of the total power lost which is dissipated in ohmic heating is high in the present configuration, the ohmic heating density is relatively low. In the case of operation at 125 kW and a frequency of 120 GHz–demonstrated in this experiment with a 23 cm mirror separation and a 47 kG magnetic field–the average heating density (during the pulse) on the mirrors was 0.6 kW/cm$^2$. This is well within the ohmic heating limit of a few kW/cm$^2$ for CW applications. The peak heating density (at the center of the mirror) for this case was 3 kW/cm$^2$. The resonator used in this experiment has $g \sim 0.3$. The ohmic heating density could be reduced by a factor of four without changing the interaction parameters (except for mode density) by decreasing $g$ to -0.65 and increasing the mirror separation to 75 cm.

In conclusion, a CW relevant quasi-optical gyrotron experiment has been performed that substantiates many of the pertinent theories and demonstrates an understanding of the basic physics of the QOG. The model used for the annular beam predicted very well the change in the threshold current as the electron beam was translated relative to the cavity

standing wave pattern. Threshold currents themselves were also in good agreement with calculated values, with differences attributable to the imprecise knowledge of some of the relevant parameters such as the $\alpha$ value of the electron beam. Frequency measurements were obtained for several widely varied values of the magnetic field, electron beam current, electron gun voltage, mirror separation, and electron beam alignment relative to the cavity fields. With the exception of a few observed frequencies attributable to oscillations in the drift tube region (i.e. near the peak of the magnetic field), each frequency measurement was consistent with a $TEM_{00}$ mode oscillating in the resonant cavity. Essentially, the higher-order TEM modes were effectively suppressed due to their higher diffraction losses. As discussed above, regions of single-mode operation and efficiency are well predicted by a relatively recently developed theory. Finally, efficiency optimization as a function of current and mirror separation has been demonstrated. To within the limits that $\alpha$ is known, if the value of $QI/d \sim I/T$ is held constant, the efficiency remains unchanged.

A series of several experiments are planned for the future. Immediate plans include the incorporation of a higher-power electron gun capable of producing 50 amps at 80 kV. This electron beam has a diameter of 1 cm in the resonant cavity, necessitating modification of the drift tube, and the collector will also be modified to handle the higher-power beam. During these modifications, a probe will be added to measure any buildup of charge that may be trapped between the two peaks of the magnetic field. One benefit of using this electron gun will be a better characterized electron beam, with average values of $\alpha \approx 1.5$ considered accessible at high currents, implying a much lower spread in $\alpha$ than in the experiment described here. The higher input power from the electron gun will make possible the use of a resonator with larger output coupling, again to keep the product $I/T \sim QI/d$ the same as the lower-power experiments. Since the ohmic losses remain nearly constant, the total $Q$ value for the cavity will be essentially unaffected by the ohmic $Q$, resulting in the measured efficiency being essentially equal to the electronic efficiency. This fact will make interpretation of the data and comparison to theory more straightforward. One value to be determined by the experiment will be the maximum value of current that can be propogated through the resonant cavity. To enhance this value, provision has been

made to add a DC electric field parallel to the magnetic field, possibly increasing the amount of current that can be propogated through the cavity. A gyroklystron experiment is also planned, incorporating a quasi-optical prebunching cavity with low mode density (essentially single-moded) in addition to the overmoded output cavity. The circulating power in the prebunching cavity will be low, allowing the use of a short mirror separation while maintaining CW relevance.

# VIII Acknowledgements

We thank Drs. Steven Gold, Victor Granatstein, Robert McCowan, and John Burke for helpful discussions, and we thank Robert Lee for carrying out many of the computer calculations. This work was supported by the Office of Fusion Energy of the Department of Energy and by the Office of Naval Research.

# A Appendix: Calorimeter Calculations

The calorimeter described here consisted of a conducting plate covered with a layer of lossy dielectric material (paint). The analysis of this situation is given here for the case of a general dielectric material. The geometry is shown in Figure 19 for the case of the electric field of the incident radiation perpendicular to the plane of incidence. The electric fields of the plane wave incident ($\vec{\mathbf{E}}_1^+$) on and reflected ($\vec{\mathbf{E}}_1^-$) by the dielectric as well as the forward ($\vec{\mathbf{E}}_2^+$) and reflected ($\vec{\mathbf{E}}_2^-$) waves in the dielectric are given by:

$$\vec{\mathbf{E}}_1^{\pm} = \hat{y} E_1^{\pm} e^{\imath(\omega t - \vec{k}_1^{\pm} \cdot \vec{r})} \quad (1)$$

$$\vec{\mathbf{E}}_2^{\pm} = \hat{y} E_2^{\pm} e^{\imath(\omega t - \vec{k}_2^{\pm} \cdot \vec{r})} \quad (2)$$

where $\omega = 2\pi f$ is the angular frequency of the radiation, $\vec{k}$ is the wave number, $\vec{r}$ is the position vector, $\hat{y}$ is the unit vector in the $y$ direction and:

$$\vec{k}_1^{\pm} \cdot \vec{r} = k_1(x \sin\theta_i \pm z \cos\theta_i) \quad (3)$$

$$\vec{k}_2^{\pm} \cdot \vec{r} = k_2(x \sin\theta_t \pm z \cos\theta_t) \quad (4)$$

where $\theta_i$ is the angle of incidence and $\theta_t$ is the angle of transmittance shown in Figure 19. In region 1 (free space), the wave number is real, but $\vec{k}$ is complex in the lossy dielectric of region 2:

$$k_2 = \omega\sqrt{\mu_2 \epsilon_2} \quad (5)$$

$$\epsilon_2 = \epsilon_{r_2} \epsilon_o (1 - \imath \tan\delta) \quad (6)$$

where the permeability of the dielectric, $\mu_2$, is assumed equal to $\mu_o$, the permeability of free space, $\epsilon_o$ is the permitivity of free space, $\epsilon_{r_2}$ is the real part of the dielectric constant relative to free space, and $\tan\delta$ is the loss tangent of the dielectric. The total electric fields in regions 1 and 2 are given by:

$$\vec{\mathbf{E}}_1 = \vec{\mathbf{E}}_1^+ + \vec{\mathbf{E}}_1^- \quad (7)$$

$$\vec{\mathbf{E}}_2 = \vec{\mathbf{E}}_2^+ + \vec{\mathbf{E}}_2^- \quad (8)$$

and $E_i^{\pm}$ are the peak electric field strengths of the waves travelling in the $\pm z$ direction. Here we desire to calculate the reflection coefficient of the dielectric layer, i.e. we wish to calculate $E_1^-/E_1^+$, and do so by applying the appropriate boundary conditions.

First note that the tangential electric field is zero at $z = d$ , leading to the equation

$$E_2^+ = -E_2^- e^{i2k_2 d\cos\theta_t}. \tag{9}$$

The fact that the tangential electric field is continuous across the boundary at $z = 0$ leads to Snell's Law,

$$k_1 \sin\theta_i = k_2 \sin\theta_t, \tag{10}$$

and

$$E_1^+ + E_1^- = E_2^+ + E_2^-. \tag{11}$$

The tangential part of the magnetic intensity ($\vec{H}_{tan}$) is also continuous at $z = 0$, which implies

$$E_1^- - E_1^+ = \left(\frac{\cos\theta_t}{\cos\theta_i}\right)\frac{\epsilon_2}{\epsilon_o}(E_2^- - E_2^+). \tag{12}$$

Using Eq.(9) and performing some algebra yields an equation for the complex reflection coeficient,

$$\frac{E_1^-}{E_1^+} = \frac{1-D}{1+D}, \tag{13}$$

where

$$D = \left(\frac{\cos\theta_t}{\cos\theta_i}\right)\sqrt{\frac{\epsilon_2}{\epsilon_o}}\left\{\frac{1+e^{-i2k_2 d\cos\theta_t}}{1-e^{-i2k_2 d\cos\theta_t}}\right\}. \tag{14}$$

The power reflection coefficient is

$$R = \left|\frac{1-D}{1+D}\right|^2. \tag{15}$$

A similar calculation for the electric field of the incident radiation parallel to the plane of incidence yields

$$R = \left|\frac{1-D'}{1+D'}\right|^2, \tag{16}$$

where

$$D' = \left(\frac{\cos\theta_i}{\cos\theta_t}\right)\sqrt{\frac{\epsilon_2}{\epsilon_o}}\left\{\frac{1+e^{-i2k_2 d\cos\theta_t}}{1-e^{-i2k_2 d\cos\theta_t}}\right\}. \tag{17}$$

# B References

# References


[1] K. Felch *et al., Int. J. Elec.* **61**, 701 (1986).

[2] K.E. Kreischer and R.J. Temkin, *Phys. Rev. Lett.* **59**, 547 (1987); K.E. Kreischer, *Bull. Amer. Phys. Soc.* **33**, 1913 (1988).

[3] P. Sprangle, J. Vomvoridis and W.M. Manheimer, *Phys. Rev. A* **23**, 3127 (1981).

[4] A. Bondeson, W.M. Manheimer and E. Ott, *Infrared and Millimeter Waves*, ed. by K.J. Button, Vol. 7, Chapter 7, Academic Press (1983).

[5] B. Levush and W.M. Manheimer, *Int. J. Infrared and Millimeter Waves* **4**, 877 (1983).

[6] B. Levush *et al., Int. J. Elec.* **54**, 749 (1983).

[7] T.A. Hargreaves *et al., Int. J. Elec.* **57**, 977 (1984).

[8] M.E. Read *et al., Int. J. Elec.* **65**, 309 (1988).

[9] Y. Zhonghai and L. Shenggang, *Int. J. Elec.* **57**, 1003 (1984).

[10] X. Kongyi and L. Shenggang, *Int. J. Elec.* **57**, 1019 (1984).

[11] E.C. Morse and R.V. Pyle, *J. Vacuum Sci. and Tech. A* **3**, 1239 (1985).

[12] Y. Itoh *et al., Conference Digest of the Thirteenth International Conference on Infrared and Millimeter Waves*, Honolulu, HI (December 1988).

[13] Presented at the Thirteenth International Conference on Infrared and Millimeter Waves, Honolulu, HI (December 1988).

[14] A. Yariv, *Optical Electronics*, CBS College Publishing (1985).

[15] A. Perrenoud, T.M. Tran, M.Q. Tran, C. Rieder, M. Schleipen, and A. Bondeson, *Int. J. Elec.*, **57**, 985, (1984).

[16] J.L. Seftor, A.T. Drobot and K.R. Chu, *IEEE Trans. on Elec. Dev.* **ED-26**, 1609 (1979).

[17] W.B. Herrmannsfeldt, *SLAC Report 226*, (1979).

[18] K.E. Kreischer, B.G. Danly, J.B. Schutkeker, and R.J. Temkin, *IEEE Trans. on Plasma Science* **PS-13**, 364 (1985).

[19] A.K. Ganguly and K.R. Chu, *Int. J. Infrared and Millimeter Waves* **5**, 103 (1984).

[20] B.G. Danly and R.J. Tem n, *Phys. Fluids* **29**, 561 (1986).

[21] T.M. Tran, B.G. Danly, K.E. Kreischer, J.B. Schutkeker, and R.J. Temkin, *Phys. Fluids* **29**, 1274 (1986).

[22] M.Q. Tran, A. Bondeson, A. Perrenoud, S. Alberti, B. Isaak, and P. Muggli, *Int. J. Elec.* **61**, 1029, (1986).

[23] T. Antonsen, B. Levush and W.M. Manheimer, to be published.

[24] T.M. Antonsen, Jr. and B. Levush, *Phys. Rev. Lett.* **62**, 1488 (1989).

# TABLE I

| | | | |
|---|---|---|---|
| Mirror Diameter ($2a$) | 5.0 cm | | |
| Radius of Curvature ($R_c$) | 38.7 cm | | |
| Mirror Separation ($d$) | 20 | 24 | 28 cm |
| | | | |
| Frequency ($f$) | 120 GHz | | |
| Wavelength ($\lambda$) | 0.25 cm | | |
| Longitudinal Mode Spacing ($\Delta f/f$) | 0.63 | 0.52 | 0.45 % |
| Radiation Waist Radius ($\omega_o$) | 1.16 | 1.19 | 1.22 cm |
| $\omega_o/\lambda$ | 4.6 | 4.8 | 4.9 |
| $\mu$ ($E = 70$ keV, $\alpha = 1.0$) | 9.8 | 10.1 | 10.3 |
| | | | |
| Transmission Coefficient ($T$, round trip) | 0.5 | 1.5 | 2.2 % |
| Diffraction Quality Factor ($Q_d$) | 198,000 | 80,000 | 61,000 |
| Ohmic Quality Factor ($Q_o$) | 354,000 | 400,000 | 470,000 |
| Total Quality Factor ($Q$) | 127,000 | 67,000 | 54,000 |
| | | | |
| Fresnel Number ($a^2/\lambda d$) | 1.25 | 1.04 | 0.89 |
| G ($(1 - d/R_c)(a_1/a_2)$) | 0.48 | 0.38 | 0.28 |

# Figure Captions

**Figure 1** Schematic diagram of the NRL quasi-optical gyrotron experiment.

**Figure 2** The quasi-optical gyrotron resonator showing the geometry of the external magnetic field ($\vec{B}_o$), the RF electric field ($\vec{E}_{rf}$), and the electron beam.

**Figure 3** Open resonator stability diagram. The shaded (high-loss) areas are those in which the stability criterion ($0 \leq (1 - d/R_1)(1 - d/R_2) \leq 1$) is not satisfied. Note that the experimental design lies well within the stable region.

**Figure 4** Cavity diffraction loss as a function of mirror separation for resonant frequencies of 110, 120 and 130 GHz. The 5 cm diameter cavity mirrors had a radius of curvature of 38.7 cm.

**Figure 5** Resonant cavity quality factor ($Q$) including diffraction and ohmic losses as a function of mirror separation for resonant frequencies of 110, 120 and 130 GHz. The 5 cm diameter cavity mirrors had a radius of curvature of 38.7 cm.

**Figure 6** The ratio of power lost through ohmic heating of the cavity mirrors to the RF output power as a function of mirror separation for resonant frequencies of 110, 120 and 130 GHz. The 5 cm diameter cavity mirrors had a radius of curvature of 38.7 cm.

**Figure 7** Geometry of the annular electron beam and the standing RF electric field (with the beam centered on the peak of the electric field).

**Figure 8** Adjustable resonant cavity mirror holder shown mounted in the superconducting magnet cross-bore.

**Figure 9** Electron gun geometry modeled using the Hermannsfeldt electron trajectory code showing the calculated electron trajectories. Note in this calculation that 1 mesh unit = 0.25 mm.

**Figure 10** Alpha ($\alpha = v_\perp / v_{||}$) values for different rays calculated by the Hermannsfeldt electron trajectory code.

**Figure 11** Drift tube design showing the lossy and matching dielectric rings and the copper scrapper rings.

**Figure 12** The space charge depression of the electron beam voltage as a function of the beam current for electron gun voltages of 50, 60, 70 and 80 kV. The momentum pitch ratio was assumed to be equal to 1.

**Figure 13** Resonant cavity and associated diagnostics.

**Figure 14** The heterodyne diagnostic used for frequency measurements. The local oscillator (LO) is frequency locked by the counter (FC) and power leveled by the power monitor (PM). The RF from the gyrotron (QOG) is mixed with the LO signal by the harmonic mixer (HM) and the IF signal is filtered by one of several bandpass filters (BPF) before being amplified (A), rectified (DET), and measured on an oscilloscope.

**Figure 15** Schematic diagram of the Fabry-Perot interferometer used to measure the frequency. Radiation was input (I) from the experiment and coupled out (O) for detection through the planar mirror (A). The concave mirror (B) of the nearly semiconfocal resonator was movable through the use of a micrometer (C).

**Figure 16** Modified laser calorimeter used to measure experimental output power. The incident radiation (A) is absorbed in the layer of paint (B) on an aluminum plate (C). The temperature rise is measured by thermopiles (D).

**Figure 17** Measured (solid dots) and calculated (solid curve) calorimeter absorption as a function of lossy paint thickness . The calculations assumed $\epsilon_r = 5$ and $\tan(\delta) = 0.25$, and the thickness of each coat of paint was assumed to be equal.

**Figure 18** Measured (solid dots) and calculated (solid curve) calorimeter absorption as a function of incident RF frequency. The calculations assumed $\epsilon_r = 5$ and $\tan(\delta) = 0.25$.

**Figure 19** Geometry used to calculate the calorimeter absorption showing the angles of incidence ($\Theta_i$) and transmittance ($\Theta_t$), the dielectric constants of free space ($\varepsilon_o$) and of the absorbing paint ($\varepsilon_2$) and the RF electric ($\vec{E}$) and magnetic ($\vec{H}$) fields.

**Figure 20** Voltage waveform applied to the cathode (a) and intermediate anode (b) of the electron gun.

**Figure 21** Profile of applied axial ($B_z$, solid curve) and radial ($B_r$, dashed curves) magnetic fields measured on axis (curve 1) and 0.7 cm off axis (curve 2).

**Figure 22** Configuration of the electron gun emitter and the main and trim magnetic field coils. The trim coil nearest the emitter generated a magnetic field in the direction opposite the fields of the other coils and the origin of the z-axis (axis of symmetry) indicates the bottom of the superconducting magnet dewar flange.

**Figure 23** Schematic diagram of the 13 $\mu$sec, high-voltage modulator used in the experiments.

**Figure 24** Threshold currents for a 25 cm mirror separation. The solid dots show data with an oscillation frequency of $109.8 \pm 0.1$ GHz, and the open circles show data with an oscillation frequency of $108.8 \pm 0.1$ GHz. The solid (dashed) curves show theoretical results based on $\alpha = 1.5$ for longitudinal modes with an electric field maximum (minimum) coinciding with the electron beam axis.

**Figure 25** Threshold current dependence on $\alpha$ for a mirror separation of 25 cm. The solid curve shows the theoretical result for $\alpha = 1.5$, the dashed curve corresonds to $\alpha = 1$, and the dash–dot–dash curve corresponds to $\alpha = 2$. Other parameters are as given for Figure 24.

**Figure 26** Threshold currents for a 20 cm mirror separation. The solid dots show data with an oscillation frequency of $109.8 \pm 0.1$ GHz, and the open circles show data with an oscillation frequency of $109.2 \pm 0.2$ GHz. The solid curves show theoretical results based on $\alpha = 1.5$ and the electron beam axis located midway between the electric field maxima for adjacent longitudinal modes of the resonator. The two thicker line theoretical curves correspond to frequencies of 109.05 (minimum oscillation current at $\sim 42.8$ kG) and 109.8 GHz (minimum oscillation current at $\sim 43.2$ kG).

**Figure 27** Threshold current dependence on beam translation. The solid dots show data for a 20 cm mirror separation, a gun voltage of 54.2 kV, a magnetic field of 43 kG, and an oscillation frequency of $111 \pm 0.1$ GHz. The solid curve is proportional to the amplitude squared of the standing-wave RF field of the resonator.

**Figure 28** Output power vs. mirror separation for a 50 kG magnetic field. The solid square data corresponds to a gun voltage of $V = 66.7$ kV and a beam current of 8 A. The solid dot data corresponds to a gun voltage of $V = 71.5$ kV and a beam current of 13.5 A.

**Figure 29** Output power vs. beam current for 20 cm mirror separation and a gun voltage of 71.5 kV. The magnetic field is 44, 47, and 50 kG for the solid square, solid dot, and solid triangle data, respectively.

**Figure 30** Output efficiency vs. beam current for 20 cm mirror separation and a gun voltage of 71.5 kV. The magnetic field is 44, 47, and 50 kG for the solid square, solid dot, and solid triangle data, respectively.

**Figure 31** Typical multimode frequency spectra for a mirror separation of 20 cm and a gun voltage of 71.5 cm. (a): $B = 44$ kG, $I = 8$ A; (b): $B = 47$ kG, $I = 14$ A; (c): $B = 50$ kG, $I = 8$ A.

**Figure 32** Electronic efficiency vs. $QI/d$. The solid curve shows results from a multimode, annular beam simulation. The solid dots and triangles show the estimated electronic efficiency for the 50 kG power data shown in Figure 29. The solid dots are based on the diffraction $Q$ obtained from scalar diffraction theory, and the solid triangles are based on the $Q$ inferred from the threshold current data.

**Figure 33** Output power and efficiency operation with a 50 kG resonator magnetic field and gun voltages of 71–74 kV. The mirror separation for the data shown by the solid and open squares is 20 cm, and is 23 cm for the data shown by the solid and open circles and triangles. The resonator magnetic field has a 2% negative taper for the data shown by the solid and open circles.

**Figure 34** Frequency tuning by magnetic field variation. The oscillation frequencies are shown by +'s and the output power is shown by the solid dots. The gun voltage and beam current 66.7 kV and 12 A, respectively.

**Figure 35** Frequency tuning with gun voltage variation for a magnetic field of 50 kG, a current of $\sim$ 10 A and a 20 cm mirror separation. The oscillation frequencies are shown by the solid dots and the large dots indicate the dominant mode.

**Figure 36** Mode frequencies as a function of current for a magnetic field of 47 kG with a 2% negative taper, a fixed voltage of 71.5 kV, and a 23 cm mirror separation.

**Figure 37** A region of single-mode operation in $V - I$ space. The magnetic field is 47 kG and the frequency is 119 GHz.

**Figure 38** Output power for single-moded or near single-moded operation for a magnetic field of 47 kG and frequencies of 119–120 GHz. The mirror separation is 23, 25.5, and 28 cm for the solid dots, triangles, and squares, respectively.

**Figure 39** Resonance detuning dependence on beam current normalized to the threshold current. The detuning in (a) is uncorrected for space-charge effects, the data in (b) includes a space-charge correction. The solid dots, triangles, and squares correspond to the data shown in Figure 38.

**Figure 40** QOG normalized operating parameter space for (a):$\mu = 5$ ($\alpha = 0.65$) and (b):$\mu = 10$ ($\alpha = 1$). The solid dots, triangles, and squares correspond to the data shown in Figure 38. The solid curves indicate the boundary of the predicted region of stable operation.

**Figure 41** Comparison of theoretical and experimental electronic efficiencies for (a) $\mu = 5$ ($\alpha = 0.65$) and (b) $\mu = 10$ ($\alpha = 0.65$). The solid dots, triangles, and squares correspond to the data shown in Figure 38.

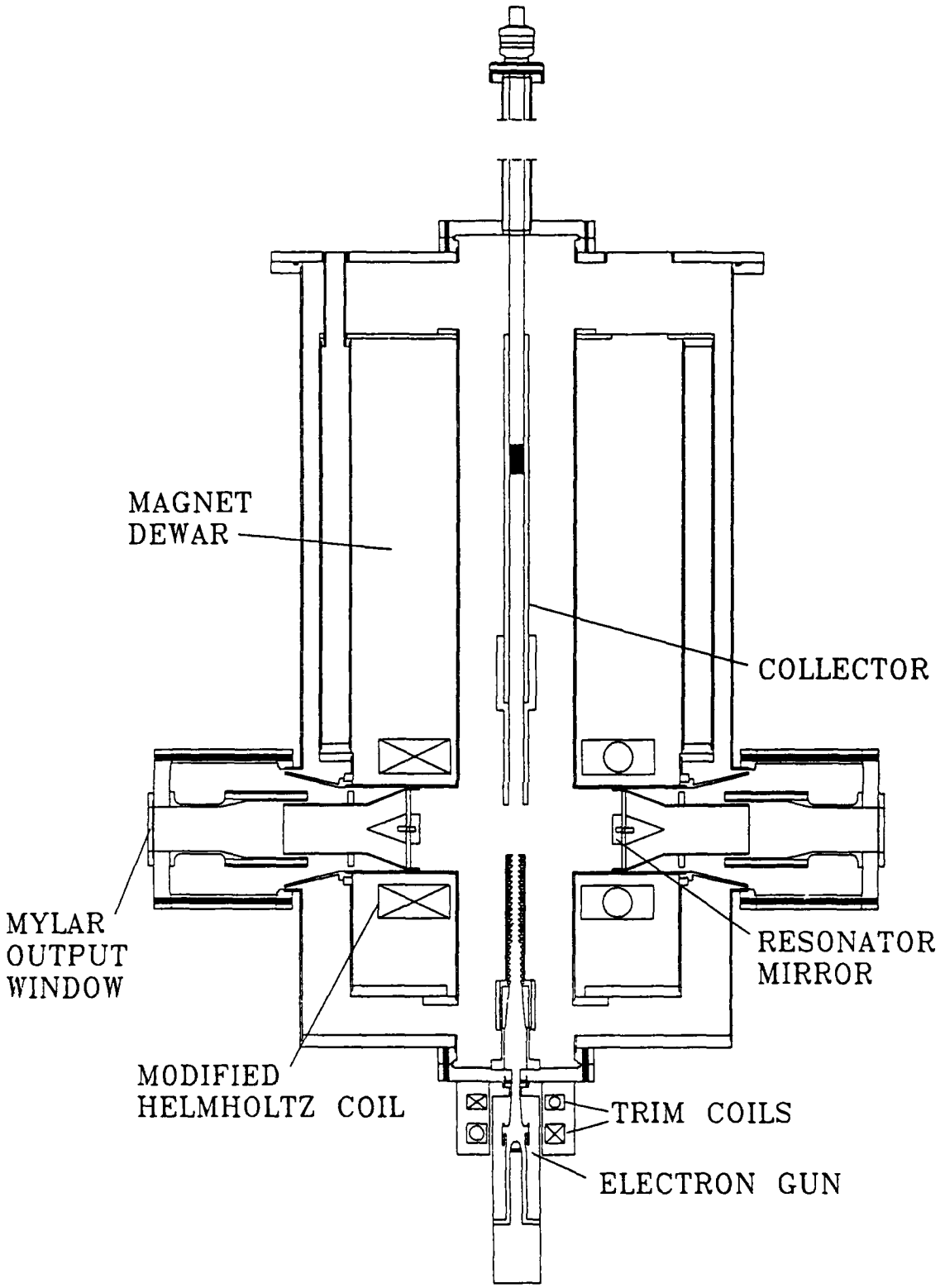

MAGNET
DEWAR
COLLECTOR
MYLAR
OUTPUT
WINDOW
RESONATOR
MIRROR
MODIFIED
HELMHOLTZ COIL
TRIM COILS
ELECTRON GUN

Figure 1

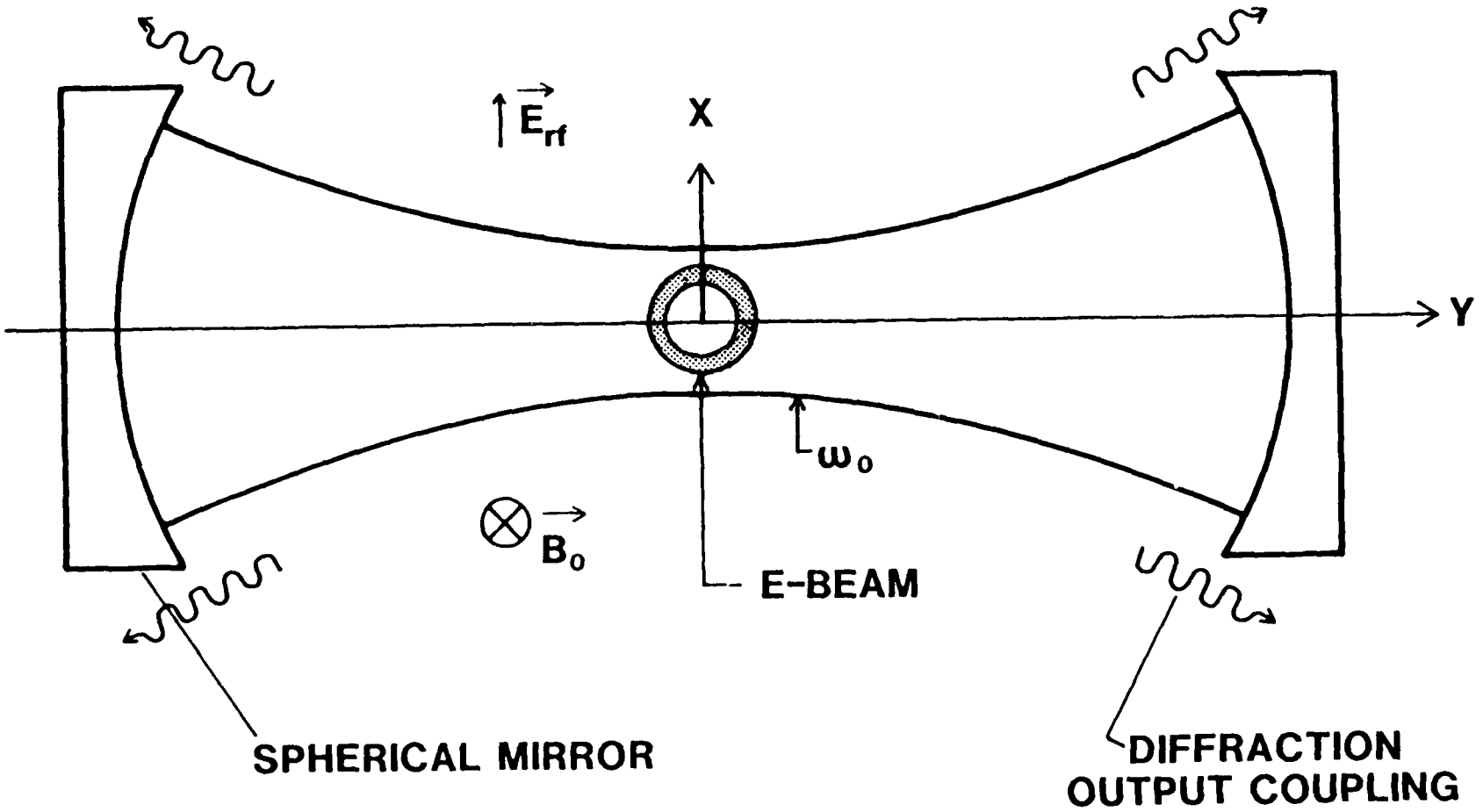

$\vec{E}_{rf}$
X
Y
$\omega_o$
$\vec{B}_o$
E-BEAM
SPHERICAL MIRROR
DIFFRACTION
OUTPUT COUPLING

Figure 2

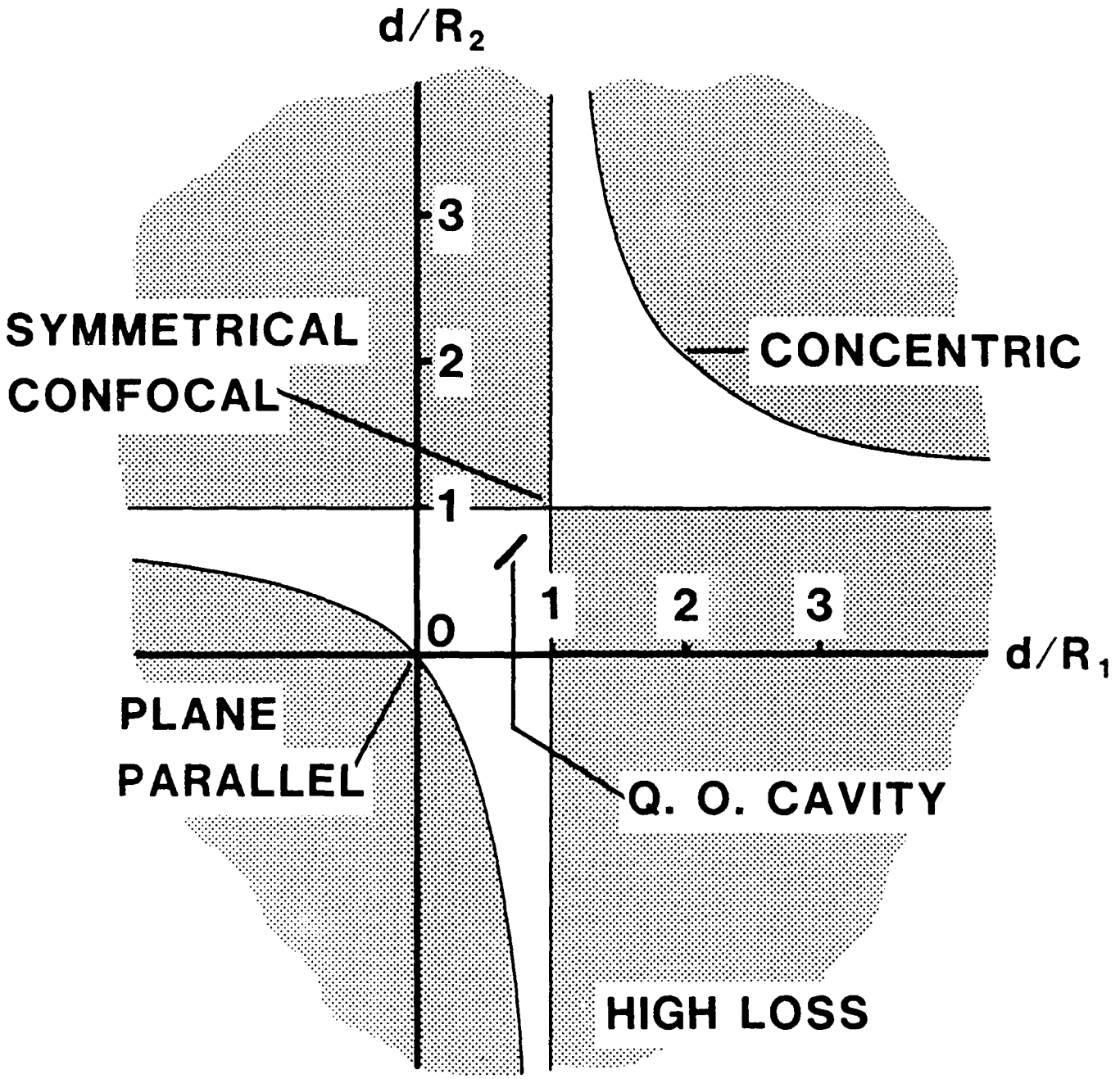

d/R2
3
2
1
0
SYMMETRICAL
CONFOCAL
CONCENTRIC
1
2
3
d/R1
PLANE
PARALLEL
Q. O. CAVITY
HIGH LOSS

Figure 3

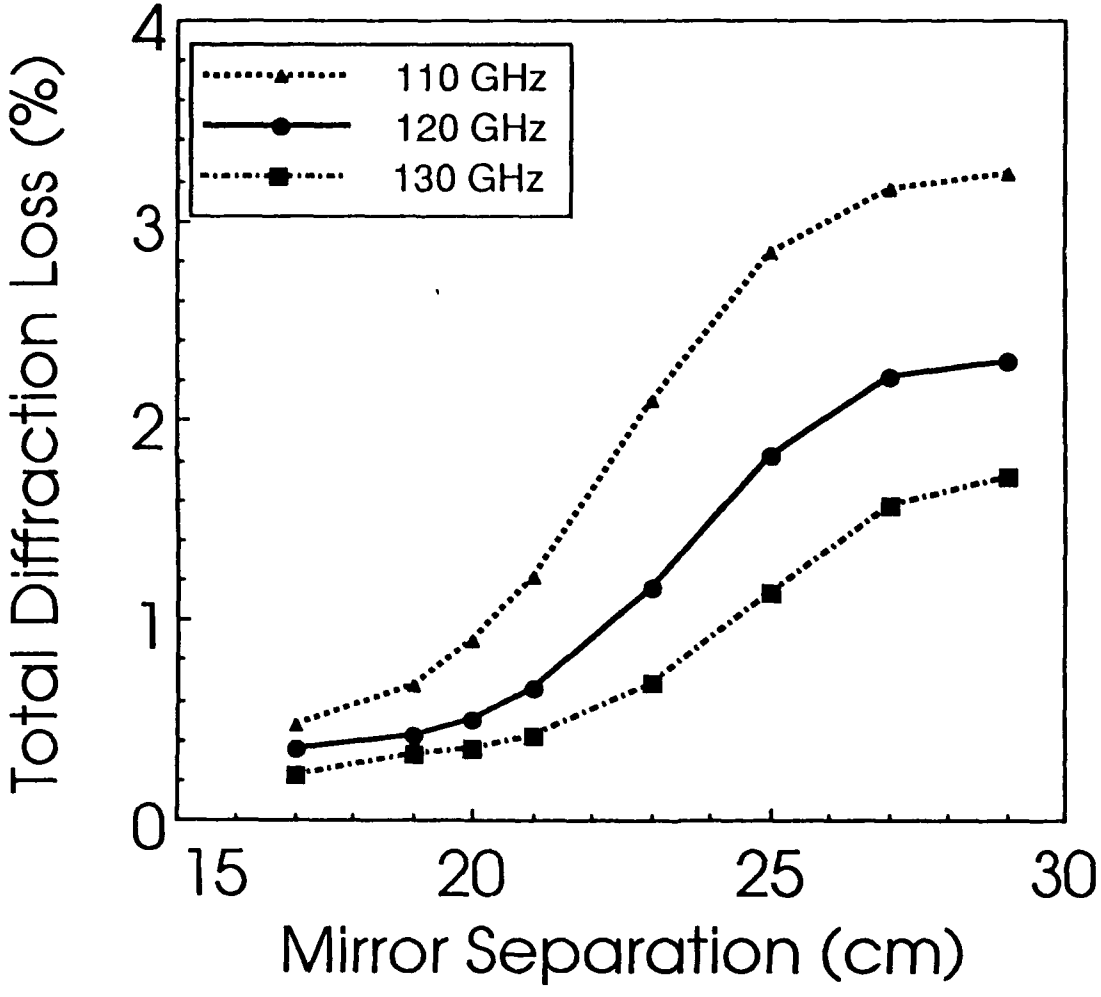

110 GHz
120 GHz
130 GHz
Total Diffraction Loss (%)
0
1
2
3
4
15
20
25
30
Mirror Separation (cm)

Figure 4

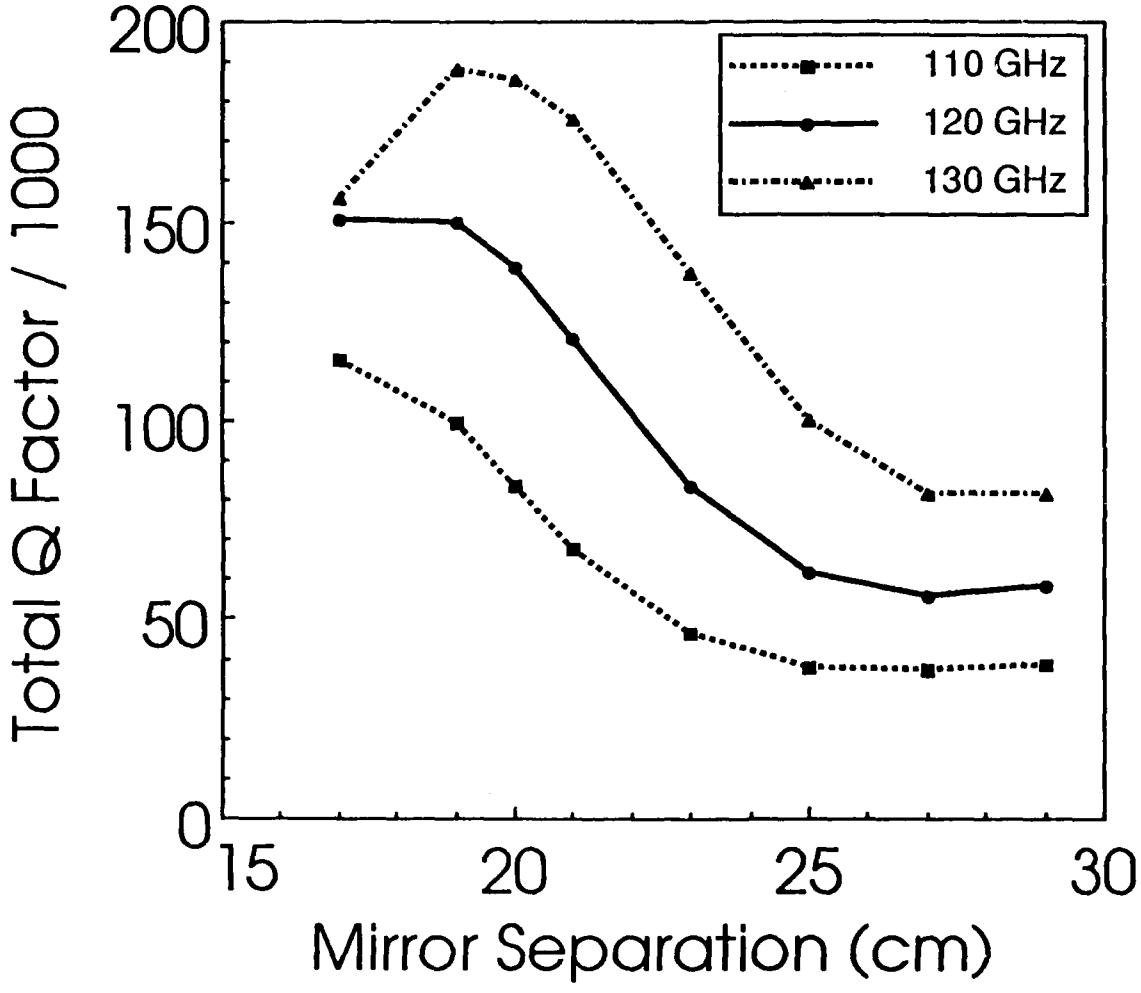

200
150
100
50
0
Total Q Factor / 1000
15
20
25
30
Mirror Separation (cm)
110 GHz
120 GHz
130 GHz

Figure 5

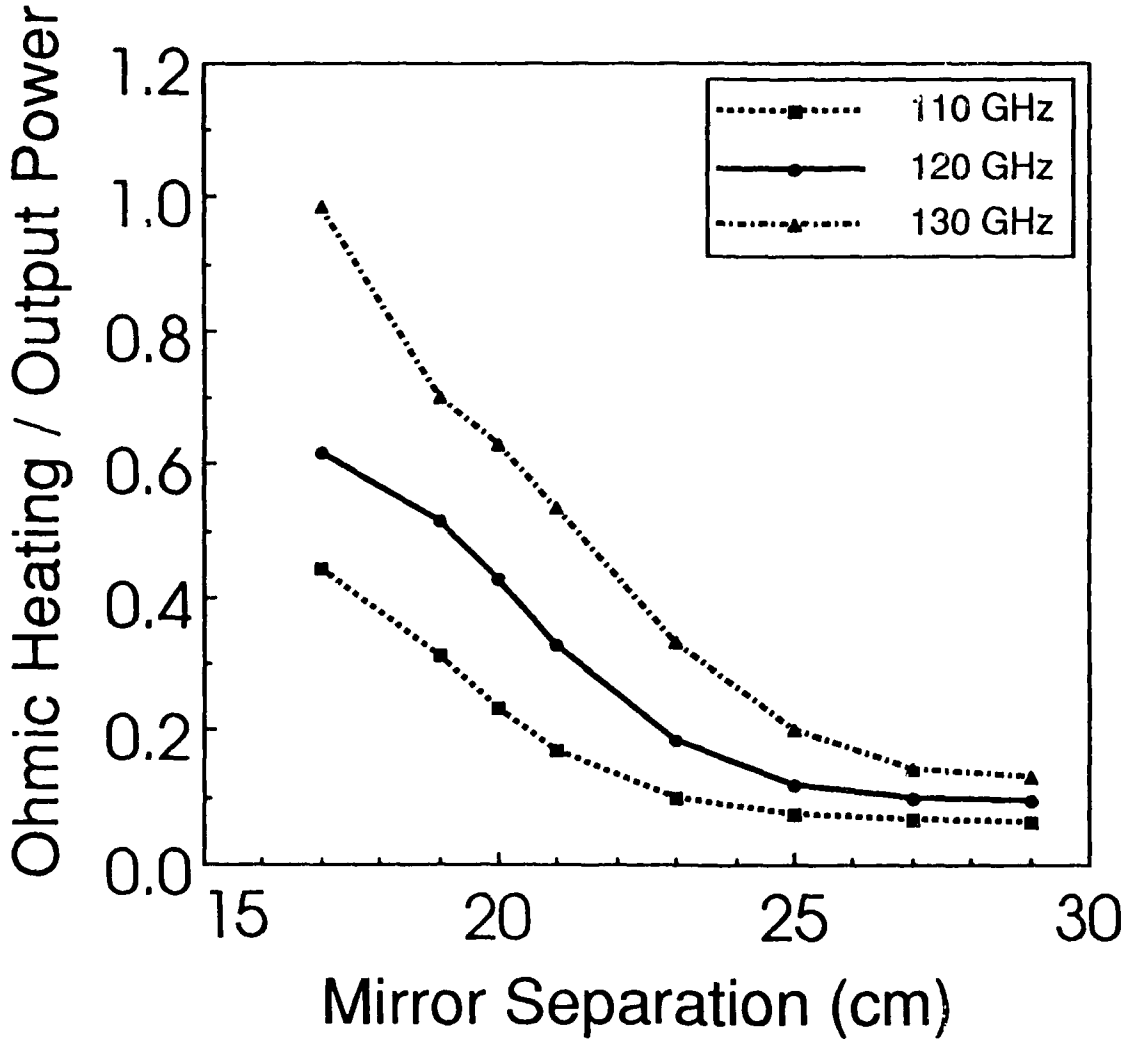

Ohmic Heating / Output Power
1.2
1.0
0.8
0.6
0.4
0.2
0.0
15
20
25
30
Mirror Separation (cm)
110 GHz
120 GHz
130 GHz

Figure 6

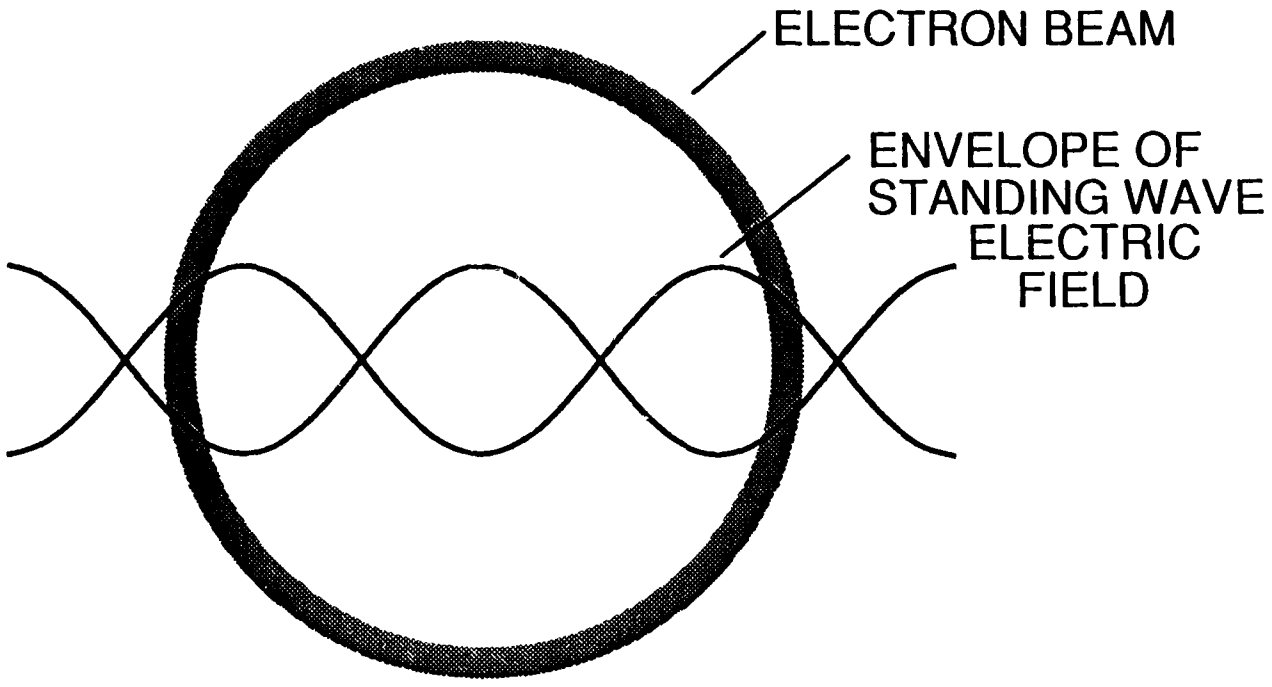



Figure 7

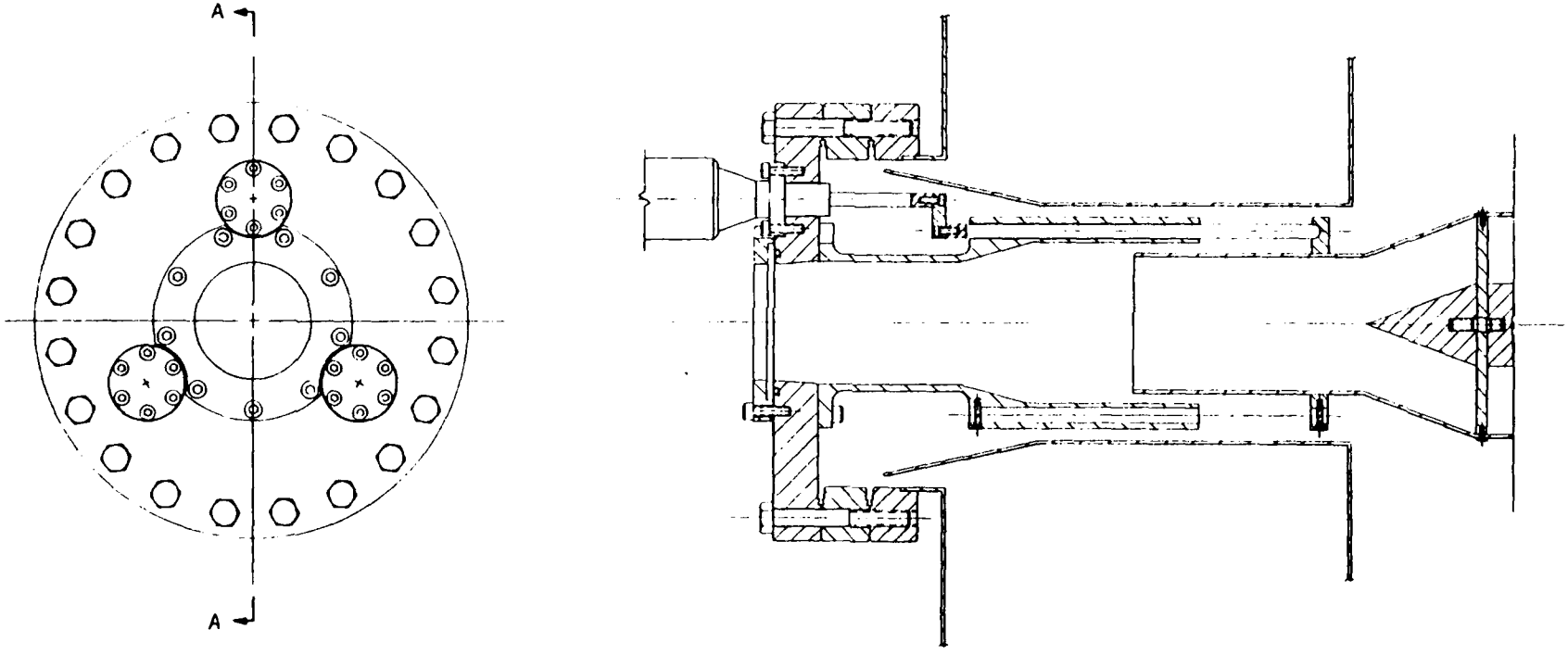



Figure 8

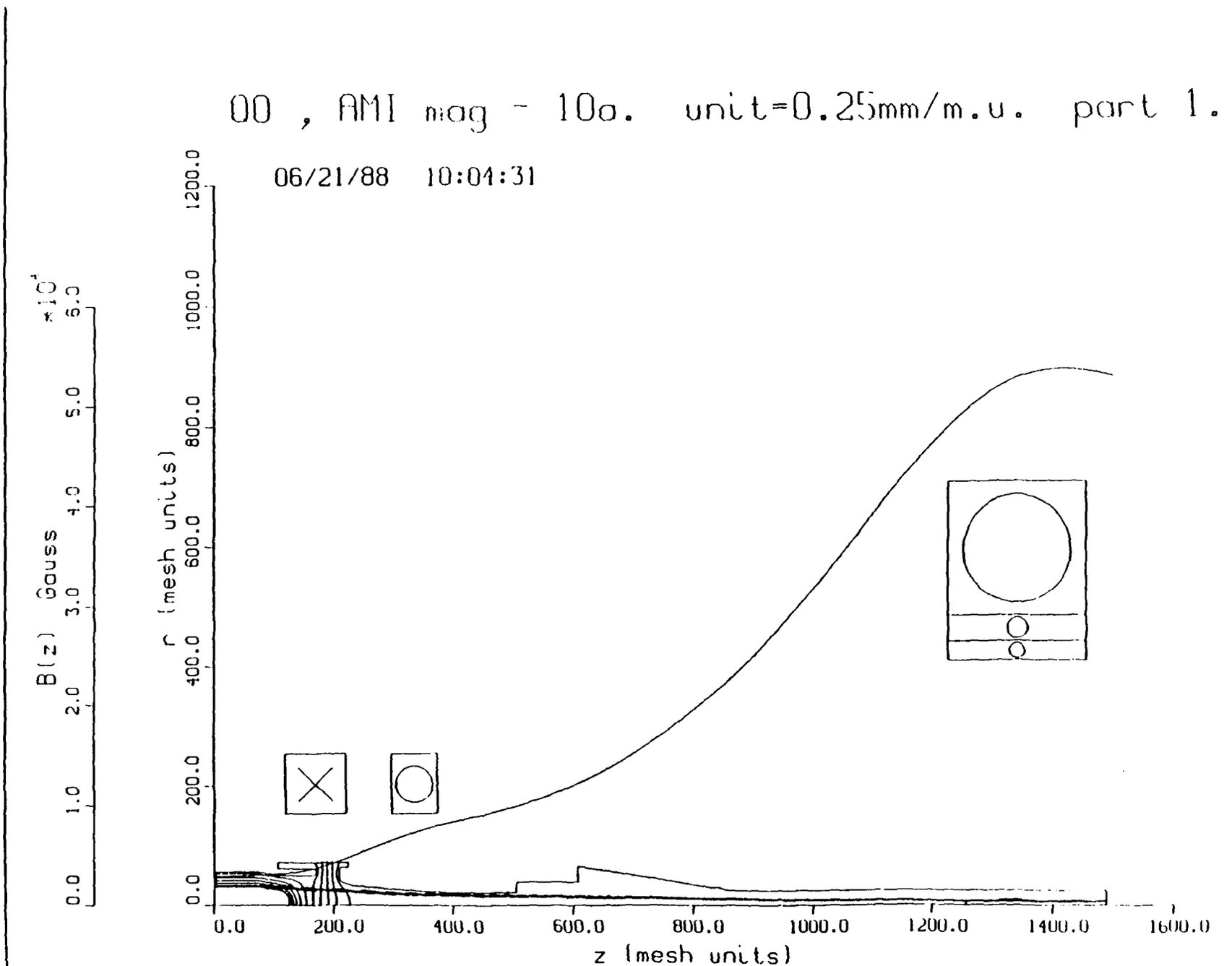

00 , AMI mag - 10a. unit=0.25mm/m.u. part 1.
06/21/88 10:04:31
B(z) Gauss
x10⁴
0.0
1.0
2.0
3.0
4.0
5.0
6.0
r (mesh units)
0.0
200.0
400.0
600.0
800.0
1000.0
1200.0
z (mesh units)
0.0
200.0
400.0
600.0
800.0
1000.0
1200.0
1400.0
1600.0

Figure 9

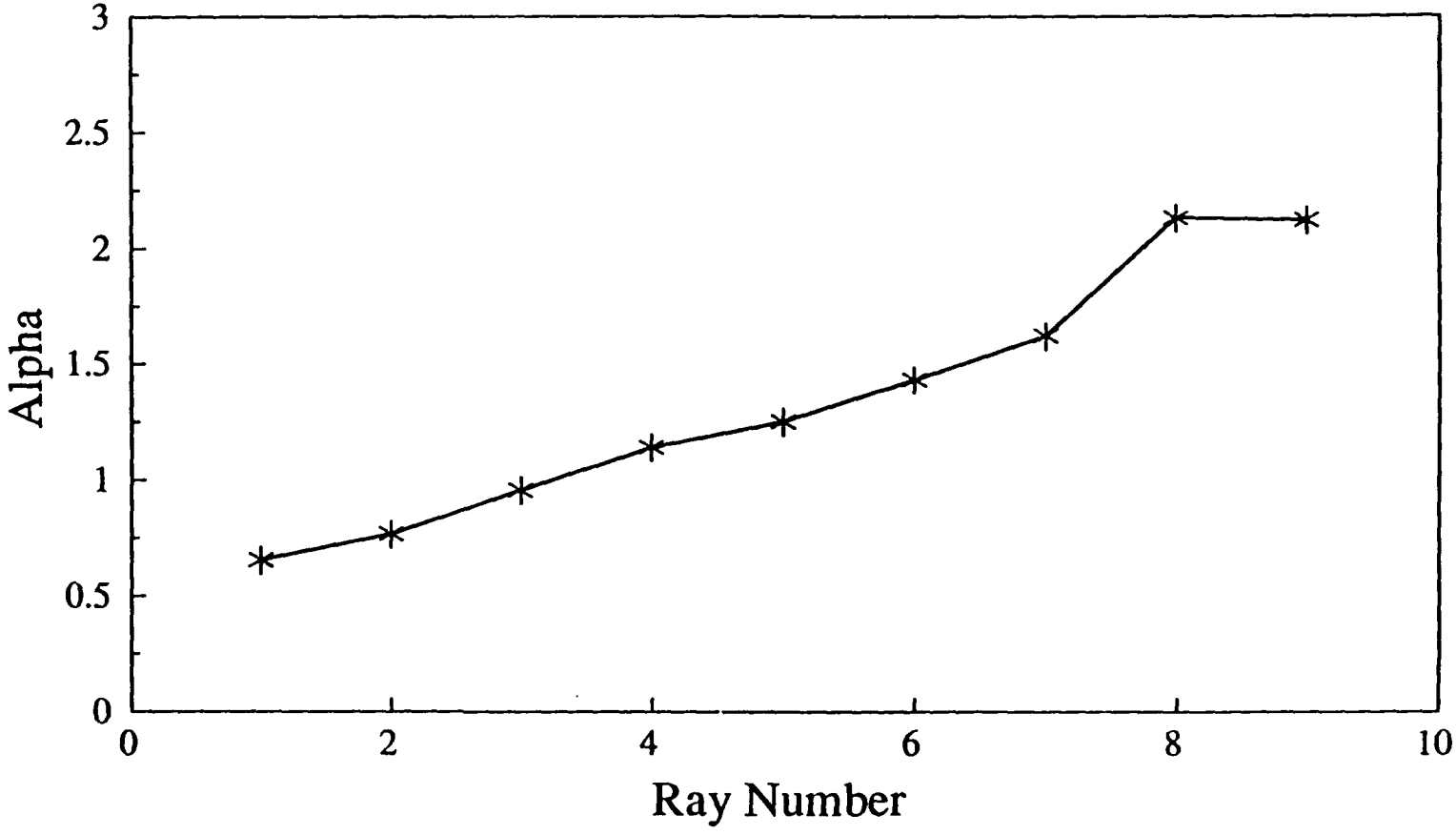



Figure 10

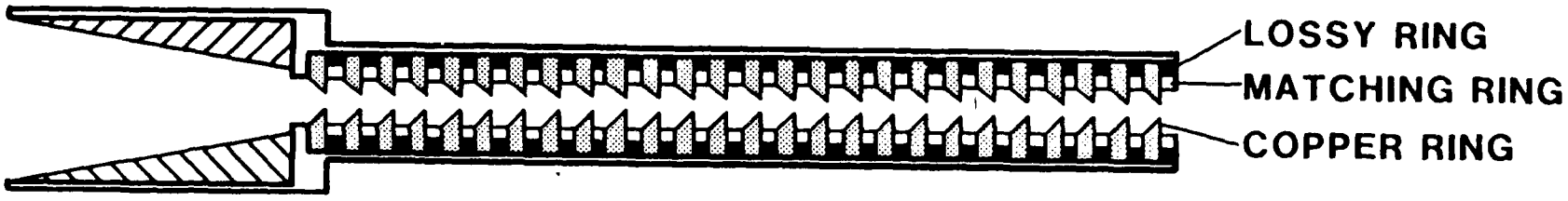



Figure 11

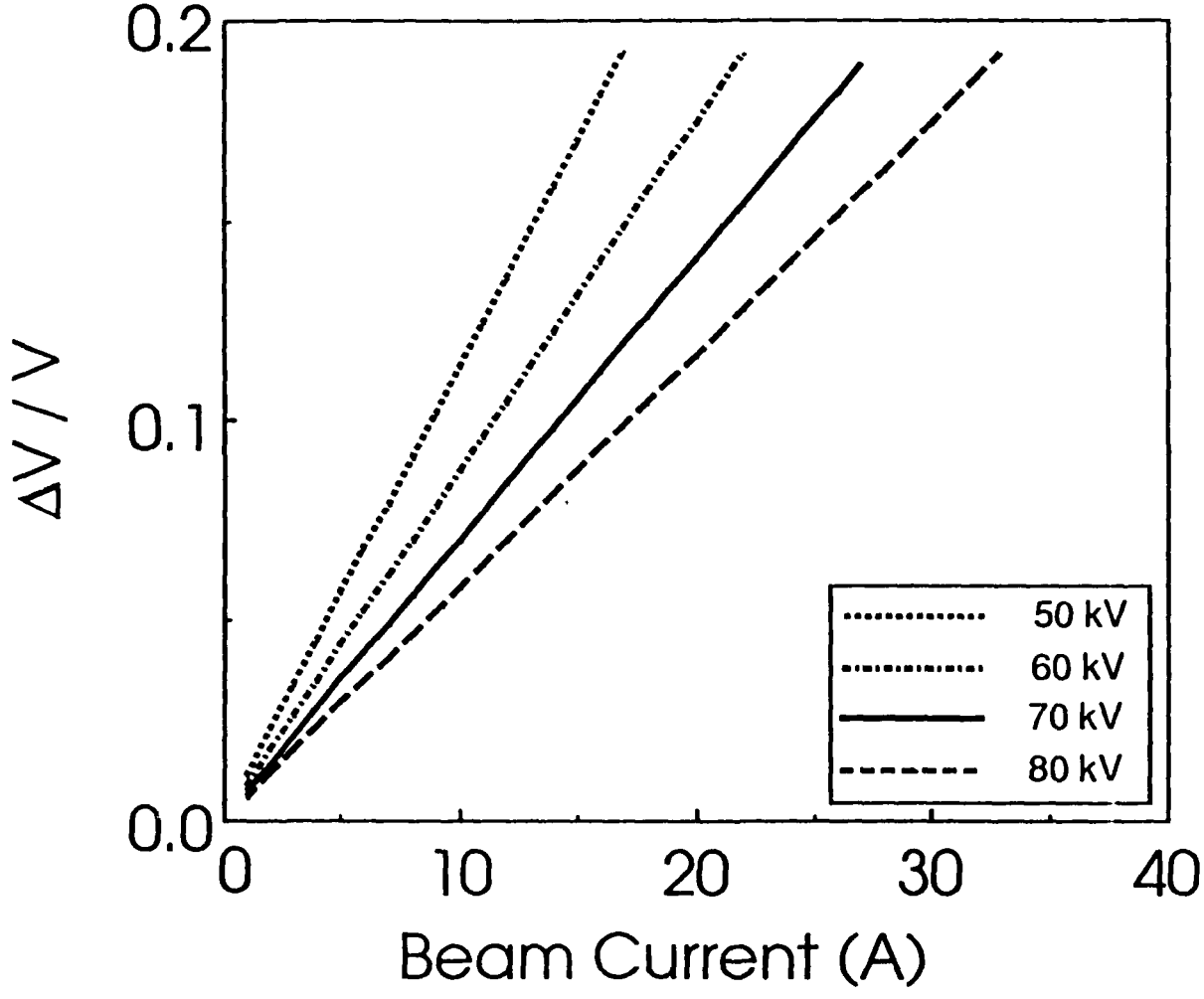



Figure 12

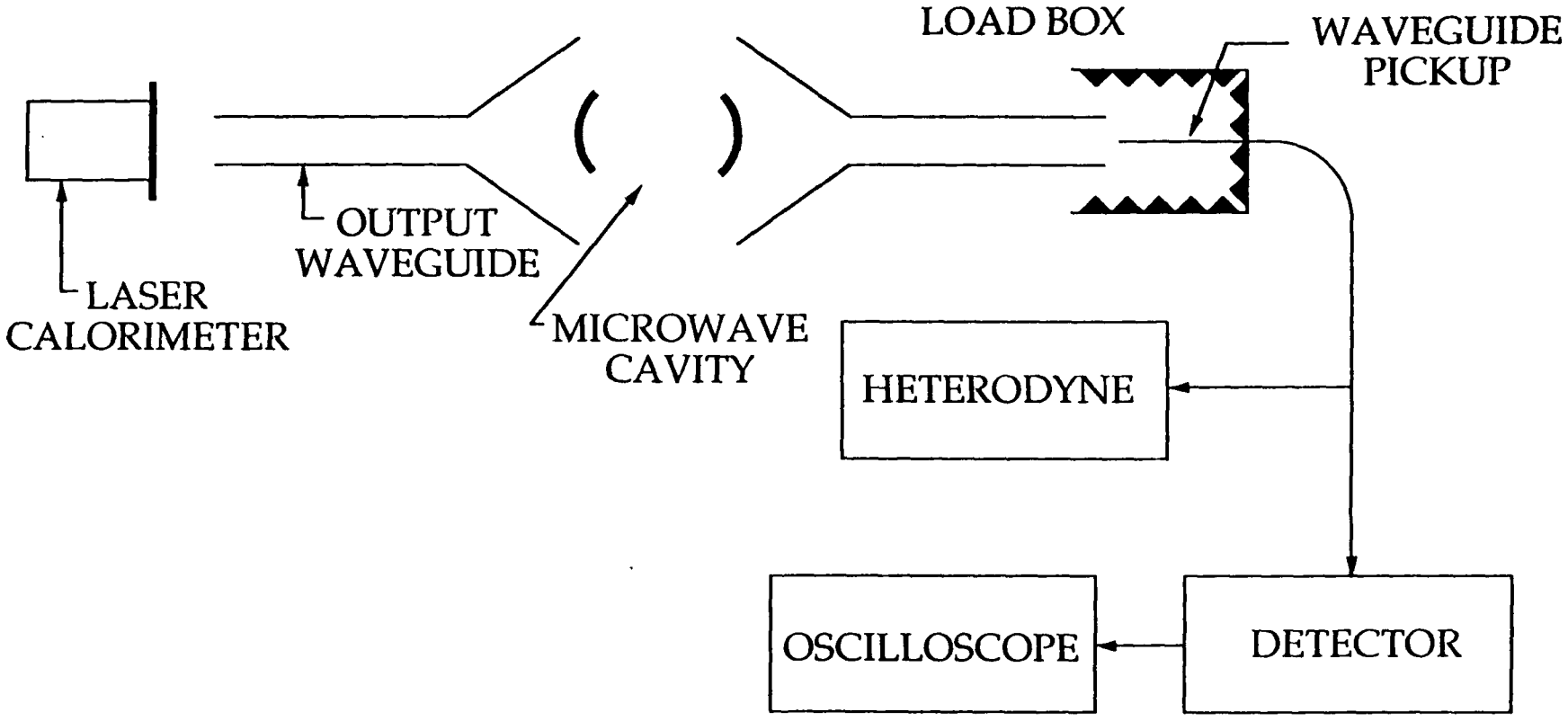

LOAD BOX
WAVEGUIDE PICKUP
OUTPUT WAVEGUIDE
LASER CALORIMETER
MICROWAVE CAVITY
HETERODYNE
OSCILLOSCOPE
DETECTOR

Figure 13

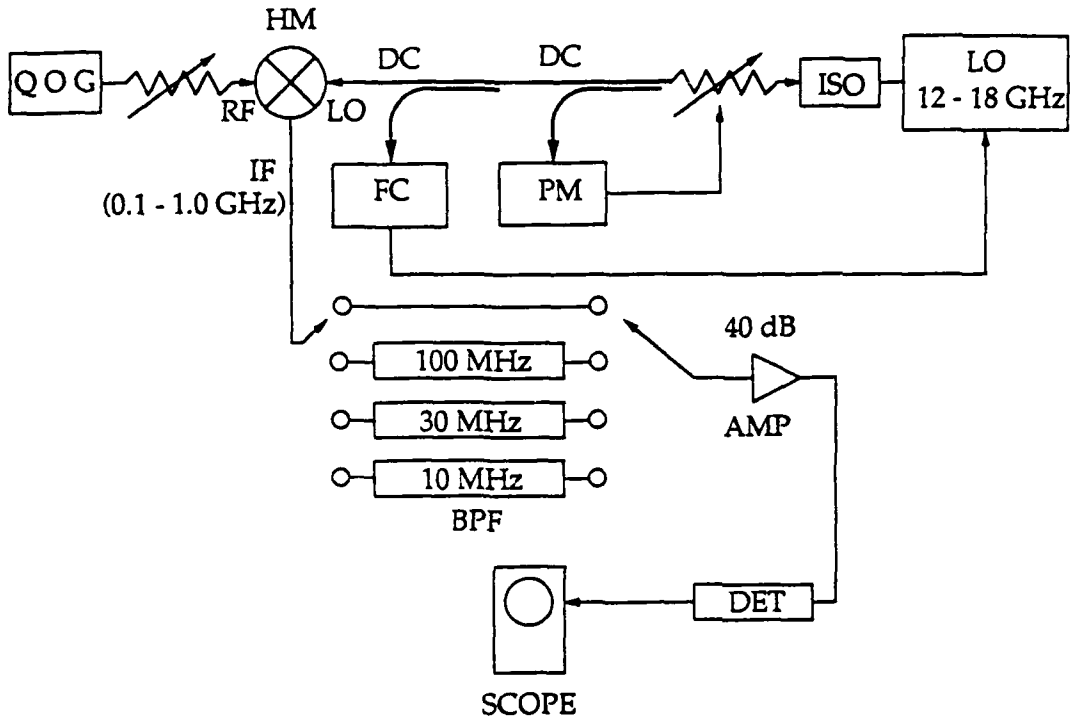

HM
QOG
RF
LO
DC
DC
ISO
LO
12 - 18 GHz
IF
(0.1 - 1.0 GHz)
FC
PM
40 dB
100 MHz
30 MHz
10 MHz
BPF
AMP
DET
SCOPE

Figure 14

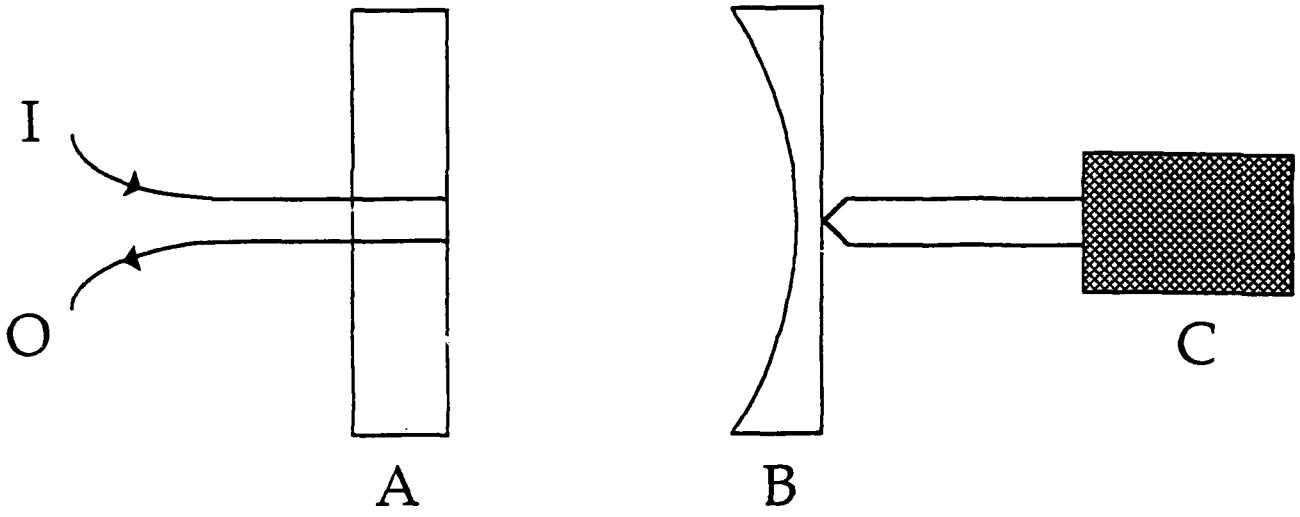



Figure 15

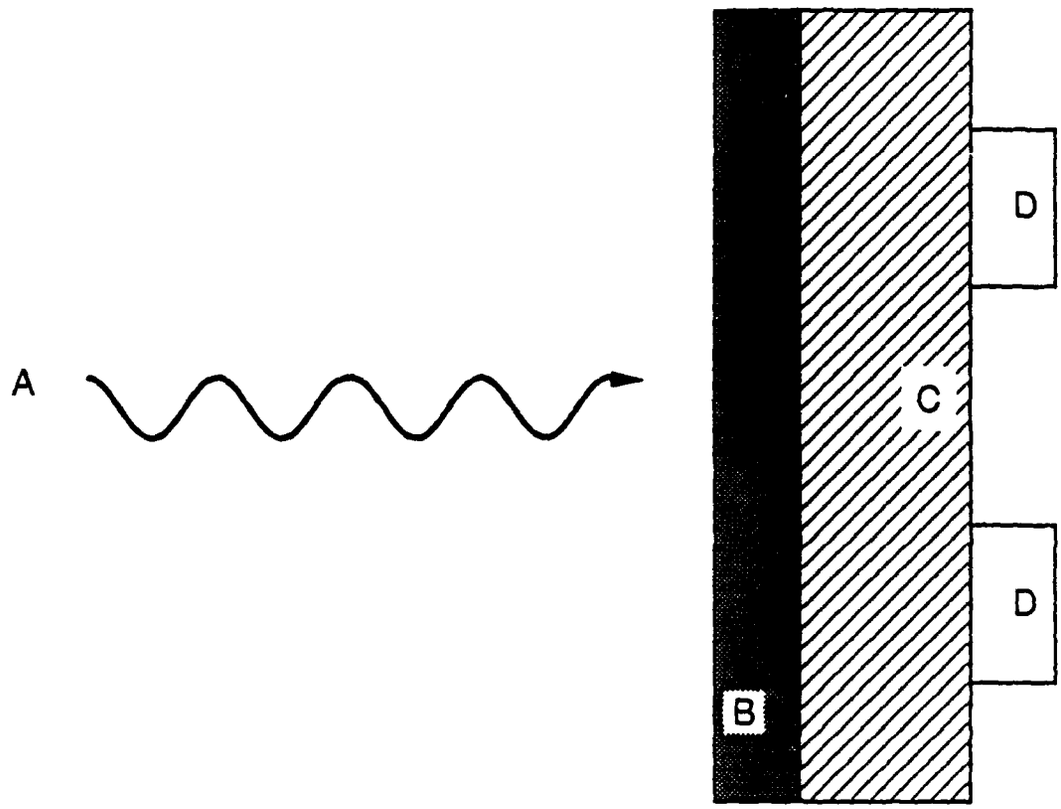



Figure 16

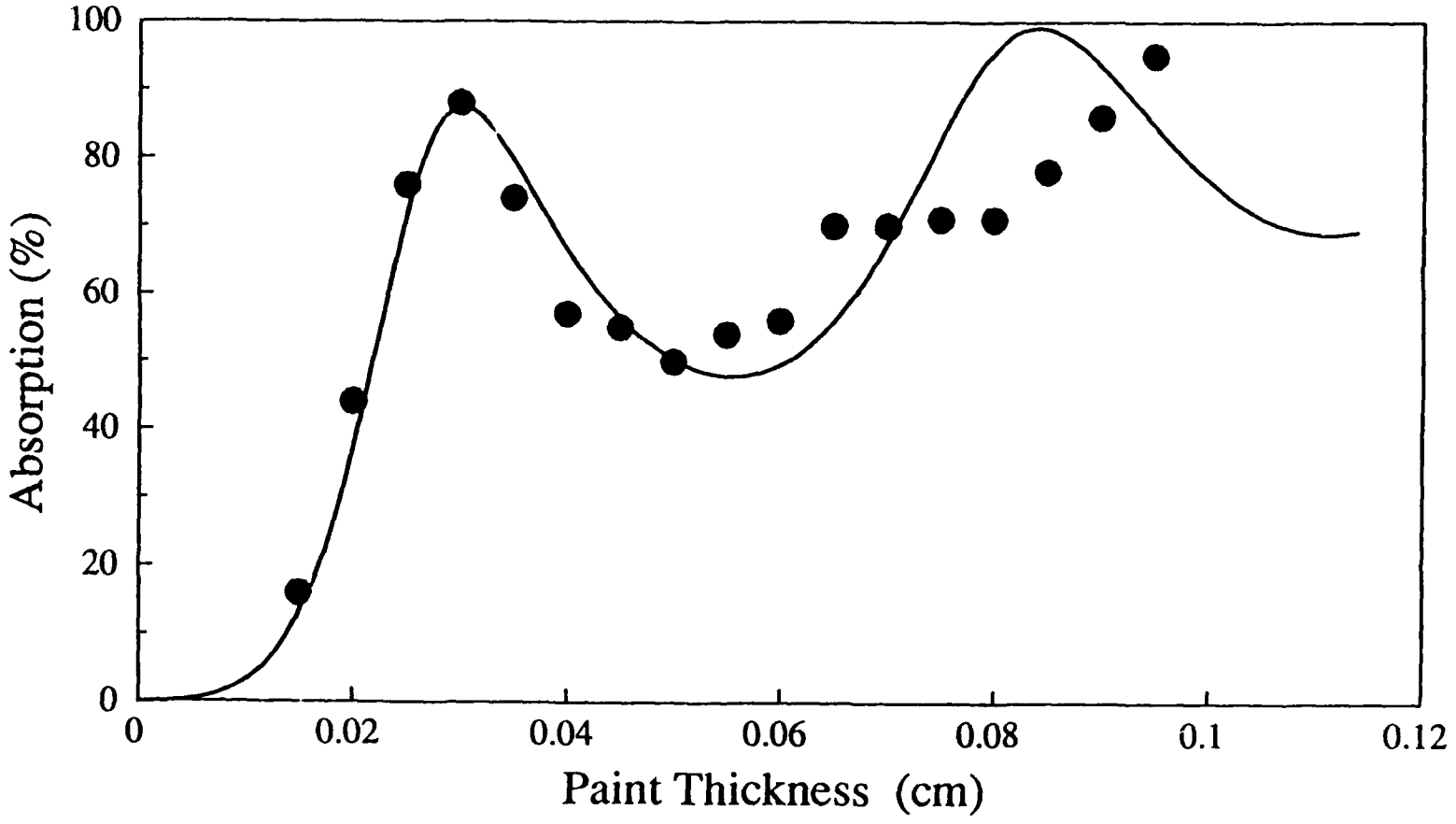

100
80
60
40
20
0
Absorption (%)
0
0.02
0.04
0.06
0.08
0.1
0.12
Paint Thickness (cm)

Figure 17

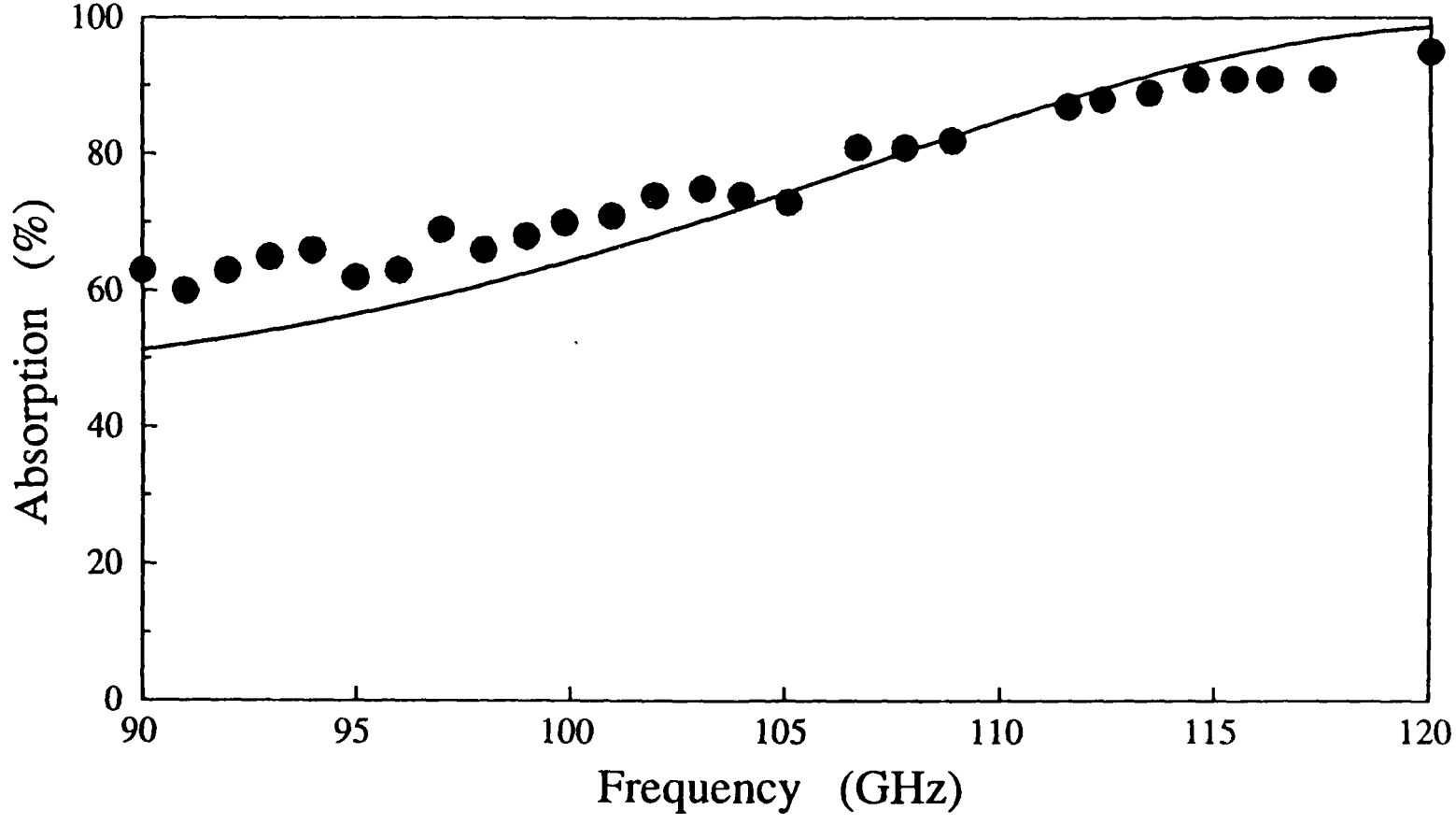

100
80
60
40
20
0
Absorption (%)
90
95
100
105
110
115
120
Frequency (GHz)

Figure 18

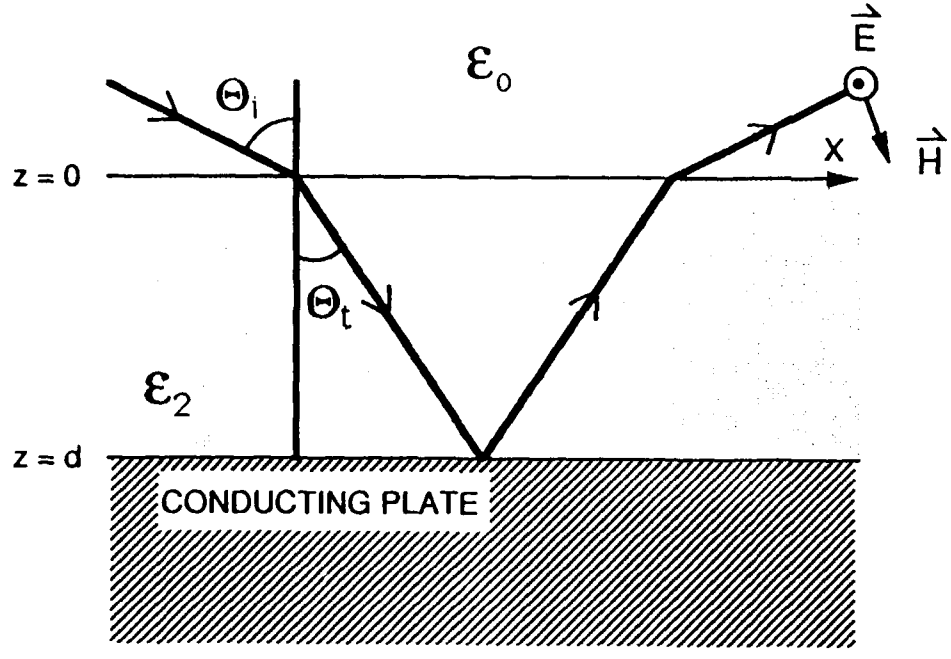

$\varepsilon_0$
$\vec{E}$
$\Theta_i$
z = 0
x
$\vec{H}$
$\Theta_t$
$\varepsilon_2$
z = d
CONDUCTING PLATE

Figure 19

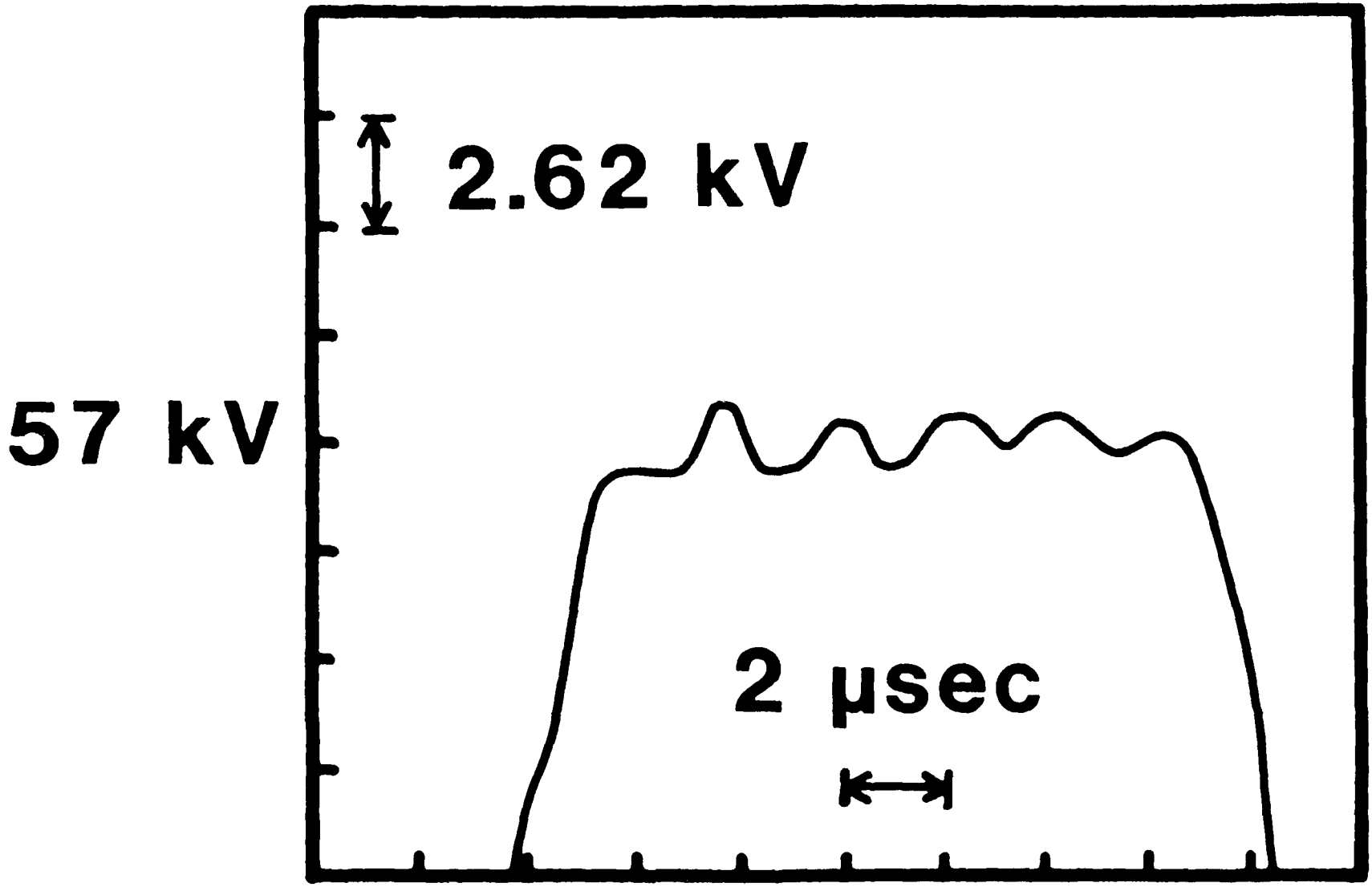



Figure 20 (a)

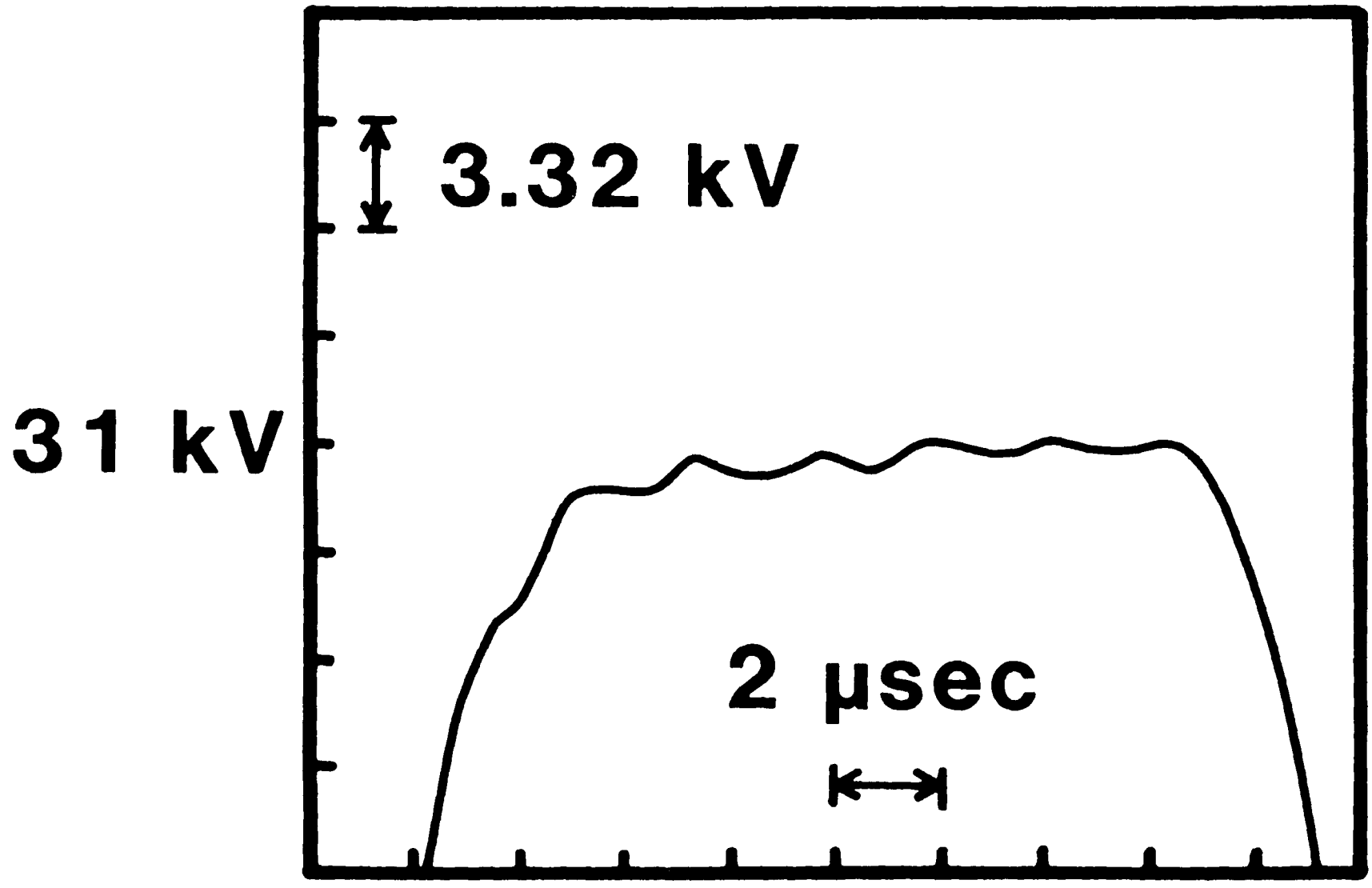



Figure 20 (b)

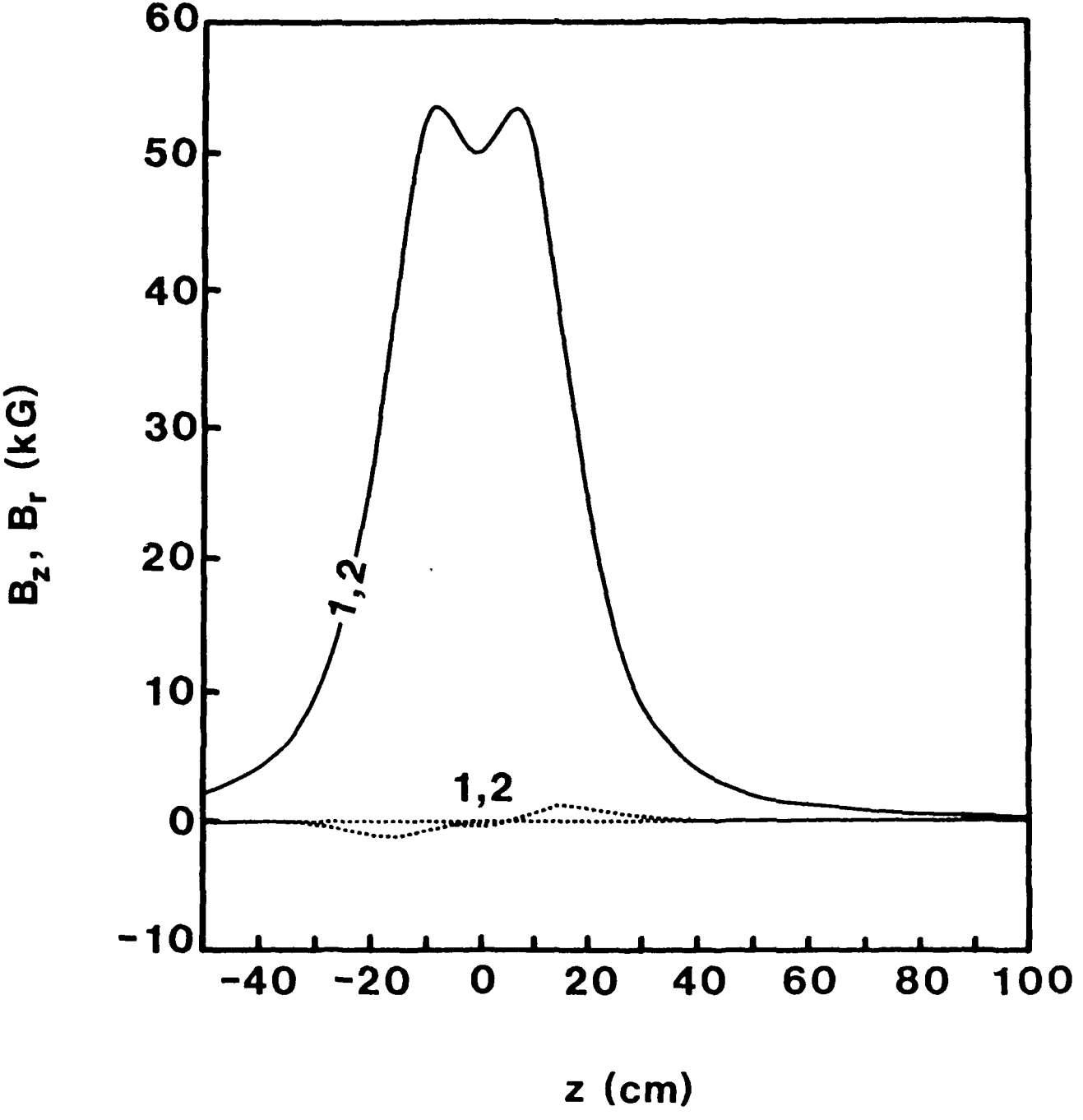



Figure 21

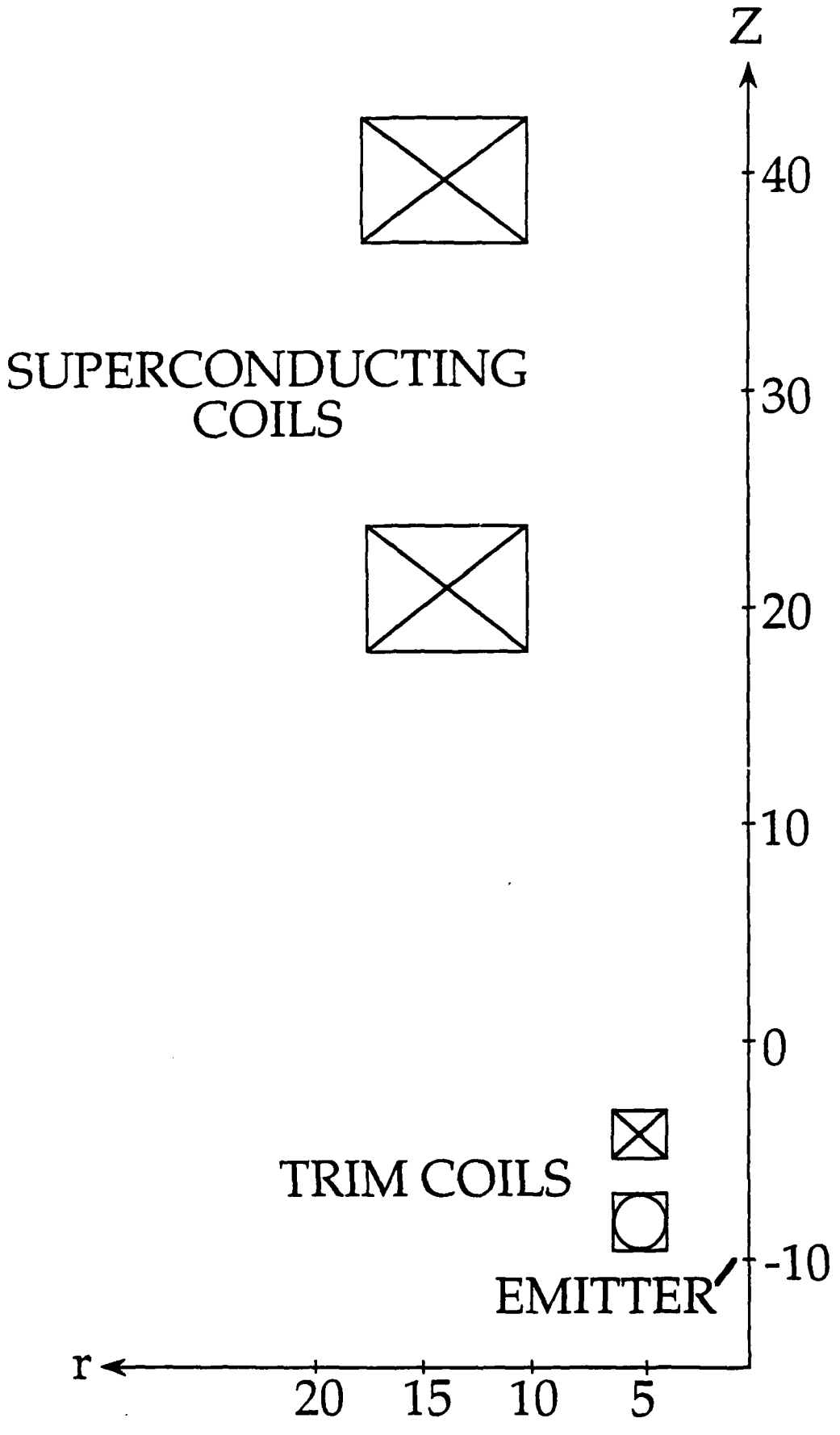

Z
40
30
20
10
0
-10
SUPERCONDUCTING
COILS
TRIM COILS
EMITTER
r
20
15
10
5

Figure 22

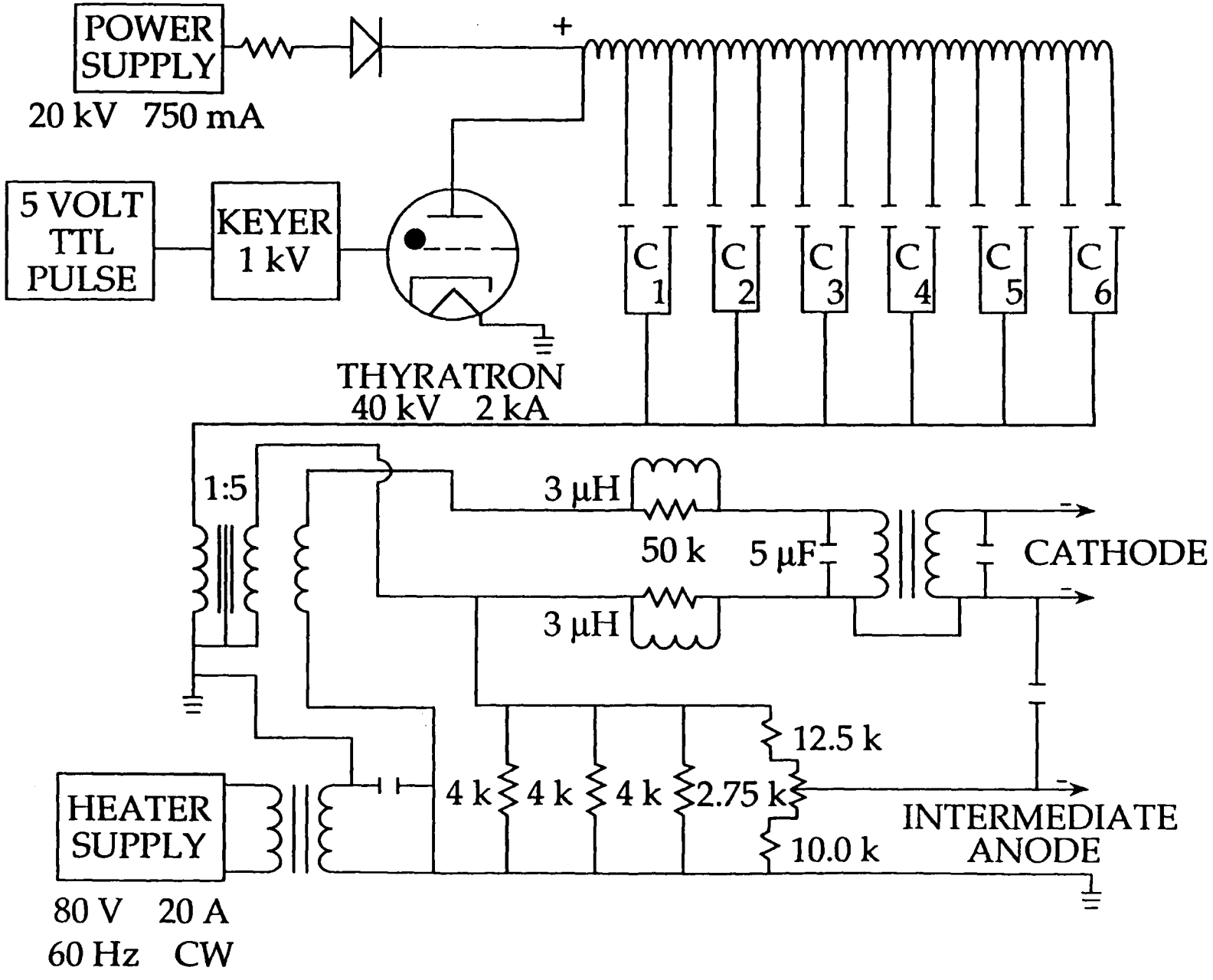

POWER SUPPLY
20 kV 750 mA
+
5 VOLT TTL PULSE
KEYER 1 kV
THYRATRON 40 kV 2 kA
C 1
C 2
C 3
C 4
C 5
C 6
1:5
3 µH
50 k
5 µF
CATHODE
3 µH
12.5 k
4 k
4 k
4 k
2.75 k
10.0 k
INTERMEDIATE ANODE
HEATER SUPPLY
80 V 20 A
60 Hz CW

Figure 23

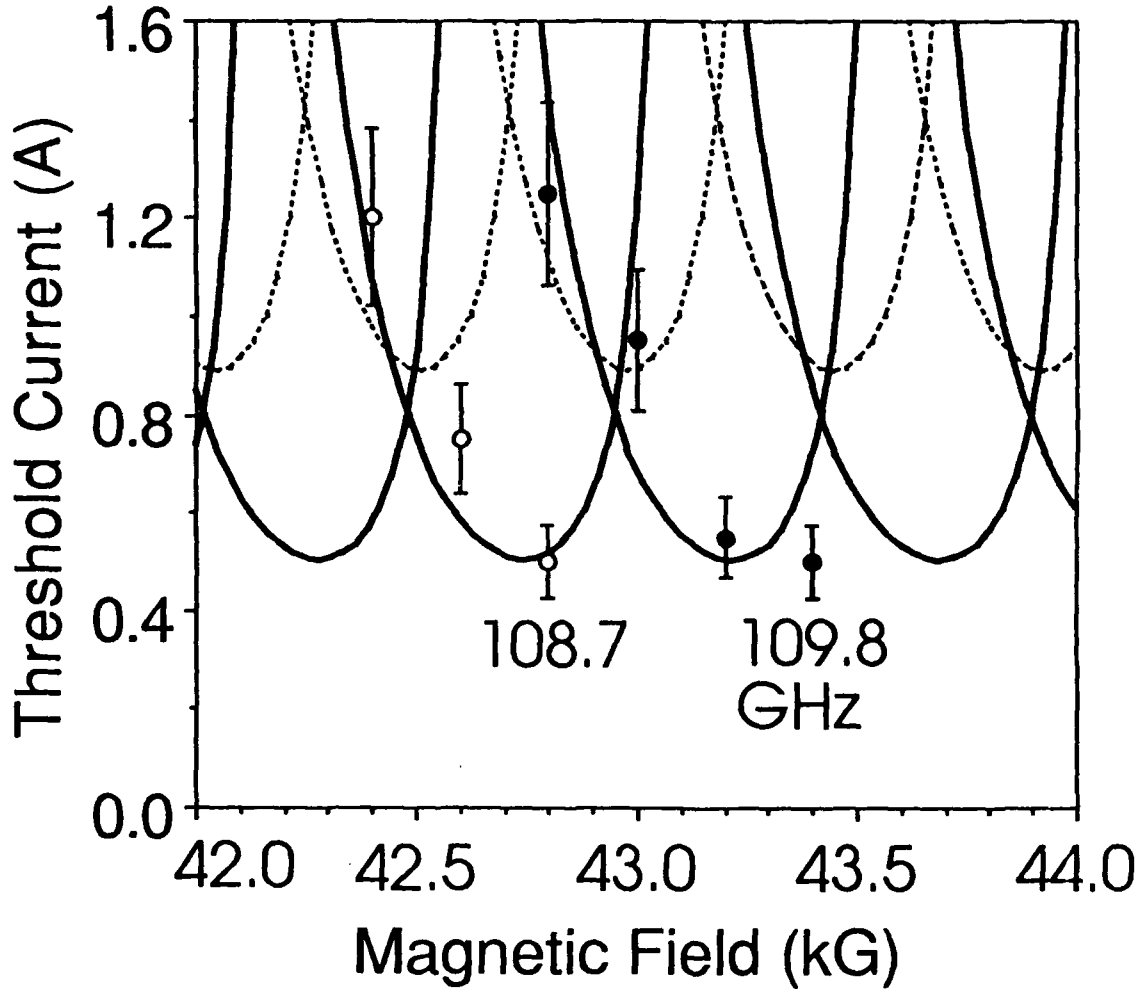

1.6
1.2
0.8
0.4
0.0
Threshold Current (A)
108.7
109.8
GHz
42.0
42.5
43.0
43.5
44.0
Magnetic Field (kG)

Figure 24

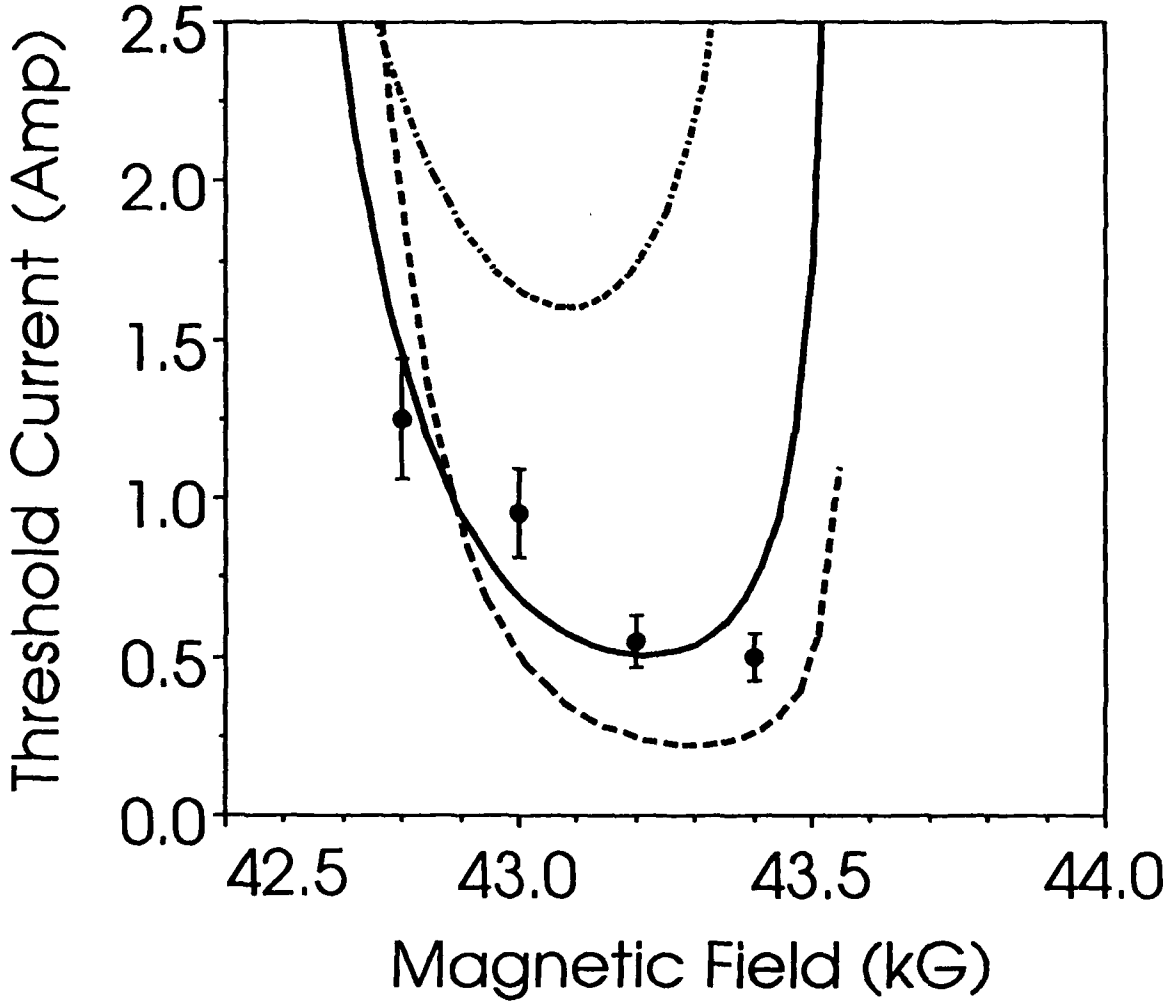

Threshold Current (Amp)
2.5
2.0
1.5
1.0
0.5
0.0
42.5
43.0
43.5
44.0
Magnetic Field (kG)

Figure 25

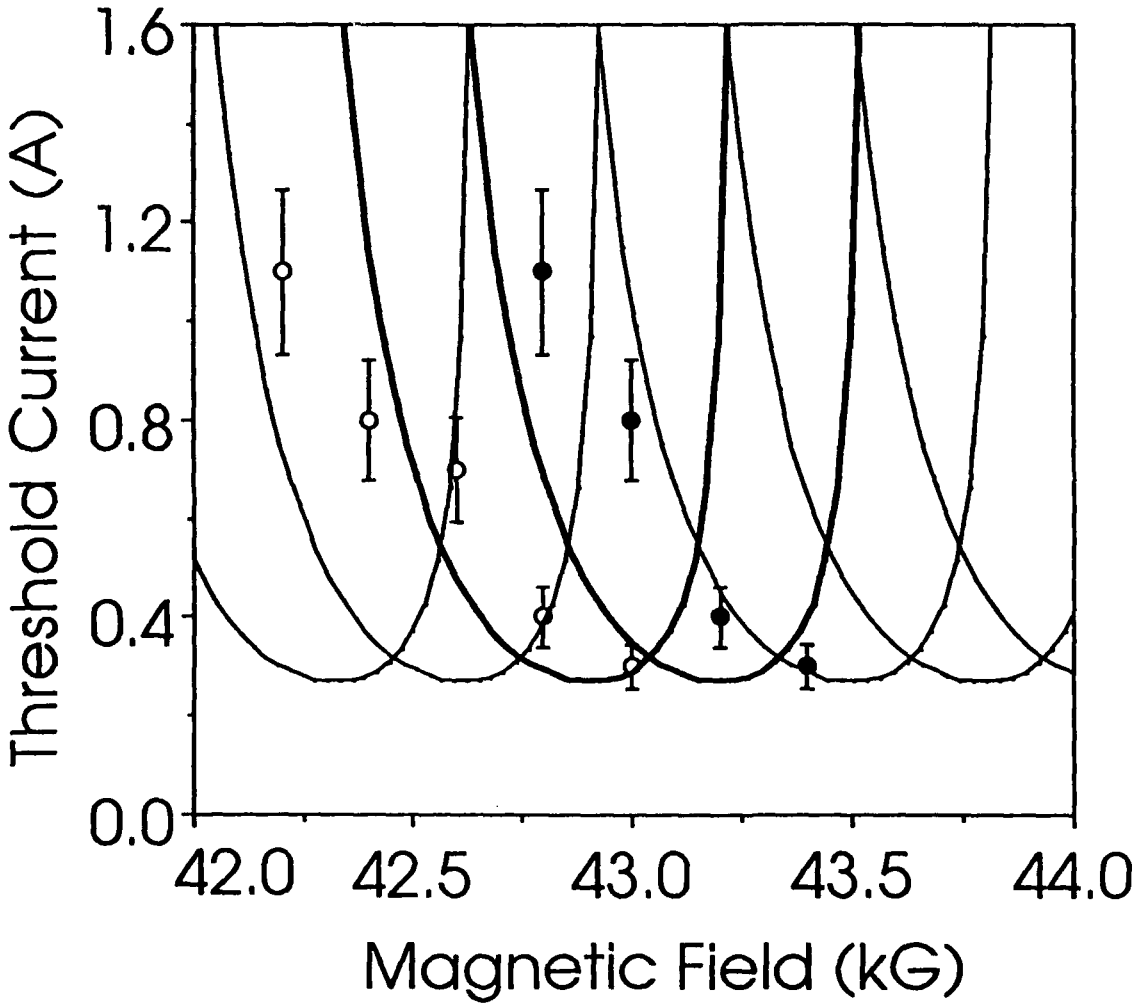

Threshold Current (A)
1.6
1.2
0.8
0.4
0.0
42.0
42.5
43.0
43.5
44.0
Magnetic Field (kG)

Figure 26

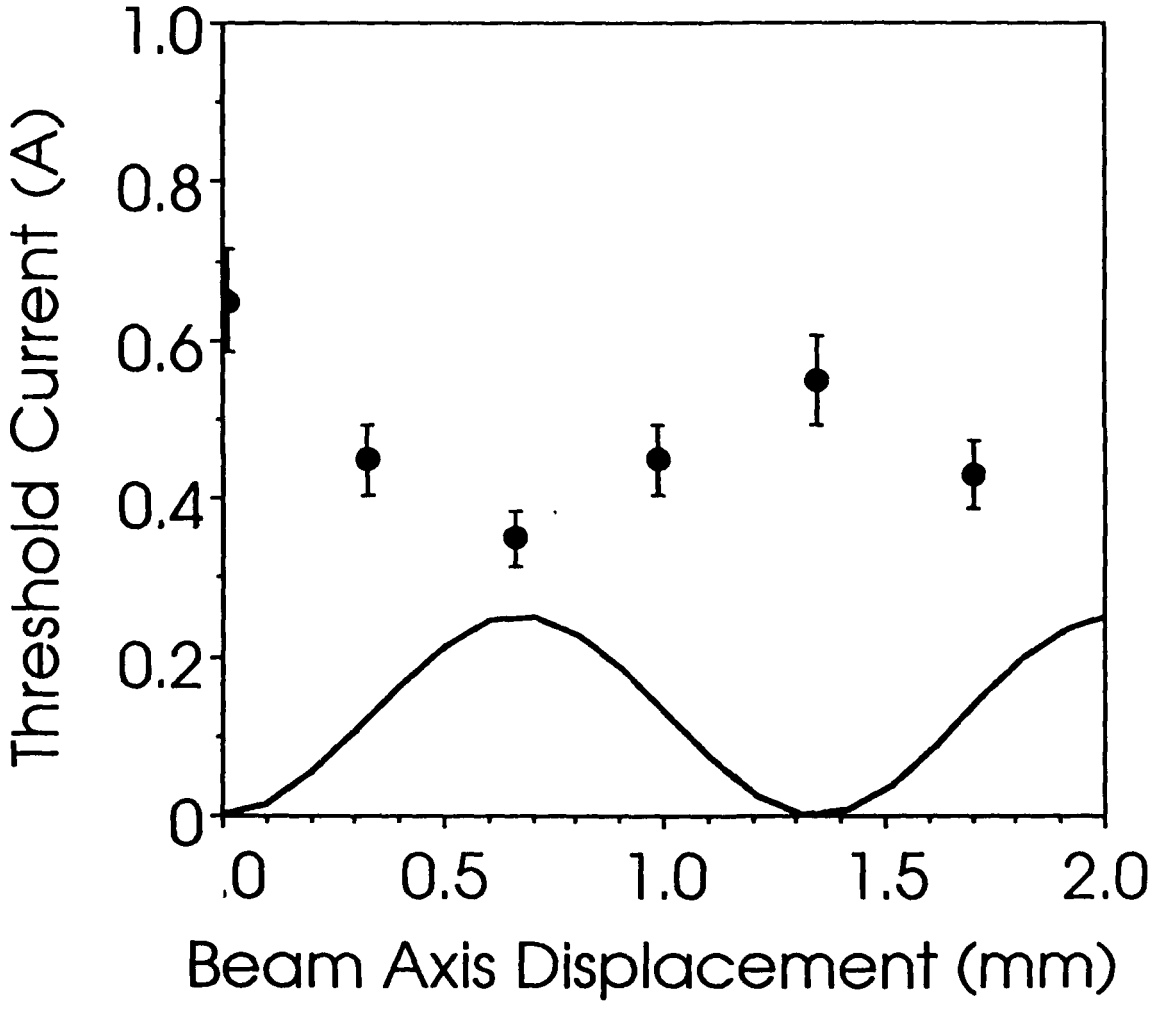

1.0
0.8
0.6
0.4
0.2
0
Threshold Current (A)
.0
0.5
1.0
1.5
2.0
Beam Axis Displacement (mm)

Figure 27

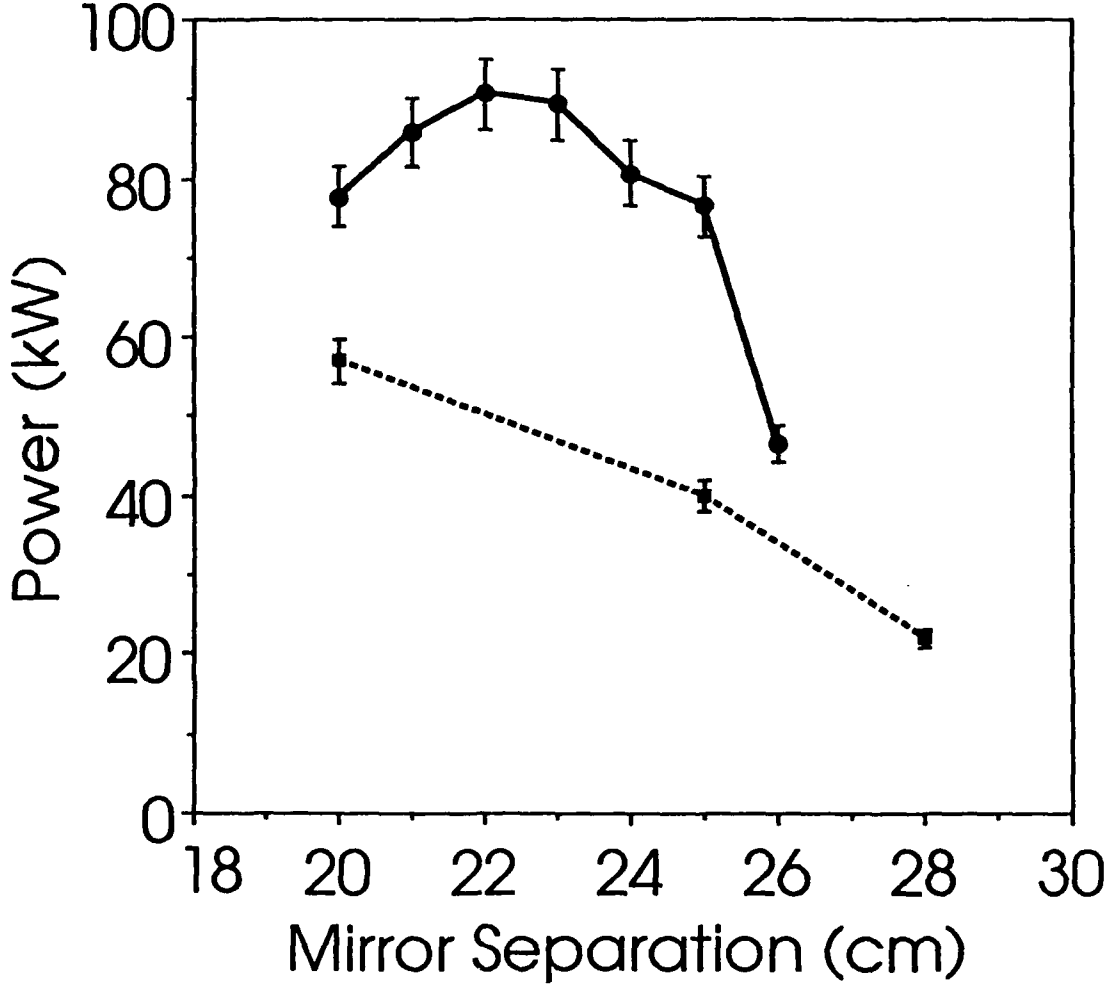

100
80
60
40
20
0
Power (kW)
18
20
22
24
26
28
30
Mirror Separation (cm)

Figure 28

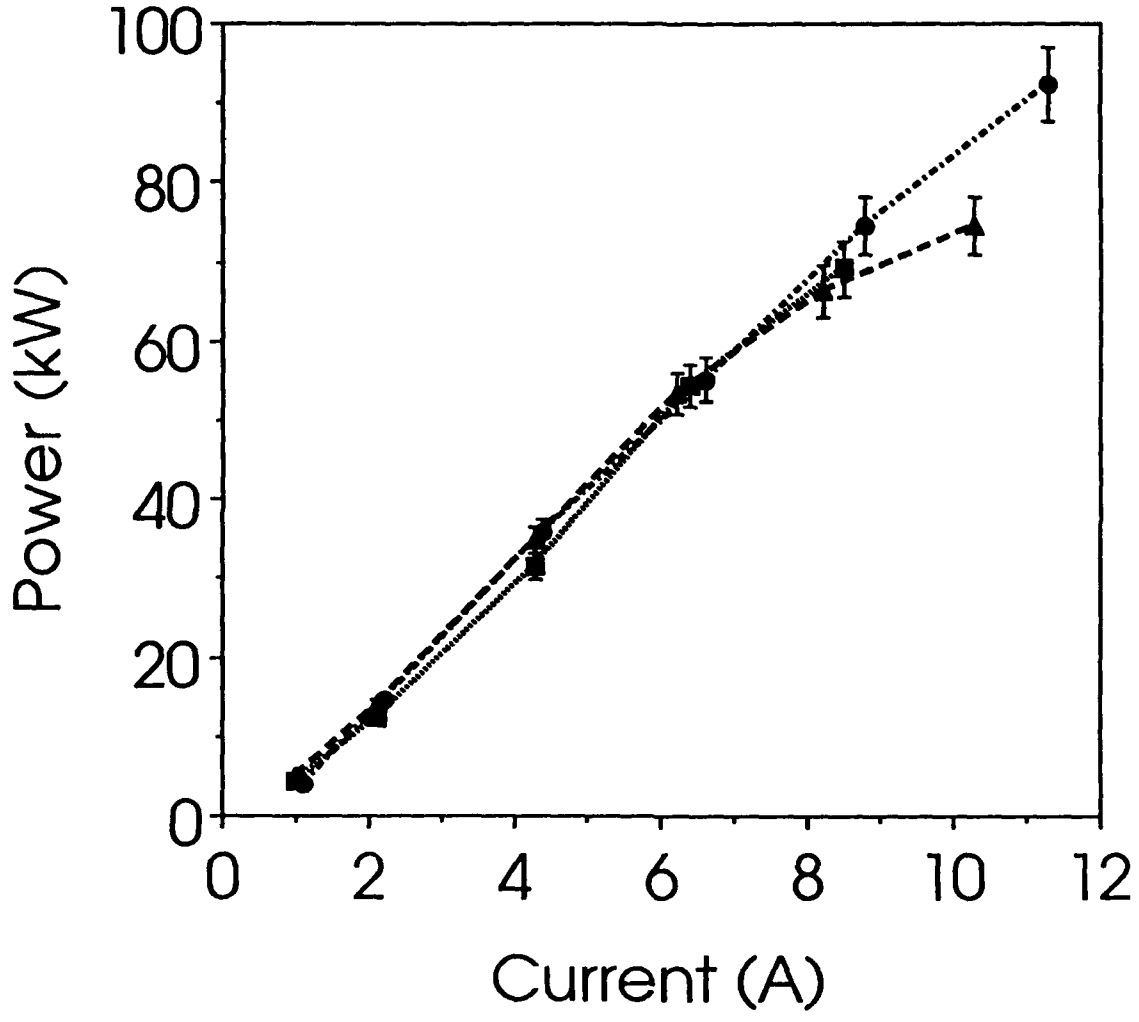



Figure 29

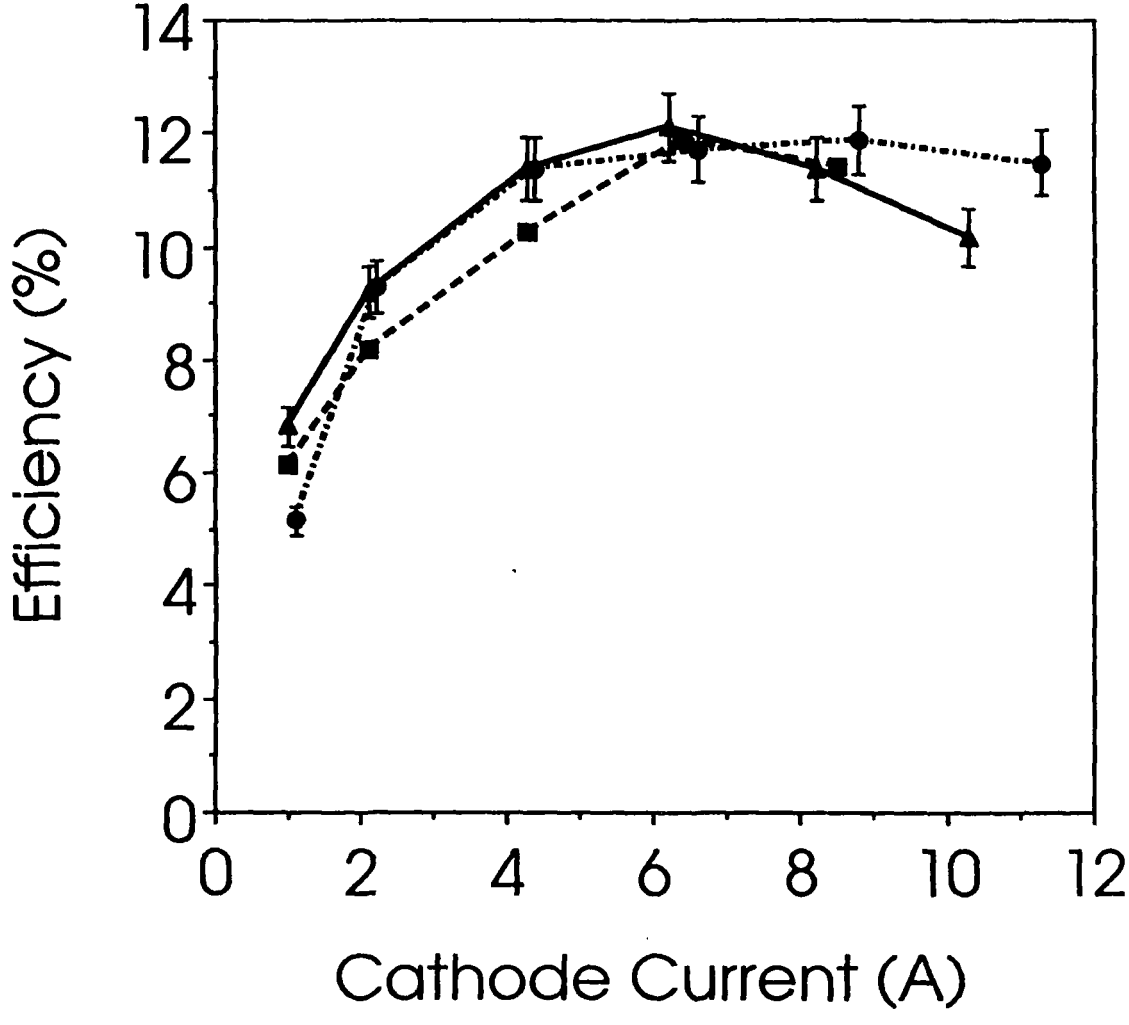



Figure 30

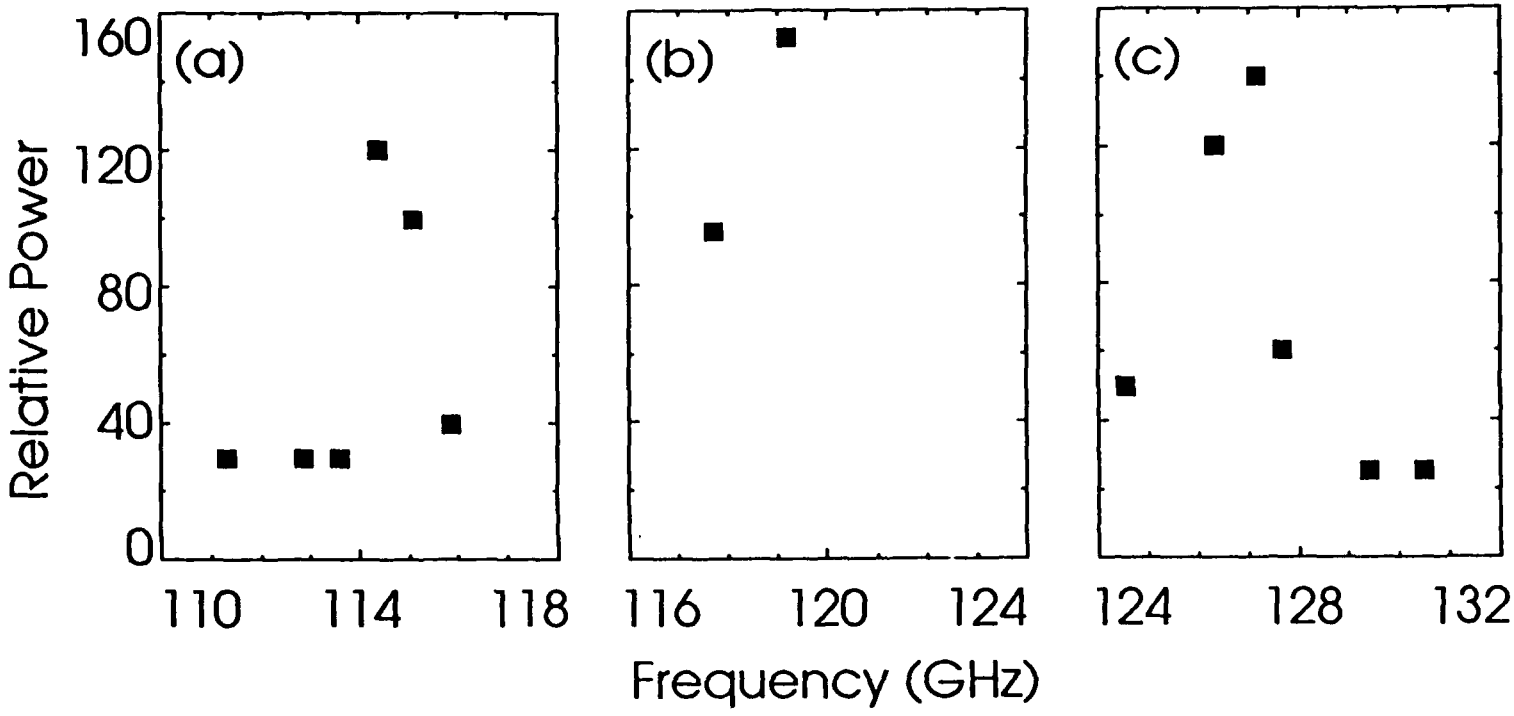

(a)
(b)
(c)
160
120
80
40
0
Relative Power
110
114
118
116
120
124
124
128
132
Frequency (GHz)

Figure 31

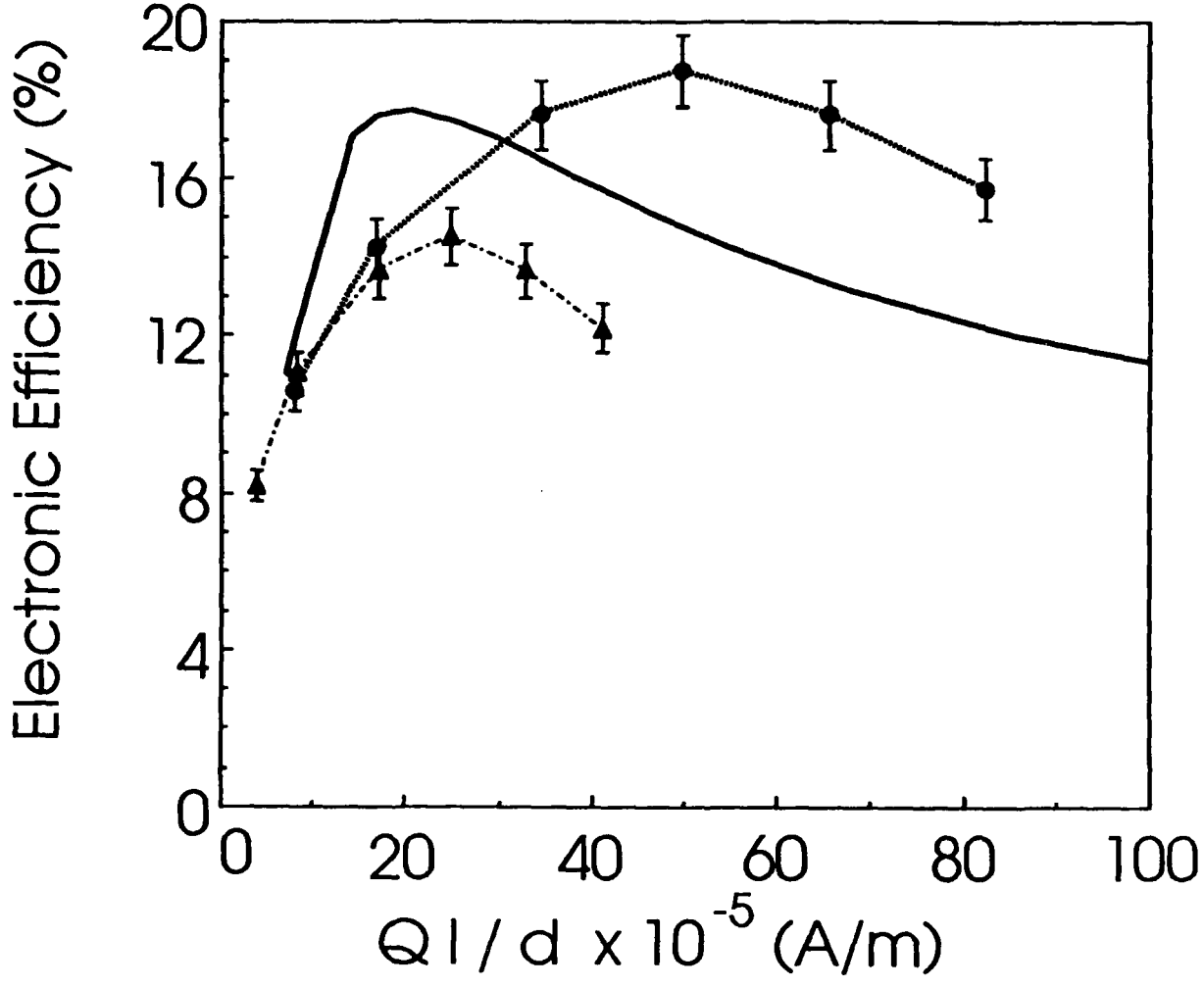

Electronic Efficiency (%)
20
16
12
8
4
0
0
20
40
60
80
100
Q I / d x 10^-5 (A/m)

Figure 32

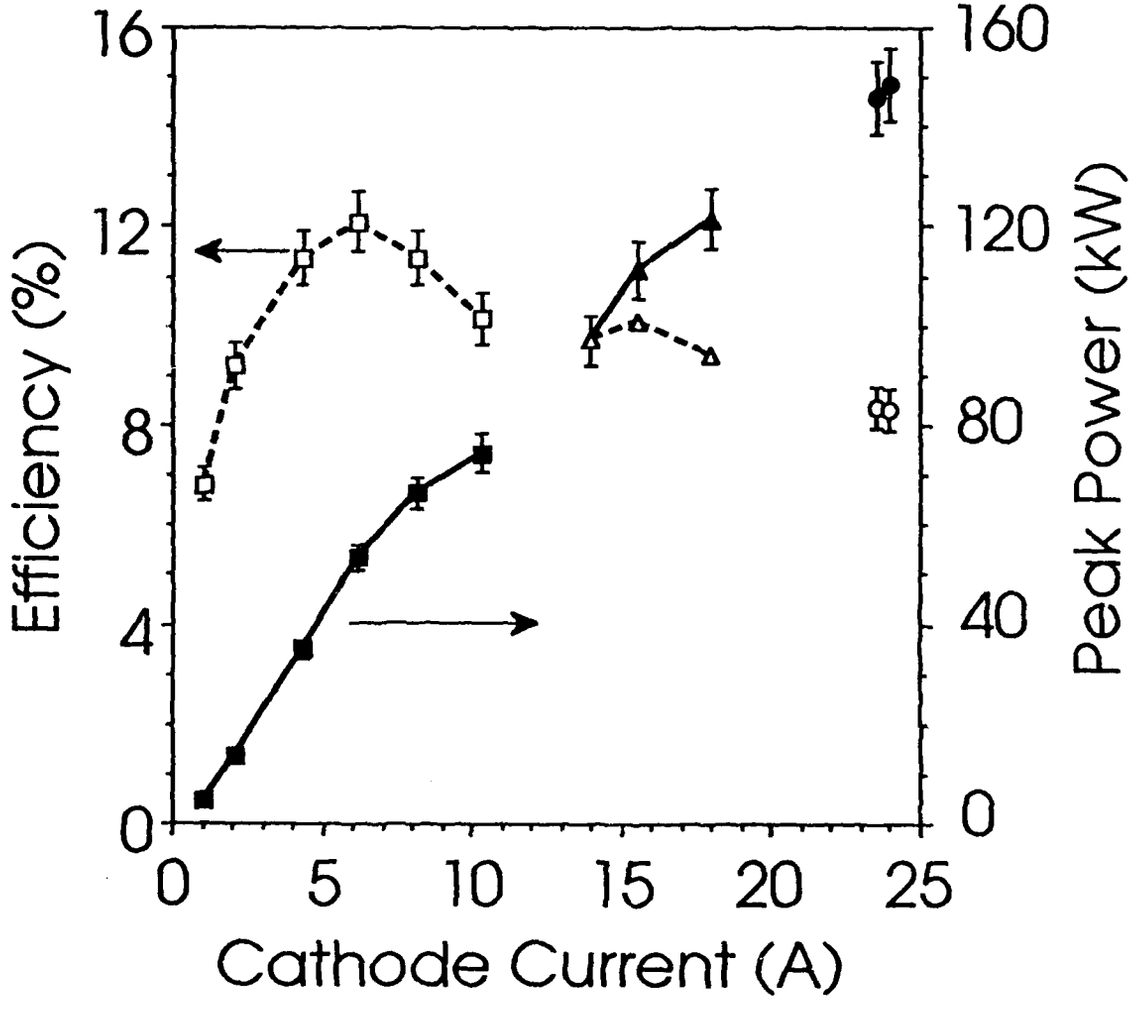

16
12
8
4
0
Efficiency (%)
160
120
80
40
0
Peak Power (kW)
0
5
10
15
20
25
Cathode Current (A)

Figure 33

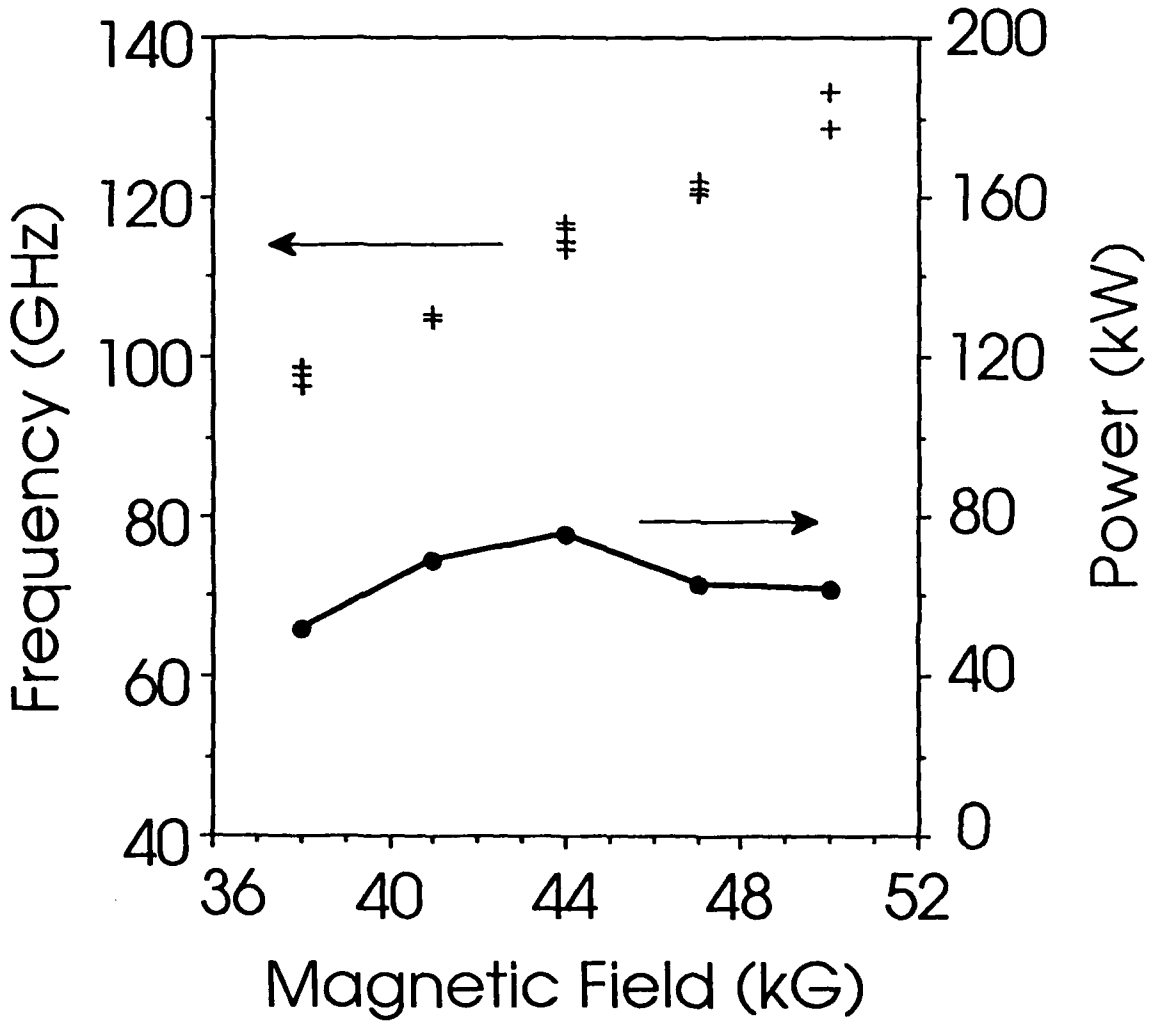

140
120
100
80
60
40
Frequency (GHz)
200
160
120
80
40
0
Power (kW)
36
40
44
48
52
Magnetic Field (kG)

Figure 34

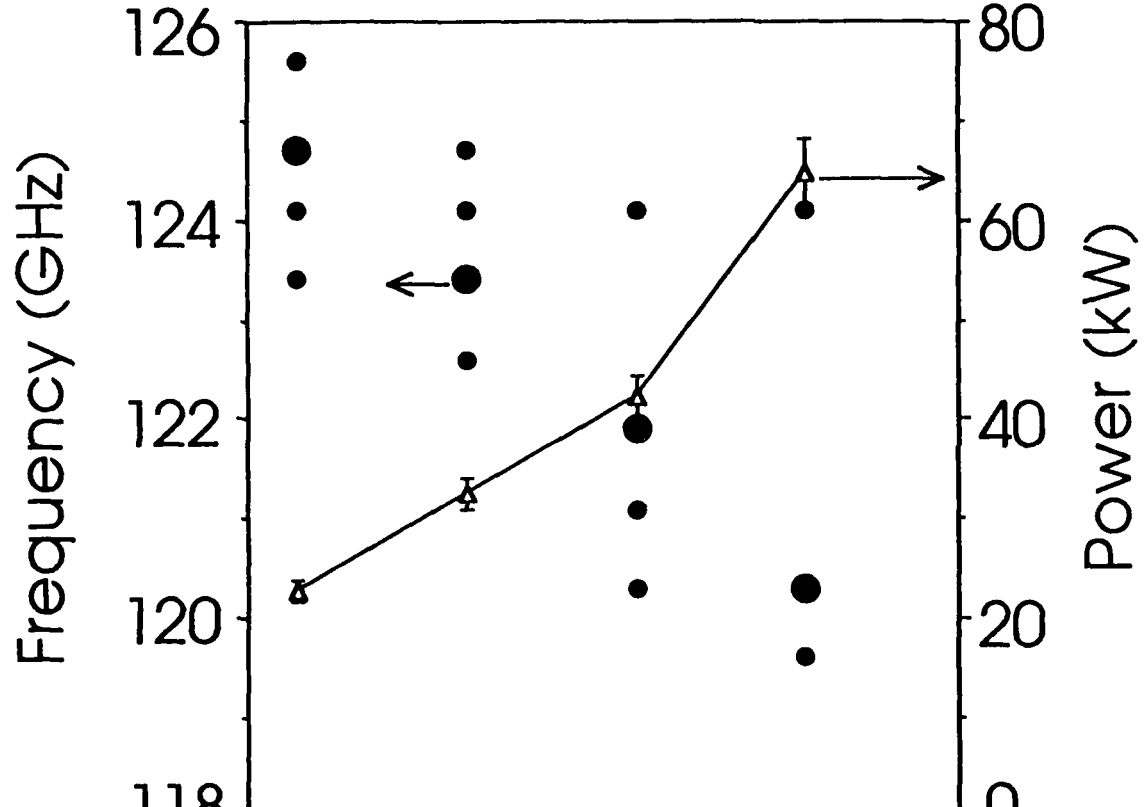

126
124
122
120
118
Frequency (GHz)
80
60
40
20
0
Power (kW)
40
50
60
70
80
Gun Voltage (kV)

Figure 35

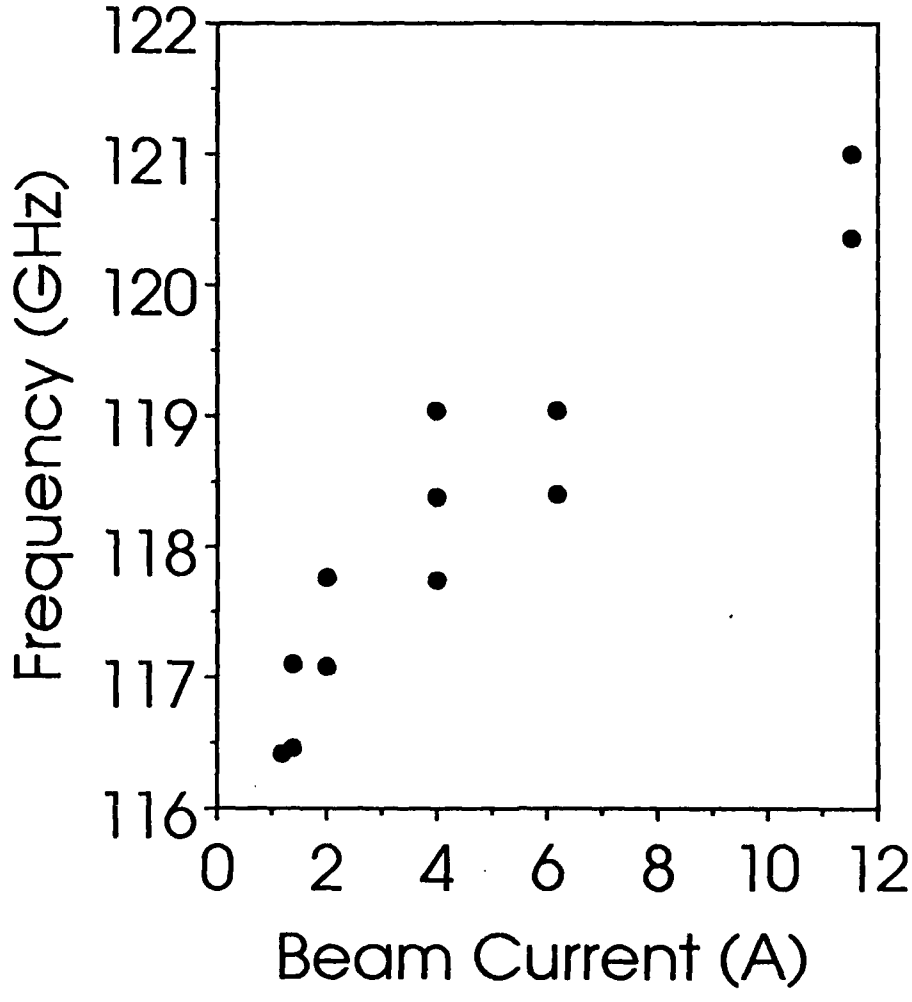

122
121
120
119
118
117
116
Frequency (GHz)
0
2
4
6
8
10
12
Beam Current (A)

Figure 36

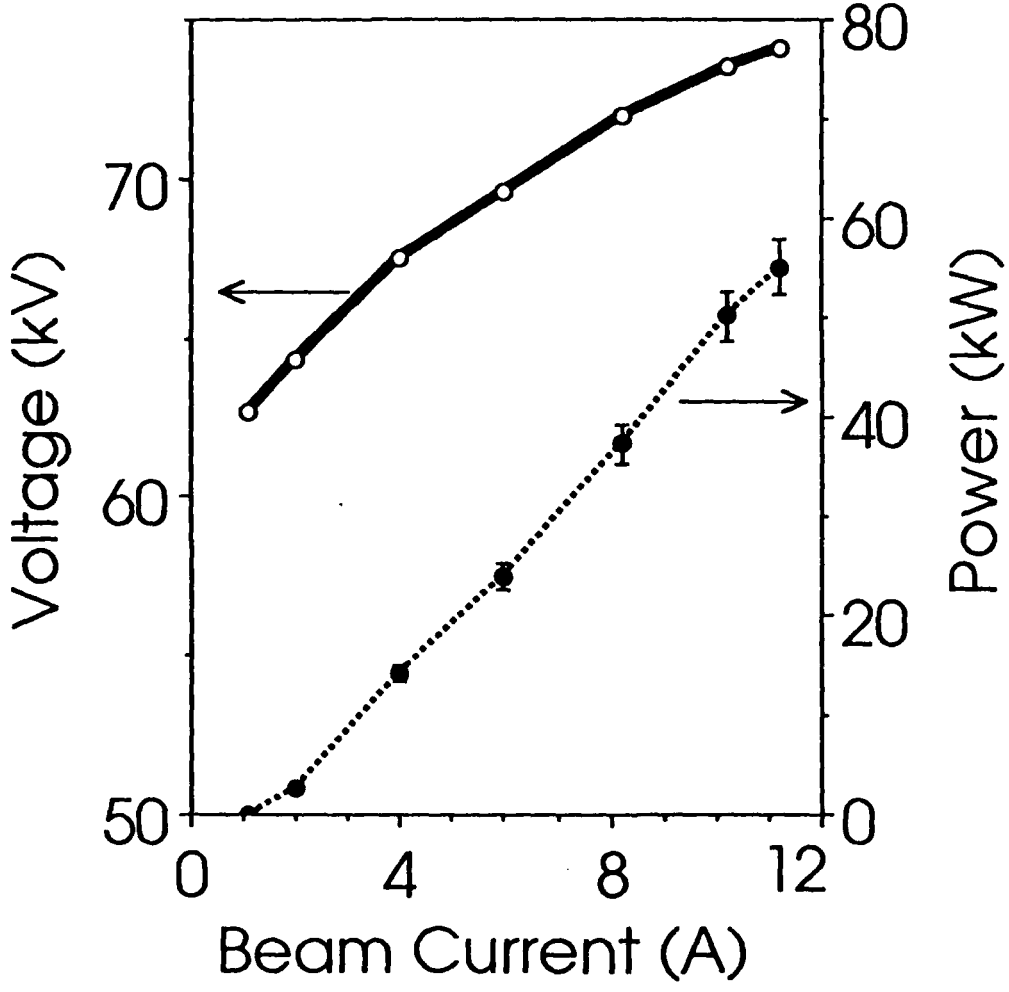



Figure 37

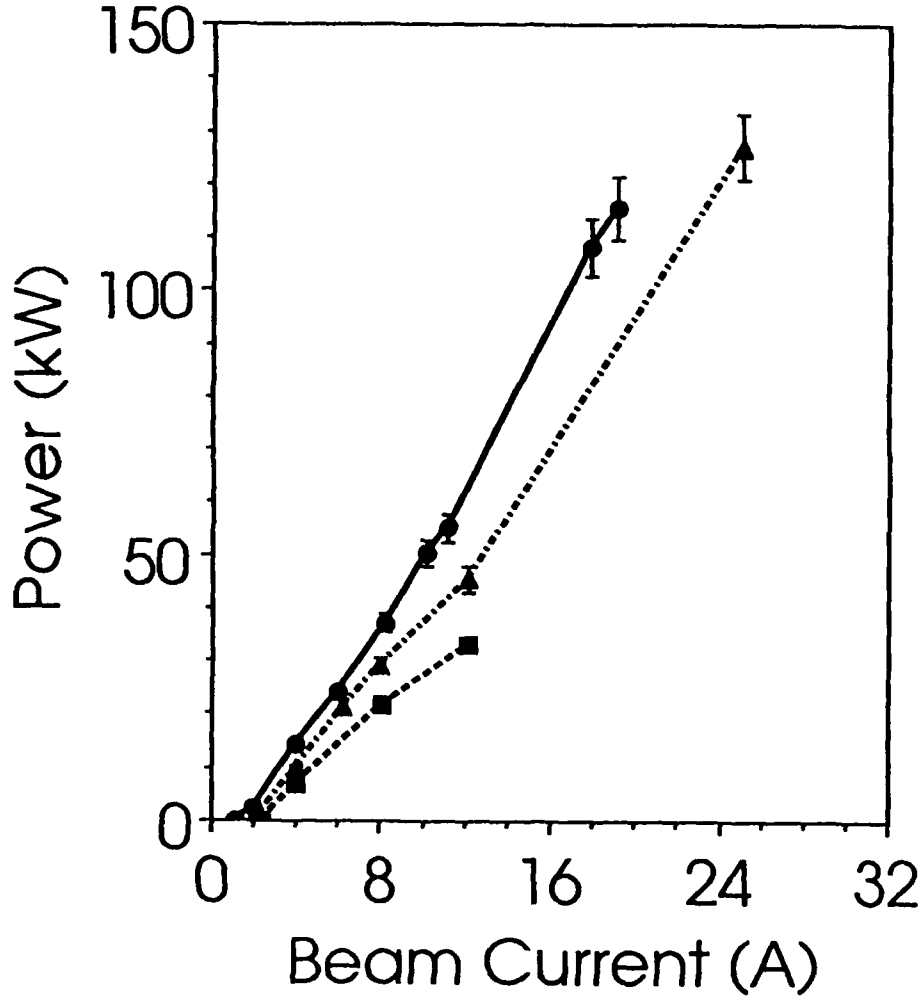



Figure 38

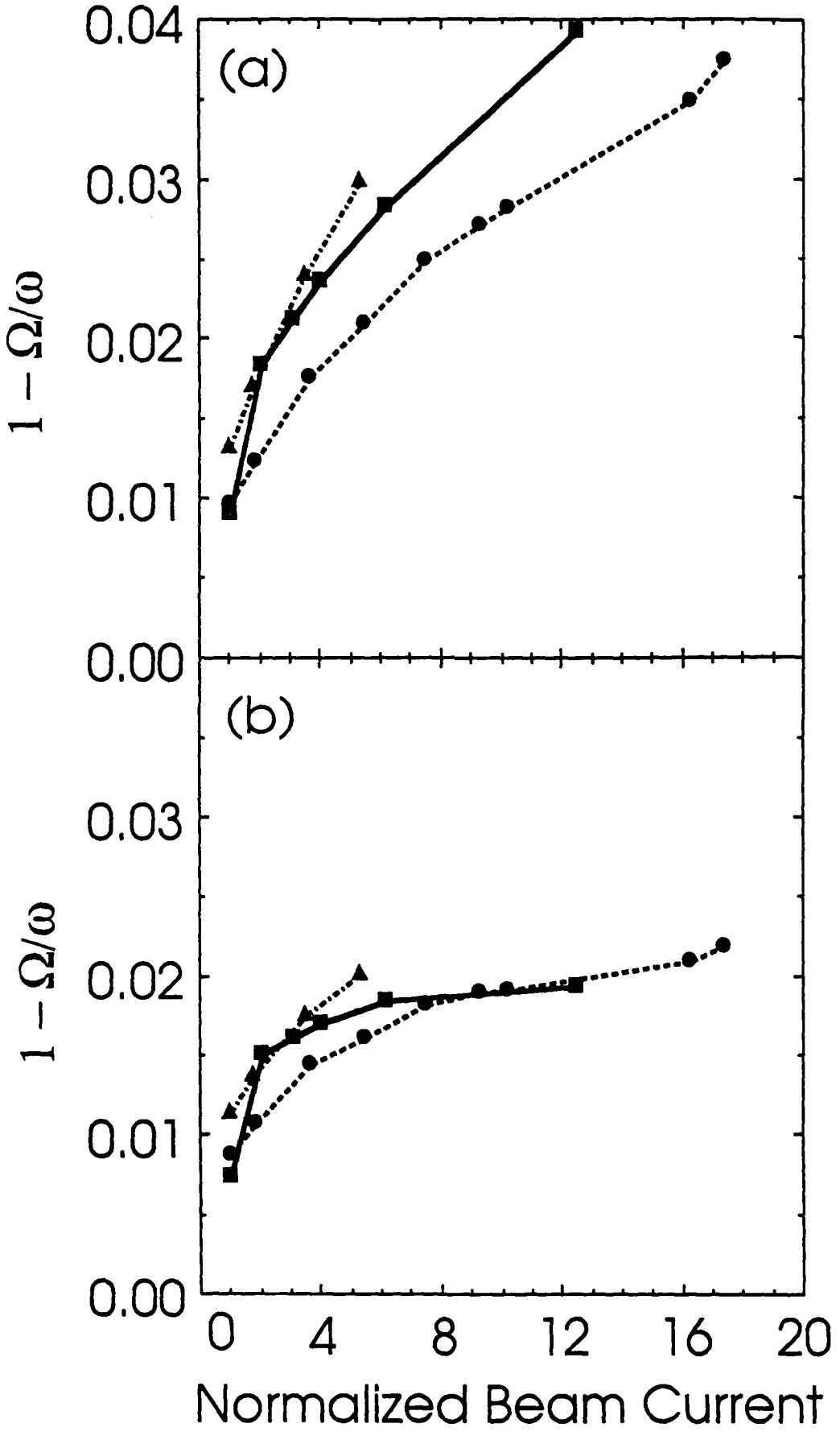

(a)
(b)
0.04
0.03
0.02
0.01
0.00
1 − Ω/ω
0
4
8
12
16
20
Normalized Beam Current

Figure 39

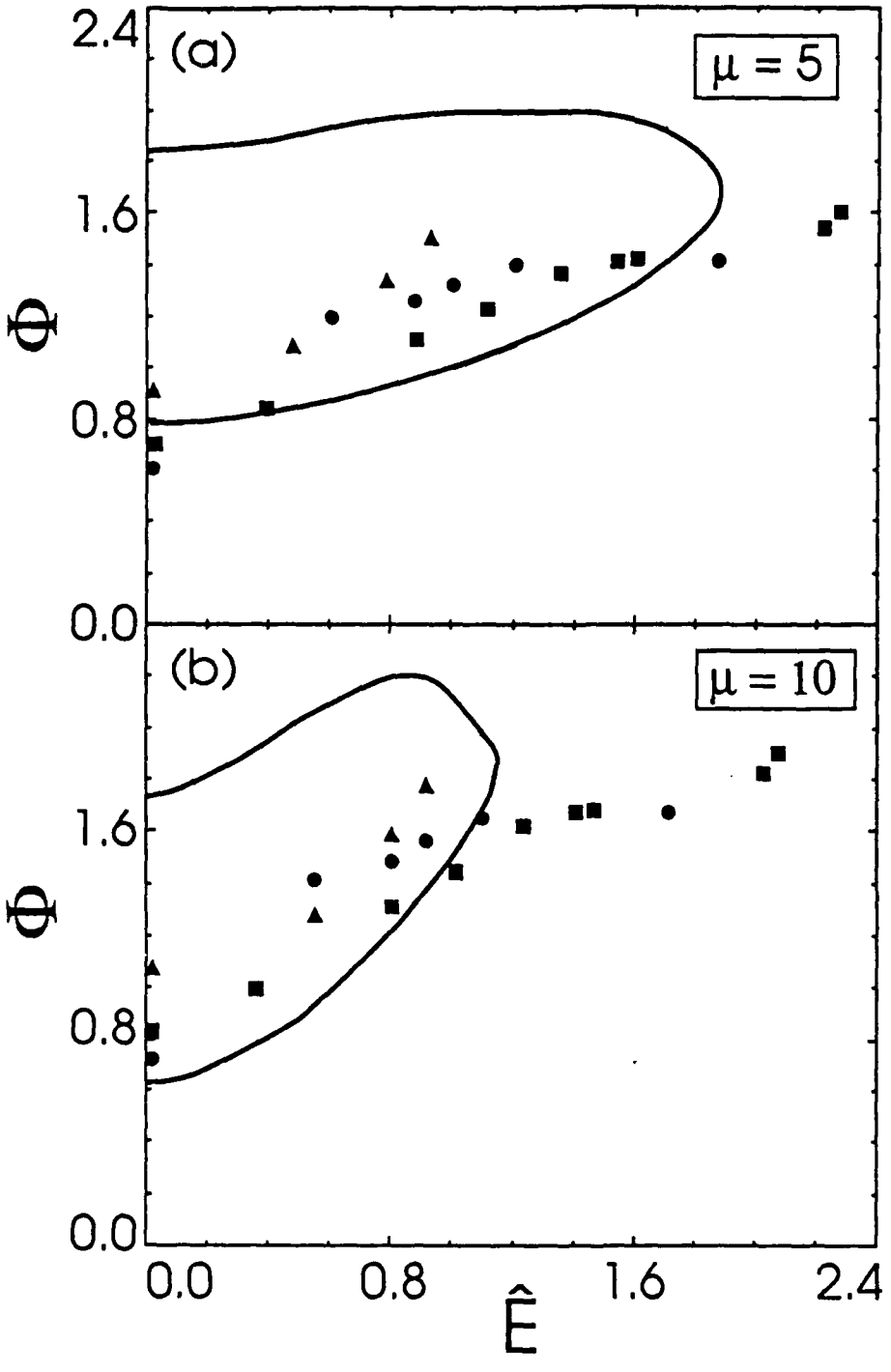



Figure 40

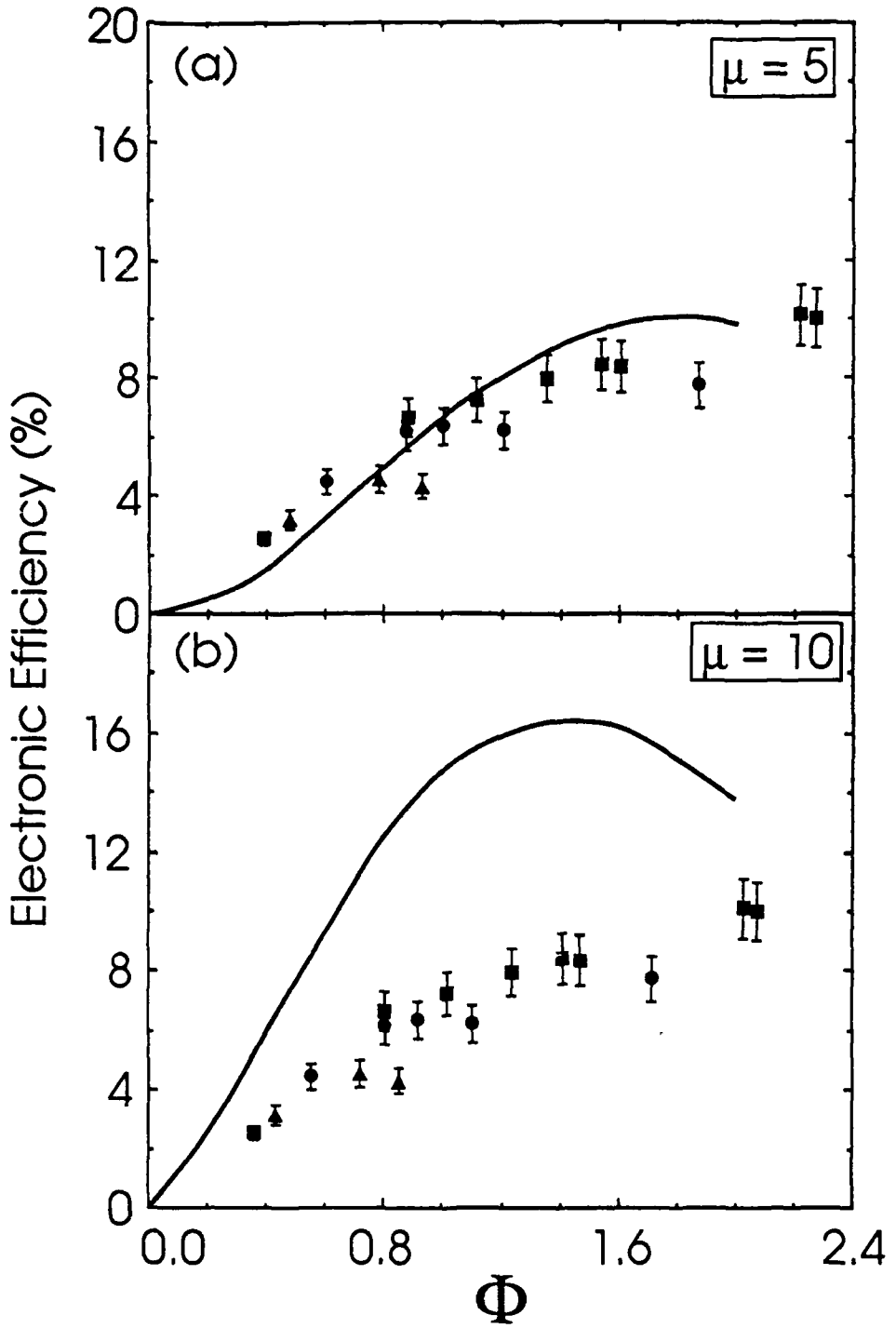



Figure 41

# APPENDIX G

## Experimental Study of a 115 GHz Quasi-Optical Gyrotron with a Large Cavity

# Experimental Study of a 115 GHz Quasi-Optical Gyrotron with a Large Cavity

M.E. Read*, M.Q. Tran**, J. McAdoo+, and M.Barsanti++

Naval Research Laboratory, Washington DC 20375

## Abstract

The operation of a gyrotron based upon a quasi-optical cavity is reported. The cavity mirrors were separated by 81 cm, allowing the use of mirrors large enough in diameter to be in principle compatible with cw operation. The pulse length in this experiment was 12 microseconds. The gyrotron operated between 113 GHz and 122 GHz, with a maximum output power of 50 kW. The highest efficiency observed was 7.3%. The observed powers and efficiencies were lower than originally anticipated, but when cavity losses and the actual performance of the electron gun was included, agreed well with theoretical predictions based on multimode simulations. The output spectra were measured, and again were in good agreement with theory.

* Currently at Physical Sciences Inc., 603 King Street, Alexandria, Va. 22314
** Centre de Recherche en Physiques des Plasma, Association Suisse-Euratom, Confederation Suisse, Ecole Polytechnique Federale de Lausanne, 21 Ave. des Bains, CH 1007, Lausanne, Switzerland
+ Currently at Mission Research Co., Alexandria, Va.
++ Jaycor, Inc., McLean, Va.

## I. Introduction

High power ($P \geq 1$ MW), continuous wave sources operating at frequencies in excess of 100 GHz are expected to be required for heating of thermonuclear fusion plasmas. The gyrotron has been shown to be a good candidate for such a source. This is due to the fact that highly overmoded cavities can be used, greatly extending the limits on power that are imposed by the ohmic heating in devices based on fundamental mode cavities. Gyrotrons based on axisymmetric cavities supporting TE modes have produced powers as high as 75 kW cw [1] and 650 kW pulse [2] at 140 GHz. As a method of going to even higher cavity volumes, it has been proposed to use a quasi-optical Fabry-Perot resonator.[3] This concept combines both the high intrinsic efficiency of the gyrotron mechanism and the potential capability of handling multimegawatt powers at high frequency. Numerical, multimode, simulations [4] of the time evolution of the wave spectrum have predicted that efficiencies up to 28% could be reached using presently available electron guns and a single quasi-optical cavity. Implementation of a buncher cavity and the use of an electron gun specifically tailored should result in efficiencies exceeding 40%.

In previous experiments, quasi-optical gyrotrons with a cavity small enough to confine operation to a single mode were tested.[5,6] The length of the cavity in the experiment of reference [5] was 4 cm. In this paper we report on the results of experimentation with a gyrotron based on a quasi-optical cavity for which simultaneous oscillation in several modes was expected. This cavity was 81 cm in length, and, in contrast to the previous cavity, could be cooled using conventional methods to allow cw operation.

The original design of the experiment called for an output power of 100 kW and an efficiency of approximately 25%. Due to the failure of the originally intended electron gun, and the substitution of one less suited to the experiment, the estimates for the power and efficiency were more than halved. However, as is shown below, the results of the experiment were in good agreement with theoretical predictions for the configuration actually realized. This agreement gives substantial credence to the simulation, and the substantially higher efficiencies and powers predicted for optimized configurations.

## II. The Experimental Apparatus

A schematic of the quasi-optical gyrotron is shown in Figure 1. The geometry is largely that of a previous experiment,[5] with the small cavity being replaced by one with a mirror separation of approximately 81 cm. As before, the magnetic field is provided by a pair of superconducting coils. One of the constraints in the design of the magnet was the incorporation of a cross bore large enough in diameter (10 cm) to avoid interference with the cavity mode. This resulted in the magnet coils being placed farther apart than required for optimum uniformity of magnetic field. The field profile is shown in Figure 2. The coils could be independently driven, allowing the field to be tapered.

The electron beam was produced by an electron gun originally designed for use in a 35 GHz gyrotron. [7] For use at the higher magnetic field of this experiment (4.5 Tesla), both the magnetic field at the cathode and the magnetic compression were increased. Operation under these conditions produced very non-laminar flow, as is shown in Figure 3. This produced high spreads in velocities, with $\Delta v_{perp} / v_{perp}$ of approximately 10 %. ($V_{perp}$ is the component of the velocity normal to the magnetic field vector. $\Delta V_{perp}$ is the standard

deviation for the distribution of perpendicular electron velocities.) In conjunction with the magnetic field profile, this velocity spread gave an upper limit to the ratio of the perpendicular to parallel electron velocities. Higher values in the ratio would result in too large a fraction of the beam being magnetically mirrored, as shown in Figure 4. As discussed below, this limited the efficiency of the gyrotron, since the only accessible electron energy in the gyrotron is that associated with motion perpendicular to the magnetic field.

An approximate value for the upper limit to the velocity ratio can be found by assuming a limit to the space charge caused by the reflection, and calculating the reflection that would create that space charge density. A 100% increase in the space charge density is equivalent to a doubling of the current. This has been shown by simulation to cause a significant increase in the velocity spread, and is a reasonable upper limit. The distance between the gun and the first maximum in the magnetic field is approximately 30 cm, and, for an average alpha of 1, the electron transit time is approximately 3.3 ns. For a mirrored electron, the round-trip time is 6.6 ns. Thus, for a pulse length of 12 microseconds, there are approximately 1800 transit times. To limit the build up of space charge to 100%, a reflection of less than 0.04% per transit is required. We assume a Maxwellian distribution in the perpendicular velocities, and use the adiabatic invariant $v_{perp}^2/B$ to calculate the conditions for mirroring. It is then found that in order to limit the reflection to less than 0.04% per pass, the maximum velocity ratio, $\alpha$ ($= v_{perp} / v_{par}$), in the cavity must be $\leq 0.95$. The calculation is not particularly sensitive to the allowed degree of build-up in the space charge. If only a 20% increase in the charge density is allowed, the maximum velocity ratio is 0.9. Since this is clearly an approximate calculation, with loss of charge by scattering, etc. not included, a value of $\alpha = 1$ has been taken for the calculation discussed below.

The other beam parameters are summarized in Table I.

The resonator consisted of two mirrors of different diameters, to allow for a single output by diffraction around the smaller mirror. This form of diffractive output was chosen over center hole coupling because the latter has been found to preferentially load the desired mode, while poorly coupling to higher modes. This results in oscillation in the higher order mode, but with little output. A partially transmissive mirror, such as a dielectric with a thin coating or a mesh, was rejected because it could not be cooled in a CW system.

The output mirror radius was determined by use of a code by K. Yoshioka,[8] in which the diffractive losses are found by use of a scalar Huygen's method. From results of multimode simulations of the gyrotron, the optimum loss per pass for the available beam current was approximately 1.5% - 2.0%. The chosen output mirror radius was 4.15 cm, yielding a total diffractive loss from the resonator of 2%. Unfortunately, not all of the power diffractively lost from the cavity is via the output coupling. Due to the finite extent of the mirrors, a significant amount of power is scattered into the dewar. For the present resonator, only 60% of the radiation is coupled out. This "efficiency" could be increased to approximately 80% by shortening the separation between the resonator mirrors or increasing the mirror radius of curvature. Neither of these changes could be made given the constraints of the present experiment.

The quality factor Q resulting from ohmic losses was calculated from the expression

$$Q_{ohmic} = (L/4)(f \pi \sigma \mu)^{1/2}$$

where L is the separation between mirrors, f is the frequency, $\sigma$ the conductivity of the mirror material (copper) and $\mu$ the permeability of free space. Taking $\sigma$ equal to $3.5 \times 10^7$ mhos/meter (60% of the dc value for copper),[9] an ohmic Q of 757,000 was calculated. This is 15% of the diffractive Q. The total calculated Q (including all diffractive and ohmic losses) was 86,000, and the total "efficiency" of the resonator was calculated to be 53%.

Actual measurements of the cavity, performed while in place on the magnet and with the magnet at operating temperature and under vacuum, indicated a total Q of 90,000 +/-10,000. This is in good agreement with the calculations.

Such a good agreement between the experiment and the calculations indicates tha the magnet cross bore diameter was large enough not to significantly interfere with the resonator mode. This conculsion is also supported by the observation that in both cold and hot tests the frequency separation between two consecutive modes is exactly c/2L. c is the velocity of light in vacuum.

A summary of the resonator parameters is given in Table II.

In order to focus the output radiation into a nearly Gaussian beam, a modified Cassegrain antenna was used. The system is shown in Figure 5. The mirror system imaged the center of the resonator, and focussed the output radiation to a 1.5 cm diameter spot. The 6 cm diameter output waveguide began at this focal point, as shown in Figure 6.

The output power was monitored by a laser calorimeter which had been modified for mm-wave operation by the application of additional layers of absorbing paint. The measured absorption coefficient was a function of frequency, but for the frequency range of interest was approximately 90%. The actual measured reflectance was incorporated in the calibration of the instrument.

The frequency spectrum was measured via a heterodyne receiver using a harmonic mixer. The harmonic number used was 8, with an intermediate frequency (IF) of 160 MHz and a IF filter bandwidth of 30 MHz. The pulse shape was monitored using a standard microwave diode. The signal for the measurements of the spectrum and pulse shape was obtained via a beam splitter consisting of a thin polyethylene film mounted at 45 degrees to the axis of the waveguide.

The pattern of the output radiation was observed using liquid crystal paper with a resistive backing.[10]

## III. Results

The gyrotron was operated with currents from 0 A to 16 A, and the magnetic field varied from 43.9 Tesla to 47.4 Tesla. At a field of 44.7 Tesla, corresponding to a radiation frequency of 115 GHz, a magnetic taper of + 5% or - 5% (over a distance of 4 times the radiation waist) could be produced without exceeding the limits of the magnet.

The results of the experimentation are summarized in Figures 7 - 13. In Figures 7 - 10, the output power and efficiency are given as a function of beam current. A maximum power of 50 kW was observed. As can be seen in the figures, the power and efficiency were improved with a negative taper (one in which the magnetic field decreased as the distance from the gun became greater). A positive taper (results not shown) tended to decrease the efficiency.

In addition to the experimental results, several points resulting from multimode simulations are given. A velocity ratio, $\alpha$, of 1.0 was used for the calculations, and a velocity spread of 0 was assumed. (Even without a spread in velocity, the run times for the simulations took between 1 and 3 hours on a CRAY I.) For the points given, the results from the code have been multiplied by the resonator output coupling efficiency 0.53 to account for calculated non-output diffractive and ohmic losses.

Frequency data, as measured with the heterodyne receiver, are shown in Figures 11-13. Oscillographs showing the actual receiver output for a beam current of 6 Amperes and an untapered magnetic field are shown in Figure 11. The oscillographs include the filtered IF signal as well as the beam voltage. The beam voltage is flat to within +/- 0.9% over 12 microseconds. The ripple appears to have little effect on the microwave signal. Traces are given for the four frequencies at which there was observable power. The modes with observable power are separated by 184 MHz, 368 MHz, and 184 MHz. 184 MHz corresponds approximately to the value of 185 MHz predicted by c/2L, where L is the cavity length (=81 cm). As predicted by theory (and is illustrated in Figures 11 - 13), the lower frequency modes grow most quickly, but are replaced by higher frequency modes at later time. For the example given, it appears that a steady state has been reached by the end of the 12 microsecond pulse. This was the case for most, but not all conditions.

The spectra for the data of Figure 11, along with those produced by the multimode simulation, are given in Figure 12. Spectra for points 3.5 microsec, 7 microsec, and 11 microsec after the beam voltage had reached 99% of the average maximum value. Spectra with a 5% negative taper with a beam of 6 Amperes are given in Figure 13. An exact agreement between theory and experiment is not seen, but the number of modes (2 - 3) is approximately the same. In addition, the prediction of average frequency as a function of time is quite good. As predicted by theory, there is no substantial difference between the spectra for the different operating conditions.

Under certain conditions single mode operation could be obtained. The factor that most effected the ability to obtain a single mode was the relative position of the beam along the cavity axis. This was expected, since movement of the cavity mode pattern relative to the beam would change the degree to which the annular beam intersected the maxima in the cavity standing wave. Indeed, the changes in the operation appeared to occur periodically with 1/2 wavelength changes in the relative positions. The output from the heterodyne receiver for a case where only a single mode was observed is given in Figure 14.

Using liquid crystal paper, measurements were made of the radiation pattern at the output window and the focal point of the Cassegrain antenna. The results are shown in Figures 15a and 15b. In 16a, the pattern at the output window is shown. As can be seen, the pattern is not uniform. Adjustment of the mirror positions and tilts could alter the pattern, but not improve it. The power does

appear localized near the edge of the output mirror, as expected. The pattern of the beam at the focal spot is shown in Figure 15b. The diameter is approximately 4 cm. This is consistent with the predicted waist of 1 cm.

## IV. Discussion

Agreement of theory and experiment is good for both the efficiency and spectra. The only major discrepancy is seen between the observed and predicted spectra near the beginning of the pulse (3.5 microseconds), which is probably due to growth during the finite rise time of the actual voltage and current. The finite rise was not modeled in these simulations. Clearly, there is need for improvement in the experiment. The non-ohmic resonator losses are large and can be somewhat reduced by better design. Without the constraints of the present experimental configuration, a resonator efficiency of 80% - 85% could be reached with an improved mirror geometry. Higher efficiencies may be obtainable with novel resonators and/or with the larger output couplings appropriate for higher output powers.

A more dramatic improvement in the efficiency is predicted for an increase in the velocity ratio of the electron beam. This can be done even with the present magnet by using an electron gun with lower velocity spread. An electron gun designed and fabricated by Hughes Aircraft Corporation has a theoretically predicted spread in the perpendicular velocities of approximately 3.5%. This would allow transmission of beams with a velocity ratio of over 1.5, as shown in Figure 4. Results of the multimode simulation code indicate that efficiencies as high as 28 % (neglecting losses) can be achieved with a single cavity similar to the one used in the present experiment. The result of a simulation with a 10 Ampere beam and a magnetic taper of - 5% is shown in Figure 16.

Of note in Figure 16 is the great increase in the number of modes, over that observed with $\alpha$=1. Thus the results of the present experiment should not be cause for concluding that the quasi-optical gyrotron will operate efficiently with the 1 - 3 modes observed in this experiment. From Figure 16 it is clear that mode selective methods such as the use of a pre-bunching cavity [4] will be required to achieve near single mode operation.

In the experiment, tuning of the output frequency was achieved over a range of 113 GHz to 122 GHz. The range was limited by interception of the beam in the drift region, which could be easily modified to allow use of a much wider range of magnetic fields, and, hence, output frequencies. Operation of a high power gun over a range of 4.5 to 9 Tesla has been reported in experiments with a microwave cavity based gyrotron.[2] A similar range could be expected with a quasi-optical gyrotron, with this device having the advantage that the transverse (i.e., output) mode would remain constant during a sweep of frequencies. In addition, by simultaneous adjustment of the cavity length and the magnetic field, a continuous sweep in the frequency should be possible.

## Conclusion

Data have been presented showing the first operation of a quasi-optical gyrotron with a resonator large enough to be relevant to megawatt cw operation. Agreement of the results with those of a multimode simulation good giving confidence in the code, which is the only method presently available for predicting the performance of a quasi-optical gyrotron with a large cavity. The

efficiencies and output powers were clearly lower than is required for applications where high average power is required, but improvements discussed above should allow a several-fold increase in these parameters.

## Acknowledgements

The authors are indebted to many people who contributed to this experiment. In particular, we would like to thank Dr. T. Hargreaves, for initial experimental designs, and Drs. A. Bondeson and B. Levush and R. Lee for assistance with the multimode code. R. Seeley helped fabricate the original apparatus, and G. Bergeron and M. Rhinewine assisted in solving the many technical problems. Many useful discussions were had with A. Fliflet, W. Manheimer, T. Antonsen and R. Temkin. P. Sprangle and J. Vomvoridis proposed the basic configuration and performed the initial (single mode) calculations which motivated the work. Dr. T.V. George of the Department of Energy supplied much encouragement and patience.

The work was supported by the Department of Energy and the Office of Naval Research. One of us (MQT) was partially supported by the Swiss Commission pour l'Encouragement de la Recherche Scientifique.

## References


1. K. Felch, et al., Proc. 11th Int. Conf. on IR and mm Waves, Piza, Italy, 43 (1986).

2. K.E. Kreischer, et al., Proc. 11th Int. Conf. on IR and mm Waves, Piza, Italy, 43 (1986).

3. P. Sprangle, et al., "Theory of Quasi-Optical Electron Cyclotron Maser," Phys. Rev A, 23, 3127 (1981).

4. A. Bondeson, et al., "Multimode Analysis of Quasi-Optical Gyrotrons and Gyroklystrons," Infrared and Millimeter Waves, 9, 309 (1983).

5. T.A. Hargreaves, K.J. Kim, J.H. McAdoo, S.Y. Park, R.D. Seeley, and M.E. Read, "Experimental Study of a Single-Mode Quasi-Optical Gyrotron", Int. J. Electronics, 57, 977 (1984).

6. E.C. Morse and R.V. Pyle, "Operation of a Quasi-Optical Electron Cyclotron Maser", J. Vacuum Science Technology A3, 1239 (1985).

7. J.L. Seftor, A.T. Drobot, and K.R. Chu, "An Invesitgation of a Magnetron Injection Gun Suitable for Use in Cyclotron Resonance Masers", IEEE Trans. on Electron Devices, ED-26, pp. 1609-1616 (1979).

8. K. Yoshioka, personal commmunication.

9. F.J. Tucher, "Experimental Attenuation of Rectangular Waveguides at Millimeter Wavelengths," IEEE Trans. Microwave Theory and Technique MTT-27, 31 (1979).

10. Y. Carmel and M.E. Read, "A Technique to Identify Modes in Oversized Waveguides", IEEE Trans on Microwave Theory and Technique, MTT (1983).

11. W.B. Herrmannsfeldt, "Electron Trajectory Program," SLAC Report 166, Stanford Linear Accelerator Center (1973).

Table I

Electron Beam Parameters

| | |
|---|---|
| Voltage | 60 kV |
| Current | 0 - 13 A |
| Radius | 0.16 cm |
| Average $\alpha$ | 1.0 |

Table II

Cavity Parameters

| | |
|---|---|
| Mirror separation | 81 cm |
| Mirror radius of curvature | 48 cm |
| Cavity material | OFHC Copper |
| Output mirror radius | 4.15 cm |
| Non-output mirror radius | 7.3 cm |
| Q factors | |
| output | 160,000 |
| non-output diffractive | 248,000 |
| ohmic | 757,000 |
| total | 86,000 |
| Total loss | 2.3% |

## Figures

Figure 1. Schematic of the quasi-optical gyrotron

Figure 2. Coil geometry and axial magnetic field profile of the superconducting magnet.

Figure 3. Geometry and plot of the electron trajectories of the electron gun. The trajectories were calculated using E-Gun [11]. One mesh unit = 0.5 mm.

Figure 4. Plot of the distribution of $v_{perp}$, assuming a gaussian distribution. Solid line is for $\Delta v_{perp} / v_{perp} = 0.1$ and $\alpha = 1.0$. The line with short dashes is for $\alpha = 1.5$. Both of these are representative of the seftor gun. The long dashed line is for $\Delta v_{prep} / v_{prep} = 0.035$ and $\alpha = 1.5$ (the Hughes Gun).

Figure 5. Schematic of the Cassegrain output system.

Figure 6. Schematic of the diagnostic system.

Figure 7. Output power as a function of beam current, with no magnetic taper.

Figure 8. Output efficiency as a function of beam current, with no magnetic taper.

Figure 9. Output power as a function of beam current, with a -5% magnetic taper. (The taper is measured over 4 optical beam waists, or approximately 5 cm. This is consistent with the definition of the taper used in the efficiency calculations.)

Figure 10. Output efficiency as a function of beam currrent, with a -5% magnetic taper.

Figure 11. Oscillographs of the output of the heterodyne receiver. The actual frequency is given by the intermediate frequency (IF) multiplied by 8, plus 160MHz.

Figure 12. Spectra of the output radiation for a beam current of 6 A and no magnetic taper. (a) T = 3.5 μs, (b) T = 7 μs, (c) T = 11 μs.

Figure 13. Spectra of the output radiation for a beam current of 6 A and -5% magnetic taper. (a) T = 3.5 μs, (b) T = 7 μs, (c) T = 11 μs.

Figure 14. Output of the heterodyne receiver with a single mode. The two lines of the spectra are the image of each other separated by twice the IF frequency (2 x 160 MHz).

Figure 15. Radiation patterns as shown by liquid crystal paper. (a) At the output mirror. The dark region in the center of (a) is actually hotter than the light regions, and therefore the beam is solid. (b) at the focal point of the Cassegrain antenna.

Figure 16. Power spectrum predicted by the simulation for $\alpha = 1.5$, a beam current of 6 A, and -5% taper.

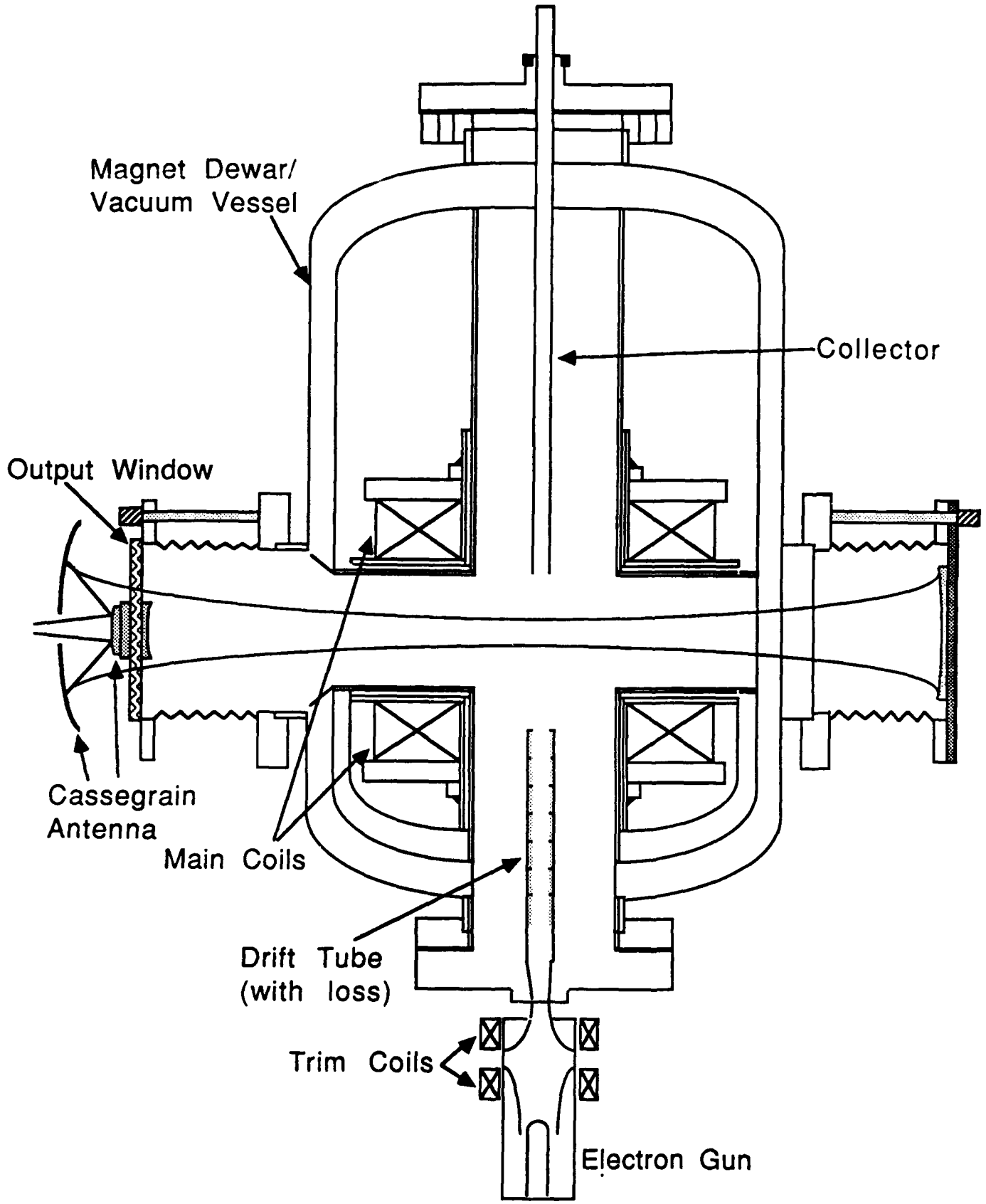

Magnet Dewar/
Vacuum Vessel
Collector
Output Window
Cassegrain
Antenna
Main Coils
Drift Tube
(with loss)
Trim Coils
Electron Gun

Figure 1

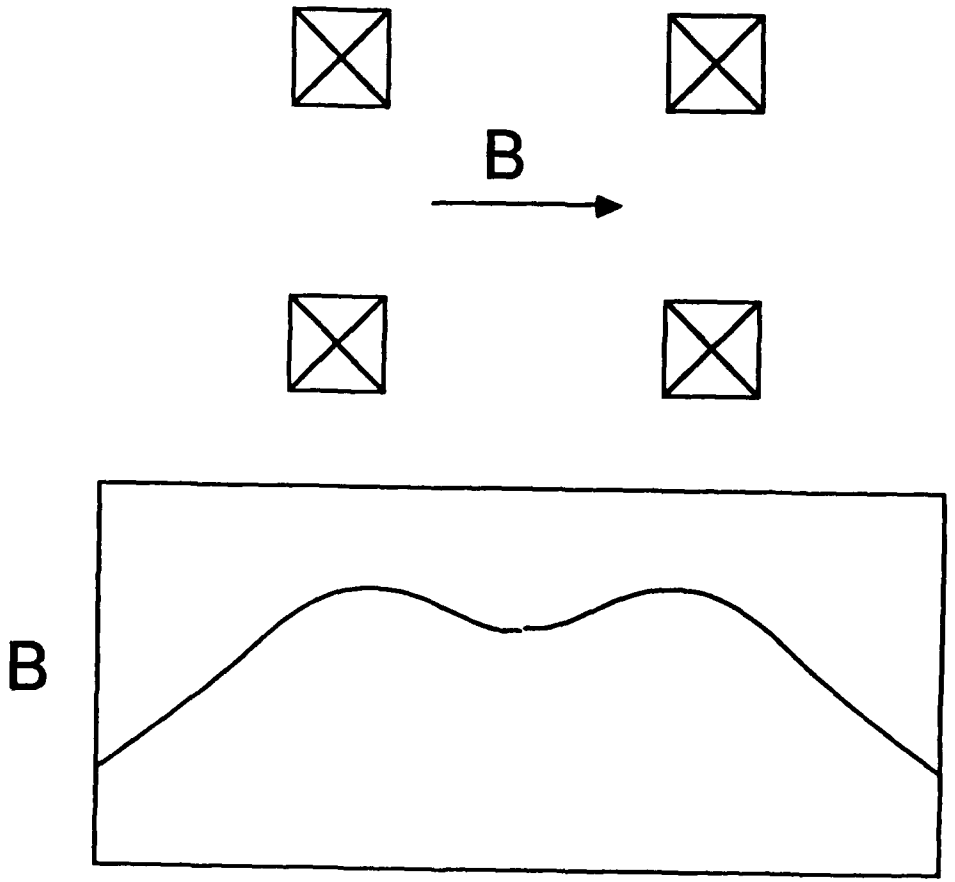



Figure 2

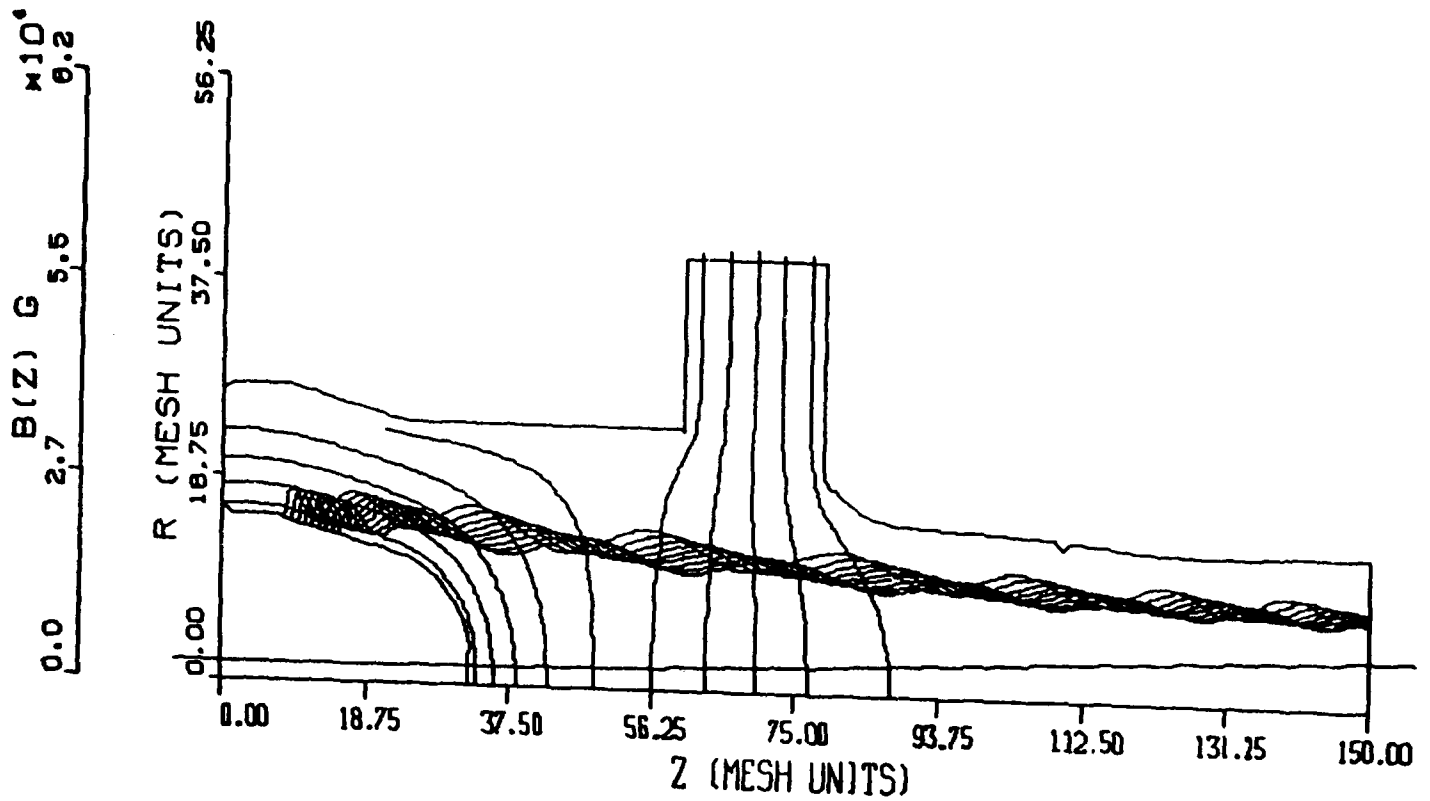
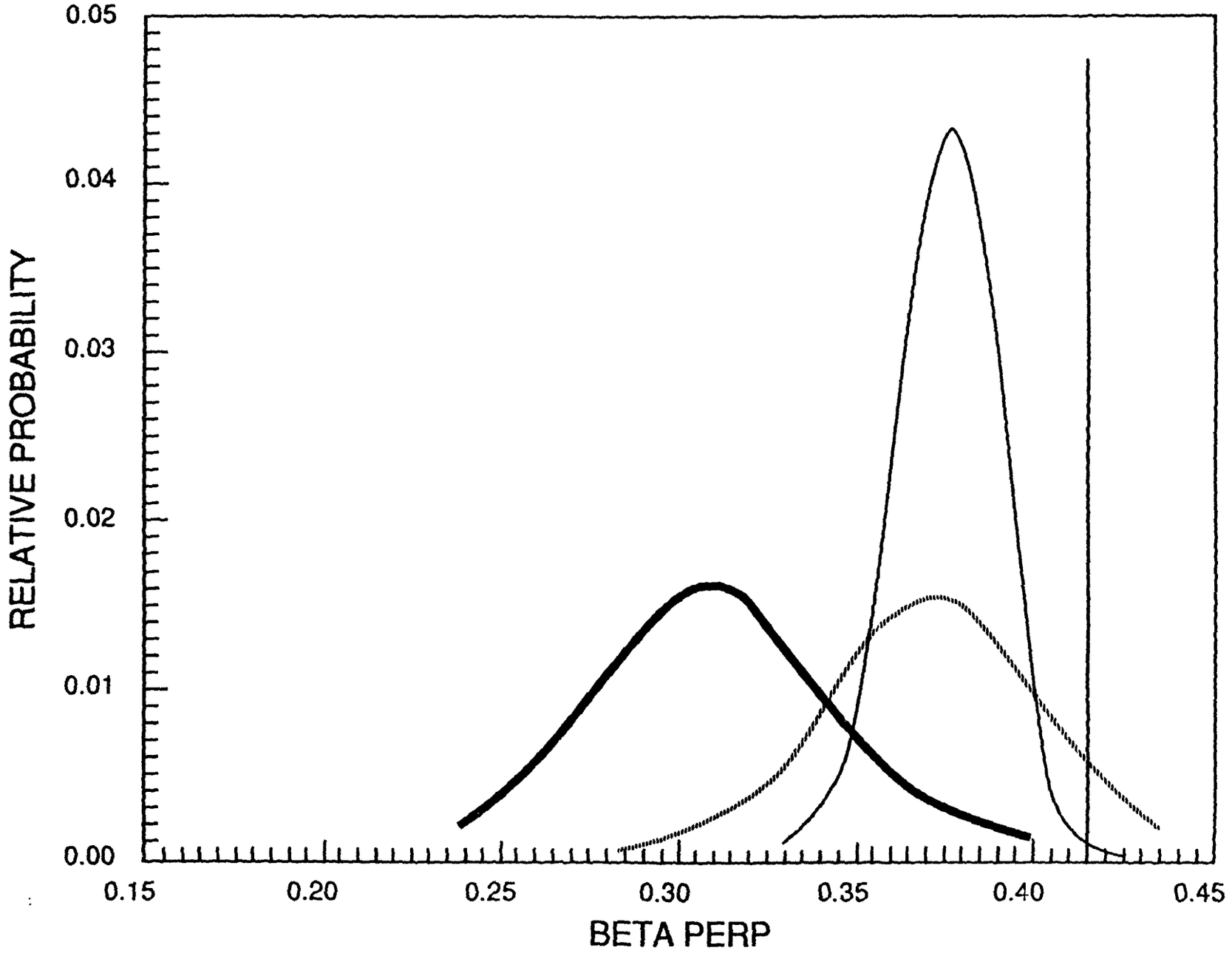

B(Z) G
×10⁴
6.2
5.5
2.7
0.0
R (MESH UNITS)
56.25
37.50
18.75
0.00
0.00
18.75
37.50
56.25
75.00
93.75
112.50
131.25
150.00
Z (MESH UNITS)

Figure 3


0.05
0.04
0.03
0.02
0.01
0.00
RELATIVE PROBABILITY
0.15
0.20
0.25
0.30
0.35
0.40
0.45
BETA PERP

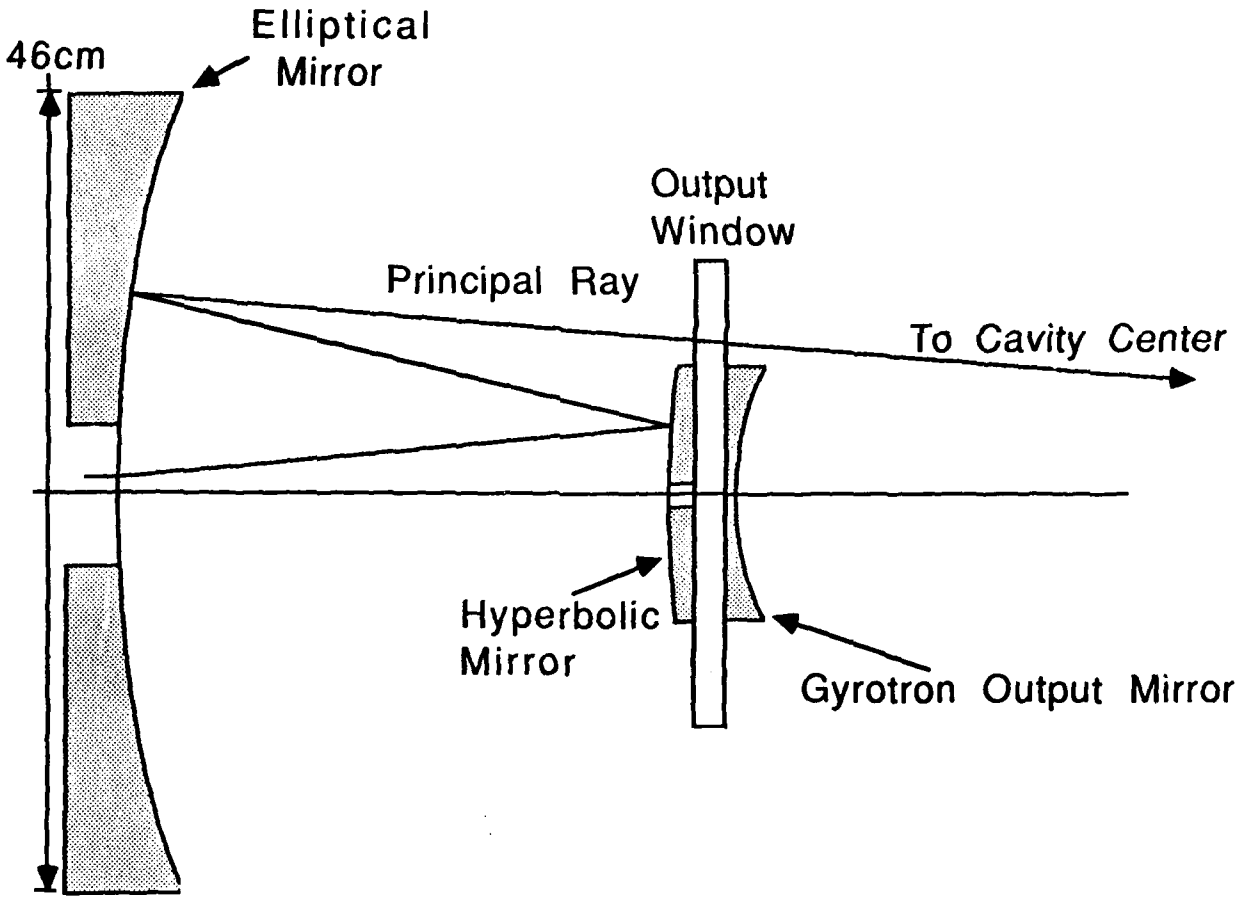

46cm
Elliptical
Mirror
Output
Window
Principal Ray
To Cavity Center
Hyperbolic
Mirror
Gyrotron Output Mirror

Figure 5

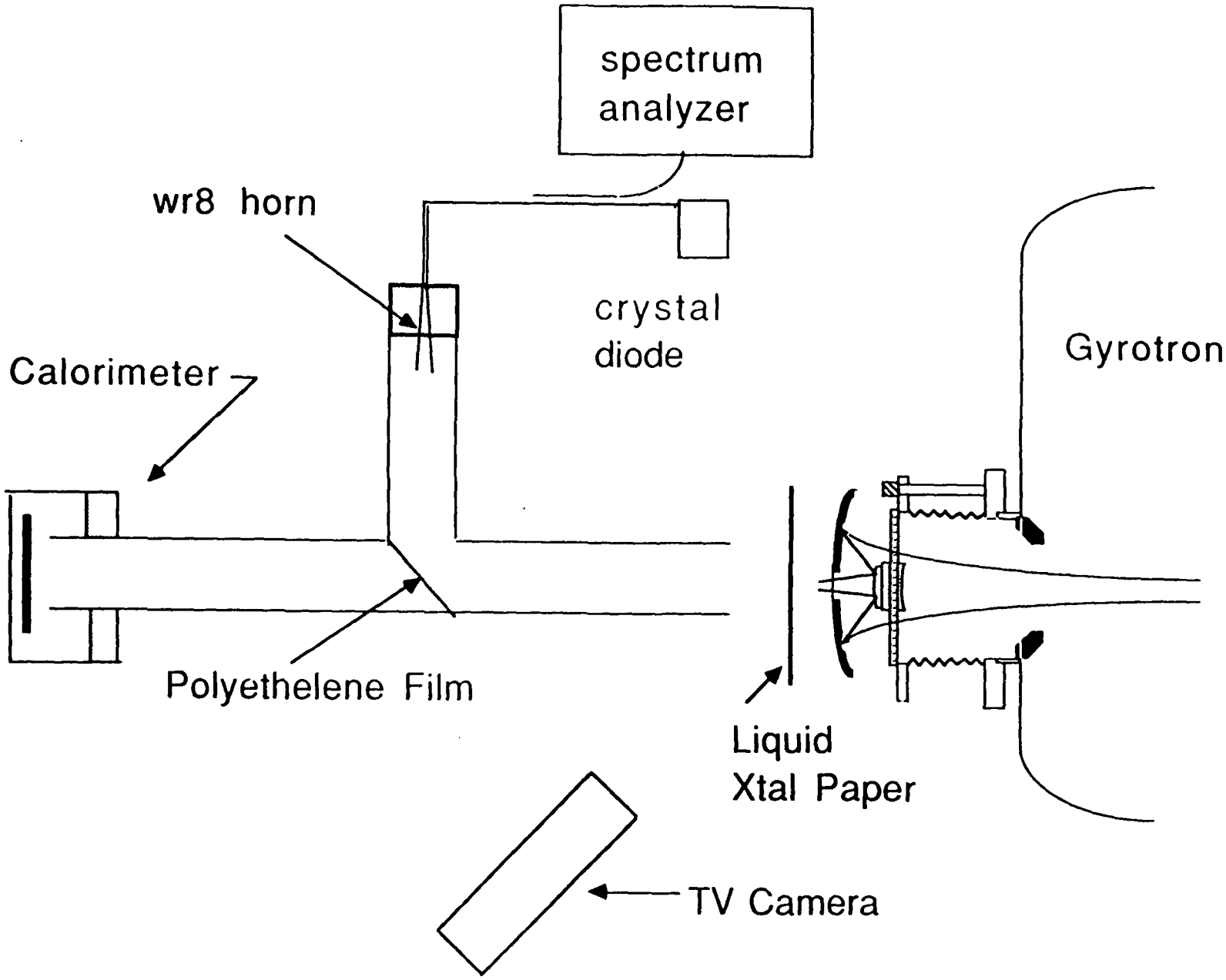

spectrum
analyzer
wr8 horn
crystal
diode
Gyrotron
Calorimeter
Polyethelene Film
Liquid
Xtal Paper
TV Camera

Figure 6

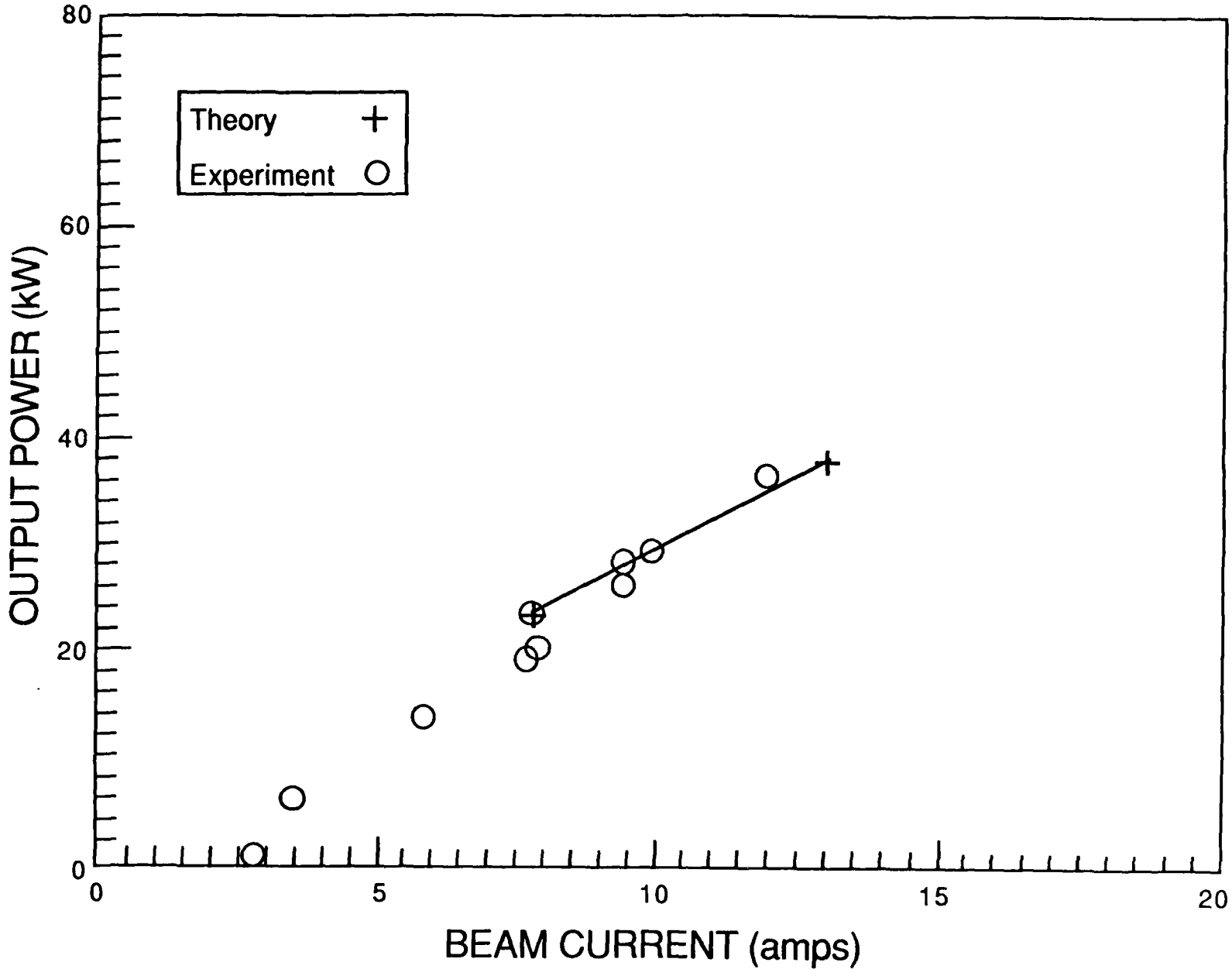

Theory
Experiment
OUTPUT POWER (kW)
BEAM CURRENT (amps)
0
20
40
60
80
0
5
10
15
20

Figure 7

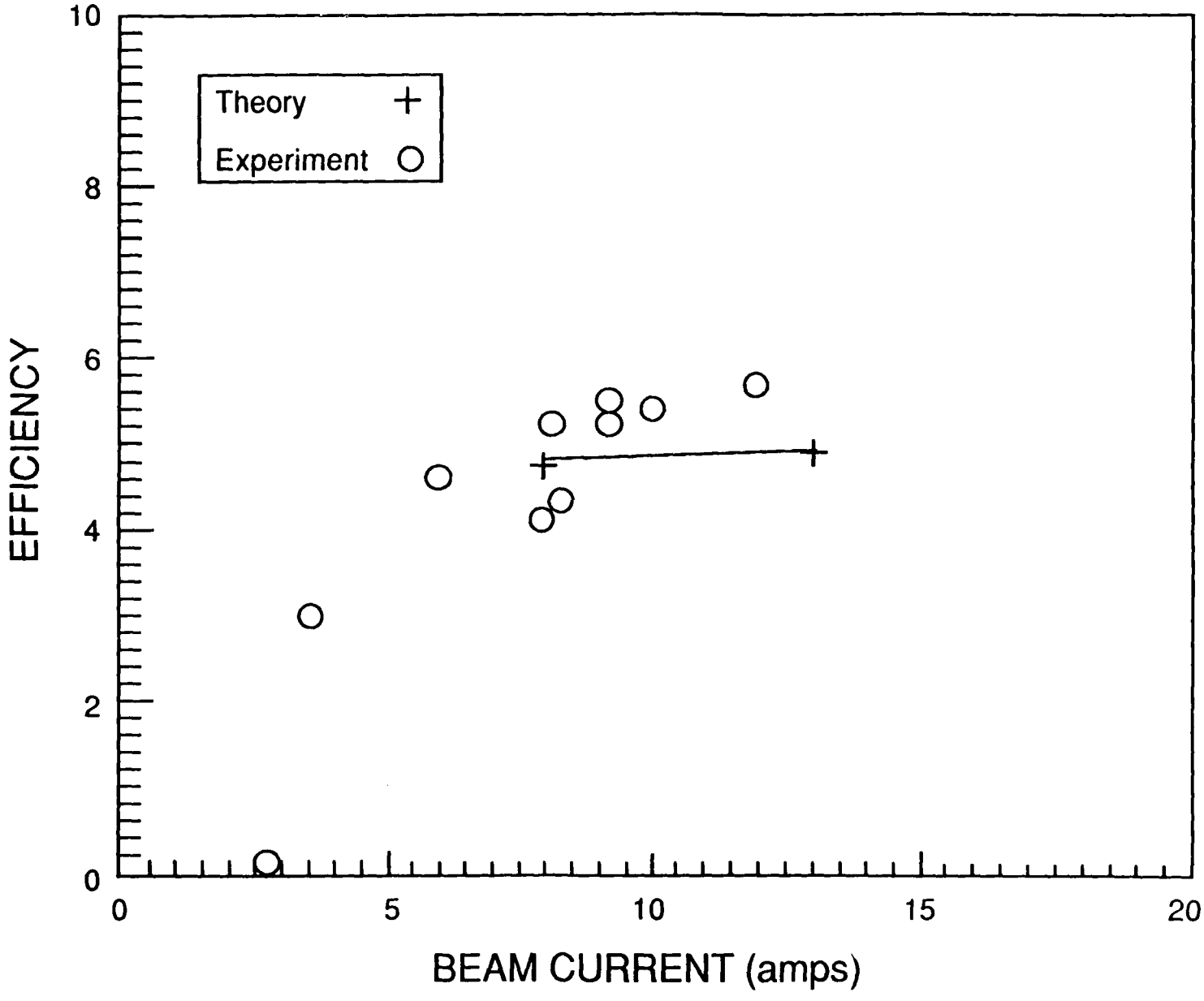

Theory
Experiment
EFFICIENCY
BEAM CURRENT (amps)
0
2
4
6
8
10
0
5
10
15
20

Figure 8

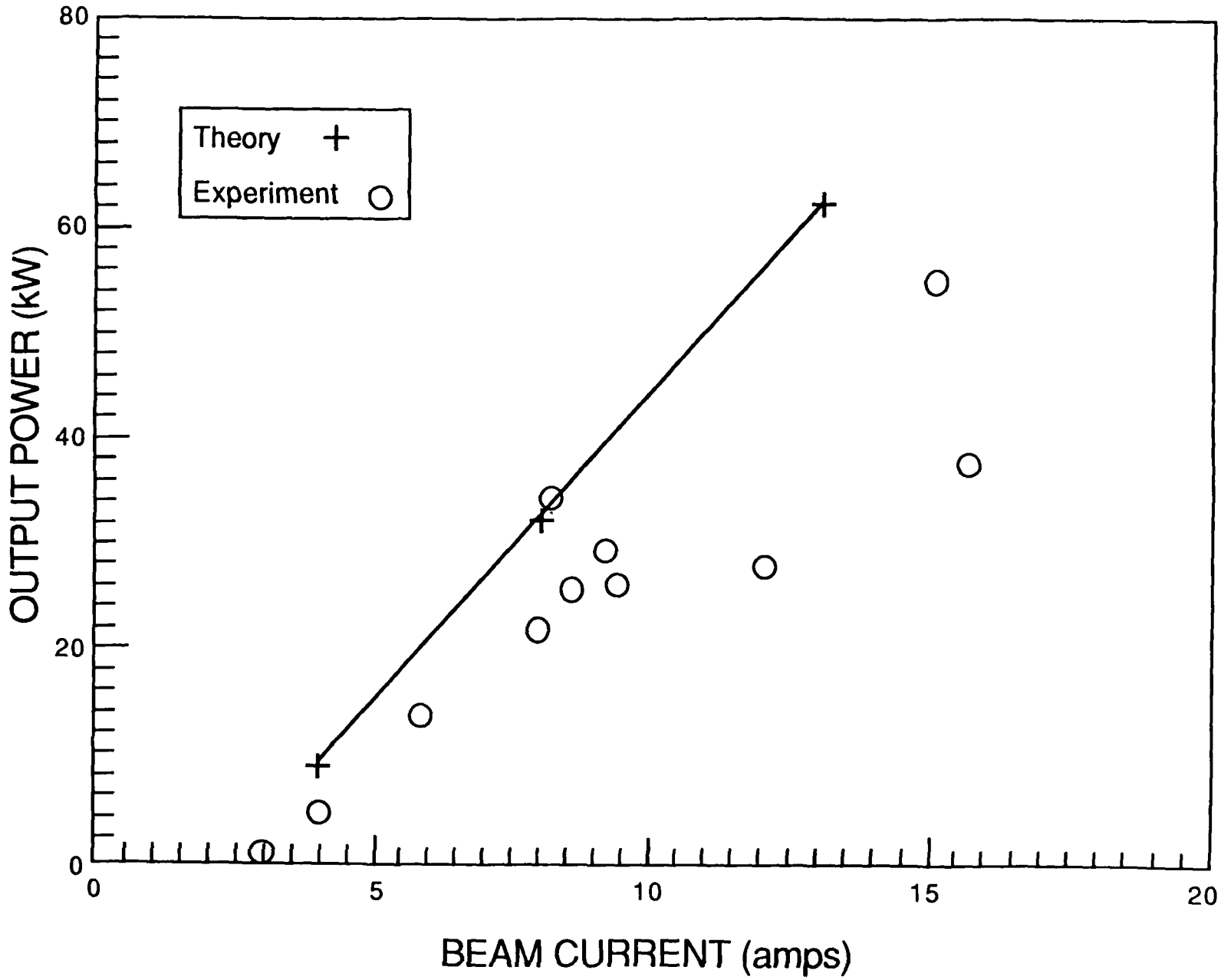

Theory
Experiment
OUTPUT POWER (kW)
BEAM CURRENT (amps)
0
20
40
60
80
0
5
10
15
20

Figure 9

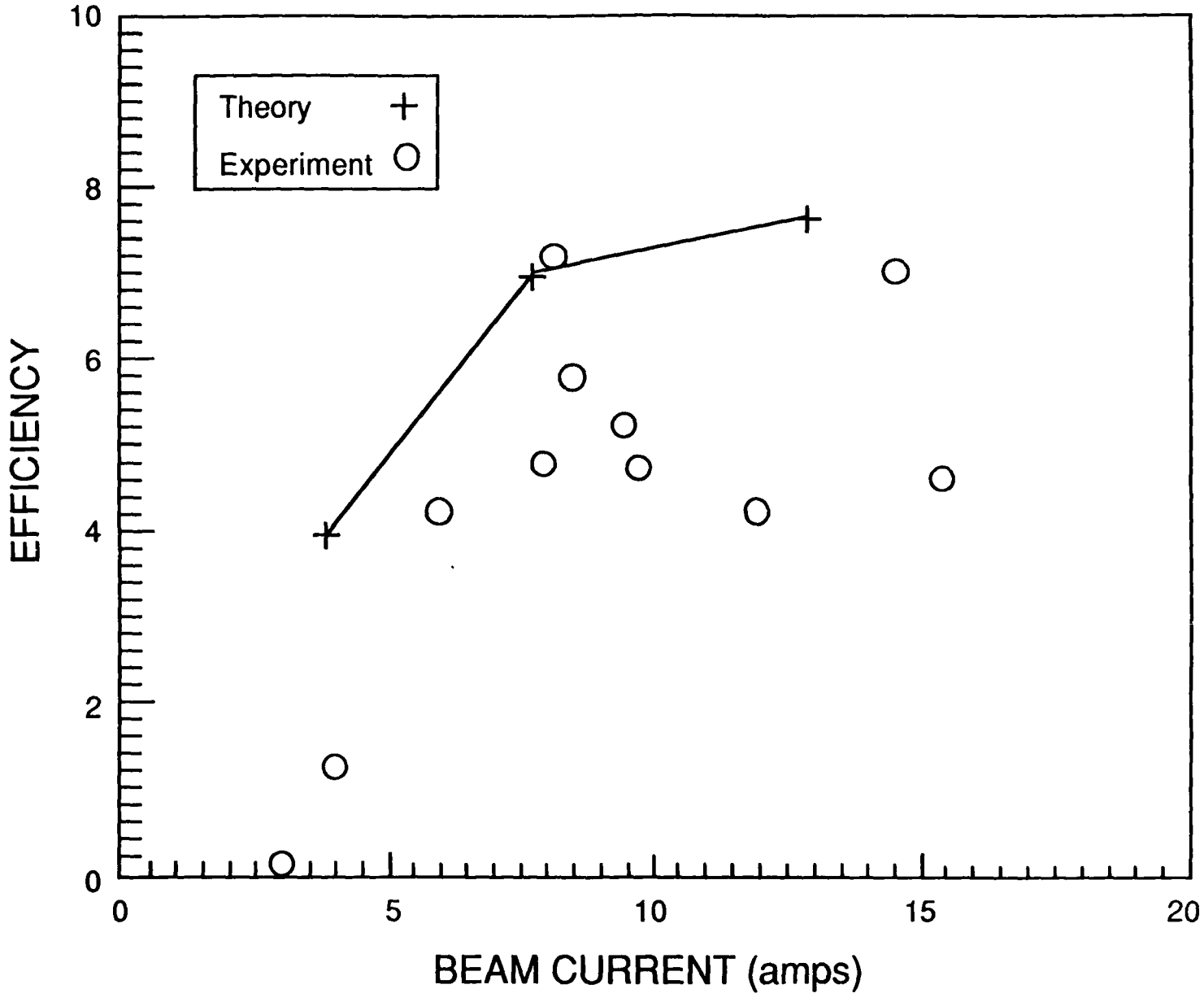

Theory
Experiment
EFFICIENCY
BEAM CURRENT (amps)
0
2
4
6
8
10
0
5
10
15
20

Figure 10

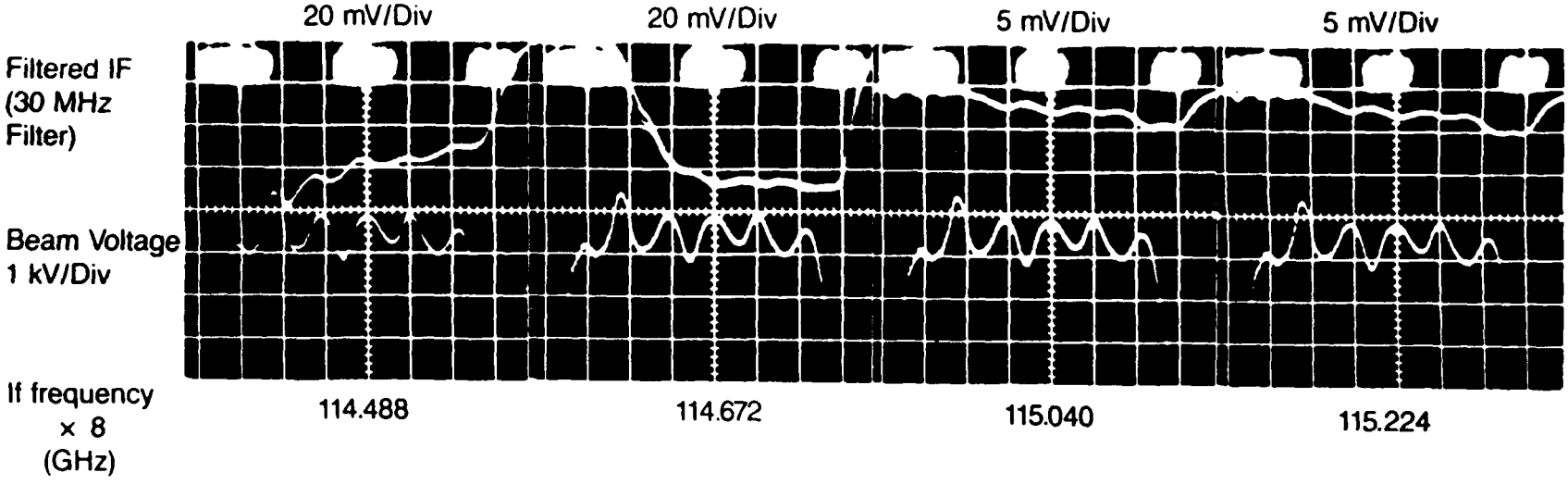

20 mV/Div
20 mV/Div
5 mV/Div
5 mV/Div
Filtered IF
(30 MHz
Filter)
Beam Voltage
1 kV/Div
If frequency
× 8
(GHz)
114.488
114.672
115.040
115.224

Figure 11

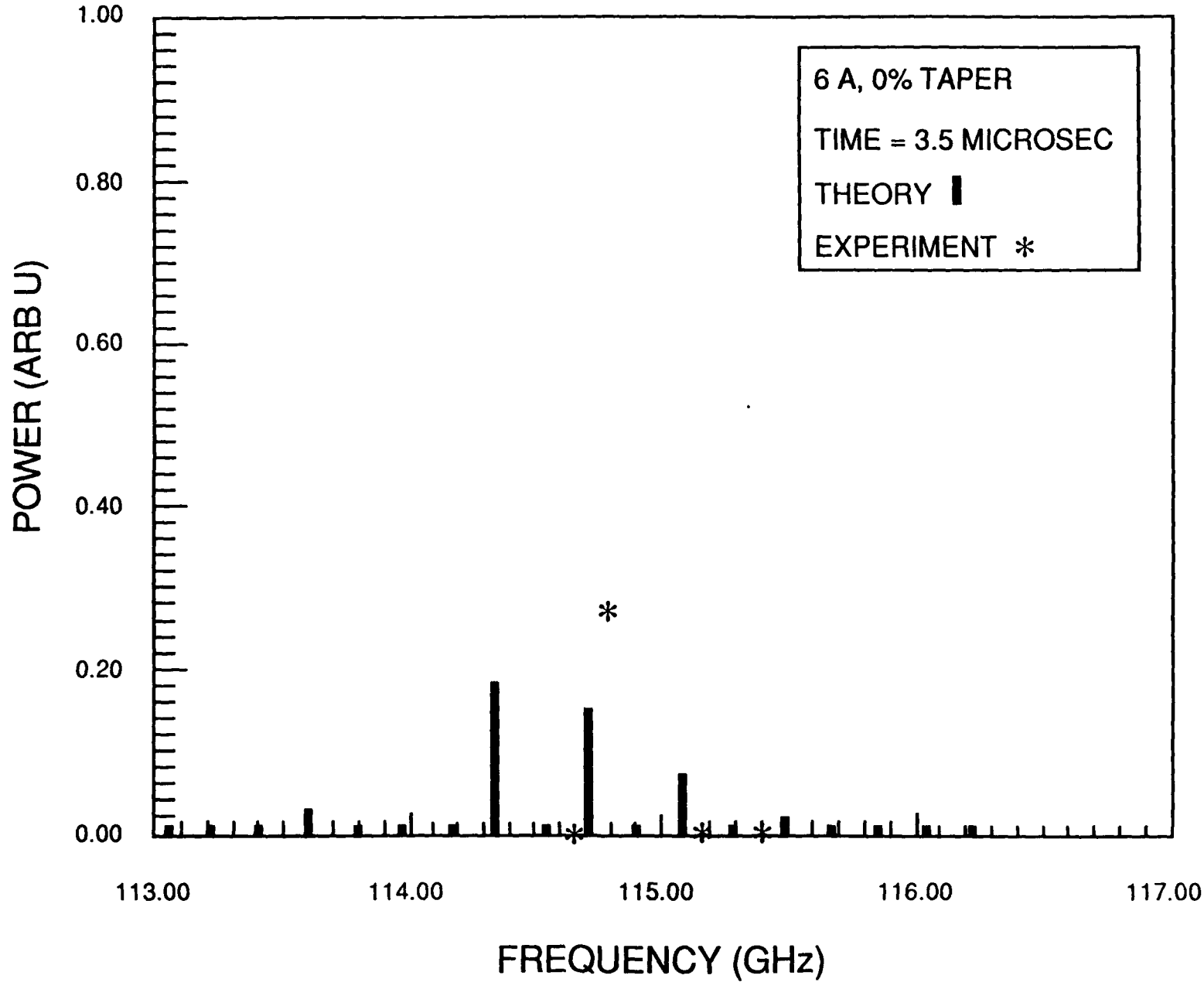

6 A, 0% TAPER
TIME = 3.5 MICROSEC
THEORY
EXPERIMENT *
POWER (ARB U)
1.00
0.80
0.60
0.40
0.20
0.00
113.00
114.00
115.00
116.00
117.00
FREQUENCY (GHz)

Figure 12a

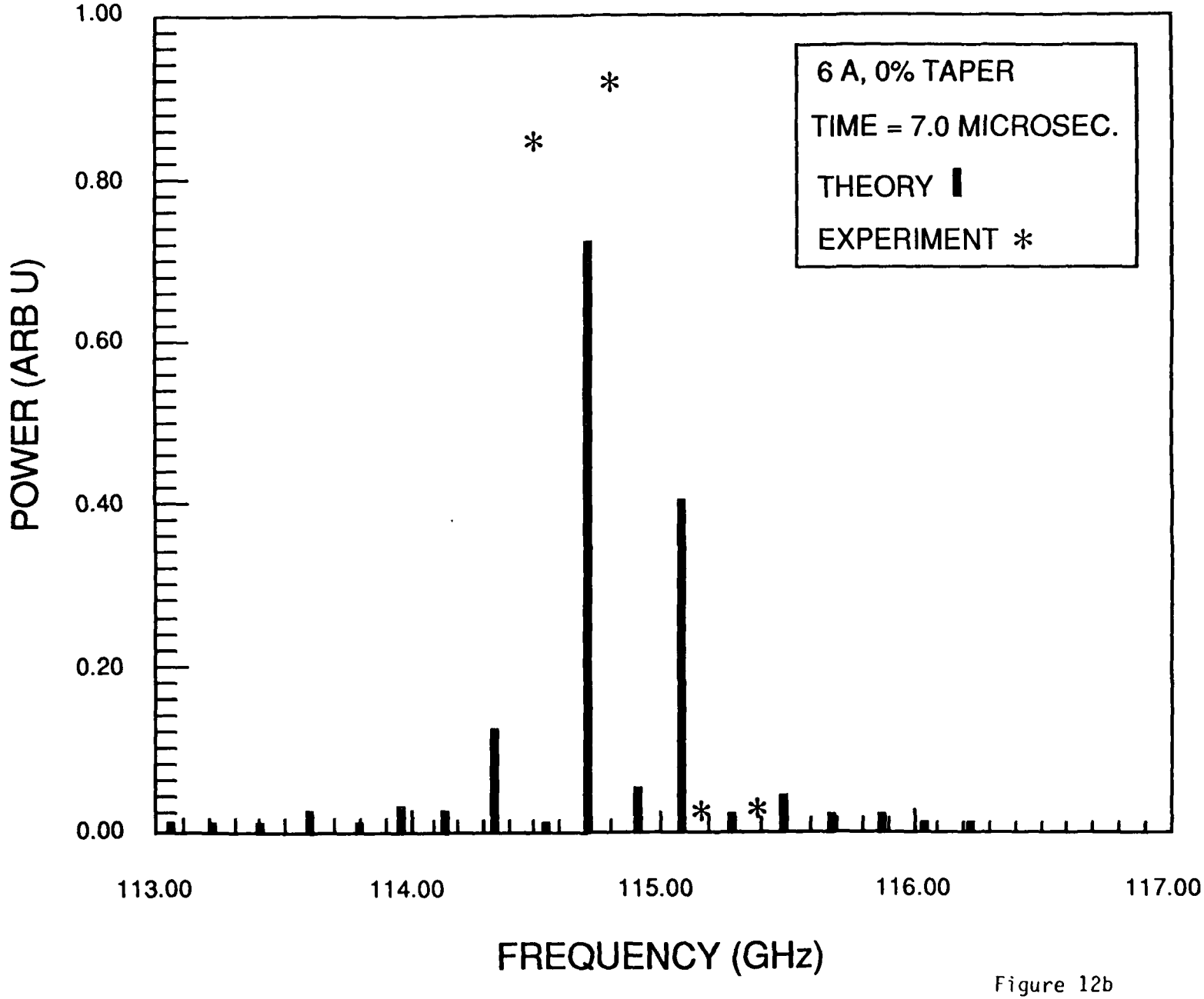

1.00
0.80
0.60
0.40
0.20
0.00
POWER (ARB U)
6 A, 0% TAPER
TIME = 7.0 MICROSEC.
THEORY
EXPERIMENT *
113.00
114.00
115.00
116.00
117.00
FREQUENCY (GHz)

Figure 12b

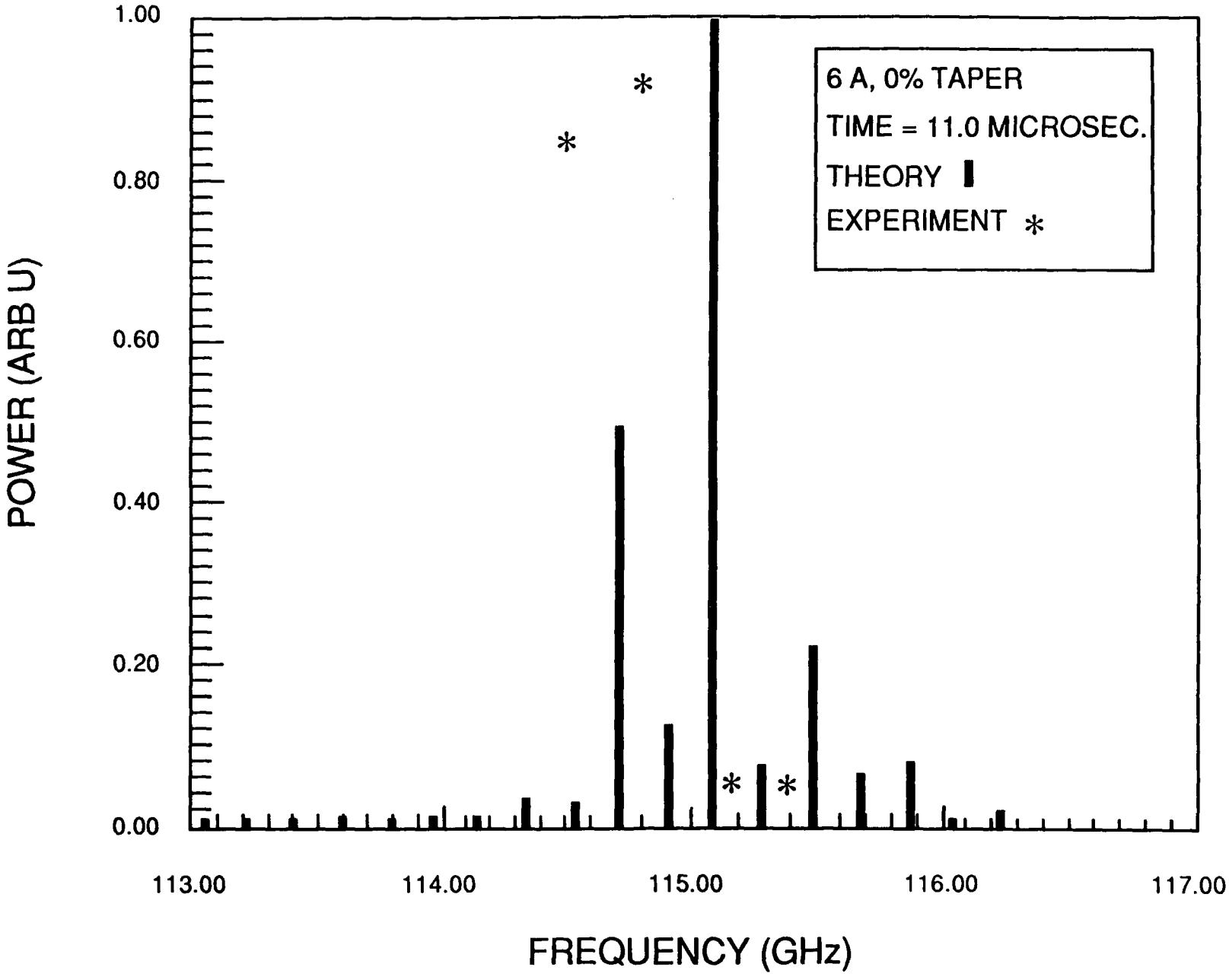

6 A, 0% TAPER
TIME = 11.0 MICROSEC.
THEORY
EXPERIMENT *
POWER (ARB U)
1.00
0.80
0.60
0.40
0.20
0.00
113.00
114.00
115.00
116.00
117.00
FREQUENCY (GHz)

Figure 12c

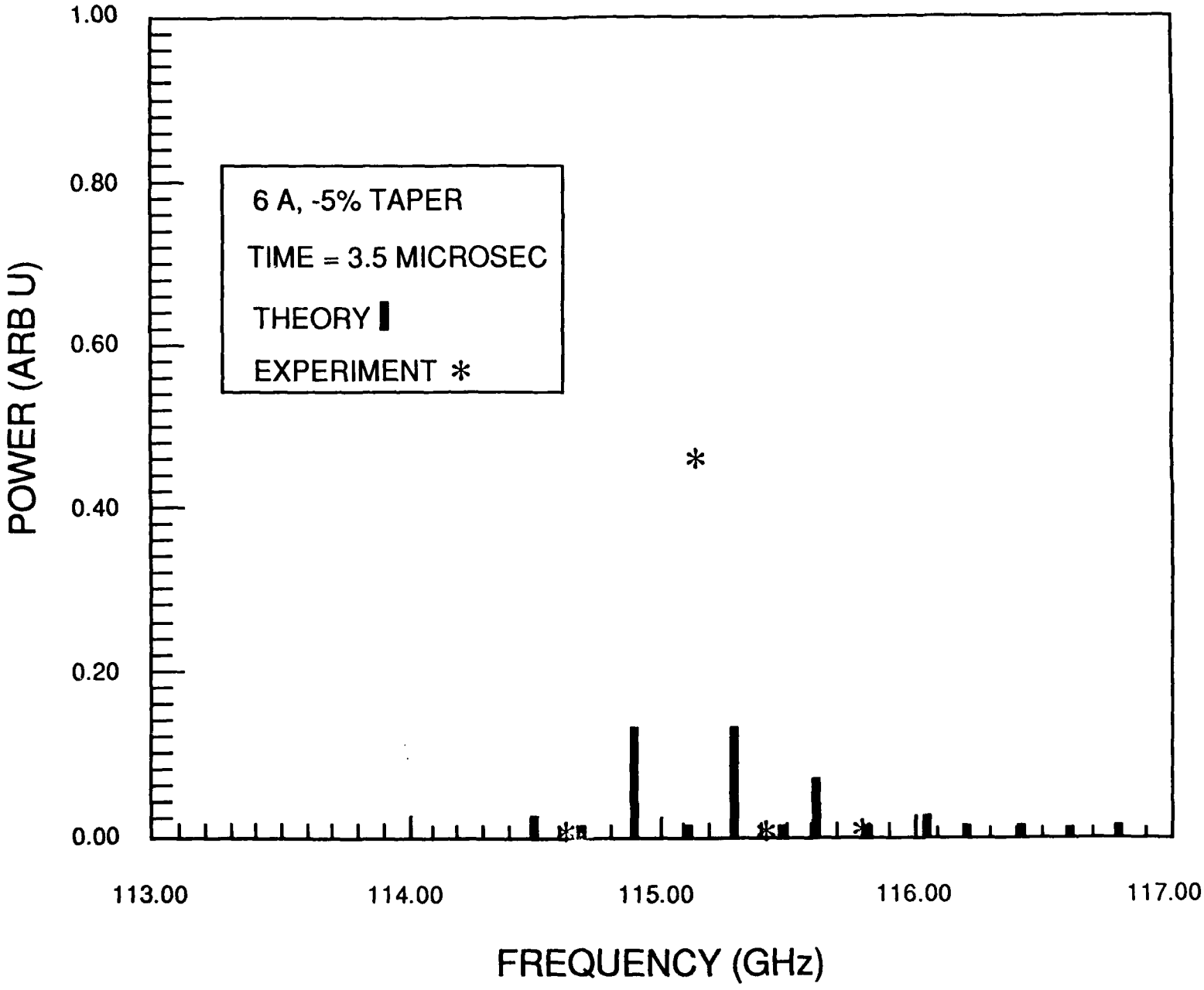

1.00
0.80
0.60
0.40
0.20
0.00
POWER (ARB U)
6 A, -5% TAPER
TIME = 3.5 MICROSEC
THEORY
EXPERIMENT *
113.00
114.00
115.00
116.00
117.00
FREQUENCY (GHz)

Figure 13a

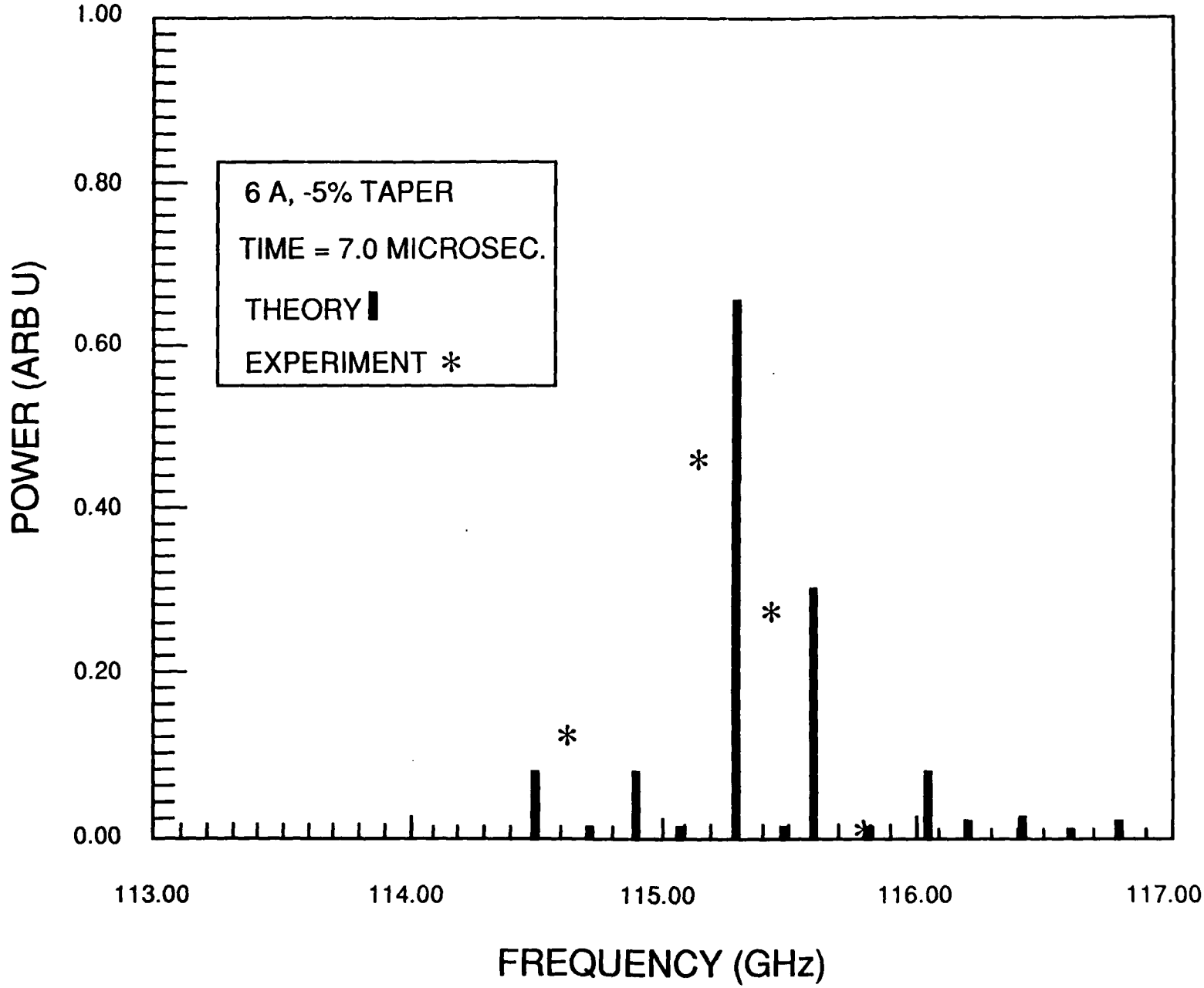

1.00
0.80
0.60
0.40
0.20
0.00
POWER (ARB U)
6 A, -5% TAPER
TIME = 7.0 MICROSEC.
THEORY
EXPERIMENT *
113.00
114.00
115.00
116.00
117.00
FREQUENCY (GHz)

Figure 13b

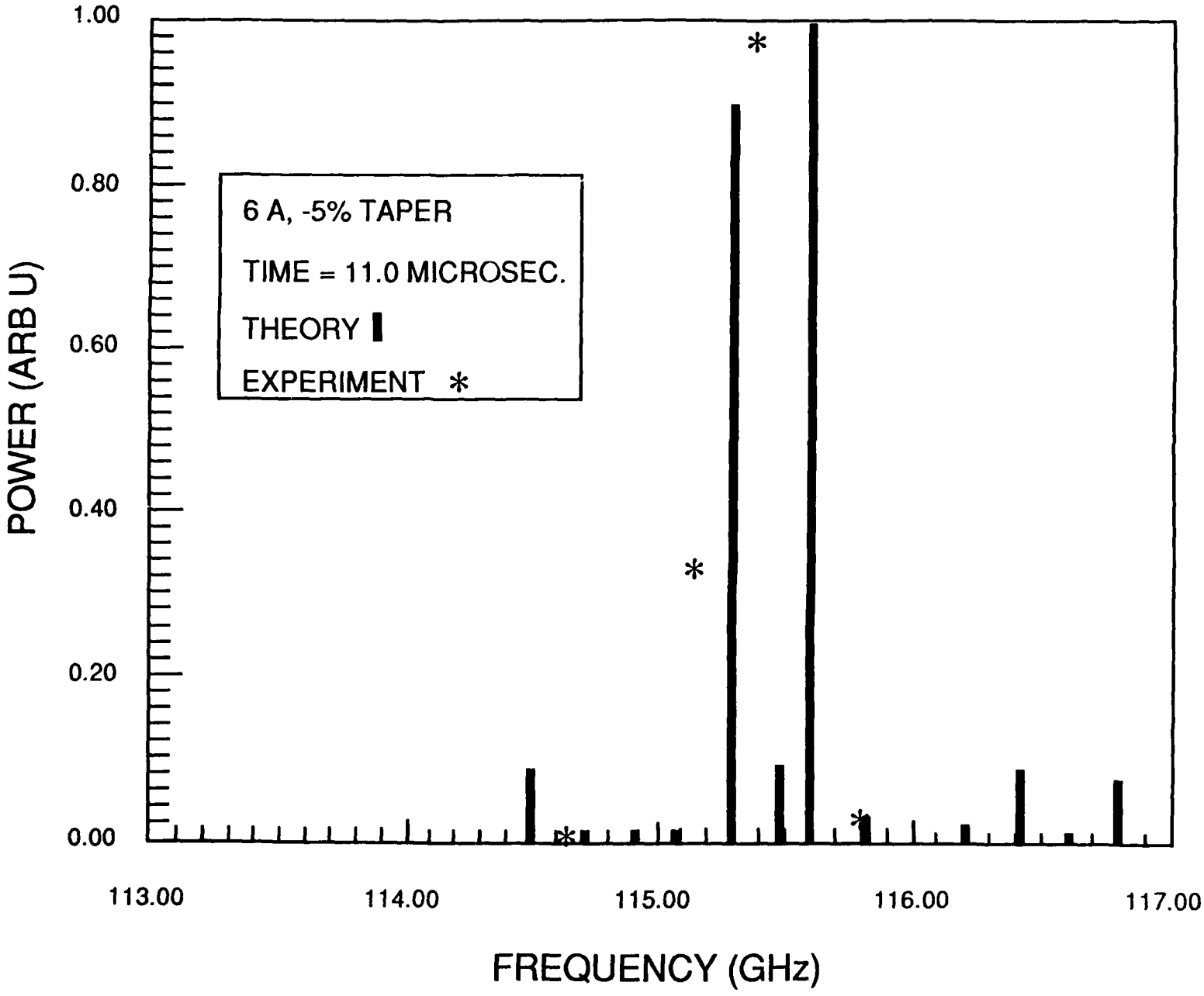

1.00
0.80
0.60
0.40
0.20
0.00
POWER (ARB U)
6 A, -5% TAPER
TIME = 11.0 MICROSEC.
THEORY
EXPERIMENT *
113.00
114.00
115.00
116.00
117.00
FREQUENCY (GHz)

Figure 13c

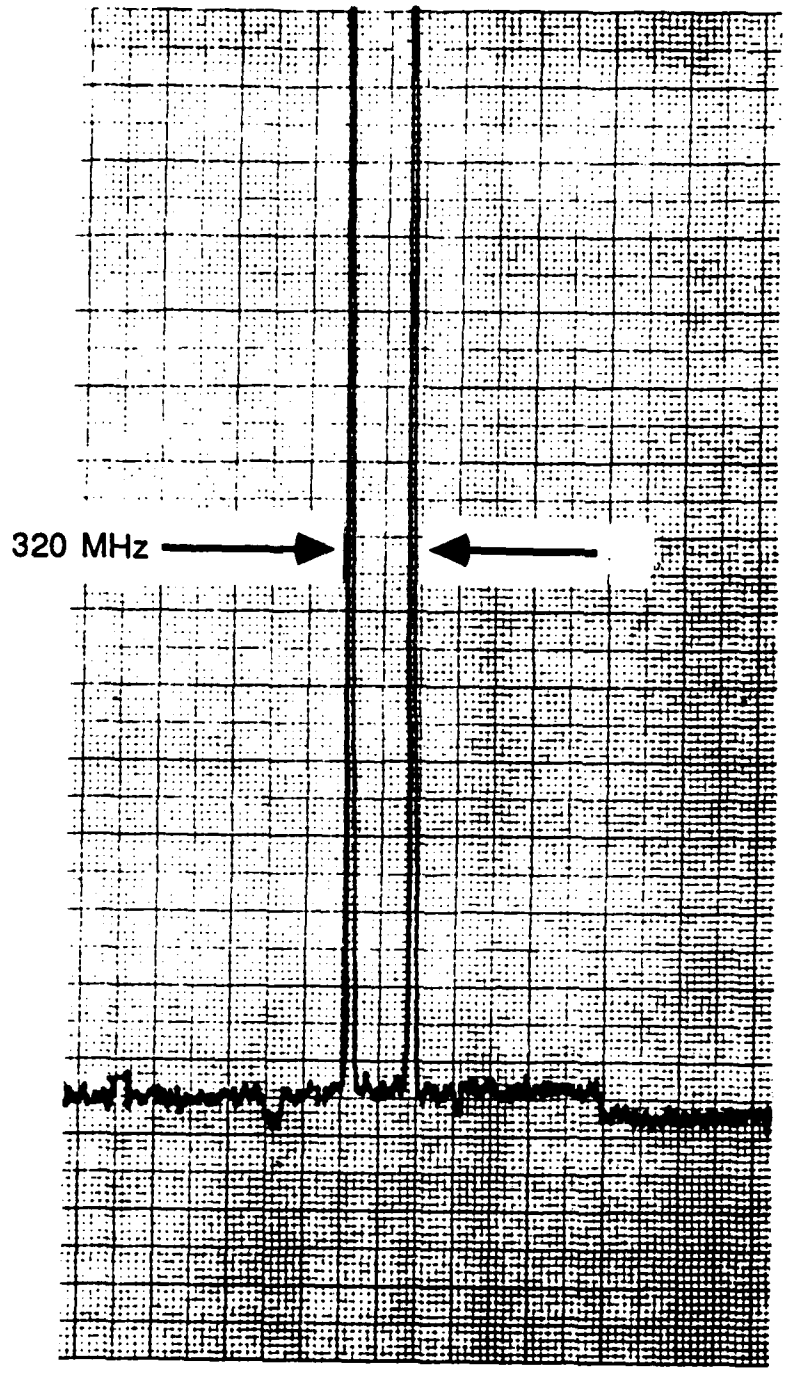
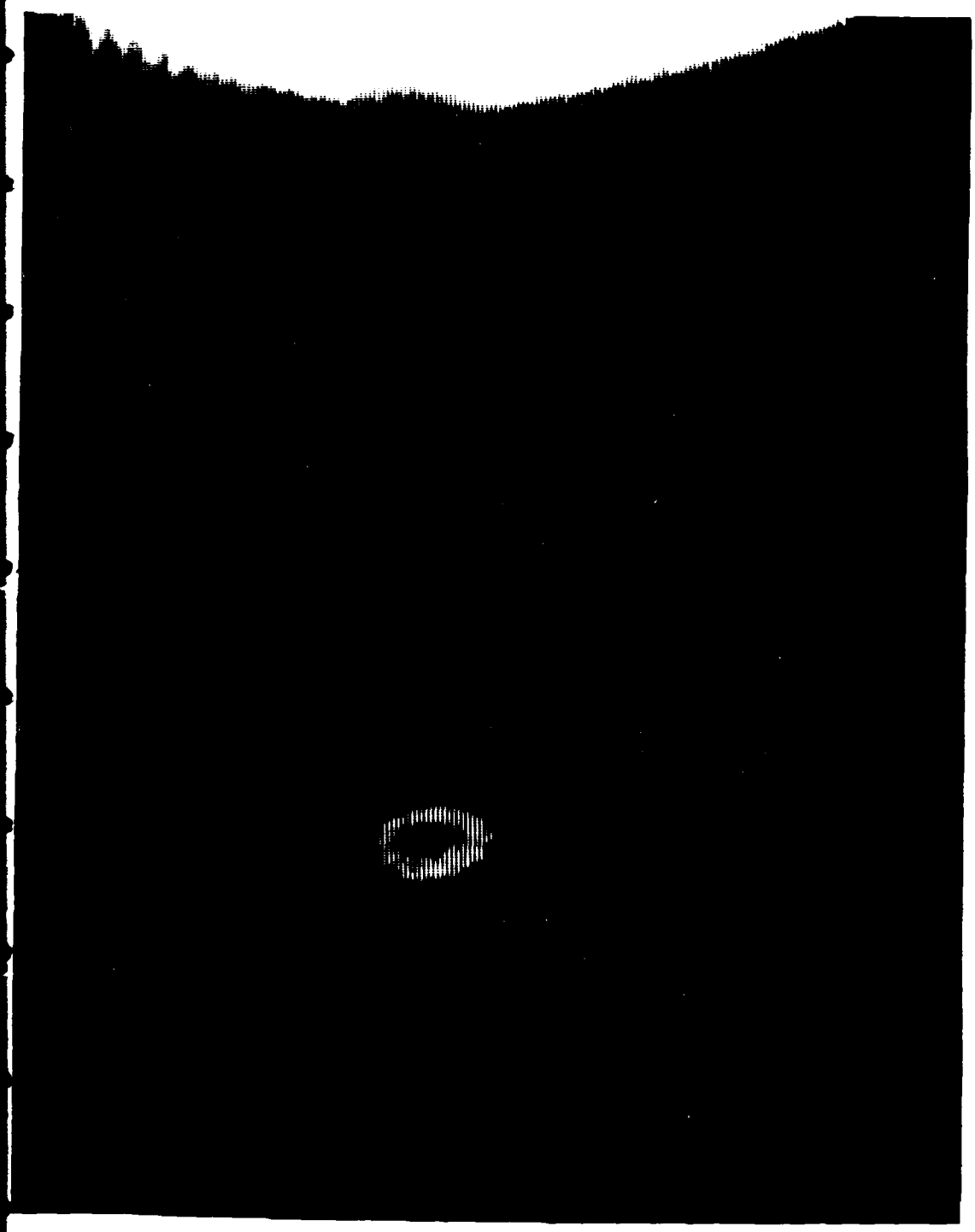



Figure 14





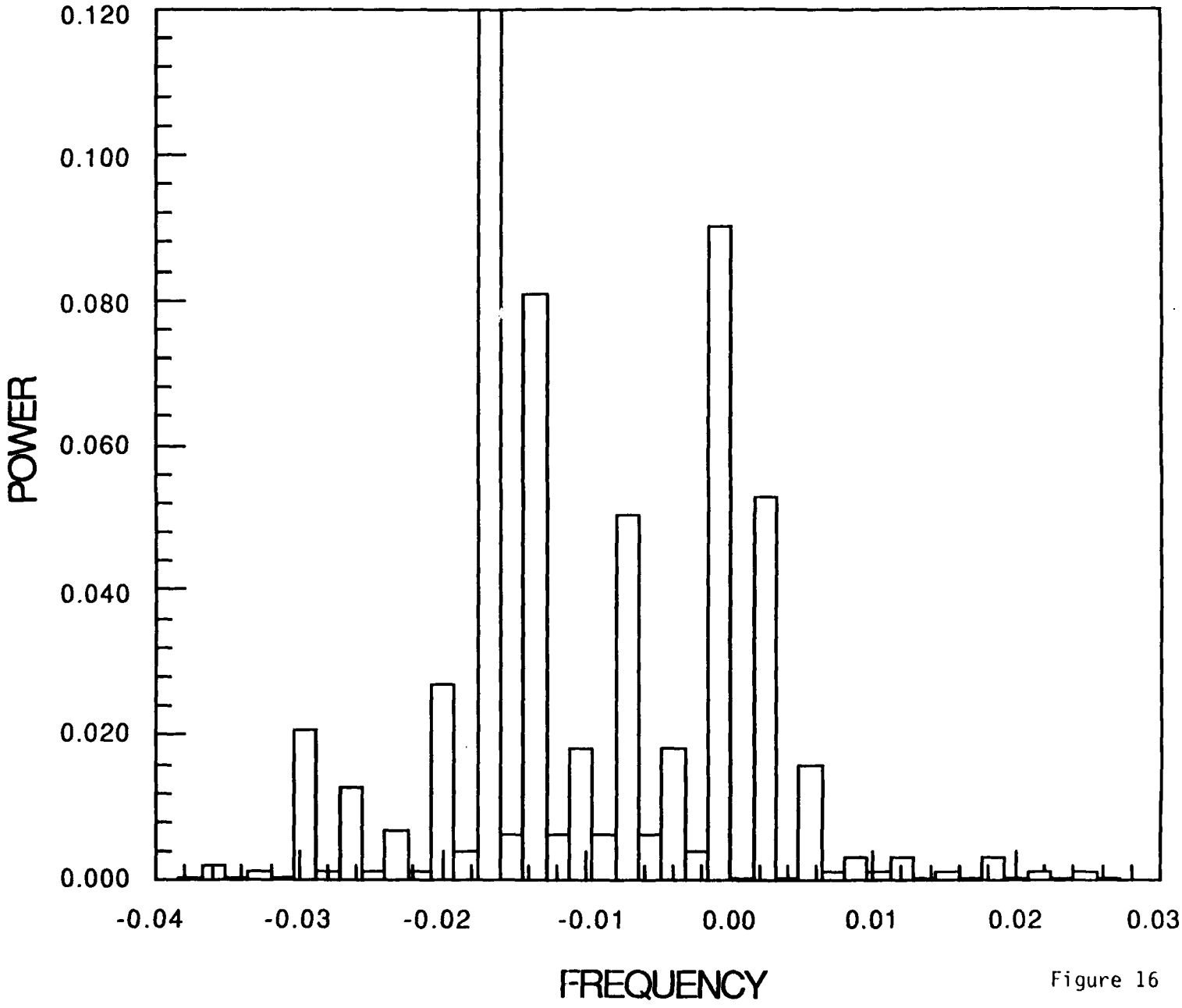

0.120
0.100
0.080
0.060
0.040
0.020
0.000
POWER
-0.04
-0.03
-0.02
-0.01
0.00
0.01
0.02
0.03
FREQUENCY

Figure 16

# APPENDIX H

## High Peak Power $K_a$-Band Gyrotron Oscillator Experiments with Slotted and Unslotted Cavities

IEEE TPS 16 2 1988

# High Peak Power $K_a$-Band Gyrotron Oscillator Experiments with Slotted and Unslotted Cavities

S. H. Gold
A. W. Fliflet
W. M. Manheimer
R. B. McCowan
R. C. Lee
V. L. Granatstein
D. L. Hardesty
A. K. Kinkead
M. Sucy

Reprinted from
IEEE TRANSACTIONS ON PLASMA SCIENCE
Vol. 16, No. 2, April 1988

# High Peak Power $K_a$-Band Gyrotron Oscillator Experiments with Slotted and Unslotted Cavities

S. H. GOLD, MEMBER, IEEE, A. W. FLIFLET, MEMBER, IEEE, W. M. MANHEIMER, SENIOR MEMBER, IEEE, R. B. MCCOWAN, R. C. LEE, V. L. GRANATSTEIN, SENIOR MEMBER, IEEE, D. L. HARDESTY, A. K. KINKEAD, AND M. SUCY

*Abstract*—A $K_a$-band gyrotron oscillator powered by a compact pulse-line accelerator has been operated using oscillator cavities with and without axial slots. The use of axial slots has been shown to suppress low starting current "whispering-gallery" modes, in particular, modes of the $TE_{m2}$ type, allowing stable operation in a linearly polarized $TE_{13}$ mode. A peak power of 35 MW has been observed at 6-percent efficiency.

## I. Introduction

GYROTRON operation is generally optimized with respect to the magnetic detuning (from exact cyclotron resonance), the interaction length, and the RF electric field at the position of the electron beam. High-power gyrotron oscillators must operate in high-order transverse modes of low-$Q$ cavities in order to increase the ratio of output power to the RF electric field at the electron beam, where $Q$ is the quality factor of the cavity. This requirement makes control of mode competition one of the major constraints in designing high-power gyrotron devices. A simple cavity with circular cross section, when utilized at frequencies well above the cutoff frequency for the lowest order $TE_{11}$ mode, can support a large number of closely spaced $TE_{mn}$ and $TM_{mn}$ modes. (Here $m$ is the azimuthal mode index, and $n$ is the radial mode index.) In earlier experiments operating at 350–775 keV, it was found that the easiest modes to excite were families of "whispering-gallery" TE modes, i.e., $TE_{mn}$ modes for which $m >> n$ [1], [2]. In particular, for electron beam radii ranging from approximately 40 to 85 percent of the radius of a 3.2-cm-diameter gyrotron cavity, it was found that cavity modes of the $TE_{m2}$ type were most readily excited. By varying the magnetic field in the cavity, $TE_{m2}$ modes from 28 to 49 GHz were excited, with $m$ ranging from 4 to 10. However, the easiest modes to excite may not always be the most desirable operating modes, either for reasons of maximizing power or efficiency, or for ease of utilization of the resulting RF emission. For instance, modes with low start-oscillation threshold currents will also have lower optimum output powers than higher starting current modes.

An alternative to operation in the modes with the lowest start oscillation threshold currents (at particular applied magnetic fields and beam radii) is to modify the simple cylindrical cavity in order to favor other modes. One straightforward means of raising the starting current of many of the whispering-gallery modes is to bifurcate the cavity by placing a pair of opposing axial slots in the cavity wall. By this means, all modes will have their total $Q$ lowered by diffraction losses through the slots. However, modes such as whispering-gallery modes, which require the presence of large wall currents at the position of the slots, will be most strongly affected. For that reason, a proper selection of slot width can often result in lowering the $Q$ for such modes substantially more than for other classes of modes. By this means, the ordering of modes with respect to start-oscillation threshold current may be changed, and modes with an initially higher starting current may be favored to start oscillation. In particular, whispering-gallery modes can generally be strongly suppressed by a pair of axial wall slots, while $TE_{1n}$ modes are less strongly affected [3]. Instead, the slots make the $TE_{1n}$ modes linearly polarized along the plane of the slots. (It is straightforward to excite $TE_{1n}$ modes with small radius electron beams, since only the $TE_{1n}$ modes couple exactly on axis. However, the beam positions in high-current devices designed to operate at very high peak powers are subject to space-charge constraints; the beams will generally be annular and cannot be too far from the conducting wall of the cavity.) The Soviet literature discusses high-peak-power gyrotron experiments at both 10 GHz [4], [5] and 40 GHz [6], [7] that employed axially slotted cavities to operate stably in linearly polarized $TE_{13}$

Manuscript received October 14, 1987; revised November 3, 1987. This work was supported by the Office of Innovative Science and Technology of the Strategic Defense Initiative Organization, and was managed by Harry Diamond Laboratories. This work was also supported in part by the Office of Naval Research.

S. H. Gold, A. W. Fliflet, W. M. Manheimer, D. L. Hardesty, and A. K. Kinkead are with the High Power Electromagnetic Radiation Branch, Plasma Physics Division, Naval Research Laboratory, Washington, DC 20375-5000.

R. B. McCowan is with Science Applications International Corporation, McLean, VA 22102.

R. C. Lee and M. Sucy are with JAYCOR, Inc., Vienna, VA 22180.

V. L. Granatstein is with the Electrical Engineering Department, University of Maryland, College Park, MD 20742.

IEEE Log Number 8819781.

0093-3813/88/0400-0142$01.00 © 1988 IEEE

modes. The 40-GHz experiment employed a 350-keV electron beam and reported 23 MW at 5-percent efficiency with a beam current of 1.3 kA.

In this paper, we describe a set of experiments comparing the performance of slotted and unslotted cavities in a high-voltage ( ~900 keV), high-current ( ~500 A) gyrotron experiment operating at frequencies between approximately 20 and 50 GHz.

## II. Experimental Setup

Fig. 1 illustrates the experimental setup. A 600-kV compact Febetron pulser with 100-Ω impedance and 55-ns output voltage pulse is used to generate an annular electron beam in a simple foilless diode geometry. The electrons are emitted from the sharpened edge of a cylindrical graphite cathode by explosive plasma formation. (In order to optimize the compression ratio for these experiments, a graphite cathode was employed that tapered down from a 1.75-cm-radius shank to a 1.27-cm emitting tip; as a result of some emission at the start of this taper, a low-current halo was produced at ~0.4 times the radius of the main gyrotron beam.) The beam is created in a uniform axial field provided by the main solenoidal magnet. The initial transverse momentum is low because the emission is predominantly along the direction of the applied magnetic field. Additional transverse momentum is induced by transit through a localized depression in the axial field, which is produced by the "pump" magnet. Finally, the beam is adiabatically compressed to its final radius by the cavity solenoid. In order to achieve separate adjustment of the electron transverse momentum, the magnetic compression ratio, and the final magnetic field in the gyrotron cavity, each of the three magnets is powered by a separate capacitor-bank discharge. The overall experimental setup has been described in more detail elsewhere [2]. The changes affecting the present work are in the cathode radius and in the gyrotron cavity design.

Three 2.34-cm-diameter cavities of identical dimensions were fabricated. A pair of opposing axial slots were machined into two of the cavities. One received 33° full-width slots, while the second received 45° full-width slots. The third cavity was left unslotted. The 45° slotted cavity is illustrated in Fig. 2. These cavities were designed to run in the $TE_{13}$ mode at 35 GHz, with the slotted cavities intended to suppress competition from other nearby modes. The calculated $Q$ factor for these cavities was ~200 for the $TE_{11}$ mode, with the axial slots not significantly lowering this value. Fig. 3 shows a map of the lowest axial wavenumber $TE_{mn}$ modes between approximately 22 and 53 GHz. ($TM_{mn}$ modes are omitted, since the gyrotron interaction couples relatively weakly to these modes.) Fig. 4 shows the effect of slots on the cavity $Q$ of the $TE_{13}$ mode and on two competing modes, the $TE_{42}$ and $TE_{32}$ modes, as well as on two modes resonant near 48 GHz, the $TE_{14}$ and $TE_{62}$ modes. (The $TE_{71}$ mode near 35 GHz is not included in Fig. 4, because coupling to it is very weak for normalized beam radii ($r_b/r_w$) less than ~0.6.) The data in this figure were generated using a theory and computer code described in [3] to calculate the effect of finite slot widths on cavity losses. In addition, the output diffraction $Q$ was calculated using a computer code employing weakly irregular waveguide theory

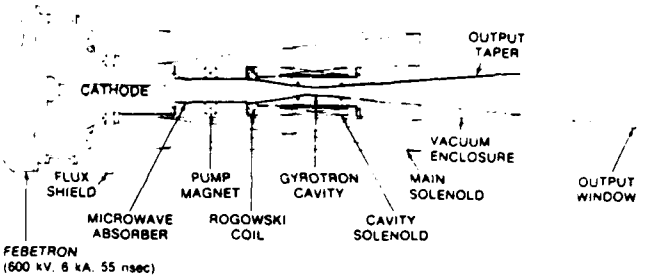



Fig. 1. Schematic diagram of the high-voltage gyrotron experimental setup.

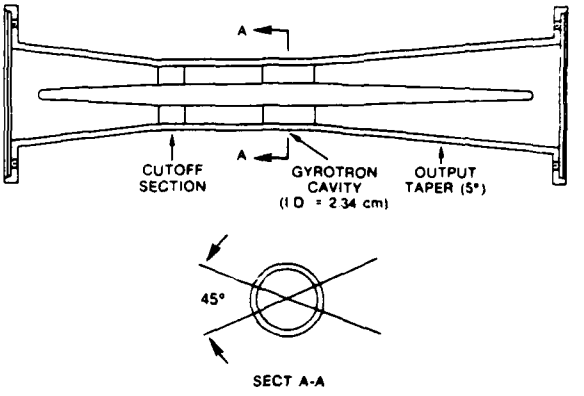



Fig. 2. Schematic of the 45° slot angle gyrotron cavity, showing a side view and a cross section through the cavity.

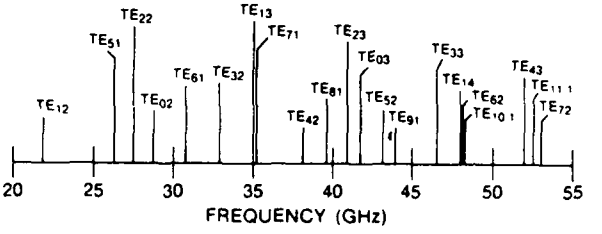



Fig. 3. Map of the cutoff frequencies of $TE_{mn}$ modes falling between 22 and 53 GHz for the unslotted $TE_{11}$ cavity.

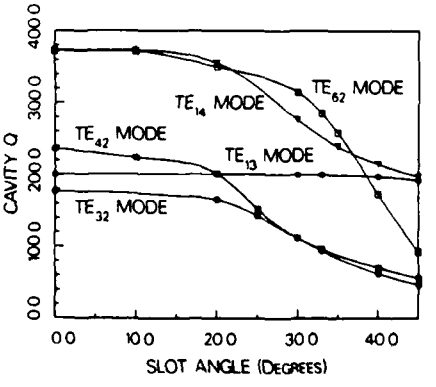



Fig. 4. Cavity $Q$ versus slot angle for selected cavity modes near 35 and 48 GHz.

[8] to calculate the diffraction $Q$ for the $TE_{13}$ mode, with the $Q$ factors for the other modes scaled from this value as the square of their resonant frequencies. (Minimum diffraction $Q$ for an $l = 1$ mode near cutoff in a gyrotron cavity of length $L$ is given by $4\pi(L/\lambda)^2$, where $l$ is the axial mode index and $\lambda$ is the free-space wavelength associated with the operating frequency.) The $Q$ values were also corrected for the calculated ohmic losses for each mode.

## III. Experimental Results and Discussion

A set of measurements were carried out on the operation of the slotted and unslotted cavities as a function of magnetic field, magnetic compression ratio, and pump-field amplitude. These measurements employed both time-resolved microwave techniques and time-integrated gas-breakdown techniques. They were intended to examine the operating modes of the slotted cavities, and in particular, to demonstrate the effect of the axial slots on the suppression of mode competition with the $TE_{13}$ mode at 35 GHz. A careful study was made of operation of the $TE_{13}$ mode in the 45°-slot-angle cavity. In addition, an attempt was made to find other possible oscillating modes of the 33° and 45° slotted cavities, in particular the $TE_{12}$ mode at ~22 GHz and the $TE_{14}$ and $TE_{62}$ modes at ~48 GHz. For the unslotted cavity, we examined the competition between the $TE_{13}$ mode and nearby whispering-gallery modes, and did a scan with magnetic field to look for other predicted modes, in particular, the $TE_{m2}$ modes seen in earlier experiments.

### A. Microwave Measurements

The microwave measurement system consists of two separate detection channels, each composed of calibrated "in-band" WR-28 components (including filters, attenuators, and directional couplers) and beginning with a small microwave aperture antenna positioned within 1 cm of the output window. In order to reduce the power density at the apertures, a 1-in-thick (~2.5 cm) phenolic vacuum window is employed, which produces a measured signal attenuation of 10 ± 0.5 dB. One aperture is maintained at a fixed position on the output window, while the second is scanned. In order to normalize the data over the large number of separate discharges needed to measure the output mode pattern, the ratio of the scanning detector to the fixed detector is calculated for each shot. These diagnostics are described in greater detail elsewhere [2].

Fig. 5 shows a scan of the operating mode of the device with the 45° slotted cavity employed, measured along a radius normal to the plane of the slots, and operating at $B_0 = 26$ kG and ~500 A, with a peak diode voltage of ~900 kV. (Very similar results could be obtained with the 33° slotted cavity.) A narrow-band (1.6-GHz FWHM) filter limited the detected signal to a narrow frequency range about 35 GHz. The peak voltage results from mismatching the diode impedance upward with respect to the Febetron output impedance. The peak beam kinetic energy should be corrected downward to ~850 keV because of space-charge depression, assuming a beam $\alpha \sim 1$, where $\alpha$ is the ratio of transverse velocity to parallel velocity. The 55-ns Febetron voltage waveform consists of two separate voltage maxima separated by ~30 ns, with the valley after the first maximum decreasing to about 67 percent of the maximum voltage, and the second maximum rising to 75 percent of the height of the first. The two voltage maxima are roughly triangular, so that the voltage is changing during all times of experimental interest, including the period during which the microwave signal is growing from noise to its maximum signal. The magnetic field is adjusted experimentally in order to place the peak of the 35-GHz microwave signal at the first peak of the voltage waveform. The implications of this time-dependent voltage on gyrotron operation for the earlier $TE_{62}$ experiment were considered in detail in [2] in the context of steady-state gyrotron theory, and have been further analyzed using time-dependent models by Lin *et al.* [9].

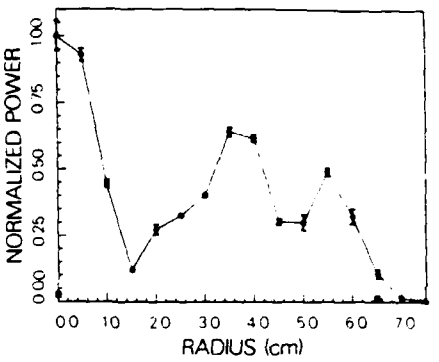



Fig. 5. Measured vertically polarized microwave power versus position across a radius along the midplane of the experimental output window. The square points at 0 and 6.5 cm correspond to horizontal polarization. The data from each experimental discharge were normalized to the signal from a fixed detector channel. Statistical error bars (standard deviation of the mean of at least three shots) are shown.

Fig. 6 plots the square of the gyrotron coupling coefficient (see [1]), which is inversely proportional to the gyrotron starting current, as a function of radius. The normalized beam radius in the cavity is 0.37. Under these conditions, with the axial slots suppressing competition from other modes that might couple to the beam at the experimental beam radius, the expected mode of operation is a linearly polarized $TE_{13}$ mode; the beam location is close to optimum for coupling to this mode on the second radial peak. The expected pattern for this mode is illustrated in Fig. 7. There is substantial agreement between experiment and calculation, although it appears that the measured mode at the output window has undergone some mode conversion after exiting the gyrotron cavity. The appearance of the measured mode suggests that the $TE_{13}$ mode has converted in part to the $TE_{14}$ mode. In order to estimate the expected mode conversion in the 5° output taper from the gyrotron cavity, calculations were carried out using a computer code [10] that integrates the differential equations for coupled transverse modes

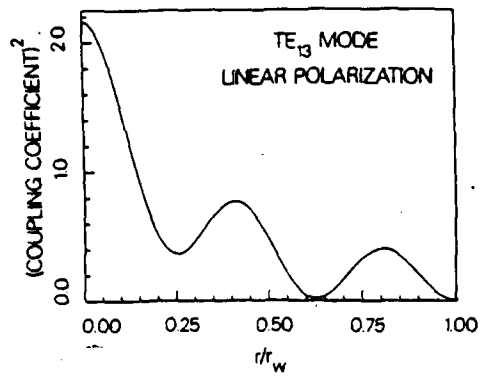



Fig. 6. Plot of the square of the gyrotron coupling coefficient versus normalized cavity radius for a linearly polarized $TE_{13}$ mode. The calculation is performed assuming an azimuthally symmetric annular electron beam.

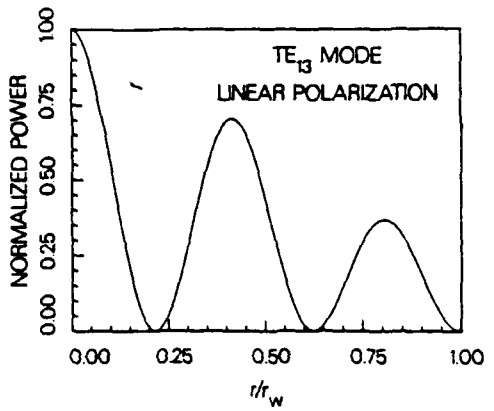



Fig. 7. Predicted microwave power as a function of position across a horizontal radius of the experimental output window for a linearly polarized $TE_{13}$ mode.

through the taper. These calculations suggest that approximately 24-percent mode conversion from the $TE_{13}$ mode should take place in the output taper, yielding approximately 12-percent mode content in the $TE_{12}$ mode, 10-percent mode content in the $TE_{14}$ mode, and less than 2-percent in other $TE_{1n}$ and $TM_{1n}$ modes. There may be additional mode conversion due to irregularities in the output waveguide.

For the data of Fig. 5, the measured mode pattern can be used to calculate the total gyrotron power by integrating over the output window, and correcting for the measured losses in the detection system. This procedure has been described in detail elsewhere [2]. For the case of a linearly polarized mode, the calculated power must be reduced by 3 dB compared to the result of integrating the measured radial pattern over the entire output window. Since the ratio of the measured power on axis to the total emitted power in the output mode pattern can be determined in this fashion, it is possible to determine power on a single-discharge basis. The best single-discharge power in this data set was 28 MW. For the voltage, magnetic field, and beam radius corresponding to Fig. 5, power was experimentally optimized by small variations in the pump magnet amplitude, producing slight changes in the net beam current. The highest power observed by this means was 35 MW at 6-percent efficiency at ~640 A. Fig. 8 shows a plot of gyrotron start-oscillation threshold currents and output power contours for a linearly polarized $TE_{13}$ mode as a function of beam current and voltage, calculated assuming a sinusoidal RF-field profile in the gyrotron cavity, and using a computer code based on the general nonlinear theory of gyrotron oscillators presented in [11]. These are steady-state calculations. They suggest that an output power between 30 and 60 MW should occur at the experimental beam current as the voltage ramps upward to the maximum of ~850 keV and subsequently decreases, in good agreement with the experimental measurement, provided that the voltage ramp provides sufficient time for saturation to occur. For operation in a linearly polarized mode, the efficiency could be improved by use of a bifurcated cathode, since the electrons near the RF null of the mode do not efficiently transfer energy to the waves.

An unsuccessful attempt was made to operate at higher output power with the beam located on the third radial maximum of the $TE_{13}$ mode. Since the starting current in this case is approximately twice as high due to the weaker coupling coefficient (see Fig. 6), the failure to observe high-power emission is believed to be related to the inability to achieve high-power oscillation during the short time provided by the Febetron voltage waveform.

### *B. Gas-Breakdown Measurements*

In order to supplement the calibrated time-resolved single-position measurements possible with microwave apertures with a more global view of the microwave emission, a time-integrated gas-breakdown technique was employed. The experimental setup is illustrated in Fig. 9. It is described in detail in [2].

Fig. 10 depicts open-shutter gas-breakdown photographs obtained under conditions corresponding to the data of Fig. 5. Photographs taken at two different ambient pressures in the gas-breakdown cell depict the key features of a linearly polarized $TE_{13}$ mode, with some possible mode impurity from other linearly polarized $TE_{1n}$ modes, most likely the $TE_{12}$ and $TE_{14}$ modes, probably due to mode conversion in the output taper and waveguide. (The small-scale azimuthal structure in the 8-torr discharge is believed to be due to phenomena in the low-pressure gas discharge, and not to reflect information relating to the small-scale structure of the microwave mode pattern.) The importance of the axial cavity slots to the stability of the $TE_{13}$ mode is shown in Fig. 11, which shows two photographs of gas-breakdown mode patterns corresponding to operation with an unslotted cavity under conditions identical to Fig. 10. In Fig. 11(a), the strong presence of a circularly polarized $TE_{13}$ mode is indicated by the appearance of a breakdown maximum on axis. However, on another shot with identical experimental parameters, the pattern in Fig. 11(b) indicates the absence of strong $TE_{13}$ mode content, and, based on data dis-

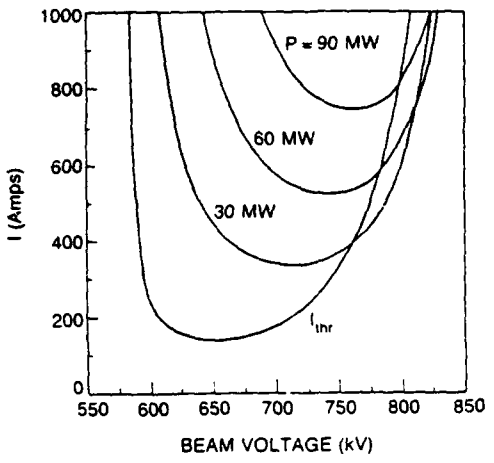



Fig. 8. Starting current and output power as a function of current and voltage for a linearly polarized $TE_{11}$ mode, assuming $B_0$ = 26 kG, $\alpha$ = 1, $r_b/r_w$ = 0.37.

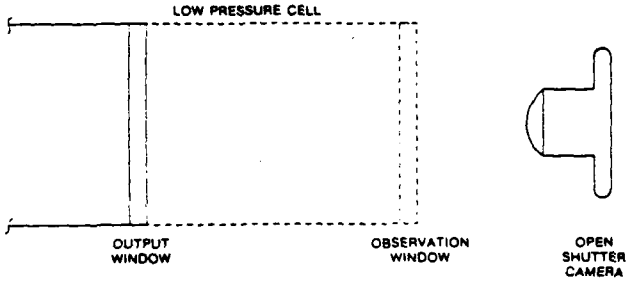
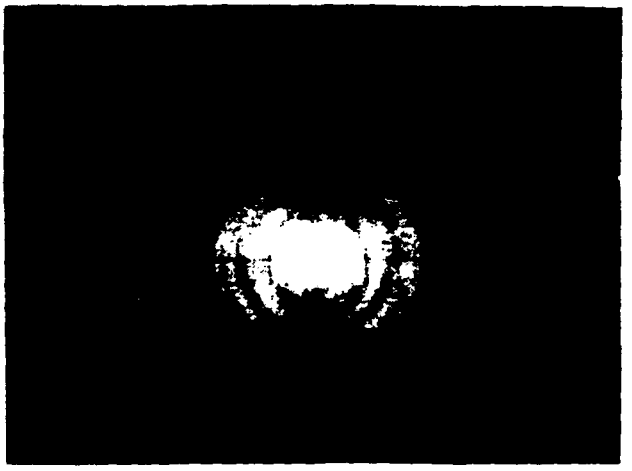


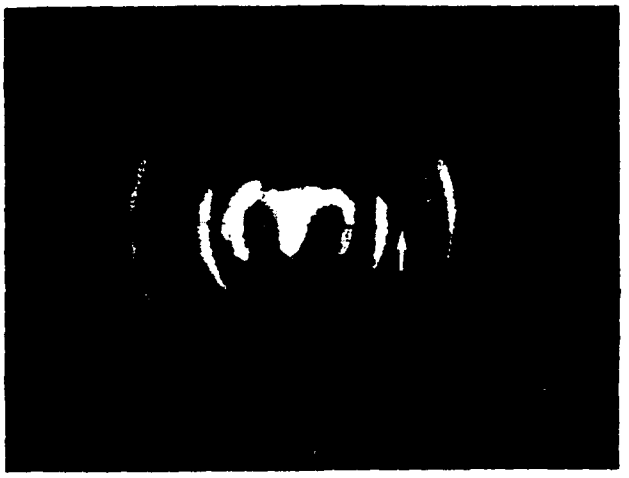

Fig. 9. Experimental setup or air-breakdown photographs of output-mode patterns.

cussed in the next paragraph for the same magnetic field and a larger radius electron beam, probably corresponds to the excitation of a circularly polarized $TE_{42}$ mode. (A comparison of the breakdown patterns of Fig. 11(a) and (b) suggests that there may be $TE_{42}$ as well as $TE_{13}$ mode content in 11(a).) An attempt was made to scan the output mode of the unslotted cavity with microwave pickups, but the large shot-to-shot variation in the 35-GHz emission as a function of radius, apparently due to the mode switching illustrated in Fig. 11, made this impossible to carry out in a systematic manner.

The very crowded mode map shown in Fig. 3 for the unslotted cavity is greatly simplified for a cavity with two large opposing axial slots, since only the $TE_{1n}$ modes remain. For the 45° cavity, an attempt was made to excite the adjacent $TE_{1n}$ modes. A very weak mode with a maximum on axis was observed via gas breakdown at $B_0 \sim$ 16 kG; this is believed to be the $TE_{12}$ mode at ~22 GHz. An unsuccessful attempt was made to observe the $TE_{14}$ mode at ~48 GHz; this attempt was somewhat constrained by the difficulty of operating at $B_0 \sim$ 36 kG, including the somewhat restricted range of magnetic compression ratios that were experimentally accessible. In the absence of the slots, operating at 26.0, 30.7, and 35.5 kG, it was straightforward to demonstrate the $TE_{42}$, $TE_{52}$, and $TE_{62}$ modes (see Fig. 12), at approximately 38,



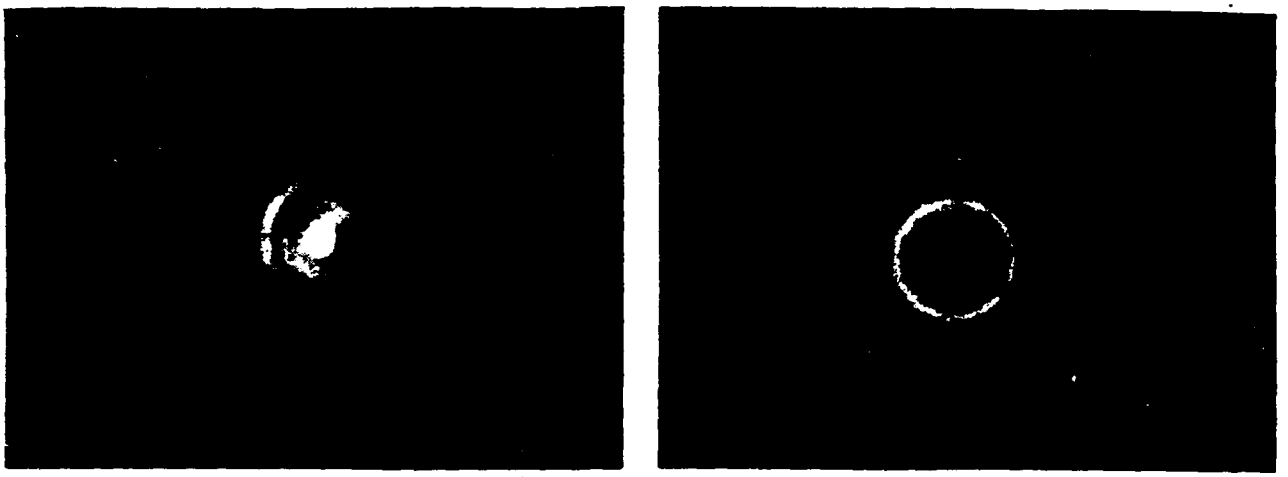
(a)



(b)

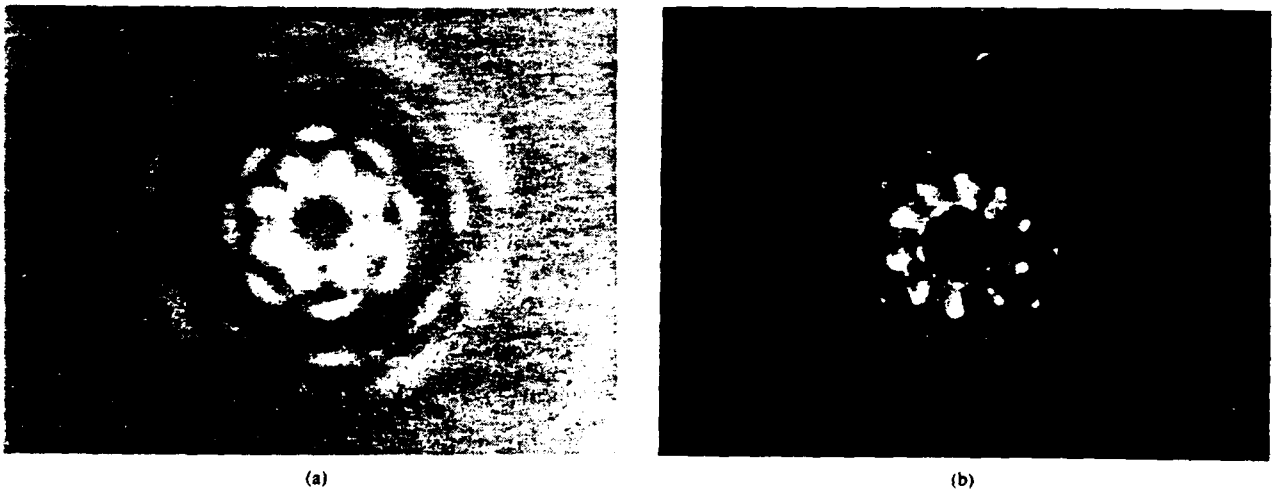
Fig. 10. End-on open-shutter photographs of microwave-induced gas breakdown for $B_0$ = 26 kG and a 2.34-cm-diameter cavity with 45° axial slots, illustrating the observation of a linearly polarized $TE_{11}$ mode at 35 GHz. Pictures are shown at two pressures in the breakdown cell: (a) 8 torr and (b) 75 torr. An arrow indicates the 7-cm radius of the output waveguide. (The outer halo is a reflection produced by the walls of the cylindrical breakdown cell. Crossing vertical and horizontal lines on the window face define the center of the aperture. The horizontal line is divided by centimeter rulings.)

43, and 48 GHz. This was done by producing an output mode with sufficient content of both of the two degenerate circularly polarized components of the specific $TE_{m2}$ mode to produce a strong "standing" component in the output mode pattern. In general, this could be made to occur by employing an electron beam radius that coupled strongly to both circularly polarized components of the specific $TE_{m2}$ mode; specifically, values of $r_h/r_w$ of ~0.60, 0.51, and 0.51, respectively, for these three cases. These observations of $TE_{m2}$ modes are similar to those reported previously in an experiment employing a 3.2-cm-diameter cylindrical cavity [2]. It is believed that the $TE_{72}$ mode was also excited, at ~53 GHz, but the resulting gas-breakdown photographs were less clear-cut than those in Fig. 12, and the difficulty of operating at ~40 kG precluded a detailed evaluation of this mode.

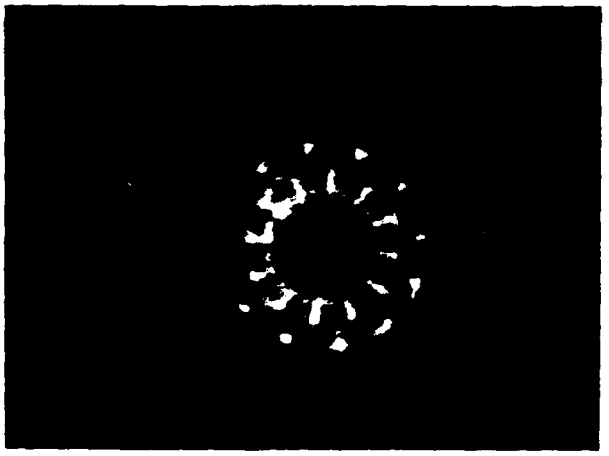


(a) (b)

Fig. 11. End-on open-shutter photographs of microwave-induced gas breakdown for $B_0 = 26$ kG and an unslotted cavity, illustrating the observation of (a) a circularly polarized $TE_{13}$ component at 35 GHz and (b) another $TE_{mn}$ mode with $m \neq 1$.



(a) (b)



(c)

Fig. 12. End-on open-shutter photographs of microwave-induced gas breakdown for (a) $B_0 = 26$ kG, (b) 30.7 kG, and (c) 35.5 kG with an unslotted cavity, illustrating the observation of standing $TE_{42}$, $TE_{52}$, and $TE_{62}$ modes at approximately 38, 43, and 48 GHz.

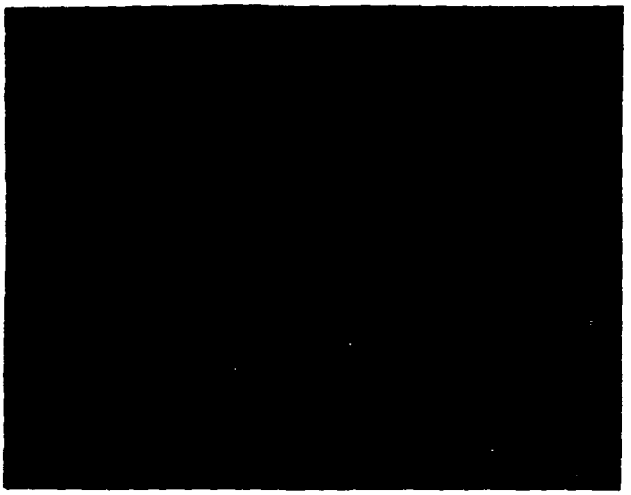


Fig. 13. End-on open-shutter photograph of microwave-induced gas breakdown for $B_0$ = 35.5 kG and a cavity with 33° axial slots, illustrating the observation of a linearly polarized $TE_{62}$ mode at 40 GHz.

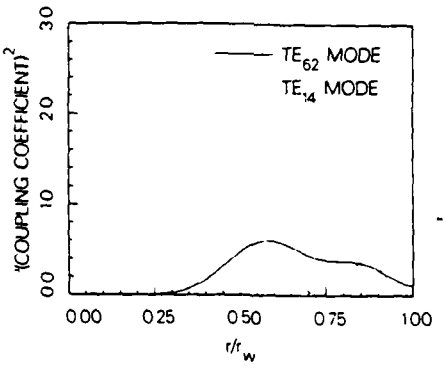



Fig. 14. Plot of the square of the gyrotron coupling coefficient versus normalized cavity radius for linearly polarized $TE_{62}$ and $TE_{14}$ modes. The calculations are performed assuming an azimuthally symmetric annular electron beam.

The width of the opposing axial slots determined the diffractive losses for particular cavity modes. Based on the calculations of cavity $Q$ versus slot angle (see Fig. 4), it was predicted that the 33° slotted cavity would not completely suppress the $TE_{62}$ mode at ~48 GHz. This prediction was confirmed by the observation of a linearly polarized $TE_{62}$ mode at 35.5 kG (see Fig. 13). This mode was completely suppressed by the 45° slotted cavity. Comparison of Fig. 13 with Fig. 12(c) demonstrates the difference between a true linearly polarized $TE_{62}$ mode, and one with a strong "standing" component that is actually elliptically polarized. The reason for the excitation of a linearly polarized $TE_{62}$ mode, rather than of the $TE_{14}$ mode that is almost degenerate in frequency with it, may be inferred from an examination of the coupling coefficients for the two modes as a function of normalized beam radius (see Fig. 14). The accessible compression ratios at 35.5 kG precluded placing the beam on either the central or second peak of the coupling coefficient for the $TE_{14}$ mode. At larger radii, in the range of $r_b/r_w \sim 0.45$–$0.6$, the $TE_{62}$ mode has a larger coupling coefficient, implying a lower starting current, assuming equal $Q$ values for the two modes. In fact, Fig. 4 indicates that for a 33° slotted cavity, the $TE_{62}$ mode has a slightly higher $Q$ value, further favoring this mode. Perhaps most important is the small radial extent of the third peak of the coupling coefficient for the $TE_{14}$ mode compared with the very broad coupling curve for the $TE_{62}$ mode, further favoring the $TE_{62}$ mode for a beam with finite spread in guiding-center radius and, in addition, slight decentering.

In summary, a 35-GHz gyrotron oscillator employing an axially bifurcated cavity has successfully operated in a linearly polarized $TE_{13}$ mode at a peak power of 35 MW with 6-percent efficiency. By comparison, an earlier $TE_{62}$ experiment at the same frequency in an unslotted cavity achieved 100 MW at 8-percent efficiency [2]. The effect of the slots on mode competition with the nearby $TE_{42}$ mode has been calculated and demonstrated experimentally, via air breakdown photographs from slotted and unslotted cavities. The unslotted cavity has been operated at high power in $TE_{42}$, $TE_{52}$, and $TE_{62}$ modes at 38, 43, and 48 GHz. A 33° slotted cavity has been shown to support a linearly polarized $TE_{62}$ mode, while 45° slots have been shown to suppress this mode, in agreement with calculations based on the theory of McDonald *et al.* [3].

## Acknowledgment

The authors gratefully acknowledge the assistance of Dr. J. Finn, who provided the computer code used to perform the slotted-cavity $Q$ calculations, and who assisted in its operation.

## References

[1] S. H. Gold *et al.*, "High voltage $K_a$-band gyrotron experiment," *IEEE Trans. Plasma Sci.*, vol. PS-13, pp. 374–382, 1985.

[2] S. H. Gold *et al.*, "High peak power $K_a$-band gyrotron oscillator experiment," *Phys. Fluids*, vol. 30, pp. 2226–2238, 1987.

[3] S. W. McDonald, J. M. Finn, M. E. Read, and W. M. Manheimer, "Boundary integral method for computing eigenfunctions in slotted gyrotron cavities of arbitrary cross-sections," *Int. J. Electron.*, vol. 61, pp. 795–822, 1986.

[4] N. S. Ginzburg, V. I. Krementsov, M. I. Petelin, P. S. Strelkov, and A. G. Shkvarunets, "Cyclotron-resonance maser with a high-current relativistic electron beam," *Pis'ma Zh. Tekh. Fiz.*, vol. 4, pp. 149–153, 1978; also, *Sov. Tech. Phys. Lett.*, vol. 4, pp. 61–62, 1978.

[5] N. S. Ginzburg, V. I. Krementsov, M. I. Petelin, P. S. Strelkov, and A. K. Shkvarunets, "Experimental investigation of a high-current relativistic cyclotron maser," *Zh. Tekh. Fiz.*, vol. 49, pp. 378–385, 1978; also, *Sov. Phys.—Tech. Phys.*, vol. 24, pp. 218–222, 1979.

[6] S. N. Voronkov, V. I. Krementsov, P. S. Strelkov, and A. G. Shkvarunets, "Stimulated cyclotron radiation at millimeter wavelengths from high-power electron beams," *Zh. Tekh. Fiz.*, vol. 52, pp. 106–108, 1982; also, *Sov. Phys.—Tech. Phys.*, vol. 27, pp. 68–69, 1982.

[7] V. V. Bogdanov *et al.*, "Measurements of millimeter-range cyclotron radiation induced by a high-current electron beam," *Zh. Tekh. Fiz.*, vol. 53, pp. 106–113, 1983; also, *Sov. Phys.—Tech. Phys.*, vol. 28, pp. 61–65, 1983.

[8] A. W. Fliflet and M. E. Read, "Use of weakly irregular waveguide theory to calculate eigenfrequencies, Q values, and RF field functions for gyrotron oscillators," *Int. J. Electron.*, vol. 51, pp. 475–484, 1981.

[9] A. T. Lin *et al.*, "Simulation of transient behavior in a pulse-line-driven gyrotron oscillator," *IEEE Trans. Plasma Sci.*, this issue, pp. 135–141.

[10] J. S. Levine, "Rippled wall mode converters for circular waveguide," *Int. J. Infrared Millimeter Waves*, vol. 5, pp. 937–952, 1984.

[11] A. W. Fliflet, M. E. Read, K. R. Chu, and R. Seeley, "A self-consistent field theory for gyrotron oscillators: Application to a low Q gyromonotron," *Int. J. Electron.*, vol. 53, pp. 505–521, 1982.

# APPENDIX I

## Review of the Tenth International Free Electron Laser Conference (Jerusalem, August 29-September 2, 1988)

# Review of the Tenth International Free Electron Laser Conference (Jerusalem, August 29–September 2, 1988)

The series of international Free Electron Laser (FEL) conferences that was initiated under the sponsorship of the U.S. Office of Naval Research (ONR) some ten years ago has developed into the most important forum for reporting research results and applications of the promising new FEL technology. The tenth conference in the series was jointly sponsored by ONR, the U.S. Air Force European Office of Aerospace Research and Development, Tel Aviv University, the Weizmann Institute of Science, the Israel Academy of Sciences and Humanities and the Israel Ministry of Science and Development. The participants in the conference represented eleven countries including the United States, Israel, the major countries of Western Europe, Austria, Poland, Japan, and the People's Republic of China. Over one hundred papers were presented.

One highlight was the scientific progress reported by the Los Alamos National Laboratory (LANL) with a high power, r.f. linac driven FEL including generation of ~400 MW of peak power at $\lambda = 10.6$ μm with over 4% efficiency. Fractional linewidth was less than 0.2%, near the limit determined by the pulse length of the electron beam, and sidebands were found to be readily suppressed by detuning. Experimental results on the use of a Littow grating in the cavity to successfully suppress sidebands was also reported.

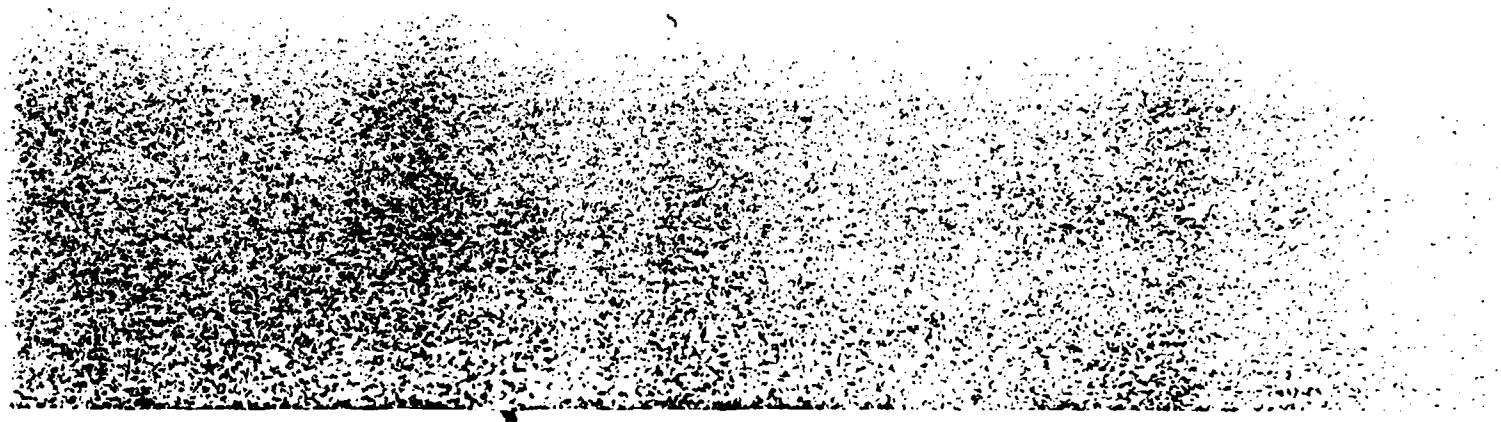
*Comments Plasma Phys. Controlled Fusion*
1989, Vol. 12, No. 4, pp. 217–222
Reprints available directly from the publisher
Photocopying permitted by license only

© 1989 Gordon and Breach.
Science Publishers, Inc.
Printed in Great Britain

Initial performance of the 10.6 μm, 45 MeV, induction linac driven FEL at the Lawrence Livermore National Laboratory (LLNL) was also reported. T. Meyer of the U.S. Strategic Defense Initiative Organization (SDIO) described the groundbased FEL planned for construction at White Sands, New Mexico and reported that a decision between deploying an r.f. linac or induction linac system would be made in the coming year.

The University of California at Santa Barbara (UCSB) reported on the early operation of a user facility employing a submillimeter wavelength FEL driven by an electrostatic accelerator; experimental studies in material science, biology and medicine are underway. Reports were presented on plans for similar user facilities at the FOM-Institute for Plasma Physics in the Netherlands, at the Weizmann Institute in Israel, at the University of Central Florida and at the National Bureau of Standards. Opportunities for FEL applications in medical research were described by C. Houston of the SDIO and A. Louis of the Hebrew University of Jerusalem. A. Lumpkin of LANL described application of FELs to research on high temperature superconductors.

Another application of FELs which was discussed was electron heating in magnetic fusion plasmas; this application requires megawatts of average power at a wavelength of about 1 mm. The leading candidate for this application to date is the CW gyrotron; FELs are of interest since they scale well to submillimeter wavelengths, are tunable and may be capable of very high average power per source. LLNL reported on progress in developing a repetitively pulsed (5 kHz), induction linac driven FEL for this application. The LLNL approach involves the production of gigawatt-level peak powers using a multi-kiloampere, 10 MeV electron beam. The University of Maryland presented a very different FEL design, involving a short-period wiggler (micro-wiggler), and a sheet electron beam, which would allow for driving the FEL with an inexpensive, conventional, d.c. power supply. Micro-wiggler development work was also presented by MIT and by the University of Tel Aviv. By reducing the beam energy (Doppler upshift) needed to operate at a given wavelength, such wigglers could significantly reduce the cost and shielding requirements of the electron accelerator. Several groups reported plans to investigate the use of electromagnetic wigglers to increase the FEL operating frequency.



ıe 10.6 μm, 45 MeV, induction linac
Livermore National Laboratory (LLNL)
ɔr of the U.S. Strategic Defense Initi-
lescribed the groundbased FEL planned
ands, New Mexico and reported that a
; an r.f. linac or induction linac system
ing year.

nia at Santa Barbara (UCSB) reported
user facility employing a submillimeter
y an electrostatic accelerator; experi-
ience, biology and medicine are under-
ed on plans for similar user facilities at
ma Physics in the Netherlands, at the
el, at the University of Central Florida
ı of Standards. Opportunities for FEL
arch were described by C. Houston of
the Hebrew University of Jerusalem.
ɔribed application of FELs to research
ɔnductors.

ELs which was discussed was electron
lasmas; this application requires mega-
wavelength of about 1 mm. The leading
on to date is the CW gyrotron; FELs
ale well to submillimeter wavelengths,
pable of very high average power per
progress in developing a repetitively
linac driven FEL for this application.
ɔs the production of gigawatt-level peak
ımpere, 10 MeV electron beam. The
esented a very different FEL design,
ɡgler (micro-wiggler), and a sheet elec-
low for driving the FEL with an inex-
power supply. Micro-wiggler devel-
ɔnted by MIT and by the University of
ɔam energy (Doppler upshift) needed
ɔngth. such wigglers could significantly
ng requirements of the electron accel-
ɔrted plans to investigate the use of
increase the FEL operating frequency.

Experiments on gyrotron powered electromagnetic wigglers were reported by MIT.

The conference included several papers on an FEL-like Cyclotron Resonance Maser configuration called the Cyclotron Auto-Resonance Maser (CARM). The CARM is of interest as a multimegawatt source of millimeter and submillimeter wavelength radiation based on a 0.5–1.5 MeV beam. Planned experimental studies of the CARM, which is also a candidate for the plasma heating application, were described by MIT and by the Naval Research Laboratory (NRL). The MIT experiments include 35 GHz and 140 GHz CARM amplifiers. The 35 GHz experiment is configured as an amplifier with r.f. input supplied by a 100 kW magnetron and based on a 1.5 MeV, 5–300 A beam obtained by emittance filtering a 20 kA beam from a field emission diode. The 140 GHz experiment will use thermionic cathode technology at voltages up to 700 kV. A 100 GHz CARM oscillator experiment based on a 600 kV, 200 A, 70 ns pulsed electron beam is in preparation at NRL, and a 250 GHz oscillator experiment based on a 500 kV thermionic cathode electron gun is also planned.

B. Newnam of LANL presented a paper on applications of FELs operating at UV wavelengths (below 300 nm). Most of these applications, which include investigation of atomic and molecular spectroscopy, surface physics, and biological structures, will require very low levels of FEL amplitude and phase noise. M. E. Couprie of LURE (Orsay, France), who had just returned from Novosibirsk, reported on an FEL driven by the VEPP-3 storage ring which had achieved lasing over the wavelength range 1000–5000 Å; this Soviet result using an optical-klystron configuration is believed to be the shortest wavelength operation of an FEL to date. Other optical klystron experiments, planned or in progress, were described by LURE and by the Brookhaven National Laboratory. Ongoing harmonic FEL studies to achieve coherent, vacuum UV radiation were described by Stanford University. Planned studies of harmonic FEL operation at millimeter wavelengths were described by NRL.

L. Shengang of the University of Electronic Science and Technology of China in Chengdu reported on two experimental FEL projects. One was a 35 GHz, pulse line accelerator driven FEL amplifier with a helical wiggler and an axial magnetic guide field.

The beam voltage is 700 kV and the current is 500 A. An Extended Interaction Oscillator provides the input signal via a quasi-optical input coupler. A peak power of 1.5 MW with 47 dB gain at 2% efficiency was reported. Multi-frequency output including superradiant emission at 37.5 GHz was observed. The other project is a Compton FEL driven by a 22 MeV r.f. linac upgraded for FEL research with a peak current of 0.5 A and a 1 μs macropulse. Operation at 10 μm is expected by 1990.

J. M. Buzzi of the École Polytechnique (Palaiseau, France) also reported on a very carefully designed, millimeter-wave FEL driven by the electron beam from a pulse line accelerator. Continuous tunability from 75 GHz to 270 GHz was demonstrated at an output power level of almost 10 MW. At 120 GHz, 20% efficiency was achieved, which is unusually high for an FEL with an untapered wiggler magnet.

K. Mima of the Institute for Laser Engineering in Osaka, Japan reported on the development of a 6 MeV, 10 kA induction linac for FEL research. Beam energy variation is designed to be <3% during the 70 ns pulse. Initial FEL experiments at reduced voltage and currents have produced ~1 MW at a wavelength of ~1 mm. Planned experiments include a 498 μm amplifier driven by a $CH_2F$ laser, and development of a UV source using a $CO_2$-laser-driven electromagnetic wiggler.

An interesting scientific controversy arose concerning the degree of coherence in the UCSB submillimeter FEL. It had been previously reported that with a 5 μs electron pulse, this FEL had operated with a single longitudinal mode having a fractional linewidth in the range $10^{-7}$–$10^{-8}$. However, at the Jerusalem conference, the University of Maryland group reported on a theoretical study of the competition between modes (with the same quality factor, $Q$) in low gain FEL oscillators. The results of this investigation showed that for such FELs to operate at a single frequency, the electron beam current must be less than four times minimum start oscillation current.[1,2] In addition, the calculations indicate that for a long pulse, low gain, FEL oscillator to operate at a single frequency at the maximum efficiency, the electron beam current should be roughly three times the minimum start-oscillation current,[1] and the last few percent of the voltage pulse rise should approach the designed value sufficiently slowly in time.[3] If one

<V and the current is 500 A. An Extended
ovides the input signal via a quasi-optical
ower of 1.5 MW with 47 dB gain at 2%
Multi-frequency output including super-
GHz was observed. The other project is
by a 22 MeV r.f. linac upgraded for FEL
irrent of 0.5 A and a 1 μs macropulse.
spected by 1990.
le Polytechnique (Palaiseau, France) also
lly designed, millimeter-wave FEL driven
om a pulse line accelerator. Continuous
270 GHz was demonstrated at an output
MW. At 120 GHz, 20% efficiency was
ally high for an FEL with an untapered

e for Laser Engineering in Osaka, Japan
nent of a 6 MeV, 10 kA induction linac
energy variation is designed to be <3%
itial FEL experiments at reduced voltage
ed ~1 MW at a wavelength of ~1 mm.
ade a 498 μm amplifier driven by a $CH_2F$
f a UV source using a $CO_2$-laser-driven

controversy arose concerning the degree
B submillimeter FEL. It had been pre-
h a 5 μs electron pulse, this FEL had
igitudinal mode having a fractional line-
$10^{-8}$. However, at the Jerusalem con-
Maryland group reported on a theoret-
n between modes (with the same quality
L oscillators. The results of this inves-
ch FELs to operate at a single frequency,
must be less than four times minimum
In addition, the calculations indicate
ain, FEL oscillator to operate at a single
n efficiency, the electron beam current
mes the minimum start-oscillation cur-
rcent of the voltage pulse rise should
lue sufficiently slowly in time.[3] If one chooses the electron beam characteristics to assure FEL operation in the stable region, the theoretical model predicts that the time scale for stable satellites to decay scales as $\epsilon^{-2}$, where $\epsilon = (v_g/v_b - 1)$ is the slippage parameter ($v_g$ is the group velocity of the radiation and $v_b$ is the electron beam velocity).[2] Thus, for small slippage parameters the time required to reach true single mode operation is long.

Furthermore, numerical simulation showed that the satellites do not perturb the amplitude of the radiation field, only its phase.[3] The results of the theoretical investigation have been extrapolated to model the UCSB FEL experiment,[4] for which $\epsilon \simeq 4.2 \times 10^{-3}$. It turns out that the time scale for stable satellites to decay is much longer than the pulse length in the UCSB experiment (5 μs). Thus, one would not expect single mode operation to be reached. The multimode simulations show that the spectrum is still rather broad (about 130 modes or relative bandwith 0.13%) at a time corresponding to the end of the beam pulse (5 μs). In fact, the estimates indicate[2] that for relative bandwidth to be of the order $10^{-6}$ the pulse duration in the UCSB experiment should be of the order $10^{-2}$ s.

The major experimental evidence offered by UCSB for single mode operation is the absence of strong amplitude modulation in temporal behavior of the FEL output signal averaged over a period of time short compared with the inverse of the frequency difference of adjacent modes but long compared with the wave period. The University of Maryland theory predicts that the long-lived satellites produce no perturbation in this quantity, and thus, their presence would be undetected. The simulation shows that at the end of the electron beam pulse (in the UCSB experiment) the amplitude of the radiation signal is relatively constant, while the phase is strongly modulated. Thus, inference of single mode operation based on the absence of strong amplitude fluctuations may be unjustified; what is required experimentally to resolve this controversy is direct measurement of the spectrum.

In summary, the Jerusalem conference revealed FELs as a maturing technology with unique capabilities over a huge wavelength span from UV to mm waves. Generally, power, efficiency and tunability are superior to other coherent radiation sources, but questions concerning the degree of coherence which is achievable

remain to be answered. FEL applications are at hand in medical and materials research. Potential applications in the future range from deployment in ballistic missile defense systems to deployment in controlled thermonuclear reactors.

V. L. GRANATSTEIN
*Laboratory for Plasma Research,*
*University of Maryland,*
*College Park, Maryland 20742*

A. W. FLIFLET
*Plasma Physics Division,*
*Naval Research Laboratory,*
*Washington, D.C. 20375*

B. LEVUSH and T. M. ANTONSEN, JR.
*Laboratory for Plasma Research,*
*University of Maryland,*
*College Park, Maryland 20742*

Received November 15, 1988
Contributed by E. Ott

**References**

1. Ya. L. Bogonolov, V. L. Bratman, N. S. Ginzburg, M. I. Petelin and A. D. Yanakovsky, Opt. Comm. **36**, 109 (1981).
2. T. Antonsen, Jr. and B. Levush, Phys. of Fluids, submitted 1988.
3. T. Antonsen, Jr. and B. Levush, Phys. Rev. Lett., submitted 1988.
4. L. R. Elias, G. Ramain, J. Hu and A. Amir, Phys. Rev. Lett. **75**, 424 (1986).

# APPENDIX J

## The Effect of the Time-Dependent Self-Consistent Electrostatic Field on Gyrotron Operation

# The effect of the time-dependent self-consistent electrostatic field on gyrotron operation

Robert G. Kleva, Thomas M. Antonsen, Jr., and Baruch Levush
*Laboratory for Plasma and Fusion Energy Studies, University of Maryland, College Park, Maryland 20742*

(Received 14 July 1987; accepted 12 October 1987)

The time-dependent self-consistent electrostatic field is shown to have a deleterious effect on gyrotron operation. As the electron beam density increases, the nonlinear efficiency is seriously degraded by the self-electrostatic field. Time-dependent multimode simulations demonstrate that at sufficiently large beam densities the electron cyclotron instability is quenched and the oscillation will not start. Contrary to previous investigations, electrostatic effects do not necessarily increase the linear growth rate of the electromagnetic cavity mode and, depending on the beam density, electrostatic effects can actually stabilize the mode. Typically, however, considerations of linear theory are not important in an overmoded, open resonator gyrotron because the system evolves nonlinearly into a state consisting of a single mode which is linearly stable, but nonlinearly the most efficient mode.

## I. INTRODUCTION

In recent years there has been a great deal of interest in the use of gyrotrons (electron cyclotron masers) for the efficient generation of short wavelength coherent radiation.[1,2] Conventional closed cavity gyrotrons have generated high power radiation at centimeter wavelengths. However, at millimeter and submillimeter wavelengths conventional gyrotrons are inadequate because the power level is limited as the cavity dimensions decrease. Conversely, if one attempts to maintain a high power level by generating the radiation in a cavity whose dimensions are much larger than a wavelength, then the presence of a dense spectrum of nearby modes makes it difficult to operate the gyrotron coherently in a single mode. The open-resonator quasioptical gyrotron is one possible solution to this dilemma.[3] The large diffraction losses suffered by the higher-order transverse modes in this open-cavity configuration lead to a mode spectrum that is essentially one-dimensional rather than three-dimensional. As a result, coherent single-mode operation at a short wavelength which is independent of the dimensions of the cavity becomes feasible.[4,5]

The electromagnetic radiation in gyrotrons is produced by the azimuthal bunching of electrons in their gyro-orbits. In addition to the electromagnetic radiation, this charge bunching also generates electrostatic fields.[6-13] In this paper we examine the nonlinear effects of the electrostatic field on gyrotron operation. Our conclusions are as follows.

(i) As the beam density increases, the nonlinear efficiency is seriously degraded because of self-electrostatic effects.

(ii) The time required for the electron cyclotron wave to saturate increases with increasing beam density, and the mode amplitude at saturation decreases.

(iii) At sufficiently large beam densities, the electron cyclotron instability is quenched and the oscillation will not start.

(iv) When the frequency mismatch is very small and the magnetic field is not tapered, the electrostatic field can sometimes actually enhance the efficiency by creating a more favorable resonance condition between the electrons and the cavity mode.

(v) Considerations of linear theory are not important in overmoded gyrotrons where the mode spectrum is dense. Typically, the system evolves nonlinearly into a state consisting of a single mode which is linearly stable. Linear theory may be relevant to operation near the lowest-order fundamental mode in a closed cavity gyrotron where the mode spectrum is sparse.

(vi) Contrary to previous results,[10-12] electrostatic effects do not necessarily increase the linear growth rate. Depending on the beam density, electrostatic effects may actually result in linear stabilization at frequencies which are otherwise unstable.

The remainder of this paper is organized as follows. In Sec. II we incorporate the effect of the self-electrostatic field in a set of model gyrotron equations. The linear and nonlinear efficiency with which the electrons transfer their energy to a single electromagnetic wave is calculated in Secs. III and IV, respectively. In Sec. V we present the results of self-consistent, time-dependent, multimode simulations of gyrotrons which include the self-electrostatic field. We summarize and discuss our results in Sec. VI.

## II. MODEL EQUATIONS

Consider the open-resonator gyrotron configuration illustrated in Fig. 1. The electron beam propagates along the external magnetic field $\mathbf{B}_0$ in the $z$ direction transverse to the

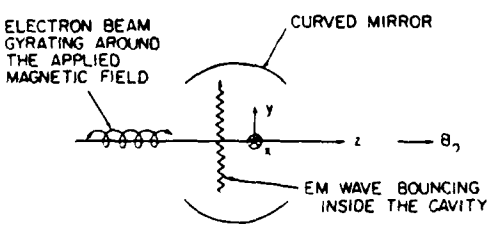



FIG. 1. Quasioptical gyrotron.

 0031-9171/88/020375-12$01.90 © 1988 American Institute of Physics 

direction of electromagnetic wave propagation. The electromagnetic wave is characterized by a vector potential $A_\perp$ which lies in the $x$ direction and the electrostatic wave is described by the scalar potential $\Phi$.

Approximate equations of motion for the electrons can be derived using a multiple time scale formulation in which the wave frequency is taken to be near the gyrofrequency. Then, the higher harmonics provide only a small amplitude, rapid oscillation on a gyroperiod time scale $t_0$ to quantities which otherwise vary slowly on a long time scale $t_1$. Averaging the equations of motion over a gyroperiod, one finds that on the slow time scale $t_1$ the equations can be written in Hamiltonian form[11]:

$$\frac{d\mu}{dt_1} = \frac{\partial H}{\partial \phi}, \tag{1a}$$

$$\frac{d\phi}{dt_1} = -\frac{\partial H}{\partial \mu}, \tag{1b}$$

$$\frac{dp_z}{dt_1} = -\frac{\partial H}{\partial z}, \tag{1c}$$

$$\frac{dz}{dt_1} = \frac{\partial H}{\partial p_z} = \langle v_z \rangle, \tag{1d}$$

where

$$\mu = mu_\perp^2/2\Omega_0 \tag{2}$$

is the magnetic moment with $\Omega_0 = qB_0/mc$ the nonrelativistic gyrofrequency, $u_\perp = \gamma v_\perp$, $u_z = \gamma v_z$, the relativistic factor $\gamma = [1 + (u_\perp^2 + u_z^2)/c^2]^{1/2}$, the canonical momentum $p_z = mu_z$, and $\phi$ is an angle related to the phase angle $\xi$ by

$$\phi = \xi + \omega t, \tag{3}$$

with $\omega = k_y c$ the electromagnetic wave frequency. The Hamiltonian $H$ is given by

$$H = \bar{\gamma} mc^2 + \langle q\Phi \rangle - \omega\mu, \tag{4}$$

with

$$\bar{\gamma} = \left[1 + \frac{1}{mc^2}\left(2\Omega_0\mu - 2\frac{q}{c}\langle \mathbf{u}_\perp \cdot \mathbf{A}_\perp \rangle + \frac{1}{m}u_z^2\right)\right]^{1/2}, \tag{5}$$

$\Phi$ the electrostatic potential and the angular bracket $\langle \cdot \rangle$ indicates a time average over the gyroperiod $T = 2\pi\gamma/\Omega_0$,

$$\langle g \rangle = \oint \frac{dt_0\,\Omega_0}{2\pi\gamma} g. \tag{6}$$

The perpendicular momentum $\mathbf{u}_\perp$ can be written in terms of the gyroangle $\xi$ as

$$\mathbf{u}_\perp = u_\perp(\hat{x}\cos\xi + \hat{y}\sin\xi). \tag{7}$$

### A. Electrostatic potential

The electrostatic potential $\Phi$ is described by Poisson's equation

$$\nabla_\perp^2 \Phi = -4\pi q \int d^3u\, f\left(\mathbf{x} + \frac{\mathbf{u}_\perp \times \hat{z}}{\Omega_0}, \mu, \phi, u_z, t_1\right), \tag{8}$$

where

$$\mathbf{x}_{\perp 0} = \mathbf{x}_\perp + \mathbf{u}_\perp \times \hat{z}/\Omega_0 \tag{9}$$

is the guiding center position and $f$ is the distribution function of guiding centers. Here we have assumed that the Laplacian operator is dominated by derivatives in the plane transverse to the direction of the beam and the applied magnetic field. This assumption is valid provided the beam thickness is smaller than the axial scale length over which quantities vary. Equation (8) can be inverted by means of the two-dimensional Green's function

$$G(\mathbf{x}_\perp, \mathbf{x}_\perp') = (1/2\pi)\ln|(\mathbf{x}_\perp - \mathbf{x}_\perp')/a|,$$

which is the solution of

$$\nabla_\perp^2 G(\mathbf{x}_\perp, \mathbf{x}_\perp') = \delta(\mathbf{x}_\perp - \mathbf{x}_\perp')$$

and where $a$ is an arbitrary scale length. In terms of the Green's function, the potential $\Phi$ can be written as

$$\Phi(\mathbf{x}_\perp) = -2q \int d^2\mathbf{x}_\perp' \int d^3u' \ln\left|\frac{\mathbf{x}_\perp - \mathbf{x}_\perp'}{a}\right| f(\mathbf{x}_{\perp 0}'). \tag{10}$$

Performing the fast time scale average indicated in Eq. (6) and using Eqs. (3), (7), and (9), one finds that

$$\langle q\Phi(\mathbf{x}_{\perp 0})\rangle = -2q^2 \int d^2\mathbf{x}_{\perp 0}' \int d^3u' \times f(\mathbf{x}_{\perp 0}', \mu', \phi', u_z', t_1) \times \oint \frac{dt_0\,\Omega_0}{2\pi\gamma} \ln\left|\frac{\mathbf{x}_{\perp 0} - \mathbf{x}_{\perp 0}' - \Delta}{a}\right|, \tag{11}$$

where

$$\Delta = [\mathbf{u}_\perp(\phi - \Omega t_0) - \mathbf{u}_\perp'(\phi' - \Omega t_0)] \times \hat{z}/\Omega_0. \tag{12}$$

Consider now a distributed beam, that is, one which is much wider than a gyroradius:

$$w \gg \rho_e,$$

where $\rho_e$ is the electron gyroradius. We assume that the distribution function varies on a scale length of $w \gg \rho_e$ in response to the electromagnetic field. In doing this we ignore the possibility of the excitation of higher harmonic electrostatic Bernstein modes which produce variations in the distribution function on the scale of a gyroradius.[6,12-14] In the simulations of Ref. 14 it was found that the fundamental mode with $\omega \simeq \Omega/\gamma_0$ with the longest scale length grew to largest amplitude. Our analysis retains only this fundamental mode. We evaluate $\langle q\Phi(x_{\perp 0})\rangle$ by taking the guiding center distribution function $f$ to be constant within a distance $R$ of $\mathbf{x}_{\perp 0}$ and zero for $|\mathbf{x}_{\perp 0}' - \mathbf{x}_{\perp 0}| > R$, where $w > R > \rho_e$. If the resulting expression is independent of $R$ (and hence $w$), then we can treat the interaction as local in the transverse coordinates.

For a distributed beam, Eq. (11) for $\langle q\Phi(\mathbf{x}_{\perp 0})\rangle$ becomes

$$\langle q\Phi(\mathbf{x}_{\perp 0})\rangle = -2q^2 \int d^3u' f \oint \frac{dt_0\,\Omega_0}{2\pi\gamma} I, \tag{13}$$

where

$$I \equiv \int_0^{2\pi} \int_0^R d^2\mathbf{s} \ln\left|\frac{\mathbf{s} + \Delta}{a}\right| \tag{14}$$

and $\mathbf{s} \equiv \mathbf{x}_\perp' - \mathbf{x}_{\perp 0}$. After a transformation of variables from $\mathbf{s}$ to $\mathbf{s}' = \mathbf{s} + \Delta$,

$$I=\int_0^{2\pi} d\theta' \int_0^{R_*(\theta')} s'\,ds' \ln\left|\frac{s'}{a}\right|, \tag{15}$$

where $R_*(\theta')$ is given by

$$(R_* \cos\theta' - \Delta)^2 + (R_* \sin\theta')^2 = R^2 \tag{16}$$

(see Fig. 2) and $\Delta = |\Delta|$. Equation (16) can be solved to yield

$$R_*(\theta') = (R^2 - \Delta^2 \sin^2\theta')^{1/2} + \Delta\cos\theta' . \tag{17}$$

After performing the integration over $s'$, one finds that Eq. (15) becomes

$$I=\frac{1}{4}\int_0^{2\pi} d\theta'\, R_*^2(\theta')\ln\frac{R_*^2(\theta')}{R^2} + \frac{1}{4}R^2\left(\ln\frac{R^2}{a^2}-1\right). \tag{18}$$

Since the second term on the right-hand side of Eq. (18) does not depend on $\mu$ or $\phi$, it will not contribute to the equations of motion and can be neglected. After inserting Eq. (17) for $R_*(\theta')$ into Eq. (18) and expanding in $\Delta/R \sim \rho_e/R \ll 1$, one can perform the integral over $\theta'$ in Eq. (18) to obtain

$$I=\pi\Delta^2/2 + \theta(1/R), \tag{19}$$

where from Eqs. (12), (7), and (3),

$$\Delta^2 = [u_\perp^2 + u_\perp'^2 - 2u_\perp u_\perp' \cos(\phi-\phi')]/\Omega_0^2 . \tag{20}$$

Inserting expression (19) for $I$ into Eq. (13) for $\Phi$ and performing the now trivial integration over $t_0$, one finds that, for large $R$,

$$\langle q\Phi(\mathbf{x}_{\perp 0})\rangle = -\frac{2\pi q^2}{m\Omega_0}\int d^3u' \times f[\mu+\mu' - (2\mu\mu')^{1/2}\cos(\phi-\phi')], \tag{21}$$

where we have used expression (2) for $\mu$. Expression (21) for $\Phi$ is indeed independent of $R$ for $R \gg \rho_e$ and, therefore, the interaction is local. Thus, in our distributed beam model, electrons interact if their guiding centers coincide. The strength of the interaction is proportional to the local electron density. In our equations we will take this local density to be a parameter.

Other beam models lead to the following expressions for the average potential. If the beam is a sheet beam with all guiding centers lying in a plane, we find

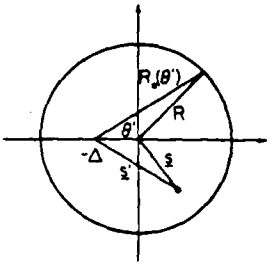



FIG. 2. Transformation of variables from $s$ to $s' = s + \Delta$ in the calculation of the electrostatic potential.

$$\langle q\Phi\rangle = -4\int dy_0' \int d^3u' f q^2 \Delta .$$

If the beam is a pencil beam with all guiding centers on a line, we find

$$\langle q\Phi\rangle = -2\int d^2x_0' \int d^3u' f q^2 \ln\Delta .$$

In the linear regime, where the beam is weakly bunched in gyroangle, all three situations give qualitatively the same potential. However, nonlinearly the pencil and sheet beam have higher harmonic content in gyroangle. We will consider only the distributed beam case because it is significantly easier to implement numerically.

### B. Equations of motion

The lowest-order electromagnetic mode in the open-resonator configuration is the $TEM_{00}$ Gaussian mode for which the vector potential $\mathbf{A}_\perp$ at the beam can be written in the form

$$\mathbf{A}_\perp = \hat{\mathbf{x}} A(z,t_1)\sin\omega t_0 , \tag{22}$$

where

$$A(z,t_1) = \pi^{-1/2}\exp[-(z/r_0)^2]\,\bar{A}(t_1) .$$

Here, $\bar{A}(t_1)$ is a slowly varying amplitude and $r_0$ is the spot size. We are restricting ourselves here to a single mode $\omega$. The generalization to many modes in an overmoded cavity is given in Sec. V. The beam has been taken to be centered between the mirrors with a sufficiently narrow width $w \ll \lambda$. The Gaussian axial profile of Eq. (22) is also an appropriate model for closed cavity gyrotrons.

To derive the equations of motion for the electrons we need to evaluate the fast time scale average $\langle \mathbf{u}_\perp \cdot \mathbf{A}_\perp\rangle$ with $\omega \simeq \Omega_0/\gamma$. Using Eqs. (22), (7), and (3) and averaging over a gyroperiod $(\Omega_0/\gamma)^{-1} \simeq \omega^{-1}$, we find that

$$\langle \mathbf{u}_\perp \cdot \mathbf{A}_\perp\rangle = \tfrac{1}{2} u_\perp \sin\phi A(z,t_1) . \tag{23}$$

The equations of motion can now be obtained by taking the appropriate derivatives of the Hamiltonian given by Eqs. (4) and (5) with Eq. (21) for $\Phi$ and Eq. (23) for $\mathbf{A}_\perp$. The result is

$$\frac{d}{dt_1}u_\perp = \frac{q}{2m}[\cos\phi(E_x + E_\phi^s) + \sin\phi\, E_\phi^c], \tag{24a}$$

$$\frac{d}{dt_1}\phi = \omega - \frac{\Omega_0}{\gamma} + \frac{1}{2}\frac{\omega_p^2}{\Omega_0} + \frac{q}{2mu_\perp} \times [\cos\phi\, E_\phi^c - \sin\phi(E_x + E_\phi^s)], \tag{24b}$$

where

$$E_x = -(\omega/c)A(z,t_1)$$

is the electromagnetic component of the electric field and $E_\phi^s$ and $E_\phi^c$ are electrostatic contributions to the electric field:

$$E_\phi^s = \frac{m}{q}\frac{\omega_p^2}{\Omega_0}\int d^3u'\, u_\perp' \sin\phi' f, \tag{25a}$$

$$E_\phi^c = -\frac{m}{q}\frac{\omega_p^2}{\Omega_0}\int d^3u'\, u_\perp' \cos\phi' f. \tag{25b}$$

In Eqs. (24) and (25) we have introduced the plasma frequency

$$\omega_p^2 = 4\pi q^2 n_0/m ,$$

where $n_0$ is the local beam density, and we have changed the normalization of the distribution function so that

$$\int d^3u' f = 1 .$$

The parameter $(\omega_p/\Omega_0)^2$ is a measure of the strength of the electrostatic effects. As a result of the nonzero beam density there are two distinct electrostatic effects: the dc frequency shift $\Delta\omega_{dc} = \omega_p^2/2\Omega_0$ and the ac fields $E_\Phi^s$ and $E_\Phi^c$.

The change in the axial momentum caused by a tapered external magnetic field $\Omega_0(z)$ is given by

$$\frac{dp_z}{dt_1} = -\frac{u}{\gamma}\frac{d\Omega_0(z)}{dz} . \tag{26}$$

In what follows we will consider devices in which the magnetic field is nearly constant, having a weak variation which can be taken to be linear in the axial distance

$$\Omega_0(z) \simeq \Omega_0(0)(1 + \epsilon z/r_0) .$$

In this limit, the axial momentum is approximately conserved and only equations evolving $u_\perp$ and $\phi$ are necessary. The dynamic equations (24)–(26) are not complete because the evolution of the electromagnetic field amplitude $\bar{A}(t_1)$ on the slow time scale $t_1$ has *not* been specified. An equation describing $\bar{A}(t_1)$ can be obtained from Maxwell's equations; we will return to this point in Sec. V, where we examine the time-dependent behavior of the electromagnetic modes in an overmoded gyrotron. Furthermore, in Appendix A the equations are put into dimensionless form, indicating that there are four relevant dimensionless parameters.

### C. Efficiency

Suppose that a beam of electrons, each with initial energy $\gamma_i mc^2$, enters a gyrotron cavity in which the electromagnetic field amplitude $E_x$ is fixed at a given magnitude. Upon traversal of the cavity the electrons will bunch in phase, with each electron losing (or gaining) energy and exiting with a final energy $\gamma_f mc^2$. The total energy of $N$ electrons upon entering the cavity is $W_i = \Sigma_{n=1}^N \gamma_{i,n} mc^2 = N\gamma_i mc^2$, and upon exiting is $W_f = \Sigma_{n=1}^N \gamma_{f,n} mc^2$. The efficiency $\eta$ with which the electrons transfer their energy to the electromagnetic wave is defined as

$$\eta \equiv \left(\gamma_i - \frac{1}{N}\sum_{n=1}^{N}\gamma_{f,n}\right)(\gamma_i - 1)^{-1} . \tag{27}$$

Note that in the absence of magnetic field tapering the maximum theoretically possible efficiency is less than 100% because the energy associated with the axial streaming of the electrons cannot be tapped by the electromagnetic wave.

## III. LINEAR THEORY

Before examining the nonlinear consequences of the electrostatic field, we first consider the effect of the electrostatic field on linear, small signal efficiency. The change in the energy of a distribution of electrons as they traverse a gyrotron cavity containing a small amplitude electromagnetic wave can be calculated by solving the linearized collisionless Boltzmann equation. The mathematical details of the calculation are presented in Appendix B. In Appendix B it is shown that the small signal efficiency $\eta$ with which the electrons transfer their energy to the electromagnetic mode is given by

$$\eta = \kappa \bar{E}_x^2 , \tag{28a}$$

where $\kappa$ is given by

$$\kappa = \pi\left(\frac{\Gamma_0^2}{2\Gamma_* \Gamma_1}\sin\theta - \cos\theta\right) \times \frac{\exp\{-\frac{1}{2}\tau_0^2[(\Delta\omega - \Gamma_1)^2 - \Gamma_*^2]\}}{8\beta_z^2\gamma_0(\gamma_0 - 1)(1 + \epsilon_*^2)^{1/2}} \tag{28b}$$

and $\bar{E}_x$ is a normalized electric field

$$\bar{E}_x = -q\omega r_0 \bar{A}/(\pi^{1/2} mc^3) .$$

We have assumed a steady electric field profile consistent with Eq. (22b):

$$A(\mathbf{r},t) = \pi^{-1/2}\sin\omega t \cos ky \exp[-r^2/r_w^2(y)]\,\bar{A} ,$$

where $r^2 = x^2 + z^2$, the radiation waist $r_w(y)$ is given by

$$r_w^2(y) = r_0^2 + 2y^2/(r_0^2 k^2) ,$$

and all electrons' guiding centers pass through $x = y = 0$. In Eq. (28b) the quantity $\epsilon_*$ is given by

$$\epsilon_* = \epsilon\Omega_0 r_0/(2\gamma_0 v_z) ,$$

with

$$\epsilon = \frac{r_0}{\Omega_0(0)}\frac{d\Omega_0(z)}{dz}$$

defining the rate of taper. The quantities $\Gamma_0$, $\Gamma_1$, and $\Gamma_*$ are frequencies:

$$\Gamma_0^2 = \omega_p^2 \beta_{\perp 0}^2/(4\gamma_0^2), \quad \Gamma_1 = \omega_p^2/(4\Omega_0) ,$$

$$\Gamma_* = (\Gamma_0^2 - \Gamma_1^2)^{1/2} .$$

The quantity $\tau_0$ is a measure of the time of flight through the radiation field,

$$\tau_0 = r_0(1 + \epsilon_*^2)^{1/2}/v_z ,$$

$\Delta\omega$ is the mismatch frequency,

$$\Delta\omega = \omega - \Omega_0/\gamma + \tfrac{1}{2}\omega_p^2/\Omega_0 ,$$

and $\theta$ is given by

$$\theta = \tau_0^2 \Gamma_* (\Delta\omega - \Gamma_1) .$$

The zero-density, constant magnetic field[3] limit of Eq. (28b) is obtained by letting $\omega_p^2$ and $\epsilon$ go to zero:

$$\kappa = \frac{\pi}{8\gamma_0(\gamma_0 - 1)\beta_z^2}\left(\frac{\Delta\omega\Omega_0 r_0^2 \beta_{\perp 0}^2}{2\gamma_0 v_z^2} - 1\right) \times \exp\left[-\frac{1}{2}\left(\frac{\Delta\omega r_0}{v_z}\right)^2\right] .$$

We see from Eq. (28b) that for moderate values of $\epsilon_*$ the effect of tapering on the linear gain is not dramatic. In fact, it is approximately equivalent to changing the spot size from $r_0$ to $r_0/(1 + \epsilon_*^2)^{1/2}$.

The self-field effects are somewhat different. The gain

can become exponentially large when the parameter $\Gamma_* r_0/v_z$ exceeds unity. The quantity $\Gamma_*$ is the temporal growth rate of the electrostatic cyclotron maser instability.[12,13] Thus we see that if the time of flight of an electron through the cavity is longer than the growth time of the electrostatic instability, the small signal efficiency is altered dramatically.

Figure 3 is a plot of the linear efficiency normalized to $\overline{E}_x^2$, given by $\kappa$ in Eq. (28b), as a function of the beam density $(\omega_{pe}/\Omega_0)^2$. The gyrotron parameters used are listed in Table I. The wave frequency $\omega$ is nearly equal to the gyrofrequency $\Omega_0/\gamma$, the difference specified by the mismatch parameter

$$\delta = (\omega - \Omega_0/\gamma)/\omega . \tag{29}$$

The curve in Fig. 3 is for $\delta = 0.02$. At small beam densities the efficiency is positive, indicating that the electrons lose energy and the small amplitude electromagnetic wave grows. As the beam density increases, the efficiency decreases and becomes negative, signifying that the electromagnetic wave is linearly stabilized by the self-electrostatic field. At still higher densities the efficiency becomes positive again.

The current necessary to start the oscillation in a given cavity mode can be obtained by examining the power balance in a gyrotron. Consider an electron beam of current $I$ accelerated through a voltage $V$. If the electromagnetic field amplitude in the gyrotron cavity is $\overline{A}$, then the beam will transfer a fraction $\eta(\overline{A})$ of its input power $P = VI$ to the field. Suppose that the electromagnetic energy $W$ stored in the cavity is extracted at the rate $\Upsilon/T$, where $\Upsilon$ is the fraction of the energy removed during a wave reflection time $T = 2L/c$, with $L$ the distance between the mirrors. Then the oscillation will start if the power input from the beam is larger than the power extracted:

$$\eta(\overline{A})\, VI > (\Upsilon/T)\, W . \tag{30}$$

For the given electric field profile, the stored energy $W$ is given by

$$W = (r_0^2 L/32\pi)\, \omega^2 \overline{A}^2/c^2 .$$

Defining the cavity $Q = \omega W/P_{\text{diss}}$, where the power dissipated $P_{\text{diss}} = W\Upsilon/T$, and using expression (28b) for $\eta$, we find that the oscillation will start if the current satisfies

$$I > (\omega L/c)\, I_0/Q\kappa(\gamma_0 - 1) , \tag{31}$$

where $I_0 = mc^3/(32q) = 5.31 \times 10^2$ A, and we have noted that the kinetic energy of an electron is given by $qV = (\gamma_0 - 1)mc^2$.

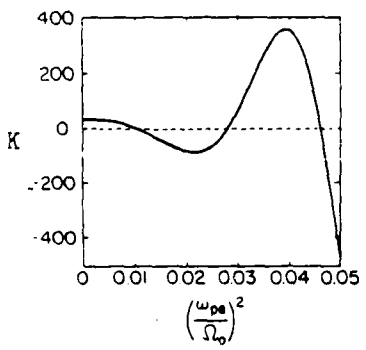



FIG. 3. Linear efficiency. The ratio $\kappa$ of the linear efficiency $\eta$ normalized to $\overline{E}_x^2$, given by Eq. (28b), is plotted as a function of the beam density $(\omega_{pe}/\Omega_0)$.

TABLE I. Gyrotron parameters.

| |
|---|
| $\Omega_0(0) = 7.23 \times 10^{11}$ rad/sec |
| $\gamma = 1.137$ |
| $\beta_\perp/\beta_\parallel = 1.5$ |
| $\epsilon = 0.02$ |
| $r_0 = 1$ cm |

## IV. NONLINEAR EFFICIENCY

In Sec. III we calculated the linear efficiency $\eta = \kappa \overline{E}_x^2$ with which an ensemble of electrons transfers its energy to a small amplitude electromagnetic wave of amplitude $\overline{E}_x$. As $\overline{E}_x$ increases beyond the linear regime, the electrons bunch in phase and the efficiency saturates. The maximum nonlinear efficiency obtained may have little relationship to the linear efficiency. That is, considering two different modes with the same gyrotron operating parameters, while one mode may be less efficient linearly, it may be more efficient nonlinearly.

In this section we calculate the effect of the electrostatic field on the nonlinear efficiency with which the electrons transfer their energy. The gyrotron parameters used are those listed in Table I. Neglecting electrostatic effects and assuming that the electron beam is only weakly relativistic, it has been found[15,16] that the efficiency of any gyrotron is a function of only three parameters: the normalized interaction length $\overline{\mu} = (\beta_\perp^2/\beta_\parallel)(2\pi r_0/\lambda)$ in our notation, the normalized current which is related to the field amplitude $\overline{E}_x$ through the power balance equation (30), and the parameter $\Delta = 2\delta/\beta_\perp^2$. The authors of Ref. 16 find that the optimal efficiency at the fundamental cyclotron resonance occurs when $\overline{\mu} \sim 15$–$20$ and $\Delta \sim 0.5$. For the gyrotron parameters in Table I that we are using, $\overline{\mu} \simeq 14.3$. Thus these parameters are close to, but not quite optimal (see Fig. 1 of Ref. 16). For the parameters in Table I and $\Delta \sim 0.5$, the optimal mismatch parameter $\delta \simeq 0.04$.

We consider $N$ electrons which are initially equally spaced in phase angle (typically, $N = 1000$), with a given beam density $(\omega_p/\Omega_0)^2$. For a fixed electromagnetic field amplitude $\overline{E}_x$, the equations of motion (24), (26), and (1d) for each electron with self-electrostatic fields described by Eqs. (25) are integrated numerically from $z = -L$ to $z = +L$, where $L = 4r_0$. The distance $L$ has been varied to ensure that the results are independent of $L$. At $z = +L$, the relativistic factor $\gamma_f$ is obtained and the efficiency $\eta$ is calculated according to Eq. (27). This process is repeated for several different values of $\overline{E}_x$ to obtain the plot of $\eta$ vs $\overline{E}_x$ shown in Fig. 4(a), with $(\omega_p/\Omega_0)^2 = 0$ (no electrostatic effects) and $\delta = 0.05$. In the small amplitude linear regime, $\eta$ increases as $\overline{E}_x^2$. At larger $\overline{E}_x$ the electrons bunch in phase

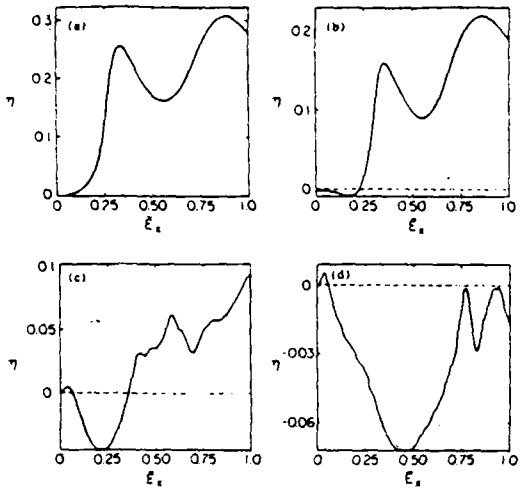


FIG. 4. Degradation of the efficiency due to electrostatic effects. The efficiency $\eta$ is plotted as a function of the normalized electromagnetic field $\bar{E}_x$ for a mode with frequency mismatch $\delta = 5\%$ and a beam density $(\omega_{pe}/\Omega_0)^2 =$ (a) 0, (b) $1\times10^{-2}$, (c) $3\times10^{-2}$, and (d) $6\times10^{-2}$.

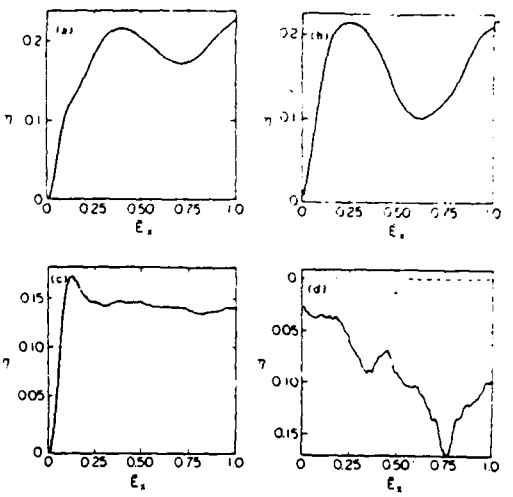


FIG. 5. Degradation of the efficiency due to electrostatic effects. The efficiency $\eta$ versus normalized electromagnetic field $\bar{E}_x$ for $\delta = 2\%$ and $(\omega_{pe}/\Omega_0)^2 =$ (a) 0, (b) $6\times10^{-2}$, (c) $1\times10^{-1}$, and (d) $2\times10^{-1}$.

and the efficiency saturates. At still larger values of $\bar{E}_x$ the electrons overbunch and the efficiency decreases. The maximum nonlinear efficiency obtained in the zero-beam-density limit is 31%. Efficiency plots for increasing beam density are shown in Figs. 4(b)–4(d). For a beam density of $(\omega_p/\Omega_0)^2 = 1\times10^{-2}$ [the corresponding value of the normalized density defined in Eq. (A6) for this case is $\bar{n} = 0.92$], the maximum efficiency drops to 22%. When the beam density increases to $(\omega_p/\Omega_0)^2 = 3\times10^{-2}$ ($\bar{n} = 2.78$), the maximum efficiency drops to 9%, and for $(\omega_p/\Omega_0)^2 \gtrsim 6\times10^{-2}$ ($\bar{n} = 5.56$), $\eta$ is negative, indicating that the field gives up energy to the electrons and the electron cyclotron instability is quenched. In these numerical simulations we have restricted the normalized electromagnetic field $\bar{E}_x < 1$. As can be seen from Eqs. (24) and (25), the ac electrostatic fields $E^s_\Phi$ and $E^c_\Phi$ for a given beam density can always be taken small if the electromagnetic field $\bar{E}_x$ is sufficiently large. However, the magnitude of $\bar{E}_x$ is limited by considerations of heat load on the mirrors. Note from Fig. 4(a) that the overbunching of the electrons in phase occurs for $\bar{E}_x \simeq 0.3$ when $\delta = 0.05$.

Efficiency plots for a lower frequency electromagnetic mode with $\delta = 0.02$ are shown in Figs. 5(a)–5(d). In the zero-beam-density limit, the maximum efficiency obtained is 22%—lower than in the $\delta = 0.05$ case. Again, as the beam density increases the efficiency with which the electrons transfer energy to the electromagnetic wave is degraded severely because of the electrostatic field. Note that although the higher frequency mode with $\delta = 0.05$ has a higher nonlinear efficiency in the zero-density limit, the lower frequency mode with $\delta = 0.02$ has a higher linear efficiency for small $\bar{E}_x$. The consequences of this will be seen in the time-dependent multimode simulations presented in Sec. V.

The density dependence of the maximum efficiency for three different cavity modes with $\delta = 0.02$, 0.04, and 0.05 is shown in Fig. 6. The critical density beyond which the efficiency is degraded decreases as the frequency mismatch (and frequency) of the cavity mode increases.

The dc contribution of the electrostatic field to the frequency, $\Delta\omega_{dc} = \omega_p^2/(2\Omega_0)$ in Eq. (24b), can actually enhance the efficiency when the zero-density frequency mismatch $\delta$ is small and the magnetic field is not tapered. Figure 7 is a plot of the density dependence of the maximum efficiency for $\delta = 0.005$ and 0.01 for both tapered (closed symbols) and untapered (open symbols) magnetic fields. As the electrons traverse a tapered magnetic field the gyrofrequency changes and a more favorable resonance condition

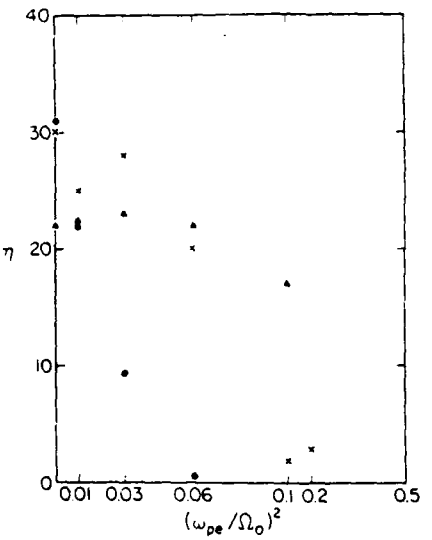


FIG. 6. Degradation of the efficiency due to electrostatic effects. The density dependence of the maximum efficiency (percent) is plotted for $\delta = 2\%$ (triangles), 4% (crosses), and 5% (circles). When no symbol appears for $(\omega_{pe}/\Omega_0)^2 = 1\times10^{-1}$ or $2\times10^{-1}$, the maximum efficiency is then negative.

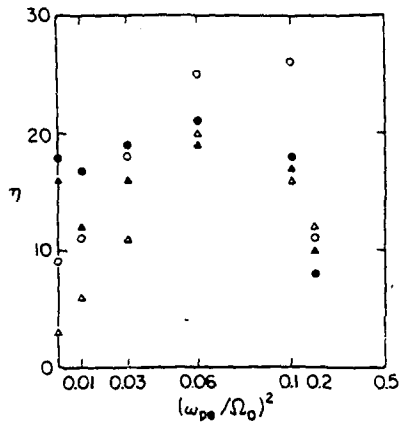



FIG. 7. The effect of the dc frequency shift. The density dependence of the maximum efficiency is plotted for $\delta = 0.5\%$ (triangles) and 1% (circles) for both tapered (closed symbols) and untapered (open symbols) magnetic fields. For $(\omega_{pe}/\Omega_0)^2 > 0.2$, the maximum efficiency is negative in all cases.

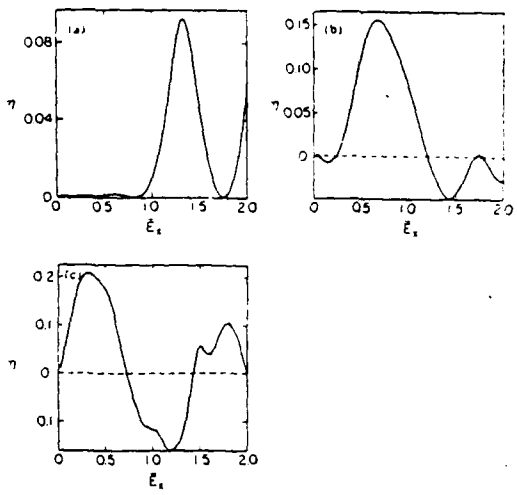



FIG. 8. The effect of the ac electrostatic fields. The efficiency $\eta$ is plotted as a function of the normalized electromagnetic field $\bar{E}_x$ for $\delta = 6\%$ and $(\omega_{pe}/\Omega_0)^2 =$ (a) 0, (b) $3\times10^{-2}$, and (c) $6\times10^{-2}$.

(frequency mismatch) for energy transfer from the electrons to the cavity mode is attained. In contrast, when the magnetic field is not tapered the electrons do not efficiently transfer their energy to cavity modes with a small frequency mismatch. However, as the beam density increases, the dc frequency shift $\Delta\omega_{dc}$ produced by the electrostatic field effectively increases the frequency mismatch so that a more favorable resonance condition is attained and the efficiency increases. Beyond a critical density, however, the electrostatic field quenches the electron cyclotron instability regardless of whether the magnetic field is tapered or not.

As can be seen from the zero-beam-density results shown in Figs. 4(a) and 5(a), as $\delta$ increases, the cavity field $\bar{E}_x$ at which the electrons first completely bunch in phase also increases. When $\delta$ exceeds 0.05, the first maximum in the efficiency does not occur until $\bar{E}_x$ is larger than 1. Since the maximum electric field at which a gyrotron can operate is limited by other considerations, the size of the mismatch $\delta$ is also restricted. However, when the frequency mismatch is large, the ac electrostatic fields $\bar{E}^s_\phi$ and $\bar{E}^c_\phi$ actually act to increase the efficiency by bunching the electrons. Figure 8(a) is a plot of the efficiency versus cavity field $\bar{E}_x$ for $\delta = 0.06$ when the beam density is zero. The maximum efficiency of only 9% occurs when $\bar{E}_x = 1.3$. Figures 8(b) and 8(c) demonstrate the effect of the ac fields; the dc frequency shift $\Delta\omega_{dc}$ produced by the electrostatic field has been neglected. When $(\omega_{pe}/\Omega_0)^2 = 6\times10^{-2}$, not only is the maximum efficiency raised to 21%, but the cavity field at which the maximum occurs is reduced to $\bar{E}_x = 0.3$. The magnitude of the electromagnetic cavity field is too small to bunch the electrons when $\bar{E}_x = 0.3$. However, if the beam density is sufficiently large, then the ac electrostatic field will bunch the electrons. The bunched electrons then radiate energy into the electromagnetic cavity mode.

## V. TIME-DEPENDENT SIMULATIONS

In Sec. IV we calculated the effect of the self-electrostatic mode on the efficiency with which electrons transfer their energy to a single electromagnetic mode of fixed magnitude. However, the quasioptical gyrotron is overmoded since it is designed to operate at a wavelength much smaller than the length of the open resonator. Conventional closed cavity gyrotrons can also be designed to operate at a wavelength much smaller than that of the lowest-order fundamental mode. Since the mode spectrum is dense in these overmoded gyrotrons, many modes may be excited and operation in a single, coherent mode may be difficult. In previous time-dependent simulations that neglected electrostatic effects it was found that it is indeed possible for an overmoded gyrotron to evolve to a steady state consisting of a single, coherent mode.[5] Here, we carry out time-dependent simulations including the self-consistent evolution of the electrostatic field in order to determine the effect of this field on gyrotron operation.

First, following Ref. 5, we generalize the equations of motion (24a) and (24b) for many modes $l$ with frequencies $\omega_l = \omega(1 + l/N)$; $l = 0, \pm 1, \pm 2, \ldots, \pm M$ with $M \ll N$. Here, the frequency separation $\Delta\omega$ between modes is given by $\Delta\omega = \omega/N = 2\pi c/L$, where $L$ is the distance between the mirrors (see Fig. 1). The expression for the electric field at the beam in the time-dependent case is

$$\mathbf{E} = \hat{x}\pi^{-1/2}\exp\left[-\left(\frac{z}{r_0}\right)^2\right]\frac{1}{2}$$

$$\times\sum_l\left\{E_{xl}(t)\exp\left[i\left(\omega t_0 + \frac{\omega l t_1}{N}\right)\right] + \text{c.c.}\right\}, \qquad (32)$$

where $E_{xl}$ is a complex amplitude having magnitude $\hat{E}_{xl}$ and phase $\theta_l$,

$$E_{xl} = \hat{E}_{xl}\, e^{i\theta_l}.$$

Then, the equations of motion [(24a) and (24b)] can be written in the form

$$\frac{du_\perp}{dt_1} = \frac{q}{2m}\left[\sum_l \hat{E}_{xl}\cos\left(\phi + \omega\frac{l}{N}t_1 + \theta_l\right)\pi^{-1/2} \times \exp\left(\frac{-z^2}{r_0^2}\right) + E_\Phi^s\cos\phi + E_\Phi^c\sin\phi\right], \quad (33a)$$

$$\frac{d\phi}{dt_1} = \omega - \frac{\Omega_0}{\gamma} + \frac{1}{2}\frac{\omega_p^2}{\Omega_0} + \frac{q}{2mu_\perp} \times\left[-\sum_l \hat{E}_{xl}\sin\left(\phi + \omega\frac{l}{N}t_1 + \theta_l\right)\pi^{-1/2} \times\exp\left(\frac{-z^2}{r_0^2}\right) + E_\Phi^c\cos\phi - E_\Phi^s\sin\phi\right], \quad (33b)$$

$$\frac{dz}{dt_1} = v_z . \quad (33c)$$

An equation for the evolution of the electromagnetic mode amplitudes $E_{xl}$ can be obtained from Maxwell's equations. Details of the derivation are given in Ref. 5. The derivation exploits the fact that for constant $E_{xl}$ the field (32) is periodic in time with period $\tau = 2\pi N/\omega$. Thus, assuming that $E_{xl}$ changes on a time scale $\bar{\tau} \gg \tau$, one can advance $E_{xl}$ as follows. Integrate the electron orbits forward over a time $\tau$, calculate $dE_{xl}/dt$ from the currents, and then step $E_{xl}$ forward in time by a time step of order $\bar{\tau} \gg \tau$. Since the electron equations of motion only have to be integrated for a time $\tau \ll \bar{\tau}$, this results in a large savings in computation time. Using this two-time scale formulation, one finds that the evolution equations for the electromagnetic mode amplitudes $E_{xl}$ are given by

$$\left(\frac{\partial}{\partial t} + \Gamma\right)E_{xl}(t) = -\frac{8\pi^{1/2}I}{r_0^2 L}\left\langle\int_{-\infty}^{\infty} dz\,\frac{u_{\perp j}}{u_{zj}}\,e^{i(\phi_j + l\omega t_1/N)}\,e^{-(z/r_0)^2}\right\rangle, \quad (34)$$

where the loss rate $\Gamma = c\Upsilon/4L$ and the angular average means averaged over an ensemble of initial phases $\phi$ and entrance times $t_{10}$, where $t_1 = t_{10} + z/v_z$. If we normalize $E_{xl}$ as

$$\bar{E}_{xl} = qr_0E_{xl}/(\pi^{1/2}mc^2) ,$$

then Eq. (34) becomes

$$\left(\frac{1}{\Gamma}\frac{\partial}{\partial t} + 1\right)\bar{E}_{xl} = \hat{I}\left\langle\int_{-\infty}^{\infty}\frac{dz}{r_0}\frac{u_{\perp j}}{u_{zj}}\,e^{-i(\phi_j + l\omega t_1/N)}\,e^{-(z/r_0)^2}\right\rangle, \quad (35)$$

where

$$\hat{I} = 32I/[\nu(mc^3/q)] .$$

Equations (33a), (33b), (25a), (25b), (26), and (35) form a complete set of self-consistent equations which describe the nonlinear evolution of the electrons and the electromagnetic and electrostatic fields. We have solved these equations numerically for a system consisting of 20 electromagnetic modes. The modes are evolved by determining the current in Eq. (35) using 2500 particles distributed uniformly in gyrophase and entrance time. In our simulations we have taken the normalized current $\hat{I} = 0.09$ and the rest of the parameters are those listed in Table I. The frequency separation of the modes is $\Delta\omega/\omega = 0.01$, which corresponds to a distance $L = 13$ cm between the mirrors for the parameters listed in Table I.

In Fig. 9 we show histograms of the electromagnetic mode amplitudes $E_{xl}$ at various times during a simulation with $(\omega_{pe}/\Omega_0)^2 = 0$ (no electrostatic effects). The system reaches a steady state which consists mainly of a single mode whose frequency mismatch parameter $\delta = 0.05$. Note that the modes which grow initially are at a lower frequency than the final steady-state mode. This is consistent with the efficiency calculations of Sec. IV, where it was found that while the lower frequency mode had a higher linear growth rate, the higher frequency $\delta = 0.05$ mode was more efficient nonlinearly. In fact, because of the loss through the mirrors, the final nonlinear steady-state mode is actually linearly stable. These results for time-dependent multimode simulations without electrostatic effects are consistent with those found previously.[5]

We now examine the effect of the electrostatic field by considering beams of nonzero density. Figure 10 is a time series of histograms of $E_{xl}$ when $(\omega_{pe}/\Omega_0)^2 = 3\times10^{-3}$. As in the zero-density case, the system evolves to a steady state consisting of a single electromagnetic mode, although it takes approximately five times longer to reach this steady state for the same initial perturbation. In addition to reducing the growth rates of the electromagnetic modes, the electrostatic field also causes a reduction of approximately 30% in the amplitude of the final steady-state mode. Thus the efficiency with which electrons transfer their energy to the electromagnetic mode is decreased.

When the beam density increases to $(\omega_{pe}/\Omega_0)^2 = 1\times10^{-2}$, the electrostatic field quenches the electron cyclotron instability entirely. As shown in Fig. 11, the initial

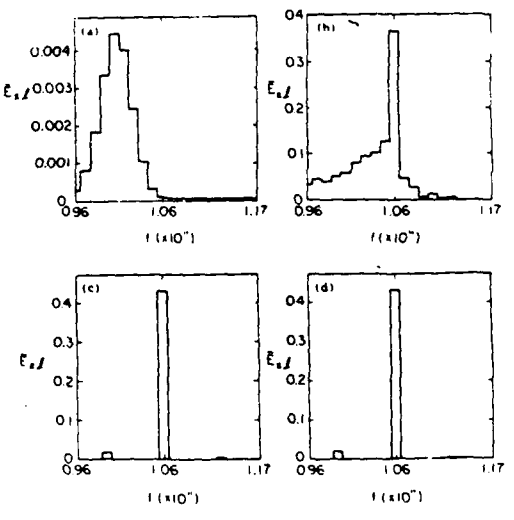



FIG. 9. Time-dependent multimode simulation. Histograms of the electromagnetic field amplitudes $E_{xl}$ are plotted as a function of frequency $f$ for $\hat{I} = 0.09$, $(\omega_{pe}/\Omega_0)^2 = 0$, and $t(\mu\text{sec}) =$ (a) 0.3, (b) 3, (c) 15, and (d) 45 after application of an arbitrary perturbation.

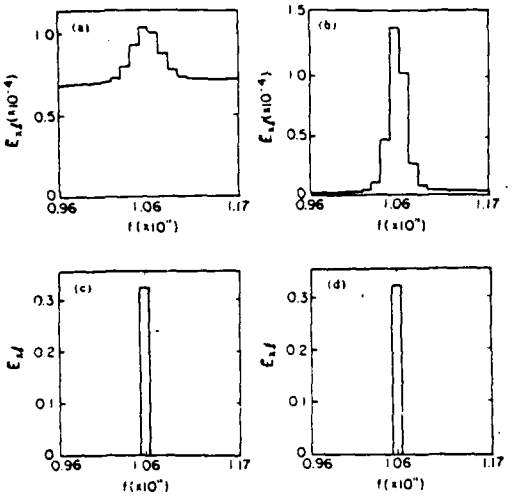


FIG. 10. Time-dependent multimode simulation. Same as Fig. 9 except $(\omega_{pe}/\Omega_0)^2 = 3\times10^{-3}$ and $t(\mu\text{sec}) =$ (a) 0.3, (b) 3, (c) 77, and (d) 106.

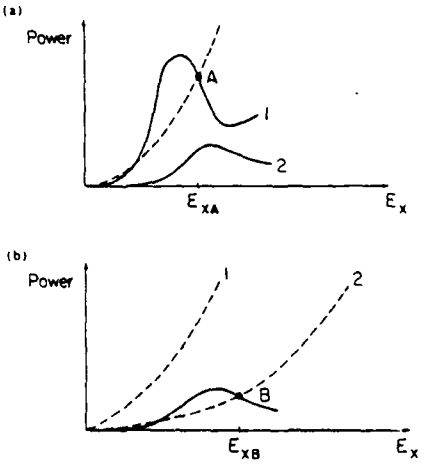


FIG. 12. Power balance in a gyrotron. The solid curves represent the functional dependence on $E_x$ of the left-hand side of the power balance equation (36), while the dashed curves represent the right-hand side.

perturbation decays away and the oscillation does not begin. The system is nonlinearly, as well as linearly, stable. For the steady state obtained in the zero-density case (see Fig. 9), when the density is increased to $(\omega_{pe}/\Omega_0)^2 = 1\times10^{-2}$, the mode then decays away rapidly and the oscillation is lost. Thus, for a sufficiently large beam density, the electrostatic effects not only degrade the efficiency, but can also lead to a failure of the gyrotron to oscillate at all.

The reason the oscillation does not begin can be understood by examining the power balance in a gyrotron. From Eq. (30) and the definitions which follow it, the power balance in a gyrotron is described by

$$\eta(E_x)VI = (\omega/Q)E_x^2 r_0^2 L/32\pi \qquad (36)$$

Neglecting electrostatic effects, the dependence of the left-hand side of Eq. (36) on $E_x$ is given typically by the efficiency curves shown in Figs. 4(a) and 5(a). This dependence is illustrated schematically by the solid curve labeled 1 in Fig. 12(a). The quadratic dependence on $E_x$ of the right-hand side of Eq. (36) is given by the dashed curve in Fig. 12(a). The intersection of these two curves, denoted by A, is the operating point. The rate at which energy is transferred from the beam to the field is equal to the rate at which energy is extracted from the cavity when $E_x = E_{xA}$. However, as the beam density increases the efficiency is degraded to the solid curve labeled 2 in Fig. 12(b). Now the energy flow from the beam to the field is less than the energy extraction rate from the cavity for all $E_x$ and the oscillation will not start. By reducing the rate at which energy is extracted from the cavity [dashed line 2 in Fig. 12(b)], one can regain operation at the point labeled B in Fig. 12(b). However, both the power and the efficiency are greatly reduced at point B as compared to point A. As the beam density increases further, the efficiency becomes negative and operation is not possible.

We have repeated a series of time-dependent simulations with the current increased to $\hat{I} = 0.9$ and with all the other parameters the same as before. The results are qualitatively the same as in the $\hat{I} = 0.09$ case, but the steady-state mode amplitude in the zero-density limit is approximately three times larger and the beam density required to stop the oscillation is roughly three times larger.

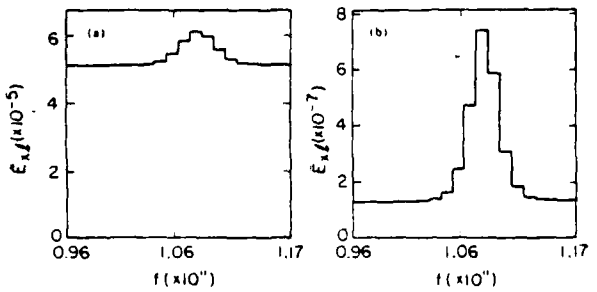


FIG. 11. Time-dependent multimode simulation. Same as Fig. 9 except $(\omega_{pe}/\Omega_0)^2 = 1\times10^{-2}$ and $t(\mu\text{sec}) =$ (a) 0.6 and (b) 6.

## VI. SUMMARY AND DISCUSSION

The time-dependent self-consistent electrostatic field has been shown to have a deleterious effect on gyrotron operation. As the electron beam density increases, the nonlinear efficiency is seriously degraded by the self-electrostatic field. Based on the dimensionless equations presented in Appendix A we anticipate that the degradation occurs for values of $\bar{n} = \omega_p^2 r_0/(v_z\Omega_0)$ of order unity. For the particular parameters considered (i.e., those in Table I) this corresponds to $\omega_p^2/\Omega_0^2 \sim 10^{-2}$ and a current density of $J = 2.0\times10^3$ A/cm$^2$.

While the maximum nonlinear efficiency appears to always be degraded, for some choices of parameters, viz., mismatch and electric field strength, the efficiency is enhanced. This is also reflected in the efficiency in the linear regime, which may be increased or decreased by space charge effects depending on the value of the mismatch.

Time-dependent multimode simulations demonstrate

that, as in the case without space charge effects, operation with a single nonlinear mode is possible. Typically, the system evolves nonlinearly to the most efficient mode even though this mode may be linearly stable. We have found that the time required to reach saturation increases and the mode amplitude at saturation decreases as the beam density is increased.


## ACKNOWLEDGMENTS

One of the authors (TMA) would like to acknowledge useful discussions with A. Bondeson.

This work was supported by the Office of Naval Research.


## APPENDIX A: DIMENSIONLESS EQUATIONS

The parameter space of our nonlinear system can be reduced by rewriting the equations of motion in dimensionless variables.[15,16] At the same time we will make the further approximation that the beam is weakly relativistic and we will replace $\gamma$ by $\gamma_0 \simeq 1$ everywhere it appears except in the combination $\omega - \Omega_0/\gamma$, which we approximate as

$$\omega - \frac{\Omega_0}{\gamma} = \omega - \frac{\Omega_0}{\gamma_0}\left(1 - \frac{1}{2}\frac{u_\perp^2 - u_{\perp 0}^2}{c^2\gamma_0^2}\right).$$

We now rewrite Eqs. (24) employing the following normalizations. Time is normalized to the time of flight through the interaction region

$$\tau = t_1 v_z / r_0 ,$$

where $v_z$ is the assumed constant axial velocity. The quantity $u_\perp$ is normalized to $\gamma_0 v_{\perp 0}$, where $v_{\perp 0}$ is the injected value of $v_\perp$:

$$u = u_\perp / \gamma_0 v_{\perp 0} .$$

The components of the electric field are normalized in the following way:

$$e_x = q r_0 E_x/(\gamma_0 v_{\perp 0} v_z m), \quad e_\Phi^{s,c} = q r_0 E_\Phi^{s,c}/(\gamma_0 v_{\perp 0} v_z m).$$

The resulting nonlinear equations can then be written as

$$\frac{d}{d\tau} u = \tfrac{1}{2}\left[(e_x + e_\Phi^s)\cos\phi + e_\Phi^c \sin\phi\right], \tag{A1}$$

$$\frac{d\phi}{d\tau} = \bar{\mu}\left(\Delta + \tfrac{1}{2}(u^2 - 1)\right) + \frac{1}{2u}\left[e_\Phi^c \cos\phi - (e_x + e_\Phi^s)\sin\phi\right], \tag{A2}$$

with

$$\bar{\mu} = (\Omega_0 r_0/\gamma_0 v_z)\,\beta_{\perp 0}^2 \tag{A3}$$

measuring the perpendicular beam energy and interaction length and

$$\Delta = \gamma_0(\omega - \Omega_0/\gamma_0 + \tfrac{1}{2}\omega_p^2/\omega_0)/(\beta_{\perp 0}^2 \Omega_0) \tag{A4}$$

measuring the frequency mismatch. The electrostatic components of the field are given by

$$e_\Phi^s = \bar{n}\int d^3u'\, u' f \sin\phi', \tag{A5a}$$

$$e_\Phi^c = \bar{n}\int d^3u'\, u' f \cos\phi', \tag{A5b}$$

where

$$\bar{n} = \omega_p^2 r_0/\Omega_0 v_z \tag{A6}$$

measures the beam density.

Thus we see that the weakly relativistic equations depend on four dimensionless parameters: the strength of the electromagnetic field $e_x$, the mismatch $\Delta$, the beam energy/interaction length $\bar{\mu}$, and the beam density $\bar{n}$. Thus, the introduction of the space charge into the model has added a new parameter $\bar{n}$. This quantity can be expressed in terms of the beam current density $J$:

$$\bar{n} = 2J\lambda r_0/\beta_z I_A ,$$

where $I_A = \beta_z \gamma_0 mc^3/e = 1.7\times 10^4 \beta_z \gamma_0$ A is the Alfvén current, and $\lambda$ is the vacuum wavelength of the radiation. For the parameters of Table I a beam current density of $2.2\times 10^3$ A/cm$^2$ is required to produce $\bar{n} = 1$. If all the current were to be confined to a pencil beam whose radius is one quarter of a wavelength $\lambda = 0.3$ cm, the value of current to which this corresponds is 40 A.

## APPENDIX B: SMALL SIGNAL EFFICIENCY

In this appendix we present the mathematical details of the calculation of the small signal efficiency $\eta$ given in Eq. (28). Consider an ensemble of electrons with a distribution function $f$ described by the Vlasov equation

$$\frac{\partial f}{\partial t_1} + v_z\frac{\partial f}{\partial z} + \frac{dp_z}{dt_1}\frac{\partial f}{\partial p_z} + \frac{d\phi}{dt_1}\frac{\partial f}{\partial \phi} + \frac{d\mu}{dt_1}\frac{\partial f}{\partial \mu} = 0, \tag{B1}$$

where $dp_z/dt_1$, $d\phi/dt_1$, and $d\mu/dt_1$ are given by Eqs. (26), (24b), and (24a), respectively. The total distribution function $f$ can be decomposed into equilibrium ($f_0$) and perturbed ($\tilde{f}$) pieces: $f = f_0 + \tilde{f}$. The equilibrium distribution function $f_0$ satisfies

$$\frac{\partial f_0}{\partial t} + \frac{p_z}{\gamma m}\frac{\partial f_0}{\partial z} - \frac{\mu}{\gamma}\frac{d\Omega_0}{dz}\frac{\partial f_0}{\partial p_z} + \left[\omega - \frac{\Omega_0}{\gamma} + \frac{\Omega_0}{2}\left(\frac{\omega_{pe}}{\Omega_0}\right)^2\right]\frac{\partial f_0}{\partial \phi} = 0 . \tag{B2}$$

Equation (B2) is satisfied by $f_0(W,\mu)$, where $f_0$ is an arbitrary function of the electron energy $W = p_z^2/2m + \mu\Omega_0$ and magnetic moment $\mu$.

Linearizing Eq. (B1), one finds that the perturbed distribution function $\tilde{f}$ obeys

$$\frac{\partial \tilde{f}}{\partial t} + v_z\frac{\partial \tilde{f}}{\partial z} + \left[\omega - \frac{\Omega_0}{\gamma}\left(1 + \epsilon\frac{z}{r_0}\right) + \frac{\Omega_0}{2}\left(\frac{\omega_{pe}}{\Omega_0}\right)^2\right]\frac{\partial \tilde{f}}{\partial \phi} + \frac{q}{2m}\left\{\left[E_\Phi^s + E_x(z)\right]\cos\phi + E_\Phi^c \sin\phi\right\}\frac{\partial f_0}{\partial u_\perp} = 0 , \tag{B3}$$

where the magnetic field has been taken to have a linear taper

$$\Omega_0(z) = \Omega_0(1 + \epsilon z/r_0) , \tag{B4}$$

where $\epsilon \equiv [r_0/\Omega_0(0)]\,d\Omega_0(z)/dz$. The perturbed distribution function has no explicit time dependence for the single-mode efficiency calculation considered here. Rather, $\tilde{f}$ de-

pends on axial distance, being zero at the point of injection ($z = -\infty$) and developing in $z$ in response to the fields. For sufficiently small $\epsilon$ (weak taper), the electron velocity along the magnetic field is nearly constant and we introduce a new time coordinate $\tau$ related to $z$ by $z = v_z\tau$ in Eq. (B3).

Let us write $\tilde{f}$ in the form $\tilde{f} = f_+ e^{i\phi} + f_- e^{-i\phi}$. Inserting this expression for $\tilde{f}$ into Eq. (B3) and then multiplying by $e^{\pm i\phi}$ and integrating, one finds the following equations for $f_+$ and $f_-$:

$$\frac{\partial f_\pm}{\partial \tau} + i\left[\omega - \frac{\Omega_0}{\gamma}\left(1 + \epsilon\frac{v_z\tau}{r_0}\right) + \frac{\Omega_0}{2}\left(\frac{\omega_{pe}}{\Omega_0}\right)^2\right] f_\pm + \frac{1}{4}\frac{q}{m}\left[E_{\Phi\pm} + E_x(v_z\tau)\right]\frac{\partial f_0}{\partial u_\perp} = 0, \tag{B5}$$

where

$$E_{\Phi\pm} = E^x_\Phi \mp iE^y_\Phi = \pm i2\pi\left(\frac{\omega_p}{\Omega_0}\right)^2\left(\frac{B_0}{c}\right)\int u_\perp^2\, du_\perp f_\pm . \tag{B6}$$

Equation (B5) can be simplified through the use of an integrating factor. Let us define $\hat{f}_\pm$ by

$$f_\pm = \exp\left(\pm i\frac{\Omega_0}{\gamma}\frac{\epsilon v_z}{r_0}\frac{\tau^2}{2}\right)\hat{f}_\pm \tag{B7a}$$

and

$$\hat{E}_{x\pm} = E_x(v_z\tau)\exp\left(\mp\frac{i\Omega_0}{\gamma}\frac{\epsilon v_z}{r_0}\frac{\tau^2}{2}\right),$$

$$\hat{E}_{x\pm} = \frac{-\omega\bar{A}}{c\pi^{1/2}}\exp\left[-\left(\frac{v_z\tau}{r_0}\right)^2 \mp i\frac{\Omega_0}{\gamma}\frac{\epsilon v_z}{r_0}\frac{\tau^2}{2}\right], \tag{B7b}$$

$$\hat{E}_{\Phi\pm}(\tau) = E_{\Phi\pm}\exp\left(\mp i\frac{\Omega_0}{\gamma}\frac{\epsilon v_z}{r_0}\frac{\tau^2}{2}\right). \tag{B7c}$$

Then in terms of $\hat{f}_\pm$ Eq. (B5) becomes

$$\frac{\partial \hat{f}_\pm}{\partial\tau} \pm i\left[\omega - \frac{\Omega_0}{\gamma} + \frac{\Omega_0}{2}\left(\frac{\omega_{pe}}{\Omega_0}\right)^2\right]\hat{f}_\pm = -\frac{1}{4}\frac{q}{m}\left(\hat{E}_{\Phi\pm} - \hat{E}_{x\pm}\right)\frac{\partial f_0}{\partial u_\perp}. \tag{B8}$$

We define the Fourier transform $\bar{f}_\pm(\bar{\omega})$ of $\hat{f}_\pm(\tau)$ by

$$f_\pm(\tau) = \int_{-\infty}^{\infty}\frac{d\bar{\omega}}{2\pi}e^{-i\bar{\omega}\tau}\bar{f}_\pm(\bar{\omega}), \quad \mathrm{Im}(\bar{\omega}) > 0, \tag{B9}$$

with a similar definition for the transforms $\bar{E}_{x\pm}(\bar{\omega})$ and $\bar{E}_{\Phi\pm}(\bar{\omega})$ of $\hat{E}_{x\pm}(\tau)$ and $\hat{E}_{\Phi\pm}(\tau)$, respectively. The inversion contour for the Fourier transform of $\hat{f}_\pm(\tau)$ defined in Eq. (B9) must be taken to lie in the upper half $\bar{\omega}$ plane. This is a consequence of the fact that $\hat{f}_\pm(\tau)$ vanishes at the point of injection $\tau = -\infty$, but does not vanish at the point of exit $\tau = +\infty$. Similar considerations apply to the Fourier transform of $\hat{E}_{\Phi\pm}$. The same contour may also be used for $\hat{E}_{x\pm}$ because it decays sufficiently rapidly as $|\tau| \to \infty$. One obtains the solution of Eq. (B8) in the form

$$\bar{f}_\pm(\bar{\omega}) = -i\frac{1}{4}\frac{q}{m}\frac{\bar{E}_{\Phi\pm}(\bar{\omega}) - \bar{E}_{x\pm}(\bar{\omega})}{\bar{\omega} \mp [\omega - \Omega_0/\gamma + (\Omega_0/2)(\omega_{pe}/\Omega_0)^2]}\times\frac{\partial f_0}{\partial u_\perp}. \tag{B10}$$

The relationship between the electrostatic field $\bar{E}_{\Phi\pm}$ and the electromagnetic field $\bar{E}_{x\pm}$ is obtained by inserting expression (B10) for $\bar{f}_\pm$ into the Fourier transform of Eq. (B6):

$$\bar{E}_{\Phi\pm}(\bar{\omega}) = -\chi_\pm(\bar{\omega})\bar{E}_{x\pm}(\bar{\omega})/[1 - \chi_\pm(\bar{\omega})], \tag{B11}$$

where

$$\chi_\pm(\bar{\omega}) = \pm\frac{\pi}{2}\left(\frac{\omega_{pe}}{\Omega_0}\right)^2\Omega_0\int\frac{u_\perp^2\, du_\perp}{\bar{\omega} \mp \Delta\omega}\frac{\partial f_0}{\partial u_\perp}, \tag{B12}$$

with

$$\Delta\omega = \omega - \frac{\Omega_0}{\gamma} + \frac{\Omega_0}{2}\left(\frac{\omega_{pe}}{\Omega_0}\right)^2 \tag{B13}$$

representing the beam's susceptibility.

The change in $\gamma$, $\Delta\gamma = \gamma_f - \gamma_i$, for a given electron is defined as

$$\Delta\gamma = \int_{-\infty}^{\infty} d\tau\frac{d\gamma}{d\tau} = \int_{-\infty}^{\infty} d\tau\frac{1}{\gamma}\frac{d}{d\tau}\frac{u_\perp^2}{2}. \tag{B14}$$

Using relationship (2) between $\mu$ and $u_\perp$ along with Eq. (24a) for $d\mu/d\tau$, one finds that the average change in $\gamma$ for a distribution of electrons is

$$\Delta\gamma = -\frac{q}{m}\int_{-\infty}^{\infty} d\tau\int u_\perp\, d\phi\, du_\perp f\frac{u_\perp}{2\gamma}E_x(v_z\tau)\cos\phi . \tag{B15}$$

After integration over $\phi$, Eq. (B15) becomes

$$\Delta\gamma = -\frac{\pi q}{2m}\int_{-\infty}^{\infty} d\tau\int\frac{u_\perp^2\, du_\perp}{\gamma}\left(\hat{E}_{x-}\hat{f}_+ + \hat{E}_{x+}\hat{f}_-\right). \tag{B16}$$

The time integration in Eq. (B16) can be replaced by a frequency integration through the use of Parseval's theorem:

$$\Delta\gamma = -\frac{\pi q}{2m}\int_{\mathrm{Im}(\bar{\omega})>0}\frac{d\bar{\omega}}{2\pi}\int\frac{u_\perp^2\, du_\perp}{\gamma}\times\left[\bar{E}_{x-}(-\bar{\omega})\bar{f}_+(\bar{\omega}) + \bar{E}_{x+}(-\bar{\omega})\bar{f}_-(\bar{\omega})\right]. \tag{B17}$$

Consider a cold beam of electrons characterized by the equilibrium distribution function

$$f_0 = (2\pi u_{\perp 0})^{-1}\delta(u_\perp - u_{\perp 0}). \tag{B18}$$

Then using the Fourier transform of relationship (B6) between $\bar{f}_\pm$ and $\bar{E}_{\phi\pm}$ in expression (B17) for $\Delta\gamma$, one obtains

$$\Delta\gamma = i\frac{q}{4(\omega_{pe}/\Omega_0)^2 B_0 mc\gamma_0}\int\frac{d\bar{\omega}}{2\pi}\times\left[\bar{E}_{\phi+}(\bar{\omega})\bar{E}_{x-}(-\bar{\omega}) - \bar{E}_{\phi-}(\bar{\omega})\bar{E}_{x+}(-\bar{\omega})\right], \tag{B19}$$

where $\gamma_0 = \gamma(u_{\perp 0})$. Finally, insertion of Eq. (B11) relating $\bar{E}_{\Phi\pm}$ and $\bar{E}_{x\pm}$ into Eq. (B19) yields

$$\Delta\gamma = -i\frac{q}{4(\omega_{pe}/\Omega_0)^2 B_0 mc\gamma_0}\int\frac{d\bar{\omega}}{2\pi} \times\left(\frac{\chi_+(\bar{\omega})\bar{E}_{x+}(\bar{\omega})\bar{E}_{x-}(-\bar{\omega})}{1-\chi_+(\bar{\omega})} - \frac{\chi_-(\bar{\omega})\bar{E}_{x-}(\bar{\omega})\bar{E}_{x+}(-\bar{\omega})}{1-\chi_-(\bar{\omega})}\right), \quad \text{(B20)}$$

where for the cold beam distribution of Eq. (B18) $\chi_\pm$ is given by

$$\chi_\pm(\bar{\omega}) = \frac{1}{2}\left(\frac{\omega_{pe}}{\Omega_0}\right)^2\left(\pm\frac{\Omega_0}{\bar{\omega}\mp\Delta\omega} - \frac{1}{2}\frac{\Omega_0^2\beta_{\perp 0}^2}{\gamma_0}\frac{1}{(\bar{\omega}\mp\Delta\omega)^2}\right). \quad \text{(B21)}$$

The Fourier transform $\bar{E}_{x\pm}(\bar{\omega})$ of $\hat{E}_{x\pm}(\tau)$ given by Eq. (B7b) is

$$\bar{E}_{x\pm}(\bar{\omega}) = \left[(-\omega\bar{A}/c)/\sqrt{\sigma_\pm}\right]\exp(-\bar{\omega}^2/4\sigma_\pm),$$
$$\sigma_\pm = (v_z/r_0)^2 \pm i(\epsilon\Omega_0 v_z/2\gamma_0 r_0). \quad \text{(B22)}$$

The integrand in Eq. (B20) contains poles at the zeros of $1-\chi_\pm(\bar{\omega})$. From Eq. (B21) the solution of $1-\chi_+(\bar{\omega})=0$ is given by $\bar{\omega}=\omega^1_{+,-}$, where

$$\omega^1_{+,-} = \Delta\omega - \Gamma_1 \pm i\sqrt{\Gamma_0^2-\Gamma_1^2}, \quad \text{(B23)}$$
$$\Gamma_0^2 = (\omega_{pe}/\Omega_0)^2\beta_{\perp 0}^2\Omega_0^2/4\gamma_0, \quad \text{(B24a)}$$
$$\Gamma_1 = (\omega_{pe}/\Omega_0)^2\Omega_0/4. \quad \text{(B24b)}$$

Similarly, the solution of $1-\chi_-(\bar{\omega})=0$ is given by $\bar{\omega}=\omega^2_{+,-}$, where

$$\omega^2_{+,-} = -\Delta\omega + \Gamma_1 \pm i\sqrt{\Gamma_0^2-\Gamma_1^2}. \quad \text{(B25)}$$

The poles corresponding to the zeros of $1-\chi_\pm$ are shown in Fig. 13. The integral in Eq. (B20) for $\Delta\gamma$ can be performed by deforming the integration contour shown in Fig. 13(a) to the real $\bar{\omega}$ axis, as shown in Fig. 13(b). First consider the contribution to the integral of the portion of the contour which lies along the real $\bar{\omega}$ axis. For real $\bar{\omega}$, $\chi_\pm(-\bar{\omega})=\chi_\mp(\bar{\omega})$ and $\bar{E}_{x\pm}(-\bar{\omega})=\bar{E}_{x\pm}(\bar{\omega})$. Because of these symmetries, the contribution of the real $\bar{\omega}$ axis to the integral is zero. Calculating the contribution of the poles to the integral in Eq. (B20), one finally obtains the expression

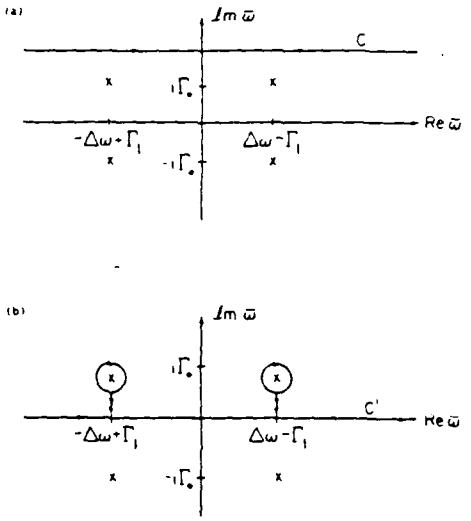



FIG. 13. Integration contours. The integration contour $C$ in the complex $\bar{\omega}$ plane in (a) is deformed to the contour $C'$ in (b).

given in Eq. (28) for the efficiency $\eta = -\Delta\gamma/(\gamma_0-1)$ in the small amplitude, linear limit.


[1] R. S. Symons and H. R. Jory, Adv. Electron. Electron Phys. 55, 1 (1981).
[2] V. L. Granatstein, Int. J. Electron. 57, 787 (1984).
[3] P. Sprangle, J. L. Vomvoridis, and W. M. Manheimer, Appl. Phys. Lett. 38, 310 (1981).
[4] A. Bondeson, B. Levush, W. Manheimer, and E. Ott, Int. J. Electron. 53, 547 (1982).
[5] A. Bondeson, W. M. Manheimer, and E. Ott, Int. J. Infrared Millimeter Waves 9, 309 (1983).
[6] I. S. Kovalev, A. A. Kurayev, S. V. Kolosov, and G. Ya. Slepyan, Radio Eng. Electron. Phys. 19, 149 (1974).
[7] J. L. Hirshfield, Int. J. Infrared Millimeter Waves 2, 695 (1981).
[8] P. Charbit, A. Herscovici, and G. Mourier, Int. J. Electron. 51, 303 (1981).
[9] L. Shenggang and Y. Zhonghai, Int. J. Electron. 51, 341 (1981).
[10] G. Döhler, Int. J. Electron. 56, 481 (1984).
[11] T. M. Antonsen, W. M. Manheimer, and B. Levush, Int. J. Electron. 61, 823 (1986).
[12] A. Bondeson and T. M. Antonsen, Int. J. Electron. 61, 855 (1986).
[13] K. R. Chen and K. R. Chu, IEEE Trans. MTT 34, 72 (1986).
[14] K. R. Chu and L.-H. Lyu, IEEE Trans. MTT 34, 690 (1986).
[15] A. I. Gaponov, U. I. Petelin, and V. K. Yulpatov, Izv. Vuz. Radiofiz. 10, 1414 (1967).
[16] B. G. Danly and R. J. Temkin, Phys. Fluids 29, 561 (1986).

# APPENDIX K

## Mode Stability in a Quasi-Optical Gyrotron

# "Mode Stability in a Quasi-Optical Gyrotron"

Wallace Manheimer, Code 4740
Naval Research Laboratory, Washington, D.C.

Thomas Antonsen and Baruch Levush
University of Maryland, College Park, Maryland

The stability of modes in a quasi-optical gyrotron is examined analytically and numerically for both free running, mode locked and phase locked equilibria. One key to the analysis is the fact that the mode eigenfrequencies are nearly integral multiples of a fundamental frequency corresponding to the reciprocal of the radiation transit time between mirrors. Analytically, results are obtained with the use of a klystron model.[1,2] Here, the radiation field in the optical resonator is approximated as essentially two delta functions separated by the radiation waste length. It is not exactly two delta functions because the field must be square integrable. However, if the separation is sufficiently large ($\mu \gg 1$, where $\mu$ is the dimensionless length unit in normalized gyrotron parameters) the klystron model is approximately valid. This model gives a good approximation to the linear and nonlinear behavior of a single moded quasi-optical gyrotron with realistic field profile as long as $0 < \mu\delta < \pi$ where $\delta$ is the dimensionless frequency mismatch parameter in normalized gyrotron parameters. Using the klystron model, one may solve analytically for the time dependence of the field amplitude. For instance one can calculate the frequency shift in the initial linear regime, as well as in the final nonlinear regime. By going to a multimode state, one can calculate analytically the condition for instability. The instability takes one of two possible characteristics. In one case the phase may be unstable; here the nearest mode is always unstable. In other cases, the amplitude may be unstable; here, it is generally not the nearest mode which is unstable. With the klystron model, one can determine the parameter space of stable and unstable single mode equilibria.

One way to control the mode in a quasi-optical gyrotron is to mode lock it in some manner. There are two basic methods of doing this which we consider. First one may directly inject a signal into the optical cavity, or second one may prebunch the beam with a separate prebunching cavity.[3] In either case, the frequency shift of the injected signal from that of the free running oscillator (or equivantly, the phase shift between the injected signal and oscillator signal) adds one additional dimension to the parameter space. If the signal used is obtained from a separate rf source, the equilibrium produced will be phase locked to this separate source. On the other hand, if the signal is obtained in some way from quasi-optical gyrotron itself[4], the signal will be mode locked. Whether a phase locked or mode locked source is desired depends on the application. The klystron model is also analytically tractable in examining the stability of a directly injected phase locked equilibrium. We find that the effect of the directly injected signal into the cavity has a small stabilizing effect on the equilibrium, principally in the stabilizing effect it has on the phase unstable mode. However the use of a directly injected signal also could have the effect of setting up the oscillator in one preferred mode out of many possible stable equilibria. For the case of the prebunched beam, the klystron model is analytically tractable only for the case of the 'ultimate prebunching', that is all particles entering at a particular phase. For this case, the stability boundary for the quasi-optical gyrotron is significantly affected.

For a more realistic field profile in the resonator, the stability is computed numerically with a modification of the multimode simulation developed earlier.[4] Once the equlibrium is obtained, perturbed orbits are calculated and inserted in the equations for the two sidebands. The growth rates for these two modes are then computed numerically. For the free running oscillator case, for a particular value of $\mu$, a plot of the stable regions in the space of $\delta$ and field amplitude parameter F is obtained. Typically a mode can be stable for values of current as high as twenty times the start oscillation threshhold current. Results will be presented for direct injection phase locked equlibria and prebunched beam phase locked equilibria, and the results will be compared with the results for free running equilibria.

* This work supported by the Department of Energy.

1. N.S. Ginzburg and S.P. Kuznitsov, in Relativistic High Frequency Electronics, p 101 IPF USSR Acad. Sci. Gorky (1981)

2. T.M. Antonsen and B. Levush, to be published; also see U.Md. Plasma Preprint 88-039

3. A. W. Fliflet and W.M. Manheimer, to be published; also see NRL Memo 6180

4. A. Bondeson, B. Levush, W. Manheimer, and E. Ott, Int. J. Electronics, 53, 547, (1982)

# APPENDIX L

## Modulation of an Intense Beam by an External Microwave Source: Theory and Simulation

# Modulation of an intense beam by an external microwave source: Theory and simulation

J. Krall[a] and Y. Y. Lau
*Plasma Physics Division, Naval Research Laboratory, Washington, DC 20375-5000*

(Received 27 July 1987; accepted for publication 1 December 1987)

A time-dependent, fully electromagnetic particle code is used to simulate the current modulation in an intense relativistic electron beam by an external rf source. It is shown that the intense beam may serve as a power amplifier with good phase stability, as suggested in earlier experiments. Increase in beam bunching by the dc space charge is demonstrated with a simple analytical model.

The experimental demonstration[1] of deep current modulation in an intense relativistic electron beam ($\sim 5$ kA, 500 keV) by a moderate external rf source ($\sim 50$ kW) suggests strong potentials[2,3] to amplify rf power to gigawatts at frequencies between 1 and 10 GHz. Several unusual properties were discovered in the experiments,[1,4] namely, the high degree of phase and amplitude stability in the output signal,[1] the ease with which the current modulation can be achieved and may be manipulated by the introduction of additional, undriven cavities downstream, and the possible avoidance of electrical breakdown at the gaps, even at a high level of beam modulation.[5] These unexpected features are only partially understood. The major obstacle to a complete understanding is the highly nonlinear interaction in complex geometries involving the kinetic energy, rf energy, *and* the potential energy of the beam, all of which are of the same order of magnitude. The crucial role played by the potential energy, which necessarily accompanies an intense beam, renders the classical picture of beam bunching invalid.

We, therefore, resort to a time-dependent, two-dimensional, fully electromagnetic particle code, CONDOR,[6] to simulate the response of an intense beam to an external rf excitation. This amplifier configuration has never been subject to particle simulation, although self-excited oscillations have been studied in the past.[7] We found that when the external rf drive is low, the induced rf current agrees well with the small signal theory.[1,7] Addition of a second cavity in the drift region significantly enhances the current modulation, without loss of phase stability, as observed in earlier experiments.[1] An analytical model is presented to show that the dc space charges associated with the intense beam may encourage current bunching as the beam traverses a modulating gap. The harmonic content is assessed. The details, together with experimental observations, will be published elsewhere.[4]

To mimic the experiments as closely as possible, the simulation geometry (Fig. 1) consists of a 500 keV, annular IREB with beam radius $r_b = 1.9$ cm and beam current $I_0 = 5$ kA propagating along a metal cylinder of radius $r_w = 2.4$ cm. A static 10 kG axial magnetic field confines the IREB. A gap feeding a coaxial cavity 5.6 cm long is inserted into the drift tube. An infinite radial transmission line (not shown) is attached to the outer wall of this cavity and "pumps" rf energy into the cavity at a frequency $f = 1.37$ GHz, the resonance frequency of the cavity. At $t = 0$, the rf drive is turned on. At $t = 6$ ns, after the fundamental mode of the cavity has saturated, the beam current is ramped up, reaching its full value at $t = 11$ ns (5 ns rise). The simulation continues until $t = 20$ ns.

For rf drives yielding gap voltages with amplitude $V_1 = 30$ kV and $V_1 = 6$ kV, the axial distribution of the normalized rf current $I_1(z)/I_0$ in steady state is shown as solid lines in Fig. 2. Curves predicted by linear theory[1,7] for these parameters, plotted as dashed lines, show close agreement and demonstrate the validity of the simulations. The temporal evolution of the beam current at a distance $z = 28$ cm from the gap center is shown in Fig. 3(a) for the $V_1 = 30$ keV case.

To obtain a current modulation comparable to $I_0$, $V_1$ should also be of the same order of the beam voltage. It is impractical to excite such a large-gap voltage directly from an external rf source. Instead, one may insert a second cavity downstream [Fig. 1(b)], at a location where the current

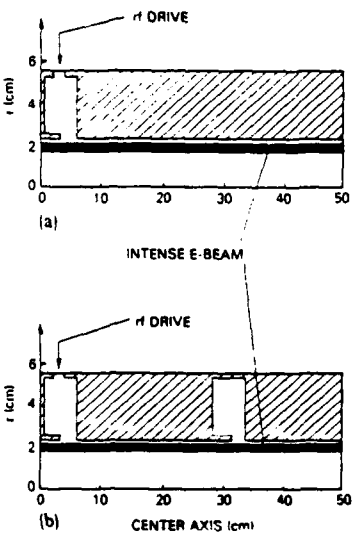



FIG. 1. (a) The geometry. Current modulation is provided by the externally driven cavity at left. (b) A second cavity is inserted to enhance current modulation.

[a] Science Applications Intl. Corp., 1710 Goodridge Drive, McLean, VA 22102.

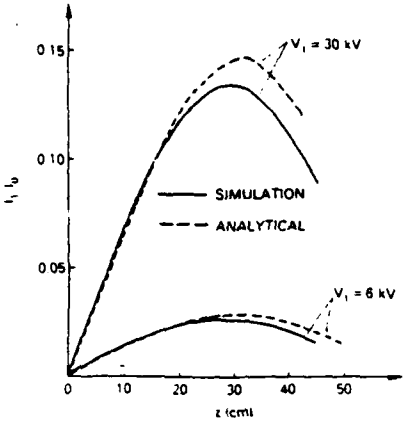



FIG. 2. Fraction of the modulated current for Fig. 1(a), at two levels of the rf drive.

modulation (by the first cavity) reaches a maximum[1]. This second cavity is identical to the first, but is not externally driven. Using the same rf drive as that for Fig. 3(a), we show in Fig. 3(b) the temporal evolution of the beam current at 6 cm downstream from the second gap, at which the gap voltage is 330 keV. The total current modulation there increases to 57%, including all harmonics. In fact, the modulation level continues to increase over the remaining 10 cm of propagation distance, reaching 85%. No particle reflections were observed at the second gap; nor were transients important. These results compare favorably to both the experimental two-cavity result, in which the cavity separation was 5 cm and modulation greater than 80% was observed at 1.328 GHz,[1] and to more recent results in which the separation is 32 cm.[4] In this situation, the harmonic content is considerable, with as many as 11 harmonics clearly observable in the

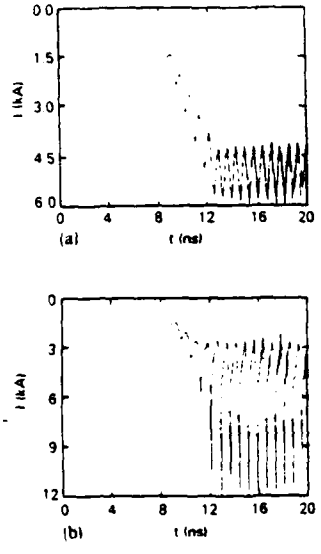



FIG. 3. (a) Current response measured at $z = 28$ cm from the gap for Fig. 1(a), with gap voltage $V_1 = 30$ kV. (b) Current response measured at 6 cm downstream of the second (right) cavity in Fig. 1(b), with $V_1 = 30$ kV at the first cavity.

current measured immediately downstream from the second gap.

The harmonic content of the beam was assessed analytically. Retaining fully the nonlinearity due to charge overtaking and accurately accounting for the change in the electron density in the drift region, we found that the $n$th harmonic in the current modulation is given by

$$I_n(z) \simeq 2I_0 J_n(n\bar{V}\sin\bar{z}), \tag{1}$$

where $J_n$ is the Bessel function of order $n$, and $\bar{V}$ and $\bar{z}$ are, respectively, the normalized gap voltage and the normalized axial distance from the gap, defined so that the small signal limit,[1,7] $I_1(z) \simeq I_0 \bar{V}\sin\bar{z}$, is recovered as $\bar{V} \to 0$. The crucial assumption used to derive Eq. (1) is that the collective forces that the electrons experience in the drift tube have been *linearized* and contain *only* the fundamental frequency component. The estimates according to Eq. (1) are in qualitative agreement with the simulations and experiments, with significant harmonic content only when $\bar{V} \gtrsim 0.3$.

One interesting property of an intense beam which is not shared with that which is characteristic of a classical klystron is the possibility of substantial current modulation immediately beyond a modulating gap. In a simple model, where a rf voltage $V_1 \sin\omega t$ is imposed across the gap, the instantaneous values $v$ (speed), $\beta$, and $\gamma$ of an electron are given by

$$\gamma_{inj} = \gamma + \frac{I_0}{I_c\beta} + \frac{|e|V_1\sin\omega t}{m_0c^2}, \tag{2}$$

where $I_c = 8.53\ \text{kA}/\ln(r_w/r_b)$ and $\gamma_{inj}m_0c^2$ is the electron energy at injection. It is easy to show that Eq. (2) does not admit a (real) solution for $\beta$ and $\gamma$ if $V_1 \sin\omega t > V_{th}$, where

$$V_{th} = \frac{m_0c^2}{e}\left\{\gamma_{inj} - \left[1 + \left(\frac{I_0}{I_L}\right)^{2/3}(\gamma_{inj}^{2/3} - 1)\right]^{3/2}\right\}, \tag{3}$$

and $I_L \equiv I_c(\gamma_{inj}^{2/3} - 1)^{3/2}$ is the limiting current from dc theory. The current modulation at the gap exit is absent if $V_1 < V_{th}$, but rises rapidly once $V_1 > V_{th}$, and becomes insensitive to $V_1$ if the latter substantially exceeds $V_{th}$. These features are also reflected qualitatively in experiments. The amount of current modulation at the gap exit is estimated to be

$$\left(\frac{I_1}{I_0}\right)_{exit} \simeq \frac{\omega}{\pi}\int_{\hat{t}-\pi}^{\hat{t}} dt\sin\omega t = \frac{2}{\pi}\left(1 - \frac{V_{th}^2}{V_1^2}\right)^{1/2}, \tag{4}$$

where $\hat{t} = (1/\omega)\sin^{-1}(V_{th}/V_1)$.

Finally, the phase locking between the external rf and the current modulation, implicit in the linear amplifier configuration, was tested for the fully modulated beam in the two-cavity geometry [Fig. 1(b)]. We varied the phase of the input signal and observed a corresponding phase shift in the peaks of the current response [see Fig. 3(b)]. We found that as the input signal is shifted by $\pi$, the fully modulated beam is phase locked to within an error of $1.1 \pm 0.6\%$, in agreement with experimental observations.[4]

In summary, several unusual features observed in experiments on the modulation of an intense beam are confirmed in the particle simulation. Useful analytic models are constructed.

We are grateful to M. Friedman and V. Serlin for many stimulating discussions, and for their support. We are also indebted to Scott Brandon and Adam Drobot for their assistance in applying CONDOR[6] to this problem. This work is supported by the Department of Energy under contract No. DE-AI05-86 ER 13585.

[1]M. Friedman and V. Serlin, Phys. Rev. Lett. **55**, 2860 (1985).
[2]M. Friedman and V. Serlin, Appl. Phys. Lett. **49**, 596 (1986).
[3]M. Friedman, V. Serlin, A. Drobot, and A. Mondelli, IEEE Trans Plasma Sci. **PS-14**, 201 (1986).
[4]M. Friedman, J. Krall, Y. Y. Lau, and V. Serlin (unpublished)
[5]M. Friedman and V. Serlin (private communication)
[6]CONDOR is an extension of the MASK particle code, discussed in A. Palevsky and A. Drobot, in Proceedings of the 9th Conference on Numerical Simulation of Plasmas, July 1980 (Northwestern University, Evanston, IL) (unpublished).
[7]M. Friedman, V. Serlin, A. Drobot, and L. Seftor, Phys Rev Lett **50**, 1922 (1983); J. Appl. Phys. **56**, 2459 (1984).

# APPENDIX M

## Nonlinear Space-Charge Waves on an Intense Relativistic Electron Beam

IEEE TPS 16 2 1988

# Nonlinear Space-Charge Waves on an Intense Relativistic Electron Beam

Y. Y. Lau
J. Krall
M. Friedman
V. Serlin

Reprinted from
IEEE TRANSACTIONS ON PLASMA SCIENCE
Vol. 16, No. 2, April 1988

# Nonlinear Space-Charge Waves on an Intense Relativistic Electron Beam

Y. Y. LAU, J. KRALL, M. FRIEDMAN, AND V. SERLIN

*Abstract*—**The propagation characteristics of the large-amplitude space-charge waves on a modulated intense relativistic electron beam are calculated. It is shown that the slow space-charge waves may cease to propagate if the modulating voltage is sufficiently high, whereas the fast waves are relatively unaffected by the nonlinearity. The limiting electron velocity inferred from the analytical theory is in excellent agreement with particle simulation. The implications are discussed.**

## I. Introduction

AN INTENSE relativistic electron beam (IREB), by definition, carries a lot of power. This beam power would be efficiently converted to radiation if the beam is modulated. Thus, the experimental demonstration [1] of complete current modulation of an IREB (500 keV, 5 kA) by a moderate RF source (50 kW, 1.3 GHz) is of great interest to particle acceleration, RF heating, and many other applications [2] which require coherent RF sources at the gigawatt level and beyond. The experiments demonstrated excellent phase and amplitude stability in the modulated current [1]. In this paper, we study the propagation of space-charge waves on a modulated IREB, paying special attention to nonlinearity and to the effects of dc space charges. These issues are clearly important to the above experiments; they have received only scanty theoretical treatment in the literature.

The significant amount of dc space charges on an IREB leads to many properties not shared by a classical tenuous, nonrelativistic electron beam. For example [3], in the dc state, an IREB cannot propagate if its current $I_0$ exceeds a critical value $I_c$. When the beam is modulated, the interaction between the RF and the beam involves not only the kinetic energy but also the potential energy. In many cases of interest, the RF, kinetic, and potential energies are all of the same order of magnitude [4]. The small-signal dispersion relation [5] shows that the phase speed of the slow space-charge waves approaches zero as $I_0$ approaches $I_c$. There are other interesting properties unique to an intense beam [6], such as the possibility of electrostatic insulation, and the enhanced current bunching in the beam–gap interaction, etc., all being caused by the dc space charges of the IREB.

Manuscript received September 2, 1987; revised October 5, 1987. This work was supported by the Department of Energy under Contract DE-AI05-86 ER 13585.

Y. Y. Lau, M. Friedman, and V. Serlin are with the Plasma Physics Division, Naval Research Laboratory, Washington, DC 20375-5000.

J. Krall is with Science Applications International Corporation, McLean, VA 22102.

IEEE Log Number 8719468.

Here, we restrict our attention to the evolution of an intense beam which is subject to a velocity modulation by an external RF source. The beam is assumed to propagate inside a straight drift tube, and is guided by a strong axial magnetic field. Only the analytic and simulation results of this relatively simple system will be given here. Experimental observation, and a detailed discussion of various other issues related to an intense beam, are given elsewhere [6].

The nonlinear evolution of space-charge waves is formulated self-consistently in terms of a single partial differential equation. This equation takes full account of charge overtaking, dc space-charge effects, and harmonic generation, and even governs the electron motion through the regime when the instantaneous beam current exceeds the limiting value. The small-signal limit [5] is easily recognized. We have not entirely solved this equation. Instead, we calculate the modification of the propagation characteristics of the space-charge waves as a result of nonlinearity (in addition to the dc space-charge effect). We show that the slow space-charge waves are considerably more affected by nonlinearity than the fast waves. Crossing of the slow-wave characteristics occurs at a relatively low modulation level, implying a stronger current modulation than the linear theory would indicate. From the governing equation, we estimate the local electron speed which may be expected as the limiting current is reached via nonlinear interaction. In that case, the (nonlinear) slow space-charge wave ceases to propagate. This limiting electron speed is also evident in the particle simulation to be reported below.

In Section II, the model is described and the governing equation for the evolution of space-charge waves is formulated. In Section III, we calculate the nonlinear propagation characteristics, using the method developed by Lin [7] and Fox [8]. Some simulation results obtained from a particle code, CONDOR,[1] will also be given there. Certain issues will be addressed in the last section.

## II. Model and Governing Equation

Consider a thin annular electron beam emerging from the anode–cathode gap with kinetic energy $(\gamma_{inj} - 1)\, m_0 c^2$ and potential energy $\Phi = 0$. This beam is con-

[1]CONDOR is an extension of the MASK code developed by A. Palevsky and A. Drobot, presented at the 9th Conference on Numerical Simulation of Plasmas (Northwestern University, Evanston, Illinois, 1980).

0093-3813/88/0400-0249$01.00 © 1988 IEEE

fined by a strong axial magnetic field and drifts inside a metallic pipe of radius $r_w$. Perpendicular motions of the electrons are ignored. The beam is assumed to be infinitesimally thin with unperturbed surface charge density $\sigma_0$. Since potential energy has been used to set up a space-charge depression in the drift region, the kinetic energy of the propagating beam is reduced to $(\gamma_0 - 1)\, m_0 c^2$.

Conservation of energy requires

$$\gamma_{inj} = \gamma_0 + I_0/I_s\beta_0 \equiv \gamma_0 + \alpha\gamma_0^3 \equiv \gamma_0 + \bar{\sigma}_0 \quad (1)$$

where $I_0$ is the beam current, $\beta_0 = (1 - \gamma_0^{-2})^{1/2}$, and

$$I_s = 2\pi\epsilon_0 m_0 c^3/e \ln(r_w/r_b) = 8.53 \text{ kA}/\ln(r_w/r_b)$$

$$\alpha = I_0/I_s\gamma_0^3\beta_0 = \bar{\sigma}_0/\gamma_0^3. \quad (2)$$

Here, $\epsilon_0$ is the free-space permittivity, $m_0$ is the rest mass of an electron, $c$ is the speed of light, $e$ is the electron charge, $r_b$ is the beam radius, and a subscript (0) in $\gamma_0$ and $\beta_0$ denotes the value of the propagating beam in the drift region in the dc state. The dimensionless parameter $\alpha$ is introduced to represent the current. Another useful dimensionless parameter $\bar{\sigma}_0 = I_0/I_s\beta_0$ is introduced in (1). It represents the potential energy and will appear in the nonlinear partial differential equation, (7), given below.

Given the injection energy $E_{inj} = (\gamma_{inj} - 1)\, m_0 c^2$ and the normalized current $I_0/I_s$, the propagating $\gamma_0$ can be determined from (1). Fig. 1 shows the solution of $\gamma_0$, for several values of $E_{inj}$. Only the branch with the higher value of $\gamma_0$ is the stable solution [3] at a given value of $I_0/I_s$ (Fig. 1). There is no meaningful solution to (1) if $I_0 > I_c$, where [3]

$$I_c = I_s(\gamma_{inj}^{2/3} - 1)^{3/2} \quad (3)$$

is the limiting current (Fig. 1).

The nonlinear evolution of the beam may be readily formulated if the beam is sufficiently close to the wall, in which case the approximation of iong axial wavelength [5], [10] may be used. The instantaneous velocity of the beam $v(z, t)$, the surface density $\sigma(z, t)$, and the axial electric field $E_z(z, t)$ experienced by the beam are governed by the following three partial differential equations:

$$\gamma^3\left(\frac{\partial}{\partial t} + v\frac{\partial}{\partial z}\right)v = \frac{e}{m_0}E_z \quad (4)$$

$$\frac{\partial\sigma}{\partial t} + \frac{\partial}{\partial z}(\sigma v) = 0 \quad (5)$$

$$-\frac{\epsilon_0}{d}\frac{\partial E_z}{\partial z} = \left(\frac{\partial^2}{\partial z^2} - \frac{1}{c^2}\frac{\partial^2}{\partial t^2}\right)\sigma. \quad (6)$$

Here, $\gamma = (1 - v^2/c^2)^{-1/2}$ denotes the instantaneous value associated with the instantaneous velocity $v(z, t)$, and $d = r_b \ln(r_w/r_b)$. Equations (4) and (5) require few comments; their solution yields the density response $\sigma$ to some imposed axial electric field pattern $E_z$, whereas the solution to (6) gives the excitation of $E_z$ due to some charge distribution $\sigma(z, t)$ at the location of the beam. The derivation of (6) is given in Appendix A (cf. (A5)) where the long-wavelength approximation [5], [10] is invoked. Note the linearity between $\sigma$ and $E_z$ in (6), a consequence of Maxwell's equations.

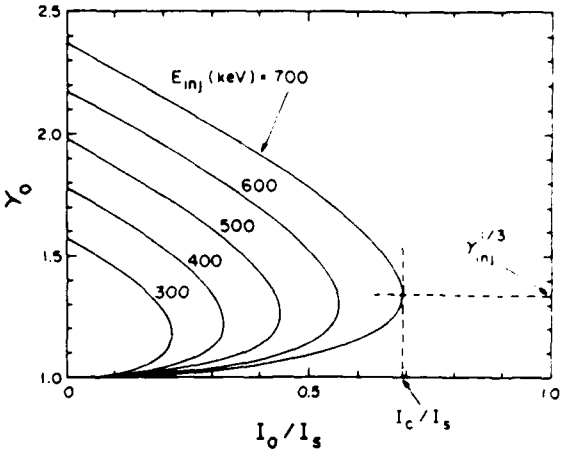



Fig. 1. The mass factor $\gamma_0$ of a propagating beam as a function of the beam current, at several injection energies, according to the dc theory (see (1)).

At the risk of some redundancy, we shall show that the system (4)–(6) includes phenomena of current limitation, say, in some steady-state solution as an example. In the steady state, $\partial/\partial t = 0$, (4)–(6) reduce to

$$\gamma m_0 c^2 + e\Phi = \gamma_{inj} m_0 c^2 = \text{constant}$$

$$\sigma v = \text{constant}$$

$$\frac{\epsilon_0}{d}\Phi = \sigma$$

which may be combined to yield

$$\gamma_{inj} = \gamma_0 + \frac{I_0}{I_s\beta_0}.$$

This is just (1) where the limiting current is discussed. We shall consider below the nonlinear evolution of the beam whose unperturbed state is characterized by $\sigma_0$, $\beta_0$, $\gamma_0$, $I_0$, and $v_0$, all of which are constants.

Without any further approximation, (4)–(6) may be combined into a single partial differential equation (see Appendix A):

$$\left(\frac{\partial}{\partial t} + v\frac{\partial}{\partial z}\right)^2 s = \frac{\bar{\sigma}_0}{\gamma^3}\left(c^2\frac{\partial^2}{\partial z^2} - \frac{\partial^2}{\partial t^2}\right)s \quad (7)$$

where $\bar{\sigma}_0 = I_0/I_s\beta_0$ is a constant already defined in (1). Physically, $s$ is the nonlinear displacement from the unperturbed position of a fluid element whose instantaneous position is $z$ at time $t$. In terms of $s$, the instantaneous current is

$$I(z, t) = I_0 + \frac{I_0}{v_0}\frac{\partial s(z, t)}{\partial t} \quad (8)$$

and the instantaneous velocity is

$$v(z, t) = v_0 + \frac{1}{1 - \partial s/\partial z}\left[\frac{\partial s}{\partial t} + v_0\frac{\partial s}{\partial z}\right] \quad (9)$$

with a corresponding value of $\gamma(z, t) = (1 - v^2/c^2)^{-1/2}$.

The derivation of (7)–(9) is given in Appendix A (cf. (A21), (A23), and (A13)).

It is interesting to note that, in the governing equation, (7), all of the complicated nonlinear processes (charge overtaking, dc and ac space-charge effects, and local transition through the limiting current, etc.) are already incorporated in the $v$ term (and through $v$ in the $\gamma^3$ term) of (7) in a rather simple manner. In other words, the way (7) is written, the beam density parameter $\bar{\sigma}_0$ remains unaffected by nonlinearity. This is not a trivial result that can be expected from the outset.

The linear dispersion relation [5]

$$(\omega - kv_0)^2 = \alpha(k^2c^2 - \omega^2) \tag{10}$$

may be readily recovered from (7) if we approximate $v$ by $v_0$ and $\gamma$ by $\gamma_0$ in that equation. The propagation constants $k_f$ and $k_s$ of the linear fast and slow waves are obtained from (10) (cf. [1] and [4]):

$$\omega = \frac{k_{f,s}v_0}{1 + \alpha}(1 \pm \alpha\mu) = \frac{k_{f,s}v_0}{\delta}\frac{1}{1 \mp \alpha\mu} \tag{11}$$

where $\alpha\mu = (\alpha^2 + \alpha/\gamma_0)^{1/2}/\beta_0$, $\delta = \beta_0^2/(\beta_0^2 - \alpha)$. The linear slow space-charge waves cease to propagate as $I_0 \to I_c$, in which case $\gamma_0 \to \gamma_{inj}^{1/3}$ and $\omega/k_s \to 0$ (cf. [4], and [5] and also Fig. 1).

The simplicity of the governing equation, (7), suggests a qualitative answer to the question: What would be the local electron speed when the current perturbation on the beam is so large that the nonlinear slow space-charge waves cease to propagate? Call this nonlinear limiting speed $v_{Nm}$ and $\beta_{Nm} = v_{Nm}/c$. Since (7) has the same structure as the corresponding equation in the linear theory, its local dispersion relation is also similar. Thus, $v_{Nm}$ is determined by

$$\beta_{Nm}^2\gamma_{Nm}^3 = \bar{\sigma}_0 \tag{12}$$

where $\gamma_{Nm} = (1 - \beta_{Nm}^2)^{-1/2}$. The solution of $\beta_{Nm}$ as a function of $\bar{\sigma}_0$ is shown in Fig. 2. The limiting velocity $v_{Nm}$ is approached nonlinearly, as the initial current $I_0$ is less than $I_c$, but it does not depend on how the large-amplitude perturbation is set up. Note that if $\beta_{Nm}^2 \ll 1$, (12) gives $\beta_{Nm} \cong \bar{\sigma}_0^{1/2} \propto (I_0/I_c)^{1/2}$. These estimates are based on a local theory of an exact formulation of the nonlinear processes, and they are in excellent agreement with particle simulation, as will be shown below. Note that the nonlinear limiting velocity $v_{Nm}$ is different from the limiting velocity $c(1 - \gamma_{inj}^{-2/3})^{1/2}$ according to the dc theory (cf. Fig. 1). The latter quantity is independent of the beam current.

## III. Propagation Characteristics and Simulation Results

Given some initial data on $s$ and $\partial s/\partial t$, (7) may be solved, in principle, for the evolution of $s$, and hence $I$ from (8), for subsequent times. The great resemblance of this nonlinear equation with the corresponding linearized one allows us to expect that the initial perturbation will propagate along the characteristics of the linear fast waves and slow waves. These characteristics are modified by nonlinearity. When the initial perturbation is small, the nonlinearity may be handled by a perturbation technique.

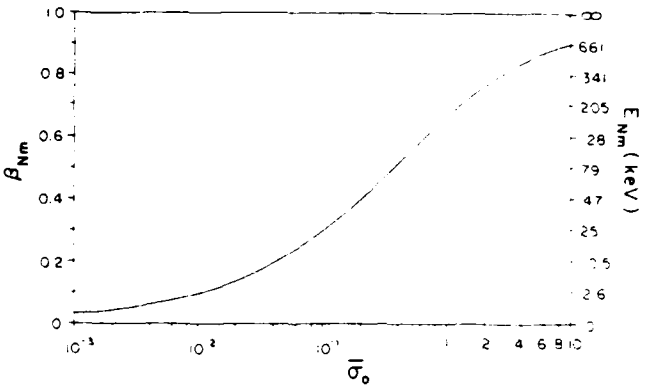



Fig. 2. The local velocity ($\beta_{Nm}c$) of the electrons when the nonlinear slow space-charge waves cease to propagate. Also labeled is the corresponding kinetic energy $E_{Nm}$.

Let us assume that a modulating gap at $z = 0$ imparts upon the beam with a velocity modulation given by

$$v_1(0, t) = (\epsilon v_0/2)\sin\omega t = v_1(t) \tag{13}$$

and

$$s(0, t) = 0 \tag{14}$$

where $\epsilon$ is the modulation depth. The initial condition (14) implies that there is no initial current modulation at $z = 0^+$. Nonlinearity modifies the propagation characteristics of the fast and slow waves, given by the $\xi$ = constant and $\eta$ = constant curves, respectively, in the $(z$–$t)$ plane. If $\epsilon$ is sufficiently small, the characteristic equations are modified to read [7], [8]

$$\begin{aligned} z - c_f t &= \xi + \epsilon G(\xi, \eta) \\ z - c_s t &= \eta + \epsilon H(\xi, \eta) \end{aligned} \tag{15}$$

to the lowest order in $\epsilon$. Here, $c_{f,s} = \omega/k_{f,s}$. In the limit $\epsilon \to 0$, the characteristic curves are straight lines in the $(z$–$t)$ plane, they represent the contours of constant phases of the linear slow and fast space-charge waves. Current modulation results from the beating of these waves.

When $\epsilon$ is small but finite, nonlinearity is introduced and the characteristics are no longer straight lines in the $(z$–$t)$ plane. The explicit forms of $G$ and $H$ are given in (B21) and (B22) of Appendix B. The approximate solution $v_1$ is given in (B15) in terms of the characteristic variables $\xi$ and $\eta$. They may even be valid beyond the time at which the characteristics intersect [7], [8].

In Figs. 3 and 4, we show the propagation characteristics over one cycle of the modulating voltage that is located at $z = 0$. Each characteristic is spaced a quarter-cycle ($\omega t = \pi/4$) from a neighboring one initially. The amplitude of the modulating voltage $V_1$ is specified in the

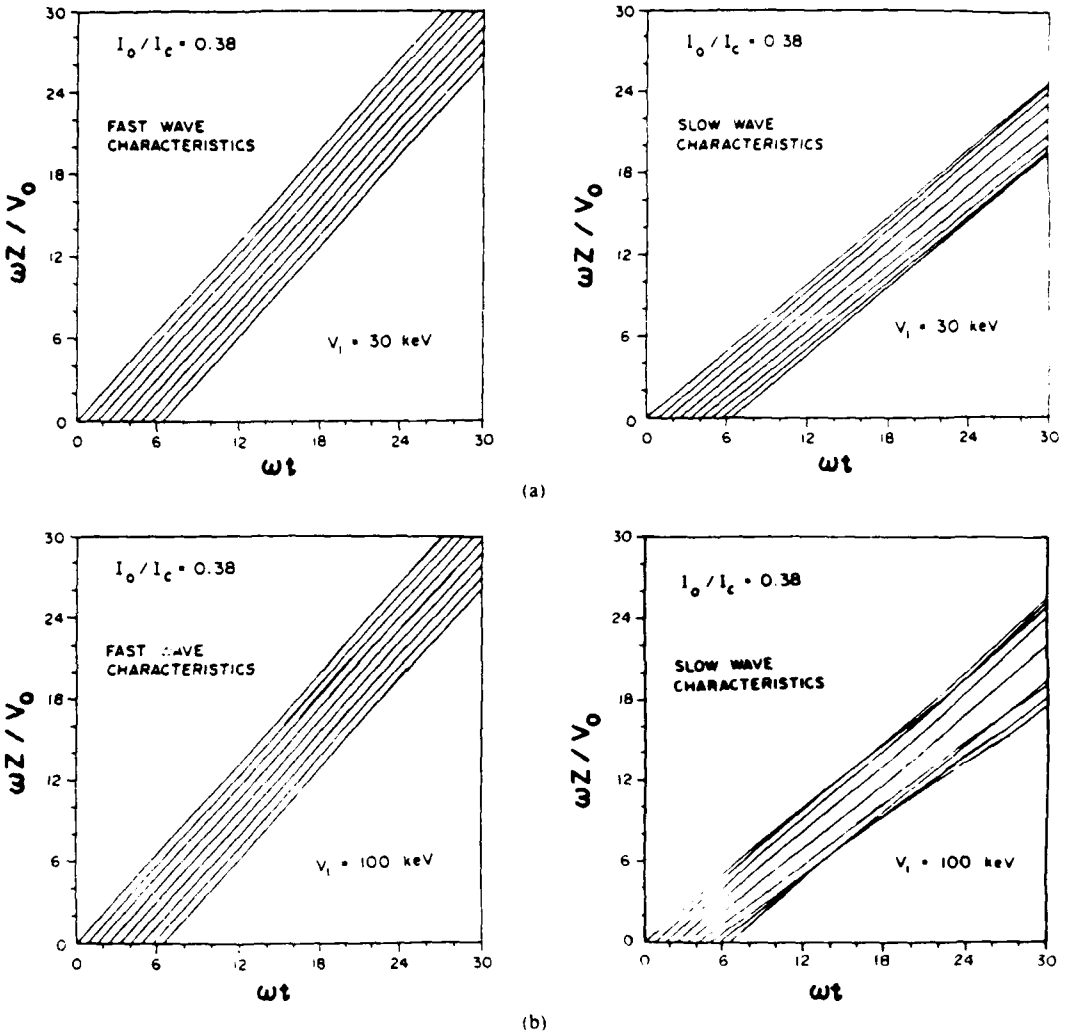



Fig. 3. The nonlinear fast- and slow-wave characteristics for $I_0/I_c = 0.38$. (a) RF voltage $V_1 = 30$ keV. (b) $V_1 = 100$ keV.

figure; it is related to the velocity modulation amplitude $v_1$ by $V_1 = v_1 v_0 m_0 \gamma_0^3/\delta$ [1], [4]. The fast-wave characteristics are shown on the left and the slow-wave characteristics on the right.

The parameters used in Fig. 3 are $E_{inj} = 425$ keV, $I_0 = 4.86$ kA, $I_s = 36.5$ kA, $I_c = 12.8$ kA, $\gamma_0 = 1.665$, and $\beta_0 = 0.8$. When the modulating RF voltage $V_1$ is low, the fast- and slow-wave characteristics are not significantly different from the linear theory, as shown in the $V_1 = 30$ keV case in Fig. 3. There, crossing of the slow-wave characteristics occur at a considerable distance downstream. When $V_1$ is raised to 100 keV, the fast-wave characteristics remain essentially unchanged, whereas the slow-wave characteristics cross at about one wavelength downstream, implying a stronger current modulation as a result of nonlinearity.

The modification of the slow-wave characteristics is more apparent if the dc beam current $I_0$ is raised to approach the limiting value $I_c$, as shown in Fig. 4. In Fig. 4, $E_{inj} = 425$ keV, $\gamma_{inj} = 1.83$, $I_0 = 10.3$ kA, $I_s = 36.5$ kA, $I_c = 12.8$ kA, $\gamma_0 = 1.44$, $\beta_0 = 0.72$, and $I_0/I_c = 0.8$. The fast-wave characteristics are hardly modified by the nonlinearity even if $V_1$ is as high as 100 keV. However, the slow-wave characteristics are significantly modified even if $V_1$ is only 30 keV; crossing of the slow-wave characteristics occur half a wavelength from the modulating gap. When $V_1$ is raised to 100 keV, crossing of characteristics occurs at $z = 0$, implying a strong current modulation at the exit of the modulating gap. Comparing the slow-wave characteristics between Figs. 3 and 4, we see that *the dc space charges of an IREB have a strong and favorable nonlinear effect on the current modulation.* It is interesting to note, for the $V_1 = 100$ keV case of Fig. 4, that the slow-wave characteristics orginating at $\omega t = 3\pi/2$ has an almost zero slope, whereas those originating at $\omega t = 5\pi/4$ and at $\omega t = 7\pi/4$ show some soliton-like behavior.

When the gap voltage $V_1$ is high, the perturbation method, given in Appendix B, based on small $\epsilon(V_1)$, would be invalid. Particle simulation has been used to analyze the response of the electrons when $V_1$ is large. The simulation code used in the present study, CON-

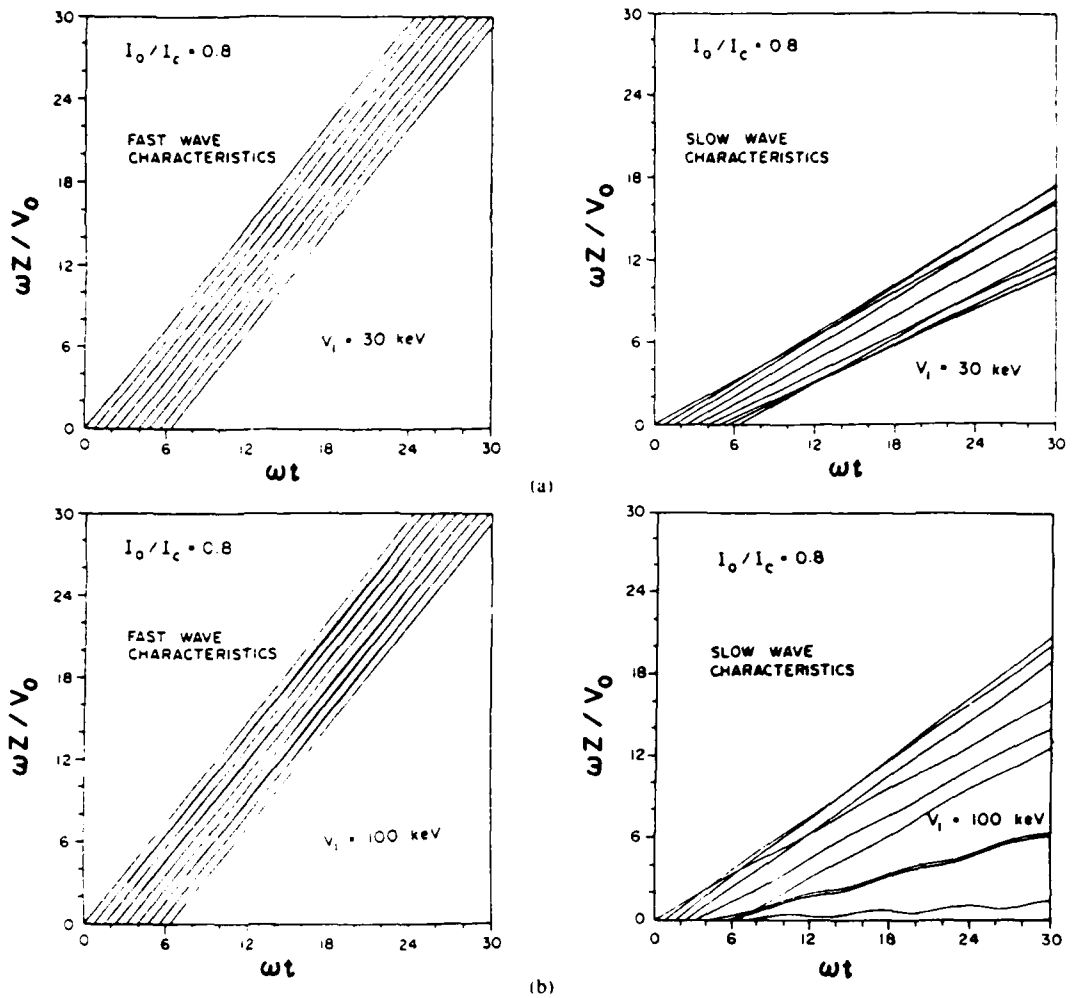



Fig. 4. (a) and (b) Same as in Fig. 3, except $I_0 = 0.8\, I_c$.

DOR.[1] is time dependent, two dimensional, and fully electromagnetic. The simulated model consists of a gap feeding a coaxial cavity, resonant at 1.37 GHz, which is inserted into a drift tube. The drift tube and the beam parameters are the same as in Fig. 3: $I_0 = 4.8$ kA, $I_s = 36.5$ kA, $I_c = 12.8$ kA, and $\gamma_0 = 1.67$. The cavity is externally driven at the resonant frequency by a radial transmission line, producing gap voltages of amplitude $V_1 = 150$, 200, 250, and 330 keV. Phase-space plots for these four cases are shown in Fig. 5. The particles are injected at $z = 0$ and cross the modulating gap at $z = 5$ cm. These plots are given for a time late enough in the simulation that transient effects due to the finite beam rise time are not significant.

Several features are noteworthy. 1) A low-energy population emerges from the gap region at the high values of $V_1$ given in Fig. 5. (This population vanishes for lower values of $V_1$.) 2) The mean axial velocity of this second population coincides with $\beta_{Nm}c$ given in Fig. 2. This velocity is represented by the dash-dot curve in Fig. 5 and is independent of $V_1$ (cf. (12)). 3) There are few or no reflected particles, even when $V_1$ is high. Further simulations of this nature, which more closely mimic the modulation experiments, are given in [6].

## IV. Discussion

The present nonlinear study partially fills the gap between the small-signal regime and the highly nonlinear state analyzed via particle simulation. Whereas detailed agreement has been obtained between experiments, theory, and simulation in the linear regime, only highly idealized models have been constructed to understand the fully nonlinear state [6]. We believe that the "simple looking" equation, (7), provides an accurate description of the essential nonlinear processes.

The nonlinear solutions in terms of the characteristic variables $(\xi, \eta)$ contain harmonic components. To extract this information would require a transformation of the solutions back to the $(z, t)$ variables. This may be done analytically in an iterative manner. A simpler, perhaps less accurate, assessment of the harmonic content is given elsewhere [6], [9]. There, we show that the harmonic content is significant only if the fundamental component of the current modulation is a sizable fraction of the dc current of the beam.

In summary, this paper provides insight into some of the mechanisms by which an intense relativistic electron beam is more readily modulated than a classical (tenuous, nonrelativistic) beam. These mechanisms are a result of

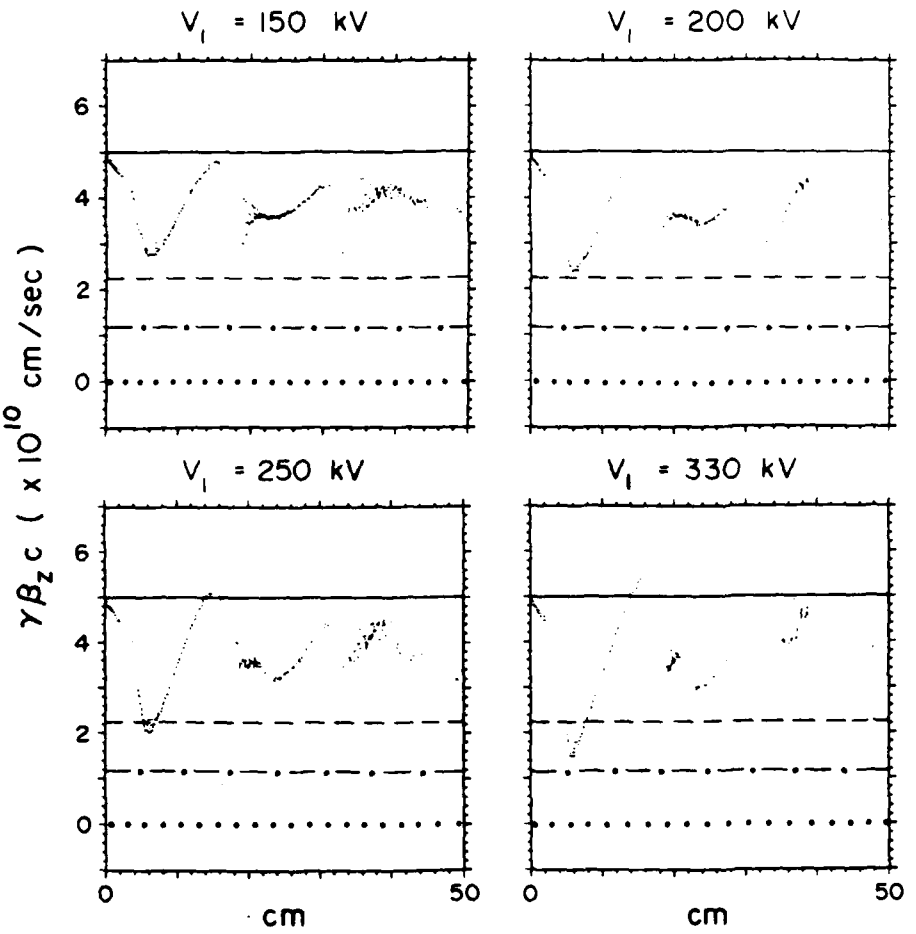



Fig. 5. Phase-space plots of the electrons at high values of modulating voltage. The modulating gap is located 5 cm from the left. The four reference lines represent (from top) the axial momentum associated with the diode voltage, the limiting velocity according to the dc theory (see (1)), the limiting velocity according to the nonlinear theory (see (12)), and zero energy.

the beam's significant dc space charges. We found that there is a rapid nonlinear deceleration of the slow waves, especially when the beam current is a substantial fraction of the limiting current.

## Appendix A
## Derivation of (6)–(9)

In this Appendix, we shall first derive (6) from Maxwell's equations under the long-wavelength approximation. We next show that the nonlinear system, (4)–(6), is equivalent to (7)–(9).

A surface charge $\sigma(z, t)$ on a thin annular beam excites electromagnetic fields with components $E_r(r, z, t)$, $E_z(r, z, t)$, $H_\theta(r, z, t)$. In the vacuum region between the sheet beam ($r = r_b$) and the outer conducting wall ($r = r_w$), these fields satisfy Faraday's law

$$-\frac{\partial H_\theta}{\partial t} = \frac{1}{\mu_0}\left(\frac{\partial E_r}{\partial z} - \frac{\partial E_z}{\partial r}\right) \tag{A1}$$

and the $r$ component of $\nabla \times \vec{H} = \epsilon_0 \partial \vec{E}/\partial t$ gives

$$\frac{\partial H_\theta}{\partial z} = -\epsilon_0 \frac{\partial E_r}{\partial t}. \tag{A2}$$

Operate (A1) by $\partial/\partial z$, (A2) by $\partial/\partial t$, add the resultants, and then integrate from $r = r_b$ to $r_w$ to yield

$$\left(\frac{1}{c^2}\frac{\partial}{\partial t^2} - \frac{\partial^2}{\partial z^2}\right)\int_{r_b}^{r_w} E_r(r, z, t)\, dr = \frac{\partial}{\partial z} E_z(r_b, z, t) \tag{A3}$$

where we have used the boundary condition of a perfectly conducting pipe: $E_z(r_w, z, t) = 0$. No approximation has been made to obtain (A3). We now introduce the long-wavelength approximation [5], [10]:

$$E_r(r, z, t) = \frac{1}{\epsilon_0}\frac{r_b}{r}\sigma(z, t). \tag{A4}$$

Equation (A3) then becomes

$$\left(\frac{1}{c^2}\frac{\partial^2}{\partial t^2} - \frac{\partial^2}{\partial z^2}\right)\frac{\sigma}{\epsilon_0} r_b \ln\left(\frac{r_w}{r_b}\right) = \frac{\partial}{\partial z} E_z(r_b, z, t) \tag{A5}$$

which is just (6) of the main text where we use $E_z(z, t)$ to denote $E_z(r_b, z, t)$, the axial electric field experienced by the beam. (The validity of the long-wavelength ap-

proximation may be justified in a number of circumstances, one of which is when the beam is sufficiently close to the wall. A detailed examination of this long-wavelength approximation has been given in [10].)

To derive (7)–(9), we shall now assume that the beam in equilibrium is characterized by constant density $\sigma_0$, uniform drift speed $v_0$, and current $I_0$. Instead of using the Eulerian variables $(z, t)$, we introduce the "polarization variable" $(z_0, \tau)$ which is related to $(z, t)$ by [11]

$$z = z_0 + z_1(z_0, \tau) \tag{A6}$$

$$t = \tau \tag{A7}$$

where $z_0$ is the coordinates of an electron fluid element at time $t$ in the absence of perturbation, and $z_1$ is its displacement from $z_0$ in the presence of perturbation. We do not assume $z_1$ to be small. Thus, $z$ is the instantaneous position of the fluid element at time $t$. The instantaneous velocity of this fluid element is, from (A6),

$$v = dz/dt = v_0 + v_0 \frac{\partial z_1(z_0, \tau)}{\partial z_0} + \frac{\partial z_1(z_0, \tau)}{\partial \tau} \tag{A8}$$

or

$$v \equiv v_0 + v_1 \tag{A9}$$

where the perturbation velocity $v_1$ is

$$v_1 = v_0 \frac{\partial z_1(z_0, \tau)}{\partial z_0} + \frac{\partial z_1(z_0, \tau)}{\partial \tau}. \tag{A10}$$

Let us denote the displacement by $s$:

$$z_1(z_0, \tau) \equiv s(z, t) \tag{A11}$$

in the Eulerian variable. Since $v$ is also the Eulerian velocity of the fluid element which, at time $t$, occupies position $z$, we have

$$v_1 = \left(\frac{\partial}{\partial t} + v \frac{\partial}{\partial z}\right) s(z, t). \tag{A12}$$

Using (A9) in (A12), we have

$$v = v_0 + \frac{\partial s/\partial t + v_0 \partial s/\partial z}{1 - \partial s/\partial z} \tag{A13}$$

which is (9) of the main text. Alternatively, we obtain (A13) from (A6) and (A7), which give

$$(\partial/\partial z_0)_\tau = (1 + \partial z_1/\partial z_0)(\partial/\partial z)_t \tag{A14}$$

$$(\partial/\partial \tau)_{z_0} = (\partial/\partial t)_z + (\partial z_1/\partial \tau)(\partial/\partial z)_t. \tag{A15}$$

Apply $z_1$ to the left-hand sides and $s$ to the right-hand sides of (A14) and (A15) to yield

$$\frac{\partial z_1(z_0, \tau)}{\partial z_0} = \frac{\partial s(z, t)/\partial z}{1 - \partial s(z, t)/\partial z} \tag{A16}$$

$$\frac{\partial z_1(z_0, \tau)}{\partial \tau} = \frac{\partial s(z, t)/\partial t}{1 - \partial s(z, t)/\partial z}. \tag{A17}$$

Substitution of (A16) and (A17) into (A8) gives (A13).

In the unperturbed state, the amount of charge between $z_0$ and $z_0 + dz_0$ is $\sigma_0 dz_0$. In the presence of perturbation, the electron at $z_0$ moves to $z_0 + z_1(z_0, \tau)$ and the electron at $z_0 + dz_0$ moves to $(z_0 + dz_0) + z_1(z_0 + dz_0, \tau)$. Let $\sigma$ be the instantaneous charge density in the presence of perturbation. Conservation of charge requires

$$\sigma_0 dz_0 = \sigma\big[z_0 + dz_0 + z_1(z_0 + dz_0, \tau) - (z_0 + z_1(z_0, \tau))\big]$$

which gives, as $dz_0 \to 0$,

$$\sigma = \frac{\sigma_0}{1 + \partial z_1(z_0, \tau)/\partial z_0} = \sigma_0\left(1 - \frac{\partial s}{\partial z}\right). \tag{A18}$$

In writing the last expression, we have used (A16). Substitution of (A18) into (6) gives

$$-\frac{\epsilon_0}{d} E_z = -\sigma_0 \left(\frac{\partial^2}{\partial z^2} - \frac{1}{c^2}\frac{\partial^2}{\partial t^2}\right) s. \tag{A19}$$

Since

$$\left(\frac{\partial}{\partial t} + v \frac{\partial}{\partial z}\right) v = \left(\frac{\partial}{\partial t} + v \frac{\partial}{\partial z}\right)^2 s \tag{A20}$$

by (A9) and (A12), we substitute (A19) and (A20) into (4) to obtain

$$\left(\frac{\partial}{\partial t} + v \frac{\partial}{\partial z}\right)^2 s = \frac{\bar{\sigma}_0}{\gamma^3}\left(c^2 \frac{\partial^2}{\partial z^2} - \frac{\partial^2}{\partial t^2}\right) s \tag{A21}$$

which is (7) of the main text, where the constant $\bar{\sigma}_0$ is defined.

Finally, the instantaneous current $I(z, t)$ is given by

$$I(z, t) = I_0\left(\frac{\sigma v}{\sigma_0 v_0}\right). \tag{A22}$$

Inserting (A13) and (A18) into (A22), we obtain

$$I(z, t) = I_0\left[1 + \frac{1}{v_0}\frac{\partial s}{\partial t}\right] \tag{A23}$$

which is (8) of the main text.

## Appendix B
## Nonlinear Characteristics of the Fast and Slow Space-Charge Waves

In this Appendix, we calculate the nonlinear propagation characteristics of the fast and slow space-charge waves governed by (7), by a perturbation technique developed in [7] and [8]. We shall restrict our discussion to the evolution of nonlinear space-charge waves when the beam is subject to a weak velocity modulation at $z = 0$:

$$v_1(t) = (\epsilon v_0/2) \sin \omega t. \tag{B1}$$

The beam itself need not be weak; that is, $\bar{\sigma}_0$ need not be small.

In the linearized theory, the characteristics of the fast and slow waves are straight lines in the $(z, t)$ plane:

$$p = z - c_f t \tag{B2}$$

$$q = z - c_s t \tag{B3}$$

where $p$ and $q$ are the characteristic variables for the fast and slow waves, respectively, whose propagation speeds $c_{f,s} = \omega/k_{f,s}$ are constant and $k_{f,s}$ are given by (11) of the main text. In the small-signal theory, it is easy to show that the RF velocity $v_1$ may be expressed as

$$v_1 = -\frac{\epsilon}{2}\left(\frac{\omega_f}{\Delta k}\right)\sin k_f p + \frac{\epsilon}{2}\left(\frac{\omega_s}{\Delta k}\right)\sin k_s q \tag{B4}$$

in terms of the characteristic variables $p$ and $q$. Here,

$$\omega_f \equiv \omega - k_f v_0$$

$$\omega_s \equiv \omega - k_s v_0 \tag{B5}$$

$$\Delta k \equiv k_s - k_f \tag{B6}$$

Because of the nonlinearity in (7), the characteristic curves are no longer straight lines. Instead of $p$ and $q$, we shall use $\xi$ and $\eta$ to denote the nonlinear characteristics associated with the fast and slow waves. If the initial velocity perturbation ($\epsilon$) is small, these nonlinear characteristics may be obtained by a perturbation method. In several cases, this technique has been proven [7] to be uniformly valid. To the lowest order in $\epsilon$, the characteristics equations, (B2) and (B3), are modified to read

$$z - c_f t = \xi + \epsilon G(\xi, \eta) \tag{B7}$$

$$z - c_s t = \eta + \epsilon H(\xi, \eta) \tag{B8}$$

where $G$ and $H$ are to be determined. Since (7) is quite complicated, based on physical argument, we expect the characteristics in the $(z, t)$ plane to be governed by

$$\frac{\partial z}{\partial \eta} = u_f \frac{\partial t}{\partial \eta} \qquad (\xi = \text{constant}) \tag{B9}$$

$$\frac{\partial z}{\partial \xi} = u_s \frac{\partial t}{\partial \xi} \qquad (\eta = \text{constant}) \tag{B10}$$

where the nonlinear phase speeds $u_f$, $u_s$ are the solution to the local dispersion relation (cf. (7)):

$$(u_{s,f} - v)^2 = \frac{\bar{\sigma}_0}{\gamma^3}(c^2 - u_{s,f}^2). \tag{B11}$$

Note that $u_{s,f}$ depends on the amplitude of the perturbation. If $v = v_0 + v_1$, and if $v_1 \ll v_0$, we obtain from (B11), after some algebra,

$$u_s = c_s + \Delta u_s$$

$$u_f = c_f + \Delta u_f \tag{B12}$$

where

$$\Delta u_{f,s} = R_{f,s} v_1 \tag{B13}$$

$$R_{f,s} \equiv \frac{(c_{f,s} - v_0)\left[2 - 3\gamma_0^2\beta_0(c_{f,s} - v_0)/c\right]}{2(c_{f,s} - v_0 + \alpha c_{f,s})} \tag{B14}$$

to first order in $v_1$. Here, $v_1$ is understood to be expressed in terms of the $\xi, \eta$ variables. To proceed further, we need one crucial observation as $v_1$ itself is unknown at this point. In the theory of perturbation of characteristics, to the lowest order, the solution in terms of the characteristic variables remains the same as the linearized theory, only the dependence of the characteristic variables on $(z, t)$ is modified by the nonlinearity [7], [8]. Thus, from (B4), we have the lowest order solution:

$$v_1 = \frac{-\epsilon}{2}\left(\frac{\omega_f}{\Delta k}\right)\sin k_f \xi + \frac{\epsilon}{2}\left(\frac{\omega_s}{\Delta k}\right)\sin k_s \eta \tag{B15}$$

in terms of $\xi$ and $\eta$. This solution is to be inserted into (B13).

To determine $G$ and $H$, from (B7) and (B8), we obtain

$$t = \frac{1}{\Delta c}\left[\xi - \eta + \xi(G - H)\right] \tag{B16}$$

$$z = \left(\frac{1}{\Delta c}\right)\left[c_s\xi - c_f\eta + \epsilon\,(c_s G - c_f H)\right] \tag{B17}$$

where

$$\Delta c = c_s - c_f \equiv \frac{\omega}{k_s} - \frac{\omega}{k_f} \tag{B18}$$

Substituting (B16), (B17), and (B12) into (B9), we obtain, after some manipulation,

$$\epsilon\frac{\partial G(\xi, \eta)}{\partial \eta} \approx \frac{-\Delta u_f}{\Delta c} \qquad (\xi = \text{constant}) \tag{B19}$$

to first order in $\epsilon$. Similarly, (B10) gives

$$\epsilon\frac{\partial H(\xi, \eta)}{\partial \xi} = \frac{\Delta u_s}{\Delta c} \qquad (\eta = \text{constant}) \tag{B20}$$

to first order in $\epsilon$. Equations (B19) and (B20) are now easily integrated, since their right-hand sides are linear combinations of $\sin k_f \xi$ and $\sin k_s \eta$ by virtue of (B13) and (B15). This integration yields, upon using the boundary conditions for $z = 0$,

$$G(\xi, \eta) = -\left(\frac{R_f}{\Delta c}\right)\left(\frac{1}{2\Delta k}\right)\left[\omega_f(\eta - c_s\xi/c_f)\sin k_f\xi + \frac{\omega_s}{k_s}(\cos k_s\eta - \cos k_f\xi)\right] \tag{B21}$$

$$H(\xi, \eta) = \left(\frac{R_s}{\Delta c}\right)\left(\frac{1}{2\Delta k}\right)\left[\frac{\omega_f}{k_f}(\cos k_f\xi - \cos k_s\eta) + \omega_s(\xi - c_f\eta/c_s)\sin k_s\eta\right]. \tag{B22}$$

In (B21) and (B22), $R_f$ and $R_s$ are defined in (B14); $\Delta c$ is defined by (B18), $\Delta k$ by (B6), $\omega_{f,s}$ by (B5), and $k_{f,s}$ by

(11) of the main text; and $c_{f,s} = \omega/k_{f,s}$. Note that in the derivation given in this Appendix, we only assume that the velocity modulation $\epsilon$ is small. We did not assume $\bar{\sigma}_0$ to be small.

## REFERENCES


[1] M. Friedman and V. Serlin, "Modulation of intense relativistic electron beams by an external microwave source," *Phys. Rev. Lett.*, vol. 55, pp. 2860-2863, 1985.

[2] M. Friedman and V. Serlin, "Particle accelerators powered by modulated intense relativistic electron beams," *Appl. Phys. Lett.*, vol. 49, pp. 596-598, 1986.
M. Friedman, V. Serlin, A. Drobot, and A. Mondelli, "High-power modulated intense relativistic electron sources with applications to RF generation and controlled thermonuclear fusion," *IEEE Trans. Plasma Sci.*, vol. PS-14, pp. 201-214, 1986.

[3] R. B. Miller, *An Introduction to the Physics of Intense Charged Particle Beams*. New York: Plenum, 1982, ch. 3.

[4] M. Friedman, V. Serlin, A. Drobot, and L. Seftor, "Propagation of intense relativistic electron beams through drift tubes with perturbed walls," *Phys. Rev. Lett.*, vol. 50, p. 1922, 1983.
M. Friedman, V. Serlin, A. Drobot, and L. Seftor, "Self modulation of intense relativistic electron beams," *J. Appl. Phys.*, vol. 56, pp. 2459-2475, 1984.

[5] R. J. Briggs, "Space-charge waves on a relativistic unneutralized electron beam and collective ion acceleration," *Phys. Fluids*, vol. 19, pp. 1257-1258, 1976.

[6] M. Friedman, J. Krall, Y. Y. Lau, and V. Serlin, *J. Appl. Phys.*, accepted for publication.

[7] C. C. Lin, "On a perturbation theory based on the method of characteristics," *J. Math. Phys.*, vol. 33, pp. 117-134, 1954.

[8] P. A. Fox, "Perturbation theory of wave propagation based on the method of characteristics," *J. Math. Phys.*, vol. 34, p. 133, 1955.
A. Neyfeh, *Perturbation Methods*. New York: Wiley, 1973, ch. 3.

[9] J. Krall and Y. Y. Lau, "Modulation of an intense beam by an external microwave source: Theory and simulation," *Appl. Phys. Lett.*, vol. 52, pp. 431-433, 1988.

[10] Y. Y. Lau, "Some design considerations on using modulated intense annular electron beams for particle acceleration," *J. Appl. Phys.*, vol. 62, pp. 351-356, 1987.

[11] D. L. Bobroff, "Independent space variables for small-signal electron beam analysis," *IRE Trans. Electron Devices*, vol. ED-6, pp. 68-78, 1959.

# APPENDIX N

## Externally Modulated Intense Relativistic Electron Beams

# Externally modulated intense relativistic electron beams

M. Friedman, J. Krall,[a] Y. Y. Lau, and V. Serlin
*Plasma Physics Division, Naval Research Laboratory, Washington, DC 20375-5000*

(Received 12 October 1987; accepted for publication 23 May 1988)

The physics of modulation of an intense relativistic electron beam by an external microwave source is studied in this paper via experiment, theory, and simulation. It is found that the self-fields of the electron beam, in general, intensify the current modulation produced by the external source. The linear and nonlinear theory, together with the simulation, show that the classical klystron description in the drift tube region is substantially modified by the beam's high density. In the modulating gap, electron bunches may be generated instantaneously without the necessity of propagating the beam through a long drift tube. These properties, which have no counterparts in low-density beams, lead to the generation of large amplitude, coherent, and monochromatic current modulation on an intense beam. The excellent amplitude stability and the phase-locking characteristics ( $< 2°$) of the modulated current, demonstrated in experiments, open new areas of research in high-power microwave generation and compact particle accelerators.

## I. INTRODUCTION

In the last two decades there has been considerable interest in generating pulses of high-power rf radiation. This interest has risen, in part, from the availabilty of intense relativistic electron beams (IREBs) with power $10^9$–$10^{12}$ W and, in part, from demands for high-power rf sources, especially from the accelerator community.[1]

There are many different mechanisms for generating rf power; one of these is based on longitudinal bunching of electrons. This mechanism transforms a velocity nonuniformity into density nonuniformities in the electron distribution, i.e., bunching.

It is possible to extract rf radiation from electron bunches with an intensity

$$I \doteq G N_b n_b^2, \tag{1}$$

where $N_b$ is the number of bunches/unit time, $n_b$ is the number of electrons in a bunch, and $G$ is a form factor which strongly depends on the microshape of the bunches and is large for bunches with sizes $< \lambda/2$, where $\lambda$ is the wavelength of the extracted rf radiation.

Equation (1) reflects the requirement of having a large $n_b$ in order to produce high rf power. A necessary condition to achieve a large $n_b$ is to employ high-current electron beams (e.g., IREBs).

Recently, a new mechanism capable of completely modulating IREBs was discussed in the literature.[2,3] This mechanism hinges on the intense space charge of the beam. The fact that the modulation of an IREB can be significantly different from a classical (tenuous, nonrelativistic) beam is already apparent in the small-signal theory. As we shall see below, nonlinearity accentuates such differences. Using this mechanism, one can get a large $n_b$ which can be used in high-power rf klystronlike oscillators and amplifiers.

The simplicity and the experimentally demonstrated high efficiency of generating modulated IREBs suggest several advantages of rf amplifiers based on the new mechanism over a more conventional approach (klystrons) for generating high rf power. Such new devices would be useful in (a) generating trains of nanosecond and subnanosecond high-voltage pulses,[4] (b) wake-field[5] acceleration of electrons or ions, and (c) other applications which require monochromatic, amplitude stable, and phase-locked bunches of electrons.

This paper addresses the development of rf amplifiers based on IREB modulation by an external rf source. Unlike the previous work,[2] self-excited oscillations and transient behavior are unimportant here.

In Sec. II, studies of the small-signal regime are given. In Sec. III, we report our findings in the nonlinear regime. In both sections, results from experiments, analytical models, and particle simulation are presented. In Sec. IV, some potential applications of modulated IREBs are indicated. The conclusion and a summary of our findings are given Sec. V.

## II. SPACE-CHARGE WAVES ON INTENSE RELATIVISTIC ELECTRON BEAMS—SMALL-SIGNAL REGIME

### A. Introduction

As we have stated earlier, the bunching mechanism occurs while the IREB propagates through a drift region, and is strongly influenced by the electric and magnetic fields of the electron beam. At a high-current level, the electric self-field of the IREB generates a potential hill through which the electrons are moving. The energy of an individual electron is split between kinetic and potential energies. From the conservation of energy, the following relationship is obtained:

$$\gamma_{inj} = \gamma_0 + I_0/I_s\beta_0 \equiv \gamma_0 + \alpha_0\gamma_0^3, \tag{2}$$

where

$$\alpha_0 = I_0/(I_s\gamma_0^3\beta_0),$$

$$I_s = 2\pi\epsilon_0 m_0 c^3/(e \ln r_w/r_b),$$

[a] Present address: Science Applications International Corp., McLean, VA 22102.

 0021-8979/88/193353-27$02.40 © 1988 American Institute of Physics 

$I_0$ is the IREB current, $m_0c^2(\gamma_0 - 1)$ is the electron kinetic energy,

$$\gamma_0 = (1 - \beta_0^2)^{-1/2}, \quad \beta_0 = v_0/c,$$

$v_0$ is the electron drift velocity,

$$m_0c^2(\gamma_{inj} - 1) = eV_0$$

is the electron total energy at injection, and $r_w$ and $r_b$ are the respective radii of the drift tube (assumed round) and of the IREB (assumed to be annular in shape). From Eq. (2) it is obvious that by increasing the IREB current, the kinetic energy of the electrons will be reduced. At a current level $I_c$, where

$$I_c = \frac{8.5(\gamma_{inj}^{2/3} - 1)^{3/2}}{\ln(r_w/r_b)} kA = I_s(\gamma_{inj}^{2/3} - 1)^{3/2}, \tag{3}$$

the electrons cannot lose anymore kinetic energy and beam propagation is disrupted.[6] At this current level, the kinetic energy of the electrons is $m_0c^2(\gamma_{inj}^{1/3} - 1)$ and the potential energy is

$$\phi = m_0c^2(\gamma_{inj} - \gamma_{inj}^{1/3})/e.$$

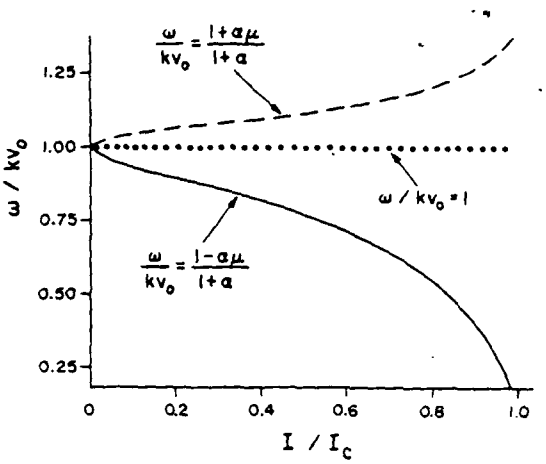



FIG. 1. Dispersion relation of waves on a magnetically focused IREB in a metallic pipe. Broken line represents fast space-charge waves; solid line represents slow space-charge waves; dotted line represents the "beam line."

### 1. The dispersion relation

The classical dispersion relation that was obtained for space-charge waves on low-density electron beams is invalid for IREBs. Briggs derived[7] a dispersion relation for space-charge waves on IREBs under a long wavelength assumption $\lambda \gg 2r_w$. More generally, for frequencies $f < f_c = 2.405c/2\pi r_w$, the dispersion relation reads[8]

$$(\omega - kv_0)^2 = \alpha_0(k^2c^2 - \omega^2)R, \tag{4}$$

where $R$ ($\leq 1$) is a reduction factor that depends on the geometry and frequency and $\alpha_0$ is defined in Eq. (2). Without loss of generality we can write $\alpha_0 R = \alpha$ and we can assume in the rest of the discussion that $R \simeq 1$.[7,8] Solving Eq. (4), one gets

$$\omega = \frac{k_{f,s}v_0}{1+\alpha}(1 \pm \alpha\mu) = \frac{k_{f,s}v_0}{\delta}\frac{1}{1 \mp \alpha\mu}, \tag{5}$$

where

$$\alpha\mu = (\alpha^2 + \alpha/\gamma_0^2)^{1/2}/\beta_0,$$

$$\delta = \beta_0^2/(\beta_0^2 - \alpha),$$

and the subscripts $f$ and $s$ stand for fast and slow (waves). The quantity $\omega/(k_{f,s}v_0)$ versus the electron beam current for the case $\gamma_{inj} = 2$ is shown in Fig. 1. Unlike in classical electron beams, the dispersion relation curves for the fast and slow waves are not symmetric with respect to the beam line $\omega/(kv_0) = 1$. This asymmetry makes the bunching mechanism for IREBs unique and novel.

### 2. Transmission line model of space-charge waves on IREBs

Bloom and Peter[9] described a useful analog between a classical (tenuous, nonrelativistic) electron beam and a transmission line. This analog is extended here to include IREBs. It expresses the rf currents and voltages on the beam in terms of the values upstream.

Assuming that the ac current consists of two components associated with slow and fast space-charge waves, one obtains the ac current and ac voltage on the beam:

$$\tilde{I}_1 = I_{f,s} \exp j(\omega t - k_{f,s}z), \tag{6a}$$

$$\tilde{V}_1 = \frac{m_0v_0\gamma_0^3}{e\delta}\frac{I_{f,s}}{I_0}\left(\frac{\omega - k_{f,s}v_0}{\omega}\right)v_0 \exp j(\omega t - k_{f,s}z), \tag{6b}$$

which may be written in a matrix form (see Appendix A):

$$\begin{pmatrix}\tilde{I}_1\\ \tilde{V}_1\end{pmatrix} = (A)\begin{pmatrix}I_{10}\\ V_{10}\end{pmatrix}\exp j(\omega t - \theta), \tag{7}$$

in terms of the current and voltage modulation $I_{10}$ and $V_{10}$ at $z = 0$. Here,

$$(A) = \begin{pmatrix}\cos(\alpha\mu\theta) - j\zeta\sin(\alpha\mu\theta) & j(1/Z)\sin(\alpha\mu\theta)\\ jZ(1-\zeta^2)\sin(\alpha\mu\theta) & \cos(\alpha\mu\theta) + j\zeta\sin(\alpha\mu\theta)\end{pmatrix}, \tag{8}$$

$$\theta = \omega\delta z/v_0, \quad \zeta = (1-\delta)/\alpha\mu\delta = -1/\beta_0^2\mu \quad (\zeta < 0),$$

$$Z = m_0c^2\gamma_0^3\beta_0^2\alpha\mu/eI_0 = R_0/(-\zeta),$$

$$R_0 = 60[\ln(r_w/r_b)/\beta_0] \quad (\Omega). \tag{9}$$

Note that $\mathrm{Det}(A) = 1$, and that the inverse of $(A)$ is obtained from $(A)$ with $\theta$ replaced by $-\theta$.

### 3. IREB interaction with gaps

Equation (7) predicts the ac current and kinetic voltage behavior in a drift tube. Similar transform matrices describe

the change in the ac current and voltage as the IREB traverses a gap.

*a. First gap interaction with the IREB.* With the boundary conditions $I_1 = 0$ and $V_1 = V_{10}\exp j(\omega t)$ imposed at the modulating gap $z = 0$, one obtains from Eq. (7) the following rf quantities at $z = z_1$:

$$I_1 = j\frac{V_{10}}{Z}\sin(\alpha\mu\theta_1) \quad \theta_1 = \frac{\omega\delta z_1}{\beta_0 c},$$
$$V_1 = V_{10}[\cos(\alpha\mu\theta_1) + j\zeta\sin(\alpha\mu\theta_1)]. \tag{10}$$

Unlike in the interaction of a low-density (classical) electron beam with a gap, $I_1$ and $V_1$ are partially in phase.

*b. Second gap interaction.* If at $z = z_1$ the IREB encounters a second gap feeding a structure of impedance $Z_c$, a new kinetic voltage $V_1'$ and a current $I_1'$ will develop:

$$\begin{pmatrix} I_1' \\ V_1' \end{pmatrix} = B\begin{pmatrix} I_1 \\ V_1 \end{pmatrix}; \quad B = \begin{pmatrix} 1 & 0 \\ Z_c & 1 \end{pmatrix}. \tag{11}$$

When a resonant cavity is used as a structure, $Z_c$ ( $= R_s$ ) is a real number and one gets

$$V_1' = V_{10}\{\cos(\alpha\mu\theta_1) + j[(R_s/Z) + \zeta]\sin(\alpha\mu\theta_1)\}. \tag{12}$$

Defining a kinetic gain as $GA$,

$$GA = |(V'/V_0)|$$
$$= (1 + \{[(R_s/Z) + \zeta]^2 - 1\}\sin^2(\alpha\mu\theta_1))^{1/2}. \tag{13}$$

A sufficient condition for the gain $GA > 1$ is

$$R_s/Z + \zeta > 1. \tag{14}$$

Since $\zeta < 0$, (14) is equivalent to

$$R_s > R_0(1 - 1/\zeta),$$
$$R_0 = 60[\ln(r_w/r_b)/\beta_0]\Omega, \tag{15}$$

Eq. (15) can be easily satisfied.

#### 4. ac power relationship

The physics of space-charge waves on an IREB is different from the physics of space-charge waves on a classical electron beam. This can be seen from the ac power relationship.

The relativistic Tonk's theorem[10] states that

$$-\nabla\cdot\left(\mathbf{E}\times\mathbf{H} + \frac{T}{e}\mathbf{J}\right) = \frac{\partial}{\partial t}\left(\frac{1}{2}\mu H^2 + \frac{1}{2}\epsilon E^2 + \frac{T}{e}\rho\right), \tag{16}$$

where $T$ is the relativistic kinetic energy per electron. Assuming small-signal behavior, one obtains

$$\text{Real}\{\nabla\cdot[\mathbf{E}_1\times\mathbf{H}_1 + (T_1/e)\mathbf{J}_1]\} = 0. \tag{17}$$

Integrating Eq. (17) over a volume of a drift tube enclosed between two surfaces of cross sections $S_1$ and $S_2$, we have

$$\text{Real}\oint(\mathbf{E}_1\times\mathbf{H}_1)\,dS = -\text{Real}\oint_{S_1}^{S_2}\frac{T_1}{e}\mathbf{J}_1\,dS, \tag{18}$$

where $T_1/e = V_1$ is the kinetic voltage. The integral $\int\mathbf{J}_1\,dS$ is the ac current flowing through a cross section $S$. Locating $S_1$ at a position where $I_{10} = 0$ one gets [using Eq. (10)]

$$\text{Real}\oint(\mathbf{E}_1\times\mathbf{H}_1)\,dS = -\frac{V_{10}^2}{Z}\zeta\sin^2(\alpha\mu\theta) > 0, \tag{19}$$

since $\zeta < 0$.

The above relationship means that the dc energy of the beam has been extracted and converted into ac kinetic energy which in turn is converted into electromagnetic energy so as to maintain power conservation.

In contrast, for a low-density classical electron beam, Eq. (19) will become

$$\text{Real}\oint\mathbf{E}_1\times\mathbf{H}_1\,dS \equiv 0. \tag{20}$$

### B. Experimental investigation of IREB modulation in the small-signal regime

#### 1. Description of the experiment

The experimental arrangement shown in Fig. 2 consisted of a foilless diode[11] emitting an annular IREB of radius $r_b \simeq 1.9$ cm and thickness $\simeq 0.3$ cm. A 10-kG quasi-dc magnetic field confined the IREB inside a metal tube of radius $r_w \simeq 2.35$ cm. A gap feeding a coaxial cavity was inserted in the drift tube. The characteristic impedance of the cavity was 45 Ω and its length was $L = 17$ cm corresponding to a resonance frequency of 410 MHz. Four thin Nichrome wires connected the inner wall of the coaxial cavity to its outer wall so as to reduce the $Q$ of the cavity at 410 MHz. The wires did not influence the $Q$ of the cavity at the 1328-MHz resonance ($Q > 1000$). The presence of the wires shifted the first resonance from 410 to 610 MHz and reduced the $Q$ to below 30. An external rf source (a magnetron) "pumped" microwave energy into the cavity for a duration of 3 μs at a frequency $f = 1328$ MHz. Sometime during the 3-μs period a Blumlein transmission line with an output of 500 kV energized the foilless diode for 120 ns, and a ~5 kA electron beam was launched through the drift region. The base pressure in the drift region was $< 10^{-5}$ Torr.

#### 2. Diagnostics

The electron beam current was measured by magnetic probes ($B_\theta$ loops). The voltage that appeared on the probes was proportional to the product of the current and frequency of the modulated IREB and even for small probe areas could

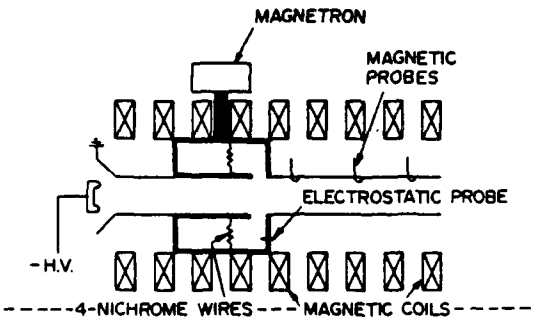



FIG. 2. Experimental arrangement when only one cavity was used.

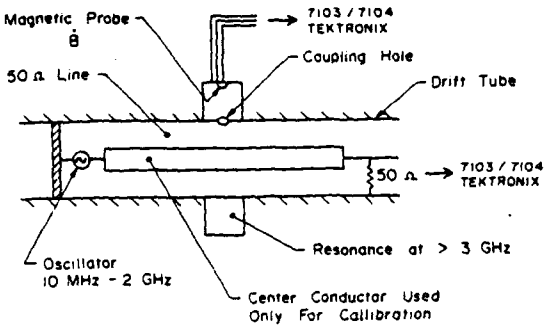



FIG. 3. Magnetic probes and the calibration arrangements.

exceed a 1000 V. In order to reduce the probe sensitivity and IREB disruption by the probe mountings the arrangement shown in Fig. 3 was used. The probes were inserted inside an enclosed toroidal metallic enclosure that was coupled electromagnetically through holes to the drift tube.

The probes were calibrated *in situ* at different frequencies. This was done by placing a center conductor coaxially within the drift tube, converting it into a 50-Ω coaxial line. This coaxial line was connected at one end to an oscillator and at the other end to an oscilloscope or a power meter. The magnetic probe signal was measured as a function of amplitude and frequency of the oscillator. From these measurements probe sensitivity was derived.

The signal from the probe due to the IREB current was displayed on the Tektronix digitizing system and/or on Tektronix oscilloscope model 7104/7103. The signals were corrected for the attenuation of the cables, oscilloscope, amplifiers, probe sensitivity, etc.

After the corrections were made, the $dI/dt$ signals were Fourier analyzed and integrated to obtain the ac current. Figure 4 shows the typical probe signal and processing. (Note that the results obtained from the digitizing system are distorted due to the discrete nature of the signal acquisition system. For example, $dI/dt$ and $I$ signals showed low-frequency amplitude modulation and the fast Fourier transform had spurious harmonic contents and a possible error in frequency of $\pm$ 50 MHz.)

Electrostatic probes were inserted inside the cavities to measure the electric field. The calibration of the probes was done after connecting the cavity in series between two 50-Ω transmission lines. The current $I_t$ that was flowing in the system was measured directly and compared with the voltage $V_p$ developed on the probes. The voltage developed in the cavity is

$$V_t = jI_tZ_c \tan[(\pi/2)(f/f_c)], \quad f \neq f_c, \tag{21}$$

where $f_c$ is the resonance frequency of the cavity and $Z_c$ is the characteristic impedance. $V_p$ and $V_t$ were used to obtain the calibration factor for frequencies $f \neq f_c$. The calibration factor of the probe for $f = f_c$ was interpolated.

### 3. Frequency and phase measurements

For many applications the purity of the rf spectrum and phase locking are necessary requirements. Figure 5 shows the arrangement that was used to measure the phase-locking capabilities and the purity of spectrum of the modulated IREB.

A signal from a magnetic probe (A) was passed through attenuators and a 700 MHz high pass filter. The signal was then split into two parts which were attenuated further. The rf signals were passed through coaxial cables (C) and (C') whose lengths differed by an amount $(2n+1)\lambda/2$ ($n$ is an

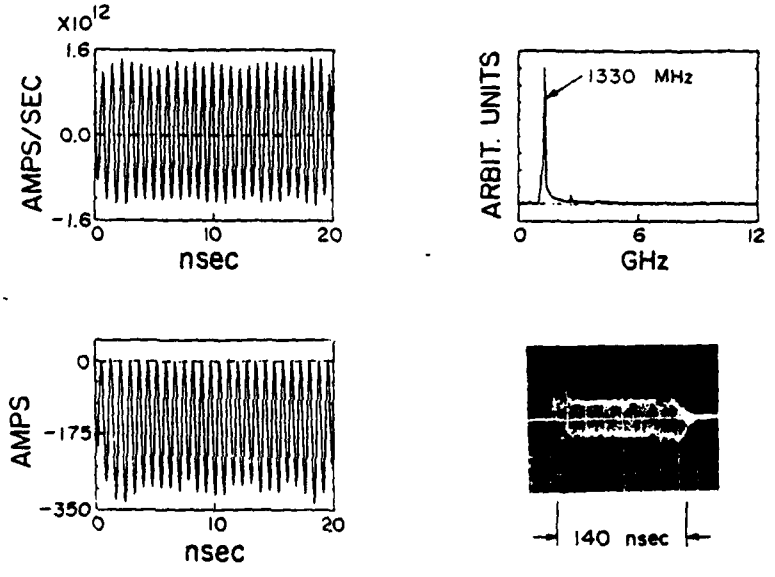



FIG. 4. Experimental results when only one cavity was used. Top left: $dI/dt$. Bottom left: $I_1$, the rf component of the current. Top right: spectrum of $dI/dt$. Bottom right: $dI/dt$ detected using a Tektronix 1 GHz oscilloscope 7104.

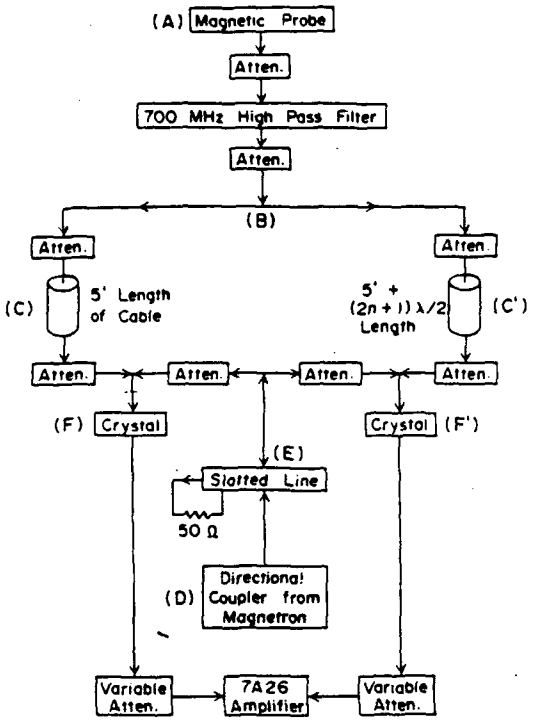



FIG. 5. Block diagram of the experimental arrangement that was used to measure phase locking.

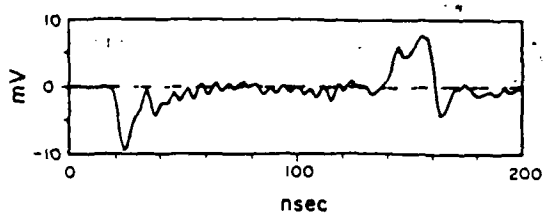



FIG. 6. Experimental result showing phase locking $< 2°$, obtained from the arrangement of Fig. 5.

A similar technique was used to measure the frequency of the modulation. One of the variable attenuator settings was increased by a factor of 100. With this arrangement the magnetron rf output was mixed with the magnetic probe signal. No oscillating signal was recorded. However, when we replaced the magnetron with an oscillator of frequency $f$, an oscillating voltage appeared at the output with a frequency $(f - 1.328)$ GHz. Hence, we conclude that the frequency of the modulated IREB is the same as the frequency of the rf from the magnetron.

### 4. Experimental results and comparison with theory

Four magnetic probes spaced 15 cm apart, the first of which was located 12 cm from the gap of the cavity, were used to analyze the electron beam that emerged from the cavity. Figure 7 displays the variation of the current ampli-

integer). The signals were then fed into crystal detectors. The two outputs were equalized by variable attenuators before being electrically subtracted by a 7A26 Tektronix amplifier (zero voltage output was obtained). At the same time an rf signal from the magnetron (D) that was used to modulate the IREB was passed through a slotted transmission line into a matched load. Out of the slotted line an rf signal, whose phase could be controlled, was picked up (E) and split into two parts. These two signals were fed into the crystal detectors (F) and (F') and mixed with the signal from the magnetic probe. The output of the 7A26 amplifier did not change as long as the experimental parameters were kept constant. Moreover, once the slotted line was adjusted for a minimum output signal of the 7A26 amplifier, any consecutive operation also showed the same minimum output (Fig. 6). Under this condition the phase between the rf signals from the magnetron and the magnetic probe would be

$$\Delta\Phi = V_s/2\sqrt{V_{s1}V_{s2}},$$

where $V_s$ was the voltage amplitude from the 7A26 preamplifier and $V_{s1}$ and $V_{s2}$ were the output voltages from the crystal detector when either the magnetron or the IREB was turned off and one of the variable attenuator values was increased manyfold. $V_s$ was always $\lesssim 0.5$ mV, $V_{s1}$ and $V_{s2} \simeq 5$ mV, hence $\Delta\Phi \lesssim 0.05$ rad or $\Delta\Phi \lesssim 3°$. Thus, the magnetron output and the modulated IREB were phase locked to better than 3°.

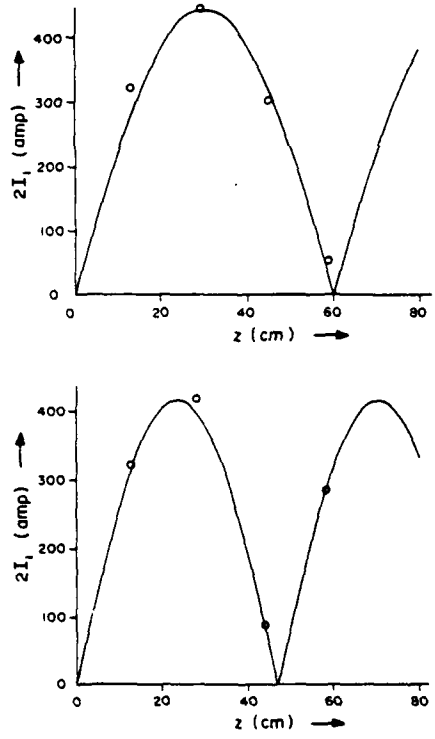



FIG. 7. Peak bunch current as a function of propagation distance from the modulating gap.

tude versus propagation distance for two different IREB voltages. Best fits to the results are in the following form:

for $V_0 = 500$ keV,

$$2I_1 = 450|\sin[0.0523z(\text{cm})]| \quad \text{A};$$

for $V_0 = 400$ keV,

$$2I_1 = 425|\sin[0.0671z(\text{cm})]| \quad \text{A}.$$

The theoretical prediction is [Eq. (10)]

$$2|I_1| = 2(V_{10}/Z)|\sin[\alpha\mu(\omega\delta/\beta_0 c)z]|; \tag{22}$$

since the rf amplitude $V_{10}$ was kept constant the following conclusions were drawn: (i) $Z$ is insensitive to the IREB electron energy $eV_0$. (ii) $\alpha\mu\omega\delta/\beta_0 c$ depends on the IREB electron energy $eV_0$.

Using the small-signal theory we plotted $Z$ and $L = [(\pi\beta_0 c)/\alpha\mu\omega\delta]$ as a function of $V_0$ under the assumption that $V_0/I_0 = \text{const}$. As a reference point we took $V_0 = 500$ kV and $I_0 = 5.6$ kA. Figure 8 agreed with the experimental results. The weak dependence of $Z$ on $V_0$ (and $I_0$) could explain the excellent stability of $I_1$ even under conditions where $V_0$ (and $I_0$) was varying during the operation of the high-voltage electron source.

The amplitude of $I_1$ depends linearly on $V_{10}$. We recorded $I_1$ as a function of the input rf power $P$. Since $P \propto V_{10}^2$ we get from Eq. (22)

$$I_1^2 = KP \quad \text{or} \quad \log(I_1^2) = \log P + \log K, \tag{23}$$

where $K$ is a constant that does not depend on $V_{01}$ and $I_1$. Figure 9 displays experimental of $\log(I_1^2)$ vs $\log(P)$. The slope of the best-fit straight line is unity in accordance with Eq. (23).

The interaction of the modulated beam with a cavity was investigated. A small cavity was introduced in the drift tube 15 cm downstream of the gap of the modulating cavity. The impedance of the cavity at 1.328 GHz can be written as $Z_c = j\omega L$, $L \simeq$ (calculated from geometry). The current amplitude downstream, was 40% higher than

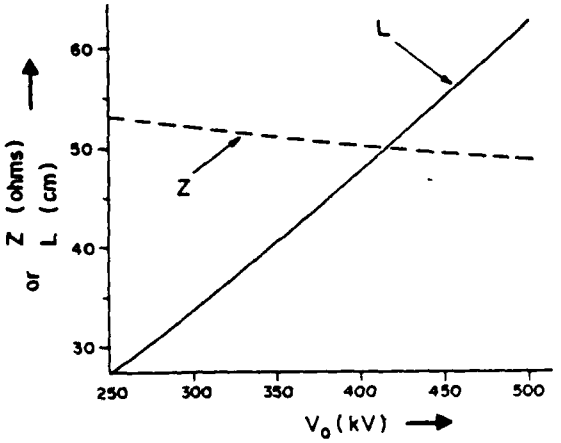



FIG. 8. Dependence of the parameters $L$ and $Z$ on the IREB voltage.

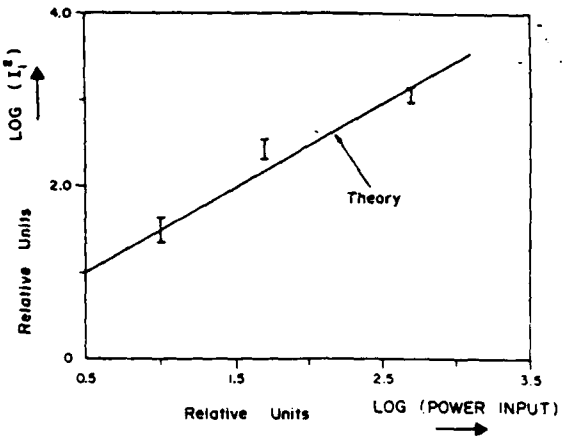



FIG. 9. Dependence of the IREB rf current on the input rf power.

without the presence of the small cavity. Using Eqs. (10), (11), and (8) we get, for $z_1 \leq 15$ cm,

$$I_1 = j(V_{10}/Z)\sin(\alpha\mu\theta_1), \quad \theta_1 = \omega\delta z_1/\beta_0 c. \tag{24}$$

At $z_2 = 30$ we have

$$I_2 = j\frac{V_{10}}{Z}\sin(\alpha\mu\theta_2) + j\frac{V_{10}}{Z} \times \frac{\omega L}{Z}\sin\alpha\mu\theta_1 \sin[\alpha\mu(\theta_2 - \theta_1)], \tag{25}$$

$$\theta_2 = \omega\delta z_2/\beta_0 c,$$

since $z_2 = 2z_1 = 30$ cm we get

$$\frac{I_2}{I_2^*} = \left(1 + \frac{\omega L}{Z}\frac{\sin(\alpha\mu\theta_1)}{2\cos(\alpha\mu\theta_1)}\right) = \left(1 + \frac{\omega L}{2Z}\tan\frac{\alpha\mu\theta_2}{2}\right) \simeq 1.5, \tag{26}$$

where

$$I_2^* = j(V_{10}/Z)\sin(\alpha\mu\theta_2),$$

in complete agreement with the experimental result.

### C. Particle simulation

#### 1. Introduction

Later in this paper we investigate the generation and propagation of a fully modulated IREB. The physics of fully modulated IREBs is highly nonlinear and the theory is not yet completely developed. Theoretical models will be developed to explain the nonlinear processes involved. Some of these models are not self-consistent and in order to check their validity we rely on numerical simulations.

The computer simulation code, CONDOR,[12] was extensively used in this research.[13] This code is fully electromagnetic, time dependent, and considers self-consistent interactions between azimuthally symmetric electromagnetic fields and an electron beam. These simulations provide us with insight into dynamical processes which are impossible to measure by experimental diagnostic techniques.

As we shall see throughout this paper, the numerical simulations confirmed experimental results and theories, showing that the mutual interaction between IREBs and cavities loaded with rf energy caused beam modulation. These calculations also showed that complete modulation does not require particle reflections. Only two cases of IREB propagation through the drift region were found to be of importance in the calculations:

(a) The "static case" of IREB propagation in which the presence of gaps leads to enhanced electrostatic potential depression and (b) the "time dependent case" in which the dynamics of the individual electrons is influenced by the external rf sources or by the mutual interactions of parts of the electrons and their response at the cavities. *In either case, transients of the IREB current are of no importance.*

Although we tried to simulate the experiment as accurately as possible, there was one major difference. Unlike in the experiment in which the current and the voltage of the beam injected into the drift region have an interdependent time varying form, in the numerical simulation, particles were injected with constant energy and the beam current was allowed a finite constant rise time. A less significant difference between the experiments and the simulations should also be noted. In the experiments, the external rf source was fixed at 1.328 GHz, and the cavity was adjusted until resonance was achieved. In the simulations, the geometry of the cavity was fixed, and the frequency was adjusted to obtain resonance. As a result, the simulations utilized rf energy at 1.37 GHz.

The calculations summarized in this section deal with a relatively low rf current ($I_1 \ll I_0$). The geometry of the simulation is shown in Fig. 10 (top).

The simulations presented here proceeded as follows: At $t = 0$ ns, the rf drive was turned on. The $Q$ of the cavity was chosen in such a way that the saturation of the fundamental TEM mode was reached at $t = 6$ ns. At this time, the IREB was injected with a current rise time of 5 ns. The simulation continued until $t = 20$ ns. Simulation parameters were $\Delta r = 0.2$ cm, $\Delta z = 0.4$ cm, $\Delta t = 2 \times 10^{-12}$ s, and, typically, $n_p \simeq 2800$ particles. The results did not vary when $\Delta z \to \Delta z/2$, $\Delta t \to \Delta t/2$, or $n_p \to 4n_p$.

### 2. Simulation in the small-signal regime

When the simulations were restricted to cases for which $I_1 \ll I_0$ nonlinear effects were of little importance and complete agreement between the linear theory and particle simulation calculations were obtained.

The initial IREB conditions were as follows: current of 5 kA, energy of 500 keV, and the geometry of the IREB was annular, with a radius of 1.9 cm. This IREB was injected through the drift tube into which a coaxial cavity has been inserted. This cavity was loaded with rf energy via a radial transmission line at the outer wall of the cavity. The impedance of the radial transmission line was 15 Ω. rf-gap voltages, $V_{10}$, of 6, 18, and 30 kV, always at a frequency of 1.37 GHz, were used. The gap voltage introduced nonuniformities in the electron velocity distribution which were translated, after propagation, into density modulation. The amplitude of the rf current versus propagation distance showed excellent agreement with linear theory (Fig. 7) and with the experimental results.

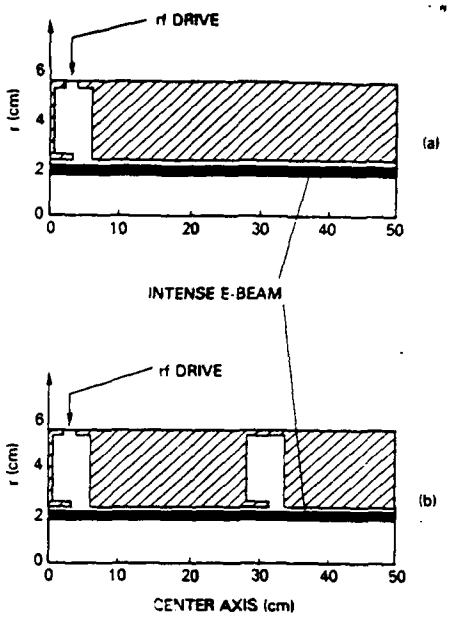



FIG. 10. (a) Top: geometry of the computer simulation when only one cavity was used. (b) Bottom: geometry of the computer simulation when two cavities were used.

As in conventional klystrons, the amplitude of the rf current varied sinusoidally. The axial position $z_m$, where maximum modulation occurred, agreed very well with the linear theory:

$$z_m = \pi\beta_0 c/2\alpha\mu\delta\omega = 28 \text{ cm}.$$

Changing $V_{10}$ did not change $z_m$; only $I_1$ varied. For example, for $V_{10} = 6$, 18, and 30 kV the peak currents in the electron bunches were $2I_1 = 270$, 800, and 1400 A, respectively. These results confirmed that $I_1$ was proportional to $V_{10}$, in agreement with Eq. (10). However, when $V_{10}$ exceeded a critical value, deviations from Eq. (24) were seen (Fig. 11). These nonlinear aspects of the simulation will be discussed later.

The amplitude stability and phase-locking characteristics were also investigated. The dc current $I_0$ and the dc voltage $V_0$ were changing in the same way as in the experiment ($V_0/I_0 = Z_0 = \text{const}$). It was found that even though $V_0$ was changing, the amplitude of the rf current did not change much. To check the phase-locking capability, the phase of the rf signal was varied. We found that the phase of the electron bunches changed in accordance with the input rf, with an uncertainty error of $2^\circ \pm 1^\circ$, in agreement with experiments.

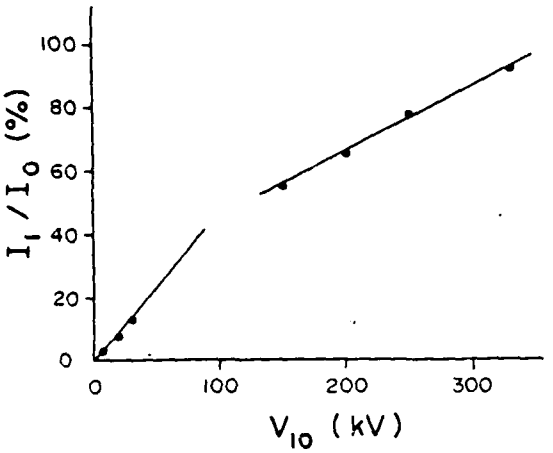



FIG. 11. Percentage modulation as a function of the rf gap voltage according to computer simulation. The three points near the origin are in the linear regime.

## III. FULLY MODULATED INTENSE RELATIVISTIC ELECTRON BEAMS

### A. Experiment

#### 1. Introduction

It is well known that nonlinear effects in rf devices become important when the rf current $I_1$ is of the order of the dc current $I_0$.

Pretending that Eq. (10) is valid even for cases for which $I_1$ is of the order of $I_0$, one can estimate the rf voltage that has to be imposed on the gap so as to fully modulate a 5 kA IREB. For the present experimental setup this voltage is of the order of 100 kV, corresponding to 20 MW of injected rf power. Since an rf source with this kind of power was not available, we used instead the partially modulated IREB to energize a second coaxial cavity (Fig. 12) and to generate a high oscillating voltage ($\sim 150$ kV) on its gap.

The gap of the second cavity was inserted in the drift tube at an axial position for which $I_1$ was maximum (29 cm). The second cavity with a $Q > 2000$ was tuned to the frequency $f = 1.328$ GHz $\pm$ 1 MHz.

The IREB that emerged from the second cavity was highly modulated. The peak current in the bunches was $\sim 80\%$ of the dc current (Fig. 13). However, on many occasions the amplitude of the dc current varied erratically and the amplitude of the rf current decayed to almost zero. We found that by reducing the rf power from the magnetron, the dc current behaved normally and the amplitude of the rf current (still 80% of the dc) did not vary with time. The explanation for such a behavior was that the two-cavity system was operating in the nonlinear region and that saturation of the bunching mechanism was achieved.

#### 2. Generation and propagation of highly modulated IREBs—Experimental results

In order to explore the physics of highly modulated IREBs, a few experiments involving modulated IREBs were performed. The results will be used to compare with the theory and the computer simulation, which were later developed in response to these experiments.

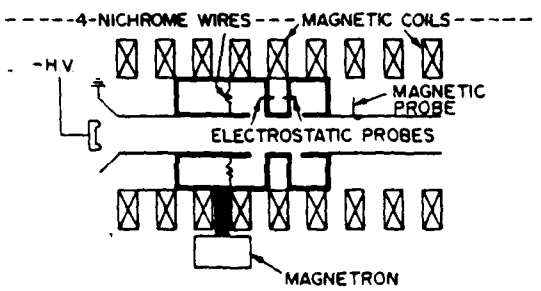



FIG. 12. Experimental arrangement when two cavities were used.

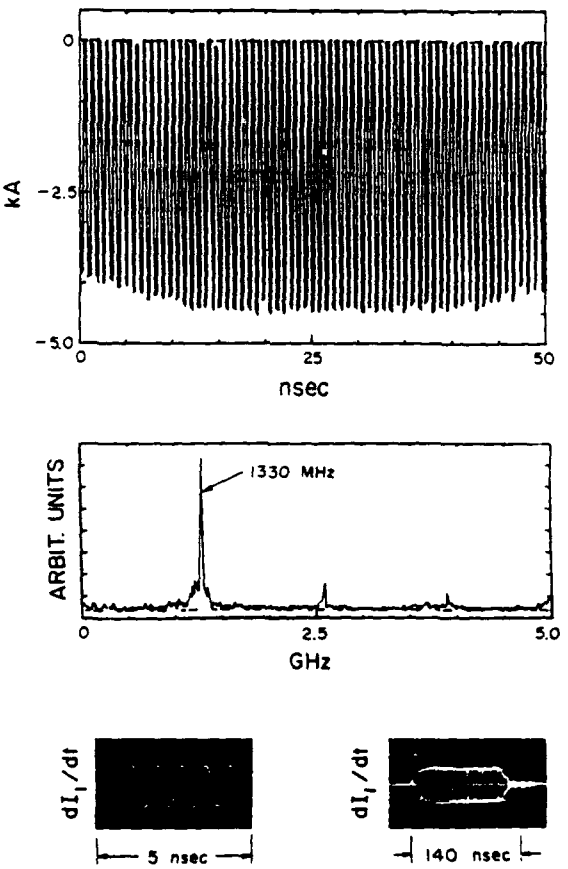



FIG. 13. Experimental results when the configuration of Fig. 12 was used. Top: rf current of the modulated IREB. Middle: Spectrum of $dI/dt$. Bottom: $dI/dt$ traces obtained from a 1 GHz Tektronix oscilloscope 7104.

In the first experiment, the propagation of a highly modulated IREB was investigated. The peak current of the bunches, $2I_1$, was measured at 12, 27, 42, and 57 cm downstream from the second gap. We found that the rf current varied in an oscillatory fashion: $2I_1$ (peak bunch current) varied between a maximum of 4.5 kA to a minimum of 2.5 kA. At any axial position the spectrum was monochromatic (to within $\pm 2$ MHz) and the phase-locking characteristic was observed. When a third cavity, tuned to $\sim 2$ GHz, was placed 12 cm downstream, the amplitude of the rf current increased so that $2I_1 \simeq 7$ kA. The third cavity behaved as an inductor of $\sim 5$ nH to the 1.328 GHz rf current.

In a different experiment the second cavity was replaced by a variable length cavity. With this cavity, the resonance frequency could be varied between 800 MHz and 2.9 GHz. The cavity $Q$ was $<400$ (at a frequency of 1.3 GHz). Because of the low $Q$, the input impedance of the gap was complex, i.e., $Z_s = R_s + jX$, even at frequencies close to the resonance frequency. It was found that by raising the magnetron rf power, no disruption of the IREB current was observed. Moreover, the rf current amplitude of the IREB increased by a factor of $\sim 1.6$ to $2I_1 \simeq 7$ kA. Figure 14(a) shows the experimental setup. Figure 14(b) shows the variation of $2I_1$ as a function of the resonance frequency of the second cavity and of the position where the measurements were taken.

### 3. Harmonic generation

Previous experimental investigations of the generation of modulated IREBs showed that when $I_1$ was of the order of $I_0$, harmonics of the main frequency appeared.[14] Here, harmonics are not shown in the spectrum of the current. The reason for it is the high attenuation of signal cables and oscilloscopes at frequencies above 1.3 GHz.

The presence of the second and third harmonics in the current modulation was detected by mixing the signals from magnetic probes with local oscillators working at frequencies $\sim 2.5$ and $\sim 3.8$ GHz (Fig. 15). The rf current at the second harmonic was measured relative to the rf current at the fundamental. When the configuration of the high $Q$ cavities was used, the rf current ratio of the second harmonic to the fundamental was 0.3.

As was found in an earlier work by the authors, the spectrum of modulation can be modified by propagating the modulated IREB through additional cavities.[14] A similar approach was used here to change the level of the current of the second harmonic. For example, when a third cavity tuned to 2.6 GHz was placed downstream of the second cavity, the ratio of currents increased to 0.8. When the third cavity was tuned to $\sim 2$ GHz this ratio decreased to $\sim 0.1$.

## B. A quasi-dc theory

The linear theory [Eq. (10)] gives good agreement between the calculated depth of the current modulation (using the measured second gap voltage $\sim 150$ kV) and the measured peak bunch current. However, the current modulation is at maximum at the second gap. The linear theory is

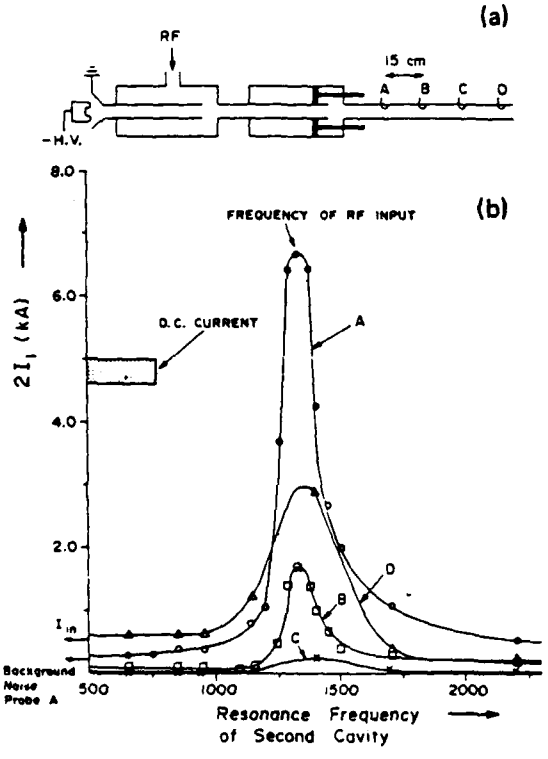



FIG. 14. (a) Top: Experimental arrangement. (b) Bottom: Peak bunch current as measured by the four magnetic probes. The shaded area represents the dc current. The arrow marked $I_{in}$ is the level of the peak bunch current measured between the cavities. The arrow at the lower left-hand corner shows the level of the background noise.

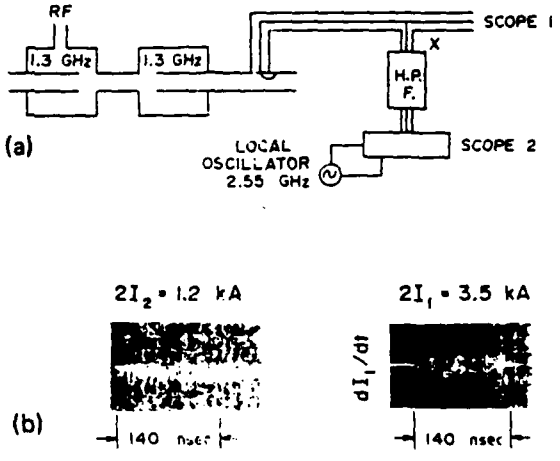



FIG. 15. (a) Top: experimental arrangement that was used to measure the fundamental and second harmonic of the modulated IREB. (b) Bottom left displays a signal after passing through a high pass filter (H.P.F) and beating it with a local oscillator. Bottom right displays $dI/dt$.

not applicable here since $I_1$ is of the order of $I_0$ and it is unlikely that low amplitude slow and fast space-charge waves can truly explain the nonlinear mechanism involved in the physics of modulated IREBs. Later on in the discussion we will use particle simulation techniques to investigate nonlinear mechanisms involved in the modulation of IREBs. In this section we chose to discuss a simpler model that has given us insight into the nonlinear process. This model calculates equipotentials for the geometry of a cavity such as in Fig. 2 when a time-independent voltage $V_g$ is applied on the gap. The potential $V$ is found at any point inside the geometry by numerically solving $\Delta V = -\rho/\epsilon$, assuming $\rho u_0 = \text{const}$, where $\rho$ is the electron charge density.

We found that the presence of the gap with the applied voltage influences the maximum IREB current $I_m$ that can propagate. Figure 16 shows potential profiles in the vicinity of the gap at the position of the IREB for various gap voltages and for currents close to $I_m$. Assuming that the IREB flow through the cavity is laminar and that the current is controlled by $V_g$ we can construct (as in a high-power electron tube) a "dynamic transfer" curve that gives an oscillating current as a response to a sinusoidally time-dependent voltage. However, the IREB flow is not laminar and when an oscillating voltage is applied on the gap the following happens: (1) The flow of the IREB is disrupted when $V_g < 0$ and a time-dependent "virtual cathode" is formed reducing the propagating IREB current well below the current, $I_m$, calculated above. (2) When $V_g > 0$ the "virtual cathode" disappears and the flow of the IREB is restored to its original level. In the case of nonlaminar flow of an IREB, Fig. 16 (bottom) should be modified by reducing the values of $I_m$ for $V_g < 0$ but keeping the same values of $I_m$ for $V_g > 0$. Hence, an oscillating $V_g$ will induce current oscillations larger than the ones shown in Fig. 16 (bottom). This picture resembles a "classical" electron tube amplifier with a negatively dc biased grid. $V_g$ corresponds to the grid ac voltages. When the amplitude of $V_g$ is small compared to the dc grid voltage (the dc grid voltage corresponds to the potential near the gap when $V_g = 0$) the system will behave like a class "A" amplifier; for $V_g$ large enough the system will behave like a class "B" amplifier.

### C. Computer simulation—Nonlinear results

The nonlinear processes that take part in the generation of fully modulated IREBs can be found from computer simulations in which the rf current is comparable to the dc current. To achieve this situation we first simulated the experimental configuration as accurately as possible. The goals of the simulation were to obtain macroscopic results such as electron beam current profiles at various axial positions, the harmonic contents, phase locking characteristics, etc., and to compare them with the experimental results. Once these results were obtained and compared favorably, we looked at microscopic quantities, such as phase space pictures, in order to reveal the nonlinear mechanisms responsible for IREB modulation.

Similar to the experimental arrangement of Fig. 2, the simulation geometry was arranged by placing an undriven

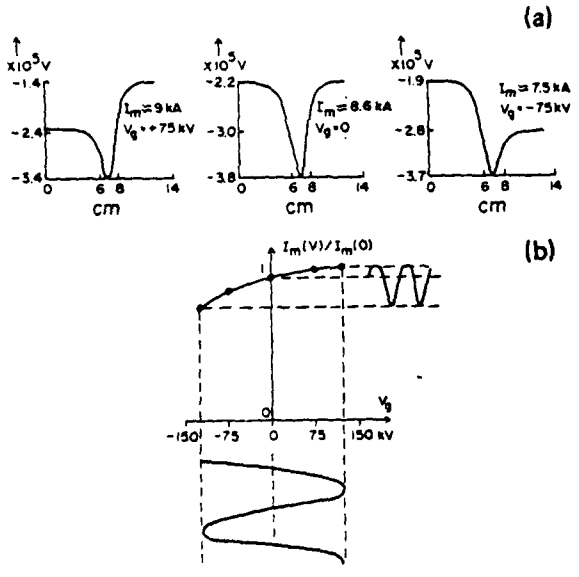



FIG. 16. (a) Top: potential profiles near the gap of a cavity for a quasi-dc current $I_m$ and a quasi-dc gap voltage $V_g$. The gap is located at axial position 6–8 cm. (b) Bottom: dynamic transfer curve showing the current response to an oscillating gap voltage.

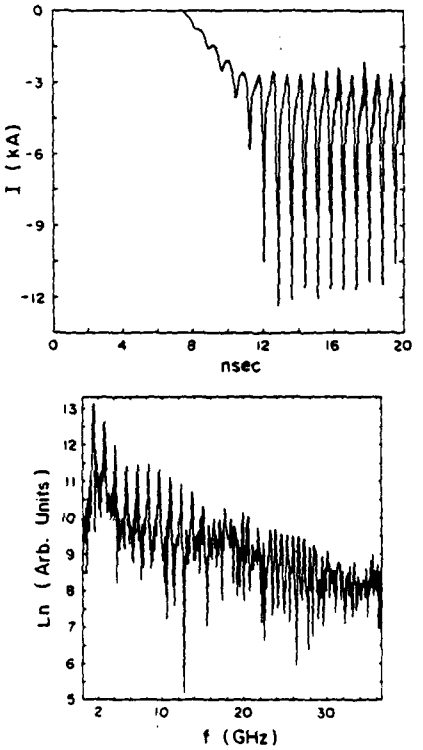



FIG. 17. Simulation result for the geometry in Fig. 10(b), showing (a) the current at 6 cm downstream of the second gap (top), and (b) the Fourier power spectrum of this modulated current (bottom).

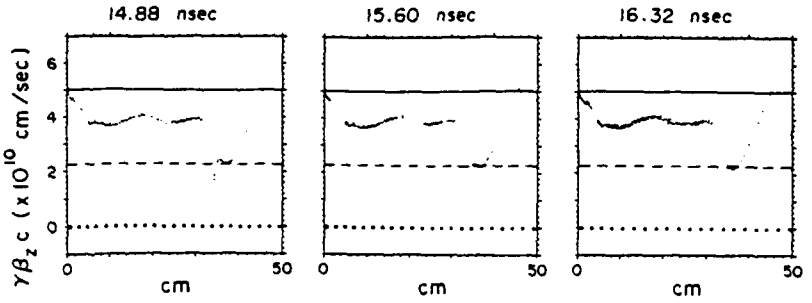



FIG. 18. Phase space plots for the two-cavity case at intervals of a cycle $T = 0.73$ ns. Solid lines show $\gamma\beta_z c$ at injection. Broken lines show $\gamma\beta_z c$ at a condition of dc limiting current ($\gamma = \gamma_{lim}^{1/3}$). Dotted lines show $\gamma\beta_z c = 0$.

second cavity into the drift tube at an axial position where the rf current reached maximum (Fig. 10, bottom). This cavity was excited by the fundamental frequency component of the partially modulated IREB current. The voltage that appeared on the second gap depended on $V_{10}$ and was typically of the order of the voltage applied on the IREB diode $V_0$. For example, for $V_{10} = 30$ kV, the voltage at the second gap $V_{20} \simeq 330$ kV. The current modulation of the IREB after passing the second gap is shown in Fig. 17.

The percentage of IREB modulation was calculated assuming a current profile of $I = I_0 + I_1 \cos(\omega t)$. This was done so as to compare simulation results with experimental results. We found that $I_1/I_0 = 13.3\%$ before the IREB entered the second cavity and $I_1/I_0 = 58\%$ 6 cm downstream

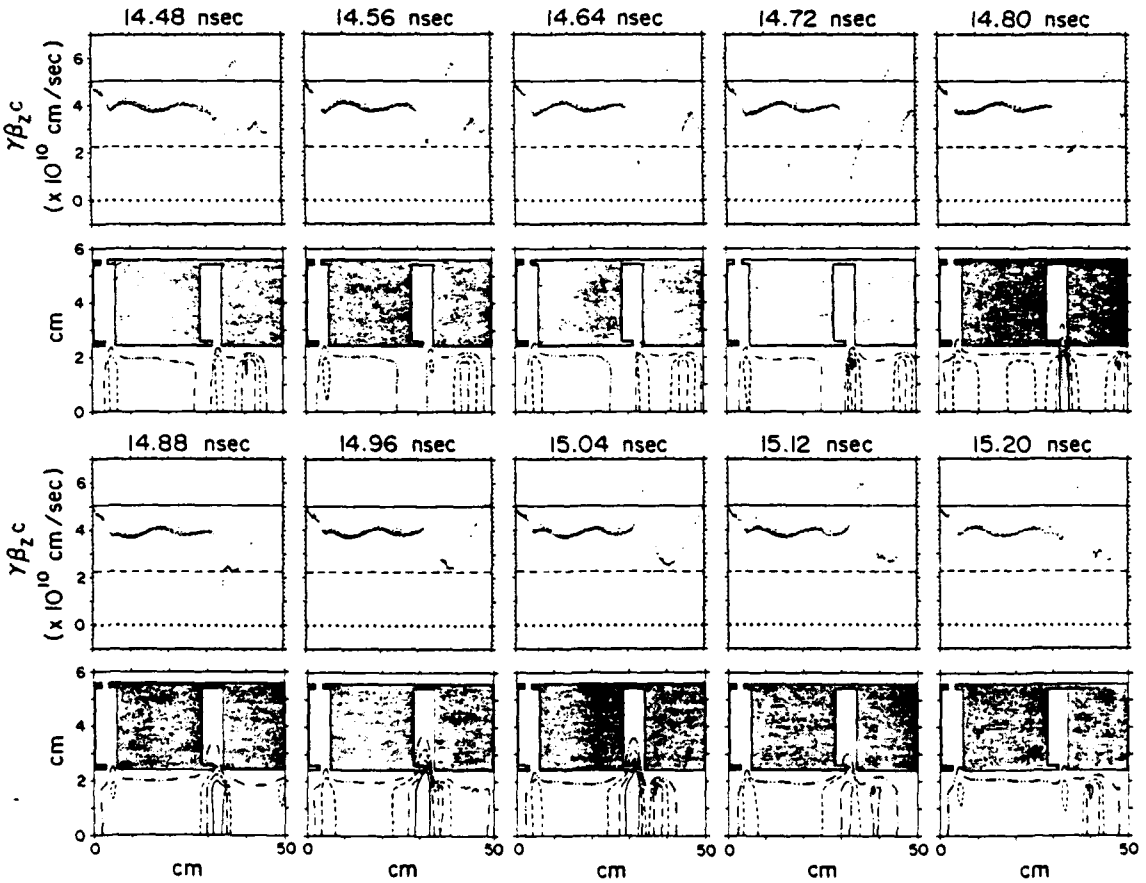



FIG. 19. Phase space plots and electrostatic potential contours for the two-cavity case. The interval between plots is 0.08 rs. In the phase space plots, solid lines show $\gamma\beta_z c$ at injection, broken lines show $\gamma\beta_z c$ at condition of dc limiting current ($\gamma = \gamma_{lim}^{1/3}$), and dotted lines show $\gamma\beta_z c = 0$. In the electrostatic potential contour plots, the potential is 0.21 MeV on the dotted curves, 0.18 MeV on the solid curves, 0.15 MeV on the dash-dot curves, 0.10 MeV on the dashed curves, and 0.05 MeV on the dash-dot-dot curves.

of the second gap. Other macroscopic results such as phase-locking features ( $<2°$) and the variation of $I_1/I_0$ versus the axial position were obtained. All these results agreed with experimental observations.

Inspecting phase space plots ($\beta\gamma c$ vs $z$) of the electrons revealed important information. These plots were obtained for different times, from time $t=0$ ns to $t=18$ ns at regular intervals. We found that the bunching mechanism reached equilibrium almost instantaneously. Figure 18 shows phase space pictures at different times but at a similar phase of three different rf cycles. The three nearly identical plots show that the mechanism is highly stable from cycle to cycle. Figure 19 shows a sequence of phase space pictures and the corresponding electrostatic field contours, all obtained during one rf cycle. Three straight lines were drawn in Fig. 19 to guide the interpretation of the physics. The first line (solid) is $\beta\gamma c$ of the injected electrons. The second line (broken) is $\beta\gamma c$ of the electrons moving at a velocity corresponding to the quasi-dc critical current [Eq. (3)]. The third line (dotted) is $\beta=0$; any particle with a "signature" that appears below this line moves backward to the diode.

Figure 19 gives the following results:

(1) No reflected electrons ($\beta\gamma<0$) exist.

(2) During part of any rf cycle, $\beta\gamma c$ of the electrons drops below the value associated with critical current. This in turn reduces the propagating current, but no reflection of the electrons occurs.

(3) Half a rf cycle later, $\beta\gamma$ of the electrons near the second gap increases above the injected $\beta\gamma$.

(4) Two distinct particle populations emerge from the second gap. The bulk of electrons has high kinetic energy while the second population consists of slow electrons with energy below 50 keV.

(5) One can see electron bunches moving from left to right on the electrostatic field contour figures. The contours are proportional to electron density.

The first result points out that the bunching mechanism is different from the one discussed for the self-modulation of IREBs.[2] The second and the third results confirm the qualitative quasi-dc theory given earlier. The fourth result is in excellent agreement with nonlinear theory and will be discussed in the nonlinear theory section that follows. It follows from the behavior of the nonlinear space-charge waves near and below the critical current. The last result shows that electron bunches are created near the second gap at a time when $\beta\gamma$ is minimum.

As was shown in Fig. 11 once the rf excitation voltage $V_{10}$ exceeded a threshold voltage $V_t$, the rf current $I_1$ was no longer proportional to $V_{10}$. We investigated the IREB modulation by a single cavity when $V_{10}$ exceeded $V_t$ ( Fig. 20). We found that the high-voltage gap behaves in a way analogous to a gate. When the gate is closed instantaneously current stops flowing and potential energy is increased. For a finite time charge accumulates at the gate without reflection. If after this time (and before reflection occurs) the gate reopens, current flow resumes and the potential energy is converted into kinetic energy.

In the simulation (or experiment) the rf voltage opens and closes the "gate." From the simulation we found that

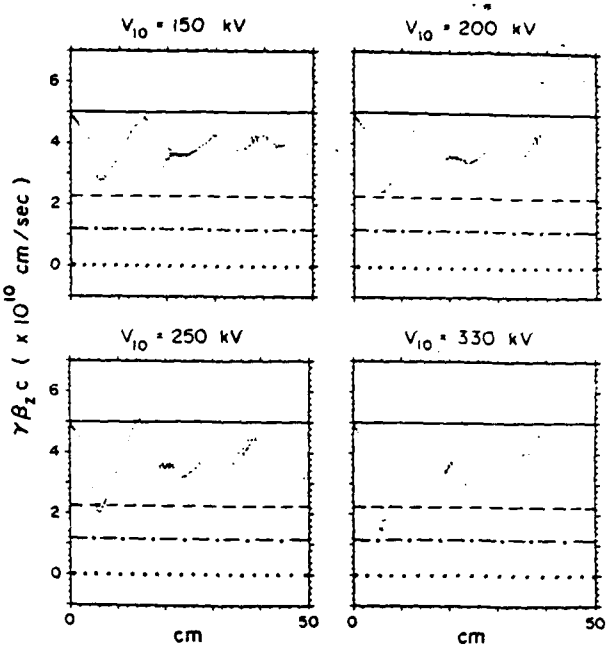



FIG. 20. Phase space plots of the electrons at high values of the modulating voltages, using a single cavity. The gap is located at 5 cm from the left. Solid line: $\gamma\beta_z c$ at injection. Broken line: $\gamma\beta_z c$ at dc limiting current ($\gamma=\gamma_{im}^{1/3}$). Dash-dot line: $\gamma\beta_z c$ at the limiting velocity according to the nonlinear theory. Dotted line: $\gamma\beta_z c=0$.

this threshold voltage was $V_t \simeq 200$ kV. It should be noted that once $V_1 \geq V_t$ the second population of slow electrons appeared in phase space with $\beta\gamma c \leq 1.2\times 10^{10}$ cm/s (see Figs. 19 and 20). This result corresponds to $\beta \leq \beta_{Nm}$ where $\beta_{Nm}$ is the nonlinear limiting velocity (to be discussed below in the nonlinear theory section, where the threshold voltage is also estimated). $\beta_{Nm}$ is independent of $V_{10}$.

Since the length of the geometry in the computer simulation was limited, the only way to see the evolution of the IREB bunching versus distance was to use a single-cavity geometry in which $V_{10}=330$ kV. Figure 21 shows phase space plots and the electrostatic potential contours (which are proportional to the electron density). In this figure one can see electron bunches being generated near the gap and propagating through the drift tube. In this case we found that $I_1/I_0$ saturated at 92% at $z=26$ cm from the gap. Only at $z=46$ cm did the electron bunches start to decay, dropping to $I_1/I_0=79\%$.

### D. Nonlinear theory

#### 1. Introduction

The highly nonlinear behavior exhibited in the experiments and in the computer simulations given above cannot be expected to be adequately described by the small-signal theory. Harmonic generation, substantial slowdown of the electrons as the instantaneous local current reaches $I_c$, etc.,

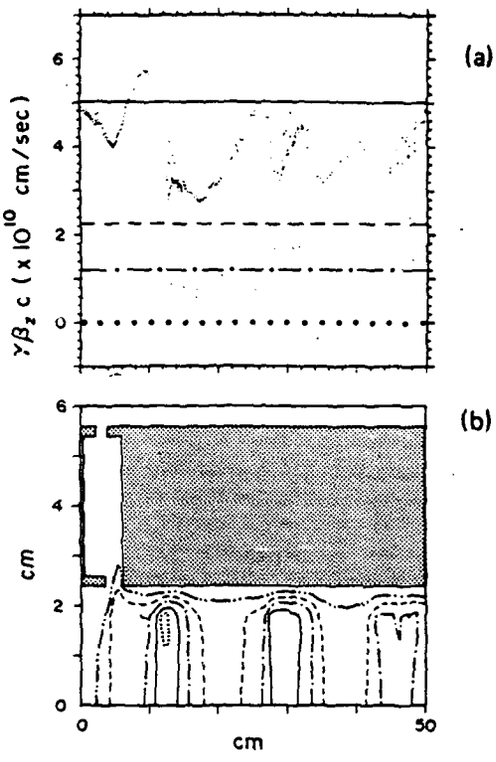



FIG. 21. (a) Top: Phase space plot for a strongly driven single cavity with $V_{10} = 330$ keV; The solid lines, broken lines, dash-dot lines, and dotted lines are the same as in Fig. 20. (b) Bottom: Corresponding contour plot of the electrostatic potential showing bunching of beam electrons. The potential is $-0.187$ MeV on the dotted curves, $-0.147$ MeV on the solid curve, $-0.111$ MeV on the dash-dot curve, $-0.0744$ MeV on the dashed curves, and $-0.0377$ MeV on the dash-dot-dot curves.

cannot be accounted for with a linear theory of space-charge waves. Given below are some analytical models which incorporate these nonlinear processes.

To gain insight with the least amount of complication, we shall treat the drift region and the gap region separately. We shall emphasize the novel effects of the dc space charge of the intense beam on the evolution of the beam current.

In the drift region, the nonlinear evolution of space-charge waves is formulated self-consistently in terms of a single partial differential equation. This equation takes full account of charge overtaking, dc space-charge effects, harmonic generation, and even governs the electron motion through the regime when the instantaneous beam current exceeds the limiting value. The small-signal limit is easily recognized. We have not entirely solved this equation. Instead, we extract certain information. This includes the modification of the propagation characteristics of the space-charge waves as a result of nonlinearity (in addition to the dc space-charge effect). This equation also allows us to estimate the local electron speed which may be expected as the limiting current is reached via nonlinear interaction. In that case, the (nonlinear) slow space charge ceases to propagate.

The harmonic content cannot be readily quantified without a complete solution to the self-consistent formulation mentioned above. We therefore introduce several assumptions. Chief among them is that the individual electrons are assumed to respond to a linearized force, while keeping the nonlinearity due to charge overtaking accurately. This is in line with the classical picture of beam bunching where charge overtaking can be shown to be the dominant nonlinear process (see Appendix D). The main result of this simplified "quasilinear" study is that harmonic generation in the drift region would be significant only if the rf drive were sufficiently strong to cause substantial current modulation in the fundamental component. Another result is that the axial location at which the maximum current modulation occurs shifts toward upstream as the modulating voltage increases. These are in qualitative agreement with experiments.

The nonlinear interaction between the beam and the gap is far more difficult to handle accurately in a self-consistent manner because of the complex geometry. Here, we only employ a rather crude model to illustrate some novel properties of beam bunching associated with an intense beam. Specifically, we show that the presence of a quasi-dc potential barrier tends to strengthen the current modulation. When the rf drive at the gap is sufficiently strong, a substantial amount of current modulation may result even at the exit of the gap. This is a result which is not expected from the classical klystron theory, but may have occurred in the experiments. (We should caution that our description of beam-gap interaction in the presence of a dc space-charge potential is highly idealized. It is not self-consistent, but portrays what is conjectured to be happening in experiments.)

### 2. A self-consistent formulation

We shall first give a self-consistent formulation of the evolution of space-charge waves in the drift region. In keeping with the small-signal theory outlined above, we shall assume (1) that the annular electron beam is infinitesimally thin, (2) that the axial magnetic field is so strong that only axial motion is considered, and (3) that the beam is sufficiently close to the drift tube to permit the use of a long wavelength approximation[7,8] on the Maxwell equations.

Under the above assumptions, the nonlinear evolution of the beam velocity $v(z,t)$, the beam surface density $\sigma(z,t)$, and the axial electric field $E_z(z,t)$ experienced by the beam are governed by the following three partial differential equations:

$$\gamma^3\left(\frac{\partial}{\partial t} + v\frac{\partial}{\partial z}\right)v = \frac{e}{m_0}E_z, \tag{27}$$

$$\frac{\partial \sigma}{\partial t} + \frac{\partial}{\partial z}(\sigma v) = 0, \tag{28}$$

$$-\frac{\epsilon_0}{d}\frac{\partial E_z}{\partial z} = \left(\frac{\partial^2}{\partial z^2} - \frac{1}{c^2}\frac{\partial^2}{\partial t^2}\right)\sigma. \tag{29}$$

Here $\gamma = (1 - v^2/c^2)^{-1/2}$ denotes the instantaneous $\gamma$ associated with the instantaneous velocity $v(z,t)$, and $d = r_b \ln(r_w/r_b)$. Equations (27) and (28) require little comment since their solution yields the density response $\sigma$ to

some imposed axial electric field pattern $E_z$, whereas the solution to Eq. (29) gives the excitation of $E_z$ due to some charge distribution $\sigma(z,t)$ at the location of the beam. The derivation of Eq. (29) is given in Appendix B [cf. Eq. (B5)] where the long wavelength approximation is invoked. Note the linearity between $\sigma$ and $E_z$ in Eq. (29), a consequence of the Maxwell equations.

Before proceeding further, we shall show that the system of Eqs. (27)–(29) would indeed include phenomena of current limitation, say, in some steady-state solution as an example. In the steady state, $\partial/\partial t = 0$. Equation (27) becomes

$$\gamma^3 v \frac{\partial v}{\partial z} = c^2 \frac{\partial \gamma}{\partial z} = \frac{e}{m_0} E_z = \frac{-e}{m_0} \frac{\partial \Phi}{\partial z}.$$

This is just the energy conservation relation

$$\gamma m_0 c^2 + e\Phi = \gamma_{inj} m_0 c^2 = \text{const}, \tag{27a}$$

where we use $\gamma_{inj}$ to denote the value at injection, before the space-charge potential $\Phi$ is set up. Equation (28) gives the conservation of charge

$$\sigma v = \text{const}, \tag{28a}$$

whereas Eq. (29) gives

$$(\epsilon_0/d)\Phi = \sigma, \tag{29a}$$

which relates the electrostatic potential to the surface charge density under the long wavelength approximation. Equations (27a)–(29a) combine to yield

$$\gamma_{inj} = \gamma_0 + (I_0/I_s\beta_0),$$

which is just Eq. (2) where the limiting current is discussed. We shall consider below the nonlinear evolution of the beam whose unperturbed state is characterized by $\sigma_0$, $\beta_0$, $\gamma_0$, $I_0$, and $v_0$, all of which are constants.

Without any further approximation, Eqs. (27)–(29) may be combined into a single partial differential equation (see Appendix B)

$$\left(\frac{\partial}{\partial t} + v\frac{\partial}{\partial z}\right)^2 s(z,t) = \frac{\bar{\sigma}_0}{\gamma^3}\left(c^2\frac{\partial^2}{\partial z^2} - \frac{\partial^2}{\partial t^2}\right)s(z,t), \tag{30}$$

where $\bar{\sigma}_0 = I_0/I_s\beta_0$ is a constant. Physically, $s$ is the nonlinear displacement from the unperturbed position of a fluid element whose instantaneous position is $z$ at time $t$. In terms of $s$, the instantaneous current is

$$I(z,t) = I_0 + \frac{I_0}{v_0}\frac{\partial s(z,t)}{\partial t}, \tag{31}$$

and the instantaneous velocity is

$$v(z,t) = v_0 + \frac{1}{1 - \partial s/\partial z}\left(\frac{\partial s}{\partial t} + v_0\frac{\partial s}{\partial z}\right), \tag{32}$$

with a corresponding value of $\gamma(z,t) = (1 - v^2/c^2)^{-1/2}$.

The derivation of (30)–(32) is given in Appendix B [cf. Eqs. (B21), (B23), and (B13)].

### 3. Propagation characteristic

It is interesting to note that, in the governing Eq. (30), all of the complicated nonlinear processes such as charge overtaking, dc and ac space-charge effects, local transition through the limiting current, etc., are all incorporated in the $v$ term (and through $v$ in the $\gamma^3$ term) of Eq. (30) in a rather simple manner. In other words, the way Eq. (30) is written, the beam density parameter $\bar{\sigma}_0$ remains unaffected by nonlinearity. This is not a trivial result that can be expected from the outset. The linear dispersion relation (4) may be readily recovered from Eq. (30) if we approximate $v$ by $v_0$ and $\gamma$ by $\gamma_0$ in that equation.

Given some initial data on $s$ and $\partial s/\partial t$, Eq. (30) may be solved, in principle, for the evolution of $s$, and hence $I$, for subsequent times. The great resemblance of this nonlinear equation with the corresponding linearized one allows us to expect that the initial perturbation propagates along the characteristics of the fast waves and slow waves. These characteristics are modified by the nonlinearity. When the initial perturbation is small, the nonlinearity may be handled by a perturbation technique.[15,16] In terms of the small parameter $\epsilon \equiv v_1/2v_0$, which is a measure of the depth in the velocity modulation, the $\xi$ and $\eta$ characteristics of the fast and slow waves are modified (see Appendix C):

$$\begin{aligned} z - (\omega/k_s)t &= \xi + \epsilon G(\xi,\eta), \\ z - (\omega/k_f)t &= \eta + \epsilon H(\xi,\eta), \end{aligned} \tag{33}$$

because of the nonlinearity. The explicit forms of $G$ and $H$ are given in Eqs. (C21) and (C22) of Appendix C. Some of these characteristics are shown in Fig. 22. The approximate solution $v_1$ is given in Eq. (C15) in terms of the characteristic variables $(\xi,\eta)$. It is possible that they may be valid beyond the time at which the characteristics intersect.[15]

In Figs. 22(a) and 22(b), we show the propagation characteristics over one cycle of the modulating voltage that is located at $z = 0$. Each characteristic is spaced a quarter cycle ($\omega t = \pi/4$) from a neighboring one initially. The amplitude $V_{10}$ of the rf gap voltage is held at 30 keV. The parameters used in Fig. 22(a) are: $E_{inj} = (\gamma_{inj} - 1)m_0c^2 = 425$ keV, $I_s = 36.5$ kA, $I_c = 12.8$ kA, $I_0 = 4.86$ kA, $\gamma_0 = 1.67, \beta_0 = 0.8$. Neither the fast wave nor the slow wave characteristics in this figure are significantly different from the linear theory. Crossing of the slow wave characteristics—a property of nonlinearity—occurs at a considerable distance downstream. Thus, the current response within a wavelength of the modulating gap can be adequately described by the small-signal theory.

In Fig. 22(b), we raise $I_0$ to 0.8 $I_c$, keeping the rest of the input parameters the same as in Fig. 22(a): $E_{inj} = 425$ keV, $I_s = 36.5$ kA, $I_c = 12.8$ keV, $I_0 = 10.3$ kA, $\gamma_0 = 1.44$, $\beta_0 = 0.72$. We see here that the fast wave characteristics remain unchanged, whereas crossing of the slow wave characteristics occur only half a wavelength downstream from the modulating gap. Comparing with Fig. 22(a), we see that, at the same rf voltage drive, an intense beam is able to produce a stronger current modulation as a result of nonlinearity and dc space-charge effects. Further discussion of the nonlinear space-charge waves may be found in Ref. 17.

The bending of the characteristics in the $(z,t)$ plane implies that the current modulation contains harmonic content. However, the harmonic content cannot be readily extracted from the solutions in terms of the characteristic variables $(\xi,\eta)$, since the conversion from the $(\xi,\eta)$ variables to the $(z,t)$ variables cannot be obtained in a simpler

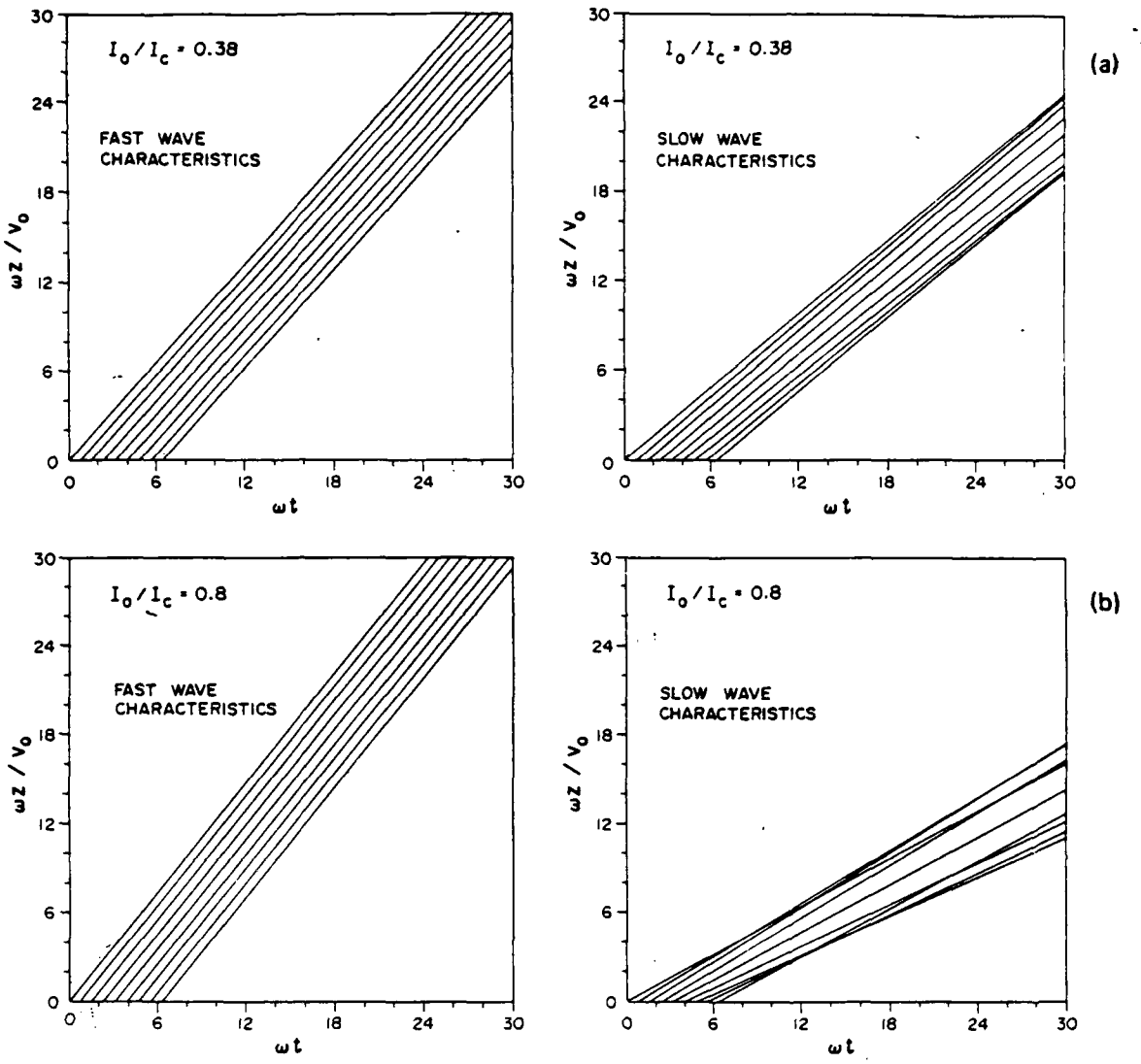



FIG. 22. Nonlinear propagation characteristics of the fast and slow space-charge waves for $E_{inj} = 425$ keV, $I_c = 12.8$ kA, $V_{10} = 30$ keV. (a) Top: $I_0 = 4.86$ kA ($I_0/I_c = 0.38$). (b) Bottom: $I_0 = 10.3$ kA ($I_0/I_c = 0.8$).

manner. (We shall estimate the harmonic content via a different approximation in the next subsection.) Instead, from the structure of Eq. (30), we estimate here the local electron speed when the limiting current is reached nonlinearly.

From the small-signal theory, we recall that as the dc beam current approaches the limiting value, the beam's unperturbed drift speed approaches the value $v_{0m} = c(1 - 1/\gamma_{inj}^{2/3})^{1/2}$, which depends only on the injection energy. Under this condition, the small-signal slow space-charge wave ceases to propagate. In the present problem of a nonlinear amplifier, the situation is different. Here, both $\gamma_{inj}$ and $I_0$ are specified, which in turn determines the unperturbed drift speed $v_0$ and hence $\bar{\sigma}_0 = I_0/I_c\beta_0$. [cf. Eq. (2)]. The question then becomes: What would be the local electron speed when the current perturbation is so strong that the nonlinear slow space-charge wave ceases to propagate? Call this nonlinear limiting speed $v_{Nm}$ and $\beta_{Nm} \equiv v_{Nm}/c$. Since (30) has the same structure as the corresponding equation in the linear theory, its local dispersion relationship is also similar. Thus, $v_{Nm}$ is determined from

$$\beta_{Nm}^2 \gamma_{Nm}^3 = \bar{\sigma}_0, \tag{34}$$

where $\gamma_{Nm} = (1 - \beta_{Nm}^2)^{-1/2}$. The solution of $\beta_{Nm}$ as a function of $\bar{\sigma}_0$ is shown in Fig. 23. The limiting speed is approached nonlinearly, as the initial current $I_0$ is below the critical current $I_c$. However, the above estimate of the limiting speed $v_{Nm}$ does not depend on how the large amplitude perturbation is set up. It is based only on a local theory of an

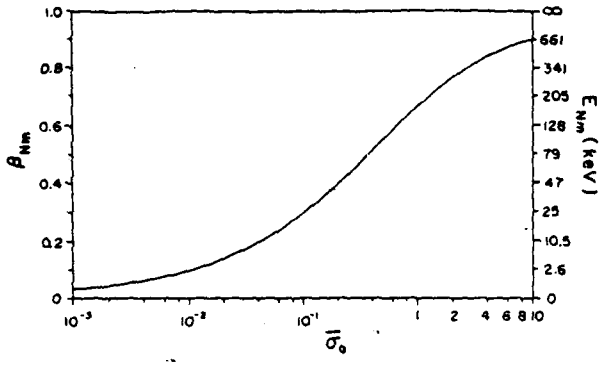



FIG. 23. Normalized local electron speed $\beta_{Nm}$ when the nonlinear space-charge waves cease to propagate. Also labeled is the corresponding kinetic energy $E_{Nm}$.

exact formulation of the nonlinear processes. Note that if $\beta_{Nm}^2 \ll 1$, Eq. (34) gives $\beta_{Nm} \simeq (\bar{\sigma}_0)^{1/2} \propto (I_0/I_s)^{1/2}$.

The estimate according to (34) is in close agreement with the simulations (Fig. 20), where we have $(I_0/I_s)^{1/2} = 0.3708$. This corresponds to an energy of 39.34 kV and a momentum, $\gamma\beta c = 1.198 \times 10^{10}$ cm/s. This value corresponds closely to the low-energy population of particles that can be seen in the phase space plots of Figs. 20 and 21. In addition, these simulations verified that $\beta_{nm}$ is independent of $V_{10}$, as predicted. This can be seen in Fig. 20, in which phase space plots for $V_{10} = 150$, 200, 250, and 330 kV are plotted. Note that in all cases, the low-energy population of particles has $\gamma\beta c \simeq \gamma_{nm}\beta_{nm}c = 1.198 \times 10^{10}$ cm.

#### 4. Harmonic content

Equation (30) allows us to assess the harmonic content, especially when the unperturbed current is sufficiently small ($\bar{\sigma}_0 \ll 1$). In that case the right-hand member of Eq. (30) becomes small and may be treated perturbatively. For the amplifier problem, we are interested in the current downstream at $z$, when an external rf signal causes an initial displacement $s(0,t)$ and initial velocity $v_1(0,t)$ at $z = 0$:

$$s(0,t) = 0,$$
$$v_1(0,t) = \tfrac{1}{2}\epsilon v_0 \sin \omega t. \tag{35}$$

These initial conditions are equivalent to imposing an rf current $I_1$ and rf beam voltage $V_1$ at $z = 0$:

$$I_1(0,t) = 0,$$
$$V_1(0,t) = V_1 \sin \omega t, \tag{36}$$

where, from Eq. (A11),

$$V_1 = \epsilon(m_0c^2/e)\gamma_0^3\beta_0^2/2\delta. \tag{37}$$

We now introduce two assumptions for the right-hand side of Eq. (30), which physically represent the collective force acting on the electron displacement $s$. (a) Since $\bar{\sigma}_0$ is assumed small, we linearize this force by replacing the factor $\gamma^3$ by $\gamma_0^3$. (b) We assume that only the fundamental frequency component ($\omega$) of this force would act on the electron. As a consequence, we may approximate $\partial^2/\partial z^2$ by $-\omega^2/v_0^2$ in the right-hand side of Eq. (30). Thus, Eq. (30) becomes

$$\left(\frac{\partial}{\partial t} + v\frac{\partial}{\partial z}\right)^2 s(z,t) = \frac{\bar{\sigma}_0}{\gamma_0^3}\left(\omega^2 - \frac{\omega^2}{\beta_0^2}\right)s(z,t), \tag{38}$$

in which $v(z,t)$ depends on $s$ nonlinearly [cf. Eq. (32)]. In essence, Eqs. (38) and (32) take full account of nonlinearity due to charge overtaking and charge conservation whereas we pretend that the electrons are subject to a linear collective field with only one frequency component. In some sense, this procedure may be regarded as a quasilinear approximation. (We shall show in Appendix D that such a quasilinear approximation yields excellent agreement with particle simulation when the procedure is applied to the conventional klystron model,[18] in both the space-charge-dominated regime and the high amplitude nonlinear regime. See Fig. 32 in Appendix D.)

The calculation outlined in Appendix D allows us to solve the coupled nonlinear partial differential equations (32) and (38). The instantaneous current (31) at time $t$ at position $z$ reads

$$I(z,t) = I_0 + \sum_{n=1}^{\infty} I_n(z)\cos n\omega\left(\frac{t-z}{v_0}\right), \tag{39}$$

where the $n$th harmonic component is given by

$$I_n(z) = 2I_0J_n(n\bar{V}\sin\bar{z}). \tag{40}$$

Here, $J_n$ is the Bessel function of order $n$,

$$\bar{V} = (eV_1/m_0c^2)\delta/(\gamma_0^2\beta_0\alpha^{1/2}),$$
$$\bar{z} = (\omega z/c)\alpha^{1/2}/\beta_0^2\gamma_0,$$

and the rest of the symbols have been defined earlier. The fundamental component $I_1(z) = 2I_0J_1(\bar{V}\sin\bar{z})$ may be approximated by

$$I_1(z) \simeq I_0\bar{V}\sin\bar{z}$$

when $\bar{V} < 0.3$, indicating that the maximum value of $I_1(z)$ occurs at $\bar{z} = \pi/2$. The last expression is simply the familiar result from the linear theory and has been shown to be in excellent agreement with simulation. When $\bar{V}$ becomes large, the maximum value of $I_1(z)$ saturates, it occurs at a value $\bar{z} < \pi/2$ [cf. Eq. (40), Fig. 32]. Thus, when the rf drive is very strong, the location at which maximum current modulation occurs shifts toward upstream. This is in qualitative agreement with experimental observation.

The estimate given by Eq. (39) suggests that the harmonic components ($n > 2$) would decrease rapidly with $\bar{V}$ if $\bar{V} < 0.3$. However, they become nontrivial if the beam is driven very hard. Figure 24 shows the peak value of the harmonic content at different levels of $V_1$ according to Eq. (40). In this figure, we see that significant harmonics would be excited if the rf gap voltage drives the fundamental component to a high level. This result is also in qualitative agreement with experiments and simulation, as discussed in earlier sections.

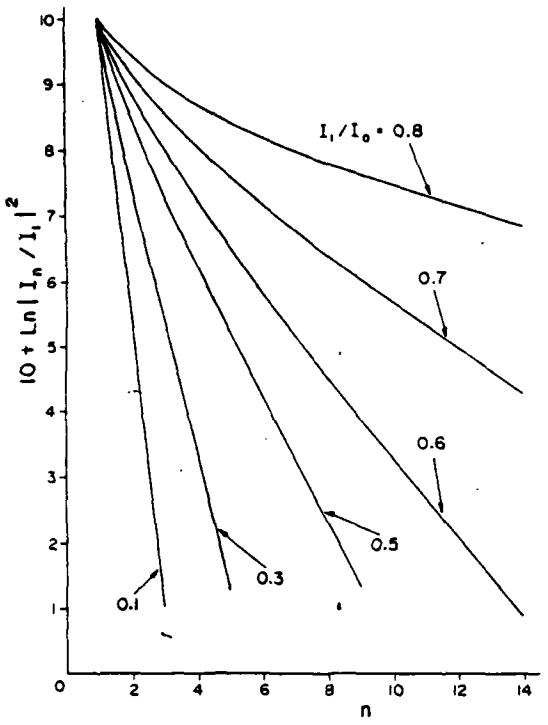



FIG. 24. Harmonic content of the modulated current as a function of the rf voltage drive (which gives rise to the peak value of $I_1/I_0$ as labeled).

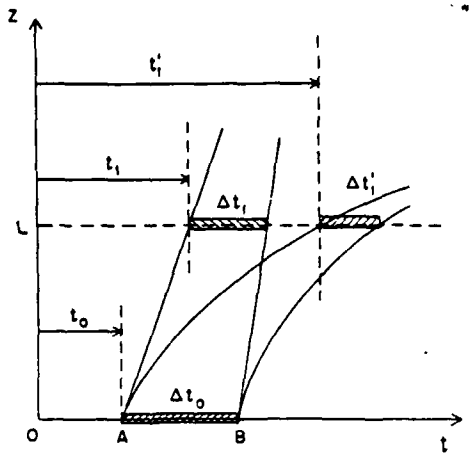



FIG. 25. Trajectories of two electrons, labeled A and B, in the absence (straight lines) and in the presence (curved lines) of a.dc retarding field.

### 5. Increase in current modulation by the dc space-charge effect

In this subsection, we shall give an intuitive argument which strengthens our perception that current modulation may be more readily achieved in an intense beam than in a classical tenuous beam. Such a difference has its origin in the dc retarding potential caused by the self-field of the intense beam. Specifically, by means of a simple model, we illustrate how a velocity modulation on the beam would be more readily converted to current modulation if the beam drifts against an electrostatic barrier than when such a barrier is absent.

Consider an electron beam which, at $z = 0$, is velocity modulated: $v = v_0 + v_1(t)$. If the electrostatic barrier is absent, an electron (A) arriving at $z = 0$ at time $t_0$ will reach $z = L$ at time $t_1 = t_0 + L/[v_0 + v_1(t_0)]$ (Fig. 25). Similarly, an electron (B) arriving at $z = 0$ at a later time $t_0 + \Delta t_0$ will reach $z = L$ at $t_1 + \Delta t_1$ (Fig. 25), where

$$\Delta t_1 = \Delta t_0 + \left(\frac{L}{v_0 + v_1(t_0)} - \frac{L}{v_0 + v_1(t_0 + \Delta t_0)}\right).$$

Charge conservation requires

$$I_0 \Delta t_0 = (I_0 + I_1)\Delta t_1,$$

which yields

$$I_1 \simeq -I_0\left(\frac{L}{v_0^2}\right)\frac{\partial v_1(t_0)}{\partial t_0}, \tag{41}$$

when $v_1$ and $\Delta t_0$ are small. This equation simply illustrates the conversion of a velocity modulation to a current modulation according to the classical klystron theory.[18]

To see how a dc retarding potential influences the bunching, for simplicity, we assume that there is an almost constant electric field $E_0 \equiv \Phi_s/L$ between $z = 0$ and $z = L$. Thus, electrons are decelerated between $z = 0$ and $z = L$ with a deceleration

$$a_0 \simeq -|eE_0/\gamma_0^3 m_0| \equiv -|e\Phi_s/\gamma_0^3 m_0 L|.$$

Thus, electron A will arrive at $z = L$ at time $t_1'$ (Fig. 25) where $t_1'$ is to be solved from

$$L = [v_0 + v_1(t_0)](t_1' - t_0) - \tfrac{1}{2}a_0(t_1' - t_0)^2,$$

whereas electron B will arrive at $z = L$ at time $t_1' + \Delta t_1'$ which is to be computed from

$$L = [v_0 + v_1(t_0 + \Delta t_0)]\left[(t_1' + \Delta t_1') - (t_0 + \Delta t_0)\right] - \tfrac{1}{2}a_0\left[(t_1' + \Delta t_1') - (t_0 + \Delta t_0)\right]^2.$$

From the last two equations, we obtain, for small $\Delta t_0$ and $v_1$,

$$\Delta t_1' = (\Delta t_0)\left(1 + \frac{L}{v_0^2}\frac{\partial v_1(t_0)}{\partial t_0}M\right), \tag{42}$$

where

$$M \equiv \frac{2}{X}\left(\frac{1}{\sqrt{1-X}} - 1\right), \tag{43}$$

with

$$X \equiv 2|e\Phi_s|/m_0c^2\gamma_0^3\beta_0^2. \tag{44}$$

Again, charge conservation requires

$$I_0 \Delta t_0 = (I_0 + I_1')\Delta t_1', \tag{45}$$

yielding

$$I_1' \simeq -I_0\left(\frac{L}{v_0^2}\right)M\frac{\partial v_1(t_0)}{\partial t_0}, \tag{46}$$

which is the current modulation at $z = L$ in the presence of a dc potential retardation. Comparing Eq. (46) with Eq. (41), we see that the presence of a potential barrier has the same effect as increasing the velocity modulation by a factor of $M$. The dependence of $M$ on $X$ is shown in Fig. 26. For small $X$, $M \simeq 1 + X$. Note from Eq. (44) that $M$ depends only on the height of the potential barrier $\Phi_s$, but is independent of the distance $L$ over which the electron is decelerated.

The physical reason for the increase in current bunching by a dc retarding potential may be understood by referring to Fig. 25. In this figure, electron B has a higher initial velocity than electron A. Under the same deceleration, it would take electron A a longer time to reach $z = L$ than electron B. Another way to see this is that electron B would travel a shorter distance to eventually catch up with electron A, when a retarding potential is present. Thus $\Delta t_1' < \Delta t_1$, which is the reason for the enhancement in current modulation.

It can be shown that the same enhancement in the current modulation persists if between the region $z = L$ and $z = 2L$ there is an *accelerating* electric field of the same magnitude. That is, at $z = 2L$, the current modulation is increased by the same factor $M$ if there is a retarding electric field between $z = 0$ and $z = L$ and an accelerating field of the same magnitude between $z = L$ and $z = 2L$.

Finally, we remark that the above account may have already underestimated the effect of the dc potential. The nonlinear acceleration is proportional to $E_0/\gamma^3$, (not $E_0/\gamma_0^3$). It would have a stronger effect on the slower electrons, especially when the rf voltage is high.

The simple illustration of the physical processes which lead to the enhancement factor $M$ given above is strongly suggestive, even if the dc potential barrier has not been solved self-consistently.

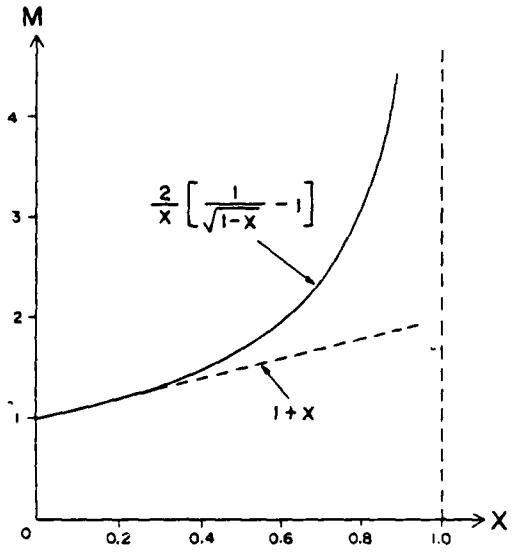



FIG. 26. Magnification factor $M$ as a function of the normalized static potential $X \equiv 2|e\Phi_s|/m_0c^2\gamma_0^2\beta_0^2$.

### 6. Current modulation at the gap exit

Toward the end of Sec. III D 3, we indicated that, for a given injection $\gamma$ and the dc current, there exists a minimum electron speed below which the rf current ceases to propagate. When an intense beam passes a modulating gap, it experiences a rather strong retarding dc potential associated with the space charge. If the rf modulating voltage is high, the kinetic energy of the beam, the rf voltage across the gap, and the retarding dc potential at the gap would all be of the same order of magnitude. Thus, it is possible that, for a sufficiently strong rf gap voltage, there is a portion of the rf cycle during which the rf voltage, together with the dc self-voltage of the beam, would reduce the propagating speed below the critical speed. This would then lead to an effect similar to a periodic "gate" for the beam current (see also Sec. III C). As a result (contrary to the classical klystron theory), substantial current modulation may arise once the beam exits the modulating gap.

We shall now estimate the minimum rf gap voltage for the above phenomena to occur. We next estimate the current modulation at the gap exit once the rf voltage exceeds this threshold value.

Let the gap be short and the rf voltage across it be $V_1 \sin \omega t$. The instantaneous speed $v$, and the corresponding values of $\beta$ and $\gamma$ of an electron are approximately given by

$$\gamma_{inj} = \gamma + \frac{I_0}{I_s\beta} + \frac{|e|V_1 \sin \omega t}{m_0c^2}. \tag{47}$$

It is easy to show that Eq. (47) does not admit a (real) solution for $\beta$ and $\gamma \equiv (1-\beta^2)^{-1/2}$ if

$$V_1 \sin \omega t > V_{th}, \tag{48}$$

where

$$V_{th} \equiv \frac{m_0c^2}{|e|}\left\{\gamma_{inj} - \left[1 + \left(\frac{I_0}{I_c}\right)^{2/3}(\gamma_{inj}^{2/3} - 1)\right]^{3/2}\right\}. \tag{49}$$

In (49), $I_c \equiv I_s(\gamma_{inj}^{2/3} - 1)^{3/2}$ denotes the limiting current. Thus, if $V_1 < V_{th}$, the modulating process at a short gap is similar to the classical picture—there is no current modulation immediately beyond a short gap which provides the (velocity) modulation.

However, if $V_1 > V_{th}$, we expect a strong current modulation by the gap. The amount of current modulation at the gap exit is estimated to be

$$(I_1)_{exit} \simeq \frac{\omega}{\pi} I_0 \int_{\hat{t}-\pi}^{\hat{t}} dt \sin \omega t$$
$$= I_0(2/\pi)\sqrt{1 - V_{th}^2/V_1^2}. \tag{50}$$

In (50), $\hat{t} = (1/\omega)\sin^{-1}(V_{th}/V_1)$. The rf current $(I_1)_{exit}$ at the gap exit as a function of $V_1/V_{th}$ is shown in Fig. 27. As shown in this figure, the current modulation is absent if $V_1 < V_{th}$, but rises rapidly once $V_1 > V_{th}$, and becomes insensitive to $V_1$ if the latter substantially exceeds $V_{th}$. These features are also reflected qualitatively in experiments and simulations, and are a (yet another) novel property associated with an intense beam.

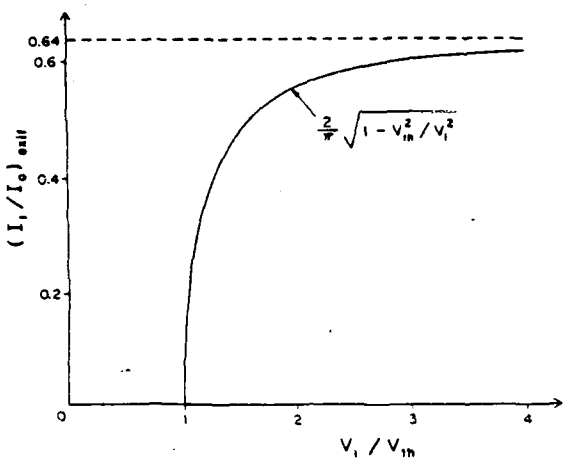



FIG. 27. Current modulation at the gap exit as a function of modulating gap voltage.

$$E_A = (m_0c/eT)(\beta_A\gamma_A - \beta_K\gamma_K) - (Q/2\epsilon A_0), \quad (51)$$

where $T$ is the transit time of an electron across the gap, $Q$ is the total charge/length stored between the plates, $A_0$ is the plate area, and the subscripts $A$ and $K$ indicate parameters measured at plate A and K, respectively. It was shown that for any $V_0$ there is an electron current for which $E_A$ (and $E_K$) was positive. Hence, no electron emission from the electrodes can occur.

The one-dimensional representation of a gap is not realistic. Typically, a gap is of two dimensions. Such a gap is used in our experimental work, and is shown in Fig. 28. Solving numerically Poisson's equation for a two-dimensional gap, we obtained equipotential lines for different gap voltages and IREB parameters. We observed that, in general, the intensity of the electric field on the negatively charged electrode was reduced and with some critical IREB parameters a po-

## IV. APPLICATIONS OF MODULATED IREBs

### A. Electrostatic insulation

There are many processes which limit the power flow in rf devices. Two of these processes are associated with high-voltage gaps: (1) multipactor effect[19] and (2) arcing and vacuum breakdown.[20] These processes result from electron emission from the negative electrode. Electron emission depends on many parameters, such as electric field, geometry, frequency of rf, etc. The above limiting processes can at best divert the rf power by acting as a shunt load, and at worst cause vacuum breakdown and "shorting" the cavity.

At first sight, these processes may limit the power that the modulated IREB can deliver. However, we show here that using an IREB offers ways to suppress electron emission. This possibility is based on our recent research showing electrostatic insulation of high-voltage gaps.[21] We found that the electric self-field of an IREB with a current in the kiloamp range can modify the electric field configuration in a high-voltage gap in such a way that the voltage gradient on the negatively charged electrode is reduced and even reversed in sign. When this happens emission of electrons is suppressed, eliminating the conditions necessary for vacuum breakdown.

The research on electrostatic insulation was presented elsewhere; here we give only the results necessary for this discussion.

Electrostatic insulation can be qualitatively investigated in a simple geometry of two parallel plates A and K through which an electron beam of particle density $\rho$ is flowing (from electrode A to electrode K). A voltage $V_0$ is applied on electrode K changing the electron energy. The electric field on electrode A can be calculated using Poisson's equation $\Delta V = -\rho e/\epsilon$ and the equation of conservation of charges $e\rho v = \text{const}$:

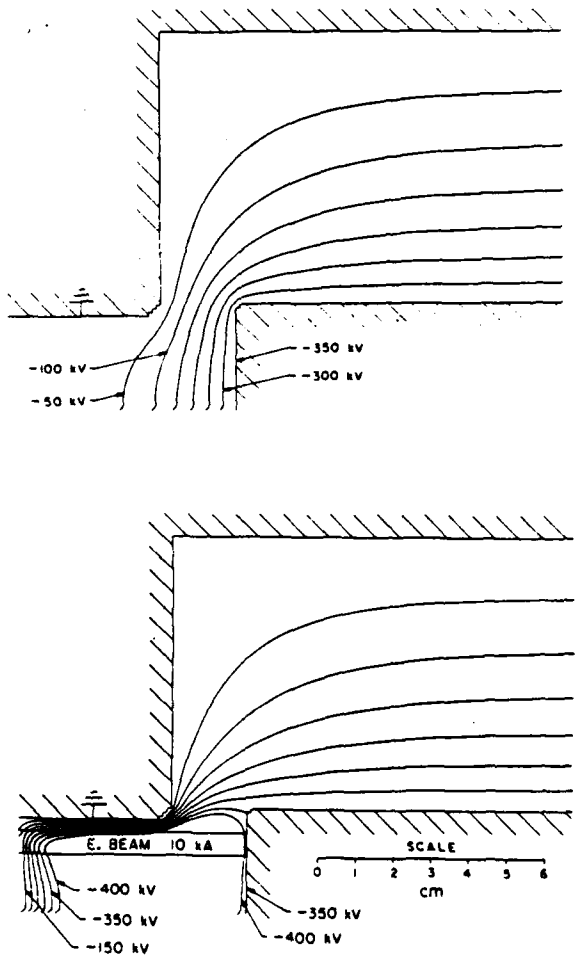



FIG. 28. Equipotential lines in a two-dimensional geometry in which the voltage between electrodes is 350 keV. Top figure does not include the IREB. In the bottom figure, an electron beam of 10 kA propagates from left to right. Note the potential reversal near the the high-voltage electrode in the bottom figure.

tential hill was established. Figure 28 shows an example of the existence of a potential hill inside a two-dimensional decelerating gap. A 10 kA electron beam with infinite energy propagated through the gap. The applied voltage on the gap was $-350$ kV. For the above example secondary electrons with energy less than 50 keV were reflected back, eliminating the multipactor effect and quenching vacuum breakdown. This picture remains the same for the propagation of a finite energy IREB through a similar gap.

### B. rf extraction from modulated IREBs

Many applications (e.g., rf accelerator) demand high rf power in a $TE_{01}$ mode of a rectangular waveguide. In this section we describe extraction of rf at a frequency of 1.328 GHz from a modulated IREB. The experimental setup is shown in Fig. 29. It consists of the device shown in Fig. 12 and an rf converter.[22] The rf converter consisted of a coaxial line which intersects a rectangular waveguide through its broad side. Two movable plungers were used to vary the lengths of the coaxial line and of the rectangular waveguide. The input impedance seen by the input of the coaxial line is

$$Z_{in} = Z_c \frac{Z_L + jZ_c \tan(kl)}{Z_c + jZ_L \tan(kl)}, \tag{52}$$

where $Z_c$ is the characteristic impedance of the coaxial line, $Z_L$ the impedance connected at the end of the coaxial line, $l$ the length of the coaxial line, $k = 2\pi/\lambda$, and $\lambda$ the wavelength ($\lambda = 2\pi c/\omega$).

The modulated electron beam that was used to excite the coaxial line had a current $I_0 = 5$ kA, for a duration of $T_0 \sim 100$ ns, energy $eV_0 = 600$ keV, and a frequency $f = \omega/2\pi = 1328$ MHz. The voltage at the input of the coaxial line was

$$V_{in} = IZ_{in}. \tag{53}$$

The following conditions had to be satisfied for $Z_{in}$ and the geometry of the coaxial line: (1) $Z_{in}$ be real at the frequency $f_0$ in order to extract power from the modulated beam. (2) $Z_{in}$ be chosen such that (a) $V_0 > IZ_{in}$ for the frequency $f_0$ and (b) $Z_{in}$ be small for frequencies around $f \simeq 1/T_0$. (3) The coaxial line with a large transverse dimension to reduce the electric field on the metallic surfaces but small enough to fit inside the magnetic field coil.

In order to satisfy the above conditions we chose $l = \lambda_0 = c/f_0$. This translates into $Z_{in} = Z_L$. $Z_L$ was adjusted by the two movable plungers to satisfy conditions (1) and (2a). Condition (2b) was satisfied by reducing $Z_c$. Condition (3) could not be satisfied. At the high power planned for the converter, electric field greater than 500 kV/cm could be generated. In order to circumvent a possible vacuum breakdown the coaxial line was immersed in a strong axial magnetic field. The rectangular waveguide dimensions were $16.6 \times 8.3$ cm$^2$, ensuring operation at the $TE_{01}$ mode. The rectangular guide was connected to an rf horn. A vacuum window was placed on the horn and was monitored during the operation by a still camera in order to detect flashover or rf breakdown. The whole converter was kept at a base pressure of less than $10^{-5}$ Torr.

The power inside the rectangular waveguide and in free space was monitored by electrostatic probes. These probes were absolutely calibrated. A known rf power at 1328 MHz was fed into the "coaxial line" through a 50-Ω slotted mission line. The movable plungers were adjusted so that voltage standing wave ratio (VSWR) of 1 was achieved. Under this condition all of the input power $P_s$ was transferred to the rectangular guide. From the response of a probe $V_s$ the required calibration was found relating voltage $V$ to power $P$:

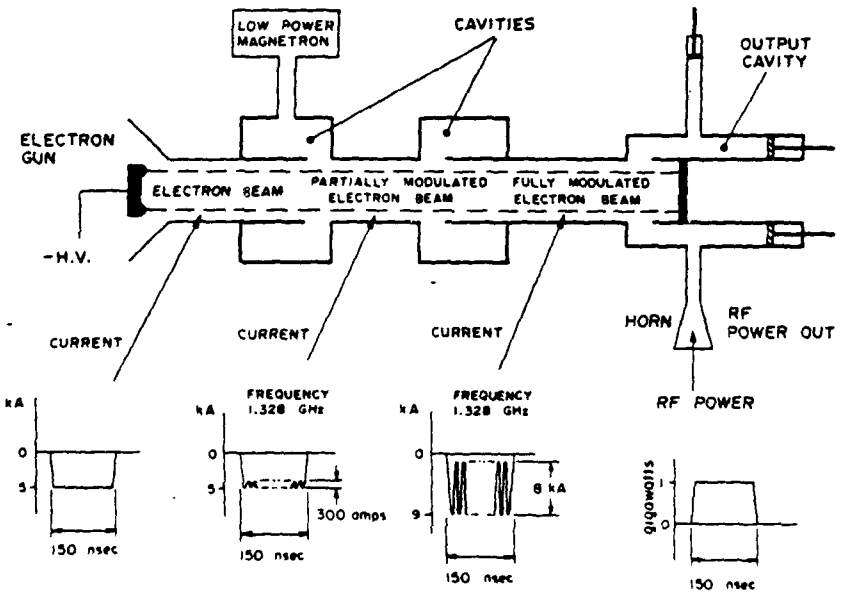



FIG. 29. Experimental arrangement used to generate rf power and to inject it into the atmosphere. The bottom figure shows the evolution of the IREB as it traverses, from the diode, through the first and the second cavity, and the rf extraction.

$$P = P_s(V/V_s)^2. \quad (54)$$

Even though the rf power in the modulated MIREB was of the order of $\sim 3$ GW for a duration of 140 ns, only a fraction of the rf energy was extracted out. Typically we got 1.8 GW of rf power for 30–50 ns. The easy access to the rectangular waveguide helped us to determine that vacuum breakdown, at the junction coaxial cavity-rectangular waveguide, occurred. Only after reducing the IREB power to 1.2 GW we extracted 500 MW of rf power for the IREB duration (140 ns).

### C. Particle accelerators powered by modulated intense relativistic electron beams (Ref. 5)

Future progress in accelerators and their applications may depend critically on development of new mechanisms capable of generating high-voltage gradients. It was shown that a high electric field can be established in structures by MIREBs (of power $> 10^9$ W). The simplicity and the high efficiency of generating MIREBs suggest possible advantages of accelerators powered by MIREBs over a more conventional approach (e.g., rf linac) for generating high currents of high-energy particles.

The mechanism of the new accelerator employs two beams of particles which interact via a metallic structure. The first beam generates an electromagnetic field which in turn accelerates a second beam. This effect is large, only, when the second beam is much weaker and shorter in duration than the first.

The new accelerator is shown schematically in Fig. 30. The major parts of the new accelerator are:

(1) An IREB generator that injects an annular electron beam of radius $R$, voltage $V$, current $I$ for a duration $T$ into the bunching region (e.g., $V = 1$ MV, $I = 10$ kA, and $T = 10^{-7}$ s). The electron beam is confined by a strong axial magnetic field.

(2) A bunching region which is immersed in the magnetic field and where a low-level rf source (magnetron) modulates the IREB.

(3) The modulated annular electron beam is guided by the axial magnetic field into a cylindrical cavity of radius $B$. The cavity is loaded with a structure that consists of thin metallic disks, of radius $A$ and thickness $\delta$, which are spaced along the cavity with a separation $\Lambda$. The disks are supported longitudinally by thin metallic rods, cantilevered from the end wall of the cavity.

The MIREB is terminated at the first disk. The frequency of modulation and the cavity geometry are chosen such that a resonance interaction between the MIREB and the cavity occurs, leading to the transfer of energy from the beam to the structure.

(4) After some predetermined time a second electron beam traverses the cavity through holes located at the centers of the disks, draining the stored energy. This electron beam is initiated and controlled by a laser beam that illuminates the center of the first metallic disk. Since the laser light can be intensity modulated by the external rf source the second electron beam will be also modulated at the same frequency. If the second bunched electron beam is in the "right" phase with the electromagnetic wave in the structure, all the electrons are accelerated by the electric field and gain the same energy.

The accelerator community often uses the SUPERFISH computer code[23] to find axial symmetric modes in cavities. We have applied this code to the geometry of a structure consisting of 12 radial cavities. This program calculates the electric field configurations, shown in Fig. 31.

The maximum voltage that can be developed along the axis of any radial line $V(r = 0)$ depends on the voltage that decelerates the MIREB $V(r = R)$:

$$V(r = 0) = V(r = R)J_0(0)/J_0(kR). \quad (55)$$

From a previous work done by the authors on inverse diodes, one finds that $V(r = R) \geq 0.5\, E_{\text{kin}}/e$, where $E_{\text{kin}}$ is the kinetic energy of the electrons in the bunch. By choosing a large diameter MIREB ($R \simeq A$) one gets $J_0(0)/J_0(kA) = 10$. Hence for $E_{\text{kin}} = 1$ MeV, $V(r = 0) \geq 5$ MV, and since the axial distance between two disks is a few cm, the electric field along the axis is $\geq 100$ MV/cm.

In order for the structure to be loaded uniformly with electromagnetic energy the following condition has to be satisfied: $T > L_t/V_g$, where $L_t$ is the total length of the structure (e.g., 3 m). For the proposed structure $L_t/V_g = 50$ ns, which is smaller in comparison with the MIREB duration of $T = 150$ ns. The unloaded energy gain of a constant-impedance accelerating section is[1]

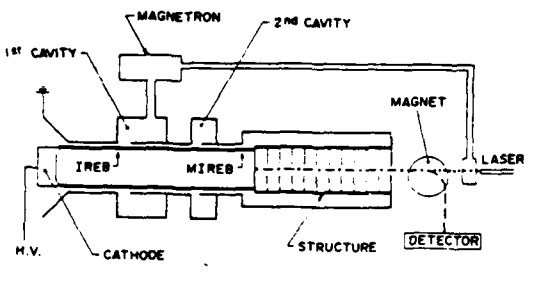



FIG. 30. Experimental arrangement proposed for particle acceleration using a modulated IREB.

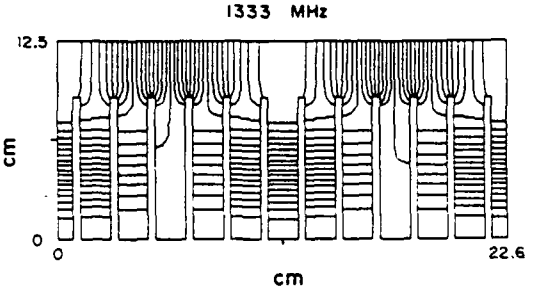



FIG. 31. Electric field configuration, obtained from the SUPERFISH code, for particle acceleration.

$$V_0 = (\rho L_t P_0)^{1/2}[(2/\tau)^{1/2}(1 - e^{-\tau})],$$
$$\tau = \omega L_t / 2 V_g Q. \quad (56)$$

For $L_t = 3$ m, $V_0 \simeq 3 \times 10^8$ V, the shunt impedance $\rho = 3 \times 10^7\ \Omega/\text{m}$, and $Q \sim 10^4$, one gets that $P_0 \simeq 3 \times 10^9$ W which is a level of power that can be obtained from a MIREB.

Conventional linear accelerators have scaling laws for voltage gain, instability thresholds, cost, etc., as a function of wavelength, power input, geometry, etc. The only point that differs here from a conventional accelerator is the power of modulated intense relativistic electron beams. Since we believe that the power of a MIREB is independent of wavelength, the scaling law for the accelerating voltage that can be derived from Eq. (56) is $V \sim \lambda^{\alpha}$, where $-1 \leqslant \alpha \leqslant 0.5$ and $\alpha$ is a function of $\lambda$ too. For large values of $\lambda$, $\alpha \simeq 1$; for a small value of $\lambda$, $\alpha \simeq 0.5$. The maximum accelerating voltage corresponds to $\lambda = 5$ cm.

The shortest wavelength of an externally induced MIREB achieved to date is $\lambda \simeq 22$ cm. However, the theory behind MIREB generation predicts that reducing $\lambda$ by a factor of 2–4 is possible.

The total energy in the MIREB is another important parameter for various applications. IREB generators of power $> 5 \times 10^{10}$ W are available and beam duration of 250 ns is possible. The total energy in a single pulse is $> 12$ kJ. Above these value of power and energy IREB generators become too cumbersome to operate. IREB generators are typically one-shot devices. However, recent developments in the technology of spark-gap switches and magnetic switches make it possible to construct an IREB generator with a repetition rate of 1000 pulses/s.[24]

Although our discussion was centered on electron acceleration one can use the same technique to accelerate protons. The phase velocity of waves in the structure can be slowed down to $V_\phi \simeq 0.3c$ and even lower. The phase velocity can be easily changed by varying the geometry in order to match the velocity of the protons.

## V. SUMMARY AND CONCLUSIONS

In this paper, the interactions between intense relativistic electron beams ( $\sim 500$ keV, $> 5$ kA) and active rf structures were investigated. Experiments, theory, and numerical simulations have provided us with a view of the mechanisms involved in IREB modulation by an external rf source. We have identified linear and nonlinear mechanisms capable of coherently bunching IREBs with power levels in the gigawatt range and above.

Modulation of an IREB was found to differ from the conventional klystron mainly in the potential energy (dc space charge) residing with the IREB. In the cases studied the potential energy and the kinetic energy of the beam were of the same order of magnitude. The beam-gap interaction, the evolution of space-charge waves, and the resulting current modulation on the beam were significantly modified from the situation of the classical, tenuous electron beam (whose potential energy can usually be neglected). In general, the dc space charge of an IREB was shown to have a strong and favorable effect on current modulation. The space charge can also provide significant electrostatic insulation against breakdown at a modulating gap. We have discussed several potential applications which exploit these unusual properties of an intense beam.

In the small-signal regime, where the beam is subject to a weak velocity modulation throughout, we found complete agreement between experiments, particle simulation, and analytic theory. This comparison, together with the details of the experimental diagnostics and the transmission line model presented in Sec. II, is given here for the first time. These results strengthen our perception that an intense beam may serve as an amplifier when it is modulated by an external signal. While there might be considerable similarities with the conventional klystron, we note that, even at the small-signal level, there are two important features unique to an intense beam:

(a) A dc beam, upon exiting a modulating gap, carries an ac current which is partially in phase with the ac beam voltage. This is a consequence of the dc space charge of the beam. As a result, the dc energy of the beam is extracted and converted into ac kinetic energy which in turn is converted into electromagnetic energy, by power conservation (relativistic Tonk's theorem).

(b) Both the fast and slow space-charge waves are nondispersive, when the annular beam is close to the wall of the drift tube. The slow space-charge waves do not propagate as the dc beam current approaches the limiting value.

In the nonlinear regime, the experiments show that the beam may be fully modulated by a moderate rf source ( $\sim 50$ kW) if a second cavity (undriven, but properly tuned) is placed at an appropriate distance downstream of the first modulating gap (Figs. 12–14). The output rf current exhibited excellent amplitude and phase stability throughout the beam pulse. The harmonic content was measured and found to be in qualitative agreement with numerical simulation and analytical models. Harmonic content may also be manipulated by additional cavities.

The particle simulations confirm much of what was observed in the experiments, in particular we demonstrated phase locking even when the beam was fully modulated. In addition, the simulations showed that transients are unimportant and that particle reflections (virtual cathodes) are absent, again demonstrating that an intense beam may serve as a power amplifier in the highly nonlinear state. The phase space plots (Fig. 19) illustrate the strong nonlinear modulation of the beam at the modulating gap. This effect, where a drift region is not required for bunching to occur, is due to the dc space charge of the beam and is described in a qualitative manner in Secs. III B and Sec. III D 6.

The analytical models developed here include the formulation of nonlinear space-charge waves. The simple-looking Eq. (30) governs all of the complicated nonlinear processes such as nonlinear charge bunching, harmonic generation, dc and ac space-charge effects, and local transitions through the limiting current. The nonlinear propagation characteristics of the fast and slow space-charge waves were calculated. They imply an increase in the current modulation as a result of the substantial slowdown of the slow

space-charge wave in the decelerating portion of the modulation cycle. The predicted nonlinear limiting velocity, occurring when the propagation of the slow space-charge wave ceases, was observed in the simulations. The harmonic content was evaluated analytically. The beneficial effects of the dc space charge on the beam's current modulation are further illustrated in the simple analytic models in Secs. III D 5 and III D 6. The predicted threshold gap voltage for the onset of the strong nonlinear modulation was observed in the particle simulations.

From the experiments, and the supporting theories and simulations summarized above, we conclude the following:

(1) IREBs can be modulated by rf sources of low power with high efficiency.

(2) The modulated IREB current has a stable amplitude and is phase locked to the external rf source.

(3) The shape of the electron bunches can be tailored by changes in the geometry.

(4) The bunching mechanism for a fully modulated IREB is unique in its behavior and, using this mechanism, a long drift region is unnecessary for operation (unlike a classical klystron).

Experiments, theory, and numerical simulations showed that the self and induced electric fields generated by IREBs play important parts in the bunching mechanism. The numerical simulation showed that quasi-dc virtual cathodes need not be formed and that electrons are not reflected even at high levels of modulation. Transients and shock excitation of cavities are unimportant in the amplifier configuration studied in this paper.

Many applications for modulated IREBs by an external rf source can now be envisioned. Out of these applications, we mention here the two that are now being actively pursued at the Naval Research Laboratory: (a) Wakefield acceleration of particles by modulated IREBs and (b) ultrahigh power rf generation.

## ACKNOWLEDGMENTS

We are grateful to Scott Brandon and Adam Drobot for their assistance in applying CONDOR[12] to this problem. This work was supported by the Department of Energy Contract No. DE-AI05-86 ER 13585.

## APPENDIX A: DERIVATION OF THE TRANSFORMATION MATRIX [EQ. (8)]

From the continuity equation

$$\frac{\partial J}{\partial z}+\frac{\partial \rho}{\partial t}=0, \tag{A1}$$

where $J$ is the current density and $\rho$ is the charge density, one gets, after expanding the variables into the zero-order (subscript 0) and the first-order wavelike perturbations (subscript 1),

$$\frac{\partial J_1}{\partial z}+\frac{\partial \rho_1}{\partial t}=0, \quad J_1=\rho_0 v_1+v_0\rho_1. \tag{A2}$$

Assuming that the ac current consists of two components associated with slow and fast space-charge waves one obtains the ac current and ac velocity,

$$\tilde{I}_1=I_{f,s}\exp j(\omega t-k_{f,s}z), \tag{A3}$$

$$\tilde{v}_1=\frac{I_{f,s}}{I_0}\left(\frac{\omega-k_{f,s}v_0}{\omega}\right)v_0\exp j(\omega t-k_{f,s}z), \tag{A4}$$

and with the use of Eq. (5)

$$\begin{aligned}\tilde{I}_1&=I_1\exp j(\omega t-\theta)\\&=[I_f\exp j(\alpha\mu\theta)+I_s\exp -j(\alpha\mu\theta)]\\&\quad\times\exp j(\omega t-\theta),\end{aligned} \tag{A5}$$

$$\begin{aligned}\tilde{v}_1&=v_1\exp j(\omega t-\theta)\\&=(v_0/I_0)\{I_f[1-\delta(1-\alpha\mu)]\exp j(\alpha\mu\theta)\\&\quad+I_s[1-\delta(1+\alpha\mu)]\exp -j(\alpha\mu\theta)\}\\&\quad\times\exp j(\omega t-\theta),\end{aligned} \tag{A6}$$

where $\theta=(\omega\delta z)/(\beta_0 c)$. At time $t=0$ and position $z=0$, $I_1=I_{10}$ and $v_1=v_{10}$. Inserting values $I_f$ and $I_s$ into Eqs. (A5) and (A6) one obtains

$$\begin{aligned}I_1&=I_{10}[\cos(\alpha\mu\theta)-j\zeta\sin(\alpha\mu\theta)]\\&\quad+jv_{10}(I_0/\alpha\mu\delta v_0)\sin(\alpha\mu\theta),\end{aligned} \tag{A7}$$

$$\begin{aligned}v_1&=I_{10}[j(v_0/I_0)\delta\alpha\mu(\zeta^2-1)\sin(\alpha\mu\theta)]\\&\quad+v_{10}[\cos(\alpha\mu\theta)+j\zeta\sin(\alpha\mu\theta)],\end{aligned} \tag{A8}$$

where

$$\zeta=(1-\delta)/\alpha\mu\delta=-1/\beta_0^2\mu.$$

Note that $\zeta<0$.

Equation (A8) may be rewritten in terms of the "kinetic voltage" $V_1$. This quantity is derived as follows: The total energy of an electron is

$$E=m_0c^2(\gamma-1), \tag{A9}$$

hence the change in energy $\Delta E$ due to the change in the drift velocity $\Delta\beta_0$ (or vice versa) is

$$\Delta E=m_0c^2\frac{\partial\gamma}{\partial\gamma_0}\frac{\partial\gamma_0}{\partial\beta_0}\Delta\beta_0. \tag{A10}$$

At $z=0$, $\Delta E=v_{10}\exp j(\omega t)$, $\Delta\beta_0=(V_{10}/c)\exp j(\omega t)$. Using Eq. (2) and assuming $I_1\ll I_0$, one gets after some manipulation

$$eV_{10}=v_{10}v_0m_0\gamma_0^3/\delta \quad \text{at} \quad z=0. \tag{A11}$$

We similarly define the small-signal kinetic voltage at any point as

$$V_1=v_1v_0m_0\gamma_0^3/\delta e. \tag{A12}$$

Substituting Eq. (A12) into Eq. (A8) we get the transmission line analog for an IREB, Eqs. (7) and (8).

## APPENDIX B: DERIVATION OF EQS. (29)–(32)

We shall first derive Eq. (29) from Maxwell equations under the long-wavelength approximation.[7,8] We next show that the nonlinear system, Eqs. (27)–(29), is equivalent to Eqs. (30)–(32).

A surface charge $\sigma(z,t)$ on a thin annular beam excites electromagnetic fields with components $E_r(r,z,t)$, $E_z(r,z,t)$, $H_\theta(r,z,t)$. In the vacuum region between the sheet beam ($r=r_b$) and the outer conducting wall ($r=r_w$), these fields satisfy Faraday's law

$$-\frac{\partial H_\theta}{\partial t}=\frac{1}{\mu_0}\left(\frac{\partial E_r}{\partial z}-\frac{\partial E_z}{\partial r}\right), \tag{B1}$$

and the $r$ component of $\nabla\times\mathbf{H}=\epsilon_0\partial\mathbf{E}/\partial t$ gives

$$\frac{\partial H_\theta}{\partial z}=-\epsilon_0\frac{\partial E_r}{\partial t}. \tag{B2}$$

Operate (B1) by $\partial/\partial z$, (B2) by $\partial/\partial t$, add the resultants, and then integrate from $r=r_b$ to $r_w$ to yield

$$\left(\frac{1}{c^2}\frac{\partial}{\partial t^2}-\frac{\partial^2}{\partial z^2}\right)\int_{r_b}^{r_w}E_r(r,z,t)dr = -\frac{\partial}{\partial z}E_z(r_b,z,t), \tag{B3}$$

where we have used the boundary condition of a perfectly conducting pipe: $E_z(r_w,z,t)=0$. No approximation has been made to obtain (B3). We now introduce the long-wavelength approximation[7,8]:

$$E_r(r,z,t)\simeq(1/\epsilon_0)(r_b/r)\sigma(z,t). \tag{B4}$$

Equation (B3) then becomes

$$\left(\frac{1}{c^2}\frac{\partial^2}{\partial t^2}-\frac{\partial^2}{\partial z^2}\right)\frac{\sigma}{\epsilon_0}r_b\ln\left(\frac{r_w}{r_b}\right)=\frac{\partial}{\partial z}E_z(r_b,z,t), \tag{B5}$$

which is just Eq. (29) where we use $E_z(z,t)$ to denote $E_z(r_b,z,t)$, the axial electric field experienced by the beam. (The validity of the long-wavelength approximation may be justified in a number of circumstances, one of which is the beam being sufficiently close to the wall. A detailed examination of this long-wavelength approximation has been given in Ref. 8.)

To derive (30)–(32), we shall now assume that the beam in equilibrium is characterized by constant density $\sigma_0$, uniform drift speed $v_0$, and current $I_0$. Instead of using the Eulerian variables $(z,t)$, we introduce the "polarization variable"[25] $(z_0,\tau)$, which is related to $(z,t)$ by

$$z=z_0+z_1(z_0,\tau), \tag{B6}$$

$$t=\tau, \tag{B7}$$

where $z_0$ is the coordinates of an electron fluid element at time $t$ in the absence of perturbation and $z_1$ is its displacement from $z_0$ in the presence of perturbation. We do not assume $z_1$ to be small. Thus, $z$ is the instantaneous position of the fluid element at time $t$. The instantaneous velocity of this fluid element is, from (B6),

$$v=\frac{dz}{dt}=v_0+v_0\frac{\partial z_1(z_0,\tau)}{\partial z_0}+\frac{\partial z_1(z_0,\tau)}{\partial\tau} \tag{B8}$$

or

$$v\equiv v_0+v_1, \tag{B9}$$

where the perturbation velocity $v_1$ is

$$v_1=v_0\frac{\partial z_1(z_0,\tau)}{\partial z_0}+\frac{\partial z_1(z_0,\tau)}{\partial\tau}. \tag{B10}$$

Let us denote the displacement by $s$

$$z_1(z_0,\tau)\equiv s(z,t) \tag{B11}$$

in the Eulerian variable. Since $v$ is also the Eulerian velocity of the fluid element which, at time $t$, occupies position $z$, we have

$$v_1=\left(\frac{\partial}{\partial t}+v\frac{\partial}{\partial z}\right)s(z,t). \tag{B12}$$

Using (B9) in (B12), we have

$$v=v_0+\frac{\partial s/\partial t+v_0\partial s/\partial z}{1-\partial s/\partial z}, \tag{B13}$$

which is Eq. (32). Alternatively, we obtain, from (B6) and (B7),

$$\left(\frac{\partial}{\partial z_0}\right)_\tau=\left(1+\frac{\partial z_1}{\partial z_0}\right)\left(\frac{\partial}{\partial z}\right)_t, \tag{B14}$$

$$\left(\frac{\partial}{\partial\tau}\right)_{z_0}=\left(\frac{\partial}{\partial t}\right)_z+\left(\frac{\partial z_1}{\partial\tau}\right)\left(\frac{\partial}{\partial z}\right)_t. \tag{B15}$$

Apply $z_1$ to the left-hand sides and $s$ to the right-hand sides of (B14) and (B15) to yield

$$\frac{\partial z_1(z_0,\tau)}{\partial z_0}=\frac{\partial s(z,t)/\partial z}{1-\partial s(z,t)/\partial z}, \tag{B16}$$

$$\frac{\partial z_1(z_0,\tau)}{\partial\tau}=\frac{\partial s(z,t)/\partial t}{1-\partial s(z,t)/\partial z}. \tag{B17}$$

Substitution of (B16) and (B17) into (B8) gives (B13).

In the unperturbed state, the amount of charge between $z_0$ and $z_0+dz$ is $\sigma_0 dz_0$. In the presence of perturbation, the electron at $z_0$ moves to $z_0+z_1(z_0,\tau)$ and the electron at $z_0+dz_0$ moves to $(z_0+dz_0)+z_1(z_0+dz_0,\tau)$. Let $\sigma$ be the instantaneous charge density in the presence of perturbation. Conservation of charge requires

$$\sigma_0 dz_0=\sigma\{z_0+dz_0+z_1(z_0+dz_0,\tau)-[z_0+z_1(z_0,\tau)]\},$$

which gives, as $dz_0\to 0$,

$$\sigma=\frac{\sigma_0}{1+\partial z_1(z_0,\tau)/\partial z_0}=\sigma_0\left(1-\frac{\partial s}{\partial z}\right). \tag{B18}$$

In writing the last expression, we have used (B16). Substitution of (B18) in (29) gives

$$-\frac{\epsilon_0}{d}E_z=-\sigma_0\left(\frac{\partial^2}{\partial z^2}-\frac{1}{c^2}\frac{\partial^2}{\partial t^2}\right)s. \tag{B19}$$

Since

$$\left(\frac{\partial}{\partial t}+v\frac{\partial}{\partial z}\right)v=\left(\frac{\partial}{\partial t}+v\frac{\partial}{\partial z}\right)^2 s \tag{B20}$$

by (B9) and (B12), we substitute (B19) and (B20) into (27) to obtain

$$\left(\frac{\partial}{\partial t}+v\frac{\partial}{\partial z}\right)^2 s=\frac{\bar{\sigma}_0}{\gamma^3}\left(c^2\frac{\partial^2}{\partial z^2}-\frac{\partial^2}{\partial t^2}\right)s, \tag{B21}$$

which is (30), where the constant $\bar{\sigma}_0$ is defined.

Finally, the instantaneous current $I(z,t)$ is given by

$$I(z,t)=I_0(\sigma v/\sigma_0 v_0). \tag{B22}$$

Inserting (B13) and (B18) into (B22), we obtain

$$I(z,t)=I_0\left(1+\frac{1}{v_0}\frac{\partial s}{\partial t}\right), \tag{B23}$$

which is Eq. (31).

## APPENDIX C: NONLINEAR CHARACTERISTICS OF THE FAST AND SLOW SPACE-CHARGE WAVES

We calculate the nonlinear propagation characteristics of the fast and slow space-charge waves governed by Eq. (30), by a perturbation technique pioneered by Lin[15] and Fox.[16] We shall restrict to the evolution of nonlinear space-charge waves when the beam is subject to a weak velocity modulation at $z = 0$:

$$v_1(t) = (\epsilon v_0/2)\sin \omega t. \tag{C1}$$

The beam itself need not be weak, that is, $\bar{\sigma}_0$ need not be small.

In the linearized theory, the characteristics of the fast and slow waves are straight lines in the $(z,t)$ plane:

$$p = z - c_f t, \tag{C2}$$

$$q = z - c_s t, \tag{C3}$$

where $p$ and $q$ are the characteristics variables for the fast and slow waves, respectively, whose propagation speeds $c_{f,s} = \omega/k_{f,s}$ are constant and given by Eq. (5). In the small-signal theory, it is easy to show that the rf velocity $v_1$ may be expressed as

$$v_1 = -\frac{\epsilon}{2}\left(\frac{\omega_f}{\Delta k}\right)\sin k_f p + \frac{\epsilon}{2}\left(\frac{\omega_s}{\Delta k}\right)\sin k_s q, \tag{C4}$$

in terms of the characteristics variables $p$ and $q$. Here

$$\omega_f \equiv \omega - k_f v_0, \quad \omega_s = \omega - k_s v_0, \tag{C5}$$

$$\Delta k \equiv k_s - k_f. \tag{C6}$$

Because of the nonlinearity in Eq. (30), the characteristic curves are no longer straight lines. Instead of $p$ and $q$, we shall use $\xi$ and $\eta$ to denote the nonlinear characteristics associated with the fast and slow waves. If the initial velocity perturbation ($\epsilon$) is small, these nonlinear characteristics may be obtained by a perturbation method. In several cases, this technique has been proven to be uniformly valid.[15] To the lowest order in $\epsilon$, the characteristics Eqs. (C2) and (C3) are modified to read

$$z - c_f t = \xi + \epsilon G(\xi,\eta), \tag{C7}$$

$$z - c_s t = \eta + \epsilon H(\xi,\eta), \tag{C8}$$

where $G$ and $H$ are to be determined. Since Eq. (30) is quite complicated, based on physical argument, we expect the characteristics in the $(z,t)$ plane to be governed by

$$\frac{\partial t}{\partial \eta} = u_f \frac{\partial t}{\partial \eta} \quad (\xi = \text{const}), \tag{C9}$$

$$\frac{\partial z}{\partial \xi} = u_s \frac{\partial t}{\partial \xi} \quad (\eta = \text{const}), \tag{C10}$$

where the phase speeds $u_f$, $u_s$ are the solution to the local dispersion relation [cf. (30)].

$$(u_{s,f} - v)^2 = (\bar{\sigma}_0/\gamma^3)(c^2 - u_{s,f}^2). \tag{C11}$$

Note that $u_{s,f}$ depends on the amplitude of the perturbation. If $v = v_0 + v_1$ and if $v_1 \ll v_0$, we obtain from (C11), after some algebra,

$$u_s = c_s + \Delta u_s, \quad u_f = c_f + \Delta u_f \tag{C12}$$

where

$$\Delta u_{f,s} = R_{f,s} v_1, \tag{C13}$$

$$R_{f,s} \equiv \frac{(c_{f,s} - v_0)[2 - 3\gamma_0^2\beta_0(c_{f,s} - v_0)/c]}{2(c_{f,s} - v_0 + \alpha_0 c_{f,s})}, \tag{C14}$$

to first order in $v_1$. Here, $v_1$ is understood to be expressed in terms of the $\xi$ and $\eta$ variables. To proceed further, we need one crucial observation as $v_1$ itself is unknown at this point. In the theory of perturbation of characteristics, to the lowest order, the solution in terms of the characteristic variables remains to be the same as in the linearized theory, only the dependence of the characteristic variables on $(z,t)$ are modified by the nonlinearity. Thus, from Eq. (C4), we have the lowest-order solution

$$v_1 = \frac{-\epsilon}{2}\left(\frac{\omega_f}{\Delta k}\right)\sin k_f \xi + \frac{\epsilon}{2}\left(\frac{\omega_s}{\Delta k}\right)\sin k_s \eta, \tag{C15}$$

in terms of $\xi$ and $\eta$. This solution is to be inserted in (C13).

To determine $G$ and $H$, from (C7) and (C8), we obtain

$$t = (1/\Delta c)[\xi - \eta + \epsilon(G - H)], \tag{C16}$$

$$z = (1/\Delta c)[c_s\xi - c_f\eta + \epsilon(c_s G - c_f H)], \tag{C17}$$

where

$$\Delta c = c_s - c_f \equiv (\omega/k_s) - (\omega/k_f). \tag{C18}$$

Substituting (C12), (C16), and (C17) into (C9), we obtain, after some manipulation,

$$\epsilon\frac{\partial G(\xi,\eta)}{\partial \eta} = \frac{-\Delta u_f}{\Delta c} \quad (\xi = \text{const}) \tag{C19}$$

to first order in $\epsilon$. Similarly, (C10) gives

$$\epsilon\frac{\partial H(\xi,\eta)}{\partial \xi} = \frac{\Delta u_s}{\Delta c} \quad (\eta = \text{const}) \tag{C20}$$

to first order in $\epsilon$. Equations (C19) and (C20) are now easily integrated, since their right-hand sides are linear combinations of $\sin k_f\xi$ and $\sin k_s\eta$ by virtue of (C13) and (C15). This integration yields, upon using the boundary conditions for $z = 0$,

$$G(\xi,\eta) = \left(\frac{R_f}{\Delta c}\right)\left(\frac{1}{2\Delta k}\right)\left(\omega_f(\tilde{\eta} - c_s\xi/c_f)\sin k_f\xi + \frac{\omega_s}{k_s}(\cos k_s\eta - \cos k_f\xi)\right), \tag{C21}$$

$$H(\xi,\eta) = \left(\frac{R_s}{\Delta c}\right)\left(\frac{1}{2\Delta k}\right)\left(\frac{\omega_f}{k_f}(\cos k_f\xi - \cos k_s\eta) + \omega_s(\xi - c_f\eta/c_s)\sin k_s\eta\right). \tag{C22}$$

In (C21) and (C22), $R_f$ and $R_s$ are defined in (C14), $\Delta c$ by (C18), $\Delta k$ by (C6), $\omega_{f,s}$ by (C5), $k_{f,s}$ by Eq. (5), and $c_{f,s} = \omega/k_{f,s}$. Note that in the derivation given in this Appendix, we only assume that the velocity modulation $\epsilon$ is small. We did not assume $\bar{\sigma}_0$ to be small, however.

## APPENDIX D: DERIVATION OF EQS. (39) AND (40) AND A COMPARISON WITH THE CLASSICAL THEORY

When the collective force acting on an electron fluid element is assumed to be proportional to the displacement,

as in Eq. (38), the harmonic content may be analyzed rather accurately using the technique developed in the classical theory of electron bunching in a drift tube.[18,26] Even if such a theory is based on the assumption of small perturbation, we shall see that the analytical results thus obtained compare very well with particle simulation even when the modulating gap voltage is very large. Perhaps what is meant by such a close "agreement" is that the most important nonlinearity originates from charge overtaking and from charge conservation, which is treated accurately.

Let us recapitulate here the classical theory of nonlinear evolution of a nonrelativistic electron beam. In keeping with the literature, instead of using the Eulerian description for the displacement $s(z,t)$ and the polarization description $z_1$ $(z_0,\tau)$, we shall use the Lagrangian variable to describe the displacement $\chi(t,t_1)$:

$$\chi = s = z_1 = \chi(t,t_1). \tag{D1}$$

That is, $\chi(t,t_1)$ denotes the displacement, at time $t$, from the equilibrium position of an electron which arrives the modulating gap at an earlier time $t_1$. The gap is assumed to be located at $z=0$, upstream of which the beam propagates with a uniform speed $v_0$ and a current $I_0$. If the "debunching" force due to the ac space-charge effects is assumed to be proportional to $\chi$, the equation of motion reads

$$\frac{d^2\chi}{dt^2} = -\omega_p^2\chi, \tag{D2}$$

where $\omega_p$ is the (reduced) plasma frequency associated with the electron beam. For a short gap, the electron receives a velocity modulation

$$\dot{\chi} = (\epsilon v_0/2)\sin\omega t_1, \tag{D3}$$

which depends on the phase $\omega t_1$ of the gap voltage at the time of arrival. Here, $\epsilon$ is the "modulation depth." The solution to (D2) subject to (D3) is

$$\chi(t,t_1) = (\epsilon v_0/2\omega_p)\sin\omega t_1 \sin\omega_p(t-t_1), \tag{D4}$$

where we have used the initial condition $\chi = 0$ at $t = t_1$.

We are interested in the current at $z = L$. From the definition of $\chi$, the electron arrives at $z = L$ at time $t = T$, where $T$ and $L$ are related by

$$L = v_0(T-t_1) + (\epsilon v_0/2\omega_p)\sin\omega t_1 \sin\omega_p(T-t_1). \tag{D5}$$

We now introduce the small-signal assumption (small $\epsilon$) to express $T$ in terms of $t_1$:

$$T \simeq t_1 + \frac{L}{v_0} - \frac{\epsilon}{2\omega_p}\sin(\omega t_1)\sin\left(\frac{\omega_p L}{v_0}\right). \tag{D6}$$

The total current $I(L,T)$ at $z = L$ contains all harmonic frequencies and may be represented in a Fourier series as

$$I(L,T) = \sum_{n=-\infty}^{\infty}[a_n(L)\cos n\omega T + b_n(L)\sin n\omega T]. \tag{D7}$$

The Fourier coefficient is given by

$$a_n(L) = \frac{\omega}{2\pi}\int_{-\pi/\omega}^{\pi/\omega} dT\, I(L,T)\cos(n\omega T), \tag{D8}$$

and a similar expression for $b_n(L)$. Since the amount of charge passing through the gap at $z=0$ in time $dt_1$ is the same as that passing the point $Z = L$ in time $dT$, we have, by charge conservation,

$$I_0\, dt_1 = I(L,T)dT. \tag{D9}$$

With this change of variable, (D8) becomes

$$a_n(L) = \frac{\omega I_0}{2\pi}\int_{-\pi/\omega}^{\pi/\omega} dt_1 \cos[n\omega T(t_1)], \tag{D10}$$

where $T(t_1)$ is given by (D6). The integral in (D10) can be calculated explicitly:

$$a_n(L) = I_0 J_n\left[n\frac{\epsilon\omega}{2\omega_p}\sin\left(\frac{\omega_p L}{v_0}\right)\right]\cos\left(\frac{n\omega L}{v_0}\right), \tag{D11}$$

where $J_n$ is the Bessel function of order $n$. Use of (D11) and a similar expression for $b_n$ in (D7) gives

$$I(z,t) = I_0 + \sum_{n=1}^{\infty} I_n(z)\cos[n\omega(t - z/v_0)], \tag{D12}$$

where we have replaced $L$ by $z$ and $T$ by $t$, and

$$I_n(z) = [J_n(n\bar{V}\sin\bar{z})]2I_0, \tag{D13}$$

in which

$$\bar{V} = \tfrac{1}{2}(\epsilon\omega/\omega_p) \tag{D14}$$

$$\bar{z} = \omega_p z/v_0. \tag{D15}$$

In Eq. (D12), $I_n(z)$ is the axial distribution of the $n$th harmonic of the current modulation at distance $z$ downstream of a gap which provides a velocity modulation $(\epsilon v_0/2)\sin\omega t$ on the beam there. Its derivation has been based on two assumptions: Linear dependence of the force on the displacement $\chi$ [cf. (D2)] and weak modulation (low $\epsilon$) to permit the inversion from (D5) to (D6). To test the validity of (D12), we compare the axial distribution of the fundamental component $I_1(z)$ according to (D13) with that obtained from particle simulation.[26] This comparison is shown in Fig. 32 for various values of $\bar{V}$, whose values range from $\bar{V} = 1/(2\times 0.12) = 4.17$ to $\bar{V} = 1/(2\times 1.8) = 0.277$. Highly nonlinear current modulation is present within this range of $\bar{V}$. The close agreement between simulation and the analytical theory over such a wide range suggests that the nonlinearity associated with charge overtaking and charge conservation [cf. (D9)] are the decisive factors in determining the current modulation, and these factors are handled accurately [cf. (D9)] in the present analytical theory. Perhaps in the averaging process over a cycle which is involved in the evaluation of the $a_n(L)$ in (D10), the error committed in the approximate expression $T(t_1)$ [cf. (D6)] is considerably reduced, thereby leading to good agreement with simulation over a much wider range of $\bar{V}$ than can be expected from the outset.

Let us return to the problem of harmonic generation in an intense beam as discussed in Sec. III D 4. We see that Eq. (38) is *identical* to (D2) if we identify $\omega_p^2$ in (D2) by

$$(\bar{\sigma}_0/\gamma_0^3)\omega^2(-1+1/\beta_0^2),$$

whereas the velocity modulation parameter $\epsilon$ appearing in (D3) is the same as in (35) and (37). With such a substitution in (D12), we immediately obtain the solution (39) and (40). We thus see that Eq. (39) takes into full consideration of the nonlinearity associated with charge overtaking and

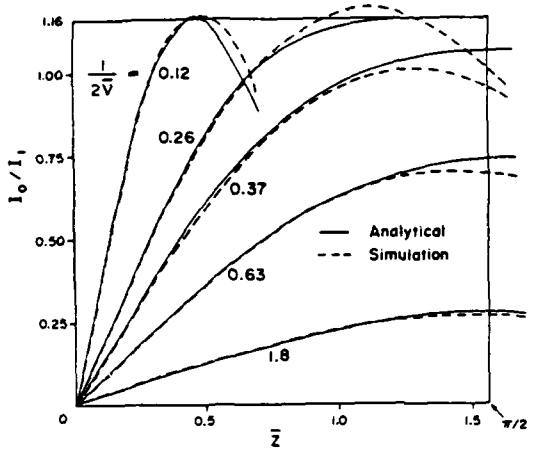



FIG. 32. Comparison of the analytic theory and particle simulation for the classical klystron model. Excellent agreement is found, ranging from the small-signal, space-charge-dominated regime ($1/2\bar{V} = \omega_p/\epsilon\omega = 1.8$) to the highly nonlinear, ballistic regime ($1/2\bar{V} = \omega_p/\epsilon\omega = 0.12$). A similar analytic theory is used to generate Fig. 24.

charge conservation and, as described above, these are the dominant nonlinear processes as long as the collective force is linear, as in Eq. (38). Therefore, whenever $\bar{\sigma}_0$ is small, it is highly likely that (38) gives a reliable account of the harmonic content. However, when $\bar{\sigma}_0$ is of order unity, the approximations leading to Eq. (38) may no longer be valid, and the harmonic content would need to be calculated from the original Eq. (30).


[1]P. B. Wilson, in *Physics of High Energy Accelerators*, edited by R. A. Carrigan, F. R. Huson, and M. Month, AIP Conference Proceedings No. 87 (American Institute of Physics, New York, 1982), pp. 450–563.
[2]M. Friedman, V. Serlin, A. Drobot, and L. Seftor, Phys. Rev. Lett. **50**, 1922 (1983); J. Appl. Phys. **56**, 2459 (1984).
[3]M. Friedman and V. Serlin, Phys. Rev. Lett. **55**, 2860 (1985).
[4]M. Friedman and V. Serlin, Rev. Sci. Instrum. **54**, 1764 (1983).
[5]M. Friedman and V. Serlin, Appl. Phys. Lett. **49**, 596 (1986).
[6]See, e.g., R. B. Miller, *An Introduction to the Physics of Intense Charge Particle Beams* (Plenum, New York, 1982), Chap. 3.
[7]R. J. Briggs, Phys. Fluids **19**, 1257 (1976).
[8]Y. Y. Lau, J. Appl. Phys. **62**, 351 (1987).
[9]S. Bloom and R. W. Peter, RCA Rev. **15**, 95 (1954).
[10]A. Bers and P. Penfield, IRE Trans. Electron Devices **ED-9**, 12 (1962).
[11]M. Friedman and M. Ury, Rev. Sci. Instrum. **41**, 1334 (1970).
[12]CONDOR is an extension of the MASK code developed by A. Palevsky and A. Drobot, in Proceedings of the 9th Conference on Numerical Simulation of Plasmas, Northwestern University, Evanston, IL, 1980 (unpublished).
[13]J. Krall and Y. Y. Lau, Appl. Phys. Lett. **52**, 431 (1988); J. Krall, M. Friedman, V. Serlin, and Y. Y. Lau, *12th IEEE International Conference on Infrared MM Waves* (Orlando, FL, Dec. 1987), IEEE Catalog No. 87CH2490-1, Conference Digest, p. 103.
[14]M. Friedman and V. Serlin, Phys. Rev. Lett. **54**, 2018 (1985).
[15]C. C. Lin, J. Math. Phys. **33**, 117 (1954).
[16]P. A. Fox, J. Math. Phys. **34**, 133 (1955). See also A. Neyfeh, *Perturbation Methods* (Wiley, New York, 1973), Chap. 3.
[17]Y. Y. Lau, J. Krall, M. Friedman, and V. Serlin, IEEE Trans. Plasma Sci. **PS-16**, 249 (1988).
[18]See, e.g., M. Chodorow and C. Susskind, *Fundamentals of Microwave Electronics* (McGraw-Hill, New York, 1964); J. W. Gewartowski and H. A. Watson, *Principles of Electron Tubes* (Van Nostrand, New York, 1965); Y. Y. Lau, Phys. Rev. Lett. **53**, 395 (1984).
[19]See, e.g., S. Humphries, *Principles of Charged Particle Acceleration* (Wiley, New York, 1986), pp. 478–482.
[20]W. D. Kilpatrick, University of California, Radiation Lab Report No. UCRL-2321 (1953).
[21]M. Friedman and V. Serlin, IEEE Trans. Electr. Insul. **EI-23**, 51 (1988).
[22]M. Friedman and V. Serlin, Rev. Sci. Instrum. **58**, 58 (1987).
[23]K. H. Halbach and R. F. Holsinger, Lawrence Berkeley Lab Report No. LBL-5040 (1976).
[24]D. L. Birx, E. J. Lauer, L. L. Reginato, D. Rogers, Jr., M. W. Smith, and T. Zimmerman, *Proceedings of the 3rd IEEE International Pulsed Power Conference*, Albuquerque, NM, June 1981, edited by T. H. Martin and A. H. Gunter (IEEE, New York, 1981), pp. 262–268, IEEE Cat. No. 81CH1662-6.
[25]D. L. Bobroff, IRE Trans. Electron Devices **ED-6**, 68 (1959).
[26]See, e.g., Fig. 9.3-5 on p. 335 of J. W. Gewartowski and H. A. Watson, *Principles of Electron Tubes* (Van Nostrand, New York, 1965).

# APPENDIX O

## Relativistic Klystron Amplifier

Reprinted from SPIE Vol 873—Microwave and Particle Beam Sources and Propagation
© 1988 by the Society of Photo-Optical Instrumentation Engineers, Box 10, Bellingham, WA 98227-0010 USA

# Relativistic klystron amplifier

M. Friedman, J. Krall,* Y. Y. Lau and V. Serlin

Plasma Physics Division
Naval Research Laboratory, Washington, DC 20375-5000

*Science Application, Inc., McLean, VA 22102

## ABSTRACT

The physics of modulation of an intense relativistic electron beam by an external microwave source and its usefulness for klystron-like devices are studied in this paper via experiment, theory, and simulation. It is found that the self fields of the electron beam, in general, intensify the current modulation produced by the external source. In the modulating gap, electron bunches may be generated instantaneously without the necessity of propagating the beam through a long drift tube. The excellent amplitude stability and the phase locking characteristics ($<2°$) of the modulated current, demonstrated in experiments, open new areas of research in high power microwave generation.

## 1. INTRODUCTION

In the last two decades there has been considerable interest in generating pulses of high power rf radiation. This interest has risen, in part, from the availability of intense relativistic electron beams (IREBs) with power $10^9 - 10^{12}$ Watts and, in part, from demands for high power rf sources. There are many different mechanisms for generating rf power; one of these is based on longitudinal bunching of electrons.

RF radiation can be extracted from electron bunches with an intensity

$$I = G\, N_b\, n_b^2 \tag{1}$$

where $N_b$ is the number of bunches/unit time, $n_b$ is the number of electrons in a bunch, and $G$ is a form factor which strongly depends on the micro-shape of the bunches and is large for bunches with sizes $< \lambda/2$, where $\lambda$ is the wavelength of the extracted rf radiation. Equation (1) reflects the requirement of having a large $n_b$ in order to produce high rf power. A necessary condition to achieve a large $n_b$ is to employ high current electron beams (e.g. IREBs).

This paper addresses the development of rf amplifiers based on IREB modulation by an external rf source.[1] Unlike in the previous work,[2] self excited oscillations and transient behavior are unimportant here.

## 2. SPACE CHARGE WAVES ON INTENSE RELATIVISTIC ELECTRON BEAMS—SMALL SIGNAL REGIME

### 2.1 Theory

The bunching mechanism occurs while the IREBs propagate through drift regions, and is strongly influenced by the electric and magnetic fields of the electron beam. At a high current level, the electric self field of the IREB generates a potential hill through which the electrons are moving. The energy of an individual electron is split between kinetic and potential energies. From the conservation of energy, the following relationship is obtained

$$\gamma_{inj} = \gamma_o + \alpha\gamma_o^3 \tag{2}$$

where $\alpha = I_o/(I_s\gamma_o^3\beta_o)$, $I_s = 2\pi\epsilon_o m_o c^3/(e \ln r_w/r_b)$, $I_o$ is the IREB current, $m_o c^2(\gamma_o - 1)$ is the electron kinetic energy, $\gamma_o = (1 - \beta_0^2)^{-1/2}$, $\beta_o = v_o/c$, $v_o$ is the electron drift velocity, $m_o c^2(\gamma_{inj} - 1) = e V_0$ is the electron total energy at injection and $r_w$ and $r_b$ are the respective radii of the drift tube (assumed round) and of the IREB (assumed to be annular in shape). From Eq. (2) it is obvious that by increasing the IREB current, the kinetic energy of the electrons will be reduced. At a current level $I_c$, where

$$I_c = \frac{8.5(\gamma_{inj}^{2/3} - 1)^{3/2}}{\ln(r_w/r_b)}\, kA = I_s\,(\gamma_{inj}^{2/3} - 1)^{3/2} \tag{3}$$

the electrons cannot lose anymore kinetic energy and beam propagation is disrupted.[3] At this current level, the kinetic energy of the electrons is $m_o c^2\,(\gamma_{inj}^{1/3} - 1)$ and the potential energy is $\phi = m_o c^2\,(\gamma_{inj} - \gamma_{inj}^{1/3})/e$.

The classical dispersion relation for space charge waves on low density electron beams is invalid for IREBs. Briggs derived[4] a dispersion relation for space charge waves on IREBs under a long wavelength assumption $\lambda >> 2r_w$.[5]

$$(\omega - kv_0)^2 = \alpha\,(k^2c^2 - \omega^2) \tag{4}$$

Solving Eq. (4), one gets

$$\omega = \frac{k_{f,s} v_o}{1+\alpha}(1 \pm \alpha\mu) = \frac{k_{f,s} v_o}{\delta} \frac{1}{1 \mp \alpha\mu} \tag{5}$$

where $\alpha\mu = (\alpha^2 + \alpha/\gamma_o^2)^{1/2}/\beta_o$, $\delta = \beta_o^2/(\beta_o^2 - \alpha)$, the subscripts $f$ and $s$ stand for fast and slow (waves). Unlike in classical electron beams, the dispersion relation curves for the fast and slow waves are not symmetric with respect to the beam line $\omega/(kv_0) = 1$. This symmetry makes the bunching mechanism for IREBs unique and novel.

Bloom and Peter[6] described a useful analogue between a classical (tenuous, nonrelativistic) electron beam and a transmission line. This analogue can be extended here to include IREBs. It expresses the rf currents and voltages on the beam in terms of the values upstream ($z = 0$).

$$I_1 = I_{10}\{\cos(\alpha\mu\theta) + j\zeta \sin(\alpha\mu\theta)\} - j\,(V_{10}/Z)\sin(\alpha\mu\theta)$$

$$V_1 = -j\,I_{10}\,Z(1-\zeta^2)\sin(\alpha\mu\theta) + V_{10}\{\cos(\alpha\mu\theta) - j\zeta\sin(\alpha\mu\theta)\} \tag{6}$$

Here, $\theta = (\omega\delta z)/\beta_o c$, $Z = m_o c^2 \gamma_o^3 \beta_o^2 \alpha\mu\delta/(el_o) = R_o/(-\zeta)$, $\zeta = (1-\delta)/\alpha\mu\delta = -1/\beta_o^2\mu$, $R_o = (60\Omega/\beta_o)\ln(r_w/r_b)$, and $V_{10}$, $I_{10}$ are the excitation voltage and modulating current at $z = 0$.

With the boundary conditions $I_1 = 0$ and $V_1 = V_{10}\exp j(\omega t)$ imposed at the modulating gap $z = 0$, one obtains from Eq. (6) the following rf quantities at $z = z_1$

$$I_1 = -j\frac{V_{10}}{Z}\sin(\alpha\mu\theta_1); \quad \theta_1 = \frac{\omega\delta z_1}{\beta_o c}, \quad V_1 = V_{10}(\cos(\alpha\mu\theta_1) - j\zeta\sin(\alpha\mu\theta_1)) \tag{7}$$

Unlike in the interaction of a low density (classical) electron beam with a gap, $I_1$ and $V_1$ are partially in phase.[1,7]

## 2.2 Experimental investigation of IREB modulation in the small signal regime

The experimental arrangement shown in Fig. (1) consisted of a foilless diode[8] emitting an annular IREB of radius $r_b = 1.9$ cm and thickness $= 0.3$ cm. A 10-kG quasi-DC magnetic field confined the IREB inside a metal tube of radius $r_w = 2.35$ cm. A gap feeding a coaxial cavity was inserted in the drift tube. The characteristic impedance of the cavity was 45Ω and its length was $L = 17$ cm corresponding to a resonance frequency of 410 MHz. Four thin Nichrome wires connected the inner wall of the coaxial cavity to its outer wall so as to reduce the $Q$ of the cavity at 410 MHz. The wires did not influence the $Q$ of the cavity at the 1328-MHz resonance ($Q > 1000$). The presence of the wires shifted the first resonance from 410 to 610 MHz and reduced the $Q$ to below 30. An external rf source (a magnetron) "pumped" microwave energy into the cavity for a duration of 3 μsec at a frequency $f = 1328$ MHz. Sometime during the 3 μsec period a Blumlein transmission line with an output of 500 kV energized the foilless diode for 120 nsec, and a ~5 kA electron beam was launched through the drift region. The base pressure in the drift region was $\leq 10^{-5}$ Torr.

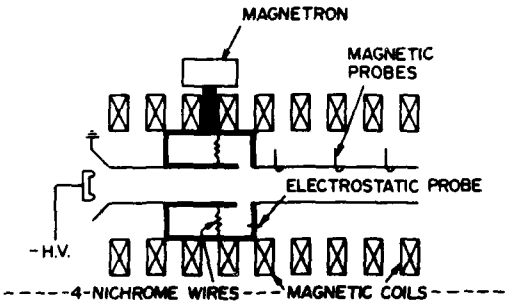



Fig. 1. Experimental arrangement when only one cavity was used.

For many applications the purity of the rf spectrum and phase locking are necessary requirements. The arrangement that was used to measure the phase locking capabilities[1] and the purity of spectrum of the modulated IREB, is shown elsewhere.[7] We found that the magnetron output and the modulated IREB were phase locked to better than 3°, and that the frequency of the modulated IREB is the same as the frequency of the rf from the magnetron.

Four magnetic probes spaced 15 cm apart, the first of which was located 12 cm from the gap of the cavity, were used to analyze the electron beam that emerged from the cavity. Best fits to the results are in the form

for $V_o = 500$ keV $\quad 2I_1 = 450 \mid \sin(0.0523z(cm)) \mid$ Amps, $\quad$ for $V_o = 400$ keV $\quad 2I_1 = 425 \mid \sin(0.0671z(cm)) \mid$ Amps

The experimental result is favorably compared with the theoretical prediction (Eq. (7))

$$2\,|I_1| = 2\frac{V_{10}}{Z}\left|\sin\left(\alpha_\mu \frac{\omega\delta}{\beta_o c}\, z\right)\right| . \tag{8}$$

Since the rf amplitude $V_{10}$ was kept constant the following conclusions were drawn

(i) $Z$ is insensitive to the IREB electron energy $eV_o$ and (ii) $\alpha_\mu\omega\delta/\beta_o c$ depends on the IREB electron energy $eV_o$.

The amplitude of $I_1$ depends linearly on $V_{10}$. We recorded $I_1$ as a function of the input rf power $P$. Since $P \propto V_{10}^2$ we get from Eq. (8)

$$I_1^2 = KP \quad \text{or} \quad \log(I_1^2) = \log P + \log K \tag{9}$$

where $K$ is a constant that does not depend on $V_{o1}$ and $I_1$. Figure 2 displays experimental results of $\log(I_1^2)$ vs $\log(P)$. The slope of the best fit straight line is unity in accordance with Eq. (9).

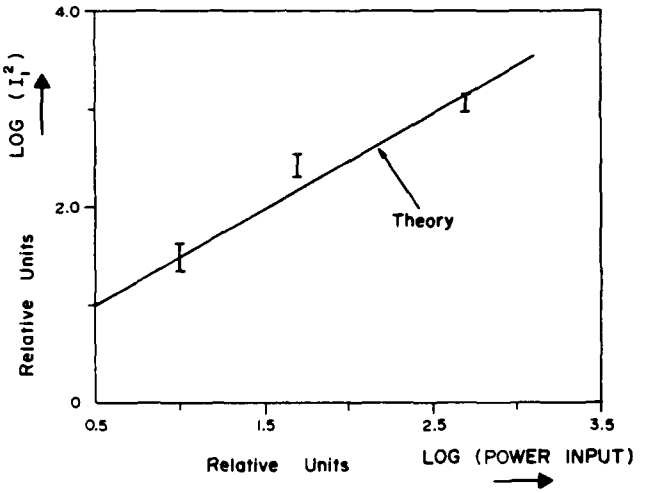



Fig. 2. Dependence of the IREB rf current on the input rf power.

## 2.3 Particle simulation

The physics of fully modulated IREBs is highly non-linear and the theory is not yet completely developed. Theoretical models will have to be used to explain the non-linear processes involved. Some of these models are not self-consistent and in order to check their validity, we rely on numerical simulations. The computer simulation code, CONDOR[9] was extensively used in this research.[10] The calculations summarized in this section deal with a relatively low rf current ($I_1 << I_o$). The geometry of the simulation is shown in Fig. 3 (top).

The simulations presented here proceeded as follows: At $t = 0$ ns, the rf drive was turned on. The $Q$ of the cavity was chosen in such a way that the saturation of the fundamental TEM mode was reached at $t = 6$ ns. At this time, the IREB was injected with a current risetime of 5 ns. The simulation continued until $t = 20$ ns.

The initial IREB conditions were as follows, current of 5 kA, energy of 500 keV, and the geometry of the IREB was annular, with a radius of 1.9 cm. This IREB was injected through the drift tube into which a coaxial cavity has been inserted. This cavity was loaded with rf energy via a radial transmission line at the outer wall of the cavity. The impedance of the radial transmission line was 15Ω. Rf-gap voltages, $V_{10}$, of 6, 18, and 30 kV, always at a frequency of 1.37 GHz were used. The gap voltage introduced nonuniformities in the electron velocity distribution which were translated, after propagation, into density modulation. The amplitude of the rf current versus propagation distance showed excellent agreement with linear theory [Fig. 4] and with the experimental results.

As in conventional klystrons, the amplitude of the rf current varied sinusoidally. The axial position, $z_m = 28$ cm, where maximum modulation occurred agreed very well with the linear theory, [c.f. Eq. (8)]. Changing $V_{10}$ did not change $z_m$; only $I_1$ varied. For example, for $V_{10} = 6$ kV, 18 kV and 30 kV the peak currents in the electron bunches were $2I_1 = 270$ Amps, 800 Amps, and 1400 Amps, respectively. These results confirmed that $I_1$ was proportional to $V_{10}$, in agreement with Eq. (7). However, when $V_{10}$ exceeded a critical value, deviations from Eq. (7) were seen. This non-linear aspects of the simulation will be discussed later.

To check the phase locking capability, the phase of the rf signal was varied. We found that the phases of the electron bunches changed in accordance with the input rf, with an uncertainty error of $2° \pm 1°$, in agreement with experiments.

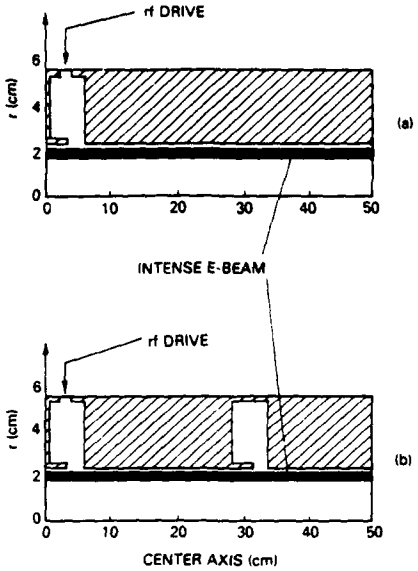



Fig. 3. (a) Top, geometry of the computer simulation when only one cavity was used. (b) Bottom, geometry of the computer simulation when two cavities were used.

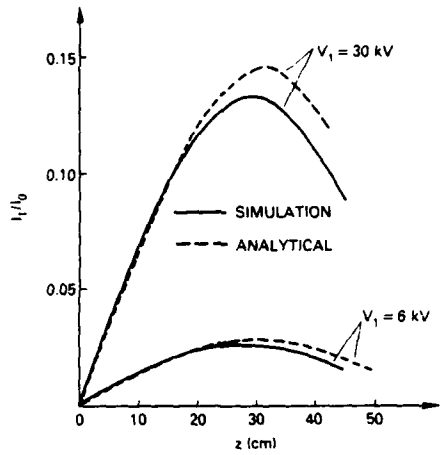



Fig. 4. Fraction of the modulated current for Fig. 3a, at two levels of the rf drive.

## 3. FULLY MODULATED INTENSE RELATIVISTIC ELECTRON BEAMS

### 3.1 Experiment

It is well known that non-linear effects in rf devices become important when the rf current $I_1$ is of the order of the DC current $I_o$. Pretending that Eq. (7) is valid even for cases for which $I_1$ is of the order of $I_o$, one can estimate the rf voltage that has to be imposed on the gap so as to fully modulate a 5 kA IREB. For the present experimental set-up this voltage is of the order of 100 kV corresponding to 20 MW of injected rf power. Since an rf source with this kind of power was not available, we used, instead, the partially modulated IREB to energize a second coaxial cavity [Fig. 5] and to generate a high oscillating voltage ($\sim$150 kV) on its gap. The gap of the second cavity was inserted in the drift tube at an axial position for which $I_1$ was maximum (29 cm). The second cavity with a $Q > 2000$ was tuned to the frequency $f = 1.328$ GHz $\pm$ 1 MHz. The IREB that emerged from the second cavity was highly modulated. The peak current in the bunches was $\sim$80% of the DC current [Fig. 6].

In a different experiment the second cavity was replaced by a variable length cavity. With this cavity, the resonance frequency could be varied between 800 MHz and 2.9 GHz. The cavity $Q$ was $\leq$400 (at a frequency of 1.3 GHz). Because of the low $Q$, the input impedance of the gap was complex, i.e., $Z_i = R_i + jX$, even at frequencies close to the resonance frequency. It was found that by raising the magnetron rf power, no disruption of the IREB current was observed. Moreover, the rf current amplitude of the IREB increased by a factor of $\sim$1.6 to $2I_1 = 7$ kA. Figure 7 shows the experimental setup. It also shows the variation of $2I_1$ as a function of the resonance frequency of the second cavity and of the position where the measurements were taken.

### 3.2 Computer simulation—non-linear results

The non-linear processes that take part in the generation of fully modulated IREBs can be found from computer simulations in which the rf current is comparable to the DC current. Similar to the experimental arrangement of Fig. 5, the simulation geometry was arranged by placing an undriven second cavity into the drift tube at an axial position where the rf current reached maximum (Fig. 3, bottom). This cavity was excited by the fundamental frequency component of the partially modulated IREB current. The voltage that appeared on the second gap depended on $V_{1o}$ and was typically of the order of the voltage applied on the IREB diode, $V_o$. For example, for $V_{1o} = 30$ kV, the voltage at the second gap $V_{2o} = 330$ kV. The current modulation of the IREB after passing the second gap is shown in Fig. 8. The percentage of IREB modulation was calculated assuming a current profile of $I = I_o + I_1 \cos(\omega t)$. This was done so as to compare simulation results with experimental results. We found that $I_1/I_o = 13.3\%$ before the IREB entered the second cavity and $I_1/I_o = 58\%$ 6 cm downstream of the second gap. Other macroscopic results such as phase locking features ($<2°$) and the variation of $I_1/I_o$ vs the axial position were obtained. All these results agreed with experimental observations.

Phase space plots ($\beta\gamma c$ vs z) of the electrons revealed important information. These plots were obtained for different times, from time $t = 0$ nsec to $t = 18$ nsec at regular intervals. We found that the bunching mechanism reached equilibrium almost instantaneously. The phase space plots are nearly identical from cycle to cycle, implying transients are unimportant. Figure 9 shows a sequence of phase space pictures and the corresponding electrostatic field contours, all obtained during one rf cycle.

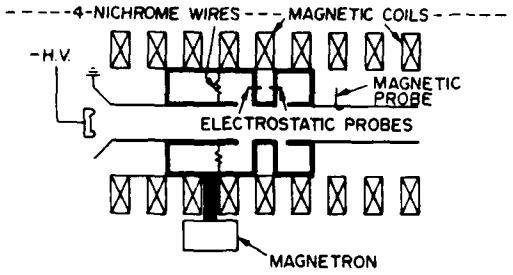



Fig. 5. Experimental arrangement when two cavities were used.

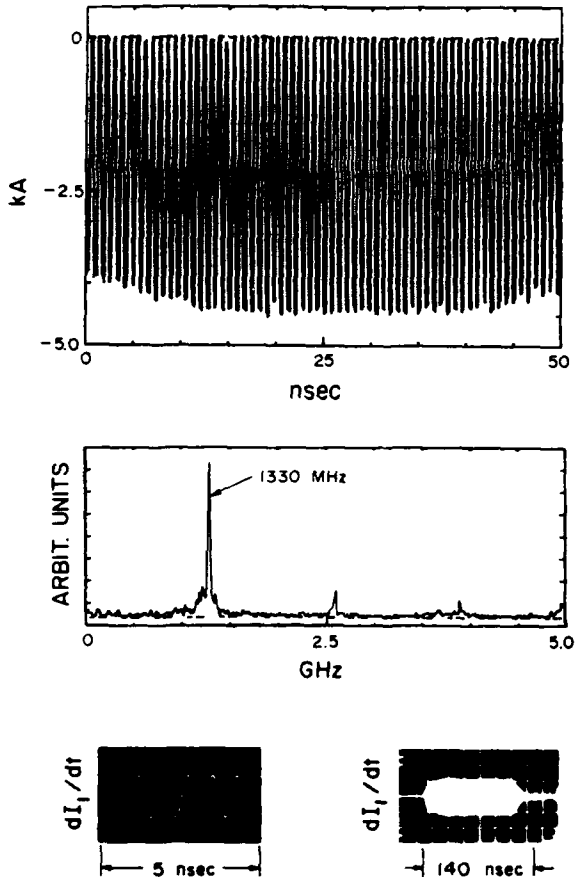



Fig. 6. Experimental results when the configuration of Fig. 5 was used. Top: rf current of the modulated IREB. Middle: Spectrum of $dI/dt$. Bottom: $dI/dt$ traces obtained from a 1 GHz Tektronix oscilloscope 7104.

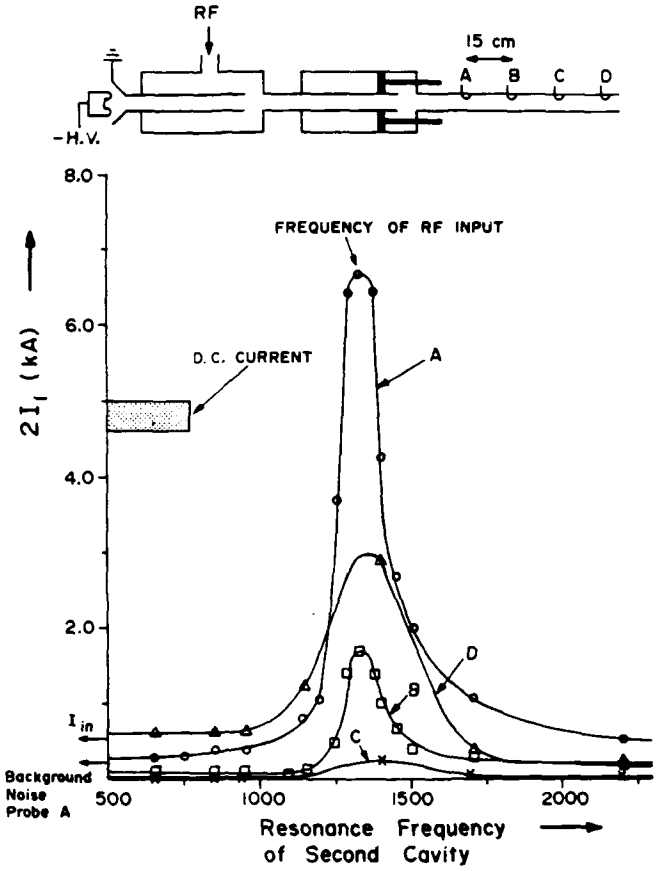



Fig. 7. (a) Top: Experimental arrangement. (b) Bottom: Peak bunch current as measured by the four magnetic probes. The shaded area represents the DC current. The arrow marked $I_{in}$ is the level of the peak bunch current measured between the cavities. The arrow at the lower left corner shows the level of the background noise.

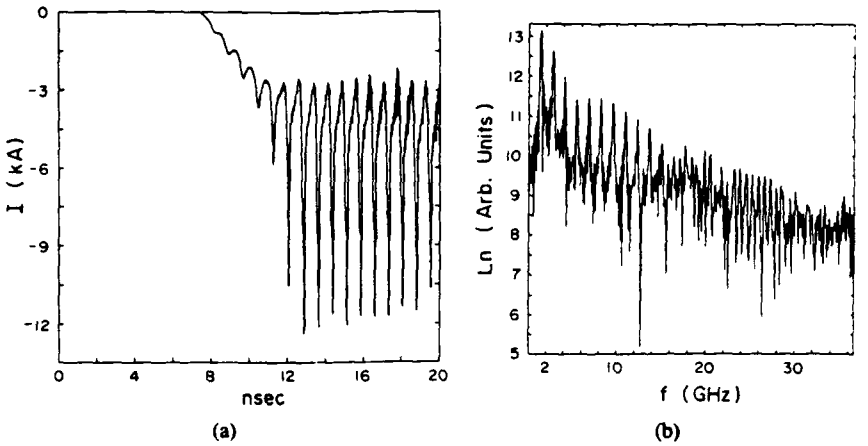



Fig. 8. Simulation result for the geometry in Fig. 3b, showing (a) the current at 6 cm downstream of the second gap (left), and (b) the Fourier power spectrum of this modulated current (right).

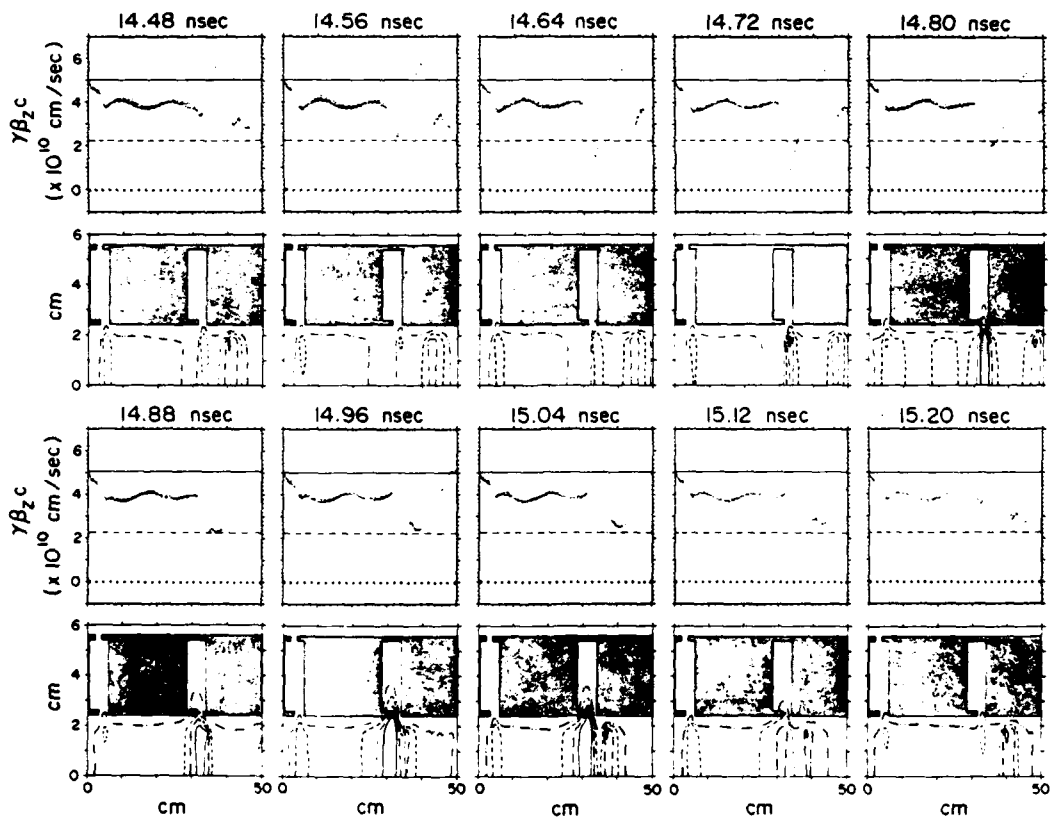



Fig. 9. Phase space plots and electrostatic potential contours for the two cavity case. The interval between plots is 0.08 nsec. In the phase space plots, solid lines show $\gamma\beta_z c$ at injection, broken lines show $\gamma\beta_z c$ at condition of DC limiting current ($\gamma = \gamma_{inj}^{1/3}$), and dotted lines show $\gamma\beta_z c = 0$. For the electrostatic potential contours: ..... 0.21 MeV, _____ 0.18 Mev, -.-.-.-.-. 0.15 MeV, - - - - - 0.10 MeV, -.-.-.-.- 0.05 MeV

Figure 9 gives the following results:

(1) No reflecting electrons ($\beta\gamma < 0$) exist.

(2) During part of any rf cycle, $\beta\gamma c$ of the electrons drops below the value associated with critical current. This in turn reduces the propagating current, but no reflection of electrons occurs.

(3) Half an rf cycle later $\beta\gamma$ of the electrons near the second gap increases above the injected $\beta\gamma$.

(4) Two distinct particle populations emerge from the second gap. The bulk of electrons has high kinetic energy while the second population consists of slow electrons with energy below 50 keV.

(5) One can see electron bunches generated at the second gap and moving from left to right on the electrostatic field contour figures. The contours are indicative of the electron density.

The first result points out that the bunching mechanism is different from the one discussed for the self-modulation of IREBs.[2]

The second and the third results confirm the qualitative quasi-DC theory given elsewhere.[1,7] The fourth result is in excellent agreement with non-linear theory and will be discussed at the non-linear theory section. It follows from the behavior of the nonlinear space charge waves near and below the critical current. The last result shows that electron bunches are created near the second gap at a time when $\beta\gamma$ is minimum.

As was indicated earlier once the rf excitation voltage $V_{10}$ exceeded a threshold voltage, $V_t$, the rf current $I_1$ was no longer proportional to $V_{10}$. We investigated the IREB modulation by a single cavity when $V_{10}$ exceeded $V_t$ (Fig. 10). We found that the high voltage gap behaves in a way analogous to a gate. When the gate is closed instantaneously current stops flowing and potential energy is increased. For a finite time charge accumulates at the gate without reflection. If after this time (and before reflection occurs) the gate reopens, current flow resumes and the potential energy is converted into kinetic energy.

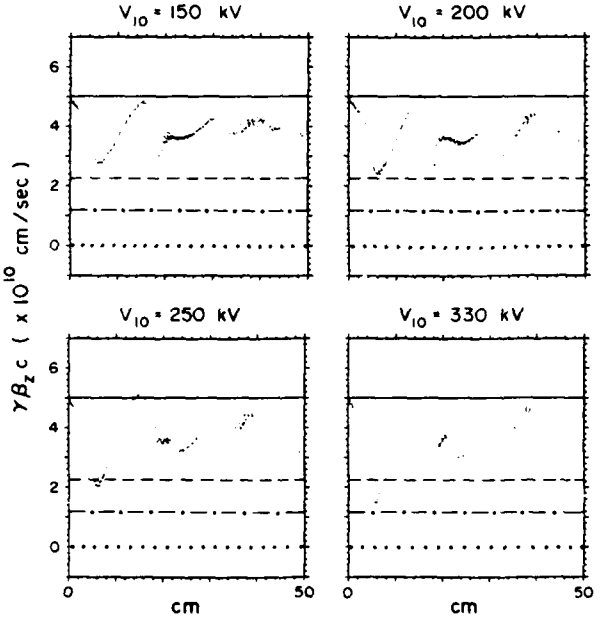



Fig. 10. Phase space plots of the electrons at high values of the modulating voltages, using a single cavity. The gap is located at 5 cm from left. Solid line: $\gamma\beta_z c$ at injection. Broken line: $\gamma\beta_z c$ at DC limiting current ($\gamma = \gamma_{inj}^{1/3}$). Dash-dot line: $\gamma\beta_z c$ at the limiting velocity according to the nonlinear theory [cf. Eq. (12)]. Dotted line: $\gamma\beta_z c = 0$.

In the simulation (or experiment) the rf voltage opens and closes the "gate." From the simulation we found that this threshold voltage was $V_t = 200$ kV. It should be noted that once $V_1 \geq V_t$ the second population of slow electrons appeared in phase space with $\beta\gamma c \leq 1.2 \times 10^{10}$ cm/sec (see Figs. 9, 10). This result corresponds to $\beta \leq \beta_{Nm}$ where $\beta_{Nm}$ is the non-linear limiting velocity (to be discussed below in the Non-Linear Theory section, where the threshold voltage is also estimated). $\beta_{Nm}$ is independent of $V_{10}$.

Since the length of the geometry in the computer simulation was limited, the only way to see the evolution of the IREB bunching vs distance was to use a single cavity geometry in which $V_{10} = 330$ kV [Fig. 10]. In this case we found that $I_1/I_o$ saturated at 92% at $z = 26$ cm from the gap. Only at $z = 46$ cm did the electron bunch start to decay, dropping to $I_1/I_o = 79\%$.

## 3.3. Non-linear theory

3.3.1. Introduction To gain insight with the least amount of complication, we shall treat the drift region and the gap region separately. The non-linear evolution of space charge waves is formulated self-consistently in terms of a single partial differential equation. This equation takes full account of charge overtaking, DC space charge effects, harmonic generation, and even governs the electron motion through the regime when the instantaneous beam current exceeds the limiting value. The small signal limit is easily recognized. We show the modification of the propagation characteristics of the space charge waves as a result of non-linearity (in addition to the DC space charge effect). We estimate the local electron speed ($\beta_{Nm}c$) which may be expected as the limiting current is reached via non-linear interaction. In that case, the (non-linear) slow space charge ceases to propagate. We shall also show via a simple model that when the rf drive at the gap is sufficiently strong, a substantial amount of current modulation may result even at the exit of the gap, in contrast to the classical klystron theory.

3.3.2. Formulation of non-linear space charge waves In keeping with the small signal theory we shall assume (1) that the annular electron beam is infinitesimally thin, (2) that the axial magnetic field is so strong that only axial motion is considered, and (3) that the beam is sufficiently close to the drift tube to permit the use of a long wavelength approximation[4,5] on the Maxwell equations.

Under the above assumptions, the non-linear evolution of the displacement $s(z,t)$ is governed by[12,7]

$$\left(\frac{\partial}{\partial t} + v\,\frac{\partial}{\partial z}\right)^2 s(z,t) = \frac{\bar{\sigma}_o}{\gamma^3}\left(c^2\,\frac{\partial^2}{\partial z^2} - \frac{\partial^2}{\partial t^2}\right) s(z,t). \tag{10}$$

Here, $\gamma = (1 - v^2/c^2)^{-1/2}$, $\bar{\sigma}_o = I_o/I_s\beta_o$ is a constant determined from the equilibrium state, and $s$ is the non-linear displacement from the unperturbed position of a fluid element whose instantaneous position is $z$ at time $t$. In terms of $s$, the instantaneous current is $I(z,t) = I_o + (I_o/v_o)\partial s/\partial t$ and the instantaneous velocity is

$$v(z,t) = v_o + \frac{1}{1 - \partial s/\partial z}\left[\frac{\partial s}{\partial t} + v_o\,\frac{\partial s}{\partial z}\right] \tag{11}$$

It is interesting to note that, in the governing Eq. (10), all of the complicated non-linear processes such as charge overtaking, DC and AC space charge effects, local transition through the limiting current, etc., are all incorporated in the $v$ term (and through $v$ in the $\gamma^3$ term) of Eq. (10) in a rather simple manner. In other words, the way Eq. (10) is written, the beam density parameter $\bar{\sigma}_o$ remains unaffected by non-linearity. This is not a trivial result that can be expected from the outset. The linear dispersion relation (4) may be readily recovered from Eq. (10) if we approximate $v$ by $v_o$ and $\gamma$ by $\gamma_o$ in that equation.

3.3.3. Propagation characteristics and the nonlinear limiting velocity Given some initial data on $s$ and $\partial s/\partial t$, Eq. (10) may be solved, in principle, for the evolution of $s$ (and hence $I$) for subsequent times. The propagation characteristics of fast and slow waves are modified by non-linearity. When the initial perturbation is small, the non-linearity may be handled analytically by a perturbation technique.[11] The details are given in Refs. (7), (12). Some of the characteristics are shown in Fig. 11. We see here that the fast wave characteristics remain unchanged whereas crossing of the slow wave characteristics occur only half a wavelength downstream from the modulating gap, implying a stronger current modulation as a result of non-linearity.

The simplicity in the structure of Eq. (10) provides a qualitative estimate of the local electron speed when the current perturbation is so strong that that non-linear slow space charge wave ceases to propagate. Call this non-linear limited speed $v_{Nm}$ and $\beta_{Nm} \equiv v_{Nm}/c$. Since (10) has the same structure as the corresponding equation in the linear theory, its local dispersion relationship is also similar. Thus, $v_{Nm}$ is determined from

$$\beta_{Nm}^2\gamma_{Nm}^3 = \bar{\sigma}_o \tag{12}$$

where $\gamma_{Nm} \equiv (1 - \beta_{Nm}^2)^{-1/2}$. The solution of $\beta_{Nm}$ as a function of $\bar{\sigma}_o$ is shown in Fig. 12. Note that the limiting speed $v_{Nm}$ does not depend on how the large amplitude perturbation is set up. It is based only on a local theory of an exact formulation of the non-linear processes. The estimate according to (12) is in close agreement with the simulations [Fig. 10].

3.3.4. Current modulation at the gap exit When an intense beam passes a modulating gap, it experiences a rather strong retarding DC potential associated with the space charge. It is possible that, for a sufficiently strong rf gap voltage, there is a portion of the rf cycle during which the rf voltage together with the DC self voltage of the beam would reduce the propagating speed below the critical speed. This would then lead to an effect similar to a periodic "gate" for the beam current. As a result, (contrary to the classical klystron theory), substantial current modulation may arise once the beam exits the modulating gap.

Let the gap be short and the rf voltage across it be $V_1 \sin \omega t$. The instantaneous speed $v$, and the corresponding values of $\beta$ and $\gamma$ of an electron are approximately given by

$$\gamma_{inj} = \gamma + \frac{I_o}{I_s\beta} + \frac{|e|V_1 \sin \omega t}{m_o c^2}. \tag{13}$$

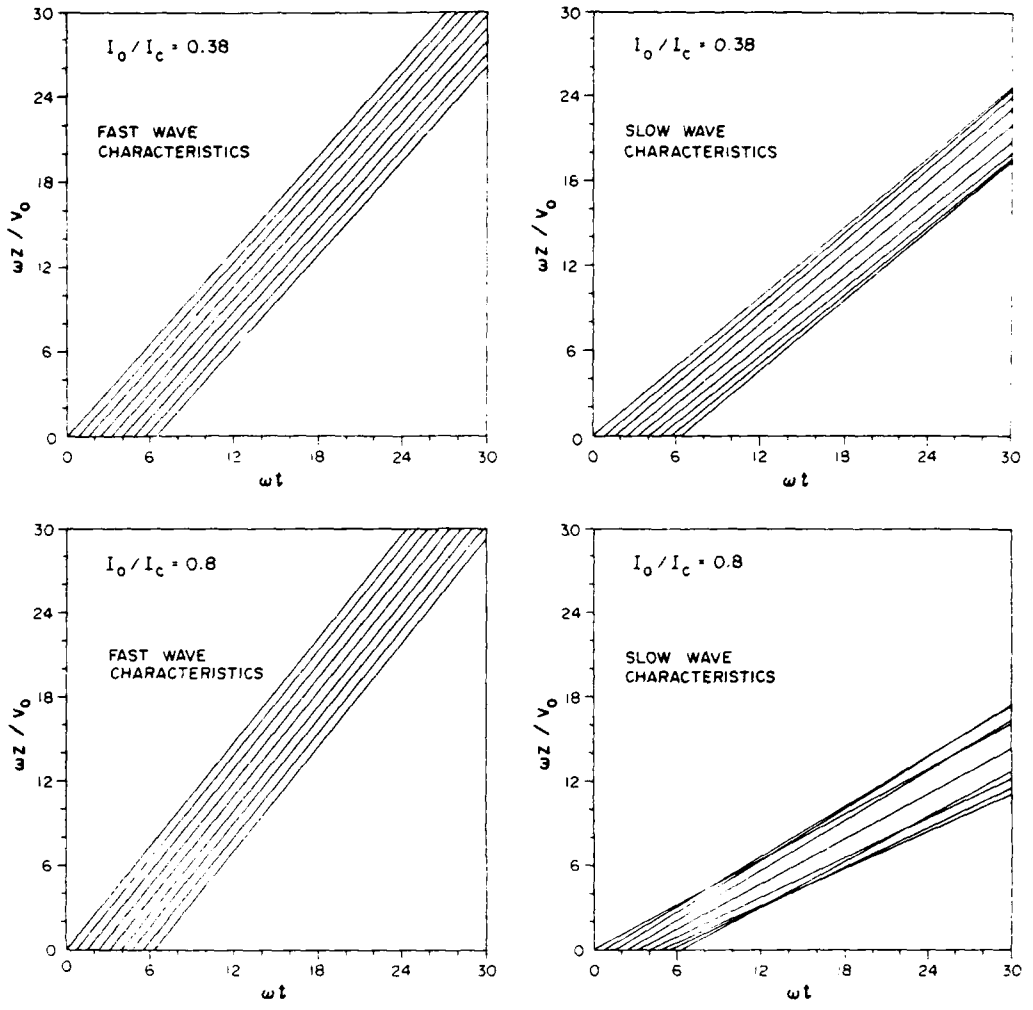



Fig. 11. Nonlinear propagation characteristics of the fast and slow space charge waves for $E_{inj}$ = 425 keV, $I_c$ = 12.8 kA, $V_{1o}$ = 30 KeV. (a) Top: $I_o$ = 4.86 kA ($I_o/I_c$ = 0.38) and (b) Bottom: $I_o$ = 10.3 kA ($I_o/I_c$ = 0.8).

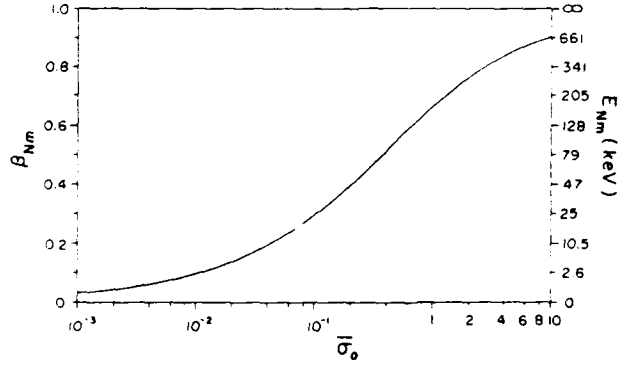



Fig. 12. The normalized local electron speed $\beta_{Nm}$ when the nonlinear space charge waves cease to propagate. Also labeled is the corresponding kinetic energy $E_{Nm}$.

Equation (13) does not admit a (real) solution for $\beta$ and $\gamma \equiv (1 - \beta^2)^{-1/2}$ if

$$V_1 \sin \omega t > V_{th} \tag{14}$$

where

$$V_{th} \equiv \frac{m_o c^2}{|e|} \left\{ \gamma_{inj} - \left[ 1 + \left( \frac{I_o}{I_c} \right)^{2/3} \left( \gamma_{inj}^{2/3} - 1 \right) \right]^{3/2} \right\}. \tag{15}$$

Thus, if $V_1 < V_{th}$, the modulating process at a short gap is similar to the classical picture—there is no current modulation immediately beyond a short gap which provides the (velocity) modulation. However, if $V_1 > V_{th}$, we expect a strong current modulation by the gap. The amount of current modulation at the gap exit is estimated to be $(I_1)_{exit} = I_o(2/\pi)(1 - V_{th}^2/V_1^2)^{1/2}$. This current modulation rises rapidly once $V_1 > V_{th}$, and becomes insensitive to $V_1$ if the latter substantially exceeds $V_{th}$ [Fig. 13]. These features are also reflected qualitatively in experiments and simulations, and are yet (another) novel property associated with an intense beam.

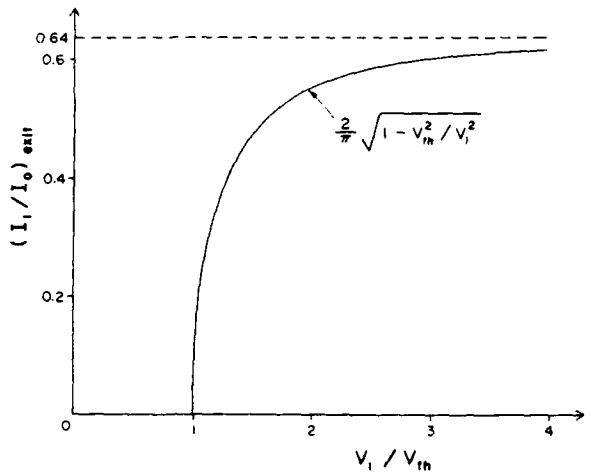



Fig. 13. Current modulation at the gap exit as a function of modulating gap voltage.

## 4. RF EXTRACTION FROM MODULATED IREBS

Many applications demand high rf power in a $TE_{01}$ mode of a rectangular waveguide. In this section we describe extraction of rf at a frequency of 1.328 GHz from a modulated IREB. The experimental set-up is shown in Fig. 14. It consists of the device shown in Fig. 5 and an rf converter.[13] The rf converter consisted of a coaxial line which intersects a rectangular waveguide through its broad side. Two movable plungers were used to vary the lengths of the coaxial line and of the rectangular waveguide. The input impedance seen by the input of the coaxial line is

$$Z_{in} = Z_c \frac{Z_L + jZ_c \tan(kl)}{Z_c + jZ_L \tan(kl)}, \tag{16}$$

where $Z_c$ is the characteristic impedance of the coaxial line, $Z_L$ the impedance connected at the end of the coaxial line, $l$ the length of the coaxial line, $k = 2\pi/\lambda$, and $\lambda$ the wavelength ($\lambda = 2\pi c/\omega$).

The modulated electron beam that was used to excite the coaxial line had a current $I_o = 5$ kA, for a duration of $T \sim 100$ ns, energy $eV_o = 600$ keV, and a frequency $f = \omega/2\pi = 1328$ MHz. The voltage at the input of the coaxial line was

$$V_{in} = IZ_{in}. \tag{17}$$

The following conditions had to be satisfied for $Z_{in}$ and the geometry of the coaxial line: (1) $Z_{in}$ be real at the frequency $f$ in order to extract power from the modulated beam. (2) $Z_{in}$ be chosen such that (a) $V_o \geq IZ_{in}$ for the frequency $f$ and (b) $Z_{in}$ be small for frequencies around $1/T$. (3) The coaxial line with a large transverse dimension to reduce the electric field on the metallic surfaces but small enough to fit inside the magnetic field coil.

Even though the rf power in the modulated MIREB was of the order of $\sim 3$ GW for a duration of 140 nsec, only a fraction of the rf energy was extracted. Typically we got 1.8 GW of rf power for 30 - 50 nsec. The easy access to the rectangular waveguide helped us to determine that vacuum breakdown, at the junction coaxial cavity-rectangular waveguide, occurred. Only after reducing the IREB power to 1.2 GW we extracted 500 MW of rf power for the IREB duration (140 nsec).

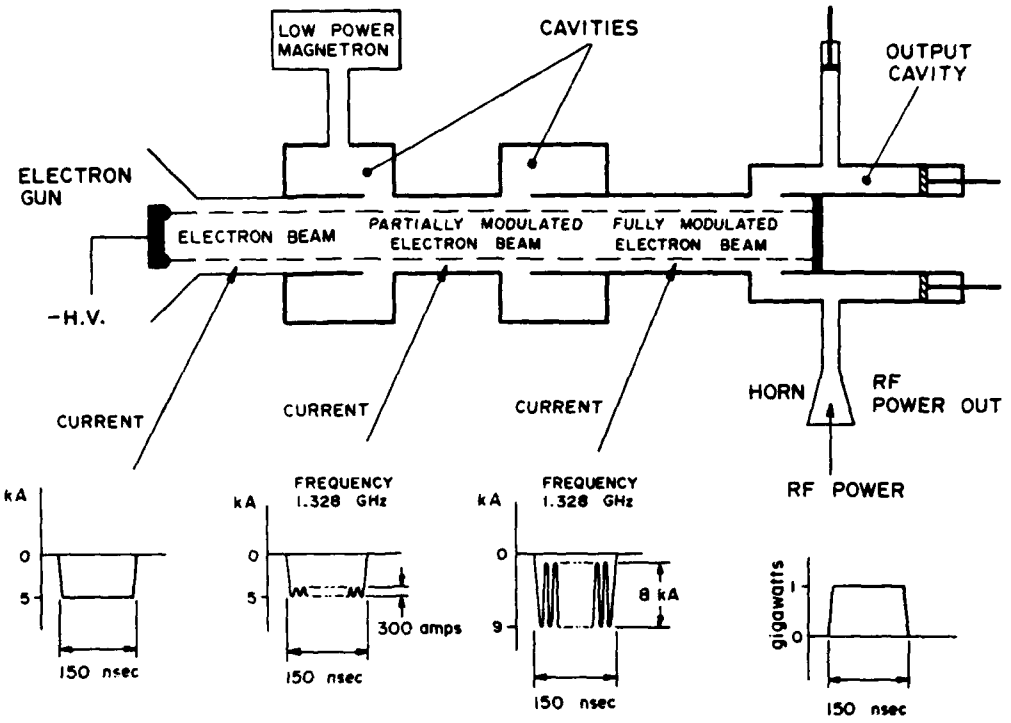



Fig. 14. Experimental arrangement used to generate rf power and to inject it into the atmosphere. The bottom figure shows the evolution of the IREB as it traverses, from the diode, through the first and the second cavity, and the rf extraction.

## 5. CONCLUSIONS

In this paper, the interaction between intense relativistic electron beams and active rf structures was investigated. Experiments, theory, and numerical simulations have provided us with a picture of the mechanisms involved in IREB modulation by an external rf source. We have identified linear and non-linear mechanisms capable of coherently bunching IREBs with power levels in the gigawatt range and above.

In this paper we showed experimentally that

(1) IREBs can be modulated by rf sources of low power with high efficiency.

(2) The modulation of the IREB current has stable amplitude and the bunches are phase locked to the external rf source.

(3) The shape of the electron bunches can be tailored by changes in the geometry.

(4) The bunching mechanism for a fully modulated IREB is unique in its behavior, and using this mechanism, a long drift region is unnecessary for operation (unlike in classical klystrons).

A simple theoretical model based on linear theory successfully explains the experimental results associated with low modulation levels (i.e., linear region). Numerical simulation extended our understanding to the non-linear region, where several simple analytical models were constructed to help to interpret the simulation and experiments.

Experiments, theory, and numerical simulations showed that the self and induced electric fields generated by IREBs play important parts in the bunching mechanism. The numerical simulation showed that quasi-DC virtual cathodes need not be formed and that electrons are not reflected even at high levels of modulation. Transients and shock-excitation of cavities are unimportant in the amplifier configuration studied in this paper.

Many applications for modulated IREBs by an external rf source can now be envisioned. One of the applications which is now being actively pursued at the Naval Research Laboratory is ultrahigh power rf generation.

## 6. ACKNOWLEDGMENT

We are grateful to Scott Brandon and Adam Drobot for their assistance in applying CONDOR[9] to this problem. The relativistic klystron amplifier research is sponsored by the Strategic Defense Initiative Organization Office of Innovative Science and Technology and managed by the Harry Diamond Laboratory.

## 7. REFERENCES


1. M. Friedman and V. Serlin, Phys. Rev. Lett. **55**, 2860 (1985).
2. M. Friedman, V. Serlin, A. Drobot and L. Seftor, Phys. Rev. Lett. **50**, 1922 (1983); J. Appl. Phys. **56**, 2459 (1984).
3. See, e.g., R.B. Miller, *An Introduction to the Physics of Intense Charge Particle Beams* (Plenum, New York, 1982), Ch. 3.
4. R.J. Briggs, Phys. Fluids **19**, 1257 (1976).
5. Y.Y. Lau, J. Appl. Phys. **62**, 351 (1987).
6. S. Bloom and R.W. Peter, RCA Rev. **15**, 95 (1954).
7. M. Friedman, J. Krall, Y.Y. Lau and V. Serlin, to be published.
8. M. Friedman and M. Ury, Rev. Sci. Inst. **41**, 1334 (1970).
9. CONDOR is an extension of the MASK Code developed by A. Palevsky and A. Drobot, in Proc. 9th Conf. Numerical Simulation of Plasmas (Northwestern Univ., Evanston, IL, 1980), unpublished.
10. J. Krall and Y.Y. Lau, to be published; J. Krall, M. Friedman, V. Serlin and Y.Y. Lau, to be published.
11. C.C. Lin, J. Math. and Phys. **33**, 117 (1954).
12. Y.Y. Lau, J. Krall, M. Friedman, and V. Serlin, to be published.
13. M. Friedman and V. Serlin, Rev. Sci. Instrum. **58**, 58 (1987).

# APPENDIX P

## Operation of a Multigigwatt Relativistic Klystron Amplifier

# OPERATION OF A MULTIGAGWATT RELATIVISTIC KLYSTRON AMPLIFIER*

M. FRIEDMAN, V. SERLIN, Y. Y. LAU, AND J. KRALL**

PLASMA PHYSICS DIVISION

NAVAL RESEARCH LABORATORY, WASHINGTON, DC 20375-5000

*This work is a part of a complete paper to be published later.
**Present address S.A.I.C., McLean, VA 22101

ABSTRACT

This paper addresses the new development of high pcwer RF Klystron - like amplifiers using modulated intense relativistic electron beams. This research followed an earlier work in which the interaction between a high impedance ( 120 ohm) intense relativistic electron beam and a low power RF pulse resulted in the generation of coherent bunches of electrons with excellent amplitude and phase stabilities.

In the present experiment a low impedance (30 Ohm) large diameter ( 14 cm ) annular electron beam of power ~ 8 gigawatts was modulated using an external RF source (Magnetron) of 0.5 megawatt power. The sequential interaction of the modulated electron beam with a structure generated a 3-gigawatt RF pulse that was radiated into the atmosphere.

## 1. INTRODUCTION

In this paper we describe the construction and operation of new RF amplifiers that use intense relativistic electron beams (IREB'S). These amplifiers exploit the unique properties of IREB's - the high self electric field-to generate electron bunches and to prevent RF breakdown of high voltage gaps.

In 1983, we found that a high level of coherent current oscillation appeared on IREB'S propagating through a drift region consisting of a smooth metallic tube in which two or more coaxial cavities were inserted[1]. The following characteristics[2] were observed in these early experiments of self modulation.

(1) The frequency of oscillation depended strongly on the geometry and weakly on the IREB current and voltage.
(2) The frequency of modulation was monochromatic.
(3) Electron beams of voltage of up to 3 MV and current of up to 50 kA were fully modulated with efficiency approaching 100%.

A simple theoretical model[1-4] showed that the "classical" space charge waves on tenuous electron beams were modified by the self-electric field of the beams. The modified space charge waves played an

important role in the new bunching mechanism. The theoretical model agreed with the experimental results. Numerical simulation agreed with the theory and extended our understanding of the mechanism into the non-linear region. Both theory and simulations showed that the self fields of the IREB and the induced electric field that originate from IREB propagation through cavities caused redistribution of energy and density within the beam in such a way that coherent bunches of electrons were formed.

The theory and simulation predicted that the modified space charge waves could also be launched by external RF source and used in klystron-like amplifiers. This theoretical prediction was verified experimentally in 1986 [3]. Later on, a series of experiments combined with theory and numerical simulations showed that[4]:

(1) IREB's could be modulated, by external RF source of low power, with high efficiency.

(2) The amplitude of the current modulation was stable and the electron bunches were phase locked to the external RF source.

(3) The shape of the electron bunches could be tailored by changes in the geometry.

(4) The bunching mechanism for a fully modulated IREB was unique in its behavior and using this mechanism a long drift region was unnecessary for operation (unlike in a classical klystron).

It is known that RF power can be extracted from modulated electron beams. We demonstrated extraction of RF power from modulated IREB'S with efficiencies of about 40%.

A drawback of RF sources based on this mechanism was the high impedance (120 ohms) of the IREB, necessary for the mechanism to work. This drawback makes it difficult to efficiently match the high impedance electron beam to the relatively low impedance of IREB generators (30 ohms). To achieve an efficient transfer of energy, the impedance of the IREB generator has to be equal to the impedance of the electron beam. However, low IREB impedance can easily be obtained by increasing the diameter of the electron beam.

In this paper, the construction and operation of an RF amplifier that employs a large diameter IREB is described. The IREB parameters were: diameter 14 cm, thickness 0.3 cm, current 16 kA, beam impedance 30 ohms, total power ~ 8 gigawatts, and beam duration 120 nsec. This electron beam was strongly modulated by an external RF source at a frequency of 1.328 GHz (Section 2). About 3 gigawatts of RF power was extracted from the modulated IREB and radiated into the atmosphere (Section 3). Summary and conclusions are given in the last section.

## 2. MODULATION OF A LARGE DIAMETER HIGH CURRENT IREB

The physics of externally modulated IREB'S was detailed in our earlier paper [4]. Here, we shall give only results needed to explain the construction and operation of the amplifier. Specifically, we will discuss three aspects:

(a) First gap interaction-small signal analysis.

(b) Second gap interaction-large signal analysis.

(c) Electrostatic insulation of high voltage gaps.

(A) First gap interaction-small signal analysis.

Following similar arrangement as in our previous work, an IREB was partially modulated by the first cavity (Fig 1). Here a

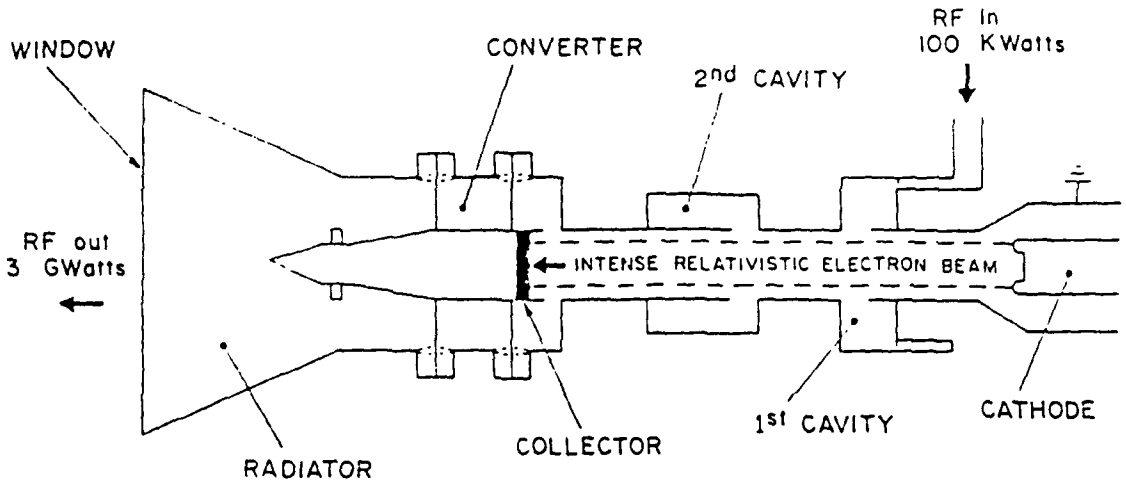



FIGURE 1 Experimental Arrangement

voltage pulse of 500 kV and 120 nsec duration was applied on a foiless diode. As a result, the diode emitted and launched an IREB inside a 14 cm diameter metallic drift tube. The IREB diameter was 13.2 cm with a thickness of 0.3 cm. The IREB current was 16 kA. The drift tube was immersed in a quasi dc magnetic field of 10 kgauss and was evacuated to a base pressure of less then $10^{-5}$ Torr. A gap feeding a cavity was inserted in the drift tube. This cavity supported many resonance

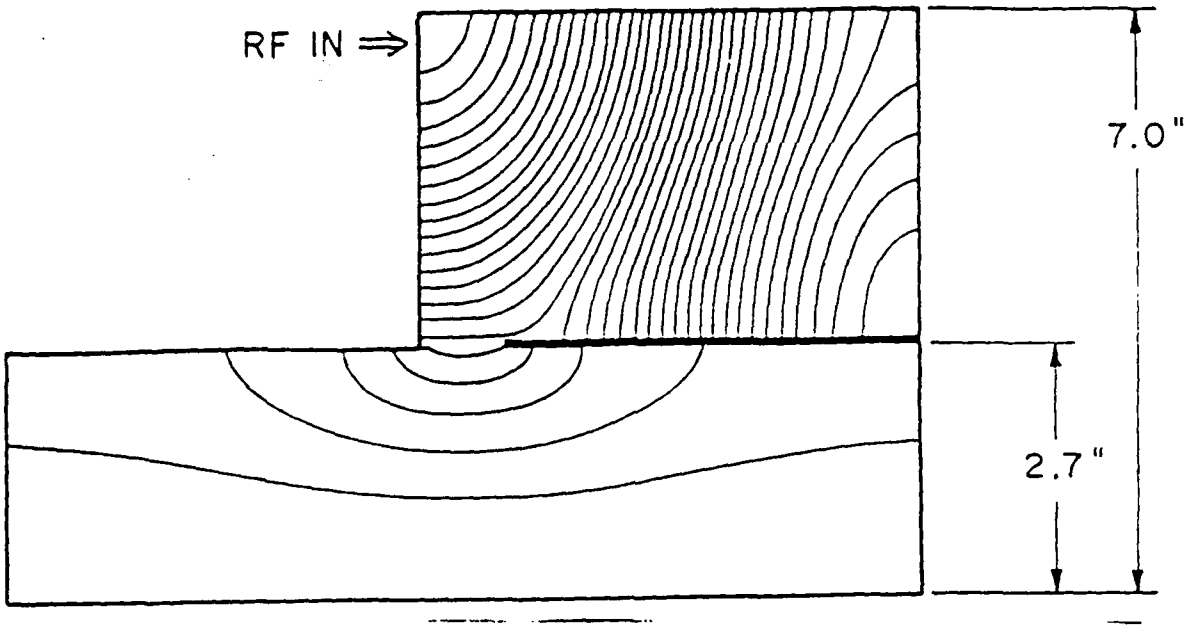



FIGURE 2 Electric Field Configuration Inside 1st Cavity

modes, one of which was a hybrid of a coaxial TEM and TM modes (Fig 2) with a frequency of 1.328 GHz. The "Q" factor of the cavity was 1100. An external RF source pumped power into the cavity for a duration of 1 $\mu$sec. The electrical parameters of the cavity were calculated using the SUPERFISH computer code. We found:

(1) That the gap voltage, Vg was half as high as the largest voltage in the cavity.

(2) The electrical parameters of a same geometry cavity made out of copper. (power dissipation P, energy stored W, quality factor Q and gap voltage Vg).

Using these parameters one can calculate the relationship between input power and Vg for any real cavity of the same geometry. It is easy to show that for two cavities (subscript 0 and 1) of the same geometry but of different "Q" the following relationship exists:

$$Vg_1 = Vg_o \left(\frac{P_1 Q_1}{P_o Q_o}\right)^{\frac{1}{2}} \qquad (1)$$

From SUPERFISH code one calculates that for a cavity made of copper

$Q_o = 39700$ and for $P_o = 5.25 \times 10^4 W$ One gets $Vg_o = 87$ kV

Hence, Eq (1) will give that: $Vg_1 = 63.2P_1^{\frac{1}{2}}$ (2)

The power injected into the cavity in the experiment was typically 0.5 Megawatt. Using Eq (2), we found the gap voltage to be:

$$Vg_1 = 45 \text{ kV}$$

Sometime after the voltage at the gap reached its maximum value a Blumlein Transmission line energized the diode, resulting in IREB propagation through the gap of the cavity.

The oscillatory voltage $Vg_1$, imposed on the gap partially modulated the IREB generating at point z an RF current $I_1$ (z) and RF voltage $V_1$ (z)

$$I_1(z) = j \frac{M\, Vg_1}{Z} \sin(kz) \qquad (3)$$

$$V_1(z) = M\, Vg_1 \left[\cos(kz) - j\zeta \sin(kz)\right] \qquad (4)$$

where Z, k and $\zeta$ are quantities that depend on the geometry and beam parameters, (4) and M<1 is the gap factor due to finite transit times[5]. (Note that unlike in a classical klystron, $I_1(z)$ and $V_1(z)$ are partially in phase.(See Ref 3) ).

Using the experimental parameters and the equations in Ref. 3 one gets:

$$Z = 16 \text{ ohms}, \; k = 0.039 \text{ cm}^{-1} \text{ and } \zeta = -0.35$$

M was evaluated from a particle simulation Code "CONDOR" (which was discussed in Ref. 4). We found M = 0.6 . From Eq (2) we obtain that maximum $I_1$ = 1800 Amps at a distance 40 cm downstream.

"CONDOR" gave $I_1$ = 3200 Amps at a distance of 44 cm from the gap, using an oscillating voltage of 50 kV amplitude.

Experimentally we found that the IREB RF current reached the maximum at a point z = 35 cm. At this point $I_1$ = 1750 Amps.

We believe that the discrepancies came from assumptions made on the values of the experimental parameters, e.g., the geometry of the cavities in the simulation differ from those used in the experiment.

(B) Second Gap Interaction-Large Signal Analysis.

At a point z = 35 cm downstream of the first gap a second gap was inserted in the drift tube. This gap was feeding a coaxial cavity of low impedance, Zc = 10 ohms. The length of the cavity was 3/4 $\lambda$ ($f = (c/\lambda) = 1.328$ GHz). In this cavity (Fig 1) 4 resistive wires were placed radially, connecting the inner and outer conductors. The purpose of the wires was to reduce the "Q" of the cavity at resonance frequencies lower than 1.328 GHz.

The geometry of the second cavity was chosen such that:

(a) The ratio of gap voltage to peak voltage was maximized.

(b) The shunt impedance of the cavity, Rs, was maximized.

Using SUPERFISH[6] computer code and experimenting with various cavities we found the best cavity geometry that fulfilled the above conditions (Fig 3). For this cavity the ratio the of gap voltage to

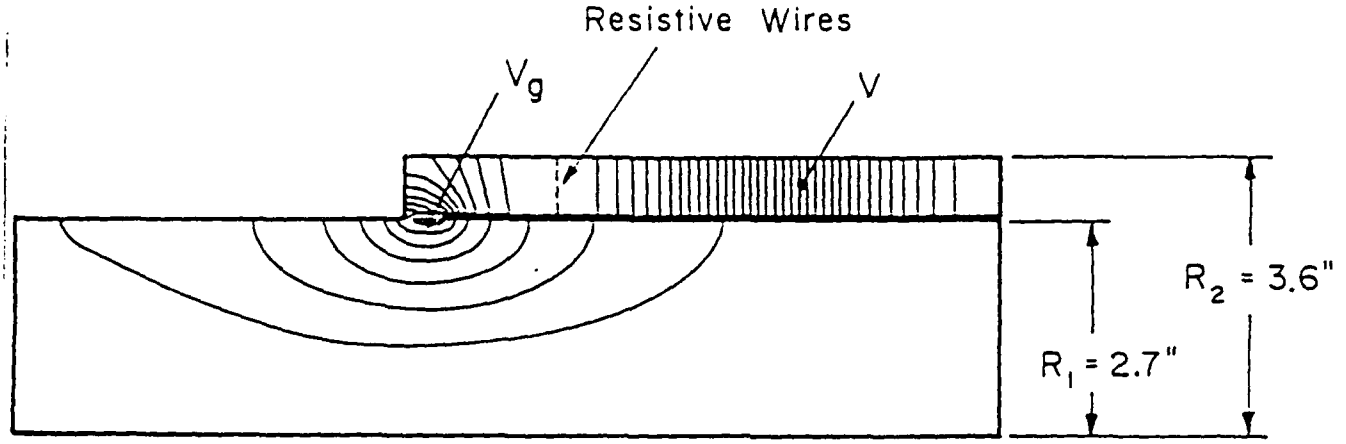



FIGURE 3 Electric Field Configuration Inside 2nd Cavity

the peak voltage was 0.8. The shunt impedance of this 3/4 $\lambda$ cavity was

$$Rs = 0.8(3\pi/4)Q(Zc) \qquad (5)$$

When a modulated IREB traversed such a cavity, an induced RF voltage appeared on the gap increasing the depth of the current

modulation by a gain factor GA which reached maximum at an axial position L = 1/k cm

$$GA = (M^2 (Rs/Z + \zeta)) \qquad (6)$$

GA was evaluated and found to be GA=30.

Using this gain an RF current exceeding the DC current was obtained. The result indicates that a non-linear treatment is needed to explain experimental observations.

The IREB current downstream from the second gap was found (Fig 4) to have the following time dependence

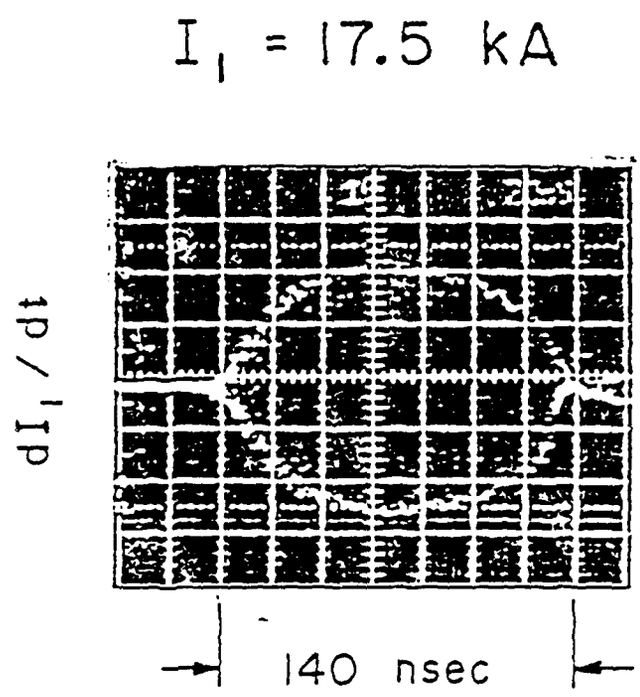



FIGURE 4 Time Derivative of the IREB Current Measured by 1 GHz 7104 Oscilloscope

$$I = I_0 + I_1 \cos(\omega t) + \ldots\ldots\ldots$$

$I_1$ reached a maximum value of 8.5 kA at a distance 39 cm from the second gap.

Large changes in the RF power input into the first cavity affected $I_1$ only marginally. Hence, we assumed that saturation of the mechanisms was achieved. But unlike our previous experiment[3] in which $I_1 / I_o = 0.8$, here $I_1 / I_o = 0.5$ and could not be further increased. Since the RF current measurements were inferred from measuring the magnetic field associated with the electron bunches we investigated whether this magnetic field differed from the one associated with DC IREB current. Using linear theory[5] we estimated that:

$$I_1 \text{ (REAL)} \tilde{=} I_1 \text{ (MEASURED)} \times \frac{2}{1 + \varepsilon} \qquad (7)$$

where

$$\varepsilon = \exp - \left\{ \frac{4\pi \left( \frac{rw - rb}{\lambda} \right) \beta_o}{1 - I/I_c} \right\} \qquad (8)$$

$I_1$ (real) is the real RF current and $I_1$ (measured) is the measured RF current and where rw and rb are the radii of the drift tube and the IREB respectively, $\beta_o = v_o / c$, $v_o$ is the speed of the electrons in the drift tube and $I_c$ is the critical current in the drift tube. Substituting the experimental results one gets

$$I_1 \text{ (real)} = 1.4 * I_1 \text{ (measured)} = 12 \text{ kA} \qquad (9)$$

Note that (1) Eq (7) was not solved self-consistently since we substitute $I = I_o + I_1$ (real) and (2) only linear theory was used to derive Eq (8). We can conclude that the measured RF current is probably lower than the value of the true RF current.

(C) Electrostatic Insulation[7]

The output power of a classical RF generator is limited by voltage breakdown across cavity gaps. The factors that influence the breakdown are electric field, geometry, frequency of the the RF, material used, vacuum and cleanliness. These factors are optimized in high power RF devices so that the largest voltage possible can be sustained across a gap. Most of these factors cannot be optimized in the environment of IREB generators. Moreover, in the experiments discussed earlier no special care was taken to prevent vacuum breakdown. Even so we found that voltage of the order of 0.5 MV appeared and sustained on the gaps without any indication of vacuum breakdown.

The reason for such behavior were discussed by us before. It is rooted in the unique properties of IREB'S, properties that do not exist for tenuous electron beams. We found that the self electric field of an IREB modifies the electric field configuration of a high voltage gap in such a way that the voltage gradient on a negatively charge electrode is reduced and for high IREB current can even reverse its sign. This effect suppresses emission of secondary electrons and eliminates conditions necessary for vacuum breakdown. We called this effect electrostatic insulation.

In the next section we shall show that electrostatic insulation plays a role also in RF power extraction. This effect is of critical importance in any device in which IREB's interact with high voltage gaps.

## 3. RF EXTRACTION FROM MODULATED IREB'S

It is well known that RF power can be extracted from a modulated electron beam. Since the electrons in an IREB are relativistic there will be less reduction in particle velocity (or IREB current) while electrons are loosing energy. Hence, we can model the modulated IREB as a constant current source I

$$I = I_o + I_1 \cos(\omega t) + \ldots\ldots\ldots \qquad (10)$$

The interaction of this current source with an RF structure can lead to transfer of power from the electrons to a load. The structure can be described as an electrical element with an input impedance of $Z_{in}$. A voltage $V_{in}$ will develop across the electrical element

$$V_{in} = Z_{in} * I \qquad (11)$$

To extract maximum RF power, from the IREB, with a frequency $\omega/2\pi$ the following requirements have to be fulfilled:

(a) $V_{in} < V_o$ otherwise the constant current source model for the IREB will not be correct and the flow of IREB will be disrupted.

(b) $Z_{in}$ $(= Z(\omega))$ has to be real at the frequency of the extracted RF.

(c) The absolute value of $Z_{in}$ at other frequencies has to be smaller than $Z(\omega)$.

(d) $Z_{in} = 0$ at low frequencies of the order of $1/T$ where T is the beam duration (in the experiment T = 120 nsec).

In order to transport this power into a load an additional requirement has to be fulfilled:

(e) Elimination of RF breakdown.

The device shown in Fig. 1 addresses all of the above requirements and consists of the following parts:

(1) A high voltage gap across which the electron bunches are moving and losing energy. Electrostatic insulation is of importance here since voltages of the order of 0.5 MV will appear across the gap when efficient extraction of RF power is taking place. The maximum current that can propogate across the gap is given in Ref. 5.

(2) The gap is connected to an antenna via a coaxial transmission line. The center conductor is supported by thin metallic rods which are terminated in ¼λ cavities (Fig 1). The axial positions of these rods are the locations of zero-amplitude node points of standing waves. The total impedance of the parallel circuits formed by the rods is large and can be considered infinite for the 1.328 GHz component of the RF current. This impedance is lower for higher frequencies and zero for the low frequency and the DC components of the current.

At the far end of the inner conductor an RF "obstacle" in a shape of a disc was placed. The axial position and diameter of the disc could be varied. This part of the convertor was modeled using transmission line calculations. Fig. 5 shows the model. The gap is

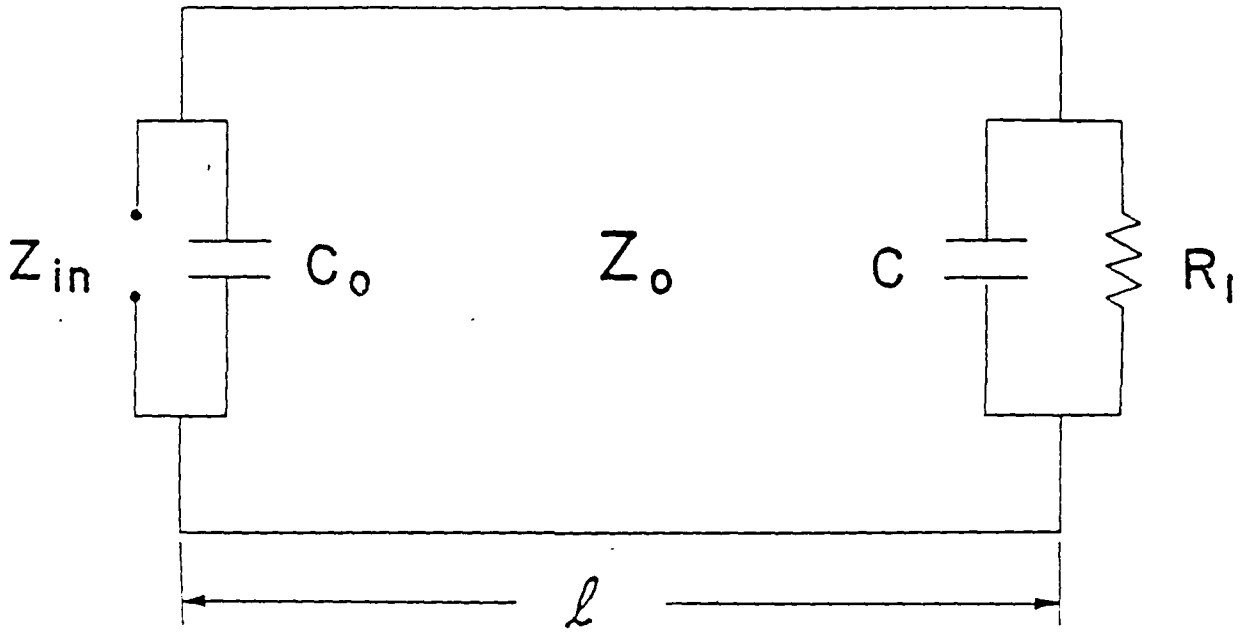



FIGURE 5 Equivalent Circuit of the RF Convertor

represented by a capacitor of value $C_o$, the obstacle is represented by a capacitor C, the load is $R_l$ and the transmission line is of length $\ell$ and impedance $Z_o$. Realistic values for the parameters in the model

were found in the following way: $C_o$ was calculated from the shift of the resonance frequency of an ideal ½λ cavity with a similar gap geometry

$$\frac{1}{j\, Z_o\, tg\left(\frac{\pi}{2}\,\frac{f}{f_o}\right)} + j2\pi f C_o = 0 \qquad (12)$$

where $f_o$ is the resonance frequency of the ideal ½λ cavity and f is the resonance frequency of a cavity with a gap of capacitance $C_o$. We found that $C_o$ = 6pF.

The value for $R_1$ was assumed to be equal to Z. The reason for this was that when the obstacle was removed the VSWR was close to 1 over a wide range of frequency. C and $\ell$ were left as free parameters that we tried to optimize so that the input impedance $Z_{in}$ = R + jX would be real at 1.328 GHz and of value a between 50 ohms to 100 ohms. Note that $\ell$ can have a series of solutions separated by ½ wavelength. Fig. 6 displays one solution for

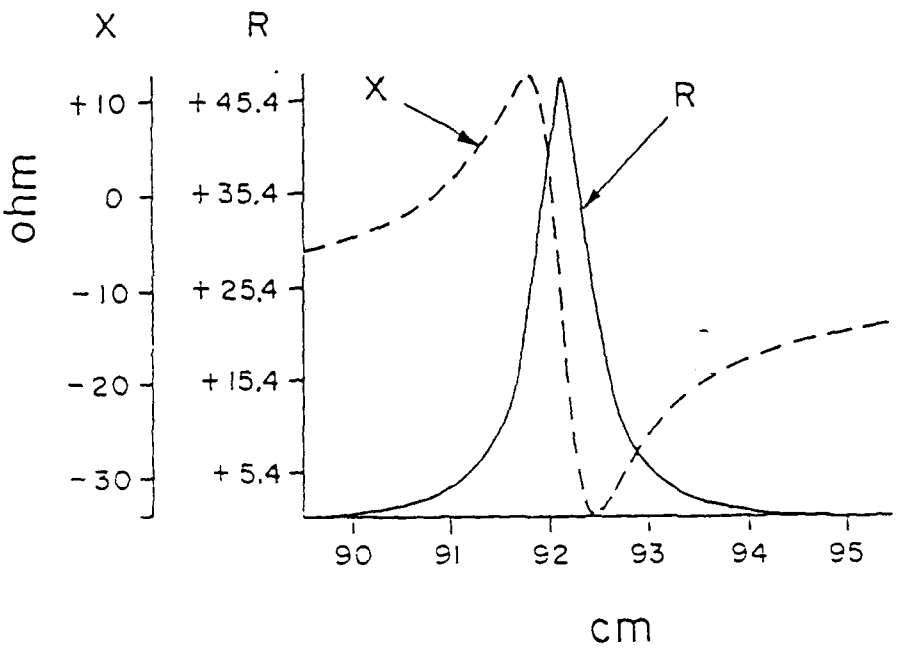



FIGURE 6 Real and Imaginary Components of the Imput Impedance $Z_{in}$ vs Length

R and X. We found that had to be chosen with great accuracy and that the value of R increased when C was increased.

The model is only qualitative in nature since it does not take into account the existence of non TEM modes at various places inside the convertor.

(3) The last part of the convertor was the antenna which has a conical shape for both the inner and outer parts. The length of the antenna was a few wavelengths. A lucite plate 5 cm thick acted as a window.

A set of experiments were performed in which and C were adjusted so as to get maximum radiated power. With optimum conditions we observed radiated power (outside the horn) of 2.7 gigawatts (Fig. 7). The IREB parameters were: 16 kA current and 500 kV voltage. (Note that the lucite window attenuates the RF power by 10%).

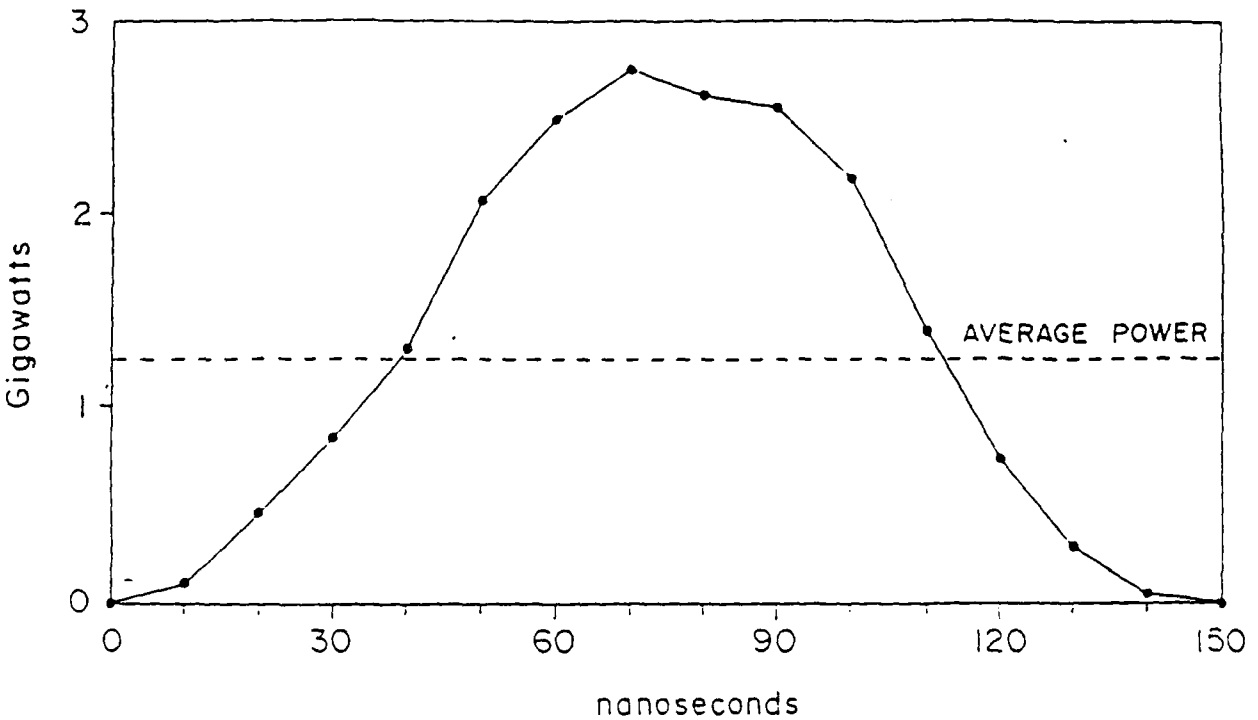



FIGURE 7 RF Power Vs Time for Shot No 1118

The total radiated power was derived in two ways:

(1) The radiation pattern was measured and the power/cm$^2$ was obtained. The total radiated power was then obtained by integration.

(2) An external RF source of 50 ohms impedance was connected at the gap via a slotted transmission line. The electrical parameters of the convertor were adjusted to achieve a VSWR of 1 measured by the slotted line. This implied that the convertor acted as a matched load to the external source. Measuring the input power and the response of a receiving horn yield the calibration factor. Excellent agreement of the two power measurements were achieved.

In the power measurements cases the receiving horn was connected to a 7103 Tektronix 1 GHz oscilloscope. All of the electrical components that were used in measuring the power were calibrated whenever a series of experiments were performed.

From Fig. 7 one can see that the radiated RF power had a slow rise time, about 60 nsec. It takes a time $\tau$ to fill a cavity with RF

$$\tau \simeq \frac{2}{M} \tau_{1/e} \; ; \quad \tau_{1/e} = 2Q/\omega \qquad (13)$$

Experimentally, we found $Q \simeq 80$, hence, $\tau \simeq 60$ nsec. At low RF output power the decay time of the power also lasted 60 nsec. At high power the decay time was shorter and at a power of 2.7 gigawatts this time was 30 nsec long. We speculate that the gap lost its electrostatic insulation due to the drop of the current at the end of the IREB pulse.

On occasion when the current was terminated earlier due to flash over in the diode the falltime of the current and the duration of the RF power was even shorter.

## 4. SUMMARY AND CONCLUSIONS

In this paper, the construction and operation of a high power amplifier were detailed. An intense relativistic electron beam of low impedance (30 ohms) and of high power (8 gigawtts) energized the amplifier. The gain of the amplifier was 37 dB and radiated power was 3 gigawatts. Power efficiency was 35% and energy efficiency 20%. Unlike in the classical klystron, long drift tubes were not necessary.

## 5. ACKNOWLEDGMENT

This research is sponsored by the Strategic Defense Initiative Organization, Office of innovative Science and Technology and managed by the Harry Diamond Laboratory.

## REFERENCES


(1) M. Friedman, V. Serlin, A. Drobot and L. Seftor, Phys. Rev. Lett. 50, 1922 (1983)

(2) M. Friedman, V. Serlin, A. Drobot and L. Seftor, J. Appl. Phys. 56. 2459 (1984)

(3) M. Friedman, V. Serlin, Phys. Rev. Lett, 55, 2860 (1985)

(4) M. Friedman, J. Krall, Y. Y. Lau, V. Serlin, J. Appl Phys. 64, 3353 (1988)

(5) Y. Y. Lau, J. Krall, M. Friedman, V. Serlin, published in the proceedings of this Conference

(6) K. H. Halbach and R. F. Holsinger, Lawrence Berkely Lab Report No. LBL-5040 (1976)

# APPENDIX Q

## On Certain Theoretical Aspects of Relativistic Klystron Amplifiers

# On certain theoretical aspects of relativistic klystron amplifiers

Y. Y. Lau, J. Krall*, M. Friedman and V. Serlin

Plasma Physics Division, Naval Research Laboratory
Washington, DC 20375-5000

* Science Applications International Corp.
McLean, VA 22102

## ABSTRACT

This paper addresses several issues which are relevant to the high power klystron amplifier experiments at the Naval Research Laboratory. To a large extent, these issues originate from the DC self field of the intense beam and therefore are not treated in the conventional klystron theory. Among them include electrostatic insulation, limiting current which can flow through a gap in the presence of a biased gap voltage, and the modification of the transit time effects by the beam's space charge. We examine the proper interpretation of magnetic probe measurements of current modulation on an intense beam. Particle simulation of the large diameter beam yields excellent agreement with experiments and theory. Magnetic insulation in the coaxial rf extraction structure is shown to be adequate, in agreement with experimental observations.

## INTRODUCTION

In this paper, we consider several issues which arose from our high power klystron amplifier experiments.[1] The resolution of these issues requires extension of the conventional theory, as an extremely high perveance beam was being used (500 kV, 20 kA).

With simulation and analytical theory, we demonstrate here

(a) that a large diameter beam carrying a high current can indeed be modulated efficiently by an external rf source of low power, and

(b) that significant electrostatic insulation[2,3] against rf breakdown across the gap is obtainable. These results are strongly supported (and suggested) by the present experiments.

Also given is an analysis of

(c) the limiting current which can be transported across a gap that is subject to a biased gap voltage,

(d) the significant modification of transit time effects in a gap when the space charge of the beam can no longer be neglected, and

(e) the proper interpretation of magnetic probe measurement and the inferred current modulation on the intense beam.

Item (a) is an extension of our earlier simulation.[3,4] Results from Item (b) are a corroboration of the experimental observation that rf breakdown at the gap could be considerably reduced[1] by the electrostatic self-field of the beam. Item (c) gives some constraint on the efficiency of the relativistic klystron amplifier. It also gives an estimate of the maximum amount of charge which can be maintained in a diode. Items (d) and (e) are yet other novel properties associated with the space charge of the intense beam, not shared by conventional klystron amplifiers. Finally, we verify that the external magnetic field which was used in our

experiment is sufficient to prohibit electron or ion flow across the coaxial geometry in the rf extraction section, in agreement with experiments.

A. Modulation of a Large Diameter Beam

The particle simulation [3,4] previously used (CONDOR code) may readily be extended to determine whether a large diameter beam is as easily modulated as a beam of smaller diameter. Although some preliminary studies suggest the answer to be positive,[5] the simulation given here shows excellent agreement with experiments.[1] We shall present results on the current modulation, energy modulation, and phase space evolution of the beam.

The geometry for the two-cavity simulations is given in Fig. 1. The first cavity was driven by an external RF source, starting at t = 0 nsec. The low Q of the (numerical) cavity was such that at t = 6 nsec, the fundamental TEM mode of the cavity saturates, producing a gap voltage of 40 kV at 1.24 GHz. At this time the beam was injected with a current rise time of 5 nsec. The simulation continues until t = 20 nsec. The impedance of the radial transmission line from which the first cavity is driven is 6.25 ohms, so that the DC energy of the beam is lowered as it crosses the first gap. The RF interaction is unaffected. The gaps are located at z = 2.8 and z = 36.8 cm.

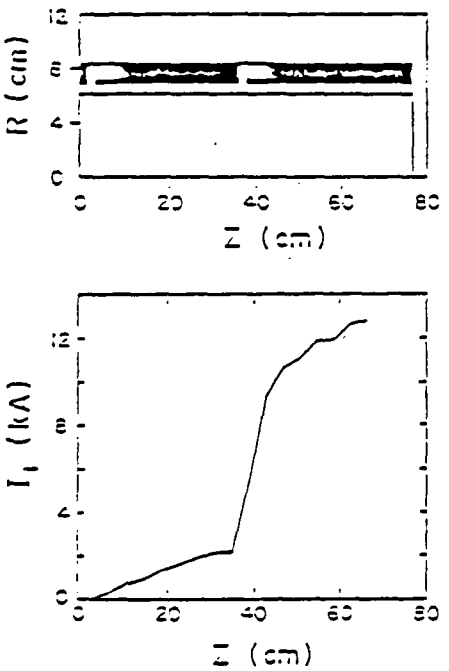



Fig. 1. The geometry (top) and the rf current modulation (bottom).

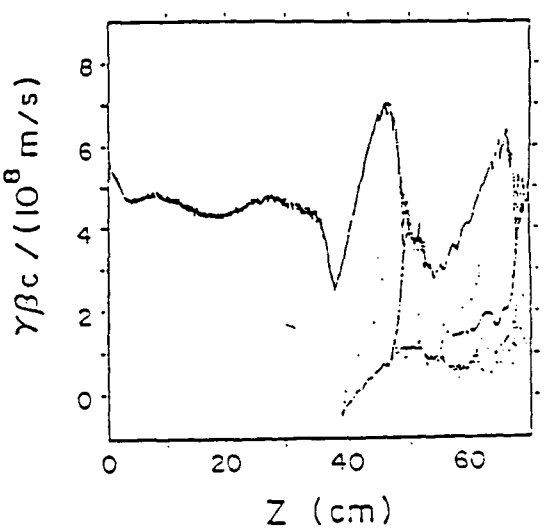



Fig. 2. Phase space plots at t = 20 ns.

The initial IREB conditions are as follows: Current 16 kA, energy 600 keV (500 KeV after the first gap), diameter 12.6 cm, thickness 0.2 cm. The first gap produced rf current $I_1$ = 2.16 kA at 30 cm from the first gap. This current modulation due to the first gap, being in good agreement with the linearized theory, excited the fundamental TEM mode of the second cavity to produce an

oscillating voltage of 425 kV at the second gap. The rf current increases to 12.8 kA, 34 cm beyond the second gap. $I_1$ versus z is plotted in Fig. 1. Figure 2 is the phase space plot of the particles at t = 20 nsec. This figure shows modulation of particle energy and the bunching of electrons at the second gap. Our simulation verified the following results for the large diameter beam:

(1) The bunching mechanism reaches steady-state after a few RF cycles. Phase-space plots, electrostatic potential plots, and modulated current are identical from RF cycle to RF cycle.

(2) Transients are of no importance and particle reflections are not necessary for the mechanism.

(3) During each cycle, the energy of the beam is decreased at the gap to a critical value at which point theoretical analysis indicates that the propagation of the slow space charge wave is halted and electrons are slowed to a nonlinear limiting velocity, corresponding to $\gamma\beta c = 1.2 \times 10^{8}$ m/sec shown in Fig. 2. An artifact of this interaction is the low energy population of particles that can be seen in this figure.

(4) Half a cycle later, the energy of the particles is increased beyond the injection value. These particles have a narrow energy spread.

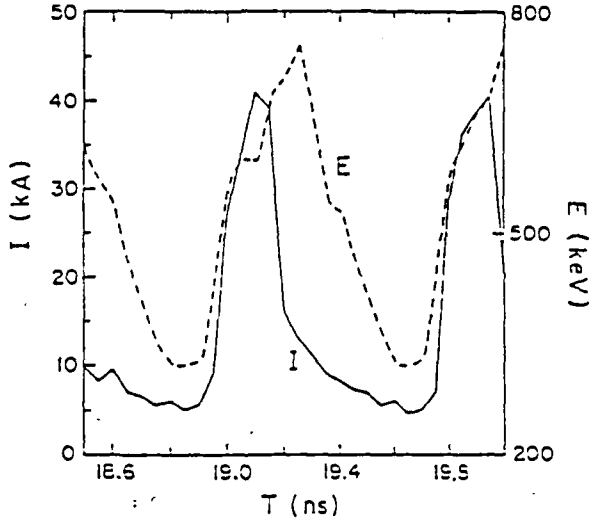



Fig. 3. Current modulation and energy modulation at z = 66.8 cm.

For the present case, we additionally diagnosed the MIREB in some detail at z = 66.8 cm, where the peak modulation was observed in the experiments. Total beam energy (potential plus kinetic) and current are plotted versus time over two rf cycles, from t = 18.5 nsec to t = 20 nsec, in Fig. 3. This figure contains the following results:

(1) The particle energy is modulated as $E(t) = E_o + E_1 \sin\omega t$ with $E_o$ = 175 keV and is stable from cycle to cycle. The energy modulation appears to be out of phase with the current modulation, but the small population of particles at high energy and low current carry very little power.

(2) The 500 keV beam was not modulated by the full 425 kV amplitude of the voltage at the second gap, indicating a finite transit time effect. [See Section D below.] The coupling coefficient, M, appears to be = 0.7 at low current and = 0.3 at peak current.

(3) Significant compression of RF power has occurred with more than 60% of the power compressed into less than 30% of the RF cycle.

(4) Comparison of these results with those obtained when the first gap voltage is increased to 50 kV shows only a 3.1% increase in the peak modulation at z = 66.8 cm, from 12.8 kA to 13.2 kA, indicating near saturation of the mechanism.

B. Electrostatic Insulation

The fact that gigavatt level of rf pover has been extracted without evidence of breakdown difficulties at the gaps can be attributed to the electrostatic insulation provided by the annular intense beam.~ To corroborate these experimental findings, we perform simulations on the geometry shown in Fig. 1 in which the second gap is sealed. An annular intense beam is injected into a drift tube with E = 500 keV and I = 16 kA, with a current rise time of 5 ns, past the radial cavity. The gap voltage is controlled externally via a radial transmission line which has an impedance of 6.25 ohms. At t = 6 nsec, the externally applied voltage across the gap is increased linearly from zero to 400 kV over 4 nsec, and a second beam, I = 1 amp, E = 1 kV, is injected continuously from the left-hand gap wall at z = 2 cm. The simulation continues until t = 10 nsec.

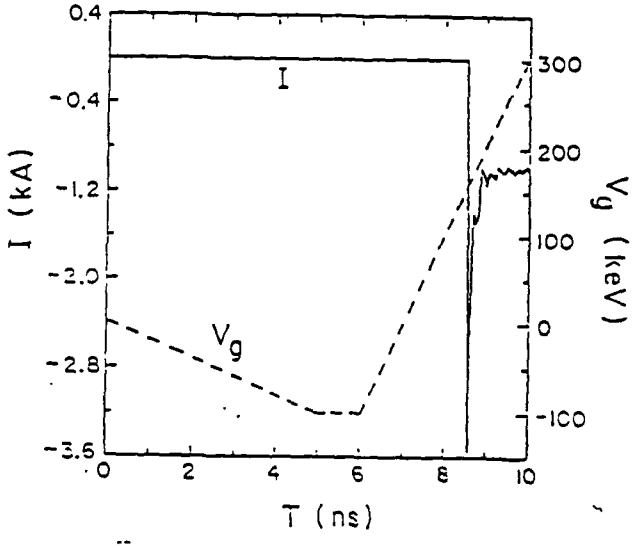



Fig. 4. Imposed gap voltage ($V_g$) and the leakage current (I) across the gap.

Voltage across the gap versus time is plotted in Fig. 4. Figure 4 also shows the leakage current crossing the gap as a function of time, measured at z = 3.2 cm. Initially, the rising DC current of the beam and the transmission line impedance cause a voltage drop which reaches 100 kV at t = 5 nsec. The effect of the externally applied voltage can be seen thereafter. The sudden increase in gap leakage current at t = 8.6 nsec indicates insulation for voltages less than 150 kV.

The effect of the electrostatic field of the intense beam has been verified by plots of particles in ($\gamma\beta_z c$,z) phase-space at t = 8.4 nsec and at t = 8.8 nsec. In the former, the gap is insulated and the low-energy particles in the gap are reflected. In the latter case, the particles are transmitted, obtaining 150 kV as they cross the gap.

Theoretical analysis indicates that as the limiting current is approached, the kinetic energy of the intense beam will be lowered near the gap, causing an increase in the net charge near the gap and a corresponding increase in the electrostatic insulation.

C. Limiting Current Across a Gap with a Biased Voltage

The modulated beam yields its kinetic energy to rf when it is retarded by the decelerating voltage across the gap of the extraction section. One limit on the extraction efficiency is governed by the maximum retarding voltage which the gap can substain without the formation of a virtual cathode. Equivalently, we may ask: Given a biased gap voltage, what is the maximum current which can be transmitted without the formation of a virtual cathode? Here, we analyze this question via the use of the simple parallel plate model. The extension to the actual experimental setup will be given toward the end of this section. We also point out that this analysis is also of interest to diode (or inverse diode) physics, as it yields the maximum charge which can be held within the diode region. This problem was treated in some limiting cases in Refs. 6-9.

Consider an ideal gap consisting of two parallel plates of area $A_o$, separated by a distance D. The left plate K (Fig. 5) is grounded and the right plate A is held at a voltage $V_1 \cos \omega t$. In this section, we assume that the transit times of the electrons are so small compared with the rf period $2\pi/\omega$ that we may pretend $\omega = 0$. Thus, when traversing the gap, the electrons see only an essentially static field and the charges are adjusted instantaneously within the diode to be consistent with the instantaneous diode voltage and current. A strong axial magnetic field allows only one-dimensional motion.

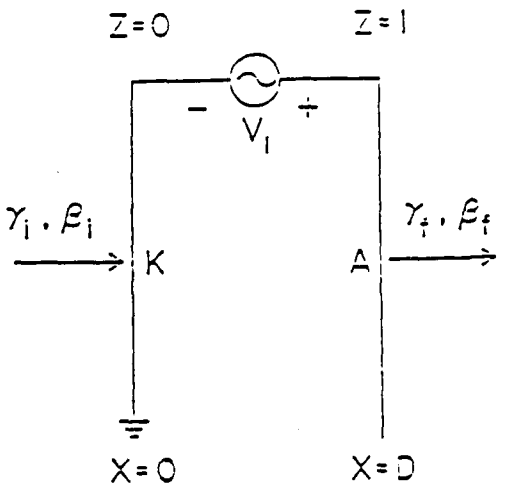



Fig. 5. A simplified model for beam-gap interaction.

Let J be the current density of the electrons impinging on plate K. Let $\beta_i \equiv v_i/c$, $\gamma_i \equiv (1-\beta_i^2)^{-1/2}$ be the normalized velocity and normalized energy of the electrons when they enter plate K, and $\beta_f \equiv v_f/c$ and $\gamma_f$ be the corresponding values when the electrons exit plate A. Since we are now dealing with a static problem, conservation of energy gives $\gamma_f = \gamma_i - |e|V_1/m_o c^2$ and conservation of charge gives

$J = |e|nv = I/A_o$, a constant everywhere, where n and v are the number density and velocity of the electrons. Let E be the electric field. We need to solve the force law and the Poisson equation:

$$\beta \frac{\partial}{\partial z} (\gamma\beta) = - \varepsilon \tag{1}$$

$$\frac{\partial \varepsilon}{\partial z} = - \bar{J}/\beta. \tag{2}$$

Here, we have introduced the normalized variables: $z \equiv x/D$, $\varepsilon \equiv |e|ED/m_o c^2$, $\bar{J} \equiv |e|D^2 J/m_o c^3 \varepsilon_o$ ($> 0$). Equations (1) and (2) may be combined to yield

$$\beta \frac{\partial}{\partial z} \left[\beta \frac{\partial}{\partial z} (\gamma\beta)\right] = \bar{J} = \text{constant}, \tag{3}$$

whose solution is

$$\gamma\beta = \frac{1}{2} \bar{J}\xi^2 + c_1 \xi + \gamma_i \beta_i, \tag{4}$$

where $\xi$ is a time-like independent variable related to z by

$$z = \int_0^\xi \beta(\xi')d\xi' \tag{5}$$

and $c_1$ is a constant to be determined. In writing (4), we have used the boundary condition at plate K: $\gamma\beta = \gamma_i\beta_i$ when $\xi = z = 0$. The constant $c_1$ is related to the normalized transit time $\xi_f$:

$$\gamma_f\beta_f = \frac{1}{2} \bar{J}\xi_f^2 + c_1 \xi_f + \gamma_i \beta_i. \tag{6}$$

It can be shown[8] that the total amount of charge, Q, within the plates is proportional to $\xi_f$:

$$Q = - C\bar{J}\xi_f \times (511 \text{ keV}), \tag{7}$$

where C is the capacitance of the gap, which in this case is simply $A_o\varepsilon_o/D$. Note that $\xi_f$ is determined from [cf. Eq. (5)]

$$1 = \int_0^{\xi_f} \beta(\xi')d\xi'. \tag{8}$$

It can be shown that, with

$$\Lambda \equiv \xi_f\sqrt{\bar{J}}, \tag{9}$$

Eq. (8) may be rewritten as

$$\sqrt{\bar{J}} = \Lambda \int_0^1 d\eta \sqrt{\frac{P_1(\eta)}{1-P_1(\eta)}}, \tag{10}$$

where

$$P_1(\eta) = \left[\frac{1}{2}\Lambda^2(\eta^2-\eta) + \gamma_i\beta_i + \eta(\gamma_f\beta_f - \gamma_i\beta_i)\right]^2. \tag{11}$$

Equation (10) determines the limiting current as a function of the biased gap voltage as follows. Suppose that we specify $\gamma_i$ and $\gamma_f$ (i.e., initial beam energy and gap voltage), the right-hand side of (10), denoted by $F(\Lambda)$, is a function of $\Lambda$. The critical value of $\sqrt{\bar{J}}$ is then given by the stationary value of F, and the critical amount of charge within the plates (i.e., $\xi_f$) is determined from (9) using those values of $\Lambda$ which yield stationary values of F.

In general, there are two critical currents $\bar{J}_{c1}$, $\bar{J}_{c2}$ for given values of $\gamma_i, \gamma_f$. The one with the lower value, $\bar{J}_{c1}$, is given by

$$\bar{J}_{c1} = \sqrt{2}\left\{f\left(\sqrt{\gamma_i\beta_i}\right) + f\left(\sqrt{\gamma_f\beta_f}\right)\right\} \tag{12}$$

where

$$f(z) = \int_0^z dt\, t^2/\sqrt{1-t^4} \tag{13}$$

whose properties are described in considerable detail in Ref. 9. Physically, $\bar{J}_{c1}$ is the minimum value of $\bar{J}$ which is required to retard some electron to zero velocity somewhere within the diode, at a given value of $\gamma_i, \gamma_f$ ($\gamma_f > 1$). The other critical current, $\bar{J}_{c2}$ is the maximum amount of current which can be transmitted, at a given value of $\gamma_i, \gamma_f$. At the moment, we have not found an analytic solution for $\bar{J}_{c2}$. Shown in Fig. 6 are the values of $\bar{J}_{c1}$ and $\bar{J}_{c2}$ as a function of the gap voltage $V_g = V_i$ when $\gamma_i = 2$. Also shown in Fig. 6 is $\xi_f$ corresponding to $\bar{J}_{c2}$.

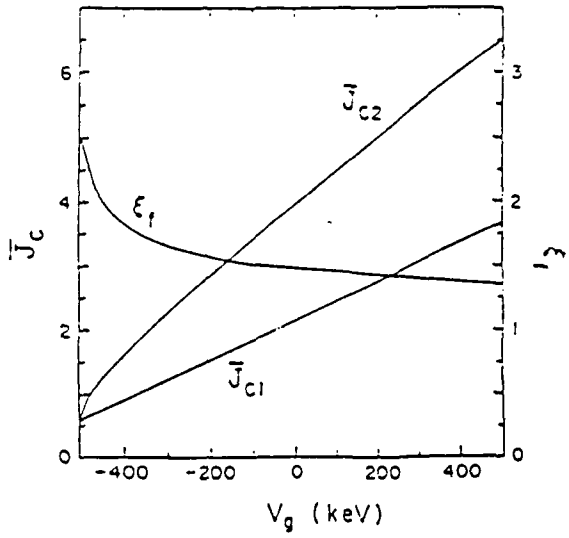



Fig. 6. The normalized limiting currents $\bar{J}_{c1}$, $\bar{J}_{c2}$ and the normalized transit time $\xi_f$ corresponding to $\bar{J}_{c2}$.

Finally, we comment on the extension of our analysis and the use of Fig. 6 for other realistic geometries. The crucial quantity is the current scale, $I_s$, which enters in the definition of the normalized current $\bar{J}$. In general, we write

$$\bar{J} = \frac{I}{I_s} \tag{14}$$

where

$$I_s = C(m_o c^2/e)/T, \tag{15}$$

and C is the capacitance (in vacuo) and T is the time required for light to traverse the system. In the parallel plate system, $C = A_o \varepsilon_o/D$ and $T = D/c$, and the normalized current $\bar{J}$ in (14) is consistent with the one introduced in Eq. (3). It is of interest to note that the current scale $I_s$ introduced in (15) is also an adequate one to describe an entirely different system--that of a thin annular beam of radius $r_b$ drifting in a circular waveguide of radius $r_w$ and length $\ell$. In this geometry, $C = 2\pi\varepsilon_o \ell/\ell n(r_w/r_b)$ and $T = \ell/c$. Equation (15) then yields $I_s = 8.53$ kA/$\ell n(r_w/r_b)$, which is the current scale which enters repeatedly in our studies of this system. Finally, for the present rf extraction experiment, C is the capacitance at the extraction gap and $T = D/c$ where D is the gap length. [See Ref. 1 for the determination of C]. For C = 6 picofarad and D = 2 cm, $I_s = 46$ kA. If $\gamma_i = 2$ and $\gamma_f = 1$, Fig. 6 gives $\bar{J}_{cr2} = \bar{J}_{cr1} = 0.55$ and $I_o = I_s \bar{J}_{cr2} \cong 25$ kA. Note that this value of 25 kA is very close to the peak current observed in the experiment.

D. Transit Time Effects Across A Finite Gap

Transit time effects, which are ignored in the previous section, are now considered. These effects are well-known for the case of a tenuous beam. Here we extend the classical analysis for an IREB. The estimates given here show that the

space charge effects are significant if the beam current is a sizable fraction of the limiting current.

For our geometry of an annular beam, the transit time effect can be analyzed by solving the equation

$$\left(\frac{\partial}{\partial t} + v\,\frac{\partial}{\partial z}\right)^2 S = \frac{\bar{\sigma}_0}{\gamma^3}\left(c^2\,\frac{\partial^2}{\partial z^2} - \frac{\partial^2}{\partial t^2}\right) S + \frac{eE_z(z)}{m_0\gamma^3}\sin\omega t. \tag{16}$$

In this equation, S is the (nonlinear) displacement of an electron at position z at time t and $\bar{\sigma}_0 = I_0/(I_s\beta_0)$. The last term in the right-hand side of this equation represents the modulating electric field $E_z(z)$ at the gap, and the remaining terms on the right-hand side represent the collective forces due to the space charges of the beam. We shall assume that $E_z(z)$ is a nonzero constant for $0 < z < D$ and is zero elsewhere. The classical transit time effect is deduced from (16) if we set $\bar{\sigma}_0 \to 0$.

A linearized study of Eq. (16), to be published elsewhere, shows that the electrons, as they cross the gap, experience an equivalent electric field which is reduced by a factor

$$M = M_c\,|\cos\phi| \tag{17}$$

where $M_c \equiv [\sin(\omega D/2v_0)]/(\omega D/2v_0)$ is the well-known transit time factor for a weak beam and $\phi = \alpha_u\delta\omega D/v_0$. Here, $\alpha = I_0/(I_s\gamma_0^3\beta_0)$, $\alpha_u = (\alpha^2 + \alpha/\gamma_0^2)^{1/2}/\beta_0$, $\delta = \beta_0^2/(\beta_0^2 - \alpha)$.

For D = 2 cm, $\omega = 2\pi \times 1.3$ GHz, $v_0 = 0.8\,c$, $\alpha/\beta_0^2 = 0.5$ (beam current is 50 per cent of the limiting current), then $M_c = 0.97$ and $|\cos\phi| = 0.733$. For d = 3 cm and the remaining parameters unchanged, $M_c = 0.95$ and $|\cos\phi| = 0.434$. There is a substantial reduction in the effective gap voltage which the beam experiences due to space charge effects. Thus, in the energy distributions of the electrons [cf. Fig. 3], the peak energy is not necessarily equal to the sum of the peak gap voltage and the peak kinetic energy.

## E. Relationship Between Magnetic Field $B_{1\theta}$ and $I_1$

The value of $B_{1\theta}$ measured at the cylindrical waveguide wall ($r_w$) depends on the beam current $I_1$ in a rather complicated manner if the beam current is highly modulated. The DC relationship $B_{1\theta} = \mu_0 I_1/2\pi r_w$ no longer holds. How one should interpret the modulated current $I_1$ from the measured value of $B_{1\theta}$ requires a more careful consideration, to be given here.

Consider a thin annular electron beam of radius $r_b$ carrying an axial current $I_1(z,t) = I_1 \exp(j\omega t - jkz)$ where $I_1$ is a constant and $\omega, k$ are constants. This annular electron sheet gives rise to a value of $B_{1\theta}$ at $r = r_w$, related to $I_1$ by

$$I_1 = B_{1\theta} \times 2\pi r_w \times \frac{J_0(pr_w)}{J_0(pr_b)} \tag{18}$$

where

$$p^2 \equiv \frac{\omega^2}{c^2} - k^2$$

and $J_o$ is the Bessel function of order zero. In the DC limit, $\omega \to 0$, $k \to 0$ and $p \to 0$, (18) gives

$$I_1(DC) = H_{1\theta} \quad \times 2\pi r_w \tag{19}$$

which is the well-known relation. This relationship has been frequently used to infer the beam current from B-dot loop measurements.

In the present experiment, the beam current $I_1$ is a superposition of the fast and slow space charge waves. Since we are considering the relationship between $I_1$ and $B_{1\theta}$ through Maxwell's equations (which are linear) we may separately consider the fast wave component and the slow wave component. For the present geometry $\omega$ and k are governed by the dispersion relation[10]

$$(\omega - kv_o)^2 = \alpha\,(k^2c^2 - \omega^2) \tag{20}$$

which yields $k_f, k_s$, the wave number of the fast and slow waves.

Let us denote

$$\varepsilon \equiv \frac{J_o(pr_w)}{J_o(pr_b)} \equiv \frac{I_o(\Gamma r_w)}{I_o(\Gamma r_b)} \tag{21}$$

where $\Gamma^2 \equiv - p^2$, and $I_o$ is the modified Bessel function of order zero. Referring to Eq. (18) we see that if $\varepsilon > 1$, the true value of $I_1$ would be greater, by a factor of $\varepsilon$, than the value inferred from $B_{1\theta}$ under the assumption of the DC relationship (19). Of interest are the values $\varepsilon_{f,s}$ corresponding to the fast and slow waves. Useful expressions may be obtained for the low current limit ($\alpha \to 0$) and in the high current limit, as the limiting current is approached ($\alpha/\beta_o^2 \to 1$).

In the limit of very weak current, $\alpha \to 0$, both $k_f$ and $k_s$ approach

$$k_s = k_f = \omega/v_o$$

by Eq. (20). Thus,

$$\Gamma_f = \Gamma_s = \sqrt{k_{f,s}^2 - \omega^2/c^2} = \frac{\omega}{c}\left(\frac{1}{\beta_o\gamma_o}\right) = \frac{2\pi}{\lambda}\left(\frac{1}{\beta_o\gamma_o}\right)$$

and we have

$$\varepsilon_s = \varepsilon_f = \exp\left\{\frac{2\pi}{\lambda}\left(\frac{1}{\beta_o\gamma_o}\right)(r_w - r_b)\right\}. \tag{22}$$

In obtaining (22), we have used the asymptotic expressions for $I_0(\Gamma r_w)$. For $\lambda$ = 23 cm, $r_w - r_b$ = 0.4 cm, $\beta_{0z}$ = 1.8, the enhancement factor $\varepsilon_f$, $\varepsilon_s$ are approximately equal to 1.063. Thus, for very low DC current, one may use the DC relationship, the error being of the order of six per cent. This is in good agreement with our simulation using the CONDOR Code.

When the limiting current is approached, $k_f \to \omega(1 + \beta_0^2)/2v_0$. Then $\Gamma_f \to (\omega/c)(1 - \beta_0^2)/2\beta_0 = \pi/(\lambda\gamma_0^2\beta_0)$ and

$$\varepsilon_f = \exp\left\{\frac{\pi}{\lambda\gamma_0^2\beta_0}\left(r_w - r_b\right)\right\}. \tag{23}$$

In our experiment, $\varepsilon_f = 1$ to within three per cent. Thus, the fast wave component of the current modulation would give rise to $B_{1\theta}$ with a magnitude close to the DC case.

The above conclusion does not apply to the slow wave component of the current modulation when the limiting current $I_c$ is approached. After some manipulation, we find

$$\Gamma_s \equiv \sqrt{k_s^2 - \omega^2/c^2} = \frac{2\omega}{c}\frac{\beta_0}{(1 - I_0/I_c)} = \frac{4\pi}{\lambda}\frac{\beta_0}{(1 - I_0/I_c)},$$

as $I_0 \to I_c$. Thus,

$$\varepsilon_s = \exp\left\{\frac{4\pi}{\lambda}\frac{\beta_0}{(1 - I_0/I_c)}(r_w - r_b)\right\}, \tag{24}$$

which gives a large value if $I_0 \to I_c$. The presence of the slow wave component may lead to an underestimation of the current modulation (when the limiting current is approached), if one applies only the DC relationship (19) to the measured value of $B_{1\theta}$. In fact, one might even be tempted to use I, the instantaneous current, in place of $I_0$ in Eq. (24) when the beam is highly modulated.

For example, take $r_b$ = 6.3 cm, $r_w$ = 6.8 cm (c.f. Fig. 1), $\beta_0$ = 0.8, $\lambda$ = 23 cm, $I/I_c$ = 0.75, then $\varepsilon_f$ = 1 and $\varepsilon_s$ = 2.4. If we further assume that the fast and slow wave components of the current modulation are about equal, then $I_1 = B_{1\theta} \times 2\pi r_w \times 2\varepsilon_f\varepsilon_s/(\varepsilon_f + \varepsilon_s) = B_{1\theta} \times 2\pi r_w \times 1.4$. Thus, the use of (18) may underestimate the modulated current by as much as forty per cent - a point suggested by our experiment[1] and consistent with our simulations.

F. Magnetic Insulation in a Coaxial Geometry

The ability to extract high power microwaves depends critically on the suppression of electron and ion flows across the coaxial line by the externally imposed axial magnetic field $B_0$. The following estimates show that the axial magnetic field (~ 10 kG) used in the current experiment is sufficient to provide the required insulation.

Since the rf frequency, $\omega$, is considerably less than the relativistic electron cyclotron frequency, we may treat the rf fields as essentially static as far as

electronic motions are concerned. Under this assumption, the relativistic Hull cut-off condition used in magnetron studies would give the magnetic field required for insulation. For a coaxial line of inner radius a and outer radius b the required magnetic field to provide magnetic insulation is given by[11]

$$B_o(kG) = \frac{1.07\ kG}{D(cm)}\left\{\left(\frac{Z_o}{10\Omega}\right)\left(\frac{I}{10\ kA}\right) + 0.098\left[\left(\frac{Z_o}{10\Omega}\right)\left(\frac{I}{10\ kA}\right)\right]^2\right\}, \tag{25}$$

where $Z_o = (60\Omega) \times \ell n(b/a)$ is the characteristic impedance of the coaxial line, I is the current flowing along it and $D \equiv (b^2 - a^2)/2a$ is the equivalent gap width. If a = 6.8 cm, b = 11.5 cm, then D = 6.3 cm and $Z_o = 31.53\ \Omega$. For a maximum current of $I_o + I_1 = 30$ kA, say, $B_o = 0.73$ kG. The imposed magnetic field is 10 kG, which is about 14 times higher than $B_o$, the value required for magnetic insulation. Thus, magnetic insulation against electron flow is virtually guaranteed.

For the ions, their cyclotron frequencies $\omega_{ci}$ are much smaller than the rf frequency, we may not use the static formula. Instead we solve the equation of motion and place an upper bound on their displacement across the field line.

The ions satisfy the nonrelativistic force law, $m_i d\vec{v}/dt = e(\vec{E} + \vec{v} + \vec{B}_o)$ where, for simplicity, we ignore the rf magnetic field in comparison with the external magnetic field, and E is the radial rf electric field. One can readily show that, if x(0) = 0, and x(0) = 0,

$$|x(t)| < eE_o/m_i\omega_{ci}|\omega - \omega_{ci}|. \tag{26}$$

For $m_i = 1840\ m_e$, $B_o = 10$ kG, $\omega_{ci} = 0.06$ GHz, and $\omega = 2\pi \times 1.3 \times 10^9\ sec^{-1}$, then (26) gives $|x| < 0.78$ mm if $E_o < 300$ kV/5 cm. Thus, magnetic insulation for the ions are also assured.

## ACKNOWLEDGMENT

This work was supported by the Strategic Defense Initiative Organization, Office of Innovative Science and Technology and managed by the Harry Diamond Laboratory.

## REFERENCES

1. M. Friedman, V. Serlin, Y. Y. Lau and J. Krall, the preceding paper in these proceedings.
2. M. Friedman and V. Serlin, IEEE Trans. Electr. Insul. EI-23, 51 (1988).
3. M. Friedman, J. Krall, Y. Y. Lau and V. Serlin, J. Appl. Phys. 64, 3353 (1988).
4. J. Krall and Y. Y. Lau, Appl. Phys. Lett. 52, 401 (1988).
5. Y. Y. Lau, J. Appl. Phys. 62, 351 (1987).
6. H. Jory and A. Trivelpiece, J. Appl. Phys. 40, 3924 (1969).
7. V. S. Voronin, Yu T. Zozulya and A. N. Lebedev, Sov. Phys. Tech. Phys. 17, 432 (1972).
8. M. Friedman and V. Serlin, J. Appl. Phys. 58, 1460 (1985).
9. Y. Y. Lau, J. Appl. Phys. 61, 36 (1987).
10. R. J. Briggs, Phys. Fluids 19, 1257 (1976).
11. See, e.g., Eq. (6.5) on p. 217 of R. B. Miller, "Physics of Intense Charge particle Beams", Plenum Press, New York (1982).

# APPENDIX R

## Simulation Studies of Particle Acceleration Powered by Modulated Intense Relativistic Electron Beams

**Naval Research Laboratory**

Washington, DC 20375-5000



NRL Memorandum Report 6425

# Simulation Studies of Particle Acceleration Powered by Modulated Intense Relativistic Electron Beams

J. KRALL*, V. SERLIN, M. FRIEDMAN AND Y. Y. LAU

**Science Applications Intl. Corp., McLean, VA*

*Plasma Theory Branch*
*Plasma Physics Division*

March 14, 1989

Approved for public release; distribution unlimited.

## CONTENTS


| | | |
|---|---|---|
| I. | INTRODUCTION | 1 |
| II. | FIELDS IN THE RF STRUCTURE | 3 |
| III. | NUMERICAL SIMULATIONS | 5 |
| IV. | NUMERICAL EFFECTS | 10 |
| V. | CONCLUSIONS | 11 |
| | ACKNOWLEDGEMENTS | 12 |
| | REFERENCES | 13 |
| | DISTRIBUTION LIST | 29 |

# SIMULATION STUDIES OF PARTICLE ACCELERATION POWERED BY MODULATED INTENSE RELATIVISTIC ELECTRON BEAMS

## I. Introduction

Future progress in accelerators and their applications may depend critically on the development of physical mechanisms capable of generating high voltage gradients. It has been shown that a high electric field can be established in rf structures by modulated intense relativistic electron beams (MIREBs) of power greater than $10^9$ W and that such a beam may be used as an rf source to power an accelerator, obtaining voltage gradients as high as 100 MeV/m or greater.[1,2] Such accelerators, in which a low power, high current beam interacts via a metallic structure with a low current beam to obtain very high energies have been suggested by an number of authors, including Voss and Weiland,[3] in addition to the accelerator outlined in Ref. 2. Wakefield acceleration has recently been observed in experiments carried out by Figueroa et al.[4]

Theoretical discussions of accelerators powered by MIREBs[2,5] have suggested unusual properties that may be present in the following devices: Firstly, the demonstrated conversion of the high dc power of an intense relativistic electron beam (IREB) to high rf power in the MIREB by the use of tuned radial cavities implies that the MIREB may be coupled to an rf structure so as to drain significant power (> 1 GW) from the beam at high efficiency and, secondly, geometrical effects may allow for sizeable variations in efficiency, field gradient, and coupling between the high power MIREB and the rf structure with small changes in the experimental parameters.

In the present paper we study these issues via an axisymmetric particle simulation using the CONDOR[6] code, which has been previously and successfully applied to the physics of such intense beams.[7] The accelerator configuration to be studied is similar to that outlined in Ref. 2 and is pictured in Fig. 1.

Manuscript approved December 28, 1988.

(1) An annular IREB generator injects a beam of radius $r_b \simeq 6.3$ cm, current $I_o = 16$ kA, energy $E_{inj} = 500$ keV and duration $T = 150$ ns into a drift tube of radius $r_w = 6.8$ cm. The IREB is guided by an axial field, $B_o = 10$ kG.

(2) The IREB is fully modulated at $f \simeq 1.3$ GHz by a pair of tuned radial cavities, the first of which is externally driven by a low level rf source (magnetron). The modulation region is immersed in the axial magnetic field.

(3) The MIREB is guided into a cylindrical cavity of radius 9.6 cm. The cavity is loaded with thin disks of radius 9.0 cm and separation 1.88 cm. The MIREB, which has a frequency of modulation corresponding to the desired mode of the rf structure, is terminated at the first disk. A resonant interaction occurs at the gap defined by the end of the drift tube and the first disk of the rf structure, transferring energy from the beam to the rf structure.

(4) An emitter, located on-axis on the surface of the first disk, emits electrons when the fields within the structure reach a sufficiently high value. This secondary beam is then accelerated by the rf fields, guided by the axial magnetic field.

The modulation stage of this device has been studied in some detail for a 1.9 cm radius annular beam in a 2.4 cm radius drift tube[5,7,8] and has been successfully repeated at $I_o = 16$ kA and $r_b = 6.3$ cm in a drift tube of radius 6.8 cm.[9]

In the present paper, we will investigate the coupling between the modulated beam and the rf structure and the subsequent acceleration of the secondary beam and shall proceed as follows. In Sec. II, we give theoretical background on the expected field gradients in the rf structure, define a transformer ratio for this acceleration scheme, and present

numerical results from the Superfish[10] code on the modes of the rf structure. In Sec. III, which contains the main results of this paper, we will simulate particle acceleration and will see that power in excess of 1 GW may be transferred between the primary and secondary beams. Here we will consider the effect of geometrical variations on the beam-rf structure coupling and on the transformer ratio. Section IV will contain a detailed discussion of the numerical issues that effect the ability of these simulations to correctly predict experimental results. Section V concludes.

## II. Fields in the RF Structure

The process of energy transfer between the primary and secondary beams in this accelerator resembles that of the wakefield schemes described in Refs. 3 and 4 in the use of fields excited by the primary beam in a disk loaded structure. In these schemes, the two beams travel colinearly such that the transformer ratio is defined as $R = E_2/E_1$ where $E_1$ is the magnitude of the decelerating field experienced by the primary beam and $E_2$ is the accelerating gradient experienced by secondary beam. In the present case, however, the interaction of the primary beam with the rf structure takes place only as the beam traverses the gap near the first disk of the rf structure, where the beam is terminated, while the secondary beam is accelerated along the entire length of the rf structure. The transformer ratio is then defined as

$$R = \frac{\langle E_{axis} \rangle L}{E_{gap} d} , \qquad (1)$$

where d is the gap length, L is length of the rf structure, $E_{gap}$ is the decelerating field in the gap (assumed spatially constant) and $\langle E_{axis} \rangle$ is the average field experienced by the accelerated secondary beam particles.

This geometry has been modelled as an interaction between a sinusoidally varying current source and a transmission line consisting of a series of R-L-C circuit elements.[2] This model exhibited many features that have been found in the numerical simulations, but such a model has a limited predictive capability.

Some insight into this problem may be obtained by assuming that the disk structure will behave like a resonant cavity. The normal modes of this cavity may be solved for by neglecting the interaction region at the gap.[2] For the purposes of this discussion, however, we may consider the only fundamental mode of a disk-loaded cavity of length $L = n\lambda/2$ where $\lambda$ is the wavelength of the rf and n is a positive integer. In this case, the z-component of the electric field of the fundamental mode varies sinusoidally along the axis and radially as

$$E_z(r)/E_z(r=0) = J_0(kr)/J_0(r=0) \ , \qquad (2)$$

where $J_0$ is a Bessel function and $k = 2\pi/\lambda$. In the analysis of Ref. 2, it was conjectured via a heuristic argument that the ratio of the field experienced at the gap by the primary beam, $r = r_b$, to the peak field on-axis, $r = 0$, would follow this radial variation. This suggests that the radial position of the primary beam in relation to the mode structure within the rf cavity is of some importance for the strength of the interaction, the efficiency, and the obtainable transformer ratio.

The normal modes for a given axisymmetric cavity may be calculated numerically by using the Superfish[10] code. The Superfish result for one such cavity is shown in Fig. 2. Here, a disk loaded cavity of length $L = \lambda$

is used and the gap region is included. Except for the metallic boundary condition imposed at the right-hand wall, this geometry closely resembles that of Fig. 1, where the right-hand boundary is an open drift tube for which the 1.33 GHz cavity mode is below cutoff. This result and a series of similar results, where the location of the right-hand wall was varied, show that the expected cavity mode is obtained.

## III. Numerical Simulations

The simulation geometry (Fig. 3) consists of a short drift tube region with radius $r_w$ = 6.8 cm, a gap of length d = 1.57 cm and a disk-loaded structure of length L = 22.2 cm $\simeq \lambda$, where $\lambda = c/f$, and f = 1.27 GHz is the frequency of the accelerating mode of the cavity, and was determined numerically.

The primary beam is injected from the left-hand wall with radius $r_b$ = 6.4 cm, energy $E_{inj}$ = 2.0 MeV and current $I_{inj}(kA) = g(t)$ $[16 + 8\sin(2\pi ft)]$, where g(t) is an envelope function that increases linearly from zero to unity during the time $0 < t < 15$ ns and remains constant thereafter. At a selected time, $t > 15$ ns, the secondary beam with $I_2$ = 10 Amperes and $E_2$ = 0.1 MeV is injected continuously from the center of the first disk and is accelerated along the axis by the rf fields. Each simulation continues until t = 30 ns.

Note that in order for the cavity-mode approximation of Sec. II to be of use the parameters L, $v_g$ and T must be such that $L/v_g \ll T$, where $v_g$ is the group velocity of E-M radiation within the disk-loaded structure and T is the duration of the primary beam pulse. If this relation is not satisfied, the disk structure will behave, not like a cavity, but like a travelling wave tube. In the numerical geometry of Fig. 3, we have arranged the separation between the outer disk edges and the cavity wall so

that $v_g/c \approx 1$. In this case the condition, $L/v_g \ll T$, is easily satisfied within the 30 ns duration of the simulations.

Several differences between this configuration and that of a practical experiment must be noted.

(1) In a practical experiment the disk structure would be longer so as to obtain higher energies in the secondary beam. Another difficulty is that the high group velocity of the E-M waves in the simulation structure and its short length and small volume would allow rf fields to build up so quickly that they might reflect the primary beam in an actual device.

(2) An actual device would have support rods to hold the disks in place. These would also provide a path for the dc current of the primary beam. Because such supports cannot be modelled axisymmetrically and because we require a dc current path, we inserted a center conductor to serve this purpose. It will be seen in Sec. IV, below, that the presence of this center conductor does not significantly effect the results.

(3) In the simulation geometry, the left-hand boundary is a metallic wall. In an actual device and in Fig. 1, this boundary is an open drift tube, for which the 1.27 GHz frequency of the rf field is below cutoff. The metal boundary of the simulations will have the similar effect of reflecting incident radiation at this frequency, but is clearly not the same.

(4) The simulation structures are defined on a grid such that the effective skin depth of the material is one grid cell ($\Delta r = 0.2$ cm, $\Delta z = 0.3133$ cm), making the cavity extremely lossy, with Q of order 10. A typical value for a metallic structure is of order 1000.

Figures 4 and 5 show the z-component of the electric field plotted vs. time in the gap and on-axis, respectively, for a simulation with parameters

described above. The plot on-axis is taken at the spatial location of the peak electric field. We see that the fields increase continuously, reaching values of 56.3 MV/m at the gap and 94.2 MV/m on-axis before the simulation is halted. The plot of the gap electric field shows evidence of a weak, lower frequency mode which may have been excited by the increase in dc current from t = 0 to t = 15 ns. The rf cavity mode, as expected, is a standing wave, varying sinusoidally in z and as a Bessel function, $J_0(kr)$, radially. This is seen in Figs. 6 and 7 which show $E_z$ vs. z and $E_z$ vs. r, respectively, at fixed time.

For the simulation shown, the secondary beam was injected continuously for t > 17 ns with $I_2$ = 10 A and $E_2$ = 0.1 MeV and was bunched and accelerated by the rf fields. This acceleration may be observed in Fig. 8, which plots particle positions in phase space, $\gamma\beta c$ vs. z, where $\beta$ is the axial particle velocity normalized to c and $\gamma = (1 - \beta^{-2})^{-1/2}$. The particle positions, plotted at fixed time at intervals of 0.2 ns, show a maximum energy increase of 8.60 MeV over 22.2 cm to give an accelerating gradient of 39.2 MV/m. With this result and the observed 56.3 MV/m at the gap, we see that for this case a transformer ratio R = 9.85 has been achieved.

Several interesting aspects of this simulation should be noted.

(1) The build-up of rf in the cavity is of a transient nature. Were the simulation not halted at t = 30 ns, the field amplitudes would increase beyond the observed 94.2 MV/m until limited by reflection of the primary beam. In an actual device, other limitations may include breakdown in the rf structure, losses due to the Q of the cavity, termination of the primary beam, or acceleration of a sufficiently high quantity of secondary beam current.

(2) The conjectured relationship between the gap field, $E_{gap}$, and the peak axial field, $E_{axis}$, which was discussed in connection with Eq. (2) above, does not hold. Here, we have $E_{axis}/E_{gap} = 1.67$ and $J_0(0)/J_0(kr_b) = 2.51$. While the conjectured relation does not hold in a precise way, it may still be useful as a qualitative guide. We sill expect that an increase in $J_0(0)/J_0(kr_b)$, obtainable by increasing $r_b$, will result in an increased $E_{axis}/E_{gap}$. This will be investigated below.

(3) The electric field of 56.3 MV/m that is observed across the 1.57 cm gap indicates that the primary beam loses 0.883 MV as it traverses the gap. This energy loss is verified in the phase-space plots of Fig. 8, where the primary beam particles, which have $0 < z < 10$ cm, are deflected in momentum space by the gap voltage. This indicates a power drain of 7.07 GW at 1.27 GHz and is sufficient power to accelerate secondary beam current in the 500 A range over this short distance. With a longer accelerating structure, lower currents may be accelerated to higher energies.

To test our conjecture that higher current may be accelerated to obtain high power in the secondary beam, we repeated the simulation of Figs. 4-8 with the secondary beam current increased to 200 A. We found $E_{gap} = 51.6$ MV/m and $E_{axis} = 91.3$ MV/m. Secondary beam particles, injected at 0.1 MeV, were accelerated to 8.02 MeV to give $\langle E_{axis} \rangle = 35.7$ MV/m so that $R = 9.78$. A comparison of these results with those of Figs. 4-8 indicates that the 200 A secondary beam does not significantly load the cavity. We also see that 1.58 GW of rf power has been transferred from the primary to the secondary beam.

While the supposed relationship between $E_{gap}$ and $E_{axis}$ discussed in connection with Eq. (2) has already been proven imprecise, the possibility of obtaining very high transformer ratios as the primary beam radius

approaches $r_b = j_{0,1}/k$, where $J_0(j_{0,1}) = 0$, remains intriguing. We investigated this by repeating the simulation of Figs. 4-8 with $r_b = 8.0$ cm. This necessitated an increase in the drift tube radius to $r_w = 8.4$ cm, a change in geometry which shifted the resonance slightly to 1.34 GHz. At this frequency, $j_{0,1}/k = 8.57$ cm. The results of the simulation are shown in Figs. 9-12. We found field gradients of $E_{gap} = 13.5$ MV/m and $E_{axis} = 34.4$ MV/m. Particle plots (not shown) indicated that the secondary beam particles, injected at 0.1 MeV, were accelerated to 3.27 MeV to give $\langle E_{axis} \rangle = 14.3$ MV/m so that R has been increased to 15.0. Figures 9-12 contain the following results:

(1) With $r_b = 8.0$, we have $E_{axis}/E_{gap} = 2.55$, an increase from the value of 1.67 that was obtained at $r_b = 6.4$ cm, but not nearly as large as $J_0(0)/J_0(kr_b) = 11.9$. Note that the transformer ratio was similarly increased, from 9.85 to 15.0. As stated above, we have only a qualitative ability to predict results as $r_b$ is changed.

(2) Figures 9 and 10 show that the build-up of rf fields in the cavity is of a transient nature, as before, but much lower amplitudes are reached at t = 30 ns than in the $r_b = 6.4$ cm case. This indicates that as the $E_{axis}/E_{gap}$ ratio is increased, the interaction between the primary beam and the rf structure is weakened. This occurs because, at a higher transformer ratio, the same accelerating field in the rf structure gives a lower decelerating field at the gap and less energy is drained from the primary beam per cycle. The low frequency excitation of the cavity, apparent in Figs. 4 and 9, is unchanged, making it more prominent in the latter case where the rf fields are weaker.

(3) The peak electric field on-axis, plotted in Fig. 10, appears to be saturating as the simulation is terminated. It is not clear whether this is a result of the low Q of the numerical structure or if we are driving

the cavity slightly off resonance. We can also see, from Figs. 11 and 12, that the mode structure is unchanged from the previous cases.

Finally, we must note that at $r_w$ = 8.4 cm, f = 1.34 GHz is very close to the cutoff frequency, $f_c = j_{0,1}c/2\pi r_w$ = 1.37 GHz. In a practical device, it may not be possible to increase $r_b$ and $r_w$ to such large values at this frequency.

## IV. Numerical Effects

To understand the applicability of the simulation results to an actual device, it is necessary to examine the differences between such a device and the numerical model. Many of these have already been addressed. One which was not is the addition of a center conductor to the drift tube region of the simulation geometry, which provides a path for the dc component of the primary beam current. The significance of this addition may be examined by considering equivalent circuit elements for the rf structure, a capacitive load, and the center conductor, an inductive load. These elements are connected in parallel and are driven by an oscillatory current source. The inductance of a coaxial line varies as $L \propto \log(r_w/r_c)$, where $r_c$ is the radius of the center conductor. The equivalent circuit model suggests that an increase in $r_c$ will lower the inductive load relative to the capacitive load, lowering the voltage across the capacitance. This was verified by increasing the radius of the center conductor to $r_c$ = 5.0 cm in the $r_b$ = 6.4 cm case. This had the effect of lowering the field amplitudes in the gap and on-axis by a factor of 1.7, but left the transformer ratio unchanged. Conversely, the circuit model suggests that for sufficiently small values of $r_c$, the inductance will be so high that it will behave as an open circuit. In this ideal case, the entire load lies across the capacitance.

To discover whether or not the radius of the center conductor is sufficiently small, we repeated the $r_b$ = 6.4 cm simulation with the dc component of the primary beam current removed, so that $I_{inj}$(kA) = g(t)8sin(2πft), where g(t) is an envelope function as before. This was accomplished by superimposing an appropriately modulated electron beam with a dc positron beam, and allowed us to compare results with and without the presence of the center conductor. With the center conductor, we found $E_{gap}$ = 56.1 MV/m, $E_{axis}$ = 92.6 MV/m and $\langle E_{axis} \rangle$ = 38.8 MV/m, comparable to the results of Figs. 4-8. Without the center conductor, we found $E_{gap}$ = 60.0 MV/m, $E_{axis}$ = 103.6 MV/m and $\langle E_{axis} \rangle$ = 41.5 MV/m. This indicates that the presence of the center conductor reduces the fields by 5-10 %.

## V. Conclusions

We have demonstrated that high fields and transformer ratios can be supported by a MIREB-driven accelerator, with several interesting properties. The most crucial of these is that the MIREB is so strongly coupled to the disk-loaded rf structure that power in excess of 1 GW may be transferred from the primary to the secondary beam, despite the low Q of the numerical structure.

We have found that the build-up of the rf fields in the structure is transient by nature and, in the simulations, peak accelerating gradients were limited only by the brevity of the simulations. In an actual device, these fields will continue to increase in amplitude until limited by breakdown in the rf structure, reflection of the primary beam at the gap or by termination of the primary beam pulse.

We have also considered variations of the geometry to successfully obtain an increased transformer ratio, but at the cost of weakening the coupling between the primary beam and the rf structure. We have also found

that the conjectured relationship between the decelerating field experienced by the primary beam at the gap and the peak accelerating gradient on-axis, which is discussed in connection with Eq. (2), provides only a qualitative guide to these geometric variations. As the original conjecture, contained in Ref. 2, is heuristic in nature and pertains to an idealized physical model, this is not a surprising result.

Finally, the differences between these simulations and a practical experimental configuration have been discussed in some detail, suggesting that similar power levels, fields and transformer ratios may be obtainable experimentally.

## Acknowledgements

This work was supported by the Department of Energy under Contract No. DE-AI05-86-ER13585.

## References


1. M. Friedman and V. Serlin, Phys. Rev. Lett. 55, 2860 (1985).

2. M. Friedman and V. Serlin, Appl. Phys. Lett. 49, 596 (1986).

3. G. Voss and T. Weiland, Desy Report M82-10 and Desy Report M82079, 1982.

4. H. Figueroa, W. Gai, R. Konecny, J. Norem, A. Ruggiero, P. Schoessow and J. Simpson, Phys. Rev. Lett. 60, 2144 (1988).

5. M. Friedman, J. Krall, Y.Y. Lau and V. Serlin, J. Appl. Phys. 64, 3353 (1988).

6. CONDOR is an extension of the MASK particle code, discussed in A. Palevsky and A. Drobot, in Proceedings of the 9th Conference on Numerical Simulation of Plasmas, July 1980 (Northwestern University, Evanston, IL) (unpublished).

7. J. Krall and Y.Y. Lau, Appl. Phys. Lett. 52, 431 (1988).

8. Y.Y. Lau, J. Krall, M. Friedman and V. Serlin, IEEE Trans. Plas. Sci. 16-2, 249 (1988).

9. M. Friedman, V. Serlin, Y.Y. Lau and J. Krall, to be published.

10. K. H. Halbach and R. F. Holsinger, LBL report LBL-5040, 1976.

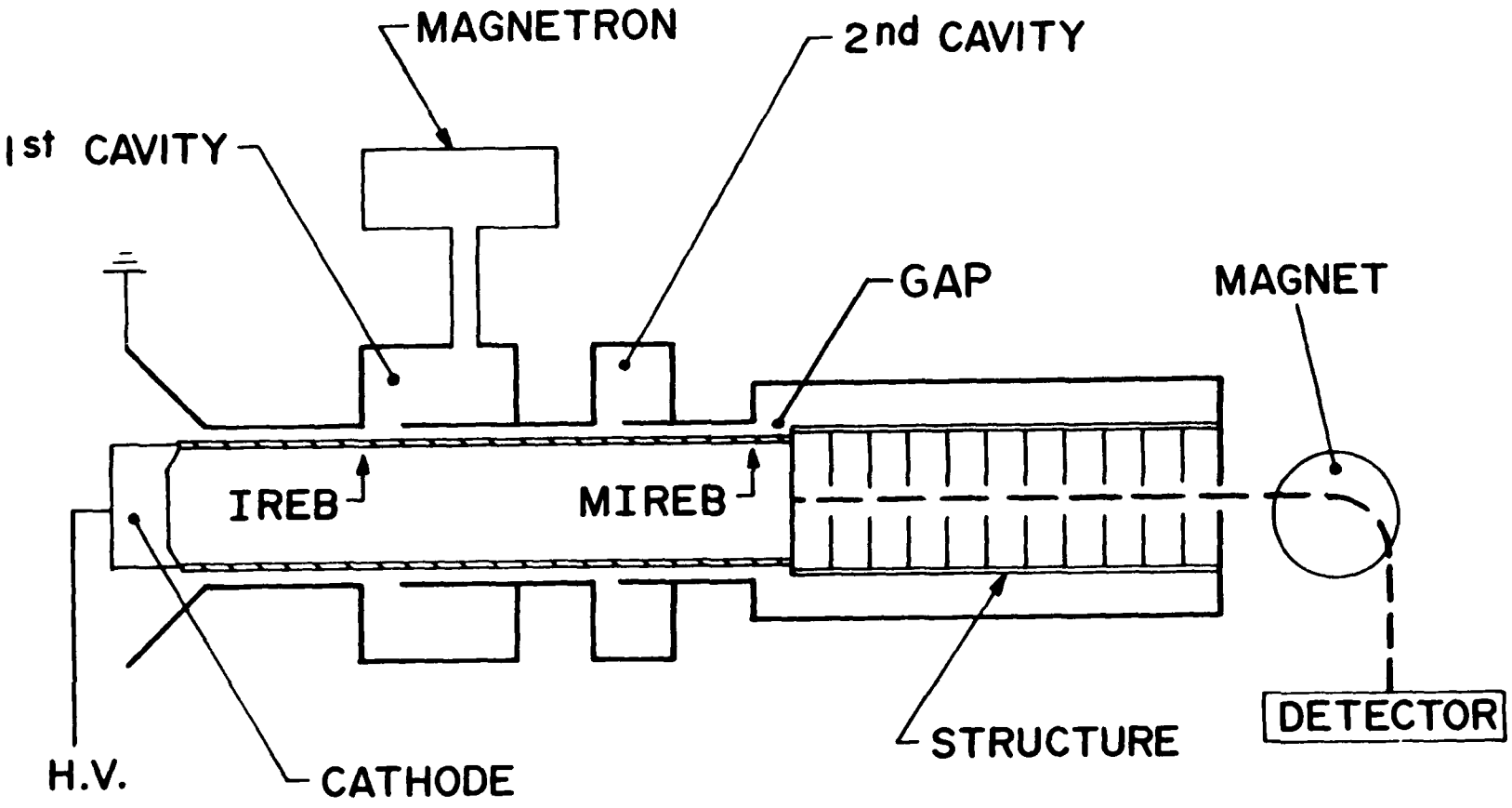



Fig. 1. MIREB-driven accelerator schematic.

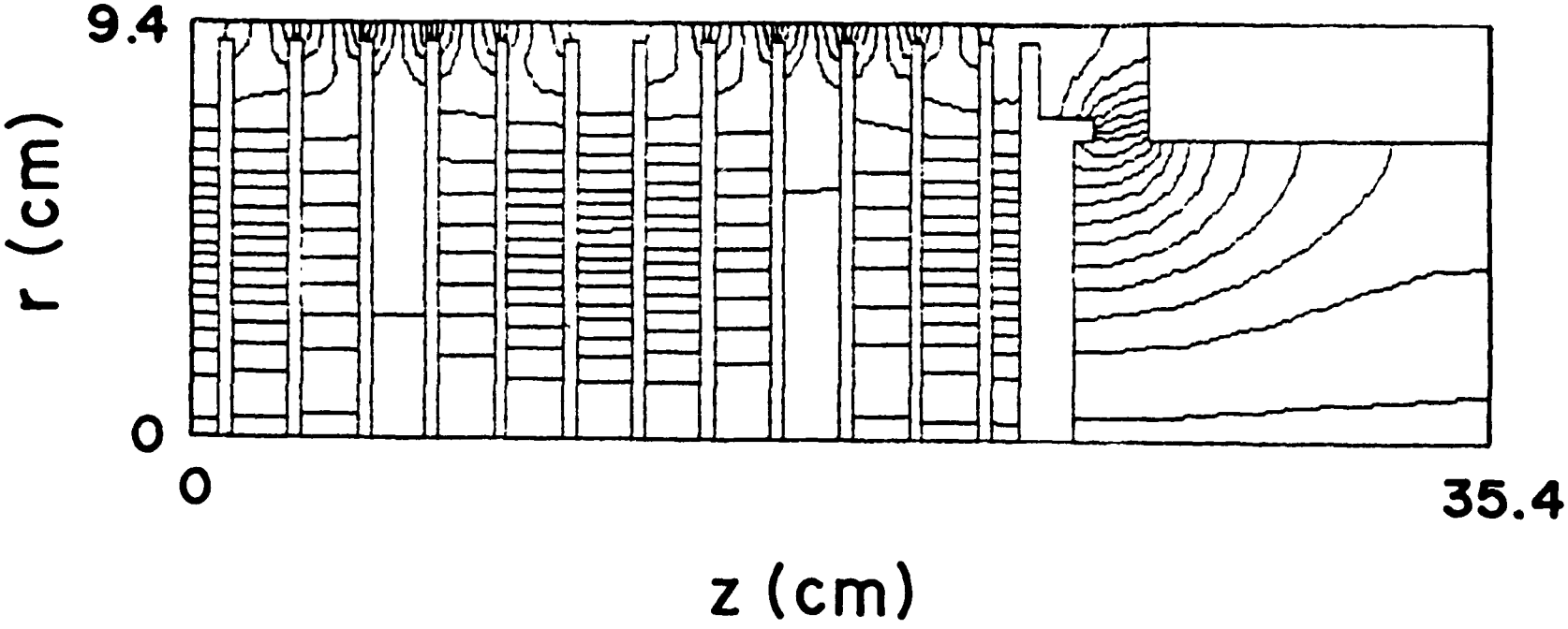



Fig. 2. Superfish result showing the electric field configuration of an rf structure cavity mode with frequency 1.33 GHz.

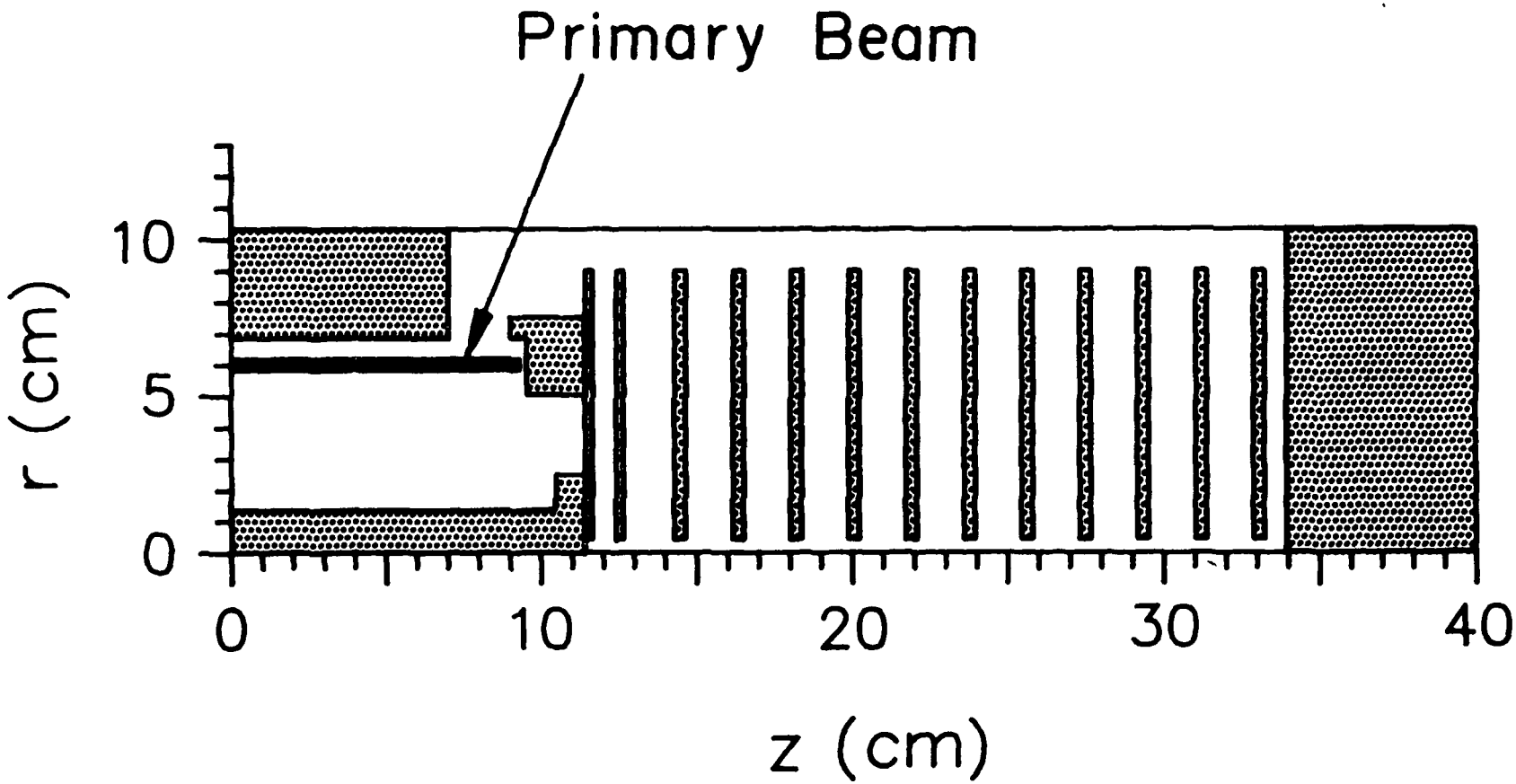



Fig. 3. Simulation geometry showing the primary beam and the disk-loaded rf structure. The primary beam enters the drift tube region from the left, passes near the gap at z ≈ 8 cm and is terminated at z ≈ 9 cm. The secondary beam is injected at z ≈ 12 cm and is accelerated along the axis.

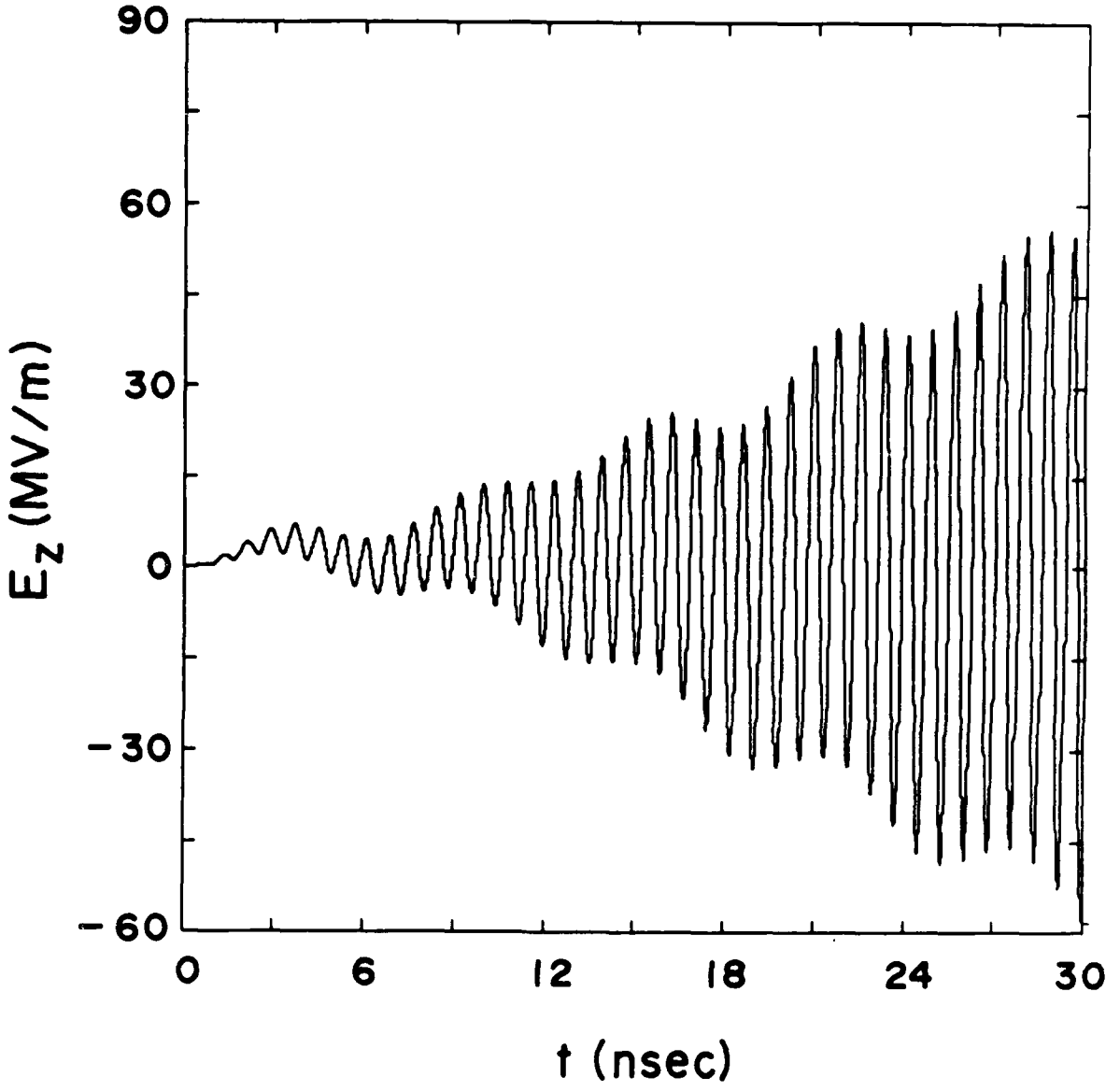



Fig. 4. $E_z$ plotted versus time at the gap for the $r_b$ = 6.4 cm case.

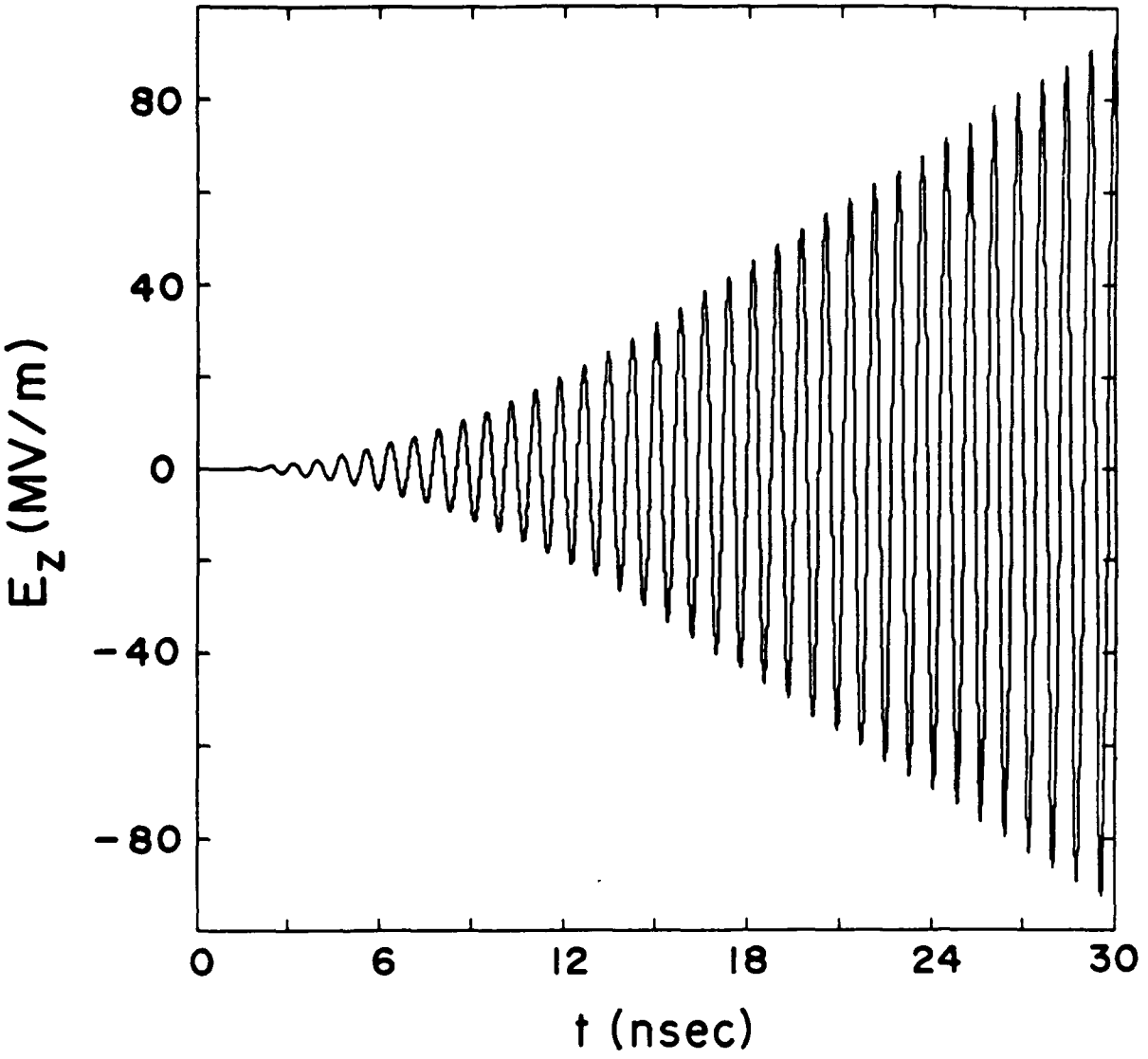



Fig. 5. $E_z$ versus time on-axis at z = 20.6 cm, near the point of peak axial field.

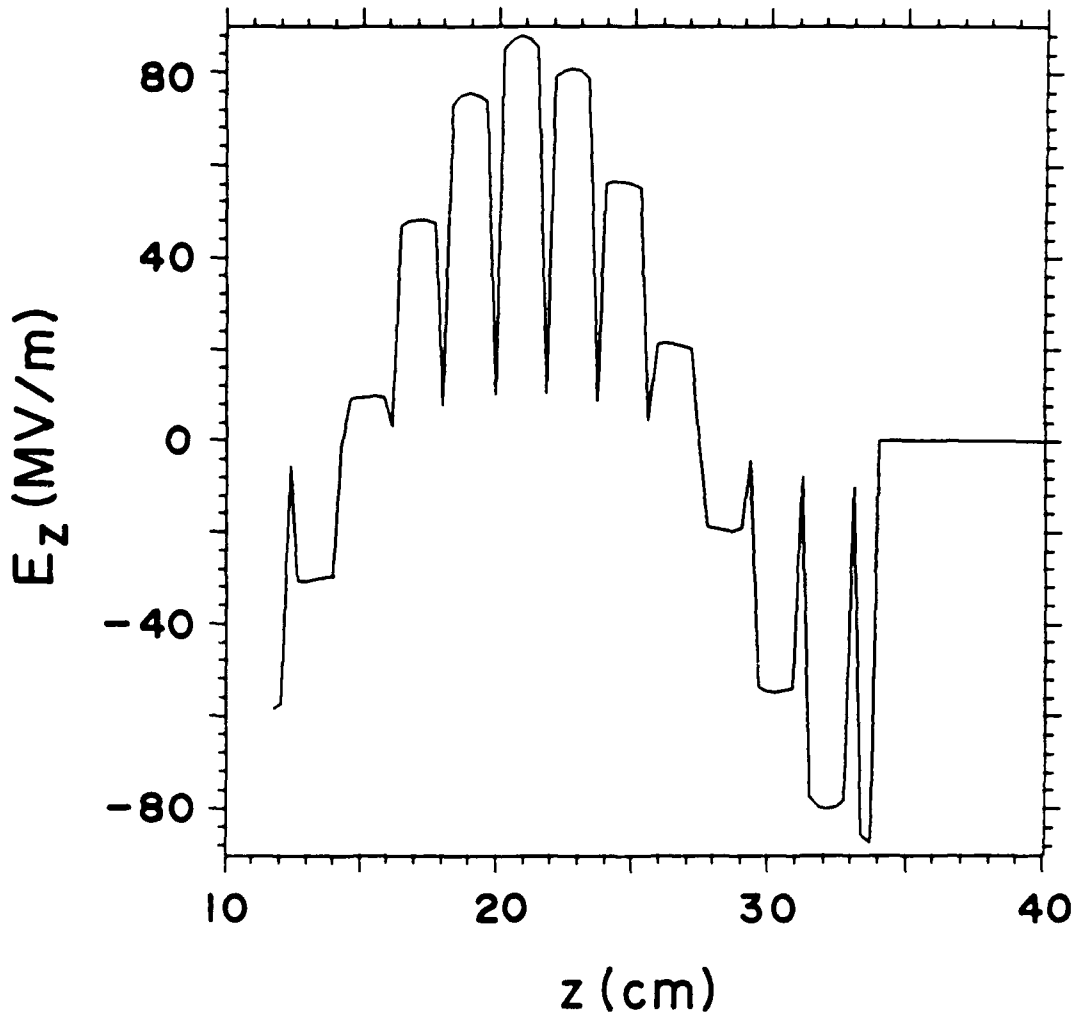



Fig. 6. $E_z$ versus z plotted on-axis at t = 28.4 ns.

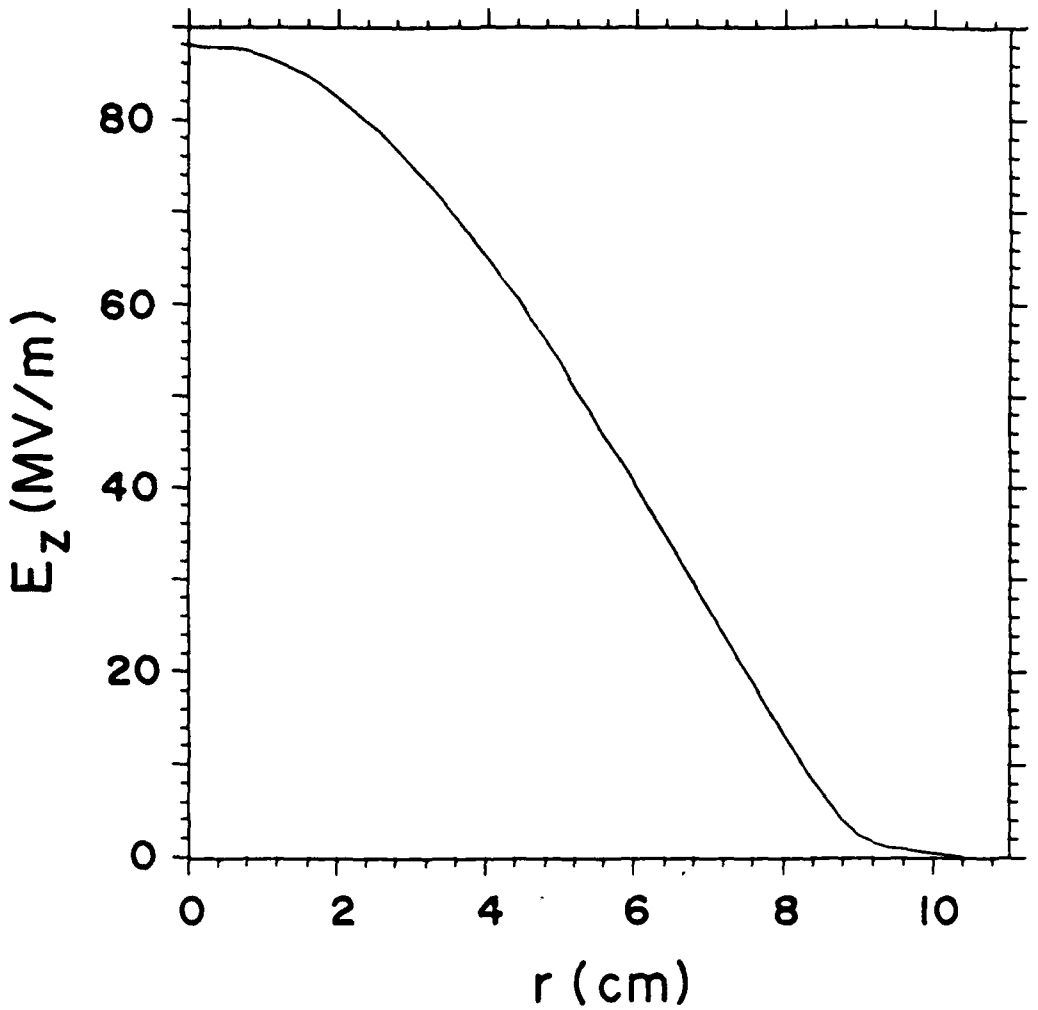



Fig. 7. $E_z$ versus r plotted near the point of peak axial field, z = 20.6 cm, at t = 28.4 ns.

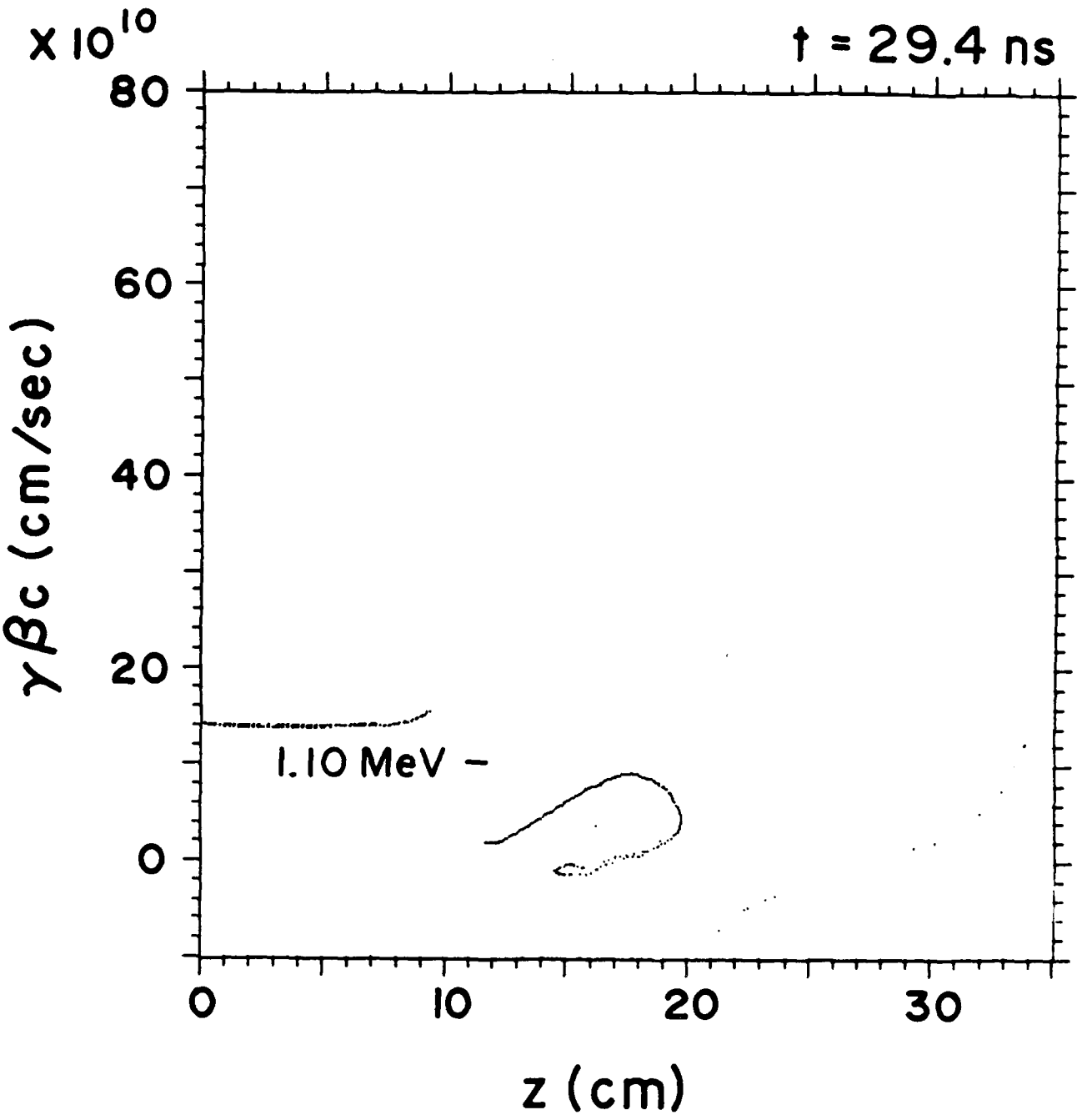



Fig. 8 — Particle positions in phase-space, $\gamma\beta_z c$ versus z, at intervals of 0.2 ns. The primary beam is on the left, $0 < z < 10$ cm. The peak energy of the accelerating secondary beam particles is noted on each plot.

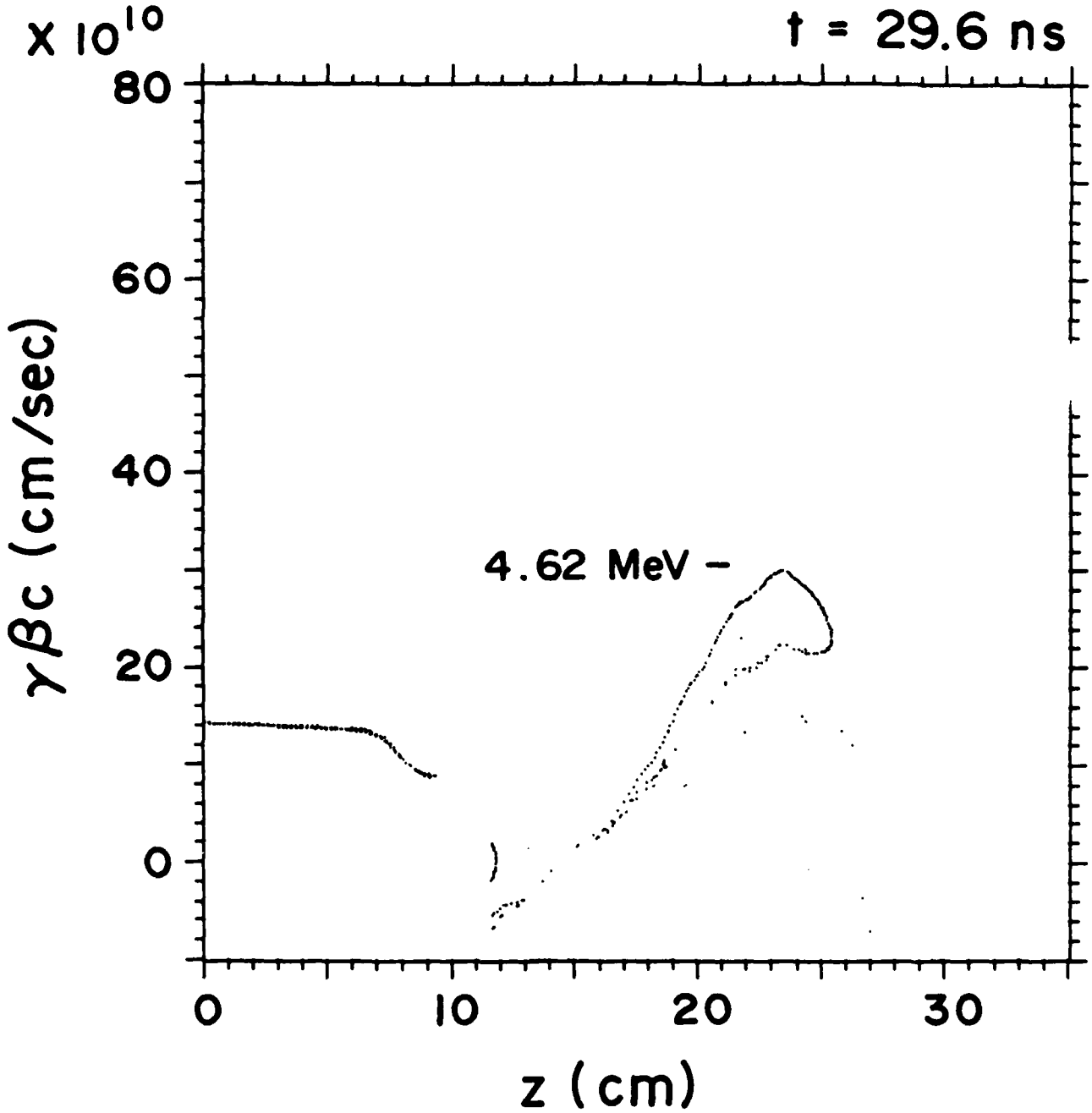



Fig. 8 (Continued) — Particle positions in phase-space, $\gamma\beta_z c$ versus z, at intervals of 0.2 ns. The primary beam is on the left, $0 < z < 10$ cm. The peak energy of the accelerating secondary beam particles is noted on each plot.

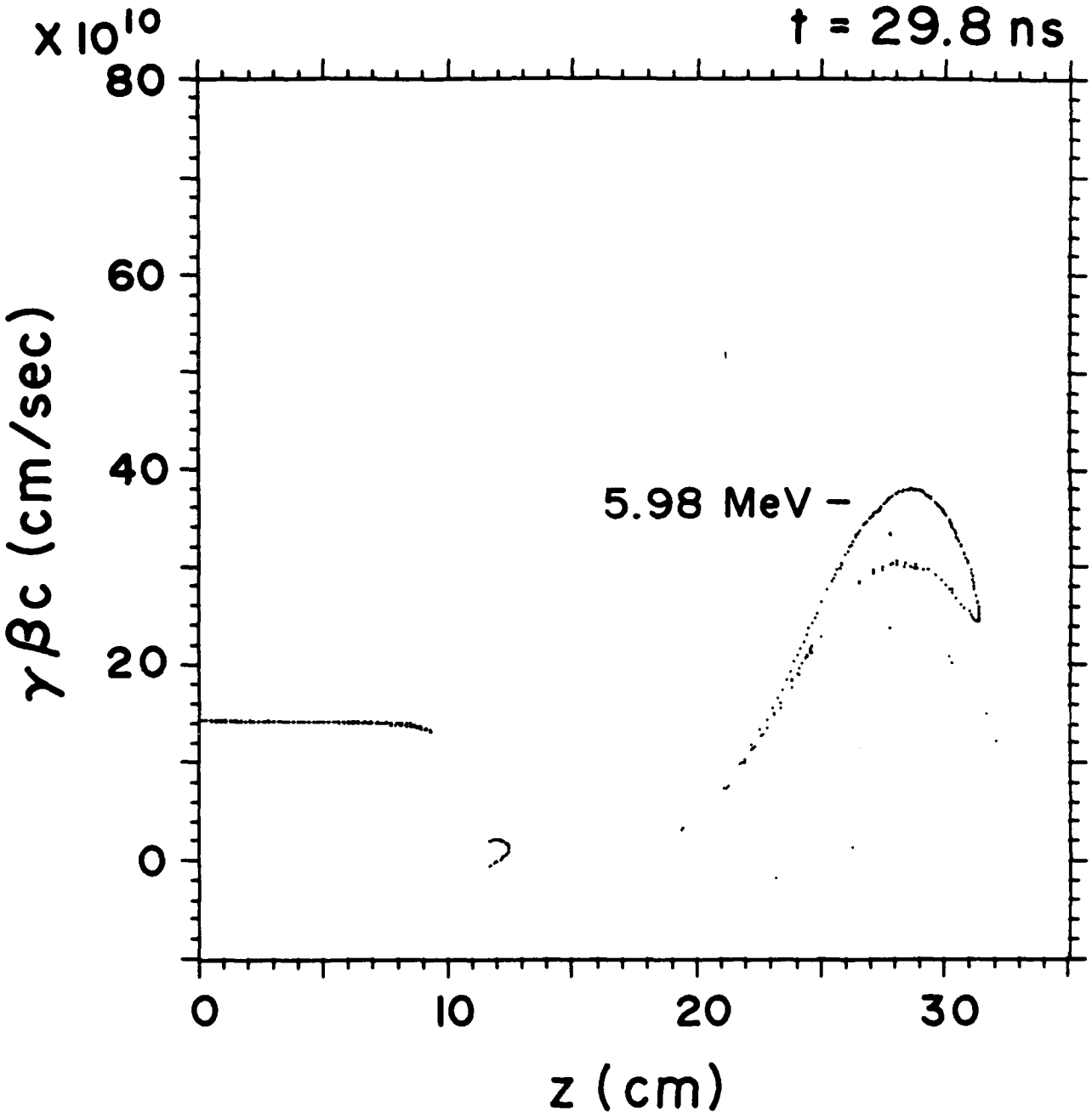



Fig. 8 (Continued) — Particle positions in phase-space, $\gamma\beta_z c$ versus z, at intervals of 0.2 ns. The primary beam is on the left, $0 < z < 10$ cm. The peak energy of the accelerating secondary beam particles is noted on each plot.

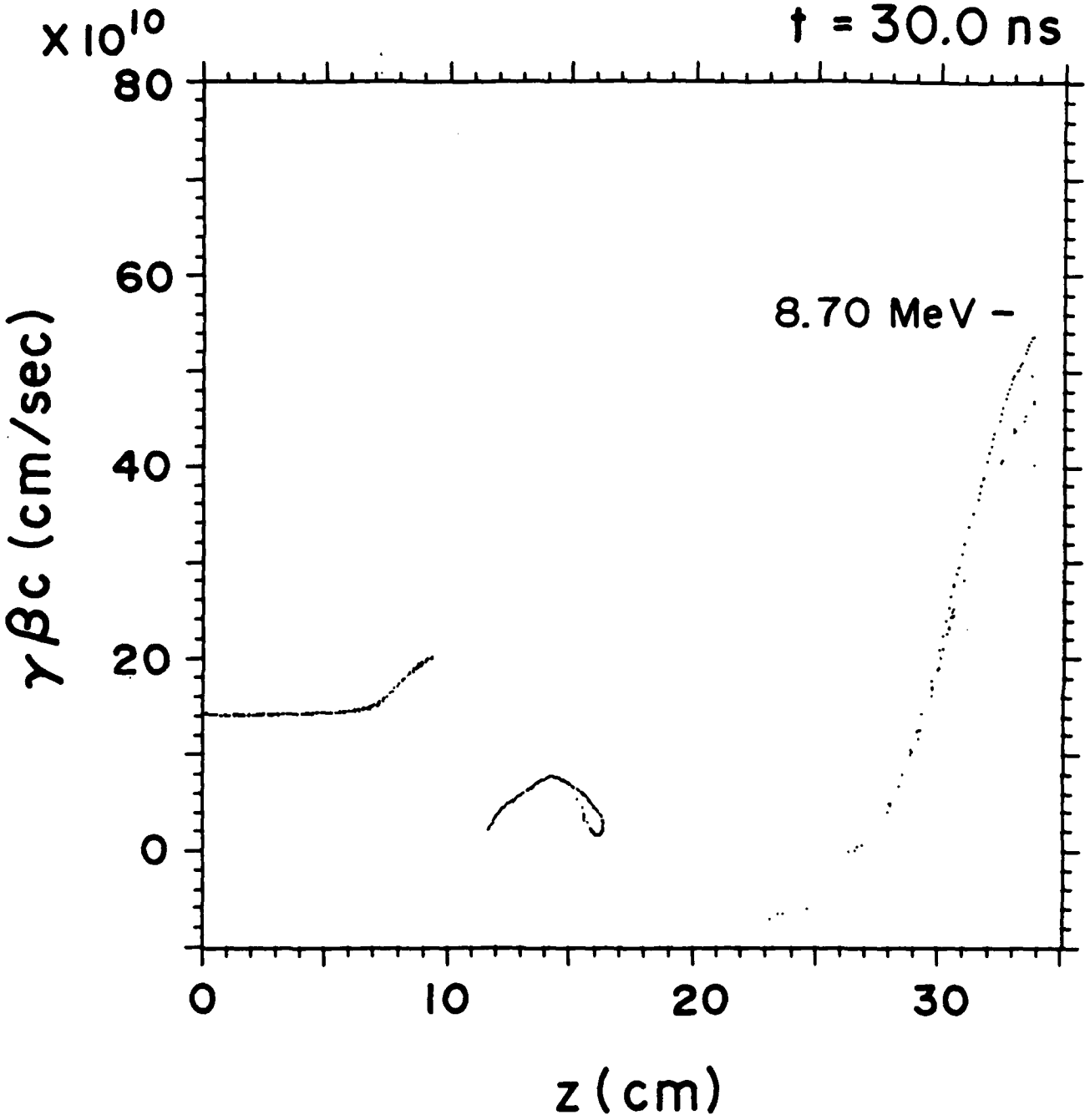



Fig. 8 (Continued) — Particle positions in phase-space, $\gamma\beta_z c$ versus z, at intervals of 0.2 ns. The primary beam is on the left, $0 < z < 10$ cm. The peak energy of the accelerating secondary beam particles is noted on each plot.

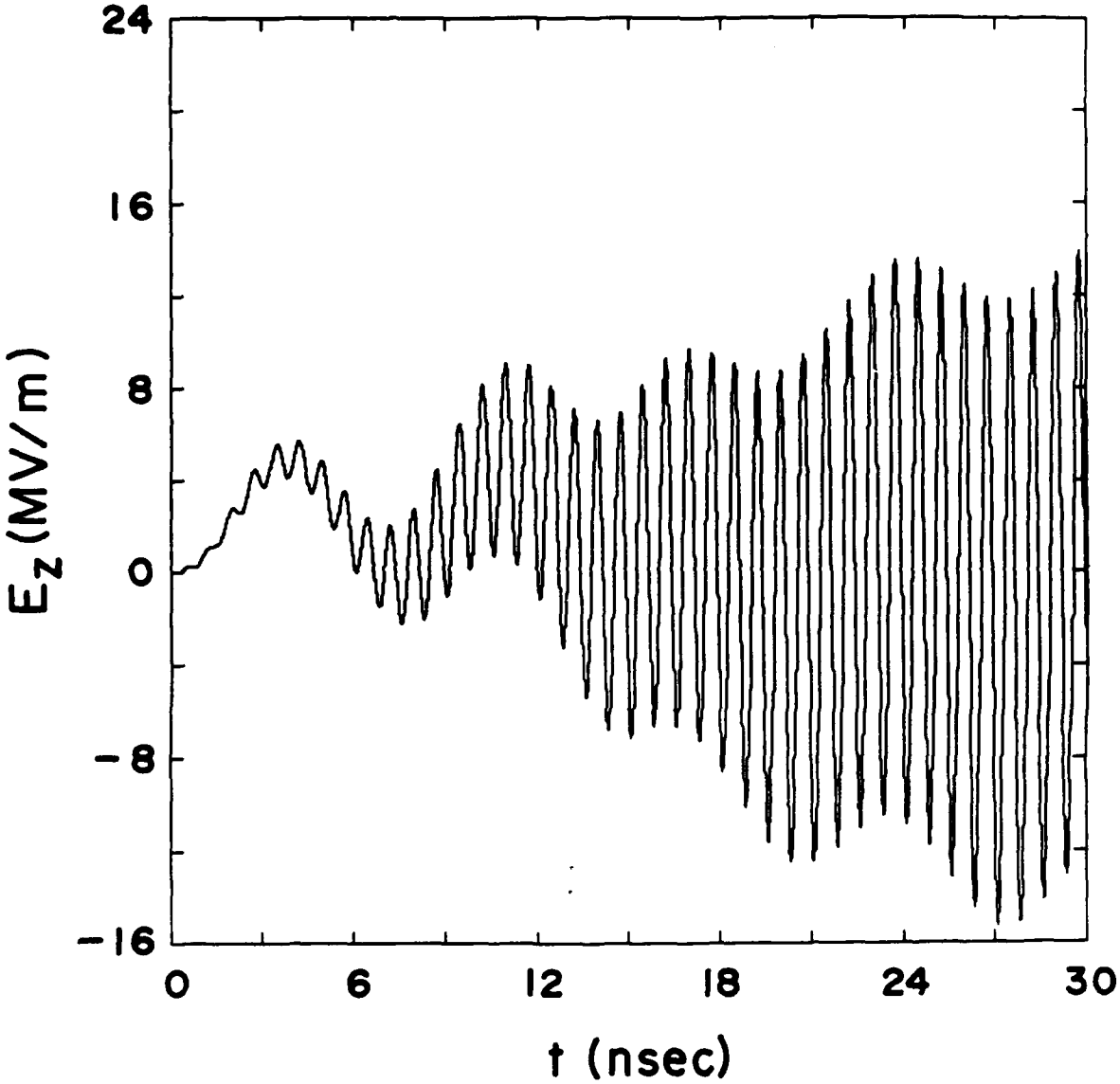



Fig. 9. $E_z$ versus t at the gap for the $r_b$ = 8.0 cm case.

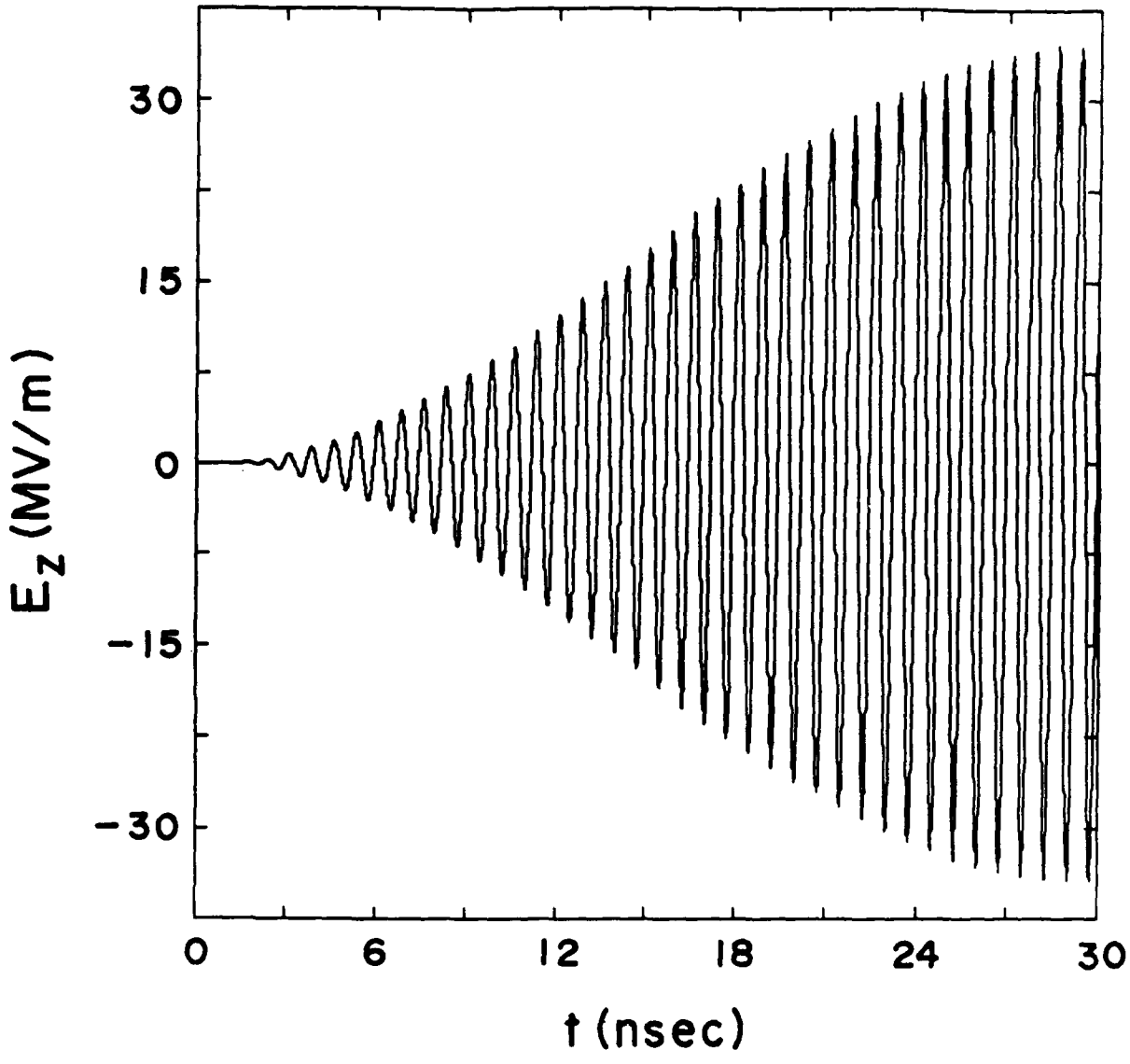



Fig. 10. $E_z$ versus t on-axis at z = 22.6 cm, near the point of peak axial field.

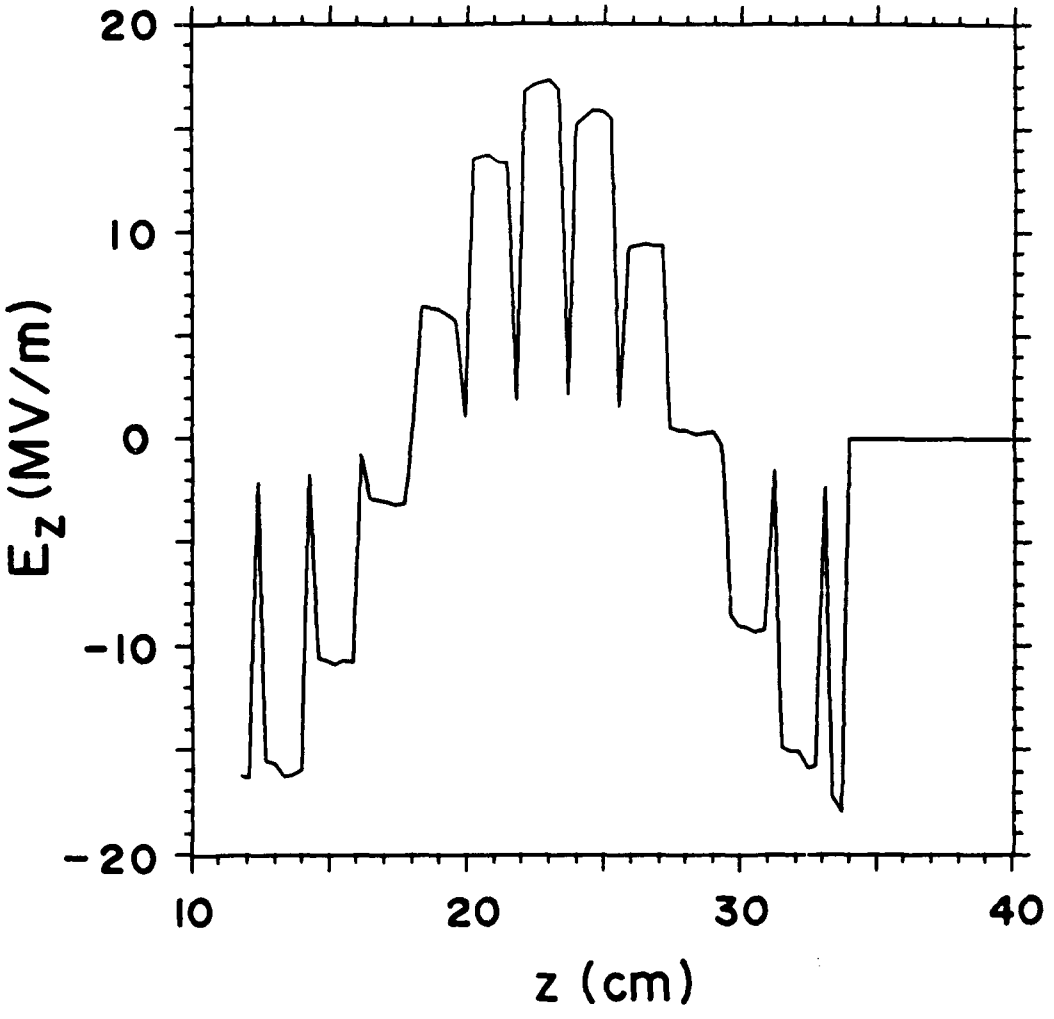



Fig. 11. $E_z$ versus z on-axis at t = 30.0 ns.

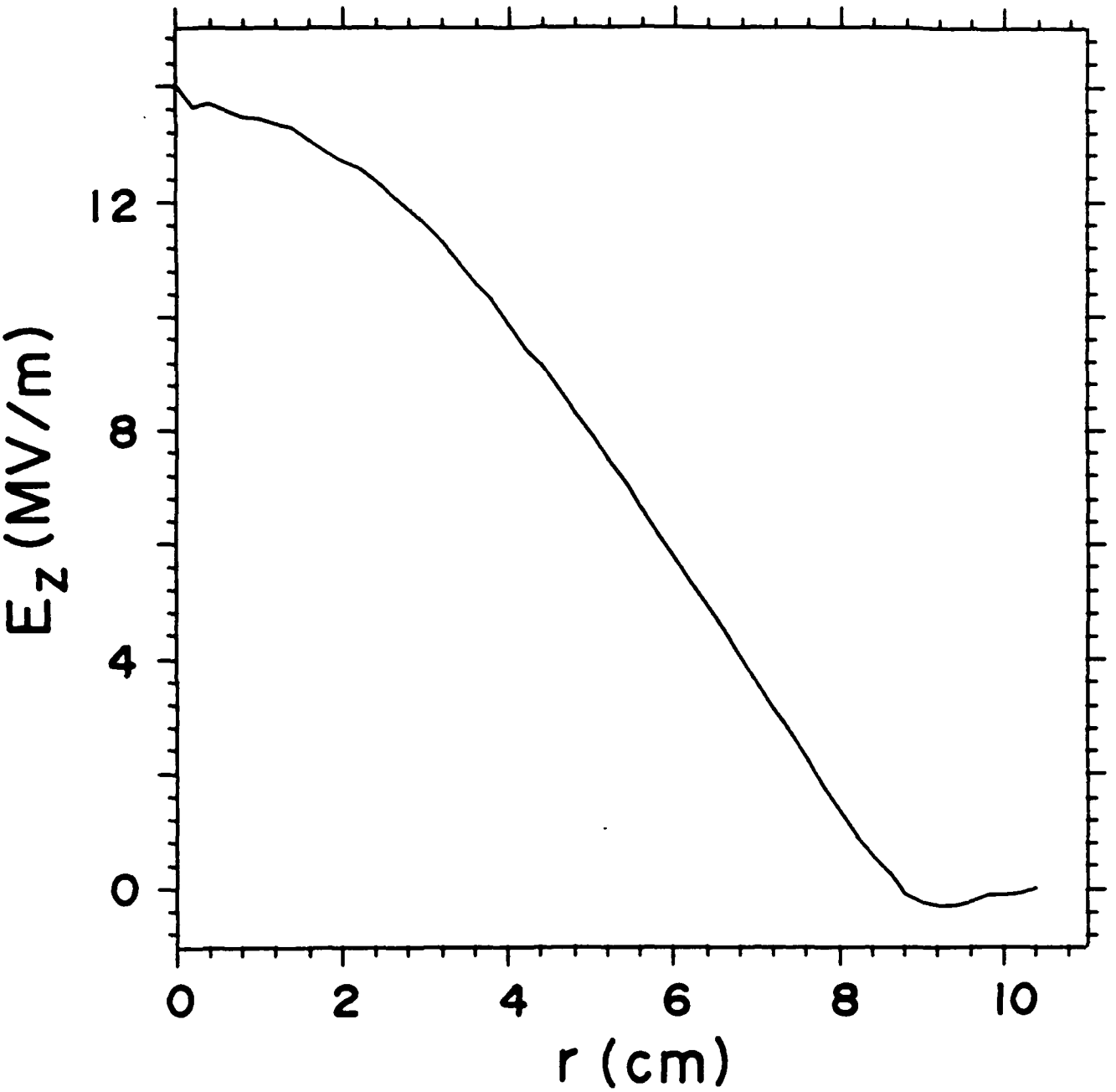



Fig. 12. $E_z$ versus r near the point of peak axial field, z = 20.6 cm, at t = 30 ns.

# APPENDIX S

## A Compact Accelerator Powered by the Relativistic Klystron Amplifier

# A compact accelerator powered by the relativistic klystron amplifier

V. Serlin, M. Friedman, Y.Y. Lau, and J. Krall*

Plasma Physics Division

Naval Research Laboratory, Washington, DC 20375-5000

*Present address: S.A.I.C., McLean, VA 22101

## ABSTRACT

The high field-gradient accelerator employs two beams of electrons which interact through an RF structure. The first, a large-diameter modulated intense relativistic electron beam (MIREB), generates an electromagnetic field which in turn accelerates a second beam. This effect is large, only, when the second beam is much weaker and shorter in duration than the first. The accelerating structure is designed in a way to produce a resonance interaction with the MIREB, leading to the energy transfer from the beam to the structure. The electromagnetic wave induced in the structure, converges radially, generating an average electric field of the order of 100 MV/m on the axis. The short duration of the MIREB pulse (140 nsec) allows us to establish these high electric fields in the accelerating region and complete the acceleration before breakdown can occur.

A secondary particle beam is injected on the axis and accelerated by the high electric field. This particle beam can be initiated and controlled by a modulated laser light, phase-locked to the RF source used to modulate the MIREB. The high power RF established in the structure by the MIREB allows acceleration of up to 100 Amps of electrons, in the present experimental configuration.

Preliminary results show electron acceleration of at least 3MeV with a beam current of about 100 Amps.

## 1.INTRODUCTION

Progress in particle accelerator technology requires the development of new mechanisms capable of generating high voltage gradients and means of avoiding the resulting electrical breakdown. Modulated Intense Relativistic Electron Beams (MIREB'S)[1] can easily provide the high power necessary to establish the accelerating gradient. Also, the interaction of intense beams with high-voltage gaps can enhance the electrical insulation at these gaps and prevent breakdown. This mechanism is due to the high electric self-field of MIREB'S and doesn't exist for "classsical" low density beams.[2]

The mechanism behind the new accelerator[3] employs two beams of particles which interact via a metallic structure. The first beam generates an electromagnetic field which in turn

SERLIN

accelerates a second beam. This effect is large, only, when the second beam is much weaker and shorter in duration than the first. The accelerating structure is designed in a way to produce a resonance interaction with the MIREB, leading to the energy transfer from the beam to the structure. The electromagnetic wave induced in the structure, converges radially, generating an average electric field of the order of 100 MV/m on the axis. A secondary particle beam is injected on the axis and accelerated by the high electric field. This particle beam can be initiated and controlled by a modulated laser light, phase-locked to the RF source used to modulate the MIREB. This scheme results in a modulated secondary particle beam, traversing the accelerating structure in phase with the electromagnetic wave.

This concept is a variant of Wakefield accelerator schemes[4-5] proposed in the past few years. The main differences with respect to the original proposal by Voss and Weiland[4] are that the primary beam in our experiment consists of a long shell of electrons that is terminated before the accelerating structure. Thus, the two beams propagate in separate axial regions and can interact only via the passive accelerating structure.

In this paper, we describe the construction and initial operation of the wakefield accelerator. Section 2 describes the conceptual design, supported by theoretical considerations and numerical simulations. Section 3 describes the actual experimental setup and the inital results of electron acceleration.

## 2. DESIGN OF THE WAKEFIELD ACCELERATOR

The new accelerator takes advantage of the very high power RF fields that can be extracted from MIREB's[6-7]. Elsewhere in these proceedings[7-8], the operation of the Relativistic Klystron Amplifier (RKA) is described. RKA is the power source for the accelerator described here. The concept of the wakefield accelerator is shown schematically in figure 1.

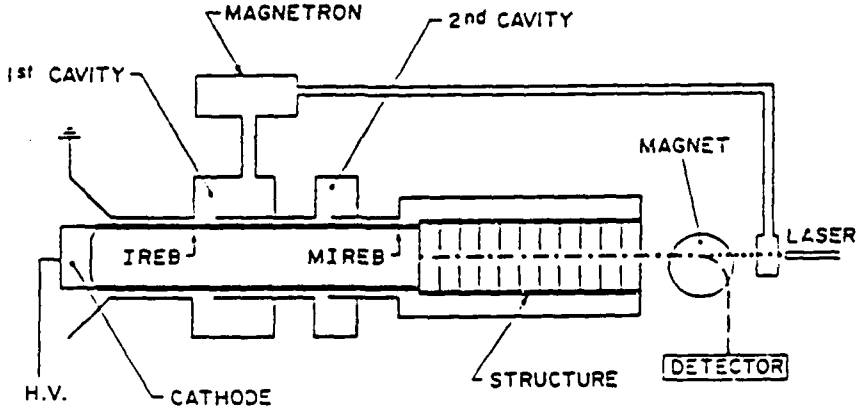



Figure 1. Schematics of the wakefield accelerator.

The major parts of the new accelerator are:

(1) An IREB generator that injects an annular electron beam of radius R, voltage V, current I for a duration T into the bunching region (e.g., V = 1 MV, I = 10kA, and T = $10^{-7}$ s). The electron beam is confined by a strong axial magnetic field.

(2) A bunching region (RKA) which is immersed in the magnetic field and where a low level rf source (magnetron) modulates the IREB.

(3) The modulated annular electron beam is guided by the axial magnetic field into a cylindrical cavity of radius B. The cavity is loaded with a structure that consists of thin metallic discs, of radius A and thickness $\delta$, which are spaced along the cavity with a separation $\lambda$. The discs are supported longitudinally by thin metallic rods, cantilevered from the end wall of the cavity.

The MIREB is terminated at the first disc. The frequency of modulation and the cavity geometry are chosen such that a resonance interaction between the MIREB and the cavity occurs, leading to the transfer of energy from the beam to the structure.

(4) After some predetermined time a second electron beam traverses the cavity through holes located at the centers of the discs, draining the stored energy. This electron beam may be initiated and controlled by a laser beam that illuminates the center of the first metallic disc. Since the laser light can be intensity modulated by the external rf source the second electron beam will be also modulated at the same frequency. If the second bunched electron beam is in the "right" phase with the electromagnetic wave in the structure, all the electrons are accelerated by the electric field and gain the same energy.

The process of energy transfer from the primary beam (MIREB) to the secondary (accelerated) beam, is of major importance. The two beams couple via the passive accelerating structure. The primary modulated beam is terminated immediately beyond the input gap of the accelerating structure. The resonance frequency of the structure is adjusted to match the frequency of the primary beam. The SUPERFISH[9] computer code, which calculates axisymmetric RF modes in cavities and accelerating structures, was used to design a structure supporting the necessary modes. Figure 2 shows the SUPERFISH output for a structure of length L = $\lambda$, with the input gap region included. The structure's geometry closely matches the experiment, except for the overall length and the ommission of radial support rods and other non-axisymmetric elements, that could not be modelled by SUPERFISH.

SERIN

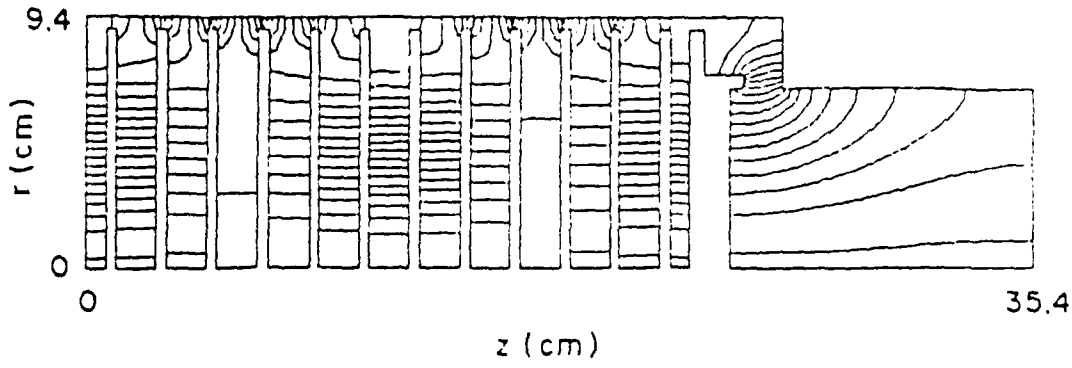



Figure 2. Electric field configuration for the structure and input gap

The phase velocity and the dispersion relation for RF waves established in the structure were obtained from electromagnetic field theory[3] and SUPERFISH. Figure 3 shows the dispersion relation and the phase velocity calculated for the structure used in the experiment.

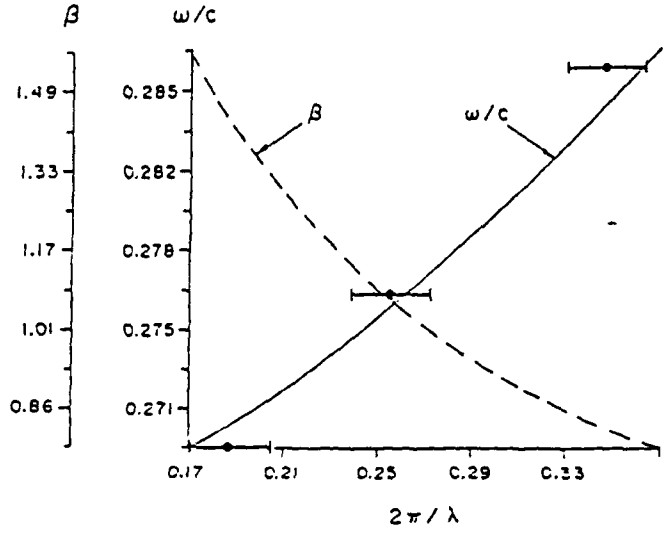



Figure 3. Phase velocity and ω-k diagram of the experimental structure

The horizontal bars are obtained from SUPERFISH. The middle bar corresponds to a mode with phase velocity close to c, and frequency matched to that of the RKA.

The transfer of power between the primary and secondary beams is characterized by a "transformer ratio", defined as $R=V_2/V_1$, where $V_1$ is the decelerating voltage in the input gap and $V_2$ is the accelerating potential experienced by the secondary beam. In our geometry,

$$R = \langle E_{axis} \rangle L \; / \; \langle E_{gap} \rangle d \; , \qquad (1)$$

where d is the gap length, L is the length of the RF structure, $\langle E_{gap} \rangle$ is the average electric field in the gap, and $\langle E_{axis} \rangle$ is the average field experienced by the secondary beam. By treating the accelerating structure like a resonant cavity of length $L = n\lambda/2$, where n is integer and $\lambda$ is the wavelength of the RF, we can obtain the following relationship for the axial components of the electric field,

$$E_z(r=0) = E_z(r) \; J_0(r=0) \; / \; J_0(kr) \; , \qquad (2)$$

where $J_0$ is the Bessel function and $k = 2\pi/\lambda$. For large r the ratio $J_0(0)/J_0(kr)$ can be as high as 10. It is conjectured that this relation holds for the ratio of the decelerating field at the input gap to the peak accelerating field on the structure's axis. Hence, the importance of using a large diameter MIREB as a power source. In addition a large diameter beam allows for higher propagating currents, increasing the power content of the primary beam.

The RF structure described here can operate either in a traveling wave mode or in a resonant cavity mode, depending on the relationship between the length of the structure - L, the group velocity of the RF wave - $v_g$, and the duration of the primary beam - T. If $L/v_g \ll T$ then the structure is filled quickly with RF energy and the resonant cavity mode will be established, provided $L=n\lambda/2$ . If, on the other hand, $L/v_g \ll T$ is not satisfied, the structure will operate as a traveling wave amplifier. The group velocity may be adjusted by simple changes in the geometry of the structure.

In order to simulate the acceleration mechanism, a time dependent, fully electromagnetic particle code CONDOR[10] was applied[11] to a geometry and beam parameters similar to those in the experiment. Figure 4 shows the z-component of the electric field versus time, on the axis of the accelerating structure. The plot is taken at a spatial location where the electric field is maximum. The field amplitude increases continuously, reaching 94.2 MV/m before simulation is halted. The RF cavity mode is, as expected, a standing wave varying sinusoidally in z and as a Bessel function $J_0(kr)$ radially.

The simulation results show that the accelerating gradient on axis is 39.2 MV/m and the resulting transformer ratio is R=9.85. The MIREB is shown to be strongly coupled to the RF structure,

SERLIN

resulting in power transfer in excess of 1 GW from the primary to the secondary beam.

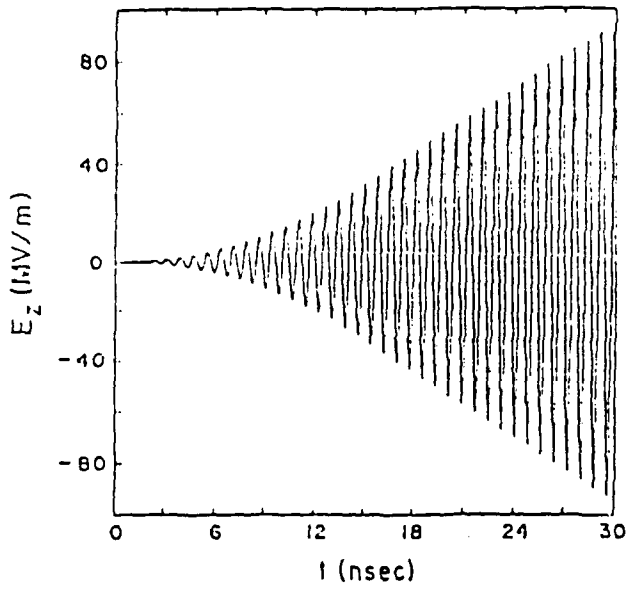



Figure 4. Plot of $E_z$ vs. time on axis.

Consideration has to be given to instabilities affecting the secondary beam. One of the most serious of those is the beam break-up (BBU) instability[12]. The excitation and growth of BBU was analyzed[13] for our experimental parameters and it does not appear to be a significant problem.

## 3. EXPERIMENTAL RESULTS

Figure 5 shows the actual setup used in the initial experiments.

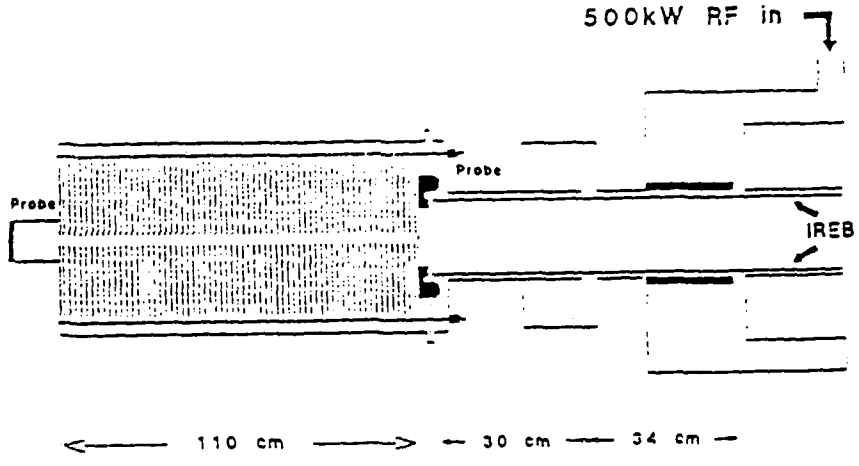



Figure 5. Experimental arrangement for wakefield acceleration.

SERLIN

An annular IREB with the following characteristics was generated by a high voltage diode and launched into a 13.6cm diameter drift-tube:

voltage ~ 500 kV
current ~ 16 kA
duration ~ 140 nsec
diameter ~ 13.1 cm
beam thickness ~ 0.3 cm

This IREB was subsequently modulated by the RKA mechanism. RKA is extensively described in 2 papers elswhere in these proceedings[7-8]. The RKA part of the setup consists of the two coaxial cavities on the right, both tuned to 1.328 GHz, the frequency of the external RF source (magnetron) feeding the first cavity. The IREB is partially modulated by the first gap. The depth of this current modulation varies along z. At a point 34 cm downstream from the first gap, where the amplitude of modulation is maximum, a second gap was inserted, feeding a passive coaxial cavity. This second cavity was excited by the premodulated beam and in turn increased the bunching on the beam, resulting in a peak AC current of (15±5)kA. The gap feeding the accelerating structure is located, again, at a point 30 cm downstream of the second gap where the modulation reaches its maximum of ~ 15 kA.

The accelerating structure consists of 57 thin round plates, held by 6 longitudinal rods, placed at a radial position corresponding to a minimum electric field, as given by SUPERFISH. These rods are fed through small $1/4\lambda$ cavities, tuned to the beam frequency, located on the input side of the RF structure. This is done to choke off the RF path to ground that would bypass the structure. The structure is also supported by 6 radial rods in the input section, used to prevent sagging, and similarly fed through $1/4\lambda$ cavities. The structure's diameter is 18.8 cm, while the plates have a diameter of 18.0 cm. The plates are 1 mm thick and have a 1 cm diameter hole in the center, through which the secondary beam is accelerated. The distance between plates is 1.84 cm and the overall length is 110 cm, corresponding to about 5 wavelengths. The MIREB is terminated on a thick graphite ring, immediately following the structure input gap. The graphite is surrounded by lead, to prevent any X-rays from reaching the RF structure and initiate breakdowns.

The primary beam was diagnosed by a magnetic loop probe located just in front of the structure input gap. The current of the secondary accelerated beam was diagnosed by a magnetic probe on the output of the RF structure. The whole experiment was evacuated to better than $10^{-5}$ Torr and immersed in a quasi-DC magnetic field of ~10 kG. Figure 6 shows the magnetic probes' signals of the primary (top) and secondary (bottom) beams. The MIREB current is ~15 kA. The secondary current is ~100 Amps, consistent with theoretical predictions.

In this geometry, the group velocity is $v_g \approx 0.07c$ .

Consequently, $L/v_g \approx 50$ nsec, where L = 110 cm is the length of the structure. The beam duration is T = 140 nsec, which means that the structure is operating in a traveling wave mode.

The short duration of the secondary beam was probably due to several electrical breakdowns occuring in the structure, and to the reflection of the RF wave from the end of the structure. One breakdown took place along the external magnetic field lines, across the 1/4λ cavities housing the radial rods, which supported the front end of the RF structure. The other breakdown occured radially, from the edges of the plates to the outer wall, which was only 4 mm away. This latter breakdown may have been also related to the reflection of the RF wave.

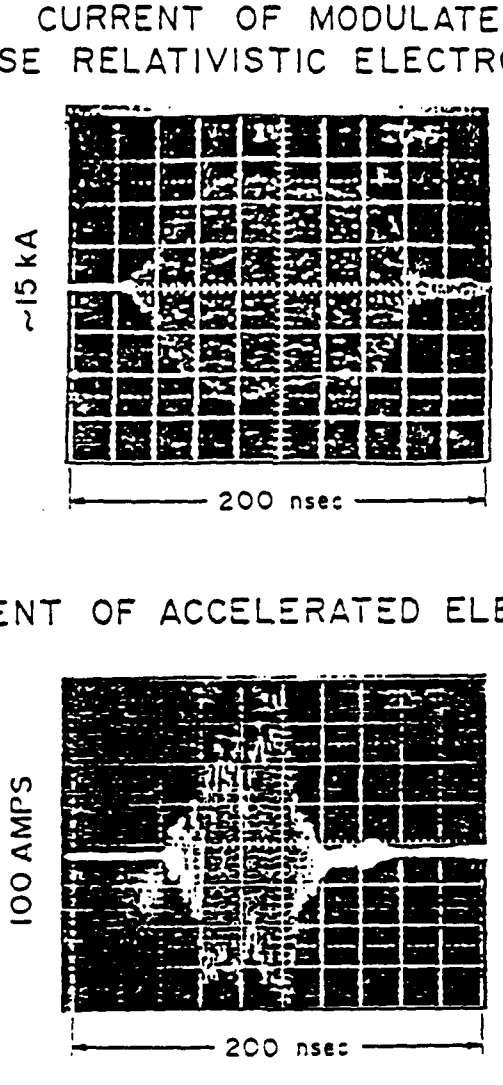



Figure 6. Magnetic probes' signals showing the currents.

The energy of the secondary beam was approximately

obtained from the depth of penetration of the accelerated electrons into a lucite target. The "tree" left in the target was about 1 cm long. This length gives the lower bound on the range of the accelerated electrons in lucite. From range-energy tables we obtained ~ 3 MeV as the peak energy of the secondary beam. There was no attempt to use more sophisticated energy diagnostics, since the acceleration process was obviously disrupted by breakdowns in the structure, and this problem had to be addressed first.

The upper limit on the temperature of the secondary beam was deduced from the size of the beam diameter ( 0.4 cm diameter spot on a witness plate ). Equating this diameter to 2 Larmor radii in the external magnetic field yielded ~ 10 keV as the upper bound on the transverse electron energy.

## 4. CONCLUSIONS

Electrons were accelerated by the wakefield mechanism to about 3 MeV. The accelerated beam current was ~ 100 Amps, the beam diameter ~ 0.4 cm, and the transverse energy ≤ 10 keV. The accelerating structure was plagued by electrical breakdowns, resulting in a much lower electron energy than anticipated. A new structure has been constructed, alleviating most of the problems encountered by the previous one. This new structure is currently being tested.

## 5. ACKNOWLEDGEMENTS

This work is supported by the Department of Energy, contract No. DE-AI05-86-ER13585

## 6. REFERENCES

1. M. Friedman, V. Serlin, A. Drobot and L. Seftor, Phys. Rev. Lett. 50, 1922 (1983); M. Friedman and V. Serlin, Phys. Rev. Lett. 55, 2860 (1985).
2. M. Friedman and V. Serlin, IEEE Trans. Elect. Insul. EI-23, 51 (1988).
3. M. Friedman and V. Serlin, Appl. Phys. Lett. 49, 596 (1986).
4. G. Voss and T. Weiland, DESY Report M82-10 (1982) and DESY Report 82-079 (1982), Hamburg, Germany.
5. K. L. F. Bane, P. Chen, and P. B. Wilson, IEEE Trans. Nucl. Sci. NS-32, 3524 (1985).
6. M. Friedman, J. Krall, Y.Y. Lau, and V. Serlin, J. Appl. Phys. 64, 3353 (1988).
7. M. Friedman, V. Serlin, Y.Y. Lau, and J. Krall, "Operation of a multigigawatt relativistic klystron amplifier", elsewhere in these proceedings.
8. Y.Y Lau, J. Krall, M. Friedman, and V. Serlin, "On certain theoretical aspects of relativistic klystron amplifiers", elsewhere in these proceedings.

9. K. H. Halbach and R. F. Holsinger, LBL Report LBL-5040, 1976.
10. CONDOR is an extension of the MASK Code developed by A. Palevsky and A. Drobot, in Proc. 9th Conf. Numerical Simulation of Plasmas, Northwestern Univ., Evanston, IL, 1980, (unpublished).
11. J. Krall, M. Friedman, Y.Y. Lau, and V. Serlin, to be published.
12. W. K. H. Panofsky and M. Bander, Rev. Sci. Instrum. 39, 206 (1968).
13. Y. Y. Lau, NRL Memorandum Report 6237 (1988).

# APPENDIX T

## Numerical and Experimental Studies of Particle Acceleration

# NUMERICAL AND EXPERIMENTAL STUDIES OF PARTICLE ACCELERATION

# POWERED BY MODULATED INTENSE RELATIVISTIC ELECTRON BEAMS

J. Krall*, M. Friedman, V. Serlin and Y.Y. Lau
Plasma Physics Division
Naval Research Laboratory
Washington, DC 20375-5000

*Science Applications Intl. Corp.
McLean, VA 22102

Abstract: A fully electromagnetic particle code is used to simulate the transfer of energy from an annular modulated intense relativistic electron beam to a secondary low current electron beam via a disk-loaded structure. It is shown that the modulated intense beam can be used to drive such an accelerator at a high transformer ratio (R = 10) with an accelerating gradients in the ~ 100 MV/m range. Power in excess of 1 GW was transferred from the primary to the secondary beam. An experiment was performed in which such a beam (diameter 13 cm, peak power 8 GW) dumped RF power into a disk-loaded structure of length one meter. This RF power was transferred from the structure to a secondary electron beam resulting in acceleration of electrons to an energy much greater than 10 MeV with current of the order 300 Amps.

## Introduction

It has been shown that high electric fields of the order of 100 MV/m can be established in RF accelerating structures by modulated intense relativistic electron beams (MIREB's) of power greater than $10^9$ W.[1,2] Novel accelerators, in which a *low voltage, high current beam interacts via a* metallic structure to power a low current beam to very high energies have been suggested by Voss and Weiland,[3] among others. Wake field acceleration has been observed in experiments by Figueroa et al.[4]

Accelerators powered directly by MIREB's have several advantages over conventional accelerators:[2,5]

(1) Previous results[5] suggest that the high RF power of a MIREB may be coupled to an RF structure so as to drain significant power (> 1 GW) from the beam at high efficiency.

(2) Geometrical effects may allow for sizeable variations in efficiency, field gradient, and coupling between the MIREB and the RF structure.

In the present paper we study these issues via an axisymmetric particle simulation using the CONDOR[6] code and present preliminary experimental results.

The accelerator configuration to be studied is similar to that outlined in Ref. 2 and is pictured in Fig. 1.

(1) An IREB of radius $r_b$ = 6.3 cm, current $I_o$ = 16 kA and energy $E_{inj}$ = 500 keV is injected into an evacuated drift tube of radius $r_w$ = 6.8 cm. The IREB is focussed by an axial field $B_o$ = 10 kG throughout.

(2) The IREB is fully modulated at a frequency f = 1.3 GHz by two tuned cavities. The first cavity is externally driven by a low level RF source (magnetron). The second cavity is undriven.

(3) The MIREB is guided into a drift tube of radius 9.6 cm. The tube contains an accelerating structure which consists of thin disks of radius 9.0 cm and separation 1.88 cm. The MIREB, which has a frequency of modulation corresponding to the desired mode of the RF structure, is terminated at the first disk. A resonant interaction occurs between the MIREB and the RF fields, extracting energy from the MIREB at the gap (defined by the end of the drift tube and the first disk of the RF structure).

(4) An emitter, located on axis on the surface of the first disk, emits a secondary beam which is accelerated by the RF fields.

Modulation of an IREB has been previously reported[5,7,8] and has been repeated experimentally with the present parameters.[9]

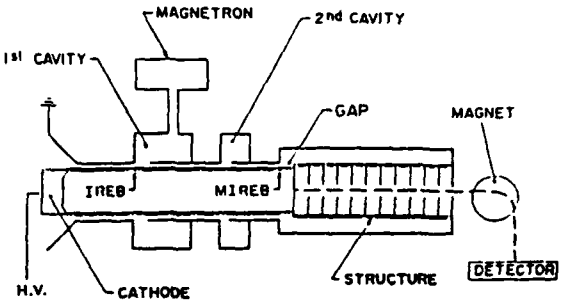



Fig. 1. MIREB-driven accelerator schematic.

## Fields in the RF Structure

The interaction between the primary and secondary beams in this accelerator is different than the wake field schemes of Refs. 3 and 4, where the two beams travel colinearly. Here, the interaction of the primary beam with the RF structure takes place only as the beam traverses the gap, while the secondary beam is accelerated along the entire length of the RF structure. The transformer ratio is defined as

$$R = \frac{\langle E_{axis} \rangle L}{E_{gap} d} , \qquad (1)$$

where d is the gap length, L is RF structure length, $E_{gap}$ is the gap field and $\langle E_{axis} \rangle$ is the average field experienced by the accelerated particles.

The normal modes of the RF structure can be solved for by neglecting the interaction region at the gap.[2] Here, we consider the only fundamental mode of a disk-loaded cavity of length $L = n\lambda/2$ where $\lambda$ is the wavelength of the RF and n is a positive integer. The z-component of the electric field of the fundamental mode varies sinusoidally along the axis and radially as

$$E_z(r)/E_z(r=0) = J_0(kr)/J_0(r=0) , \qquad (2)$$

where $J_0$ is a Bessel function and $k = 2\pi/\lambda$. It was conjectured in Ref. 2 that the ratio of the field experienced at the gap by the primary beam to the peak field on axis would follow this radial variation so that $E_{axis}/E_{gap} = 1/J(kr_b)$.

The normal modes for a given axisymmetric cavity may be calculated numerically by using the Superfish[10] code. Superfish calculations have been performed for a disk-loaded cavity of length $L = \lambda$ with the gap region included. A series of such calculations showed that the expected cavity mode was obtained.[11]

The nonaxisymmetric modes for this structure have also been studied to show that beam breakup growth due to such modes is benign for the parameters of the present proof-of-principle experiment.[12]

## Numerical Simulations

The simulation geometry (Fig. 2) consisted of a short drift tube region with radius $r_w$ = 6.8 cm, a gap of length d = 1.57 cm and a disk-loaded structure of length L = 22.2 cm = $\lambda$, where $\lambda = c/f$, and f = 1.27 GHz is the frequency of the accelerating mode of the cavity, and was determined numerically.

The primary beam was injected from the left-hand wall with radius $r_b$ = 6.4 cm, energy $E_{inj}$ = 2.0 MeV and current $I_{inj}(kA) = g(t)[16 + 8\sin(2\pi ft)]$, where g(t) is an envelope function that increases linearly from zero to unity during the time $0 < t < 15$ ns and remains constant thereafter. At t = 17 ns, the secondary beam with $I_2$ = 10 Amps and $E_2$ = 0.1 MeV was injected continuously from the center of the first disk and was accelerated along the axis by the RF fields. The simulation continued until t = 30 ns.

Note that in order for this structure to behave like a cavity, the parameters L, $v_g$ and T must be such that $L/v_g << T$, where $v_g$ is the group velocity of E-M radiation within the disk-loaded structure and T is the duration of the primary beam pulse. In the geometry of Fig. 2, $v_g/c$ is a sizable fraction of unity, satisfying this constraint within the 30 ns duration of the simulation.

Several differences between this configuration and that of an experiment must be noted.

(1) In an experiment the disk structure would be longer so as to obtain a higher energy secondary beam.

(2) An actual device would have support rods to hold the disks in place, providing a DC current path for the primary beam. Because such supports cannot be modelled in two dimensions, we added a center conductor between the first disk and the left-hand boundary (ground). This did not significantly effect the results.[11]

(3) In the simulation geometry, the left-hand boundary was a metallic wall. In reality, this boundary is an open drift tube, for which symmetric RF modes at a frequency of 1.27 GHz are below cutoff.

(4) The simulation structures were defined on a grid such that the effective skin depth of the material is one grid cell ($\Delta r$ = 0.2 cm, $\Delta z$ = 0.3133 cm), making the cavity extremely lossy, with Q of order 10. A typical value for the experimental structure is of order 1000.

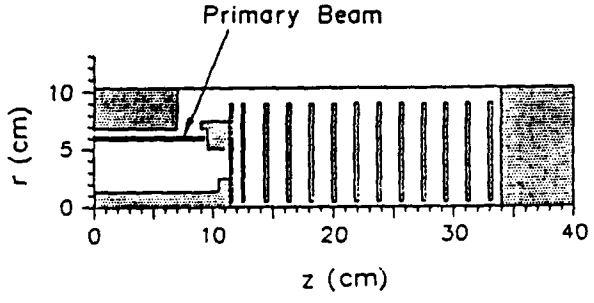



Fig. 2. Simulation geometry. The secondary beam is injected on axis at z = 12 cm.

Figure 3 shows the z-component of the electric field plotted versus time in the gap and on the axis of the RF structure. These fields increased continuously, reaching values of 56.3 MV/m at the gap and 94.2 MV/m on axis before the simulation was halted. The plot of the gap electric field shows evidence of a weak, lower frequency mode which may have been excited by the increase in DC current from t = 0 to t = 15 ns. The RF cavity mode, as expected, was a standing wave, varying sinusoidally in z and radially as a Bessel function, $J_0(kr)$.

The acceleration of the secondary beam can be seen in Fig. 4. Here, particle positions were plotted in phase space, $\gamma\beta c$ vs. z, where $\beta$ is the axial particle velocity normalized to c and $\gamma = (1 - \beta^{-2})^{-1/2}$. The particle positions, plotted at fixed time at intervals of 0.2 ns, show a maximum energy increase of 8.60 MeV over 22.2 cm to give an accelerating gradient of 39.2 MV/m. With this result and the observed 56.3 MV/m at the gap, a transformer ratio R = 9.85 has been achieved.

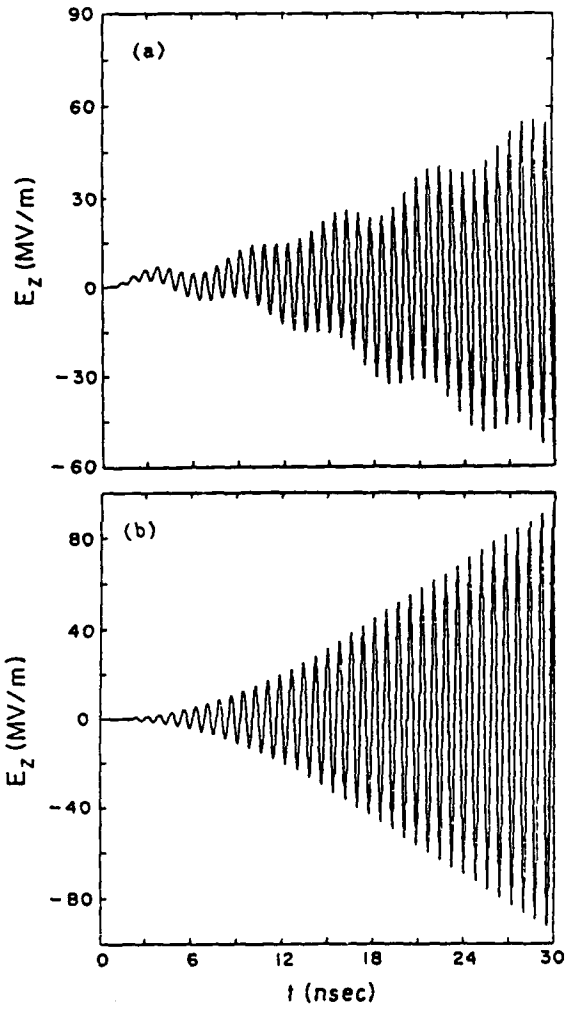



Fig. 3. $E_z$ versus time at the gap and on axis (at peak field) for the $r_b$ = 6.4 cm case.

Several interesting aspects of this simulation should be noted.

(1) The build-up of RF in the cavity was of a transient nature. Were the simulation not halted at t = 30 ns, the field amplitudes would increase beyond the observed 94.2 MV/m. Realistically, limitations may include breakdown in the RF structure, low Q, termination of the primary beam, or loading due to high current in the secondary beam.

(2) The conjectured relationship between $r_b$ and $E_{axis}/E_{gap}$, discussed in connection with Eq. (2) above, did not hold. Here, we have $E_{axis}/E_{gap}$ = 1.67 and $1/J_0(kr_b)$ = 2.51. The effect of varying $r_b$ will be investigated below.

(3) The electric field of 56.3 MV/m that was observed across the 1.57 cm gap indicates that the primary beam loses 0.883 MV as it traverses the gap. This energy loss is verified by the phase-space plots of Fig. 4, where the primary beam particles, which have $0 < z < 10$ cm, were deflected in momentum space by the gap voltage. This indicates a power drain of 7.07 GW at 1.27 GHz and is sufficient power to accelerate secondary beam current in the 500 Amp range over this short distance. With a longer accelerating structure, lower currents may be accelerated to higher energies.

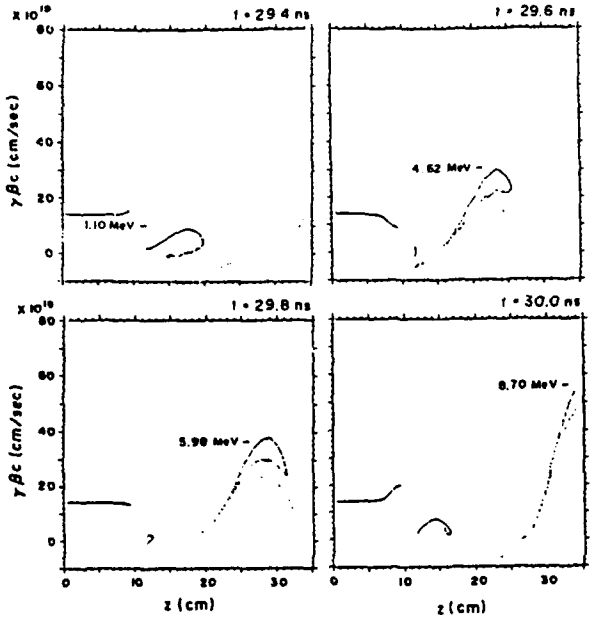



Fig. 4. Particle positions in phase-space, $\gamma\beta_z c$ versus z, at intervals of 0.2 ns. The primary beam is on the left, $0 < z < 10$ cm. The peak energy of the accelerating secondary beam particles is noted.

The simulation of Figs. 3 and 4 was repeated with 200 Amps secondary beam current. We found $E_{gap}$ = 51.6 MV/m, $E_{axis}$ = 91.3 MV/m, $\langle E_{axis} \rangle$ = 35.7 MV/m and R = 9.78. We obtained secondary beam RF power of 1.58 GW without significantly loading the cavity.

The effect of varying $r_b$ was investigated by repeating the simulation of Figs. 3 and 4 with $r_b$ = 8.0 cm, necessitating an increase in the drift tube radius to $r_v$ = 8.4 cm. This shifted the resonance slightly, to 1.34 GHz. We have obtained the following results:

(1) We found $E_{gap}$ = 13.5 MV/m, $E_{axis}$ = 34.4 MV/m and $\langle E_{axis} \rangle$ = 14.3 MV/m. R was increased to 15.0.

(2) With $r_b$ = 8.0, we have $E_{axis}/E_{gap}$ = 2.55 and $1/J_0(kr_b)$ = 11.9. The conjectured relation between $r_b$ and $E_{axis}/E_{gap}$ held only in a qualitative sense.

(3) The fields in the cavity reached much lower amplitudes at t = 30 ns than in the $r_b$ = 6.4 cm case, indicating a weakening of the interaction between the primary beam and the RF structure.

(4) The mode structure was unchanged from the previous case. Note that at $r_v$ = 8.4 cm, f = 1.34 GHz is very close to the cutoff frequency $f_c$ = 1.37 GHz. Realistically, it may not be possible to increase $r_b$ and $r_v$ to such values at this frequency.

## Experimental Results

An experiment has been performed in which a 13 cm diameter annular IREB of DC current 16 kA and voltage 500 kV was fully modulated at a frequency of 1.328 GHz. The modulated electron beam was terminated in such a way that the RF energy was transferred into the disk-loaded structure as in Fig. 1. A cold emission cathode was placed at the center of the first disk. The electron beam emitted from this cathode had a diameter of 1 mm and current of 300 Amps. This electron beam propagated along the length of the structure (1 meter) without loss of current or radial expansion.

Preliminary diagnostics based on the stopping range of the accelerated electrons in absorbers indicate that electrons with energy much greater than 10 MeV were present. More sophisticated diagnostics are currently being designed.

## Conclusions

We have demonstrated that high fields and transformer ratios can be supported by a MIREB-driven accelerator, with power in excess of 1 GW transferred from the primary to the secondary beam, despite the low Q of the numerical structure.

We have found that the build-up of RF fields in the structure is transient by nature with peak accelerating gradients limited only by the brevity of the simulations. In an actual device, field amplitudes will continue to increase until limited by such mechanisms as saturation (low Q) or termination of the primary beam pulse.

We have also shown that by varying the primary beam radius, the transformer ratio may be increased, but at the cost of weakening the coupling between the primary beam and the RF structure.

Finally, in a preliminary experiment electrons were accelerated to energies in excess of 10 MeV and with peak current of 300 Amps.

## Acknowledgement

This work was supported by the Department of Energy under contract number DE-AI05-86-ER13585.

## References

1. M. Friedman and V. Serlin, Phys. Rev. Lett. 55, 2860 (1985).
2. M. Friedman and V. Serlin, Appl. Phys. Lett. 49, 596 (1986).
3. G. Voss and T. Weiland, Desy Report M82-10 and Desy Report M82079, 1982.
4. H. Figueroa, W. Gai, R Konecny, J. Norem, A. Ruggiero, P. Schoessow and J. Simpson, Phys. Rev. Lett. 60, 2144 (1988).
5. M. Friedman, J. Krall, Y.Y. Lau and V. Serlin, J. Appl. Phys. 64, 3353 (1988).
6. CONDOR is an extension of the MASK particle code, discussed in A. Palevsky and A. Drobot, in Proceedings of the 9th Conference on Numerical Simulation of Plasmas, July 1980 (Northwestern University, Evanston, IL) (unpublished).
7. J. Krall and Y.Y. Lau, Appl. Phys. Lett. 52, 431 (1988).
8. Y.Y. Lau, J. Krall, M. Friedman and V. Serlin, IEEE Trans. Plas. Sci. 16-2, 249 (1988).
9. M. Friedman, V. Serlin, Y.Y. Lau and J. Krall, to be published.
10. K. H. Halbach and R. F. Holsinger, LBL report LBL-5040, 1976.
11. J. Krall, V. Serlin, M. Friedman and Y.Y. Lau, to be published.
12. Y.Y. Lau, Bull. Am. Phys. Soc. 33, 2040 (1988), Also in these proceedings.

# APPENDIX U

## IFR Conditioning and Transport

# IFR CONDITIONING AND TRANSPORT

R. F. Hubbard, G. Joyce, J. Krall+, S. P. Slinker, and M. Lampe
Naval Research Laboratory
+Science Applications International Corporation

## I. INTRODUCTION

IFR (Ion-Focused Regime) propagation is extensively employed in ATA and other electron beam experiments to transport and condition the beam before injection into the atmosphere. Laser-guided IFR is used within the ATA accelerator to guide the beam and damp transverse oscillations. It is also employed in the airline section of ATA to recenter the beam after it has passed through a bending magnet. ATA and other devices have employed beam-generated IFR transport in a conditioning cell to taper the beam radius prior to injection into the atmosphere. The ATA beamline also contains regions where vacuum solenoidal transport and thin magnetic lenses control the beam. In addition, scattering foils and apertures are inserted at various points. The complexity of the ATA beamline introduces a number of transitions where beam current, emittance, or transverse noise can be degraded.

The Livermore propagation code BEAMFIRE[1-3] is an axisymmetric particle simulation which can treat many of the situations described above. As in the NRL IFR code HOTH,[4] secondary electrons are assumed to be instantaneously ejected. This paper describes modifications to the NRL FRIEZR code[5] which make it possible to treat the variety of IFR and magnetic transport regions found in ATA. Because FRIEZR must follow secondary electrons, it is an intrinsically slower code than BEAMFIRE. We believe the code to be best suited to studying the detailed physics of matching from one transport region to another.

## II. CODE DESCRIPTION

Overview: FRIEZR is similar to conventional particle simulations in that particles are advanced in time t with a fully-relativistic particle pusher and Maxwell's equations are solved without the ultrarelativistic approximations often employed in beam codes. However, the axial variable is $\zeta = ct - z$ rather than z, so relativistic beam particles tend to stay within the same slice. Beam and secondary plasma particles are pushed in the same way but are separated for diagnostics purposes. Since only particles from one $\zeta$-slice are in the system at any one time, careful bookkeeping and I/O management is required to keep track of particles slipping from one slice to the next.

Pre-existing ion channels: In laser-generated IFR, the beam head encounters new plasma at each time step. In FRIEZR, new plasma electron particles are created in such a way as to follow the ion channel density $\rho_i(r)$. As the propagating beam passes, the plasma electrons are accelerated radially while plasma ions remain fixed. (Some versions of FRIEZR follow ion particle motion.) The channel density is defined by a channel strength $f = N_i/N_b$, where $N_i$ and $N_b$ are the ion and beam line densities, and a channel radius $a_c$.

Beam-generated IFR: Beam-generated IFR is important when the pressure P is in the 10-100 mtorr range. The ionization rate $\nu_i \approx 10^6$ $sec^{-1}$-$mtorr^{-1}$, and the number of secondary electron-ion pairs produced in a time step $\Delta t$ is $\Delta N_s^* = \nu_i \Delta t N_b^*$. Here $N_b^*$ is the number of simulation particles in a beam slice. At each time step and $\zeta$-step, $\Delta N_s^*$ simulation particles are chosen at random, and the secondaries are loaded at the same locations as the chosen subset of beam particles. (The code usually holds $\Delta N_s^*$ constant and adjusts particle weights accordingly.)

Other optional features: The code allows an axial guide magnetic field $B_z$, so solenoidal transport can be studied with or without an ion channel present. Magnetic focusing lenses are modeled using the thin lens approximation: a lens of focal length F is specified at some location z, and beam particles are given velocity kicks $\Delta v_x = -x/F$ and $\Delta v_y = -y/F$ when they pass that location. Algorithms for treating foil scattering are contained in HOTH but not yet implemented in FRIEZR.

Axial variations in parameters: Treating transitions between regions requires that f,P, and $B_z$ vary with z. This is implemented in FRIEZR by defining nominal values $f_o$, $P_o$, and $B_{zo}$ and generating multipliers $\alpha_f$, $\alpha_p$, and $\alpha_B$ at specified axial positions $z_k$. The individual quantities vary linearly between $z_k$ and $z_{k+1}$. The position $z_k$ generally defines the location of a transition between one type of transport (e.g., laser guiding) to another (e.g., beam-generated IFR).

## III. ATA TRANSPORT EXAMPLES

Laser-generated IFR and tapered Benzene channels: FRIEZR is particularly well-suited for treating such cases because of the importance of plasma electron motion. Contour plots of plasma electron density $n_e(r,\zeta)$ reveal that they are ejected in an annular shell. The finite ejection time affects ohmic erosion and the shape of the beam head. The

beam does not usually taper except in the beam head. "Benzene tapering", a method employed successfully in the December, 1985 ATA experiments to tune the beam shape, has been modelled with FRIEZR by varying $f(z) = \alpha_f(z) f_o$. The pressure P is usually small in these regions.

IFR Conditioning cells: In a conditioning cell, the pressure P is usually chosen so that $\nu_i \tau_p \leq 1$ where $\tau_p$ is the pulse length. FRIEZR simulations in the ATA regime appear to be insensitive to secondary electron motion because $n_e << n_b$ near the beam at all times. In these cases, the beam pulse is tapered in radius as it propagates through the cell. An example with a higher pressure, resulting in $\nu_i \tau_p = 2$ revealed that plasma electrons are well-ejected from the beam head, but remained close to the beam in the beam tail. This did not appear to disrupt propagation, however. This overneutralized regime, which corresponds to P = 100-500 mtorr for ATA, has not yet appeared to be disruptive in the simulations.

Multi-region example: Figures 1-3 are taken from an ATA simulation with an 80 cm long laser-guided IFR region with f = 0.5 followed by an 80 cm vacuum expansion region and a 160 cm long IFR conditioning cell with P = 100 mtorr. The beam radius shows little taper in the first two regions (Figs. 1 and 2) but emerges with a substantial taper at z = 320 cm when it emerges from the conditioning cell. Similar radius variations have been produced in the ATA experiment.

Conclusions: The ATA experiment contains several different regions of IFR and vacuum transport. The recent modifications to the FRIEZR code allows detailed simulations of these regions and should prove useful in suggesting methods for improving the performance of the machine.

## REFERENCES


1. W. Fawley, Proc. 1986 DARPA CPB Propagation Review, p. 27.
2. S. S. Yu, et al., ibid, p. 62.
3. W. Fawley, to appear in Proc. 1987 DARPA CPB Propagation Review.
4. R. F. Hubbard, et al., Proc. 1986 DARPA CPB Propagation Review, p. 519.
5. G. Joyce, et al., to appear in Proc. 1987 DARPA CPB Propagation Review.

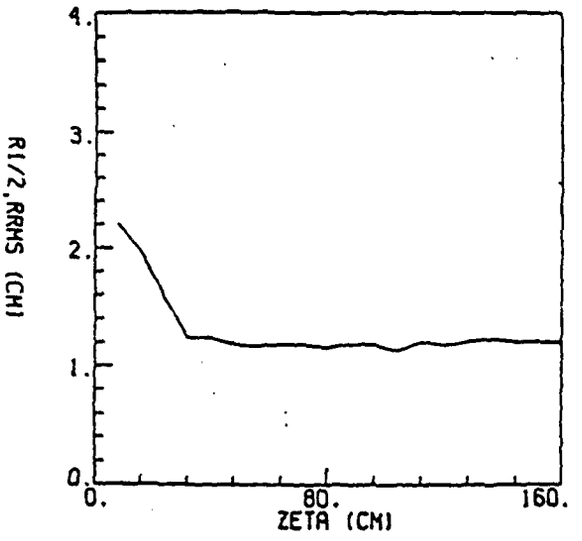



Fig. 1 Beam radius a(ζ) in the laser-guiding region z(z = 80 cm) of a multi-region ATA simulation

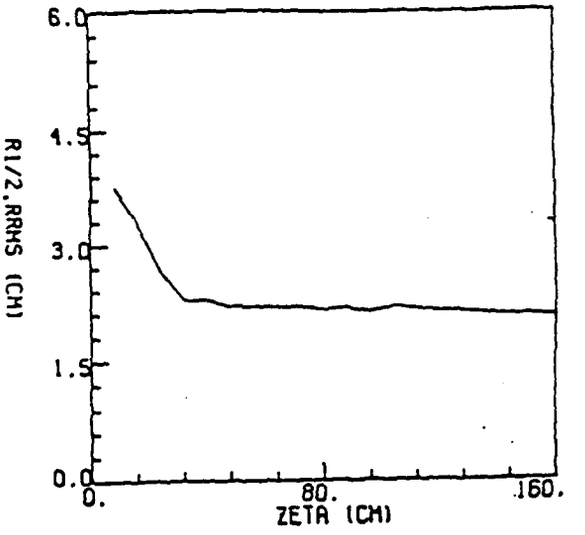



Fig.2 Radius a(ζ) at the end of a vacuum expansion region for the same simulation (z = 160 cm)

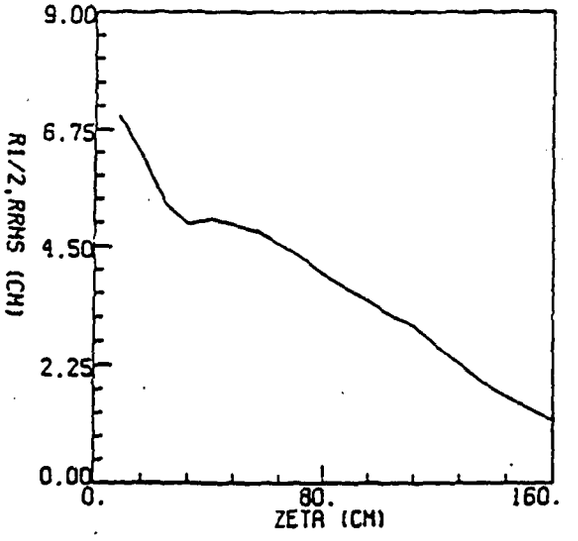



Fig. 3 Radius a(ζ) at the end of an IFR conditioning cell (z = 320 cm) for the same simulation

# APPENDIX V

## Numerical Simulations of Axisymmetric Erosion Processes in Ion Focused Regime-Transported Beams

# NUMERICAL SIMULATIONS OF AXISYMMETRIC EROSION PROCESSES IN ION FOCUSED REGIME-TRANSPORTED BEAMS

Jonathan Krall[a], Khanh Nguyen[b] and Glenn Joyce

Plasma Physics Division
Naval Research Laboratory
Washington, DC 20375-5000

Erosion rates for a relativistic electron beam propagating through a low density plasma channel in the ion-focused regime are computed via axisymmetric particle simulation. Steady-state inductive (ohmic) erosion rates are found that are in quantitative agreement with new theoretical results which correctly account for the relativistic dynamics of electrons at the beam head. In cases where the finite emittance of the beam is expected to be the dominant loss mechanism, the beam does not develop steady-state erosion, as suggested by previous analyses. Asymptotically, such a beam is characterized by a low emittance population at the beam head, a long rise length, and an erosion rate that tends toward zero.

a) Science Applications Intl. Corp., McLean, VA
b) Naval Surface Warfare Center, Silver Spring, MD

## I. Introduction

An electron beam propagating along a low density plasma channel in the ion focused regime (IFR) is characterized by a freely expanding head, a pinch region, where the plasma electrons are ejected from the channel and the beam pinches to its equilibrium value, and the beam body. When $N_c < N_b$, where $N_c$ is the line density of the plasma channel electrons and $N_b$ is the line density of the beam electrons, the channel electrons are fully expelled from the vicinity of the beam and the remaining ions reduce its space charge potential. This has allowed stable propagation of intense beams over distances of several tens of meters, as demonstrated, for example, in the Advanced Test Accelerator.[1] The pinch region of the beam is associated with increasing net current and azimuthal magnetic field and an inductive $E_z$ spike. Energy loss, due to the inductive field, causes electrons to be removed from the beam head. Additional particle losses can result from the finite emittance of the portion of the beam that is not fully pinched. Both of these processes cause the pinch point to erode backwards in the beam frame. These beams are also subject to instabilities, such as the transverse two-stream and ion hose instabilities.[2,3,4] In the present paper, we work within the constraint of azimuthal symmetry, in which the dominant (transverse) instabilities are not present.

The physics of IFR propagation has developed over a number of years and was recently discussed in some detail.[2,5] We will focus on the transport losses associated with inductive and emittance effects at the beam head. To complement and illuminate the previous analyses, we perform particle simulations in sufficient detail that erosion rates can be measured directly from the motion of the pinch point relative to the motion of the beam body. Such simulations have not been previously presented.

The simulations are a product of FRIEZR, a fully electromagnetic two-dimensional (r,z) particle code that has recently been developed to study IFR propagation and transport of electron beams. It features fully relativistic beam and channel electrons and treats the ions as an immobile fluid. A notable feature of the code is that it solves Maxwell's equations and propagates the beam in a coordinate system which moves at the speed of light. The coordinates are $r, \zeta, \tau$ where $\zeta = ct - z$ and $\tau = t$. An eroding beam appears to move slowly backwards in these coordinates. FRIEZR is discussed in the appendix.

The remainder of this paper proceeds as follows. In Sec. II we derive a new expression for steady-state inductive erosion which is valid in cases where scattering and secondary ionization may be neglected. Simulation results are then presented for comparison. In Sec. III, we cite previous analyses of emittance-driven erosion and compare these results with simulations. Here, we will find that the assumption of self-similar radial expansion of the beam head that is contained in these analyses does not hold. The simulations provide some insights into the relevant physics. Section IV concludes.

## II. Inductive Erosion

In IFR propagation, where energy losses due to scattering may be neglected, the inductive (ohmic) erosion rate per unit propagation distance of a beam pulse may be simply approximated by

$$\frac{\beta_o - \beta_p}{\beta_p} = \frac{\Delta\zeta}{\Delta z} = \frac{\zeta_{max}}{\text{range}} , \qquad (1)$$

where $\zeta_{max}$ is the pulse length, $\beta_o$ is the beam velocity normalized to c and $\beta_p$ is the velocity of the pinch point so that $\beta_o - \beta_p$ is the rate of beam

loss with respect to time. Note that the first equality above implies that losses are confined to the beam head, as is the case when scattering and radiation losses may be neglected. This also requires that the beam be matched to the plasma channel, so that the beam body is in equilibrium.

The range, which appears in Eq. (1) above, may be calculated from the beam energy that is lost to the inductive axial electric field per unit propagation distance and the available energy of the beam electrons. Using a reduced set of Maxwell's equations for relativistic beams, the electric field at a fixed radius $r = r_c$ has been calculated to be[2]

$$E_z(r_c,\zeta) = \frac{2}{c} \log\left(\frac{r_w}{r_c}\right) \frac{\partial}{\partial\zeta}(fI_b) , \qquad (2)$$

where $r_c$ is the radius of the plasma channel, $f = N_c/N_b$ is the ratio of the line densities of channel ions to beam electrons and $I_b$ is the beam current (taken to be positive), rises from zero at $\zeta = 0$ to reach a constant value behind the pinch point. In deriving (2) it was assumed that the plasma electrons are ejected from the channel and move out to a conducting boundary at a finite radius $r_w$. Beam energy lost to the induced field is transferred to the channel electrons as they are moved to large radii and the channel potential is established. The assumption of a finite conducting boundary is necessary because of the logarithmic nature of this potential. Averaged over the entire pulse (2) gives

$$\bar{E}_z = \frac{1}{\zeta_{max}} \int_0^{\zeta_{max}} E_z(r_c,\zeta)\, d\zeta$$

$$= \frac{L_c f I_b}{c\zeta_{max}} \Big|_{\zeta=\zeta_{max}} , \qquad (3)$$

where $L_c = 2\log(r_w/r_c)$ is a dimensionless inductance. The range may now be calculated as

$$\text{range} = \frac{(\gamma_{inj} - \gamma_f)mc^2}{e|\bar{E}_z|} \tag{4}$$

where m is the electron mass, $(\gamma_{inj} - 1)mc^2$ is the energy of the beam upon injection, and $(\gamma_f - 1)mc^2$ is the final energy of the particles as they are lost from the beam. Note that unless the beam is fully neutralized by the plasma channel (f = 1) the propagating gamma of the beam, $\gamma_o$, is less than $\gamma_{inj}$:

$$\gamma_{inj} = \gamma_o + \gamma_U \tag{5}$$

where $\gamma_U mc^2$ is the field potential energy:

$$\gamma_U = \frac{eI_b L_b (1 - f)}{mc^3} . \tag{6}$$

Here, $L_b = 2\log(r_w/r_b)$ is a dimensionless inductance and $r_b$ is the beam radius. Note that for the vacuum case (f = 0) the above gives the familiar expression for the limiting current of a beam with $\gamma = \gamma_U$ propagating in a drift tube of radius $r_w$. Using Eqs. (3), (4) and (5), the erosion rate may be written in terms of equilibrium beam and channel parameters, $\beta_p$ and $\gamma_f$:

$$\beta_o - \beta_p = \frac{efI_b L_c \beta_p}{mc^3(\gamma_o + \gamma_U - \gamma_f)} . \tag{7}$$

The value of $\gamma_f$ can be estimated via a simple argument. In the case where Eq. (7) holds, the erosion process establishes a constant velocity for the pinch point, $v_p = \beta_p c$. Assuming the energy of the beam is lost to the $E_z$ spike adiabatically, a particle with a velocity infinitesimally less

than $v_p$ will fall behind the pinch region, where the $E_z$ spike is localized. The final velocity of this beam particle, $v_f$, is therefore approximated by

$$\beta_p = \beta_f = (1 - \frac{1}{\gamma_f^2})^{1/2} \simeq 1 - \frac{1}{2\gamma_f^2} \qquad (8)$$

Substituting $\beta_p$ from (8) into (7), we obtain a cubic equation which determines $\gamma_f$:

$$\gamma_f^3 - (\gamma_o + \gamma_U + 2C\gamma_o^2)\gamma_f^2 - \gamma_o^2\gamma_f + (\gamma_o + \gamma_U + C)\gamma_o^2 = 0 \qquad (9)$$

where

$$C = \frac{efI_bL_c}{mc^3} . \qquad (10)$$

Note that $\gamma_f$ may be solved for numerically without the approximation of the $(1 - 1/\gamma_f^2)^{1/2}$ term included in Eq. (8) above. For the examples to be given below, however, this approximation is reasonable as it has an order 1% effect on the results.

To verify the theoretical inductive erosion rates predicted by Eq. (7), simulations with FRIEZR were performed over a range of values for the beam current, $I_b$ = 2-10 kA, and the plasma ionization fraction, f = 0.2-1.0, with $\gamma_o$ = 10. The beams generally showed the characteristic trumpet shape as expected, but also had features that were not accounted for in the simple model that produced Eq. (7), such as the multiple $E_z$ spikes that were observed at high $I_b$ and f values. In these cases, oscillatory behavior at the beam head was characteristic of the relativistic electron-electron two-stream instability.

In the relativistic limit, where the beam electrons have longitudinal and transverse effective masses which differ significantly, the fastest

growing mode of the two-steam instability is characterized by a wave vector that is not parallel to the direction of propagation. Here, we consider a cold beam interacting with a cool plasma of density $n_c$, where $n_c$ is the channel electron density. Typically[6,2] the fastest growing wave vector features $k_{\parallel} = \omega_c/v_b$ and $k_{\perp} = k_r \simeq r_b^{-1}$, where $\omega_c^2 = 4\pi n_c e^2/m$ and $r_b^{-1}$ is taken to be the lowest available $k_{\perp}$. Because we are constrained by axisymmetry, $k_{\theta} = 0$, giving the mode a sausage-like structure in r and $\zeta$. Results of a FRIEZR run in which these oscillations were observed are shown in Fig. 1. The plot of $E_z$ versus $\zeta$ on axis shows the oscillations and corresponding plot of $R_{1/2}$, the radius within which one-half of the initial beam current is enclosed at a given $\zeta$, shows the sausage structure of the instability. Note that in the figures, the beam is moving to the left. Note also that the beam has been assigned a positive charge so that $E_z < 0$ is decelerating. As can be seen in the figures, the oscillatory behavior is confined to the beam head, where the channel electrons have not yet been fully ejected. This means that over the length of the interaction region, the channel electron density is dropping from its peak initial value to zero. In this run, $I_b = 5$ kA, $r_b = 1$ cm, $r_c = 2$ cm and $f = 1$. With these parameters, the initial average channel electron density is $n_c = 8.3 \times 10^{10}$ $cm^{-3}$ so that the oscillations will have an initial wavelength of $\lambda_c = 11.6$ cm which increases as the channel density drops. The three distinct peaks in the $E_z$ plot of Fig. 1 show increasing separation consistent with this scenario. Channel electron and beam electron densities on axis are also plotted in Fig. 1. Note that the oscillations in $E_z$ and $R_{1/2}$ correspond to oscillations in $n_c$. Note also that the $n_c$ and $n_b$ plots show the value on axis, rather than the lower average value in the channel. Because the values of all parameters are changing over the course of each oscillation wavelength, the instability does not lend itself to a more detailed

analysis. It is of interest, however, that this phenomena is confined to the beam head and, as we shall see below, does not adversely affect the argument that produced Eq. (7).

Beam head erosion is ideally measured from simulation results by observing the movement of the pinch point, as a function of time, to larger $\zeta$ values, where $\zeta = ct - z$. In the presence of the complicated beam head dynamics discussed above, however, the location of the pinch point is sometimes difficult to define. In all cases, we looked at a number of features, but the most reliable measurement has proven to be $I_{encl}$ versus $\zeta$, where $I_{encl}$ is defined to be the current enclosed inside the radius $r = 5\ r_b$. Examples of this diagnostic are given in Figs. 2 and 3. Figure 2 shows superimposed plots of $I_{encl}$ versus $\zeta$ at $c\tau = 5$ meters and 10 meters for the beam pictured in Fig. 1. The superimposed plots give a reasonable measurement of the erosion rate, despite the dynamics at the beam head. Figure 3 is a similar superposition of $I_{encl}$ versus $\zeta$ plots at $c\tau = 30$ and 40 meters. The parameters are $I_b = 2$ kA, $f = 0.2$, $r_b = 1$ cm and $r_c = 2$ cm. Corresponding plots of $E_z$, $R_{1/2}$, $n_b$ and $n_c$ versus $\zeta$ (see Fig. 4) show that this beam lacks the instabilities seen in Fig. 1, having a well defined pinch point and $E_z$ spike. In such cases, these other features corroborated the erosion rate estimated from the $I_{encl}$ plots.

Erosion rates for various values of $I_b$ and f are shown in Table I. In all cases, $\gamma_o = 10$, $r_b = 1$ cm, $r_c = 2$ cm, $r_w = 33$ cm, $\zeta_r$ (beam rise length) $= 50$ cm, and $\zeta_{max} = 100$-$400$ cm. The erosion rate predicted by Eq. (7) is also given. These rates were seen to be insensitive to the channel radius, as expected, and additional runs at $I_b = 10$ kA and $f = 0.2$ showed correct scaling with $\gamma_o$ and with $r_w$. It is interesting that the results agree so closely with theory, even when the beam dynamics are complicated. It is also true, however, that as long as the energy losses are confined to the

beam head, as in these cases, the energy balance argument that produced Eq. (7) still applies.

It is important to note that Eq. (7) differs from previous analyses mainly in the treatment of $\gamma_f$, which is calculated by solving Eq. (9). A common feature of previous treatments[2] of inductive erosion in this regime is to assume either $\gamma_o >> \gamma_f$ or $\gamma_f = 1$. It is easy to see that, for our $I_b = 2$ kA cases, either of these approximations will cause the erosion rate to be underestimated by as much as 50%, because the particle dynamics limit the amount of energy that can be extracted from the beam. Another consequence of these dynamics is that a population of particles with $\gamma = \gamma_f$ may remain behind the beam head. In those cases where $\gamma_f$ is large, as in the $I_b = 2$ kA cases, a significant portion of these particles may remain at small radii, near the beam, and will show up in the $I_{encl}$ plots as an apparent current enhancement behind the beam head (see Fig. 3). Because these particles are behind the pinch region, they are an artifact with no effect on the beam head dynamics.

## III. Emittance Driven Erosion

For a beam propagating in near-equilibrium, transverse emittance losses are confined to the beam head, where the pinch force is not sufficient for confinement. In cases where this is the dominant erosion mechanism, the loss of particles in the radial direction causes the length scale for pinching to increase so that an increasing portion of the beam is susceptible. One expects these losses to be significant only when the pinch force and inductive $E_z$ spike at the head of the beam are weak, as in the case of low current. When considering the decrease in the erosion rate as the current is lowered, emittance losses would appear to place a lower bound on the erosion rate given by Eq. (7).

This issue was recently addressed in this regime by Buchanan,[2] who employed the envelope equations of Lee and Cooper,[7] which require that the radial profile of the beam be a function that is parameterized by $R(\zeta,z)$, the root mean square radius. This radial function is specified and $R(\zeta,z)$ is solved for. In Buchanan's analysis, a Gaussian profile was used. The resulting equations could not be solved analytically, but the lack of an equilibrium solution (characterized by $\partial/\partial z = 0$) was demonstrated, indicating a nonzero erosion rate for all time. When the equations were solved numerically for a wide range of parameters it was found that the asymptotic erosion rate is a constant given by empirical expression

$$\beta_o - \beta_p = 0.18 \frac{1}{\sqrt{\gamma_o}} \left(\frac{r_b}{r_c}\right)^{2(1+f)} f^{0.9} \quad . \tag{11}$$

This was addressed independently by Nguyen and Uhm,[8] who again applied the envelope equations of Lee and Cooper to a beam with a Gaussian radial profile. They made the additional assumption that, after a short transient, the erosion rate is constant and the axial profile of the beam is fixed so that all relevant qualities vary only as $X = v_p t - z$, where $v_p$ is the velocity of the eroding pinch point. As above, the envelope equations were solved numerically with resulting erosion rates summarized by the expression:

$$\beta_o - \beta_p = \frac{1}{\sqrt{\gamma_o}} \left(\frac{r_b}{r_c}\right)^3 \times \begin{cases} 0.094\, f^{0.85} & f > 0.1 \\ 0.044\, f^{0.5} & f < 0.1 \end{cases} \quad . \tag{12}$$

From Eq. (7) and Eqs. (11) and (12) we expect that emittance erosion should not contribute significantly to losses in high current beams, which is apparently the case for the parameters used in Table I. At low current

(< 1 kA) and high $\gamma_o$ (> 20), however, these equations suggest that significant effects should be observable in the simulations.

We investigated this possibility by making several runs with $I_b$ = 1 kA, $\gamma_o$ = 20, $\zeta_r$ = 10 cm, $\zeta_{max}$ = 100-400 cm. The values used for the ionization fraction, $0.055 \leq f \leq 1.0$, and the ratio of beam to channel radius, $1.0 \leq r_b/r_c \leq 3.0$, were chosen so as to satisfy two conditions: (1) we require $n_c \leq n_b$ throughout the channel so that all channel electrons will be expelled and (2) the predicted emittance erosion rate must dominate over the inductive effects. From Eqs. (11) and (12) erosion rates ranging from $\beta_o - \beta_p < 0.01$ up to $\beta_o - \beta_p > 0.08$ were expected for these parameters.

As in the inductive cases, erosion was measured from plots of $I_{encl}$ versus $\zeta$ once steady-state erosion was established. In contrast with the inductive case, where this could be determined from the average particle energy in the beam head, we had to rely on axial profiles of beam quantities to indicate steady-state, or near steady-state behavior. In all cases, we found erosion rates of $.01 < \beta_o - \beta_p < .03$, which varied only sluggishly with f and $r_b/r_c$. The measured rates also varied with the numerical parameters, $\Delta\zeta$ and $\Delta\tau$, indicating that the erosion rates were less than or of the order of the numerical errors.

To clarify these data, we repeated several of the runs with $\gamma_o$ = 5. This reduction in $\gamma_o$ should double the rate of emittance erosion, according to (11) and (12). Inductive erosion effects were removed in these cases by specifying $E_z$ = 0 in the part of the simulation where the beam particles are acted on by the fields (the particle push routine). In all cases, we found $\beta_o - \beta_p$ = 0.005, a reduction in the erosion rate that is opposite the scaling predicted in (11) and (12). Because the measurements were made in the asymptotic limit as required to obtain steady-state behavior, we

concluded that the rate of erosion due to the finite emittance of the beam tends toward zero in the asymptotic limit. This conclusion is supported by further analysis of the simulations.

To further investigate the results, the beam was diagnosed for average transverse emittance as a function of $\zeta$ throughout the simulation. Plots of $I_{encl}$ versus $\zeta$ from a run in which $\gamma_o = 5$, $f = 1$, $r_b = r_c = 2$ cm, $I_b = 1$ kA and in which $E_z = 0$ were specified in the particle push routine as shown in Fig. 5. Early in the simulation, at $c\tau = 4$ meters, the initial rise length of 10 cm has increased to 100 cm, and a low emittance population of particles, with $T < T_o/2$, has developed at the beam head, where $T_o$ is the initial transverse temperature of the beam. Beyond $c\tau = 4$ meters, the axial profile evolves slowly, with both the rise length and the low-emittance population continuing to increase and the rate of increase in these quantities tending toward zero. Note that because of the low energy, $\gamma_o = 5$, $\beta_o = 0.98$, the beam motion relative to the coordinates will be discernible over the course of the simulation, which continues until $c\tau = 40$ meters. This motion can be seen in the the $c\tau = 4$ m and $c\tau = 40$ m plots of Fig. 5. When measuring the cumulative effects of the transient erosion process over a long distance, this must be taken into account.

The progress toward an asymptotic state can be seen in Fig. 6, where the growth of the low emittance population is shown by plotting $\zeta_T$ versus $z$, where $\zeta_T$ is the coordinate of the point at which the beam particles have transverse temperature $T = T_o/2$ and $z = c\tau$. Particles with $\zeta < \zeta_T$ will have lower emittance. As the beam reaches an asymptotic state, the motion of $\zeta_T(z)$ will match the motion of the beam body, $\zeta_b(z) = (1 - \beta)z$, so that $\zeta_T(z)$ and $\zeta_b(z)$ will have the same slope. A line with slope $d\zeta/dz = 1 - \beta$ is also plotted in Fig. 6. Note that for $z \gtrsim 20$ m the two slopes have converged to within numerical fluctuations.

The result of an asymptotically vanishing erosion rate is clearly a departure from the predictions of Eqs. (13) and (14). The discrepancy resides in the assumption of self-similar radial dynamics which is fundamental to the derivation of the envelope equations.[7] Note that self-similarity implies that $\langle v_r \rangle = (r/R)dR/dt$, where the beam density profile is a fixed function with a scale radius R and the brackets indicate an average over particles within a thin annulus of radius r. In other words, a Gaussian beam remains Gaussian as it expands. Departures from self-similar dynamics have been observed in our simulation results via plots (not shown) of beam density versus radius both in the head and in the body of the beam. We found that the beam profile at the head of the beam, initially zero for $r \gg r_b$, developed "wings" at large radii while remaining peaked on axis. The formation of this highly non-Gaussian profile occurred early in time, when the high temperature particles escaped the weak pinch potential. Low temperature particles, which remained trapped near the axis, contributed to the increased rise length of the beam. The radial profile was preserved in the beam body throughout.

## IV. Conclusions

We have seen that numerical simulations of inductive erosion agree closely with the theory over a wide range of parameters, even when the beam dynamics are complicated by unstable behavior in the beam head. These results demonstrate that at low energies (< 5 MeV) careful consideration of the relativistic dynamics of the beam particles are required for accurate prediction of inductive erosion rates. This, in effect, limits ones ability to reduce the erosion rate by various means because a lower erosion rate results in a higher $\gamma_f$. At higher energies, the $\gamma_o \gg \gamma_f$ approximation holds, and our results are in agreement with previous formulations.[2]

In the case of emittance erosion, simulations indicate that a steady-state erosion rate is not established and that the radial expansion at the beam head is not self-similar, thereby departing from previous theoretical assumptions.[2,8] As the beam-channel equilibrium is established, these beams develop a long rise length of low-emittance particles, with an erosion rate that tends towards zero. Because the simulations show that this asymptotic behavior establishes itself only over large propagation distances, this may not be easily observable in laboratory cases of interest. For these cases a new analysis, in which the radial dynamics are treated more carefully, would be required.

## Acknowledgments

We are happy to acknowledge many helpful and stimulating discussions with M. Mostrom of Mission Research Corporation.

This work was supported by the Defense Advanced Research Projects Agency, under contract number N60921-86-WR-W0233.

## Appendix: The FRIEZR Simulation Code

For these studies we have used an electromagnetic particle simulation code, FRIEZR,[9] which was written to study the propagation of high energy electron beams in the Ion Focus Regime in an axisymmetric coordinate system. The elements of the code are beam and plasma electrons which are treated as particles, and plasma ions which may be treated as an immobile background. The code is written in a transformed coordinate system $(r,\zeta,\tau)$, where $\zeta = ct - z$ and $\tau = t$. For a highly relativistic beam, the axial variable, $\zeta$, measures distance behind the beam head. The beam moves slightly slower than c so the beam head slips slowly backward in the coordinate system, but for high energy beams and short propagation distances, the slippage is not significant relative to the size of the simulation region. The particle dynamics are determined from the solution of Maxwell's equations written in the $(r,\zeta,\tau)$ variables with current and charge densities determined from the simulation particles. We write the equations for the vector and scalar potentials, $\vec{A}$ and $\phi$, in a gauge suggested by Lee which is particularly convenient for axisymmetry.[10] In this gauge, which has the condition

$$\nabla_\perp \cdot \vec{A}_\perp = 0 \ , \tag{A1}$$

we may write the parallel and perpendicular components of Ampere's law as

$$\nabla_\perp^2 \left( \frac{\partial A_z}{\partial z} + \frac{1}{c} \frac{\partial \phi}{\partial t} \right) = \frac{4\pi}{c} \nabla_\perp \cdot \vec{J}_\perp \tag{A2}$$

and

$$\nabla_\perp^2 A_z + \frac{1}{c} \frac{\partial E_z}{\partial t} = - \frac{4\pi}{c} J_z \ . \tag{A3}$$

We change variables to the $(r, \zeta=ct-z, \tau=t)$ coordinate system and write

$$\nabla_\perp^2\left(-\frac{\partial a}{\partial \zeta} + \frac{1}{c}\frac{\partial \phi}{\partial \tau}\right) = \frac{4\pi}{c}\nabla_\perp \cdot \vec{J}_\perp \tag{A4}$$

and

$$\nabla_\perp^2(a + \phi) + \left(\frac{1}{c}\frac{\partial}{\partial \tau} + \frac{\partial}{\partial \zeta}\right)E_z = -\frac{4\pi}{c}J_z \ , \tag{A5}$$

where

$$a = A_z - \phi \tag{A6}$$

and

$$E_z = -\left(\frac{1}{c}\frac{\partial}{\partial \tau} + \frac{\partial}{\partial \zeta}\right)a - \frac{1}{c}\frac{\partial \phi}{\partial \tau} \ . \tag{A7}$$

Using the continuity equation,

$$\nabla_\perp \cdot \vec{J}_\perp - \frac{\partial J_z}{\partial \zeta} + \frac{\partial \rho}{\partial \tau} + c\frac{\partial \rho}{\partial \zeta} = 0 \ , \tag{A8}$$

and Gauss' law,

$$\nabla_\perp^2 \phi + \frac{\partial E_z}{\partial \zeta} = -4\pi\rho \ , \tag{A9}$$

we may write equations (A4) and (A5) as

$$\nabla_\perp^2\left(-\frac{\partial a}{\partial \zeta} + \frac{1}{c}\frac{\partial \phi}{\partial \tau}\right) = \frac{4\pi}{c}\left(\frac{\partial J_z}{\partial \zeta} - \frac{\partial \rho}{\partial \tau} - c\frac{\partial \rho}{\partial \zeta}\right) \tag{A10}$$

and

$$\nabla_\perp^2 a + \frac{1}{c}\frac{\partial E_z}{\partial \tau} = \frac{4\pi}{c}(\rho c - J_z) \ . \tag{A11}$$

In axisymmetry, $A_r = 0$ and the $A_\theta$ equation is decoupled from the a and $\phi$ equations, so that

$$\nabla^2 A_\theta - \frac{A_\theta}{r^2} - \frac{1}{c}\frac{\partial}{\partial\tau}\left(\frac{1}{c}\frac{\partial}{\partial\tau} + 2\frac{\partial}{\partial\zeta}\right)A_\theta = -\frac{4\pi}{c}J_\theta \,. \tag{A12}$$

These equations determine the dynamics of the system and are solved at each time step to determine the potentials from the charge and current densities. The electric and magenetic fields are then obtained from the potentials in the usual way. The field equations are differenced implicitly in both the radial and axial directions, but an alternate version with explicit differencing in the axial direction has also been used. Once the fields are calculated, the code pushes all particles relativistically in Cartesian coordinates using standard techniques. In order to determine the densities, we use a particle lay-down scheme which is quadratic in the radial direction and linear (or Nearest Grid Point in the alternate version) in the axial direction. The code should be valid for moderate energy as well as high energy beam propagation studies.

## References


1. G. J. Caporaso, F. Rainer, W. E. Martin, D. S. Prono, and A. G. Cole, Phys. Rev. Lett. 57, 1591 (1986).
2. H. L. Buchanan, Phys. Fluids 30, 221 (1987) and references within.
3. W. M. Sharp and M. Lampe, Phys. Fluids 23, 2383 (1980).
4. K. T. Nguyen, R. F. Schneider, J. R. Smith, and H. S. Uhm, Appl. Phys. Lett. 50, 239 (1987).
5. M. A. Mostrom, D. Mitrovich, B. B. Godfrey, D. R. Welch, and R. M. Clark, Bull. Am. Phys. Soc. 33, 1883 (1988).
6. S. A. Bludman, K. M. Watson, and M. N. Rosenbluth, Phys. Fluids 3, 747 (1960).
7. E. P. Lee and R. C. Cooper, Particle Accelerators 7, 83 (1976).
8. K. T. Nguyen and H. S. Uhm (private communication).
9. G. Joyce, J. Krall, S. Slinker and R. Hubbard (private communication).
10. W. S. Sharp, S. S. Yu, and E. P. Lee, (private communication).

| $I_b$ (kA) | f | $\beta_o-\beta_p$ (FRIEZR) | $\beta_o-\beta_p$ [Eq. (7)] |
|---|---|---|---|
| 2 | 0.2 | 0.024 | 0.022 |
| 2 | 0.5 | 0.039 | 0.046 |
| 2 | 1.0 | 0.094 | 0.084 |
| 5 | 0.2 | 0.043 | 0.040 |
| 5 | 0.5 | 0.085 | 0.090 |
| 5 | 1.0 | 0.16 | 0.17 |
| 10 | 0.2 | 0.061 | 0.062 |
| 10 | 0.5 | 0.15 | 0.14 |
| 10 | 1.0 | 0.28 | 0.26 |

Table I. Erosion rates from simulation results and corresponding values predicted by Eq. (7).

Fig. 1 $E_z$ versus $\zeta$, $R_{1/2}$ versus $\zeta$, and $n_c$ and $n_b$ versus $\zeta$ are plotted separately at $c\tau = 7$ meters for a beam with parameters: $I_b = 5$ kA, $f = 1.0$, $\gamma_o = 10$, $r_b = 1$ cm, $r_c = 2$ cm and $r_w = 33$ cm.

Fig. 2 $I_{encl}$ versus $\zeta$ plots overlayed for $c\tau = 5$ meters (solid) and 10 meters (dashed) show erosion of the current. $I_{encl}$ is the total current within $r = 5r_b$. Here, parameters are the same as for Fig. 1. Such plots were used to measure the erosion rates given in Table I.

Fig. 3 $I_{encl}$ versus $\zeta$ plots are overlayed for $c\tau = 30$ meters (solid) and 40 meters (dashed) for a beam with parameters: $I_b = 2$ kA, $f = 0.2$, $\gamma_o = 10$, $r_b = 1$ cm, $r_c = 2$ cm and $r_w = 33$ cm.

Fig. 4 $E_z$ versus $\zeta$, $R_{1/2}$ versus $\zeta$, and $n_c$ and $n_b$ versus $\zeta$ are plotted separately at $c\tau = 30$ meters. The parameters are the same as in Fig. 3.

Fig. 5 $I_{encl}$ versus $\zeta$ plotted at $c\tau = 4$ and 40 meters shows an increase in the rise length, $\zeta_r$, and the development of a low-emittance population at the beam head. Areas with low transverse temperature, $T < T_o/2$, are shaded. Parameters are $I_b = 1$ kA, $f = 1$, $\gamma_o = 5$ and $r_b = r_c = 2$ cm. $E_z = 0$ is specified in the particle push routine.

Fig. 6 The coordinate location of the $T = T_o/2$ point, $\zeta_T$, is plotted versus $c\tau$ for the simulation pictured in Fig. 5. As the asymptotic near-equilibrium state is reached, this point will become stationary with respect to the beam body, attaining a slope $d\zeta_T/dz = d\zeta_b/dz = 1 - \beta$, where $d\zeta_b/dz$ is the velocity of the beam body relative to the simulation coordinate frame and $z = c\tau$. A line with slope $1 - \beta$ is also plotted.

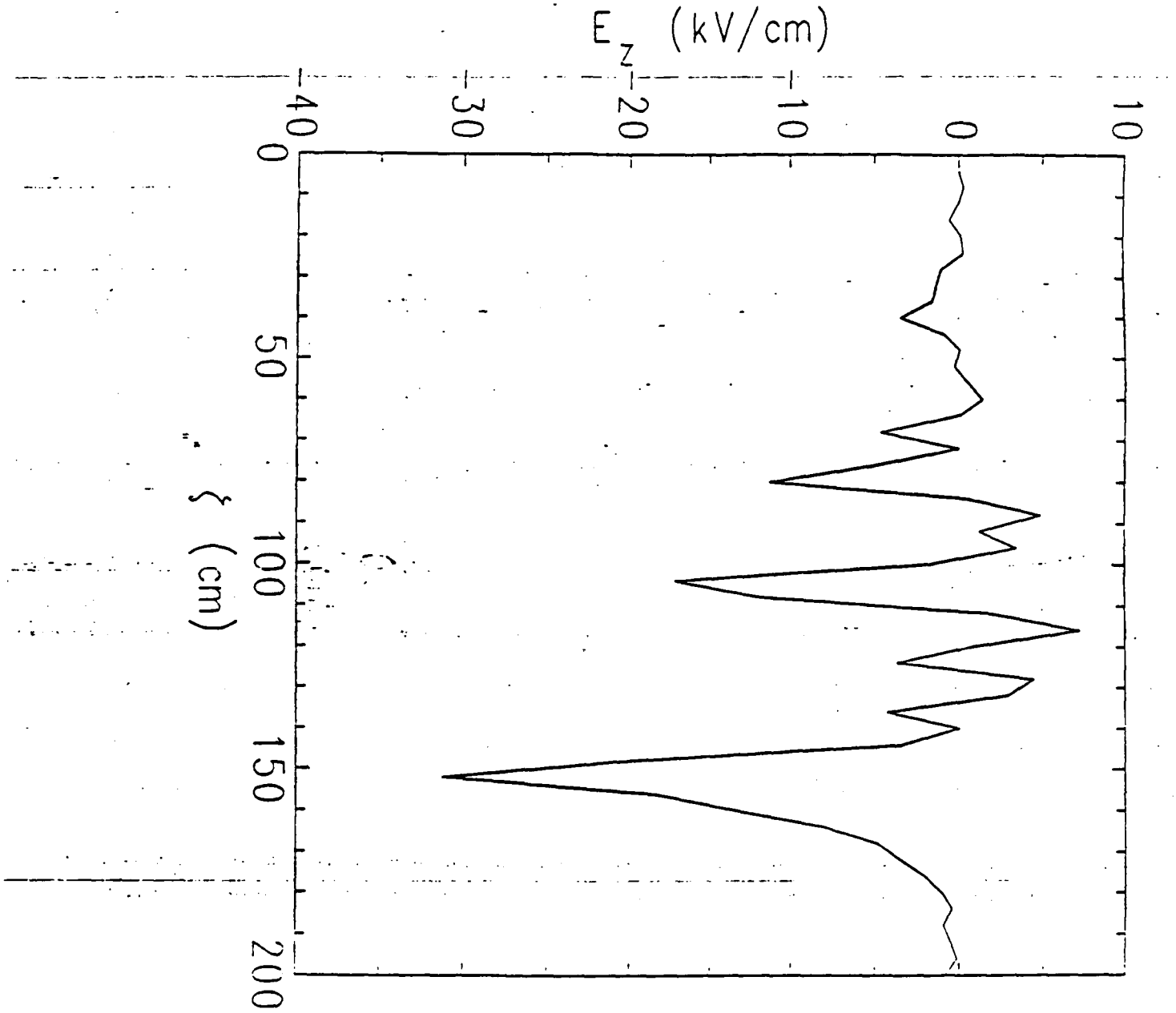



Figure 1(A)

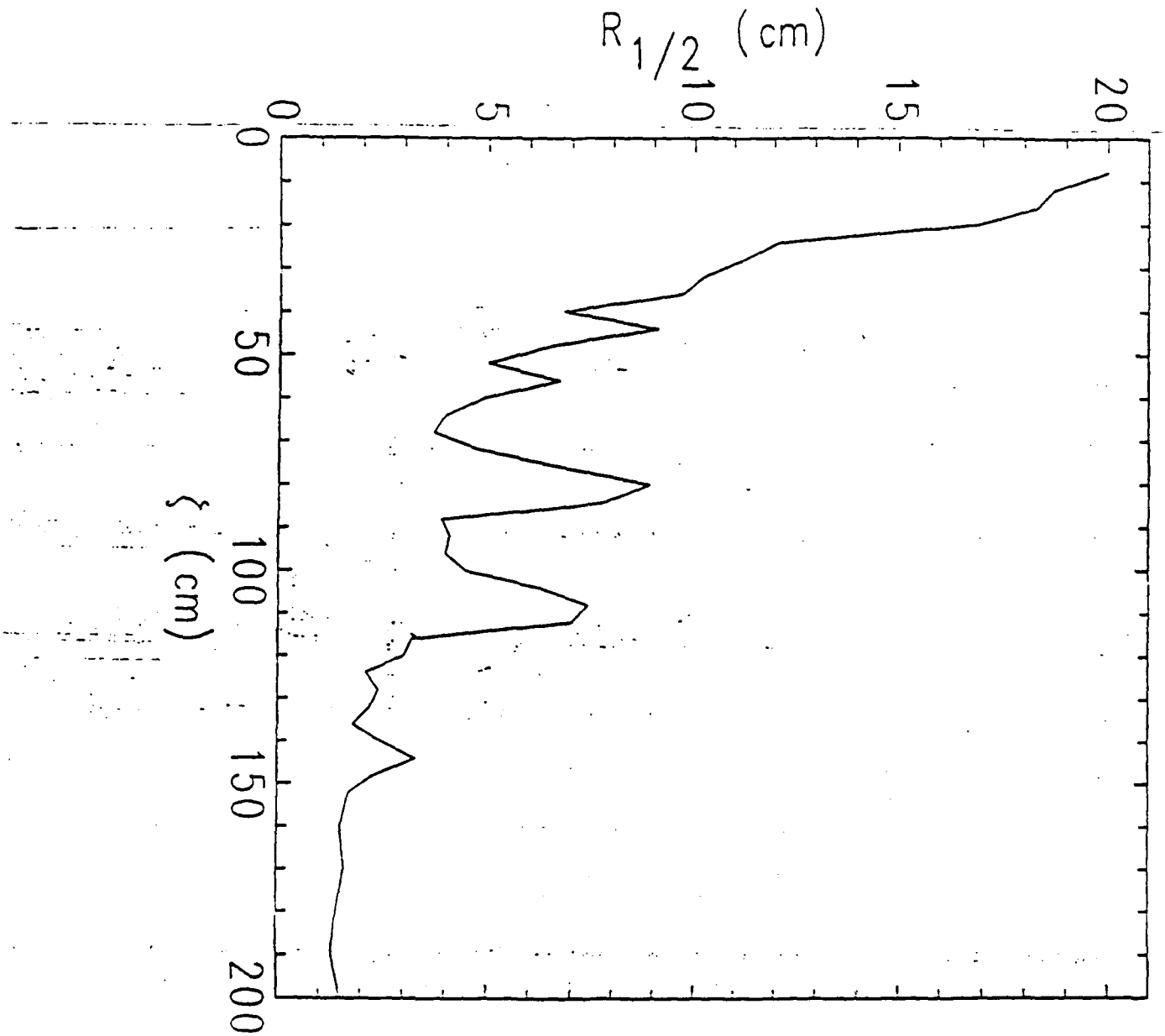



Figure 1(B)

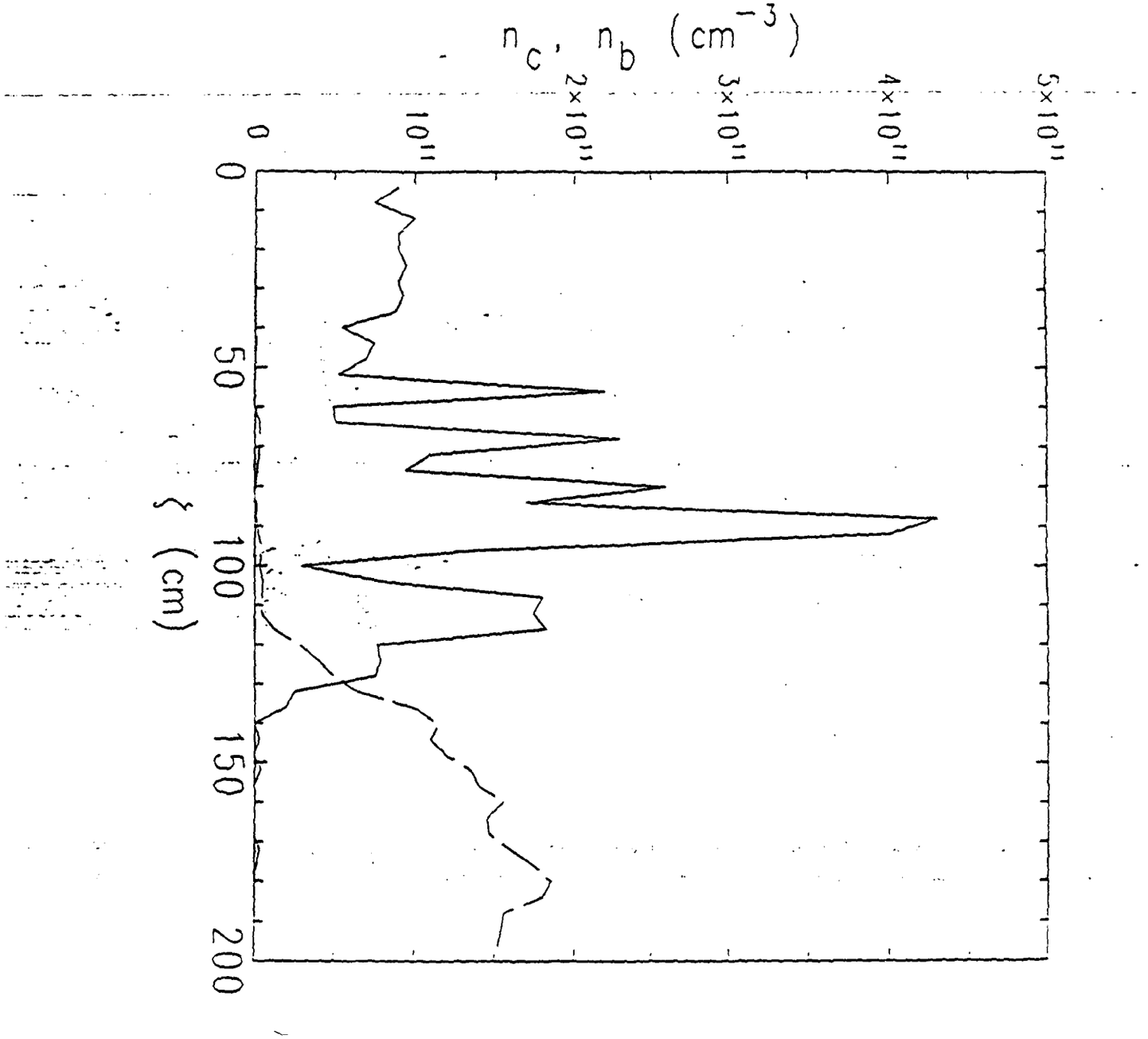

$n_c$, $n_b$ ($cm^{-3}$)
0
$10^{11}$
$2\times10^{11}$
$3\times10^{11}$
$4\times10^{11}$
$5\times10^{11}$
0
50
100
150
200
$\zeta$ (cm)

Figure 1(C)

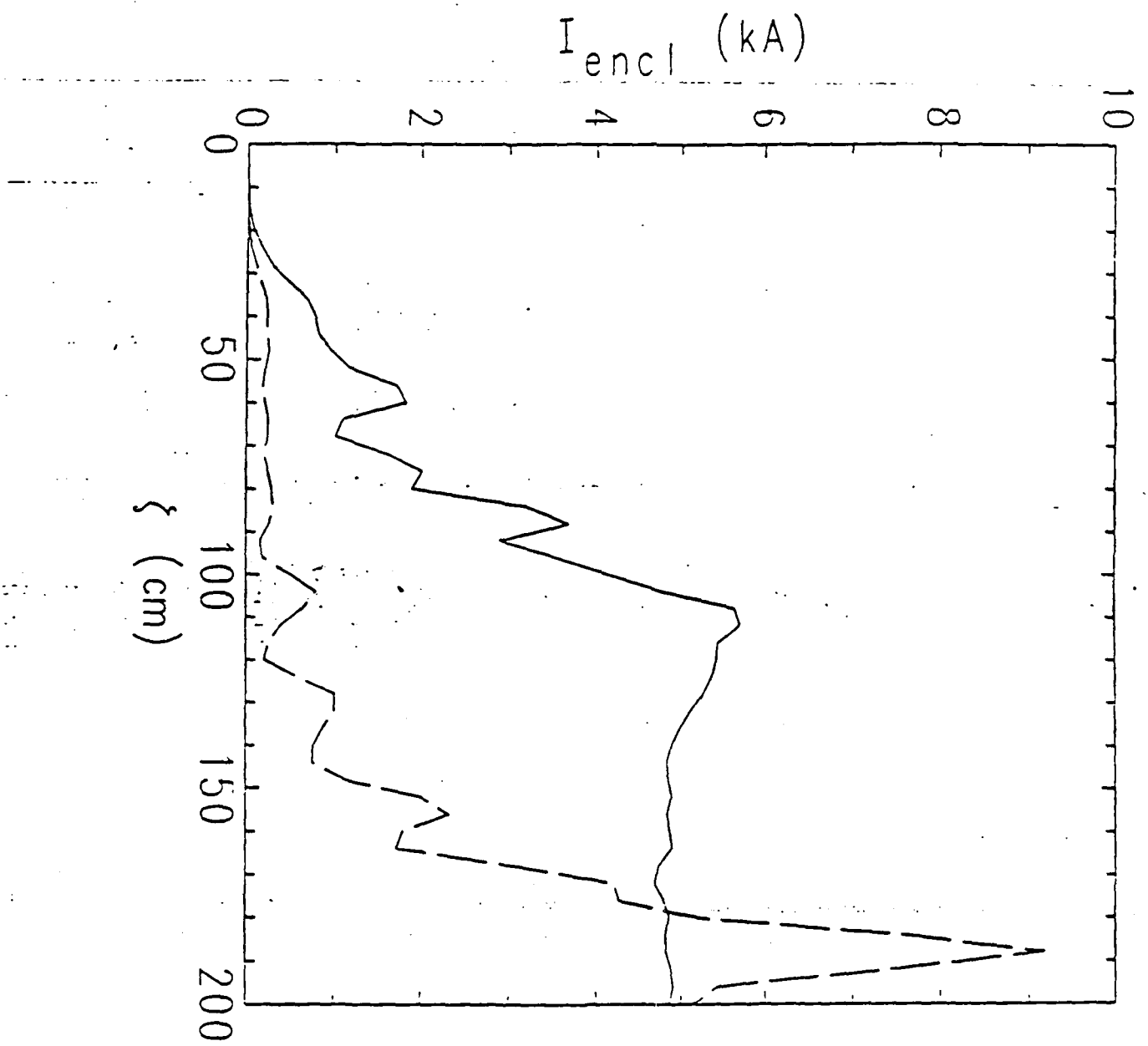



Figure 2

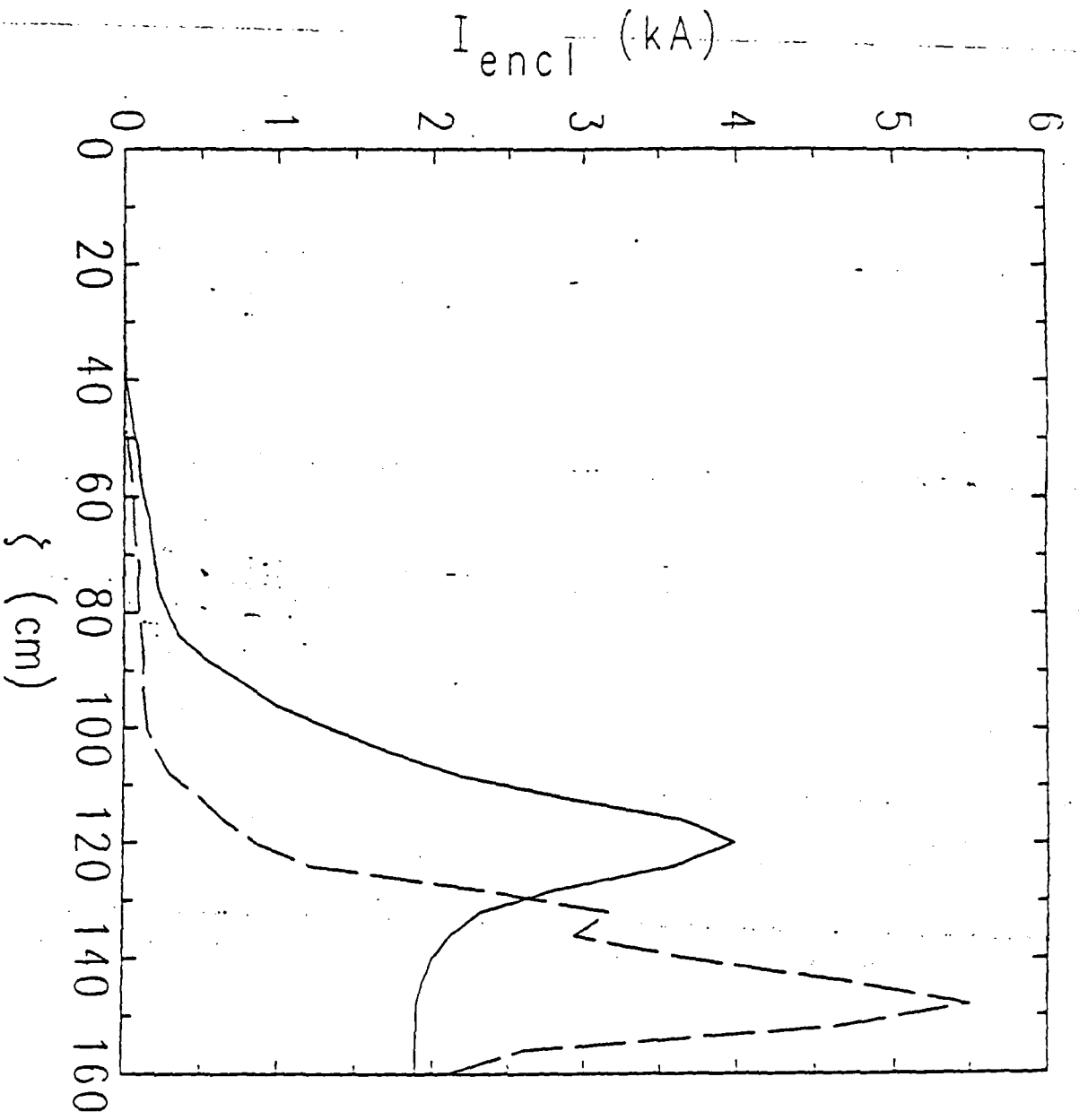



Figure 3

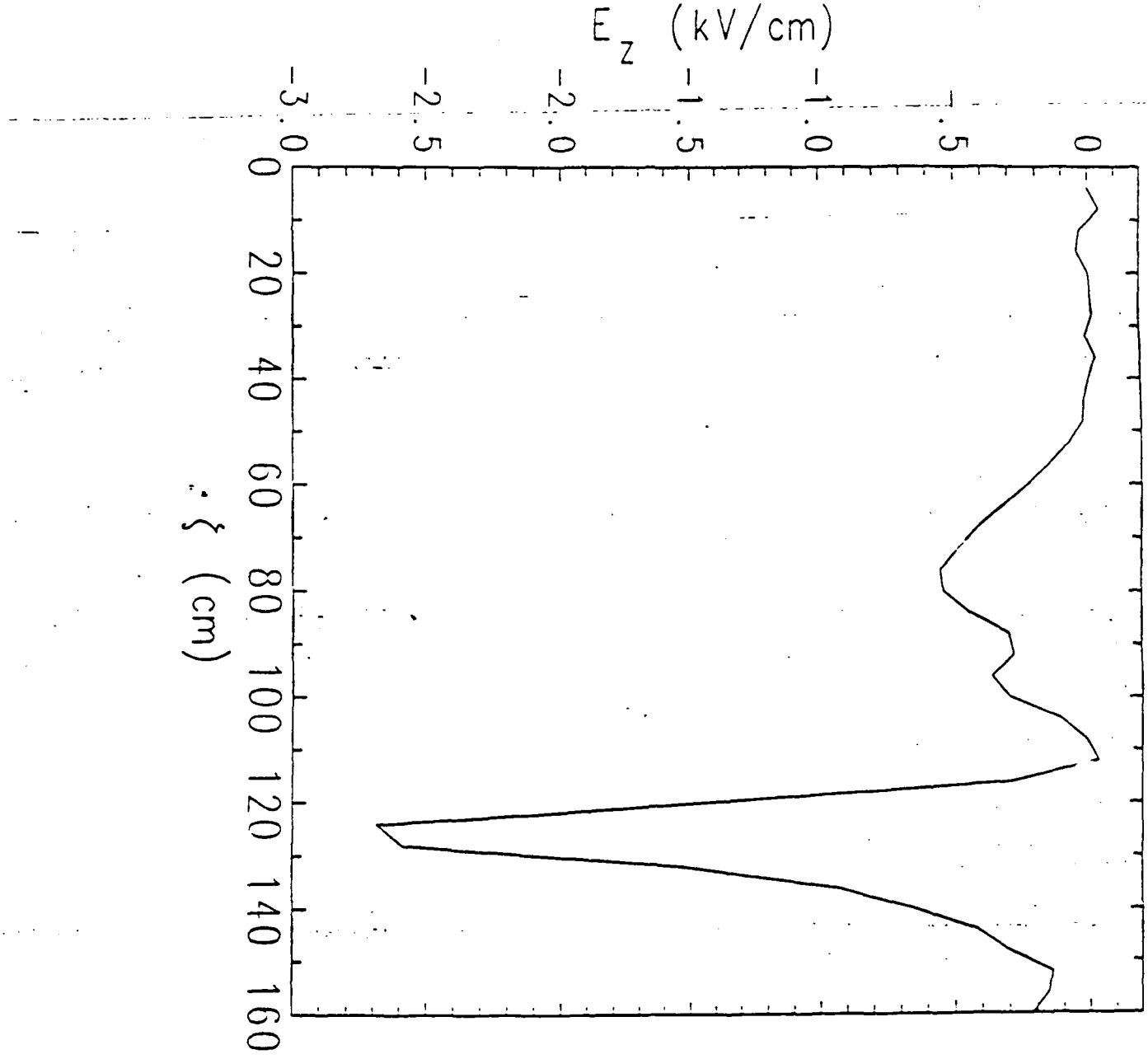



Figure 4(A)

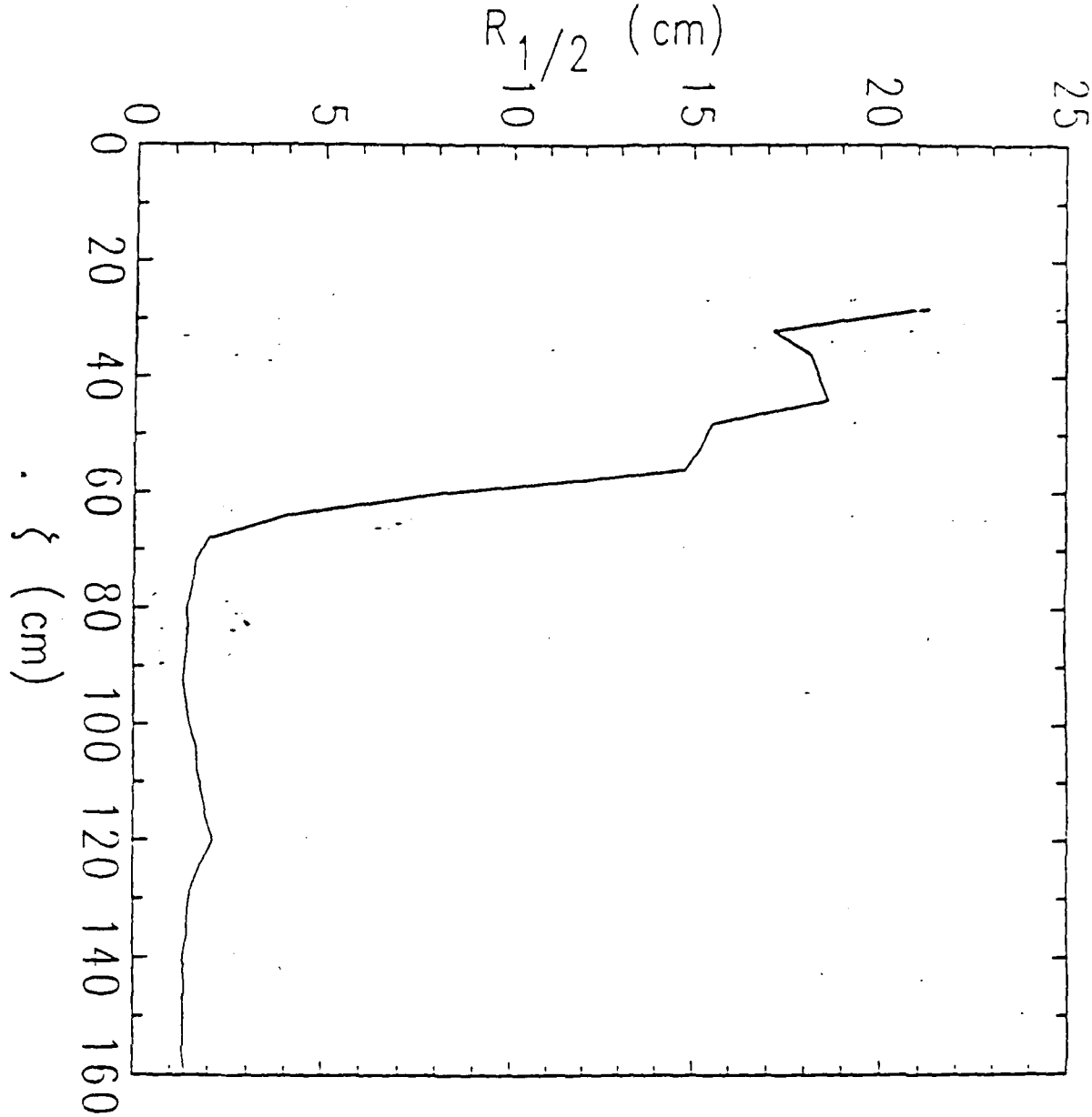



Figure 4(B)

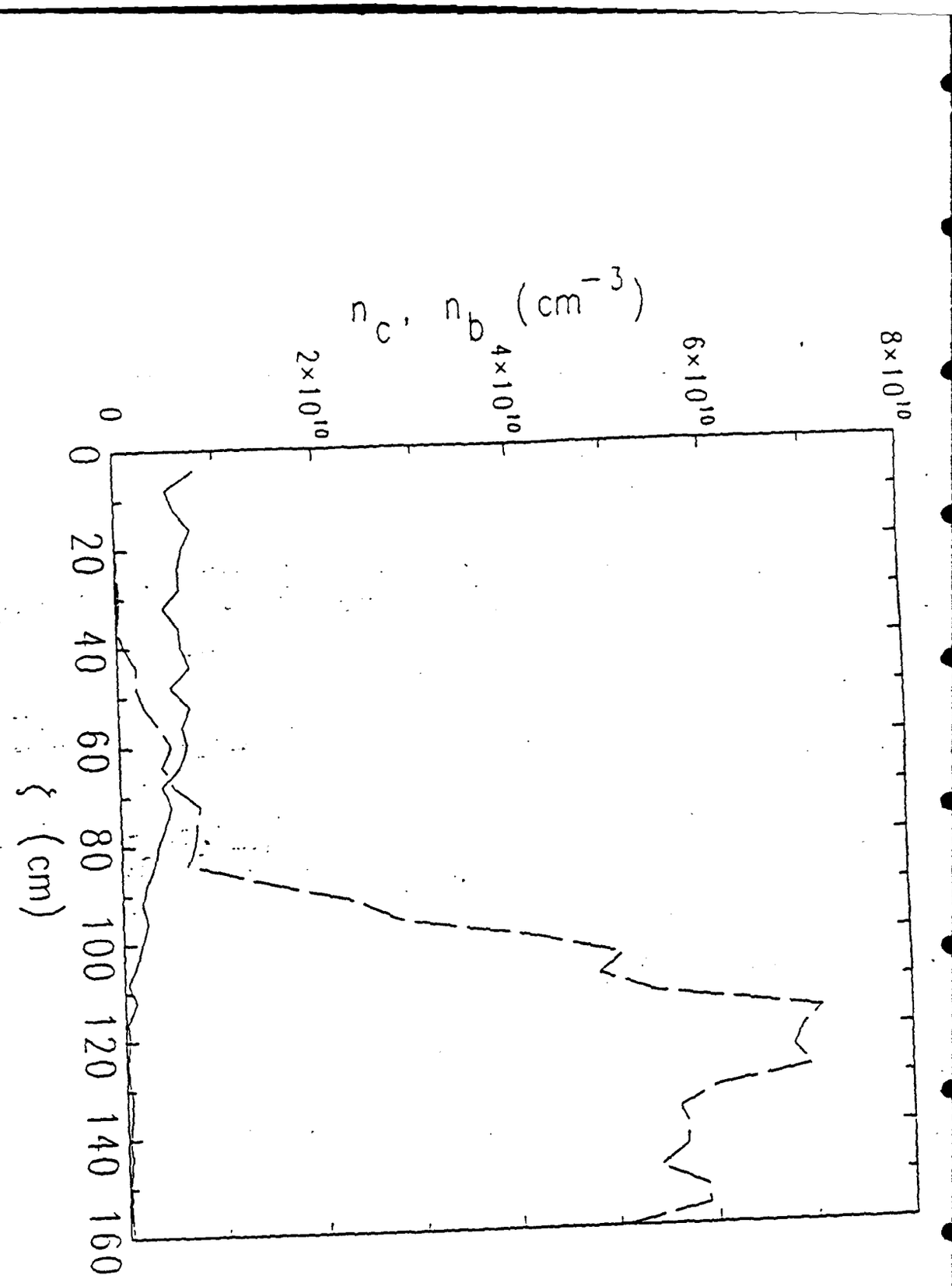

$n_c$, $n_b$ $(cm^{-3})$
0
$2\times10^{10}$
$4\times10^{10}$
$6\times10^{10}$
$8\times10^{10}$
0
20
40
60
80
100
120
140
160
ζ (cm)

Figure 4(C)

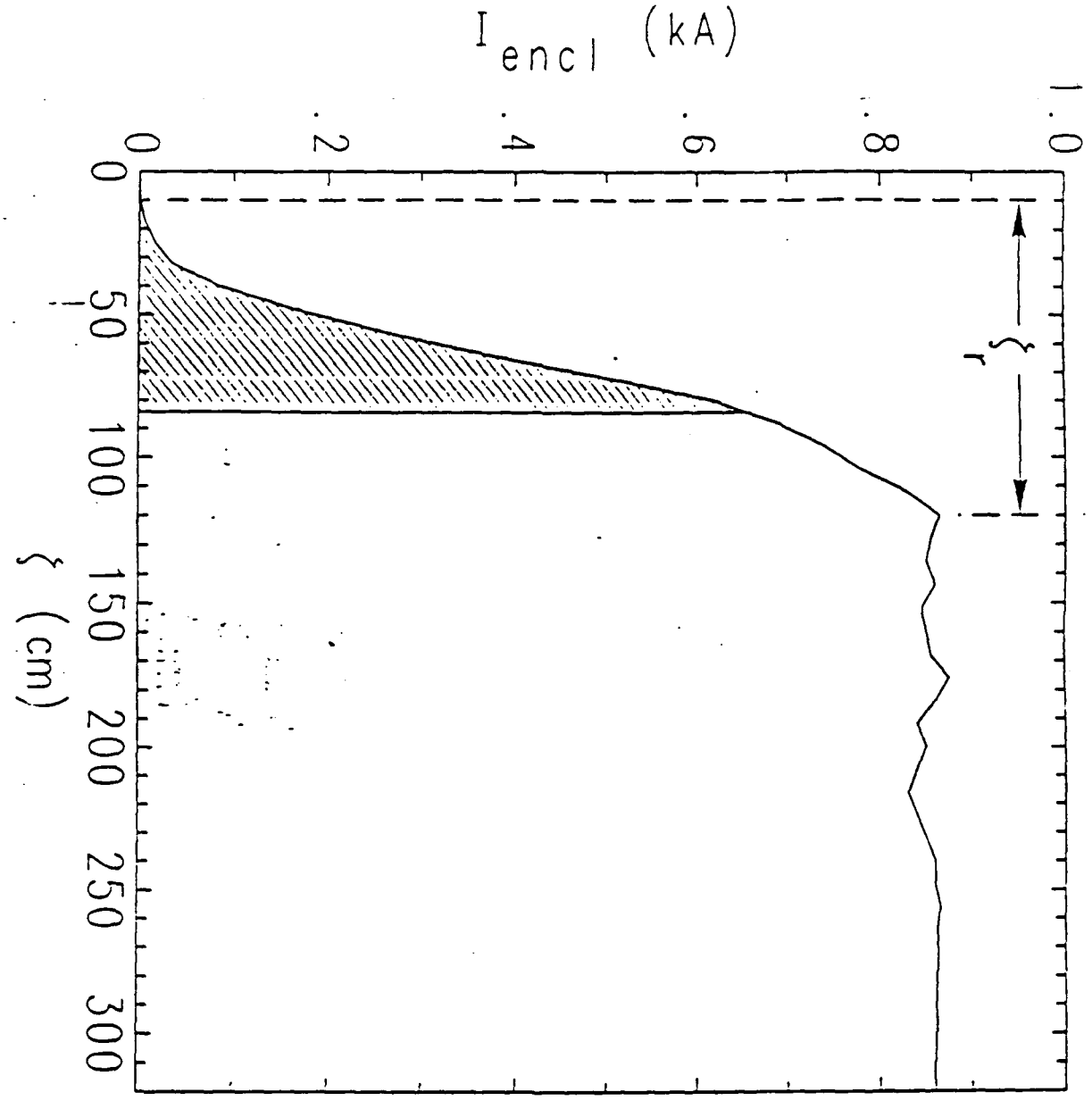



Figure 5(A)

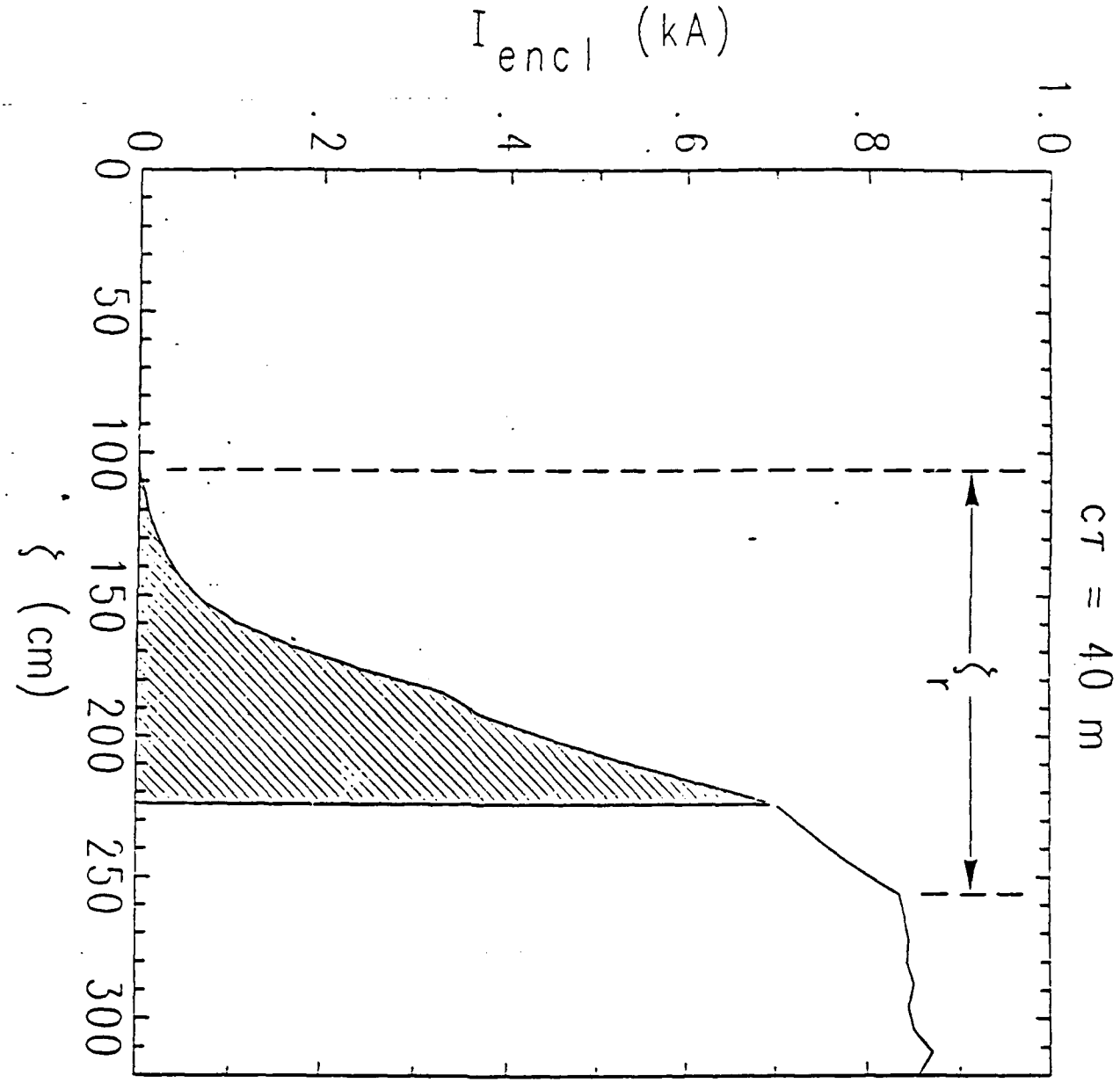



Figure 5(B)

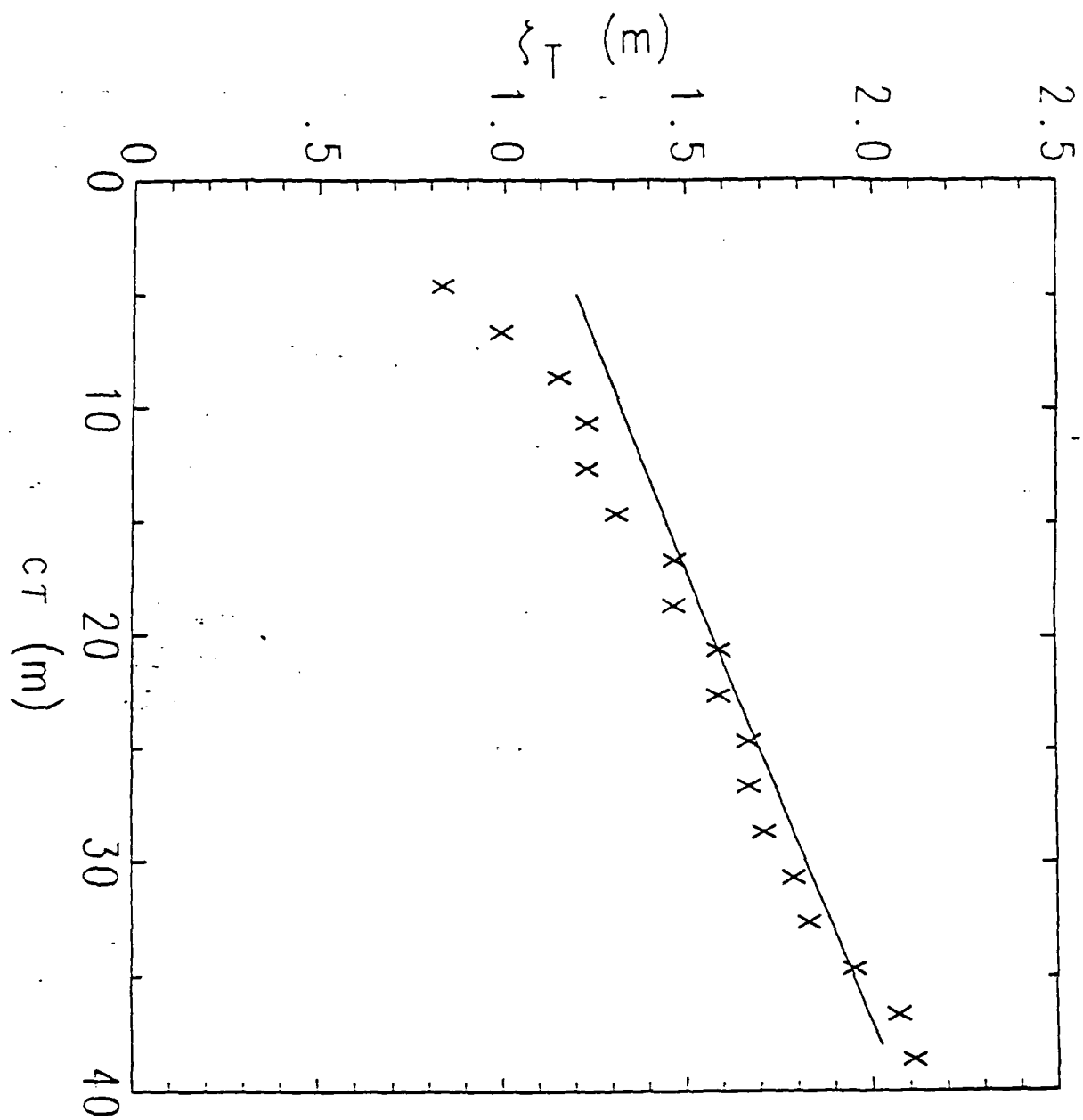



Figure 6

# APPENDIX W

## Analysis of the NSWC Beam Erosion Experiment

# ANALYSIS OF THE NSWC BEAM EROSION EXPERIMENT

K. Nguyen, J. Smith*, R. Schneider, H. Uhm
and J. Krall**

Naval Surface Warfare Center
*Titan/Spectron
**Science Applications Intl. Corp.

Recently an experiment was performed at NSWC[1]. The objective of this experiment was to quantify beam head erosion as a result of energy loss due to the inductive axial electric field in propagating through a preformed IFR plasma channel, i.e., inductive erosion[2-4]. Inductive erosion occurs at the beam head where the channel electrons are expelled to set up a potential minimum (the positive ion channel) so that the rest of the beam pulse can follow. In this paper, a theoretical analysis of the experimental results is presented. Theoretical calculations and experimental data are found to be in good agreement. A detailed description of the experimental setup can be found in reference (1).

The inductive axial electric field can be found from Poisson's equation, together with the pertinent component of generalized Ampere s and Faraday's equations. In cylindrical coordinates, these equations can be written as

$$\frac{1}{r}\frac{\delta}{\delta r}(rE_r) + \frac{\delta E_z}{\delta z} = 4\pi e(n_i - n_e - n_b), \tag{1}$$

$$\frac{1}{r}\frac{\delta}{\delta r}(rB_\theta) = \frac{4\pi}{c}(J_{zb} + J_{ze}) + \frac{1}{c}\frac{\delta E_z}{\delta t}, \tag{2}$$

$$\frac{\delta E_z}{\delta r} - \frac{\delta E_r}{\delta z} = \frac{1}{c}\frac{\delta B_\theta}{\delta t}, \tag{3}$$

where the subscripts (i, e, b) denote ions, channel electrons and beam, respectively. Assuming beam electrons are moving at speed $v_z \approx c$ so that we can neglect beam self-fields, then Eqs. (1) and (2) can be combined by using Gallilean transformation $\zeta = ct - z$ to give (assuming ions do not move)

$$\frac{1}{r}\frac{\delta}{\delta r}[r(E_r - B_\theta)] = 4\pi e\,[n_i(r) - n_e(r,\zeta)] - \frac{4\pi}{c}J_{ze}(r,\zeta) \tag{4}$$

Whereas, Eq. (3) can be rewritten as

$$\frac{\delta E_z}{\delta r} = -\frac{\delta}{\delta \zeta}(E_r - B_\theta). \tag{5}$$

We can combine Eqs. (4) and (5) to have

$$E_z(r,\zeta) = 2\frac{\delta}{\delta \zeta}\int_r^{R_w}\left[\frac{eN_e(r',\zeta)}{r'} + \frac{I_{ze}(r',\zeta)}{cr'}\right]dr', \tag{6}$$

or

$$E_z(r,\zeta) = \frac{\delta}{\delta \zeta}[\phi_e(r,\zeta) - A_{ze}(r,\zeta)]. \tag{7}$$

Here $R_w$ is the conducting wall radius, $\phi$ and A are the scalar and vector potential, respectively. If we neglect any axial motion of the channel electrons, then Eq. (7) can be further reduced to

$$E_z(r,\zeta) = \frac{\delta \phi_e}{\delta \zeta}(r,\zeta). \tag{8}$$

In this form, we can readily relate the inductive axial electric field and hence beam energy loss to the expulsion of the channel electrons. It is important to note that if, due to some physical reasons, the channel electrons can return before hitting the wall, then Eq. (8) indicates that the beam electrons can also be accelerated.

Thus beam energy loss (or gain) can be found from Eq. (8) to be

$$m_e c^2 \frac{d}{dz}[\gamma(\zeta) - 1] = - e \frac{\delta}{\delta \zeta} \phi_e(\zeta). \tag{9}$$

For steady state erosion where beam current and energy axial profiles are uniform, Eq. (9) can be integrated to yield an erosion rate [3-5]

$$\frac{\Delta \zeta}{\Delta z} = \frac{eN_e c \ln (R_T/R_e)}{8.5 (\gamma - 1)}. \tag{10}$$

Here N is the line density, $R_e$ is the channel radius, and $R_T$ is the final radius where most of the channel electrons are trapped. However, for part of the initial rise time of the beam pulse, no steady state erosion exists since not all the channel electrons are promptly expelled.[6] The propagation range required for complete erosion of this transient portion of the beam is given by

$$\Delta Z_t = \frac{17 \int_0^{\zeta_1} [\gamma(\zeta') - 1] d\zeta'}{I_b(\zeta_1) L}, \tag{11}$$

where $\zeta_1$ is defined as $N_b(\zeta_1) = N_e$, and $L = \ln (R_T/R_e)$ is a dimensionless inductance. No meaningful erosion can be measured unless the propagation range is larger than $\Delta Z_t$. Furthermore, no steady state erosion exists if beam current and energy axial profiles are not flat, even after the initial transient period. In this case, the erosion formula is given by

$$\Delta Z_e = \Delta Z_t + \frac{17}{L} \int_{\zeta_1}^{\zeta_e} \frac{[\gamma(\zeta') - 1]}{I_e(\zeta')} d\zeta', \tag{12}$$

where we have defined

$$I_e(\zeta) = \begin{cases} eN_e c & \text{for } N_e < N_b(\zeta), \\ I_b(\zeta) & \text{for } N_e > N_b(\zeta). \end{cases} \tag{13}$$

In obtaining Eq. (12), we have assumed that the beam only expelled a sufficient number of channel electrons to neutralize its own space charge and these electrons remain trapped at radius $R_T$. Eq. (12) is the main equation that we use in analyzing the data of the present experiment.

The experiment was performed with the Febetron 705X accelerator which was capable of producing a beam with peak energy of 2.8 MeV. However, for the

present experiment the accelerator was only charged up to 2 MeV at peak which gave us a nominal triangular shape beam of 30 ns long ( ~15 ns rise, ~15 ns fall time), with peak current of about 4.5 kA for a 2 cm diameter fine grain graphite cathode or 6.5 - 7.5 kA if a velvet cathode of the same size was used. The beam was injected into a stainless steel drift tube of 25 cm in radius which was filled with Argon at $2 \times 10^{-4}$ Torr. The drift tube was also immersed in a 120 Gauss axial magnetic field. This field was necessary in order to confine the plasma channel created by direct ionization with a low energy electron beam (400 Volts) from a Godfrey gun[4]. The channels were carefully diagnosed with a Langmuir probe to have a nominal radius of 1 cm and line densities ranging from $5 \times 10^{11}$ $cm^{-1}$ to more than $1 \times 10^{12}$ $cm^{-1}$ depending on the adjustable low energy beam current.

It is important to note at this point several effects of the 120 Gauss axial field will have on this experiment. Firstly, at moderate current (i.e., 4.5 kA), the energy gained by the channel electrons are not sufficient to allow their escape to the wall and they are consequently trapped at some large radius. Secondly, the gyro-motions of trapped electrons can modulate the beam pulse at the gyro-frequency. Thirdly, trapped channel electrons can return during current fall time, upon seeing a positive net charge, and accelerate the beam tail end. Finally, plasma wakefield effects[5] due to the diffuse plasma at large radius are expected to be much reduced by the axial magnetic field and the beam long rise time in this experiment. To verify these phenomena,a simulation was performed with the NRL's FRIEZR code. In this simulation, the beam was injected with a triangular current profile of 30 ns long (15 rise, 15 fall) and a corresponding triangular voltage trace that starts at 800 kV, peaks at 2 MV, and falls back to 800 kV as expected from the experiment. Snapshots of beam current profile and contour plot of the channel electrons density at ct = 800 cm are shown in Figures 1-a and 1-b, respectively. The channel line density was $5 \times 10^{11}$ $cm^{-1}$. The fact that the channel electrons are trapped at large radius and eventually return at the beam tail are clearly observed. Beam current modulation also begins to show at this point. After 9 meters of propagation, beam tail energy is accelerated to 1.3 MV from an initial 800 kV and the beam profile is clearly seen to be modulated at gyro-frequency.

Two series of shots were performed in the experiment. In the first series of shots, a graphite cathode was employed to obtain a beam with peak current of 4.5 kA (13 ns rise, 17 ns fall times). The corresponding voltage trace peaks at 2 MV with a base that starts and ends at 800 kV. Input and output current traces were obtained with Rogowski coils (7.5 cm radius) as new sections of drift tube were inserted (at 8', 16', 28', and 40'). In most of these shots, the channel line density was about $9.3 \times 10^{11}$ $cm^{-1}$($I_{emax}$ = 4.3 kA) or larger. Input and output traces for $I_{emax}$ = 4.3 kA case at 8' and 28' are shown in Figs. 2-a and 2-b, respectively. No erosion was observed at 8' as expected due to transients. At 28 ft., the beam had eroded about 17 ns as measured from the initial beam edge to the leading edge of the remaining pulse where the current is half of the observed peak. Theoretically, we expected about 14 ns by using Eq. (12) and assuming $R_T$ = 15 cm (Fig. 1-b). The discrepancy can probably be attributed to the transient beam head emittance driven erosion[5] due to the large initial transverse temperature ( ~35 kV) as measured by vacuum free expansion[7]. Current traces at 40 ft. was observed to be indistinguishable from those at 28 ft. indicating substantial energy gain of the beam tail as expected for these experimental parameters. 4 ns more of beam pulse would have eroded

away if there was no energy gain. We also note that for case in which channel exceeds beam peak line density, experimental data was observed to be similar to the case presented here, where $N_e = N_{bmax}$. This observation justifies the assumption that the beam only expels a sufficient number of channel electrons to neutralize its own space charge. In order to avoid channel trapping by the axial field and to reduce the beam emittance, a velvet cathode was employed which allowed us to increase beam peak current to about 6.5 - 7.5 kA (15 ns rise, 15 ns fall) for a peak beam energy of 2 MV. The higher current allowed us to perform the experiment at $N_e < N_{bmax}$ and still observe substantial erosion. The propagation range in these cases was 40 ft. Input and output current traces were obtained with Rogowski coils. A simultaneous current trace was obtained at 25' (or 14') by using a B-dot probe located 25 cm from the beam axis. The experimental results are shown in Figs. 3-a to 3-d. Fig. 3-d is the result of two shots under similar conditions. It is interesting to note the oscillations seen in the B-dot current traces which are near the electron gyro-frequency. These oscillations were not picked up by the Rogowski coils which had a 7.5 cm radius. A plausible explanation for this observation is that the beam may have perturbed the diffuse plasma at large radii and/or a small fraction of the expelled channel electrons may have been trapped near the wall, thus the electron gyro-motions are only picked up by the B-dot probe which locates near the wall. Comparisons between theoretical predictions and experimental data are shown in table 1. Excellent agreement between theory and experiment strongly indicates that inductive erosion has been observed.

| Figure | $I_{bmax}$ (kA) | $N_e/N_{bmax}$ | Z(ft) | Exp (ns) | Theory (ns) |
|---|---|---|---|---|---|
| 3-a | 6.5 | 0.65 | 25 | 13 | 15 |
| | | | 40 | 20 | 21 |
| 3-b | 6.5 | 0.92 | 25 | 17 | 19 |
| | | | 40 | 23 | 26 |
| 3-c | 7 | >1 | 25 | 22 | 21 |
| | | | 40 | 30 | 27 |
| 3-d | 7.5 | >1 | 14 | 18 | 15 |
| | | | 25 | 24 | 22 |
| | | | 40 | 30 | 28 |

Table 1. Comparisions Between Experiment and Theory [Eq. (12)].

## References


1. J. Smith et al., these proceedings.
2. W. M. Fawley, LLNL-UCID-19556 (July 1982).
3. H. L. Buchanan, Phys. Fluids 30, 221 (1987).
4. B. Godfrey et al., AMRC-R-741 (Nov 1985).
5. J. Krall et al., these proceedings.
6. K. Nguyen et al., LLNL-UCID-8709146, p. 365 (1987)
7. K. Nguyen et al., Bull. APS 33, p. 1951 (1988).

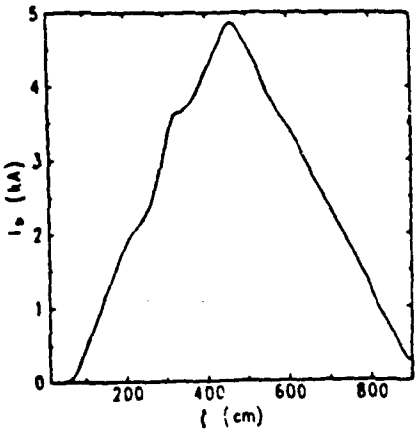



Fig. 1-a: Snapshot of beam current at ct=800 cm

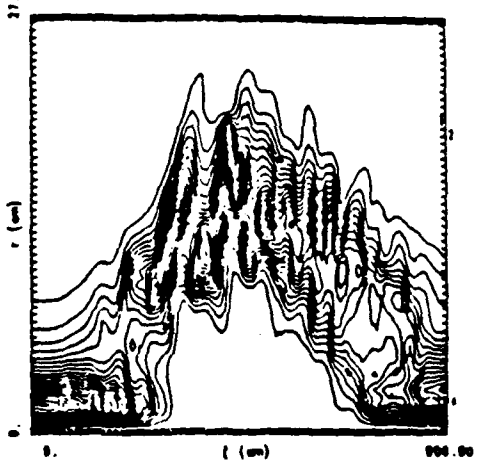


Fig. 1-b: Snapshot of channel electrons density contours at ct = 800 cm

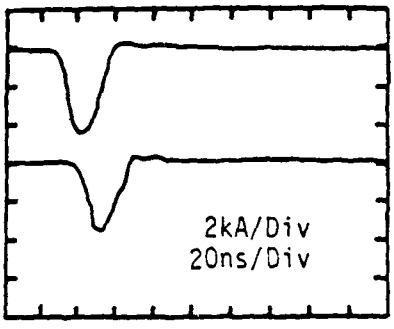



Fig. 2-a: Input (top) and output traces for Z = 8'

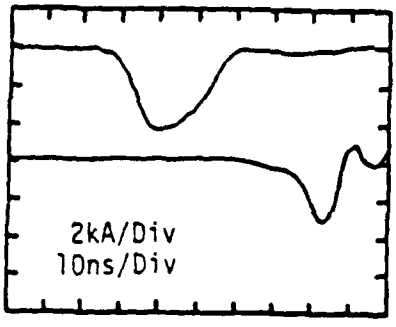



Fig. 2-b: Input (top) and output traces for Z = 28'

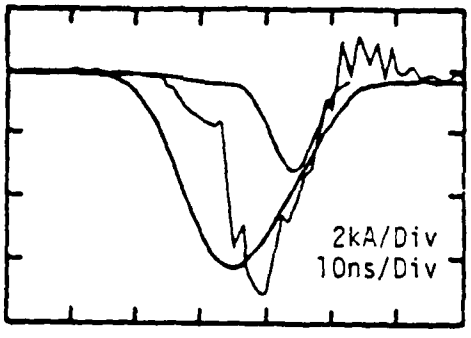



Fig. 3-a: Current traces at input, 25' and 40'

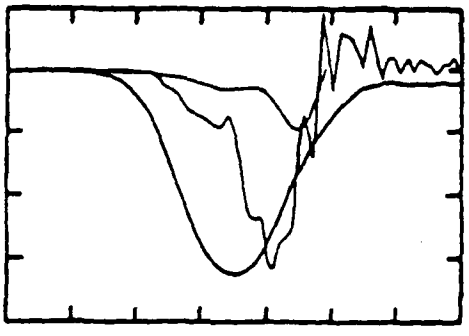


Fig. 3-b: Current traces at input, 25' and 40'

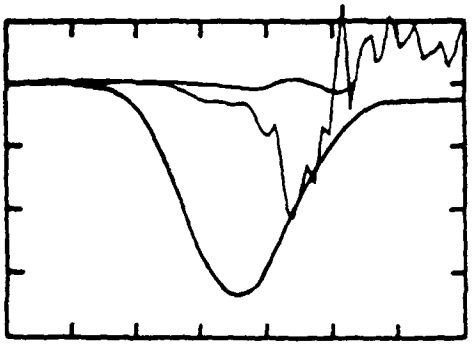


Fig. 3-c: Current traces at input, 25' and 40'

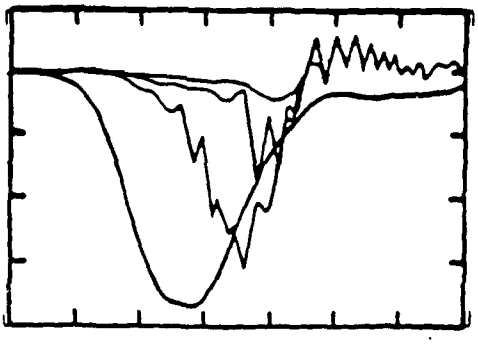


Fig. 3-d: Current traces at input, 14', 25' and 40'

# APPENDIX X

## Delphi Theory Axisymmetric Erosion and Wake Field Effects

# DELPHI THEORY
# AXISYMMETRIC EROSION AND WAKE FIELD EFFECTS

Glenn Joyce, Martin Lampe, Richard Hubbard, and Steve Slinker
Naval Research Laboratory
and
Jon Krall and K. Popadopoulos
Science Applications International Corporation, McLean, VA

A laser guided relativistic electron beam experiences a loss of energy as it propagates due to the expulsion of plasma electrons from the plasma channel produced by the laser. The energy loss occurs mostly at the head and results in an erosion of the beam front. A number of studies of this phenomenon have established the amount of erosion as a function of the beam and plasma parameters. If, in addition to the laser generated channel there is an ambient plasma in the vicinity of the beam, the beam can produce large amplitude plasma oscillations which can extract energy from the beam. These oscillations look like standing waves to the beam and cause the beam to lose energy in some axial regions and to gain energy in other regions. The effects are similar to those of a plasma wake field accelerator although the maximum energy which can be gained by any beam segment is twice the initial energy. One of the effects of the wake field is an enhanced erosion of the beam but another consequence is that the beam may lose its equilibrium and break up into bunches of shorter beams. The consequences of this beam break up are not fully understood. We have studied both inductive erosion and wake field effects using the axi-symmetric particle simulation code FRIEZR.

The theoretical formula for axi-symmetric erosion is given by

$$\text{Erosion rate} = fI_b L/17\gamma_o$$

where f is the channel neutralization fraction, $I_b$ is the beam current, L is the system inductance, and $\gamma_o$ is the beam energy.

The table on following page shows the results of a number of code runs and compares the erosion measured in the numerical experiments with the theoretical result. We have chosen a beam energy comparable to the energy we expect from the SUPER_IBEX experiment at NRL and have used propagation ranges similar to what we expect from that experiment. Some of the methods of measuring the erosion, such as monitoring the position of the Ez spike as it moves backward from the beam head, are easy to determine in a numerical simulation but may be quite difficult to measure in an experiment, while others may be easier to duplicate experimentally. The results obtained from a number of methods give erosion values which are close to each other and to the theoretical result.

The plasma wake field is an electrostatic wave which is set up by the beam. As the beam propagates in the plasma, electrons are repulsed by the beam head and travel radially outward leaving behind an ion charge. If the rise time of the beam is sufficiently long, a volume of electrons will move out to a radius such that the beam plus the surrounding ion cloud will be charge neutral. If, however, the rise time is short, the electrons will overshoot the charge neutral radius and an excess of positive charge around the beam will attract the electrons. The oscillation of the plasma across this boundary occurs at the plasma frequency and will result in a wave of wavelength $2\pi c/\omega_p$ as measured from the beam head. This wave has an associated electric field whose axial component, Ez, alternates sign. During half the period, the field extracts energy from the beam and during the other half, the field adds energy. An example of the field structure is shown in Fig. 1. Over long distances of propagation, the effect of the electric field is to deplete the energy from some axial regions of the beam and to energize other regions.

For beams propagating in plasmas whose boundaries are far from the beam, there may be situations in which wake field effects do not occur since there are beams with so much charge that electrons will be pushed to such a large radius before reaching charge neutrality that they either never return (for practical purposes), or they lose any coherence with be beam before they return. This radius appears to be on the order of the electromagnetic skin depth, $(c/\omega_p)$ since past this distance the fields of the beam cannot easily penetrate the plasma. If we require that the skin depth be equal to or greater than the radius for charge neutrality, we obtain

$$I_b \leq 17/4 \text{ Ka.}$$

Note that the plasma density does not occur in the inequality and the condition is on the beam current only. For beams with currents less than about 4 kiloamperes, the structure and size of the plasma wave depends little on the beam, but mainly on the diffuse plasma. The wave can exist for a number of periods with only slight variations of the peak Ez field from peak to peak.

An examination of the equations governing the electromagnetic fields and the beam dynamics shows that a number of physical parameters scale with the beam radius. That is, if we know the properties of the beam propagation at one radius and diffuse plasma density, we can infer the properties at other radii and densities. The figure on the following page shows the dependence of the peak Ez field over a large range of plasma densities. In addition, this figure shows that the peak field is relatively independent of the beam radius at a constant plasma density. Using this information, we can understand some of the implications of the energy loss due to the wake fields. For example, $\Delta\gamma \approx 2*Ez*z$ where z is the propagation distance, and if $\gamma_o=40$, and $n_{p1}=10^4$, some segments of the beam will lose most of their energy after a propagation distance of about 10 kilometers. Most of this energy will be transferred to the other portions of the beam.

The portions of the beam which lose energy will eventually be lost from the beam. There are three mechanisms for the loss. The first and strongest can occur if the returning plasma electrons create a region around the beam in which there is an excess of negative charge. In this case, the radial confining force is reversed and becomes defocussing which causes the beam electrons to quickly spread to large radii. The second occurs even if the returning plasma is too diffuse to reverse the confining force. In this case, the beam eventually loses equilibrium because beam emittance is mismatched for the lower energy segments of the beam. Finally, the low energy particles may simply slow down and be left behind. Any of these effects will cause the beam to evolve into a train of beams with a length of half a plasma period. The front half wavelength of the beam which always loses energy will relatively quickly erode away and the half wavelength following will then become the beam front. As this happens, the phase of the plasma wave with respect to the beam will change and the long term consequences of this are not completely understood. We have done a simulation of this effect for a relatively high density, low energy beam ($n_{pl}$~$10^{9}$, $\gamma$~10) and in this case, the beam becomes fairly incoherent after the beam front disappears. The plasma density, for this example, was high enough to quickly disperse the low energy portions of the beam.

Wake fields may have important consequences in the propagation of laser guided beams. Even with fairly low density plasmas surrounding the beam, if the propagation distance is long enough, the beam may be broken into a train of pulses. The combination of beam head erosion and wake fields can cause the shorter pulses to be broken up as well.

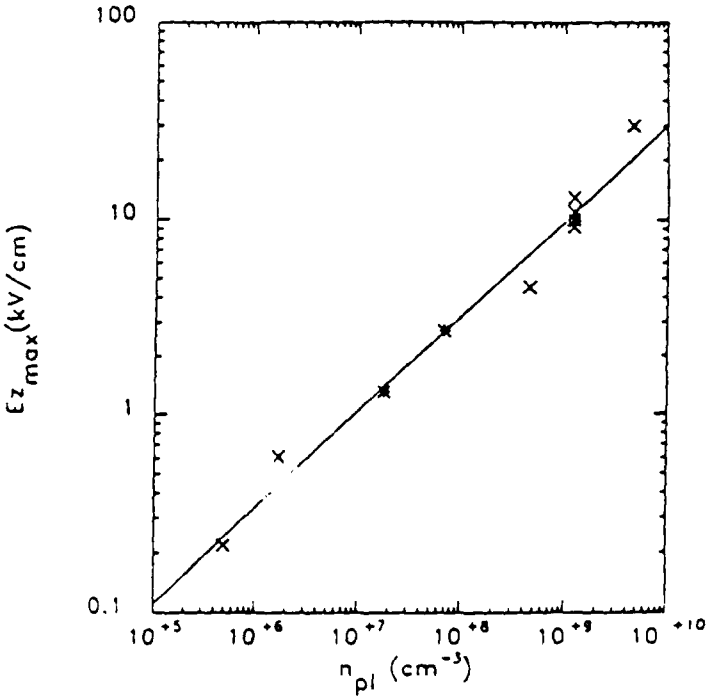
SIMULATION RESULTS

$\gamma$ = 10 $R_w$ = 30 cm

$R_b$ = 1 cm $\zeta_r$ = 50 cm

$R_c$ = 2 cm $\zeta_{max}$ = 100-400 cm

| I (kA) | f | $\sigma$ (FRIEDR) | $\sigma^{in}$ (L=5) |
|---|---|---|---|
| 2 | 1.0 | 0.058 | 0.059 |
| 2 | 0.5 | 0.031 | 0.030 |
| 2 | 0.2 | 0.024 | 0.012 |
| 5 | 1.0 | 0.156 | 0.147 |
| 5 | 0.5 | 0.085 | 0.074 |
| 5 | 0.2 | 0.035 | 0.029 |
| 10 | 1.0 | 0.25 | 0.294 |
| 10 | 0.5 | 0.13 | 0.148 |
| 10 | 0.2 | 0.052 | 0.058 |



# APPENDIX Y

## Numerical Studies of Erosion and Transport of Chopped and Unchopped Beams

# NUMERICAL STUDIES OF EROSION AND TRANSPORT OF CHOPPED AND UNCHOPPED BEAMS

J. Krall*, G. Joyce and K. Nguyen**

Naval Research Laboratory
*Science Applications Intl. Corp.
**Naval Surface Warfare Center

An electron beam propagating along a low density plasma channel in the ion focused regime (IFR) is characterized by a freely expanding head, a pinch region, where the plasma electrons are ejected from the channel and the beam pinches to its equilibrium value, and the beam body.

The pinch region of such a beam is associated with increasing net current and azimuthal magnetic field and an inductive $E_z$ spike. Energy loss in the beam electrons due to $E_z$ causes electrons to be lost from the beam head. Additional losses can result from the finite emittance of the portion of the beam that is not fully pinched. In this study, we use the FRIEZR simulation code to measure these effects and make comparisons with theoretical results.

In cases where a diffuse background plasma is present, it has been observed that wake fields are excited at the beam head as long as the rise length is less than the plasma wavelength, $\lambda_p = 2\pi c/\omega_p$.[1] These wake fields move with the beam, causing periodic disruptions, and have been observed in IPROP simulations where they are not reduced by 3-D effects.[2] Mostrom et al.[2] have observed, using IPROP simulations, that chopping the beam at a frequency $\omega_c > \omega_p$ will reduce wake field effects, apparently as a result of the ability of a chopped beam to maintain a long rise length. Here we use FRIEZR to verify these results, survey values of $\omega_c/\omega_p$ for optimum conditions, and contribute our own insights.

## INDUCTIVE EROSION

In IFR propagation, where energy losses due to scattering may be neglected, the inductive erosion rate of a beam pulse is given by[3]

$$\beta_o - \beta_p = \frac{efI_b L_c \beta_p}{mc^3(\gamma_o + \gamma_U - \gamma_f)}, \qquad (1)$$

where $\beta_o$ is the beam velocity, $\beta_p$ is the velocity of the pinch point, $(\gamma_f - 1)mc^2$ is the final energy of the particles as they are lost from the beam, $L_c = 2\log(r_w/r_c)$ is a dimensionless inductance and $r_c$ is the plasma channel radius. The field energy, which erodes with the beam energy, is given by $\gamma_U mc^2$, where

$$\gamma_U = \frac{e\tau_b L_b(1 - f)}{mc^3}. \qquad (2)$$

Here, $L_b = 2\log(r_w/r_b)$ is a dimensionless inductance and $r_b$ is the beam radius. For the vacuum case ($f = 0$) the above gives the familiar expression for the limiting current of a beam with $\gamma = \gamma_U$ propagating in a drift tube of radius $r_w$.

The value of $\gamma_f$ is determined by solving a cubic equation which is the result of a simple argument given in reference 4:

$$\gamma_f^3 - (\gamma_o + \gamma_U + 2C\gamma_o^2)\gamma_f^2 - \gamma_o^2\gamma_f + (\gamma_o + \gamma_U + C)\gamma_o^2 = 0 \ , \qquad (3)$$

where $C = efI_bL_b/mc^3$. Note that for $\gamma_o \gg 1$, the $\gamma_U = 0$, $\gamma_f = 1$ approximation used in previous treatments[5] holds. Some of our own results at $\gamma_o = 10$ are within this regime.

Numerically determined erosion rates for various values of $I_b$ and f are shown in Table 1. In all cases, $\gamma_o = 10$, $r_b = 1$ cm, $r_c = 2$ cm, $r_w = 33$ cm, $\zeta_r$(beam rise length) = 50 cm, and $\zeta_{max} = 100 - 400$ cm. The erosion rate predicted by Eq. (1) is also given. We see that the results agree closely with theory.

| $I_b$ (kA) | f | $\beta_o-\beta_p$ (FRIEZR) | $\beta_o-\beta_p$ [Eq. (1)] |
|---|---|---|---|
| 2 | 0.2 | 0.024 | 0.022 |
| 2 | 0.5 | 0.039 | 0.046 |
| 2 | 1.0 | 0.094 | 0.084 |
| 5 | 0.2 | 0.043 | 0.040 |
| 5 | 0.5 | 0.085 | 0.090 |
| 5 | 1.0 | 0.16 | 0.17 |
| 10 | 0.2 | 0.061 | 0.062 |
| 10 | 0.5 | 0.15 | 0.14 |
| 10 | 1.0 | 0.28 | 0.26 |

Table 1. Erosion rates from simulation results and corresponding values predicted by equation (1).

## EMITTANCE DRIVEN EROSION

This issue was recently addressed in this regime by Buchanan,[5] and independently by Nguyen and Uhm.[6] Both analyses employed the envelope equations of Lee and Cooper,[7] which require the radial structure of the beam be parameterized by $R(\zeta,z)$, the RMS radius. The radial function is specified and $R(\zeta,z)$ is solved for. In both cases, a Gaussian profile was used. The resulting equations could not be solved analytically, but numerical solutions over a wide range of parameters demonstrated nonzero erosion rates and resulted in empirical expressions for each case.

From these analyses we expect that emittance erosion should not contribute significantly to losses in high current beams, which is the case for the parameters used in Table 1 above. At low current (< 1 kA) and high $\gamma_o$ (> 20), however, they suggest that significant effects should be observable in the simulations.

We performed several runs with $I_b = 1$ kA, $\gamma_o = 20$, $\zeta_r = 10$ cm, $\zeta_{max} = 100$-400 cm. The values used for the ionization fraction, $0.055 \leq f \leq 1.0$, and the

ratio of beam to channel radius, $1.0 \leq r_b/r_c \leq 3.0$, were chosen so as to satisfy two conditions: (1) we require $n_c \leq n_b$ throughout the channel so that all channel electrons will be expelled and (2) the predicted emittance erosion rate must dominate over the inductive effects. Erosion rates ranging from $\beta_o - \beta_p < 0.01$ up to $\beta_o - \beta_p > 0.08$ were expected for these parameters. In all cases, we found erosion rates of $.01 < \beta_o - \beta_p < .03$, which varied only sluggishly with f and $r_b/r_c$. The measured rates also varied with the numerical parameters, $\Delta\zeta$ and $\Delta\tau$, indicating that the erosion rates were less than or of the order of the numerical errors.

We repeated several of the runs with $\gamma_o = 5$, which should double the rate of emittance erosion, according to the analytic expressions which scale as $\gamma^{-1/2}$. Inductive erosion effects were removed in these cases by specifying $E_z = 0$ in the FRIEZR particle push routine. In all cases, we found $\beta_o - \beta_p \approx 0.005$, a reduction in the erosion rate that is opposite the predicted scaling. We conclude from this that the rate of erosion due to the finite emittance of the beam tends toward zero in the asymptotic limit. This conclusion is supported by further analysis of the simulations.

To further investigate the results, the beam was diagnosed for average transverse emittance as a function of $\zeta$ throughout the simulation. Analysis of a run in which $\gamma_o = 5$, $f = 1$, $r_b = r_c = 2$ cm, $I_b = 1$ kA and in which $E_z = 0$ was specified in the particle push routine showed an increase in rise length from 10 cm at $z = c\tau = 0$ to 100 cm at $z = 4$ meters to 150 cm at $z = 40$ meters. Within this long rise length the emittance diagnostic showed that the high emittance particles were lost, so that an increasing portion of the rise length is composed of very low emittance particles. From $z = 4$ m to $z = 40$ m the axial profile evolved slowly, with both the rise length and the low-emittance population continuing to increase and the rate of increase in these quantities tending toward zero.

## PROPAGATION IN A DIFFUSE PLASMA

A Delphi beam propagating through a diffuse plasma will excite a plasma wave which will travel in phase with and disrupt the beam, unless the beam rise length is longer than the plasma wavelength, $\lambda_p = 2\pi c/\omega_p$. It has been observed, however, that such a beam will self-sharpen at the beam head so as to eventually excite these waves.[1] Recent simulations have shown that a rapidly chopped beam will develop and preserve a long rise length, reducing the amplitude of the plasma waves.[2]

In these studies we considered an $I_b = 2$ kA, $\gamma_o = 10$, $r_b = 1$ cm, $\zeta_{max} = 350$ cm, beam propagating in an $f = 0.5$ channel with a background density $n_p = 10^9$. This results in a plasma oscillation of wavelength $\lambda_p = 110$ cm. In our initial survey, we considered sinusoidally chopped beams with chopping wavelengths of $\lambda_c = \lambda_p/1.5$, $\lambda_p/2.0$ and $\lambda_p/2.5$ respectively. These runs were carried out to ten meters where, in an unchopped case, the electric field amplitude is 25 kV/cm. We found in the $\lambda_c = \lambda_p/1.5$ case that each pulse in the pulse train appeared to act independently of the others, exciting a 25 kV/cm wake field behind each pulse. In the $\lambda_c = \lambda_p/2$ case, the wakes from the beam head disrupted alternate beam pulses so that after ten meters, this beam resembled the unchopped result with correspondingly high electric fields. In the $\lambda_c/\lambda_p = 2.5$ case, the beam did not undergo severe disruptions and peak field amplitudes were less than 15 kV/cm. In this case, the beam experienced high transient fields before the rise length increased and the the field amplitudes decreased.

In an effort to understand the effects of this transient, we ran two cases with $\lambda_c = \lambda_p/2.5$, one with a rise length $\zeta_r = 5$ cm $<< \lambda_c$ and one with $\zeta_r = 50$ cm $> \lambda_c$, as well as an unchopped beam with $\zeta_r = 50$ cm. We measured the average energy per unit length in the beam as $U = (\gamma_{<5} - 1)I_{<5}$, where $\gamma_{<5}$ is the average gamma and $I_{<5}$ is the average current for particles enclosed within $r \leq 5r_b$. The presumption is that particles at radii greater than $5r_b$ are not useful for Delphi applications. This was compared with an ideal value, $U_I$, where the only losses are due to inductive erosion at the beam head as calculated via Eq. (1). After 18 meters, the $\zeta_r = 50$ cm chopped case developed a rise length of 150 cm with $E_z$ less than 6 kV/cm. The energy diagnostic showed $U/U_I = 0.69$ for this case, $U/U_I = 0.62$ for the unchopped case and $U/U_I = 0.38$ for the $\zeta_r = 5$ cm case, indicating the importance of the transient fields in developing the long rise length. Note that with the 350 cm of beam used in the simulations, we are modelling only the region near the beam head and expect the low field amplitudes in the $\zeta_r = 50$ cm chopped case to cause significantly less disruption of the beam body than is expected in the unchopped case.

## CONCLUSIONS

We have seen that numerical simulations of inductive erosion agree closely with the theory over a wide range of parameters. These results demonstrate that at low energies (< 5 MeV) careful consideration of the relativistic dynamics and field self-energy of the beam are required for accurate prediction of inductive erosion rates.

The result of asymptotically vanishing emittance erosion rates is clearly a departure from the analytic models. The discrepancy resides in the assumption of self-similar radial structure which is fundamental to the derivation of the envelope equations. This assumption appears to be too limiting in this case, where the beam must be parameterized, at the very least, by $\varepsilon(\zeta,z)$ as well as $R(\zeta,z)$, where $\varepsilon(\zeta,z)$ is the average emittance of the particles at a given $\zeta$ and $z$. The beam may in fact assume a highly non-Gaussian profile at early times, when high temperature particles escape from and low temperature particles remain trapped by the weak pinch potential.

The survey of frequencies for fast chopping of these beams indicates that $\lambda_p/\lambda_c > 2$ is required for effective suppression of wake fields in a background plasma. We also find that the transient fields can cause significant energy losses in the beam head of a chopped beam unless the pulse train has an initial rise length $\zeta_r > \lambda_c$. With this initial rise length, we find that energy losses in the region of the beam head are reduced relative to the unchopped case and that field amplitudes are reduced by a factor greater than four.

## REFERENCES


1. G. Joyce, M Lampe, R. Hubbard, S. Slinker, J. Krall and K. Papadopoulos, LLNL Report No. CONF 8709146, 361 (1987).
2. M. Mostrom et al., these proceedings.
3. J. Krall, K. Nguyen and G. Joyce, to be published.
4. J. Krall, K. Nguyen, R. Hubbard, G. Joyce, and M. Lampe, LLNL Report No. CONF 8709146, 395 (1987).
5. H. L. Buchanan, Phys. Fluids 30, 221 (1987) and references within.
6. K. T. Nguyen and H. S. Uhm, LLNL Report No. CONF 8506141, 533 (1985).
7. E. P. Lee and R. C. Cooper, Particle Accelerators 7, 83 (1976).

# APPENDIX Z

## Relativistic Beam Propagation Through Diffuse Plasmas

# RELATIVISTIC BEAM PROPAGATION THROUGH DIFFUSE PLASMAS

Glenn Joyce, Martin Lampe, Richard Hubbard, Steve Slinker
Naval Research Laboratory

Jonathan Krall
SAIC, McLean, Va.

A relativistic electron beam injected into a laser produced plasma channel can propagate for long distances while being guided by the channel. This propagation mode is known as Ion Focussed Regime (IFR) propagation. If, in addition to the laser generated channel, there is an ambient plasma in the vicinity of the beam, the beam can, under certain conditions, excite large amplitude electrostatic plasma oscillations or wake fields which can extract energy from the beam. These oscillations are standing waves in the beam frame and cause the beam to lose energy in some axial regions and to gain energy in other regions. One of the effects of the wake field is an enhanced erosion of the beam but another consequence which may be more important is that the beam may lose its equilibrium and break up into bunches of shorter beams. In addition to the generation of wake fields which are primarily axisymmetric, the beam is unstable to a transverse electrostatic instability called the transverse two stream instability. We have studied the wake field effects using the axisymmetric particle simulation code FRIEZR, and have developed a dispersion relation to help understand the transverse electrostatic instability.

## I. AXISYMMETRIC EFFECTS

The plasma wake field is an electrostatic wave which is set up by the beam. As the beam propagates in the plasma, electrons are repulsed by the beam head and travel radially outward leaving behind an ion charge. If the rise time of the beam is sufficiently long, the electrons will move out to a radius such that the beam plus the surrounding ion cloud will be charge neutral. If, however, the rise time is short, the electrons will overshoot the charge neutralization radius. The oscillation of the plasma across this boundary occurs at the plasma frequency and will result in a wave of wavelength $2\pi c/\omega_p$ as measured from the beam head. This wave has an associated electric field whose axial component, $E_z$, alternates sign. During half the period, the field extracts energy from the beam and during the other half, the field adds energy. An example of the field structure is shown in Fig. 1. Over long distances of propagation, the effect of the electric field is to deplete the energy from some axial regions of the beam and to energize other regions.

For beams propagating in plasmas whose boundaries are far from the beam, there may be situations in which wake field effects do not occur since there are beams with so much charge that electrons will be pushed to such a large radius

before reaching charge neutrality that they either never return (for practical purposes), or they lose any coherence with be beam before they return. This radius appears to be on the order of the electromagnetic skin depth, $(c/\omega_p)$. If we require that the skin depth be equal to or greater than the radius for charge neutrality, we obtain $I_b \leq 17/4$ kA. Note that the plasma density does not occur in the inequality and the condition is on the beam current only. For beams with currents less than about 4 kiloamperes, the structure and size of the plasma wave depends little on the beam, but mainly on the diffuse plasma. The wave can exist for a number of periods with only slight variations of the peak Ez field from peak to peak.

An examination of the equations governing the electromagnetic fields and the beam dynamics shows that a number of physical parameters scale with the beam radius. That is, if we know the properties of the beam propagation at one radius and diffuse plasma density, we can infer the properties at other radii and densities. Figure 2 shows the dependence of the peak Ez field over a large range of plasma densities. Using this information, we can understand some of the implications of the energy loss due to the wake fields. For example, $\Delta\gamma=2zE_z$ where z is the propagation distance, and if $\gamma_o=20-40$, and $n_{pl}=10^4-10^5$, some segments of the beam will lose most of their energy after a propagation distance of about 10-20 kilometers. Most of this energy will be transferred to the other portions of the beam.

The portions of the beam which lose energy will eventually be lost from the beam. There are several mechanisms for the loss. The first and strongest can occur if the returning plasma electrons create a region around the beam in which there is an excess of negative charge. In this case, the radial confining force is reversed and becomes defocusing which causes the beam electrons to quickly spread to large radii. A second occurs even if the returning plasma is too diffuse to reverse the confining force. In this case, the beam eventually loses equilibrium because beam emittance is mismatched for the lower energy segments of the beam. In addition, the low energy particles may simply slow down and be left behind. Any of these effects will cause the beam to evolve into a train of beams with a length of half a plasma period. The front half wavelength of the beam which always loses energy will relatively quickly erode away and the half wavelength following will then become the beam front. As this happens, the phase of the plasma wave with respect to the beam will change and the long term consequences of this are not completely understood. We have done a simulation of this effect for a relatively high density, low energy beam ($n_{pl}\sim10^9$, $\gamma\sim10$) and in this case, the beam becomes fairly incoherent after the beam front disappears. The plasma density, for this example, was high enough to quickly disperse the low energy portions of the beam.

## II. TRANSVERSE EFFECTS

A set of three-dimensional simulations of a beam propagating in a flat-topped IFR channel surrounded by a diffuse plasma by Mostrom[1] show a strong transverse instability which disrupts the beam on a much shorter time scale than the axisymmetric effects of wake fields. The instability appears to be electrostatic in nature and is similar to one studied by Sharp and Yu[2] for the PURE mode. We have derived a dispersion relation for transverse electrostatic oscillations which can be applied to either the PURE case, or that of IFR propagation in a channel. The results are similar to Sharp and Yu for PURE and the details of the calculation are presented by Lampe, et al.[3] The major difference between PURE and IFR propagation is that the beam particles in the IFR channel oscillate in the potential well of the channel and generally have a spread of betatron frequencies which cause the instability to be convective instead of absolute. The dispersion relation is given by

$$\frac{\omega^2}{\omega_{po}^2} = 1 + \frac{\frac{1}{4}\frac{1}{1-f_{ch}}\left(\frac{n_p}{n_{ch}}\right)\left[1 + G\left(\frac{\Omega}{\Omega_\beta}\right)\right]}{1 - 1/2\,\frac{n_b}{n_{ch}}\left[1 + G\left(\frac{\Omega}{\Omega_\beta}\right)\right]},$$

where $n_p$, $n_b$, $n_{ch}$ are the plasma, beam, and channel densities,
$f_{ch}$ is the charge neutralization fraction of the channel,

$$\omega_{po}^2 = \frac{4\pi n_p e^2}{m_e}, \qquad \Omega_\beta^2 = \frac{4\pi n_{ch} e^2}{2\gamma c^2 m},$$

and $G\left(\frac{\Omega}{\Omega_\beta}\right)$ is the spread mass dispersion function.[4]

For the case of a beam propagating in a Bennett-like channel we can estimate the maximum growth at the beam tail.

When $n_b = n_{ch} >> n_p$ the amplification is approximately given by

$$\exp\left[N\left(\frac{n_p}{n_{ch}}\right)\frac{1}{1-f_{ch}}\right]$$

where N is the number of plasma wavelengths from the head to the tail of the beam. For typical Delphi parameters, we expect N=20, $n_p/n_{ch}=10^{-3}$ and $f_{ch}=1/2$. The growth, then, is quite small. If the channel were flat-topped as in the case of Mostrom's simulation, the instability would be absolute and catastrophic. Later simulation work has confirmed this result.[5]

Wake fields may have important consequences in the propagation of laser guided beams. Even with fairly low density plasmas surrounding the beam, if the

propagation distance is long enough, the beam may be broken into a train of pulses. The combination of beam head erosion, nonlinear effects, and wake fields can cause the shorter pulses to be broken up as well. The transverse instability effects do not seem to be important for beams propagating in diffuse plasmas if the plasma density is much less than the beam or channel density.


1. M. Mostrom, "Effects of Background Plasma and Beam Chopping on IFR Propagation", This Volume (1988)
2. W.M. Fawley, et. al., "A Pure Primer", UCID-21374 (1988).
3. M. Lampe, "PURE Mode Instabilities", this Volume (1988)
4. See, for example, M. Lampe, W. Sharp, R. F. Hubbard, E. P. Lee and R. J. Briggs, Phys. Fluids 27, 2921 (1984).
5. D. Welch, "Background Plasma Effects on Transverse Instabilities in E-Beam IFR Propagation, this volume (1988).

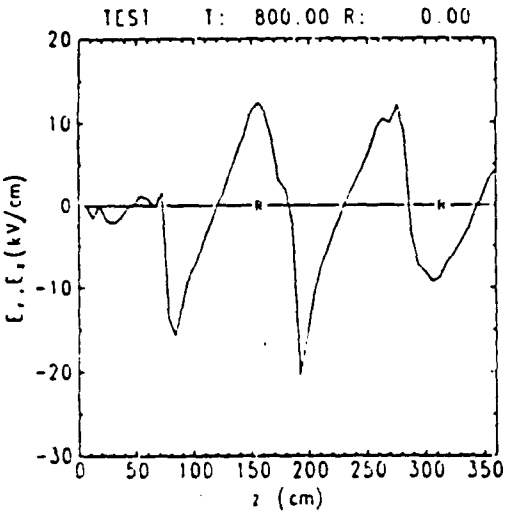




Figure 1. $E_z$ field along the beam axis for a beam with I=2kA, a=1cm propagating through a plasma with $n_p=10^9$/cc. The beam has propagated 8 meters.

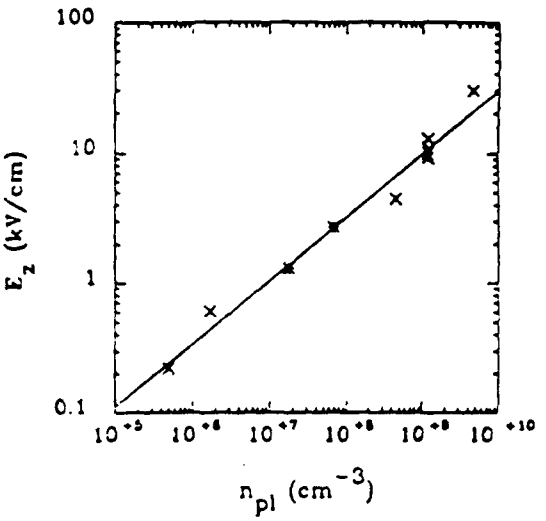



Figure 2. The maximum $E_z$ on axis for beams with $n_b=2\times10^{11}$/cc propagating through plasmas of different densities.

# APPENDIX AA

## Diamagnetic Effects in Endoatmospheric Electron Beam Propagation

# Diamagnetic Effects in Endoatmospheric Electron Beam Propagation

## 1. Overview

The current theoretical understanding of relativistic electron beam (REB) propagation as developed in the steady state treatment of Sharp and Lampe (Phys. Fl. 23, 2383 (1980)) is as follows. The head of the REB propagating into the predominantly neutral gas expands freely due to its emittance since the radial forces due to the space charge and the beam self magnetic field nearly cancel at the beam head. Behind the head ionization of the ambient gas raises the conductivity and neutralizes the space charge in such a way as to pinch the beam at a backward point, called the "pinch point", to an equilibrium radius determined by the balance of the beam pressure and the radial magnetic force. As a result the beam takes on a characteristic "trumpet" shape (Fig. 1). A similar picture arises during for propagation in a preionized gas, with the only difference that beam pinching occurs as the return current decays resistively. Further on beam front "erosion" due to expansion coupled with energy loss results in an almost constant motion of the pinch point backwards while the beam front erodes. In a simplified fashion we can view the beam head to pinch point geometry (Fig. 1) as stationary in the

reference frame moving with the pinch point.

For REP propagation in the earth's atmosphere the useful propagation range of the beam as well as its targeting accuracy depends on the motion of the pinch point as well as the backward part of the beam. In the presence of the earth's ambient magnetic field $B_o$, it is usually assumed that the beam motion is controlled by its gyromotion caused by $B_o$. Such an analysis implicitly assumes that during the propagation of the beam head, which occurs during a time $t = \zeta/c$, the induced plasma currents do not have any significant effect on the value of the ambient magnetic field. This appears to be the cause for currents carried by the bulk of the plasma due to their high collisionality. However, electrons whose mean path $\lambda > vt = n/c\xi$ have the potential to generate diamagnetic currents thereby reducing the ambient $B_o$ and altering many of the targeting considerations. For endoatmospheric REB propagation δ-rays (i.e. electrons with transverse energy ~ 10 keV), satisfy this condition. The purpose of the present work is to assess the extent to which diamagnetic currents caused by δ-rays modify the magnetic field seen by the "pinch point" and the subsequent part of the REB and its consequences to targeting.

## 2. The Physics of the Diamagnetic Effect for Axisymmetric Situations (Simple Physical Considerations)

In order to visualize the physics of the diamagnetic

currents generated by the trumpet like part of the beam we examine a simple axisymmetric situation, where the beam propagates along $\underline{B}_o$ (Fig.2 ). We, of course, realize that for this case changes in the value of $\underline{B}_o$ do not affect the REB targeting, and the transverse propagation is the relevant one. However, this case provides an easier visualization of the physical effects, and thus facilitates the discussion of transverse propagation.

Referring to Fig. 2 the relevant question is "What is the value and spatial distribution of the diamagnetic current caused by the motion of the δ-rays generated by the beam head on a time equal to the transit time $t = \xi/c$?"

In the absence of an ambient magnetic field (i.e. $\underline{B}_o = 0$), the δ-rays expand radially with initial velocity $v_r$. Since they feel no forces in the azimuthal direction $j_\theta = 0$. The presence of an ambient magnetic field however forces the electrons to gyrate about it, thereby transforming part of $v_r$ to $v_\theta$. Since the transit time $t \ll \Omega_e^{-1}$ ($\Omega_e \approx 6\times10^7$), the δ-rays rotate only a small fraction (i.e. $\Omega_e t$) of their gyro-orbit. A diamagnetic electron current layer rotating in the θ-direction is thus created during the transit time t. The value of the magnetic field inside the beam at the "pinch point" and behind can be computed easily on the basis of the electron equation of motion

$$\frac{dv_\theta}{dt} = \frac{e}{m}\left[E_\theta - \frac{v_r B_z}{c}\right] \qquad (1)$$

and the spatial and temporal production rate of δ-rays. For our purposes it is sufficient to consider the value of the field inside the diamagnetic current by viewing it as a solenoid. It will be given by

$$2B_d\xi = \frac{4\pi j_\theta(v_r t)\xi}{c} \qquad (2)$$

so that the field inside the layer will be

$$B_d = \frac{2\pi}{c}(v_r t)\,(n_\Delta e v_\theta) \qquad (3)$$

where $n_\Delta$ is the density of the δ-rays. Solving Eq. (1) we find $v_\theta$ at time t as

$$v_\theta \approx -\frac{eB_o}{mc}(v_r t) \qquad (4)$$

Note that since $eB_o/mc\ t \ll 1$ we can take $v_r$ as almost constant. From (3) and (4) we find that the total magnetic field at the "pinch point" is given by

$$B = B_o - \frac{2\pi n_\Delta e^2}{mc^2} B_o (v_r t)^2$$

or

$$\frac{B}{B_o} = \left[1 - \frac{1}{2} \frac{\omega_{e\Delta}^2}{c^2} (v_r t)^2\right] \qquad (5)$$

Complete diamagnetic situation occurs if

$$\boxed{\frac{1}{2} \frac{\omega_{e\Delta}^2}{c^2} (v_r t)^2 > 1} \qquad (6)$$

Criterion (6) implies

$$\frac{n_\Delta}{\#/cm^3} > 1.5 \times 10^{10} \left[\frac{10\ keV}{\epsilon_\Delta}\right] \left[\frac{10^{-9}}{t}\right]^2 \qquad (7)$$

where $\epsilon_\Delta$ is the energy of the $\delta$-rays.

A complete self consistent solution to the axisymmetric problem will be given later.

3. Diamagnetic Effect for Cross Field Propagation (Simple Physical Consideration)

We proceed next to examine the diamagnetic effect of δ-rays for the most important case, that of REB propagation across $\underline{B}_o$. The essential question concerns the critical value $n_\Delta$ of the δ-rays required to achieve in a position $z=z_o$ a time dependent magnetic profile with a time variation such as shown in Fig. 4. Namely, at any point Z along the propagation path and for a magnetic field $\underline{B} = B_o\hat{e}_y$, the diamagnetic current induced by the δ-rays to be sufficient to exclude the field from the propagation region in a time t. The analysis can be performed in a planar geometry and assuming the beam to have a finite tranverse thickness Δx, while it is infinite in the field aligned y direction. The relevant δ-rays are emitted in the x direction and in the presence of $\underline{B} = \hat{e}_y B_o$ turn in the z-direction forming diamagnetic current sheets $J_z$ on both sides of the beam which tend to reduce the value of $B_o$ inside Δx. The relevant equations are

$$\frac{\partial B_y}{\partial x} = \frac{4\pi}{c} J_z \tag{8}$$

$$J_z = en_\Delta v_z \tag{9}$$

$$\frac{dv_z}{dt} = \frac{e}{mc} v_x B_y \qquad (10)$$

Integrating (10) for $\Omega_e t \ll 1$ we have

$$v_z = \frac{eB_o}{mc} v_x t \qquad (11)$$

and from (8) and (9)

$$B_y(t) = B_o - \frac{4\pi n_\Delta e^2}{mc^2} (v_x t)^2 B_o \qquad (12)$$

In deriving Eq. (12) we integrated form 0 to $x = v_x t$. Therefore

$$\frac{B_y(t)}{B_o} = 1 - \frac{\omega_{e\Delta}^2}{c^2} (v_x t)^2 \qquad (13)$$

The condition is similar to the axisymetric case Eq. (6). it is equivalent to

$$\frac{n_\Delta}{\#/cm^3} > 7 \times 10^9 \left[ \frac{10 \text{ keV}}{\epsilon_\Delta} \right] \left[ \frac{10^{-9}}{t} \right]^2 \qquad (14)$$

## 4. The Role of the Transverse Electric Field of the Beam

In the equations of motion of δ-rays [Eqs. (1) and (12)] we have neglected the influence of the beam fields. Since the dominant force is due to the radial electric field, the above results will not be affected except for replacing the energy $\epsilon$ of the δ-rays in Eqs. (17) and (14) by the potential $U_\Delta = \epsilon_r(v_r t)$ where $\epsilon_r$ is the part of the radial electric field transverse to $\underline{B}_o$.

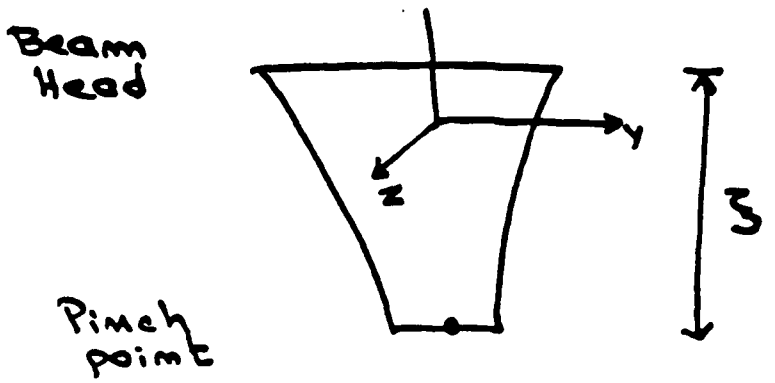



Fig. 1

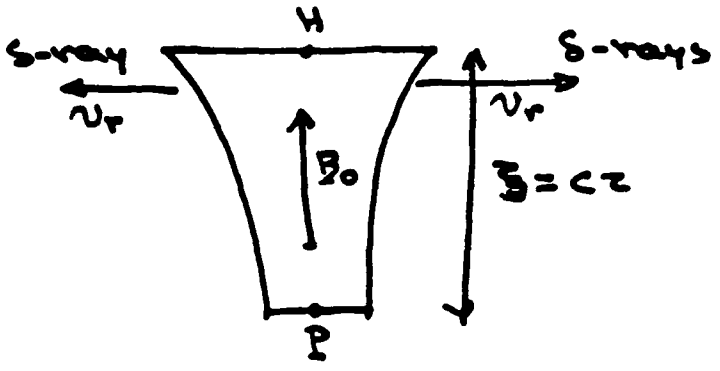



Fig. 2

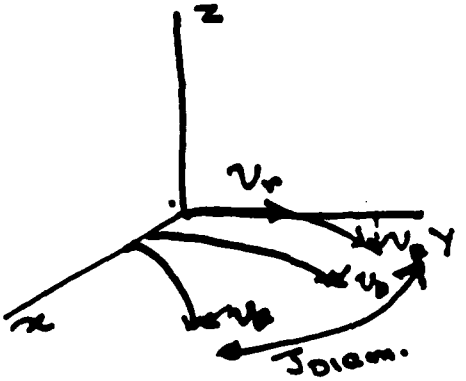



Fig. 3

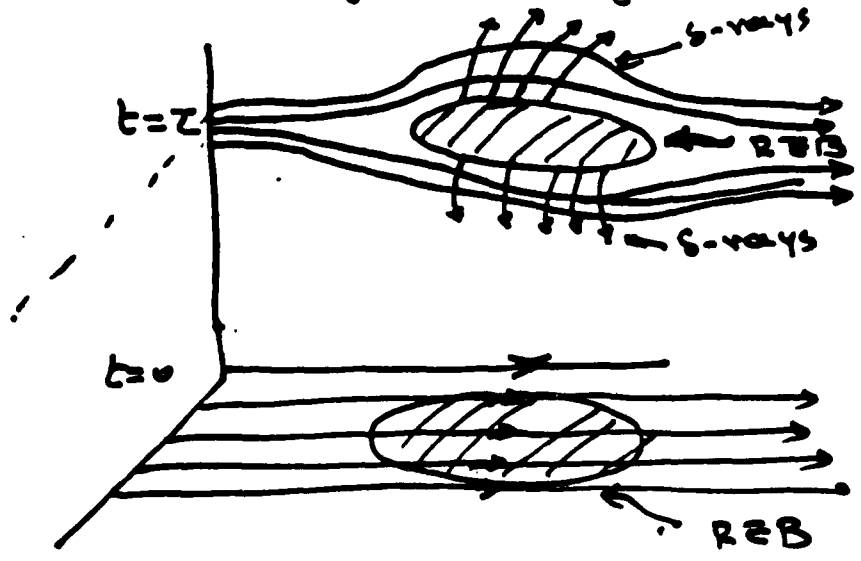



Fig. 4

# APPENDIX BB

## Diamagnetic Cavity Formed During the Formation of a Laser Channel in the Ionosphere

# Diamagnetic Cavity Formed During the Formation of a Laser Channel in the Ionosphere

## 1. Overview

Relativistic electron beam (REB) tracking through the use of ionization channels in the IFR mode appears to be a viable mode for propating REB's in the ionosphere across the ambient magnetic field. The value of the ambient magnetic field $B_o$ inside the ionization channel is a critical parameter determining many of the beam and channel requirements for a desired range. For example

(i) The value of the line density ratio of channel to beam electrons (f) required to electrostatically overcome the magnetic forces, depends linearly on the value of $B_o$.

(ii) The rate of magnetic erosion scales also linearly with $B_o$.

(iii) The beam current at which the ohmic range equals the magnetic range scales quadratically $B_o$.

In the calculations today, the value of the magnetic field inside the channel was taken as equal to the earth's magnetic field $B_o(\sim 1/3G)$. This implies that the diamagnetic currents due to the channel formation as well as

the ones potentially induced by the front of the beam in the plasma can be neglected. Such an assumption is highly questionable at least for a range of heights and can result in lower rates of magnetic erosion and values of f. In this work we make a preliminary study of the diamagnetic effect due to the channel formation and before the REB is injected. Diamagnetic effects caused by the beam front will be addressed elsewhere.

## 2. The Dynamics of the Channel Formation

Following the ionization stage by the laser the expected density and temperature profiles are shown in Fig. 1. In our preliminary analysis we assume complete ionization of the ambient neutral gas, while leaving the electron temperature $T_e$ specified at this stage. In the regime of interest (100-600km) the value of the ambient plasma density $n_o \sim 10^3$-$10^6 cm^{-3}$ of the ambient temperature $T_{eo} \sim .05$-$.2$ eV and of the ambient neutral density $N \sim 10^{13}$-$10^7 cm^{-3}$. Relevant graphs are shown as Fig. 2. The ambient magnetic field is of the order of $B_o$=1/3G giving an energy density $B_o^2/8\pi = 3.6\times10^{-3}$ erg/cm$^3$ $= 2\times10^9$ eV/cm$^3$. Typical values of $\beta_o = n_o T_{eo}/B_o/8\pi \sim 10^{-4}$-$10^{-7}$.

If we assume complete ionization in the channel and take $T_e$=1eV the resulting values of $\beta \sim 5\times10^3$-$10^{-2}$. It is obvious that for a wide range of altitudes $\beta > 1$, and the magnetic field will not be able to prevent the expansion of the

channel electrons. We therefore expect that the expansion will create diamagnetic currents that will alter the value of the magnetic field inside the channel. The time scale for this to occur is of the order of $10^{-7}$-100$\mu$sec. Since the reduction of the field greatly decreases the rate of magnetic erosion and targeting is not affected by even 100$\mu$sec time long, it might be desirable for relevant altitudes to delay the beam pulse by the appropriate time. Figure 3 shows a particular 1-D hybrid simulation of the plasma expansion for values of the channel $\beta$~4. The value of the magnetic field inside the channel has been reduced by a factor of five.

3. Practical Consideration

If we assume a complete channel ionization and $T_e$~1eV the expected value of $\beta$ as a function of altitude is shown in Fig. 4. Values pf $\beta$~1 can be achieved up to 280km altitude. If the channel temperature can be controlled so that higher values of $T_e$ can be achieved the maximum altitude can be raised substantially. The dynamics of the expansion for $\beta$~.1- have not been studied in detail and can possibly help in raising the altitude. Another area in need of study is the effect of shaping the laser profile.

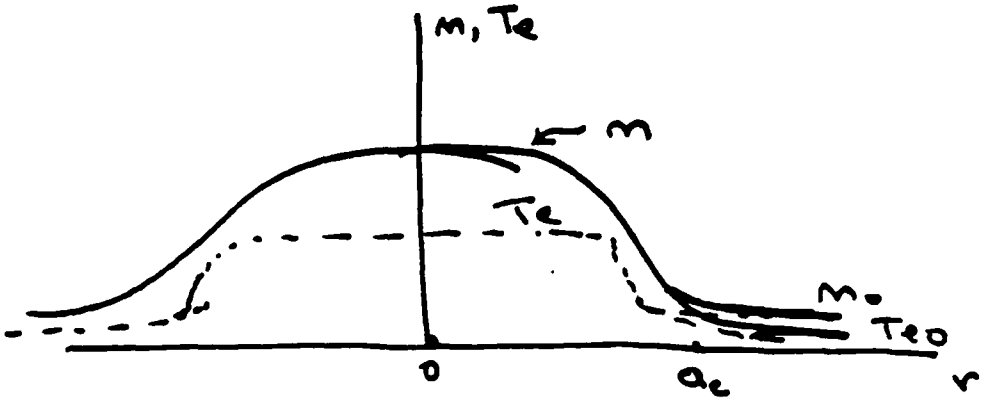



Fig. 1

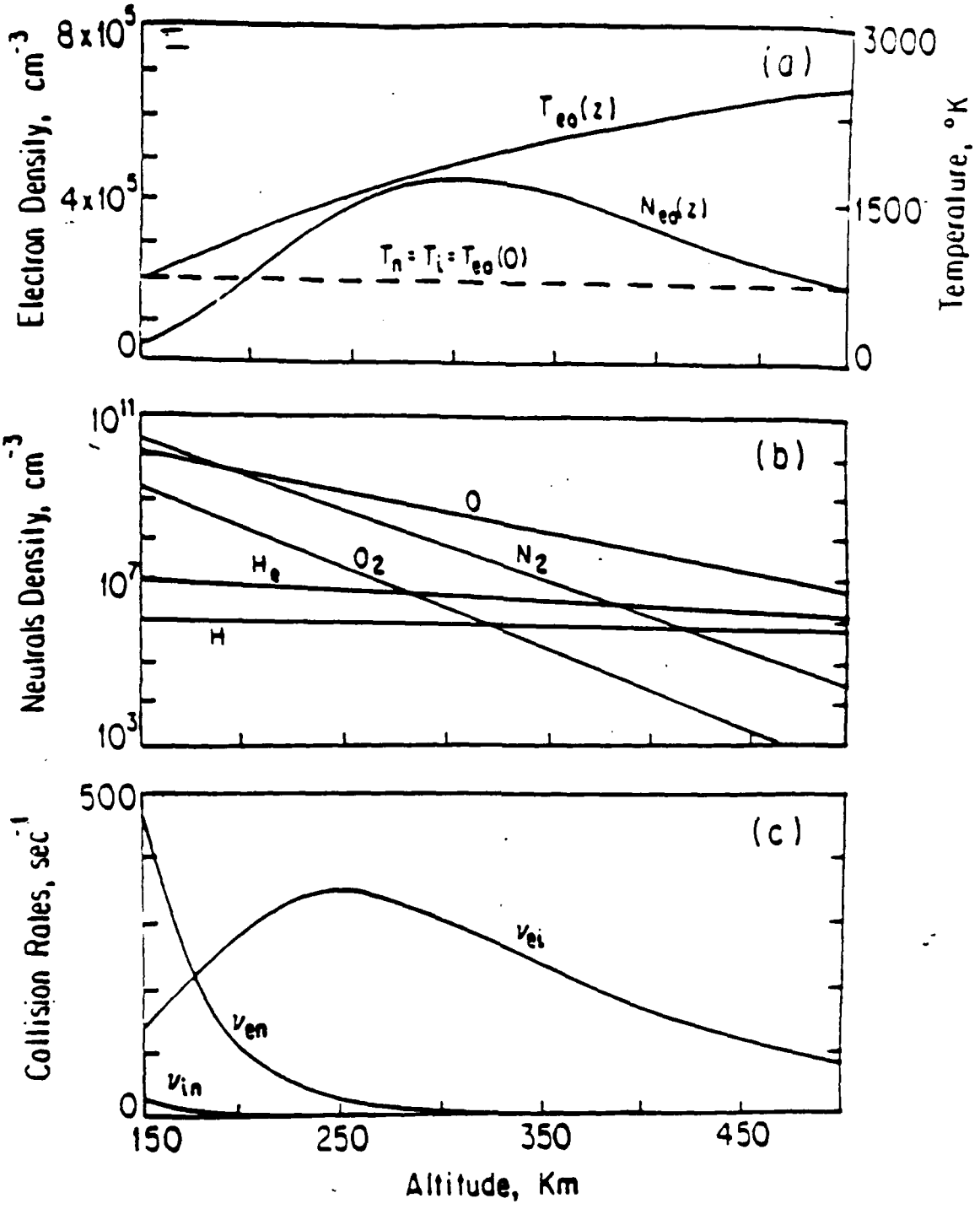



Figure 2 The ionospheric F-region model: a) zero order Chapman electron density and temperature profiles; b) density profiles of various neutral components; c) elastic momentum transfer collision profiles.

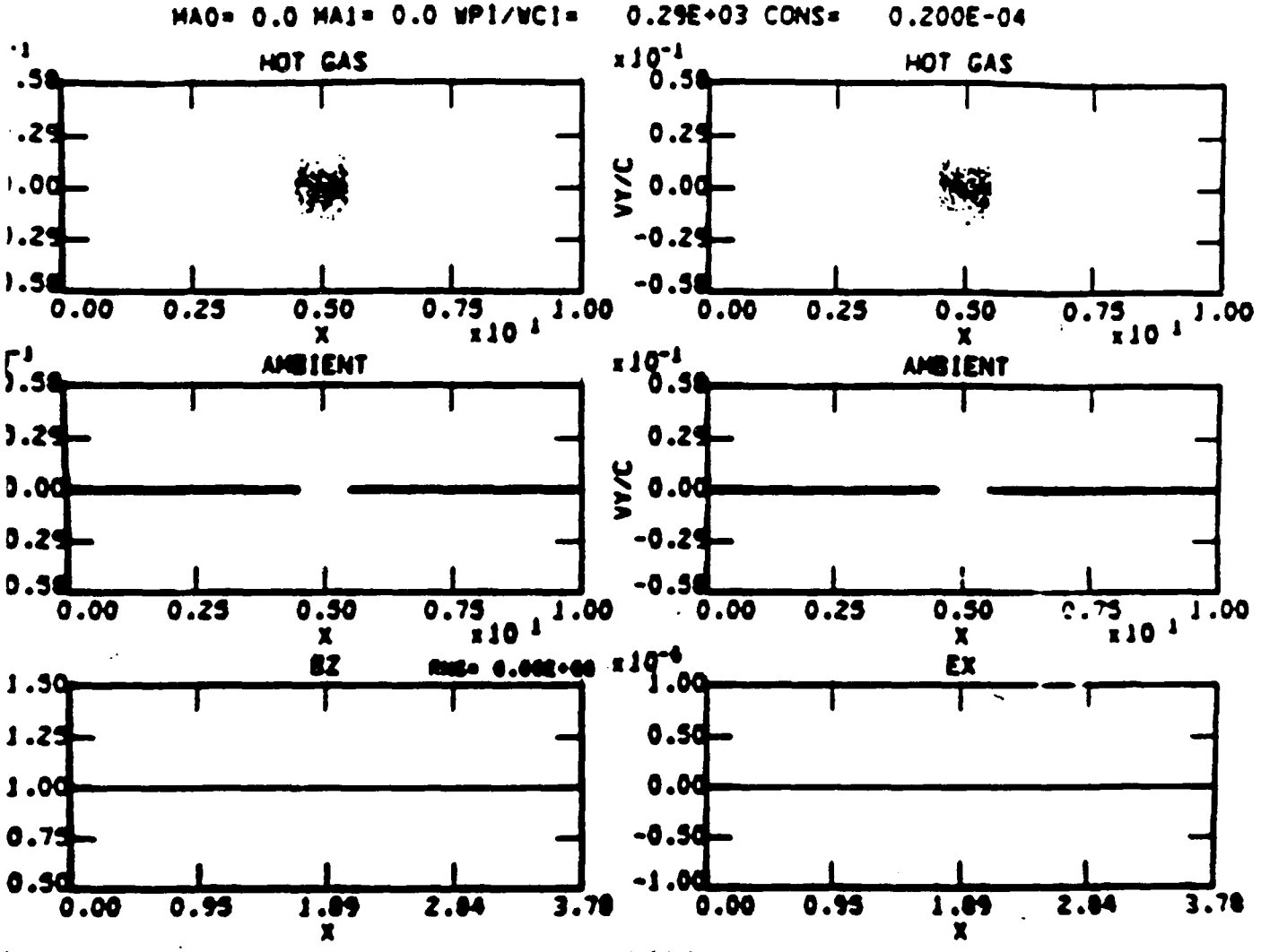

MA0= 0.0 MA1= 0.0 WPI/WCI= 0.29E+03 CONS= 0.200E-04
HOT GAS
HOT GAS
AMBIENT
AMBIENT
BZ
EX
VY/C
VY/C
X
X
X
X
0.00
0.25
0.50
0.75
1.00
0.00
0.95
1.89
2.84
3.78
IT= 0, TIME= 0.000

Fig. 3a

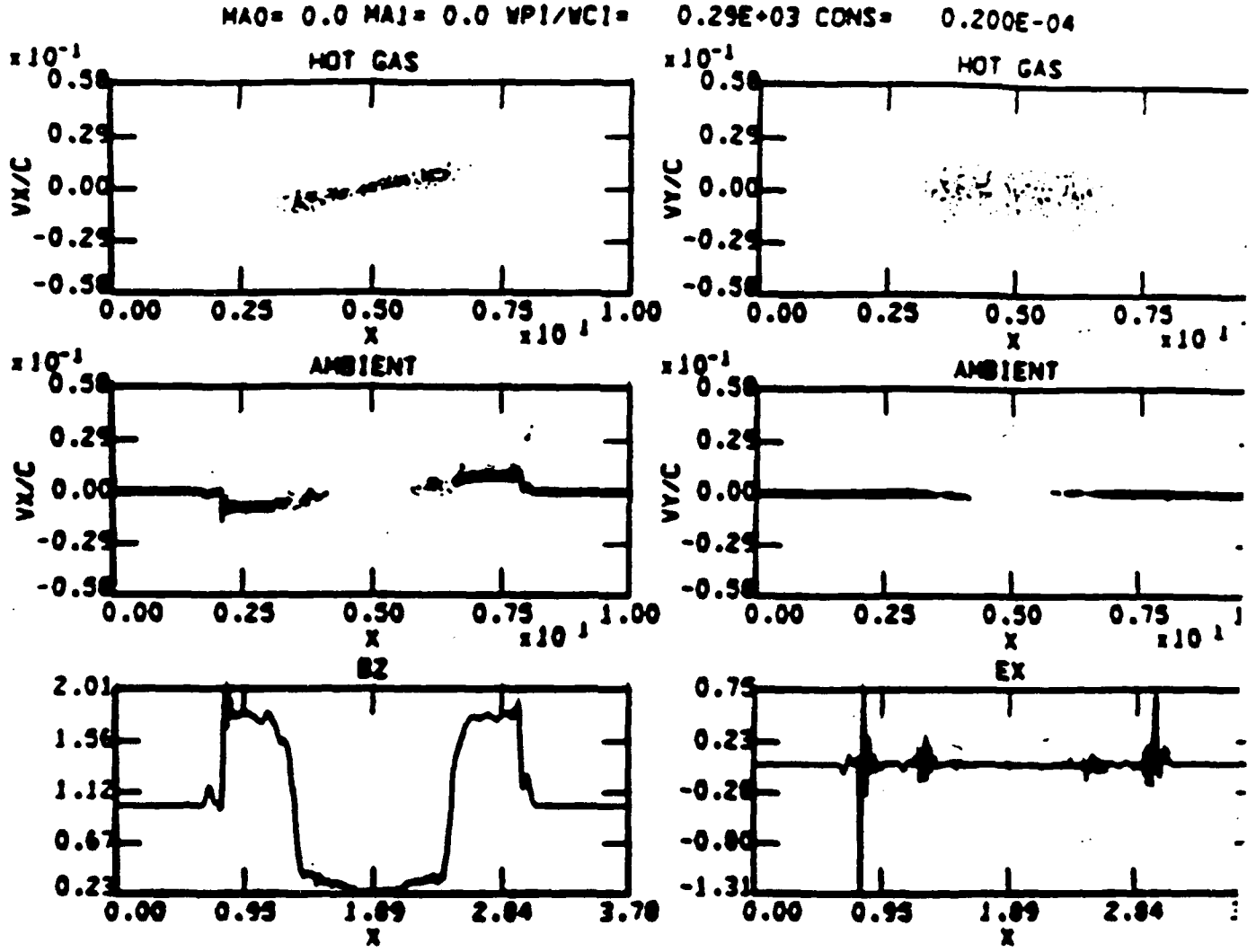
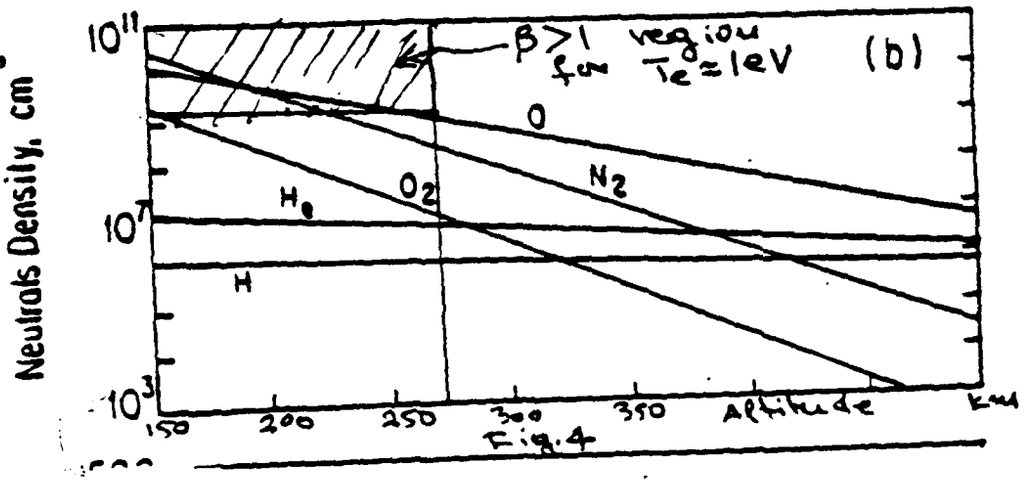

MA0= 0.0 MA1= 0.0 WPI/WCI= 0.29E+03 CONS= 0.200E-04
HOT GAS
VX/C
VY/C
AMBIENT
BZ
EX
X
IT= 490, TIME= 0.445

Fig. 8b


Neutrals Density, cm$^{-3}$
$10^{11}$
$10^{7}$
$10^{3}$
$\beta > 1$ region for $T_e = 1eV$ (b)
O
$N_2$
$O_2$
$H_e$
H
150
200
250
300
350
Altitude
Km
Fig. 4

# APPENDIX CC

## Guided Radiation Beams in Free Electron Lasers

Nuclear Instruments and Methods in Physics Research A272 (1988) 536-542
North-Holland, Amsterdam

# GUIDED RADIATION BEAMS IN FREE ELECTRON LASERS

P. SPRANGLE, A. TING [1], B. HAFIZI [2] and C.M. TANG

*Plasma Theory Branch, Plasma Physics Division, Naval Research Laboratory, Washington, DC 20375-5000, USA*
*[1] Berkeley Research Assoc., Inc., Springfield, VA 22150, USA*
*[2] Science Applications Intl. Corp., McLean, VA 22102, USA*

In a free electron laser (FEL), the radiation field, wiggler field and electron beam resonantly couple and modify the refractive index in the vicinity of the electron beam, such that the radiation beam will tend to focus upon the electron beam. From the radiation envelope equation derived from the source dependent expansion (SDE) method of solving the 3-D wave equation in FELs, conditions and parameters necessary to achieve guided radiation beams (constant radius) in the Compton exponential gain regime are obtained for FELs driven by either induction linacs or rf linacs with various transverse profiles of the electron beam. From the efficiency of the guided radiation beam, the trapping potential of the ponderomotive potential prior to saturation and the required beam quality of the electron beam can be obtained. The wiggler field could be tapered to further increase the operating efficiency. The possibility of bending or steering radiation beams in FELs is discussed and a condition necessary for radiation guiding along a curved electron beam orbit is obtained.

## 1. Introduction

In many short wavelength free electron laser devices the radiation beam will not be confined or guided by a structure such as a waveguide. Furthermore, in order to provide high gain and efficiency, it is usually necessary for the interaction length (length of wiggler field) to be long compared to the diffraction length (Rayleigh length) associated with the radiation beam. In the FEL the tendency of the radiation beam to diffract away over a distance of a few Rayleigh lengths can be overcome by a focusing phenomenon arising from the resonant coupling of the radiation and wiggler fields with the electron beam [1,2]. This radiation focusing effect plays a central role in the practical utilization of the FEL [3]. This phenomenon was first analyzed for the low gain FEL with transverse effects where it was shown that the diffractive spreading of the radiation beam could be overcome by a focusing effect arising from the modified index of refraction [1]. Experimental evidence indicating optical guiding in the FEL has also been observed recently [4-7].

Optical guiding in FELs operating in the small signal exponential gain regime has been studied for the asymptotic behavior of the radiation beam [8-11], indicating that it is possible for the propagation of self-similar transverse modes. Recently, a general formalism for optical focusing, guiding and steering, called the Source Dependent Expansion (SDE) method, has been developed and applied to FELs [12]. The SDE method is an excellent analytical and numerical technique for solving the wave equation that governs the FEL interaction. An envelope equation for the radiation beam in the FEL can be derived using the SDE method, and it is very appropriate for studying perfect guiding of the radiation beam in FELs operating in the exponential regime. We have obtained analytic expressions for the spot size, wavefront curvature, phase shift and growth rate of the perfectly guided radiation beam in FELs operating in the Compton regime for different transverse profiles of the electron beam. The intrinsic efficiency of the FEL in the exponential gain regime with guided radiation can be calculated from these expressions, and from which the trapping potential and desired beam quality at injection can be estimated. It is found that high current rf linacs [13,14] with their higher energy and better beam quality, are quite suitable for driving relatively short wavelength FELs to beyond saturation where the wiggler is tapered to enhance the efficiency. These results have been verified by simulations based on the SDE method for FELs driven by either induction or rf linacs.

One of the consequences of optical guiding in FEL is the bending of the optical beam by a curved or misaligned electron beam [17]. The SDE formalism allows us to obtain a condition on the curvature of the electron beam in an FEL that the radiation beam will remain guided.

0168-9002/88/$03.50 © Elsevier Science Publishers B.V.
(North-Holland Physics Publishing Division)

## 2. Refractive index associated with FELs

In our model, the vector potential of an axially symmetric, linearly polarized, radiation field is

$$A_R(r, z, t) = A(r, z)\, e^{i(\omega z/c - \omega t)}\hat{e}_x/2 + \text{c.c.}, \qquad (1)$$

where $A(r, z)$ is the complex radiation field amplitude, $\omega$ is the frequency and c.c. denotes the complex conjugate.

The wave equation governing $A_R$ is

$$\left(\frac{1}{r}\frac{\partial}{\partial r}\left(r\frac{\partial}{\partial r}\right)+\frac{\partial^2}{\partial z^2}-\frac{1}{c^2}\frac{\partial^2}{\partial t^2}\right)A_R=-\frac{4\pi}{c}J_x\hat{e}_x, \quad (2)$$

where $J_x(r, z, t)$ is the driving current density. Substituting eq. (1) into eq. (2) leads to the following reduced wave equation,

$$\left(\frac{1}{r}\frac{\partial}{\partial r}\left(r\frac{\partial}{\partial r}\right)+2i\frac{\omega}{c}\frac{\partial}{\partial z}\right)a(r, z)=S(r, z, a), \quad (3)$$

where $a(r, z)=|e|A/m_0c^2=|a|\exp(i\phi)$ is the normalized complex radiation amplitude and we have assumed that $a(r, z)$ is a slowly varying function of $z$, i.e., $|(\partial a/\partial z)/a| \ll \omega/c$. The source function, $S$, is given by,

$$S=-\frac{4\omega}{c}\int_0^{2\pi/\omega}J_x(r, z, t)\,e^{-i(\omega z/c-\omega t)}\,dt. \quad (4)$$

It is possible to relate the source function, $S$, to the index of refraction associated with the medium by noting that the wave equation for $A_R$ in a nonmagnetic, time-independent, nonlinear medium is

$$\left(\nabla^2-\left(n^2(r, z, a)/c^2\right)\partial^2/\partial t^2\right)A_R=0,$$

where $n$ is the index of refraction associated with the medium and is, in general, complex and a nonlinear function of $a(r, z)$. Comparing the reduced wave equation written in terms of $n(r, z, a)$ with eq. (3) we find that the source function can be written in terms of $n$,

$$S(r, z, a)=(\omega/c)^2\left(1-n^2(r, z, a)\right)a(r, z). \quad (5)$$

The refractive index associated with FELs can be obtained from the following derivation, where a number of simplifying assumptions are made. For example: the beam electrons are monoenergetic without betatron oscillations and that the radiation is of a single frequency [15]. We write the nonlinear driving current density, $J_x$, as

$$J_x=-|e|n_b(r)v_w(z)v_{0z}\int\delta\left(z-\bar{z}(t, t_0)\right)dt_0, \quad (6)$$

where $n_b(r)$ is the ambient beam density, $v_{0z}$ is the axial electron velocity at $z=0$, $t_0$ is the time a given electron crosses the $z=0$ plane,

$$v_w(z)=\left(|e|A_w/\gamma m_0c\right)\left(e^{ik_wz}+\text{c.c.}\right)\hat{e}_x/2$$

is the wiggle velocity, $\gamma$ is the Lorentz factor, $A_w$ is the vector potential amplitude of the planar wiggler field and $k_w=2\pi/\lambda_w$ is the wiggler wave number. Substituting eq. (6) into the expression for $S$, eq. (4) gives

$$S=\left(\frac{\omega_b(r)}{c}\right)^2a_w\int_0^{2\pi/\omega}dt\frac{\omega}{2\pi}\times\int dt_0\exp\left(-i\left(\left(\frac{\omega}{c}+k_w\right)z-\omega t\right)\right)\times\delta\left(t-\tau(z_0, t_0)\right)/\gamma, \quad (7)$$

where

$$a_w=\frac{|e|A_w}{m_0c^2}, \qquad \tau=t_0+\int_0^z\frac{dz'}{v_z(z', t_0)}$$

and the $t_0$ integration is over all entry times. Equating eq. (7) with eq. (5) and carrying out the integration over $t_0$, we find the index of refraction associated with the FEL to be given by

$$n_{FEL}(r, z, a)=1+\left(\frac{\omega_b^2(r)}{2\omega^2}\right)\frac{a_w}{|a|}\langle e^{-i\psi}/\gamma\rangle_{\psi_0}, \quad (8)$$

where

$$\psi=\int_0^z\left(\frac{\omega}{c}+k_w-i\ln\frac{a}{|a|}-\frac{\omega}{v_z(z, \psi_0)}\right)dz+\psi_0$$

is the relative phase between the electron and the ponderomotive wave, $\psi_0=-\omega t_0$ is the initial phase of a given electron and $\langle\ \rangle_{\psi_0}=(2\pi)^{-1}\int_0^{2\pi}d\psi_0$ is an ensemble average over the initial phases. The radial profile of the index of refraction as given by eq. (8) supports self-focusing of the radiation in an FEL. It should be noted, for completeness, that the relative phase satisfies the pendulum equation given by

$$\frac{\partial^2\psi}{\partial z^2}=\frac{\partial k_w}{\partial z}-\gamma^{-2}\left(\frac{\omega}{c}\right)\left[\frac{1}{4}\frac{\partial a_w^2}{\partial z}-k_wa_wa\sin\psi\right]. \quad (9)$$

## 3. Radiation beam envelope equation

In order to solve eq. (3) we will use the source dependent expansion (SDE) method [12]. This formalism has the merit that with only a few modes it permits an accurate solution of the wave equation throughout the interaction region. In this method, we choose the following representation for $a(r, z)$ in terms of Laguerre–Gaussian functions,

$$a(r, z)=\sum_m a_m(z)L_m\left(\frac{2r^2}{r_s^2(z)}\right)\times\exp\left(-(1-i\alpha(z))r^2/r_s^2(z)\right), \quad (10)$$

where $m=0, 1, 2, \ldots$. In eq. (10), $a_m(z)$ are the complex amplitude coefficients, $r_s(z)$ is the radiation spot size, $\alpha(z)$ is related to the radius of curvature of the radiation beam wavefront, $R=-(\omega/2c)r_s^2/\alpha$ and $L_m$ is the Laguerre polynomial. Solving for the unknown quantities $a_m$, $r_s$ and $\alpha$ in terms of the source term $S$ allows us to completely describe the radiation dynamics. The representation in eq. (10) is underspecified, since, when eq. (10) is substituted into eq. (3) and moments of the source function taken, there remain more unknown quantities than available equations. The additional degrees of freedom in our representation allow us to

specify a particular functional relationship for the unknown quantities $r_s$ and $\alpha$ in such a way that, if the radiation beam profile remains approximately Gaussian, the number of modes needed to accurately describe the radiation beam is small. This yields the following first order coupled differential equations for $r_s$ and $\alpha$,

$$r_s' - 2c\alpha/\omega r_s = -r_s H_I, \tag{11a}$$

$$\alpha' - 2(1+\alpha^2)c/\omega r_s^2 = 2(H_R - \alpha H_I), \tag{11b}$$

and a set of first order ordinary differential equations for the complex amplitudes $a_m(z)$,

$$a_m' + A_m a_m = -i\left[F_m - mBa_{m-1} - (m+1)B^* a_{m+1}\right], \tag{11c}$$

where $H = F_1/a_0$, $' \equiv \partial/\partial z$, and $(\ )_{R,I}$ denotes the real and imaginary part of the enclosed function. In eqs. (11a–c), the functions $A_m$, $B$, and $F_m$ are given by

$$A_m(z) = \frac{r_s'}{r_s} + i(2m+1)\left((1+\alpha^2)\frac{c}{\omega_s^2} - \alpha\frac{r_s'}{r_s} + \frac{\alpha'}{2}\right),$$

$$B(z) = -\left(\alpha\frac{r_s'}{r_s} + \frac{(1-\alpha^2)c}{\omega r_s^2} - \frac{\alpha'}{2}\right) - i\left(\frac{r_s'}{r_s} - \frac{2\alpha c}{\omega r_s^2}\right),$$

$$F_m(z) = \frac{c}{2\omega}\int_0^\infty d\zeta\, S(\zeta, z) L_m(\zeta) \exp(-\tfrac{1}{2}(1+i\alpha)\zeta),$$

where $\zeta = 2r^2/r_s^2$.

Eqs. (11a, b) can be combined to give the following envelope equation for the radiation beam

$$r_s'' + K^2 r_s = 0, \tag{12}$$

where

$$K^2 = (2c/\omega)^2\left(-1 + C^2\langle\sin\psi\rangle^2 + 2C\langle\cos\psi\rangle + (\omega/2c)r_s^2 C'\langle\sin\psi\rangle\right) r_s^{-4}, \tag{13}$$

$C(z) = (2\nu/\gamma)G(z)a_w/|a_0(z)|$, measures the coupling between the radiation and electron beam, $\nu = (\omega_{b0} r_b/2c)^2 = I_b/17\times 10^3$ is Budker's constant, $I_b$ is the electron beam current in amperes, $G(z) = (1-f)/(1+f)^2$ and $f(z) = (r_b/r_s)^2$ is the filling factor associated with a Gaussian electron beam density profile. The first term on the right-hand side of eq. (13) is the usual diffraction term, the second and third terms are focusing while the last term provides a focusing or defocusing contribution. In the high gain trapped particle regime, $\langle\sin\psi\rangle$ and $\langle\cos\psi\rangle$ are approximately constant, while $|a_0(z)|$ increases with $z$. Hence, $K$ depends on $z$ and a guided beam ($r_s' = 0$) cannot be exactly maintained in this regime, although the radiation envelope is still reasonably well-confined. In the low gain trapped particle regime $|a_0(z)|$ increases slightly and, therefore, a guided beam can be approximately achieved. In the Compton exponential gain regime, we can obtain the necessary conditions to achieve stable guided radiation beams.

## 4. Guided radiation beams in the exponential gain regime

By considering the lowest order transverse mode (Gaussian profile) of the radiation beam, we find that the source term appropriate for the high gain Compton regime is

$$S(r, z) = \frac{(\omega_b(r)/c)^2 (a_w k_w f_B)^2}{\gamma(1 + a_w^2/2)(\Delta k - i\Gamma)^2} a(r, z), \tag{14a, b}$$

where $\Delta k$ and $\Gamma$ are the wave number shift and growth rate respectively and $f_B$ is the usual difference of Bessel functions due to the linear wiggler. The lowest order mode is taken to have the form

$$a(r, z) = a_0(0)\exp\left(i\int_0^z (\Delta k - i\Gamma)\, dz' - (1 - i\alpha)r^2/r_s^2\right). \tag{15}$$

For the purposes of illustration, we will consider the Compton FEL regime in which the electron beam has a Gaussian density profile, $n_b(r) = n_0 \exp(-r^2/r_b^2)$. The conditions for a guided radiation beam required that the waist and curvature of the radiation beam remain constant ($r_s' = \alpha' = 0$). Setting $r_s' = \alpha' = 0$ in eqs. (11a, b) and solving for $\Gamma$, $\Delta k$, $r_s$, and $\alpha$ (see Appendix), the following results for a guided beam are obtained.

$$\Gamma = (1+\alpha^2)^{-1}(1+2f)^{-1}\Gamma_0, \quad \Delta k = \alpha\Gamma, \tag{16a, b}$$

$$r_s = \left(\frac{\gamma}{\nu}\right)^{1/4} \frac{\lambda_w}{2^{7/4}\pi\gamma f_B^{1/2}} \frac{(1 + a_w^2/2)^{3/4}}{a_w^{1/2}} \times \frac{f^{1/4}(1+2f)^{3/2}}{(1+3f/2)^{3/4}}, \tag{16c}$$

$$\alpha = (f/(2+3f))^{1/2}, \tag{16d}$$

where $\Gamma_0 = 2f_B(\nu/\gamma)^{1/2} a_w k_w (1 + a_w^2/2)^{-1/2}$ and $f = r_b^2/r_s^2$ is the filling factor. In the special case of $f = 1$,

$$r_s(f=1) = 0.25\lambda_w\left(\frac{\gamma}{\nu}\right)^{1/4} \frac{(1 + a_w^2/2)^{3/4}}{\gamma f_B^{1/2} a_w^{1/2}}.$$

Similar procedures can be performed for other transverse profiles of the electron beam. Conditions for guided radiation beams in the Compton regime for Gaussian, parabolic, and flat-top transverse electron beam profiles are summarized in table 1.

In fig. 1, we show the spatial evolution of the radiation waist for the induction linac-driven FEL parameters in table 2. The parameters in table 2 are consistent with eq. (16) and have been chosen to produce a guided radiation beam in the Compton exponential gain regime. The guided beam conditions can be shown to be

Table 1
Guided radiation beam conditions for compton exponential gain regime

| Electron beam profile | $\frac{r_s^2 k_s \Gamma_0}{2\alpha(1+\alpha^2)}$ | $\alpha^2$ | $(1+\alpha^2)\Gamma/\Gamma_0$ | $\Delta k/\Gamma$ | $\frac{\Gamma_0}{(2k_s k_w \nu/\gamma)^{1/2}}$ |
|---|---|---|---|---|---|
| Gaussian | $(1+2f)^2$ | $f/(3f+2)$ | $1/(1+2f)$ | $\alpha$ | $\frac{f_B a_w}{\gamma}$ |
| Parabolic | $\frac{\sqrt{2}f(e^{-2f}+2f-1)}{(1-(1+2f)e^{-2f})^{3/2}}$ | $\frac{(f-1)+(1+f)e^{-2f}}{(3f-1)+(1-f)e^{-2f}}$ | $\frac{(1-(1+2f)e^{-2f})^{1/2}}{\sqrt{2}f}$ | | |
| Flat-top | $\frac{1-e^{-2f}}{2fe^{-3f}}$ | $\frac{1-(1+2f)e^{-2f}}{3-(3-2f)e^{-2f}}$ | $e^{-f}$ | | |

stable [16], and fig. 2 shows that irrespective of the initial value, the spot size asymptotes to the matched (guided) beam value. Fig. 3 shows the evolution of the spot size for the rf linac-driven FEL parameters in table 3. As in table 2, the parameters in table 3 have been chosen to produce a guided radiation beam in the Compton exponential gain regime and are consistent with eqs. (16).

Free electron lasers driven by either induction or rf linacs could initially operate in the guided, exponential gain regime until saturation occurs. Immediately prior to saturation, the ponderomotive potential can be large enough, as in the above illustrations, to trap a significant fraction of the beam electrons. At this point, the wiggler field can be spatially tapered to achieve a significant increase in the operating efficiency and a somewhat smaller input signal into the FEL amplifier.

To determine the viability of tapering the wiggler, prior to saturation, the trapping potential associated with the ponderomotive wave is needed. For linearly polarized waves, the fractional trapping potential is

$$\frac{|e|\phi_{trap}}{\gamma m_0 c^2} = 2\sqrt{2}\left(\frac{a a_w}{1+a_w^2/2}\right)^{1/2}. \tag{17}$$

The radiation amplitude at saturation can be obtained from the intrinsic efficiency of the FEL. Using arguments based on electron trapping in the ponderomotive wave, we find that the intrinsic efficiency in the exponential (maximum) gain regime is

$$\eta = \Delta k/k_w. \tag{18}$$

Using the induction linac parameters in table 2 as an illustration, we find that the intrinsic efficiency is $\eta = \Delta k/k_w = 0.66\%$. From this, the fractional trapping potential at the end of the exponential gain regime is $|e|\phi_{trap}/\gamma m_0 c^2 = 6\%$, making it possible to trap the electron beam while tapering the wiggler field. In

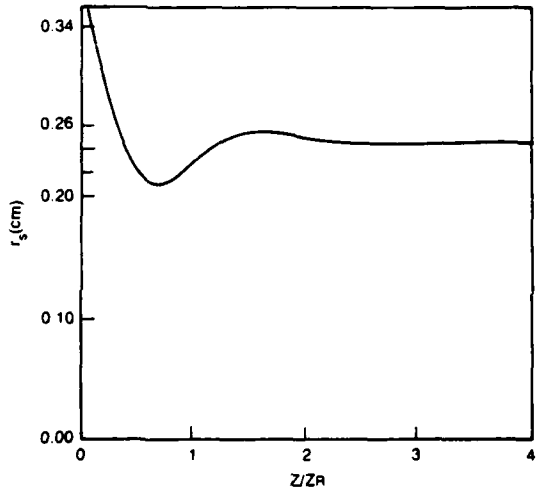



Fig. 1. Spatial evolution of the radiation spot size in the exponential gain regime for induction linac-driven FEL parameters given in table 1.

Table 2
Parameters associated with an induction linac-driven FEL in the exponential gain regime

| | |
|---|---|
| Electron beam | |
| current | $I_b = 2$ kA ($\nu = 0.118$) |
| energy | $E_b = 50$ MeV ($\gamma = 100$) |
| radius | $r_b = 0.3$ cm |
| emittance | $\epsilon_n < 34\times10^{-3}$ cm rad |
| Wiggler field | |
| wavelength | $\lambda_w = 8$ cm |
| wiggler strength | $B_w = 2.3$ kG ($a_w = 1.72$) |
| Radiation beam | |
| wavelength | $\lambda = 10.6\ \mu$m |
| spot size | |
| (guided beam) | $r_s = 0.25$ cm ($Z_R = 2$ m) |
| e-folding length | $L_e = 1/\Gamma = 94$ cm |
| Intrinsic efficiency | $\eta = \Delta k/k_w = 0.66\%$ |
| Saturated power | $p_{sat} = 660$ MW ($a = 7\times10^{-4}$) |
| Trapping potential | $\lvert e\rvert\phi_{trap}/\gamma m_0 c^2 = 6.0\%$ |

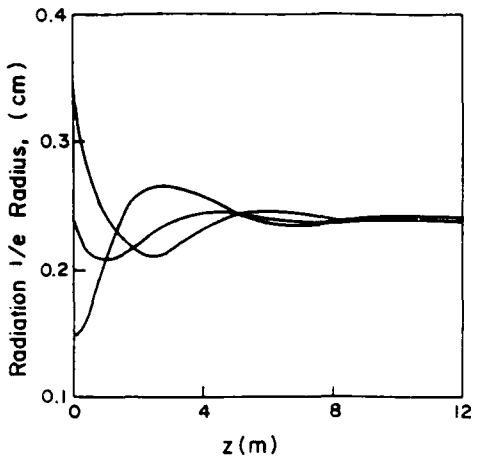



Fig. 2. Spatial evolution of the radiation spot size in the exponential gain regime for initial spot sizes: (a) 0.35 cm, (b) 0.24 cm, and (c) 0.15 cm.

addition, the initial fractional energy spread of the electron beam must be somewhat less than $\eta$. This places a limitation on the fractional energy spread of the electron beam, $\delta E/E_b < 0.66\%$. One contribution to the beam energy spread is the transverse emittance, $\delta E/E_b = (1/2)(\epsilon_n/r_b)^2$. Therefore, the normalized beam emittance must satisfy $\epsilon_n < (2\Delta k/k_w)^{1/2} r_b = 0.034$ cm rad.

Similar estimates can be carried out for the rf linac parameters in table 3. Even though the intrinsic efficiency is only 0.25%, the fractional trapping potential of 2% prior to saturation is still large enough to trap the electron beam and the wiggler field can be tapered. However, the small intrinsic efficiency puts a more stringent requirement on the beam quality, $\epsilon < 0.007$ cm rad, in an rf linac-driven FEL.

Table 3
Parameters associated with an rf linac-driven FEL in the exponential gain regime

| | |
|---|---|
| Electron beam | |
| peak current | $I_b = 500$ A |
| energy | $E_b = 150$ MeV |
| radius | $r_b = 1$ mm |
| emittance | $\epsilon_n \leq 7 \times 10^{-3}$ cm rad |
| Wiggler field (planar) | |
| wavelength | $\lambda_w = 12$ cm |
| wiggler strength | $B_w = 900$ G $(a_w = 1)$ |
| Radiation beam | |
| wavelength | $\lambda = 1\ \mu$m |
| spot size | |
| (guided beam) | $r_s(0) = 1.1$ mm $(Z_R = 3.8$ m) |
| e-folding length | $L_e = 1/\Gamma = 196$ cm |
| Intrinsic efficiency | $\eta = \Delta k/k_w = 0.25\%$ |
| Saturated power | $P_{sat} = 180$ MW $(a = 7.25 \times 10^{-5})$ |
| Trapping potential | $\lvert e \rvert \phi_{trap}/\gamma m_0 c^2 = 2\%$ |

Fig. 4 shows the relative power for ten transverse modes used in a simulation of the guided radiation beam for parameters in table 2. The fundamental mode is at least three orders of magnitude larger than any of the higher modes, indicating the SDE method is an excellent numerical scheme and the analytic results obtained with only the fundamental mode are well justified.

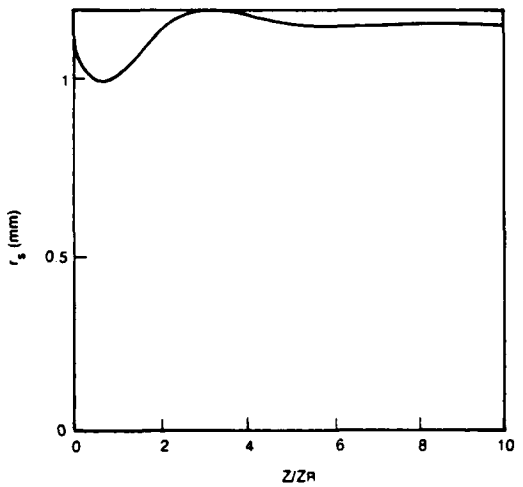



Fig. 3. Spatial evolution of the radiation spot size in the exponential gain regime for rf linac-driven FEL parameters given in table 3.

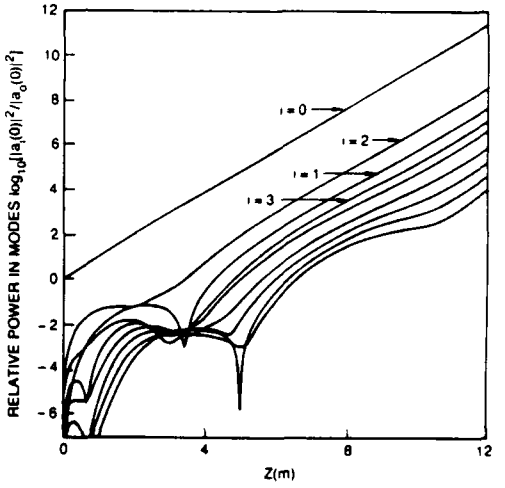



Fig. 4. Spatial evolution of the power in 10 SDE modes, $|a_i(z)|^2/|a_0(0)|^2$, $i = 0,\ldots,9$, for FEL parameters given in table 2.

## 5. Bending and guiding of radiation beams

Using the SDE formalism, it is possible to discuss the bending of a radiation beam by a curved electron beam in an FEL. For small displacements of the electron beam centroid, a nonaxisymmetric modal expansion similar to eq. (10) can be performed and the spatial evolution of the centroid of the radiation beam found. Fig. 5 shows the centroids of the electron and radiation beams for an FEL in the trapped particle regime with parameters given in table 2. Steering of the radiation beam by the electron beam is clearly demonstrated in this figure.

It is interesting to consider the conditions under which the radiation beam could be guided by a curved electron beam. We denote the radial position by $r = R_0 + x$, where $R_0$ is the radius of curvature of the electron beam and $x$ is the radial displacement from the center of the curved electron beam, as shown in fig. 6. The FEL refractive index (correct to order $x/R_0$) is

$$n = n_{FEL} + x/R_0, \tag{19}$$

where $n_{FEL}$ is given by eq. (8) In the exponential gain regime, a guided radiation beam in a curved FEL is possible if $R_0 \geq R_{min}$ where

$$R_{min} = r_s/|\mathrm{Re}(1 - n_{FEL})|. \tag{20}$$

Substituting the expressions for $\Gamma$, $\Delta k$ and $r_s$, from eq. (16), into eq. (20) yields

$$R_{min} = 4(1+f)f\gamma^2 r_b\left[(1+2f)(3f+2)^{1/2} f_B a_w \times \left(1 + a_w^2/2\right)^{1/2}(\nu/\gamma)^{1/2}\right]^{-1}, \tag{21a}$$

$$R_{min}(f=1) = 1.2\gamma^2 r_b\left[f_B a_w\left(1 + a_w^2/2\right)^{1/2}(\nu/\gamma)^{1/2}\right]^{-1}. \tag{21b}$$

For a numerical example of $R_{min}$, consider the following parameters, $\gamma = 100$, $I = 2$ kA, $r_b = 0.3$ cm, $a_w = 1.72$, $f = 1$ and $f_B = 0.85$ (table 2). For these parameters, the minimum turning radius required for a guided radiation beam is $R_{min} = 455$ m.

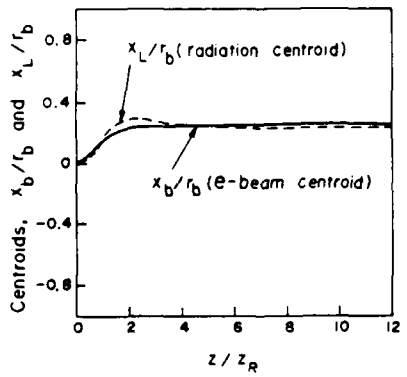



Fig. 5. Electron and radiation beam centroids, $x_b$ and $x_L$ for a displaced electron beam, $x_b = x_c(1 - \mathrm{sech}(k_c z))$ with $x_c = r_b/4$ and $\lambda_c = 2\pi/k_c = 4Z_R$.

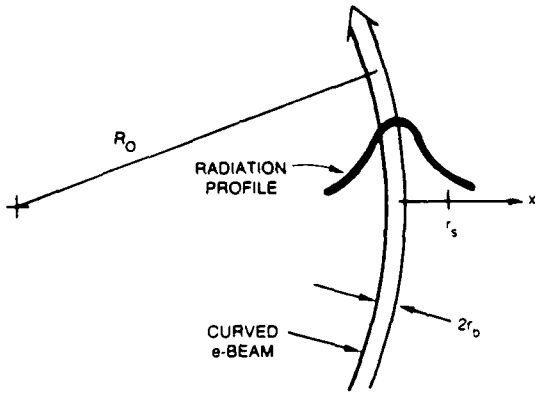



Fig. 6. Configuration showing guiding of radiation beam by a curved electron beam with radius of curvature, $R_0$.

## 6. Conclusion

The Source Dependent Expansion (SDE) method provides an excellent analytical and numerical technique for studying optical focusing, guiding and steering in FELs. We find that guided radiation beams in the FEL can be achieved in the Compton exponential gain regime but cannot be maintained in the high gain trapped particle (tapered wiggler) regime. Conditions for guided radiation beam with different transverse profiles of the electron beam have been derived in the Compton exponential gain regime of an FEL.

Free electron lasers driven by either induction linacs, such as the ATA, or high current rf linacs can operate in the guided, exponential gain regime until saturation occurs. At this point, the wiggler field could be spatially tapered so as to operate the FEL in the trapped particle regime in order to further increase the operating efficiency.

We also examined the possibility of bending or steering radiation beams in FELs. We found a condition which places a lower limit on the radius of curvation of the electron beam necessary for the radiation to be guided along a curved path.

### Acknowledgement

This work is supported by SDIO and managed by SDC.

## Appendix

Derivation of the conditions for guided radiation beam in the Compton exponential gain regime is shown in the following. When the transverse radiation beam profile is represented by the fundamental mode, eq. (15), one can combine eqs. (11a–c) to give the three-dimensional dispersion relation for the Compton exponential regime,

$$(\Delta k - i\Gamma) + \frac{2c}{\omega r_s^2}(1 - i\alpha) + \left(\frac{F_0}{a_0} + \frac{F_1}{a_0}\right) = 0. \qquad \text{(A1)}$$

where $F_0$, $F_1$ are the overlap integrals of the source function, eq. (14a), with the zeroth and first Gaussian–Laguerre modes. It can be shown that for the Compton source term, $F_0 = F_1(1 + 2f)$, where $f$ is the filling factor, $r_b^2/r_s^2$. The dispersion relation eq. (A1) is then reduced to

$$(\Delta k - i\Gamma) + \frac{2c}{\omega r_s^2}(1 - i\alpha) + 2\frac{F_1}{a_0}(1 + f) = 0. \qquad \text{(A2)}$$

By setting $r_s' = 0$ and $\alpha' = 0$ in eq. (11a, b) for guided radiation beams, we have

$$(1 - i\alpha)^2 = -\left(\frac{F_1}{a_0}\right)\frac{\omega r_s^2}{c}. \qquad \text{(A3)}$$

Evaluating $F_1/a_0$ and substituting in eq. (A3) gives the relations between the growth rate $\Gamma$, phase shift $\Delta k$ and wavefront curvature factor $\alpha$, eqs. (16a, b). Substituting eqs. (A3) into eq. (A2) provides a second set of relations between $\Gamma$, $\Delta k$, $\alpha$ and the guided radiation beam radius $r_s$,

$$\Delta k + \frac{2c}{\omega r_s^2}\left[\alpha^2(1 + f) - f\right] = 0,$$

$$\Gamma + \frac{2c\alpha}{\omega r_s^2}(2f - 1) = 0. \qquad \text{(A4)}$$

Eliminating $\Delta k$ and $\Gamma$ from eqs. (16a, b) and (A4) gives the relations of $r_s$ and $\alpha$ with the filling factor $f$, eqs. (16c, d). These algebraic equations can be easily solved numerically for the guided radiation beam values of $r_s$, $\alpha$, $\Delta k$ and $\Gamma$.

## References


[1] P. Sprangle and C.M. Tang, Appl. Phys. Lett. 39 (1981) 677.

[2] N.M. Kroll, P.L. Morton and M.N. Rosenbluth, IEEE J. Quantum Electron. QE-17 (1981) 1436.

[3] E.T. Scharlemann and D. Prosnitz, eds. Free Electron Laser, Proc. 7th Int. Conf. on FELs, Tahoe City, Sept. 8–13, 1985 (North-Holland, Amsterdam 1986).

[4] J. Fajans, J.S. Wurtele, G. Bekefi, D.S. Knowles and K. Xu, Phys. Rev. Lett. 57 (1986) 579;
F. Hartemann, K. Xu, G. Bekefi, J.S. Wurtele and J. Fajans, Phys. Rev. Lett. 59 (1987) 1177.

[5] T.J. Orzechowski, E.T. Scharlemann and B.D. Hopkins, Phys. Rev. A35 (1987) 2184.

[6] J.E. LaSala, D.A.G. Deacon and J.M.J. Madey, Phys. Rev. Lett. 59 (1987) 2047.

[7] S.Y. Cai, S.P. Chang, J.W. Dodd, T.C. Marshall and Hua Tang, these Proceedings (9th Int. FEL Conf., Williamsburg, VA, 1987) Nucl. Instr. and Meth. A272 (1988) 136.

[8] G.T. Moore, Nucl. Instr. and Meth. A239 (1985) 19.

[9] E.T. Scharlemann, A.M. Sessler and J.S. Wurtele, Phys. Rev. Lett 54 (1985) 1925.

[10] J.E. LaSala, D.A.G. Deacon and E.T. Scharlemann, Nucl. Instr. Meth. A250 (1986) 389.

[11] M. Xie and D.A.G. Deacon, Nucl. Instr. Meth. A250 (1986) 426.

[12] P. Sprangle, A. Ting and C.M. Tang, Phys. Rev. Lett. 59 (1987) 202; Phys. Rev. A36 (1987) 2773; also in Proc. 8th Int. FEL Conf., Glasgow, Scotland (Sep. 1–5, 1986) ed. M.W. Poole (North-Holland, Amsterdam 1987) p. 136.

[13] G. Mavrogenes, W. Ramler, W. Wesolowski, K. Johnson and G. Clifft, IEEE Trans. Nucl. Sci. NS-20 (1973) 919.

[14] R.L. Sheffield and J.M. Watson, A High-Power RF Linear Accelerator For FELs, AIAA-87-1226, AIAA 19th Fluid Dynamics, Plasma Dynamics and Lasers Conf., Honolulu, Hawaii (June 8–10, 1987).

[15] P. Sprangle, C.M. Tang and W. Manheimer, Phys. Rev. A21 (1980) 302.

[16] B. Hafizi, P. Sprangle and A. Ting, Phys. Rev. A36 (1987) 1739.

[17] B.D. McVey and R.W. Warren, Nucl. Instr. and Meth. A259 (1987) 158.

# APPENDIX DD

## Optical Gain, Phase Shift, and Profile in Free-Electron Lasers

PHYSICAL REVIEW A VOLUME 36, NUMBER 4 AUGUST 15, 1987

# Optical gain, phase shift, and profile in free-electron lasers

B. Hafizi,* P. Sprangle, and A. Ting†
*Naval Research Laboratory, Washington, D.C. 20375-5000*
(Received 2 March 1987)

The gain, phase shift, wave-front curvature, and radius of the radiation envelope in a free-electron-laser amplifier are obtained in the small-signal regime. The electron beam is assumed to have a Gaussian density distribution in the transverse direction. Numerical calculations indicate that the radius and curvature of the radiation beam entering a wiggler asymptote to unique spatially constant values after a finite transition region. However, in the asymptotic region the wave fronts are divergent. Analytical expressions for the gain, phase shift, curvature, and spot size are derived. It is shown analytically that small perturbations of the optical waist and curvature about the matched value are spatially damped out, indicating the stability of the matched envelope. When the electron-beam envelope is modulated in space, the optical spot size oscillates with an almost identical wavelength but is delayed in phase. In the case of small-amplitude long-wavelength betatron modulation of the electron-beam envelope, generation of optical sidebands in wave-number space is examined and the effect on the dispersion characteristics of the primary wave is found to be negligible for typical experimental parameters.

## I. INTRODUCTION

A well-known feature of the free-electron laser (FEL) is that the refractive index of the medium is a complex function and hence the radiation is amplified and to some extent focused in the vicinity of the electron beam.[1,2] It may then be possible for the electron and radiation beams to interact over an extended length along the wiggler, with the diffractive tendency being compensated by the FEL interaction, thereby enhancing the efficiency of the process.

Considerable progress has been made in studying this process by several authors.[3-8] The purpose of this paper is to apply the formalism of the Gaussian-Laguerre modal source-dependent expansion (SDE) of Ref. 8 to examine the propagation and guiding of the optical wave in an amplifier operating in the exponential gain regime, for a variety of operating conditions.

The plan of this paper is as follows. In Sec. II the formalism of the SDE is employed to obtain the evolution equations for the radius and the curvature for the lowest-order mode of the optical beam, along with the relevant dispersion relation for a Gaussian electron beam driving an FEL amplifier in the small-signal regime. In Sec. III numerical solutions of the single-mode equation for the radius of the optical beam are presented and compared to the result from a multimode truncation of the radiation field. In this case, and for cases not presented herein, the single-mode and multimode results indicate that the radiation-beam profile entering the wiggler asymptotes to a *unique* form after an initial transient. Additionally, the numerical values of the radius of the radiation envelope and of the wave-front curvature are in fair agreement, irrespective of the degree of mode truncation, indicating the usefulness of the single-mode equations. Limiting ourselves to these equations, the electron beam is then allowed to oscillate at the betatron wavelength and the resulting radiation profile is examined. It is found that the optical-beam envelope follows that of the electrons with almost identical wavelength, but retarded in phase. Section IV discusses the results, deriving formulas for the matched radiation-beam profile (i.e., radius and curvature) in terms of the electron-beam and wiggler parameters. It is shown analytically that perturbations of the profile are spatially damped out, consistent with the numerical observations indicating a unique, asymptotic matched radius and curvature. Appendix A presents the necessary details required to derive the source term, for the wave equation, for a planar wiggler and an electron beam with uniform density along the direction of propagation. Appendix B considers the effect of the modulation of the electron beam on the optical wave. Specifically, a simple analysis, taking into account sideband generation, indicates that the dispersion characteristics of the primary wave are only slightly modified for typical experimental parameters. Appendix C presents the details of the stability calculation.

## II. MATHEMATICAL FORMULATION

The purpose of the present section is to present the salient features of the source-dependent expansion method[8] so as to fix the notation and for reference in the subsequent sections.

For a planar wiggler, it is appropriate to assume a linearly polarized radiation vector potential

$$\mathbf{A}=\tfrac{1}{2}A(r,\theta,z)\exp\left[i\left[\frac{\omega z}{c}-\omega t\right]\right]\mathbf{e}_x+\text{c.c.}\ ,$$

with angular frequency $\omega$ and complex amplitude $A$. In the slowly-varying-envelope approximation, the wave equation reduces to

 ©1987 The American Physical Society

$$\left[\frac{1}{r}\frac{\partial}{\partial r}r\frac{\partial}{\partial r}+\frac{1}{r^2}\frac{\partial^2}{\partial\theta^2}+\frac{2i\omega}{c}\frac{\partial}{\partial z}\right]a=S(r,\theta,z)\ , \tag{1}$$

where $a=|e|A/m_0c^2$, and the source function is given by

$$S(r,\theta,z)=-\frac{8\pi|e|}{m_0c^3}\left\{J_x(r,\theta,z)\exp\left[-i\left[\frac{\omega z}{c}-\omega t\right]\right]\right\}_{\text{slow}}\ . \tag{2}$$

Here $e$ is the charge on an electron of (rest) mass $m_0$, $J_x(r,\theta,z)$ is the current density, and $\{\}_{\text{slow}}$ indicates that only the spatially and temporally slow part of the quantity in braces is to be retained.

The basic premise of the work presented herein is that the radiation field is azimuthally symmetric and the vector potential is expressible as

$$a(r,\theta,z)=\sum_{m=0}^{\infty}a_m(z)D_m(\xi,z)\ , \tag{3}$$

with $D_m=L_m(\xi)\exp\{-[1-i\alpha(z)]\xi/2\}$, where $\xi=2r^2/r_s^2(z)$, $r_s(z)$ is related to the radiation spot size, $\alpha(z)$ is proportional to the curvature of the wave front, and $L_m(\xi)$ is the Laguerre polynomial of order $m$.

Now, if the transverse profile of the radiation beam is close to a Gaussian, the lowest-order mode is expected to dominate,[3,5,7,8] and, following Ref. 8, it is simple to show that the associated vector potential evolves according to

$$\left[\frac{\partial}{\partial z}+A_0\right]a_0\simeq -iF_0\ , \tag{4}$$

and the spot size and wave-front curvature evolve via

$$\frac{d}{dz}r_s-\frac{2c\alpha}{\omega r_s}=-r_s\left[\frac{F_1}{a_0}\right]_I\ , \tag{5a}$$

$$\frac{d}{dz}\alpha-2(1+\alpha^2)\frac{c}{\omega r_s^2}=2\left[\left[\frac{F_1}{a_0}\right]_R-\alpha\left[\frac{F_1}{a_0}\right]_I\right]\ , \tag{5b}$$

where

$$A_0=\frac{1}{r_s}\frac{d}{dz}r_s+i\left[(1+\alpha^2)\frac{c}{\omega r_s^2}-\frac{\alpha}{r_s}\frac{d}{dz}r_s+\frac{1}{2}\frac{d}{dz}\alpha\right]\ ,$$

the $F$'s are given by the following overlap integral:

$$F_m(z)=\frac{c}{2\omega}\int_0^{\infty}d\xi\,S(\xi,z)D_m^*(\xi,z)\ , \tag{6}$$

and the label $R$ ($I$) indicates the real (imaginary) part.

Noting that $L_0(\xi)=1$, the normalized vector potential is seen to be given by [Eq. (3)]

$$a(r,\theta,z)\simeq a_0(z)\exp\left[-[1-i\alpha(z)]\frac{r^2}{r_s^2(z)}\right]\ , \tag{7}$$

where, in the exponential gain, small-signal regime,

$$a_0(z)\simeq a(0)\exp\left[i\int_0^z dz_1[\Delta k(z_1)-i\Gamma(z_1)]\right]\ . \tag{8}$$

Here $a(0)$ is the input signal at $z=0$, and the two components of the refractive index are given by

$$n_z=\left[1+\frac{c\Delta k}{\omega}\right]-i\frac{c}{\omega}\left[\Gamma-r^2\frac{\partial}{\partial z}\frac{1-i\alpha}{r_s^2}\right]\ , \tag{9a}$$

$$n_r=\frac{2cr}{\omega r_s^2}(\alpha+i)\ . \tag{9b}$$

Assuming the electron-beam profile to be given by

$$n_b(z)=n_{b0}\left[\frac{r_{b0}}{r_b(z)}\right]^2\exp\left[-\frac{r^2}{r_b^2(z)}\right]\ , \tag{10}$$

where $r_b(z)$ is the electron-beam radius at $z$ and $n_{b0}$ is the beam density at $r_b(z)=r_{b0}$, the source term in Eq. (1) may be readily evaluated (Appendix A) to obtain

$$S(r,z)=f_B^2\frac{\omega_{b0}^2}{2\gamma^3c^2}\left[\frac{r_{b0}}{r_b(z)}\right]^2\exp\left[-\frac{r^2}{r_b^2}\right]\frac{\omega k_w a_w^2 a}{c(\Delta k-i\Gamma)^2}\ , \tag{11}$$

where the vector potential of the planar wiggler of periodicity $2\pi/k_w$ is given by

$$\mathbf{A}_w=A_w\cos(k_wz)\mathbf{e}_x\ , \tag{12}$$

$$a_w=|e|A_w/m_0c^2\ , \tag{13}$$

$\gamma$ is the relativistic mass factor, $f_B$ is the usual difference of Bessel functions, $f_B=J_0(\xi)-J_1(\xi)$, $\xi=(1/4)a_w^2/[1+(1/2)a_w^2]$, and

$$\omega_{b0}=(4\pi|e|^2n_{b0}/m_0)^{1/2}$$

is the plasma frequency of the electron beam with density $n_{b0}$.

Substituting Eqs. (8) and (11) into Eq. (6) and making use of Eqs. (4) and (5), it is simple to show that the equations reduce to

$$\frac{d\alpha}{d(k_wz)}=2(1+\alpha^2)\left[\frac{ck_w}{\omega}\right]\frac{1}{(k_wr_s)^2}+2\left[\left[\frac{F_1}{k_wa_0}\right]_R-\alpha\left[\frac{F_1}{k_wa_0}\right]_I\right]\ , \tag{14a}$$

$$\frac{d(k_wr_s)^2}{d(k_wz)}=4\alpha\left[\frac{ck_w}{\omega}\right]-2\left[\frac{F_1}{k_wa_0}\right]_I(k_wr_s)^2\ , \tag{14b}$$

$$\frac{\Delta k}{k_w}-i\frac{\Gamma}{k_w}+2\left[\frac{ck_w}{\omega}\right]\frac{1-i\alpha}{(k_wr_s)^2}+2\left[\frac{F_1}{k_wa_0}\right]\left[1+\left[\frac{r_b}{r_s}\right]^2\right]=0\ , \tag{14c}$$

where

$$\frac{F_1}{k_wa_0}=f_B^2\left[\frac{\omega_{b0}}{ck_w}\right]^2\left[\frac{r_{b0}}{r_b(z)}\right]^2\frac{a_w^2}{2\gamma^3}\frac{(r_b/r_s)^2}{[1+2(r_b/r_s)^2]^2}\times\left[\frac{\Delta k}{k_w}-i\frac{\Gamma}{k_w}\right]^{-2}\ . \tag{14d}$$

The spatial evolution of the system is governed by the differential system (14a) and (14b) along with the dispersion relation (14c), the solution of which yields $\alpha(z)$, $r_s(z)$, $\Delta k(z)$, and $\Gamma(z)$.

## III. NUMERICAL RESULTS

Having obtained the single-mode system of Eqs. (14), it is of interest to determine the extent to which it approximates the general solution in (3). Once it is established that Eqs. (14) provide an adequate representation of the general solution, it is then possible to study a variety of problems of interest by solving a simple set of equations. Briefly, the numerical procedure for solving an initial-value problem is the following. Substituting Eq. (14d) into Eq. (14c) yields a cubic (algebraic) equation for $\Delta k - i\Gamma$ which may be solved, at each $z$, in terms of $r_s(z)$, $\alpha(z)$, and $r_b(z)$, thus enabling Eqs. (14a) and (14b) to be stepped forward in $z$. Since in the absence of source terms an input radiation signal diffracts away on the scale length defined by the Rayleigh range $z_R$,

$$z_R = \left.\frac{\omega r_s^2(z)}{2c}\right|_{z=0}, \tag{15}$$

it is informative to present the numerical results with the distance along the wiggler measured in units of the Rayleigh range. In all the numerical results to be presented, the radiation field is assumed to be in the form of plane waves at the entrance to the wiggler, i.e., $\alpha(z=0)=0$.

### A. Case I

To begin with, Fig. 1 shows the results for the following parameters: beam current $I_b = 270$ A, $r_{b0}=0.01$ cm, $\gamma=2000$, $2\pi/k_w=10$ cm, $a_w=6.15$, and $r_s(z=0)=0.02$ cm. Noting the factor of $2^{1/2}$ difference between the definition of $a_w$ in Eq. (13) and that in Ref. 4, it is clear from Fig. 1(a) that after a transient oscillation over a distance of about 20 Rayleigh ranges, the radiation spot size approaches a value quite close to that obtained with the two-dimensional FEL code FRED at the Lawrence Livermore National Laboratory (LLNL).[4] We also find that for all the numerical cases examined, a unique, asymptotic spot size is obtained irrespective of the initial optical waist. Figure 1(b) shows the spatial evolution of $\alpha$, indicating that it, too, approaches a constant value after an initial transient behavior.

The solid curve in Fig. 2 shows the evolution of the $1/e$ width of the radiation amplitude with a five-mode ($m=0,1,2,3,4$) source-dependent expansion calculation using the same set of FEL parameters. The radiation field is represented by Eq. (3) and the source term is given by Eq. (11). With the assumption that the fundamental mode dominates, only the $\Delta k$ and $\Gamma$ of $a_0(r,z)$ are involved in the source function and they are obtained from Eqs. (14c) and (14d). It is found that the fundamental mode remains dominant over many Rayleigh lengths. For comparison, the dashed curve in Fig. 2 shows the fundamental mode spot size of Fig. 1(a), and the asymptotic results are seen to differ by about 10%. This suggests that the single-mode system of Eqs. (14) may be regarded as a reasonably accurate simplification of Eq. (3). Henceforth, the results presented pertain to Eqs. (14).

### B. Case II

Figure 3 presents the results for a case where the electron beam is not matched, i.e., the envelope of the electron beam is modulated:

$$r_b(z) = r_{b0} + \delta r_b \sin(k_\beta z), \tag{16}$$

where $\delta r_b$ is the amplitude of the modulation and for simplicity $k_\beta$ is chosen to be equal to the betatron wave number[9] $k_w a_w/(\sqrt{2}\gamma\beta_z)$, neglecting self-fields.[10] $\beta_z$ is the beam speed along the wiggler axis normalized to $c$. The

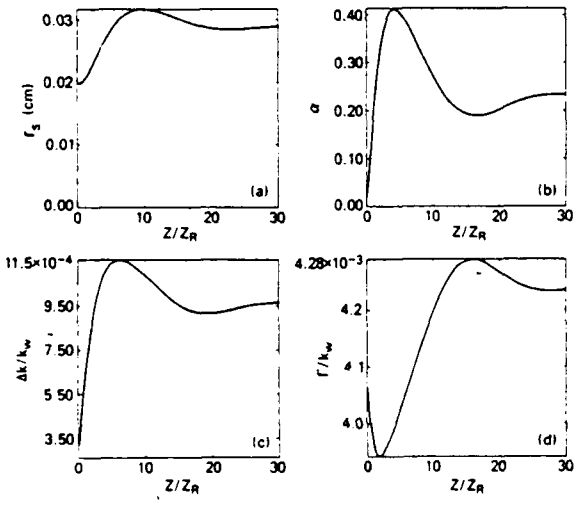



FIG. 1. Spot size ($r_s$), $\alpha$, phase shift ($\Delta k$), and gain ($\Gamma$) vs distance along the wiggler. $z$ is normalized to the Rayleigh range $z_R$.

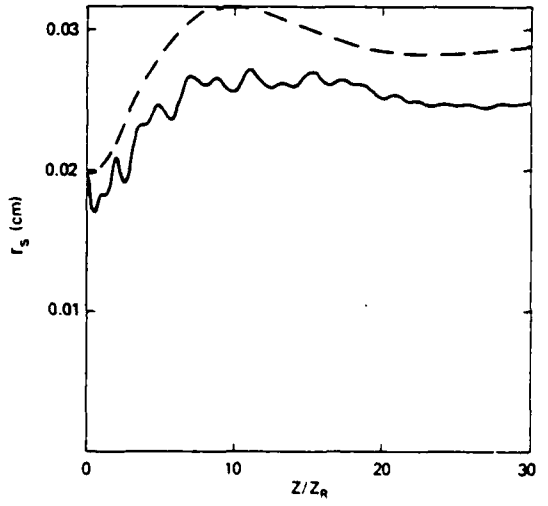



FIG. 2. ($1/e$) width of the optical field vs distance along the wiggler. Solid curve, five-mode system; dashed curve, one-mode system.

parameters, typical of the Advanced Test Accelerator experiment at LLNL, are $I_b=2$ kA, $r_{b0}=0.3$ cm, $\gamma=100$, $2\pi/k_w=8$ cm, $a_w=1.72$, and $r_s(z=0)=0.35$ cm. (The reader is referred to Refs. 9 and 11 for details.) In Fig. 3, where $\delta r_b/r_{b0}=0.1$, it is observed that the optical spot size follows the modulations in the electron envelope apparently identically. Specifically, a number of cases were examined with $\delta r_b/r_{b0}$ up to 0.4. In all cases the electron and optical beams oscillate with almost identical wavelength, although the radiation beam appears to lag behind in phase. Defining the modulation depth $\Delta=[(r)_{\max}-(r)_{\min}]/[(r)_{\max}+(r)_{\min}]$, it is found from Fig. 3(a) that $\Delta_s=0.087$ whereas, from Eq. (16), $\Delta_b=\delta r_b/r_{b0}=0.1$. Although the modulation depth of the electron beam differs from that of the radiation beam, it is found that $\Delta_s$ increases with $\delta r_b$.

More generally, allowing for the defocusing effect of self-fields, there is always the possibility of a small-amplitude ripple on the electron-beam envelope and hence on the radiation-beam envelope. In Appendix B, generation of sidebands is considered in a simplified model and found to have, for typical cases, an insignificant effect on the linear dispersion characteristics of the primary optical wave, as implicitly assumed by employing the source term in Eq. (11) in the present case.

## IV. ANALYSIS OF RESULTS

One interesting feature of the numerical results is that in all cases the radiation spot size has a unique, asymptotic limit irrespective of the initial value. The asymptotic value of $r_s$ and of $\alpha$ is determined by the fixed points of Eqs. (14a) and (14b), i.e., at the fixed point

$$2(1+\alpha^2)\frac{ck_w}{\omega}\frac{1}{(k_w r_s)^2}+2\left[\left[\frac{F_1}{k_w a_0}\right]_R-\alpha\left[\frac{F_1}{k_w a_0}\right]_I\right]=0\,, \tag{17a}$$

$$4\alpha\frac{ck_w}{\omega}-2\left[\frac{F_1}{k_w a_0}\right]_I(k_w r_s)^2=0\,. \tag{17b}$$

Combining Eqs. (17a) and (17b) one obtains

$$(1-i\alpha)^2\frac{ck_w}{\omega}+(k_w r_s)^2\left[\frac{F_1}{k_w a_0}\right]=0\,,$$

which, upon making use of Eq. (14d), yields

$$\Delta k=\frac{k_w^2 r_b \eta^{1/2}}{1+2f}\frac{\alpha}{1+\alpha^2},\quad \Gamma=\Delta k/\alpha\,,$$

where

$$\eta=f_B^2\left[\frac{\omega}{ck_w}\right]\left[\frac{\omega_{b0}}{ck_w}\right]^2\left[\frac{r_{b0}}{r_b}\right]^2\frac{a_w^2}{2\gamma^3}\,,$$

and $f=(r_b/r_s)^2$ is the filling factor. Substituting the expressions for $\Delta k$ and $\Gamma$ into the dispersion relation (14c), one obtains

$$\alpha=[f/(3f+2)]^{1/2}\,,$$

$$r_s=\frac{(\gamma/\nu)^{1/4}}{2^{3/4}k_w\gamma f_B^{1/2}}\frac{(1+a_w^2/2)^{3/4}}{a_w^{1/2}}\frac{f^{1/4}(1+2f)^{3/2}}{(1+3f/2)^{3/4}}\,,$$

where $\nu=(\omega_{b0}r_{b0}/2c)^2$ is Budker's parameter. These expressions may be used to obtain the asymptotic spot size for a given filling factor, and then one obtains the corresponding electron-beam radius via $r_b=r_s f^{1/2}$. To avoid complications arising at the outer edges of the optical beam, where the field amplitude is small, typically a filling factor $f\lesssim\frac{1}{2}$ is appropriate. It is also possible to rearrange the expression for $r_s$ to obtain

$$f^3+f^2+(\tfrac{1}{4}-\tfrac{3}{2}q)f-q=0\,,$$

where

$$q=\left[a_w^2\left[\frac{2f_B^2}{\gamma/\nu}\right]\left[\frac{\gamma r_b k_w}{2}\right]^4\right]^{1/3}\frac{1}{1+a_w^2/2}\,.$$

The cubic equation for $f$ may be solved to obtain an explicit expression for $r_s$. Noting that the sum and the product of the three roots of the cubic equal $-1$ and $q$, respectively, it follows that there is a unique, real value for the asymptotic spot size $r_s$.

To examine stability, it is convenient to define

$$Y\equiv\frac{\Delta k}{k_w}-i\frac{\Gamma}{k_w}\,,$$

and subsititute Eq. (14d) into Eq. (14c) to obtain the local dispersion relation

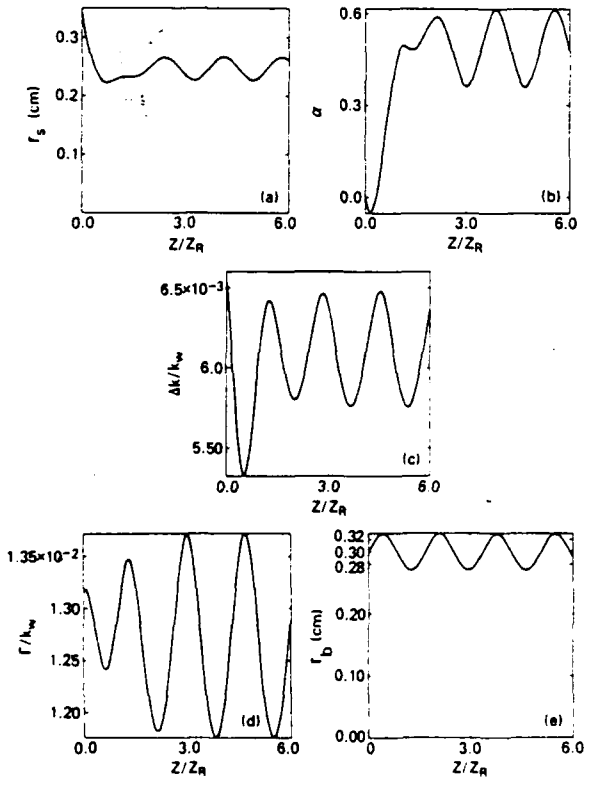



FIG. 3. Spot size ($r_s$), $\alpha$, phase shift ($\Delta k$), gain ($\Gamma$), and radius of electron beam ($r_b$) vs distance along wiggler.

$$Y^3+2\left|\frac{ck_w}{\omega}\right|\frac{1-i\alpha}{(k_w r_s)^2}Y^2=-2\frac{ck_w}{\omega}\eta\left|\frac{r_b}{r_s}\right|^2\times\frac{1+(r_b/r_s)^2}{[1+2(r_b/r_s)^2]^2}, \quad (18)$$

which may be solved iteratively. It turns out that for the parameters of case I, at the lowest order, the right-hand side balances the quadratic term on the left. The relevant root, with $\Delta k$, $\Gamma>0$, may be substituted into Eq. (14d) to obtain, for $\alpha>0$,

$$\frac{F_1}{k_w a_0}\simeq\frac{-ck_w}{\omega}\frac{1-i\alpha}{(k_w r_s)^2+(k_w r_b)^2}-\frac{1}{2}\left|\frac{\eta}{2(1+\alpha^2)}\right|^{1/2}\frac{\alpha-i[1+(1+\alpha^2)^{1/2}]}{[1+(1+\alpha^2)^{1/2}]^{1/2}}\frac{(k_w r_s)^2}{(k_w r_s)^2+2(k_w r_b)^2}\frac{(k_w r_s)(k_w r_b)}{[(k_w r_s)^2+(k_w r_b)^2]^{1/2}}. \quad (19)$$

Perturbing Eqs. (14a) and (14b) about the fixed point and making use of Eq. (19), it is simple to show that the perturbation is spatially damped, thus indicating the stability of the fixed point. The algebraic details are relegated to Appendix C.

Another aspect of the results which is of interest pertains to the nature of the phase fronts and the flux of optical power in the asymptotic region. From Eqs. (7) and (8) it is simple to check that, in differential form, the surfaces of constant phase are given by $(\omega/c+\Delta k)\delta z+(2r\alpha/r_s^2)\delta r=0$, and hence, noting that $\Delta k$, $\alpha>0$, the wave fronts are divergent in the direction of propagation. Consistent with this, there is a nonvanishing transverse component of the Poynting flux. Specifically, for $r/r_s\lesssim 1$ the ratio of flux of optical energy in the transverse direction to that along the $z$ axis is $\sim\alpha r/kr_s^2\ll 1$.

## V. CONCLUSION

Based on the results presented herein, the simplicity and accuracy of the single-mode Gaussian-Laguerre approximation to the solution of Maxwell's equations have been demonstrated. It is shown that, in the exponential gain regime of operation of an FEL amplifier, there is a unique, asymptotic spot size for the radiation beam irrespective of that at the entrance of the wiggler. There is, however, a transverse flux of optical power. It is shown analytically that the asymptotic profile (i.e., the radius and the curvature at large $z$) is stable to small-amplitude perturbations. With a spatially modulated electron-beam envelope, that of the optical beam is found to oscillate on the same spatial scale.

## ACKNOWLEDGMENTS

Discussions with Dr. W. P. Marable and Dr. C. M. Tang are gratefully acknowledged. This work was sponsored by U.S. Army Strategic Defense Command.

## APPENDIX A: SOURCE TERM

In this appendix, the details of the evaluation of the source term $S$ in Eq. (11) are presented.

The FEL source current, $J_x(r,\theta,z)$ in a linear wiggler is given by

$$J_x(r,\theta,z)=-|e|\delta n_b(r,\theta,z)v_x=\frac{-|e|^2\delta n_b e^{-ik_w z}}{2\gamma m_0 c}A_w+\text{c.c.},$$

where $\delta n_b$ is the perturbed beam density and the relation $v_x\simeq v_w=|e|A_w\cos(k_w z)/\gamma m_0 c$ has been used. Equation (2) can then be written as

$$S(r,\theta,z)=\left[\frac{4\pi|e|^2\delta n_b a_w}{\gamma m_0 c^2}e^{-i[(k+k_w)z-\omega t]}\right]_{\text{slow}}, \quad (A1)$$

where $k=\omega/c$.

The perturbed beam density can be evaluated from the continuity equation

$$\frac{d\delta n_b}{dt}=-n_b\frac{\partial\delta v_z}{\partial z}, \quad (A2)$$

and the equation of motion in the $z$ direction,

$$\frac{dv_z}{dt}=-\frac{|e|}{\gamma m_0}\left[\frac{v_x B_y}{c}-\frac{v_z(v_x E_x)}{c^2}\right], \quad (A3)$$

where electron self-field effects are neglected. Taking the convective time derivative of Eq. (A2), and incorporating the linearized version of Eq. (A3), one can arrive at the following equation for the perturbed beam density:

$$\frac{d^2\delta n_b}{dt^2}=\frac{-|e|n_b}{\gamma m_0}\frac{\partial}{\partial z}\left[\frac{\partial}{\partial z}+\frac{v_z}{c^2}\frac{\partial}{\partial t}\right]\Phi_{\text{pond}}, \quad (A4)$$

where

$$\Phi_{\text{pond}}=\frac{-|e|A_w A}{4\gamma m_0 c^2}e^{i[(k+k_w)z-\omega t]}+\text{c.c.}$$

With the assumption that $A(r,\theta,z)$ is a slowly varying function of $z$, i.e., $|\partial\ln A/\partial z|\ll k_w\ll k$, Eq. (A4) becomes

$$\frac{d^2\delta n_b}{dt^2}=\frac{|e|^2 n_b A_w A}{2\gamma^2 m_0^2 c^2}k_w k e^{i[(k+k_w)z-\omega t]}+\text{c.c.}, \quad (A5)$$

where the resonance condition $\omega=v_z(k+k_w)$ is used.

For a near-Gaussian radiation field in the exponential gain regime,

$$A(r,\theta,z) \simeq A_0(r,\theta,z) = A_0(0)\exp\left\{ i\int_0^z [\Delta k(z_1) - i\Gamma(z_1)]dz_1 - [1-i\alpha(z)]\frac{r^2}{r_s^2(z)} \right\}$$

and assuming that $\Delta k$, $\Gamma$, $\alpha$ and $r_s$ are slowly varying functions of $z$, Eq. (A5) can be integrated immediately to give

$$\delta n_b = \frac{|e|^2 n_b A_w A k k_w}{2\gamma^2 m_0^2 c^4 (\Delta k - i\Gamma)^2} e^{i[(k+k_w)z-\omega t]} + \text{c.c.} \qquad \text{(A6)}$$

When Eq. (A6) is substituted into Eq. (A1), taking into account the usual difference of Bessel functions for a planar wiggler, and Eq. (10) for the beam profile, the source function in Eq. (1) is then given by Eq. (11).

## APPENDIX B: SIDEBAND GENERATION

In this appendix generation of sidebands to the primary optical wave, due to the spatial modulation of the electron beam, is analyzed. It is to be emphasized that the following analysis is intended merely to show that the dispersion characteristics of the primary optical wave are only slightly modified [$\sim(\delta N_0/N_0)^2$] for typical experimental parameters, as implicitly assumed in applying the results of Appendix A to the case of a modulated electron beam in Sec. III. The development of the linear theory herein generalizes that of Sprangle *et al.*,[12] to which reference should be made for further details.

The form of the vector potential of a planar wiggler employed in this appendix is slightly different than that given by Eq. (12),

$$\mathbf{A}_w \simeq A_w[\exp(ik_w z) - \text{c.c.}]\mathbf{e}_x ,$$

where $A_w$ is purely imaginary, and that of the linearly polarized radiation field is taken to be of the form

$$\mathbf{A} = [A_+\exp(ik_+ z - i\omega t) + A_-\exp(ik_- z - i\omega t) + A_0\exp(ikz - i\omega t) + \text{c.c.}]\mathbf{e}_x ,$$

where it is assumed that the electron density, modulated at the betatron wavelength $2\pi/k_\beta$, has the simple form

$$n_0 = N_0 + \frac{\delta N_0}{2}[\exp(ik_\beta z) + \text{c.c.}] ,$$

with $k_\beta \ll k_w \ll k$, and $k_+ = k + k_\beta$, $k_- = k - k_\beta$.

Following Ref. 12, the wave equation is found to be

$$\left[\frac{\partial^2}{\partial z^2} - \frac{1}{c^2}\frac{\partial^2}{\partial t^2} - \frac{\omega_b^2}{\gamma_0 c^2}\right]\mathbf{A} = \frac{4\pi|e|^2}{\gamma_0 m_0 c^2}\delta n\,\mathbf{A}_w ,$$

where $\gamma_0$ is the relativistic factor in the absence of the radiation field, $\omega_b = (4\pi n_0|e|^2/m_0)^{1/2}$, and $\delta n$ is the density perturbation caused by the radiation. Note that the velocity $v_{z0}$ along the wiggler axis is not affected by the betatron oscillation and hence $\gamma_0$, to lowest order in $|eA_w/\gamma_0 m_0 c^2|^2$, is not a function of $z$. Defining the ponderomotive potential

$$\Phi_{\text{pond}} = \frac{-|e|}{\gamma_0 m_0 c^2}\mathbf{A}_w \cdot \mathbf{A} ,$$

the momentum, continuity, and Poisson's equations may be combined to obtain

$$\frac{d^2}{dt^2}\delta n - \frac{v_{z0}}{n_0}\left[\frac{\partial n_0}{\partial z}\right]\frac{d}{dt}\delta n + \frac{4\pi n_0|e|^2}{m_0\gamma_0\gamma_z^2}\delta n + \frac{|e|}{m_0\gamma_0\gamma_z^2}\left[\frac{\partial n_0}{\partial z}\right]\frac{\partial\Phi}{\partial z} = \frac{-|e|}{m_0\gamma_0}\frac{\partial}{\partial z}n_0\left[\frac{\partial}{\partial z} + \frac{v_{z0}}{c^2}\frac{\partial}{\partial t}\right]\Phi_{\text{pond}} , \qquad \text{(B1)}$$

where $\gamma_z = (1 - v_{z0}^2/c^2)^{-1/2}$, $\Phi$ is the scalar potential, and terms such as $\partial^2 n_0/\partial z^2$, which are on the order of $k_\beta^2$, have been neglected.

Writing $k_+ = k + k_\beta$, $k_- = k - k_\beta$,

$$\delta n = \{\delta n_+\exp[i(k_+ + k_w)z - i\omega t] + \delta n_-\exp[i(k_- + k_w)z - i\omega t] + \delta n_0\exp[i(k + k_w)z - i\omega t] + \text{c.c.}\} ,$$

noting that, on the left-hand side of Eq. (B1), the ratio of the fourth to the third term is on the order of $k_\beta/k \ll 1$, one finds that

$$\begin{bmatrix} m_{11}+\epsilon^2 a_- & \epsilon m_{12} & m_{13} \\ \epsilon m_{21} & m_{22}+\epsilon^2 a_{22} & \epsilon m_{23} \\ m_{31} & \epsilon m_{32} & m_{33}+\epsilon^2 a_+ \end{bmatrix}\begin{bmatrix} A_+ \\ A_0 \\ A_- \end{bmatrix} = 0 ,$$

where $\epsilon = (\delta N_0/2N_0)$ and $m_{13}, m_{31} = O(\epsilon^2)$. It is then simple to show that, correct to $O(\epsilon^2)$, the dispersion relation is given by

$$m_{22} - \left[\frac{\delta N_0}{2N_0}\right]^2\left[\frac{m_{32}m_{23}}{m_{33}} + \frac{m_{12}m_{21}}{m_{11}}\right] + \left[\frac{\delta N_0}{2N_0}\right]^2\left[a_{22} + m_{22}\left[\frac{a_+}{m_{33}} + \frac{a_-}{m_{11}}\right]\right] = 0 ,$$

where

$$m_{22} = m_{22}(k) \equiv \left[[\omega - (k + k_w)v_{z0}]^2 - \frac{\omega_{b0}^2}{\gamma_0\gamma_z^2}\right] \times \left[k^2 - \frac{\omega^2}{c^2} + \frac{\omega_{b0}^2}{\gamma_0 c^2}\right] - \frac{2\omega_{b0}^2}{\gamma_0^3}kk_w a_w^2 ,$$

is the usual matrix element for the primary wave, $m_{11} = m_{22}(k_+)$, $m_{33} = m_{22}(k_-)$,

$$m_{12}=m_{12}(k_+,k,k_\beta)$$
$$=\frac{\omega_{b0}^2}{\gamma_0 c^2}\left[[\omega-(k_++k_w)v_{z0}]^2-\frac{\omega_{b0}^2}{\gamma_0\gamma_z^2}\right]$$
$$+\left[k_\beta v_{z0}[\omega-(k+k_w)v_{z0}]-\frac{\omega_{b0}^2}{\gamma_0\gamma_z^2}\right]$$
$$\times\left[k^2-\frac{\omega^2}{c^2}+\frac{\omega_{b0}^2}{\gamma_0 c^2}\right]-\frac{2\omega_{b0}^2}{\gamma_0^2}k_+k_w a_w^2 ,$$

$$m_{21}=m_{12}(k,k_+,-k_\beta),\quad m_{23}=m_{12}(k,k_-,k_\beta) ,$$

$$m_{32}=m_{12}(k_-,k,-k_\beta) ,$$

$$a_{22}=-\frac{2\omega_{b0}^4}{\gamma_0^2\gamma_z^2c^2}+\frac{2\omega_{b0}^2k_\beta^2v_{z0}^2}{\gamma_0c^2} ,$$

$$a_\mp=\frac{\omega_{b0}^2}{\gamma_0c^2}\left[k_\beta v_{z0}[\omega-(k+k_w)v_{z0}]\mp\frac{\omega_{b0}^2}{\gamma_0\gamma_z^2}\right] ,$$

and $\omega_{b0}=(4\pi e^2N_0/m_0)^{1/2}$. Note that with the definition chosen for $A_w$ in this appendix, $a_w^2=(eA_w/m_0c^2)^2<0$.

To proceed along the lines of Ref. 12, it is convenient to write

$$m_{22}=M_{22}+C_{22} ,$$

where

$$M_{22}=\left[[\omega-(k+k_w)v_{z0}]^2-\frac{\omega_{b0}^2}{\gamma_0\gamma_z^2}\right]$$
$$\times\left[k^2-\frac{\omega^2}{c^2}+\frac{\omega_{b0}^2}{\gamma_0c^2}\right] ,$$

and

$$C_{22}=\frac{-2\omega_{b0}^2}{\gamma_0^3}kk_wa_w^2$$

is the "coupling" term. The dispersion relation then becomes

$$\left[1+\left[\frac{\delta N_0}{2N_0}\right]^2\left[\frac{a_+}{m_{33}}+\frac{a_-}{m_{11}}\right]\right]M_{22}$$
$$=-\left[1+\left[\frac{\delta N_0}{2N_0}\right]^2\left[\frac{a_+}{m_{33}}+\frac{a_-}{m_{11}}\right]\right]C_{22}$$
$$+\left[\frac{\delta N_0}{2N_0}\right]^2\left[\frac{m_{12}m_{21}}{m_{11}}+\frac{m_{32}m_{23}}{m_{33}}-a_{22}\right] . \tag{B2}$$

$M_{22}$ yields the dispersion relation for uncoupled electromagnetic and space-charge waves. The right-hand side of Eq. (B2) introduces the FEL interaction and coupling to sidebands, and its effect is included iteratively. At the lowest order, $M_{22}=0$ for some $(\omega,k)$. Substituting in the right-hand side, the second set of terms vanishes; the term proportional to $C_{22}$ survives.

Substantial modification of this dispersion relation is expected if

$$1+\left[\frac{\delta N_0}{2N_0}\right]^2\left[\frac{a_+}{m_{33}}+\frac{a_-}{m_{11}}\right]\ll 1$$

i.e., if

$$\frac{\delta N_0}{N_0}\sim 2k_\beta c\omega_{b0}^{-3/2}(2kv_{z0})^{1/2}\gamma_z^{1/2}\gamma_0^{3/4} .$$

For typical experimental parameters, the right-hand side of this equation exceeds unity, whereas $\delta N_0/N_0\ll 1$, implying the insignificance of the effect of modulation on the dispersion relation.

## APPENDIX C: STABILITY ANALYSIS

The purpose of this appendix is to establish the stability of the fixed point $(r_s,\alpha)$ of Eqs. (14).

Perturbing Eqs. (14a) and (14b) about the fixed point and making use of Eq. (19), it is seen that the perturbation evolves according to

$$\frac{d}{d(k_wz)}\begin{bmatrix}\delta a\\ \delta x\end{bmatrix}=2\begin{bmatrix}a_{11}&a_{12}\\ a_{21}&a_{22}\end{bmatrix}\begin{bmatrix}\delta a\\ \delta x\end{bmatrix} ,$$

where $x=(k_wr_s)^2$, $y=(k_wr_b)^2$,

$$a_{11}=\frac{-\alpha(ck_w/\omega)}{x+y}+X_I+\frac{\partial}{\partial\alpha}(X_R-\alpha X_I) ,$$

$$a_{12}=\frac{-(1+\alpha^2)(ck_w/\omega)y(2x+y)}{x^2(x+y)^2}+\frac{\partial}{\partial x}(X_R-\alpha X_I) ,$$

$$a_{21}=\frac{xX_I}{\alpha}-x\frac{\partial}{\partial\alpha}X_I ,$$

$$a_{22}=-\frac{\alpha(ck_w/\omega)}{(x+y)^2}-\frac{\partial}{\partial x}(xX_I) ,$$

and

$$X=-\tfrac{1}{2}\left[\frac{\eta}{2(1+\alpha^2)}\right]^{1/2}\frac{\alpha-i[1+(1+\alpha^2)^{1/2}]}{[1+(1+\alpha^2)^{1/2}]^{1/2}}$$
$$\times\frac{x}{x+2y}\left[\frac{xy}{x+y}\right]^{1/2} . \tag{C1}$$

Assuming that $\delta\alpha,\delta x\sim\exp(\lambda k_wz)$, one finds that

$$\lambda=-\left[\frac{\alpha(ck_w/\omega)(x+2y)}{(x+y)^2}+S_2+S_1\right]$$
$$\pm\left[\left[\frac{-\alpha(ck_w/\omega)x}{(x+y)^2}+S_2-S_1\right]^2-S_3\right]^{1/2} ,$$

where

$$S_1=-\frac{\partial X_R}{\partial\alpha}+\alpha\frac{\partial X_I}{\partial\alpha} ,$$

$$S_2=\frac{\partial}{\partial x}(xX_I) ,$$

$$S_3=-4x\left[\frac{X_I}{\alpha}-\frac{\partial X_I}{\partial\alpha}\right]\left[\frac{-(1+\alpha^2)(ck_w/\omega)y(y+2x)}{x^2(x+y)^2}\right.$$
$$\left.+\frac{\partial}{\partial x}(X_R-\alpha X_I)\right] .$$

(Note that all the variables in this appendix are evaluated at the fixed point.) Making use of Eq. (C1), it is simple to show that $X_I/\alpha - \partial X_I/\partial\alpha > 0$, $\partial(X_R - \alpha X_I)/\partial x < 0$, whence $S_3 > 0$ and hence, noting that $S_2 + S_1 > 0$, and that the perturbation solution for Eq. (18) implies $S_1 < \alpha(ck_w/\omega)/(x+y)$, one finds that $\mathrm{Re}\lambda < 0$, thus indicating the stability of the fixed point to small-amplitude perturbations.

---

*Permanent address: Science Applications Intl. Corp., McLean, VA 22102.

†Permanent address: Berkeley Research Assoc., Inc., Springfield, VA 22150.

[1]N. M. Kroll, P. L. Morton, and M. N. Rosenbluth, IEEE J. Quantum Electron. QE-17, 1436 (1981).

[2]P. Sprangle and C. M. Tang, Appl. Phys. Lett. 39, 677 (1981).

[3]G. T. Moore, Nucl. Instrum. Methods Phys. Res. A 239, 19 (1985).

[4]E. T. Scharlemann, A. M. Sessler, and J. S. Wurtele, Phys. Rev. Lett. 54, 1925 (1985).

[5]G. T. Moore, Nucl. Instrum. Methods, Phys. Res. A 250, 381 (1986).

[6]J. E. LaSala, D. A. G. Deacon, and E. T. Scharlemann, Nucl. Instrum. Methods, Phys. Res. A 250, 389 (1986).

[7]M. Xie and D. A. G. Deacon, Nucl. Instrum. Methods, Phys. Res. A 250, 426 (1986).

[8]P. Sprangle, A. Ting and C. M. Tang, Phys. Rev. Lett. (to be published); Phys. Rev. A (to be published).

[9]E. T. Scharlemann, J. Appl. Phys. 58, 2154 (1985).

[10]E. P. Lee and R. K. Cooper, Part. Accel. 7, 83 (1976).

[11]D. Prosnitz, and A. Szoke and V. K. Neil, Phys. Rev. A 24, 1436 (1981).

[12]P. Sprangle, C. M. Tang and C. W. Roberson, Nucl. Instrum. Methods, Phys. Res. A 239, 1 (1985).

# APPENDIX EE

## Comparison of Sideband Growth in Tapered and Untapered Free Electron Lasers

Nuclear Instruments and Methods in Physics Research A272 (1988) 392-396
North-Holland, Amsterdam

*Section III. Theory: (b) Beam transport and sidebands*

# COMPARISON OF SIDEBAND GROWTH IN TAPERED AND UNTAPERED FREE ELECTRON LASERS

B. HAFIZI *, A. TING **, P. SPRANGLE, C.M. TANG and I. HABER

*Naval Research Laboratory, Washington, DC 20375-5000, USA*

Development of sideband frequencies in a free electron laser is studied numerically and analytically in axisymmetric geometry. In the case of small input power the sidebands grow independently in the exponential gain regime. For large input power an instability develops whereby the carrier is coupled to the sidebands via the synchrotron oscillation of the electrons. In a tapered system, the growth rate of sidebands decreases with increasing rate of taper. However, maximum extraction and efficiency is obtained when the particle motion is marginally nonadiabatic.

## 1. Introduction

In a free electron laser (FEL) the synchrotron oscillation of electrons trapped in the ponderomotive potential well may couple energy into sideband frequencies. The ensuing instability leads to the modulation of the output signal and, in consequence, to an increase in its spectral width.

The growth of sideband frequencies has been the subject of discussion in a number of papers [1-7]. In the work presented herein this process is examined by means of a time-dependent code in an assumed axisymmetric geometry. Both tapered and untapered wigglers are examined. Two regimes of sideband development are examined in detail. In one, the carrier amplitude is small and all frequencies within the linear gain spectrum develop independently. In the other, the initial amplitude of the carrier is large and hence coupled to the sideband modes via the synchrotron oscillation of the electrons. Simplified analytical models of sideband growth are outlined.

The purpose of this work is to contrast the development of sideband growth in tapered and untapered FEL systems. In this connection, the issue of sideband start-up from the spontaneous emission appropriate to the electron beam and wiggler parameters employed is not addressed.

## 2. Basic equations

This section presents the equations that form the basis for the investigation of the FEL interaction.

The optical field is taken to be of the form

$$\boldsymbol{a}_r(r, z, t) = \tfrac{1}{2}a(r, z, t)\exp\left[i\left(\frac{\omega}{c}z - \omega t\right)\right]\boldsymbol{e}_x + \text{c.c.},$$

where $\boldsymbol{A}_r = mc^2\boldsymbol{a}_r/|e|$ is the radiation vector potential. The wiggler field is assumed to be plane-polarized, of amplitude $B_w$ and period $2\pi/k_w$:

$$\boldsymbol{B}_w(z) = \frac{-i}{2}B_w\exp(ik_w z)\boldsymbol{e}_y + \text{c.c.},$$

where transverse variations of the wiggler field are neglected. The equations of motion of the $j$th electron are then given by

$$\frac{d\gamma_j}{dt} = \frac{i\omega a_w f_B}{4\gamma_j}\sum_n a_n L_n\left(2r_j^2/r_s^2\right) \times\exp\left[i\psi_j - (1 - i\alpha)r_j^2/r_s^2\right] + \text{c.c.}, \quad (1)$$

$$\frac{d\psi_j}{dt} = ck_w\left(1 - \gamma_r^2/\gamma_j^2\right), \quad (2)$$

where

$$\gamma_r^2 = \tfrac{1}{2}(\omega/ck_w)\left(1 + a_w^2/2\right) \quad (3)$$

defines the resonant (i.e., synchronous) relativistic factor, $a_w = |e|B_w/mc^2k_w$ is the normalized vector potential of the wiggler, $r_j$ is the radial distance of the $j$th electron, and $\psi_j = (\omega/c + k_w)z_j - \omega t$ is the relative phase. The results to be presented in this paper pertain to the case where only $a_w$ is tapered and the period of the wiggler is taken to be constant.

The envelope of the radiation field is expanded as follows:

$$a(r, z, t) = \sum_n a_n(z, t)L_n\left[2r^2/r_s^2\right] \times\exp\left[-(1 - i\alpha)r^2/r_s^2\right].$$

Here, $\alpha(z, t)$ is related to the curvature of the optical

* Science Applications International Corporation, McLean, VA, USA.
** Berkeley Research associates, Springfield, VA, USA.

0168-9002/88/$03.50 © Elsevier Science Publishers B.V. (North-Holland Physics Publishing Division)

wavefronts, $r_s(z, t)$ is the spot size, and $L_n(2r^2/r_s^2)$ is the Laguerre polynomial of degree $n$. Following Sprangle et al. [8,9], the optical field evolves according to:

$$\left(\frac{\partial}{\partial t} + c\frac{\partial}{\partial z}\right) r_s = \frac{2c^2\alpha}{\omega r_s} - r_s c B_I, \tag{4}$$

$$\left(\frac{\partial}{\partial t} + c\frac{\partial}{\partial z}\right) \alpha = \frac{2c^2(1+\alpha^2)}{\omega r_s^2} + 2c(B_R - \alpha B_I), \tag{5}$$

$$\left(\frac{\partial}{\partial t} + c\frac{\partial}{\partial z} + cA_n\right) a_n = inBca_{n-1} + i(n+1)B^* c a_{n+1} - icF_n, \tag{6}$$

where

$$F_n = \frac{-\nu}{N\omega c}\left(\frac{2c}{r_s}\right)^2 \sum_j \left(\frac{f_B a_w}{\gamma}\right)_j L_n\left(2r_j^2/r_s^2\right) \times \exp\left[-i\psi_j - (1+i\alpha)r_j^2/r_s^2\right], \tag{7}$$

$$A_n = \frac{2ic}{\omega r_s^2}(2n+1-i\alpha) + i(2nB_R + B),$$

and

$$B = F_1/a_0 \equiv B_R + iB_I. \tag{8}$$

In eq. (7) the sum on $j$ runs over the electrons in a given ponderomotive bucket and $N$ denotes the number of electrons initially therein, and $\nu = I_b/(mc^2\upsilon_z/|e|)$ is the Budker parameter, where $I_b$ is the electron beam current.

## 3. Numerical results

For definiteness the parameters for the computations presented herein correspond to those of the Paladin experiment at the Lawrence Livermore National Laboratory [10], and are listed in table 1.

In the linear regime the maximum growth rate obtains at the resonance wavelength $\lambda_{res} = 10.34\ \mu$m. In what follows, where appropriate, a wavelength $\lambda$ will be denoted in terms of the relative shift $\delta \equiv (\lambda/\lambda_{res}) - 1$ from the resonant value. Note that the wavelength of the carrier is given by $2\pi c/\omega$.

Table 1
Parameters of the Paladin experiment

| | |
|---|---|
| Electron beam | |
| Current | 2 kA |
| Energy | 50 MeV |
| Radius | 0.45 cm |
| Magnet | |
| Induction | 2.3 kG |
| Period | 8 cm |
| Length | 25 m |
| Radiation field | |
| Wavelength | 10.6 μm |
| Initial spot size | 0.36 cm |

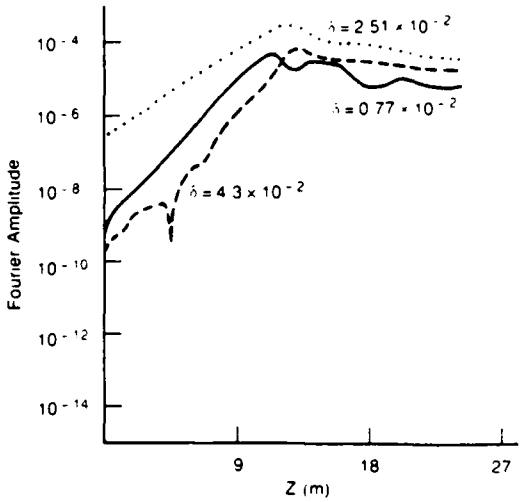



Fig. 1. Evolution of three spectral components along the wiggler when 100 W is input into the 10.6 μm wavelength ($\delta = 2.51 \times 10^{-2}$) at the entrance to the wiggler.

### 3.1. Multifrequency, small input power

Fig. 1 shows the development of three spectral components of the optical field when the input signal is at 10.6 μm ($\delta = 2.51 \times 10^{-2}$) and 100 W. Of course there are many other spectral components besides those shown in fig. 1; however, the curves shown do indicate the general trend in the development of the sideband frequencies. Note in particular that in the exponential regime the growth rate of the component at $\delta = 0.77 \times 10^{-2}$ exceeds that of the main signal. This result is discussed in section 4.

### 3.2. Multifrequency, untapered magnet

Fig. 2 shows the development of the carrier for the case where 800 MW of 10.6 μm radiation ($\delta = 2.51 \times 10^{-2}$) is injected into an untapered magnet. Again, there are many modes in the spectrum that grow along the length of the wiggler. The dashed curve in fig. 2 indicates the maximum amplitude, or the envelope, of the rest of spectrum as a function of $z$. Fig. 2 also shows in detail the evolution of one of the fastest growing modes, at $\delta = 5.71 \times 10^{-2}$, indicating the trend in the development of the instability. At the end of the wiggler (25 m) the amplitude of the sidebands is large enough to modulate the optical field by about 30%.

### 3.3. Multifrequency, tapered magnet

As is well known, for practical purposes the magnet employed in an FEL device must be tapered so as to

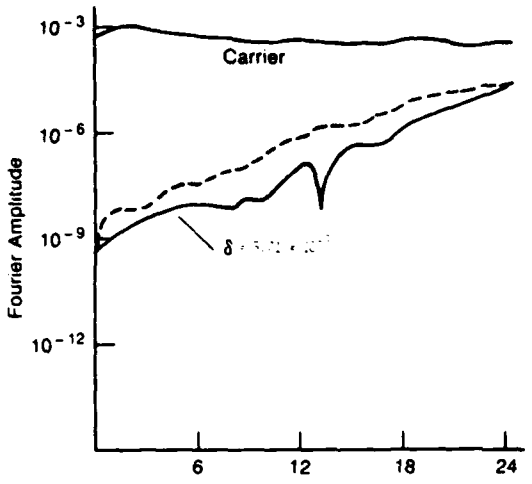



Fig. 2. Evolution of carrier (10.6 $\mu$m) starting from 800 MW in an untapered wiggler. The dashed curve indicates the upper bound for (or the envelope of) the rest of the spectrum. Also shown is the evolution of the sideband at $\delta = 5.71 \times 10^{-2}$ (10.93 $\mu$m).

enhance its efficiency and extraction. Fig. 3 shows the development of the carrier and of the maximum amplitude of all the sidebands through a device where the normalized vector potential $a_w = |e| B_w/mc^2 k_w$ is tapered. The form of the tapering employed in the computations is obtained by simply prescribing a constant rate of decrease of energy for a synchronous electron, at an assigned radius. From eq. (3) with $d\gamma_r/dz$ = constant, one obtains $a_w(z)$. Comparing figs. 2 and 3 it is apparent that in the tapered device the

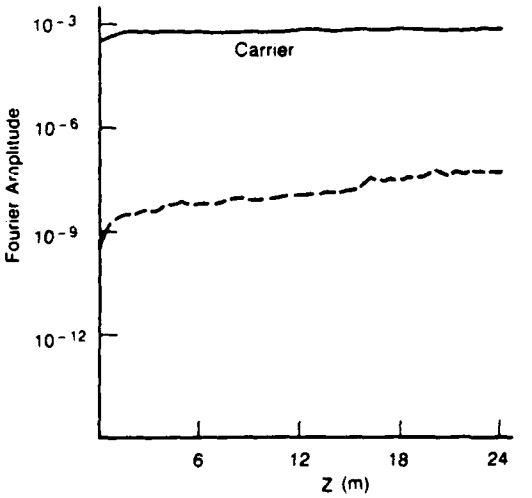



Fig. 3. Evolution of carrier (10.6 $\mu$m) starting from 800 MW in a tapered wiggler. The dashed curve indicates the upper bound for the rest of the spectrum.

sidebands saturate at a level substantially below that of the carrier. As expected, the optical field is observed to be only slightly modulated. The efficiency of the tapered system is 16% at the wiggler exit.

## 4. Analysis of results

An understanding of fig. 1 may be obtained by performing a *single-bucket* linear stability analysis of eqs. (1)–(7). The presentation is limited to the fundamental optical mode, and a monochromatic electron beam of energy $\gamma_0 mc^2$ per electron.

Defining $\dot{\psi}_0 = ck_w(1 - \gamma_r^2/\gamma_0^2)$, $\tilde{\psi}_j = \psi_j - \dot{\psi}_0 t$, $\Gamma_j = \gamma_j/\gamma_0$, $A = ia \exp(i\dot{\psi}_0 t)$, the equilibrium corresponds to $A = 0$, $\Gamma_j = 1$, $\sum_j \exp(-in\tilde{\psi}_j) = 0$ $(n = 1, 2, \cdots)$.

Perturbing eqs. (1)–(7), defining collective variables as in ref. [11], and assuming a temporal dependence of the form $\exp(-i\Upsilon t)$, the following dispersion relation is obtained

$$\Upsilon^3 + \left[\dot{\psi}_0 - 2c^2(1 - i\alpha)/\omega r_s^2\right]\Upsilon^2 + \frac{\nu(a_w f_B)^2}{N\gamma_0^3}\left(\frac{c}{r_s}\right)^2 \sigma\Upsilon - 2ck_w\left(\frac{\gamma_r}{\gamma_0}\right)^2 \frac{\nu(a_w f_B)^2}{N\gamma_0^3}\left(\frac{c}{r_s}\right)^2 \sigma = 0,$$

where

$$\sigma = 2\sum_j \left(1 - r_j^2/r_s^2\right) \exp\left(-2r_j^2/r_s^2\right).$$

Perturbing $B$ (defined by eq. (8)), and numerically solving eqs. (4) and (5) along with the cubic in $\Upsilon$, one obtains the growth rate, efficiency, spot size, and $\alpha$ in the exponential regime for any given angular frequency $\omega$.

Fig. 4 shows the growth rate $\Gamma$ and efficiency $\eta$, in the case of a small input power as a function of $\delta = (\lambda/\lambda_{res}) - 1$, where $\lambda = 2\pi c/\omega$. The crosses are the results of single-bucket simulations. The curves are obtained from the linear stability analysis of the preceding paragraph. It is seen that the agreement is quite good.

An important feature of fig. 1 may now be understood with reference to fig. 4. In the small signal regime – and therefore prior to particle trapping – eqs. (1)–(7) may be linearized to show that there is no coupling between the various spectral components. In other words, the development of the spectral components proceeds independently and at a rate approximately equal to that indicated in fig. 4. Referring to fig. 1, it is thus seen that the larger growth rate of the sideband at $\delta = 0.77 \times 10^{-2}$ as compared to the carrier at $\delta = 2.15 \times 10^{-2}$ is consistent with fig. 4.

It is also possible to set up and analyze a simple model of the FEL interaction so as to obtain an under-

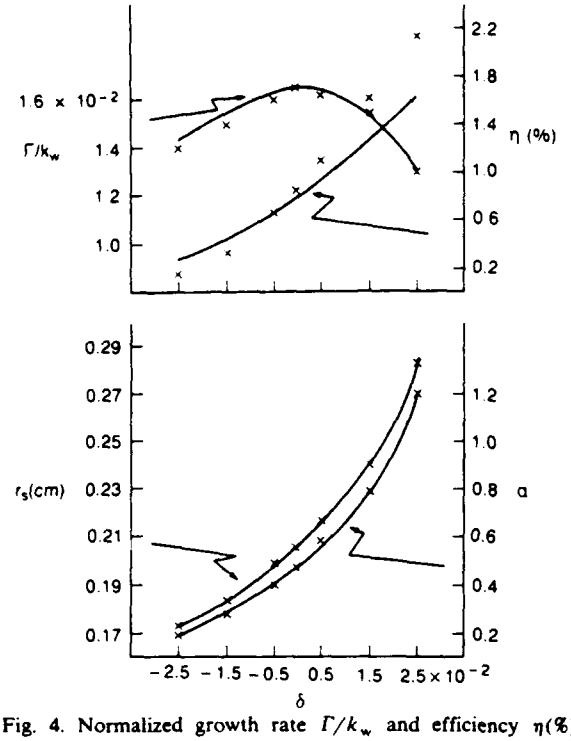



Fig. 4. Normalized growth rate $\Gamma/k_w$ and efficiency $\eta(\%)$ versus $\delta \equiv (\lambda/\lambda_{res}) - 1$, where $\lambda_{res} = 10.34\ \mu$m. Crosses represent results of simulations. Curves are obtained from the linearized equations for the exponential, matched-optical-field regime. The electron beam radius is 0.3 cm.

standing of the gross features of the sideband instability ensuing from the synchrotron oscillation of the electrons in a large-amplitude carrier wave.

Neglecting diffraction and considering the fundamental mode of the optical field only, writing $\gamma_j = \gamma_r + \Delta\gamma_j(t)$, $\psi_j = \psi_{j0} + \Delta\psi_j(t)$, $a = |a^{(0)}| \exp[i\phi^{(0)}]$, the equilibrium is described by $\psi_{j0} + \phi^{(0)} + \alpha r_j^2/r_s^2 = 2n_j\pi$ ($n_j$ an integer), $|a^{(0)}| \simeq$ constant,

$$\frac{d^2}{dt^2}\Delta\psi_j \simeq -\Omega_j^2 \Delta\psi_j, \tag{9}$$

$$\left(\frac{\partial}{\partial t} + c\frac{\partial}{\partial z}\right)\phi^{(0)} = \frac{\nu}{N\omega|a^{(0)}|}\left(\frac{2c}{r_s}\right)^2 \sum_j \frac{f_B a_w}{\gamma_r}\epsilon_j, \tag{10}$$

where the synchrotron frequency is given by $\Omega_j = [ck_w\omega a_w f_B |a^{(0)}| \epsilon_j/\gamma_r^2]^{1/2}$, $\epsilon_j = \exp(-r_j^2/r_s^2)$, and $\gamma_r$ is defined by eq. (3). Note that eq. (10) describes a linear increase in the *equilibrium* phase. Inserting an average value for $r_s$ (between 9 m and 25 m) the rate obtained from eq. (10) is within several tens of percent of the numerical value.

Next, perturbing the equilibrium state and assuming a dependence of the form $f^{(1)} \sim \exp[-i(\Delta\omega t - \Delta k z)]$ for the perturbation, one obtains the following dispersion relation [12]:

$$1 = \frac{1}{\chi^2} + \frac{(2\beta c k_w/\Omega_B)^2}{(\chi - \zeta)^2} - \frac{\beta}{\chi(\chi - \zeta)}. \tag{11}$$

where

$$\chi = \Delta\omega(1 + a_w^2/2)/2\Omega_B\gamma_r^2,$$

$$\zeta = c\Delta k(1 + a_w^2/2)/2\Omega_B\gamma_r^2,$$

$$\beta = \frac{\nu a_w f_B}{2|a^{(0)}|\gamma_r^5}\left(\frac{1 + a_w^2/2}{k_w r_s}\right)^2\left(\sum_j \epsilon_j/N\right),$$

and

$$\Omega_B^2 = \sum_j \Omega_j^2/N. \tag{12}$$

The dispersion relation in eq. (11) is similar to that given in ref. [6]. Inserting numerical values into eq. (11), one finds that the range of unstable modes encompasses that obtained in the simulations. The maximum growth rate obtained is about a factor of 5 larger than the average value observed for one of the fastest growing modes in the simulations (cf. fig. 2.) That the growth rate deduced from eq. (11) should exceed that observed in the simulations is to be expected for two reasons. First, diffraction of the optical field (neglected in deriving eq. (11)) is bound to reduce growth rates. Second, in the simulations the electrons are distributed throughout the ponderomotive bucket with synchrotron frequencies ranging from $\Omega_j$ down to zero, whereas the analysis leading to eq. (11) assumes all electrons to bounce at the bottom of the ponderomotive wells, at the largest synchrotron frequency (cf. eq. (9)).

Turning next to the case of the tapered magnet, the question arises as to why the growth rate of the sidebands is about a factor of 6 smaller than that in the untapered magnet (cf. figs. 2 and 3). As is well known, upon tapering, the electrons separate into roughly two groups. For the tapering employed, the decelerating group – which is responsible for stimulated emission – comprises 25–30% of the total number of electrons. However, the sideband growth rate for such a fraction of the number of electrons is still large compared to the observed value. There appear to be additional reasons for the small growth rate of the sidebands. In the context of a high-extraction FEL with a tapered magnet it is generally assumed that the change of parameters ($a_w$ and/or $k_w$) is slow enough so that the action $I_j \equiv \int d\psi_j(\gamma_j - \gamma_r)$ is an adiabatic invariant [1]. For the case considered here, however, it turns out that $d\gamma_r/dt = \Omega_j(\gamma_j - \gamma_r)$, implying that the action $I_j$ is not an invariant [12]. Additionally, the $\gamma_j$ of trapped electrons decrease more or less monotonically with time, modifying the "equilibrium" electron distribution on the same time scale as that of the synchrotron motion. Physically,

as the radiation pulse slips relative to the electrons, it is modulated not only by the synchrotron motion but also by the temporal variation of $\gamma_r$. This has a detuning effect and renders the sideband quasistable. Indeed, by increasing the rate of tapering and therefore the rate of variation of $\gamma_r$, the modulation of the optical pulse is reduced further, although the efficiency is also diminished due to increased particle detrapping.

Finally, it is important to remark that the tapering employed here leads to the same efficiency for a single-bucket, single-frequency case as for a many-bucket, multifrequency case. In other words, for the given analytical form for $a_w(z)$, the optimal rate of tapering naturally leads to the observed reduction in the growth rate of sideband modes.

## 5. Conclusion

The work presented here contrasts the development of sideband frequencies in an untapered and in a tapered magnet. For the tapering employed, optimal operation (i.e., maximum efficiency) is achieved when the electrons trapped in the ponderomotive buckets are nonadiabatically decelerated, leading to substantial suppression of the sideband frequencies relative to the untapered system.

## Acknowledgement

Discussions with Dr. W.P. Marable are gratefully acknowledged. This work was supported by SDIO and managed by SDC.

## References

[1] N.M. Kroll, P.L. Morton and M.N. Rosenbluth, IEEE J. Quantum Electron. QE-17 (1981) 1436.
[2] J.C. Goldstein and W.B. Colson, in: Proc. Int. Conf. on Lasers, STS, McLean, VA (1982) p. 218.
[3] A.T. Lin, in: Physics of Quantum Electronics, eds. S.F. Jacobs, G.T. Moore, H.S. Pillof, M. Sargent III, M.O. Scully and R. Spitzer (Addison-Wesley, Reading, MA, 1982) vol. 9, p. 409.
[4] R.A. Freedman and W.B. Colson, Opt. Commun. 52 (1985) 409.
[5] D.C. Quimby, J.M. Slater and J.P. Wilcoxon, IEEE J. Quantum Electron. QE-21 (1985) 979.
[6] R.C. Davidson and J.C. Wurtele, Phys. Fluids 30 (1987) 557.
[7] R. Riyopoulos and C.M. Tang, Nucl. Instr. and Meth. A259 (1987) 226.
[8] P. Sprangle, A. Ting and C.M. Tang, Phys. Rev. Lett. 59 (1987) 202; and Phys. Rev. A36 (1987) 2773.
[9] B. Hafizi, P. Sprangle and A. Ting, Phys. Rev. A36 (1987) 1739.
[10] T.J. Orzechowski, E.T. Scharlemann, B. Anderson, V.R. Neil, W.M. Fawley, D. Prosnitz, S.M. Yarema, D.B. Hopkins, A.C. Paul, A.M. Sessler and J.S. Wurtele, IEEE J. Quantum Electron. QE-21 (1985) 831.
[11] R. Bonifacio, C. Pellegrini and L.M. Narducci, Opt. Commun. 50 (1984) 373.
[12] B. Hafizi, A. Ting, P. Sprangle and C.M. Tang, Phys. Rev. A (1988).

# APPENDIX FF

## Development of Sidebands in Tapered and Untapered Free-Electron Lasers

PHYSICAL REVIEW A VOLUME 38, NUMBER 1 JULY 1, 1988

# Development of sidebands in tapered and untapered free-electron lasers

B. Hafizi,* A. Ting,† P. Sprangle, and C. M. Tang
*Naval Research Laboratory, Washington, D.C. 20375-5000*
(Received 19 October 1987)

A time-dependent, axisymmetric code is employed to examine the development of sidebands in a free-electron laser. For the case where the input signal undergoes an extended period of exponential growth, a broad spectrum of sidebands with growth rates comparable to that of the signal is excited. In general, in an untapered system the optical field displays considerable modulation after several synchrotron periods. An analytical model, in qualitative agreement with a number of features of the simulations, is discussed. In a tapered system the amplitude of the sidebands approaches a quasisteady level that is several orders of magnitude below that of the untapered case, and the output optical field displays only a slight modulation. The optimal rate of tapering employed, to maximize efficiency, leads to substantial reduction in the growth rate of sidebands. This result is discussed in connection with the nonadiabatic nature of particle motion in the tapered system.

## I. INTRODUCTION

In a free-electron laser (FEL) the synchrotron oscillation of electrons trapped in the ponderomotive potential well may couple energy into sideband frequencies. The ensuing instability leads to the modulation of the output signal and, in consequence, to an increase in its spectral width.

The growth of sideband frequencies has been the subject of discussion in a number of papers.[1-7] In the work presented herein, this process is examined by means of a time-dependent code in an assumed axisymmetric geometry. Both tapered and untapered wigglers are examined. Two regimes of sideband development are examined in detail. In one, the carrier amplitude is small and all frequencies within the linear gain spectrum develop independently. In the other, the initial amplitude of the carrier is large and hence coupled to the sideband modes via the synchrotron oscillation of the electrons. Simplified analytical models of sideband growth in the two regimes are presented as an aid to understanding the important features of the simulations.

It should be emphasized at the outset that the numerical work reported herein is intended to contrast the development of sidebands in untapered and in tapered FEL systems. In this connection, the important issue of sideband startup from the noise spectrum appropriate to the electron-beam and wiggler parameters employed is not addressed.

## II. NUMERICAL MODEL

This section presents the equations that form the basis for the investigation of the FEL interaction.

The electrons move under the influence of the ponderomotive force due to the beating of the wiggler field with the optical field. The computations are simplified by employing the Gaussian-Laguerre source-dependent expansion (SDE) technique,[8,9] thereby minimizing the number of Laguerre polynomials required for an accurate description of the optical field.

The optical field is taken to be of the form

$$\mathbf{a}_r(r,z,t)=\tfrac{1}{2}a(r,z,t)\exp\left[i\left[\frac{\omega}{c}z-\omega t\right]\right]\hat{\mathbf{e}}_x+\text{c.c.}\ ,$$

where $\mathbf{A}_r=mc^2\mathbf{a}_r/|e|$ is the radiation vector potential, $m$ is the rest mass of an electron, $|e|$ is the magnitude of the electronic change, $c$ is the speed of light *in vacuo*, $\omega$ is the radian frequency, and $\hat{\mathbf{e}}_x$ is the unit vector along the $x$ axis. The wiggler field is assumed to be plane polarized, of amplitude $B_w$ and period $2\pi/k_w$,

$$\mathbf{B}_w(z)=\frac{-i}{2}B_w\exp(ik_wz)\hat{\mathbf{e}}_y+\text{c.c.}\ ,$$

where transverse variations of the wiggler field are neglected, and $\hat{\mathbf{e}}_y$ is the unit vector along the $y$ axis. The equations of motion of the $j$th electron, of energy $\gamma_j mc^2$, are then given by

$$\frac{d\gamma_j}{dt}=\frac{i\omega a_w f_B}{4\gamma_j}\sum_n a_n L_n(2r_j^2/r_s^2)\times\exp[i\psi_j-(1-i\alpha)r_j^2/r_s^2]+\text{c.c.}\ , \tag{1}$$

$$\frac{d\psi_j}{dt}=ck_w(1-\gamma_r^2/\gamma_j^2)\ , \tag{2}$$

where

$$\gamma_r^2=\tfrac{1}{2}(\omega/ck_w)(1+a_w^2/2) \tag{3}$$

defines the resonant (i.e., synchronous) relativistic factor, $a_w=|e|B_w/mc^2k_w$ is the normalized vector potential of the wiggler, $r_j$ is the radial distance of the $j$th electron, $\psi_j=(\omega/c+k_w)z_j-\omega t$ is the relative phase with $z_j$ the axial location of the $j$th electron, and $f_B=J_0(\xi)-J_1(\xi)$ is the usual difference of Bessel functions, with

 ©1988 The American Physical Society

$$\xi=(a_w/2)^2/(1+a_w^2/2)\ .$$

The results to be presented in this paper pertain to the case where only $a_w$ is tapered and the period of the wiggler is taken to be constant.

Following Sprangle *et al.*,[8] the envelope of the radiation field is expanded as follows:

$$a(r,z,t)=\sum_n a_n(z,t)L_n(2r^2/r_s^2)\exp[-(1-i\alpha)r^2/r_s^2]\ .$$

Here $\alpha(z,t)$ is related to the curvature of the optical wavefronts, $r_s(z,t)$ is the spot size, and $L_n(2r^2/r_s^2)$ is the Laguerre polynomial of degree $n$. The method of SDE then permits a complete specification of the optical field by solving[8]

$$\left[\frac{\partial}{\partial t}+c\frac{\partial}{\partial z}\right]r_s=\frac{2c^2\alpha}{\omega r_s}-r_s cB_I\ , \tag{4}$$

$$\left[\frac{\partial}{\partial t}+c\frac{\partial}{\partial z}\right]\alpha=\frac{2c^2(1+\alpha^2)}{\omega r_s^2}+2c(B_R-\alpha B_I)\ , \tag{5}$$

$$\left[\frac{\partial}{\partial t}+c\frac{\partial}{\partial z}+cA_n\right]a_n =inBca_{n-1}+i(n+1)B^*ca_{n+1}-icF_n\ , \tag{6}$$

where

$$F_n=\frac{-\nu}{N\omega c}\left[\frac{2c}{r_s}\right]^2\sum_j\left[\frac{f_B a_w}{\gamma}\right]_j L_n(2r_j^2/r_s^2) \times\exp[-i\psi_j-(1+i\alpha)r_j^2/r_s^2]\ , \tag{7}$$

$$A_n=\frac{2ic}{\omega r_s^2}(2n+1-i\alpha)+i(2nB_R+B)\ ,$$

and

$$B=F_1/a_0 \equiv B_R+iB_I\ . \tag{8}$$

In Eq. (7) the sum on $j$ runs over the electrons in a given ponderomotive bucket and $N$ denotes the number of electrons initially therein, and $\nu=I_b/(mc^2v_z/|e|)$ is the Budker parameter, where $I_b$ is the electron-beam current.

A detailed presentation of the SDE approach is given in Ref. 8. For orientation, however, it should be noted that, *in vacuo*, one has the well-known result,

$$r_s(z)=r_s(0)(1+z^2/z_R^2)^{1/2},\quad \alpha=z/z_R\ ,$$

where $r_s(0)$ is the minimum spot size (at $z=0$) and $z_R=(\omega/2c)r_s^2(0)$ is the Rayleigh range. These results follow from Eqs. (4) and (5) upon neglecting $B$, i.e., neglecting the electron beam.

Typically ten optical modes ($n=0,\ldots,9$) are included in the computations. As noted in the Introduction, the question of the proper spectrum and noise level for the sidebands due to spontaneous emission is not considered [illegible]. The result from the sideband frequencies may be incorporated in several ways. As an example, the noise level may be estimated from the Larmor formula and spread uniformly but with random phase over the computational spectrum. Although there are fluctuations between runs with different initial random phases, the general trend of sideband development is as described herein. Finally, in all the computations, the initial electron distribution is taken to be monoenergetic, the radial profile of the electron beam is taken to be parabolic, and betatron motion is neglected.

## III. NUMERICAL RESULTS

For definiteness, the parameters for the computations presented herein correspond to those of the experiment of Orzechowski *et al.* at the Lawrence Livermore National Laboratory,[11] and are listed in Table I. In the linear regime the maximum growth rate is obtained at the resonance wavelength $\lambda_{res}=10.34\ \mu$m. In what follows, where appropriate a wavelength $\lambda$ will be denoted in terms of the relative shift $\delta\equiv(\lambda/\lambda_{res})-1$ from the resonant value. Note that the wavelength of the carrier is given by $2\pi c/\omega$. Spectra are obtained by performing a spatial Fourier-*series* analysis of the optical field $a(r=0,z,t)$ along the mesh. The result, displayed in the figures as Fourier amplitude, is dimensionless.

(a) *Multiple frequencies, small input power, untapered magnet.* Simulations of a pulse of radiation extending over many ponderomotive buckets, formed by the interaction of the wiggler and optical fields, permit the development of frequencies besides that of the input signal and, as electrons slip relative to the radiation pulse, the sideband instability may develop.

Figure 1 shows the development of three spectral components of the optical field when the input signal is set at 10.6 $\mu$m ($\delta=2.51\times10^{-2}$) and 100 W. Of course, there are many other spectral components besides those shown in Fig. 1; however, the curves shown do indicate the general trend in the development of the sideband frequencies. Note, in particular, that in the exponential regime the growth rate of the component at $\delta=0.77\times10^{-2}$ exceeds that of the main signal. This result is discussed in Sec. IV.

(b) *Multiple frequencies, large input power, untapered magnet.* Figure 2 shows the development of the carrier for the case where 800 MW of 10.6 $\mu$ m radiation ($\delta=2.51\times10^{-2}$) is injected into an untapered magnet. Again, there are many modes in the spectrum that grow

TABLE I. Parameters of the experiment of Orzechowski *et al.*

| | |
|---|---|
| Electron beam | |
| Current | 2 kA |
| Energy | 50 MeV |
| Radius | 0.45 cm |
| Magnet | |
| Induction | 2.3 kG |
| Period | 8 cm |
| Length | 25 m |
| Radiation field | |
| Wavelength | 10.6 $\mu$m |
| Initial spot size | 0.16 cm |

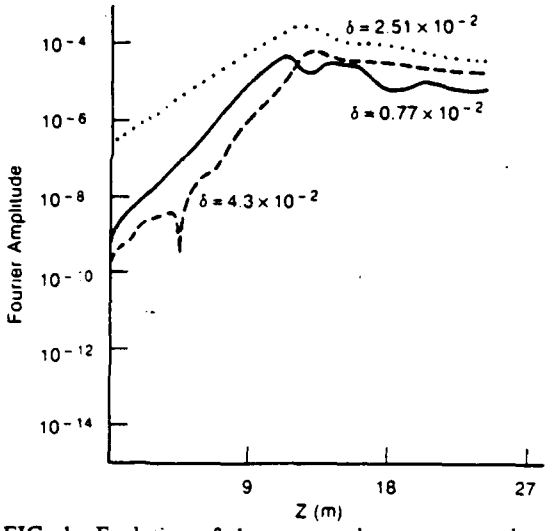



FIG. 1. Evolution of three spectral components along the wiggler when 100 W are input into the 10.6-$\mu$m wavlength ($\delta = 2.51 \times 10^{-2}$) at the entrance of the wiggler.

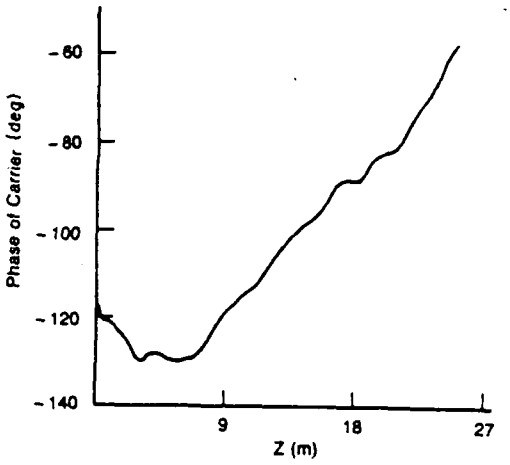



FIG. 3. Development of the phase of the carrier (in degrees) along the wiggler.

along the length of the wiggler. The dashed curve in Fig. 2 indicates the maximum amplitude, or the envelope, of the rest of spectrum as a function of $z$. Figure 2 also shows in detail the evolution of one of the fastest growing modes, at $\delta = 5.71 \times 10^{-2}$, indicating the trend in the development of the instability. At the end of the wiggler (25 m) the amplitude of the sidebands is large enough to spatially modulate the optical field by about 30%. Figure 3, which shows the phase of the carrier along the wiggler, will be discussed in connection with the analytical model for the instability in Sec. IV. At the wiggler exit the electron-beam distribution function has a clear multistream character as indicated in Fig. 4. The spectrum of the optical field at this point consists principally of the carrier with a group of Stokes and anti-Stokes modes on either side, Fig. 5. The approximately symmetrical form of the spectrum, which is a reflection of comparable growth rates for modes symmetrically disposed with respect to the carrier, is discussed in Sec. IV.

(c) *Multiple frequencies, tapered magnet.* As is well known, for practical purposes the magnet employed in an FEL device must be tapered so as to enhance its efficiency and extraction. Figure 6 shows the development of the carrier and of the maximum amplitude of all the sidebands through a device where the normalized vector potential $a_w = |e| B_w / mc^2 k_w$ is tapered as shown in Fig. 7. The form of the tapering employed in the computations is obtained simply by prescribing a constant rate of decrease of energy for a synchronous electron, at an assigned radius. From Eq. (3), with $d\gamma_r/dz = \text{const}$, one obtains $a_w(z)$. Comparing Figs. 2 and 6, it is apparent that in the tapered device the sidebands saturate

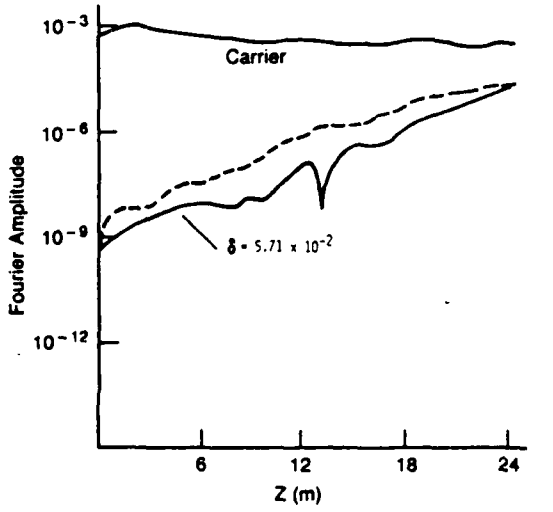



FIG. 2. Evolution of carrier (10.6 $\mu$m) starting from 800 MW in an untapered wiggler. The dashed curve indicates the upper bound for (or the envelope of) the rest of the spectrum. Also shown is the evolution of the sideband at $\delta = 5.71 \times 10^{-2}$ (10.93 $\mu$m).

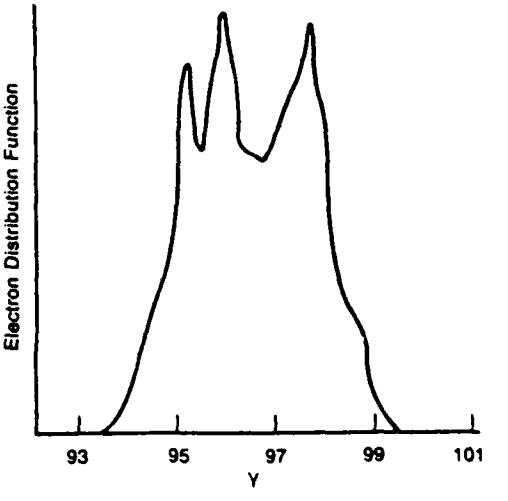



FIG. 4. Electron distribution function (i.e., number of electrons) vs relativistic mass factor $\gamma$ at the end of the wiggler. (Ordinate scale is linear.)

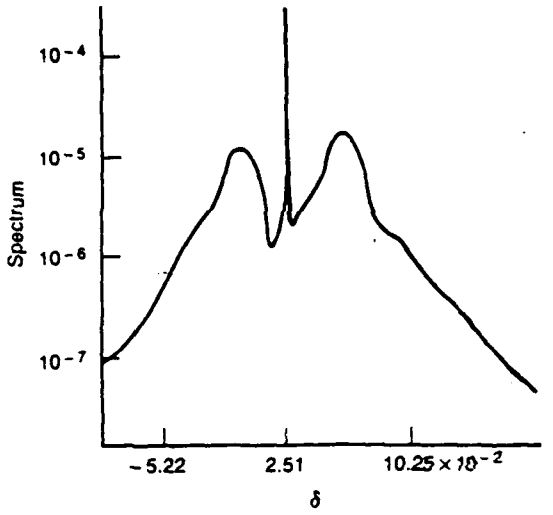



FIG. 5. Spectrum of optical field vs $\delta\equiv\lambda/\lambda_{res}-1$ at the end of the wiggler.

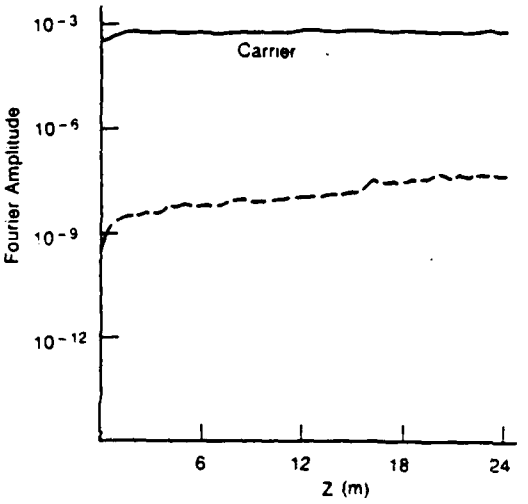



FIG. 6. Evolution of carrier (10.6 $\mu$m) starting from 800 MW in a tapered wiggler. The dashed curve indicates the upper bound for the rest of the spectrum.

at a level that is substantially below that of the carrier. As expected, the optical field is observed to be only slightly modulated in space. The electron distribution function (not shown here) consists principally of two groups, an untrapped group and a trapped group at lower energy. Finally, Fig. 7 also shows the efficiency of the FEL, with 16% being a tenfold improvement over the peak efficiency for the untapered device.

## IV. ANALYSIS OF RESULTS

An understanding of Fig. 1 may be obtained by performing a *single-bucket* linear stability analysis of Eqs. (1)–(7). The presentation is limited to the fundamental optical mode, and a monochromatic electron beam of energy $\gamma_0 mc^2$ per electron.

Defining

$$\dot{\psi}_0=ck_w(1-\gamma_r^2/\gamma_0^2)\ ,$$

$$\tilde{\psi}_j=\psi_j-\dot{\psi}_0 t\ ,$$

$$\Gamma_j=\gamma_j/\gamma_0\ ,$$

$$A=ia\exp(i\dot{\psi}_0 t)\ ,$$

the equilibrium corresponds to $A=0$, $\Gamma_j=1$, $\sum_j\exp(-in\tilde{\psi}_j)=0$ $(n=1,2,\ldots)$. Perturbing Eqs. (1)–(7), defining collective variables as in Ref. 12, and assuming a temporal dependence of the form $\exp(-i\Upsilon t)$, the following dispersion relation is obtained:

$$\Upsilon^3+[\dot{\psi}_0-2c^2(1-i\alpha)/\omega r_s^2]\Upsilon^2+\frac{\nu(a_w f_B)^2}{N\gamma_0^3}\left[\frac{c}{r_s}\right]^2\sigma\Upsilon-2ck_w\left[\frac{\gamma_r}{\gamma_0}\right]^2\frac{\nu(a_w f_B)^2}{N\gamma_0^3}\left[\frac{c}{r_s}\right]^2\sigma=0\ ,$$

where $\sigma=2\sum_j(1-r_j^2/r_s^2)\exp(-2r_j^2/r_s^2)$. Perturbing $B$ [defined by Eq. (8)], and numerically solving Eqs. (4) and (5) along with the cubic in $\Upsilon$, one obtains the growth rate, efficiency, spot size, and $\alpha$ in the exponential regime for any given angular frequency $\omega$.

Now, as is well known, the FEL interaction has the rather important property that the optical field tends to be guided by the electron beam. In an amplifier operating in the exponential regime, it is found that, irrespective of the initial spot size, the radiation beam asymptotically approaches a unique spot size $r_s$ and wave front curvature ($\sim\alpha^{-1}$) (Refs. 8 and 9). Figure 8 shows the growth rate $\Gamma$, efficiency $\eta$, *matched* spot size $r_s$, and *matched* $\alpha$ in the case of a small input power as a function of $\delta=(\lambda/\lambda_{res})-1$, where $\lambda=2\pi c/\omega$. The crosses are the results of single-bucket simulations. The curves are obtained from the linear stability analysis of the preceding paragraph. It is seen that the agreement is quite good.

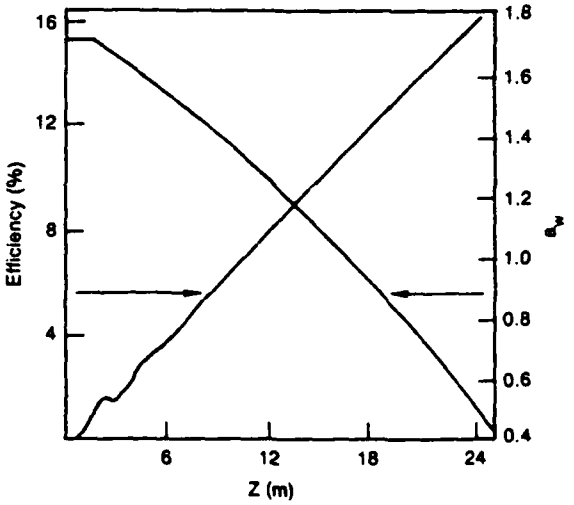



FIG. 7. Efficiency (%) and $a_w$ along the length of the tapered magnet.

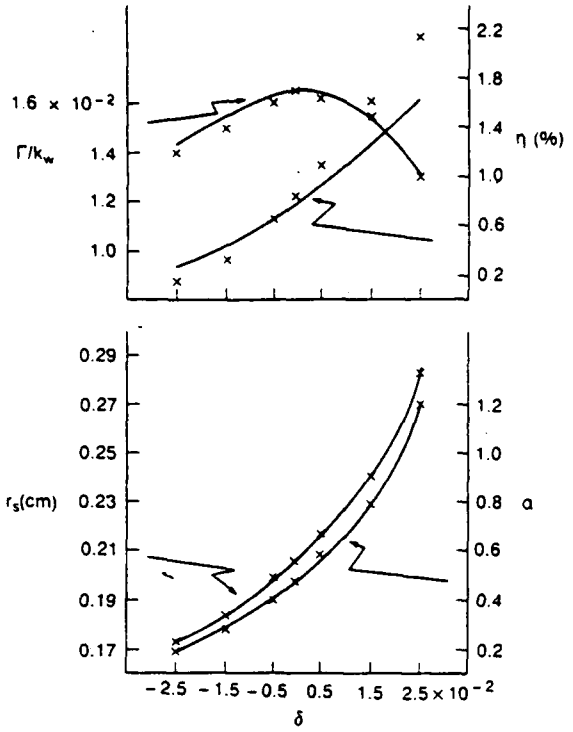



FIG. 8. Normalized growth rate $\Gamma/k_w$, efficiency $\eta$ (%), spot size $r_s$, and $\alpha$ vs $\delta \equiv (\lambda/\lambda_{res}) - 1$, where $\lambda_{res} = 10.34\ \mu m$. Crosses represent results of simulations. Curves are obtained from the linearized equations for the exponential, matched-optical-field regime. The electron-beam radius is 0.3 cm.

An important feature of Fig. 1 may now be understood with reference to Fig. 8. In the small signal regime—and therefore prior to particle trapping—Eqs. (1)–(7) may be linearized to show that there is no coupling between the various spectral components. In other words, the development of the spectral components proceeds independently and at a rate approximately equal to that indicated in Fig. 8. Referring to Fig. 1, it is thus seen that the larger growth rate of the sideband at $\delta = 0.77 \times 10^{-2}$ as compared to the carrier at $\delta = 2.51 \times 10^{-2}$ is consistent with Fig. 8.

It is also possible to setup and analyze a simple model of the FEL interaction so as to obtain an understanding of the gross features of the sideband instability ensuing from the synchrotron oscillation of the electrons in a large-amplitude carrier wave.

Neglecting diffraction and considering the fundamental mode of the optical field only, writing $\gamma_j = \gamma_r + \Delta\gamma_j(t)$, $\psi_j = \psi_{j0} + \Delta\psi_j(t)$, $a = |a^{(0)}| \exp(i\phi^{(0)})$, the equilibrium is described by

$$\psi_{j0} + \phi^{(0)} + \alpha r_j^2/r_s^2 = 2n_j\pi \quad (n_j \text{ is an integer}) ,$$

$$\frac{d^2}{dt^2}\Delta\psi_j \simeq -\Omega_j^2 \Delta\psi_j , \tag{9}$$

$$|a^{(0)}| \simeq \text{const} ,$$

$$\left(\frac{\partial}{\partial t} + c\frac{\partial}{\partial z}\right)\phi^{(0)} \simeq \frac{\nu}{N\omega|a^{(0)}|}\left(\frac{2c}{r_s}\right)^2 \sum_j \frac{f_B a_w}{\gamma_r}\varepsilon_j , \tag{10}$$

where the synchrotron frequency is given by

$$\Omega_j = \left[\frac{ck_w\omega a_w f_B}{\gamma_r^2}|a^{(0)}|\varepsilon_j\right]^{1/2} ,$$

$\varepsilon_j = \exp(-r_j^2/r_s^2)$, and $\gamma_r$ is defined by Eq. (3). Note that Eq. (10) describes a linear increase in the *equilibrium* phase. Inserting numerical values corresponding to the wiggler entrance, Eq. (10) yields a rate of increase that is about a factor of 4 greater than that observed in Fig. 3 (beyond 9 m). Due to diffraction, however, the spot size $r_s$ increases along the wiggler. Thus, inserting an average value for $r_s$ (between 9 and 25 m), the rate obtained from Eq. (10) is within 10–30 % of the numerical value.

Next, perturbing the equilibrium state and assuming a dependence of the form $f^{(1)} \sim \exp[-i(\Delta\omega t - \Delta kz)]$ for the perturbation, one obtains the following dispersion relation (Appendix A):

$$1 = \frac{1}{\chi^2} + \frac{(2\beta ck_w/\Omega_B)^2}{(\chi-\zeta)^2} - \frac{\beta}{\chi(\chi-\zeta)} , \tag{11}$$

where

$$\chi = \Delta\omega(1 + a_w^2/2)/2\Omega_B\gamma_r^2, \quad \zeta = c\Delta k(1 + a_w^2/2)/2\Omega_B\gamma_r^2 ,$$

$$\beta = \frac{\nu a_w f_B}{2|a^{(0)}|\gamma_r^5}\left[\frac{1 + a_w^2/2}{k_w r_s}\right]^2 \left[\sum_j \varepsilon_j/N\right] ,$$

and

$$\Omega_B^2 = \sum_j \Omega_j^2/N . \tag{12}$$

The dispersion relation is obtained in the *diagonal* approximation, wherein terms of the form $f^{(1)}\Delta\psi_j$, $f^{(1)}\Delta\gamma_j$ are neglected. The dispersion relation in Eq. (11) is similar to that given in Ref. 6. The last term on the right-hand side of Eq. (11), which is due to terms proportional to $\gamma_j^{(1)}$ and is neglected in Ref. 6, increases the growth rate by about 10%. In reference to the electron distribution function shown in Fig. 4, it is interesting to note the similarity of Eq. (11) to the dispersion relation for a multistream system. Neglecting the third term on the right-hand side of Eq. (11), it is seen that—as discussed in Ref. 6—the dispersion relation has a symmetrical form about the carrier ($\Delta k = 0$), with identical growth rate for $(-\Delta\omega, \Delta k)$ and $(\Delta\omega, \Delta k)$. The spectrum in Fig. 5 is consistent with this general feature of Eq. (11).

Inserting numerical values into Eq. (11), one finds that the range of unstable modes encompasses that obtained in the simulations. The maximum growth rate obtained is about a factor of 5 larger than the average value observed for one of the fastest growing modes in the simulations (cf. Fig. 2). That the growth rate deduced from Eq. (11) should exceed that observed in the simulations and the discrepancy in the rate of increase of the phase of the carrier are to be expected for two reasons. First, diffraction of the optical field [neglected in deriving Eq. (11)] is bound to reduce growth rates. Second, in the simulations, the electrons are distributed throughout the pondermotive bucket with synchrotron frequencies ranging from $\Omega_j$ down to zero, whereas the analysis leading to Eq. (11) assumes all electrons to bounce at the bottom of

the ponderomotive wells, at the largest synchrotron frequency [cf. Eq. (9)].

Turning next to the case of the tapered magnet, the question arises as to why the growth rate of the sidebands is about a factor of 6 smaller than that in the untapered magnet (cf. Figs. 2 and 6). As is well known, upon tapering the electrons separate into roughly two groups. For the tapering employed, the decelerating group—which is responsible for stimulated emission—comprises 25–30 % of the total number of electrons. However, the sideband growth rate for such a fraction of the number of electrons is still large compared to the observed value. There appears to be additional reasons for the small growth rate of the sidebands. In the context of a high-extraction FEL with a tapered magnet, it is generally assumed that the change of parameters ($a_w$ and/or $k_w$) is slow enough so that the action $I_j \equiv \int d\psi_j(\gamma_j - \gamma_r)$ is an adiabatic invariant.[1] For the case considered here, however, *it turns out* that $d\gamma_r/dt \simeq \Omega_B(\gamma_j - \gamma_r)$, implying that the action $I_j$ is *not* an invariant (Appendix B). Additionally, the $\gamma_j$ of trapped electrons decrease more or less monotonically with time, modifying the "equilibrium" electron distribution on the same time scale as that of the synchrotron motion. Physically, as the radiation pulse slips relative to the electrons, it is modulated not only by the synchrotron motion but also by the temporal variation of $\gamma_r$. This has a detuning effect and renders the sidebands quasistable. Indeed, by increasing the rate of tapering and therefore the rate of variation of $\gamma_r$, the modulation of the optical pulse is reduced further, although the efficiency is also diminished due to increased particle detrapping.

Finally, it is important to remark that the tapering employed here leads to the same efficiency for a single-bucket, single-frequency case as for a many-bucket, multifrequency case. In other words, for the given analytical form for $a_w(z)$, the optimal rate of tapering naturally leads to the observed reduction in the growth rate of sideband modes.

## V. CONCLUSION

The work presented here contrasts the development of sideband frequencies in an untapered and in a tapered magnet. For the tapering employed, optimal operation (i.e., maximum efficiency) is achieved when the electrons trapped in the ponderomotive buckets are nonadiabatically decelerated, leading to substantial suppression of the sideband frequencies relative to the untapered system.

## ACKNOWLEDGMENTS

Discussions with Dr. W. P. Marable are gratefully acknowledged. This work was supported by the Strategic Defense Initiative Organization and managed by the Strategic Defense Command.

## APPENDIX A: MULTIFREQUENCY LINEAR STABILITY ANALYSIS

In this appendix some of the details leading to the dispersion relation in Eq. (11) are presented. Upon writing $\gamma_j = \gamma_r + \Delta\gamma_j + \gamma_j^{(1)}$, $\psi_j = \psi_{j0} + \Delta\psi_j + \psi_j^{(1)}$, $\phi = \phi^{(0)} + \phi^{(1)}$, $|a| = |a^{(0)}| + |a^{(1)}|$, and neglecting terms comprising products of the form $\Delta\gamma_j\psi_j^{(1)}$, $\Delta\psi_j\gamma_j^{(1)}$, etc., one obtains, at first order,

$$\left[\frac{\partial}{\partial t} + c\frac{\partial}{\partial z}\right]|a^{(1)}| \simeq \frac{\nu}{N\omega}\left[\frac{2c}{r_s}\right]^2 \sum_j \frac{f_B a_w}{\gamma_r}\varepsilon_j(\psi_j^{(1)} + \phi^{(1)}) ,$$

$$|a^{(0)}|\left[\frac{\partial}{\partial t} + c\frac{\partial}{\partial z}\right]\phi^{(1)} \simeq -\frac{\nu}{N\omega}\left[\frac{2c}{r_s}\right]^2 \sum_j \frac{f_B a_w}{\gamma_r}\varepsilon_j\left[\frac{|a^{(1)}|}{|a^{(0)}|} + \frac{\gamma_j^{(1)}}{\gamma_r}\right] , \tag{A1}$$

$$\frac{d}{dt}\gamma_j^{(1)} \simeq -\frac{\omega a_w f_B}{2\gamma_r}\varepsilon_j |a^{(0)}|(\psi_j^{(1)} + \phi^{(1)}) ,$$

$$\frac{d}{dt}\psi_j^{(1)} = 2ck_w\gamma_j^{(1)}/\gamma_r .$$

Note that the term proportional to $\gamma_j^{(1)}$ on the right-hand side of Eq. (A1) was neglected in Ref. 6 where a similar analysis of sideband growth was presented.

Defining collective variables

$$\chi_k = \sum_j \varepsilon_j^k \psi_j^{(1)}/N, \quad y_k = \sum_k \varepsilon_j^k \gamma_j^{(1)}/N, \quad E_k = \sum_j \varepsilon_j^k/N ,$$

one obtains

$$\left[\frac{\partial}{\partial t} + c\frac{\partial}{\partial z}\right]|a^{(1)}| = \frac{\nu}{\omega}\left[\frac{2c}{r_s}\right]^2 \frac{f_B a_w}{\gamma_r}(\chi_1 + E_1\phi^{(1)}) ,$$

$$|a^{(0)}|\left[\frac{\partial}{\partial t} + c\frac{\partial}{\partial z}\right]\phi^{(1)} = -\frac{\nu}{\omega}\left[\frac{2c}{r_s}\right]^2 \frac{f_B a_w}{\gamma_r}\left[\frac{y_1}{\gamma_r} + \frac{E_1|a^{(1)}|}{|a^{(0)}|}\right] ,$$

$$\frac{d}{dt}\chi_1 = \frac{2ck_w}{\gamma_r}y_1 ,$$

$$\frac{d}{dt}y_1 = -\frac{\omega a_w f_B}{2\gamma_r}|a^{(0)}|(\chi_2 + E_2\phi^{(1)}) ,$$

$$\frac{d}{dt}\chi_2 = \frac{2ck_w}{\gamma_r}y_2 ,$$

etc. This hierarchy may be truncated by assuming that $\chi_2 = \sum \varepsilon_j\chi_1/N$, $E_2 = \sum \varepsilon_j E_1/N$, whence

$$\frac{d^2}{dt^2}\chi_1 = -\Omega_B^2(\chi_1 + E_1\phi^{(1)}) ,$$

$$\frac{d}{dt}y_1 = -\frac{\gamma_r\Omega_B^2}{2ck_w}(\chi_1 + E_1\phi^{(1)}) ,$$

where $\Omega_B$ is defined by Eq. (12). Assuming perturbations of the form $\exp[-i(\Delta\omega t - \Delta kz)]$, one obtains the dispersion relation in Eq. (11), where the third term on the right-hand side is due to the term proportional to $\gamma_j^{(1)}$ on the right-hand side of Eq. (A1).

## APPENDIX B: TEMPORAL VARIATION OF ADIABATIC INVARIANT

In this appendix the law of variation of the action variable for the tapered magnet is obtained. For a synchronous particle, the energy and phase evolve according to

$$\frac{d}{dt}\gamma_r = -\frac{\omega a_w f_B}{2\gamma_r} |a| \varepsilon_r \sin(\psi_r+\phi+\alpha r_r^2/r_s^2) ,$$

$$\frac{d}{dt}\psi_r = 0 .$$

Defining $\gamma_j=\gamma_r+\delta\gamma_j$, $\psi_j=\psi_r+\delta\psi_j$, the Hamiltonian for small-amplitude oscillations is

$$H=\frac{ck_w}{\gamma_r}\delta\gamma_j^2+\frac{\omega a_w f_B |a|}{4\gamma_r}\varepsilon_r\cos(\psi_r+\phi+\alpha r_r^2/r_s^2)\delta\psi_j^2 .$$

Defining the synchrotron frequency of such a particle,

$$\Omega_{syn}=[ck_w\omega a_w f_B |a| \varepsilon_r\cos(\psi_r+\phi+\alpha r_r^2/r_s^2)]^{1/2}/\gamma_r ,$$

following Ref. 13, the action ($I_j$) angle ($w_j$) variables are found to evolve according to

$$\frac{d}{dt}I_j = -\frac{I_j}{\gamma_r}\frac{d\gamma_r}{dt}\cos(2w_j) ,$$

$$\frac{d}{dt}w_j = \Omega_{syn}+\frac{1}{2\gamma_r}\frac{d\gamma_r}{dt}\sin(2w_j) .$$

These formulas are valid for the length of the magnet lying between 6 and 21 m where $\Omega_{syn}$ is found to be remarkably constant in the simulations. Thus the variation of $\gamma_r$ is the only factor contributing to the breaking of the adiabatic invariant $I_j$. (Generalization of the formulas to include the variation of $\Omega_{syn}$ in the other sections of the magnet is straightforward.) The change in the action variable over a synchrotron period is then found to be given by

$$\frac{|\Delta I|}{I} \lesssim \left|\frac{d\gamma_r/dt}{2\gamma_r\Omega_{syn}}\right|^{1/2}$$

$$\sim 10^{-3} .$$

It is important to notice that although this variation is relatively small, it is nevertheless much faster than the usual case for an adiabatic invariant where $\Delta I \to 0$ *exponentially* as $d\gamma_r/dt \to 0$.

---

*Also at Science Applications International Corporation, McLean, VA.

†Also at Berkeley Research Associates, Springfield, VA.

[1]N. M. Kroll, P. L. Morton, and M. N. Rosenbluth, IEEE J. Quantum Electron. **QE-17**, 1436 (1981).

[2]J. C. Goldstein and W. B. Colson, in *Proceedings of the International Conference on Lasers '82, New Orleans, LA, 1982,* edited by R. C. Powell (STS, McLean, VA, 1983), p. 218.

[3]A. T. Lin, in *Physics of Quantum Electronics,* edited by S. F. Jacobs, G. T. Moore, H. S. Pillof, M. Sargent III, M. O. Scully, and R. Spitzer (Addison-Wesley, Reading, MA, 1982), Vol. 9, p. 409.

[4]R. A. Freedman and W. B. Colson, Opt. Commun. **52**, 409 (1985).

[5]D. C. Quimby, J. M. Slater, and J. P. Wilcoxon, IEEE J. Quantum Electron. **QE-21**, 979 (1985).

[6]R. C. Davidson and J. S. Wurtele, Phys. Fluids **30**, 557 (1987).

[7]S. Riyopoulos and C. M. Tang, Nucl. Instrum. Methods **A259**, 226 (1987).

[8]P. Sprangle, A. Ting, and C. M. Tang, Phys. Rev. Lett. **59**, 202 (1987); Phys. Rev. A **36**, 2773 (1987).

[9]B. Hafizi, P. Sprangle, and A. Ting, Phys. Rev. A **36**, 1739 (1987).

[10]P. Sprangle, C. M. Tang, and I. Bernstein, Phys. Rev. Lett. **50**, 1775 (1983); Phys. Rev. A **28**, 2300 (1983).

[11]T. J. Orzechowski, E. T. Scharlemann, B. Anderson, V. K. Neil, W. M. Fawley, D. Prosnitz, S. M. Yarema, D. B. Hopkins, A. C. Paul, A. M. Sessler, and J. S. Wurtele, IEEE J. Quantum Electron. **QE-21**, 831 (1985).

[12]R. Bonifacio, C. Pellegrini, and L. M. Narducci, Opt. Commun. **50**, 373 (1984).

[13]L. D. Landau and E. M. Lifshitz, *Mechanics* (Pergamon, New York, 1976), Sec. 49.

# APPENDIX GG

## An X-Ray Source for Lithography Based on A Quasi-Optical Maser Undulator

# AN X-RAY SOURCE FOR LITHOGRAPHY BASED ON A QUASI-OPTICAL MASER UNDULATOR

P. Sprangle, B. Hafizi* and F. Mako+

Plasma Theory Branch
Plasma Physics Division
Naval Research Laboratory
Washington, DC 20375-5000

## Abstract

We propose the use of electromagnetic waves as an undulator in order to generate x-rays in the wavelength range required for fabrication of integrated circuits. The configuration consists of a quasi-optical maser cavity through which a beam of relativistic electrons is made to propagate, spontaneously emitting x-rays of the desired energy. For 5" silicon wafers covered with a sensitive resist such as PBS, this translates into a throughput of 26 wafers/hr using an aggressive stepper. The scaling of x-ray power with wavelength indicates that the throughput can be increased substantially using resists which are sensitive to shorter wavelength x-rays.

*Science Applications International Corp., McLean, VA

+FM Technologies, Inc, Alexandria, VA

## I. Introduction

A major contributor to the tremendous developments taking place in our ability to process information is the miniaturization of semiconductor devices marketed by the electronics industry. It is now recognized that over the next few decades the economic well-being of the United States is dependent on its ability to maintain a leadership position in the fast-developing technology for fabricating smaller and cheaper integrated circuits (IC) (see Ref. 1).

A process by which IC's are mass produced is lithography. Using this technique, a predetermined pattern can be rapidly replicated on the surface of a semiconductor chip using a beam of radiation or particles. A reliable, efficient and compact source of radiation or particles is critical to the economic viability of lithography. This is especially so because of the high capital expenditure required for the sources necessitated by further miniaturization.

In this report we propose a novel design concept for a source of x-ray radiation for the purposes of lithography. In order to motivate the design concept and to provide a comparison with other sources presently being considered, the following section is devoted to a brief description of the salient aspects of the lithographic technique. Section III describes the x-ray sources currently under study and/or development. Our proposed scheme is detailed in Sec. IV, followed by a derivation of the x-ray power formula in Sec. V. In Sec. VI we consider the availability of the two major components (electron beam and electromagnetic undulator) required by the proposed scheme, and we present parameters for an actual device based on a preliminary analysis of the power-formula scaling. In Sec. VII we compare our design-parameters with an x-ray source based on a conventional bending-magnet storage ring. Our conclusions are contained in Sec. VIII.

## II. Lithography[2]

The crystal-growing industry routinely provides silicon crystals about 5" or more in diameter. Once a single-crystal ingot is grown, it is sliced into thin wafers, which are then used for device fabrication. Planar technology consists, for example, in selective introduction of dopant atoms into small precisely predetermined areas of the silicon surface to form regions of p- and n-type material. Dopant atoms can be introduced simultaneously into many separate, small regions of a wafer. Therefore, the use of larger diameter wafers and smaller device dimensions minimizes processing cost per device.

The technique for replication of a predetermined pattern on a silicon wafer is referred to as lithography. The pattern may correspond, for example, to an opening for introduction of dopant atoms by diffusion or implantation. Lithography consists in the application of a thin film of a radiation-sensitive plastic -- called a photoresist -- onto the surface of the wafer. The photoresist is then exposed to radiation through a mask, bearing the desired feature, to create a shadow image on the resist.

### A. Resolution

Current state-of-the-art miniaturization requirements by the IC industry call for the ability to resolve submicron minimum features of patterns to be replicated. However, for mass-production of critical, leading-edge circuits for computers, memories, signal processors and other devices, resolutions approaching $\leq 0.1$ μm will be required. Resolution, therefore, is a determining factor in the quest for greater device density. However, as is well-known, diffraction provides a fundamental barrier for resolution. If d is the line width of the feature on the mask to be replicated and $\lambda$ is the wavelength of the radiation, the diffraction angle is $\lambda/d$, so that if s is the mask-to-resist separation, the blur on the

resist is $(\lambda/d)s$. Thus, to reduce blur, it is necessary to use short wavelength radiation (x-rays) or energetic particle beams.

B. Sources

As far as resolution is concerned, x-ray radiation or particle beams are satisfactory sources. It is, however, necessary to consider other factors such as throughput and yield in order to be able to select the most appropriate source for lithographic purposes. Direct-write with tightly focussed electron or ion beams is frequently used for extremely high-resolution processes. The wavelength $\lambda$ of an electron of momentum p is $\lambda = h/p$ where h is Planck's constant. Thus, for a 20 keV electron beam $\lambda \approx 2.5 \times 10^{-2}$ Å. With such short wavelengths, computer-controlled particle beams are ideal for making high-quality patterns on masks which are then used for resist exposure in quantity. However, the main problem with the electron-beam direct-write process for mass production is that it is slow compared to parallel exposure through a mask. In addition, particle beams spread out upon impinging on a resist, and there is also some backscattering and thus possible damage to the mask.

## III. X-Ray Lithography

Since x-ray sources have high throughput compared to direct-write techniques, we now concentrate on three sources of x-ray radiation that are envisioned for lithography. These are: a) electron-impact (x-ray tube), b) high-temperature plasma, and c) synchrotron radiation. To compare these, we list the important characteristics that must be considered in making a choice between different sources.

i) Emission intensity

ii) Efficiency of x-ray generation and usage

iii) Spectral character of radiation (lines, continuum, etc.)

iv) Energy range of emitted photons

v) Source size (important for resolution)

vi) Emission solid angle (determines collimation and exposure area)

vii) Pulsed or cw

In comparing the different x-ray sources, we shall consider the material polymethyl methacrylate (PMMA) which is a popular, high-resolution resist suitable for submicron work. To fully expose PMMA one requires 1 $J/cm^2$ of 12 Å radiation. More generally, the range of useful photon energies is 0.5 - 1.5 keV (20-8 Å). Photon energy influences resist absorption which, along with the intensity, determines the exposure time. In common with ordinary photography, faster resists than PMMA are found to exhibit poorer resolution. We now enumerate the properties of the three common sources of x-ray radiation.

### A. Electron-Impact

X-ray tubes were the first to be used for x-ray lithography. The radiation is uncollimated and is in the form of lines (bound-to-bound transitions) and a continuum (free-to-free transitions in the nuclear Coulombic field). X-ray tubes are inefficient, with typically less than 1% of the electron beam energy being converted into (total) x-ray radiation.

B. High-Temperature Plasmas

X-ray radiation from plasmas at $10^6$-$10^7$ °K is in the form of a line spectrum (bound-to-bound transitions), continua with a high-energy cut-off (free-to-bound transitions), and a continuum (free-to-free, bremsstrahlung). Heating of the plasma is via a discharge (as in a z-pinch) or a high-power laser,[3] and the radiation is spread over a large solid angle ($2\pi$ to $4\pi$). The process is necessarily pulsed with a lifetime of 10-100 ns for discharge heating and 1-10 ns for laser heating. Efficiencies are in the range of 1-10%.

Some of the problems associated with high-temperature plasma lithography are the following:

i) Contamination of mask and/or resist by debris from the plasma

ii) Low repetition rate

iii) Thermal response of mask and/or resist to very intense, pulsed heating

iv) Significant shot-to-shot variability of plasma sources.

C. Synchrotron Radiation

Synchrotron radiation is generated by electrons in synchrotron accelerators and storage rings. It is basically magnetic bremsstrahlung due to the curved motions of the particles in the bending (dipole) magnets. Although the radiation process is efficient, usage of the emitted radiation is quite inefficient due to the large fraction that is lost onto the vacuum chamber walls. Since the radiation is highly collimated ($\lesssim$ 1 mrad for a 1 GeV electron beam), the mask-wafer separation and wafer flatness are less critical than with x-rays from a point-source with highly-diverging rays. The spectrum is continuous so that filters and/or mirrors must be used to select the desired wavelength band for lithography work.

In existing and proposed storage rings electrons are typically injected at low energy (~ 150 MeV) and then accelerated to about 1 GeV while the bending magnets are ramped up to about 4-5 T. These are designed for compactness, with linear dimensions on the order of several meters. Superconducting magnet designs are also available and somewhat more compact, although there is the added cost and extra space for the cryogenic system. Thus far, the most important source of x-ray synchrotron radiation is that provided by dedicated storage rings to be found in many national laboratories throughout the world. However, these machines are extremely expensive and occupy a great deal of space. On the other hand, the commercial storage rings for x-ray lithography are only now becoming available.

Since there are inherent difficulties associated with each of the three x-ray sources we have mentioned, in what follows we propose the use of an electromagnetic undulator as another means of generating x-rays which may prove to be suitable for lithographic applications.

## IV. X-Ray Radiation in an Electromagnetic Undulator

The use of periodic undulators and of wigglers to achieve higher brightness (energy radiated per unit bandwidth per unit solid angle) and to modify the spectral character of the radiation by storage rings is by now well-established.[4] Due to complexity and construction costs of electromagnets (conventional or superconducting) recent developments in the fabrication of high-field, rare-earth cobalt permanent magnets[5,6] have led to their almost-universal use as insertion devices in storage rings.

Defining the dimensionless magnetic field parameter

$$K = \frac{|e|B_o\lambda_o}{2\pi mc^2}, \tag{1}$$

where e is the charge and m is the rest-mass of an electron, c is the speed of light in vacuo, $B_o$ is the peak magnetic induction and $\lambda_o$ is the period of the planar undulator or wiggler, the wavelength $\lambda$ of the radiation emitted along the beam direction is given by

$$\lambda = \frac{\lambda_o(1+K^2/2)}{2\gamma^2}, \tag{2}$$

where $\gamma$ is the relativistic mass factor. Typically, $\lambda_o$ ranges over 1-10 cm so that for x-ray radiation in the required range (8-20 Å) electron energies upwards of several GeV are required. On the other hand, one might use lower energy electrons, say 150 MeV, and use extremely short-period insertion devices. However, to maintain the same magnetic field strength there has to be a corresponding decrease in the gap spacing between opposite poles of the magnet.[6] This implies very thin filamentary electron beams and correspondingly high electron-beam brightness.

As an alternative to the permanent magnet designs mentioned in the preceding, we propose herein to employ a high-power electromagnetic wave of moderate wavelength ($\lesssim$ 1 mm) to generate x-ray radiation in the required wavelength range using moderate energy electrons ($\lesssim$ 1/4 GeV). It is expected that with use of moderate energy electrons and one of a variety of recently-developed, efficient, high-power sources of coherent radiation, a compact source of x-ray radiation may be designed for commercial use without an excessive capital outlay.

## V. Technical Discussion

As is well-known, the radiation emitted by a charged particle in instantaneous circular motion is confined to cone of half-angle $1/\gamma$ about the direction of dominant motion.[7] It is also well-known that for motion in a periodic magnetic or electromagnetic field the transverse particle orbit is periodically deflected through an angle

$$\theta_d = K/\gamma. \tag{3}$$

We can now distinguish two limiting cases. For $K \lesssim 1$ we see that the transverse angular deflection of the particle lies within the natural opening angle of the emitted radiation. In this case, the insertion device is referred to as an undulator and the emitted radiation is confined to a very narrow angle about the direction of propagation and is thus of high brightness. For an insertion device for which $K > 1$ (referred to as a wiggler) we see from Eq. (3) that the emitted radiation is spread over an angle $K/\gamma$, which may be considerably larger than the natural opening angle $1/\gamma$, depending on the magnitude of K. In the limit $K >> 1$, the wiggler radiation is similar to that from a bending magnet where particles undergo substantial deflection on traversing the bending field.

For the electromagnetic pump wave to be considered herein, one can define an equivalent parameter K as in Eq. (1). It turns out that for our configuration $K << 1$, so that the electromagnetic pump behaves like an undulator. Therefore, unlike wiggler fields and the commercially available bending-magnet designs, the radiation from the electromagnetic undulator would be highly collimated and entirely available for resist exposure. Additionally, for $K << 1$ the higher harmonics are negligible compared to the fundamental.

To evaluate the radiated power for the case of the electromagnetic undulator, we refer to Fig. 1. This is a schematic (not to scale) of a configuration wherein the electron beam propagates along the z-axis and interacts with the electromagnetic pump field stored in the cavity. If L is the interaction length, the cavity mirror on the right-hand side includes an orifice of diameter $2L/\gamma$ to permit extraction of the x-ray radiation. The opening in the mirror is connected to a Bragg reflector,[8] which is simply a long, corrugated metallic tube, to effectively plug the resonant cavity against microwave power loss. Alternatively, the orifice may be connected to a tube across which a jet of neutral gas is pumped. If the gas density is sufficiently high, the microwaves will be reflected due to cutoff if the microwave electric field exceeds the breakdown field for ionization of the neutral gas.[9,10]

From a well-known formula of electrodynamics the instantaneous power radiated by a single electron in arbitrary, relativistic motion is given by[11]

$$P = \frac{2e^2}{3c}\gamma^6\left[\dot{\underline{\beta}}^2 - (\underline{\beta}\times\dot{\underline{\beta}})^2\right], \tag{4}$$

where $\underline{\beta} = \underline{v}/c$ is the particle velocity normalized to the speed of light, and $\dot{\underline{\beta}} = \dot{\underline{v}}/c$, where $\dot{\underline{v}} = \frac{d}{dt}\underline{v}$ is the acceleration. Making use of the Lorentz force formula, Eq. (4) may be rewritten as

$$P = \frac{2e^4}{3m^2c^3}\gamma^2\left[(\underline{E}+\underline{\beta}\times\underline{B})^2 - (\underline{E}\cdot\underline{\beta})^2\right], \tag{5}$$

where $\underline{E}$ and $\underline{B}$ are the electric and the magnetic fields. Since the x-ray radiation field is small compared to the electromagnetic undulator field, we may neglect the excited radiation fields in Eq. (5). For the undulator field we take plane waves of the form

$$\underline{E} = E_o \sin(k_o z + \omega_o t)\hat{e}_x, \tag{6}$$

$$\underline{B} = -\frac{cE_o k_o}{\omega_o} \sin\left(k_o z + \omega_o t\right)\hat{e}_y, \tag{7}$$

where $E_o$ is the amplitude of the electric field, $\omega_o$ is the radian frequency and $\underline{k}_o = (0,0,k_o)$ is the wave-vector. $\hat{e}_z$ is a unit vector along the direction of propagation of the electron beam, with $\hat{e}_x$ out of the plane of the paper and $\hat{e}_y$ in the plane of the paper. We note that the electric and the magnetic field may be obtained from the following vector potential

$$\underline{A} = \frac{c}{\omega_o} E_o \cos\left(\underline{k}_o \cdot \underline{r} + \omega_o t\right)\hat{e}_x, \tag{8}$$

where $\underline{r}$ is the radius vector. Since the vector potential is not an explicit function of the x coordinate, the canonical momentum along the x-axis is conserved, whence

$$\beta_x \equiv v_x/c = (K/\gamma)\cos\left(\underline{k}_o \cdot \underline{r} + \omega_o t\right), \tag{9}$$

where

$$K = \frac{|e|(cE_o/\omega_o)}{mc^2}, \tag{10}$$

is the undulator parameter [cf. Eq. (1)]. To evaluate the power according to the formula in Eq. (5) we make use of the Lorentz equation and after a simple analysis we obtain, for a single electron,

$$P \approx \frac{e^2\gamma^2\omega_o^2K^2}{3c}(1 + \beta_z)^2. \tag{11}$$

The distribution in frequency and angle of energy radiated by the particle is obtained from[12]

$$\frac{d^2\mathcal{E}_s}{d\Omega_s d\omega_s} = \frac{e^2\omega_s^2}{4\pi^2 c}\left|\int_{-L/2c}^{L/2c} dt\ \hat{n}\times(\hat{n}\times\underline{\beta})e^{i\omega_s\left[t-\frac{\hat{n}\cdot\underline{r}(t)}{c}\right]}\right|^2, \quad (12)$$

where $\hat{n}$ is the unit vector in the direction of observation, and L is the length over which the electron interacts with the undulator. It is important to note that $\omega_s$ in Eq. (12) refers to the radian frequency of the scattered radiation (in the x-ray region), which is to be distinguished from the frequency of the electromagnetic undulator, denoted by $\omega_o$ in Eqs. (6)-(8). Expressing the unit vector $\hat{n}$ in terms of the polar ($\theta$) and azimuthal ($\phi$) angles,

$$\hat{n} = \hat{e}_z\cos\theta + (\hat{e}_y\sin\phi + \hat{e}_x\cos\phi)\sin\theta,$$

the distribution of the scattered radiation for $\theta \lesssim \frac{1}{\gamma}$ is given by

$$\frac{d^2\mathcal{E}_s}{d\Omega_s d\omega_s} \approx \frac{1}{c}\left[\frac{e\omega_o LK\gamma}{\pi c(1+\gamma^2\theta^2)}\right]^2\left[1-\frac{4\gamma^2\theta^2\cos^2\phi}{(1+\gamma^2\theta^2)^2}\right]\left(\frac{\sin x}{x}\right)^2, \quad (13a)$$

where

$$x \equiv \frac{\omega_o L}{c}(1+\beta_z)\left[\frac{\omega_s(1-\beta_z\cos\theta)}{\omega_o(1+\beta_z)}-1\right]. \quad (13b)$$

From Eqs. (13) we find that for long interaction lengths ($L\omega_o/c \gg 1$) the scattered radiation has a peak centered at

$$\omega_s = \frac{\omega_o(1+\beta_z)}{(1-\beta_z\cos\theta)}, \quad (13c)$$

$$\approx \frac{4\gamma^2\omega_o}{1+\gamma^2\theta^2}.$$

It must be noted that the forward scattered wavelength predicted by Eq. (13c) is half of that given by Eq. (2). This is well-known and is due to the travelling-wave nature of the electromagnetic undulator considered in this Section.

It is important to note that the frequency distribution given by Eq. (13) pertains to a single electron. The determination of the actual frequency distribution, in general, presents a complex problem. The factor $(\sin x/x)^2$ in Eq. (13a) indicates a line width on the order of $\lambda_o/2L$ about the central frequency (13c). For long interaction lengths, however, a number of other mechanisms limit the line width. Besides the damping due to the emission of radiation itself, there are several other causes which broaden a line. These include Doppler broadening, collisional broadening, and radiative widths induced by the high power microwaves inside the resonator cavity.

It is useful to express the power emitted as x-ray radiation, Eq. (11), in terms of the power in the electromagnetic pump rather than the undulator parameter K. To do so, we assume the fundamental Gaussian (resonator) mode is proportional to $\exp(-r^2/\sigma^2)$ where $\sigma$ is the spot-size. It is simple to show that the undulator power and the undulator parameter K are related via

$$P_u = \left(\frac{m\omega_o K}{4e}\right)^2 c^3 \sigma^2, \tag{14}$$

whence the total power (in x-rays) of an electron beam of current $I_b$ emitted over a length L of interaction is expressible as

$$P_{x\text{-ray}} = \frac{64|e|^3 \gamma^2 I_b L}{3\sigma^2 \beta_z m^2 c^5} P_u, \tag{15}$$

where use has been made of Eqs. (11) and (14). For applications it is necessary to refine this formula in two respects. First, in order to take into account the variation of the spot-size of the undulator field inside the resonator, we assume the waist to be at the center of cavity, z=0. From elementary diffraction theory, we have

$$\sigma(z) = \sigma_o(1+z^2/z_R^2)^{1/2}, \tag{16}$$

Where $\sigma_o$ is the waist and $z_R = \pi\sigma_o^2/\lambda_o$ is the Rayleigh range corresponding to microwaves of wavelength $\lambda_o$. Substituting Eq. (16) into Eq. (15) and averaging over the interaction length L, one obtains

$$\langle P_{x\text{-ray}} \rangle = \frac{32\pi|e|^3 I_b P_u}{3\beta_z m^2 c^5 \lambda_s} \tan^{-1}(L/2z_R), \tag{17}$$

where $\lambda_s$ is wavelength of the x-rays.

A further refinement pertains to the angular distribution of the x-rays. From Eq. (13a) the power radiated per unit solid angle (in terms of the electrons' time) is given by

$$\frac{dP_{x\text{-ray}}}{d\Omega_s} = \frac{2}{\pi}\frac{e^2}{c}|\dot{\underline{\beta}}|^2 \frac{1}{(1+\gamma^2\theta^2)^3}\left[1-\frac{4\gamma^2\theta^2\cos^2\phi}{(1+\gamma^2\theta^2)^2}\right].$$

Integrating over the cone of semi-angle $1/\gamma$ around the forward direction, Eq. (17) is modified to

$$\langle P_{x\text{-ray}} \rangle = \frac{25\pi|e|^3 I_b P_u}{3\beta_z m^2 c^5 \lambda_s} \tan^{-1}(L/2z_R),$$

or, in practical units.

$$\langle P_{x\text{-}ray} \rangle [W] = 0.045 \frac{I_b[A] P_u[MW]}{\lambda_s[\mathring{A}]} \tan^{-1}(L/2z_R) \qquad (18)$$

where the x-ray radiation power is in watts, the electron beam current is in Amperes, the undulator stored power is in megawatts, and the x-ray wavelength is in Ångstroms.

## VI. Design Parameters for Electromagnetic Undulator

As a concrete example of a synchrotron radiation source based on the electromagnetic undulator we present a set of design parameters which would be useful for x-ray lithography. There are basically two main components in our proposed device, the electromagnetic pump wave (undulator) and the electron beam. The goal is to have a powerful source of x-rays to be able to expose a commercially interesting number of wafers. Bearing this in mind and noting the scaling of the x-ray-power formula in Eq. (18) we consider each of these components separately.

For the undulator we have examined several sources of radiation. A good candidate is a pulsed $CO_2$ laser since gigawatt power levels are readily available from such a source. One of the problems, though, with using such high power levels is the difficulty in designing beam-line optical elements that can operate at high powers.

Our present choice for the undulator is the quasi-optical gyrotron.[13] Quasi-optical gyrotrons employ an open resonator cavity containing a gyrating electron beam which propagates perpendicular to the resonator axis. Among the attractive features of this source are high cw operating powers and high efficiency. Quasi-optical gyrotrons are routinely and reliably operated at the Naval Research Laboratory.[14] A schematic of the NRL quasi-optical gyrotron is shown in Fig. 2.

The other major component of the x-ray source is the electron beam. With the use of a short-wavelength electromagnetic undulator, we require moderately energetic electron beams at high average current levels. For electron beam energies of interest ($\lesssim$ 1/2 GeV) race-track microtrons may be appropriate. Typically, microtrons are limited to very low currents ($\lesssim$ 1 mA), and the linacs that are suitable are fairly expensive. Storage rings appear to be most suitable for our purposes.[15] A closed vacuum

chamber threads through the components of the storage ring which include the bending magnets and the rf cavity. Electron injection can be below the energy of operation in which case the ring is used to accelerate the particles to their final energy within several minutes. The lifetime of the beam may be several hours depending on the average pressure in the ring.

If we assume the stored (circulating) power in the quasi-optical cavity is 1/4 GW, using a 1/4 GeV, 1/2 A (average current) storage ring, from Eq. (18) we find that the power emitted as x-ray radiation is about 3/4 W. From Eq. (13c) we find that if the x-rays are centered at about 12 Å then the undulator (that is, the microwave radiation in the quasi-optical resonator) has a wavelength $\lambda_o$ of about 1.2 mm, which should be readily available with current quasi-optical technology. In making use of Eq. (18) we have assumed that the intramirror separation L in the quasi-optical cavity is much larger than the Rayleigh range $z_R$ of the microwaves. This is true provided the waist of the microwaves is on the order of or less than several centimeters and L is on the order of 1 meter or longer. It is important to note that for $L/z_R \gg 1$, $\tan^{-1}(L/2z_R) \to \pi/2$ and the power formula in Eq. (18) is then independent of the cavity dimensions, the microwave spot-size and wavelength, and the electron beam energy. However, the latter two parameters determine the required x-ray wavelength, which is constrained by the composition of the resist material.

If we consider using gas breakdown instead of the Bragg reflector to stop microwave leakage through the mirror orifice, then for this configuration the electric field of the microwaves passing through the orifice in the right-hand cavity mirror exceeds the breakdown field of a typical gas at 20 torr. At this pressure, x-ray absorption is negligible, but the plasma density exceeds the microwave frequency and may therefore completely eliminate the loss of microwaves from the cavity.

## VII. Comparison of X-Ray Sources for Lithography

In order to put the expected performance of the electromagnetic undulator x-ray source in perspective, we now briefly compare such a device with a conventional, bending-magnet source, such as a storage ring.

We assume the silicon wafer diameter is 5" and divided into chips of area $A_C$ = 3X3 $cm^2$. When such a wafer is covered with a high-quality resist such as PMMA (resist sensitivity ≈ 1 $J/cm^2$) and placed at about 8.5 m from the source, we find that with the design parameters of Sec. VI the chip exposure time $T_E$ is 12.3 sec. The throughput T of the lithography process, in terms of wafers/hr, can then be estimated from[16]

$$T = \frac{3600}{T_{L/U} + T_G + \frac{A_W}{A_C}\left(T_S + T_A + \frac{\sqrt{A_C}}{V} + T_E\right)},$$

where

| | Aggressive | Very Aggressive |
|---|---|---|
| $T_{L/U}$ = wafer load/unload time, (sec), | 20 | 12 |
| $T_G$ = global alignment time, (sec), | 6 | 3 |
| $T_S$ = stage acceleration and settle time, (sec), | 1/5 | 1/10 |
| $T_A$ = chip alignment time, (sec), | 1/2 | 1/5 |
| V = stage velocity, (cm/sec), | 1/2 | 10 |

and $A_W$ is the area of the wafer.

The columns on the right of the table indicate typical values for an aggressive and for a very aggressive stepper used in exposing the chips on a wafer.

Using an aggressive stepper, the wafer throughput is found to be 12 wafers/hr. With a more sensitive resist such as PBS (polybutene-ℓ-sulfone; resist sensitivity $\leq$ 100 mJ/cm$^2$) the throughput rises to 26 wafers/hr, which compares favorably with plasma and with storage ring throughputs. It is of interest to note that the demands on the quasi-optical gyrotron and the electron beam can be significantly reduced by using a very aggressive stepper. For example, a very modest gyrotron (50 MW) and electron beam (100 mA, 1/4 GeV), used in conjunction with PBS and a very aggressive stepper, have a throughput of 8 wafers/hr.

## VIII. Conclusion

In this report we propose a novel application of an electromagnetic undulator; namely, as an x-ray source for lithography in the fabrication of high-density integrated circuits. The preliminary conclusion of this work is that it may very well be possible to design such a compact source of x-rays with a commercially-attractive throughput. A significant attribute of this system is that its throughput can be substantially enhanced should resists sensitive to shorter wavelength x-rays be available. In such a case it is necessary to adjust appropriately either the microwave wavelength in the quasi-optical maser or the electron beam energy.

In closing, we mention several problem areas requiring further investigation:

(i) Heat loading of the resonator mirrors in the quasi-optical cavity.

ii) Effect of the transverse distribution of the undulator field on electron motion and the generated x-rays.

iii) Effect of finite electron-beam emittance on x-ray emission.

iv) System design and cost for commercial applications.


### Acknowledgment

The authors have greatly benefitted from technical discussions with Dr. D. J. Nagel, Dr. A. Fliflet and Dr. V. L. Jacobs. This work was supported in part by the Office of Naval Research.

## References


1. Report of the Third Workshop Program for X-ray Lithography Development, Nov 17-18, 1986, Edited by J. B. Godel, W. Marcuse and G. P. Williams, Brookhaven National Laboratory Report 52046.

2. In preparing this and the following Section, we have borrowed heavily from a series of articles by Dr. D. J. Nagel and co-workers. The collection is entitled "X-ray Lithography Research: A Collection of NRL Contributions", Edited by R. R. Whitlock, Naval Research Laboratory Memorandum Report 5731 (1987).

3. D. J. Nagel, M. C. Peckerar, R. R. Whitlock, J. R. Greig, and R. E. Pechacek, Electron. Lett. 14, 781 (1978).

4. H. Winick and A. Bienenstock, Phys. Today 36, 49 (1983).

5. K. Halbach, Nucl. Instr. and Meth. 169, 1 (1980).

6. K. Halbach, J. Chin, E. Hoyer, H. Winick, R. Cronin, J. Yang, and Y. Zambre, IEEE Trans. Nucl. Sci. NS-28, 3136 (1981).

7. L. D. Landau and E. M. Lifshitz, The Classical Theory of Fields (Pergamon, New York, 1975) Section 73.

8. V. L. Bratman, G. G. Denisov, N. S. Ginzburg and M. I. Petelin, IEEE J. Quantum Electron. QE-19, 282 (1983).

9. A. D. MacDonald, Microwave Breakdown in Gases, (Wiley, New York, 1966).

10. F. Mako, J. A. Pasour, C. W. Roberson, R. Lucey, Rev. Sci. Instrum. 55, 712 (1984).

11. In Ref. 7, Section 73.

12. In Ref. 7, Section 77.

13. P. Sprangle, J. L. Vomvoridis, and W. M. Manheimer, Phys. Rev. A 23, 3127 (1981).

14. T. A. Hargreaves, K. J. Kim, J. H. McAdoo, S. Y. Park, R. D. Seelers, and M. E. Read, Int. J. Electronics 57, 977 (1984). Figure 2 was made available courtesy of Dr. A. Fliflet.

15. S. Penner (private correspondence).

16. A. D. Wilson, Solid State Technology 29, 249 (1986).

## Figure Captions

Fig. 1 Schematic top-view of an electron ring (thick line) interacting with the electromagnetic-undulator field inside a quasi-optical resonator cavity bounded by mirrors M. The x-ray radiation is confined to a cone of half-angle $1/\gamma$, $\gamma$ being the electron beam relativistic factor. L is the interaction length. The function of the Bragg reflector is to reduce the loss of microwave power through the orifice in the right-hand mirror. It may be possible to replace the quasi-optical gyrotron with a $CO_2$ laser.

Fig. 2 Schematic of the quasi-optical gyrotron. The electron beam propagates along the magnetic field (~ 5 T) which is directed transverse to the axis of the resonator. Extremely high circulating power levels (~ 100 MWs) can be achieved at short wavelengths (~ 1 mm) with this configuration. The opening in the mirror allows for out-coupled radiation.

# A SYNCHROTRON RADIATION X-RAY SOURCE BASED ON AN ELECTROMAGNETIC UNDULATOR

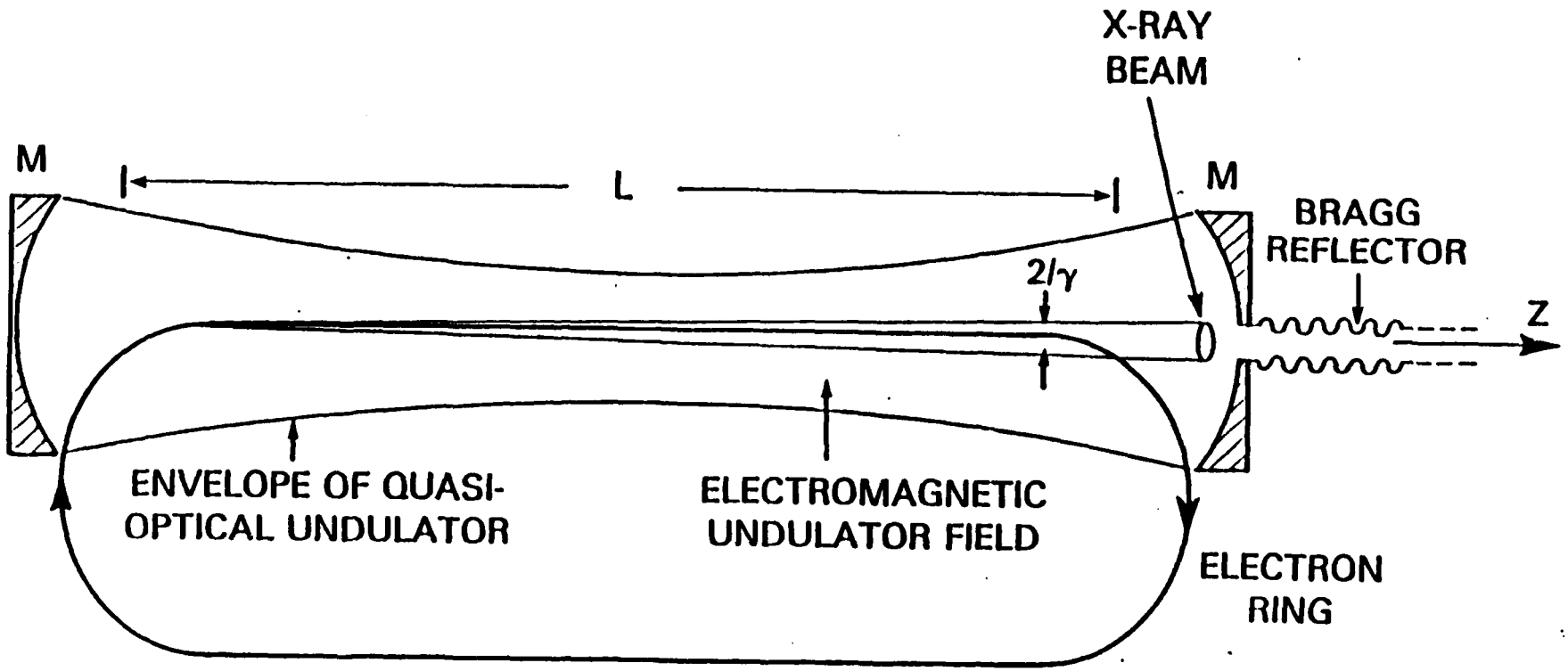
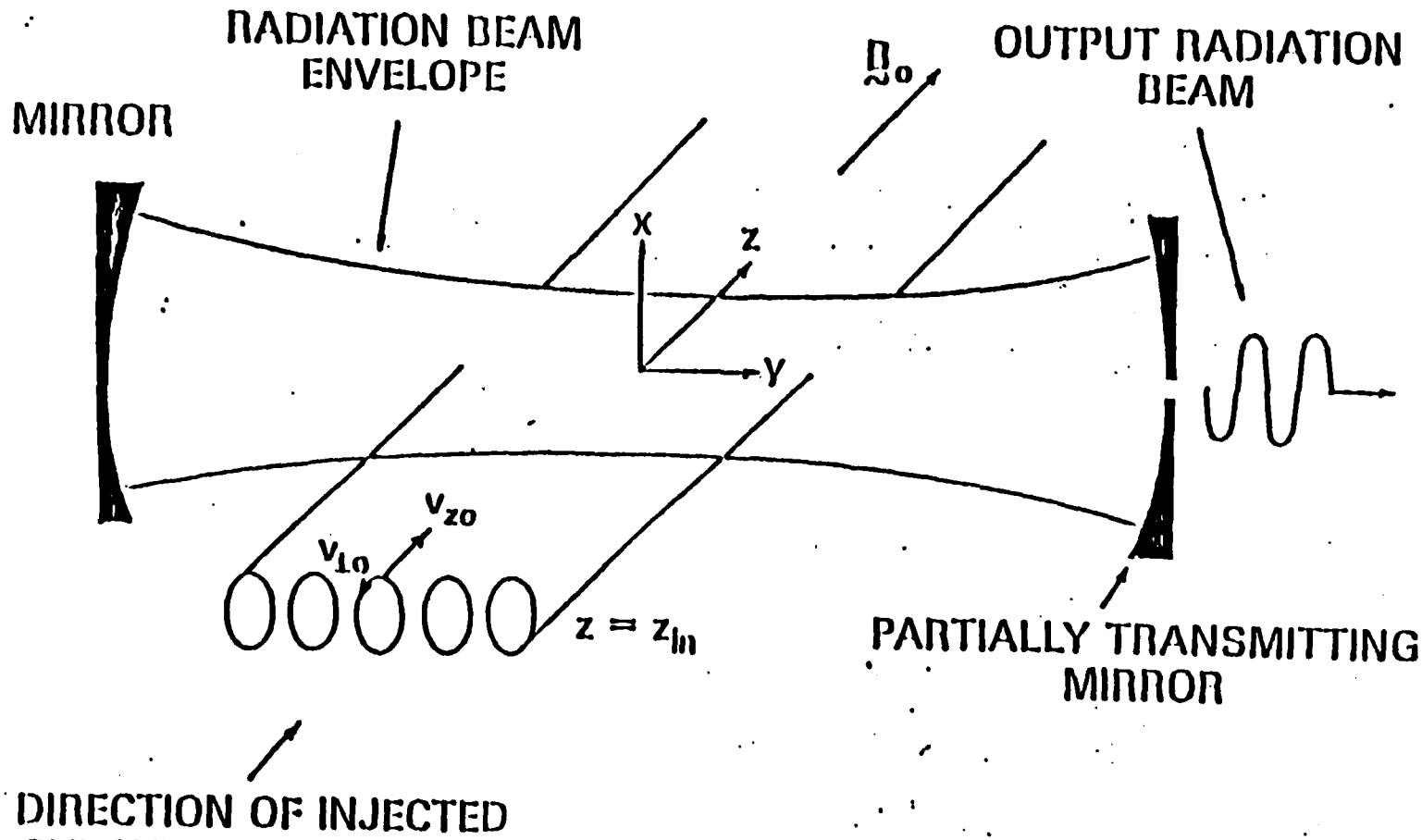



Fig 1

# QUASI-OPTICAL MASER



# APPENDIX HH

## Small Signal Analysis of the Induced Resonance Electron Cyclotron Maser

**Naval Research Laboratory**

Washington, DC 20375-5000

NRL Memorandum Report 5986

# Small Signal Analysis of the Induced Resonance Electron Cyclotron Maser

S. RIYOPOULOS,* C. M. TANG AND P. SPRANGLE

*Plasma Theory Branch*
*Plasma Physics Division*

**Science Applications, Intl. Corp., McLean, VA*

May 20, 1987

Approved for public release; distribution unlimited.

CONTENTS


I. INTRODUCTION ..... 1

II. FIELD AND PARTICLE DYNAMICS ..... 2

III. EFFICIENCY ..... 5

a. Small Signal Efficiency ..... 6

b. Start-up Current ..... 9

IV. CONCLUSION AND SUMMARY ..... 10

ACKNOWLEDGMENT ..... 11

REFERENCES ..... 12

# SMALL SIGNAL ANALYSIS OF THE INDUCED RESONANCE ELECTRON CYCLOTRON MASER

## I. Introduction

Generation of intense radiation in the microwave regime utilizing electron cyclotron interaction has been proposed independently by a number of researchers in the late 1950's.[1-4] Electrons gyrating in resonance with the radiation field can experience a bunching in the relative wave-particle phase through the dependence of the cyclotron frequency on the relativistic mass. High amplification of the radiation field, known as masing action, results for Doppler shifted frequencies slightly above the electron cyclotron frequency. Electron cyclotron masers, also called gyrotrons,[5-30] have demonstrated efficient high power generation of electromagnetic waves at centimeter wavelengths.

For many purposes it is of practical interest to develop high power generation capability at millimeter and submillimeter wavelengths. Potential areas of application include advanced accelerators, short wavelength radar, plasma heating in fusion reactors and spectroscopy. The shortest wavelength for single mode operation in a closed resonator is tied to the transverse dimension of the cavity. For radiation wavelengths much shorter than the transverse dimensions, a multimode excitation will result from the small frequency separation among nearby modes. The mode selectivity is greatly improved by the use of an open resonator configuration, the quasi-optical maser.[19,20]

A new configuration has recently been proposed[29,30] which utilizes the benefits of the open resonators and at the same time minimizes the detrimental effects of the injected electron beam energy spread. The operating frequency in the induced resonance electron

Manuscript approved February 18, 1987

cyclotron (IREC) quasi-optical maser is upshifted by a factor $\gamma^2$ relative to the relativistic electron cyclotron frequency. It has been shown that for operation at the optimum index of refraction the efficiency is relatively insensitive to the beam energy spread and the sensitivity to the effect of pitch angle spread can be minimized. The index of refraction is adjustable by varying the angle between the resonators (see Fig. (1)) and the guide field, and can be chosen to minimize the effects of finite beam quality. Finally, by spatially tapering the magnetic field the operating efficiency can be increased.

In this paper we limit ourselves to analyzing the small signal efficiency characteristics of such a device. We include the effects of the Gaussian profile for the radiation envelope considering a uniform magnetic field for simplicity. Nonlinear effects and the role of the magnetic field tapering are treated elsewhere.[30]

The remainder of this paper is organized as follows. In Sec. II we describe the field configuration and the equations of motion. In Sec. III we derive the linear energy, power efficiency and start-up current condition. In Sec. IV numerical results and conclusions are presented.

## II. Field and Particle Dynamics

The configuration for the induced resonance electron cyclotron (IREC) quasi-optical maser is shown schematically in Fig. 1. The interaction cavity is formed by two quasi-optical resonators intersecting at an angle $2\alpha$ where $\alpha$ is the angle relative to the external magnetic field $B_o$ in the $z$-direction.

The beam radius is much smaller than the Gaussian width $r_o$ (spot size) for the radiation envelope. In the limit of small Larmor radius $\rho$ compared to the perpendicular wavelength $k_\perp \rho << 1$ we can approximate the vector potential in the interaction regime by

$$\underset{\sim}{A}_T = A_R(z)\, \exp[i\Phi(z,t)]\, \frac{1}{2}\,(\hat{e}_x + i\hat{e}_y) + cc$$

$$+ A_L(z)\, \exp[i\Phi(z,t)]\, \frac{1}{2}\,(\hat{e}_x - i\hat{e}_y) + cc. \qquad (1)$$

Since we are interested in the synchronous interaction of the gyrating electrons with the radiation, we have kept only the forward propagating wave component $\Phi(z,t) = k_z z - \omega t + \Phi_o$. The amplitudes $A_R$ and $A_L$ for the right- and left-handed polarized wave component, respectively are given by

$$A_{R,L}(z) = A^o_{R,L} \exp[-z^2/L^2],$$

$$A^o_{R,L} = A_o\,(\cos\alpha \pm 1),$$

$$L = r_o/\sin\alpha, \qquad (2)$$

where $A_o$ and $r_o$ are the amplitude and spot size for each individual resonator beam.

We use the guiding center description for the particle orbits

$$x = x_g + \rho\sin\zeta, \qquad y_g = y - \rho\cos\zeta,$$

$$p_x = p_{gx} + p_\perp\cos\zeta, \quad p_y = p_{gy} + p_\perp\sin\zeta, \qquad (3)$$

to obtain the nonlinear relativistic equations of motion. In this representation $(x_g, y_g)$ and $(p_{gx}, p_{gy})$ denote the transverse coordinates

and momentum of the particle's guiding center, $\rho$ is the Larmor radius, $p_\perp$ is the magnitude of the transverse momentum and $\zeta$ is the momentum space angle. We assume that x, y, $p_x$, $p_y$, $\rho$ and $p_\perp$ are slowly changing, on the spatial scale of a gyroperiod. An additional condition for ignoring finite $k_\perp$ effects is that the guiding center shift in the x direction be small $k_\perp \Delta x \ll 1$, valid for $\alpha \ll 1$ where $k_\perp$ is k sin$\alpha$. Using the Lorentz force equation together with Maxwell's equations and retaining only the right-hand polarized wave component the nonlinear relativistic equations of motion are cast into the form

$$u_\perp' = - [(\omega\gamma/cu_z)-k_z]a(z)\cos\psi + a'(z)\sin\psi, \tag{4a}$$

$$u_z' = - (u_\perp/u_z)[k_z a(z)\cos\psi + a'(z)\sin\psi], \tag{4b}$$

$$\psi' = - (\gamma\Delta\omega/cu_z) + (1/u_\perp)\left[\left((\omega\gamma/cu_z)-k_z\right)a(z)\sin\psi + a'(z)\cos\psi\right], \tag{4c}$$

The prime (') in Eqs. (4) signifies the d/dz derivative, $\underset{\sim}{u} = \underset{\sim}{p}/m_o c = \gamma\underset{\sim}{v}/c$, $\gamma = (1 + u_\perp^2 + u_z^2)^{1/2}$ is the relativistic mass factor, $a(z) = |e|A_R(z)/m_o c^2$ is the normalized radiation amplitude, $\psi = \zeta + \Phi$ is the relative phase between the radiation field and particle, $n = ck_z/\omega = \cos\alpha$ is the refractive index associated with the radiation field, $\Delta\omega = [\omega(1-n\beta_z) - \Omega_o/\gamma]$ is the frequency mismatch term and $\Omega_o = |e|B_o/m_o c$ is the nonrelativistic electron cyclotron frequency. Using Eqs. (4) the rate of change of $\gamma$ is given by

$$\gamma' = - \omega(u_\perp/cu_z)a(z)\cos\psi. \tag{5}$$

The frequency mismatch $\Delta\omega$ and its dependence on the particle energy through the relativistic correction $\gamma$, provide the mechanism for the masing action (phase bunching).

## III. Efficiency

One of the central issues concerning maser operation is the efficiency of the configuration. Efficiency calculations have been carried out for various configurations in the general categories of the closed resonator gyrotron[5-18,21-28] or the open resonator quasi-optical maser.[19,20] While it is generally recognized that nonlinear saturation mechanisms are very important for the full power operation, it is useful to carry out the small signal efficiency calculation in order to compute the start-up current. Expressions for the small amplitude efficiency, obtained in closed form, provide some guidelines in selecting the optimum operating parameters.

Assuming steady state operation, with the number of particles crossing the unit area per unit time $n_o v_z$ being constant, the efficiency can be defined by

$$\eta_E = -\left\langle \frac{\gamma_f - \gamma_o}{\gamma_o - 1} \right\rangle = \langle \gamma_o - 1 \rangle^{-1} \int d^3p_o f_o(p_o) \int_{-\infty}^{\infty} dz \, \frac{\partial \gamma}{\partial z} . \quad (6)$$

In Eq. (6), the bracket $\langle\ \rangle$ signifies the average over the initial distribution in phase space, the subscript $\pm\infty$ stands for the initial and final values at $z = \pm\infty$ respectively and $\partial\gamma/\partial z$ is a function of the initial conditions $\gamma = \gamma(z; p_{\perp o}, p_{zo}, \psi_o)$. In the cold beam limit with the initial distribution function given by $f_o(p_\perp, p_z, \psi) = (n_o/2\pi p_\perp)$ $\delta(p_\perp - p_{\perp o})\delta\,(p_z - p_{zo})$ the average reduces to an average over $\psi_o = \zeta_o + \Phi_o$.

a. Small Signal Efficiency

We proceed to compute the small signal power efficiency by evaluating the right-hand side of Eq. (6) using Eq. (5). A first order expansion for the quantities $u_\perp = u_\perp^{(o)} + u_\perp^{(1)}$, $\gamma = \gamma^{(o)} + \gamma^{(1)}$, $\psi = \psi^{(o)} + \psi^{(1)}$ will suffice for a quadratic expression in the wave amplitude a. The integrand on the right-hand side of Eq. (6) is expanded using the linear solutions from Eqs. (4a)-(4c). The evaluation of the final result is considerably simplified by performing the phase space average over the angle $\psi_o$ before the spatial integration over z. Expanding the products of the trigonometric terms inside the integral in Eq. (6) into sums and averaging over $\psi_o$ leads to

$$\left\langle \int_{-\infty}^{\infty} dz \, \frac{\partial \gamma}{\partial z} \right\rangle = - \left(\frac{\omega}{cu_{zo}}\right)\left[\left(1 + \frac{1}{2}\frac{u_{\perp o}^2}{u_{zo}^2}\right)\int_{-\infty}^{\infty} dz a(z) \int_{-\infty}^{z} dz' \, \frac{da(z')}{dz'} \sin \Delta_o(z-z')\right.$$

$$+ \left\{k_z\left(1 + \frac{1}{2}\frac{u_{\perp o}^2}{u_{zo}^2}\right) - \frac{\omega\gamma_o}{cu_{zo}}\right\}\int_{-\infty}^{\infty} dz a(z) \int_{-\infty}^{\infty} dz' \, a(z')\cos\Delta(z-z')$$

$$- \frac{1}{2}\left\{\frac{\omega^2}{c^2}\frac{u_{\perp o}^2}{u_{zo}^2} - k_z\frac{u_{\perp o}^2}{u_{zo}^2}\left(\frac{\omega\gamma_o}{cu_{zo}} - \frac{\Omega_o}{cu_{zo}}\right)\right\}\int_{-\infty}^{\infty} dz a(z) \int_{-\infty}^{z} dz' \int_{-\infty}^{z'} dz'' a(z'')\sin\Delta_o(z-z'')$$

$$\left. + \frac{1}{2}\frac{u_{\perp o}^2}{u_{zo}^2}\left(\frac{\omega\gamma_o}{cu_{zo}} - \frac{\Omega_o}{cu_{zo}}\right)\int_{-\infty}^{\infty} dz a(z) \int_{-\infty}^{z} dz' \int_{-\infty}^{z'} dz'' \, \frac{da(z'')}{dz''} \cos\Delta_o(z-z'')\right], \qquad (7)$$

where $\Delta_o = \frac{\Omega_o}{cu_{zo}} - \left(\frac{\omega\gamma_o}{cu_{zo}} - k_z\right) = - \frac{\Delta\omega_o}{v_{zo}}$, $a(z) = a_o \exp[-z^2/L^2]$

and $a_o = |e| \, A_R^o/m_o c^2$.

We evaluate the remaining integrals in Eq. (14) and express the final result in terms of the parameters $\xi = \omega\tau = (\omega\gamma_o/cu_{zo})L$, $\tau$ being the transit time through the interaction regime, and the relative frequency mismatch $\Delta\omega_o/\omega$. We find

$$\eta_p = \frac{\pi}{2}\frac{a_o^2\,\xi^2}{\gamma_o(\gamma_o-1)} \left\{\left(1+\theta_o^2\right)n\beta_{zo}-1 + \left[\frac{1}{2}\xi^2\beta_{\perp o}^2(1-n^2)+\left(1+\theta_o^2\right)\right]\frac{\Delta\omega_o}{\omega} - \theta_o^2\, n\beta_{zo}\xi^2\left(\frac{\Delta\omega_o}{\omega}\right)^2 - \frac{\theta_o^2}{2}\,\xi^2\left(\frac{\Delta\omega_o}{\omega}\right)^3\right\} e^{-\frac{1}{2}\xi^2\frac{\Delta\omega_o^2}{\omega^2}}, \quad (8)$$

with $\theta_o = u_{\perp o}/u_{zo}$, the initial pitch angle.

The efficiency is proportional to $\exp[-1/2\ \xi^2\ \Delta\omega_o^2/\omega^2]$ where exponent $\xi(\Delta\omega_o/\omega)$ is equal to $\Delta\omega_o\tau$, the advance in the relative phase $\Delta\psi_o$ between the wave and the particle over the interaction regime. For typical values of $\xi >> 1$ and $\Delta\omega_o/\omega << 1$ the expression in braces in Eq. (8) is simplified to

$$\left\{\cdots\right\} = \left(1+\theta_o^2\right)n\beta_{zo}-1+\frac{\xi_o^2\beta_{\perp o}^2}{2}\frac{\Delta\omega_o}{\omega}-\theta_o^2\beta_{zo}\frac{\xi_o^2}{\sin^2\alpha}\left(\frac{\Delta\omega_o}{\omega}\right)^2, \quad (9)$$

where $\xi_o^2 = \xi^2(1-n^2)$ is independent of $\alpha$. In (9) we have omitted the small terms that originate from the gradient terms $\partial a/\partial z$ in the equations of motion. Treating (9) as a quadratic form in $\Delta\omega/\omega$ we find the regime for positive efficiency, given by

$$2\left(1-\left(1+\theta_o^2\right)n\beta_{zo}\right)\left(\beta_{\perp o}^2\xi_o^2\right)^{-1} < \frac{\Delta\omega_o}{\omega} < \beta_{\perp o}^2(1-n^2)\left(n\,\theta_o^2\beta_{zo}\right)^{-1}. \quad (10)$$

The upper limit in $\Delta\omega_o/\omega$ is due to a finite n and results from the negative contribution of the quadratic term $(\Delta\omega/\omega)^2$ that overtakes the positive contribution of the linear term $\Delta\omega/\omega$ for small angles $\sin^2\alpha < (2n\theta_o^2\beta_{zo}/\beta_{\perp o}^2)\ (\Delta\omega_o/\omega)$.

In order to determine the maximum efficiency within the positive regime, we parameterize Eq.(8) as a function of $x = \xi\ \Delta\omega/\omega$, since the exponential is the main factor limiting efficiency. Setting $d\eta/dx = 0$, we obtain

$$c_3x^3 - c_2\,x^2 - c_1x + c_o = 0\ , \tag{11}$$

with $c_1 = (1 + 3\theta_o^2)\beta_{zo}\ \cos\alpha - 1$, $c_3 = \theta_o^2\beta_{zo}\ \cos\alpha$ and $c_2 = c_o = (1/2)\ \beta_{\perp o}^2\xi_o\ \sin\alpha$. Observing that the terms proportional to $c_1$ and $c_3$ can be omitted provided that $c_o = c_2 >> c_3 \sim c_1 \sim 1$ or

$$\sin\alpha >> \frac{\theta_o^2\beta_{zo}}{\beta_{\perp o}^2\xi_o}, \tag{12}$$

we can show that $x \simeq 1$. In the special case $x = 1$, we obtain the maximum efficiency

$$\eta_{max} = \frac{\pi}{4}\,a_o^2e^{-1/2}\ \frac{\beta_{\perp o}^2\xi_o^3}{\gamma_o(\gamma_o-1)}\ (\sin\alpha)^{-1}. \tag{13}$$

The overall efficiency increases with decreasing $\alpha$ (increasing index of refraction) provided that inequality Eq. (12) remains valid. For very small $\alpha$ Eq. (13) fails and a solution of the cubic Eq. (11) is necessary.

b. Start-up Current

We are in position now to calculate the start-up beam current utilizing the power efficiency coefficient. Amplification of the electromagnetic field energy will result if

$$\eta P_b > \frac{d\varepsilon}{dt}, \tag{14}$$

where $\varepsilon$ is the total electromagnetic energy stored in both cavities $\varepsilon = \int U_R dV = 2V(\omega^2/c^2)(A_o^2/4\pi)$, $V=\pi r_o^2 L_T$, $d\varepsilon/dt = (\omega/Q)\varepsilon$, Q is the quality factor for the cavity and $P_b$ is the electron beam power.

The optimum power efficiency $\eta_{max}$ is given by Eq. (13). The cavity Q is given by

$$Q = \frac{2\pi}{1-R_{ef}} \frac{L_T}{\lambda}, \tag{15}$$

where $L_T$ is the effective resonator length and $\lambda$ the wavelength. Combining Eqs. (13), (14), (15) and expressing $A_o$ in terms of $a_o$ from Eq. (2) we obtain

$$P_b > \frac{\lambda}{r_o}(1-R_{ef}) \frac{\exp(\frac{1}{2})}{4\pi^2} \frac{m_o^2 c^5}{|e|^2} \frac{\beta_{zo}^3 \gamma_o(\gamma_o-1)}{\beta_{\perp o}^2} \frac{2\sin\alpha}{(1+\cos\alpha)^2}, \tag{16}$$

where $P_b = I_b V_b$, $I_b$ is the current and $V_b$ is voltage of the electron beam. For typical parameters $V_b = 0.25 \times 10^6$eV, $\lambda/r_o = 10^{-1}$, $1-R_{ef} = 0.1$, $\gamma_o = 1.5$, $\beta_{zo} \simeq 0.64$, $\beta_{\perp o} \simeq (\sqrt{3}\gamma_o)^{-1}$, and the optimum operation angle $\alpha \simeq 45°$, the start-up current is

$$I_b \gtrsim 4.6 \text{ A}.$$

## IV. Conclusion and Summary

We have performed the small signal analysis for an oscillator configuration capable of generating radiation in the millimeter and the submillimeter regime. The threshold for the start-up current was found to be well within the existing capabilities of today's long pulse mildly relativistic beams. Our theoretical linear efficiency results are plotted as solid lines in Figs. 2-4 against the numerical results (dots) obtained by direct integration of the fully nonlinear Eqs. (4) for small wave amplitude. Plots of the linear efficiency as a function of the controlling parameter $\xi\ \Delta\omega/\omega$ for constant radiation amplitude $a_o$ and constant spot size $r_o$ are shown in Fig. 2, with each curve corresponding to a different index of refraction $n = \cos\alpha$. The maximum efficiency for all plots occurs at $\xi\ \Delta\omega/\omega \simeq 1$ in agreement with Eq. (13). Small signal efficiency increases with increasing $n = \cos\alpha$ roughly proportionally to the length of the interaction regime $L = r_o/\sin\alpha$. In Fig. 3, the optimum index of refraction [29-30] $n = \beta_{zo}/(1-\beta_{\perp o}^2)$, to minimize the effects of beam energy spread, is held constant, and the interaction length L is changed by increasing the width of the radiation envelope $r_o$. Figure 4 is a comparison the theoretical small signal efficiency with the numerically calculated nonlinear efficiency as a function of wave amplitude $a_o$. The agreement is good for $a_o \leq 3 \times 10^{-4}$. Nonlinear saturation occurs for $a_o > 1 \times 10^{-3}$. Obtaining the scaling of the efficiency in the nonlinear regime is not possible analytically. Numerical studies of the high power performance, however, have demonstrated good nonlinear efficiency.

## Acknowledgment

This work is sponsored by the Department of Energy under Contract Number DE-AI05-83ER40117.

## References


1. R. Q. Twiss, Aust. J. Phys. 11, 564 (1958).
2. A. V. Gaponov, Isv. Vyssh. Uchebn, Zaved, Radiofiz., 2, 450 (1959).
3. R. H. Pantell, Proc. IRE, 47, 1146 (1959).
4. J. Schneider, Phys. Rev. Lett. 2, 504 (1959).
5. J. L. Hirshfield and J. M. Wachtel, Phys. Rev. Lett. 12, 533 (1964).
6. A. V. Gaponov, M. I. Petelin and V. K. Yulpatov, Radiophys. Quantum Electron. 10, 794 (1967).
7. V. L. Bratman, M. A. Moiseev, M. I. Petelin and R. E. Erm, Radiophys. Quantum Electron. 16, 474 (1973).
8. D. V. Kisel', G. S. Korablev, V. G. Navel'yev, M. I. Petelin and Sh. Ye. Tsimring, Radio Eng. Electron. Phys. 19, No. 4, 95 (1974).
9. N. I. Zaytsev, T. B. Pankratova, M. I. Petelin and V. A. Flyagin, Radio Eng. Electron. Phys. 19, No. 5, 103 (1974).
10. V. L. Granatstein, M. Herndon, R. K. Parker and P. Sprangle, IEEE J. Quantum Electron. QE-10 p. 651 (1974).
11. E. Ott and W. M. Manheimer, IEEE Trans. Plasma Science PS-3, 1 (1975).
12. V. L. Granatstein, P. Sprangle, R. K. Parker, and M. Herndon, J. Appl. Phys. 46, 2021 (1975).
13. P. Sprangle and W. M. Manheimer, Phys. Fluids 18, 224 (1975).
14. P. Sprangle and A. T. Drobot, IEEE Trans. Microwave Theory and Techniques MTT-25, 528 (1977).
15. J. L. Hirshfield and V. L. Granatstein, IEEE Trans. Microwave Theory and Tech. MTT-25, 522 (1977).
16. K. R. Chu and J. L. Hirshfield, Phys. Fluids 21, 461 (1978).

17. V. L. Bratman, N. S. Ginzburg and M. I. Petelin, Optics Commun. 30, 409 (1979).

18. P. Sprangle and R. A. Smith, J. Appl. Phys. 51, p. 3001 (1980).

19. P. Sprangle, J. L. Vomvoridis and W. M. Manheimer, Appl. Phys. Lett. 38, 5, p. 310 (1981), also Phys. Rev. A23, 3127 (1981).

20. J. L. Vomvoridis and P. Sprangle, Phys. Rev. A25, 931 (1982).

21. K. E. Kreischer and R. J. Temkin, Intl. J. of Infrared and Millimeter Waves, 2, p. 175 (1981).

22. V. L. Bratman, N. S. Ginzburg, G. S. Nusinovich, M. I. Petelin and P. S. Strelkov, Intl. J. Electron. 51, 541 (1981).

23. I. E. Botvinnik, V. L. Bratman, A. B. Volkov, N. S. Ginzburg, G. G. Denisov, B. D. Kol'chugin, M. N. Ofitserov and M. I. Petelin, JETP Lett. 35, p. 516 (1982).

24. Y. Y. Lau, IEEE Trans., ED-29, p 320 (1982).

25. V. L. Bratman, G. G. Denisov, N. S. Ginzburg and M. I. Petelin, IEEE J. Quantum Electron, QE-19, 282 (1983).

26. A. T. Lin, W. W. Chang and C.-C. Lin, Phys. Fluids 27, 1054 (1984).

27. C. S. Wu and L. C. Lee, Astrophysical Journal 230, 621 (1979).

28. B. Levush, A. Bondeson, W. M. Manheimer and E. Ott, Intl. J. Electr. 54, 749 (1983).

29. P. Sprangle, C. M. Tang and P. Serafim, NRL Memo Report No. 5678 (1986), also in Nucl. Instr. and Methods in Phys. Res., A250, 361 (1986).

30. P. Sprangle, C.-M. Tang and P. Serafim, Appl. Phys. Lett. 49 (18) 1154 (1986).

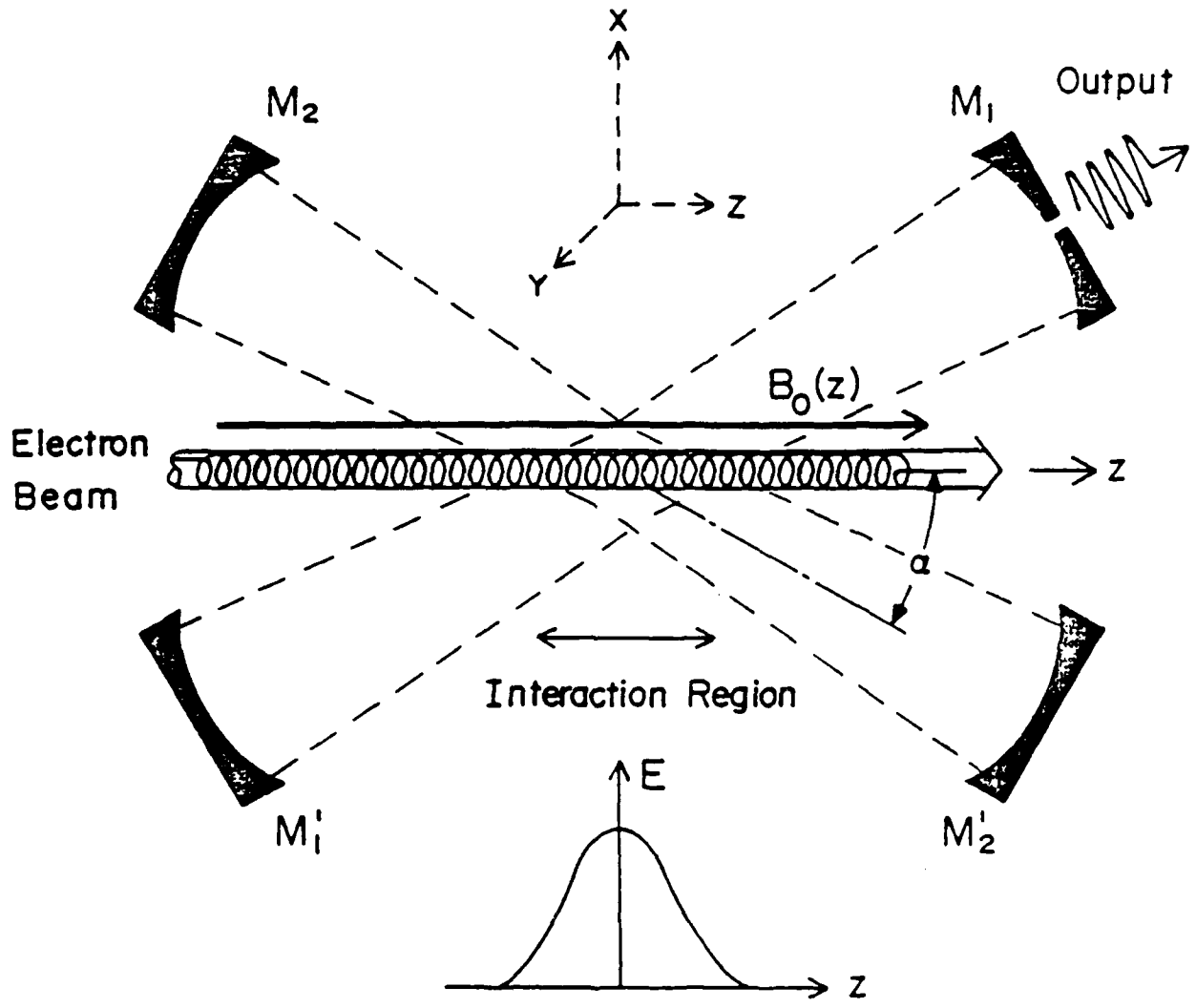



Figure 1. The configuration of the Induced Electron Resonance Maser.

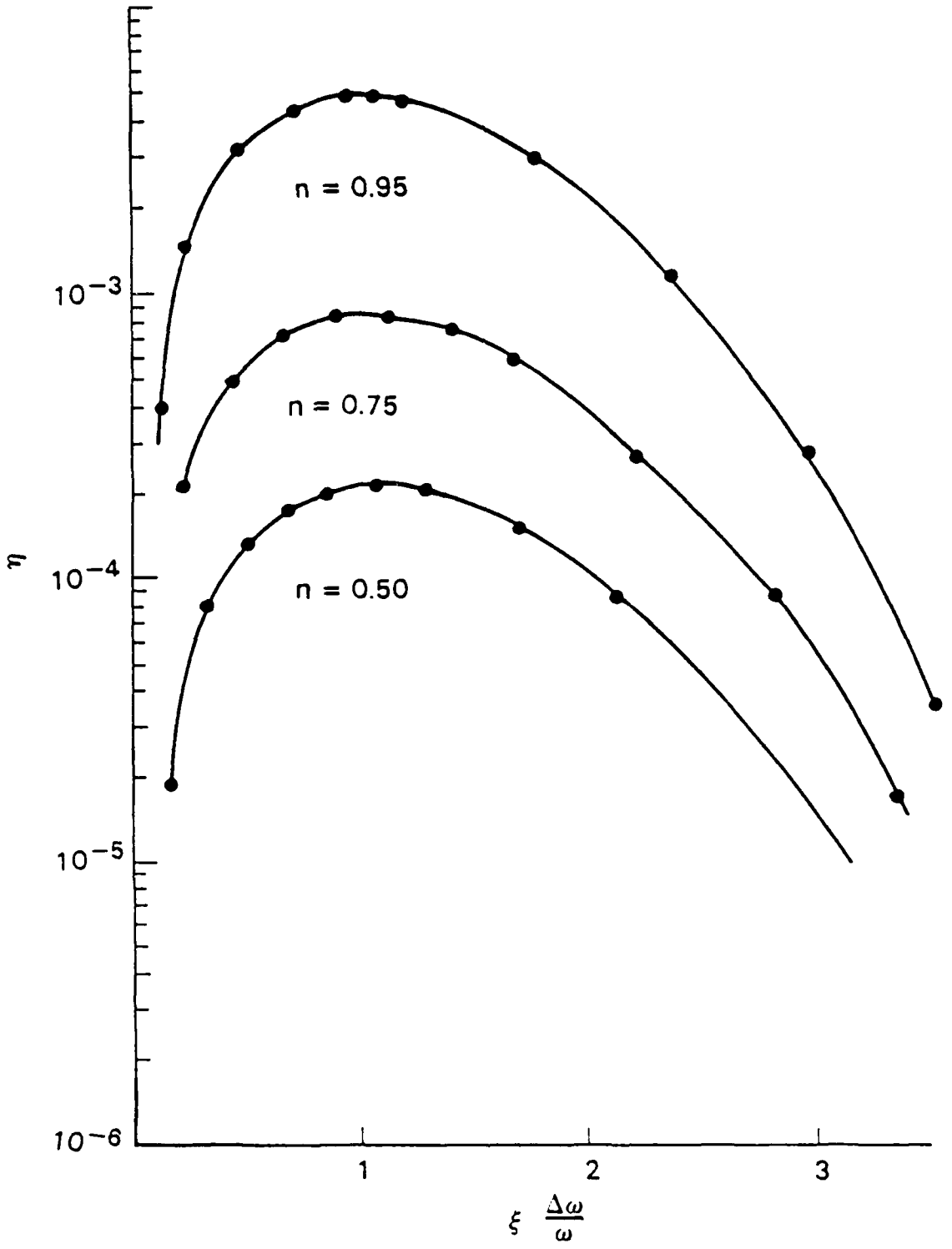



Figure 2. Theoretical (solid line) and numerical (dots) plots of linear efficiency η versus $\xi\,\Delta\omega/\omega$ for various values of index of refraction n with constant amplitude $a_o = 5\times10^{-5}$ and $\gamma = 1.5$.

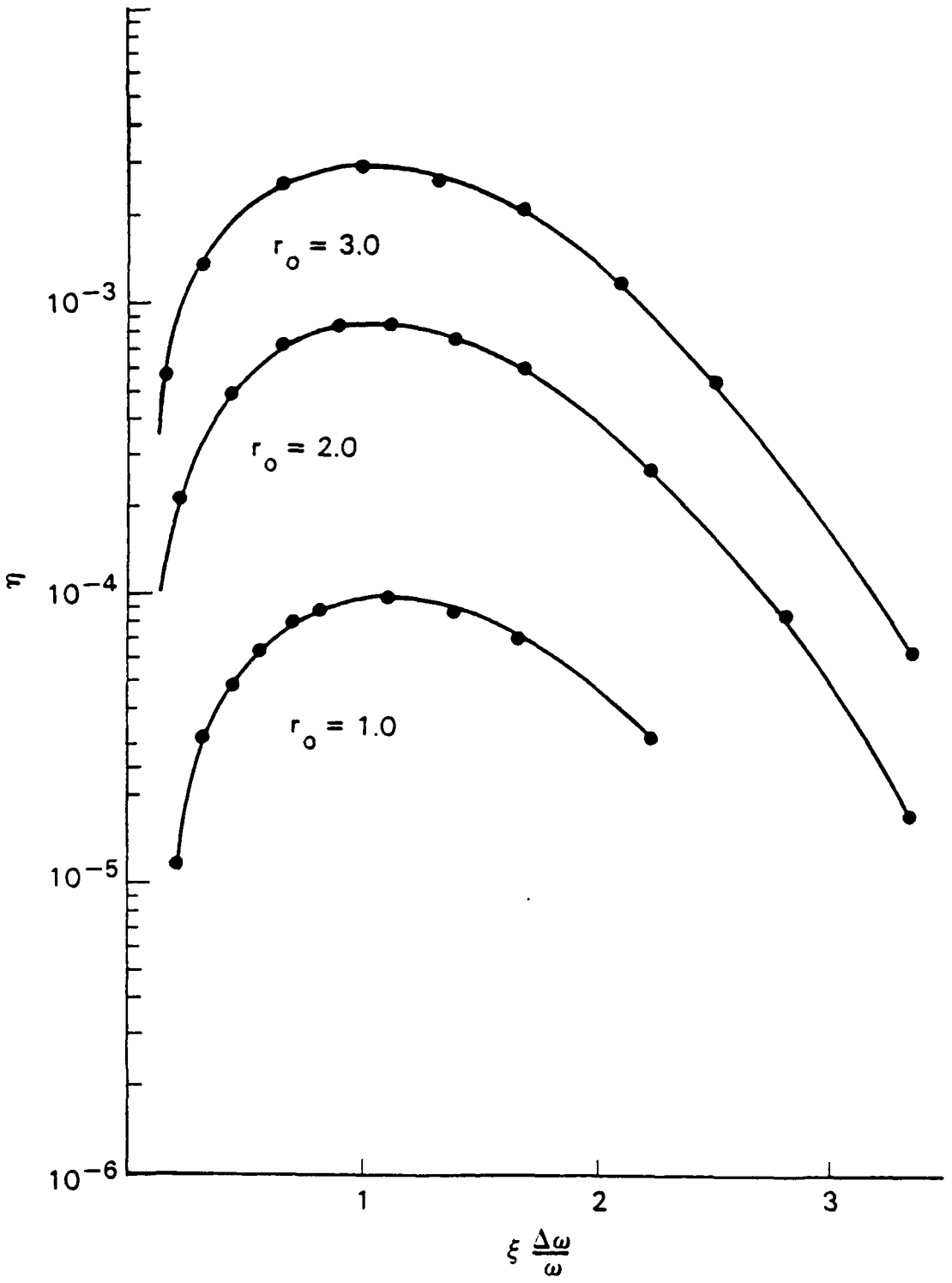



Figure 3. Theoretical (solid line) and numerical (dots) plots of linear efficiency η versus $\xi\ \Delta\omega/\omega$ for various Gaussian widths $r_o$ with constant refraction index $n_{opt}$ and $a_o = 5\times10^{-5}$, $\gamma = 1.5$.

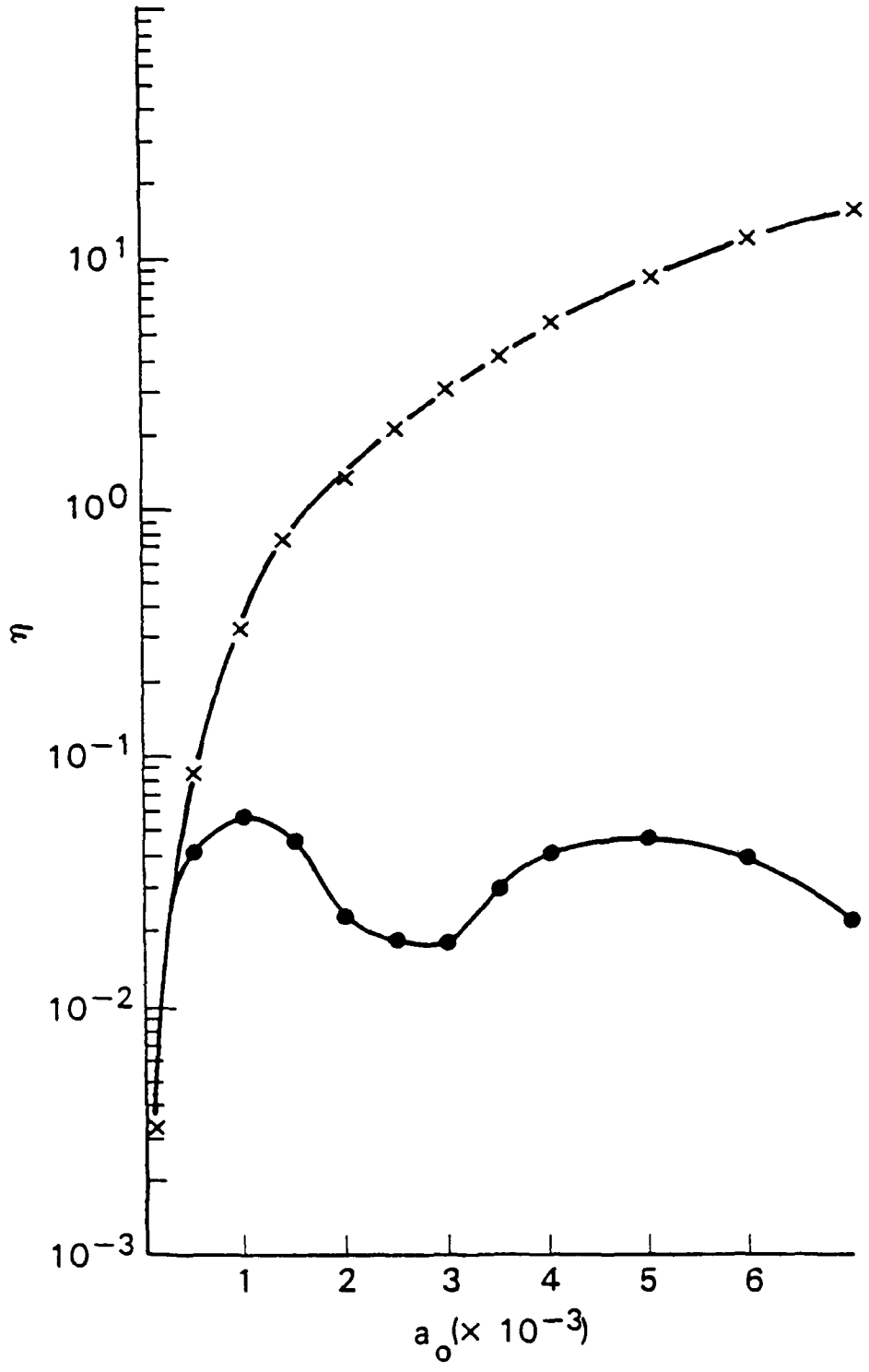



Figure 4. Comparison of linear (crosses) versus nonlinear (dots) efficiency η as a function of $a_o$ for $\xi\,\Delta\omega/\omega = 1$, $n = 0.75$ and $\gamma = 1.5$.

# APPENDIX II

## Higher Harmonic Generation in the Induced Resonance Electron Cyclotron Maser

# Higher harmonic generation in the induced resonance electron cyclotron maser

S. Riyopoulos,[a] C. M. Tang, P. Sprangle, and B. Levush[b]
*Plasma Physics Division, Plasma Theory Branch, Naval Research Laboratory, Washington, D. C. 20375-5000*

(Received 13 July 1987; accepted 5 January 1988)

Operation of the induced resonance electron cyclotron (IREC) maser [Appl. Phys. Lett. 49, 1154 (1986); Nucl. Instrum. Methods Phys. A 250, 361 (1986)] at Doppler upshifted cyclotron harmonics is studied. A set of fast-time averaged nonlinear equations of motion is derived for the particle motion near an arbitrary harmonic at any index of refraction. The small signal efficiency is computed analytically and the minimum current to start the cavity oscillations is obtained. The nonlinear equations of motion are integrated numerically. The interaction efficiency at the first few harmonics is found to be comparable to the efficiency at the fundamental. The sensitivity of the efficiency to beam thermal spreads is minimized by proper selection of the index of refraction.

## I. INTRODUCTION

Generation of intense radiation in the microwave regime through electron cyclotron interaction was proposed independently by a number of researchers[1-4] in the late 1950's. Electrons gyrating in resonance with the radiation field experience a bunching in the relative wave particle phase through the dependence of the cyclotron frequency on the relativistic mass. High amplification of the radiation field, known as masing action, results for radiation frequencies slightly above the electron cyclotron frequency. Electron cyclotron masers,[5-18] also called gyrotrons, have demonstrated efficient high power generation capability at the centimeter wavelengths. Electron cyclotron instabilities also occur in ionospheric and astrophysical plasmas.[19,20]

A variety of potential applications, such as advanced accelerators, heating of fusion plasmas, short wavelength radar, and spectroscopy, call for generation of intense radiation at even shorter wavelengths in the millimeter and submillimeter range. In a closed resonator, the shortest wavelength for single mode operation is tied to the transverse dimension of the cavity. Operation at radiation wavelengths shorter than the transverse dimensions will result in a multimode excitation[21] as a result of the small frequency separation among cavity eigenmodes. This limitation in the wavelength is considerably relaxed in the quasioptical maser[22,23] operating in an open resonator that offers much improved frequency separation.

Considerable attention has been given lately to the operation at Doppler upshifted frequencies[24-30] resulting from a finite wavenumber $k_z$ in the direction of the electron beam propagation. The operation frequency $\omega$, defined by the resonance condition $\omega - k_z z - \Omega_c = 0$, is given by

$$\omega = \Omega_c (1 - n_z \beta_z)^{-1},$$

where $\gamma$ is the relativistic factor $\gamma = (1 - \beta^2)^{-1/2}$, $\beta = v/c$, $n_z = k_z c/\omega$ is the parallel index of refraction, and $\Omega_c = \Omega_0/\gamma$ is the relativistic cyclotron frequency with $\Omega_0 = eB_0/mc$. For $n_z \simeq \beta_z \simeq 1$ the frequency is boosted to $2\gamma_z^2$ times the electron cyclotron frequency with $\gamma_z = (1 - \beta_z^2)^{-1/2}$. Note that both parallel and perpendicular kinetic energy of the electrons feed the instability in the case of a tilted resonator. So far, plane wave configurations in simple geometry [also referred to as the cyclotron autoresonance maser[24] (CARM)] have been analyzed[24-27] in conjunction with Doppler upshifting of the radiation frequency.

The induced resonance electron cyclotron (IREC) maser,[28-31] shown in Fig. 1, operates at Doppler upshifted frequencies, utilizing at the same time the advantages of the open resonators. Each resonator forms an angle $\alpha$ with the direction of the electron beam along the external magnetic field. The index of refraction $n_z = \cos\alpha$ is adjustable by varying the angle between the resonators and can be chosen to minimize the effects of finite beam thermal spreads. For operation at the optimum refraction index the efficiency is relatively insensitive to the beam energy spread. The sensi-

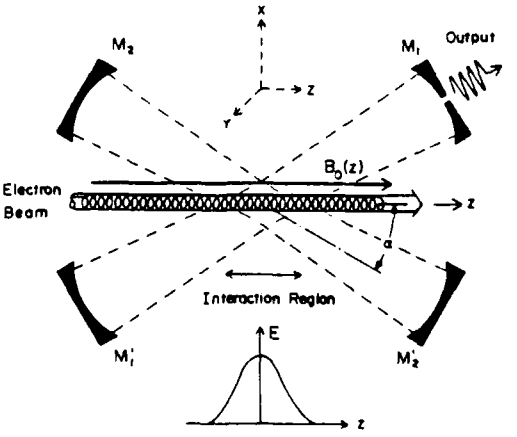



FIG. 1. Schematic illustration of the induced resonance electron cyclotron maser.

[a] Science Applications International Corporation, McLean, Virginia 22102.
[b] University of Maryland, College Park, Maryland 20742.

 0031-9171/88/040924-06$01.90 © 1988 American Institute of Physics 

tivity to the beam pitch angle spread can also be minimized. The interaction length inside the resonator that maximizes efficiency is of the order of one-half a bounce distance[14] for the trapped particles.

As the available magnetic field limits the maximum operation frequency for given $\gamma$, operation at higher harmonics[31,32] becomes very attractive. The magnetic field required to produce radiation at a given frequency is reduced to a fraction $1/(N+1)$ for operation at the $N$th harmonic. Operation at higher harmonics has been analyzed for the conventional[33,34] and quasioptical[35,36] gyrotron, showing that considerable efficiency can be achieved at the first few harmonics. Previous IREC studies have considered operation at the fundamental frequency and small Larmor radius, relevant to the case of small resonator angle and small pitch angle $\theta = v_\perp/v_z$. In the present work we analyze operation at any given harmonic $N$ and arbitrary resonator angle including finite Larmor radius effects. The effects of the Gaussian radiation profile are retained as well. A set of slow time scale equations of motion is derived by averaging over the cyclotron period time scale. The small signal efficiency is determined analytically. Nonlinear efficiency is determined by numerical integration. It is found that the efficiency for the first few harmonics is comparable to that for the fundamental in the same parameter regime. This is feasible because saturation occurs at larger radiation amplitude with higher harmonics. The effects of energy, pitch angle, and guiding center spread are also studied. An optimum resonator angle $\alpha$ exists for a given set of parameters minimizing the effects of finite beam thermal spreads. Efficiency enhancement can be achieved by properly tapering the external magnetic field,[29] inducing an extended wave particle resonance.

The remainder of this paper is organized as follows. In Sec. II we describe the field in the resonator and we obtain the fast-time averaged equation of motion. In Sec. III, the small signal efficiency and the start-up current required to trigger the oscillations in the resonator are calculated. In Sec. IV we discuss briefly the effects caused by the finite thermal spreads in the electron energy and pitch angle. In Sec. V we integrate numerically the equations of motion using velocity distributions with finite energy and pitch angle spread as well as guiding center distribution in the transverse direction. The nonlinear efficiency is computed for the first few harmonics.

## II. FIELD MODELING AND PARTICLE DYNAMICS

The configuration for the induced resonance electron cyclotron (IREC) maser is shown schematically in Fig. 1. The interaction cavity is formed by the two quasioptical resonators intersecting at an angle $2\alpha$ where $\alpha$ is the angle relative to the external magnetic field $B_0$ along the $z$ axis. The electron beam also propagates along $z$. The total vector field is the superposition of the two resonant fields

$$A(x', y', z';t)_{\alpha} + A(x', y', z';t)_{-\alpha}, \tag{1}$$

where $A(x', y', z';t)$ are eigenmodes of the Fabry–Perot-type resonator. Here we consider the lowest order Gaussian $\mathrm{TEM}_{(0)}$ modes linearly polarized along the $y$ axis

$$\begin{aligned} A(x', y', z';t) &= \hat{e}_y \tfrac{1}{4} A_0 \exp\{-i[(k/2)(x'^2+y'^2)/q(z') - \mu(z')]\} \\ &\quad \times \{\exp[i(kz'-\omega t)] + \exp[-i(kz'+\omega t')]\} \\ &\quad + \text{c.c.}, \end{aligned} \tag{2}$$

where

$$\frac{1}{q(z')} = \frac{1}{R(z')} - i\frac{\lambda}{\pi w^2(z')}, \quad R(z') = z'\left[1+\left(\frac{z'}{Z_0}\right)^2\right],$$

$$w(z') = w_0\left[1+\left(\frac{z'}{Z_0}\right)^2\right]^{1/2}, \quad \mu(z') = \tan^{-1}\left(\frac{z}{Z_0}\right),$$

$w_0$ is the beam waist at the center of the resonator, $\lambda$ is the wavelength, and $Z_0 = \pi w_0^2/\lambda$ is the Rayleigh length.

The coordinates $(x', y', z')_{\pm\alpha}$ have the $z'$ axis aligned with each resonator and are related to $(x, y, z)$ by

$$\begin{pmatrix} x' \\ z' \end{pmatrix} = \begin{pmatrix} \cos\alpha & \pm\sin\alpha \\ \pm\sin\alpha & \cos\alpha \end{pmatrix}\begin{pmatrix} x \\ z \end{pmatrix}, \quad y' = y. \tag{3}$$

The radiation field is assumed at temporarily steady state. The Gaussian width $w_0$ for the radiation envelope is much larger than the radiation wavelength $\lambda$ and the beam spot size $b$. The Rayleigh length $Z_0$ is typically much longer than the interaction length $L \sim w_0/\sin\alpha$ in the $z$ direction. In the vicinity of the beam $x \sim y \sim b$, and within the interaction regime $|z| \sim L$, we have $b/L \sim z/Z_0 \sim \epsilon \ll 1$, $b/Z_0 \sim \epsilon^2$. Combining Eqs. (1)–(3), and dropping terms of order $\epsilon^2$, the forward propagating component of the total field near the interaction area is expressed as

$$A_y(x, y, z;t) = \hat{e}_y A_0 e^{-(x^2\sin^2\alpha)/w_0^2} \cos k_\perp x \cos(k_z z - \omega t), \tag{4}$$

where $k_\perp = (\omega/c)\sin\alpha$, $k_z = (\omega/c)\cos\alpha$.

In short, Gaussian effects in the transverse direction of order $b^2/L^2 \sim \epsilon^2$ have been omitted while the electrons experience a Gaussian envelope of effective width $L = w_0/\sin\alpha$ in the $z$ direction. Only the forward propagating wave phase is considered in Eq. (4) since the synchronous interaction of an electron with the backward component occurs at downshifted cyclotron frequency, of small practical interest.

We use the guiding center description for the particle orbits

$$\begin{aligned} &x = x_g + \rho\sin\zeta, \quad y = y_g - \rho\cos\zeta, \\ &p_x = p_{gx} + p_\perp\cos\zeta, \quad p_y = p_{gy} + p_\perp\sin\zeta, \end{aligned} \tag{5}$$

with $(x_g, y_g)$ and $(p_{gx}, p_{gy})$ denoting the guiding center position and momentum, $\rho$ is the Larmor radius, $p_\perp$ is the magnitude of the transverse momentum, and $\zeta$ is the gyroangle. By averaging the exact Lorentz force equations in the vector potential representation over the fast (cyclotron) time scale, the slow time scale nonlinear relativistic equations of motion are cast in the form

$$\frac{dx_g}{dz} = -\frac{\Delta\omega}{\Omega_0}\frac{\gamma}{u_z} a J_N(k_\perp\rho)\sin\psi_N\cos g_N, \tag{6a}$$

$$\frac{dy_g}{dz} = \frac{ck_\perp}{\Omega_0}\gamma\frac{u_\perp}{u_z} a J'_N(k_\perp\rho)\cos\psi_N\cos g_N, \tag{6b}$$

$$\frac{du_\perp}{dz} = \left(\frac{\gamma\omega}{cu_z} - k_z\right) a J'_N(k_\perp\rho)\sin\psi_N\sin g_N, \tag{6c}$$

$$\frac{du_z}{dz} = k_z \frac{u_\perp}{u_z} a J'_N(k_\perp \rho)\sin\psi_N \sin g_N , \tag{6d}$$

$$\frac{d\psi_N}{dz} = -\frac{\gamma\Delta\omega}{cu_z} + \frac{N^2}{u_\perp}\left(\frac{\gamma\omega}{cu_z} - k_z\right) a \times \frac{J'_N(k_\perp\rho)}{k_\perp\rho}\cos\psi_N \sin g_N - N\frac{k_\perp}{u_z} a J_N(k_\perp\rho)\cos\psi_N \sin g_N . \tag{6e}$$

In Eqs. (6a)–(6e) the prime ( ′ ) signifies the Bessel function derivative in respect to the argument, $u$ is the normalized momentum $u = p/mc = \gamma v/c$, $\gamma$ is the relativistic factor $\gamma = (1 + u_\perp^2 + u_z^2)^{1/2}$, $\psi_N = k_z z - \omega t + N\zeta + N\pi/2$ is the relative phase between the field and the particle, $g_N = k_\perp x_g - N\pi/2$ carries the dependence on the guiding center position, $a(z) = a_0 \exp(-z^2/L^2)$ is the normalized radiation amplitude with $a_0 = eA_0/mc^2$, and the detuning in frequency $\Delta\omega$ is given by

$$\Delta\omega = \omega(1 - n_z\beta_z) - N\Omega_0/\gamma . \tag{7}$$

It is the dependence of the detuning $\Delta\omega$ on the particle energy through the relativistic correction $\gamma$ that causes the phase bunching and the radiation amplification in the linear regime. The evolution of $\gamma$ is found combining Eqs. (6c)–(6e),

$$\frac{d\gamma}{dz} = \frac{\omega}{c}\frac{u_\perp}{u_z} a J'_N(k_\perp\rho)\sin\psi_N \sin g_N . \tag{8}$$

In performing the fast-time averaging to obtain Eqs. (6)–(8) we have assumed that the particles always remain close to resonance with a single harmonic $N$, i.e., $\omega(1 - n_z\beta_z) - N\Omega_0/\gamma \simeq 0$. Therefore the change in energy $\Delta\gamma$ and consequently the radiation amplitude $a_0$ cannot exceed a certain limit. When $a_0$ is very large, the particles may also experience resonant effects from nearby harmonics $N \pm 1$. The validity conditions for a single resonant harmonic are satisfied in the parameter regime under consideration.

The nonlinear system of differential equations (6)–(8) cannot be solved analytically in terms of elementary functions, except in some special cases.[37,38] We resort to numerical integration in order to examine the nonlinear behavior while the small signal analysis is done by perturbation theory.

## III. SMALL SIGNAL EFFICIENCY

One of the issues concerning intense microwave generation is the intrinsic efficiency $\eta$ of the interaction, defined as

$$\eta = -\frac{\langle\gamma_f - \gamma_0\rangle}{\langle\gamma_0 - 1\rangle} = -\langle\gamma_0 - 1\rangle^{-1}\int dp_0^3 f(p_0) \times \int dg_0 \int d\psi_0 \int_{-\infty}^{\infty} dz \frac{d\gamma}{dz} , \tag{9}$$

where $\langle\ \rangle$ signifies the average over the initial distribution in phase space, and $\gamma$ is a function of the initial conditions $\gamma(z;p_{\perp 0},p_{z0},\psi_0,g_0)$ with $\psi_0 = \psi_N(-\infty)$ and $g_0 = g_N(-\infty)$. We compute the small signal efficiency in order to determine the beam current required to overcome losses and start the cavity oscillations. After obtaining the linearized solutions of Eqs. (6)–(8), we substitute them into the integrand on the right-hand side of Eq. (9). The evaluation of the final result is considerably simplified by taking the phase space average over $\psi_0$ before the spatial integration[22,36] over $z$. Expanding the products of trigonometric terms inside the integrand into sums, averaging over $\psi_0$, and extending the limits of the $z$ integration to $\pm\infty$, we obtain the linear efficiency in terms of the initial conditions

$$\eta = \frac{\pi}{2}\frac{a_0^2\xi^2}{\gamma_0(\gamma_0 - 1)}[J'_N(s_0)]^2 \exp\left(-\frac{1}{2}\xi^2\frac{\Delta\omega_0^2}{\omega^2}\right)\langle\sin^2 g_0\rangle \times\left[(n_z\beta_{z0} - 1)\left(1 + \frac{N^2 J_N(s_0)}{s_0 J'_N(s_0)} + \frac{s_0 J''_N(s_0)}{J'_N(s_0)}\right) + \theta_0\beta_{z0}\left(\theta_0 n_z + \frac{NJ_N(s_0)}{J'_N(s_0)}n_\perp\right) + \left(\xi^2\beta_{\perp 0}^2(1 - n_z^2) - \frac{\langle\cos^2 g_0\rangle}{\langle\sin^2 g_0\rangle}\frac{s_0 J_N(s_0)}{J'_N(s_0)}\right)\left(\frac{\Delta\omega_0}{\omega}\right) - n_z\beta_{z0}\theta_0^2\xi^2\left(\frac{\Delta\omega_0}{\omega}\right)^2\right], \tag{10}$$

where $s_0 = k_\perp\rho_0$, $g_0 = k_\perp x_{g0} - N\pi/2$, $\beta_{\perp 0} = v_{\perp 0}/c$, $\beta_{z0} = v_{z0}/c$, $\theta_0 = v_{\perp 0}/v_{z0}$, and $\langle f\rangle = (1/2\pi)\int_0^{2\pi} d(k_\perp x_g) f$ is the average over the initial guiding center position.

We have chosen to express $\eta$ in terms of the parameters $\Delta\omega_0/\omega$ and $\xi = \omega\tau$, where $\tau = \gamma_0 L/cu_{z0}$ is the transit time through the interaction regime. The argument $\xi\Delta\omega_0/\omega$ in the exponential is equal to $\Delta\omega_0\tau$, the linear advance in the relative phase $\Delta\psi_0$ over the interaction regime. The sign is determined by the angular bracket on the right-hand side of Eq. (10). Treating the bracket as a quadratic form in $\Delta\omega_0/\omega$ and keeping the lowest order contribution in $k_\perp\rho$, we find that the regime for positive efficiency is given approximately by

$$\frac{[(N+1)(1 - n_z\beta_{z0}) - \theta_0^2 n_z\beta_{z0}]}{(1 - n_z^2)\beta_{\perp 0}^2\xi_0^2} < \frac{\Delta\omega_0}{\omega} < \frac{\beta_{\perp 0}^2(1 - n_z^2)}{n_z\beta_{z0}\theta_0^2} . \tag{11}$$

The upper limit in $\Delta\omega_0/\omega$ is caused by the finite $n_z$ and results from the negative contribution of the quadratic term $(\Delta\omega/\omega)^2$ that overtakes the positive contribution of the linear terms for small angle,

$$\sin^2\alpha < (n_z\beta_{z0}\theta_0^2/\beta_{\perp 0}^2)(\Delta\omega_0/\omega) .$$

For typical operation parameters we have $\xi \gg 1$ and $\Delta\omega_0/\omega \ll 1$. In order to estimate the maximum efficiency

within the positive regime, we parametrize Eq. (10) as a function of $\zeta = \xi\Delta\omega_0/\omega$ and look for the zeros of the cubic equation resulting from $d\eta/d\zeta = 0$. If the angle $\alpha$ is not too small, $\sin^2\alpha \gg 1/\xi\beta_{\perp 0}^2$ where $\xi \gg 1$, then the maximum occurs at $\zeta \simeq 1$, yielding

$$\eta_{\max} \simeq (\pi/8)\left[a_0^2\xi_0^3\{J'_N(k_\perp\rho_0)\}^2\beta_{\perp 0}^2/(\gamma_0-1)\gamma_0\sin\alpha\right]\exp(-\tfrac{1}{2}), \quad (12)$$

where $\xi_0^2 = \xi^2(1-n_z^2) = (\omega_0\gamma_0\omega/cu_{z0})^2$ is independent of $\alpha$. The small signal efficiency increases with decreasing angle $\alpha$ (increasing index of refraction $n_z$) provided that $\sin\alpha$ satisfies the inequality above Eq. (12). When $\sin\alpha$ is too small, an exact solution of the cubic equation for $\zeta$ is required and Eq. (12) is invalid.

We now calculate the start-up beam current using the small signal efficiency. Amplification of the electromagnetic radiation is possible if

$$\eta P_b > \frac{dE}{dt} = \frac{\omega}{Q}E, \quad (13)$$

where $E = \frac{1}{4}w_0^2 L_R a_0^2(\omega^2/c^2)(m^2c^4/|e|^2)$ is the total energy stored inside both resonators, $L_R$ is the resonator length, $dE/dt$ is the combined refraction, diffraction, and transmission losses, and $Q$ is the quality factor for the cavity. Combining Eqs. (12) and (13) we obtain

$$I_s V_b > 2\frac{\beta_{z0}^3}{\beta_{\perp 0}^2}\frac{\gamma_0(\gamma_0-1)\sin\alpha\exp(-\frac{1}{2})}{\pi[J'_N(k_\perp\rho_0)]^2}\frac{m^2c^5}{|e|^2}\frac{L_R}{\omega_0 Q}. \quad (14)$$

For small Larmor radius $k_\perp\rho_0 \ll 1$ the start-up current $I_s$ increases very quickly with the harmonic $N$, $I_s \propto 2^{2N}[(N-1)!]^2/(k_\perp\rho_0)^{-(N-1)}$. It is therefore desirable to operate at $k_\perp\rho_0 \gg 1$ in order to have good coupling to the resonator modes and low start-up currents. In this case the start-up current scales roughly as the inverse maximum of the Bessel function derivative, $I_s \propto N^{2/3}$, increasing mildly with the harmonic $N$. We can achieve harmonic selection by choosing $k_\perp\rho_0$ near a maximum of $J'_N(k_\perp\rho_0)$ for the intended $N$th harmonic.

Expression (14) for the start-up current was derived using coherent resonator modes. These modes have evolved from an initial noise background of spontaneous cyclotron radiation. During the spontaneous emission stage preceding coherency most of the emitted radiation is contained within a cone of angle $1/\gamma$ around the direction of the particle velocity $v$. Since $v$ makes an angle $\Theta = \tan^{-1}(v_\perp/v_z)$ with the magnetic field the condition $|\Theta - \alpha| \lesssim 1/\gamma$ must be met to avoid excessive losses during the start-up phase.

## IV. THERMAL EFFECTS

One of the important features associated with the IREC maser is choosing the index of refraction appropriately to minimize the effects of the electron beam thermal spreads. Spreads in the initial electron momentum will cause a spread in the detuning parameters $\Delta\omega_0$ among different particles. This in turn will cause an accelerated mixing in phase space opposing the nonlinear phase bunching and reducing in efficiency. According to Eq. (7) a standard deviation

$$\delta(\Delta\omega_0) = \left[\left(\frac{\partial\Delta\omega}{\partial\beta}\right)^2\delta\beta_z^2 + \left(\frac{\partial\Delta\omega}{\partial\beta_\perp}\right)^2\delta\beta_\perp^2\right]^{1/2} = \left[(\omega n_z - N\Omega_0\gamma_0\beta_{z0})^2\delta\beta_z^2 + (N\Omega_0\gamma_0\beta_{\perp 0})^2\delta\beta_\perp^2\right]^{1/2} \quad (15)$$

in the initial detuning results from a beam distribution with velocity deviations $\delta\beta_z$ and $\delta\beta_\perp$. The choice of resonator angle

$$n_z = \cos\alpha = N\Omega_0\gamma_0\beta_{z0}/\omega \quad (16)$$

causes the minimum initial spread in $\Delta\omega_0$ for any beam thermal spreads. The minimum spread from Eqs. (15) and (16) can also be expressed in terms of the pitch angle spread $\delta\theta_0$ and the energy spread $\delta\gamma_0$. Then, the requirement for small phase mixing among various particles over the interaction length $L$, namely, $\delta(\Delta\omega)_0 L/c\beta_z \ll \pi$, suggests

$$\frac{\delta\theta_0}{\theta_0} + \frac{1}{\gamma_0^2}\frac{\delta\gamma_0}{\gamma_0} \ll \frac{\beta_{z0}}{2N_c(N\beta_{\perp 0}^2\gamma_0^2)}, \quad (17)$$

where $N_c = \Omega_0 L/(2\pi\gamma_0 c\beta_{z0})$ is the approximate number of cyclotron gyrations within the interaction length. The beam thermal spread requirements become more stringent with increasing harmonic $N$.

In the nonlinear operation regime the electrons get trapped in the wave potential[14,38] and execute synchrotron oscillations in phase space in a similar manner as in the conventional gyrotrons. The phase mixing among various particles is now determined by the dependence of the trapped particle synchrotron period on the various parameters. The efficiency deterioration involves more factors than the initial spread in the detuning $\Delta\omega_0$, which is the dominant source of phase mixing only in the small signal regime $a_0 \ll 1$. Analytic predictions similar to Eq. (16) are hard to make in the nonlinear case. Our numerical results show that when the index of refraction is optimized according to (16) the nonlinear efficiency is practically insensitive to the energy spread $\delta\gamma_0/\gamma_0$.

## V. NUMERICAL RESULTS

In this section, we investigate various aspects of the nonlinear performance by numerically integrating Eqs. (6a)–(6e). We consider an electron beam of $\gamma_0 = 2.5$ ($\sim$0.75 MeV) with $\beta_{\perp 0} = 1/\gamma_0$ and $\beta_{z0} = 0.825$ in a guide magnetic field of strength $B_0 = 40$ kG. The appropriate index of refraction to minimize the effect of energy spread is, according to Eq. (16), $n = 0.982$, which corresponds to an angle $\alpha = 11°$. The frequency is upshifted by a factor $N/(1-n\beta_{z0}) = 5.26N$ times the relativistic cyclotron frequency, and corresponds to a wavelength of 0.41 mm for the third harmonic $N = 3$ and 0.31 mm for the fourth harmonic $N = 4$. The radiation spot size $w_0$ is 0.50 cm and the Rayleigh lengths are 14.3 and 25.8 cm for $N = 3$ and $N = 4$, respectively. We consider a uniform guiding center distribution in the interval $0 < k_\perp x_g < 2\pi$.

Curves of efficiency $\eta$ vs $a_0$ for various values of the detuning $\Delta\omega_0/\omega$ are plotted for $N = 3$ and $N = 4$ in Figs. 2 and 3, respectively. These results correspond to a cold beam

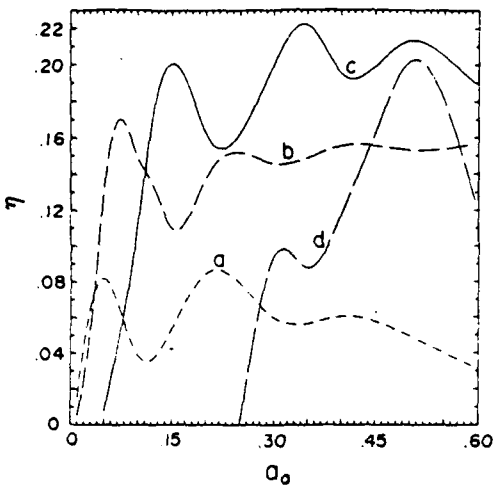



FIG. 2. Plots of efficiency $\eta$ versus the normalized radiation amplitude $a_0$ at the third harmonic $N = 3$ and for detuning parameters $\Delta\omega_0/\omega$ equal to curve a 0.025, curve b 0.050, curve c 0.075, and curve d 0.100, respectively. A cold beam of uniform guiding center spread is considered. The simulation parameters are $\gamma_0 = 2.5$, $\alpha = 11°$, $w_0 = 0.5$ cm, and $\theta_0 = 0.48$.

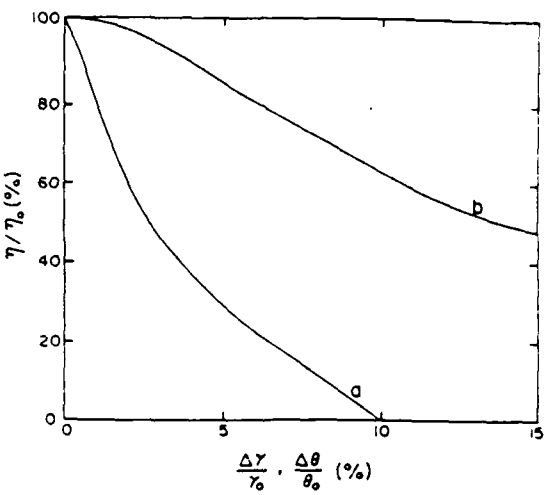



FIG. 4. Dependence of the efficiency on beam thermal spreads. Shown is the ratio of thermalized to cold beam efficiency $\eta/\eta_0$ as a function of curve a pitch angle spread $\delta\theta_0/\theta_0$ with $\delta\gamma_0 = 0$ and curve b energy spread $\delta\gamma_0/\gamma_0$ with $\delta\theta_0 = 0$. The parameters are the same as in Fig. 2 with $\Delta\omega_0/\omega = 0.075$.

without thermal spreads. We find the efficiency for the first few harmonics comparable to the efficiency for the fundamental[29] under the same operation parameters. Efficiency saturation occurs for larger amplitude $a_0$ compared to the operation at the fundamental. Figure 4 shows the effects of finite beam quality on efficiency when the electron beam has either a spread in the pitch angle or a spread in energy. We plot the ratio of the thermalized efficiency $\eta$ over the cold beam efficiency $\eta_0$ for the third harmonic $N = 3$ at fixed amplitude $a_0 = 0.20$. Curve a for zero energy spread, $\Delta\gamma_0/\gamma_0 = 0$, shows that the half-width in the pitch angle spread that reduces efficiency by 50%, is equal to $\Delta\theta_0/\theta_0 = 2\%$. Curve b for zero pitch angle spread, $\Delta\theta_0/\theta_0 = 0$, shows that the half-width in energy spread is $\Delta\gamma_0/\gamma_0 = 13\%$. Efficiency tends to be more sensitive on the spread in the pitch angle than the spread in energies; therefore, we may simulate thermal effects by including only pitch angle spreads, cutting down on computing time.

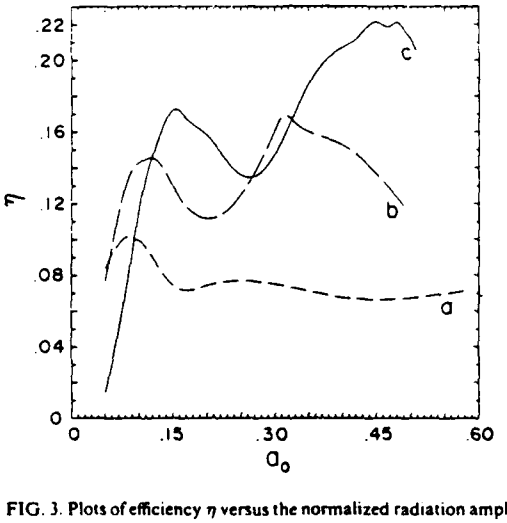



FIG. 3. Plots of efficiency $\eta$ versus the normalized radiation amplitude $a_0$ at the fourth harmonic $N = 4$ for detuning parameter $\Delta\omega_0/\omega$ equal to curve a 0.025, curve b 0.037, and curve c 0.050, respectively. The other parameters are the same as in Fig. 2.

Given that the large signal efficiency depends on few parameters, predictions about optimum operation at maximum efficiency are hard to make. One anticipates maximum efficiency when the transit time through the interaction regime is about equal to one-half the synchrotron period for a trapped particle. An optimum interaction length in the $z$ direction $L_z \simeq 2L = 2w_0/\sin\alpha$ corresponds to a given synchrotron period $\omega_b$, which, in turn, depends on the five parameters $a_0$, $\gamma_0$, $\theta_0$, $\Delta\omega_0$, and $\cos\alpha$. This is illustrated in Fig. 5, which shows efficiency as a function of the traveled distance $z$ for three different Gaussian profiles corresponding to different radiation spot sizes $w_0$, keeping the other parameters fixed. In curve a the interaction length is less than one-half the bounce distance $L_b = \pi c\beta_z/\omega_b$ and the electrons exit the resonator before reaching the point of lowest energy in their trajectories. In curve b we have a good matching of $L_z$ with $L_b$ achieving the highest efficiency. In curve c $L_z$ is larger than $L_b$ and the electrons overshoot the point of minimum energy, gaining energy back from the wave and reducing efficiency.

From the practical point of view, one would like to optimize the design parameters of the resonator $\alpha$ and $L$ for a given beam energy $\gamma_0$ and pitch angle $\theta_0$ under the maximum energy load $a_0^2$ sustained by the cavity. We already picked the operation angle $\cos\alpha$ so as to minimize the effects the beam energy spread. In Fig. 6 we show the efficiency as a function of the interaction length $L_z$ by varying the spot size $w_0$ and keeping all other parameters fixed. The upper curve shows the nonlinear efficiency for a monoenergetic electron beam of infinitesimal spot size $b \ll w_0$, and a uniform spread in the initial phase $0 < \psi_0 < 2\pi$. A uniform guiding center dis-

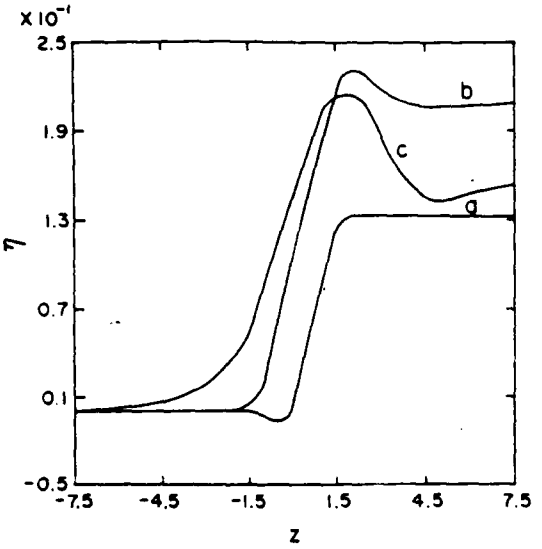



FIG. 5. Plots of efficiency $\eta$ versus traveled distance $z$ inside the resonator for various interaction lengths corresponding to different radiation spot sizes $\omega_0$. The center of the resonator is at $z = 0$. Here, $L_z$ is equal to curve a 2.64 cm, curve b 4.24 cm, and curve c 7.41 cm. The parameters are the same as in Fig. 2 with $\Delta\omega_\parallel/\omega = 0.075$.

tribution $0 \leq k_\perp x_g \leq 2\pi$ is included in the second curve. The resulting efficiency reduction is no more than 30% indicating that some bunching in the guiding center position takes place as well. The addition of a 2% energy spread $\delta\gamma_0/\gamma_0$ with zero pitch angle spread does not reduce efficiency considerably in the fourth curve. A 2% spread in the pitch angle $\delta\theta_0/\theta_0$ with zero energy spread has a more pronounced effect on efficiency shown in the lowest curve d. The overall picture shows that, for the parameters chosen, efficiency has a weak dependence on the interaction length $L$ falling off slowly after an optimum length of $L \sim 4$ cm.

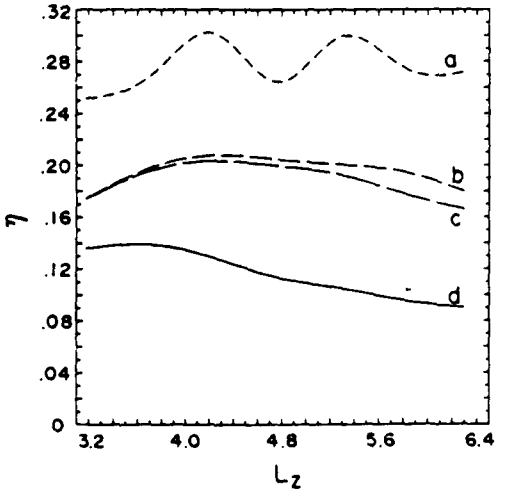



FIG. 6. Plots of efficiency $\eta$ versus interaction length $L_z$ with the same parameters as before. Curve a is for a cold beam of zero cross section and curves b–d for a uniform guiding center spread with curve b no thermal spreads, curve c 2% energy spread, and curve d 2% pitch angle spread.

## ACKNOWLEDGMENT

This work was supported by the U.S. Department of Energy under Contract No. DE-AI05-83ER40117, Modification 3.

[1] R. Q. Twiss, Aust. J. Phys. 11, 564 (1958).
[2] A. V. Gaponov, Izv. Vyssh. Uchebn. Zaved. Radiofiz. 2, 450 (1959).
[3] R. H. Pantell, Proc. IRE 47, 1146 (1959).
[4] J. Schneider, Phys. Rev. Lett. 2, 504 (1959).
[5] J. L. Hirshfield and J. M. Wachtel, Phys. Rev. Lett. 12, 533 (1964).
[6] A. V. Gaponov, M. I. Petelin, and V. K. Yulpalov, Radiophys. Quantum Electron. 10, 794 (1967).
[7] V. L. Bratman, M. A. Moiseev, M. I. Petelin, and R. E. Erm, Radiophys. Quantum Electron 16, 474 (1973).
[8] D. V. Kisel, G. S. Korablev, V. G. Navel'yev, M. I. Petelin, and Sh. E. Tsimring, Radio Eng. Electron. Phys. 19, 95 (1974).
[9] N. I. Zaytsev, T. B. Pankratova, M. I. Petelin, and V. A. Flyagin, Radio Eng. Electron. Phys. 19, 103 (1974).
[10] V. L. Granatstein, M. Herndon, R. K. Parker, and P. Sprangle, IEEE J. Quantum Electron. QE-10, 651 (1974).
[11] E. Ott and W. M. Manheimer, IEEE Trans. Plasma Sci. PS-3, 1 (1975).
[12] V. L. Granatstein, P. Sprangle, M. Herndon, and R. K. Parker, J. Appl. Phys. 46, 2021 (1975).
[13] P. Sprangle and W. M. Manheimer, Phys. Fluids 18, 224 (1975).
[14] P. Sprangle and A. T. Drobot, IEEE Trans. Microwave Theory Tech. MTT-25, 528 (1977).
[15] J. L. Hirshfield and V. L. Granatstein, IEEE Trans. Microwave Theory Tech. MTT-25, 522 (1977).
[16] K. R. Chu and J. L. Hirshfield, Phys. Fluids 21, 461 (1978).
[17] V. L. Bratman, N. S. Ginzburg, and M. I. Petelin, Opt. Commun. 30, 409 (1979).
[18] P. Sprangle and R. A. Smith, J. Appl. Phys. 51, 3001 (1980).
[19] C. S. Wu and L. C. Lee, Astrophys. J. 230, 621 (1979).
[20] P. L. Pritchett, Phys. Fluids 29, 2919 (1986).
[21] A. Bondeson, W. M. Manheimer, and E. Ott, Infrared Millimeter Waves 9, 309 (1983).
[22] P. Sprangle, J. L. Vomvorides, and W. M. Manheimer, Appl. Phys. Lett. 38, 310 (1981); Phys. Rev. A 23, 3127 (1981).
[23] J. L. Vomvorides and P. Sprangle, Phys. Rev. A 25, 931 (1982).
[24] M. I. Petelin, Radiophys. Quantum Electron. 17, 686 (1974); also V. L. Bratman, N. S. Ginzburg, and M. I. Petelin, Opt. Commun. 30, 409 (1979).
[25] V. L. Bratman, G. G. Denisov, N. S. Ginzburg, and M. I. Petelin, IEEE J. Quantum Electron. QE-19, 282 (1983).
[26] K. E. Kreisher and R. J. Temkin, Infrared Millimeter Waves 7, 377 (1983).
[27] A. W. Fliflet, Int. J. Electron. 61, 1049 (1986).
[28] P. Sprangle, C. M. Tang, and P. Serafim, Appl. Phys. Lett. 49, 1154 (1986).
[29] P. Sprangle, C. M. Tang, and P. Serafim, Nucl. Instrum. Methods Phys. A 250, 361 (1986).
[30] S. Riyopoulos, C. M. Tang, and P. Sprangle, Phys. Rev. A 36, 197 (1987).
[31] C. M. Tang, S. Riyopoulos, P. Sprangle, and B. Levush, in *Proceedings of the Eighth International Conference on Free Electron Lasers*, Glasgow, Scotland, edited by M. Poole (North-Holland, Amsterdam, 1986), p. 192.
[32] V. L. Bratman, N. S. Ginzburg, and A. S. Sergeev, Sov. Phys. JETP 55, 479 (1985).
[33] A. V. Gaponov, V. A. Flyagin, A. L. Goldenberg, G. S. Nusinovich, Sh. E. Tsimring, V. G. Usov, and S. N. Vlasov, Int. J. Electron. 51, 277 (1981).
[34] B. G. Danly and R. J. Temkin, Phys. Fluids 29, 561 (1985).
[35] B. Levush, A. Bondeson, W. M. Manheimer, and E. Ott, Int. J. Electron. 54, 749 (1983).
[36] B. Levush and W. Manheimer, IEEE Trans. Microwave Theory Tech. MTT-32, 1398 (1984).
[37] Y. Gell, J. R. Torstensson, H. Wilhelmsson, and B. Levush, Appl. Phys. B 27, 15 (1982).
[38] J. L. Vomvorides, Int. J. Electron. 53, 555 (1982).

# APPENDIX JJ

## The Structure of the Sideband Spectrum in Free Electron Lasers

# The structure of the sideband spectrum in free electron lasers

S. Riyopoulos[a] and C. M. Tang
*Plasma Physics Division, Naval Research Laboratory, Washington, D.C. 20375-5000*

(Received 17 August 1987; accepted 26 February 1988)

The one-dimensional, fast time averaged Hamiltonian is derived in a free electron laser (FEL) for electrons passing through a constant parameter wiggler and a radiation field. The exact unperturbed orbits without sidebands are obtained for all particles and arbitrary strength of the main signal. Integration, in action-angle variables, of the linearized kinetic equation with perturbing sidebands over the unperturbed orbits yields the sideband growth rate including both trapped and untrapped particles. The structure and scaling of the unstable spectrum are different from previous results obtained for electrons localized at the bottom of the ponderomotive well. It is found that upper and lower sidebands that are symmetric relative to the FEL frequency have opposite growth rates. There is no differentiation in the magnitude of the gain between upper and lower sidebands. The stability is determined by the sign of $df_0/d\omega_b$, the relative population of quantized oscillators with energy quantum $\hbar\omega_b$, where $\omega_b$ is the synchrotron frequency in resonance with the sideband. The shear $d\omega_b/dJ$, where $J$ is the action variable, is stabilizing and distributions with gradients $df_0/dJ$ localized near the separatrix have the minimum growth rates.

## I. INTRODUCTION AND SUMMARY

Free electron lasers (FEL's) have recently attracted a lot of attention as effective sources of coherent radiation generated by relativistic electron beams. This is evidenced by the ever-growing literature on the subject since the 1950's when the FEL concept was first introduced.[1-4] Theoretical studies have included small signal analysis[5-11] in both Compton and Raman regimes, nonlinear behavior and efficiency enhancement,[12-15] electrostatic effects,[16] harmonic generation,[17,18] and finally multidimensional effects.[19-21]

An increasing volume of experimental results[22-33] for FEL's operating either as amplifiers or as oscillators demonstrates the potential of successful operation in a wide range of electron beam energies ranging approximately from 1 to 200 MeV and peak currents going up to kiloamperes. Superradiant FEL operation with the signal starting from the noise level has also been considered.[34]

An oversimplified picture of an FEL is drawn in Fig. 1. Relativistic electrons traveling through the periodic magnetic structure (wiggler) oscillate emitting electromagnetic radiation according to the laws of classical electrodynamics. It follows that the frequency $\omega_r$ of the radiation emitted along the beam direction is twice Doppler upshifted relative to the electron wiggling frequency $\omega_0 = k_w v_z$, i.e.,

$$\omega_r \equiv 2\gamma_z^2\omega_0, \quad \gamma_z = \{1 - (v_z/c)^2\}^{-1/2}.$$

In addition, the radiated power is confined within a very narrow cone in the direction of the beam. The oscillating electrons at different positions in the beam interact coherently with the radiation field if their velocity $v_z$ is approximately the phase velocity

$$v_p \equiv \omega_r/(k_r + k_w)$$

of the ponderomotive wave formed by the beating of the radiation field with the wiggler field. This implies that one wavelength of the radiation passes over an electron while the electron travels one wavelength of the wiggler.

In the small signal, exponential growth regime the electrons bunch in phase space in the regimes where they decelerate giving up energy to the radiation field. Once the radiation field exceeds a certain amplitude the electrons become trapped in the ponderomotive well, executing "synchrotron" oscillations in phase space around the resonant energy $\gamma_r$, where

$$\gamma_r^2 = [1 + (ek_w\langle B_w\rangle/mc^2)^2]\gamma_z^2$$

and $\langle B_w\rangle$ and $k_w$ are the rms wiggler strength and the wavenumber, respectively. This is the saturation stage for untapered wiggler FEL's. Considerable efficiency improvement results by properly tapering the wiggler parameters. As the center of the trapped particle bucket $\gamma_r$ decelerates the kinetic energy of the beam is continuously converted into radiation energy.

An important issue for high power FEL operation at finite amplitude of the main signal is the stability of the configuration against the growth of parasitic modes. The low frequency oscillations of the trapped electrons generate current components at frequencies shifted from the electron wiggling frequency $\omega_0$ by some multiple of the synchrotron frequency $\omega_b$. Then the radiation associated with these currents will appear at frequencies separated from the carrier by a multiple of the twice Doppler upshifted synchrotron fre-

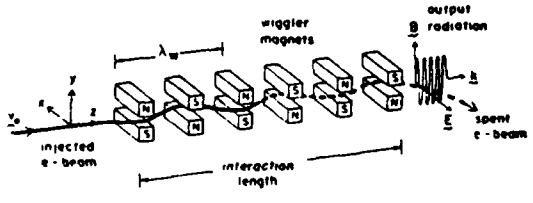



FIG. 1. Schematic illustration of a free electron laser with a linearly polarized wiggler.

[a] Permanent address: Science Applications International Corp., McLean, Virginia 22102.

 0031-9171/88/061708-12$01.90 © 1988 American Institute of Physics 

quency. It has been predicted theoretically[15] that these sideband frequencies can become unstable. Numerical simulations,[16–40] as well as experimental observations,[41,42] have shown that sidebands may develop to a significant fraction of the overall power. Degradation in the optical quality of the FEL signal is one outcome of the sideband excitation. The performance of the mirrors in an oscillator-type operation can be harmed from the modulation of the wave envelope caused by the sidebands. Last—but not least—the growth of sidebands above a certain threshold may cause chaotic electron motion leading to detrapping and loss of amplification for the radiation field.

The above have stimulated a considerable amount of theoretical work focused on sideband growth. Simple one-dimensional configurations that are analytically tractable have been used to model the situation. Two lines of approach have been considered. The single particle picture regards the particle trajectories as functions of the initial conditions and computes the gain by ensemble averaging over initial distributions.[43,44] The alternative approach assumes some adiabatic equilibrium between the particles and the main signal and examines the stability of the perturbations induced by the sidebands, solving the kinetic equation.[45–48] Continuous electron distributions have been formally included in the kinetic equation.

In both treatments so far, analytic results have been obtained only for trapped particles localized near the bottom of the ponderomotive well, and/or streaming particles far from the separatrix.[48] This implies the following limitations.

(i) The sideband spectrum is restricted to discrete frequencies

$$\omega_s = \omega_r \pm (k_r/k_w) n \omega_b(0). \tag{1}$$

The frequency mismatch between the main signal $\omega_r$ and the sideband $\omega_s$ is equal to $n$ times the Doppler upshifted bounce frequency $\omega_b(0)$ at the bottom of the ponderomotive potential.

(ii) The contribution from the majority of the trapped as well as the untrapped particles is ignored.

(iii) The effect of the shear $d\omega_b/dJ$, where $J$ is the action variable parametrizing the distance from the bottom of the well $J=0$ (see Sec. II), is neglected.

(iv) Predictions of asymmetric growth rates, with the lower sidebands $\omega_s < \omega_r$ growing much faster than the upper sidebands $\omega_s > \omega_r$, are not always supported by experimental results.[41,42]

Here canonical formalism is introduced by expressing the unperturbed particle orbits in terms of action-angle variables.[49] The unperturbed orbits are the fast time averaged "synchrotron" oscillations of the electrons in the potential well formed by the combined action of the wiggler and the radiation signal. The perturbed kinetic equation is solved in action space, starting from an equilibrium extending over all trapped and untrapped electrons. The following statements can be made.

(a) The sideband spectrum becomes continuous, replacing $\omega_b(0)$ by $\omega_b(J)$ in Eq. (1). The modes located at the peaks of the unstable spectrum grow faster, emerging as the discrete spectrum observed in simulations.

(b) More than one group of particles are in resonance with a sideband of a given frequency $\omega_s$ through different harmonics of their bounce frequency and contribute significantly to its growth rate.

(c) Upper and lower sidebands located symmetrically around the main signal frequency have opposite growth rates (complementary stability). Therefore some mode is always unstable. There is no stable distribution $f_0(J)$ except the trivial one $df_0/dJ = 0$.

(d) In general, upper and lower sidebands have comparable growth rates. A similar conclusion, applying to a special type of distribution, appeared recently in Ref. 47. Previous results, finding lower sidebands having an inherently larger gain than upper sidebands, are relevant only to the limiting case of a singular distribution $f_0(J)$ with particles localized at the bottom of the potential well. This case is unrealistic because even an ideal cold beam initial distribution $f_0(p) = \delta(p - p_0)$ corresponds to a wide, smooth distribution $f_0(J)$ in action space.

(e) For any smooth distribution, of finite $df_0/dJ$, electrons at the bottom of the ponderomotive well have a negligible effect on stability.

(f) The shear $d\omega_b/dJ$ is stabilizing. Distributions with gradients $df_0/dJ$ localized near the separatrix are found to have the minimum growth rates because of the high shear there. This type of distribution is relevant to FEL's with tapered wigglers.

(g) The gain is proportional to $[df_0(J)/d\omega_b(J)]$, the relative population of quantized oscillators with the energy quantum $\hbar\omega_b$ in resonance with the sideband frequency mismatch. This agrees with the quantum mechanical interpretation.

The nonlinear saturation levels for the unstable modes and the sideband amplitude for transition to stochastic electron motion can also be derived using canonical formalism and will be addressed in future work.

The remainder of the paper is organized as follows. In Sec. II a simple model field is used to study the particle dynamics. Action-angle variables are introduced and the exact solutions for the unperturbed orbits are found. The perturbed Hamiltonian is expanded into harmonics of the unperturbed motion. In Sec. III we obtain the linearized solution of the kinetic equation around some equilibrium $f_0(J)$. The gain is computed including all contributing trapped and untrapped electrons. In Sec. IV the interpretation and general implications of the derived formula are presented. A connection is made with quantum mechanics. In Sec. V we consider some special cases of simple distribution functions. The limit of particles localized at the bottom of the ponderomotive well is taken. In Sec. VI we examine the structure of the unstable spectrum for certain types of distributions $f_0$ and we draw conclusions about minimizing the instability.

## II. PARTICLE DYNAMICS

A one-dimensional model for the instability will be studied with relativistic electrons streaming along the $z$ direction through a linearly polarized wiggler of constant amplitude and wavelength. The components of the radiation field are

plane electromagnetic waves with constant amplitude. Electrostatic effects are ignored assuming a low current, tenuous beam. The combined vector potential is taken to be

$$A_y(z,t) = A_w \cos k_w z + A_r \cos(k_r z - \omega_r t) + A_s \cos(k_s z - \omega_s t) \tag{2}$$

composed by the wiggler field $A_w$, the main signal $A_r$, and a sideband $A_s$. Dispersive effects are generally very small, of order $(\omega_p/\omega_r)^2 \ll 1$, where $\omega_p^2 = 4\pi n_b e^2/m_e$ is the beam plasma frequency, and all electromagnetic waves propagate with the speed of light $c$. Thus corrections in the real part of the frequency $\omega_s(k_s) = ck_s$ are negligible while the imaginary part of $\omega_s$ is computed from the wave-particle energy balance equation without solving a dispersion relation.

We assume that the change in the main signal strength is slow compared to the characteristic time of interest, the synchrotron period $\tau_b$ for the trapped electrons, letting $A_r$ be a constant. Then an unperturbed electron distribution $f_0$ (without the sidebands) exists in equilibrium with the main signal, $df_0/dt = 0$. The above scenario is relevant to FEL operation characterized by high power and slow main signal growth. The sidebands are assumed suppressed during periods of fast, exponential growth for the main FEL signal. The exact equations of motion for an electron are

$$\frac{d}{dt}P_z = -\frac{\partial H}{\partial z}, \quad \frac{d}{dt}z = \frac{\partial H}{\partial P_z}, \qquad \frac{d}{dt}P_y = \frac{d}{dt}P_x = 0, \tag{3}$$

with $H(z,P_z;t)$ the relativistic Hamiltonian

$$H(z,P_z;t) = \{c^2P_{x0}^2 + c^2[P_{y0} - (e/c)A_y]^2 + c^2P_z^2 + m^2c^4\}^{1/2}. \tag{4}$$

The components $P_{x0}, P_{y0}$ of the canonical momentum $\mathbf{P} = \mathbf{p} + (e/c)\mathbf{A}$ are constants of the motion and can be set equal to zero by a proper shift of the origin, implying

$$p_x = 0, \quad p_y = -(e/c)A_y. \tag{5}$$

There are two time scales involved in the problem. The transit time of an electron through a wiggler period $\tau_w \sim \lambda_w/v_z \sim 1/k_w c$ is much shorter than the synchrotron oscillation period in phase space $\tau_b \sim 1/\omega_b$. We will deal with phenomena taking place on the slow time scale by averaging the irrelevant fast time scale out. This is done using the canonical transformation

$$P_z = \hat{P}_z + \xi\frac{\partial S}{\partial z}, \quad z = \hat{z} - \xi\frac{\partial S}{\partial z}, \tag{6}$$

where the small parameters are

$$\frac{a_r}{\gamma} \sim \frac{a_s}{\gamma} \sim \frac{a_w^2}{\gamma^2} \sim \xi \ll 1.$$

Then the generating function $S$ is chosen to cancel the fast oscillation terms of order $O(\xi) \ll 1$ in the expansion under the square root of Eq. (4),

$$2\hat{P}_z\frac{\partial S}{\partial z} + \frac{1}{2}a_w^2\cos(2k_w z) = 0. \tag{7}$$

Defining the fast time average by $\langle F\rangle = (1/\tau_w)\int_t^{t+\tau_w} dt\, F$, it follows from Eqs. (6) and (7) that $P_z$ and $\hat{z}$ are the averaged particle momentum and position,

$$\langle P_z\rangle = \hat{P}_z, \quad \langle z\rangle = \hat{z}. \tag{8}$$

By solving the equations of motion (3) to first order in $\xi$ one can see that the generating function $\partial S/\partial z$ given from Eq. (7) coincides with the wiggling motion of the electron in the external magnetic field.

Introducing the transformation (6) into the exact Hamiltonian (4) one obtains the time averaged Hamiltonian in dimensionless variables with time $t$ normalized to $\omega_r^{-1}$ and length $z$ to $k_r^{-1}$,

$$H(\hat{P}_z,\hat{z};t) = \left(M^2 + \hat{P}_z^2 + a_w a_r \sum_{n=1}^{\infty}(-1)^n[J_{n-1}(\zeta) - J_n(\zeta)]\cos\{[k_r + (2n-1)k_w]\hat{z} - \omega_r t\} + a_w a_s \sum_{n=1}^{\infty}(-1)^n[J_{n-1}(\zeta) - J_n(\zeta)]\cos\{[k_s + (2n-1)k_w]\hat{z} - \omega_s t\}\right) + O(\xi^2), \tag{9}$$

where

$$\zeta = (k_r/8k_w)(a_w/\hat{P}_z)^2, \quad M^2 = 1 + \tfrac{1}{2}(a_w^2 + a_r^2), \quad a_i = |e|A_i/mc^2.$$

Although $k_r = \omega_r = 1$ in the normalized variables, we write them down explicitly to avoid some confusion. The transformation (6) brought out higher harmonics inside the Hamiltonian (9), generated by the fast oscillation of the axial momentum $P_z \simeq \hat{P}_z - (a_w^2/4\gamma_0)\cos(2k_w z)$, where $\hat{P}_z$ is constant when $a_r = a_s = 0$. Hence FEL operation at odd harmonics of the fundamental

$$k_r = 2(2n-1)\gamma_z^2 k_w \tag{10}$$

is possible in a linear wiggler, provided that the argument of the Bessel functions is not too small, i.e., $\zeta > 2n-1$, or, upon substituting (9) and (10), $a_w^2/4 > 1$ independently of $n$. In addition to the generation of higher harmonics of $k_r$ for given $\gamma_r$, we also have additional resonances for given $k_r$ at energies $\gamma_{r,2n-1}$ $(n = 1,2,\ldots)$ that are fractions of $\gamma_r$, according to $\gamma_{r,2n-1}/\gamma_r = 1/(2n-1)^{1/2}$. These energies, however, are well outside the usual beam thermal spread. Also, the height of the separatrix for the usual field strengths is too small to cause resonance overlapping, allowing the choice of a single resonant term inside (9).

In this paper we consider operation at the fundamental $k_r$, keeping only the $n = 1$ term in the resonant Hamiltonian $H_R$, given by

$$H_R(\hat{P}_z,\hat{z};t) = \{M^2 + \hat{P}_z^2 - \Lambda a_w a_r\cos[(k_r + k_w)\hat{z} - \omega_r t] - \Lambda a_w a_s\cos[(k_s + k_w)\hat{z} - \omega_s t]\}^{1/2}, \tag{11}$$

with $\Lambda = J_0(\xi) - J_1(\xi)$. Note that for $\Lambda = 2$, $M^2 = 1 + a_w^2 + a_r^2$, the above average Hamiltonian for the linear wiggler is identical with the exact Hamiltonian for a circularly polarized (helical) wiggler where all the fields have the form

$$\mathbf{A}_i = A_i(\cos\phi_i\,\hat{y} \pm \sin\phi_i\,\hat{x}), \quad \phi_i = k_i z - \omega_i t, \tag{12}$$

and $i$ stands for $w$, $r$, or $s$ ($\omega_w = 0$). The following analysis applies to both linear and helical wigglers with the proper choice of $\Lambda, M$. In helical wigglers there is no fast oscillation in the parallel momentum; thus $P_z = \hat{P}_z$ and higher harmonics are not excited.

We introduce a final transformation treating time and energy as a second pair of conjugate variables, obtaining

$$\begin{aligned}\overline{H}(\overline{P},\psi,\overline{P}_t,\bar{t}) = {} & [M^2 + (k_w + k_z)^2\overline{P}_z^2 - \Lambda a_w a_r \cos\psi \\ & - \Lambda a_w a_s \cos(\psi - \delta_s\bar{t})]^{1/2} \\ & - \overline{P}_z + \overline{P}_t/(k_r + k_w) = 0,\end{aligned} \tag{13}$$

where

$$\begin{aligned}&\overline{P}_z = \hat{P}_z/(k_w + k_r), \quad \psi = (k_w + k_r)\hat{z} - \omega_r t, \\ &\overline{P}_t = \hat{P}_z - (k_r + k_w)E/\omega_r, \quad \bar{t} = \omega_r t.\end{aligned} \tag{14}$$

Here, $E = \gamma(t)$ is the total energy and

$$\delta_s = k_w(\omega_s - \omega_r)/k_r \simeq (\omega_s - \omega_r)/2\gamma_z^2 \tag{15}$$

is the Doppler shifted frequency mismatch between the main signal and the sideband.

In the absence of sidebands, $\overline{H}$ possesses a second invariant $\overline{P}_t = \overline{P}_t(0) = C$, following from $\partial H/\partial\bar{t} = 0$, and is reduced to the relativistic pendulum Hamiltonian

$$H_0(P,\psi) = [M^2 + (k_r + k_w)^2P^2 - \Lambda a_w a_r \cos\psi]^{1/2} - P, \tag{16}$$

where from now on we will drop the overbar. Here $H_0$ is exactly integrable with the trajectories in phase space given by

$$H_0(P,\psi) = K,$$

where the constant $K = -P_t(0)/(k_r + k_w)$ is the reduced energy determined by the initial conditions $P_0,\psi_0$. The equations of motion take the simplest possible form if they are expressed in terms of the action-angle variables

$$J = \frac{1}{2\pi}\oint P(\psi;K)\,d\psi, \quad \theta = \frac{\partial}{\partial J}\int^{\psi} P(\psi';K)\,d\psi', \tag{17}$$

putting $H_0$ in the form $H_0 = H_0(J)$ and

$$\frac{dJ}{dt} = \frac{\partial H_0}{\partial\theta} = 0, \tag{18a}$$

$$\frac{d\theta}{dt} = \frac{\partial H_0}{\partial J} = \omega_b(J). \tag{18b}$$

Performing the integrals in Eqs. (17) we obtain $J,\theta$ in terms of $P,\psi$:

$$J = \begin{cases} J_s[E_1(\lambda) - (1-\lambda^2)E_1(\lambda)], & \lambda^2 < 1, \\ 2J_s\lambda E_1(1/\lambda), & \lambda^2 > 1, \end{cases} \tag{19a}$$

$$J_s = \frac{8\sqrt{G}}{\sqrt{2}\pi A} \simeq \frac{8}{\pi}\left(\frac{\Lambda a_w a_r k_r}{4k_w}\right)^{1/2}, \tag{19b}$$

$$\sin\frac{\psi}{2} = \begin{cases} \lambda\,\mathrm{sn}\left(\dfrac{2}{\pi}E_1(\lambda)\theta\right), & \lambda^2 < 1, \\ \mathrm{sn}\left[\dfrac{1}{\pi}E_1\left(\dfrac{1}{\lambda}\right)\theta\right], & \lambda^2 > 1, \end{cases} \tag{19c}$$

where $E_1$ and $E_2$ are the complete elliptic integrals of the first and second kind; sn is the Jacobi elliptic sine function;

$$\lambda^2 = (F + G)/2G \tag{20}$$

is the trapping parameter ($\lambda^2 < 1$ for trapped particles); and the constants $A$, $F$, and $G$ are given in terms of the initial conditions

$$\begin{aligned}&A = (k_r + k_w)^2 - 1, \\ &F = (k_r + k_w)^2(K^2 - M^2), \\ &G = \Lambda a_r a_w[(k_r + k_w)^2 - 1], \\ &K = H_0(P_0,\psi_0) = H_0(J).\end{aligned} \tag{21}$$

From (17) and (18) we determine the bounce (synchrotron) frequency

$$\omega_b(J) = \begin{cases} \omega_b(0)\pi/2E_1(\lambda), & \lambda^2 < 1, \\ \omega_b(0)\pi\lambda/E_1(1/\lambda), & \lambda^2 > 1, \end{cases} \tag{22}$$

where

$$\omega_b(0) = \left(\frac{G}{2}\right)^{1/2}\frac{(k_r + k_w)^2 - 1}{(k_r + k_w)^2K} \simeq \frac{1}{\gamma_r}\left(\frac{\Lambda}{2}a_w a_r k_w k_r\right)^{1/2} \tag{23}$$

is the bounce frequency at the bottom of the well. The three constants $K$, $J$, and $\lambda^2$ are mutually related through Eqs. (19)–(21) and any of them can label a trajectory uniquely. The trajectories $H_0(J) = K$, the action $J(K)$, $\lambda^2(J)$, and the bounce frequency $\omega_b(J)$ are shown in Figs. 2(a)–2(d).

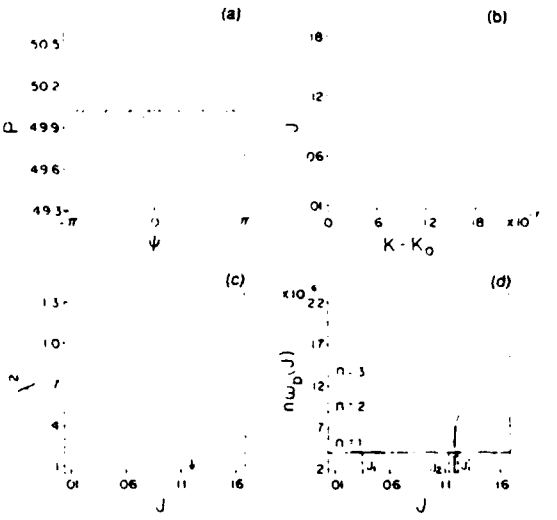



FIG. 2. Time averaged motion without the sidebands. (a) Plots in phase space of the unperturbed orbits $H_0(P,\psi) = K$. The intersections with the horizontal line $P = \text{const}$ mark the initial conditions for each orbit. (b) The action $J$ plotted against the reduced energy $K - K_0$. (c) The trapping parameter $\lambda^2$ plotted against $J$, $\lambda^2 = 1$ at $J_{cr} = 0.119$. (d) The normalized bounce frequency $\omega_b$ and the first two harmonics as functions of the action $J$. The intersections with the horizontal line $\delta = (\omega_s - \omega_r)k_w/k_r$ determine the position $J_n$ of the resonant orbits for a given $\omega_s$.

The perturbed Hamiltonian can now be expanded around $H_0(J)$ according to

$$H(J,\theta) = H_0(J) + \sum_{n=0}^{\infty} [h_n^+(J)\cos(n\theta + \delta_1 t) + h_n^-(J)\cos(n\theta - \delta_1 t)], \quad (24)$$

with

$$h_n^{\pm}(J) = \{\Lambda a_w a_r / [H_0(J) + P_r]\} Q_n^{\pm}(J). \quad (25)$$

The coefficients $Q_n^{\pm}$ are the Fourier coefficients from the decomposition of $\cos[\psi(J,\theta)]$, with $\psi$ given by Eq. (19) into the harmonics of the synchrotron angle $\theta$. They are computed by integration in the complex plane around the singularities, utilizing the double periodicity properties of the Jacobi elliptic functions to obtain

$$\begin{aligned} Q_n^{+} &= -(\pm 1)^n \frac{n\pi^2}{E_1^2(\lambda)} \frac{q^{n/2}}{1-(-q)^n}, \\ q &= \exp\left(\frac{\pi E_1'(\lambda)}{E_1(\lambda)}\right), \quad \lambda^2 < 1, \\ Q_n^{+} &= -\frac{n\pi^2\lambda^2}{E_1^2(1/\lambda)} q^n \left(\frac{1}{1-q^{2n}} \pm \frac{1}{1+q^{2n}}\right), \\ q &= \exp\left(\frac{\pi E_1'(1/\lambda)}{E_1(1/\lambda)}\right), \quad \lambda^2 > 1, \end{aligned} \quad (26)$$

for $n \neq 0$ and

$$\begin{aligned} Q_0^{+} &= \frac{E_2(\lambda)}{E_1(\lambda)} - \frac{1}{2}, \quad \lambda^2 < 1, \\ Q_0^{+} &= \frac{1}{2} - \lambda^2\left(1 - \frac{E_2(1/\lambda)}{E_1(1/\lambda)}\right), \quad \lambda^2 < 1, \end{aligned}$$

where $E_1'(\lambda^2) \equiv E_1(1-\lambda^2)$.

This expansion is similar in spirit with the more familiar case of expanding the phase of the plane wave acting on a magnetized electron into a sum of cyclotron harmonics, where the harmonic coefficients are given by Bessel functions. Plots of the first harmonic coefficients $Q_n$ are shown in Fig. 3. Here, $Q_n(J)$ vanishes for $J \to \infty$, i.e., for free-streaming particles, as well as for $J \to 0$, i.e., for trapped particles at the bottom of the ponderomotive well. One can again draw

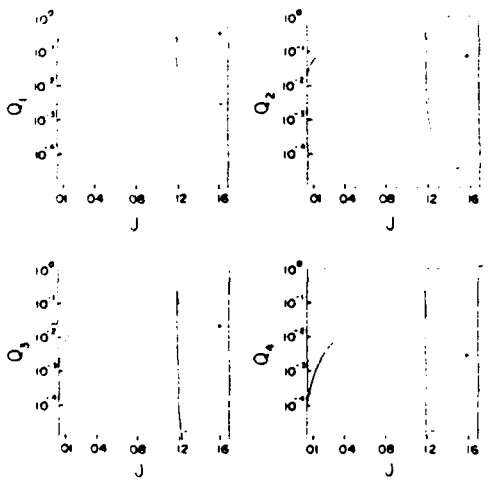



FIG. 3. Plots of the first four Fourier coefficients $Q_n^{+}(J)$.

the analogy with the finite Larmor radius effects: the vanishing action $J \to 0$ plays the role of vanishing $\rho_L \to 0$.

The equations for the perturbed motion derived from Hamiltonian (24) are

$$\begin{aligned} \frac{d}{dt} J &= \sum_{n=0}^{\infty} n[h_n^{+}(J)\sin(n\theta + \delta_1 t) + h_n^{-}(J)\sin(n\theta - \delta_1 t)], \\ \frac{d}{dt}\theta &= \omega_b(J) + \sum_{n=0}^{\infty}\left(\frac{dh_n^{+}}{dJ}\cos(n\theta + \delta_1 t) + \frac{dh_n^{-}}{dJ}\cos(n\theta - \delta_1 t)\right). \end{aligned} \quad (27)$$

Defining the phase $\Phi_n$ of the secondary ponderomotive potential induced by the sideband as

$$\Phi_n^{\pm} = n\theta \pm \delta_1 t,$$

new resonances emerge at

$$\frac{d}{dt}\Phi_n^{\pm} = n\omega_b(J) \pm \delta_1 \simeq 0.$$

This occurs for the orbits $J = J_n$ such that the $n$th harmonic of the unperturbed bounce frequency $\omega_b(J_n)$ matches the downshifted frequency difference between the sideband and the main signal

$$\pm n\omega_b(J_n) = (k_w/k_r)(\omega_r - \omega_r), \quad n = 1,2,\ldots. \quad (28)$$

In Fig. 2(d) various groups of particles are shown in resonance with a sideband of a given frequency $\omega_s$, each group interacting through a different harmonic $n$. It will be shown that the particles in the neighborhood of these synchronous (unperturbed) orbits $J = J_n$ alone determine the linear growth for the sideband.

## III. GAIN COMPUTATION FROM THE KINETIC EQUATION

We consider the evolution of the electron distribution function $f(J,\theta,t)$ under the Hamiltonian flow

$$\frac{df}{dt} = [H,f] + \frac{\partial f}{\partial t} = \frac{\partial f}{\partial t} + \frac{\partial H}{\partial J}\frac{\partial f}{\partial \theta} - \frac{\partial H}{\partial \theta}\frac{\partial f}{\partial J} = 0. \quad (29)$$

We start from a state of adiabatic equilibrium between the main signal and the electrons, described by the distribution function $f_0$ remaining invariant along the unperturbed trajectories

$$\frac{df_0}{dt} = [H_0, f_0] = 0. \quad (30)$$

Here $f_0$ satisfies the normalization condition

$$\int_0^{2\pi} d\theta \int_0^{\infty} dJ\, f_0(J) = 1.$$

We will determine the stability of such an equilibrium against perturbations $f_1$ around $f_0$ caused by the small amplitude sideband term $H_1$ in the Hamiltonian (24),

$$\frac{\partial f_1}{\partial t} + [H_0, f_1] + [H_1, f_0] = 0. \quad (31)$$

Note that Eq. (30) is satisfied by any $\theta$-independent distribution $f_0 \equiv f_0(J)$, because $\partial H_0/\partial\theta = 0$, and does not determine $f_0$ uniquely. One can do a little better using the

concept of phase mixing to show that the final asymptotic equilibrium state $f_{i\infty}$ toward which any initial distribution relaxes under the flow $H_{i\infty}$ must be of the form $f_{i0}[H_{i0}(J)]$. Using this fact and conservation of the number of particles $f_{i0}$ can be derived analytically given the initial $f_{i\infty}$ that $f_{i0}$ evolved from. If $f_{i\infty}$ is of the form $f_{i\infty}(P,\psi) = (1/2\pi)\delta(P_z - P_{i\infty})$, appropriate for cold beam injection, the final $f_{i0}(J)$ is found to be

$$f_{i0}(J) = \frac{4(K + P_{i0})}{\{(a_w a_r \Lambda)^2 - [M^2 + (k_r + k_w)^2 P_{i0}^2 - (K + P_{i0})^2]^2\}^{1/2}} \frac{\omega_{bi}(J)}{2\pi}, \tag{32}$$

with $K = H_{i0}(J)$. This formula yields an inverted distribution profile [see Fig. 6(a)]. Although diffusion in action space, caused by higher dimensionality and nonconstant $a_r(t)$, will smooth the edges of such a distribution under more realistic conditions, hollow distribution profiles should be included among the choices of $f_{i0}(J)$ to be checked for stability.

We now consider a slow change in the sideband amplitude $a_s(t)$ allowing a small imaginary part in $\omega_s$. Using Eqs. (18), (27), and casting Eq. (31) in the form

$$\frac{\partial f_{i1}}{\partial t} + \omega_{bi}(J)\frac{\partial f_{i1}}{\partial \theta} = \frac{\partial H_{i1}}{\partial \theta}\frac{df_{i0}}{dJ},$$

we obtain the perturbed distribution

$$f_{i1} = -\frac{1}{2}\left(\sum_n n \frac{h_{ni}(J)}{n\omega_{bi}(J) \pm (\delta_s + i\epsilon)} \frac{df_{i0}}{dJ} e^{i(n\theta + \psi_i)} + \text{c.c.}\right), \tag{33}$$

where $\delta_s$ in the denominator picks a small imaginary contribution $\epsilon = \text{Im}(\delta_s) = (k_w/k_r)\text{Im}(\omega_s)$. Expressing the electric field $E_s$ in terms of the vector potential $a_s$, $E_s = -(1/c)(\partial a_s/\partial t)$, we obtain the growth rate $g_s \equiv \text{Im}(\omega_s)$ from the time averaged energy balance equation

$$\frac{d}{dt}a_s^2 = 2g_s a_s^2 = \frac{4\pi c}{\omega_s}\left(\left\langle j_y(z,t)\frac{1}{2}(ia_s e^{i(k_s z - \omega_s t)} + \text{c.c.})\right\rangle + \text{c.c.}\right), \tag{34}$$

where $\langle\ \rangle$ means the fast time average over $\tau_\infty$ defined in Sec. II.

The transverse current $j_y$ is expressed in terms of the perturbed distribution $f_{i1}$,

$$j_y = n_b \int_{-\infty}^{\infty} dP \frac{1}{\gamma}(p_{yi} f_{i1} + p_{yi} f_{i0}),$$

where $P$ is the normalized $P_z$, Eq. (14). Since the equilibrium $f_{i0}[J(P,\psi)]$ is a periodic function of $\psi$, the current $j_y$ can be written as

$$j_y = \{j_y\} + \tilde{j}_y(\psi),$$

where $\{j_y\}$ is the $\psi$-averaged component

$$\{j_y\} = \frac{1}{2\pi}\int_0^{2\pi} d\psi j_y,$$

while $\tilde{j}_y$ contains the periodic dependence in $\psi$. According to the Floquet theory, applying to wave propagation in media with periodic properties, upper and lower sidebands are coupled[50] through $\tilde{j}_y$. One can show, however, using scaling arguments, that the strength of this coupling is of order $\xi \simeq (\omega_p/\omega_r)^2/(\Delta\omega^2/\omega_r^2)$, where $\Delta\omega^2 = \omega_s^2(k_+) - \omega_s^2(k_-)$ and $k_\pm = k_s \pm 2\gamma_z^2\omega_b/c$. For typical FEL parameters in the Compton regime $\Delta\omega^2/\omega_r^2 \simeq 4\gamma_z^2\omega_b/\omega_r \gg (\omega_p/\omega_r)^2$ and $\xi \ll 1$. The averaged current density $\{j_y\}$ suffices for the lowest order approximation, admitting monochromatic sideband modes. The coupling to additional wavenumbers, entering to the next order in $\xi$, will be neglected in this paper.[51]

Utilizing the property $\int\int dP\, d\psi = \int\int dJ\, d\theta$ we obtain

$$\{j_y\} = n_b \int\int dJ\, d\theta \frac{1}{\gamma(J,\theta)}[p_{wi} f_{i1}(J,\theta;z) + p_{yi} f_{i0}(J)], \tag{35}$$

with

$$p_{wi} = a_w \cos k_w z + a_r \cos(k_r z - \omega_r t), \quad p_{yi} = a_s \cos(k_s z - \omega_s t),$$

according to Eq. (2). Substituting Eqs. (33) and (35) into (34) and retaining terms to order $a_s^2$ yields

$$\begin{aligned} 2g_s a_s^2 = \frac{i}{2}\frac{4\pi}{|\omega_s|^2}\sum_n \Big\langle \int_0^{2\pi} d\theta \int dJ \frac{1}{2}\big[(F_n e^{i(n\theta + \psi_i)} + \text{c.c.}) + (F_n e^{i(n\theta - \psi_i)} + \text{c.c.})\big] \\ \times \tfrac{1}{2}\big[a_w(e^{ik_s z} + \text{c.c.}) + a_r(e^{i(k_s z - \omega_r t)} + \text{c.c.})\big]\tfrac{1}{2}(a_s\omega_s e^{i(k_s z - \omega_s t)} - \text{c.c.}) \\ + \tfrac{1}{2}(a_s e^{i(k_s z - \omega_s t)} + \text{c.c.})F_n\tfrac{1}{2}(a_s\omega_s e^{i(k_s z - \omega_s t)} - \text{c.c.})\Big\rangle + \text{c.c.}, \end{aligned} \tag{36}$$

where

$$F_n^{\pm} = -\frac{nh_n^{\pm}(J)df_0/dJ}{\gamma_r[n\omega_b(J) \pm (\delta_s + i\epsilon)]}, \quad F_0 = \frac{f_0}{\gamma_r}. \tag{37}$$

The last term in (36), the contribution from the unperturbed distribution $f_0$, time averages to zero. We combine the products of the remaining terms into sums and express the phases in the resulting exponentials in terms of $\psi = (k_w + k_r)z - \omega_r t$. Only terms proportional to $\exp\{\pm i[(n\theta \pm \delta_s t) - (\psi - \delta_s t)]\}$ survive the fast time averaging, reducing the integral in Eq. (36) into

$$\frac{a_w a_s}{8}\sum_n\sum_m\int_0^\infty dJ\int_0^{2\pi}d\theta\,\gamma_r^{-1}\left(\frac{df_0}{dJ}\right)\times\left(h_n^{+}(J)Q_m^{+}(J)\frac{e^{i(n\theta - m\psi)}}{\omega_b(J) + (\delta_s/n) + i\epsilon} - \text{c.c.} + h_n^{-}(J)Q_m^{-}(J)\frac{e^{i(n\theta - m\psi)}}{\omega_b(J) - (\delta_s/n) - i\epsilon} - \text{c.c.}\right). \tag{38}$$

In obtaining (38) the phase $\psi(\theta)$ was expanded again into harmonics of the synchrotron angle $\theta$ utilizing the familiar Fourier coefficients $Q_m^{\pm}(J)$. Integration over $\theta$ further reduces expression (38) into

$$\frac{\pi}{8}\sum_n\int_0^\infty dJ\frac{a_w^2a_s^2}{\gamma_r[H_0(J) + P_r]}\left(\frac{df_0}{dJ}\right)\times\left(\frac{|Q_n^{+}|^2}{\omega_b + \delta_s/n + i\epsilon} + \frac{|Q_n^{-}|^2}{\omega_b - \delta_s/n - i\epsilon} - \text{c.c.}\right). \tag{39}$$

For $\epsilon$ small, the main contribution in the above integral comes from the poles in the denominators. Changing variables to $dJ = d\omega_b(d\omega_b/dJ)^{-1}$, extending the limits to infinity, and applying the approximation

$$\epsilon/[(x \pm y)^2 + \epsilon^2] \to \pi\delta(x \pm y)$$

for small growth rates, we obtain the final result in normalized units,

$$g_s^{\pm} = \mp\frac{\omega_r}{\omega_s}\frac{\Lambda\pi^2\omega_p^2a_w^2}{4\omega_r^2\gamma_r}\times\sum_n\frac{|Q_n^{\pm}(J_n)|^2}{H_0(J_n) + P_r}\left(\frac{d\omega_b}{dJ}\right)_{J_n}^{-1}\left(\frac{df_0}{dJ}\right)_{J_n}. \tag{40}$$

Above, $g^+$ and $g^-$ correspond to the growth rates for the upper ($\omega_s > \omega_r$) and lower ($\omega_s < \omega_r$) sidebands, respectively. Only one of the terms, $h_n^-$ or $h_n^+$, in the integral (38) can be resonant and contributing for a given $\omega_s$, depending on whether $\delta_s$ is positive or negative, respectively. This causes the growth rates for the upper sidebands to have opposite signs from the lower sidebands in Eq. (40). The physical explanation will be given later.

Before proceeding to discussing the various aspects of (40) we provide an approximate simplified expression in estimating growth rates. Assuming that (i) the most unstable mode comes from the vicinity of the maximum gradient in $(df_0/dJ)$ located near $\lambda_n^2 = 0.5$, (ii) the main contribution comes from a single harmonic $n$, and (iii) using the derivatives of the elliptic functions[52] in Eqs. (19) and (22) to compute

$$\left(\frac{d\omega_b}{dJ}\right)_{J_n}^{-1} = \frac{2J_s}{\pi\omega_b(0)}\frac{E_1^3(\lambda_n)\lambda_n^2(\lambda_n^2 - 1)}{E_2(\lambda_n) - (1 - \lambda_n^2)E_1(\lambda_n)}$$

for trapped particles, we obtain the approximate growth rate for the most unstable mode

$$g_s \simeq \omega_r\frac{a_w}{\gamma_r a_r}\frac{3\pi^{1/2}}{128}\left(\frac{\omega_p}{\omega_r}\right)^2\nu^2. \tag{41}$$

We have used a Gaussian distribution $f_0(J)$ of width $D$ in obtaining expression (41), defining $\nu$ as the ratio $J_s/D$. Using the parameters of the Columbia FEL experiment[41] $\lambda_w = 1.45$ cm, $B_w = 0.75$ kG, $\lambda_r = 2.5\times10^{-4}$ cm, $I_b = 10^2$ A, $r_b = 2.5\times10^{-1}$ cm, $P_r \simeq 1\times10^7$ W/cm$^2$, and assuming $D = J_s/2$ ($\nu = 2$), we find from (41) the spatial growth rate $g_s/c\beta_z \sim 0.12$ cm$^{-1}$, in agreement with the experimental growth rate $\simeq 0.10$ cm$^{-1}$.

## IV. DISCUSSION OF THE RESULT

The summation over $n$ in Eq. (40) contains the contribution from all the groups of resonant trajectories among both trapped and untrapped particles. The action $J_n$, defined implicitly by Eq. (28), labels the resonant orbit having the $n$th harmonic of its bounce frequency in resonance with the sideband. For a given harmonic $n$ there are in general two solutions, $J_n$ and $J_n'$, of Eq. (28) corresponding to one group of trapped and one group of untrapped particles [see Fig. 1(d)].

In most cases of interest the majority of the electrons are trapped inside the separatrix and the effect of the untrapped particles on stability is small. Then according to Eq. (40), and using the symmetry in the coefficients $|Q_n^+(J)| = |Q_n^-(J)|$ for trapped particles, Eq. (26), upper and lower sidebands of symmetric frequencies around the main signal $|\omega_s^+ - \omega_r| = |\omega_s^- - \omega_r|$ have opposite growth rates (complementary stability),

$$\frac{g_s^+}{g_s^-} = -\left(\frac{\omega_s^-}{\omega_s^+}\right) \simeq -1 + \left(\frac{\delta\omega}{\omega_r}\right)^2. \tag{42}$$

Thus some sidebands are always unstable and there exists no globally stable distribution $f_0(J)$ except the trivial one $df_0/dJ = 0$. The sign of the growth rate for a given frequency $\omega_s$ is determined by the signs of the slope $(df_0/dJ)_{J_n}$ and the shear $(d\omega_b/dJ)_{J_n}$ near the resonant orbits $J_n$. There is no difference in the magnitude of the growth rates between upper and lower sidebands, both being equally fast to develop provided they are destabilized.

We clarify that, in general, the opposite signs do not imply that all upper sidebands have the same kind of stability, opposite to the stability of all lower sidebands. Depending upon $f_0$, the stability may change sign between two upper (or lower) frequencies because the slopes $df_0/dJ_n$ change as the location of the resonant orbits $J_n$ shift with $\omega_s$.

For a monotonic distribution $f_0$, we observe that trapped and untrapped particles of the same synchrotron period $\omega_b(J_n) = \omega_b(J_n')$ yield opposite contributions to a given mode because $d\omega_b/dJ$ changes sign across the separatrix. If trapped particles are stabilizing, untrapped are destabilizing and vice versa. High shear is stabilizing, tending to reduce the magnitude of the growth $g_s$. This is expected as the number of resonant orbits is inversely proportional to $|d\omega_b/dJ|$.

As the shear is generally higher for untrapped particles it is the trapped ones that usually dominate the instability. Shear tends to infinity near the separatrix; thus the modes in resonance with orbits near the separatrix, corresponding to small $|\omega_r - \omega_r| \ll (k_r/k_w) n\omega_b(0)$, have the smallest growth rates. Modes coming from resonances with particles localized near the bottom of the ponderomotive well $J_n \simeq 0$, corresponding to frequencies $|\omega_r - \omega_r| \simeq (k_r/k_w) n\omega_b(0)$, also have small growth rates as the coefficients $Q_n(J)$ tend to zero there. In particular, given any smooth distribution $f_0(J)$, electrons exactly at the bottom of the well have a null contribution to the instability. It takes a singular distribution of infinite gradient at $J = 0$ to create an instability at the bottom.

Although Eq. (40) was based on purely classical arguments it nevertheless admits the correct quantum mechanical interpretation. By rewriting

$$\left(\frac{df_0}{dJ}\right)\left(\frac{d\omega_b}{dJ}\right)^{-1} = \frac{df_0}{d\omega_b} \tag{43}$$

in the right-hand side of (40), the growth simply depends on the energy distribution of quanta $f_0(\hbar\omega_b)$ among the quantized trapped particle oscillators. In the ponderomotive frame the elementary physical process is a second order, two-photon transition, where an incident wiggler "photon" $\omega'_w$ is inelastically scattered into a sideband photon $\omega'_s$ with the parallel absorption or emission of $n$ oscillation quanta $\omega'_b$ by the trapped electron (Raman scattering). Conservation of energy in the ponderomotive frame moving at $v_p = \omega_r/(k_r + k_w)$, where $\omega'_w = \omega'_r$, requires

$$\hbar(\omega'_s - \omega'_r) = \pm n\hbar\omega'_b. \tag{44}$$

Substituting $\omega'_r = \gamma_z(1 - \beta_z)\omega_r$, $\omega'_s = \gamma_z(1 - \beta_z)\omega_s$, and $\omega'_b = \gamma_z\omega_b$ for the Doppler shifted frequencies, we recover the resonance condition in the laboratory frame, Eq. (28).

Consider the process in Fig. 4(a), where one wiggler "photon" is absorbed with the emission of a sideband photon plus the absorption of $n$ oscillation quanta $\hbar\omega'_r - \hbar\omega'_s + n\hbar\omega'_b$. The inverse process is taking place at the same time where the emitted sideband photon is reabsorbed and a main signal photon is emitted, $\hbar\omega'_s + n\hbar\omega'_b - \hbar\omega'_r$. The growth in the number of sideband photons $n_s$ is given by the balance between the induced emission and absorption

$$\frac{dn_s}{dt} = [\Pi_{12} n_w (n_s + 1) f_0(E_1) - \Pi_{21}(n_w + 1) n_s f_0(E_2)] \times \delta(E_1 - E_2 \pm n\hbar\omega'_b), \tag{45}$$

where $f_0(E)$ is the number of oscillators at a given energy level $E$; $n_w$ and $n_s$ are the photon densities for the wiggler and the sideband, respectively; $\Pi_{ij} > 0$ is the transition probability per unit time; and the factor $+1$ represents the contribution from spontaneous emission. The minus sign inside the $\delta$ function corresponds to upper sideband emission, requiring that the oscillator fall into a lower energy state $E_1 - E_2 = \hbar\omega'_b$. Given that the transition probabilities between the two inverse processes are the same, $\Pi_{12} = \Pi_{21} = \Pi$, and using $E_1 - E_2 = \mp n\hbar\omega_b$, $df_0/dE = -|d\omega_b/dE|(df_0/d\omega_b)$, we obtain, for $n_w, n_s \gg 1$,

$$g_s = \mp\left(\frac{\Pi n_w}{\gamma}\right)\left|\frac{d\omega_b}{dE}\right| \hbar\omega_b \frac{df_0}{d(\hbar\omega_b)}. \tag{46}$$

An electron at the higher energy state is an emitter for the upper sideband while an electron at the lower state is an emitter for the lower sideband. Also, $df_0/dE$ has opposite sign to $df_0/d\omega_b$ for trapped electrons since $\omega_b$ decreases with increasing energy. Hence distributions with a higher electron population at higher energy levels corresponding to $df_0/d\omega_b < 0$ are unstable to upper sidebands, while those with higher populated lower levels $df_0/d\omega_b > 0$ are unstable to lower sidebands. This explains the opposite signs in Eq. (40) and the complementary stability among higher and lower frequencies.

The emission probability $\Pi$ from trapped electrons, having zero streaming velocity in the ponderomotive frame, is equal for symmetric Stokes and anti-Stokes lines. On the other hand, the untrapped electrons, having a nonzero streaming velocity in the ponderomotive frame, see a slightly different wiggler frequency $\omega''_w \neq \omega'_w = \omega'_r$. They scatter symmetrically around $\omega''_w$, resulting in unequal scattering probabilities for Stokes and anti-Stokes lines that are symmetric relative to $\omega'_r$. This is reflected in the Fourier coefficients in Eq. (26) where $|Q_n^+(J)| \neq |Q_n^-(J)|$ for untrapped particles while $|Q_n^+(J)| = |Q_n^-(J)|$ for trapped particles.

In both (40) and (46) the growth rate depends explicitly on the wiggler strength $a_w^2 \sim n_w$ alone and not on the carrier $a_r$. To the lowest order the sideband emission is the inelastic backscattering of a wiggler photon, Fig. 4(a), competing with the elastic backscattering (negligible electron recoil) that generates the FEL carrier signal. The decay of a carrier photon into a sideband photon plus oscillation quanta, Fig. 4(b), will enter (40) as a higher order correction, if perturbations of order $a_s a_r \sim \epsilon^2 \ll a_w a_r$ are kept in the Hamiltonian (16). Consequently the development of sidebands does not necessarily deplete the carrier signal; instead it offers additional modes to channel the electron beam energy into. The source of energy for all the radiation modes is the electron deceleration. The fractional change in momentum due to electron recoil for a single-photon emission is of order $\Delta p/p \sim \hbar\omega_b/\gamma mc^2$, too small to modify the resonance

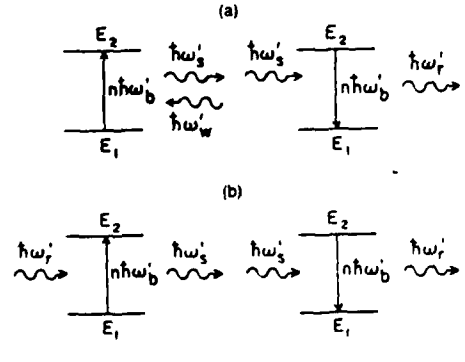



FIG. 4. Schematic illustration of the two elementary processes, stimulated sideband emission and reabsorption, that determine the overall sideband gain. (a) Inelastic backscattering of a wiggler virtual photon, the dominant process. (b) Decay of a carrier photon, a higher order correction.

condition [Eq. (28)]. It takes a large number of emitted photons in the given frequency regime (optical wavelengths or longer) to slow an electron down, justifying the use of the classic equations to describe the process.

In terms of the overall energy extraction from the electron beam, the excitation of sidebands may have varying effects. Efficiency enhancement (at the expense of optical quality) may result in untapered wiggler FEL's since the beam energy keeps being converted into radiation in the sideband frequencies even after the saturation of the carrier signal. In tapered wiggler FEL's, where the free energy comes from the deceleration of the trapped electron bucket, excitation of high amplitude sidebands will eventually cause chaotic electron motion and detrapping. Depending on how fast electrons leak outside the bucket, this may cause a reduction in efficiency and eventually a loss of amplification for all the radiation modes.

## V. LIMITING CASES

The general expression (40) for the growth rate can be further simplified for certain types of distributions $f_0(J)$. First we consider the case of a $\delta$-function distribution $f_0(J) = \delta(J - J_0)/2\pi$, the so-called hydrodynamic limit. Integrating the right-hand side of Eq. (39) by parts we find

$$(g_s')^2 = -(nk_r/k_w)^2[\Delta_s^2 \mp (k_w/nk_r)\Gamma G_n'], \quad (47)$$

where the primes (') denote the derivative $d/dJ$ and

$$\Delta_s = n\omega_b(J_0) \mp (\omega_s - \omega_r)(k_w/k_r), \quad (48)$$

$$\Gamma = \frac{\omega_r}{\omega_s}\frac{\pi\omega_p^2}{4\gamma_r\omega_r^2}, \quad G_n = \frac{\Lambda|Q_n(J_0)|^2}{H_0(J_0) + P_r}. \quad (49)$$

Since the electrons are localized at $J = J_0$, there is only one resonant harmonic $n$ determined by $\Delta_s = 0$ in Eq. (48). The growths between symmetric sidebands of equal $|\Delta_s| = |\Delta_{-s}|$ are no longer opposite. In the limit $\Delta_s \to 0$ we observe that only the upper or the lower sidebands can be unstable for a given $\delta$ function, depending on the sign of $G_n'(J_0)$. The maximum growth occurs for $\Delta_s = 0$ and is given by

$$g_{max} = |n(k_r/k_w)\Gamma G_n'|^{1/2}, \quad (50)$$

scaling proportionally to $\omega_p/\omega_r \sim n_b^{1/2}$.

Next we compute the growth rate for a uniformly filled type of distribution $f_0(J) = (1/2\pi J_0)[1 - S(J - J_0)]$, where $S(J - J_0)$ is the step function $dS/dJ = \delta(J - J_0)$. Performing the integration (39) and substituting into (36) we find that the growth $g_s$ is peaked near the resonant frequencies $\omega_s$ satisfying relation (49). At most, one harmonic $n$ can be in resonance with $\omega_s$ for given $J_0$, with a growth rate

$$(g_s')^2 = \mp 2\omega_r^2 \frac{\omega_s k_r}{\gamma_r^2\omega_s k_w}\frac{\omega_p^2}{\omega_r^2}\frac{|Q_n'(J_0)|^2}{J_0} \quad (51)$$

for $|\Delta_s| \ll \epsilon$. Thus, to the lowest order in $\Delta_s$, only lower frequency sidebands $g^-$ can be unstable for a uniformly filled-type distribution. In particular, we may take the limit $J_0 = 0$ to obtain the growth rate for a distribution localized exactly at the bottom of the ponderomotive well. Expressing $J_0$ and $Q_n(J_0)$ in terms of $\lambda_0$ from Eqs. (26) and (19) and then taking the limit[52] $\lambda_0 \to 0$, we obtain

$$|Q_n'(J_0)|^2/J_0 \to (1/2J_0)\delta_{1n}. \quad (52)$$

According to (51) and (52), the first lower sideband of frequency $\omega_s \simeq \omega_r - (k_w/k_r)\omega_b(0)$ is the only unstable mode in the case of a singular electron distribution localized at the center of the bucket. Particles localized at the bottom of the ponderomotive well are at the ground state of the oscillator and cannot fall into a lower state required for the emission of an upper sideband. Similar conclusions have been drawn in Ref. 35, where the relative growth rate of the sideband to the carrier $g_s/g_r$ has been obtained. In case of a constant parameter wiggler, the sideband growth rate cannot be determined from $g_s/g_r$ because the growth of the carrier $g_r$ goes to zero when all particles are assumed at the center of the bucket, and the expression[15] for $g_s/g_r$ diverges.

The cases of singular, localized distributions with infinite gradients yield higher growth rates, proportional to $\omega_p/\omega_r$ rather than $(\omega_p/\omega_r)^2$ as in Eq. (40). However, such distributions are of little practical interest since even the case of an ideal cold beam distribution $\delta(p_z - p_0)$ is described in action space by a smooth $f_0(J)$ of finite width $\Delta J$ [see Fig. 2(a)].

## VI. NUMERICAL EXAMPLES AND CONCLUSIONS

The normalized growth rate $g_s/\omega_r$ is plotted against the percentage mismatch $(\omega_s - \omega_r)/\omega_r$ for both upper and lower sidebands in Figs. 5(a)–5(d). The contribution up to the third harmonic $n \leq 4$ in Eq. (40) is included in these plots. The parameters chosen correspond to a wiggler wavelength $\lambda_w = 6$ cm, $a_w = 2$, main signal strength $a_r = 5 \times 10^{-5}$, beam energy of 37 MeV ($\gamma = 72$), and current $I = 1$ kA

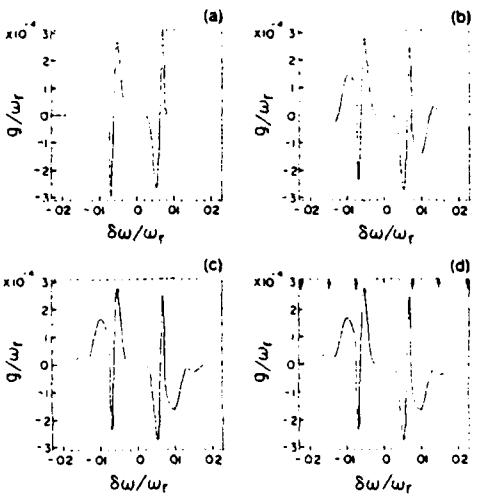



FIG. 5. Growth rate for a Gaussian distribution $f_0(J) = C\exp[-(J - J_0)^2/2D^2]$ centered halfway inside the trapped particle island $J_0 = J_s/2$ and of width $D$ equal to $J_s$. The normalized growth rate $g_s/\omega_r$ is plotted versus $\delta\omega/\omega_r$ for (a) the fundamental contribution $n = 1$ in Eq. (16), (b) including the first harmonic $n = 2$, (c) two harmonics, and (d) three harmonics. The most unstable modes do not correspond to harmonics of the bounce frequency at the bottom $\omega_b(0)$ indicated by the arrows.

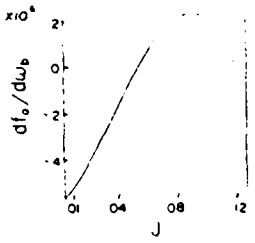


FIG. 6. Plot of $df_0(J)/d\omega_b(J) = (df_0/dJ)(d\omega_b/dJ)^{-1}$ as a function of $J$ for the distribution $f_0$ of Fig. 5. The slope goes to zero near the separatrix $J_s$ because of the infinite shear $d\omega_b/dJ$.

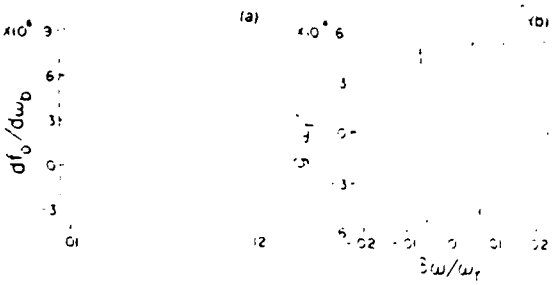


FIG. [illegible] ...tion for an inverted Gaussian distribution with ... (a) Plot of $df_0(J)/d\omega_b(J)$ (b) The normalized growth r... $\omega/\omega_r$.

(beam density $6.25 \times 10^{11}$ cm$^{-3}$). The normalized equilibrium distribution is a Gaussian $f_0(J) = (2\pi^3 D^2)^{-1/2} \exp[-(J-J_0)^2/2D^2]$ centered halfway inside the island, $J_0 = J_s/2$, and of width $D$ equal to half the separatrix action $D = J_s/2$. We plot the contribution of only the fundamental, $n = 1$ in Eq. (40), in Fig. 5(a), adding the second harmonic $n = 2$ in (b), the third harmonic in (c), and the fourth harmonic in (d). New unstable bands emerge with each harmonic while the gain for already unstable bands is modified. For example, we observe two upper and two lower unstable bands in (b) but only one upper and three lower bands in (d). We find the contributions from higher than the third harmonics $n > 4$ generally negligible. The upper frequency $\omega_+ > \omega_r$ and the lower frequency $\omega_- < \omega_r$ parts of the unstable spectrum come from the regimes of negative and positive slope $df_0/d\omega_b$, respectively, shown in Fig. 6. The lower sideband growth is peaking at frequencies corresponding to $n\omega_b(J_{max})$, the value of $J$ maximizing $df_0/d\omega_b(J)$. The peaks for the upper sideband growth, however, do not occur at $J = 0$, which minimizes $df_0/d\omega_b(J)$, but at $J$ halfway inside the negative slope regime. This is because $Q_n(J)$ and, consequently, $g_-$ are zero at $J = 0$, showing the negligible contribution from electrons at the bottom of the well. The analogous effect in plasma physics is the elimination of the thermal effects when $\rho_L$ goes to zero. In any case the most unstable modes are far from the frequencies $|\omega_- - \omega_r| = (k_r/k_w)n\omega_b(0)$ pointed out by the arrows in Fig. 6(d).

In Fig. 7 we plot the equilibrium distribution without sidebands, $f_{EQ}(J)$ given in Eq. (32), associated with a cold beam initial distribution $f_{in}(P,\psi) = (2\pi)^{-1}\delta(P - P_0)$. Here, $f_{EQ}(J) \equiv f(H_0(J))$ is constant along the trajectories $H_0(J) = K(P_0,\psi_0)$ such as those shown in Fig. 2(a). The initial conditions $P = P_0$ with $P_0 = (1+d)P_s$,

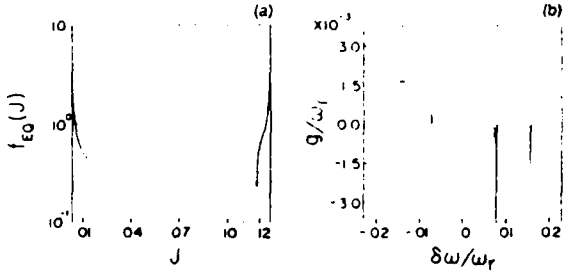


FIG. 7. (a) The equilibrium $f_{EQ}(J)$ that evolves from an original cold beam distribution $f_{in}(P) = (1/2\pi)\delta(P - P_0)$, shown by the horizontal line in Fig. 2(a). (b) Normalized growth rate versus frequency for $f_{EQ}(J)$

$d = 2 \times 10^{-4}$, are given by the intersections with the horizontal line. The sharp gradients that are localized at the two edges $J_{min} = J(P_0,\psi_0 = 0)$ and $J_{max} = J(P_0,\psi_0 = \pi)$ of the distribution are likely to be smoothed by diffusion across the trajectories in the case where three-dimensional effects are included. We choose a more diffuse density profile as an example of a hollow distribution, given by the inverted Gaussian $f_0(J) = C\{1 - \frac{1}{2}\exp[-(J-J_0)^2/D^2]\}$, with $J_0 = J_s/2$, $D = J_s/2$, and $C$ the normalizing constant. We plot $df_0/d\omega_b$ in Fig. 8(a) and the growth in Fig. 8(b).

Since sidebands cannot be eliminated completely it remains debatable whether a distribution function can be tailored experimentally minimizing their growth rate. From the previous discussion a flat distribution inside the trapped regime with sharp gradients localized at the separatrix seems the appropriate choice. Instabilities will then localize near the separatrix and the gain will be suppressed by the strong shear. To check this we plot the growth rates from Eq. (40) for two types of distributions $f_0(J)$: (i) two Gaussians $f_0(J) = (2\pi^3 D^2)^{-1/2}\exp(-J^2/2D^2)$ centered at the bottom of the island and of characteristic lengths $D$ equal to half the island width $D = J_s/2$ in Fig. 9(a) and one island width $D = J_s$ in Fig. 9(b), and (ii) two steplike distributions of the form $f_0(J) = (\pi^{1/2}\alpha D)^{-1}\exp[-(J/\alpha D)^N]$ with $N = 16$. Selecting $\alpha = (N/N-1)^{1/N}$ places the sharp gradient at $J = D$ and we plot the case $D = J_s/2$ in Fig. 9(c) and $D = J_s$ in Fig. 9(d).

Comparing Fig. 9(a) to Fig. 9(b) and Fig. 9(c) to Fig. 9(d) it is seen that the growth rates between similar types of distributions tend to decrease the closer the maximum gradient $df_0/dJ$ is placed near the separatrix. In both cases there is more than one order of magnitude reduction in the gain by shifting the maximum gradient position from $D = J_s/2$ to $D = J_s$. Because $f_0$ was chosen monotonic in all the above plots and because it was limited to trapped particles, $df_0/d\omega_b$ preserves its sign and only lower modes are unstable. The spectral width of the unstable regimes is reduced with a parallel increase in the maximum gain as one goes from the Gaussian type to the steplike type of distributions. Also, the distance of the sideband frequencies form the main signal decreases by shifting the gradient position $D$ closer to the separatrix. Distributions with sharp gradients at the separatrix such as those in Figs. 9(b) and 9(d) are perhaps more relevant to the case of variable wiggler FEL, where the

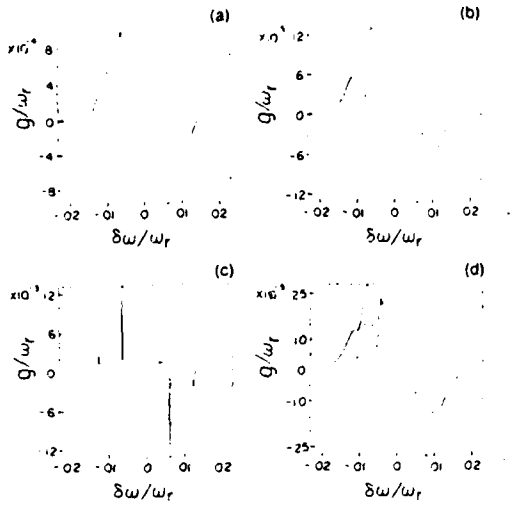



FIG. 9. Normalized growth rate for monotonic distributions centered at the bottom of the well $J = 0$ including the first three harmonics $n < 4$ in Eq. (16). (a) Gaussian distribution of width $D$ equal to half the island width $D = J_s/2$. (b) Gaussian distribution with $D = J_s$. (c) Steplike distribution with $D = J_s/2$ and (d) steplike distribution with $D = J_s$.

"bucket" of the trapped particles is decelerating in phase space leaving the untrapped particles behind, and only small diffusion occurs across the separatrix allowing sharp gradients.

Our calculations for the case of a fixed parameters wiggler can be easily extended to the case of a variable wiggler FEL provided that the same adiabatic assumptions hold. Only the functional relations (19) between the action-angle variables $(J,\theta)$ and the coordinates $(P,\psi)$ need to change. The derivation of the growth rate, performed in $J$ space, is independent of the transformation $J(P,\psi)$ and the result, Eq. (40), stands as is. It is the high gain of tapered wiggler FEL's that seems to challenge the adiabatic approach to the problem. In this case the change of the signal amplitude $a_s(t)$ in time together with the dependence of the equilibrium $f_0$ on both time and $\theta$ should be included for a more realistic treatment.

If the growth time for $a_s(t)$ is long compared to the synchrotron period $\tau_b$, the WKB approximation is applicable. The growth rate $g_s$ for a given frequency $\omega_s$ becomes time dependent as the distribution profile $f_0(J,t)$ and the synchrotron frequency $\omega_b(J,t)$ in Eq. (40) change in time. The most unstable sideband frequencies vary with time. A continuous sideband spectrum emerges in this case[53] as the maximum amplification shifts among various modes during the interaction time. If, on the other hand, the growth time for the main FEL signal is comparable or shorter than the synchrotron period, then $\omega_b(J)$ cannot be defined and resonance conditions of the form (28) do not exist. It is reasonable to speculate, supported by numerical results,[19] that the sideband instability does not appear in this case. Instead, the slow frequency components in the electron motion generate only incoherent (spontaneous) emission in the sideband frequency regime. The threshold in the growth rate of the main signal that causes the transition from coherent sideband emission (instability) to incoherent emission (noise) is an intriguing question that has yet to be answered.

## ACKNOWLEDGMENT

This work was supported by the U.S. Army Strategic Defense Command.

[1] H. Motz, J. Appl. Phys. 22, 527 (1951).
[2] J. M. J. Madey, J. Appl. Phys. 42, 1906 (1971).
[3] L. R. Elias, W. M. Fairbanks, J. M. J. Madey, G. J. Ramian, H. A. Schwettmann, and T. I. Smith, Phys. Rev. Lett. 36, 717 (1976).
[4] F. A. Hopf, P. Meystre, M. O. Scully, and W. H. Louisell, Phys. Rev. Lett. 37, 1342 (1976).
[5] W. B. Colson, Phys. Lett. A 64, 190 (1977).
[6] N. M. Kroll and W. A. McMullin, Phys. Rev. A 17, 300 (1978).
[7] A. Bambini, A. Renieri, and S. Stenholm, Phys. Rev. A 19, 2013 (1979).
[8] P. Sprangle, V. L. Granatstein, and L. Baker, Phys. Rev. A 12, 1697 (1975).
[9] P. Sprangle, R. A. Smith, and V. L. Granatstein, in *Infrared and Millimeter Waves*, edited by K. J. Burton (Academic, New York, 1979), Vol. 1, p. 279.
[10] L. Friedland and A. Fruchtman, Phys. Rev. A 25, 2693 (1982).
[11] R. A. Schill and S. R. Seshadri, Phys. Fluids 29, 2298 (1986).
[12] P. Sprangle, C. M. Tang, and W. M. Manheimer, Phys. Rev. A 21, 302 (1980).
[13] N. M. Kroll, P. L. Morton, and M. N. Rosenbluth, IEEE J. Quantum Electron QE-17, 1436 (1981).
[14] N. M. Kroll, P. L. Morton, and M. N. Rosenbluth, in *Free Electron Generators of Coherent Radiation* (Addison-Wesley, Reading, MA, 1980), Vol. 7, p. 89.
[15] W. B. Colson, Phys. Quantum Electron. 8, 457 (1982).
[16] T. M. Antonsen, Jr., Phys. Rev. Lett. 58, 211 (1987).
[17] W. B. Colson, IEEE J. Quantum Electron. QE-17, 1417 (1981).
[18] R. C. Davidson and W. A. McMullin, Phys. Fluids 26, 840 (1983).
[19] C. M. Tang and P. A. Sprangle, IEEE J. Quantum Electron QE-21, 970 (1985).
[20] A. K. Ganguly and H. P. Freund, Phys. Rev. A 32, 2275 (1985).
[21] H. P. Freund and A. K. Ganguly, Phys. Rev. A 34, 1242 (1986).
[22] S. H. Gold, W. M. Black, H. P. Freund, V. L. Granatstein, P. C. Efthimion, and A. K. Kinkead, Phys. Fluids 26, 2683 (1983).
[23] T. J. Orzechowski, B. Anderson, W. M. Fawley, D. Prosnitz, E. T. Scharlemann, S. Yarmea, D. Hopkins, A. C. Paul, A. M. Sessler, and J. Wurtele, Phys. Rev. Lett. 54, 889 (1985).
[24] J. A. Pasour, R. F. Lucey, and C. A. Kapetanakos, Phys. Rev. Lett. 53, 1928 (1984).
[25] L. R. Elias, W. M. Fairbank, J. M. J. Madey, H. A. Schwettman, and T. I. Smith, Phys. Rev. Lett. 36, 717 (1976).
[26] D. A. G. Deacon, L. R. Elias, J. M. J. Madey, G. J. Ramian, H. A. Schwettman, and T. I. Smith, Phys. Rev. Lett. 38, 892 (1977).
[27] M. Billardon, P. Elleaume, Y. Lapierre, J. M. Ortega, C. Bazin, M. Bergher, J. Marilleau, and Y. Petroff, in *Proceedings of the Seventh International FEL Conference*, Tahoe City, California, edited by E. T. Scharlemann and D. Prosnitz (North-Holland, Amsterdam, 1985), p. 26.
[28] L. Elias, J. Hu, and G. Ramian, Nucl. Instrum. Methods Phys. Res. A 237, 203 (1984).
[29] S. V. Benson, J. M. J. Madey, J. Schoultz, M. Marc, W. Wadensweller, and G. A. Westenskow, in Ref. 27, p. 26.
[30] J. Fajans and G. Bekefi, Phys. Fluids 29, 3461 (1986).
[31] R. W. Warren, B. E. Newnam, J. G. Winston, W. E. Stein, L. M. Young, and C. A. Brau, IEEE J. Quantum Electron QE-19, 391 (1983).
[32] T. J. Orzechowski, B. R. Anderson, J. C. Clark, W. M. Fawley, A. C. Paul, D. Prosnitz, D. B. Hopkins, A. M. Sessler, and J. S. Wurtele, Phys. Rev. Lett. 57, 2172 (1986).
[33] C. R. Pidgeon, D. A. Jaroszynski, D. M. Tratt, S. D. Smith, W. J. Firth, M. F. Kimmitt, C. W. Cheng, M. W. Poole, G. Saxon, R. P. Walker, J. S. MacKay, J. M. Reid, M. G. Kelliher, E. W. Lang, D. V. Land, and W. A. Gillespe, IEEE J. Quantum Electron QE-21, 1083 (1985).
[34] P. Sprangle, C. M. Tang, and I. Bernstein, Phys. Rev. A 28, 2300 (1983).

[15]N. M. Kroll, P. L. Morton, and M. N. Rosenbluth, in *Free Electron Generators of Coherent Radiation* (Addison-Wesley, Reading, MA, 1980), Vol. 7, p. 147.
[16]J. C. Goldstein, B. E. Newnam, R. W. Warren, and R. L. Sheffield, in Ref. 27, p. 4.
[17]C. M. Tang and P. Sprangle, in *Proceedings, Free Electron Generators of Coherent Radiation*, Orcas Island, Washington, edited by S. F. Jacobs and M. O. Scully (SPIE, Bellingham, WA, 1983), Vol. 453, p. 11.
[18]W. B. Colson, in Ref. 27, p. 168; see also, W. B. Colson, in *Proceedings of the International Conference on Lasers* (STS, McLean, VA, 1982), p. 751.
[19]A. T. Lin, in *Free Electron Generator of Coherent Radiation* (Addison-Wesley, Reading, MA, 1982), Vol. 9, p. 867.
[20]B. Hafizi, A. Ting, P. Sprangle, and C. M. Tang, submitted to Phys. Rev. A.
[21]T. Masud, T. C. Marshall, S. P. Schlesinger, and F. G. Yee, Phys. Rev. Lett. **56**, 1567 (1986).
[22]T. Masud, T. C. Marshall, S. P. Schlesinger, F. G. Yee, W. M. Fawley, E. T. Scharlemann, S. S. Yu, A. M. Sessler, and E. J. Sternbach, Phys. Rev. Lett. **58**, 763 (1987).
[23]N. M. Rosenbluth, H. V. Wong, and B. N. Moore, in Ref. 37, p. 25.
[24]D. C. Quimby, J. M. Slater, and J. P. Wilcoxon, IEEE J. Quantum Electron. **QE-21**, 979 (1986).
[25]R. C. Davidson, Phys. Fluids **29**, 2689 (1986).
[26]R. C. Davidson, J. S. Wurtele, and R. E. Aamodt, Phys. Rev. A **34**, 3063 (1986).
[27]R. C. Davidson and J. S. Wurtele, Phys. Fluids **30**, 557 (1987).
[28]R. C. Davidson and J. S. Wurtele, Phys. Fluids **30**, 2825 (1987).
[29]S. Riyopoulos and C. M. Tang, in *Proceedings of the Eighth International FEL Conference*, Glasgow, Scotland, edited by M. Poole (North-Holland, Amsterdam, 1987), p. 226.
[30]H. V. Wong, Phys. Fluids **15**, 632 (1972).
[31]Sideband coupling in FEL's is much weaker than in the case of plasma waves, examined in Ref. 50. In the case of plasma waves, $k \gg k_n$, therefore $\Delta\omega = \omega(k + k_n) - \omega(-k_n) \neq 0$ and degenerate perturbation theory must be applied. That means that the sideband coupling in plasma waves is a strong (zeroth order) effect.
[32]See, for example, M. Abramowitz and I. A. Stegun, *Handbook of Mathematical Functions* (Dover, New York, 1972), p. 591.
[33]F. G. Yee, T. C. Marshall, and P. Schlesinger, submitted to IEEE Trans. Plasma Sci.

# APPENDIX KK

## Chaotic Electron Motion Caused by Sidebands in Free Electron Lasers

**Naval Research Laboratory**
Washington, DC 20375-5000




NRL Memorandum Report 6365

# Chaotic Electron Motion Caused by Sidebands in Free Electron Lasers

S. RIYOPOULOS

*Science Applications Intl. Corp.*
*McLean, VA 22102*

C. M. TANG

*Plasma Theory Branch*
*Plasma Physics Division*

October 27, 1988

Approved for public release; distribution unlimited.

## CONTENTS


I. INTRODUCTION ..... 1

II. GENERAL CONSIDERATIONS ..... 6

III. PORTRAIT OF THE PHASE SPACE ..... 10

IV. THRESHOLD FOR ERRATIC MOTION ..... 15

V. NARROW FREQUENCY BAND DIFFUSION ..... 19

VI. BROAD FREQUENCY BAND DIFFUSION ..... 22

A. Broad Discrete Spectrum ..... 24
B. Broad Continuous Spectrum ..... 27

VII. NUMERICAL RESULTS ..... 33

VIII. CONCLUSION ..... 36

ACKNOWLEDGEMENT ..... 37

APPENDIX A — Transformations in Action-Angle Variables ..... 39

APPENDIX B — Phase Averaging Over Constant J ..... 43

APPENDIX C — Computation of the Quasilinear Diffusion Coefficient ..... 45

APPENDIX D — Summation of Fourier Coefficients ..... 49

REFERENCES ..... 52

DISTRIBUTION LIST ..... 67

# CHAOTIC ELECTRON MOTION CAUSED BY SIDEBANDS IN FREE ELECTRON LASERS

## I. INTRODUCTION

Multifrequency effects in Free Electron Lasers (FELs) become increasingly important as progress is made towards high power operation. Growth of parasitic frequencies (sidebands[1-5]) has been predicted theoretically and has been observed in experiments[6,7] as well as in simulations[8-11] with either constant or tapered wigglers[11]. The efficiency for the carrier signal is reduced and the optical quality is degraded as power is channeled into frequencies apart from the intended operation frequency. Another potential hazard that has attracted little attention so far is the onset of chaotic electron motion caused by the presence of even a single frequency sideband. This may lead to extensive particle detrapping and premature loss of the amplification for all the radiation modes independent of frequency.

Two of the main issues concerning FEL operation are: (a) whether unstable parasitic frequencies exist that can grow to significant amplitude and (b) what is the effect of potentially unstable modes on the trapped electron trajectories. Considerable attention has been devoted to the linear stability issue. The gain for small sideband signal has been computed analytically[1-5] invoking either ensemble averaging over single particle trajectories or solutions of the perturbed kinetic equation for the distribution function. Initial results, obtained for particles localized near the bottom of the ponderomotive well, and, in particular, more recent results including all trapped and untrapped particles[2] with arbitrary distributions, have demonstrated that every nontrivial distribution $df_o/dJ \neq 0$ is unstable to sideband growth.

Manuscript approved August 29, 1988.

Given that sidebands cannot be eliminated, the growth of the unstable modes to a finite amplitude may have serious effects on the unperturbed trajectories. It has been known that stochastic behavior[12] is an intrinsic property of perturbed Hamiltonian systems[13,14]. Accordingly, the electron motion in a FEL will become chaotic when the sideband amplitude exceeds a certain threshold. This, in turn, will result in significant electron detrapping. Since it is the deceleration of the trapped electron bucket that provides the energy for the radiation in case of tapered wigglers, detrapping will cause loss of amplification for the FEL signal.

In the present work we investigate the nonlinear effects caused by sidebands. The threshold for stochasticity, above which unbound chaotic motion occurs, is determined. Once the stochastic transition takes place, the action J, a constant of motion in the unperturbed system, changes in a random manner. The ensemble average $\langle \Delta X^2 \rangle$ of any physical quantity X is described by a diffusion equation. Diffusion of the action invariant provides a measure of the leakage rate across the separatrix. If D is the effective diffusion coefficient in action space then the diffusion length $L_d = J_s^2/D$, where $J_s$ is the action at the separatrix, signifies the length over which approximately half of the deeply trapped particles get detrapped. We show that a single frequency sideband at a modest fraction of the carrier amplitude suffices to spread irregular motion over a significant fraction of the trapped particle domain. However, given that the interaction time of an electron in a FEL is short, we are mainly concerned on how fast this diffusion occurs. The diffusion rate increases and the diffusion length $L_d$ decreases with increasing sideband amplitude(s). Thus, a critical sideband level $a_c$ can be defined above which the diffusion length $L_d$

becomes shorter than the wiggler length $L_w$. Obviously the power level for the sidebands in a FEL cannot exceed $a_c$, otherwise, extensive diffusion and premature detrapping will occur. On the other hand, enough electrons can remain trapped during the interaction period even though their motion has turned stochastic, because we find that usually the critical amplitude $a_c$ is much larger than the threshold for stochasticity $\alpha_s$.

A clear-cut relation between the diffusion rate under constant total sideband power and the type of the excited sideband spectrum is discovered. More specifically we observe three regimes in the simulation parameters defining the sideband spectrum, corresponding to a narrow, a wide discrete and a wide continuous spectrum. The transition from one spectral type to another is accompanied by an abrupt change in the diffusion rates. In all cases we find the diffusion coefficient proportional to the ratio of the total power in the sidebands to the FEL carrier power. The coefficients of this proportionality depend on the spectral type. A general conclusion is that the diffusion rate under constant sideband power ratio decreases with increasing number of spectral components. The diffusion rate for a single sideband frequency exceeds that of a broad continuous spectrum by orders of magnitude while a broad discrete spectrum causes intermediate diffusion rates.

For practical purposes we measure the diffusion length in terms of the number of wiggler periods, $N_d = L_d/\lambda_w$, while $\langle \Delta J^2 \rangle$ is normalized to the action $J_s$ at the (unperturbed) separatrix. We compute the normalized diffusion coefficient D analytically for the cases of broad discrete and continuous spectra. In the latter case the quasilinear diffusion coefficient in action space $D_q(J)$ is obtained in closed form. This expression for $D_q(J)$ is quite general, valid for any choice of

unperturbed Hamiltonian $H_o(J)$. The analysis also shows that the normalized diffusion coefficient does not depend on the beam energy $\gamma_r$. The numerical results agree well with the theory.

We evaluate the loss of trapped particles for typical short wavelength FEL parameters. We find that a single frequency sideband with a sideband to carrier power ratio of $\lesssim 1$ can cause half of the particles to detrap over 100 wiggler periods; we have observed total loss of trapped particles for power ratios of $\simeq 1$. In cases of wide but discrete sideband spectrum the diffusion length becomes comparable to the wiggler length only at large power ratios ($\gtrsim 1$). The case of a wide continuous spectrum seems to cause insignificant electron detrapping for the same parameters as above; the typical diffusion length is of the order of 1000 wiggler periods for sideband to carrier power ratios of 1.

In our investigation we have assumed all electromagnetic fields as given. The changes in the particle trajectories are decoupled from the evolution of the fields. At the expense of self-consistency we are able to analyze the situation theoretically and determine the scaling of the diffusion rates on the various FEL parameters. Deterioration in the extraction efficiency has been observed in self-consistent numerical simulations of high power FEL oscillators[10] with high level sideband excitation. The gain per pass in a tapered wiggler is progressively limited as the sideband power goes up and the rate of electron detrapping is accelerated. In an untapered wiggler, on the other hand, particle detrapping is not so important for the main signal efficiency. The total extraction efficiency may actually increase with the sidebands since there are more modes to channel the electron beam energy into.

The remainder of this paper is organized as follows. In Sec. II we construct our analytic model for the study of the stochastic diffusion and discuss the various approximations. To elucidate the analysis we start with a single sideband mode and give a sketchy description of how this can lead to electron detrapping. In Sec. III we examine the structure of the phase space for a monochromatic sideband in detail, using canonical formalism. The threshold for the stochastic transition and the extent of the chaotic regime in phase space are obtained in Sec. IV. In Sec. V the diffusion rate caused by a single sideband mode is examined in connection with the various FEL parameters. In Sec. VI the study is extended to broad (multifrequency) sideband spectra. A distinction is drawn between continuous and discrete spectra. Subsection VI.a covers the case of a broad discrete spectrum and the related diffusion coefficient. Subsection VI.b deals with a broad continuous spectrum and the corresponding quasilinear diffusion coefficient. In Sec. VII the theoretical models are compared with numerical results. The differences in the induced diffusion rates among the three different types of spectra are emphasized. The reduction in the extraction efficiency in a tapered wiggler FEL is computed as a function of the diffusion coefficient. Results and conclusions are summarized in Sec. VIII.

## II. GENERAL CONSIDERATIONS

We consider relativistic electrons streaming along the z-direction through the static magnetic wiggler and the radiation fields of the carrier and the sideband. We take all fields to be circularly polarized and of constant amplitude. To simplify the analysis and make the underlying ideas clearer we start out with monochromatic waves for the carrier and the sideband. The total vector potential is then,

$$A(z,t) = \frac{1}{2}\left[(e_x - ie_y)A_w e^{i\phi_w} - (e_x + ie_y)A_r e^{i(k_r z - w_r t)} - (e_x + ie_y)A_s e^{i(k_s z - w_s t)}\right] + cc\ , \tag{1}$$

where the subscripts w, r, and s stand for wiggler, carrier and sideband respectively. We assume that all waves propagate with the speed of light c, ignoring the small correction of order $\omega_p^2/\omega_r^2$ from the dielectric contribution of the beam. Electrostatic contributions to the fields are neglected for operation in the Compton regime. The phase of the wiggler is given by $\phi_w(z) = \int^z k_w(z')dz'$, where the wave number $k_w(z)$ may change slowly in z on a scale length much longer than the wiggler wavelength $\lambda_w = 2\pi/k_w$. The main signal wave number $k_r$ is doubly Doppler upshifted from the wiggler wavenumber $k_w$,

$$k_r = 2\gamma_z^2 k_w\ , \tag{2}$$

with the upshifting factor $\gamma_z = (1 - \beta_r^2)^{-1/2}$ and $\beta_r = \omega_r/c(k_r + k_w)$.

We have ignored variations in the x- and y-directions. Increased number of dimensions is known to facilitate the transition to chaotic

motion. Therefore, the threshold for stochasticity for variations in the z-direction only will be useful in providing a neccessary condition to avoid fast large-scale diffusion. Slow diffusion due to higher dimensionality will in fact persist for the real system below this threshold. As far as particle detrapping is concerned, three dimensional effects are comparatively insignificant, provided that the dependence on x and y is adiabatic. This requires that the frequency of the betatron oscillation, caused by the transverse field gradients[15], be small compared to the electron synchrotron frequency in the ponderomotive bucket.

We have also assumed that the radiation amplitudes remain constant. In case of fast growth rate of the carrier amplitude the particle trajectories are not analytically tractable, even in the absence of sidebands. It is generally expected that the fraction of trapped particles decreases with decreasing carrier amplitude. Therefore the spreading of the radiation beam due to diffraction[16,17] can also cause detrapping by reducing the carrier amplitude $a_r$. This detrapping mechanism is independent of the diffusive detrapping caused by sidebands that is examined here.

Normalizing the time t to $\omega_r^{-1}$, the length z to $k_r^{-1}$, the mass to $m_e$ and the vector potentials according to $a_i = |e|A_i/m_e c^2$ the dimensionless Hamiltonian describing the electron motion in the fields of Eq. (1) is,

$$H = \left[\mu^2 + p_z^2 - 2\Lambda\, a_w a_r \cos(\phi_w + k_r z - \omega_r t) - 2\Lambda\, a_w a_s \cos(\phi_w + k_s z - \omega_s t)\right]^{1/2} \tag{3}$$

$$\mu^2 = 1 + M(a_w^2 + a_r^2 + a_s^2) ,$$

with $M = 1$ and $\Lambda = 1$. Eq. (3) also describes the fast-time averaged Hamiltonian for a linearly polarized wiggler by setting $M = 1/2$, $\Lambda = [J_o(\zeta) - J_1(\zeta)]/2$ and $\zeta = a_w^2/(4 + 2a_w^2)$.

The terms proportional to $a_w a_r$ and $a_w a_s$ are the ponderomotive potentials due to the combined action of the wiggler with the main signal and the sideband respectively. The resonant velocities for each ponderomotive potential are given by $\beta_i = k_i/(k_i + k_w)$ corresponding to resonant energies,

$$\gamma_i = \left(\frac{\mu^2}{1 - \beta_i^2}\right)^{1/2}, \qquad i = r, s. \tag{4}$$

In the vicinity of $\gamma_i$ the motion of the electrons is determined by the corresponding resonant term inside (3). We may drop the nonresonant term for small radiation amplitudes and linearize (3) for small excursions $\delta\gamma$ around $\gamma_i$. From the resulting pendulum equation we find that trapped electrons will undergo oscillations of frequency $\omega_b$ around $\gamma_i$, forming islands of width $\delta\gamma_i$ in phase space, where $\omega_b$ and $\delta\gamma_i$ are given by,

$$\omega_b = \frac{1}{\gamma_i^2}\left(a_w a_i \mu^2\right)^{1/2}, \qquad \delta\gamma_i = \gamma_i \left(\frac{a_w a_r}{\mu^2}\right)^{1/2}. \tag{5}$$

We call these islands, due to the direct wave-particle resonances, primary islands.

Roughly speaking, irregular motion breaks out as a result of nearby island overlapping[14]. The amplitudes $a_r$, $a_s$ must increase to the point where,

$$\delta\gamma_r + \delta\gamma_s \geq |\gamma_r - \gamma_s|, \tag{6}$$

for an overlapping between the two primary islands to take place. The difference in resonant energies $\Delta\gamma = \gamma_r - \gamma_s$ is given by $\Delta\gamma \simeq \gamma_z\gamma_r^2\,\Delta\beta$ where $\Delta\beta = |\beta_s - \beta_r| = (1/2\gamma_z^2)|k_r - k_s|/k_r$. Given that typically $k_s - k_r \sim 2\gamma_z^2\omega_b$ we find,

$$\Delta\gamma \sim \gamma_r(a_w a_r)^{1/2}. \tag{7}$$

It then follows from (5) to (7) that overlapping and transition to chaotic behavior can take place at $a_s \sim a_r$. This crude estimate demonstrates the potential of chaotic behavior for large amplitude sidebands. The above threshold becomes even smaller in case of a multifrequency sideband spectrum.

We will be interested in evaluating the fraction of the phase space that becomes chaotic as a function of the sideband amplitude. This requires the use of a more refined overlapping criterion. Electrons trapped inside the primary island of the main signal still experience perturbations in their motion caused by the sideband. The perturbation is especially felt by these electrons that have the synchrotron frequency $\omega_b$ matching the difference between the frequencies of the main signal and the sideband. This condition defines new secondary resonances between the electrons and the sideband. It is the overlapping among the nearby secondary islands, formed inside the primary island, that determines more accurately the break out and extent of the stochastic behavior.

## III. PORTRAIT OF THE PHASE SPACE

The electrons are injected into a FEL with energies near the resonant energy $\gamma_r$ for the main signal $\omega_r$. Expression (3) can be linearized for small excursions $\delta\gamma/\gamma_r << 1$ for electrons not too far from the separatrix. Introducing $\tilde{\gamma} = \gamma - \gamma_r$ and $\psi = (k_w + k_r)z - \omega_r t$ as a new pair of canonical variables and approximating the time $t(z) \simeq z/c\beta_r$ we obtain,

$$\tilde{H}(\tilde{\gamma},\psi;z) = \frac{k_w}{\gamma_r}\tilde{\gamma}^2 + \frac{a_w a_r}{\gamma_r}(\cos\psi + \psi \sin\psi_r) + \frac{a_w a_s}{\gamma_r}\cos(\psi - \delta_s z). \tag{8}$$

In (8) the phase flow is parametrized by the traveled length z inside the wiggler rather than the time t. It was also assumed that the wiggler parameters change slowly compared to the wiggler wavelength $2\pi/k_w$. The term $\sin\psi_r$ parametrizes the rate of change for the resonant energy caused by the change in the wiggler wavelength,

$$\frac{d}{dz}\gamma_r = \frac{k_r a_w a_r}{\gamma_r}\sin\psi_r \ , \tag{9}$$

where $\psi_r = \pi$ corresponds to an untapered wiggler. The term $\delta_s$ in the sideband phase is the Doppler downshifted difference between the signal and the sideband wave numbers,

$$\delta_s = \frac{k_w}{k_r}(k_s - k_r) \ . \tag{10}$$

In the absence of sidebands, $a_s = 0$, the Hamiltonian $H_o$ is integrable. The unperturbed trajectories in the ponderomotive well are given by $H_o(\tilde{\gamma},\psi) = K$ where K is the reduced energy in the ponderomotive frame. These orbits take the simplest possible form expressed in terms of the action-angle variables (J, $\theta$), defined as,

$$J = \frac{1}{2\pi}\oint d\psi\ \tilde{\gamma}(K,\psi), \qquad \theta = \frac{\partial}{\partial J}\int^{\psi} d\psi'\,\tilde{\gamma}(K,\psi')\ , \qquad (11)$$

where $K = H_o(J)$ and the path of integration is over the unperturbed orbits. For trapped particles in closed trajectories, the action J is related to the area in phase space enclosed by the orbit. For untrapped particles in open trajectories, the path of integration in Eq. (11) depends on the wiggler type. In case of an untapered wiggler, the orbits are periodic and the limits of $\psi$ integration are from 0 to $2\pi$. In case of a tapered wiggler the path of integration is the segment of the trajectory that begins and ends at $\psi = \psi_s$, enclosing the separatrix. Thus, J remains finite, avoiding an infinite jump in action across the separatrix that would result by considering the full orbit length for unbound orbits[18]. J is always periodic in $\psi$, $J(\tilde{\gamma},\psi_1) = J(\tilde{\gamma},\psi_2)$ for $\psi_1 = \psi_2 + 2\pi$, even when $H_o$ is not (case of tapered wiggler).

Hamiltonian (8) is now transformed under the canonical transformation defined by Eq. (11) into,

$$H(J,\theta;z) = H_o(J) + \frac{a_w a_s}{\gamma_r}\sum_{n=0}^{\infty} Q_n^{+}(J)\cos(n\theta + \delta_s z) + Q_n^{-}(J)\cos(n\theta - \delta_s z). \qquad (12)$$

$Q_n^{+}(J)$ are the Fourier coefficients obtained by the decomposition of the perturbing sideband phase $\psi(J,\theta) - \delta_s z$ into harmonics of the angle $\theta$,

where $\psi(J, \theta)$ is obtained by inverting Eq. (11). In case of constant parameter wiggler J, $\theta$ and $Q_n$ (J) are expressed in closed forms given in Appendix A.

$H_o(J)$ is independent of $\theta$ so the unperturbed orbits in (J, $\theta$) space are straight lines,

$$J = \text{const.}, \qquad \theta = \theta_o + \kappa_b(J)z \ .$$

The synchrotron wave number $\kappa_b(J)$ is connected to the bounce length $L_b$ and the synchrotron frequency in the laboratory frame $\omega_b(J)$ with the relation,

$$\kappa_b(J) = \frac{dH_o(J)}{dJ} = \frac{2\pi}{L_b(J)} = \frac{\omega_b(J)}{c\beta_z} \ . \tag{13}$$

Since c = 1 in the normalized units and $\beta_z$ = 1 in the cases of interest, we may use $\omega_b(J)$ in place of $\kappa_b(J)$ as well.

Expression (12) for the transformed Hamiltonian reveals the new resonances emerging when a sideband is turned on. Defining the phase of the nth sideband induced harmonic $\theta^{(n)} = n\theta \pm \delta_s z$, the stationary phase condition reads,

$$\pm n\kappa_b(J) - \delta_s = 0, \quad \text{or} \quad \pm n\beta_z\omega_b(J) - \delta_s = 0. \tag{14}$$

Thus, particles, originally in unperturbed orbits $J = J_n$, resonate with the sideband when the nth harmonic of their synchrotron period $\omega_b(J_n)$ matches the downshifted frequency difference between the sideband and the carrier signal.

For a given n and sufficiently small $a_s$ we may keep only the resonant term $\theta^{(n)}$ to examine the motion in the vicinity of $J_n$. This is formally achieved by the canonical transformation,

$$\Theta = n\theta - \delta_s z \ , \quad I = \frac{1}{n} J \ ,$$
$$Z = \delta_s z \ , \qquad I_Z = \frac{1}{\delta_s} K + \frac{1}{n} J \ , \tag{15}$$

coming from the generating function $F(\theta,z,I,I_Z) = (n\theta - z)I - zI_Z$. The resulting Hamiltonian is,

$$H_n(I,I_Z,\Theta,Z) = H_o(nI) + \delta_s(I_Z - I) + \frac{a_w a_s}{\gamma_r} Q_n(nI) \cos\Theta + O(a_s^2) \ . \tag{16}$$

The fixed points $(J_n, \theta_n)$ are found from,

$$\frac{d\Theta}{dZ} = \frac{\partial H_n}{\partial I} = \frac{\partial H_o}{\partial I} - \delta_s = 0, \tag{17a}$$

$$\frac{dI}{dZ} = - \frac{\partial H_n}{\partial \Theta} = \frac{a_w a_s}{\gamma_r} Q_n(nI) \sin\Theta = 0. \tag{17b}$$

Using relations (15) for the transformed variables we recover from (17a) the resonant condition (14) while (17b) indicates $\theta_n = k\pi / n$, $k = 0,1,\ldots,n-1$.

In short, a single frequency sideband causes chains of secondary islands to appear inside the original primary island. Each chain corresponds to a given harmonic n and is centered around the stable fixed points $J_n$, $\theta_n$. The structure of the phase space is shown in Figs. 1 and 2. They are surfaces of section, created by numerically

integrating the original equations of motion from Hamiltonian Eq. (8) and then recording the intersection point of each trajectory with the plane $z = 2\pi/\delta_s$. The $\tilde{\gamma}$ vs. $\psi$ plots are on the left side in Figs. 1 and 2. The plots on the right side show the same surfaces of section in action-angle variables, produced by the transformations (11). The bounce frequency around a given secondary island is found by linearly expanding the resonant Hamiltonian (16) in $\delta I = I - I_n$. From the resulting pendulum equation and from relations (15) one finds that the secondary synchrotron period $\Omega_n$ near the center is given by,

$$\Omega_n = n \left[ \left( \frac{d\omega_b}{dJ} \right)_{J_n} \frac{a_w a_s}{\gamma_r} Q_n^{\pm}(J) \right]^{1/2}, \tag{18a}$$

while the half-width of the island $\delta J_n$ is

$$\delta J_n = \left[ 2 \frac{a_w a_s}{\gamma} \frac{Q_n(J_n)}{(d\omega_b/dJ)_{J_n}} \right]^{1/2}. \tag{18b}$$

Representation (12) for the Hamiltonian (8) is formally independent on the details of the transformations (11). Consequently, the same stability analysis applies for constant as well as variable parameter wigglers.

## IV. THRESHOLD FOR ERRATIC MOTION

When the sideband amplitude exceeds a certain amplitude $\alpha_s$ regarded as the stochasticity threshold, the presence of even one sideband frequency suffices to transform the regular coherent motion, such as in Fig. 1, to the irregular unbounded motion shown in Fig. 2. The mechanism for this radical change in behavior can be briefly described as follows. The trajectories emanating from the unstable fixed points (X-points) of a secondary island do not actually join smoothly around that island. They intersect infinite times with each other[12,13] due to the effect of the other harmonics $n' \neq n$ that were ignored during the local approximation Eq. (16). A thin layer of fuzzy motion thus surrounds each island chain of given n. As the amplitude $a_s$ increases, the width of each island increases according to (18b) and so does the thickness of the stochastic layer around that island. At a given point the stochastic layers around the two neighboring island chains n and n+1 overlap[14], allowing particles to hop from one island to another. This signifies the beginning of unbounded, random motion in J characterized as stochastic diffusion.

Various methods of different accuracy have been developed for estimating the stochasticity threshold[12,14]. An approximate criterion that works well in most cases is,

$$\delta J_n + \delta J_{n+1} \geq \frac{2}{3} \Delta J_n \ , \tag{19}$$

where $\delta J_n$, $\delta J_{n+1}$ are the separatrix half-widths and $\Delta J_n = J_{n+1} - J_n$ is the distance between the separatrix centers for the n and n+1 harmonics respectively. For small widths $\delta J$ and distances $\Delta J$ compared to J we may expand

$$\omega_b(J_{n+1}) - \omega_b(J_n) = \left(\frac{\partial \omega_b}{\partial J}\right)_{J_n} \Delta J_n \simeq \frac{\omega_b(J_n)}{n} , \qquad (20)$$

and use (18b) with $J_{n+1} \simeq J_n$ to obtain the amplitude $a_s(n)$ for overlapping

$$a_s(n) \simeq \left(\frac{2}{3n}\right)^2 \frac{\omega_b(J_n)}{(d\omega_b/dJ)_{J_n}} \left(\frac{\gamma_r}{2a_w Q_n(J_n)}\right) . \qquad (21)$$

The outermost islands centered at $J_n \simeq J_s$, correspond to larger shear $d\omega_b(J)/dJ$, smaller $\omega_b(J)$ and higher harmonics n, for given $\omega_s - \omega_r$. According to (21) the threshold $a_s(n)$ is lower near the separatrix and the outermost secondary islands will be the first to overlap. The overlapping is progressively extending to smaller $J_n$ and lower n as $a_s$ increases. The macroscopic stochastic layer first appears near the original separatrix of the primary island and spreads to the interior of the trapped particle bucket. We take the amplitude when the two innermost harmonics overlap as the threshold for "global" stochastic transition, $\alpha_s \equiv a_s(n_1)$. The lowest possible harmonic $n_1$ for given frequency $\omega_s$ is defined by the resonant condition (14). For $J_n$ small we have both $\delta J$ and $\Delta J$ of order J and the approximations that led to (21) are not valid. In this case, the exact expressions for J and $\omega_b(J)$ must be applied inside the criterion (19).

We may obtain the dependence of $a_s(n)$ on the various parameters using Eqs. (A4) and (A7), setting $d/dJ = (d\lambda/dJ)\, d/d\lambda$ and utilizing the properties of the elliptic integrals to compute the derivatives in Eq. (21). We find that,

$$\frac{a_s(n)}{a_r} \simeq \frac{1}{n^2} F^2(\lambda_n) , \qquad (22)$$

where

$$F(\lambda_n) = \left\{ \frac{E_1(\lambda_n)\, \lambda_n^2\, (\lambda_n^2 - 1)}{E_2(\lambda_n) - (1 - \lambda_n^2)\, E_1(\lambda_n)} \right\}^{1/2} \left( 2Q_n(\lambda_n) \right)^{-1/2} .$$

The threshold for extensive stochasticity $\alpha_s \equiv a_s(n_1)$ is independent of $\gamma$ and $a_w$. The trapping parameter $\lambda_n$ is determined uniquely from $J_n$ according to $\lambda_n = H_o(J_n)\gamma_r/a_w a_r + 1/2$ (see Appendix A). Thus, the sideband frequency $\omega_s$, related to $\omega_b(J_n)$ through the resonant condition (14), is the only parameter that $\alpha_s/a_r$ depends on. The scaling in (22) is still valid in case of large secondary island width with a modification in the numerical factor F.

In Fig. 3a we plot in solid line the threshold $\alpha_s$ for extensive stochasticity, when the two innermost secondary island chains overlap, as a function of the frequency difference $\omega_c - \omega_r$. The dotted line shows the threshold for overlapping between the next two secondary island chains. Some deeply trapped orbits, near the center of the original primary island, still persist when $a_s$ is close to $\alpha_s$. The extent of the area unaffected by the irregular motion when $a_s \simeq \alpha_s$ is given approximately by $J < J_c$ where $J_c \simeq J_n - \delta J_n$. In Fig. 3b we plot the portion $J_c/J_s$ of the remaining "good" trajectories when the sideband amplitude equals $\alpha_s$ as a function of $\omega_s - \omega_r$. It is seen that the threshold $\alpha_s$ is larger and the extent of the stochastic regime is maximized as well for frequency mismatch near a harmonic of the synchrotron frequency $\omega_b(0)$ at the bottom of the ponderomotive well.

The threshold $\alpha_s$ for overlapping is considerably lower but the extent of the stochastic regime also diminishes for frequencies far from a harmonic of the central synchrotron frequency.

A typical phase portrait for a sideband amplitude $a_s$ slightly above $\alpha_s$ is shown in Fig. 2b. Two different kinds of regions coexist: a stochastic regime where diffusive behavior prevails, interrupted here and there by islands of regular motion, remnants of the original regular motion. The stochastic regimes are interconnected allowing unbounded particle transport. The rate of diffusion as well as the decorrelation times are not uniform in phase space but depend on both J and $\theta$.

When $a_s$ is increased well above $\alpha_s$ the chaotic motion engulfs almost 100% of the phase space (Fig. 2c). The decorrelation time is short everywhere in phase space. In this parameter regime the behavior of the system can be described by a diffusion coefficient D(J) depending on the action J only and insensitive to the frequency of the driving sideband. Total stochastization of the island interior occurs roughly when the sideband amplitude grows to the point where the stable fixed point $\tilde{\gamma} = 0$, $\psi = \pi + \psi_r$ at the center of the original island becomes unstable.

## V. NARROW FREQUENCY BAND DIFFUSION

We will examine first the diffusion caused by the presence of one single frequency, large amplitude sideband. This is a relevant approximation in case of a narrow sideband spectrum. The term narrow implies a spectral width $D\omega_s$ much smaller than the frequency separation $\omega_s - \omega_r$, typically of the order $2\gamma_z^2\omega_b$. We examine the evolution of a monoenergetic distribution $f(J;z=0) = \delta(J - J_o)$ by numerically integrating the equations of motion. We plot $\langle\Delta J^2\rangle$, $\langle J\rangle$ and $2\langle\Delta J^2\rangle/z$ against the distance z in Figs. 4a, 4b, and 4c respectively. The electrons are initially uniformly distributed in $\theta$ with constant action $J_o = 0.7\ J_s$. Different curves in the same frame correspond to different sideband amplitudes $a_s$ at a given frequency $\omega_s$.

For a constant diffusion coefficient D, independent of J, the average $\langle J\rangle$ and the mean square deviation $\langle\Delta J^2\rangle = \langle J^2\rangle - \langle J\rangle^2$ would evolve as $\langle\Delta J^2\rangle = (1/2)\ D\ z$, $\langle J\rangle = J_o$. The dashed curves in Figs. 4a - 4c correspond to a sideband amplitude $a_s$ below the stochasticity threshold $\alpha_s$. The deviation $\langle\Delta J^2\rangle$ asymtotes to a constant after an initial increase while the ratio $\langle\Delta J^2\rangle/z$ tends to zero for large z. In this case stochasticity is localized. Different stochastic regimes are still separated by "good" integrable orbits (KAM surfaces) located in between. Electrons diffuse until they are stopped at the boundaries of the stochastic regimes that "compartmentalize" the phase space. The solid curves in Figs. 4a - 4c correspond to sideband amplitude above the global stochasticity threshold $\alpha_s$. This means that the last good orbit has been destroyed allowing different stochastic regimes to interconnect. $\langle\Delta J^2\rangle$ now increases monotonically and the ratio $\langle\Delta J^2\rangle/z$ remains finite for large z. The fact that the diffusion rate is not

constant, and that the average <J> changes away from the initial value $J_o$, shows that D depends strongly on J.

In principle, one could determine a local D(J) by advancing test distributions $\delta(J-J_o)$ of various $J_o$ over short distances z. Then the Fokker-Planck equation for any initial distribution $f_o(J)$ could be solved numerically using D(J). Here, instead, we elect to measure directly the effective diffusion rate associated with a given type of initial distribution. We do so by integrating numerically the equations of motion, Hamiltonian (8), for a number of particles (typically 400) assuming constant amplitude for the electromagnetic fields. A uniform initial distribution in phase space with trapped particles inside the (unperturbed) separatrix is chosen, $f_o(J) = [1 - S(J - J_s)]/J_s$ where S is the step function. This situation is relevant with the operation of tapered wiggler FELs where the trapped particles in the ponderomotive bucket are decelerating, falling quickly behind the untrapped particles and thus creating large distribution gradients near the separatrix.

The two questions of practical interest are (a) what percentage of the particles will eventually get detrapped and (b) how fast do they leak outside the separatrix. For our uniform initial distribution the maximum fraction of particles becoming detrapped equals the fraction of the inside of the separatrix area that becomes chaotic. In Fig. 5a we plot the fraction $f_d$ of the particles that cross the original separatrix $J_s$ as a function of the traveled wiggler length for values of $q = a_s/a_r$ below the threshold for extended stochasticity. In all cases an initial stage of quick diffusion is followed by a long period where the average number of untrapped particles remains practically constant. The results are consistent with the existence of a boundary in phase space (KAM surface) separating two regimes: the one of unbounded, chaotic motion

from the one filled with regular, coherent orbits of particles that remain trapped. Only electrons in the area between the last integrable surface and the old unperturbed separatrix will diffuse until that area is depleted. A fraction $1 - f_d$ of the original primary island area will remain trapped for an arbitrarily long time, as long as $a_s$ remains below the threshold $\alpha_s$ associated with the particular sideband frequency. This fraction is shrinking as $a_s$ increases and the bucket "peels off". The situation when $a_s$ exceeds $\alpha_s$ is shown in Fig. 5b. The fraction of untrapped particles $f_d$ reaches 1 in all cases, meaning complete absence of particle confinement in the bucket. All particles can eventually escape with a rate that increases with increasing $a_s$.

Numerical results showing the fraction of detrapped particles $f_d$ after 100 wiggler periods as a function of $a_s/a_r$ are plotted in Fig. 6 for various sideband frequencies $|\omega_s - \omega_r|$. The length over which approximately half of the initially trapped particles get detrapped will be discussed in the next section, in comparison with the diffusion rates from other types of sideband spectra.

## VI. BROAD FREQUENCY BAND DIFFUSION

So far stochastic electron detrapping caused by a single frequency sideband has been examined. It was argued that when the excited sideband spectrum is narrow enough, i.e., $D \ll 2\gamma_z^2\omega_b$, the situation can be reasonably approximated by a single frequency sideband. Here, we consider the situation when a broad spectrum of frequencies have been excited, $D\omega_s \geq 2\gamma_z^2\omega_b$. We will make a distinction between a continuous and a discrete spectrum. In case of a discrete spectrum the distance between two nearby sideband frequencies is much larger than the width of an individual spectral line. In the opposite case, when various peaks in the spectrum merge together, we will talk about a continuous spectrum. We may model numerically both cases by introducing a modulation in the sideband phase of Hamiltonian Eq. (11),

$$\tilde{H}(\tilde{\gamma},\psi;z) = \frac{k_w}{\gamma_r}\tilde{\gamma}^2 + \frac{a_w a_r}{\gamma_r}(\cos\psi + \psi\sin\psi_r) + \frac{a_w a_s}{\gamma_r}\cos(\psi + A\sin\nu z - \delta_s z), \tag{23}$$

that is transformed in action-angle variables as

$$H(J,\theta;z) = H_o(J) + H_1(J,\theta;z),$$

$$H_1(J,\theta;z) = \tag{24}$$

$$\frac{a_w a_s}{\gamma_r}\sum_{m=-\infty}^{\infty} J_m(A)\sum_{n=0}^{\infty} Q_n^+(J)\cos[n\theta + \delta_s(m)z] + Q_n^-(J)\cos[n\theta - \delta_s(m)z].$$

The frequency mismatch values $\delta_s(m)$ and the corresponding sideband frequencies $\omega_s(m)$ are given by,

$$\delta_s(m) = \delta_o + m\,\nu, \qquad \omega_s(m) = \omega_{so} + 2\,m\,\gamma_z^2\nu, \tag{25}$$

where $\omega_{so} = \omega_r + 2\gamma_z^2\delta_o$. Since the Bessel function coefficients become vanishingly small, $J_m(A) << 1$ for $A > m$, the width of the spectrum is given by $D\delta_s \sim A\,\nu$ or $D\omega_s \simeq 2\gamma_z^2 A\nu$.

In order to examine the connection between diffusion rates and the types of the sideband spectra, we divide the latter into three general categories: narrow, broad discrete and broad continuous. The passage from one regime to the other is not gradual but characterized by abrupt changes in the diffusion coefficients. Thus, from the diffusion point of view, the distinction among the spectral types is not arbitrary but based on certain relations between the parameters A and $\nu$. In all three regimes of the parameter space the rate of diffusion is proportional to the ratio of the total sideband power to the carrier power. The scaling of the coefficients of this proportionality on the various FEL parameters, however, differs from one regime to the other.

Both cases of the broad spectrum are characterized by a width $D\omega_s$ in the excited frequencies that is larger than the upshifted synchrotron frequency $\omega_b$,

$$D\omega_s > 2\,\gamma_z^2\omega_b \quad \text{, equivalent to} \quad \nu > \frac{\omega_b}{A}\ , \tag{26}$$

with $A >> 1$. The further distinction between discrete or continuous spectrum is related to the separation between nearby frequencies. We find that when $\omega_b/A^{1/2} > \nu > \omega_b/A$ the diffusion rate agrees well with the quasilinear diffusion coefficient. A different coefficient is derived for the case when $\nu > \omega_b/A^{1/2} > \omega_b/A$, in agreement with the numerical simulations. Consequenlty the separation $\omega_b/A^{1/2}$ between

nearby modes marks the transition from a discrete to a continuous type of behavior. Departure from the quasilinear diffusion coefficient has also been observed numerically in previous literature[19] when the frequency separation between nearby modes was not "small enough". Here a condition for the discrete-to-continuous transition has beeen obtained.

For any spectral type, the sideband amplitude must be above the stochastisity threshold in order to trigger electron diffusion. Using the same method of nearby resonance overlapping as in Sec. III, and the Hamiltonian Eq. (25) we find that the threshold in case of a multifrequency spectrum is given by,

$$\tilde{\alpha}_s \simeq \frac{\nu}{\omega_b J_m(A)} \alpha_s \ , \tag{27}$$

where $\alpha_s$ is the threshold for the single sideband frequency. Thus $\tilde{\alpha}_s$ decreases with decreasing frequency separation $\nu$. Condition (27) guarantees the stochastization of the particle orbits. The frequency separation among sidebands must be limited by the additional condition $\nu < \omega_b/A^{1/2}$, as stated in the previous paragraph, if one wishes to simulate quasilinear diffusion with a discrete spectrum.

A. Broad Discrete Spectrum.

We now evaluate the diffusion coefficient for a broad, discrete spectrum. The equation of motion for J can be written as,

$$\frac{dJ}{dz} = -\frac{\partial H_1}{\partial \theta} = -\frac{\partial H_1}{\partial \psi}\frac{d\psi}{d\theta} = \Lambda \frac{a_w a_s}{\gamma_r} \sin\left(\psi + A\sin\nu z - \delta_s z\right) \left|V(\psi_{mx}) - V(\psi)\right|^{1/2},$$

using Eq. (A2) for $d\psi/d\theta$. Due to the presence of many frequencies in the spectrum J(z) executes a complicated oscillatory motion with the average $< J >$ changing very little most of the time. J however receives a large kick $\Delta J$ near resonances, where the phase $\Phi = \psi + A \sin \nu z - \delta_s z$ of the multifrequency perturbation $H_1$ varies slowly. The resonant condition is,

$$\frac{d\Phi}{dz} = \frac{k_w \tilde{\gamma}}{\gamma_r} + A \nu \sin \nu z - \delta_s = 0, \tag{28}$$

at some $z = z_i$. Given that $k_w \tilde{\gamma}/\gamma_r \leq \omega_b$, collective effects due to many frequencies are important for the resonance in Eq. (28) when $A \nu > \omega_b$. On this basis inequality (27) signifies the transition from a narrow to a broad spectrum. Let us consider the case $A \nu >> \omega_b$. Then the resonances occur at $z_i \simeq i\pi/\nu$, i integer, and the interval between successive resonances is $\Delta z \simeq \pi/\nu$. Expanding the phase $\Phi(z)$ in the equation of motion for J around the resonance $z_i$,

$$\Phi(z) \simeq \Phi_i + \frac{1}{2}\left[\omega_b^2(\sin\psi_i + \sin\psi_r) + A \nu^2 \cos \nu z_i\right](z - z_i)^2, \tag{29}$$

and extending the limits of integration to $z = \pm\infty$ we obtain,

$$DJ_i \simeq \frac{a_w a_r}{\gamma_r}\left(\frac{2\pi}{\omega_b^2}\right)^{1/2} \frac{\cos\left(\Phi_n \pm \frac{\pi}{4}\right) \left|V(\psi_{mx}) - V(\psi_i)\right|^{1/2}}{\left((\sin\psi_i + \sin\psi_r) + A\left(\frac{\nu}{\omega_b}\right)^2\right)^{1/2}}, \tag{30}$$

where $\psi_{mx}(J)$ is the turning point for an unperturbed trajectory of given J. When $A \nu^2 >> \omega_b^2$ both $\Delta z$ and $\Delta J$ depend on the features $\nu$ and A of the sideband spectrum and not on the bounce frequency $\omega_b$. We classify the cases with frequency separation $\nu > \omega_b/A^{1/2}$ as broad discrete spectra. They obey a distinct scaling in the diffusion coefficient that will be

derived below. We find the cases with $\nu < \omega_b/A^{1/2}$ to agree numerically with the quasilinear diffusion that will be studied in the next subsection.

The resonant phases $\Phi_i$ between two successive jumps of $\Delta J$ become quickly decorrelated when $a_s$ grows above the stochastisity threshold. Because the relation between $\Phi_i$ and $\psi_i$ involves the distance $z_i$, $\Phi_i$ and $\psi_i$ will also become decorrelated, $\langle \cos\Phi_i \cos\psi_i \rangle = 0$. Assuming complete decorrelation between two successive jumps we obtain,

$$D_w = \frac{2 \langle \Delta J_i^2 \rangle}{Dz} = \frac{2 a_w^2 a_r^2}{\gamma_r^2 A \nu} \langle |V(\psi_{mx}) - V(\psi_i)| \rangle, \qquad (31)$$

where the angular brackets $\langle ... \rangle$ signify the average over $\psi_i$ for constant J. For practical purposes it is more convenient to rescale the diffusion coefficient so that the distance $\underline{z} = z/\lambda_w$ is measured in terms of wiggler wavelengths and the action $\underline{J} = J/J_s$ signifies the location relative to the separatrix. In these units, using Eq. (A4) for $J_s$ and setting $\nu / \omega_b(0) = r$ we obtain,

$$\underline{D}_w = \frac{2\pi}{k_w} \frac{D_w}{J_s^2} \sim \frac{\pi^3}{8} \frac{g^2 \zeta}{A r} \left( \frac{a_w a_r}{1 + a_w^2} \right)^{1/2} \frac{a_s^2}{a_r^2} . \qquad (32)$$

The term g is a scaling factor, the ratio of the separatrix area for an untapered wiggler to that of a tapered wiggler, $g = J_s(\psi_r=\pi)/J(\psi_r)$, and depends only on $\psi_r^1$. The term $\zeta \sim 1$, coming from the averaging over $\psi_i$ in Eq. (31), is computed in Appendix B. The typical diffusion length $L_d$, the traveled distance inside the wiggler over which the average trapped particle crosses the separatrix, is estimated from the diffusion Eq.

(22) by taking $\langle \Delta J^2 \rangle = J_s^2$, $L_d \sim J_s^2/D_w$. Thus, the diffusion length in wiggler periods $N_d = L_d/\lambda_w$ is the inverse of $\underline{D}_w$,

$$N_d \sim \frac{1}{\underline{D}_w}. \tag{33}$$

B. Broad Continuous Spectrum

Next we consider the case of a sideband wave package,

$$a_s(z,t) = \frac{1}{2\pi} \int dk_s a_s(k_s)\, e^{ik_s z - i\omega(k_s)t}, \tag{34}$$

of finite spectral width $Dk_s$ centered around $k_{so}$. Our purpose is to obtain the diffusion coefficient for a continuous spectrum using the methods of the quasilinear theory. Upon using exression (34) for the fields, the Hamiltonian representation in action-angle variables assumes the form,

$$H(J,\theta;z) = H_o(J) + \frac{a_w}{\gamma_r} \sum_{n=0}^{\infty} Q_n^{\pm}(J) \int dk_s a_s(k_s) \cos\left[n\theta \pm \delta(k_s)z\right], \tag{35}$$

where $\delta(k_s)$ is given by,

$$\delta(k_s) = \delta_{so} + (k_s - k_{so}) \frac{k_w}{k_r} + \left(\frac{v(k_s) - v(k_r)}{c}\right) k_{so}, \tag{36}$$

and $\delta_{so} = (k_w/k_r)(k_{so} - k_r)$ in the spirit of Eq. (10). The last parenthesis in the right-hand side of (36) is of order $(\omega_p/\omega_r)^2$ resulting from the dispersive effects in the sideband spectrum. The

finite $k_w$ provides phase slippage among the ponderomotive phases of various wavenumbers $k_s$, a necessary condition for the validity of the quasilinear theory, even when the dispersive effects of the last term in (36) are negligible, i.e., $\gamma_z^2(\omega_p/\omega_r)^2 \ll Dk_s/k_s$.

The resonant condition between a sideband wavelength $k_s$ and a given harmonic n now reads $\pm n\omega_b(J_n) = \delta(k_s)$. For each harmonic n there exists a wide band of resonant orbits centered around $J_{no}$ and of width $DJ_n$ defined by,

$$DJ_n = (d\Omega_b/dJ)_{Jno}^{-1} (k_w/k_r)\, Dk_s, \quad \pm n\omega_b(J_{no}) = \delta_{so}. \tag{37}$$

One condition for the applicability of the quasilinear theory is that the phase mixing due to $Dk_s$ occurs much faster than the bounce period around a secondary island in phase space. In this way, electrons, that otherwise would execute periodic orbits around some fixed point, lose coherence sufficiently fast to allow random motion of the Fokker-Planck type. Taking the decorrelation length for the phase $l_d \sim 2\pi/D\delta(k_s)$ and applying Eq. (18a) for the bounce period around the nth harmonic we obtain

$$\frac{Dk_s}{k_s} >> \frac{n}{2}\left(\frac{\pi Q_n^{\pm}}{\sqrt{2}}\right)^{1/2}\left(\frac{\Lambda a_w a_r}{1 + a_w^2}\right)^{1/2}. \tag{38}$$

Inequality (38) guarantees the diffusive behavior within the band $DJ_n$ around $J_{no}$ given by (37). Large scale diffusion, permitting transport of deeply trapped particles across the separatrix $J_s$ of the original primary island, requires that different stochastic bands touch each other, $DJ_n + DJ_{n+1} \geq \Delta J_n$, or, using a similar approach as in Eqs. (19) and (20),

$$\frac{Dk_s}{k_s} > \frac{1}{8n}\left(\frac{\pi Q_n^{\pm}}{\sqrt{2}}\right)^{1/2}\left(\frac{\Lambda a_w a_r}{1+a_w^2}\right)^{1/2} . \tag{39}$$

The right-hand sides of Eqs. (38) and (39) are of the same order as the upshifted synchrotron period for the main bucket. Thus both conditions are satisfied when,

$$\frac{Dk_s}{k_s} >> 2\,\gamma_z^2\,\frac{\kappa_b(0)}{k_r} . \tag{40}$$

Note that (40) is the same as the condition (26) that defines the wide spectrum, obtained in the previous subsection using different arguments. Then the evolution of the initial distribution $f_o(J)$ is globally described by a diffusion equation,

$$\frac{\partial f}{\partial z} = \frac{\partial}{\partial J} D_q(J) \frac{\partial f}{\partial J} . \tag{41}$$

Applying the standard procedures of the quasilinear theory[20,21] (see appendix C) and taking the limit of small growth rate for the sidebands, $Im(k_s)/k_s << 1$, we obtain,

$$D_q(J) = \frac{k_r}{4}\frac{k_r}{k_w}\frac{a_w^2}{\gamma_r^2}\sum_{n=0}^{\infty} n^2 \left|Q_n^{\pm}(J)\right|^2 \int dk_s W_s(k_s)\,\delta(k_s - k_n),$$

$$k_n = k_r \pm \frac{k_r}{k_w}\, n\, \kappa_b(J) . \tag{42}$$

According to the condition (40) for the validity of the quasilinear

theory, the wave package has a wide spectrum $Dk_s \sim N(k_r/k_w)\omega_b(0)$ with N large. The wave components $a_s(k_n)$ fall off slowly for $n < N$ while the Fourier coefficients $Q_n(J)$ decay rapidly with n. Then we may factor out the average spectral power density $W_s = (1/Dk_s)\int dk_s\, W_s(k_s) \simeq a_s^2/Dk_s$ in Eq. (34) getting,

$$D_q(J) \simeq \frac{k_r}{4}\frac{k_r}{k_w}\frac{a_w^2}{\gamma_r^2} W_s \sum_{n=0}^{\infty} n^2 |Q_n^{\pm}(J)|^2. \tag{43}$$

The infinite sum in the right-hand side of (43) is computed in Appendix C. The summation technique does not require the knowledge of the individual coefficients $Q_n(J)$ and the result depends only on the quantities J and $\omega_b(J)$ for the unperturbed Hamiltonian $H_o(J)$. We then obtain the diffusion coefficient in closed form,

$$D_q(J) = \frac{k_r\, a_w^2\, \gamma_z^2\, W_s\, k_w\, J}{\gamma_r^3 \omega_b(J)} \quad . \tag{44}$$

We note in passing that the method used to obtain expression (44) for $D_q(J)$ is quite general and valid for any integrable dynamical system $H_o(J)$ that is subject to an external perturbation. In particular, it should be applicable to a variety of RF heating methods in fusion plasmas, commonly involving a strong, narrow-band pump wave embedded in a wide, parametrically excited, fluctuation spectrum.

Using the expressions (A3) and (A7) for the action J and the synchrotron frequency $\omega_b(J)$ we find that the diffusion coefficient goes to zero at the centre of the primary island $J = 0$, has a logarithmic singularity at the separatrix $J = J_s$ and falls off away from it. In

normalized units, with the wiggler wavelength $\lambda_w$ as the unit length and the action $J_s$ at the separatrix as the unit action, we have,

$$\underline{D}_q(J) = \frac{2\pi}{k_w} \frac{D_q(J)}{J_s^2} . \tag{45}$$

Choosing the value $J = J_s/2$ inside $D_q(J)$ we obtain an estimate for the effective diffusion coefficient associated with the uniformly filled distribution,

$$\underline{D}_q \sim \frac{\pi}{4} \frac{g\, a_w a_r}{\Lambda\,(1+a_w^2)} \frac{a_s^2}{Dk_s\, a_r^2} , \tag{46}$$

where g is the same scaling factor as in Eq. (32).

Note that both expressions (32) and (46), corresponding to the two different spectral types, are independent of $\gamma_r$. Thus, for the same wiggler parameters and total sideband power, the detrapping distance in wiggler periods is independent of the electron beam energy. The dependence of the effective diffusion rate on the wiggler tapering enters through the form factor $g(\psi_r) = J_s(\pi)/J(\psi_r)$. As the rate of tapering increases and $\psi_r$ shifts further from $\pi$, g inreases[1] and accelerates the effective diffusion rate. This happens because the trapped area in phase space, parametrized by $J_s$, is shrinking as the tapering progresses, while the sideband induced excursions remain the same, depending mainly on the sideband strength and spectrum. This

shortens the average detrapping time for a particle. The diffusion by broad discrete spectrum, Eq. (32) scales as $g^2$, while the quasilinear diffusion, Eq. (46), scales as $g$. Thus the former is affected more by tapering than the latter.

## VII. NUMERICAL RESULTS

The numerically computed diffusion coefficient $\underline{D}$ and the diffusion length in wiggler periods $N_d = 1/\underline{D}$ are plotted against the sideband to carrier power ratio $P = \sum_n a_s^2(\omega_n)/a_r^2 = W_s/W_r$ in Figs. 7 and 8 respectively for the three different types of spectra. We have integrated numerically the equations of motion for 400 particles of a uniform initial distribution inside the bucket. The field intensities remained constant at $a_r = 5\times10^{-5}$, $a_w = 2$ and $\gamma_r = 25$. All the numerical results in this paper correspond to a tapered wiggler with $\psi_r = 7\pi/6$. A clear separation in the diffusion rates is observed among the various spectral types. The narrow frequency results (triangles) were obtained using the Hamiltonian (8) with a single sideband frequency $\omega_s/\omega_r = 1.016$. The results for a broad discrete spectrum (circles) were obtained using (23) with $A = 20$, $\omega_s/\omega_r = 1.016$ and $\nu = 0.5\ \delta_s$. The continuous spectrum (squares) was modeled by $A = 100$, $\nu = 0.05\ \delta_s$. The solid lines, corresponding to the theoretical results of Eqs. (32) and (46), are in good agreement with the numerics. Theoretical predictions for the single frequency case were not made. We stress, however, the difference between single frequency results and quasilinear theory in this case. The agreement that has been observed in some other cases[22] is not generic but particular to certain systems.

Figure 9 illustrates the difference of the electron response to different sideband spectra. The plots on the left side are typical orbits J(z) for selected particles along the wiggler. The trajectories in all plots are generated by the same initial conditions for the electrons and the same FEL parameters $a_w$, $a_r$ and $k_w$, as well as the same mean square sideband power $\langle a_s^2 \rangle$. The spectral parameters A and $\nu$,

however, are different so that each of the figures (a) to (c) corresponds to one of the three spectral types defined earlier. The dashed line marks the position of the unperturbed separatrix $J_s$. The corresponding distribution functions f(J,z) at the beginning, z = 0, halfway inside, $z = 50\lambda_w$, and at the end, $z = 100\lambda_w$ of the wiggler are plotted in the right-hand side of Figs. 9a-9c respectively.

In Fig. 10 we plot the diffusion coefficient for a uniformly filled bucket as a function of the energy $\gamma_r$, fixing the wiggler parameters. It is clear that the diffusion rate (measured again in number of wiggler periods) is independent of the beam energy, provided the synchrotron frequency $\omega_b$ stays in the same parameter regime.

Once the diffusion coefficients are known, some estimate can be made of the related reduction in efficiency over the wiggler length. The number of trapped particles at any point z is given by

$n_b = \int_0^{J_s} dJ\ f(J,z)$. Using the diffusion Eq. (41) with D(J=0) = 0 one obtains the rate of change in the number of trapped particles,

$$\frac{dn_b}{dz} = n_b(z)\ D(J_s)\ \frac{\partial f(J_s,z)}{\partial z}\ . \qquad (47)$$

The leakage rate for trapped particles changes along z as the slope of the distribution f(J,z) changes. To estimate the average leakage rate we assume that f(J,z) remains Gaussian in J with an average width equal to the separatrix action $J_s$. We estimate from (47) the e-folding length $L_d = -\ n_b^{-1}(dn_b/dz)$ for the number $n_b$ of trapped particles,

$$L_d = D(J_s)\ J_s^{-2}. \qquad (48)$$

Assuming that $n_b(z) = n_b(0)\exp(-z/L_d)$, the number of detrapped particles between z and $z + \Delta z$ is $\Delta n(z) = n_b(0)L_d^{-1}\exp(-z/L_d)\,\Delta z$. These particles gave up an amount of energy $\Delta E(z) = [\gamma_r(0) - \gamma_r(z)]\,\Delta n(z)$ as radiation. Integrating $\Delta E(z)$ over the wiggler length for a linearly tapered wiggler $\gamma_r(z) = \gamma_r(0) - z\Delta\gamma/L_w$, we find the total energy extracted from the particles that were detrapped at some point inside the wiggler. Adding the contribution $[\gamma_r(0) - \gamma_r(L_w)]\,n_b(L_w)$ from the particles that remained trapped throughout the wiggler length, we come up with,

$$\eta = \eta_o \frac{L_d}{L_w}\left(1 - \exp\left(-\frac{L_w}{L_d}\right)\right) , \qquad (49)$$

where $\eta_o = \Delta\gamma/\gamma_r(0)$ is the efficiency without induced diffusion. The loss of amplification will, in general, be distributed among all the radiation modes and (49) reflects the total power loss in all frequencies. The extraction efficiency $\eta$ for a linearly tapered wiggler is plotted in Fig. 11 versus the sideband to carrier power ratio P, obtaining the corresponding value for $L_d/L_w$ from the results in Fig. 8.

## VIII. CONCLUSION

The diffusion in phase space caused by sideband excitation during FEL operation was studied. It was shown that the characteristic rates for this process depend on the structure of the sideband spectrum, falling into one of the following general categories: narrow, wide discrete or wide continuous spectrum. In all cases, the diffusion coefficient was found proportional to the ratio of the total power in the sidebands to the power in the main FEL signal $D \propto C\, W_s/W_r$. The coefficient C, however, is connected to the spectral type under consideration. From Eqs. (32) and (46) we see that, apart from numerical factors of order unity, C scales as $(a_w a_r)^l$ with $l = 1/2$ for a discrete and $l = 1$ for a continuous spectrum. Therefore, given the typical FEL values of $a_w \leq 10$ and $a_r \leq 10^{-3}$ an order of magnitude reduction in diffusion occurs in the transition from a discrete to a continuous sideband spectrum. It was also observed numerically that the highest diffusion rate occurs when all the sideband power is in a single frequency. In this case, however, a portion of the particles will remain trapped for arbitrary long wigglers if the sideband amplitude is below the threshold for extensive stochasticity. The stochasticity threshold is progressively reduced as the sideband power is distributed into an increasing number of frequencies. Yet the rate of diffusion also slows down with increasing spectral width and decreasing mode separation. Thus, the minimum reduction in the FEL energy extraction efficiency will occur for continuous sideband spectra. Although control of the sideband structure does not seem plausible, experiments show that a wide spectrum is naturally excited during FEL operation. This would allow enough power build-up before serious deterioration in efficiency, due to detrapping,

to occur. The diffusion length, measured in wiggler periods, is independent of the beam energy $\gamma$ under the same wiggler parameters, for all the spectral types. Our results have been obtained for radiation fields of constant amplitude. Inclusion of the time evolution for both the carrier and the sidebands will modify the detrapping rates by changing both the diffusion rate as well as the size of the separatrix. This subject is left for future investigation.

## ACKNOWLEDGEMENT

This work was supported by SDIO and managed by SDC.

## APPENDIX A: TRANSFORMATIONS IN ACTION-ANGLE VARIABLES

The relations between $\tilde{\gamma}$, $\psi$ and the action-angle variables J, $\theta$ are given in closed forms in case of an untapered wiggler. Starting from the general expression (11) and using (8) we have,

$$\frac{1}{\pi}\int_{\psi_{mn}}^{\psi_{mx}} d\psi \left( \frac{\gamma_r H_o}{k_w} - V(\psi) \right)^{1/2} , \tag{A1}$$

$$\theta = \frac{\gamma_r K_b(J)}{2k_w} \int_0^{\psi} d\psi' \left( \frac{\gamma_r H_o}{k_w} - \frac{a_w a_r}{k_w} V(\psi) \right)^{-1/2} , \tag{A2}$$

where

$$V(\psi) = \left( \cos\psi + \psi \sin\psi_r \right) .$$

Using $H_s = -(a_w a_s/\gamma_r)\, V(\psi_r)$ we obtain the action at the separatrix,

$$J_s = \left(\frac{a_w a_r}{\gamma_r}\right)^{1/2} \frac{1}{\pi}\int_{\psi_{mn}}^{\psi_{mx}} d\psi \left( V(\psi) - V(\psi_r) \right)^{1/2} .$$

In case of an untapered wiggler $\psi_r = 0$ Eqs. (A1)-(A2) yield,

$$J = \begin{cases} J_s \left[ E_2(\lambda) - (1-\lambda^2) E_1(\lambda) \right] , & \lambda^2 < 1 \\ 2J_s \lambda\, E_2\left(\frac{1}{\lambda}\right) , & \lambda^2 > 1 \end{cases} \tag{A3}$$

$$J_s = \frac{8}{\pi}\left(\frac{\Lambda a_w a_r k_r}{4k_w}\right)^{1/2} , \tag{A4}$$

$$\sin\frac{\Psi}{2} = \begin{cases} \lambda\, sn\left(\frac{2}{\pi} E_1(\lambda)\theta\right) , & \lambda^2 < 1, \\ sn\left(\frac{1}{\pi} E_1\left(\frac{1}{\lambda}\right)\theta\right) , & \lambda^2 > 1, \end{cases} \tag{A5}$$

where $E_1$ and $E_2$ are the complete elliptic integrals of the first and second kind, sn is the Jacobi elliptic sine function, and

$$\lambda^2 = \frac{\gamma_r H_o}{2a_w a_r} + \frac{1}{2} , \tag{A6}$$

is the trapping parameter ( $\lambda^2 < 1$ for trapped particles). Using $\kappa_b(J) = (\partial J/\partial H_o)^{-1}$ and (A1) we determine the bounce (synchrotron) frequency

$$\kappa_b(J) = \begin{cases} \kappa_b(0)\, \frac{\pi}{2E_1(\lambda)} , & \lambda^2 < 1 \\ \kappa_b(0)\, \frac{\pi\lambda}{E_1(1/\lambda)} , & \lambda^2 > 1 \end{cases} \tag{A7}$$

where

$$\kappa_b(0) = \frac{1}{\gamma_r}\left(\frac{\Lambda}{2} a_w a_r k_w k_r\right)^{1/2} , \tag{A8}$$

is the bounce frequency at the bottom of the well. J and $\lambda^2$ are mutually related through (A3) - (A6) and they uniquely label the trajectories.

The Fourier coefficients of the expansion (12) can also be expressed in closed form. They are computed by integration in the complex plane around the singularities, utilizing the double periodicity properties of the Jacobi elliptic functions to obtain,

$$Q_n^{\pm} = -(\pm 1)^n \frac{n\pi^2}{E_1^2(\lambda)} \frac{q^{\frac{n}{2}}}{1-(-q)^n} , \quad q = \exp\left(\frac{\pi E_1'(\lambda)}{E_1(\lambda)}\right), \quad \lambda^2 < 1, \tag{A9}$$

$$Q_n^{\pm} = - \frac{n\pi^2\lambda^2}{E_1^2(1/\lambda)} q^n \left( \frac{1}{1-q^{2n}} \pm \frac{1}{1+q^{2n}} \right) , \quad q = \exp\left( \frac{\pi E_1'(1/\lambda)}{E_1(1/\lambda)} \right) , \quad \lambda^2 > 1$$

for $n \neq 0$ and,

$$Q_0^{\pm} = 2 \frac{E_2(\lambda)}{E_1(\lambda)} - 1 \qquad \lambda^2 < 1 , \qquad Q_0^{\pm} = 1 - 2\lambda^2 \left( 1 - \frac{E_2(1/\lambda)}{E_1(1/\lambda)} \right) , \quad \lambda^2 < 1,$$

where $E_1'(\lambda^2) \equiv E_1(1 - \lambda^2)$.

## APPENDIX B : PHASE AVERAGING OVER CONSTANT J

The phase average $< |V(\psi_{mx}) - V(\psi_i)| >$ over constant J is given, for $\psi_r = 0$, by,

$$<.....> = \frac{1}{2\pi} \int_0^{2\pi} d\theta_i \; | \cos\psi_{mx}(J) - \cos\psi_i(J,\theta_i) |$$

$$= \frac{4}{2\pi} \int_0^{\psi_{mx}} d\psi_i \left(\frac{d\theta_i}{d\psi_i}\right) | \cos\psi_{mx}(J) - \cos\psi_i | . \qquad (B1)$$

Substituting $d\theta_n/d\psi_i$ from (A2) and using $\cos \psi_{mx} = \gamma_r H(J)/a_w a_r$ one obtains,

$$<.....> = \frac{\gamma_r K_b}{\pi\, a_w a_r} \int_0^{\psi_{mx}} d\psi_i \left( \frac{\gamma_r H}{k_w} - \frac{a_w a_r}{k_w} \cos \psi_i \right)^{1/2}$$

$$= \sqrt{2} \left( \frac{E_2(\lambda^2)}{E_1(\lambda^2)} - ( 1 - \lambda^2) \right) , \qquad (B2)$$

where $\lambda^2$ was defined in (A6).

## APPENDIX C : COMPUTATION OF THE QUASILINEAR DIFFUSION COEFFICIENT

We consider the evolution of the electron distribution in the presence of a sideband wave package,

$$a_s(z,t) = \frac{1}{2\pi} \int dk_s a_s(k_s)\, e^{ik_s z - i\omega(k_s)t} , \qquad (C1)$$

of width $Dk_s$. The interaction Hamiltonian in action-angle variables, derived in Sec. IV.(b) is,

$$H(J,\theta;z) = H_o(J) + \frac{a_w}{\gamma_r} \sum_{m=0}^{\infty} Q_n^{\pm}(J) \int dk_s a_s(k_s) \cos\left[n\theta \pm \delta(k_s)z\right] . \qquad (C2)$$

The evolution of the distribution function $f(J,\theta;z)$, under the Hamiltonian flow,

$$\frac{d\theta}{dz} = \frac{\partial H}{\partial J} , \quad \frac{dJ}{dz} = - \frac{\partial H}{\partial \theta} , \qquad (C3)$$

is given by,

$$\frac{\partial f}{\partial z} + \frac{d\theta}{dz}\frac{\partial f}{\partial \theta} + \frac{dJ}{dz}\frac{\partial f}{\partial J} = 0 . \qquad (C4)$$

We separate the distribution $f(J,\theta;z)$ into a slowly varying part $f_o(J;z) = \langle f \rangle$ and a fluctuating part $\delta f(J,\theta;z) = f - \langle f \rangle$. The averaging operator is defined by,

$$\langle f \rangle = \int_0^L \frac{dz}{L} \int_0^{2\pi} \frac{d\theta}{2\pi} f .$$

It is implied in the above definition that the characteristic length for $f_o(J;z)$ is longer than the synchrotron length $L = 2\pi/\kappa_b$. We then obtain from (C4),

$$\frac{\partial \tilde{f}}{\partial z} + \frac{d\theta}{dz}\frac{\partial \tilde{f}}{\partial \theta} + \frac{dJ}{dz}\frac{\partial \tilde{f}}{\partial J} = -\frac{dJ}{dz}\frac{\partial f_o}{\partial J} - \frac{\partial}{\partial J}\left[\frac{dJ}{dz}\tilde{f} - \left\langle \frac{dJ}{dz}\tilde{f}\right\rangle\right], \quad (C5)$$

$$\frac{\partial}{\partial z} f_o = -\frac{\partial}{\partial J}\left\langle \frac{dJ}{dz}\tilde{f}\right\rangle . \quad (C6)$$

Using Eqs. (C2) and (C3) inside Eq. (C5) and ignoring the last bracketed term in the right-hand side we obtain,

$$\tilde{f} = -\frac{a_w}{2\gamma_r}\sum_{n=1}^{\infty}\int dk_s \frac{n\, Q_n^{\pm}(J)\, a_s(k_s)}{n\,\kappa_b(J) \pm \delta(k_s)}\frac{\partial f_o}{\partial J} e^{i[n\theta \pm \delta(k_s)]} + cc . \quad (C7)$$

Substituting (C7) in (C6) we have,

$$\frac{\partial}{\partial z} f_o = \frac{1}{(2\pi)^2}\int_{-\infty}^{\infty} dk_s \int_{-\infty}^{\infty} dq_s \int_0^L \frac{dz}{L}\int_0^{2\pi}\frac{d\theta}{2\pi}\frac{a_w^2}{4\gamma_r^2}$$

$$\times \frac{\partial}{\partial J}\left\{\left[\sum_{m=0}^{\infty} i\, m\, Q_m^{\pm}(J)\, a_s(q_s)\, e^{i[m\theta \pm \delta(q_s)z]} + cc\right]\right. \quad (C8)$$

$$\left.\left[\sum_{n=0}^{\infty}\frac{n\, Q_n^{\pm}(J)\, a_s(k_s)}{n\,\kappa_b(J) \pm \delta(k_s)}\frac{\partial f_o}{\partial J} e^{i[n\theta \pm \delta(k_s)]} + cc\right]\right\},$$

where again $\delta(k_s) = (k_w/k_r)[(k_s - k_r) + i\varepsilon]$, $\varepsilon = \mathrm{Im}(k_s)$. Integration of the right-hand side of (C8) over $\theta$ yields,

$$\int_0^{2\pi}\frac{d\theta}{2\pi}\{\ldots\} = -\sum_{n=0}^{\infty}\left[i\bar{n}^2\,\frac{|Q_n^{\pm}|^2\, a_s^*(q_s)\, a_s(k_s)}{n\,\kappa_b(J) \pm \delta(k_s)} e^{\pm[\delta^*(q_s) - \delta(k_s)]z} + cc\right]. \quad (C9)$$

Spatial integration yields

$$\frac{1}{L}\int_0^L dz\, a^*(q_s)\, a\,(k_s)\, e^{\pm\frac{k_w}{k_r}[(q_s - k_s) + 2\,i\,\varepsilon]z} = 2\pi\, W(q_s,z)\, \delta(q_s - k_s)\,, \tag{C10}$$

where $W_k(z) = a^2(k_s,z)/L$ is the spectral energy density. Substitution of the results (C9) and (C10) back in (C8) yields,

$$\frac{\partial f}{\partial z} = \frac{\partial}{\partial J}\, D_q(J)\, \frac{\partial f}{\partial J}\,,$$

where

$$D_q(J) = \frac{k_r}{4\pi}\,\frac{a_w^2}{\gamma_r^2}\,\frac{k_r}{k_w}\sum_{n=1}^{\infty}\int dk_s\, \frac{n^2 W_{k_s}(z)\,|Q_n^{\pm}|^2\,\varepsilon}{\left[\frac{k_r}{k_w}\,n\,\kappa_b(J) \pm (k_s - k_r)\right]^2 + \varepsilon^2}. \tag{C11}$$

In the limit of small growth rate $\varepsilon/k_s \ll 1$, (C11) is reduced to Eq. (42), Sec. IV,

$$D_q(J) = \frac{k_r}{4}\,\frac{k_r}{k_w}\,\frac{a_w^2}{\gamma_r^2}\sum_{n=0}^{\infty}|Q_n^{\pm}|^2\int_{-\infty}^{\infty}dk_s\, W_{k_s}(z)\,\delta(k_s - k_n)\,, \tag{C12}$$

where $k_n = k_r \pm 2\gamma_z^2 k_w$.

## APPENDIX D: SUMMATION OF FOURIER COEFFICIENTS

We present a general technique of computing sums of the form,

$$\sum_{n=0}^{\infty} n^2 \left[ |Q_n^+(J)|^2 + |Q_n^-(J)|^2 \right] . \qquad \text{(D1)}$$

The quantities $Q_n^{\pm}(J)$ are the Fourier coefficients from the decomposition of the phase $\exp[i\psi(J,\theta)]$ of the perturbation into harmonics of the angle variable $\theta$ for the unperturbed system. The knowledge of the individual $Q_n^{\pm}(J)$ is not required in the computation. The technique should be applicable to a wide class of integrable systems experiencing a periodic perturbation with only minor modifications. In our case $Q_n^{\pm}(J)$ are defined by,

$$\cos [\psi(J,\theta) + \delta_s z] = \sum_{n=0}^{\infty} Q_n^+(J) \cos(n\theta + \delta_s z) + Q_n^-(J) \cos(n\theta - \delta_s z). \qquad \text{(D2)}$$

Closed forms for $Q_n^{\pm}(J)$, obtained in Ref. 2 for the case of an untapered wiggler, appear in Appendix A.

For untrapped particles we have,

$$Q_{2m}{}^{\pm} = Q_{2m} , \qquad Q_{2m+1}{}^{\pm} = \pm Q_{2m+1} .$$

Setting $\delta_s = 0$ in (D2) and differentiating in $\theta$, we obtain,

$$\frac{\partial}{\partial\theta} \cos \psi = - \frac{d\psi}{d\theta} \sin \psi = - \sum_{m=1}^{\infty} (2m)\, 2Q_{2m} \sin 2m\theta , \qquad \text{(D3a)}$$

$$\frac{\partial}{\partial\theta} \sin\left[\theta - \frac{\pi}{2}\right] = \frac{d\psi}{d\theta} \cos q = \sum_{m=0}^{\infty} (2m+1)\ 2Q_{2m+1}\ \cos[(2m+1)\theta]. \tag{D3b}$$

Squaring the right-hand sides of (D3a), (D3b), adding them and integrating over $\theta$ we obtain,

$$\sum n^2 \left[|Q_n^{+}|^2 + |Q_n^{-}|^2\right] = 2 \sum n^2 |Q_n|^2 = \frac{1}{2\pi} \int_0^{2\pi} \left(\frac{d\psi}{d\theta}\right)^2 (\cos^2\psi + \sin^2\psi)\, d\theta \tag{D4}$$

Applying the same procedure to untrapped particles we obtain,

$$\frac{\partial}{\partial\theta} \cos\psi = -\frac{d\psi}{d\theta} \sin\psi = -\sum_{m=1}^{\infty} n\,(Q_n^{+} + Q_n^{-}) \sin n\theta\,, \tag{D5a}$$

$$\frac{\partial}{\partial\theta} \sin\left[\theta - \frac{\pi}{2}\right] = \frac{d\psi}{d\theta} \cos q = -\sum_{m=0}^{\infty} n\,(Q_n^{+} - Q_n^{-}) \cos n\theta\,, \tag{D5b}$$

and, after squaring, adding (D5a) and (D5b) and integrating over $\theta$ ,

$$\sum_{n=0}^{\infty} n^2 \left(|Q_n^{+}|^2 + |Q_n^{-}|^2\right) = \sum_{n=0}^{\infty} \frac{n^2}{2} \left(|Q_n^{+} + Q_n^{-}|^2 + |Q_n^{+} - Q_n^{-}|^2\right)$$
$$= \frac{1}{2\pi} \int_0^{2\pi} \left(\frac{d\psi}{d\theta}\right)^2 (\cos^2\psi + \sin^2\psi)\, d\theta\,. \tag{D6}$$

Thus in both cases,

$$\sum_{n=0}^{\infty} n^2 \left(|Q_n^{+}|^2 + |Q_n^{-}|^2\right) = \frac{1}{2\pi} \int_0^{2\pi} \left(\frac{d\psi}{d\theta}\right)^2 d\theta\,. \tag{D7}$$

Using the definition Eq. (11) for $\theta(\psi)$, and Eq. (8) for the unperturbed Hamiltonian ($a_s = 0$ ) in the right-hand side of (D7) we have,

$$\frac{1}{2\pi}\int_0^{2\pi}\left(\frac{d\psi}{d\theta}\right)^2 d\theta = \frac{1}{2\pi}\,2\int_{\psi_{mn}}^{\psi_{mx}}\frac{d\psi}{\left(\frac{d\theta}{d\psi}\right)}$$

$$= \frac{2\,k_w}{\gamma_r\omega_b(J)}\,\frac{1}{\pi}\int_{\psi_{mn}}^{\psi_{mx}} d\psi\,\left(\frac{\gamma_r H_o(J)}{k_w} - \frac{a_w a_r}{k_w}\left[\cos\psi + \psi\sin\psi_r\right]\right)^{1/2}. \tag{D8}$$

The last integral in (D8) is by the definition (11) the action J for the unperturbed Hamiltonian, yielding the final result,

$$\sum_{n=0}^{\infty} n^2\left(|Q_n^{+}|^2 + |Q_n^{-}|^2\right) = \frac{2\,k_w}{\gamma_r\omega_b(J)}\,J\ . \tag{D9}$$

## REFERENCES


1. N. M. Kroll, P. L. Morton and M. N. Rosenbluth, IEEE Journal Quantum Electronics, QE-17, 1436 (1981).
2. S. Riyopoulos and C. M. Tang, in Proceedings of the Eighth International FEL Conference, Glasgow, Scotland, edited by M. Poole (North Holland, Amsterdam, 1987), p. 226.
3 S. S. Yu, W. M. Sharp, W. M. Fawley, E. T. Scharlemann, A. M. Sessler and E. J. Sternbach, in Proceedings of the Eighth International FEL Conference, Glasgow, Scotland, edited by M. Poole (North Holland, Amsterdam, 1987), p. 219.
4. R. C. Davidson and J. S. Wurtele, Phys. Fluids 30, 557 (1987).
5. R. C. Davidson and J. S. Wurtele, Phys. Fluids 30, 2825 (1987).
6. T. Masud, T. C. Marshall, S. P. Schlesinger and F. G. Yee, Phys. Rev. Lett. 56, 1567 (1986).
7. T. Masud, T. C. Marshall, S. P. Schlesinger, F. G. Yee, W. M. Fawley, E. T. Scharlemann, S. S. Yu, A. M. Sessler and E. J. Sternbach, to appear in Transactions on Plasma Science (1988).
8. C. M. Tang and P. Sprangle in Proceedings, Free Electron Generators of Coherent Radiation, Orcas Island, Washington, edited by S. F. Jacobs and M. O. Scully, 1983, (SPIE, Bellingham, WA, 1983), Vol. 453, p. 11.
9. W. B. Colson, in Proceedings of The Seventh International FEL Conference, Tahoe City, edited by E. T. Scharlemann and D. Prosnitz (North Holland, Amsterdam, 1985), p. 168; also W. B. Colson, in Proceedings of the International Conference on Lasers, (STS Press, McLean, VA, 1982) p. 751.

10. J. C. Goldstein, B. E. Newnam, R. W. Warren and R. L. Sheffield, in Proceedings of The Seventh International FEL Conference, Tahoe City, edited by E. T. Scharlemann and D. Prosnitz (North Holland, Amsterdam, 1985), p. 4; also R. W. Warren, J. C. Goldstein and B. E. Newnam, same as above, p. 19.

11. D. C. Quimby, J. M. Slater and J. P. Wilcoxon, IEEE J. Quant. Elec. 21, 979 (1986).

12. See, for example, A. J. Lichtenberg and M. A. Lieberman, Regular and Stochastic Motion (Springer-Verlag, New York, 1983), and references therein.

13. H. Poincare, New Methods of Celestial Mechanics, (Dover, New York, 1957).

14. B. V. Chirikov, Phys. Reports 52, 265 (1979)

15. P. Sprangle and C. M. Tang, Phys. Fluids 28, 2019 (1985).

16. P. Sprangle, A. Ting and C. M. Tang, Phys. Rev. Lett. 59, 202 (1987).

17. P. Sprangle, A. Ting and C. M. Tang, Phys. Rev. A36, 2773 (1987).

18. In case of a tapered wiggler, there is a jump $\Delta J$ in action on crossing a boundary in phase space between two untrapped particle regimes. Since J also parametrizes the distance from a given island center $\psi_r$, the jump $\Delta J$ reflects the shift in the fixed point $\psi_r \rightarrow \psi_r + 2\pi$ from which we measure this distance.

19. A. K. Ram, K. Hizanidis and A. Bers, Phys. Rev. Lett. 56, 147 (1986).

20. A. Vedenov, E. Velikhov and R. Z. Sagdeev, Nucl. Fusion 1, 82 (1961); also W. E. Drummond and D. Pines, Nucl. Fusion, Suppl. 3, 1049 (1962).

21. C. F. Kennel and F. Engelmann, Phys. Fluids 9, 2377 (1966).

22. C. F. F. Karney, Phys. Fluids 21, 1584 (1978).

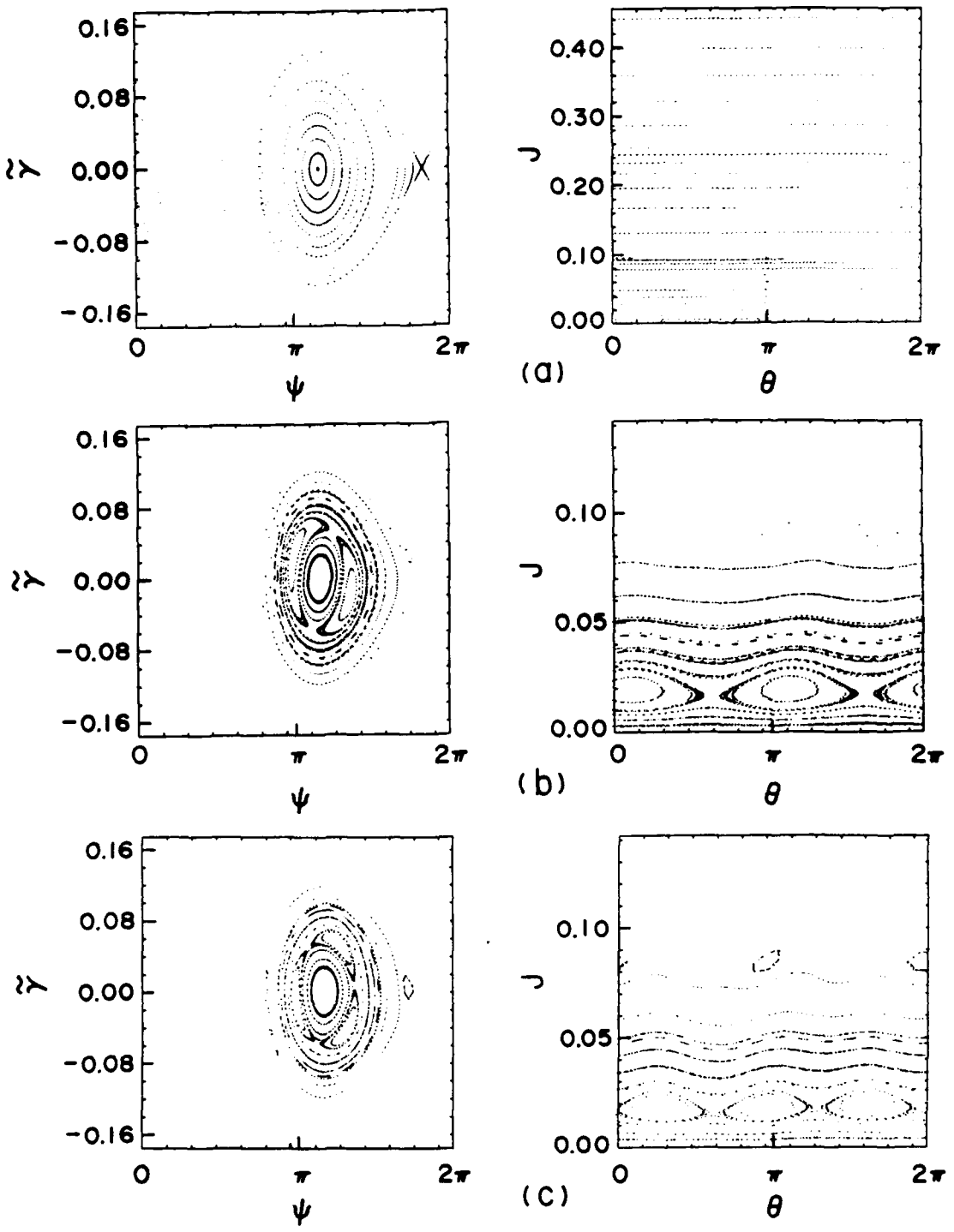



Figure 1. Surfaces of section expressed in $\gamma$, $\psi$ coordinates on the left side and action-angle coordinates on the right side. The parameters are $a_w = 2$, $a_r = 5\times10^{-5}$, $\psi_r = 7\pi/6$, $\gamma_r = 25$ and (a) $a_s = 0$ , (b) $a_s = 5\times10^{-7}$, $\omega_s/\omega_r = 1.016$, (c) $a_s = 2\times10^{-6}$, $\omega_s/\omega_r = 1.024$ .

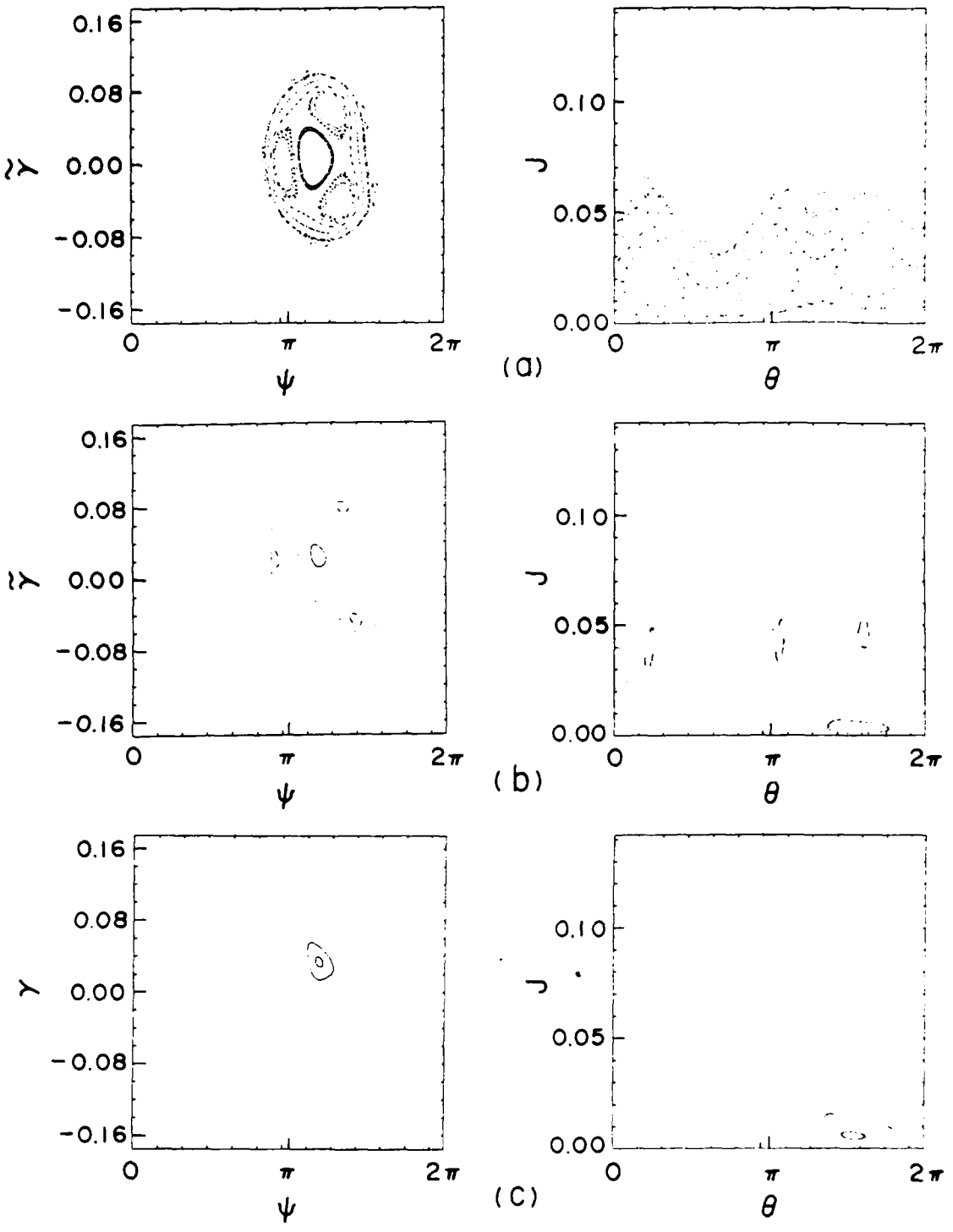



Figure 2. Transition to chaotic behavior. Plotted again are surfaces of section in both $\tilde{\gamma}$, $\psi$ and J, $\theta$ representations. The parameters are $a_w = 2$, $a_r = 5\times10^{-5}$, $\psi_r = 7\pi/6$, $\gamma_r = 25$ and $\omega_s/\omega_r = 1.024$. The sideband amplitude increases from (a) $a_s = 1\times10^{-5}$ to (b) $a_s = 3\times10^{-5}$ to (c) $a_s = 5\times10^{-5}$.

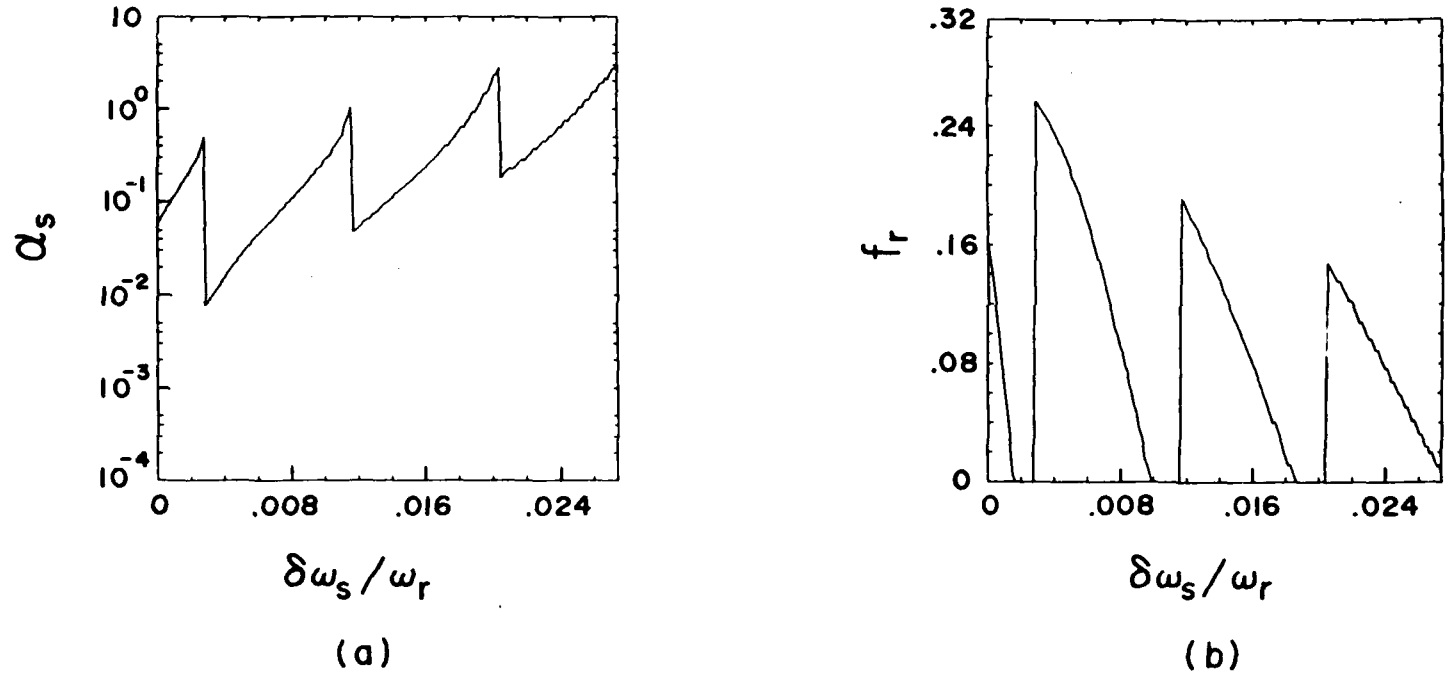



Figure 3. Stochasticity threshold $\alpha_s$ for single frequency sideband. (a) Plot of $\alpha_s$ against the sideband frequency mismatch $\delta\omega/\omega_r$ (solid line), signifying the overlapping of the two innermost secondary island chains (extended stochastic behavior). The dashed line $\alpha_s'$ signifies the overlapping of the next two islands on the outside (limited stochastic behavior). (b) The fraction $f_s$ of the phase area inside the separatrix that remains integrable when $a_s = \alpha_s$ (solid) and when $a_s = \alpha_s'$ (dashed) line.

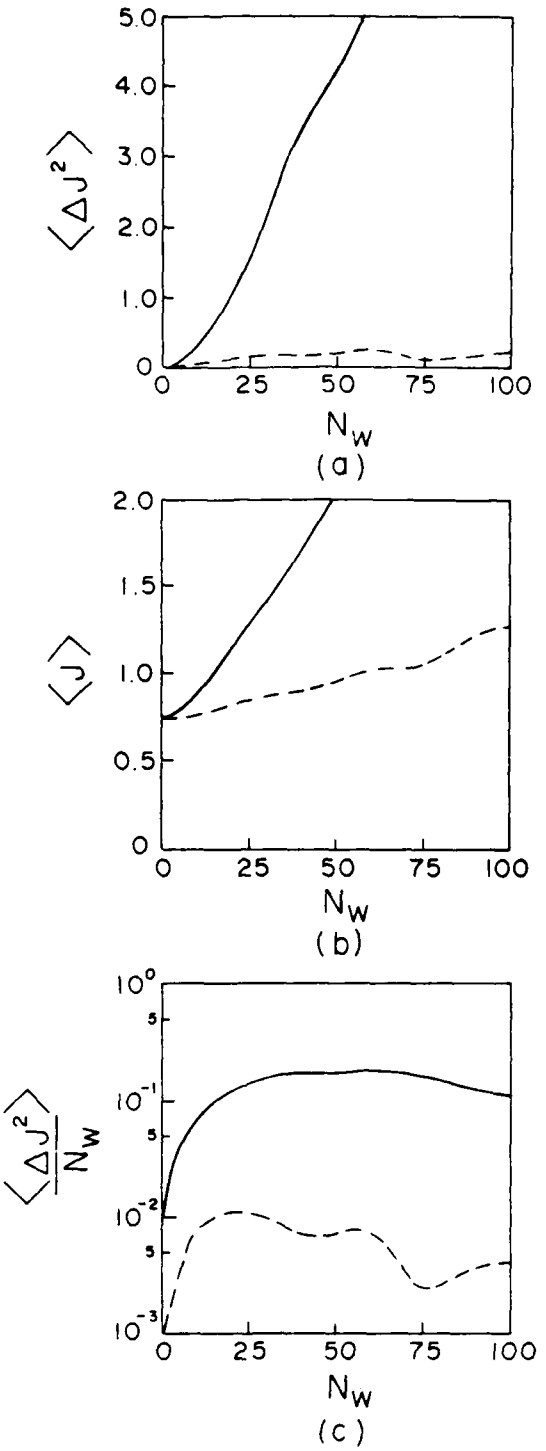



Figure 4. Diffusive behavior of a "monoenergetic" initial distribution $J_o = 0.7\ J_s$ with $a_w = 2$, $a_r = 5\times10^{-5}$, $\psi_r = 7\pi/6$, $\gamma_r = 25$ and $\omega_s/\omega_r = 1.016$. Plotted are (a) $\langle \Delta J^2 \rangle$ (b) $\langle J \rangle$ and (c) $\langle \Delta J^2 \rangle / z$ as functions of $N_w = z / \lambda_w$. The solid curves correspond to $a_s = 1.5\times10^{-5}$ and the dashed ones to $a_s = 5\times10^{-5}$.

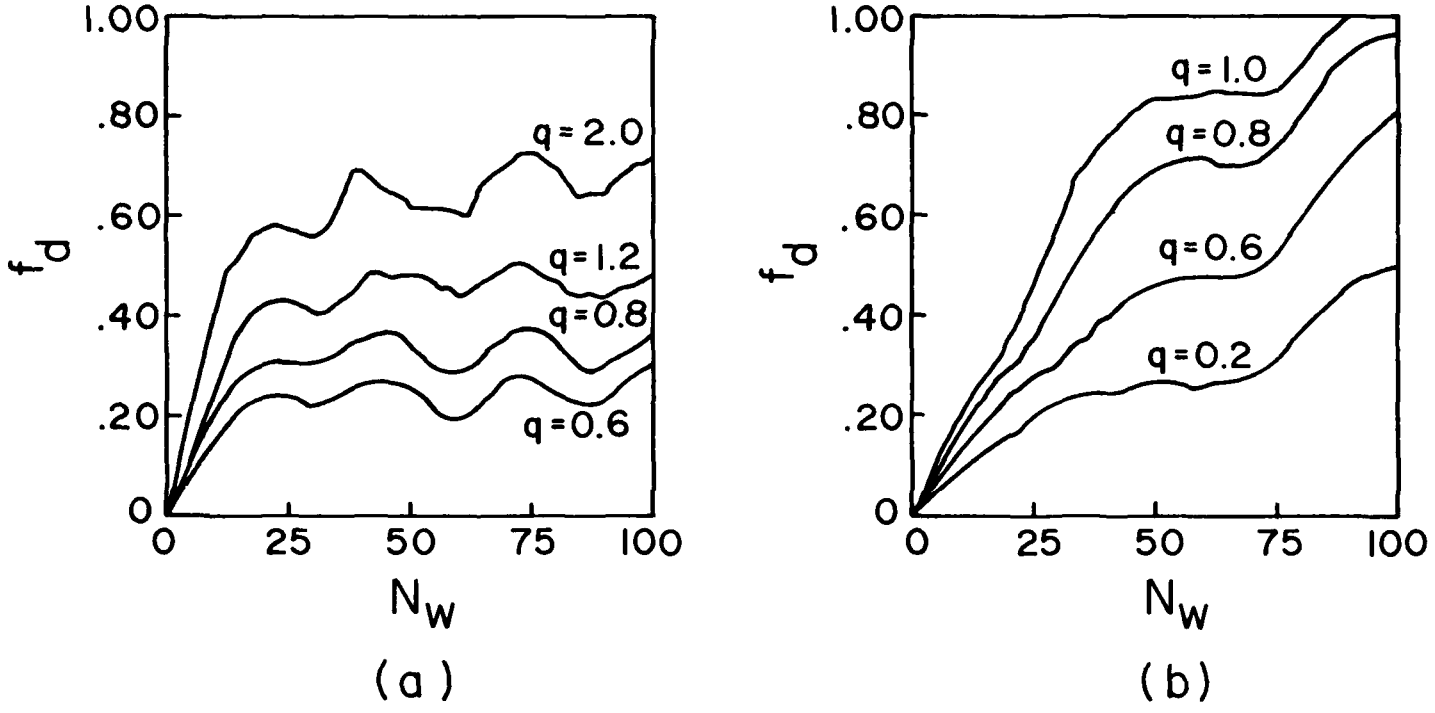



Figure 5. The fraction $f_d$ of detrapped particles against the distance in wiggler periods $N_W = z / \lambda_W$. Different curves correspond to various sidebands to carrier amplitude ratios $q = a_s/a_r$. Parameters are $a_w = 2$, $a_r = 5\times10^{-5}$, $\psi_r = 7\pi/6$, $\gamma_r = 25$ and (a) $\omega_s/\omega_r = 1.016$ , (b) $\omega_s/\omega_r = 1.024$.

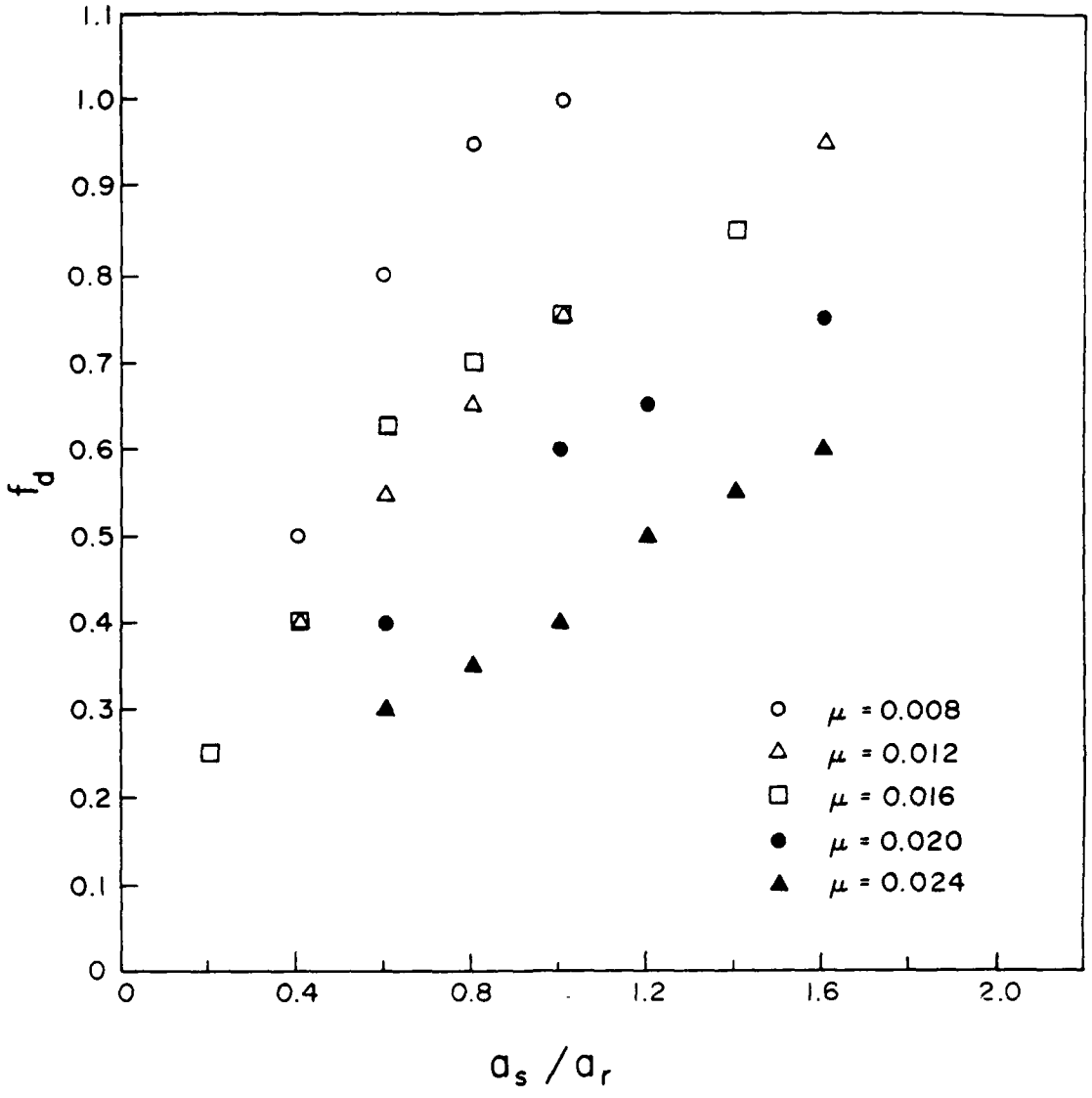



Figure 6. The fraction $f_d$ of detrapped particles after 100 wiggler periods for an initially uniformly filled bucket. Results for various sideband frequency ratios $\mu = \omega_s/\omega_r$ are plotted against the relative sideband amplitude $q = a_s/a_r$ for $a_w = 2$, $a_r = 5\times10^{-5}$ and $\psi_r = 7\pi/6$, $\gamma_r = 25$.

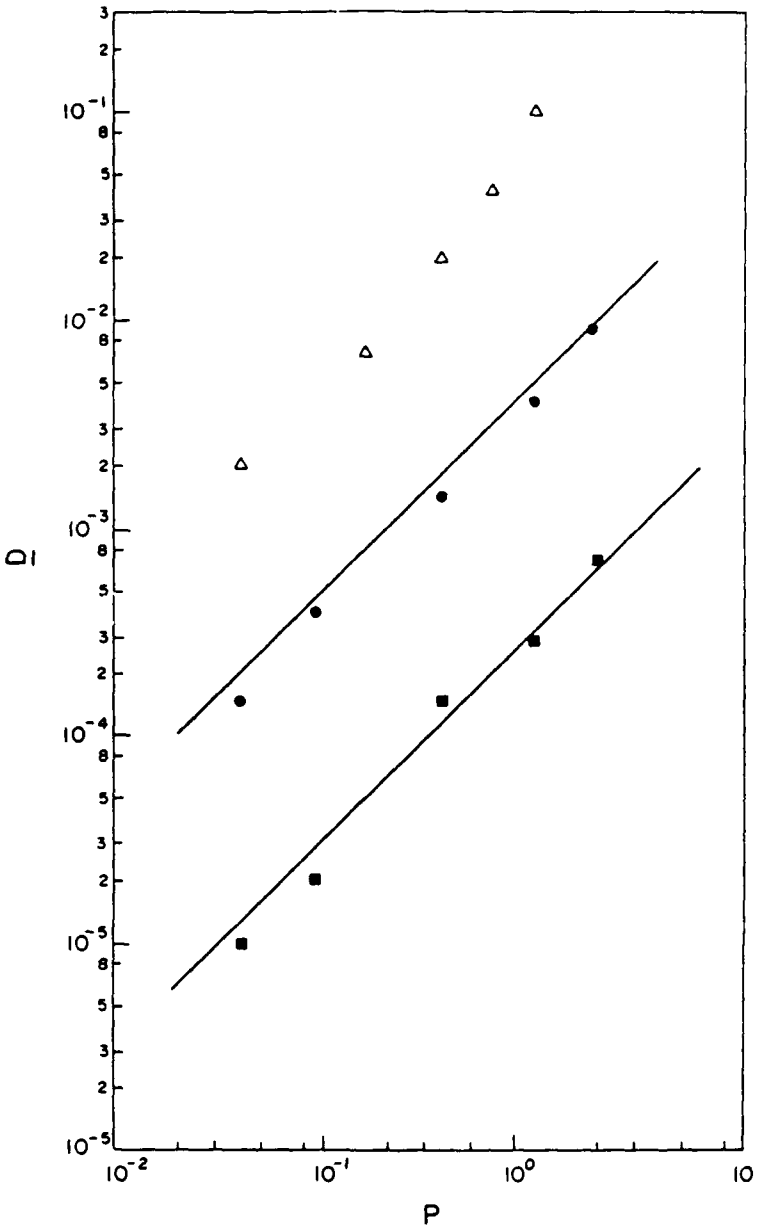



Figure 7. The normalized diffusion coefficient $\underline{D}$ as a function of the sideband power ratio $P = W_s/W_r$ for $a_w = 2$, $a_r = 5\times10^{-5}$ and $\psi_r = 7\pi/6$, $\gamma_r = 25$. Squares correspond to a continuous type of spectrum, peaked at $\omega_s/\omega_r = 1.016$ with $A = 100$ and $\nu = 0.1$. Dots correspond to a wide discrete peaked at $\omega_s/\omega_r = 1.024$ with $A = 20$ and $\nu = 0.5$. Triangles correspond to a single frequency spectrum with $\omega_s/\omega_r = 1.016$. The upper and lower solid lines correspond to the theoretical results from Eqs. (36) and (42) respectively.

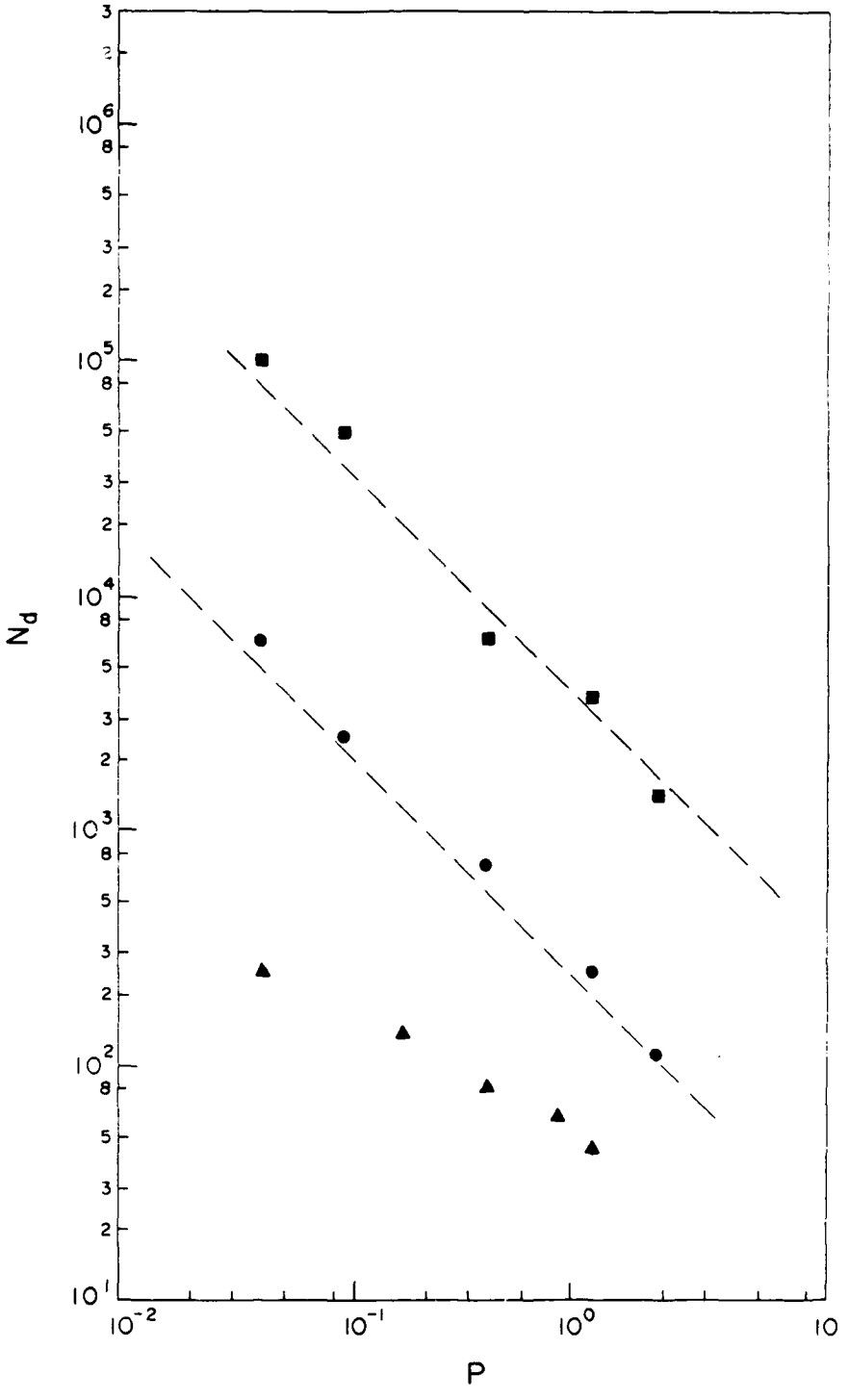



Figure 8. The e-folding diffusion length $N_d$ in wiggler periods for the number of trapped particles. Parameters and semantics are the same as in Fig. 7.

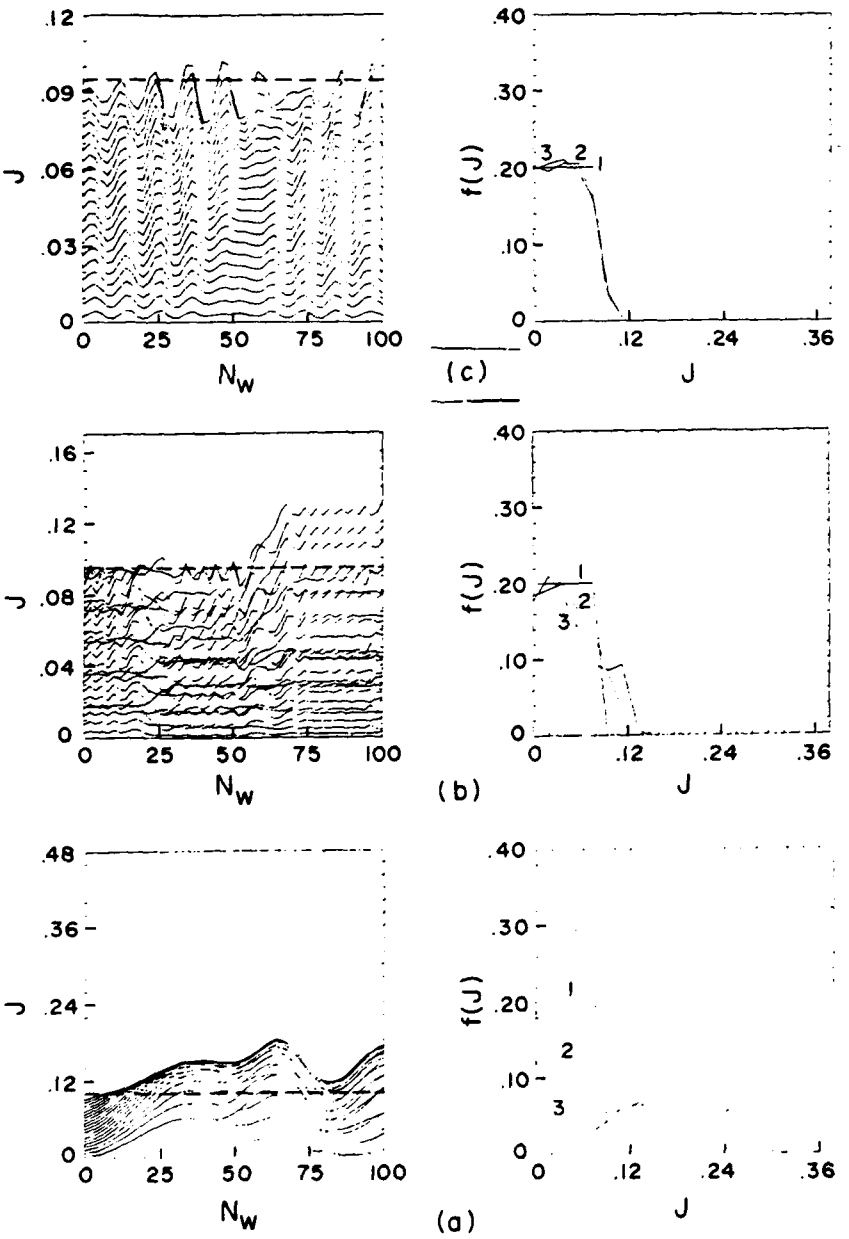



Figure 9. Particle response under different sideband spectra. On the left-hand side we plot the action J against the number of wiggler periods $N_w$ for selected particles. On the right-hand side we plot the corresponding distribution function f(J) at $N_w$ = 0, 50, and 100. In all cases the total sideband power ratio $P = W_s/W_r = 0.36$ and $a_w = 2$, $a_r = 5\times10^{-5}$, $\gamma_r = 25$. (a) corresponds to a wide continuous sideband spectrum (b) corresponds to a wide discrete spectrum and (c) to a single frequency $\omega_s/\omega_r = 1.016$.

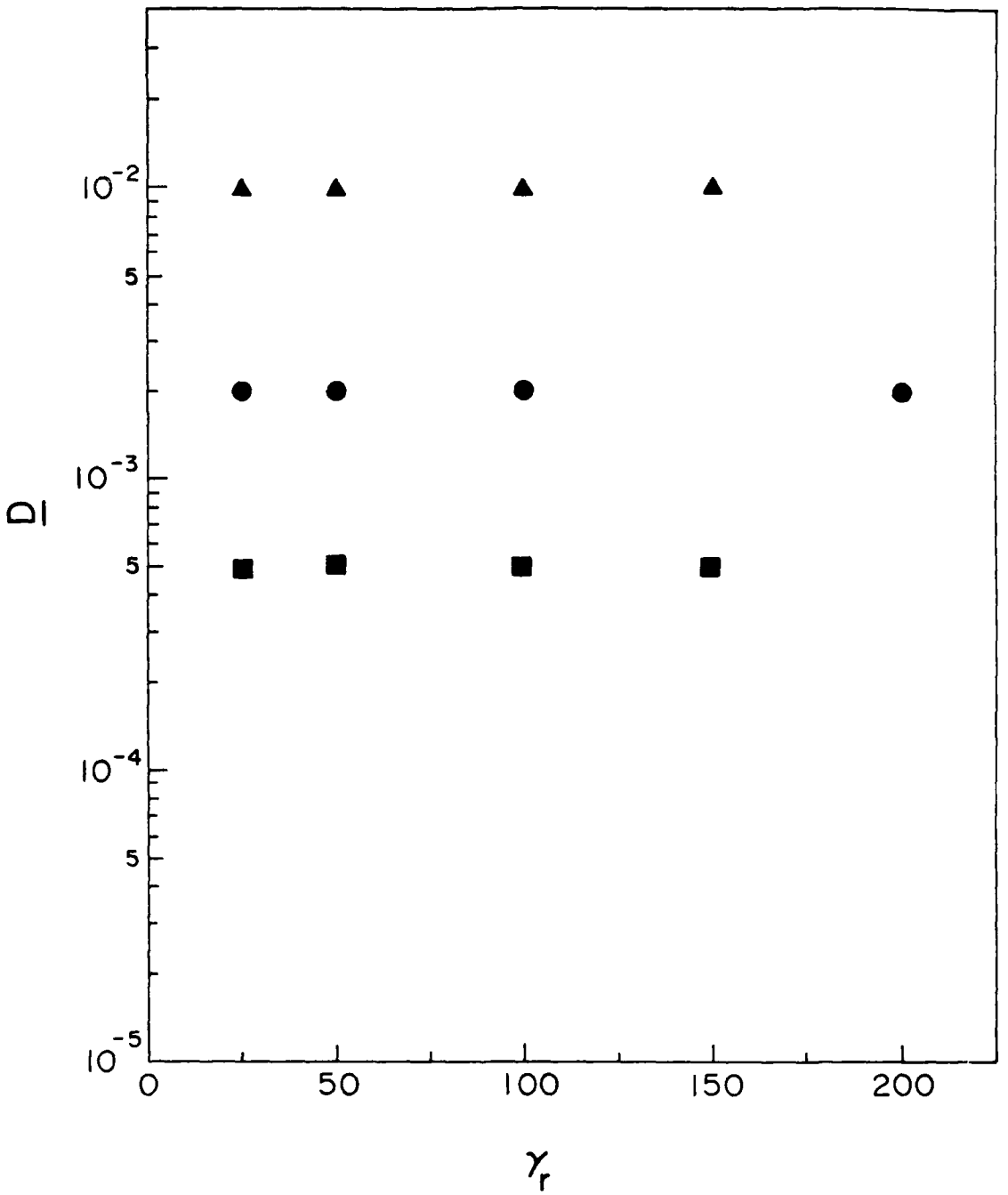



Figure 10. Plots of the normalized diffusion coefficient $\underline{D}$ against the electron energy $\gamma_r$. Parameters are $a_w = 2$, $a_r = 2 \times 10^{-4}$, $a_s = 7.5 \times 10^{-5}$ and $\omega_s = 1.024$. Squares correspond to a continuous, dots to a wide discrete and triangles to a single frequency spectrum.

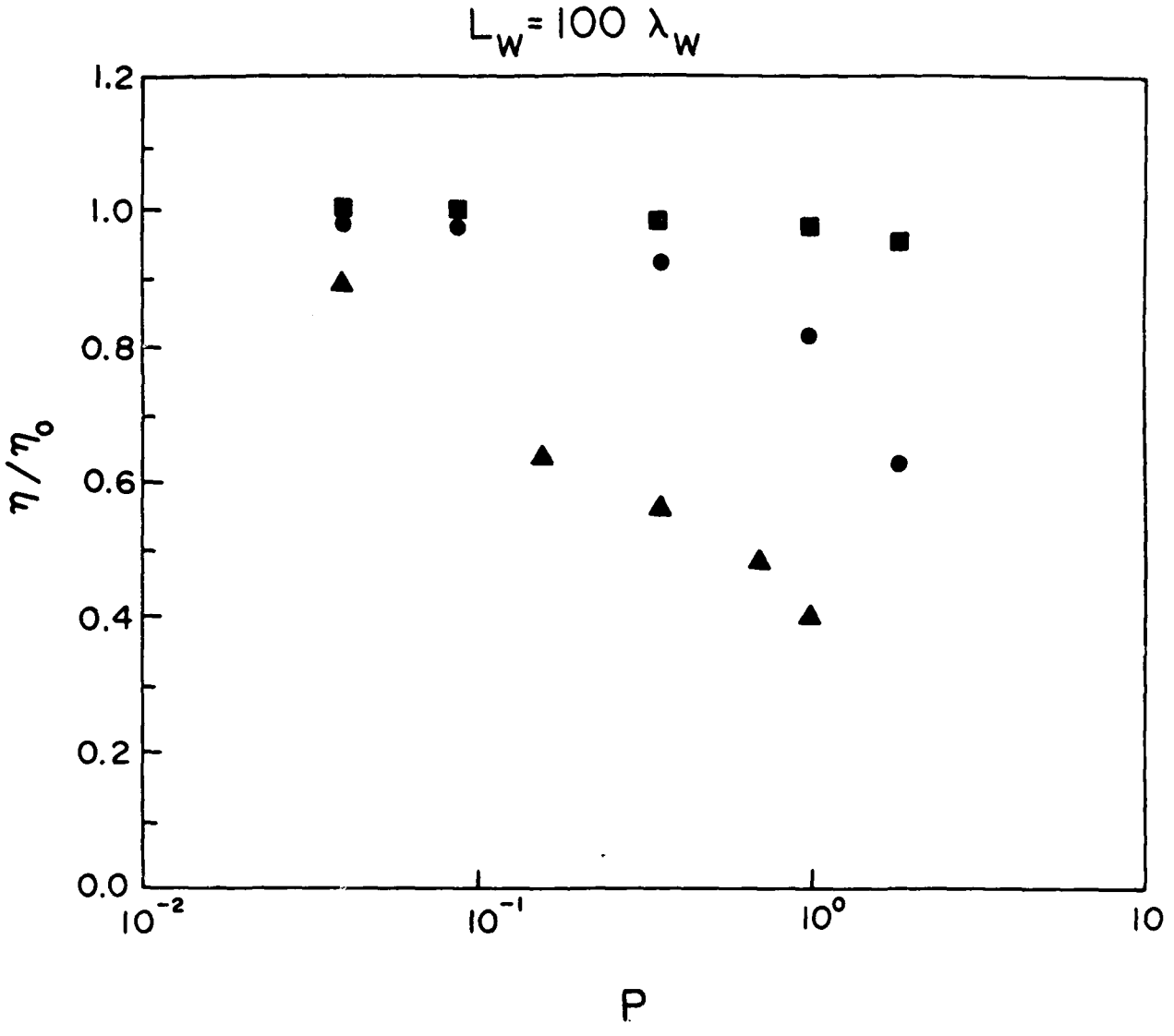



Figure 11. Deterioration of the extraction efficiency for various spectral types. Plotted is the ratio $\eta/\eta_o$ for a wiggler length of 100 periods as a function of the sideband power ratio P. The numerical results in Fig. 8 were used in Eq. (49) to create this plot. The symbolism and the parameters are the same as in Fig. 8.

# APPENDIX LL

## Transformations of Gaussian Light Beams Caused by Reflection in FEL Resonators

**Naval Research Laboratory**
Washington, DC 20375-5000




NRL Memorandum Report 6347

# Transformations of Gaussian Light Beams Caused by Reflection in FEL Resonators

S. RIYOPOULOS

*Science Applications Intl. Corp.*
*McLean, VA 22102*

C. M. TANG AND P. SPRANGLE

*Plasma Theory Branch*
*Plasma Physics Division*

October 27, 1988

Approved for public release; distribution unlimited.

## CONTENTS


| | | |
|---|---|---|
| I. | INTRODUCTION | 1 |
| II. | OUTLINE OF THE METHOD | 4 |
| III. | MIRROR SURFACE | 11 |
| IV. | COMPUTATION OF THE REFLECTION MATRIX | 13 |
| V. | LIMITING CASES | 19 |
| VI. | REFLECTION OF THE LOWEST ORDER MODE | 22 |
| VII. | CROSS-POLARIZATION EFFECTS | 26 |
| | ACKNOWLEDGMENT | 28 |
| | APPENDIX A — Computation of the Hermitian Matrix Elements | 29 |
| | APPENDIX B — Computation of the First Matrix Elements in Laguerre Representation | 32 |
| | APPENDIX C — Computation of the Cross-Polarization Matrix Element | 36 |
| | APPENDIX D — Small Aperture Limit | 37 |
| | REFERENCES | 41 |
| | DISTRIBUTION LIST | 51 |

# TRANSFORMATIONS OF GAUSSIAN LIGHT BEAMS CAUSED BY REFLECTION IN FEL RESONATORS

## I. INTRODUCTION

Free Electron Lasers (FELs) operating as oscillators[1-7] require the trapping of light pulses between systems of mirrors (resonators).[8,9] These pulses are repeatedly amplified via synchronous interaction with electron pulses passing through the wiggler. The radiation produced by the stimulated emission is confined within a narrow cone along the beam axis. Therefore, the vector potential can be represented as a superposition of Gaussian modes. Those are the free space eigenmodes $A_{mn}(r) = e_{mn}A_{mn}(r)e^{ikz}$ where $e_{mn}$ is the polarization vector, of the paraxial equation,[10]

$$\nabla_{\perp}^2 A - 2ik \frac{\partial A}{\partial z} = 0. \qquad (1)$$

Equation (1) is the $k_{\perp} << k = \omega/c$ limit of the exact wave equation. The simplest oscillator configuration is that of an open resonator with two opposed identical mirrors. The vacuum eigenmodes for this arrangement are also expressed in terms of the paraxial eigenmodes. Their detailed structure can be described in terms of either Gaussian-Hermite functions in rectangular coordinates, or Laguerre functions in polar coordinates. In both representations all the eigenmodes with given wave number k are characterized by two independent parameters: the waist $w = (2b/k)^{1/2}$ and the curvature of the wave front $1/R = z/(z^2 + b^2)$, where z is the distance from the waist position and b is the Rayleigh length (Fig. 1).

The electron beam is an optically active medium that alters the characteristic parameters of the radiation after each passage. During the build-up period the modal content and the structure of the light pulses inside the oscillator will change. A numerical method has been developed recently optimizing the representation for the amplified radiation. In the source dependent expansion[11,12] the waist size and the curvature of the elected modal basis is tailored according to the driving source term. That

Manuscript approved August 8, 1988.

minimizes the number of modes required to describe the light beam. In general, the curvature and waist size of these modes does not match the curvature and waist of the vacuum eigenmodes for the resonator. Therefore, the transfer matrix for a given mirror must be known for arbitrary incoming modes. This need stems from computational as well as physical reasons. The knowledge of the cavity reflection matrix R, together with the gain matrix G through the wiggler, is necessary in determining the potential for steady state operation.

The study of the reflection matrix must include the effects of deflecting the light beam, in addition to finite mirror size and curvature mismatches. During high power operation, grazing mirror incidence may be necessary to avoid exceeding the dielectric breakdown limit for the reflecting surface. Also, in case of a high per-pass gain with optical guiding, the spot size for the reflected radiation could be much larger than the incoming. In two mirror resonators, the reflected radiation could then damage the wiggler. Therefore, ring resonators, including three or more mirrors, must be employed for the deflection and recirculation of the light pulses.

We are interested in cases when the reflected radiation remains focused along some direction $\hat{z}_o$ making an angle $\phi$ with the incoming $\hat{z}_i$. Then the reflected vector potential will also be expandable in free space eigenmodes $A_{pq}(r_o)$ of the paraxial equation in the new direction. The mirror surface generating focused reflection in the desired direction can not be arbitrary but must be appropriately defined. The angle of deflection $\phi$ will enter the equation defining the mirror surface. The other surface parameter, namely the curvature $1/R_m$, is a free parameter. It determines the curvature $1/R_o$ for the outgoing modes given the curvature $1/R_i$ of the incoming modes. In case of reflection by an arbitrary surface,

the scattered radiation cannot, in general, be covered by the paraxial modes that do not form a complete set in three dimensions.

A single incident mode $A_{mn}(r_i)$ will, in general, be partially reflected into different modes $A_{pq}(r_o)$ where $(m,n)\neq(p,q)$. This is caused by the deflection of the light beam, the finite size of the mirror and the curvature mismatches. Reflection into other modes will affect the interaction between the electron beam and the radiation in a number of ways. First, the rms radius of the light beam will change, affecting the matching beam condition. Second, the light pulse will spread axially because of dispersion among different modes, since the phase velocity depends on the modal number (m,n). Third, different phase shifts among the various modes during reflection may render these modes out of phase after a number of bouncings off the resonator. For the above reasons the fraction of radiation scattered into other modes will contribute to the losses in FEL oscillators.

The method for obtaining the reflection matrix is outlined in Sec. II. The definition of the appropriate mirror surface is given in Sec. III. In Sec. IV the integral expressions for the matrix elements are derived. An analytic expansion in powers of a small parameter (of the order of the diffraction angle) is given in the same section. Some limiting cases are examined in Sec. V. In Sec. VI the reflection of the fundamantal mode (0,0) is studied in detail. Section VII deals with cross-coupling effects among the vector components of the radiation.

## II. OUTLINE OF THE METHOD

The free space eigenmodes $A_{mn}(r)$ of the paraxial wave equation have the general form

$$A_{mn}(r) = \frac{u_{mn}(r;W)}{\left(1 + \frac{z^2}{b^2}\right)^{1/2}} e^{i\left[kz + \frac{k(x^2 + y^2)}{2R(z)}\right]} e^{i\delta_{mn}(z)} . \qquad (2)$$

The first exponential in (2) contains the rapidly varying phase on the wavelength scale $\lambda = 2\pi/k$. The wavefronts are spherical with radius of curvature R(z) given by $1/R(z) = z/(z^2 + b^2)$. The spot size of the radiation envelope is $W(z) = w(1 + z^2/b^2)^{1/2}$, where $w = (2b/k)^{1/2}$ is the waist, and the distance z is measured from the position of the waist. The amplitude squared of the mode drops by 1/2 over a distance equal to the Rayleigh length b (also known as confocal parameter). Most of the radiation is confined within a cone parametrized by the diffraction angle $\theta_d = W/z \simeq (\lambda/b\pi)^{1/2}$. The structure of the amplitude profile $u_{mn}(r;W)$ depends on the elected coordinate system. $u_{mn}(r;W)$ contains the slow spatial variation equivalent to a small wave number perpendicular to the z-direction. Higher modes correspond to an increasing effective $k_\perp$, producing the slow phase shift expressed by the term exp $[i\delta_{mn}(z)]$. For a given k, the mode is completely defined by the two independent parameters R and w (or any combination of two out of the four quantities R, w, z and b).

The geometry of the reflection is illustrated in Fig. 2. The subscripts i and o denote the coordinate system used for expressing incoming and outgoing modes. $r_i$ is defined with the $\hat{z}_i$ axis along the direction of incidence and $r_o$ has the $\hat{z}_o$ axis along the direction of reflection. The origins are displaced from the mirror center by $l_i$ and $l_o$ respectively, where $l_i$ is the distance of the minimum waist $w_i$ for the

incoming radiation and $l_o$ is the distance of the minimum waist $w_o$ for the reflected mode. A third coordinate system $r_s$ with the origin at the mirror center and $\hat{z}_m$ aligned with the mirror axis will be useful in the computations. Underlined quantities $\underline{r}_i$, $\underline{r}_o$ and $\underline{r}_s$ stand for the mirror surface coordinates in each reference frame. The transformations among the various frames are defined by

$$x_i = x_s \cos\frac{\Phi}{2} - z_s \sin\frac{\Phi}{2}, \qquad x_o = x_s \cos\frac{\Phi}{2} + z_s \sin\frac{\Phi}{2},$$

$$y_i = y_s, \qquad (3a) \qquad y_o = y_s, \qquad (3b)$$

$$z_i = z_s \cos\frac{\Phi}{2} + x_s \sin\frac{\Phi}{2} + l_i, \qquad z_o = z_s \cos\frac{\Phi}{2} - x_s \sin\frac{\Phi}{2} + l_o.$$

We consider incoming radiation of given curvature and of arbitrary amplitude profile $A^i(r_i)$, consisting of various modes (m,n) with the same $R_i(z)$. If both incident and reflected radiation are expanded into eigenmodes,

$$A^i(r_i) = e^{i\Phi_i(r_i)} \sum_{m,n} c^i_{mn} \frac{u_{mn}(r_i)}{\left[1 + \frac{z_i^2}{b_i^2}\right]^{1/2}} e^{i\delta_{mn}}, \qquad (4a)$$

$$A^o(r_o) = e^{i\Phi_o(r_o)} \sum_{p,q} c^o_{pq} \frac{u_{pq}(r_o)}{\left[1 + \frac{z_o^2}{b_o^2}\right]^{1/2}} e^{i\delta_{pq}}, \qquad (4b)$$

where

$$\Phi_i(r) = k\left[z + \frac{x^2 + y^2}{2R_i(z)}\right], \qquad (4c)$$

the relation among the incident and reflected expansion coefficients $c^{i}_{mn}$, $c^{o}_{pq}$ is formulated by

$$c^{o} = \mathbf{R}\, c^{i}, \tag{5a}$$

or

$$c^{o}_{pq} = \sum_{m,n} R^{mn}_{pq}\, c^{i}_{mn}, \tag{5b}$$

where $R^{mn}_{pq}$ are the elements of the reflection matrix $\mathbf{R}$.

We examine the case when the mirror dimensions $\rho$ are much larger than the wavelength $\lambda$, $\lambda << \rho$ (otherwise diffraction rather than reflection would prevail). We also assume that the angle $\zeta$ subtended by the mirror $\zeta = \rho/R_m$, where $R_m$ parametrizes the radius of curvature, is small, of the order of the diffraction angle $\theta_d$, $\zeta \sim \theta_d \sim \varepsilon$. The $\nu$-th component of the reflected vector potential at distance $|\mathbf{r}_o - \underline{r}_o| >> \lambda$ from the mirror surface S is then given by

$$A^{o}_{(\nu)}(\mathbf{r}_o) = -\frac{ik}{2\pi} \iint_S ds\, \frac{e^{ik|\mathbf{r}_o - \underline{r}_o|}}{|\mathbf{r}_o - \underline{r}_o|} A^{S}_{(\nu)}(\underline{r}_o)\, (\hat{n} \cdot \hat{\delta r}). \tag{6}$$

In Eq. (6) $\hat{n}\cdot\hat{\delta r}$ is the obliqueness factor where $\hat{\delta r} = (\mathbf{r}_o - \underline{r}_o)/|\mathbf{r}_o - \underline{r}_o|$ and $\hat{n}$ is the normal unit vector to the reflecting surface. The surface element ds is given by $ds = \delta[z_o - f(x_o, y_o)]dx_o dy_o dz_o$ where $z_o = f(x_o, y_o)$ is the surface equation. Equation (6) is the convolution of a source term $A^{S}(\underline{r}_o)$ at the mirror surface with the propagator $\exp(ik|\mathbf{r}_o - \underline{r}_o|)/|\mathbf{r}_o - \underline{r}_o|$, i.e., a superposition of spherical waves originating at S. The source term $\mathbf{A}^{S}(\underline{r}_o)$ is specified from the incoming vector potential $\mathbf{A}^{i}(\underline{r}_i)$ through the boundary conditions and the coordinate transformations (3). We will assume a perfectly conducting surface, where the incident and reflected fields are related by

$$A^s = -A^i + 2\,(\hat{n}\cdot A^i)\,\hat{n}, \tag{7a}$$

and $\hat{n}$ is the normal unit vector to the reflecting surface. The second term in (7a) introduces a coupling among different vector components, caused by the mirror curvature. This cross-coupling is small and disappears in the plane mirror limit,

$$A^s_{(\nu)} = -A^i_{(\nu)}, \tag{7b}$$

where $A^i$ and $A^s$ are expressed in the incoming and outgoing coordinate systems respectively. Because of the linear superposition principle, Eq. (6), the cross-coupling contribution can be added separately, and will be deferred until Sec. VII. In the next three sections we will treat the reflected vector components as independent scalars, according to (7b), that corresponds to a phase shift by $\pi$ during reflection. Most of the computations will be performed on the mirror surface. To simplify the notation from now on, we drop the bar ($\underline{\ }$) under the mirror coordinates $\underline{r}$. Subscripted quantities such as $r_i$, $r_o$, $r_s$ will signify the mirror coordinates in each reference frame. Unsubscripted coordinates will denote the observation point in the reflected radiation frame of reference.

We seek cases when the reflected radiation propagates along $z_o$, contained within a cross section of dimensions $x,y \ll z-z_o$. The expansion $|r-r_o| \simeq (z-z_o)\,\{1 + [(x-x_o)^2 + (y-y_o)^2]/2(z-z_o)^2\}$ replaces the full propagator inside (6) with the paraxial propagator in that direction,

$$A^o(r) = \iint_S ds\; A(r_o)\;(\hat{n}\cdot\delta\hat{r})\; U_{-k}(r,r_o), \tag{8a}$$

where

$$U_{-k}(r, r_o) = \frac{ik}{2\pi} \frac{e^{-ik(z-z_o)}}{z-z_o} e^{-ik \frac{(x-x_o)^2 + (y-y_o)^2}{2(z-z_o)}} . \qquad (8b)$$

Expression (8) is the approximation of the exact solution (6) to order $[(x-x_o)^2 + (y-y_o)^2]/2(z-z_o)^2 \sim \varepsilon^2$. It is valid provided the surface S produces focused reflection along the desired direction. Otherwise the paraxial limit will fail to encompass all the radiation contained in the original expression (6). The geometry of the mirror that is compatible with the above approximation will be obtained during the computation of the reflection matrix.

It is known that the profile of a given eigenmode $A_{mn}(x_o,y_o,z_o)$ at $z_o$ is generated by the propagator $U_k(r,r_o)$ acting on the mode $A_{mn}(x,y,0)$ at $z = 0$. The inverse propagator $U_{-k}(r,r_o)$ therefore reproduces $A_{mn}(x,y,0)$ from $A_{mn}(x_o,y_o,z_o)$,

$$\iint_S dx_o dy_o \frac{u_{mn}(x_o,y_o,z_o)}{\left[1 + \frac{z_o^2}{b_o^2}\right]^{1/2}} e^{-ik\left[z_o + \frac{x_o^2 + y_o^2}{2R(z_o)}\right]} U_{-k}(r,r_o) = u_{mn}(x,y,0). \qquad (9)$$

This suggests multiplying and dividing the integrand inside (8a) by $\exp[i\Phi(r_o)] / [1 + z_o^2/b_o^2]^{1/2}$, recasting (8a) in the form,

$$A^o(r) = \iint ds\, e^{i\Delta(r_o)} S(r_o)\, e^{-i\Phi_o(r_o)} U_{-k}(r,r_o), \qquad (10)$$

where the source term $S(r_o)$ is,

$$S(r_o) = A^i[r_i(r_o)]\, (\hat{n} \cdot \delta\hat{r}) \left[1 + \frac{z_o^2(r_o)}{b_o^2}\right]^{1/2}, \qquad (11)$$

and the phase term $\Delta(r_o) = \Phi_i[r_i(r_o)] + \Phi_o(r_o)$ is given by,

$$\Delta(r_o) = k\left[z_i(r_o) + z_o + \frac{x_i^2(r_o) + y_i^2(r_o)}{2R_i(r_o)} + \frac{x_o^2 + y_o^2}{2R_o(r_o)}\right]. \quad (12)$$

The phase $\Delta(r_o)$ depends on the angle $\phi$ through the coordinate transformations Eqs. (3).

The term $\exp[i\Delta(r_o)]$ is varying rapidly, on the scale of the wavelength $\lambda$. Therefore, its convolution with the slowly varying source term over an arbitrary surface will be vanishingly small. In general, this corresponds to radiation scattering where only a small fraction of the incoming radiation is reflected along the considered direction $\phi$. The integral (10) will be finite only when it is possible to satisfy the condition $\Delta(r_o) \simeq$ constant over some surface S. If, in addition, S is much larger than $\lambda$, expression (10) will be finite only within a narrow angle $\delta\phi$ around $\phi$. This guarantees that the reflected radiation remains focused along that direction. Therefore, a condition that the exact reflected radiation (6) be fully covered by the paraxial limit (10) is that

$$\Delta(r_o) = \text{constant}, \quad (13)$$

along the surface S. Accordingly, the optical path is the same along the rays connecting an incoming wave front with its mirror image (reflected) wave front.

Requirement (13) defines the appropriate mirror surface $z_o = f_o(x_o, y_o; \phi)$ for reflection in the elected direction. Assuming that $f_o$ is found, we may express $z_o$ in terms of $x_o$, $y_o$ and use the constancy of $\Delta(r_o)$ over S, reducing (10) into

$$A^o(r) = \iint_S dx_o dy_o\ \sigma(x_o, y_o)\ e^{-i\Phi_o(x_o, y_o)}\ U_{-k}(r, r_o). \quad (14)$$

$\sigma(x_o,y_o) \equiv S[x_o,y_o,z_o(x_o,y_o)]$ is fully expanded in terms of $u_{mn}(x_o,y_o)$ that form a complete set in two dimensions,

$$\sigma(x_o,y_o) = \sum_{m,n} R^{mn}\, u_{mn}(x_o,y_o;W_o). \tag{15}$$

The expansion coefficients $R^{mn}$ for Gaussian incoming radiation of arbitrary profile $\sigma(x_o,y_o)$ are given by

$$R^{mn} = \iint dx_o dy_o\ \sigma(x_o,y_o)\ u_{mn}(x_o,y_o;W_o) / \iint dx_o dy_o u_{mn}^{\,2}(x_o,y_o;W_o). \tag{16}$$

The radiation spot size $W_o$ at the location of the mirror center is a free parameter, yet to be specified. Each choice of $W_o$ generates an equivalent representation for $\sigma(x_o,y_o)$.

Upon substituting expansion (15) inside the integral (14) and using the property (9) for the inverse propagator $U_{-k}$, the reflected vector potential assumes the final form

$$A^o(x,y,0) = \sum_{m,n} R^{mn}\, u_{mn}(x,y;W_o), \tag{17}$$

where $W_o(z) = w_o\ (1 + z^2/b_o^{\,2})^{1/2}$, $w_o = (2b_o/k)^{1/2}$. Expression (17) is a complete decomposition of the reflected radiation into paraxial eigenmodes for incident radiation of arbitrary profile. Therefore, condition (13) that defines the mirror surface is sufficient for the full reflection of paraxial (Gaussian) incoming light beams into paraxial beams only. The fraction of the electromagnetic flux incident on the mirror is conserved after reflection. If, on the other hand, (13) is seriously violated, the paraxial modes are inadequate to include all reflected radiation, and the incident flux is not conserved by expressions similar to (17).

## III. MIRROR SURFACE.

To obtain the equation for S we express all quantities inside (12) in the mirror coordinate frame applying the transformations (3a) and (3b). Using the scaling $x_s/R_m \sim y_s/R_m \sim \varepsilon << 1$, $z_s/R_m \sim \varepsilon^2$ we obtain from (13)

$$z_s = -\frac{1}{2R_m \cos\frac{\phi}{2}}\left[x_s^2 \cos^2\frac{\phi}{2} + y_s^2\right], \tag{18a}$$

where

$$\frac{1}{R_m} = \frac{1}{2R_o} + \frac{1}{2R_i}. \tag{18b}$$

Equation (18a) is the analytic expression for a paraboloid surface. $R_m$ parametrizes the mirror curvature, being positive or negative for a convex or concave mirror respectively. The surface is reflection symmetric with $(zx)_s$ and $(zy)_s$ as the symmetry planes; there is no rotational symmetry around $\hat{z}_s$. Surface (18a) can also be approximated, to second order in $(x_s/R_m)^2$, $(y_s/R_m)^2$ by hyperboloids or ellipsoids defined by

$$\left(z_s - R_m\cos\frac{\phi}{2}\right)^2 - x_s^2\cos^2\frac{\phi}{2} - y_s^2 = R_m^2\cos^2\frac{\phi}{2}, \tag{19a}$$

$$\left(z_s + R_m\cos\frac{\phi}{2}\right)^2 + x_s^2\cos^2\frac{\phi}{2} + y_s^2 = R_m^2\cos^2\frac{\phi}{2}. \tag{19b}$$

All the surfaces become spherical in the limit of perpendicular incidence $\phi = 0$, and plane mirrors when $R_m \to \infty$. Using the definition of the curvature for the paraxial modes, Eq. (2), and the fact that $R >> b$ in cases of interest, we obtain from (18b)

$$\frac{1}{R_o} = \frac{2}{R_m} - \frac{1}{R_i}. \tag{20}$$

Relation (20) defines the curvature of the reflected modes from the incoming mode curvature and the curvature of the mirror.

Equations (18)-(20) imply that

$$\Delta(r_s) \equiv \Delta[r_i(r_s), r_o(r_s)] = \text{const.} + O\left[ k\rho \left(\frac{\rho}{R_m}\right)^2 \right], \qquad (21)$$

where $\rho$ parametrizes the mirror size. A more complicated surface equation (higher than quadratic in x, y, z) is required to improve the constancy to a higher order. In the next section the reflection matrix will be computed by expansion in powers of $W_o/R_m \simeq \rho/R_m$. Since $k\rho >> 1$, the approximation $\Delta(r_s) = \text{constant}$ is satisfactory for a first order expansion as long as $\rho/R_m \sim 1/k\rho$. In case that $\rho/R_m > 1/k\rho$, $\Delta(x_s, y_s)$ is a slowly varying function over S. Large mirrors require the inclusion of the phase slippage term $\exp[i\Delta(x_s, y_s)]$ next to the source term $\sigma(x_s, y_s)$ in Eq. (16).

The unit vector $\hat{n}$ normal to the mirror surface is given by

$$\hat{n} = \frac{\nabla f}{|\nabla f|} \simeq \cos\frac{\phi}{2}\frac{x_s}{R_m}\hat{x}_s + \frac{1}{\cos\frac{\phi}{2}}\frac{y_s}{R_m}\hat{y}_s + \left(1 + \frac{z_s}{R_m \cos\frac{\phi}{2}}\right)\hat{z}_s,$$

where $f(x_s, y_s, z_s)$ is given by Eq. (18a).

## IV. COMPUTATION OF THE REFLECTION MATRIX

According to the definition (5b), the $R_{pq}^{mn}$ element of the reflection matrix **R** is obtained from the source term $\sigma_{pq}(x_o,y_o)$ inside (14) generated by a single incident eigenmode $A_{pq}[r_i(r_o)]$. The integration is performed in the mirror-aligned coordinates, taking advantage of the existing symmetries. The coordinates $r_i$ and $r_o$, defining the incoming and outgoing wave functions, become explicit functions of $x_s$, $y_s$ through the transformations (3). The surface equation (14a) is used to express $z_s$ in terms of $(x_s,y_s)$. The mirror boundary

$$x_s^2\cos^2\frac{\phi}{2} + y_s^2 = \rho^2 \tag{22}$$

is defined by the intersection of the infinite surface (18a) with the plane $z_s = \text{const} = 2\rho^2\cos^2(\phi/2)/R_m$. After the above manipulations, the reflection matrix elements take the form

$$R_{pq}^{mn} = \iint_S dx_s dy_s \frac{\bar{u}_{mn}(x_s,y_s)\bar{u}_{pq}(x_s,y_s)}{\left[1 + \frac{l_o^2}{b_o^2}\right]^{1/2}} \left[\frac{1 + \frac{z_o^2(x_s,y_s)}{b_o^2}}{1 + \frac{z_i^2(x_s,y_s)}{b_i^2}}\right]^{1/2} e^{i\Delta(x_s,y_s)}$$

$$\times e^{i\delta_{pq}^i(x_s,y_s) - i\delta_{mn}^o(x_s,y_s)} \left[\cos\frac{\phi}{2}\left(1 - \frac{x_s}{R_m}\sin\frac{\phi}{2} - \frac{x_s^2\sin^2\frac{\phi}{2}}{R_m^2}\right)\right], \tag{23}$$

where

$$\bar{u}_{mn}(x_s,y_s) \equiv u_{mn}\left[x_o(x_s,y_s),\ y_s\right],\ \bar{u}_{pq}(x_s,y_s) \equiv u_{pq}\left[x_i(x_s,y_s),\ y_s\right]. \tag{24}$$

Expression (23) is correct to order $\rho^2/R_m^2$.

It will be seen that **R**, as given by (23), depends on four parameters

$$\mathbf{R} \equiv \mathbf{R}(\phi,\ \alpha,\ \mu;\ \xi). \tag{25}$$

$\phi$ is the reflection angle shown in Fig. 2. $\alpha$ is the ratio of the incoming to the outgoing spot size at the mirror, $\alpha = W_i(l_i)/W_o(l_o)$. $\mu = \rho/W_o$ parametrizes the mirror size compared to the radiation spot size. $\xi = W_o/R_m$ scales as the diffraction angle $\theta_d \simeq W_o/l_o$ multiplied by the curvature mismatch $R_o/R_m$ between the mirror and the radiation wavefronts. The spot size $W_o$ enters as a free parameter because only the curvature $1/R_o$ for the reflected modes is specified by the mirror geometry. Since many combinations of $W_o$ and $l_o$ apply to a given curvature according to paragraph Eq. (2), an additional selection rule for $W_o$ is needed. Note that $W_o$ does not have to match $W_i$. This is obvious in cases when the mirror size $\rho$ is smaller that $W_i$. Each value of $W_o$ defines a complete set of modes for the reflected radiation and an equivalent representation for **R**.

Parameters $\phi$, $\alpha$, and $\mu$ can be arbitrary. In most cases of interest, however, $\xi$ is small, $\xi \ll 1$, of the same order as the diffraction angle $\theta_d$. The analytic computation of the matrix elements is carried out by expanding the integral (23) in powers of $\xi$,

$$\mathbf{R} = \mathbf{R}(0) + \xi\,\mathbf{R}(1) + \xi^2\,\mathbf{R}(2). \tag{26}$$

Each representation of **R** is tied to the choice of the basis functions $u_{mn}(\mathbf{r})$. The eigenmodes $u_{mn}(\mathbf{r})$ are specified according to the coordinate geometry. In the next subsections we derive **R** in Gaussian-Hermite and Gaussian-Laguerre representations. For simplicity, it is assumed that $\Delta(x_s,y_s)$ in Eq. (23) is constant, i.e., $k\rho\ (\rho/R_m) \ll 1$.

(a). Gaussian-Hermite representation

In rectangular coordinates (x,y,z) the functions $u_{mn}(x,z;W)$ are given by

$$u_{mn}(x,y;W) = a_{mn} H_m\left(\frac{\sqrt{2}x}{W}\right) H_n\left(\frac{\sqrt{2}y}{W}\right) e^{-\frac{x^2+y^2}{W^2}}, \tag{27a}$$

where $H_m$, $H_n$ are the Hermite polynomials and $a_{mn}$ is a normalization factor, setting the total electromagnetic flux carried by the mode equal to unity,

$$a_{mn} = \frac{\sqrt{2}}{W}\left(\pi\, 2^{m+n}\, m!n!\right)^{-1/2}. \tag{27b}$$

The corresponding slow phase factor $\delta_{mn}(z)$ in Eq. (2) is

$$\delta_{mn}(z) = (m + n + 1)\, \tan^{-1}\left(\frac{z}{b}\right). \tag{27c}$$

Substituting inside (23), expanding in $\xi$ and performing the integrations, Eqs. (23)-(26) yield

$$R_{pq}^{mn}(0) = C_{pq}^{mn}\, e^{i\psi_{pq}^{mn}}\, I_{pq}^{mn}, \tag{28a}$$

$$R_{pq}^{mn}(1) = C_{pq}^{mn}\, e^{i\psi_{pq}^{mn}}\, \tan\frac{\phi}{2}\left\{M_{pq}^{mn} + i\, N_{pq}^{mn}\right\}, \tag{28b}$$

where $C_{pq}^{mn}$ is a normalization factor

$$C_{pq}^{mn} = \frac{W_o}{\pi W_i}\left(2^{m+n+p+q}\, m!n!p!q!\right)^{-1/2}, \tag{28c}$$

and the phase $\psi_{pq}^{mn}$ is expressed by

$$\psi_{pq}^{mn} = (p+q+1)\tan^{-1}\left(\frac{l_i}{b_i}\right) - (m+n+1)\tan^{-1}\left(\frac{l_o}{b_o}\right) + k(l_i+l_o). \tag{28d}$$

$$I_{pq}^{mn} = \int_{-X_s}^{X_s} dX \int_{-Y_s}^{Y_s} dY\, H_p(\alpha X)\, H_q(Y)\, H_m(X)\, H_n(Y)\, e^{-\frac{\alpha^2+1}{2}(X^2+Y^2)}, \quad (29a)$$

$$M_{pq}^{mn} = \int_{-X_s}^{X_s} dX \int_{-Y_s}^{Y_s} dY\, H_p(\alpha X)\, H_q(Y)\, H_m(X)\, H_n(Y)\, e^{-\frac{\alpha^2+1}{2}(X^2+Y^2)}$$

$$\left\{ -\frac{3}{2} X + \frac{1-\alpha^2}{\sqrt{2}} (X^2+Y^2) - \left( \alpha \frac{H_p'(\alpha X)}{H_p(\alpha X)} - \frac{H_m'(X)}{H_m(X)} \right) \frac{\sqrt{2}}{4} (X^2+Y^2) \right\}, \quad (29b)$$

$$N_{pq}^{mn} = \int_{-X_s}^{X_s} dX \int_{-Y_s}^{Y_s} dY \frac{X}{\sqrt{2}}\, H_p(\alpha X)\, H_q(Y)\, H_m(X)\, H_n(Y)\, e^{-\frac{\alpha^2+1}{2}(X^2+Y^2)}. \quad (29c)$$

In the rescaled variables $X \simeq \cos\phi/2\ \sqrt{2}x_s/W_o$, $Y = \sqrt{2}y_s/W_o$, the surface boundary is given by $X_s^2 + Y_s^2 = 2\rho^2/W_o^2$. The lowest terms can be computed directly. The matrix elements are computed, to first order in $\xi$, in Appendix A for large size mirror and $\alpha = 1$.

(b). Gaussian-Laguerre representation

In cylindrical coordinates $(r,\theta,z)$ where $\tan\theta = x/y$, $r = (x^2+y^2)^{1/2}$, $u_m^p(r,\theta;W)$ take the form

$$u_m^{\pm p}(r,\theta;W) = a_m^p \begin{pmatrix} \cos p\theta \\ \sin p\theta \end{pmatrix} \left(\frac{\sqrt{2}r}{W}\right)^p L_m^p\left(\frac{2r^2}{W^2}\right) e^{-\frac{1}{2}\frac{2r^2}{W^2}}, \quad (30a)$$

where +p(-p) signifies cosine (sine) poloidal dependence, $a_m^p$ is given by

$$a_m^p = \left(\frac{4}{\pi W^2}\right)^{1/2} \left(\frac{m!}{(m+p)!}\right)^{1/2}, \quad (30b)$$

and the $L_m^p$ are the Laguerre polynomials. The corresponding slow phase $\delta_m^p(z)$ in Eq. (2) is,

$$\delta_m^p(z) = (2m + p + 1) \tan^{-1} \left(\frac{z}{b}\right). \tag{30c}$$

The transformations among polar coordinates representing the various reference frames are

$$r_i \simeq r_s \left[1 - \sin^2\theta_s \sin^2 \frac{\phi}{2} - 2 \frac{z_s}{R_m} \sin \theta_s \sin \frac{\phi}{2} \cos \frac{\phi}{2}\right]^{1/2},$$

$$r_o = r_s \left[1 - \sin^2\theta_s \sin^2 \frac{\phi}{2} + 2 \frac{z_s}{R_m} \sin \theta_s \sin \frac{\phi}{2} \cos \frac{\phi}{2}\right]^{1/2}, \tag{31a}$$

$$\tan \theta_i = \cos \frac{\phi}{2} \tan \theta_s - \frac{z_s}{r_s} \frac{\sin \frac{\phi}{2}}{\cos \theta_s},$$

$$\tan \theta_o = \cos \frac{\phi}{2} \tan \theta_s + \frac{z_s}{r_s} \frac{\sin \frac{\phi}{2}}{\cos \theta_s}. \tag{31b}$$

The mirror surface (18a) is expressed in polar coordinates as

$$z_s = - \frac{r_s^2}{2R_m} \frac{\sin^2\theta_s \cos^2 \frac{\phi}{2} + \cos^2\theta_s}{\cos \frac{\phi}{2}}. \tag{31c}$$

Applying similar computational procedure as in the previous subsection we obtain

$$R_{mn}^{pq} = C_{mn}^{pq} e^{i\psi_{mn}^{pq}} \cos \frac{\phi}{2} \int_o^{X_s} dX \left\{D_{mn}^{pq}(X) U^{pq}(X) + \xi \sin \frac{\phi}{2} E^{pq}(X) \left[V_{mn}^{pq}(X) + i W_{mn}^{pq}\right]\right\}, \tag{32a}$$

$$C_{mn}^{pq} = \frac{1}{2\pi}\left[\frac{m!n!\ \alpha^2}{(m+p)!(n+q)!}\right]^{1/2}, \tag{32b}$$

and the phase $\psi_{mn}^{pq}$ is expressed by

$$\psi_{mn}^{pq} = (2m+p+1)\ \tan^{-1}\left(\frac{l_i}{b_i}\right) - (2n+q+1)\ \tan^{-1}\left(\frac{l_o}{b_o}\right) + k(l_i+l_o)\ . \tag{32c}$$

The integrals $D^{pq}$, $E^{pq}$, $U_{mn}^{pq}$, $V_{mn}^{pq}$ and $W_{mn}^{pq}$ are given by

$$D^{pq}(X) = \int_o^{2\pi} d\theta_m\ \frac{\cos p\left[\theta_i(\theta_s)\right]\ \cos q\left[\theta_o(\theta_s)\right]}{1 - \sin^2\frac{\phi}{2}\sin^2\theta_m}, \tag{33a}$$

$$E^{pq}(X) = \int_o^{2\pi} d\theta_m\ \frac{\sin\theta_m\ \cos p\left[\theta_i(\theta_s)\right]\ \cos q\left[\theta_o(\theta_s)\right]}{\left(1 - \sin^2\frac{\phi}{2}\sin^2\theta_m\right)^{3/2}}, \tag{33b}$$

$$U_{mn}^{pq}(X) = (\alpha^2X)^{\frac{p}{2}}\ X^{\frac{q}{2}}\ L_m^p(\alpha^2X)\ L_n^q(X)\ e^{-\frac{\alpha^2+1}{2}X}, \tag{33c}$$

$$V_{mn}^{pq}(X) = \frac{1}{\sqrt{2}}\left\{\frac{p-q}{2} - 3 - \frac{\alpha^2+1}{2}X + \left[\frac{L_m^{p\prime}(\alpha^2X)}{L_m^p(\alpha^2X)} - \frac{L_n^{q\prime}(X)}{L_n^q(X)}\right]X\right\}$$

$$(\alpha^2X)^{\frac{p}{2}}\ X^{\frac{q+1}{2}}\ L_m^p(\alpha^2X)\ L_n^q(X)\ e^{-\frac{\alpha^2+1}{2}X}, \tag{33d}$$

$$W_{mn}^{pq}(X) = \frac{1}{\sqrt{2}}\ (\alpha^2X)^{\frac{p}{2}}\ X^{\frac{q+1}{2}}\ L_m^p(\alpha^2X)\ L_n^q(X)\ e^{-\frac{\alpha^2+1}{2}X}. \tag{33e}$$

In obtaining (33a) - (33e), X was defined by $X = [1-\sin^2(\phi/2)\sin^2\theta]r^2/2W_o^2$; thus, according to (22) and (30), the boundary $X_s$ is $X_s = 2\rho^2/W_o^2$. The lowest order terms for the first few elements are given in Appendix B for arbitrary deflection angle $\phi$ and $\alpha = 1$.

## V. LIMITING CASES

When the mirror radius tends to infinity ($1/R_m \to 0$), or in cases of vertical incidence on the mirror ($\phi = 0$), the higher order corrections in the reflection matrix **R** disappear,

$$\mathbf{R} = \mathbf{R}(0) \tag{34}$$

in both representations. The nondiagonal elements in **R** stem from the finite mirror size only. If, in addition, the mirror size is very large, $\mu \gg 1$, it is appropriate to take $W_o = W_i$ as best representation for the reflected radiation. The $\alpha = 1$ limit yields

$$R^{mn}_{pq} = \delta^{mn}_{pq}. \tag{35}$$

Thus, in case of large curved mirror and vertical incidence, or large plane mirror and arbitrary incidence, the reflection matrix is the identity matrix.

The case $\alpha = 1$ is of special interest for arbitrary angle of deflection $\phi$ and mirror curvature $1/R$, as it will be explained in the next section. For finite mirror size $\rho \geq W_o$, ( $\mu \geq 1$), there exists zeroth order non-diagonal terms inside **R**(0). Since **R**(0) is independent of the angle of deflection $\phi$, the finite mirror size yields the dominant contribution to the reflection into modes different than the incoming. The effects of the deflection of the light beam enter to first order in $\xi$, **R**(1), or higher. In the Hermite representation the elements $R^{mn}_{pq}(0)$ couple mode combinations with $m + p$ = even, $n + q$ = even. The elements with either $m + p$ or $n + q$ odd vanish because of the even/odd symmetry of the Hermite functions.

As the mirror size becomes very large and the limits of integration in (23) are extended, the orthogonality among the various modes ( $_s$) becomes effective. The off-diagonal terms in **R**(0) become comparable to

the first order corrections roughly when $1/\mu^2 \sim \xi \sim \theta_d$. At the limit $\mu \to \infty$ all the nondiagonal elements of R are reduced to order $\xi$ or higher,

$$R_{pq}^{mn} = \xi R_{pq}^{mn}(1) + O(\xi^2), \quad m \neq p, \; n \neq q, \tag{36a}$$

and the only matrix elements of zeroth order in $\xi$ are the diagonal

$$R_{mn}^{mn} = R_{mn}^{mn}(0) + O(\xi^2), \tag{36b}$$

in both Hermite and Laguerre represenations. The lowest correction in the diagonal elements is of second order $\xi^2$, while the first order contribution disappears. This is consistent with flux conservation during reflection in case of large mirror.

In obtaining Eqs. (28) and (32) it was assumed that $\Delta(x_s,y_s)$ is constant over S. According to (21) the variation of $\Delta$ is parametrized by $\xi^* = (kW_i^2/R_m)\,\xi$. When $(kW_i^2/R_m) \geq 1$, $\xi^*$ becomes of order $\xi$ and the effects of the slow phase slippage must be retained in (23). This effect, known as spherical aberration, causes additional corrections $\mathbf{R}^*(1)$, of order $\xi^*$,

$$\mathbf{R} = \mathbf{R}(0) + \xi\,\mathbf{R}(1) + \xi\,\overset{*}{\mathbf{R}}(\overset{*}{1}) + \ldots..$$

Spherical aberration does not disappear at the limit of large mirror size, as opposed to the effects discussed so far. In fact, when $\xi^* > \xi$, it places a lower limit on the off-diagonal terms in the reflection matrix,

$$R_{pq}^{mn} \geq \xi^* R_{pq}^{mn}(1)^*.$$

Perfect reflection, requiring $\xi^* = 0$, is possible only for plane mirror ($R_m \to \infty$) of large size.

The superposition principle can be used to describe reflection from more complex mirror surfaces. In case of a mirror with a hole the surface integral (14) over $S_m$ is expressed as $\int_S = \int_{S1} - \int_{S2}$ where $S_1$ is defined by the mirror exterior boundary and $S_2$ is the surface of the hole. The total

reflection matrix **R** is given by $\mathbf{R} = \mathbf{R}(S_1) - \mathbf{R}(S_2)$, the difference in the reflection matrices associated with mirrors $S_1$ and $S_2$ respectively. The transmission matrix **T** through a screen with an aperture of area S is given by $\mathbf{T} = -\mathbf{R}$, **R** being the reflection matrix for a mirror matching the aperture S. The transmission matrix for radiation diffracted behind a finite size mirror is given by $\mathbf{T}' = 1 - e^{i\pi}\mathbf{R}$ where 1 is the identity matrix.

## VI. REFLECTION OF THE LOWEST ORDER MODE

The computation of all the truncated integrals for finite mirror surface is nontrivial. Most applications, however, involve the (0,0) lowest order mode as the dominant mode in both incoming and reflected radiation. The strategy here is to compute the element $R_{00}^{00}$ of the reflection matrix first. Then the waist for the reflected modes $W_o$ can be selected so that it maximizes $R_{00}^{00}$. The optimum representation condition

$$\frac{\partial R_{00}^{00}}{\partial \alpha} = 0, \tag{37}$$

puts the maximum amount of the reflected radiation in the lowest order mode (a different mode and matrix element may be chosen, if desired). It is pointed out that (37) does not improve the properties of the reflected radiation. It enables one to choose the best representation in terms of minimizing the coefficients of the undesired modes for the scattered radiation. Once $W_o$ is fixed by (37) then the exact location and size of the waist(s) for the reflected modes is determined by solving the system of equations

$$\frac{1}{R_o} = \frac{l_o}{l_o^2 + b_o^2}, \tag{38a}$$

$$W_o = w_o \left[1 + \frac{l_o^2}{b_o^2}\right]^{1/2}. \tag{38b}$$

The element $R_{00}^{00}$ is identical in both representations since the lowest order mode $u_{00}$ is the same in rectangular and cylindrical coordinates. Performing the integration (29a) yields $R_{00}^{00}$ to first order in $\xi$

$$R_{00}^{00} = \frac{2\alpha}{1+\alpha^2}\left[1 - e^{-(1+\alpha^2)\mu^2}\right] + O(\xi^2). \qquad (39)$$

Note that the first order term vanishes and the lowest correction is of second order in $\xi^2$. The exact dependence on the mirror size $\rho$ is parametrized by $\mu = \rho/W_o$, while $\alpha = W_i/W_o$ parametrizes the ratio of the incoming and scattered radiation spot sizes at the mirror. The optimization condition $\partial R_{00}^{00}(0)/\partial\alpha = 0$ yields, $\alpha^2 = 1 + \exp[-(1+\alpha^2)\mu^2][2\mu^2\alpha^4+(2\mu^2+1)\alpha^2-1]$. In case that the mirror cross section is much larger than the spot size of the incoming mode, $\mu >> 1$, $\alpha \rightarrow 1$ and the reflected spot size at the mirror matches the incoming, $W_o = W_i$.

Large mirror size is desired to maximize the total reflection coefficient. For incoming radiation of unity electromagnetic flux $P_i = |c^i|^2 = \Sigma\ |c^i{}_{pq}|^2 = 1$, the total reflection coefficient $\eta_R = P_o/P_i$ equals the reflected flux $P_o$,

$$P_o = |c^o|^2 = |\ R \cdot c^i|^2 = \sum_{mn}\sum_{pq} |R_{pq}^{mn}\ c^i{}_{pq}|^2. \qquad (40)$$

In Fig. 3 we plot $\eta_R$ for the lowest order incoming mode as a function of $\mu' = \cos(\phi/2)\ \rho/W_o = \cos(\phi/2)\ \mu$. $\mu'$ parametrizes the size of the mirror projection into the plane perpendicular to the incoming radiation direction. The incoming radiation has a wavelength $\lambda = 1\mu$ ($10^{-4}$cm), waist $w_i = 2\times10^{-1}$cm at distance $l_i = 1.8\times10^{2}$cm from the mirror and radius of curvature (at the mirror) $R_i = 8.95\times10^{3}$cm. The mirror has a radius of curvature $R_m = 8.95\times10^{3}$cm, yielding reflected modes of $R_o = 8.95\times10^{3}$ (again $l_o$ and $w_o$ depend on the choice of $W_o$). In Fig. 4 we plot the magnitude of the reflection coefficients $|R_{pq}^{00}|$ of the lowest order mode (0,0) into the firstr 25 modes (p,q) with $p \leq q \leq 5$, as a function of $\mu'$. The deflection angle is $90^o$ and the ratio of the spot

sizes is 1. Increasing mirror size maximizes the diagonal element and minimizes scattering into other modes. The spherical aberration was retained inside (23) in evaluating the matrix elements. Its effect is small, since for the above parameters $\xi^* = 0.28\xi$, and a good agreement is observed with the constant $\Delta$ theoretical limit. In particular, the dominant off-diagonal terms couple the (0,0) incoming mode to the (1,0), (3,0) and (3,2) reflected modes only, according to the selection rules, Eqs. A(10). Comparing Figs. 3 and 4 with the next plots shows that the relative mirror size to the radiation spot size is the most important parameter to determine the reflection into other than the incoming modes.

In Fig. 5 we fix the mirror size $\mu' = 2$ and the angle $\phi = 90^o$ and vary the spot size ratio $\alpha$. The best representation, maximizing $R_{00}^{00}$ and minimizing $R_{pq}^{00}$ is obtained at $\alpha = 1$. However, for small mirror $\mu' = 0.66$, the maximum for $R_{00}^{00}$ occurs at $\alpha \simeq 0.70$ (see Fig. 6). Radiation reflected off mirrors smaller than the incoming spot size is best described by outgoing modes of reduced spot size $W_o < W_i$. Also note from Fig. 6b that for small mirror size the total power reflected into the first 25 modes never exceeds 80% of the incoming flux; even with many more modes $\eta_R$ remains less than 1. In Fig. 7 the reflection coefficients $R_{pq}^{00}$ are plotted as functions of the angle of deflection $\phi$ for fixed $\alpha = 1$, $\mu' = 2$. It is seen that, for sufficiently large reflecting surface and good choice of the spot size $W_o$, the reflection matrix is not very sensitive to $\phi$ and the off-diagonal terms remain small.

The main conclusions so far are summarized as follows. When the mirror size is $\geq 2.5$ times the incoming spot size, the fraction of the incident power scatterd into different modes is of order $\xi^2$ for

$kW^2_i/R_m < 1$, or $(\xi^*)^2$ for $kW^2_i/R_m > 1$. This holds for a wide range of deflection angles $\phi$. It will be shown in the next section that cross-polarization effects are of the same order. In most applications both $\xi$ and $\xi^*$ are less than $10^{-2}$. To this end, scattering losses will be smaller than the losses caused by the finite reflectivity (i.e., absorption) by the mirror, for most dielectrics.

## VII. CROSS-POLARIZATION EFFECTS

The curvature of the mirror surface produces a cross-coupling between the transverse components of the incoming and reflected radiation. Inserting expressions (21) for the normal unit vector to the mirror inside the boundary conditions Eq. (7a), the full source term $\mathbf{A}^s = (A_x{}^s, A_y{}^s, A_z{}^s)$ for an incoming wave $\mathbf{A}^i = (A_x{}^i, A_y{}^i, 0)$ is given by

$$A_x{}^s = - A_x{}^i + 2 \tan\frac{\phi}{2} \frac{y_s}{R_m} A_y{}^i,$$

$$A_y{}^s = - A_y{}^i + 2 \tan\frac{\phi}{2} \frac{y_s}{R_m} A_x{}^i,$$

$$A_z{}^s = 2 \cos\frac{\phi}{2} \frac{x_s}{R_m} A_x{}^i + 2 \frac{y_s}{R_m} . \qquad (41)$$

In the above relations, the components of $\mathbf{A}^i$ and $\mathbf{A}^s$ are given in coordinate systems aligned with the incoming and outgoing radiation, respectively. According to (41) the reflection of a plane polarized wave generates components polarized in every direction, including $A_z$. These cross polarization effects enter to order $\xi$ and result in a small rotation of the polarization angle.

The radiation steming from the $A_z{}^s$ component will propagate perpendicularly to the direction of interest $\hat{z}_o$ and escapes the resonator as pure reflection loss. The relation between the incoming and reflected transverse components, including cross-polarization effects, is now given by

$$\begin{pmatrix} C_x{}^o \\ C_y{}^o \end{pmatrix} = \begin{pmatrix} R & Q \\ Q & R \end{pmatrix} \begin{pmatrix} C_x{}^i \\ C_y{}^i \end{pmatrix}. \qquad (42)$$

The matrix $\mathbf{R}$ has been computed in the previous section. Substitution

of the additional cross-terms in Eq. (41) inside the propagator integral (6) yields

$$Q_{(xy)pq}^{mn} = Q_{(yx)pq}^{mn} = Q_{pq}^{mn} ,$$

where

$$Q_{pq}^{mn} = \iint_S dx_s dy_s \; 2 \tan\frac{\phi}{2} \frac{y_s}{R_m} \frac{\bar{u}_{mn}(x_s,y_s)\bar{u}_{pq}(x_s,y_s)}{\left[1 + \frac{l_o^2}{b_o^2}\right]^{1/2}} \left[\frac{1 + \frac{z_o^2(x_s,y_s)}{b_o^2}}{1 + \frac{z_i^2(x_s,y_s)}{b_i^2}}\right]^{1/2}$$

$$\times \quad e^{i\delta_{pq}^{i}(x_s,y_s) - i\delta_{mn}^{o}(x_s,y_s)} \left[\cos\frac{\phi}{2}\left(1 - \frac{x_s}{R_m}\sin\frac{\phi}{2} - \frac{x_s^2 \sin^2\frac{\phi}{2}}{R_m^2}\right)\right] . \tag{43}$$

In Gaussian-Hermite representation, we obtain

$$Q_{pq}^{mn}(1) = \sqrt{2}\xi \, C_{pq}^{mn} \, e^{i\psi_{pq}^{mn}} \tan\frac{\phi}{2} \, G_{pq}^{mn} , \tag{44a}$$

with

$$G_{pq}^{mn} = \int_{-X_s}^{X_s} dX \int_{-Y_s}^{Y_s} dY \; H_p(\alpha X) \, H_q(Y) \, Y \, H_m(X) \, H_n(Y) \, e^{-\frac{\alpha^2+1}{2}(X^2+Y^2)} . \tag{44b}$$

In Gaussian-Laguerre representation, we have

$$Q_{mn}^{pq}(1) = \sqrt{2} \, \xi \sin\frac{\phi}{2} \int_o^{X_s} dX \; G_{mn}^{pq}(X) \, B^{pq}(X), \tag{45a}$$

where

$$G_{mn}^{pq}(X) = (\alpha^2 X)^{\frac{1}{2}} \, X^{\frac{q+1}{2}} \, L_m^p(\alpha^2 X) \, L_n^q(X) \, e^{-\frac{\alpha^2+1}{2}X} , \tag{45b}$$

and

$$B^{pq}(X) = \int_0^{2\pi} d\theta \; \frac{\cos\theta \cos\left[p\theta_i(\theta)\right]\cos\left[q\theta_i(\theta)\right]}{1 - \sin^2\frac{\phi}{2}\sin^2\theta} . \qquad (45c)$$

In both representations, cross polarization effects enter to order $\xi$. In case of vertical incidence ($\phi = 0$) with arbitrary curvature $1/R_m$, or plane mirror ($\xi \sim 1/R_m = 0$) and arbitrary incidence $\phi$, **Q** goes to zero. Transverse vector components are reflected independently of each other in these two limits. Some of the elements of **Q** (in both representations) are given in Appendix C for large ($\rho >> W_i$) mirror.


## Acknowledgment

*This work was supported by SDIO and managed by SDC.*

Appendix A. Computation of the Hermitian Matrix Elements.

The integrals (29) will be evaluated here in case the mirror size $\rho$ is much larger than the incoming mode spot size $W_i$, $\rho \cos \phi/2 >> W_i$. Then the limits of the surface integrals can be extended to infinity, and the spot size for the outgoing modes $W_o$ matches that of the incoming at the mirror, i.e., $\alpha = 1$. We use the notation

$$\psi_n = e^{-\frac{X^2}{2}} H_n(X), \tag{A1}$$

the recurrence relation

$$H_n'(X) = 2n\, H_{n-1}(X), \tag{A2}$$

and the orthonormality properties

$$\int_{-\infty}^{\infty} dX\, \psi_n(X)\psi_m(X) = 2^n n!\sqrt{\pi}\, \delta_{m,n}, \tag{A3}$$

$$\int_{-\infty}^{\infty} dX\, \psi_n(X)\, X\, \psi_m(X) \equiv \langle X\rangle_{m,n} = \sqrt{\pi}\left(2^{n-1} n!\, \delta_{m,n-1} + 2^n (n+1)!\, \delta_{m,n+1}\right), \tag{A4}$$

$$\int_{-\infty}^{\infty} dX\, \psi_n(X)\, X^2\, \psi_m(X) \equiv \langle X^2\rangle_{m,n}$$

$$= \sqrt{\pi}\left\{2^{n-2} n!\, \delta_{m,n-2} + 2^{n-1}(2n+1) n!\, \delta_{m,n} + 2^n (n+2)!\, \delta_{m,n+2}\right\}, \tag{A5}$$

to obtain

$$I_{pq}^{mn} = \pi\, 2^{m+n} n!m!\, \delta_{p,m}\delta_{q,n}, \tag{A6}$$

$$M_{pq}^{mn} = -\frac{3}{2} \langle X\rangle_{p,m}\left(\sqrt{\pi}\, 2^n n!\right)\delta_{q,n},$$

$$- \frac{\sqrt{2}}{4}\left[2k\langle X^2\rangle_{p-1,m} - 2m\,\langle X^2\rangle_{m-1,p}\right]\left(\sqrt{\pi}\,2^n n!\right)\delta_{q,n}$$

$$- \frac{\sqrt{2}}{4}\left[2k\,2^m m!\,\delta_{p-1,m} - 2m\,2^{m-1}(m-1)!\,\delta_{p,m-1}\right]\langle Y^2\rangle_{q,n}, \quad \text{(A7)}$$

$$N_{pq}^{mn} = \frac{1}{\sqrt{2}}\left[(m+n+1)\frac{b_i R_m}{l_i R_i} + (p+q+1)\frac{b_o R_m}{l_o R_o}\right]\langle X\rangle_{p,m}\left(\sqrt{\pi}2^n n!\,\xi\right)\delta_{q,n}. \quad \text{(A8)}$$

Inserting expressions (A3)-(A5) into Eqs. (A6)-(A8) we obtain

$$R_{pq}^{mn}(0) = \delta_{p,m}\,\delta_{q,n}, \quad \text{(A9)}$$

$$R_{pq}^{mn}(1) = \quad \text{(A10)}$$

$$\tan\frac{\phi}{2}\left\{\left\{-\left[\frac{3}{2}\left(\frac{m-1}{2}\right)^{1/2} + \frac{1}{\sqrt{2}}\left(\frac{m-1}{2}\right)^{3/2} - \left(\frac{2m-1}{4} + \frac{2n+1}{4}\right)m^{1/2}\right]\delta_{p,m-1}\right.\right.$$

$$- \left[\frac{3}{2}\left(\frac{m+1}{2}\right)^{1/2} - \frac{1}{\sqrt{2}}\left(\frac{m+1}{2}\right)^{3/2} + \frac{1}{\sqrt{2}}\left(\frac{m+1}{2}\right)^{1/2}\left(\frac{2m+1}{2} + \frac{2n+1}{2}\right)\right]\delta_{p,m+1}$$

$$\left.- \frac{1}{\sqrt{2}}\left(\frac{(m+1)(m+2)(m+3)}{8}\right)^{1/2}\delta_{p,m+3} + \frac{1}{\sqrt{2}}\left(\frac{m(m-1)(m-2)}{8}\right)^{1/2}\delta_{p,m-3}\right\}\delta_{q,n}$$

$$- \frac{1}{\sqrt{2}}\left[\left(\frac{m+1}{2}\right)^{1/2}\delta_{p,m+1} - \left(\frac{m}{2}\right)^{1/2}\delta_{p,m-1}\right]\left(\frac{(n-1)(n-2)}{4}\right)^{1/2}\delta_{q,n-2}$$

$$- \frac{1}{\sqrt{2}}\left[\left(\frac{m+1}{2}\right)^{1/2}\delta_{p,m+1} - \left(\frac{m}{2}\right)^{1/2}\delta_{p,m-1}\right]\left(\frac{(n+1)(n+2)}{4}\right)^{1/2}\delta_{q,n+2}$$

$$+$$

$$\left.\frac{i}{\sqrt{2}}\left[(m+n+1)\frac{b_i R_m}{l_i R_i} + (p+q+1)\frac{b_o R_m}{l_o R_o}\right]\left[\left(\frac{m-1}{2}\right)^{1/2}\delta_{p,m-1} + \left(\frac{m+1}{2}\right)^{1/2}\delta_{p,m+1}\right]\delta_{q,n}\right\}.$$

R is diagonal to zeroth order. The lowest order correction couples m with $m\pm1$, $m\pm3$ in the X-direction and n with n, $n\pm2$ in the Y-direction. The reflection matrix is not symmetric, $R^{mn}_{pq} \neq R^{pq}_{mn}$. Also, it is not invariant to interchanging X and Y. This means that the modes $u_{mn}(x,y)$ and $u_{nm}(x,y)$ with $m \neq n$ are reflected differently.

## Appendix B. Computation of the First Matrix Elements in Laguerre Representation.

Representation using Gaussian-Laguerre modes may be advantageous in numerical simulations because fewer Laguerre modes than Hermite modes are required to represent close-to-axisymmetric radiation profiles with the same accuracy. However, the computation of Eqs. (33a) to (33e) is not so straightforward. The integrations (33a) and (33b) for $I^{pq}$ and $K^{pq}$ over the polar angle $\theta_s$ involve trigonometric functions of complicated arguments $\theta_i(\theta_s)$ and $\theta_o(\theta_s)$, given implicitly by Eq. (31b). There is no simple recurrence formula for this calculation. The first few elements are computed here by expansions in powers of $r_s/R_m < \zeta \sim \xi$. Substituting from (31b) inside (33) and renormalizing $r_s^2/2W_o^2 = X/(1-\sin^2\phi/2\sin^2\theta)$, one obtains, to first order in $\xi$,

$$D^{00}(X) = \int_o^{2\pi} d\theta \; \frac{1}{1-\sin^2\frac{\phi}{2}\sin^2\theta}, \tag{B0}$$

$$D^{10}(X) = -I^{01}(X) = \frac{1}{2\sqrt{2}}\,\xi\, X \tan\frac{\phi}{2} \int_o^{2\pi} d\theta \; \frac{\cos^2\theta}{\left(1-\sin^2\frac{\phi}{2}\sin^2\theta\right)^2}, \tag{B1}$$

$$D^{11}(X) = \int_o^{2\pi} d\theta \; \frac{\cos^2\theta}{\left(1-\sin^2\frac{\phi}{2}\sin^2\theta\right)^2}, \tag{B2}$$

$$D^{-1-1}(X) = \cos^2\frac{\phi}{2} \int_o^{2\pi} d\theta \; \frac{\sin^2\theta}{\left(1-\sin^2\frac{\phi}{2}\sin^2\theta\right)^2}, \tag{B3}$$

$$D^{-10}(X) = -D^{0-1}(X) = -\frac{1}{2\sqrt{2}}\,\xi\, X \tan\frac{\phi}{2} \int_o^{2\pi} d\theta \; \frac{\left(1-\cos^2\frac{\phi}{2}\tan^2\theta\right)\cos^2\theta}{\left(1-\sin^2\frac{\phi}{2}\sin^2\theta\right)^2}, \tag{B4}$$

$$D^{-11}(X) = D^{1-1}(X) = 0. \tag{B5}$$

We only need $E^{pq}$ to zeroth order in $\xi$, obtaining

$$E^{-10}(X) = -E^{0-1}(X) = \int_0^{2\pi} d\theta \frac{\cos\frac{\phi}{2}\sin^2\theta}{\left(1-\sin^2\frac{\phi}{2}\sin^2\theta\right)^{3/2}}, \tag{B6}$$

and

$$E^{pq} = 0 + O(\xi) \qquad \text{for } (p,q) \neq (-1,0), (0-1). \tag{B7}$$

The integrals (B1) - (B7) are evaluated using the formula

$$\int_0^{\pi/2} dx \frac{\sin^{\mu}x \cos^{\nu}x}{\left(1-k^2\sin^2x\right)^{\rho}} = \frac{1}{2} B\left(\frac{\mu+1}{2}, \frac{\nu+1}{2}\right) F\left(\rho, \frac{\mu+1}{2}, \frac{\mu+\nu+2}{2}, k^2\right), \tag{B8}$$

where $B(p,q) = \Gamma(p)\Gamma(q)/\Gamma(p+q)$, $\Gamma$ is the factorial function and F is the hypergeometric function. The radial integrations for U, V and W are performed directly, using the expressions $L_m^p(x)$ for the Laguerre functions and the identities

$$\int_0^{\infty} e^{-x} x^{-1/2} dx = \sqrt{\pi},$$

$$\int_0^{\infty} e^{-x} x^{n} dx = n!,$$

$$\int_0^{\infty} e^{-x} x^{n+1/2} dx = \frac{1}{2} \cdot \frac{3}{2} \ldots (n+1/2)\sqrt{\pi}. \tag{B9}$$

Again, we extend the limits of integration to infinity assuming $\rho \cos(\phi/2) >> W_i$ and $\alpha = 1$. The zeroth order contribution is given by

$$R_{00}^{00}(0) = 1,$$
$$R_{11}^{00}(0) = 1,$$

$$R^{-1-1}_{1\ 1}(0) = \cos^3 \frac{\phi}{2}\, F\left(2,\frac{3}{2},2,\sin^2 \frac{\phi}{2}\right),$$

$$R^{11}_{11}(0) = \cos \frac{\phi}{2}\, F\left(2,\frac{1}{2},2,\sin^2 \frac{\phi}{2}\right),$$

$$R^{11}_{00}(0) = \cos \frac{\phi}{2}\, F\left(2,\frac{1}{2},2,\sin^2 \frac{\phi}{2}\right),$$

$$R^{-1-1}_{0\ 0}(0) = \cos^2 \frac{\phi}{2}\, F\left(2,\frac{3}{2},2,\sin^2 \frac{\phi}{2}\right). \qquad \text{(B10)}$$

The first order corrections in $\xi$ are given by

$$R^{10}_{00}(1) = -R^{01}_{00}(1) = \left(\frac{\pi}{2}\right)^{1/2} \frac{3}{8} \sin \frac{\phi}{2}\, F\left(2,\frac{1}{2},2,\ \sin^2 \frac{\phi}{2}\right),$$

$$R^{10}_{01}(1) = -R^{01}_{10}(1) = \left(\frac{\pi}{2}\right)^{1/2} \frac{9}{16} \sin \frac{\phi}{2}\, F\left(2,\frac{1}{2},2,\ \sin^2 \frac{\phi}{2}\right),$$

$$R^{00}_{01}(1) = R^{00}_{10}(1) = 0,$$

$$R^{10}_{10}(1) = -R^{01}_{01}(1) = \left(\frac{\pi}{2}\right) \quad \frac{3^{1/2}}{16} \sin \frac{\phi}{2}\, F\left(2,\frac{1}{2},2,\ \sin^2 \frac{\phi}{2}\right),$$

$$R^{10}_{11}(1) = -R^{01}_{11}(1) = -\left(\frac{\pi}{2}\right)^{1/2} \frac{39}{32} \sin \frac{\phi}{2}\, F\left(2,\frac{1}{2},2,\ \sin^2 \frac{\phi}{2}\right), \qquad \text{(B11)}$$

and

$$R^{-10}_{00}(1) = \sin \frac{\phi}{2} \left\{ \pm \left[ \left(\frac{\pi}{2}\right)^{1/2} \frac{3}{8}\, F\left(2,\frac{1}{2},2,\ \sin^2 \frac{\phi}{2}\right) - \cos^2 \frac{\phi}{2}\, F\left(2,\frac{3}{2},2,\ \sin^2 \frac{\phi}{2}\right) \right] \right.$$

$$\left. \pm \frac{1}{2} \cos^2 \frac{\phi}{2}\, F\left(\frac{3}{2},\frac{3}{2},2,\ \sin^2 \frac{\phi}{2}\right) \begin{bmatrix} -4.5 & + i2^{-1/2} \\ -3.5 & + i2^{-1/2} \end{bmatrix} \right\},$$

$$R^{-10}_{01}(1) = \sin \frac{\phi}{2} \left\{ \pm \left[ \left(\frac{\pi}{2}\right)^{1/2} \frac{9}{16}\, F\left(2,\frac{1}{2},2,\ \sin^2 \frac{\phi}{2}\right) - \cos^2 \frac{\phi}{2}\, F\left(2,\frac{3}{2},2,\ \sin^2 \frac{\phi}{2}\right) \right] \right.$$

$$\left. \pm \frac{1}{2} \cos^2 \frac{\phi}{2}\, F\left(\frac{3}{2},\frac{3}{2},2,\ \sin^2 \frac{\phi}{2}\right) \left[2 - i\ 2^{-1/2}\right] \right\},$$

$$R^{-10}_{11}(1) = \sin\frac{\phi}{2}\left\{ \pm \left[\left(\frac{\pi}{2}\right)^{1/2} \frac{39}{32} F\left(2,\frac{1}{2},2,\ \sin^2\frac{\phi}{2}\right) - \cos^2\frac{\phi}{2} F\left(2,\frac{3}{2},2,\ \sin^2\frac{\phi}{2}\right)\right],\right.$$

$$\left. \pm \frac{1}{2}\cos^2\frac{\phi}{2} F\left(\frac{3}{2},\frac{3}{2},2,\ \sin^2\frac{\phi}{2}\right)\begin{bmatrix}4.5 + i2^{-1/2}\\ 3.5 + i2^{-1/2}\end{bmatrix}\right\}. \qquad \text{(B12)}$$

The (-) sign and the lowest row inside the last square bracket in (B12) correspond to exchanging indices,

$$R^{pq}_{mn} \leftrightarrow R^{qp}_{nm}.$$

Note also that the elements $R^{1-1}_{m\ n}$, $R^{-11}_{mn}$, coupling sine and cosine modes, are of order $\xi^2$ or higher for every m, n,

$$R^{-1\ 1}_{m\ n} \sim O(\xi^2). \qquad \text{(B13)}$$

Appendix C. Computation of the Cross-Polarization Matrix Elements

We compute here some of the first order cross-polarization matrix elements in case of large mirror size $\rho >> W_i$ and $\alpha \to 1$. In the Gaussian-Hermite representation we find from (44b), using the notation of Appendix A,

$$G_{pq}^{mn} = 2^m m!\ \sqrt{\pi}\ \langle Y \rangle_{q,n} \delta_{p,m}$$

$$= \pi\ 2^m m!\ \left\{ 2^{n-1} n!\ \delta_{q,n-1} + 2^n\ (n+1)!\ \delta_{q,n+1} \right\} \delta_{p,m}, \qquad (C1)$$

yielding

$$Q_{pq}^{mn}\ (1) = \xi \sin \frac{\phi}{2} \left\{ \sqrt{n}\ \delta_{q,n-1} + \sqrt{n+1}\ \delta_{q,n+1} \right\} \delta_{p,m}. \qquad (C2)$$

In Gaussian-Laguerre representation we only have to compute $B^{pq}(X)$, Eq. (45c), to zeroth order in $\xi$. Applying the methods of Appendix B, we find

$$B^{pq} = O(\xi), \text{ if } p,q \neq (1,0), (0,1),$$

$$B^{10} = B^{01} = \int_0^{2\pi} \frac{d\theta \cos^2\theta}{\left(1 - \sin^2 \frac{\phi}{2} \sin^2\theta\right)^{3/2}}. \qquad (C3)$$

Noting that $G_{mn}(X)$ is the same as $W_{mn}^{pq}(X)$, Eq. (33e), and inserting (C3) and (33e) inside (45a), we obtain

$$Q_{10}^{10}\ (1) = Q_{01}^{01}\ (1) = 0,$$

$$Q_{00}^{10}\ (1) = Q_{00}^{01}\ (1) = \xi \sin \frac{\phi}{2}\ F\left(\frac{3}{2},\ \frac{1}{2},\ 2,\ \sin^2 \frac{\phi}{2}\right),$$

$$Q_{01}^{10}(1) = Q_{10}^{01}(1) = -\xi \sin \frac{\phi}{2}\ F\left(\frac{3}{2},\ \frac{1}{2},\ 2,\ \sin^2 \frac{\phi}{2}\right),$$

$$Q_{11}^{10}\ (1) = Q_{11}^{01}\ (1) = \sqrt{2}\ \xi \sin \frac{\phi}{2}\ F\left(\frac{3}{2},\ \frac{1}{2},\ 2,\ \sin^2 \frac{\phi}{2}\right). \qquad (C4)$$

## Appendix D. Small Aperture Limit

We have seen in Sec. V that in case of mirror surface $S_1$ with an aperture of area $S_2$ the reflection matrix is given by

$$R(S;W_o) = R(S_1;W_o) - R(S_2;W_o) \tag{D1}$$

In case that $S_2 << S_1$ the spot size $W_o$ optimizing the representation for the scattered radiation will be determined predominantly by the surface $S_1$. Thus, the formula (23) with $W_o$ given from

$$\frac{\partial R(S_1;\alpha)}{\partial \alpha} = 0, \tag{D2}$$

can be used for the modal decomposition of the scattered radiation. According to Eqs. (28a) and (29a) for the Hermite representation, and Eqs. (32a) and (33c) for the Laguerre representation, the lowest order contribution from a small aperture $\rho_2 << W_o$ scales as $R(S_2;W_o) \sim \xi^2$.

In some cases, however, it is important to know the <u>total</u> radiation diffracted through a small hole, rather than the modal decomposition. In case of small apperture $\rho_2$,

$$\rho_2^2 << l_o k^{-1} \quad \text{or} \quad \lambda >> \rho_2^2/l_o, \tag{D3}$$

where $l_o \sim z$ is the distance of the observation point from the mirror, the paraxial approximation, Eq. (8b) is taken one step further, setting

$$\frac{k}{z-z_o}\left[\left(x-x_o\right)^2 + \left(y-y_o\right)^2\right] \simeq \frac{k}{z-z_o}\left[\left(x^2+y^2\right) - 2xx_o - 2yy_o\right]. \tag{D4}$$

Substituting (D4) inside (8a) we obtain the "far field" limit of the diffracted radiation

$$A^o(x,y,z=0) = \frac{ik}{2\pi z_o}\int dx_o \int dy_o A^i(x_o,y_o)(\hat{n}\cdot\delta\hat{r})$$

$$\exp\left\{-\frac{ik}{2z_o}\left[\left(x^2+y^2\right) - 2xx_o - 2yy_o\right]\right\}, \qquad (D5)$$

also known as Fraunhoffer diffraction. The condition (D3) can only be valid for appertures much smaller than the spot size $W_o$ at the mirror, $\rho_2 << W_o$, since for $\rho_2 \sim W_o$ (D3) is violated, $k\rho_2^2 \sim kW_o^2 \sim kw_o^2\,(1+l_o^2/b_o^2) \sim b_o(1+l_o^2/b_o^2) > l_o$. Neglecting terms of order $kx_m^2/l_o \sim k\rho_2^2/l_o << 1$ means that terms of order $x_s/l_m$, $x_s/l_o << 1/kx_s$, where $kx_s > 1$, must also be neglected. The source term can be written as $A^i[x_i,y_i] \simeq A^i[x_s,y_s]$. Rescaling variables to

$$K_x = \cos\frac{\phi}{2}\,\frac{kx}{l_o}, \qquad K_y = \frac{ky}{l_o} \qquad (D6)$$

we obtain

$$A^o(x,y,0) = e^{i\left(pq_o + k\frac{x^2+y^2}{l_o}\right)} \cos\frac{\phi}{2}\,\frac{ik}{2\pi l_o}\int dx_s\int dy_s A^i(x_s,y_s)\, e^{iK_x x_s + iK_y y_s}. \qquad (D7)$$

According to (D7) the outgoing radiation is the Fourier transform of the incoming radiation in respect to $K_x$, $K_y$. Defining the "polar" coordinates $K = (K_x^2+K_y^2)^{1/2}$, $\Theta = \tan^{-1}(K_x/K_y)$, we obtain, for $A^i(x_s,y_s)$ $= \sum_{k,l} c^i_{pq}\, u_{pq}(x_s,y_s)$, the scattered radiation

$$A^o(x,y,0) = \sum_{p,q} c^i_{pq}\,\frac{ika_{pq}}{2\pi l_o}\, e^{ik\left(l_o + \frac{x^2+y^2}{2l_o}\right)} \quad X$$

$$\cos\frac{\phi}{2}\int dx_s\int dy_s\; H_p\left[\sqrt{2}\,\frac{x_s}{W_i}\cos\frac{\phi}{2}\right]H_q\left[\sqrt{2}\,\frac{y_s}{W_i}\right]e^{-\frac{x_s^2\cos^2\frac{\phi}{2}+y_s^2}{W_i^2}}$$

$$\sum_{m=-\infty}^{\infty}\sum_{n=-\infty}^{\infty}J_n(Kx_s)\,J_m(Ky_s)\,e^{i(m-n)\theta}\,i^{m+n}\,e^{in\frac{\pi}{2}}. \qquad (D8)$$

The zeroth order contribution in $x_s/W_i << 1$ yields

$$A^o(x,y,0) \simeq c_{oo}^i\,\frac{ika_{oo}}{2\pi l_o}\,e^{ik\left(l_o+\frac{x^2+y^2}{2l_o}\right)}$$

$$X\cos\frac{\phi}{2}\int dx_s\int dy_s\; J_o(Kx_s)\,J_o(Ky_s)e^{-\frac{x_s^2\cos^2\frac{\phi}{2}+y_s^2}{W_i^2}}. \qquad (D9)$$

The waist size $w_f$ for the Fraunhoffer modes is given by the zeros of the Bessel functions

$$K(w_f)\,x_s \sim \frac{kw_f}{l_o}\,\rho_2 \sim 2\pi. \qquad (D10)$$

Therefore, the diffraction angle $\theta_f$ is

$$\theta_f \simeq \frac{w_f}{l_o} \sim \frac{\lambda}{\rho_2}. \qquad (D11)$$

The requirement $\theta_f << 1$ for the validity of the paraxial approximation puts a lower limit in the aperture size $\rho_2$

$$\rho_2 >> \lambda. \qquad (D12)$$

In case the aperture size is of the order of the wavelength $\lambda$ the scattered wavefunctions are spherical rather than Gaussian. Because the overall effect of a scatterer with size $\rho_2 \sim \lambda$ is very small, the familiar from quantum mechanics Born approximation, involving perturbation theory, is applicable in that case.


## Acknowledgements

This work was supported by the Strategic Defense Initiative Organization and managed by the U. S. Army Strategic Defense Command.

## References


1. L. R. Elias, W. M. Fairbanks. J. M. J. Madey, H. A. Schwettman and T. I. Smith, Phys. Rev. Lett. 36, 717 (1976).
2. T. I. Smith, H. A. Schwettman, R. Rohatgi, Y. Lapierre and J. Edighoffer in Proceedings of the Eighth International FEL Conference, Glasgow, Scotland, edited by M. Poole (North Holland, Amsterdam, 1987), p. 1.
3. R. W. Warren, D. W. Feldman, B. E. Newnam, S. C. Bender, W. E. Stein, A. H. Lumpkin, R. A. Lohsen, J. G Goldstein, B. D. McVey and K. C. D. Chan, in Proceedings of the Eighth International FEL Conference, Glasgow, Scotland, edited by M. Poole (North Holland, Amsterdam, 1987), p. 8.
4. K. E. Robinson, T. L. Churchill, D. C. Quimby, D. M. Shemwell, J. M. Slater, A. S. Valla, A. A. Vetter, J. Adamski, T. Doering, W. Gallagher, R. Kennedy, B. Robinson, D. Shoffstall, E. Tyson, A. Vetter and A. Yeremian in Proceedings of the Eighth International FEL Conference, Glasgow, Scotland, edited by M. Poole (North Holland, Amsterdam, 1987), p. 49.
5. M. Billardon, P. Elleaume, J. M. Ortega, C. Bazin, M. Bergher, M. E. Couprie, Y. Lapierre, Y. Petroff, P. Prazeres and M. Velghe, in Proceedings of the Eighth International FEL Conference, Glasgow, Scotland, edited by M. Poole (North Holland, Amsterdam, 1987), p. 72.
6. T. Masud, T. C. Marshall, S. P. Schlesinger and F. G. Yee, Phys. Rev. Lett. 56, 1567 (1986).
7. X. K. Maruyama, S. Penner, C. M. Tang and P. Sprangle, in Proceedings of the Eighth International FEL Conference, Glasgow, Scotland, edited by M. Poole (North Holland, Amsterdam, 1987), p. 259.

8. S. Solimeno and A. Torre, Nucl. Instr. and Methods A237, 404 (1985).

9. J. A. Murphy, Intl. J. Infrared and Millimeter Waves 8, 1165 (1987).

10. See, for example, H. A. Hauss in Waves and Fields in Optoelectronics, (Prentice Hall, New Jersey, 1984), p. 180, and references therein.

11. P. Sprangle, A. Ting and C. M. Tang, Phys. Rev. Lett. 59, 202 (1987).

12. P. Sprangle, A. Ting and C. M. Tang, Phys. Rev. A36, 2773 (1987).

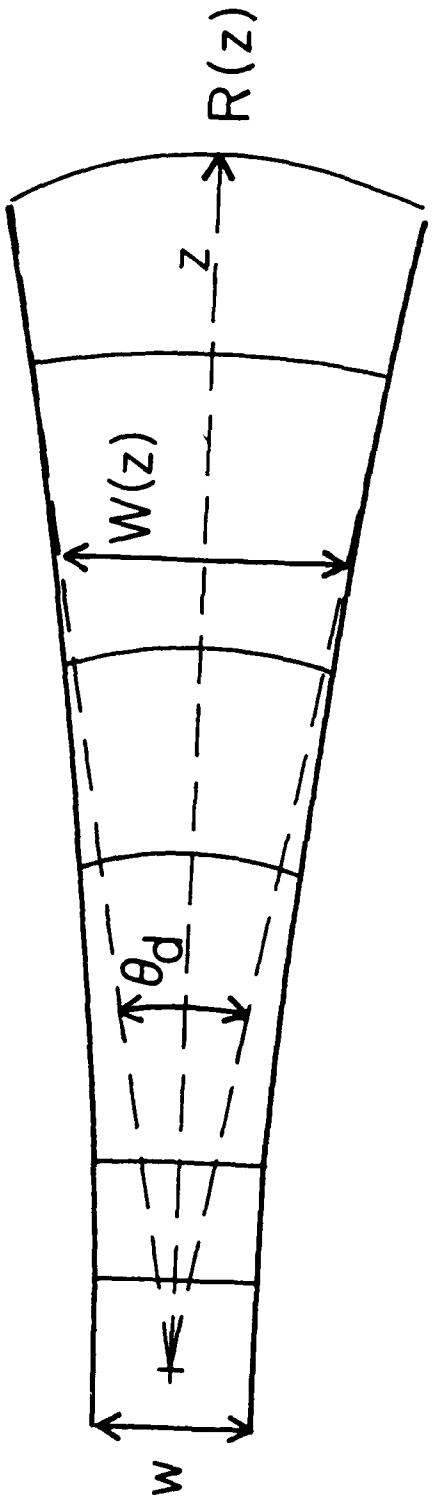



Figure 1 Schematic illustration of the radiation envelope for a Gaussian eigenmode.

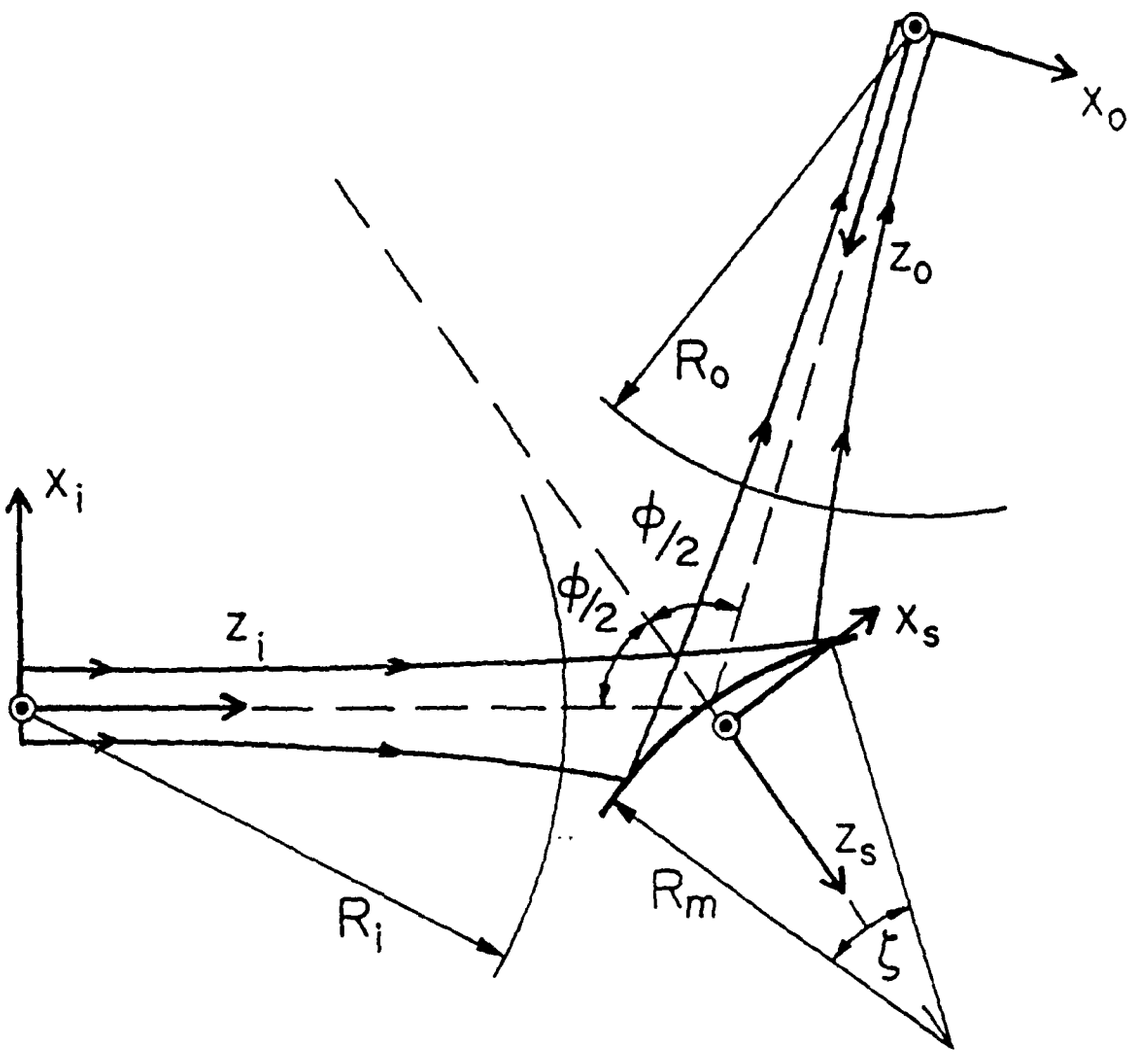



Figure 2 Reflection geometry.

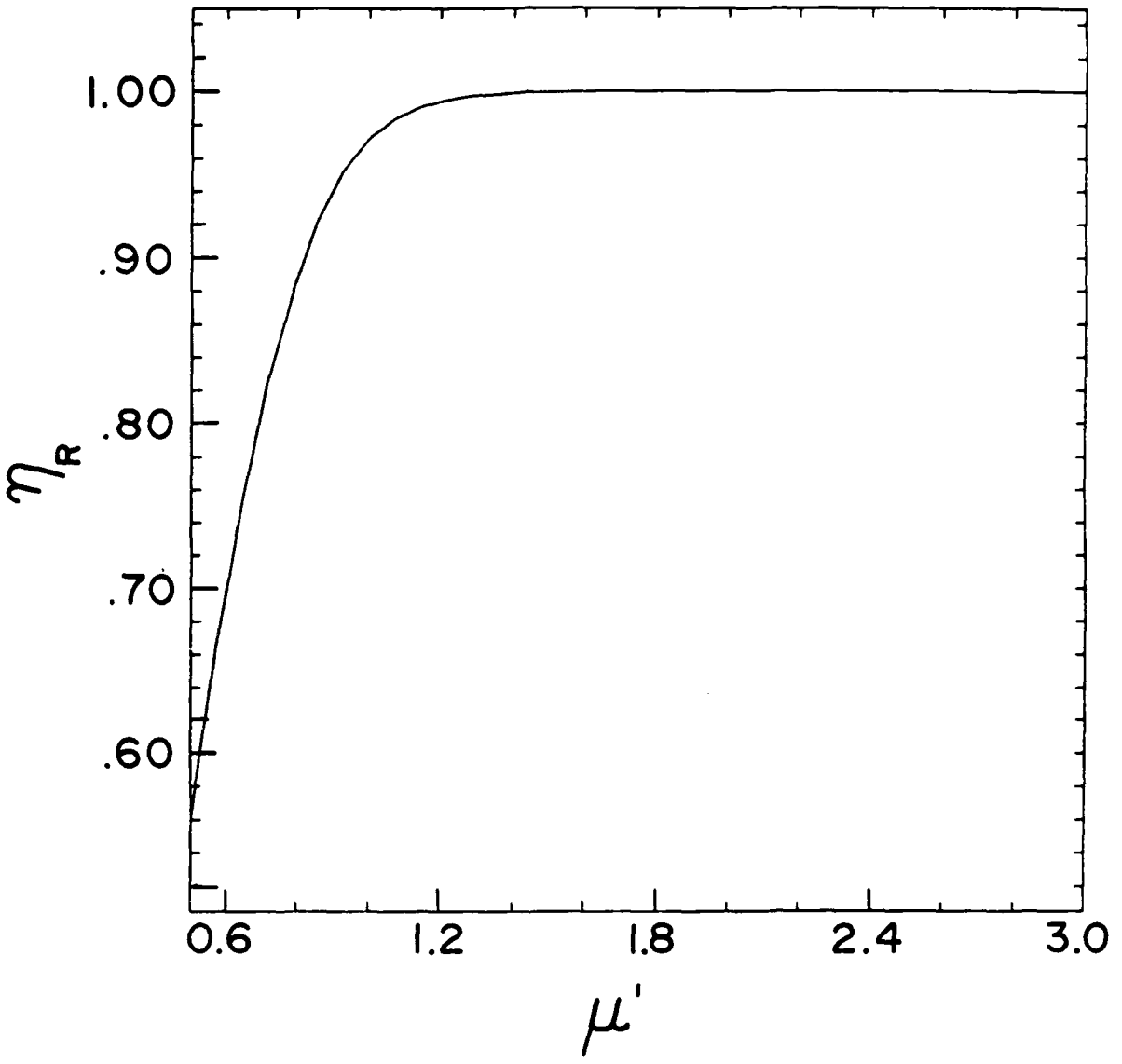



Figure 3 Plot of the total reflection coefficient $\eta_R$ for the lowest order mode as a function of the mirror size $\mu'$ for $\phi = 90°$. The radiation has wavelength $\lambda = 10^{-4}$cm, waist $w_i = 2\times10^{-1}$cm at distance $l_i = 1.8\times10^{2}$cm from the mirror and radius of curvature $R_i = R_m = 8.95\times10^{3}$cm.

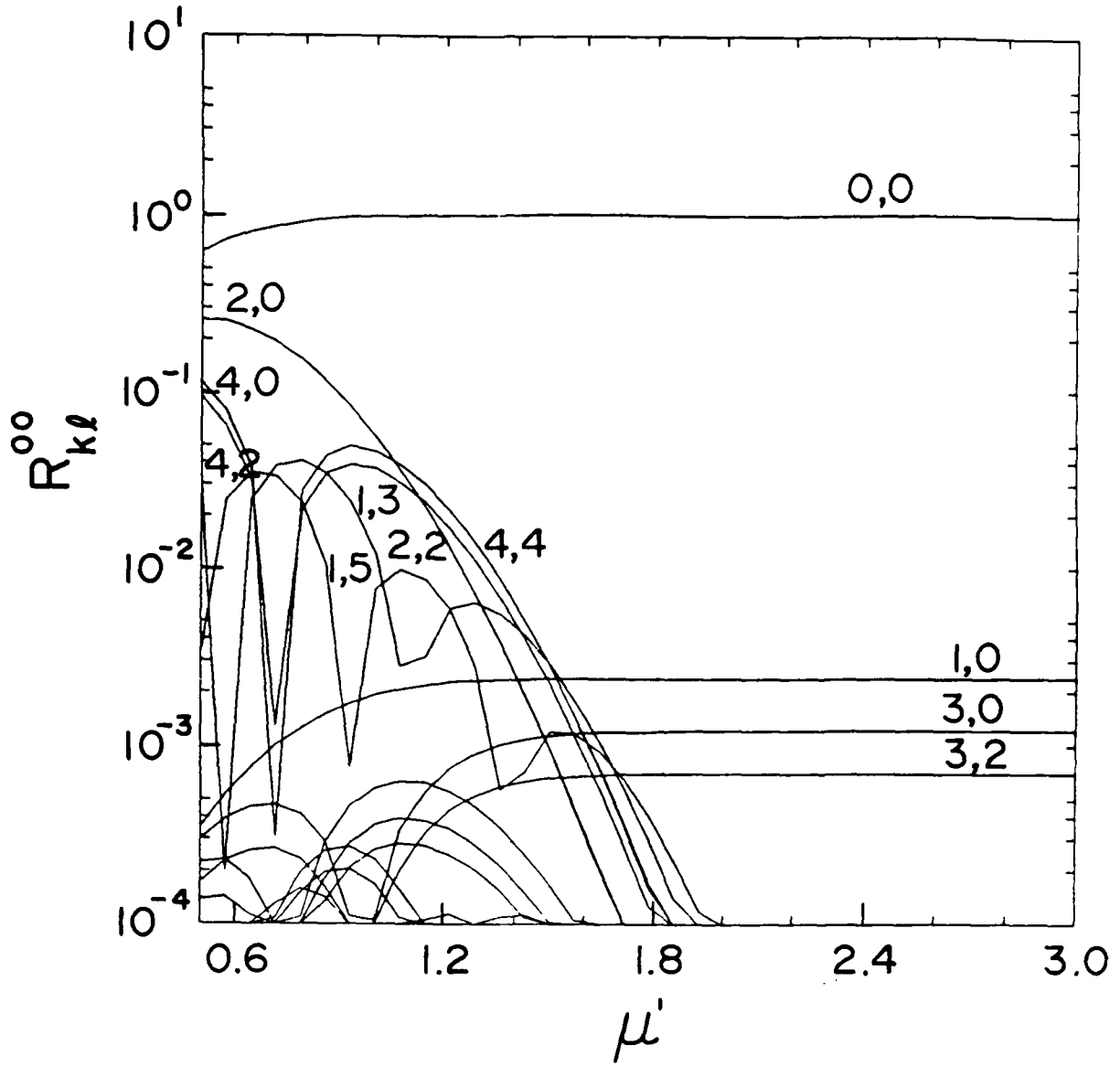



Figure 4 Reflection matrix elements for the lowest order mode (0,0) into the first 25 modes (p,q) against the relative mirror size $\mu'$. The magnitude $|R^{00}_{pq}|$ is plotted for angle of deflection $\phi = 90°$, $\alpha = 1$ ($W_i = W_o$).

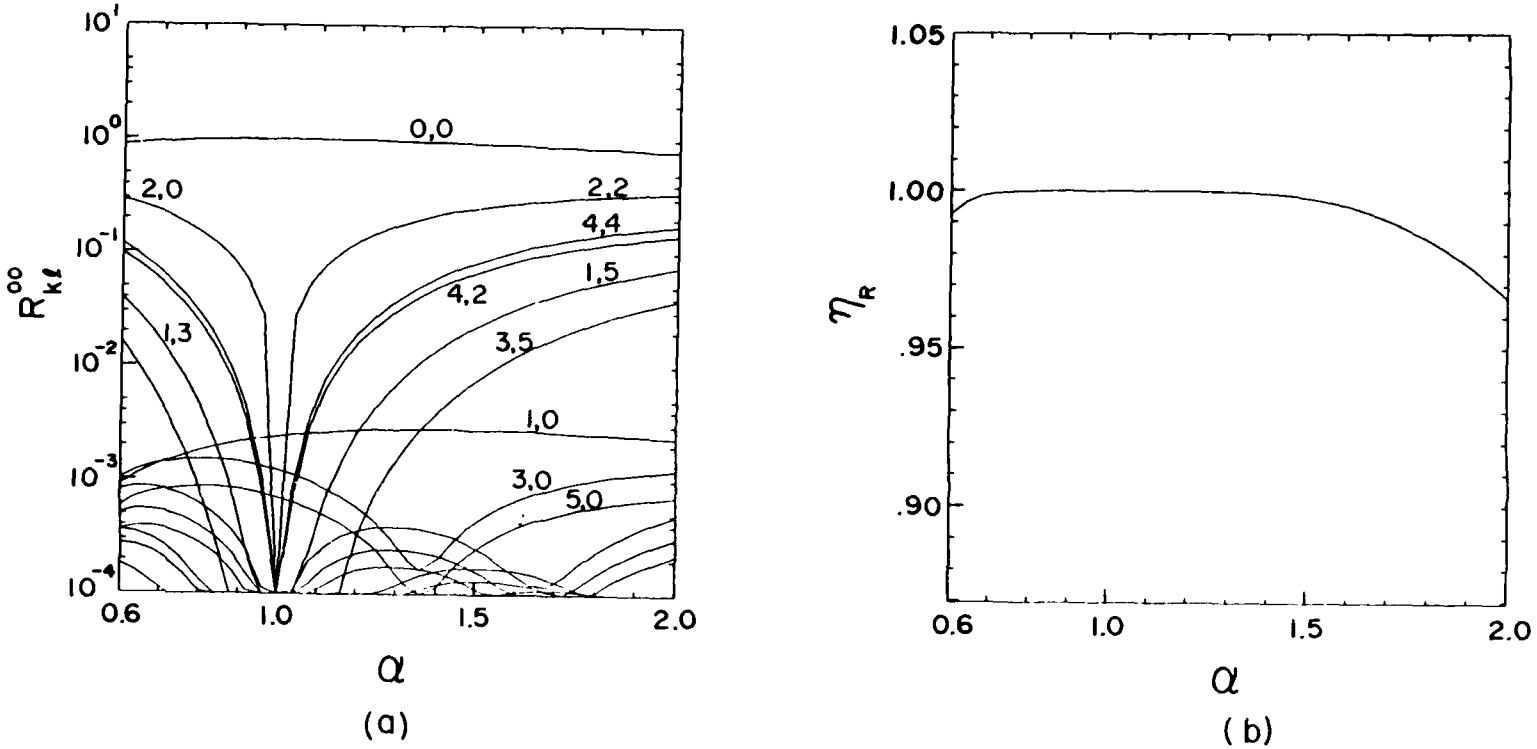



Figure 5 Plots of the reflection matrix elements $|R^{00}_{pq}|$ against the spot size ratio $\alpha$ for $\mu' = 2$ and $\phi = 90°$. Radiation parameters are the same as in Fig. 3.

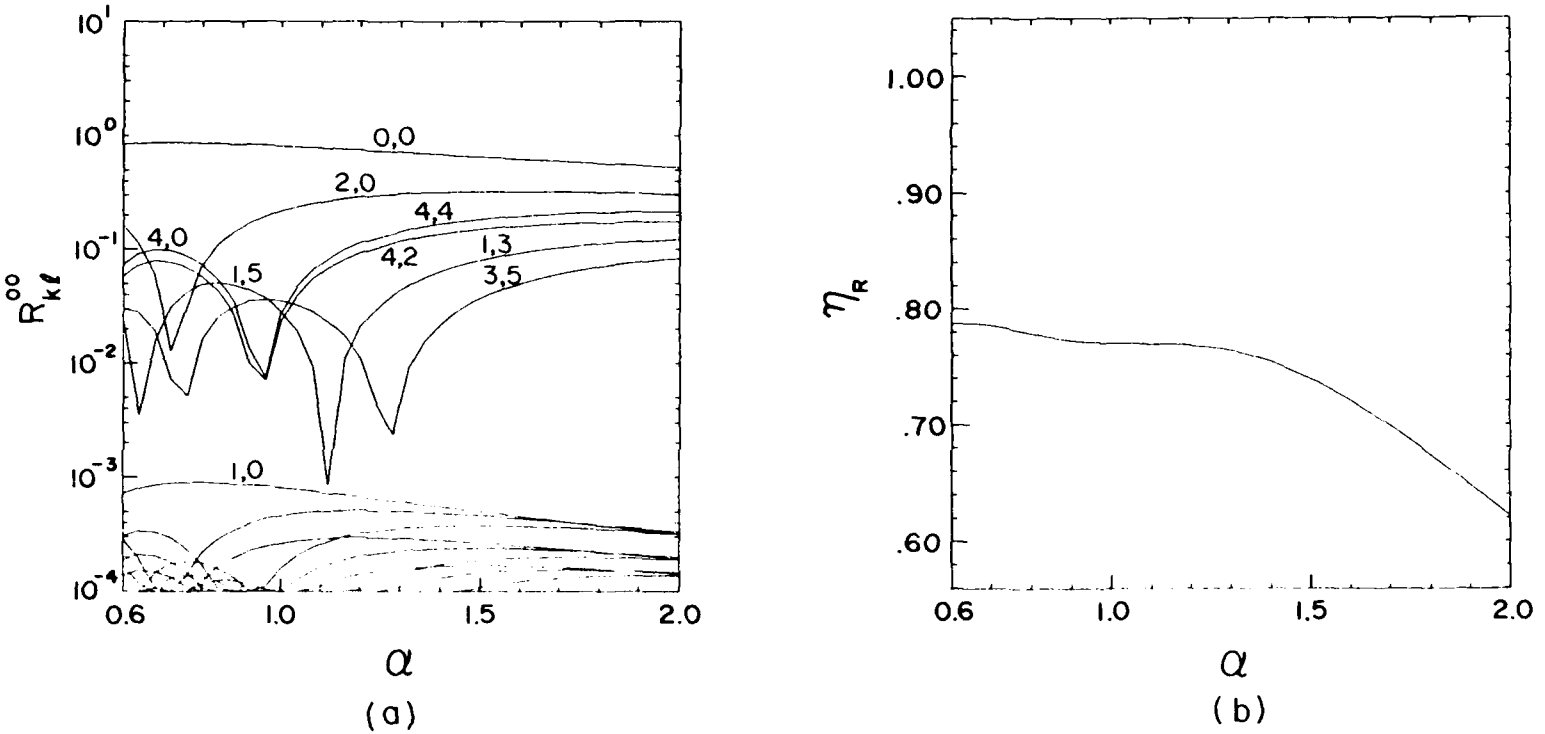



*Figure 6 Same as in Fig. 5 for* $\mu' = 0.66$.

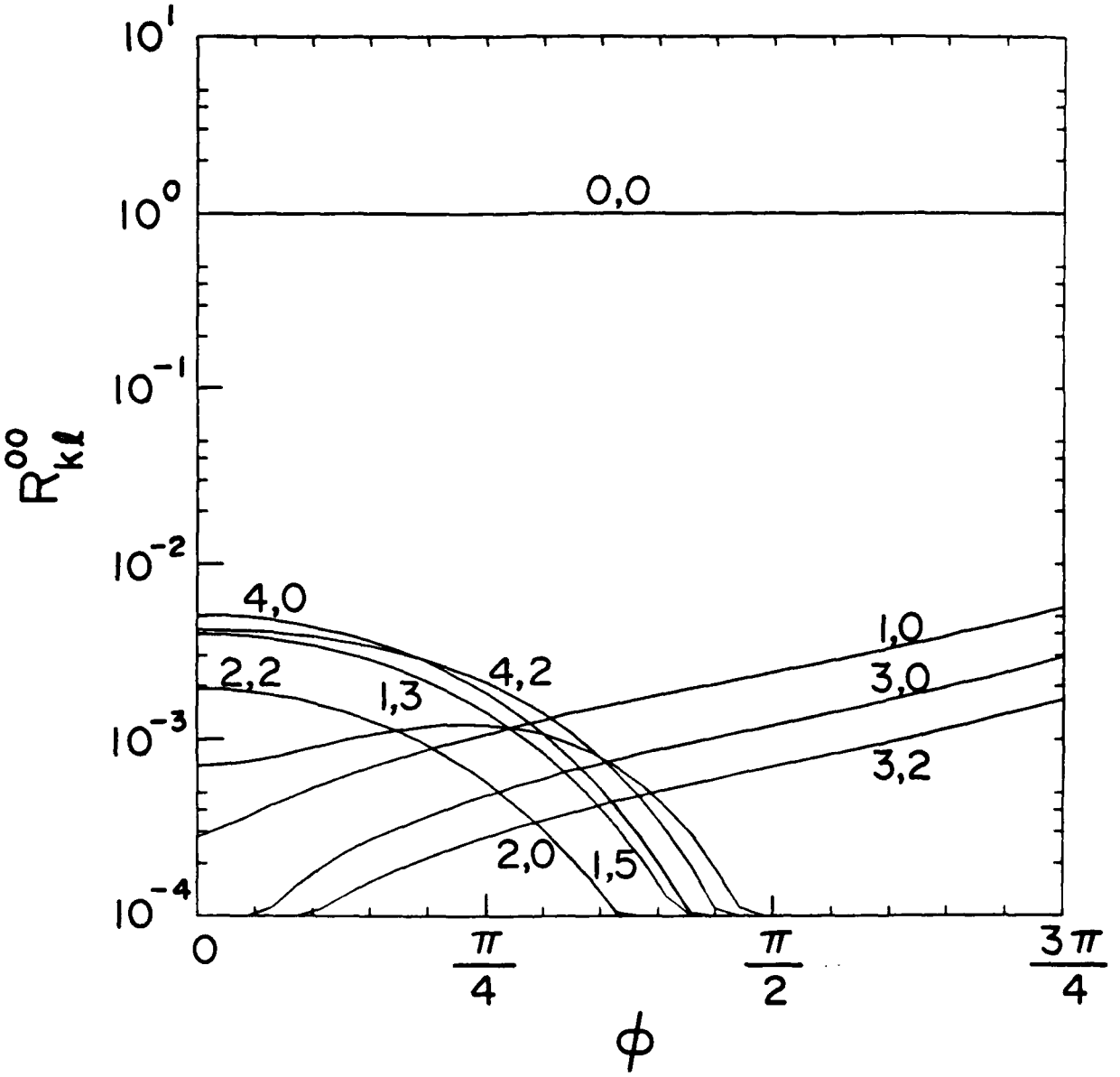



Figure 7 Plots of the reflection matrix elements $|R^{00}_{pq}|$ against the angle of deflection $\phi$ for $\mu' = 2$ and $\alpha = 1$.

# APPENDIX MM

## Reflection Matrix for Optical Resonators in FEL Oscillators

**Naval Research Laboratory**
Washington, DC 20375-5000

NRL Memorandum Report 6285

# Reflection Matrix for Optical Resonators in FEL Oscillators

S. RIYOPOULOS

*Science Applications Intl. Corp.*
*McLean, VA 22102*

P. SPRANGLE AND C. M. TANG

*Plasma Theory Branch*
*Plasma Physics Division*

A. TING

*Berkeley Research Assoc.*
*Springfield, VA 22150*

September 22, 1988

Approved for public release; distribution unlimited.

## CONTENTS


I. INTRODUCTION ..... 1

II. OUTLINE OF THE METHOD ..... 4

III. COMPUTATION OF THE REFLECTION MATRIX ..... 10

IV. LIMITING CASES ..... 12

V. REFLECTION OF THE LOWEST ORDER MODE ..... 14

ACKNOWLEDGEMENT ..... 16

REFERENCES ..... 17

DISTRIBUTION LIST ..... 26

# REFLECTION MATRIX FOR OPTICAL RESONATORS IN FEL OSCILLATORS

## I. INTRODUCTION

Free Electron Lasers (FEL) operating as oscillators[1-7] require the trapping of light pulses between systems of mirrors (resonators).[8-10] These pulses are repeatedly amplified via synchronous interaction with electron pulses passing through the wiggler. The simplest oscillator configuration is that of an open resonator with two opposed identical mirrors. The radiation vector potential for this arrangement is expressed in terms of the free space eigenmodes $A_{mn}(r) = A_{mn}(r)e_{mn}$ of the paraxial wave equation[11], where $e_{mn}$ is the polarization vector and

$$A_{mn}(r) = \frac{u_{mn}(r;W)}{\left(1 + \frac{z^2}{b^2}\right)^{1/2}} e^{i\left[kz + \frac{k(x^2 + y^2)}{2R(z)}\right]} e^{i\delta_{mn}(z)} \quad . \qquad (1)$$

The exponent $\Phi(r) \equiv k[z + (x^2+y^2)/2R(z)]$ in (1) contains the rapidly varying phase on the wavelength scale $\lambda = 2\pi/k$. The constant phase wavefronts are spherical of curvature $1/R(z) = z/(z^2 + b^2)$. The spot size of the radiation envelope is $W(z) = w\,(1 + z^2/b^2)^{1/2}$, where $w = (2b/k)^{1/2}$ is the waist, and the distance z is measured from the position of the waist. The amplitude squared of the mode drops by 1/2 over a distance equal to the Rayleigh length b (also known as confocal parameter). Most of the radiation is confined within a cone parametrized by the diffraction angle $\theta_d = W/z \simeq (\lambda/b\pi)^{1/2}$. The amplitude profile $u_{mn}(r;W)$ contains the transverse spatial variation, equivalent to a small $k_\perp$, perpendicular to the z-direction. Higher modes correspond to a larger effective $k_\perp$, responsible for the phase shift $\exp[i\delta_{mn}(z)]$. For a given k the mode is completely defined by the two independent parameters R and w (or any combination of two out of the four quantities R, w, z and b).

The functions $u_{mn}(r;W)$ depend on the elected coordinate system. In

Manuscript approved June 14, 1988.

rectangular coordinates (x,y,z) they are given by

$$u_{mn}(x,y;W) = a_{mn} H_m\left(\frac{\sqrt{2}x}{W}\right) H_n\left(\frac{\sqrt{2}y}{W}\right) e^{-\frac{x^2+y^2}{W^2}} , \qquad (2)$$

where $H_m$, $H_n$ are the Hermite polynomials, $a_{mn} = (2/W^2)^{1/2}(\pi\, 2^{m+n}\, m!\, n!)^{-1/2}$ is the normalization factor, setting the total electromagnetic flux carried by the mode equal to unity, and $\delta_{mn}(z) = (m + n + 1)\tan^{-1}(z/b)$ is the slow phase. In cylindrical coordinates $(r,\theta,z)$, where $\tan\theta = x/y$, $r = (x^2+y^2)^{1/2}$, $u_m^p(r,\theta;W)$ take the form

$$u_m^{\pm p}(r,\theta;W) = a_m^p \begin{pmatrix}\cos p\theta \\ \sin p\theta\end{pmatrix} \left(\frac{\sqrt{2}r}{W}\right)^p L_m^p\left(\frac{2r^2}{W^2}\right) e^{-\frac{1}{2}\frac{2r^2}{W^2}} , \qquad (3)$$

where +p (-p) signifies cosine (sine) poloidal dependence, $L_m^p$ are the Laguerre polynomials, $a_m^p = (1/2\pi W^2)^{1/2}\,[m!/(m + p)!]^{-1/2}$ and $\delta_m^p(z) = (2m + p + 1)\tan^{-1}(z/b)$.

The electron beam is an optically active medium that alters the characteristic parameters of the radiation after each passage. During the build-up period the modal content and the structure of the light pulses inside the oscillator will change. A numerical method has been developed recently optimizing the representation for the amplified radiation. In the source dependent expansion[12,13] the waist size and the curvature of the elected modal basis is tailored according to the driving source term. That minimizes the number of modes required to describe the light beam. In general, the curvature and waist size of these modes does not match the curvature and waist of the vacuum eigenmodes for the resonator. Therefore the transfer matrix for a given mirror must be known for arbitrary incoming modes. This need stems from computational as well as physical reasons. The knowledge of the cavity reflection matrix R, together with the gain

matrix G through the wiggler, is necessary in determining the potential for steady state operation.

During high power operation, grazing mirror incidence may be necessary to avoid exceeding the dielectric breakdown limit for the reflection surface. Also, in case of a high per-pass gain with optical guiding, the waist for the reflected radiation would be much larger than the incoming. In two-mirror resonators the reflected radiation could hit the wiggler. Therefore, ring resonators, including three or more mirrors, must be employed for the deflection and recirculation of the light pulses. The study of the reflection matrix must be extended to include the effects of deflecting the light beam, in addition to finite mirror size and curvature mismatches.

The amplitude profile of the incoming radiation will be modified by reflection. A single incident mode $A_{mn}(r_i)$ will, in general, be partially reflected into different modes $A_{pq}(r_o)$ where $(m,n) \neq (p,q)$. This is caused by the deflection of the light beam, the finite size of the mirror and the curvature mismatches. Reflection into other modes will affect the interaction between the electron beam and the radiation in a number of ways. First the rms radius of the light beam will change, affecting the matching beam condition. Second, the light pulse will spread axially because of dispersion among different modes, since the phase velocity depends on the modal number (m,n). Third, different phase advances during reflection among the various modes may render these modes out of phase after a number of bouncings off the resonator. For the above reasons the fraction of radiation scattered into other modes will contribute to the losses in FEL oscillators.

## II. OUTLINE OF THE METHOD

The geometry of the reflection is illustrated in Fig. 1. The subscripts i and o denote the coordinate system used for expressing incoming and outgoing modes. $\mathbf{r}_i$ is defined with the $z_i$ axis along the direction of incidence and $\mathbf{r}_o$ has the $z_o$ axis along the direction of reflection. The origins are displaced from the mirror center by $l_i$ and $l_o$ respectively, where $l_i$ is the distance of the minimum waist $w_i$ for the incoming radiation and $l_o$ is the distance of the minimum waist $w_o$ for the reflected mode. A third coordinate system $\mathbf{r}_s$ with the origin at the mirror center and $\hat{z}_s$ aligned with the mirror axis will be useful in the computations. Underlined quantities $\underline{r}_i$, $\underline{r}_o$ and $\underline{r}_s$ stand for the mirror surface coordinates in each reference frame. The transformations among the various frames are defined by

$$x_i = x_s \cos\frac{\phi}{2} - z_s \sin\frac{\phi}{2}, \qquad x_o = x_s \cos\frac{\phi}{2} + z_s \sin\frac{\phi}{2},$$

$$y_i = y_s, \qquad (4a) \qquad y_o = y_s, \qquad (4b)$$

$$z_i = z_s \cos\frac{\phi}{2} + x_s \sin\frac{\phi}{2} + l_i, \qquad z_o = z_s \cos\frac{\phi}{2} - x_s \sin\frac{\phi}{2} + l_o.$$

We are interested in cases when the reflected radiation remains focused along some direction $z_o$ making an angle $\phi$ with the incoming $z_i$. Then the reflected vector potential will also be expandable in free space eigenmodes $A_{pq}(\mathbf{r}_o)$ of the paraxial equation in the new direction. The mirror surface generating focused reflection in the desired direction can not be arbitrary but must be appropriately defined. The angle of deflection $\phi$ will enter the equation defining the mirror surface. The other surface parameter, namely the curvature $1/R_m$, is a free parameter. It determines the curvature $1/R_o$ for the outgoing modes given the curvature $1/R_i$ of the incoming modes. In case of reflection by an arbitrary mirror

surface, the scattered radiation cannot, in general, be covered by the paraxial modes that do not form a complete set in three dimensions.

We consider incoming radiation of given curvature and of arbitrary amplitude profile $A^i(r_i)$, consisting of various modes (m,n) with the same $R_i(z)$. If both incident and reflected radiation are expanded into eigenmodes,

$$A^i(r_i) = \sum_{m,n} c^i{}_{mn}\, A_{mn}(r_i) \quad ,$$
$$A^o(r_o) = \sum_{p,q} c^o{}_{pq}\, A_{pq}(r_o) \quad , \tag{5}$$

the relation among the incident and reflected expansion coefficients $c^i{}_{mn}$, $c^o{}_{pq}$ is formulated by

$$c^o = R\, c^i \quad , \tag{6a}$$

or

$$c^o_{pq} = \sum_{m,n} R^{mn}_{pq}\, c^i{}_{mn} \quad , \tag{6b}$$

where $R^{mn}_{pq}$ are the elements of the reflection matrix R.

We examine the case when the mirror dimensions $\rho$ are much larger than the wavelength $\lambda$, $\lambda << \rho$ (otherwise diffraction rather than reflection would prevail). We also assume that the angle $\zeta$ subtended by the mirror $\zeta = \rho/R_m$, where $\kappa_m$ parametrizes the radius of curvature, is small, of the order of the diffraction angle $\theta_d$, $\zeta \sim \theta_d \sim \varepsilon$. The j-th component of the reflected vector potential at distance $|r_o - \underline{r}_o| >> \lambda$ from the mirror surface S is then given by

$$A^o{}_{(\nu)}(r_o) = -\frac{ik}{2\pi} \iint_S ds\, \frac{e^{ik|r_o - \underline{r}_o|}}{|r_o - \underline{r}_o|}\, A^s{}_{(\nu)}(\underline{r}_o)\, (\hat{n} \cdot \Delta\hat{r}). \tag{7}$$

In Eq. (7) $\hat{n}\cdot\Delta r$ is the obliqueness factor where $\Delta r = (\underline{r}_o-\underline{r}_{oo})/|\underline{r}_o-\underline{r}_{oo}|$ and n is the normal unit vector to the reflecting surface. The surface element ds is given by $ds = \delta[z_o-f(x_o,y_o)]dx_o dy_o dz_o$ where $z_o = f(x_o,y_o)$ is the surface equation. Equation (7) is the convolution of a source term $A^s(\underline{r}_o)$ at the mirror surface with the propagator $\exp(ik|\underline{r}_o-\underline{r}_{oo}|)/|\underline{r}_o-\underline{r}_{oo}|$, i.e., a superposition of spherical waves originating at S. The source term $A^s(\underline{r}_o)$ is specified from the incoming vector potential $A^i(\underline{r}_i)$ through the boundary conditions and the coordinate transformations (4). We will assume a perfectly conducting surface, where the incident and reflected fields are related by

$$A^s = -A^i + 2\,(\hat{n}\cdot A^i)\,\hat{n}\,, \qquad (8a)$$

and $\hat{n}$ is the normal unit vector to the reflecting surface. When the solid angle subtended by the mirror is small, the last term in (8a) is very small and the boundary condition becomes,

$$A^s_{(\nu)} = -A^i_{(\nu)}\,. \qquad (8b)$$

Relation (8b) corresponds to a phase shift by $\pi$ during reflection. It is independent of the wave polarization, thus the subscript $(\nu)$ is dropped. Cross polarization effects, due to the last term in (8a) are discussed in Ref. 10. Most of the computations will be performed on the mirror surface. To simplify the notation from now on, we drop the bar ($\underline{\ }$) under the mirror coordinates $\underline{r}$. Subscripted quantities such as $r_i$, $r_o$, $r_s$ will signify the mirror surface in each reference frame. Unsubscripted coordinates will denote the observation point in the reflected radiation frame of reference.

We seek cases when the reflected radiation propagates focused along $z_o$, contained within a cross section of dimensions $x,y \ll z-z_o$. The

expansion $|r-r_o| \simeq (z-z_o)\{1 + [(x-x_o)^2 + (y-y_o)^2]/2(z-z_o)^2\}$ replaces the full propagator inside (7) with the paraxial propagator $U_{-k}$ in that direction,

$$U_{-k}(r, r_o) = \frac{ik}{2\pi} \frac{e^{-ik(z-z_o)}}{z-z_o} e^{-ik \frac{(x-x_o)^2 + (y-y_o)^2}{2(z-z_o)}} . \quad (9)$$

It is known that the profile of a given eigenmode $A_{mn}(x_o,y_o,z_o)$ at $z_o$ is generated by the propagator $U_k(r,r_o)$ acting on the mode $A_{mn}(x,y,0)$ at $z=0$. The inverse propagator $U_{-k}(r,r_o)$ therefore reproduces $A_{mn}(x,y,0)$ from $A_{mn}(x_o,y_o,z_o)$. This suggests multiplying and dividing the integrand inside (7) by $\exp[i\Phi(r_o)] / [1 + z_o^2/b_o^2]^{1/2}$, recasting (7) in the form,

$$A^o(r) = \iint ds\, e^{i\Delta(r_o)} S(r_o)\, e^{i\Phi_o(r_o)}\, U_{-k}(r,r_o) , \quad (10)$$

where the source term $S(r_o)$ is,

$$S(r_o) = A^i[r_i(r_o)]\, (\hat{n} \cdot \Delta\hat{r}) \left[1 + \frac{z_o^2(r_o)}{b_o^2}\right]^{1/2} , \quad (11)$$

and the phase $\Delta(r_o)$ is given, in outgoing coordinates $r_o$, by

$$\Delta(r_o) = k \left[z_i(r_o) + z_o + \frac{x_i^2(r_o) + y_i^2(r_o)}{2R_i(r_o)} + \frac{x_o^2 + y_o^2}{2R_o(r_o)}\right]. \quad (12)$$

The expression for $\Delta(r_o)$ depends on the angle $\phi$ through the transformations between the incoming and the outgoing coordinates, Eqs. (4). Expression (10) is the approximation of the exact solution (7) to order

$[(x-x_o)^2 + (y-y_o)^2]/2(z-z_o)^2 \sim \varepsilon^2$. It is valid provided that the surface S produces focused reflection along the desired direction. Otherwise, the paraxial limit will fail to encompass all the radiation contained in the original expression (7).

The term $\exp[i\Delta(r_o)]$ is varying rapidly, on the scale of the wavelength $\lambda$. Therefore, its convolution with the slowly varying source term over an arbitrary surface will be vanishingly small. In general, this corresponds to radiation scattering where only a small fraction of the incoming radiation is reflected along the considered direction $\phi$. The integral (10) will be finite only when it is possible to satisfy the condition $\Delta(r_o)$ = constant over some surface S. If, in addition, S is much larger than $\lambda$, expression (10) will be finite only within a narrow angle $\delta\phi$ around $\phi$. This guarantees that the reflected radiation remains focused along that direction. Therefore, a condition that the exact reflected radiation (7) be fully covered by the paraxial limit (10) is that

$$\Delta(r_o) = \text{const.}, \tag{13}$$

along the surface S. Accordingly, the optical path is the same along the various rays connecting an incoming wavefront with its mirror image (reflected) wavefront.

Requirement (13) defines the appropriate mirror surface $z_o=f_o(x_o,y_o;\phi)$ for reflection in the elected direction. Expressing all quantities inside (13) in the mirror coordinate frame, applying the transformations (4) and using the scaling $x_s/R_m \sim y_s/R_m \sim \varepsilon \ll 1$, $z_s/R_m \sim \varepsilon^2$ we obtain from (13)

$$z_s = -\frac{1}{2R_m \cos\frac{\phi}{2}}\left[x_s^2 \cos^2\frac{\phi}{2} + y_s^2\right], \tag{14a}$$

where

$$\frac{1}{R_m} = \frac{1}{2R_o} + \frac{1}{2R_i}. \qquad (14b)$$

Equation (14a) is the analytic expression for a paraboloid surface. $R_m$ parametrizes the mirror curvature, being positive or negative for a convex or concave mirror respectively. The surface is reflection symmetric with $(zx)_s$ and $(zy)_s$ as the symmetry planes; there is no rotational symmetry around $z_s$. Surface (14a) can also be approximated, to second order in $(x_s/R_m)^2$, $(y_s/R_m)^2$ by hyperboloids or ellipsoids defined by

$$\left(z_s - R_m\cos\frac{\phi}{2}\right)^2 - x_s^2\cos^2\frac{\phi}{2} - y_s^2 = R_m^2\cos^2\frac{\phi}{2}, \qquad (15a)$$

$$\left(z_s + R_m\cos\frac{\phi}{2}\right)^2 + x_s^2\cos^2\frac{\phi}{2} + y_s^2 = R_m^2\cos^2\frac{\phi}{2}. \qquad (15b)$$

All the surfaces become spherical in the limit of perpendicular incidence $\phi = 0$, and plane mirrors when $R_m \to \infty$. Relation (14b) defines the curvature of the reflected modes from the incoming mode curvature and the curvature of the mirror.

Switching Eq. (12) into the mirror-aligned coordinates $r_s$ through Eqs. (4), and using the surface constraints (14), it follows that

$$\Delta(r_s) = \text{const.} + O\left[k\rho\left(\frac{\rho}{R_m}\right)^2\right],$$

where $\rho$ parametrizes the mirror size. A more complicated surface equation (higher than quadratic in x, y, z) is required to improve the constancy to a higher order. Since $k\rho \gg 1$, the approximation $\Delta(r_s) = \text{const.}$ is satisfactory for a first order expansion of the reflection matrix in powers of $\rho/R_m$, as long as $\rho/R_m \leq (k\rho)^{-1}$. In case $\rho/R_m > (k\rho)^{-1}$, the slow variation of $\Delta(x_s,y_s)$ over S must be included. That introduces an additional contribution in the reflection matrix, known as spherical aberation.

## III. COMPUTATION OF THE REFLECTION MATRIX

The reflected radiation is expressed by

$$A^{o}(r) = \int_{S}\int dx_o dy_o \; \sigma(x_o,y_o)\; e^{-i\Phi_o(x_o,y_o)}\; U_{-k}(r,r_o)\;, \qquad (16)$$

where $\sigma(x_o,y_o) \equiv S[x_o,y_o,z_o(x_o,y_o)]$. Expanding the source $\sigma(x_o,y_o)$ in terms of $u_{mn}(x_o,y_o)$,

$$\sigma(x_o,y_o) = \sum_{m,n} R^{mn}\; u_{mn}(x_o,y_o;W_o). \qquad (17)$$

and exploiting the property of the inverse propagator $U_{-k}$, the reflected vector potential $A^{o}(r)$ at $z = 0$ becomes

$$A^{o}(x,y,0) = \sum_{m,n} R^{mn}\; u_{mn}(x,y;W_o), \qquad (18)$$

where $W_o(z) = w_o\,(1 + z^2/b_o^2)^{1/2}$, $w_o = (2b_o/k)^{1/2}$. Expression (18) is a complete decomposition of the reflected radiation into paraxial eigenmodes for incident radiation of arbitrary profile.

According to the definition (6b), the $R^{mn}_{pq}$ element of the reflection matrix **R** is obtained from the source term $\sigma_{pq}(x_o,y_o)$ inside (16) generated by a single incident eigenmode $A_{pq}[r_i(r_o)]$. The integration is performed in the mirror-aligned coordinates, taking advantage of the existing symmetries. The coordinates $r_i$ and $r_o$, defining the incoming and outgoing wave functions, become explicit functions of $x_s$, $y_s$ through the transformations (4). The surface equation (14a) is used to express $z_s$ in terms of $(x_s,y_s)$. The mirror boundary

$$x_s^2 \cos^2 \frac{\phi}{2} + y_s^2 = \rho^2 \tag{19}$$

is defined by the intersection of the infinite surface (14a) with the plane $z_s = \text{const} = 2\rho^2 \cos^2(\phi/2)/R_m$. After the above manipulations the reflection matrix elements take the form

$$R_{pq}^{mn} = \iint_S dx_s dy_s \frac{\bar{u}_{mn}^{-}(x_s,y_s)\, \bar{u}_{pq}(x_s,y_s)}{\left[1 + \frac{l_o^2}{b_o^2}\right]^{1/2}} \left[\frac{1 + \frac{z_o^2(x_s,y_s)}{b_o^2}}{1 + \frac{z_i^2(x_s,y_s)}{b_i^2}}\right]^{1/2} e^{i\Delta(x_s,y_s)} \tag{20}$$

$$\times\, e^{i\delta_{pq}^{i}(x_s,y_s) - i\delta_{mn}^{o}(x_s,y_s)} \left[\cos\frac{\phi}{2}\left(1 - \frac{x_s}{R_m}\sin\frac{\phi}{2} - \frac{x_s^2 \sin^2\frac{\phi}{2}}{R_m^2}\right)\right],$$

where

$$\bar{u}_{mn}(x_s,y_s) \equiv u_{mn}\left[x_o(x_s,y_s),\, y_s\right], \qquad \bar{u}_{pq}(x_s,y_s) \equiv u_{pq}\left[x_i(x_s,y_s),\, y_s\right].$$

Expression (20) is correct to order $\rho^2/R_m^2$.

Each representation of R is tied to the choice of the basis functions $u_{mn}(r)$. In any case R, as given by (20), depends on four parameters[10]

$$R \equiv R(\phi,\, \alpha,\, \mu;\, \xi). \tag{21}$$

$\phi$ is the reflection angle shown in Fig. 1. $\alpha$ is the ratio of the incoming to the outgoing spot size at the mirror, $\alpha = W_i(l_i)/W_o(l_o)$. $\mu = \rho/W_o$ parametrizes the mirror size compared to the radiation spot size. $\xi = W_o/R_m$ scales as the diffraction angle $\theta_d \simeq W_o/l_o$ multiplied by the curvature mismatch $R_o/R_m$ between the mirror and the radiation wavefronts. The spot size $W_o$ enters as a free parameter because only the curvature $1/R_o$ for the reflected modes is specified by the mirror geometry. Since many

combinations of $W_o$ and $l_o$ apply to a given curvature according to paragraph Eq. (1), an additional selection rule for $W_o$ is needed. Note that $W_o$ does not have to match $W_i$. This is obvious in cases when the mirror size $\rho$ is smaller that $W_i$. Each value of $W_o$ defines a complete set of modes for the reflected radiation and an equivalent representation for R.

Parameters $\phi$, $\alpha$, and $\mu$ can be arbitrary. In most cases of interest, however, $\xi$ is small, $\xi << 1$, of the same order as the diffraction angle $\theta_d$. The analytic computation of the matrix elements is carried out by expanding the integral (20) in powers of $\xi$,

$$R = R(0) + \xi R(1) + \xi^2 R(2). \tag{22}$$

The first order expansion is performed in Ref. 10. In this paper we review some of the general properties of R and focus on the reflection of the lowest mode $u_{00}$.

## IV. LIMITING CASES

When the mirror radius tends to infinity ($1/R_m \to 0$), or in cases of vertical incidence on the mirror ($\phi = 0$), the higher order corrections in the reflection matrix R disappear,

$$R = R(0) \tag{23}$$

in both representations. The nondiagonal elements in R stem from the finite mirror size only. If, in addition, the mirror size is very large, $\mu >> 1$, it is appropriate to take $W_o = W_i$ as best representation for the reflected radiation. The $\alpha = 1$ limit yields

$$R^{mn}_{pq} = \delta^{mn}_{pq} . \tag{24}$$

Thus, in case of large curved mirror and vertical incidence, or large plane mirror and arbitrary incidence, the reflection matrix is the

identity matrix.

The case $\alpha = 1$ is of special interest for arbitrary angle of deflection $\phi$ and mirror curvature $1/R$, as it will be explained in the next section. For finite mirror size $\rho \geq W_o$, ( $\mu \geq 1$), there exists zeroth order nondiagonal terms inside $R(0)$. Since $R(0)$ is independent of the angle of deflection $\phi$, the mirror size yields the dominant contribution to the reflection into modes different than the incoming. The effects of the deflection of the light beam enter to first order in $\xi$, $R(1)$, or higher.

As the mirror size becomes very large and the limits of integration are extended to infinity the orthogonality among the various modes $u_{mn}$ becomes effective. The off-diagonal terms in $R(0)$ become comparable to the first order terms $R(1)$ roughly when $1/\mu^2 \sim \xi \sim \theta_d$. At the limit $\mu \to \infty$ all the nondiagonal elements of $R$ are reduced to order $\xi$ or higher,

$$R^{mn}_{pq} = \xi R^{mn}_{pq}(1) + O(\xi^2), \quad m \neq p, \; n \neq q, \tag{25a}$$

and the only matrix elements of zeroth order in $\xi$ are the diagonal

$$R^{mn}_{mn} = R^{mn}_{mn}(0) + O(\xi^2). \tag{25b}$$

in both Hermite and Laguerre represenations. The lowest correction in the diagonal elements is of second order $\xi^2$, while the first order contribution disappears. This is consistent with flux conservation during reflection in case of a large mirror.

The superposition principle can be used to describe reflection from more complex mirror surfaces. In case of a mirror with a hole the surface integral (7) over S is expressed as $\int_S = \int_{S1} - \int_{S2}$ where $S_1$ is defined by the mirror surface including the hole surface, and $S_2$ is the surface of the hole only. The total reflection matrix R is given by R =

$R(S_1) - R(S_2)$, the difference in the reflection matrices associated with mirrors $S_1$ and $S_2$ respectively. The transmission matrix **T** through a screen with an aperture of area S is given by $\mathbf{T} = -\mathbf{R}$, **R** being the reflection matrix for a mirror matching the aperture S. The transmission matrix for radiation diffracted behind a finite size mirror is given by $\mathbf{T}' = \mathbf{1} - e^{i\pi}\mathbf{R}$ where **1** is the identity matrix.

## V. REFLECTION OF THE LOWEST ORDER MODE

The computation of all the truncated integrals for finite mirror surface is nontrivial. Most applications however involve the (0,0) lowest order mode as the dominant mode in both incoming and reflected radiation. The strategy here is to compute the element $R_{00}^{00}$ of the reflection matrix first. Then the waist for the reflected modes $W_o$ can be selected so that it maximizes $R_{00}^{00}$. The optimum representation condition

$$\frac{\partial R_{00}^{00}}{\partial \alpha} = 0, \tag{26}$$

puts the maximum amount of the reflected radiation in the lowest mode (a different mode and matrix element may be chosen, if desired). It is pointed out that (26) does not improve the properties of the reflected radiation. It enables one to choose the best representation in terms of minimizing the coefficients of the undesired modes for the scattered radiation. Once $W_o$ is fixed by (26) then the exact location and size of the waist(s) for the reflected modes is determined by solving the system of equations

$$W_o = w_o\left[1 + \frac{l_o^2}{b_o^2}\right]^{1/2}, \qquad \frac{1}{R_o} = \frac{l_o}{l_o^2 + b_o^2}. \tag{27}$$

The element $R_{00}^{00}$ is identical in both representations since the lowest order mode $u_{00}$ is the same in rectangular and cylindrical coordinates. Performing the integration (20) yields $R_{00}^{00}$ to first order in $\xi$

$$R_{00}^{00} = \frac{2\alpha}{1+\alpha^2}\left[1 - e^{-(1+\alpha^2)\mu^2}\right] + O(\xi^2). \qquad (28)$$

Note that the first order term vanishes and the lowest correction is of second order in $\xi^2$. The exact dependence on the mirror size $\rho$ is parametrized by $\mu = \rho/W_o$, while $\alpha = W_i/W_o$ parametrizes the ratio of the incoming and scattered radiation spot sizes at the mirror. The optimization condition $\partial R_{00}^{00}(0)/\partial\alpha = 0$ yields, $\alpha^2 = 1 + \exp[-(1+\alpha^2)\mu^2]\,[\alpha^4+(2\mu^2+1)\alpha^2-1]$. In case the mirror cross section is much larger than the spot size of the incoming mode, $\mu >> 1$, $\alpha \to 1$ and the reflected spot size at the mirror matches the incoming, $W_o = W_i$.

Large mirror size is desired to maximize the total reflection coefficient. The reflection coefficient $\eta_R$ is given by $\eta_R = P_o/P_i$ where the incoming flux is $P_i = |c^i|^2 = \Sigma\,|c^i_{pq}|^2$ and the outgoing flux is given by

$$P_o = |c^o|^2 = |\,R \cdot c^i|^2 = \sum_{mn}\sum_{pq} |R^{mn}_{pq}\, c^i_{pq}|^2. \qquad (29)$$

In Fig. 2 we plot $\eta_R$ for the lowest order incoming mode as a function of $\mu' = \cos(\phi/2)\,\rho/W_o = \cos(\phi/2)\,\mu$. $\mu'$ parametrizes the size of the mirror surface projection into the plane perpendicular to the incoming radiation direction. The incoming radiation has a wavelength $\lambda = 1\mu$ ($10^{-4}$cm), waist $w_i = 10^{-2}$cm at distance $l_i = 2.5\times10^3$cm from the mirror and radius of curvature (at the mirror) $R_i = 2.5\times10^3$cm. The mirror has a radius of curvature $R_m = 2.5\times10^3$cm, yielding reflected modes of $R_o$ =

$2.5 \times 10^3$ (again $l_o$ and $w_o$ depend on the choice of $W_o$). In Fig. 3 we plot the reflection coefficients $R_{pq}^{00}$ of the lowest order mode (0,0) into the first 25 modes (p,q) with $p \leq q \leq 5$, as a function of $\mu'$. The deflection angle is $90^o$ and the ratio of the spot sizes is 1. Increasing mirror size maximizes the diagonal element and minimizes scattering into other modes.

In Fig. 4 we fix the mirror size $\mu' = 2$ and the angle $\phi = 90^o$ and vary the spot size ratio $\alpha$. The best representation, maximizing $R_{00}^{00}$ and minimizing $R_{pq}^{00}$ is obtained at $\alpha = 1$. However, for small mirror $\mu' = 0.66$, the maximum for $R_{00}^{00}$ occurs at $\alpha \simeq 0.70$ (see Fig. 5). Radiation reflected off mirrors smaller than the incoming spot size is best described by outgoing modes of reduced spot size $W_o < W_i$. Also note from Fig. 5b that for small mirror size the total power reflected into the first 25 modes never exceeds 80% of the incoming flux; even with many more modes $\eta_R$ remains less than 1. In Fig. 6 the reflection coefficients $R_{pq}^{00}$ are plotted as functions of the angle of deflection $\phi$ for fixed $\alpha = 1$, $\mu' = 2$. It is seen that, for sufficiently large reflecting surface and good choice of the spot size $W_o$, the reflection matrix is not very sensitive to $\phi$. Comparison of Figs. 2 and 3 with the rest of the plots shows that the relative mirror size to the radiation spot size is the most important parameter to determine the reflection into other than the incoming modes.

## ACKNOWLEDGEMENT

This work supported by SDIO and managed by SDC.

## References


1. L. R. Elias, W. M. Fairbanks. J. M. J. Madey, H. A. Schwettman and T. I. Smith, Phys. Rev. Lett. 36, 717 (1976).
2. T. I. Smith, H. A. Schwettman, R. Rohatgi, Y. Lapierre and J. Edighoffer in Proceedings of the Eighth International FEL Conference, Glasgow, Scotland, edited by M. Poole (North Holland, Amsterdam, 1987), p. 1.
3. R. W. Warren, D. W. Feldman, B. E. Newnam, S. C. Bender, W. E. Stein, et al., in Proceedings of the Eighth International FEL Conference, Glasgow, Scotland, edited by M. Poole (North Holland, Amsterdam, 1987), p. 8.
4. K. E. Robinson, T. L. Churchill, D. C. Quimby, D. M. Shemwell, J. M. Slater, et al., in Proceedings of the Eighth International FEL Conference, Glasgow, Scotland, edited by M. Poole (North Holland, Amsterdam, 1987), p. 49.
5. M. Billardon, P. Elleaume, J. M. Ortega, C. Bazin, M. Bergher, et al., in Proceedings of the Eighth International FEL Conference, Glasgow, Scotland, edited by M. Poole (North Holland, Amsterdam, 1987), p. 72.
6. T. Masud, T. C. Marshall, S. P. Schlesinger and F. G. Yee, Phys. Rev. Lett. 56, 1567 (1986).
7. X. K. Maruyama, S. Penner, C. M. Tang and P. Sprangle, in Proceedings of the Eighth International FEL Conference, Glasgow, Scotland, edited by M. Poole (North Holland, Amsterdam, 1987), p. 259.
8. S. Solimeno and A. Torre, Nucl. Instr. A237, 404 (1985).
9. J. A. Murphy, Intl. J. Infrared and Millimeter Waves 8, 1165 (1987).
10. S. Riyopoulos and C. M. Tang, submitted for publication (1988).
11. See, for example, H. A. Hauss in Waves and Fields in Optoelectronics, (Prentice Hall, New Jersey, 1984), p. 180, and references therein.

12. P. Sprangle, A. Ting and C. M. Tang, Phys. Rev. Lett. 59, 202 (1987).

13. P. Sprangle, A. Ting and C. M. Tang, Phys. Rev. A36, 2773 (1987).

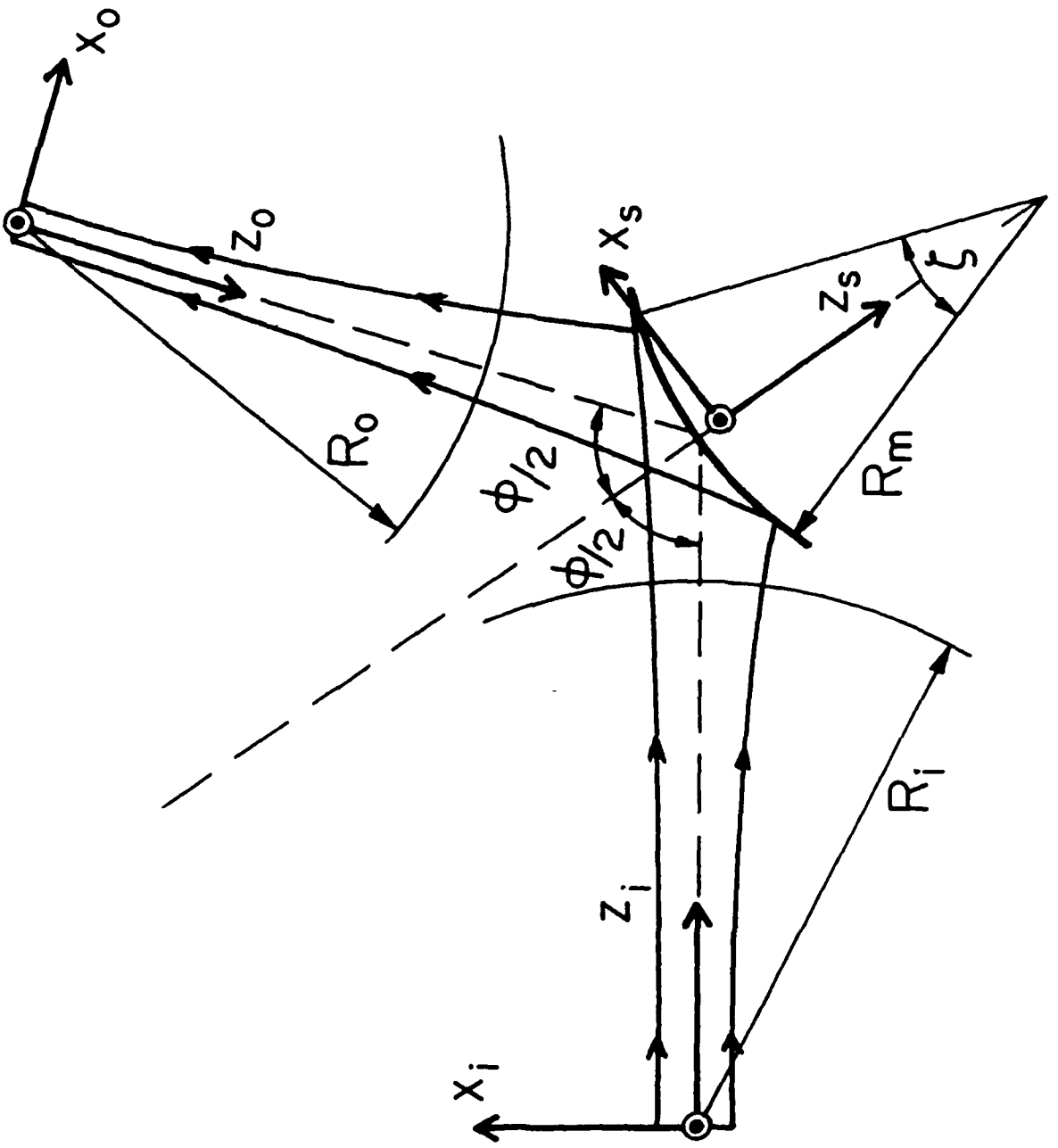



Figure 1 Reflection geometry.

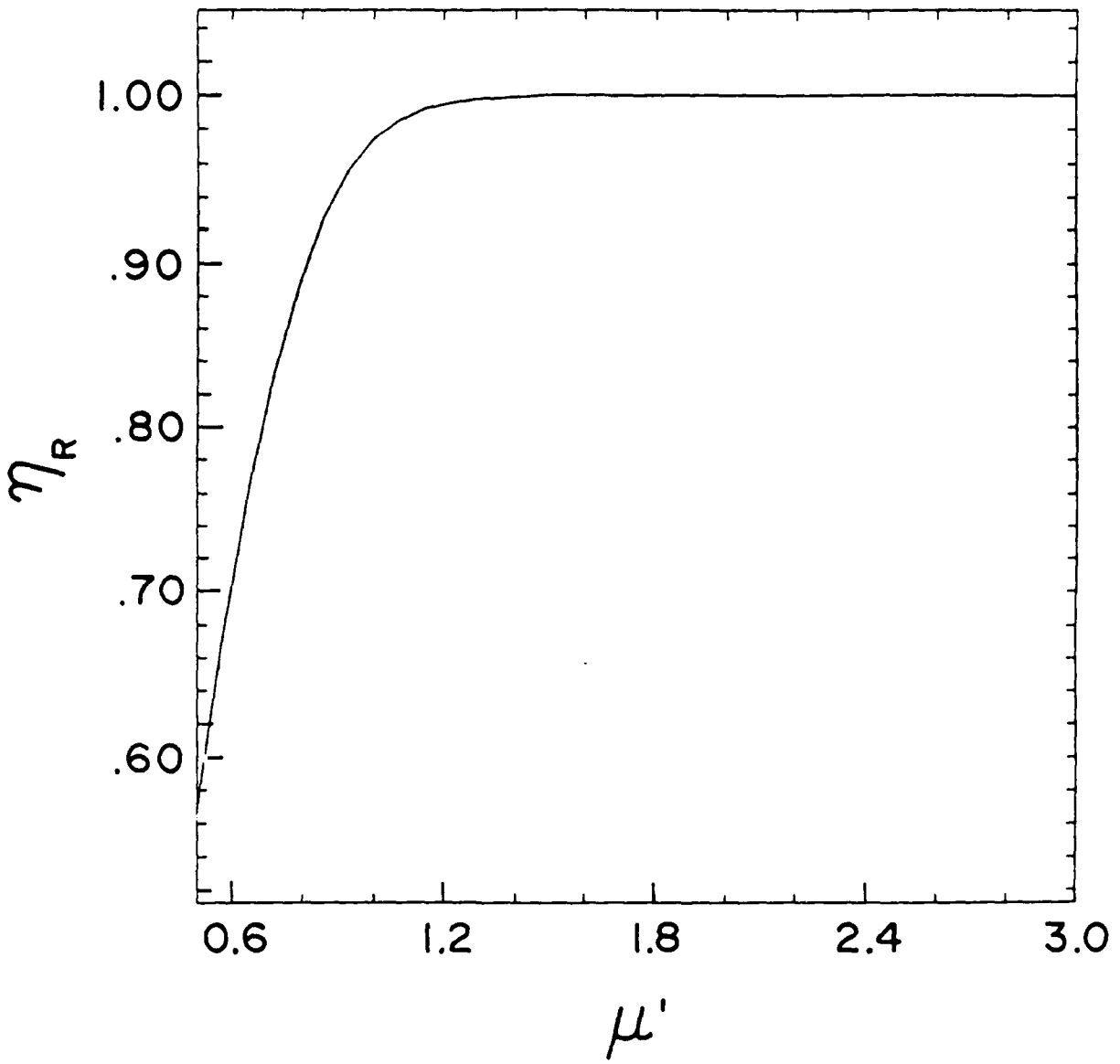



Figure 2 Plot of the total reflection coefficient $\eta_R$ for the lowest order mode as a function of the mirror size $\mu'$ for $\phi = 90°$ and $W_o = W_i$.

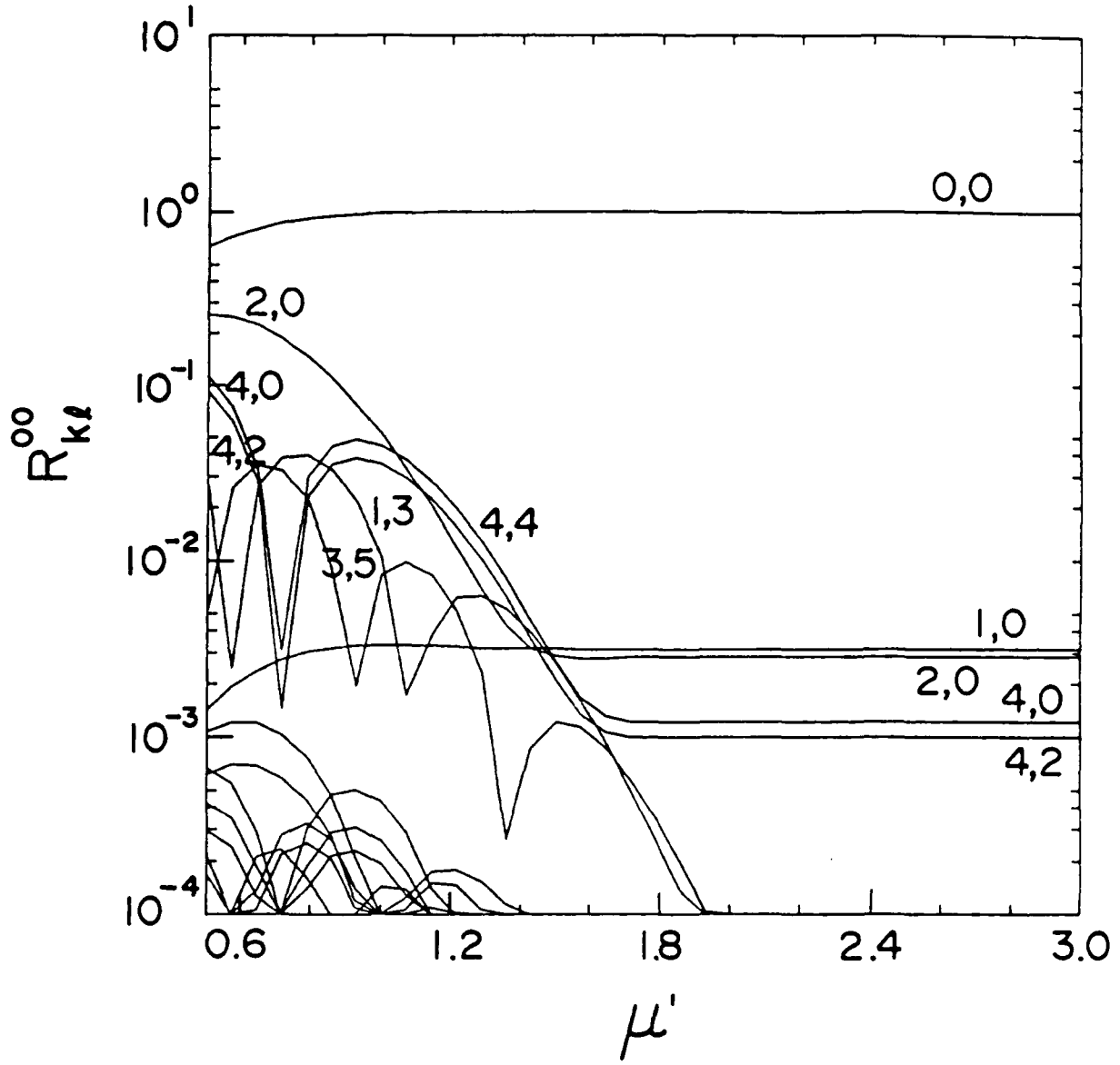



Figure 3 Plots of the reflection matrix elements of the lowest order mode (0,0) into the first 25 modes $p \leq q \leq 5$. The magnitude $|R^{00}_{pq}|$ is plotted against the relative mirror size $\mu'$. The angle of deflection $\phi = 90°$ and $\alpha = 1$ ($W_i = W_o$).

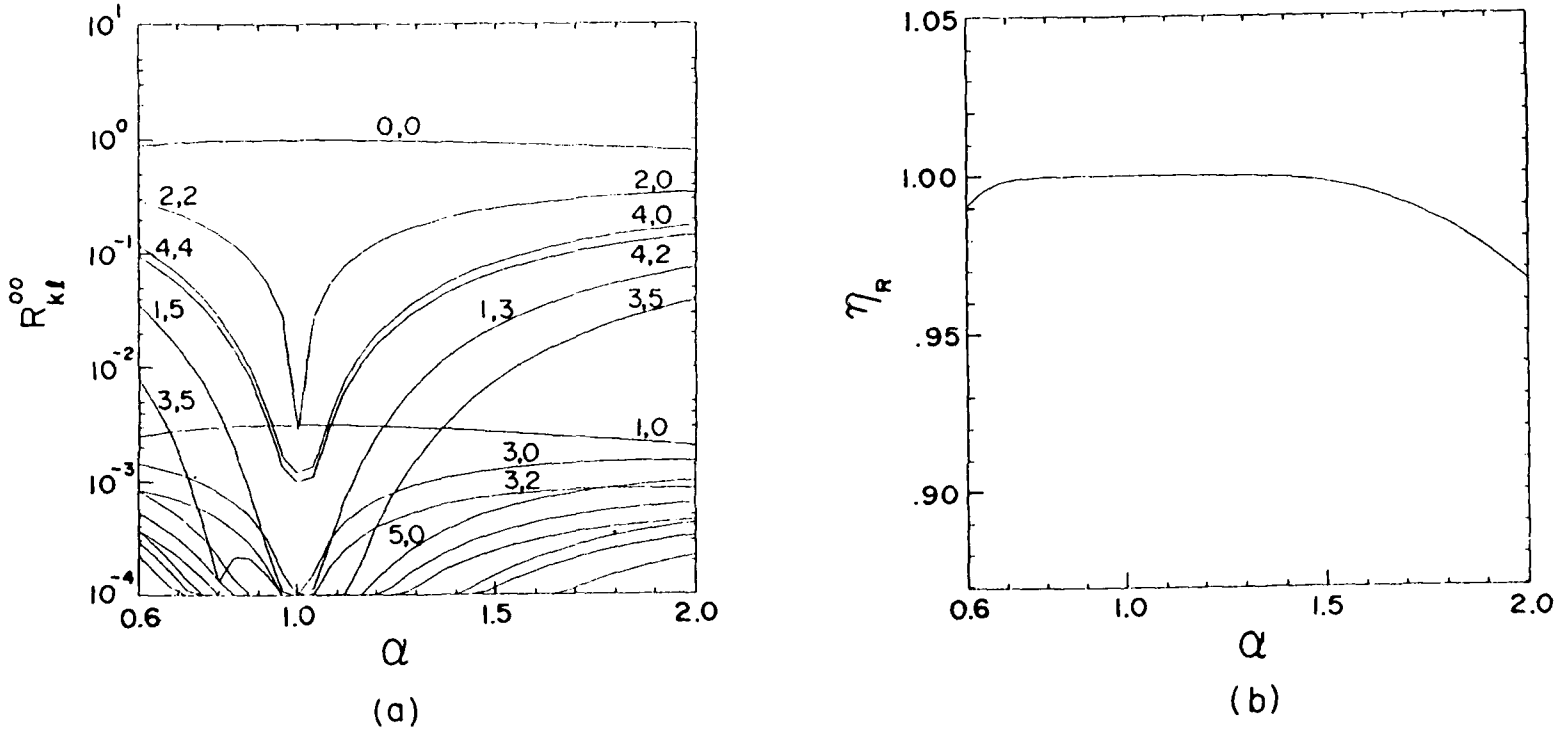



Figure 4 Plots of (a) the reflection matrix elements $|R^{00}_{pq}|$, and (b) the reflection coefficient $\eta_R$ into the first 25 modes, against the spot size ratio $\alpha$ for $\mu' = 2$ and $\phi = 90°$.

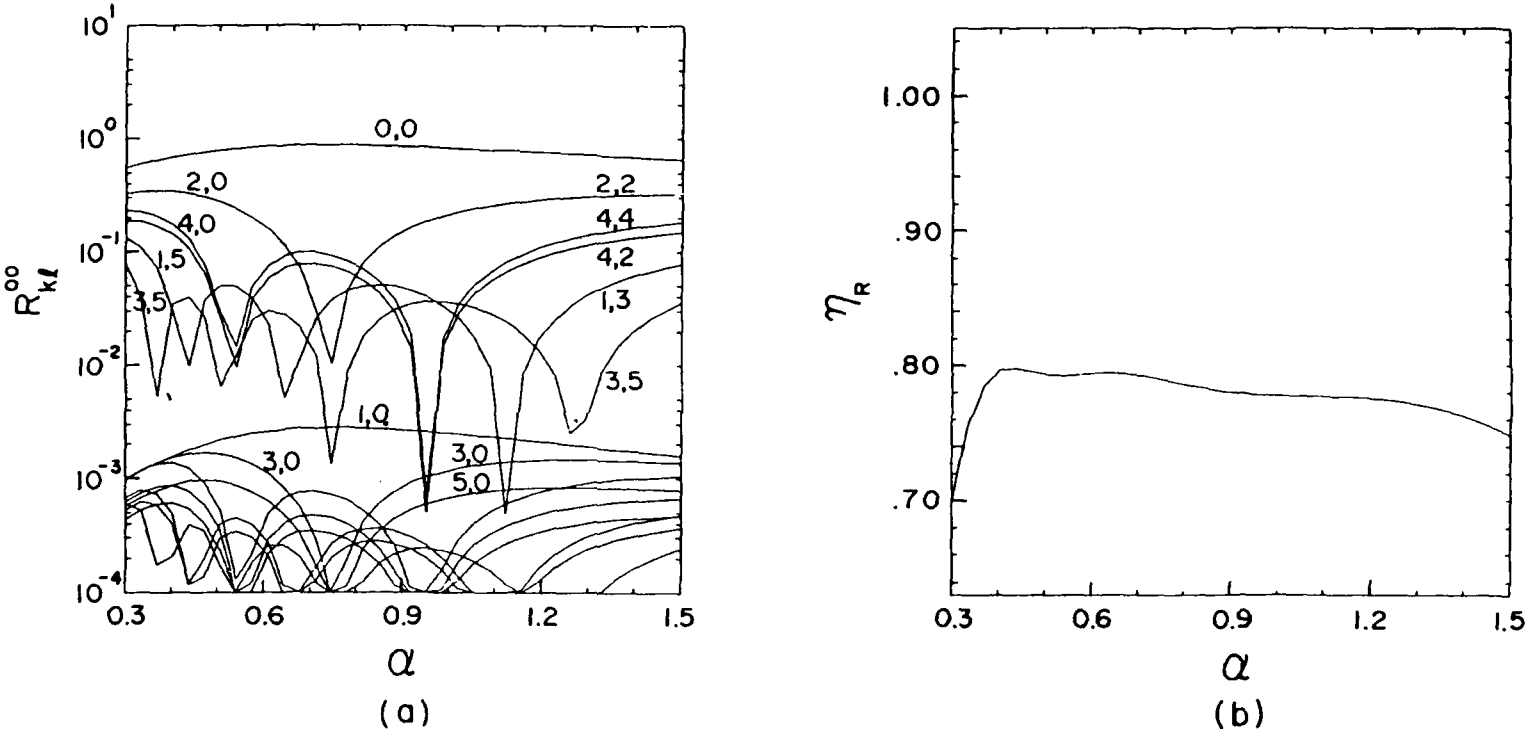



Figure 5 Same as in Fig. 4 for $\mu' = 0.5$.

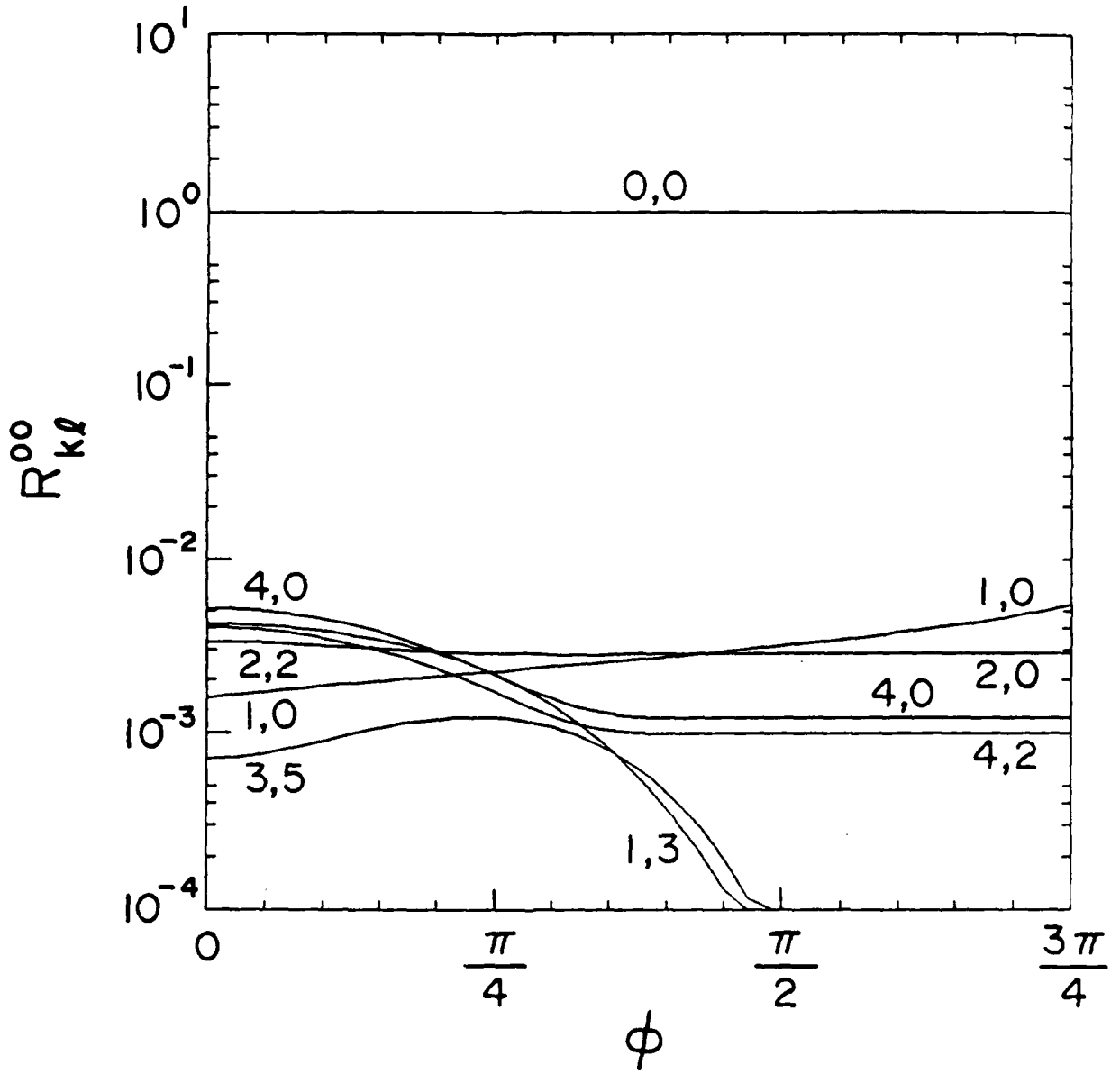



Figure 6 Plots of the reflection matrix elements $|R^{00}_{pq}|$ against the angle of deflection $\phi$ for $\mu' = 2$ and $\alpha = 1$.

# APPENDIX NN

## Cavity Eigenmodes for the NIST/NRL Free Electron Laser

# CAVITY EIGENMODES FOR THE NIST/NRL FREE ELECTRON LASER

S. Riyopoulos[a] and C. M. Tang

Naval Research Laboratory
Plasma Physics Division
Washington DC 20375

The cavity transfer matrix for the round trip of a light pulse in the optical resonator of the National Institute of Standards and Technology (NIST)/Naval Research Laboratory (NRL) Free Electron Laser (FEL) oscillator is derived. The cavity eigenmodes and the corresponding eigenvalues are obtained, using an expansion in Gaussian-Laguerre vacuum modes, by numerical diagonalization. The fractional power loss per eigenmode, caused by the finite sizes of the cavity mirrors and apertures are determined. It is found that the losses are very small over the entire wavelength regime of operation.

[a]Science Applications Intl. Corp., McLean, VA 22102

# I. INTRODUCTION

The NIST(formerly NBS)/NRL FEL oscillator powered by a CW 185 MeV racetrack microtron is currently under construction[1-3]. A simplified model of the resonator cavity, consisting of the wiggler vacuum chamber and the two mirrors, is shown schematically in Fig. 1. Since stimulated emission takes place predominantly along the electron beam path, the vector potential of the radiation $A_R$ is expressed in terms of the free space eigenmodes $A_R(r) = A_{mp}(r)\ \exp(-i\omega t)\ e_{mp}$ + cc of the paraxial wave equation[4], where $e_{mp}$ is the polarization vetor,

$$A_{mp}(r) = \frac{u_{mp}(r;W)}{\left(1 + \frac{z^2}{b^2}\right)^{1/2}}\, e^{ik\left(z + \frac{(x^2 + y^2)}{2R(z)}\right)}\, e^{i\zeta_{mp}(z)}\ , \qquad (1)$$

$k = \omega/c$ is the wavenumber and $\omega$ is the frequency. In Eq. (1) the exponent $k[z + (x^2+y^2)/2R(z)]$ contains the phase variation on the wavelength scale $\lambda = 2\pi/k$, with spherical wavefronts of curvature $1/R(z) = z/(z^2 + b^2)$. The slow phase variation is given by $\zeta_{mp}(z) = (2m + p + 1)\ \tan^{-1}(z/b)$. The spot size of the radiation envelope is $W(z) = w\ (1 + z^2/b^2)^{1/2}$, where the distance z is measured from the position of the waist $w = (2b/k)^{1/2}$. The amplitude squared of the mode drops by 1/2 over a distance equal to the Rayleigh length b (also known as confocal parameter). Most of the radiation is confined within a cone parametrized by the diffraction angle

$\theta_d = W/z \simeq (\lambda/b\pi)^{1/2}$. For given wavelength $\lambda$, any two of the four parameters R, W, b, z determine a mode uniquely.

The amplitude profile $u_{mp}(r;W)$ contains the transverse spatial variation, equivalent to a small $k_\perp$, perpendicular to the z-direction. In cylindrical coordinates $(r,\theta,z)$, where $\tan\theta = x/y$, $r = (x^2+y^2)^{1/2}$, $u_{mp}(r,\theta;W)$ takes the form

$$u^{\pm}_{mp}(r,\theta;W) = a_{mp} \begin{pmatrix}\cos p\theta \\ \sin p\theta\end{pmatrix} \xi^{p/2} L^p_m(\xi)\, e^{-\frac{\xi}{2}}, \qquad \xi = \frac{2r^2}{W^2}, \qquad (2)$$

where + (-) signifies cosine (sine) poloidal dependence, $L^p_m(\xi)$ are the associated Laguerre polynomials and the normalizing factor $a_{mp} = [1/(1+\delta_{p0})\pi W^2]^{1/2}[m!/(m+p)!]^{-1/2}$.

In the presence of conducting walls the vacuum expansion (1) still provides the best representation, because (a) the chamber inner radius is much larger than the radiation spot size and (b) the transit time through the cavity and the length of the light pulse itself are too short to allow multiple reflections on the walls, required to set up cavity eigenmodes. It can also be argued that the small fraction of the radiation reflected from the wall, acting as a perfect conductor for grazing incidence, is lost out of the resonator. The main effect of the chamber therefore comes from the two edge apertures, where the radiation spot size is maximum. The resonator is then modeled by a sequence of four optical elements, i.e. two apertures and two mirrors.

The radiation profile is altered after each encounter with an optical element. A pure incident mode $A_{mp}(r)$ will, in general, be partially

transformed into different modes. This is caused by the finite size of the apertures, and, in addition, by spherical aberration and surface imperfections in case of the mirrors. Consider the radiation incoming to a given optical element as consisting of various modes (m,p) of the same curvature $R_i(z)$. Both incident and reflected radiation are expanded into eigenmodes, respectively as follows,

$$A^i(r_i) = \sum_{m,p} c^i_{mp} A_{mp}(r_i) \quad ,$$
$$A^o(r_o) = \sum_{n,q} c^o_{nq} A_{nq}(r_o) \quad . \tag{3}$$

The relation among the incident and reflected expansion coefficients $c^i_{mp}$ and $c^o_{pq}$ is written as

$$c^o = R\, c^i \quad , \tag{4a}$$

or

$$c^o_{nq} = \sum_{m,p} R^{mp}_{nq}\, c^i_{mp} \quad , \tag{4b}$$

where $R^{mp}_{nq}$ are the elements of the reflection matrix R.

The radiation profile at the end of the round trip inside the resonator will relate to the original profile through the resonator transfer matrix M,

$$M = T_2\, R_2\, T_2\, T_1\, R_1\, T_1 \tag{5}$$

where $T_i$ and $R_i$ are the transmission matricies through the chamber apertures and the reflection matrices from the mirrors 1 and 2 respectively. The cavity eigenmodes $C_j$ with eigenvalues $\nu_j$ are given by

$$M\, C_j = \nu_j\, C_j \,. \tag{6}$$

Since M is generally nondiagonal, the eigenmodes are mixtures of vacuum modes (1).

The electron beam is an active medium that changes the radiation profile during amplification in each passage. If G is the amplification matrix, then a steady state exists finally if the matirx equation

$$G\, M\, C_s = g_s\, C_s \tag{7}$$

has solutions with $|g_s| = 1$. A steady state need not be an eigenmode of the empty resonator; this could happen only in the case of equal amplification $g_a$ for each eigenmode, i.e., $G = g_a\, I$ where I is the identity matrix. In an FEL, a different gain is associated with each free space eigenmode. However, in cases when the off-diagonal elements of both G and M become vanishingly small, both the resonator modes and the final steady states approach the pure vacuum modes (1).

In this paper we first study the vacuum performance of the optical cavity. The detailed cavity mode stucture in terms of vacuum modes and the associated eigenvalues are obtained by numerical diagonalization of the cavity matrix M. The fractional power loss $\eta_j$ per cavity mode per trip is found from the magnitude of the eigenvalue

$$\eta_j = 1 - |\nu_j|^2. \qquad (8)$$

The profiles for the cavity modes are also obtained utilizing the expansion coefficients of $C_j$ into the vacuum modes. We also examine the eigenmode structure of the combined gain-transfer matrix **G M** in cases of small gain.

## II. TRANSFER MATRIX FOR A SINGLE OPTICAL ELEMENT

The reflection of Gaussian light beams from mirrors was studied in some detail in Ref. 5 for arbitrary angle of radiation incidence. In the limit of normal incidence considered here, the reflection matrix elements are given by the surface integrals

$$R_{nq}^{mp} = \iint_S d\theta_s \, dr_s \, r_s \frac{u_{mp}(r_s,\theta_s)\, u_{nq}(r_s,\theta_s)}{\left[1 + \frac{l_o^2}{b_o^2}\right]^{1/2}} \left[\frac{1 + \frac{z_s^2(r_s)}{b_o^2}}{1 + \frac{z_s^2(r_s)}{b_i^2}}\right]^{1/2} e^{i\Delta(r_s,\theta_s)} \times e^{i\zeta_{nq}^{i}(z_s) - i\zeta_{mp}^{o}(z_s)} . \tag{9}$$

The mirror surface S is spherical, expressed in the coordinate system $(r_s,\theta_s,z_s)$ with origin located at the mirror center, by

$$(z_s - R_m)^2 + r_s^2 = R_m^2 , \tag{10}$$

where $R_m$ is the mirror radius of curvature. Equation (10) is used to express $z_s$ on the surface S in terms of $r_s$. The mirror boundary is given by

$$r_s^2 = \rho^2 , \tag{11}$$

where $\rho$ is the radius of the mirror cross-section.

The phase factor $\Delta(r_s,\theta_s)$, related to the optical path along the various rays connecting the incoming wavefront with its mirror image (reflected), must be approximately constant. Therefore, the curvature of the outgoing wavefront is related to the incoming and the mirror curvatures through

$$\frac{1}{R_o} = \frac{2}{R_m} - \frac{1}{R_i} . \tag{12}$$

The Rayleigh length $b_o$ and the waist location $l_o$ of the outgoing modes are yet to be determined.

It has been argued[5,6] that the amount of radiation scattered into other than the incoming modes, as well as that escaping behind the mirror, depends on three factors:

(a) Finite mirror size effects, of the order of

$$\exp\left(-\frac{\rho^2}{W_i^2}\right) , \tag{13}$$

where $\rho$ is the mirror cross-section radius and $W_i$ the incoming radiation spot size.

(b) Spherical aberration effets, of the order of

$$kW_i\left(\frac{W_i^2}{R_m^2}\right) , \tag{14}$$

coming from the phase term $\Delta(r_s,\theta_s)$ inside (9). Spherical aberration exists even when the mirror curvature matches the radiation curvature. It is caused by the fact that rays ending on a given spherical wavefront are not exactly perpendicular to it, since they originated from a finite size waist and not from a point at the center of curvature.

(c) Surface imperfections, for example, when the reflecting surface is not perfectly sperical.

Spherical aberration effects are usually less important. They will be addressed in future work, together with the potentially more important consequences caused by mirror deformations (buckling) due to heating.

Ignoring (b) and (c) amounts to setting $\Delta(r_s,\theta_s) = 0$ in (9). After substituting expression (2) for the eigenmodes $u_{mp}$, (9) becomes,

$$R^{mp}_{nq}(\mu,\alpha) = \delta_{pq}\, C^{mp}_{nq} \int_0^{2\mu} d\xi\, (\alpha^2\xi)^{\frac{q}{2}}\, \xi^{\frac{p}{2}}\, L^q_n(\alpha^2\xi)\, L^p_m(\xi)\, e^{-\frac{\alpha^2+1}{2}\xi}, \quad (15)$$

where $C^{mp}_{nq} = \alpha\, [m!n!/(m+p)!(n+q)!]^{1/2}$ and $\xi = 2r^2/W_i^2$. Since the surface S has rotational symmetry about the z axis, it couples modes with the same poloidal $\theta$ dependence, $p = q$. The radial integration is carried out in Appendix A.

In general, the matrix R involves two indepedent parameters, the ratio of the mirror radius $\rho$ to the radiation spot size squared, $\mu = (\rho/W_i)^2$, and the ratio of the incoming to outgoing spot sizes $\alpha = (W_i/W_o)$. Only the curvature of the reflected mode is set by the

mirror, while the outgoing spot size is still a free parameter. This can be exploited by choosing the value $W_o$ that maximizes the coefficient for the fundamental mode in the reflected radiation, i.e.,

$$\frac{\partial R_{00}^{00}}{\partial \alpha} = 0 \ . \tag{16}$$

Once $W_o$ is selected, the exact location and size of the waist(s) for the reflected modes is determined by solving the system of equations

$$W_o = w_o \left[1 + \frac{l_o^2}{b_o^2}\right]^{1/2} , \qquad \frac{1}{R_o} = \frac{l_o}{l_o^2 + b_o^2} \ . \tag{17}$$

The transmission matrix T through an aperture is given by

$$T = e^{i\pi} R \ , \tag{18}$$

where R is the reflection matrix for a plane mirror ($R_m = \infty$) of the same cross section $\rho$, while the curvature tranformation is

$$\frac{1}{R_o} = \frac{1}{R_i} \ . \tag{19}$$

Aberration and surface imperfections do not affect transmission through apertures.

## III. CAVITY EIGENMODES

We seek a class of cavity eigenmodes with the waist located in the middle of the vacuum chamber. Since the mode spot must remain unchanged $W_i = W_o$ during each transmission or reflection we elect $\alpha = 1$ inside the trasfer matrix (5) for every optical element. The curvature R is not changed during transmission through an aperture. The mirror curvature, however, must match the incoming and outgoing radiation curvature, $R_i = R_o = R_m$ in (12). Therefore, for eigenmodes to exist, the equations

$$R_1 = \frac{L_1}{L_1^2 + b^2} , \qquad R_2 = \frac{L_2}{L_2^2 + b^2} , \tag{20}$$

must admit a positive solution for b. This is possible when

$$\left( 1 - \frac{L}{R_1} \right) \left( 1 - \frac{L}{R_2} \right) > 0 , \qquad L = L_1 + L_2 . \tag{21}$$

Equation (21) is the optical stability condition for the cavity. Even with (21) satisfied the cavity modes will still decay slowly in time because of the finite size of the mirrors. According to (20), the Rayleigh length b for various wavelengths remains fixed for a given mirror configuration, while the waist w varies as $w = (b\lambda/\pi)^{1/2}$. The cross section of the electron beam is adjustable to give a good filling factor for the particular wavelength. The cross section of the chamber is oval and is approximated with a circular one of effective radius $\rho = (\rho_1 \rho_2)^{1/2}$,

where $\rho_1$ and $\rho_2$ are the major and minor aperture radii.

Because of the imposed axisymmetry we look for cavity eigenmodes involving combinations of axisymmetric vacuum modes p = q = 0. The coefficients $c_j^{(n)}$ of the modes $u_{n0}$ inside the j-th cavity mode $C_j$

$$C_j = [\, c_j^{(0)},\, c_j^{(1)},\, \ldots\, ,\, c_j^{(n)},\, \ldots\, ] \tag{22}$$

and the corresponding eigenvalues $\nu_j$ are found by numerical diagonalization of the transfer matrix M, utilizing expressions (A3) with $\alpha = 1$ for each individual optical element inside (5). Eventually, the cavity matrix M depends on the spot to aperture size ratios for the four optical elements,

$$M[\mu_1(\lambda),\, \mu_2(\lambda),\, \mu_3(\lambda),\, \mu_4(\lambda)]\ , \tag{23}$$

where in turn $\mu_i$ depends on the wavelength through

$$\mu_i(\lambda) = \left( \frac{\lambda}{\pi b} \right)^{1/2} \frac{\rho_i}{\left( 1 + L_i^2/b^2 \right)^{1/2}}\ . \tag{24}$$

Two general conclusions are made. First, it is found that, for radiation spot sizes smaller than about one third the apertures sizes, the dominant contribution in each cavity eigenmode comes from a single coefficient $c_j^{(n)}$. Cavity eigenmodes, in this case, approach pure vacuum modes, as expected from the smallness of the off-diagonal matrix elements in M. Second, if the eigenvalues are arranged according to magnitude,

$|\nu_0| > |\nu_1| > \ldots |\nu_j| > |\nu_{j+1}| \ldots$, the largest eigenvalue corresponds to the eigenmode closest to the fundamental vacuum mode $u_{00}$, i.e., the eigenmode with $|c_0^{(0)}| \approx 1$. The next largest eigenvalue corresponds to the eigenmode closest to the first radial vacuum mode, i.e., with $|c_1^{(1)}| \approx 1$, and so on. This is expected as the rms spot size for the n-th radial mode $u_{n0}(r;W)$ increases with n as $(n+1)^{1/2}W$.

The NIST/NRL oscillator has been designed for eigenmodes of Rayleigh length equal to half the vacuum chamber length. Two different arrangements, one with full and one with half length wiggler will be used for the wavelength regimes of 0.2μm to 2μm and 2μm to 10μm respectively. The design parameters are $b = L_w/2 = 107.5$cm, $L_1 = 521$cm, $L_2 = 386$cm, $R_1 = 543$cm, $R_2 = 417$cm, $\rho_1 = \rho_2 = 2.54$cm for the half wiggler and $b = L_w/2 = 198$cm, $L_1 = 431$cm, $L_2 = 477$cm, $R_1 = 521$cm, $R_2 = 559$cm for the full wiggler.

The fractional power loss $\eta_j = 1 - |\nu_j|^2$ for the first 5 cavity eigenmodes of the half wiggler arrangement is plotted in Fig. 2 as a function of the wavelength λ. Through the planned regime of operation the loss for the fundmental cavity mode never exceeds 1%. The loss factor for the next two modes is also very small, so that the mode selection is going to be determined by the differences in the radiation gain for each mode. In Fig. 3(a) we plot the expansion coefficients $c_n^{(0)}$ of the fundamental cavity mode $C_0$ into the vacuum modes $u_{n0}$. Is shows that the cavity mode profile is very close to a pure $u_{00}$ vacuum mode, with other modes contributing less than 1%. The expansion coefficients for the second and third cavity modes are shown in Figs. 3(b) and 3(c) respectively. If the

complete expansion coefficients are written as

$$c_j^{(n)} = |c_j^{(n)}| \exp(i\chi_{jn}) ,$$

then the complex amplitude for the j-th eigenmode $C_j$ is given by

$$A_j(r) = |A_j(r)| \, e^{i\Phi_j(r)} ,$$

where

$$|A_j(r)| = \left[ Ar_j^2 + Ai_j^2 \right]^{1/2}, \qquad \Phi_j(r) = \tan^{-1}\left( Ar_j / Ai_j \right) ,$$

$$Ar_j = \sum_n u_{n0}(r) \, |c_j^{(n)}| \cos\chi_{jn} , \qquad Ai_j = \sum_n u_{n0}(r) \, |c_j^{(n)}| \sin\chi_{jn} .$$

The resulting amplitude profiles for the first three modes at $z = 0$ are shown in Fig. 4 for $\lambda = 2\mu m$ and $\lambda = 10\mu m$. In Fig. 5(a) we show the power fraction $\eta_j$ for the first four cavity modes of Rayleigh length $b = L_w/6$. The vacuum expansion coefficients $c_0^{(n)}$ for the fundamental cavity mode are shown in Fig. 5(b) against the wavelength $\lambda$. The transverse amplitude profiles for the first three modes at $\lambda = 2.2\mu m$ and $\lambda = 10\mu m$, in Fig. 5(c), show considerable departure from vacuum modes.

The cavity eigenmodes for the full wiggler arrangement are extremely close to vacuum modes and the fractional power losses for the first five of them are below $10^{-3}$ over the frequency regime from $0.5\mu m$ to $2\mu m$. This is caused by the combination of a longer Rayleigh length with a spot size that gets smaller with shorter wavelength.

In case of small gain we can include the effect of the electron beam on the cavity eigenmodes by introducing the amplitude gain matrix G. In the linear regime the cross-coupling among various transverse modes is unimportant and G is diagonal, given by

$$G_{mn} = g(\lambda)\ f_n\ \delta_{mn} \tag{25a}$$

where

$$g(\lambda) = 0.5\ F_1^{\,2}\ \frac{\pi^2}{\sigma_R}\ \frac{I}{I_A}\ \frac{\lambda_w^{\,2}}{\gamma_o^{\,2}}\ K^2\ N^3 \tag{25b}$$

is the amplitude gain for the fundamental vacuum mode. In Eqs. (25) N is the number of wiggler periods, $\gamma_o$ is the initial relativistic factor, $\sigma_R = \pi w^2$ is the radiation cross section at the waist, $I_A = 17\times10^3$ A, I is the current in amperes, $K = |e|B_w\lambda_w/2\pi mc^2$ is the wiggler parameter, $B_w$ is the rms magnetic field of the wiggler, $\lambda_w$ is the wiggler wavelength, related to the radiation wavelength $\lambda$ by $\lambda_w = 2\gamma^2\lambda/(1+K^2)$, $F_1 = J_o(b)-J_1(b)$ with $b = K^2/2(1+K^2)$ and $f_n$ is the normalized (to the fundamental) filling factor

$$f_n = \int_0^\infty dr\ r\ j(r)\ u_{n0}(r)\ /\ \int_0^\infty dr\ r\ j(r)\ u_{00}(r)\ , \tag{27}$$

with the parabolic current profile given by $j(r) = j_o\ (1 - r^2/\rho_b^{\,2})$ for $r \leq \rho_b$, $j(r) = 0$ for $r > \rho_b$, $\rho_b$ being the beam radius. The round trip gain

for the j-th beam-cavity eigenmode is given by

$$g_j = [\ 1 + g(\lambda)\ ]\ \tilde{\nu}_j \ . \qquad (28)$$

where $\tilde{\nu}_j$ is the eigenvalue for the eigenmode $\tilde{C}_j$ of the combined gain-transfer matrix

$$M_g = G\ M \ . \qquad (29)$$

The fractional power loss $\tilde{\eta}_j = 1 - |\tilde{\nu}_j|^2$ for the first five eigenmodes is shown in Fig. 6(a) as a function of the wavelength, while the expansion coefficients of the fundamental eigenmode in terms of vacuum modes are shown in Fig. 6(b). The losses for the higher eigenmodes $j > 0$ are now considerably higher than the fundamental mode (compare Figs. 2 and 6(a)), thusly, mode selection among transverse modes occurs through amplification of the radiation, because of the differences in the filling factor $f_n$.


## ACKNOWLEDGEMENT

This work supported by ONR Contract No. N00014-87-0066 through National Institute of Standards and Technology (NIST).

## APPENDIX A. Computation of the Reflection Matrix Element

The associated Laguerre polynomials are given by

$$L_m^p(\xi) = \sum_{k=0}^{m} (-1)^k \frac{(m+p)!}{k!(m-k)!(p+k)!} \xi^k \ . \tag{A1}$$

Substituting (A1) inside (15) and integrating by factors, using

$$\int d\xi \ \xi^n \ e^{-\xi} = - \ e^{-\xi} \left[ \sum_{k=0}^{m} \frac{m!}{(m-k)!} \xi^{m-k} \right] , \tag{A2}$$

one obtains

$$R_{nq}^{mp}(\mu,\alpha) = \delta_{pq} \left[ m!n!(m+p)!(n+q)! \right]^{1/2} \frac{\alpha^{p+1}}{\left(\frac{1+\alpha^2}{2}\right)^{p+1}} \sum_{k=0}^{m} \sum_{l=0}^{n} \alpha^{2k} \left(\frac{2}{\alpha^2+1}\right)^{k+l}$$

$$\frac{(-1)^{k+l}(k+l+p)!}{k!l!(m-k)!(n-l)!(p+k)!(p+l)!} \left( 1 - e^{-(\alpha^2+1)\mu} \sum_{i=0}^{k+l+p} (2\mu m)^{k+l+p-i} \frac{\left(\frac{\alpha^2+1}{2}\right)^{p-i}}{(k+l+p-1)!} \right). \tag{A3}$$

## REFERENCES


1. S. Penner et al., IEEE Tras. Nucl. Sci. NS-32 (5), 2669 (1985).
2. C. M. Tang, P. Sprangle, S. Penner and X. Maruyama, J. Appl. Phys. 63, 5233 (1988).
3. S. Penner et al. Nucl. Instr. and Methods Phys. Res., A272, 73 (1988).
4. See, for example, H. A. Haus in Waves and Fields in Optoelectronics, (Prentice Hall, New Jersey, 1984), p. 180, and references therein.
5. S. Riyopoulos, C. M. Tang and P. Sprangle, IEEE J. Quant. Electronics, 25, 803 (1989).
6. S. Riyopoulos, P. Sprangle, C. M. Tang and A. Ting, Nucl. Instr. and Methods in Phys. Res. A272, 543 (1988).

## FIGURE CAPTIONS

Figure 1. Schematic illustration of the NIST/NRL optical cavity.

Figure 2. Fractional per round trip power loss versus wavelength for the first five resonator eigenmodes in vacuum. The Rayleigh length b is half the wiggler length. The cavity parameters for the half wiggler arrangement are $L_1$ = 521cm, $L_2$ = 386cm, $R_1$ = 543cm, $R_2$ = 417cm and $\rho_1 = \rho_2$ = 2.54cm.

Figure 3. Expansion coefficients into vacuum modes for (a) the fundamental (b) the first and (c) the second cavity eignmodes versus wavelength.

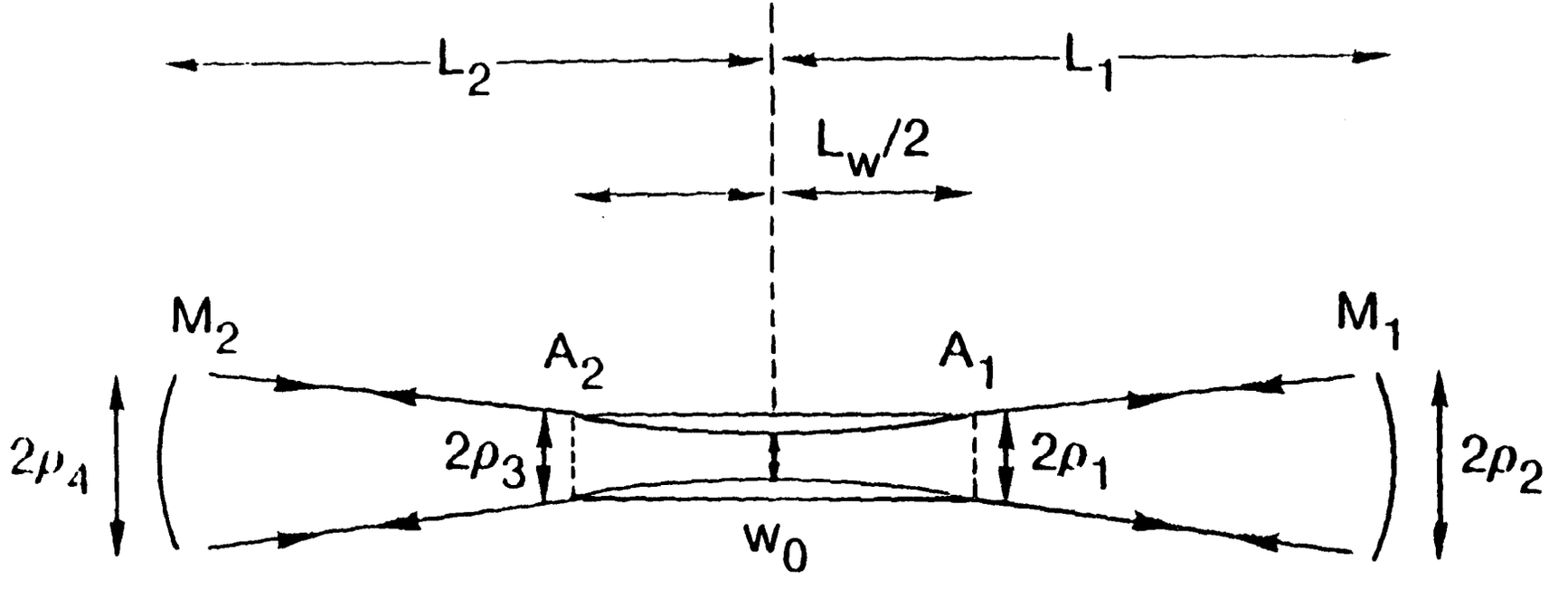
Figure 4. The transverse amplitude profiles $|A(r)|$ for the first three axisymmetric cavity modes for wavelenth (a) $\lambda$ = 2.2μm and (b) $\lambda$ = 10.0μ.

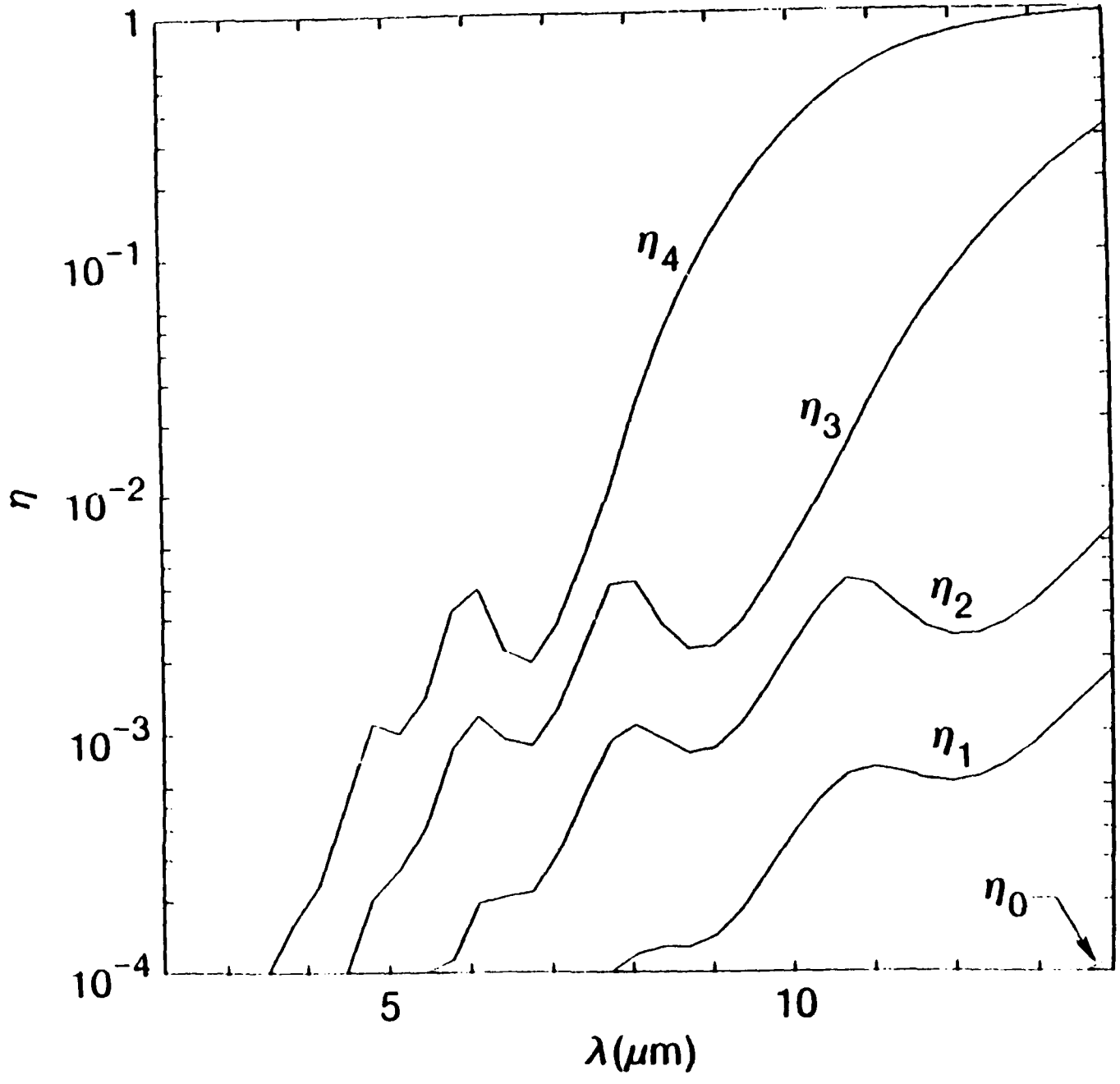
Figure 5. Fundamental cavity mode structure for Rayleigh length b = $L_w/6$ and corresponding mirror curvatures $R_1$ = 523cm and $R_2$ = 389cm. (a) fractional round trip losses for the first four eigenmodes and (b) expansion coefficients of the fundamental cavity mode in vacuum modes versus wavelength. (c)-(d) transverse profiles for the first three cavity modes at wavelengths 2.2μm and 10μm.

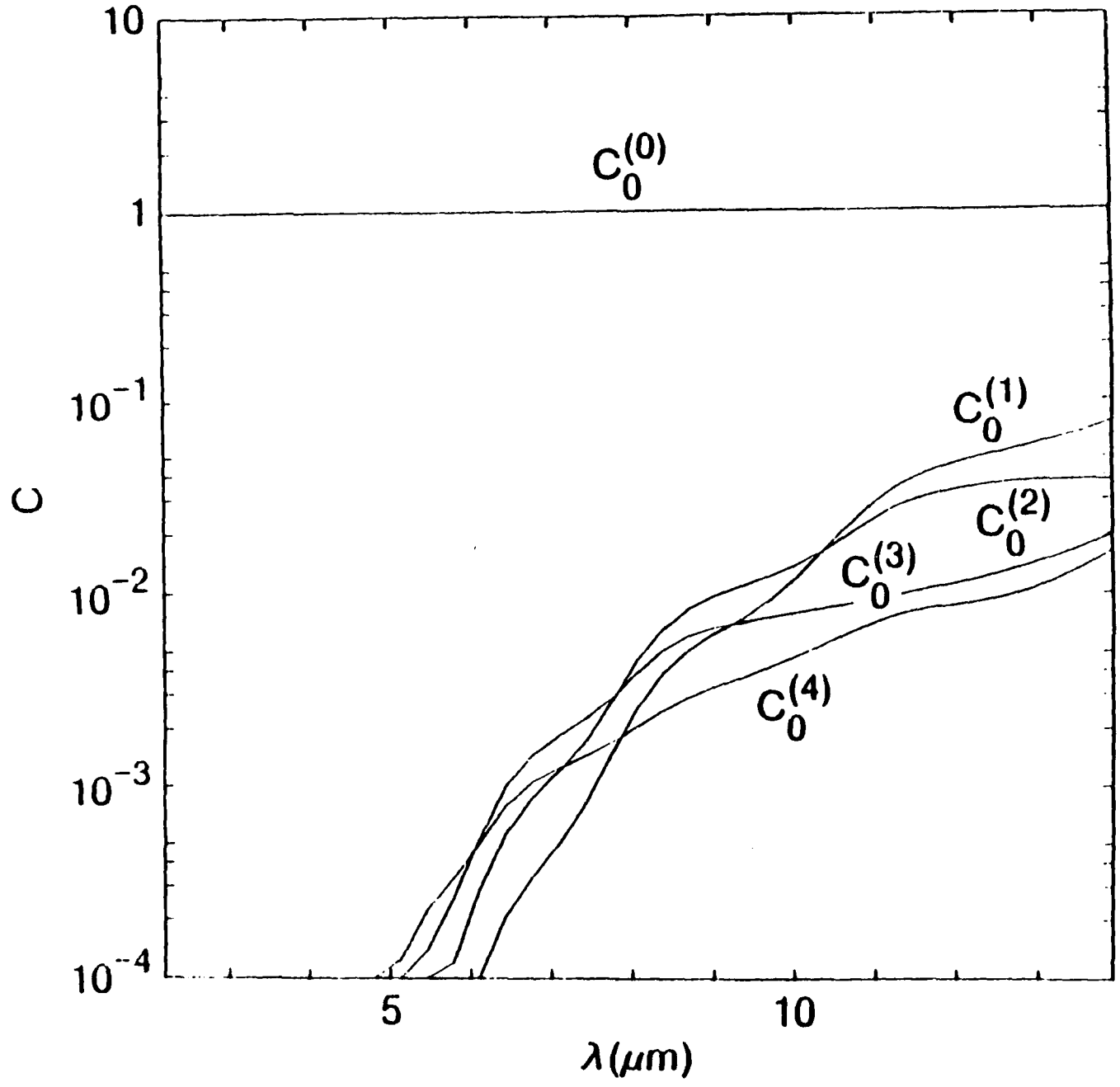
Figure 6. Same as in Fig. 2, including the effects of the beam filling factor for small gain.

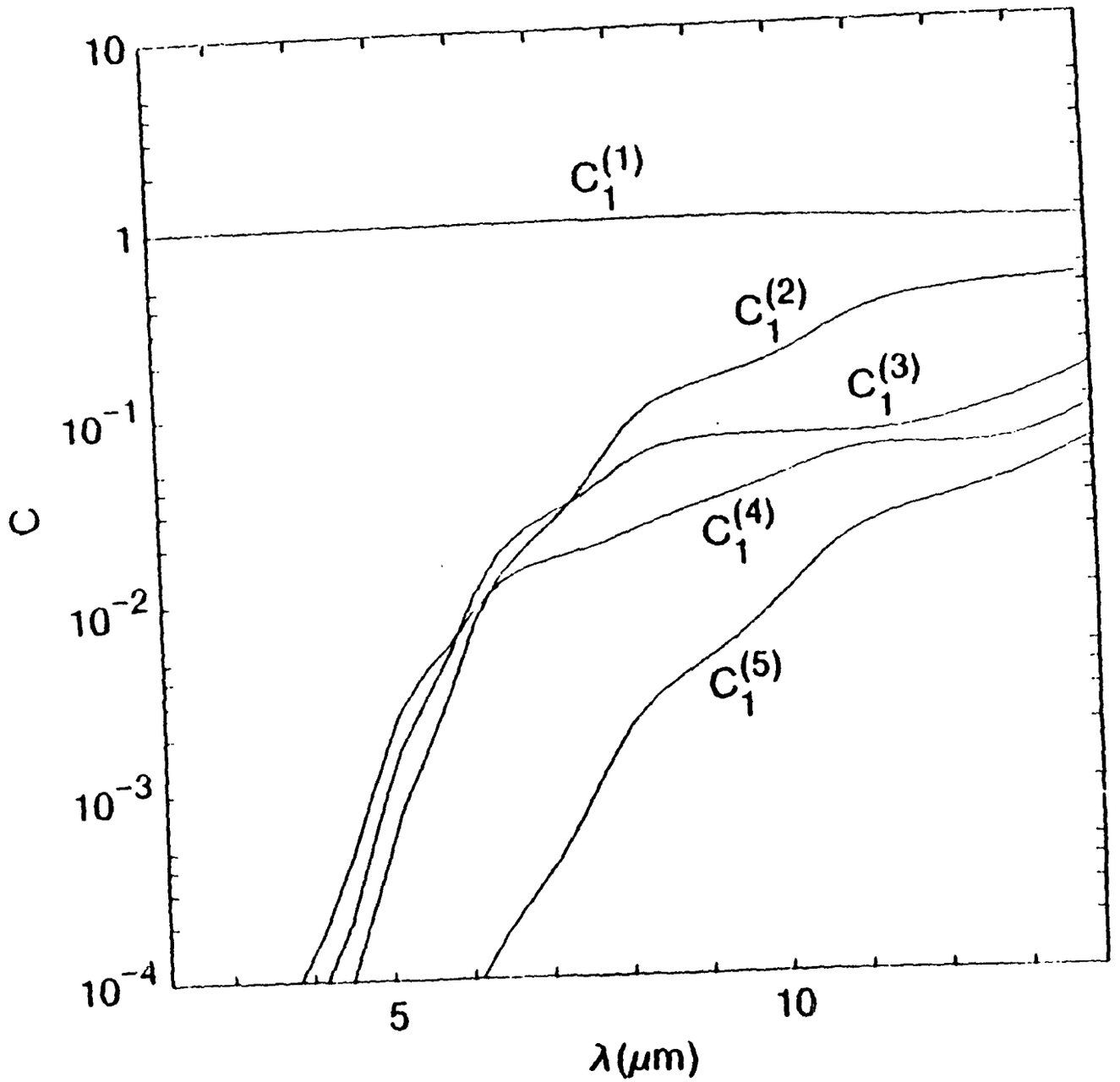
Figure 7. Structure of the combined beam-cavity eigenmodes. Same notation as in Fig. 3.

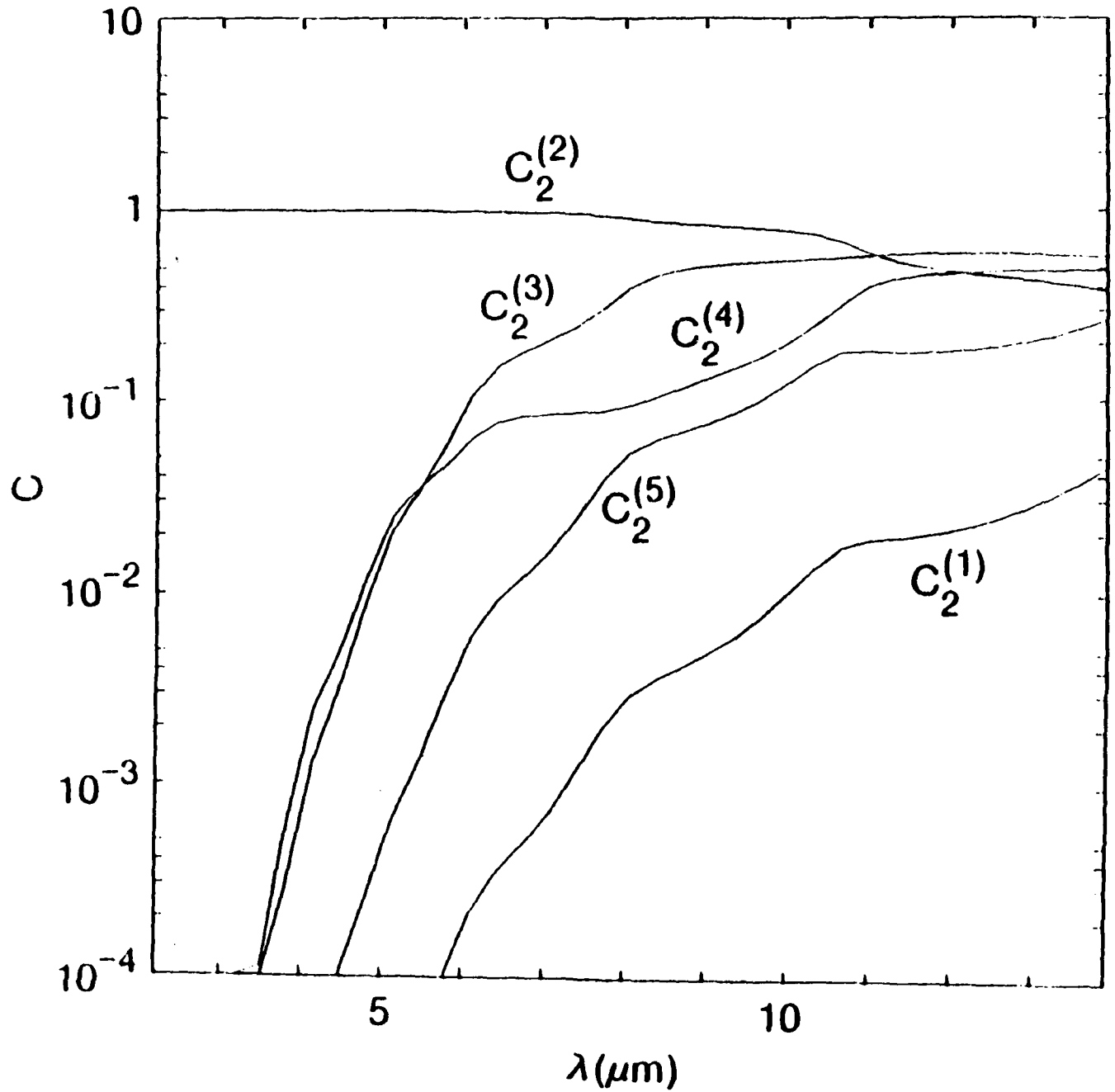
Figure 8. Profiles of the first three beam-cavity eigenmodes. Same notation as in Fig. 4.

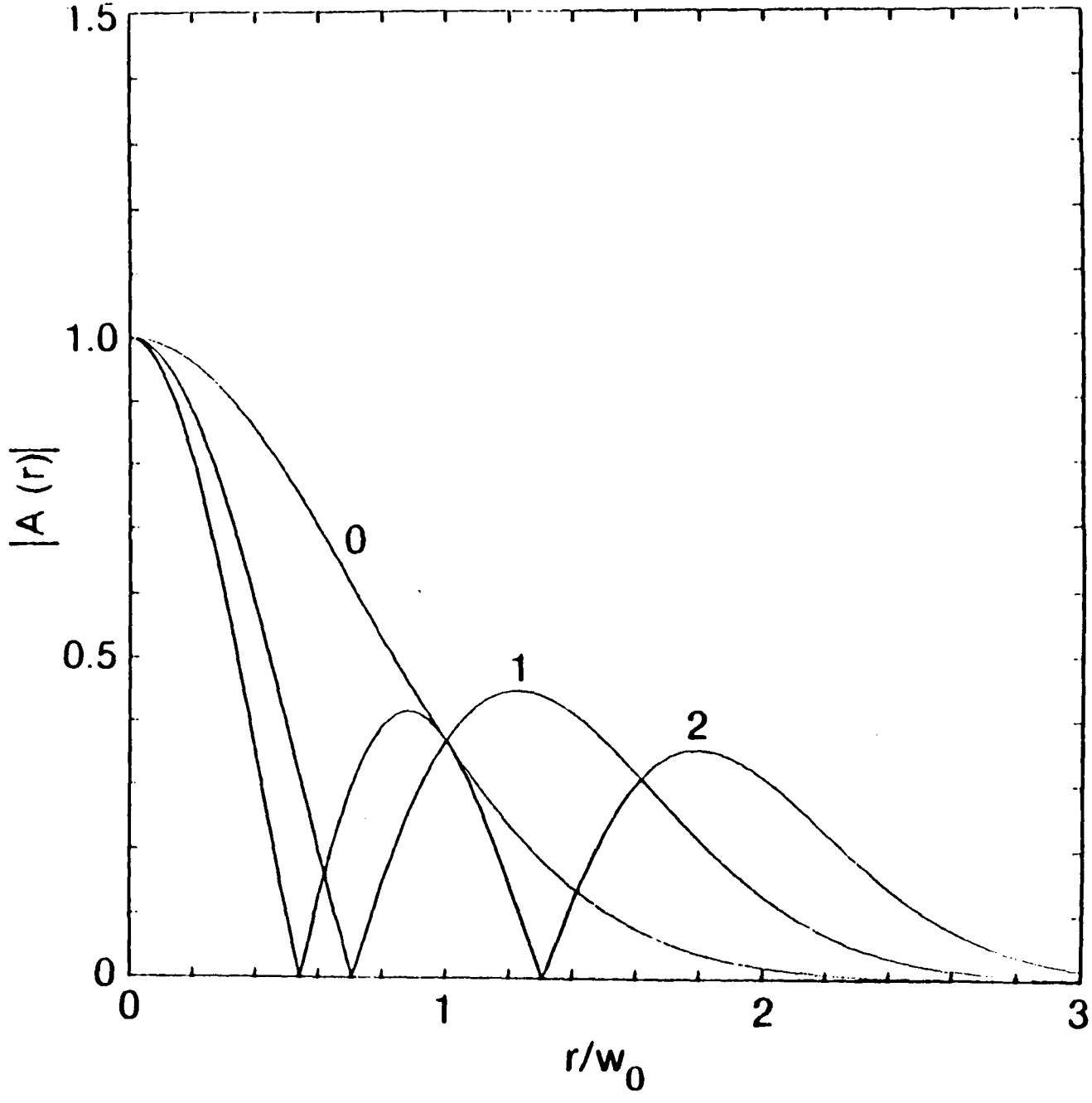

$L_2$
$L_1$
$L_w/2$
$M_2$
$A_2$
$A_1$
$M_1$
$2\rho_4$
$2\rho_3$
$2\rho_1$
$2\rho_2$
$w_0$

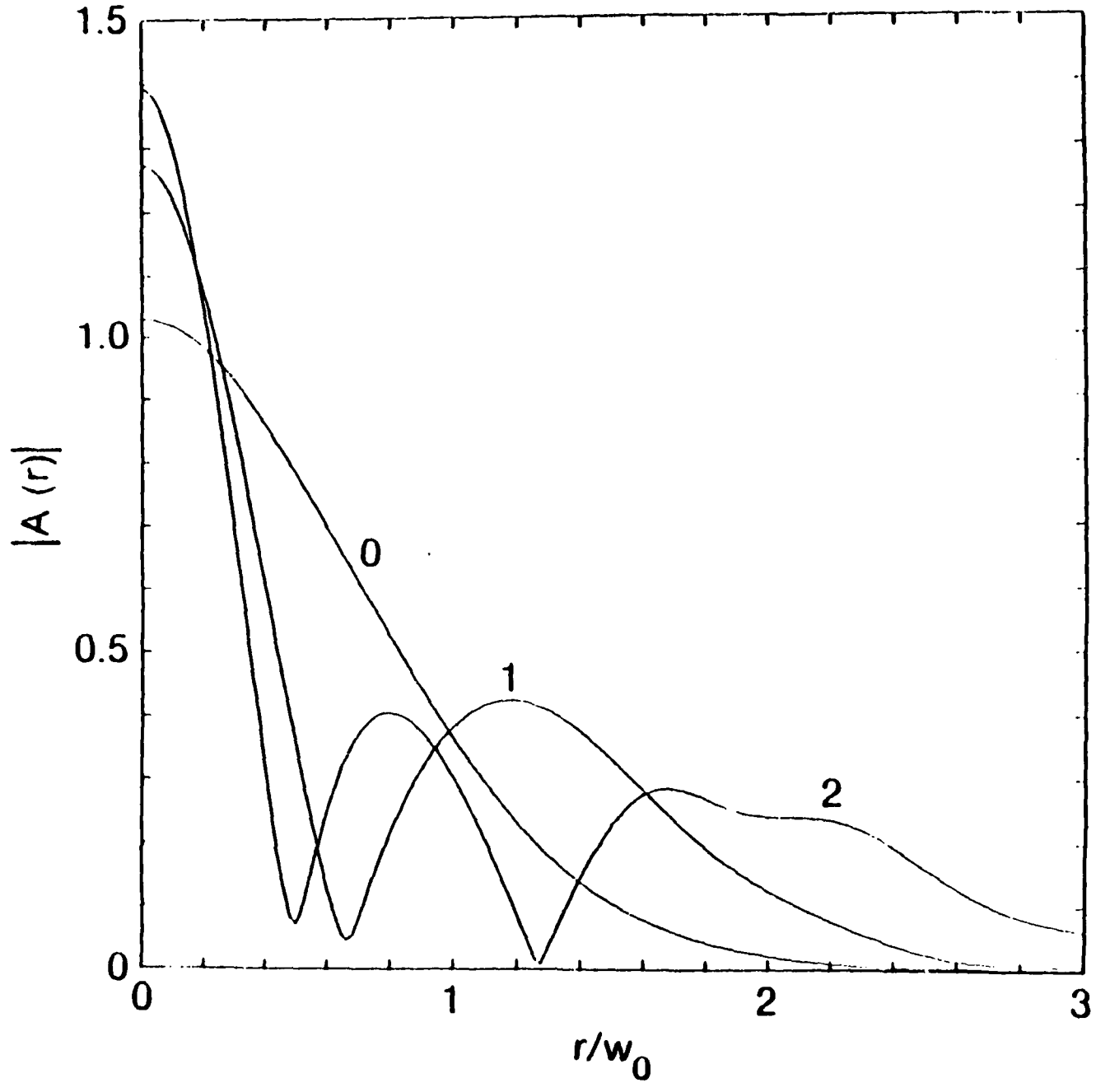

1
$10^{-1}$
$10^{-2}$
$10^{-3}$
$10^{-4}$
η
$\eta_4$
$\eta_3$
$\eta_2$
$\eta_1$
$\eta_0$
5
10
λ(μm)

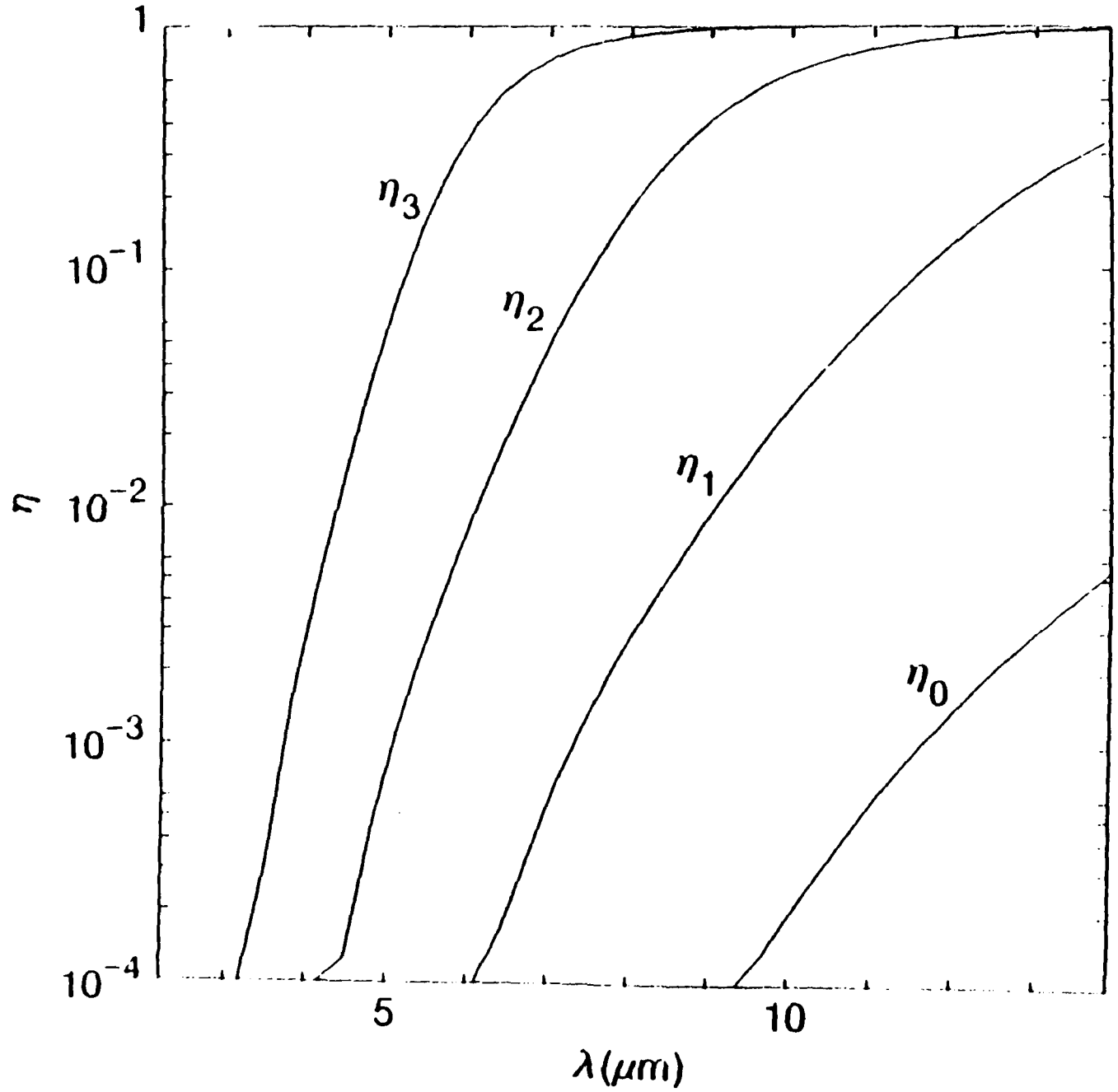

10
1
$10^{-1}$
$10^{-2}$
$10^{-3}$
$10^{-4}$
C
$C_0^{(0)}$
$C_0^{(1)}$
$C_0^{(2)}$
$C_0^{(3)}$
$C_0^{(4)}$
5
10
λ(μm)

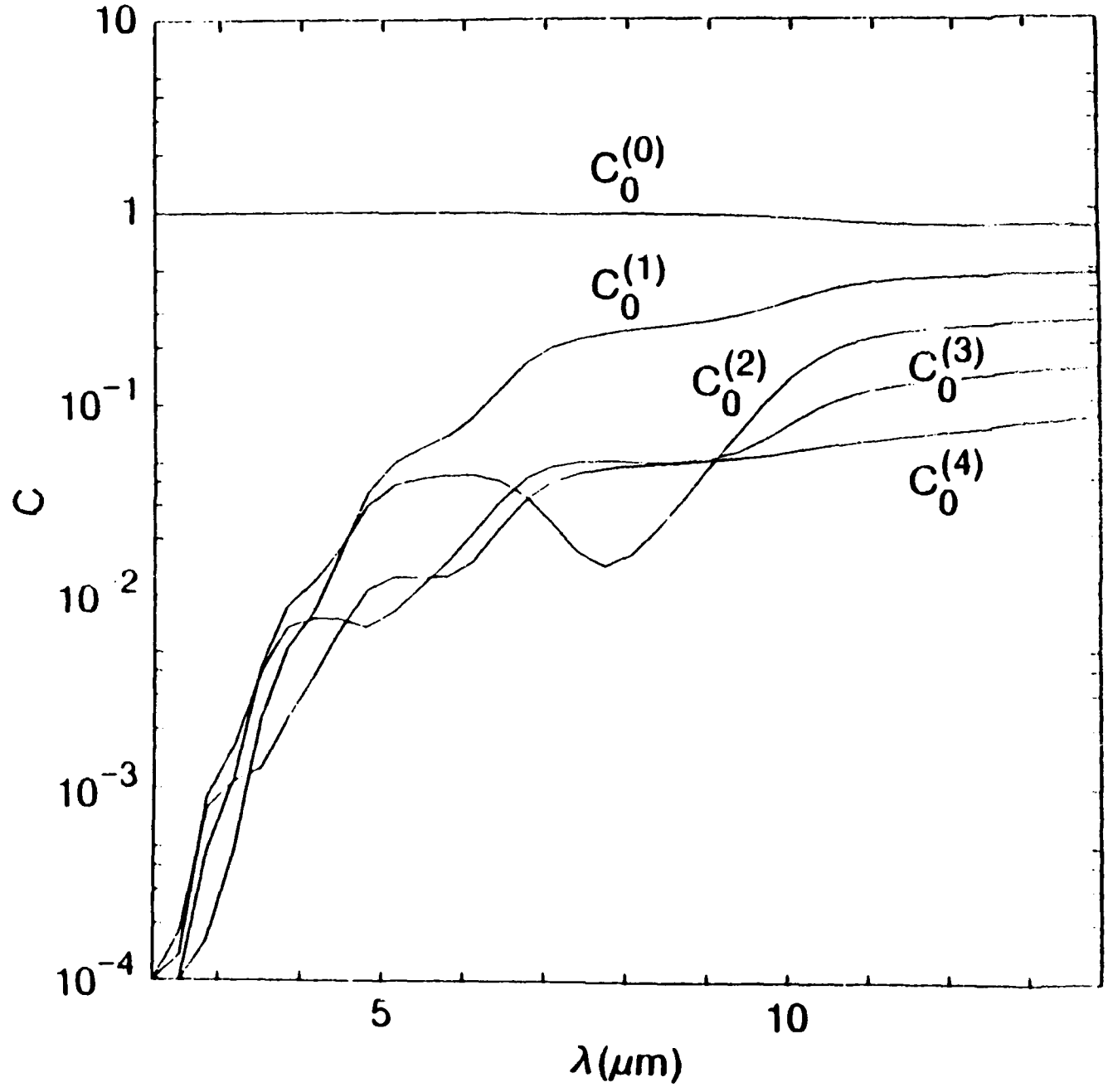

10
1
$10^{-1}$
$10^{-2}$
$10^{-3}$
$10^{-4}$
C
$C_1^{(1)}$
$C_1^{(2)}$
$C_1^{(3)}$
$C_1^{(4)}$
$C_1^{(5)}$
5
10
$\lambda(\mu m)$

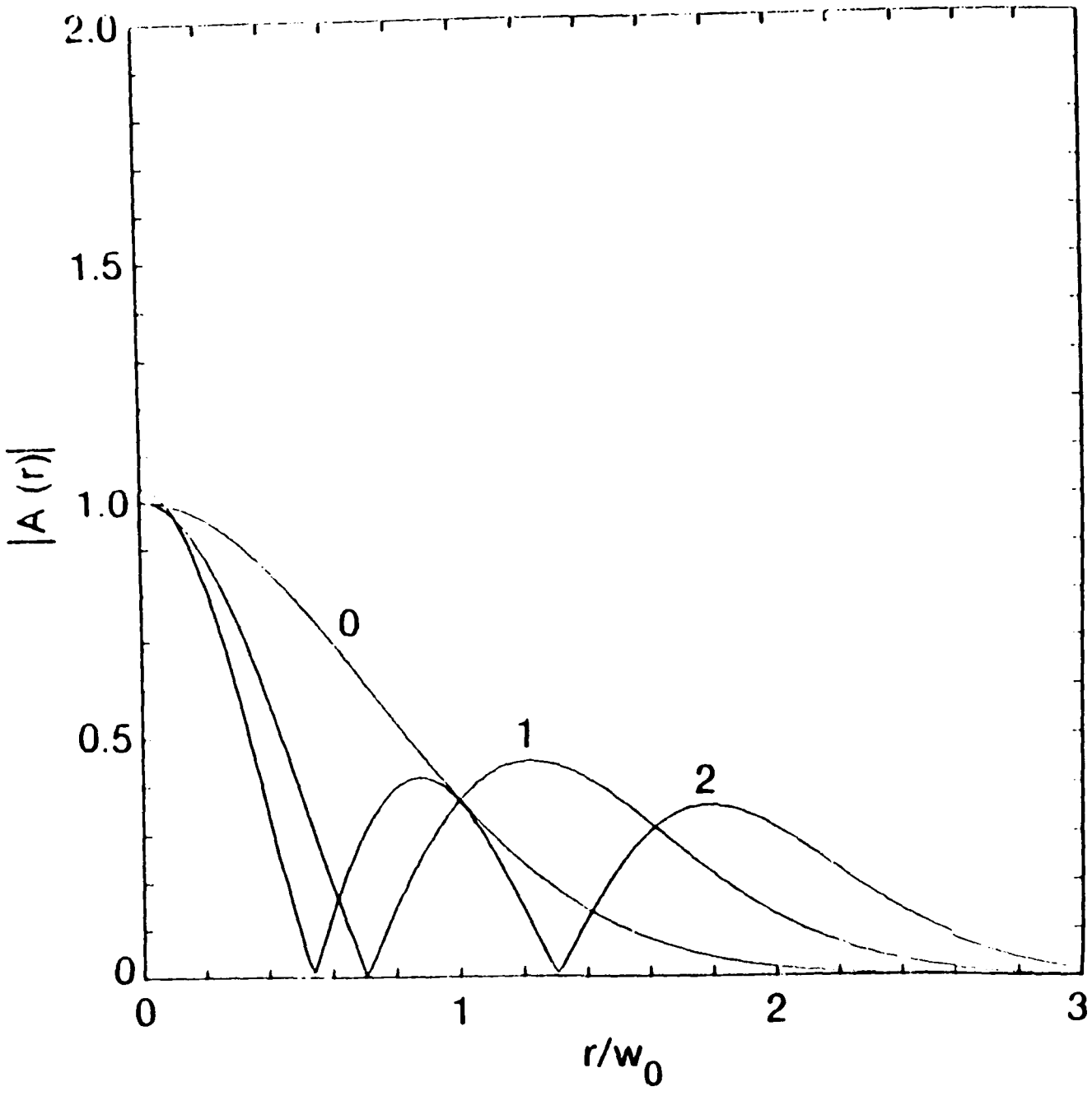

10
1
$10^{-1}$
$10^{-2}$
$10^{-3}$
$10^{-4}$
C
$C_2^{(2)}$
$C_2^{(3)}$
$C_2^{(4)}$
$C_2^{(5)}$
$C_2^{(1)}$
5
10
λ(μm)

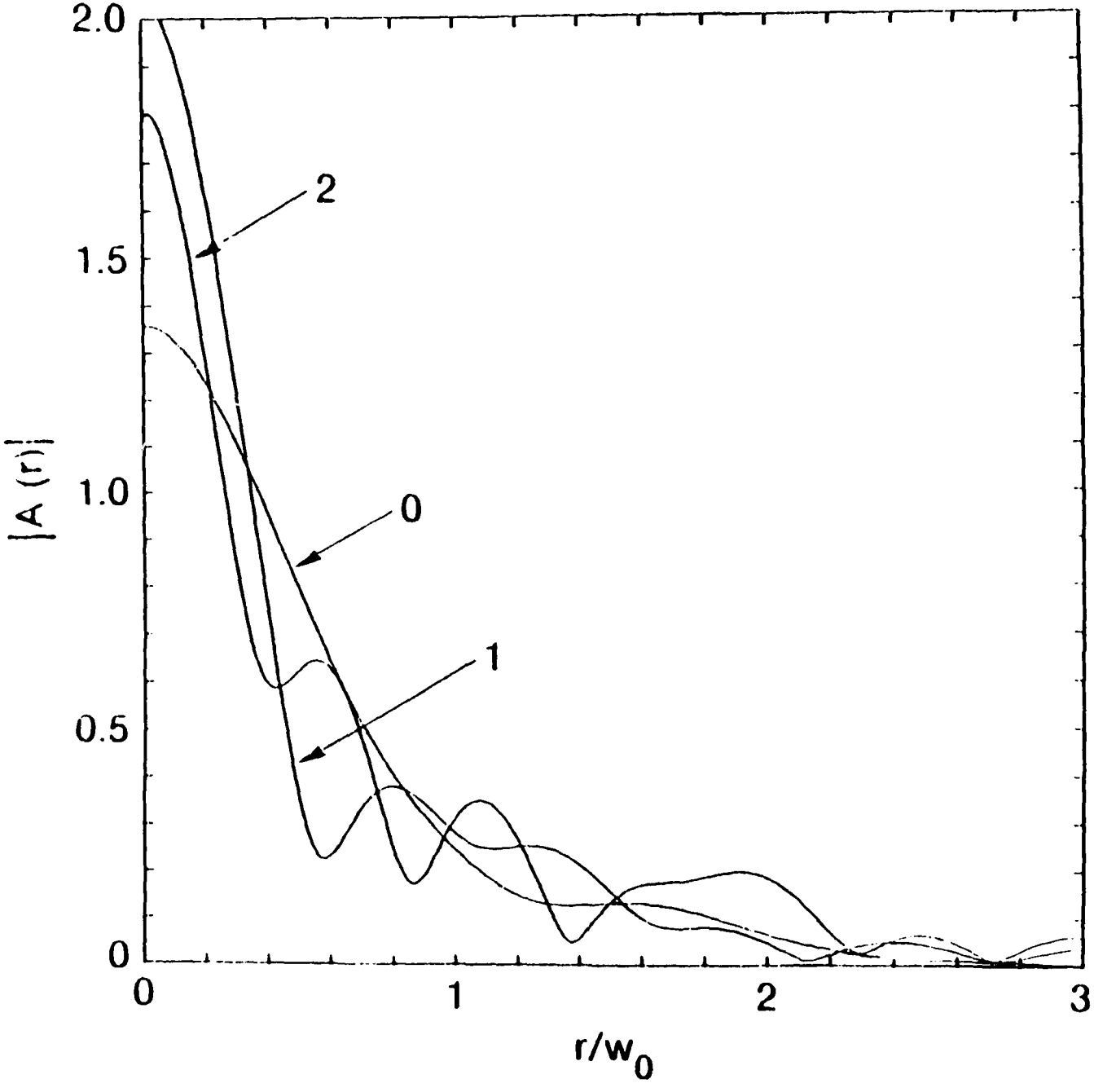

1.5
1.0
0.5
0
|A (r)|
0
1
2
3
r/w0
0
1
2

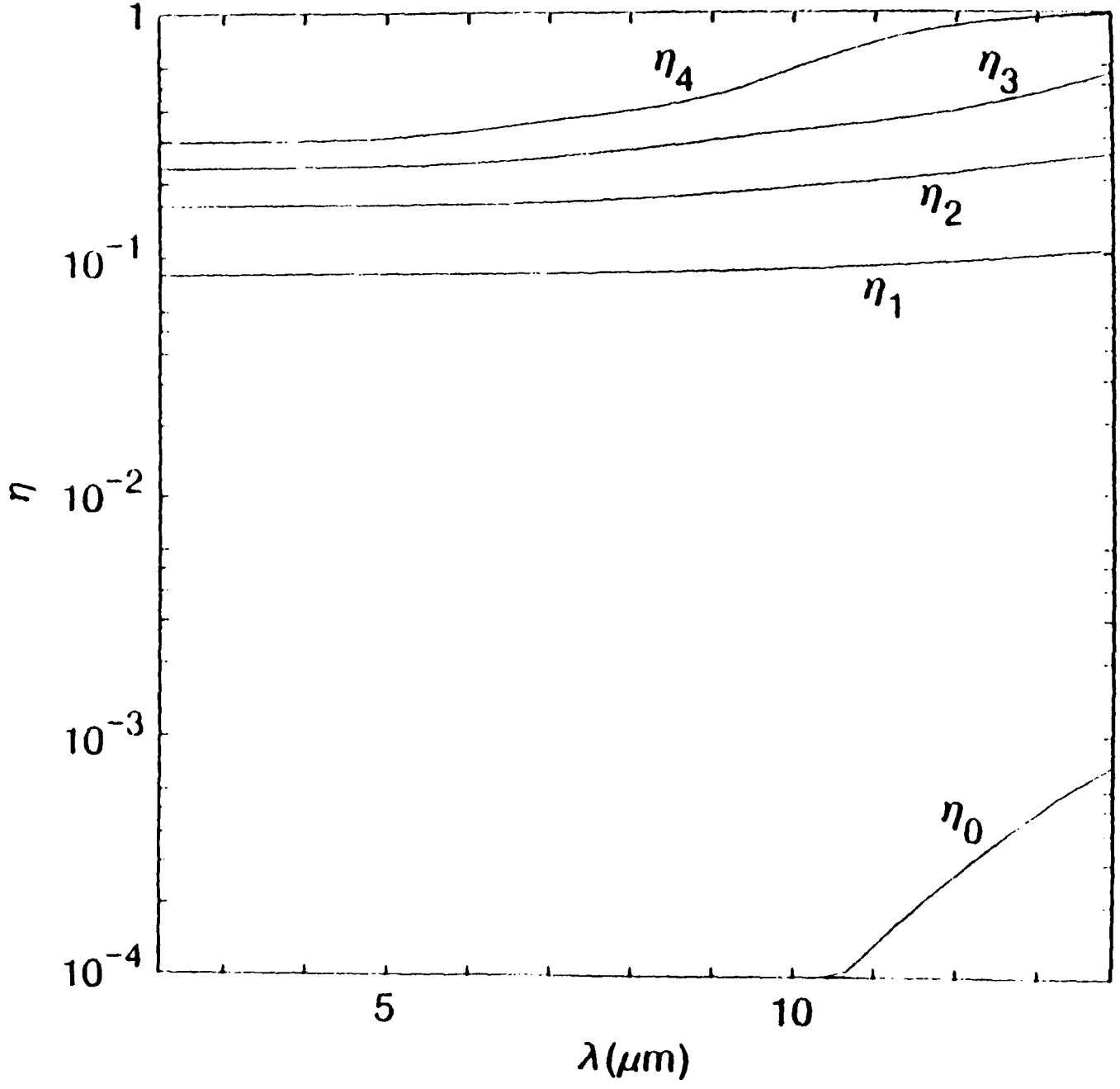

1.5
1.0
0.5
0
|A (r)|
0
1
2
3
r/w0
0
1
2

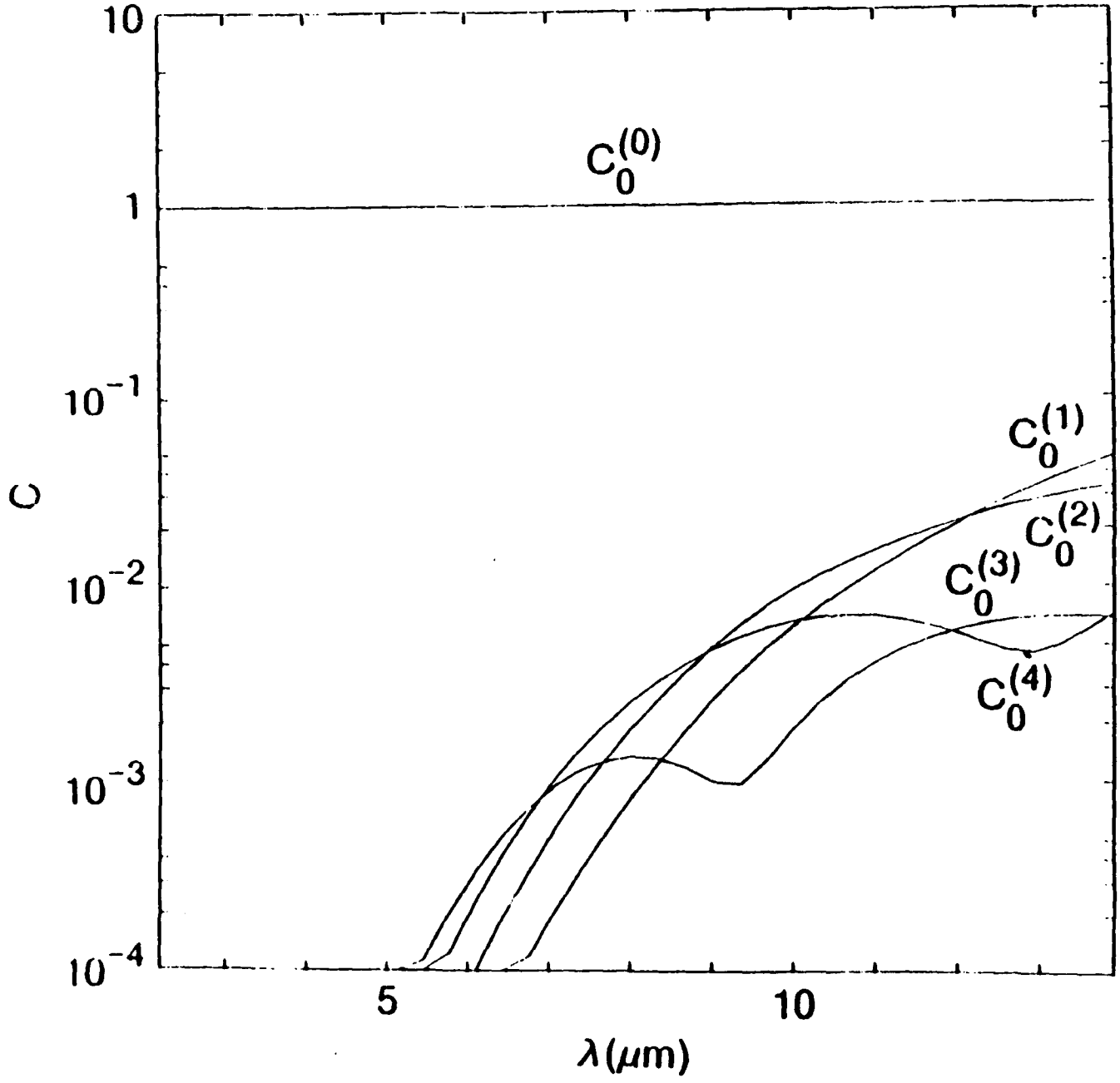

1
$10^{-1}$
$10^{-2}$
$10^{-3}$
$10^{-4}$
$\eta$
$\eta_3$
$\eta_2$
$\eta_1$
$\eta_0$
5
10
$\lambda(\mu m)$

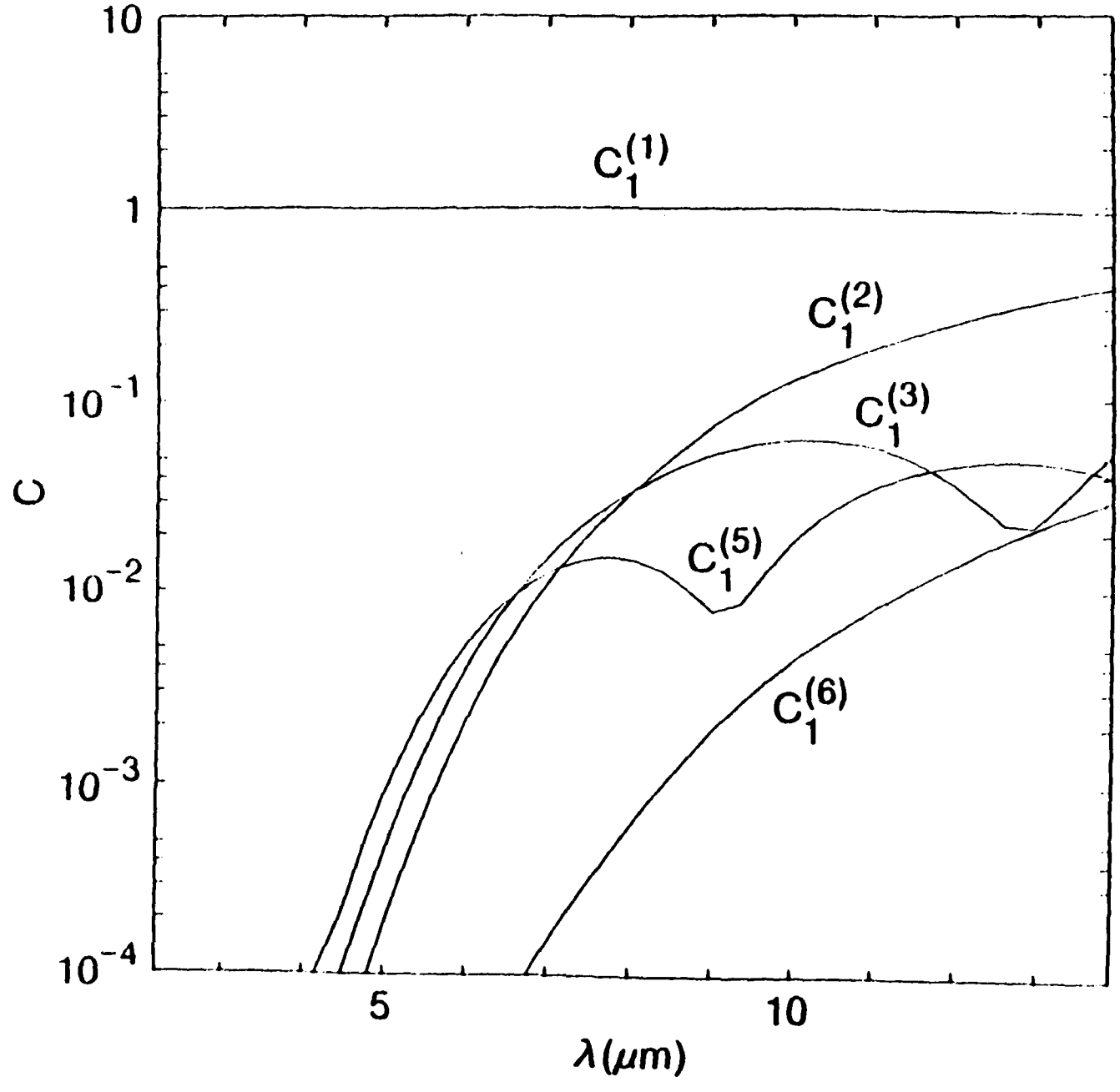

10
1
$10^{-1}$
$10^{-2}$
$10^{-3}$
$10^{-4}$
C
$C_0^{(0)}$
$C_0^{(1)}$
$C_0^{(2)}$
$C_0^{(3)}$
$C_0^{(4)}$
5
10
λ(μm)

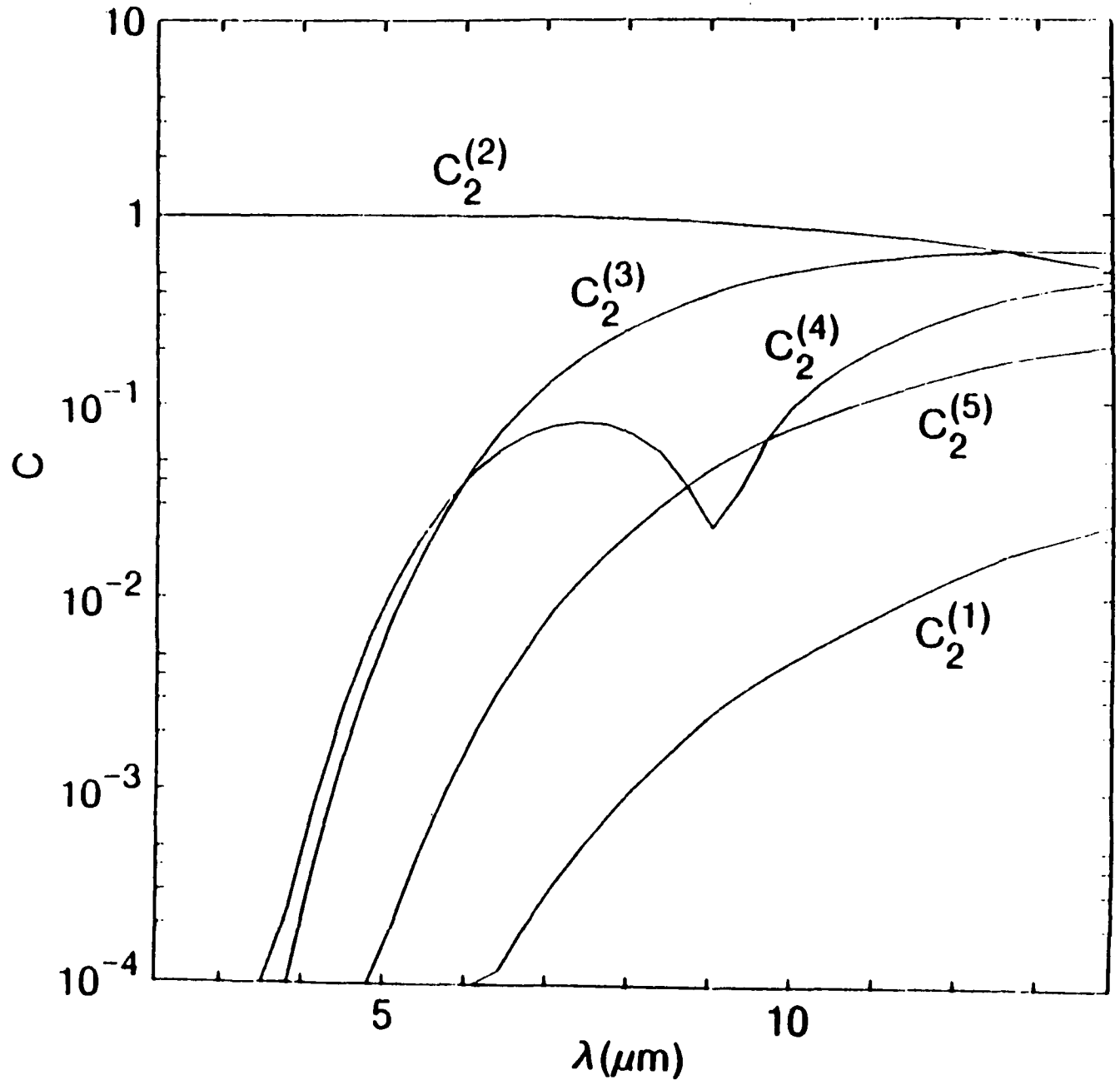

2.0
1.5
1.0
0.5
0
|A (r)|
0
1
2
3
r/w0
0
1
2

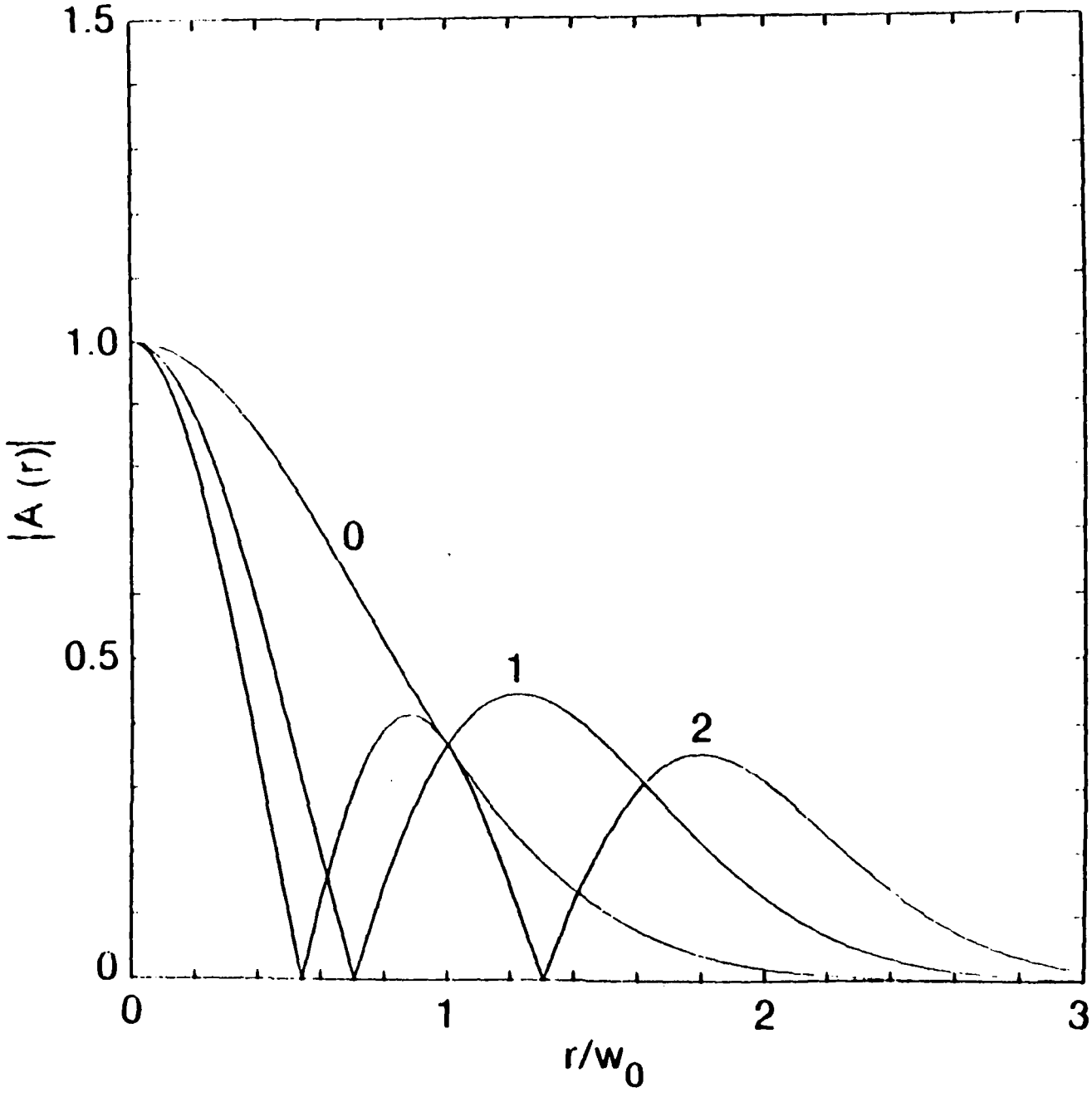

2.0
1.5
1.0
0.5
0
|A (r)|
0
1
2
3
r/w0
2
0
1

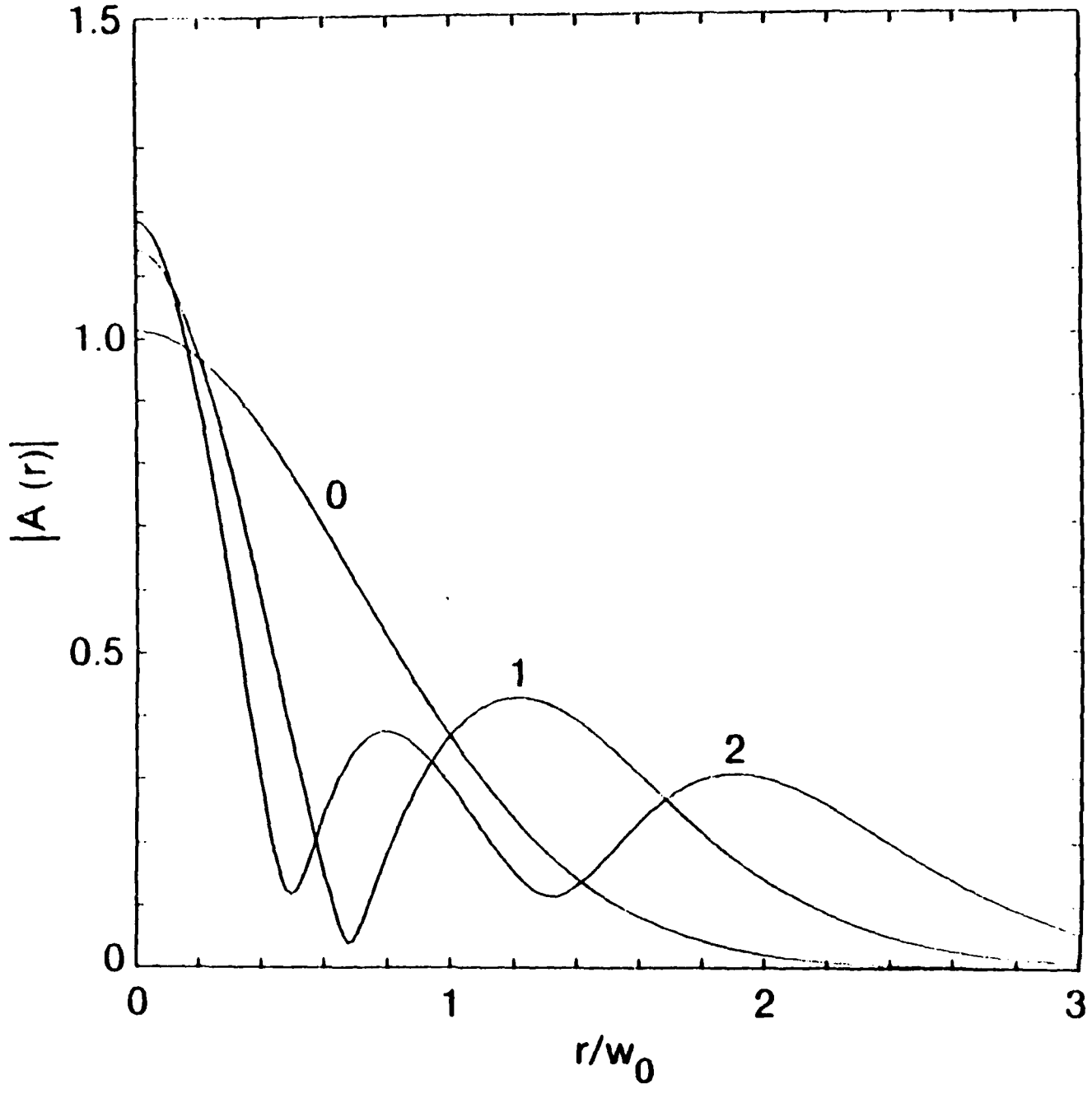

1
$10^{-1}$
$10^{-2}$
$10^{-3}$
$10^{-4}$
$\eta$
$\eta_4$
$\eta_3$
$\eta_2$
$\eta_1$
$\eta_0$
5
10
$\lambda(\mu m)$


10
1
$10^{-1}$
$10^{-2}$
$10^{-3}$
$10^{-4}$
C
$C_0^{(0)}$
$C_0^{(1)}$
$C_0^{(2)}$
$C_0^{(3)}$
$C_0^{(4)}$
5
10
$\lambda(\mu m)$


10
1
$10^{-1}$
$10^{-2}$
$10^{-3}$
$10^{-4}$
C
$C_1^{(1)}$
$C_1^{(2)}$
$C_1^{(3)}$
$C_1^{(5)}$
$C_1^{(6)}$
5
10
$\lambda(\mu m)$


10
1
$10^{-1}$
$10^{-2}$
$10^{-3}$
$10^{-4}$
C
$C_2^{(2)}$
$C_2^{(3)}$
$C_2^{(4)}$
$C_2^{(5)}$
$C_2^{(1)}$
5
10
$\lambda(\mu m)$


1.5
1.0
0.5
0
|A (r)|
0
1
2
3
r/w0
0
1
2


1.5
1.0
0.5
0
|A (r)|
0
1
2
3
r/w0
0
1
2

# APPENDIX OO

## Beam Conditioning Using Resistive Wires

# BEAM CONDITIONING USING RESISTIVE WIRES

R.F. Fernsler, Naval Research Laboratory, Washington, DC, USA
P.R. Boris, SAIC, McLean, VA, USA

## ABSTRACT

A resistive wire strung between two end plates of an evacuated metallic chamber is a simple yet effective means for centering and conditioning a relativistic electron beam. This paper presents a circuit equation for computing the charge and current induced on the wire by the beam. Use of the circuit equation is illustrated by coupling it to a beam envelope equation to determine the response of a centered, axisymmetric beam to the wire charge and current.

## INTRODUCTION

Resistive wires have been shown experimentally[1] to be capable of centering and conditioning a relativistic electron beam. Previous analyses[2-4] of wire conditioning assumed a static wire charge and no wire current. This assumption is valid, however, only in the beam body and only for selected values of the wire resistance and length. To avoid these restrictions and to model the beam front where conditioning is often most important, a dynamical model for the wire current and charge is required. Such a model is described herein and should provide a more accurate description of beam behavior.

## WIRE CIRCUIT EQUATION

Consider a wire of distributed resistance $R_w$ and length $z_w$ centered within an evacuated metallic chamber of radius b. For simplicity, assume that the wire is small and hollow with a radius $a_w \ll b$. An electron beam entering the chamber induces on the wire a distributed charge $\lambda_w$ and current $I_w$ that determine the pinch and centering forces felt by the beam. To avoid solving Maxwell's equations in full, we derive in this section a simplified circuit equation for computing $\lambda_w$ and $I_w$.

The wire circuit equation is comprised of three parts. The first follows directly from charge conservation and relates the distributed wire charge to the wire current:

$$\frac{\partial}{\partial t}\lambda_w = -\frac{\partial}{\partial z} I_w. \tag{1}$$

The second part uses Ohm's law to relate $I_w$ to the average axial electric field in the wire:

$$I_w = E_{zw}/R_w. \tag{2}$$

The third part uses Maxwell's equations plus suitable approximations to express the wire field $E_{zw}$ in terms of $\lambda_w$ and $I_w$.

To compute $E_{zw}$, we write Maxwell's equations in the form

$$\nabla^2 E_z = 4\pi \frac{\partial}{\partial z}(\rho_b + \rho_w) + \frac{1}{c}\frac{\partial}{\partial t}\left[\frac{4\pi}{c}(J_b + J_w) + \frac{1}{c}\frac{\partial}{\partial t} E_z\right] \tag{3}$$

where $E_z$ is the axial electric field, $\rho_b$ and $\rho_w$ are the charge densities of the beam and wire, respectively, and $J_b$ and $J_w$ are the axial current densities of the beam and wire, respectively. The beam current density is related to the charge density through $J_b = \rho_b \beta c$ where $\beta c$ is the axial beam velocity. For ultrarelativistic beams, $\beta \to 1$ and may be taken as constant. One can then set

$$c\frac{\partial}{\partial z}\rho_b + \frac{1}{c}\frac{\partial}{\partial t} J_b = \left[\frac{1}{\beta}\frac{\partial}{\partial z} + \frac{1}{c}\frac{\partial}{\partial t}\right] J_b$$

$$= \left[\left(\frac{1}{c}\frac{\partial}{\partial t}\right)_\zeta + \frac{1}{\beta\gamma^2}\left(\frac{\partial}{\partial \zeta}\right)_t\right] J_b \tag{4}$$

where $\zeta \equiv \beta ct - z$ measures distance behind the beam head, $\gamma^2 \equiv 1/(1-\beta^2)$ is the usual relativistic factor, and the subscript on partial derivatives indicates that the variable is to be held constant. For $\gamma^2 \gg 1$, Eqs. (3) and (4) reduce to

$$\nabla_\perp^2 E_z = 4\pi\left[\frac{\partial \rho_w}{\partial z} + c^{-2}\frac{\partial J_w}{\partial t}\right] + \frac{4\pi}{c}\left(\frac{1}{c}\frac{\partial}{\partial t}\right)_\zeta J_b$$

$$+ \left[\left(\frac{1}{c}\frac{\partial}{\partial t}\right)^2 - \left(\frac{\partial}{\partial z}\right)^2\right] E_z \tag{5}$$

where $\nabla_\perp^2$ is the Laplacian operator in the transverse plane.

A simple expression for the wire field $E_{zw}$ can be obtained from Eq. (5) by dropping the last term in brackets. Such neglect is well justified, except within a few beam radii of the end plates, provided:

$$b/\zeta_b < 1 \tag{6}$$

and

$$a_w << b < z_w \tag{7}$$

where $\zeta_b$ characterizes axial variations (rise length, etc.) of the beam. After dropping the last term, the wire field is obtained by integrating Eq. (5) using the boundary condition that $E_z = 0$ at $r = b$:

$$\begin{aligned} E_{zw} &\equiv \frac{1}{2\pi}\int_0^{2\pi} d\theta \; E_z(r=a_w,\theta,z,t) \\ &= -\int_{a_w}^{b}\frac{dl}{r}\int_0^{r} dr' \, r' \int_0^{2\pi} d\theta \, \frac{1}{2\pi} \, \nabla_\perp^2 E_z \\ &= -C_w^{-1}\frac{\partial}{\partial z}\lambda_w - L_w\frac{\partial}{\partial t} I_w - \left(\frac{1}{c}\frac{\partial}{\partial t}\right)_\zeta \left(C_b^{-1}\frac{I_b}{c}\right). \end{aligned} \tag{8}$$

Here $I_b(\zeta,t)$ is the total beam current, $C_w$ and $L_w$ are the distributed wire capacitance and inductance, respectively, defined by

$$C_w^{-1} = c^2 L_w = 2\ln(b/a_w), \tag{9}$$

and $C_b$ is the distributed beam capacitance defined by

$$C_b^{-1} = \frac{2}{I_b}\int_{a_w}^{b}\frac{dr}{r} i_b(r,\zeta,t) \tag{10}$$

where $i_b(r,\zeta,t)$ is the fraction of beam current within radius r.

Equations (2) and (8) can be combined to eliminate $E_{zw}$:

$$\left[\frac{\partial}{\partial t} + \frac{1}{\tau_o}\right] I_w = -c^2\frac{\partial}{\partial z}\lambda_w - \left(\frac{\partial}{\partial t}\right)_\zeta \left(\frac{C_w}{C_b} I_b\right) \tag{11}$$

where $\tau_o = L_w/R_w$ is the inductive decay time. Equations (1) and (9)-(11) together with suitable boundary conditions comprise a closed set for $\lambda_w(z,t)$ and $I_w(z,t)$ in terms of the beam current $I_b(\zeta,t)$ and its radial distribution $i_b(r,\zeta,t)$. Recall that the circuit equations do not apply within a short transition zone at the end plates where steep gradients in $E_z$ (but not $E_{zw}$) exist.

## BOUNDARY CONDITIONS

The conducting end plates at $z = 0, z_w$ short-circuit the transverse space-charge field of the beam and convert it into a large but localized axial field $E_z$, as required by conservation of field energy. The axial field drives current that quickly charges the wire so as to reduce and smooth $E_z$. This electrostatic charging of the wire near the end plates occurs in a time $\tau = a_w^2 R_w/4$ that is typically short compared with $\tau_o$ and all other time scales of interest. Away from the end plates, the evolution of $\lambda_w$ and $I_w$ is controlled by $\tau_o$ and the evolution of the beam.

Because the wire charges rapidly near the end plates, one can set $\lambda_w$ equal to its quasi-static equilibrium value. This value may be inferred by setting $I_w$ equal to its steady-state value, zero, and integrating Eq. (11) from $z = 0$ to $z = z_w$ using the transformation $dz = c\,dt$ for fixed $\zeta$. One then concludes that

$$\lambda_w = -\frac{C_w}{C_b}\,\frac{I_b}{c} \tag{12}$$

at $z = 0, z_w$. Previous analyses[1-4] used this steady-state value for all z and t to determine beam behavior. Here we impose the steady-state value only at the end plates and allow the wire current to relax in stages as the electromagnetic discontinuities and reflections generated by condition (12) cause $I_w \to 0$ while leaving $\lambda_w$ finite.

## BEAM DYNAMICS

Within the accuracy of the model, the transverse force on the beam electrons is given by

$$\underset{\sim}{F}_\perp(\underset{\sim}{r}_\perp,z,t) = -\frac{2e}{rc}\,[c\lambda_w(z,t) - I_w(z,t)]\,H(r-a_w)\,\hat{r} \tag{13}$$

where H is the Heaviside step function and $\hat{r}$ is the unit radial vector. The wire return current $I_w$ repels the beam and causes it to expand while the wire charge $\lambda_w$ attracts the beam and causes it to pinch. Beam conditioning requires $\lambda_w > I_w/c$ and ultimately occurs provided the pulse duration is long:

$$\tau_p > z_w/c,\ \tau_o. \tag{14}$$

The beam has time to respond to the wire force provided the beam betatron wavelength is small:

$$\lambda_\beta = 2\pi a_b U^{-1/2} < z_w \tag{15}$$

where $a_b$ is the beam radius,

$$U = 2(c\lambda_w - I_w)/I_A \tag{16}$$

is the dimensionless wire pinch potential, and $I_A = \gamma mc^3/e$ is the Alfven current. The wire pinch potential, which was derived using force equation (13) assuming $a_w << a_b$, is used in the Lee-Cooper envelope equation[5] to determine the self-similar expansion of an axisymmetric beam centered about the wire.

The beam expends energy ohmically in establishing the wire charge $\lambda_w$. Within the confines of the model, the energy loss is given by

$$\frac{d\gamma}{dt} = -\frac{eE_{zw}}{mc^2}\left(\frac{C_b}{C_w}\right) = -\frac{eI_wR_w}{mc^2}\left(\frac{C_b}{C_w}\right) \tag{17}$$

where the factor $C_b/C_w < 1$ accounts for the gradual radial fall-off of $E_z$ outside the wire. One can show that the energy loss is negligible only if

$$I_b/I_A << 2C_b^2/C_w < 1. \tag{18}$$

An important property of the wire force is that it is strongly anharmonic. The resulting spread in betatron frequencies leads to rapid phase-mix damping[3] which dissipates both sausage-like and hose-like oscillations of the beam. An off-center or mismatched beam will thus eventually stabilize about the wire but with increased beam emittance and radius. Less advantageous is that the anharmonic character of the wire force can cause the beam to develop broad wings. Neglecting cut-off at the chamber wall, the equilibrium beam current density is given by

$$J_{bo}(r,\zeta,t) = \frac{I_b(\zeta)}{\pi a_w^2}\,\frac{x}{1-x}\,(a_w/r)^{2x} \tag{19a}$$

where

$$x \equiv e(c\lambda_w - I_w)/cT_\perp \tag{19b}$$

and $T_\perp$ is the transverse beam temperature. Note that pinched equilibria

exist only if the beam is cool, $T_\perp < e(c\lambda_w - I_w)/c < eI_b/c$. Whether broad beam wings cause propagation problems outside the wire cell depends on the application. A particle code rather than an envelope model is required to address this issue.

## CONCLUSION

A dynamical circuit equation for the current and charge induced on a resistive wire by a passing relativistic electron beam has been constructed from Maxwell's equations. The circuit equation is simple to implement and provides an accurate means for computing the transverse force on beam electrons inside the wire cell. The model allows arbitrary spatial distribution for the beam current and can be used, when coupled to a particle code, to predict both conditioning and centering of the beam. To test the model, we have coupled it to an envelope code to predict the evolution of beam radius and emittance. The behavior of the beam inside the cell is controlled by varying the wire resistance and length.

This work was supported by the Defense Advanced Research Projects Agency under ARPA Order No. 4395, Amendment No. 69, and monitored by the Naval Surface Warfare Center.

## REFERENCES

1. D.S. Prono, G.J. Caporaso, J.C. Clark, E.J. Lauer and K.W. Struve, IEEE Trans. Nuc. Sci. NS-30, 2510 (1983).
2. G.J. Caporaso and A.G. Cole, IEEE Trans. Nuc. Sci. NS-30, 2618 (1983).
3. D.S. Prono, et al., Phys. Rev. Lett. 51, 723 (1983).
4. R.J. Adler, "Wire Focusing for Hollow Electron Beams", Mission Research Corporation Report AMRC-R-594 (1984).
5. E.P. Lee and R.K. Cooper, Particle Accel. 7, 83 (1976).

# APPENDIX PP

## Resistive Wire Conditioning

# RESISTIVE WIRE CONDITIONING

R. F. Fernsler and S. P. Slinker
Naval Research Laboratory
P. R. Boris
SAIC

## 1. Introduction

An evacuated resistive-wire cell is a convenient, passive device for conditioning and centering a relativistic electron beam.[1] In a previous paper[2] we derived a circuit equation for modeling the dynamical response of the wire, and illustrated use of the circuit equation through a beam envelope model. Here we extend the computational analysis by coupling the wire circuit equation to a particle pusher.

## 2. Particle Equations

Two equations are used to push the beam electrons.[3] The first is the transverse force equation:

$$\underset{\sim}{F}_{\perp}(\underset{\sim}{r}_{\perp},z,t) = \frac{2e}{rc}\left[c\lambda_w(z,t) - I_w(z,t)\right] H(r-a_w)\,\hat{r} \qquad (1)$$

where H is the Heaviside step function and $\hat{r}$ is the unit radial vector. The wire return current $I_w$ repels the beam and causes it to expand, while the wire charge $\lambda_w$ attracts the beam and causes it to pinch and center.

The second equation describes axial energy loss and is given by

$$\frac{d\gamma}{dt} = \frac{eI_wR_w}{mc}\begin{cases} \ln(b/a_w)/\ln(b/r), & r \geq a_w \\ 1, & r \leq a_w \end{cases} \qquad (2)$$

where $R_w$ is the distributed wire resistance, $a_w$ is the wire radius, and $b >> a_w$ is the wall radius. The circuit equations used to determine $\lambda_w$ and $I_w$ are given in Ref. 2.

## 3. Envelope Model Versus Particle Pusher

The above equations were solved using the following beam parameters at injection: energy $\gamma_o = 10$; peak current $I_{bo} = 10$ kA; current rise time $\tau_r =$ 5 ns, hyperbolic rise; half-current radius $a_{1/2} = 1$ cm, Bennett profile;

matching current fraction $F_m = 0.2$; and offset $\overline{x} = 0$. The wire-cell parameters were: wire radius $a_w = 0.05$ cm; wall radius $b = 14.8$ cm; resistance $R_w = 1$ Ω/cm; and length $z_w = 100$ cm.

Figures 1 and 2 compare the predictions of the envelope model with those of the particle simulation at $z_w$. Although fair aggreement is found for the beam half-radius, the envelope predictions for normalized emittance $\varepsilon_n$ differ considerably from the particle predictions. The discrepancy can be reduced by renormalizing the particle emittance to the half-radius $a_{1/2}$ rather than the rms radius $a_{rms}$; this is done in Fig. 2b which shows qualitative agreement with the envelope results in Fig. 1b.

The discrepancy has, however, a more fundamental basis. The emittance evolves because the beam profile changes shape. In general, the injected beam profile differs considerably from the equilibrium profile[2] about the wire. In the particle simulations, the beam profile and $\varepsilon_n$ change more in the tightly pinched beam body than in the weakly pinched head; see Fig. 2c. In the envelope model, however, the growth rate for $\varepsilon_n^2$ is set proportional to the radial expansion velocity.[4] The envelope model therefore predicts the largest growth in $\varepsilon_n$ near the expanding beam head. This difference demonstrates the limitations of envelope models in describing emittance growth, particularly when the pinch potential is highly anharmonic. Note that $\varepsilon_n$ should drop after the beam leaves the wire cell and enters a propagation cell with a harmonic pinch potential.

A resistive wire cell can also serve as as efficient emittance filter. Hot beam electrons reside at large radii in the anharmonic wire potential and can be removed by reducing the wall radius b or by placing a collimator near the wire-cell exit. In the run discussed, $\varepsilon_n$ could in principle be reduced by a factor of 4 by discarding only 30 percent of the beam.

## 4. Beam Centering

The particle pusher, like the circuit equation but unlike the envelope model, is valid for arbitrary spatial distribution and can accomodate off-axis beams. To demonstrate the centering capability of a wire cell, the run described above was repeated except that the beam was injected off axis at $\overline{x} = -0.5$ cm. Figure (2d) shows that the wire cell reduced the deflection by ~ 5 in the beam body. Note that the body actually overshot the wire after propagating a distance $z_w = 2\,\lambda_\beta$. Increasing either $z_w$ (to allow for more phase-mix damping) or $R_w$ (to damp $I_w$ and thereby increase the pinch force) should reduce the deflection more.

## 5. Time Step

Beam electrons in the immediate vicinity of the wire experience a pinch force that changes strongly over a wire radius $a_w$. Moreover, these electrons can attain high radial velocities, $\beta_r c$. To model these particles accurately, the time step should satisfy $\Delta\zeta < a_w/\beta_r$. By contrast, harmonic pinch forces require a less severe requirement: $\Delta\zeta < a_{1/2}/\beta_r$. The use of a small wire radius can thus dramatically increase code cost.

To illustrate the problem, consider the above simulation in which few particles attain transverse speeds above $\beta_r = 0.2$. For $a_w = 0.05$ cm, a time step of $\Delta\zeta \leq 0.25$ cm should suffice. The use of $\Delta\zeta = 0.5$ cm produced modest changes, while longer time steps produced pronounced changes and unphysical results. There are several possible techniques for overcoming this problem including an implicit particle integration scheme, or using small time steps only for those particles needing it. Note that the envelope model avoids this problem by using radially averaged quantities.

## 6. Conclusion

We have successfully coupled a particle pusher to the resistive-wire circuit equations. The new code shows distinct and important differences, particularly with regard to beam emittance, from an earlier code based on an envelope model. Future code improvements include: incorporation in the circuit solver of direct feedback from the beam while in the wire cell (presently dropped to avoid numerical instability); allowance for finite-$\gamma$ effects in the circuit solver; and developing means for bypassing the time-step limitation.

## Acknowledgements

We thank Glenn Joyce for providing the particle pusher and for helpful discussions of numerical techniques. We also thank Jay Boris for numerical assistance in the circuit solver.

## References:

1. D.S. Prono, et al., Phys. Rev. Lett. 51, 723 (1983).
2. R.F. Fernsler and P.R. Boris, "Beam Conditioning Using Resistive Wires", 7th Inter. Conf. on Particle Beams, Karlsruhe, Germany, July 1988.
3. The actual particle pusher is fully relativistic.
4. The emittance model of M. Lampe and R. Hubbard (unpublished) was used.

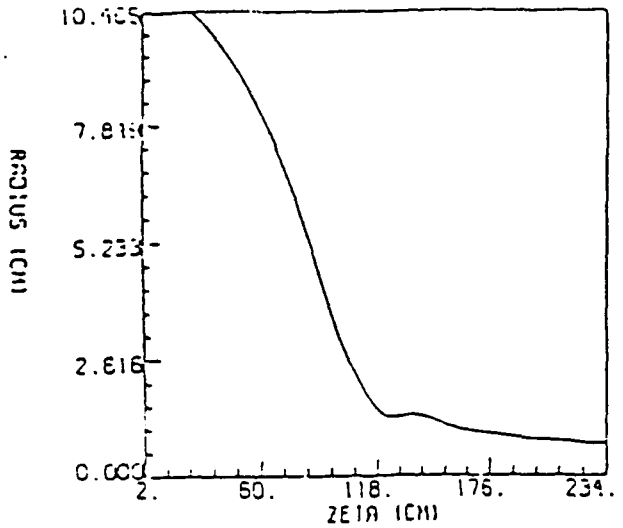



Fig. 1a. Envelope radius

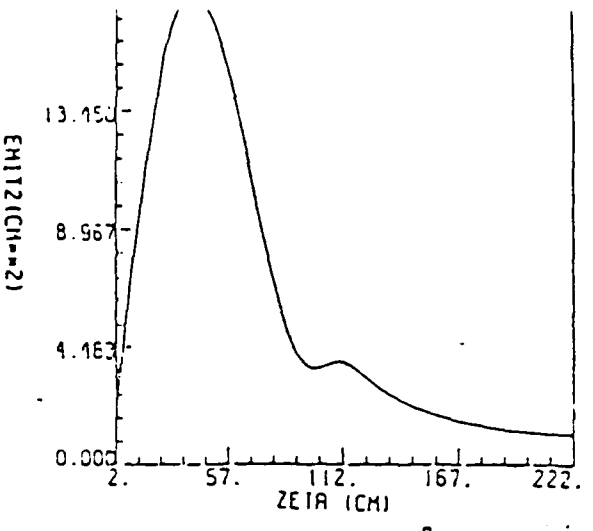



Fig. 1b. Envelope $\varepsilon_n^2$

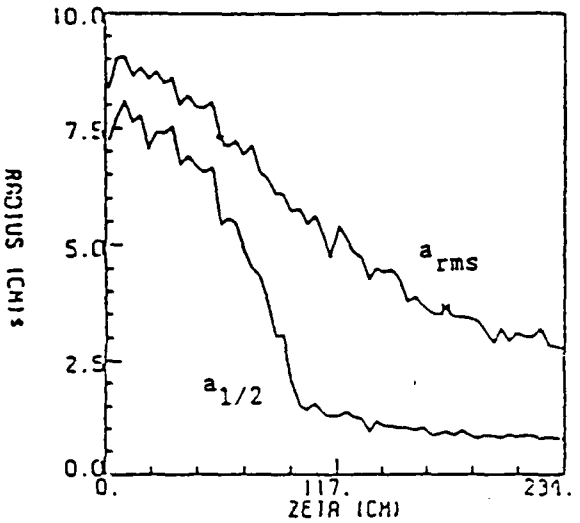



Fig. 2a. Particle radii

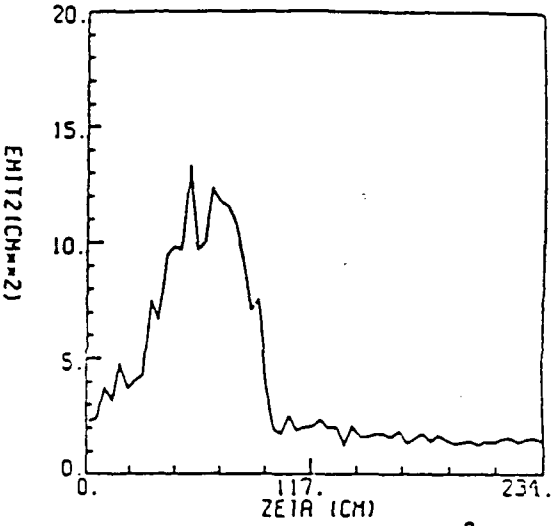



Fig. 2b. $[\varepsilon_n(a_{1/2}/a_{rms})]^2$

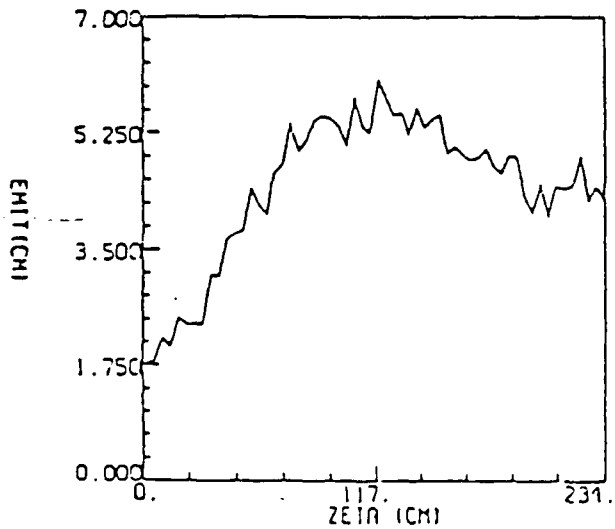



Fig. 2c Particle $\varepsilon_n$

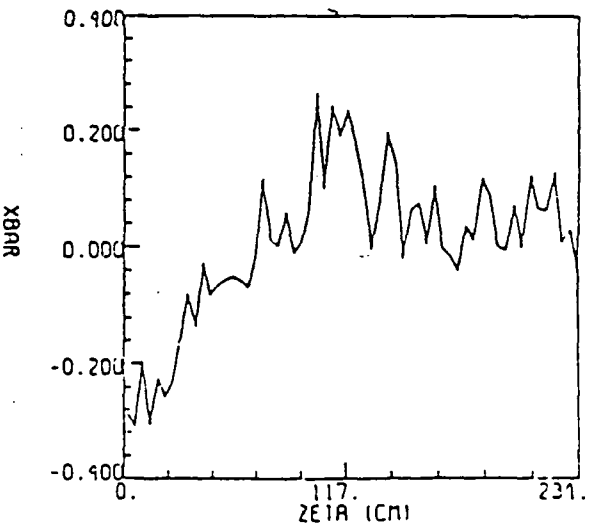



Fig. 2d Particle $\overline{x}$

# APPENDIX QQ

## SARLAC Hose and Tracking Simulations: The Movie

# SARLAC HOSE AND TRACKING SIMULATIONS: THE MOVIE

R. F. Hubbard, P. Boris*, S. P. Slinker, W. M. Fawley** and G. Joyce

Plasma Physics Division
Naval Research Laboratory
Washington, DC 20375

*Science Applications International Corp.
McLean, VA

**Lawrence Livermore National Laboratory
Livermore, CA 94550

## I. INTRODUCTION

SARLAC is a 3-D particle simulation code which can treat large deviations from axisymmetry.[1,2] We have recently modified the code to produce animations which can be run on an Atari ST micro-computer and output to a VCR tape. This paper describes the animation procedure and gives some examples of single frame output from simulations of planned experiments on ATA and Super-IBEX. These simulations are described in more detail in the companion paper.[3]

SARLAC uses the frozen approximation and uses x, y, z, and $\zeta = ct - z$ as the independent variables for pushing beam particles. In the standard version, beam particles are assumed to be ultrarelativistic and remain at a fixed distance $\zeta$ from the beam head. Each frame of the animations is a color contour plot of the line-integrated beam density $D_b(x,\zeta) = \int n_b(x,y)dy$ at a fixed position z in the lab frame. (The density $D_b$ is actually calculated by accumulating particles into bins based on their instantaneous x-coordinate). This gives a representation of the beam as viewed from the side and can clearly show hose distortions and beam expansion. The frames provide essentially the same information as the particle plots which have been used with SARLAC for some time.[2] An example of a single frame from an ATA animation is shown in Fig. 1.

## II. ANIMATION PROCEDURE

Overview: The simulations are run on a CRAY which also generates a file containing the particle density data. A translator program ships the data to a VAX which then generates animation files. An Atari ST does the

final processing and creates the finished animation. The Atari can play back the animation at any desired speed and output the screen images to a VCR tape. The entire procedure is shown schematically in Fig. 2.

CRAY processing: The CRAY creates a partitioned file containing the raw $D_b(x,\zeta)$ data at each z-step. The beam is divided into 30 equally spaced $\zeta$-slices for this diagnostic although the actual simulation axial mesh is usually finer. The CRAY then sends the raw data file to the Vax.

Vax processing: SARLAC calculates beam dynamics by pushing a single $\zeta$-slice from $z = 0$ to $z = z_{max}$, so the data must first be reordered to produce animation frames at constant z. The reordered beam density data for each z-step or animation frame is contained in a 30 x 60 array. The Vax movie generation program finds the maximum value of $D_b$ at each frame and then rescales the density based on the average maximum $\langle D_{max} \rangle$. (This prevents the color levels from being biased by a spike in the data.) The rescaled data consists of color contour levels from 0 (black) to 15 (white), and values of $D_b$ above $\langle D_{max} \rangle$ are assigned the highest level (15). The color palate runs from dull reds and oranges at the low levels to bright blues and violets at the highest levels, so the intensities are similar to what would be used for a "gray" scale plot (eg., Fig. 1).

A Vax animation library developed by Mitchell[4] converts the data, along with titles and labels, to a 320 x 200 pixel array which corresponds to the resolution of the Atari ST screen. A pixelator program transforms the data from real numbers to bytes and allows the size of the 30 x 60 data array to be scaled by an integer multiple in each direction. For the case shown in Fig. 1, the data array was transformed to a 270 x 120 array which covers 2/3 of the screen. The program then generates two animation files: a picture file containing the first frame of the animation, and a delta file containing only the changes for each subsequent frame. We chose to use contour plots rather than particle plots in part because the frame-to-frame changes for a contour plot are relatively small, making the delta file small enough so that even large simulations with 150 frames or more can reside in the 4 Mb memory of an upgraded Atari ST.

Atari ST processing: The animation files are moved from the Vax to the Atari using a standard file transfer program such as Kermit. A commercially available animation program, Cyber Paint,[5] uses the animation files to generate images on the Atari screen and allows individual frames to be modified. Normally, we choose simulation parameters so that an entire run can reside in the Atari's memory and can be played back at any desired speed. Several simulations can be concatenated together by running

Animate4, a text command file containing a list of animations to be run from a hard disc.[6] This provides a continuous process for viewing the animations and allows smooth video recordings to be made without repeatedly stopping and restarting the VCR. The Atari must be equipped with an rf modulator or video output to make such recordings.

## III. EXAMPLES

ATA in a density channel: Fig. 1 is a black-and-white frame from a SARLAC simulation of a 6 kA, 10 MeV, 0.5 cm ATA beam propagating in a 0.3 atm density channel whose nominal edge at 1.5 cm is drawn on the frame. The frame is at z = 498 cm, and its length corresponds to 750 cm (25 nsec) of pulse. Although much of the beam head has been eroded or scattered away, an intense portion in the beam tail remains in the channel. The corresponding frame from a similar case with no channel (not shown) is much more diffuse owing to the increase in scattering at the 1 atm gas density

Super-IBEX simulations: Fig. 3 is a similar plot from a simulation of a 30 kA, 5 MeV, 2 cm Super-IBEX beam propagating in full density air. At z = 498 cm, low frequency hose growth has displaced the entire pulse several cm below the axis, but there is no disruption. Frames from a more poorly-conditioned Super-IBEX simulation show violent disruption, as expected from previous experience on IBEX. Plans call for Super-IBEX to be fired into a preformed density channel. A frame from a simulation of the Fig. 3 beam propagating in such a channel is shown in Fig. 4. The beam is more intense, and hose displacements are substantially smaller.

Other simulation: A total of 9 animations have been assembled on a single VCR tape. These in include other ATA and Super-IBEX hose simulations as well as Super-IBEX tracking simulations.

## REFERENCES


1. G. Joyce, R. F. Hubbard, M. Lampe and S. P. Slinker, NRL Memo Report 6140 (1988).
2. R. F. Hubbard, M. Lampe, S. P. Slinker, and G. Joyce, Phys. Fluids 31, 2349 (1988).
3. R. F. Hubbard, S. P. Slinker, W. M. Fawley and G. Joyce, to appear in these proceedings.
4. Library developed by Horace Mitchell (SAIC/NRL).
5. Cyber-Paint is commercially-available software by Antic.
6. Animate4 is public domain software developed by Tom Hudson

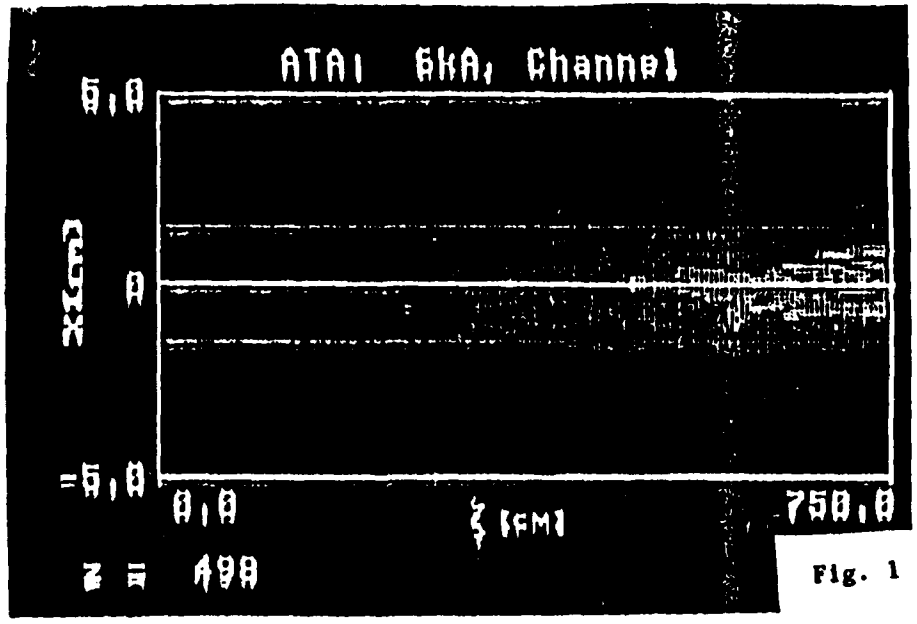



Fig. 1

ANIMATION GENERATION FLOWCHART

CRAY

Simulation codes generate data

VAX

Cray to Vax translator program

Data normalization

Horace Mitchell's (SAIC) Animation Library

Atari Screen Image: Pixelator Program

Delta Files: Picture File and Changes File

ATARI

Uniterm-Kermit: binary file transfer

Antic's Cyber Software: Cyber Paint and Animated

Fig. 2

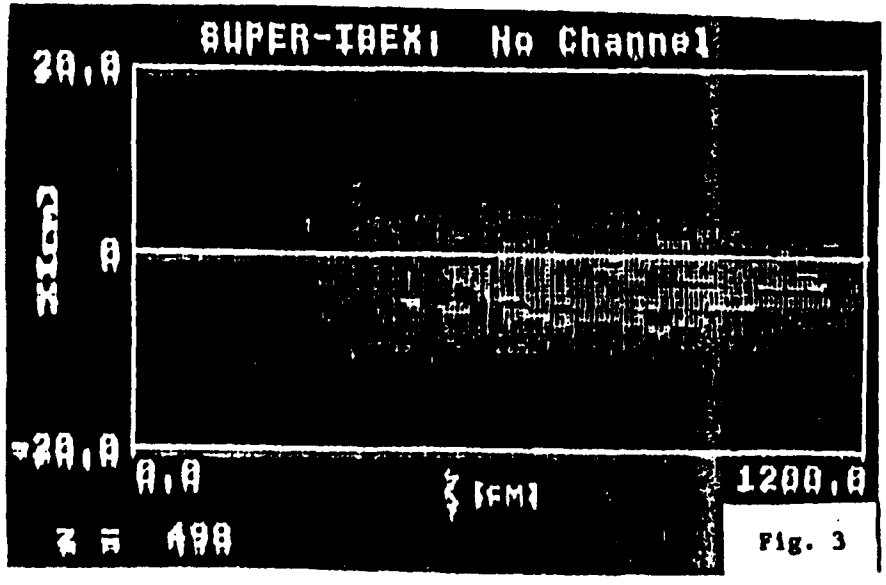



Fig. 3

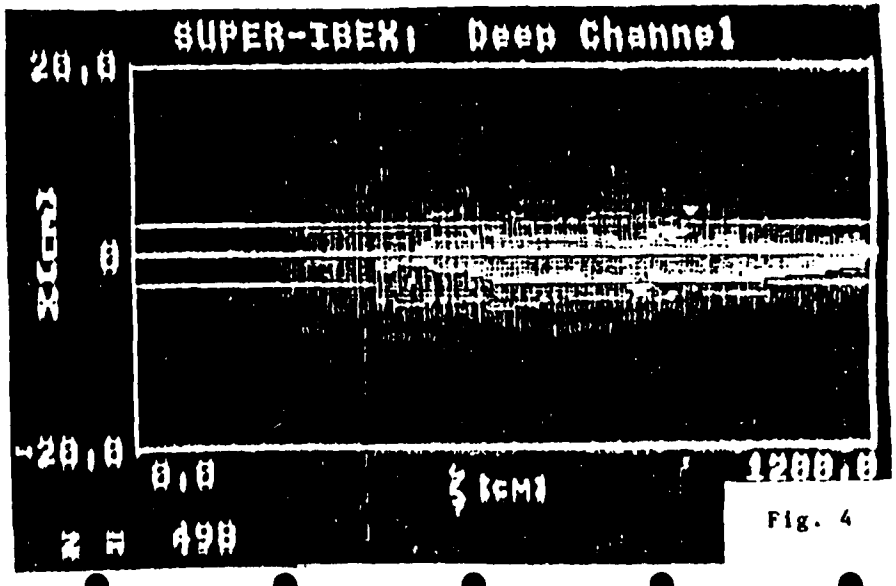



Fig. 4

# APPENDIX RR

## Improving the Current-Carrying Capability of the Modified Betatron (Presentation)

# IMPROVING THE CURRENT-CARRYING CAPABILITY OF THE MODIFIED BETATRON

(1)

PRESENTED TO THE CONFERENCE

APPLICATION OF ACCELERATORS IN RESEARCH AND INDUSTRY

DENTON, TEXAS

NOVEMBER 10 - 12, 1986


CONTRIBUTORS

C.A. KAPETANAKOS
S.J. MARSH

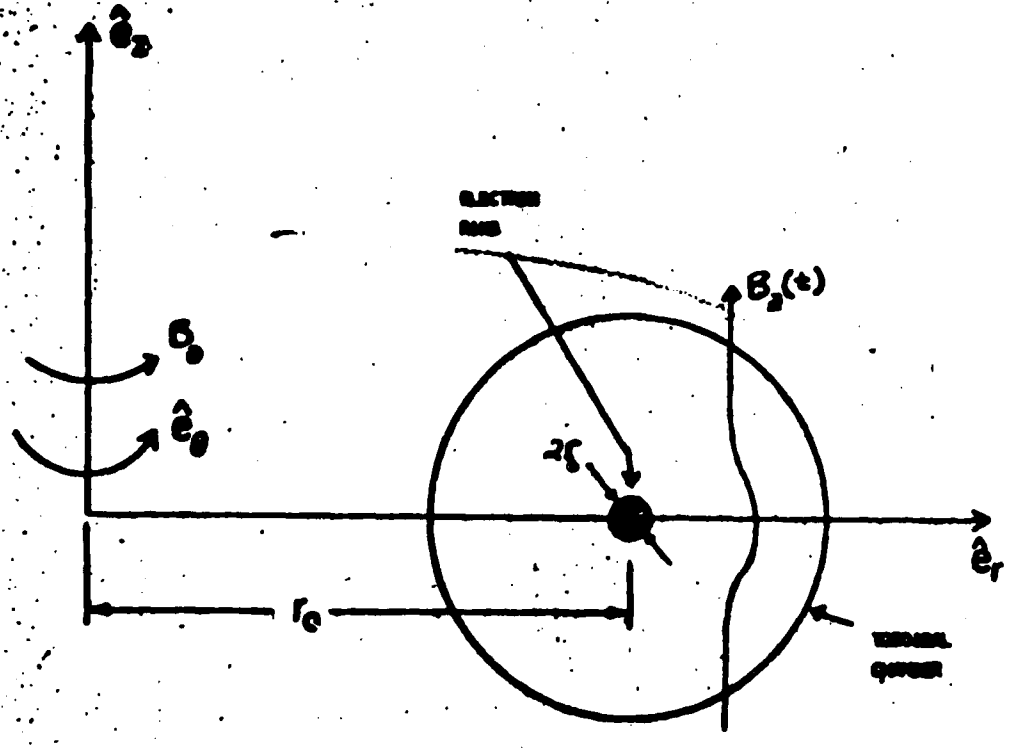
PRESENTED BY:

D. DIALETIS


[illegible] 9-12, 19[illegible]
[illegible] on the Applications
Accelerators [illegible]

# The Modified Betatron

... is a toroidal induction accelerator which includes a strong toroidal magnetic field, $B_\theta$, in addition to the vertical or betatron magnetic field, $B_z(t)$, that is responsible for the acceleration.




$B_z(t)$: controls primarily the ring major radius, $r_0$.

$B_\theta$ : controls primarily the ring minor radius, $r_b$ and the growth rate of collective modes.

# THE MODIFIED BETATRON

## ADVANTAGES

- COMPACT
- SCALABLE TO GeV ENERGIES
- CAPABLE OF GENERATING HIGH CURRENT BEAMS
- STABILITY PROPERTIES CONSIDERABLY SUPERIOR TO THAT OF THE CONVENTIONAL BETATRON
- CAN CONFINE HIGH TEMPERATURE AND EMITTANCE BEAMS

# OBJECTIVES OF THE NRL MODIFIED BETATRON

**PHASE 1A.** FORMATION OF 1 KA, 1 MEV ELECTRON RING IN A MODIFIED BETATRON CONFIGURATION USING AN INEXPENSIVE VACUUM CHAMBER WITH $r_o$ = 100 CM AND $a$ = 16 CM. WITHOUT ACCELERATING THE RING (DC RING EXPERIMENT) STUDY THE CRITICAL PHYSICS ISSUES ASSOCIATED WITH THE CONCEPT SUCH AS INJECTION, EQUILIBRIUM AND STABILITY.

**PHASE 1B.** AFTER THE INSTALLATION OF A NEW VACUUM CHAMBER ACCELERATE THE RING TO 25 MEV AND STUDY THE CRITICAL PHYSICS ISSUES ASSOCIATED WITH THE ACCELERATION.

**PHASE 2.** USING THE SAME INJECTOR, INCREASE THE CURRENT - CARRYING CAPABILITY OF THE DEVICE TO 5 - 10 KA BY ADDING TORSATRON WINDINGS. ACCELERATE THE RING TO 50 MEV.

# NRL Modified Betatron
# Summary of Experimental Results

- The beneficial effect of $B_\theta$ on the expansion of the ring's minor radius has been demonstrated.
- The drift (bounce) motion of the ring has been unambiguously confirmed with three different diagnostics.
- The pronounced effect of image forces on the ring equilibrium has been verified.
- Self trapping of the multi-kiloampere beam with efficiency in excess of 80% has been observed.
- Electron rings with circulating current 2–3 kA that remain in the system for ~4 $\mu$sec (200 revolutions) have been formed. Longer confining times are observed at 1 kA.
- Experiments are in progress to improve the confinement time and to accelerate the ring.

# SHORTCOMINGS OF THE MODIFIED BETATRON

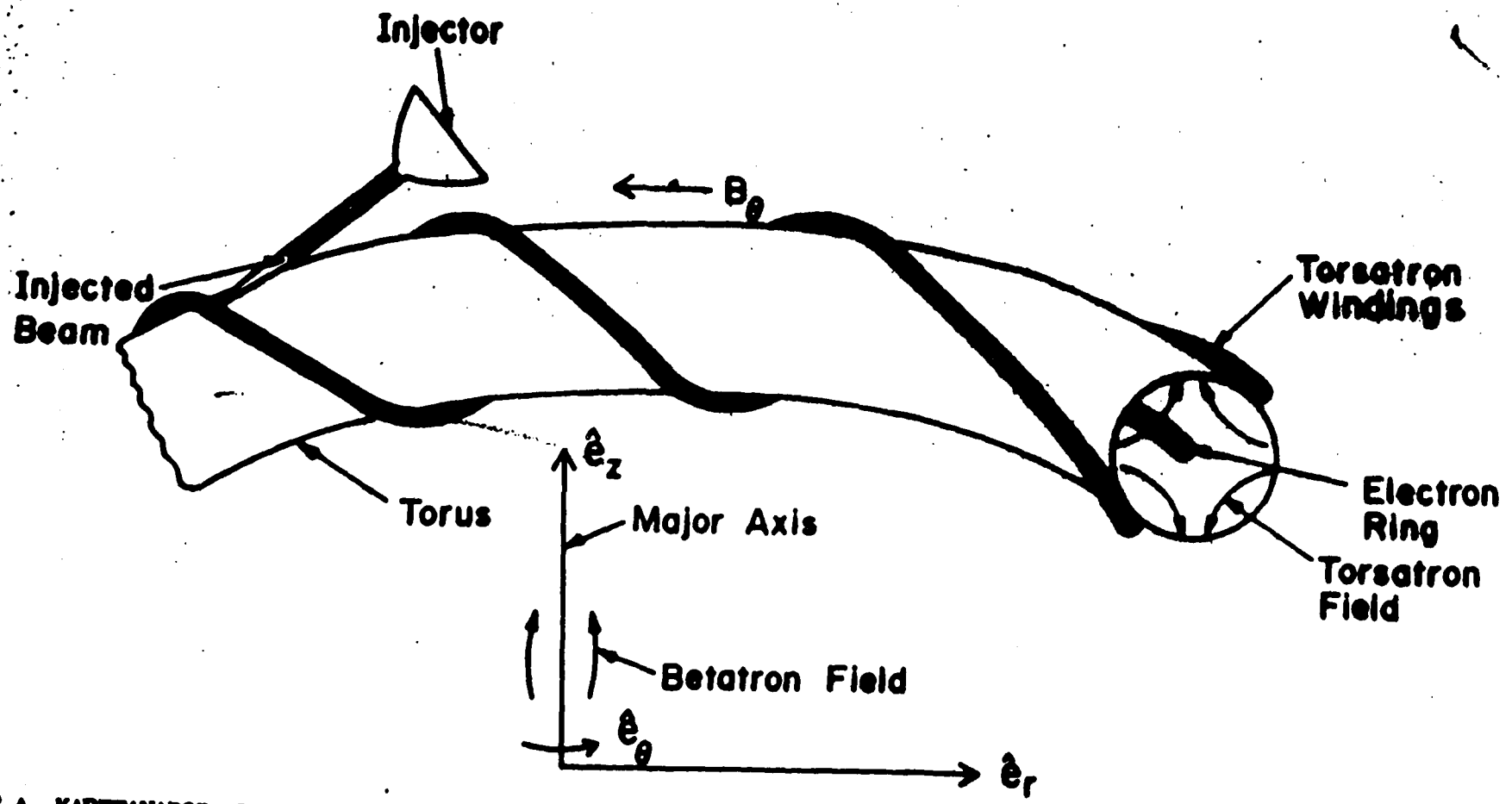
- LARGE ORBIT DISPLACEMENT RESULTING FROM THE MISMATCH BETWEEN THE BETATRON FIELD AND THE BEAM ENERGY (CONSTRAINTS ON THE INJECTOR AND FIELDS).

- REQUIRES COMPENSATING WINDINGS TO ELIMINATE ORBIT DISPLACEMENT ASSOCIATED WITH THE DIFFUSION OF SELF MAGNETIC FIELD.

- SENSITIVE TO FIELD ERRORS. (AS A RESULT, IT REQUIRES SOPHISTICATED BUS-WORK AND STIFF SUPPORT STRUCTURE)

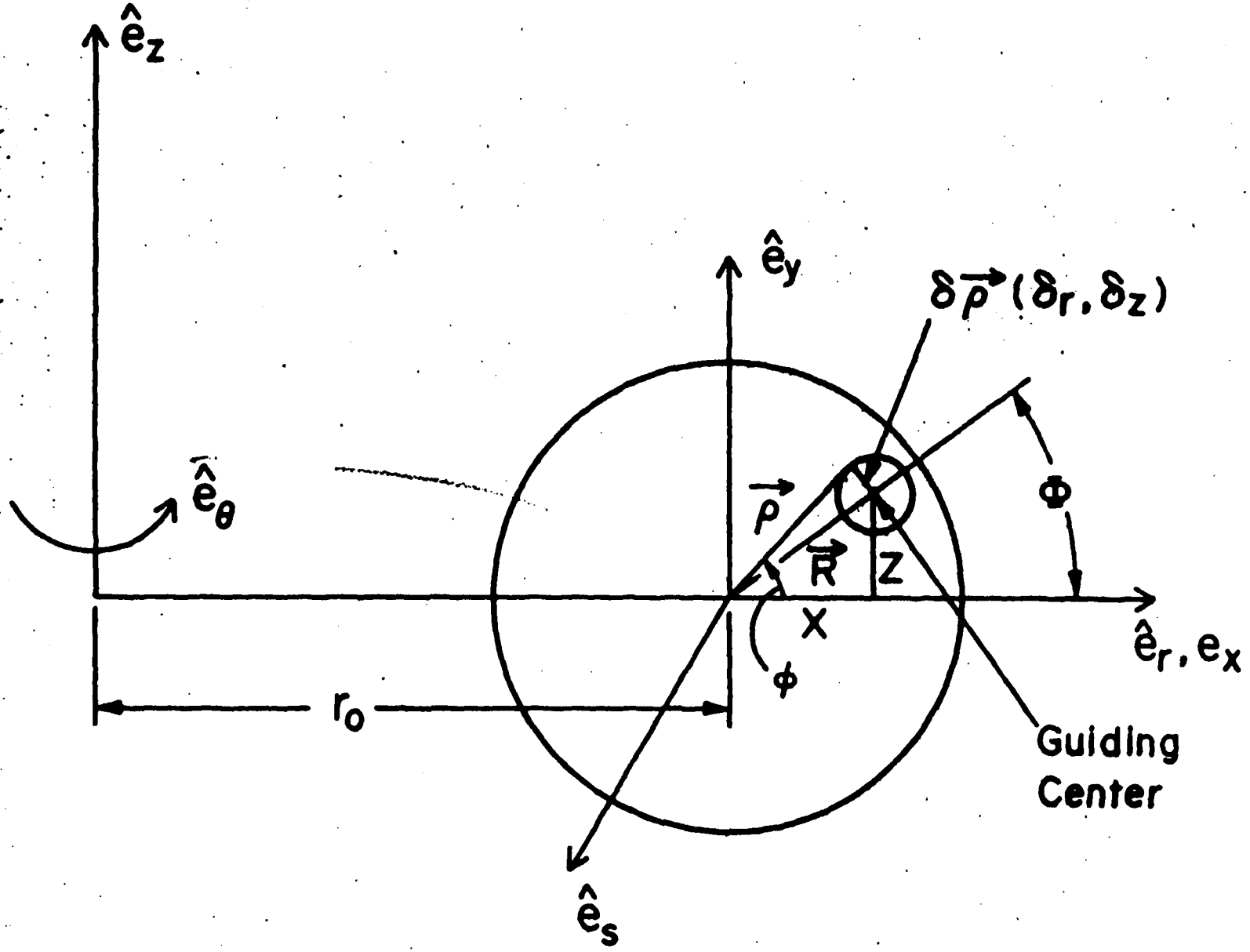
- AT LOW INJECTION ENERGIES, ITS CURRENT-CARRYING CAPABILITY IS LIMITED MAINLY BY THE DRAG INSTABILITY.

# Modified Betatron Yoked with Torsatron Windings (Mytron)




C.A. KAPETANAKOS, D. DIAKETIS,
S.J. MARSH
NRL MEMO REPORT #5619(1985)
PARTICLE ACCEL. 1986

# SYSTEMS OF COORDINATES



# COORDINATES

$$r = r_0 + X + \delta r$$

$$z = Z + \delta z$$

CENTROID GUIDING CENTER (g.c.)

CENTROID INSTANTANEOUS POSITION (REL. TO g.c.)

## INTRODUCING COMPLEX VARIABLES

$$u = r + iz = r_0 + \underbrace{X + iZ}_{U} + \underbrace{\delta r + i\delta z}_{\delta u}$$

# THE FIELDS

**TORSOTRON (NON-LINEAR)**

$$B_r^t = B_Q^t \cos\phi - B_\phi^t \sin\phi$$

$$B_z^t = B_Q^t \sin\phi - B_\phi^t \cos\phi$$

**WHERE**

$$B_Q^t = 2B_s^{ex}\,\varepsilon_t\, I_2'(2aQ) \sin[2(\phi - as)]$$

$$B_\phi^t = \frac{2B_s^{ex}}{aQ}\,\varepsilon_t\, I_2(2aQ) \cos[2(\phi - as)]$$

$a = 2\pi/L$, L = PERIOD OF WINDINGS

$\varepsilon_t = 2aB_o Q_0 K_2'(2aQ_0)/B_s^{ex}$ = FIELD STRENGTH FACTOR

$B_o = 8\pi I/cL$

ASSUMING $V_\theta$ = CONST

$\Rightarrow\ \omega_w = 2aV_\theta = -2as/t$ OR $\boxed{2as = -\omega_w t}$

THEN

$$\boxed{B_r^t + iB_z^t = B_s^{ex}\,\varepsilon_t I\ \{I_1(2aQ)\, e^{-i\phi}\, e^{-i\omega_w t} - I_3(2aQ)\, e^{3i\phi}\, e^{i\omega_w t}\}}$$

# THE FIELDS (Cont'd.)

## TOROIDAL

$$B_\theta = -(B_s^{ex} + B_0) + B_s^{ex}\,\varepsilon_t\, I_2(2aQ)\left[e^{2i\phi}\, e^{i\omega_w t} + e^{-2i\phi}\, e^{-i\omega_w t}\right]$$

EXTERNAL

TORSATRON

## BETATRON

$$B_r^b = -B_{z0}\,\frac{nz}{r_0}$$

$$B_z^b = B_{z0}\left[1 - \frac{n(r-r_0)}{r_0}\right]$$

OR

$$\boxed{(B_r^b + iB_z^b) = iB_{z0}\left[1 + n - \frac{n}{r_0}(r - iz)\right]}$$

# Induced Fields on the Ring Centroid

## Correct to order $\left(\frac{X}{a}\right)^2$ and $\left(\frac{a}{r_0}\right)$

$$E_r = -(2\,|e|\,N_l/a)\left[\frac{X}{a} + \frac{a}{2(r_0+X)}\ln\frac{a}{r_b} + \frac{r_b^2}{8(r_0+X)a}\right]$$

$$E_z = -(2\,|e|\,N_l/a)(Z/a)$$

$$E_\theta = -(2\,|e|\,N_l\beta_\theta/c)\left[\frac{X\dot{X}+Z\dot{Z}}{a^2} - \frac{\dot{X}}{2(r_0+X)}\ln\frac{a}{r_b} - \frac{2\nu}{\gamma^3}\left(1+\frac{1}{\beta_\theta^2}\right)\left(\frac{X\dot{X}+Z\dot{Z}}{a^2}\right)\left(\frac{1}{2}+\ln\frac{a}{r_b}\right)\right]$$

$$B_r = -(2\,|e|\,N_l\beta_\theta/a)(Z/a)$$

$$B_z = (2\,|e|\,N_l\beta_\theta/a)\left[\frac{X}{a} - \left(\frac{a}{2(r_0+X)}\right)\left(\ln\frac{a}{r_b}+1\right) + \frac{r_b^2}{8(r_0+X)a}\right]$$

where $N_l$ is the number of electrons per unit length.

# BASIC ASSUMPTION

**WE WILL ASSUME THAT THE REFERENCE ELECTRON ROTATES AROUND THE GUIDING CENTER WITH FREQUENCY $\pm \omega_w$**

**THEN**

$$\boxed{\delta u = \delta u_+ e^{i\omega_w t} + \delta u_- e^{-i\omega_w t}}$$

**TRUE ONLY IF**

$$\omega_w \ll \Omega_\theta/\gamma$$

$$\delta\dot{u} = i\omega_w (\delta u_+ e^{i\omega_w t} - \delta u_- e^{-i\omega_w t}) + \dot{\vec{R}} \cdot \nabla(\delta u_+ e^{i\omega_w t} + \delta u_- e^{-i\omega_w t})$$

$\dot{\vec{R}} \cdot \nabla(\delta u_+ e^{i\omega_w t} + \delta u_- e^{-i\omega_w t}) \rightarrow 0$

**WE WILL SEE THAT**

$$\delta u_\pm \sim I_1(2aQ)$$

$$\Rightarrow \nabla \delta u_\pm \sim 2a \delta u_\pm$$

$$\dot{R} \cdot \nabla \delta u_\pm \ll \omega_w \delta u_\pm$$

**OR**

$$\boxed{\dot{U} \ll v_\theta}$$

## STEPS

1. TAYLOR EXPAND THE FIELDS AND SUBSTITUTE THEM IN THE ORBIT EQUATIONS

2. MULTIPLY THE RESULTING EQUATION BY $e^{|\omega_w mt}$ AND TAKE TIME AVERAGE, OMITTING TERMS QUADRATIC IN $\delta u$

3. OMIT $\langle \ddot{U}\, e^{im\omega_w t} \rangle$

4. OMIT TERMS $(r_0 + X)^{-2}$

5. ASSUME $\dot{\gamma}/\gamma \ll \omega_w$

# NON-LINEAR EQUATIONS FOR THE SLOW (GUIDING CENTER) MOTION OF RING CENTROID

$$\dot{Z} + \frac{v_\theta(\Omega_s{}^{ex}\epsilon_t/\gamma)^2}{2(\hat{\Omega}_{\theta/\gamma})}\left[\frac{[I_2(2\alpha R)+I_0(2\alpha R)]I_1(2\alpha R)}{(\hat{\Omega}_{\theta/\gamma}-\Omega_W)} - \frac{[I_2(2\alpha R)+I_4(2\alpha R)]I_3(2\alpha R)}{(\hat{\Omega}_{\theta/\gamma}+\Omega_W)}\right]\frac{X}{R}$$

TORSATRON FIELD CONTRIBUTION

$$= -\frac{v_\theta{}^2}{(\hat{\Omega}_{\theta/\gamma})(r_0+X)} + \frac{v_\theta(\Omega_{z_0/\gamma})}{(\hat{\Omega}_{\theta/\gamma})}\left(1-\frac{n}{r_0}X\right)$$

CENTRIFUGAL — BETATRON FIELD

$$-\frac{\omega_p{}^2}{2(\hat{\Omega}_{\theta/\gamma})}\left(\frac{r_b}{a}\right)^2\left[\frac{X}{(1-R^2/a^2)\gamma^3} + \frac{a^2}{2r_0\gamma}\left[\beta^2+(1+\beta^2)\ln\frac{a}{r_b}\right]\right]$$

SELF FIELDS — TOROIDAL CORRECTION

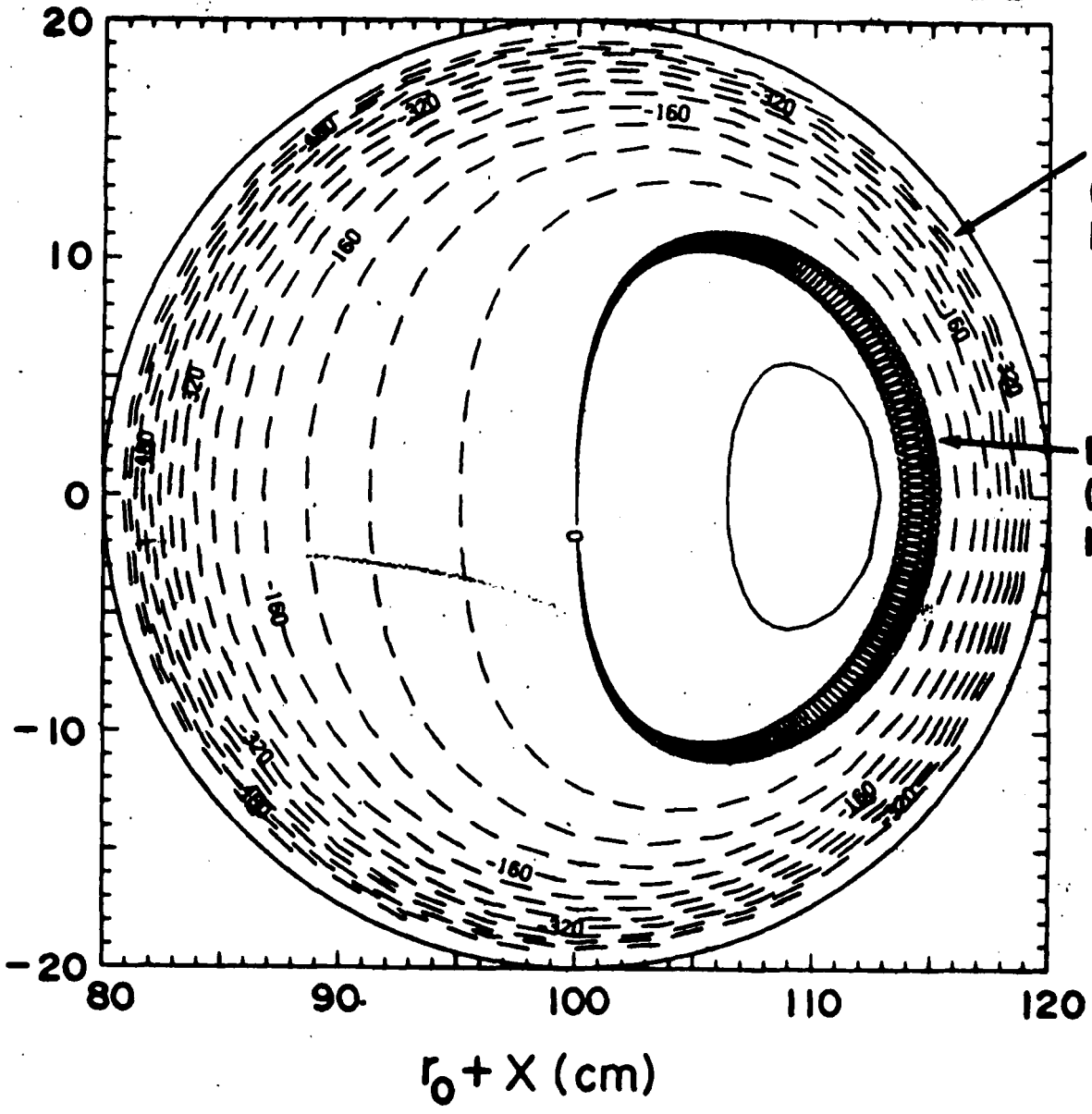
$$\dot{X} - \frac{v_\theta(\Omega_s{}^{ex}\epsilon_t/\gamma)^2}{2(\hat{\Omega}_{\theta/\gamma})}\left[\frac{[I_2(2\alpha R)+I_0(2\alpha R)]I_1(2\alpha R)}{(\hat{\Omega}_{\theta/\gamma}-\Omega_W)} - \frac{[I_2(2\alpha R)+I_4(2\alpha R)]I_3(2\alpha R)}{(\hat{\Omega}_{\theta/\gamma}+\Omega_W)}\right]\frac{Z}{R}$$

TORSATRON FIELD CONTRIBUTION

$$= -\frac{n\,v_\theta(\Omega_{z_0/\gamma})}{(\hat{\Omega}_{\theta/\gamma})}\frac{Z}{r_0} + \frac{\omega_p{}^2}{2(\hat{\Omega}_{\theta/\gamma})}\left(\frac{r_b}{a}\right)^2\frac{Z}{(1-R^2/a^2)\gamma^3}.$$

BETATRON FIELD — SELF FIELDS

# MODIFIED BETATRON WITH TORSATRON WINDINGS



# VARIATION OF $\gamma$ AS THE RING MOVES ALONG ITS SLOW ORBIT

$$\frac{d\gamma}{dt} = -\frac{|e|}{mc^2}\,\vec{v}\cdot\vec{E} - \frac{2\nu}{1+\frac{2\nu}{\gamma^3}\left(\frac{1}{2}+\ln\frac{a}{r_b}\right)}\left|\frac{d}{dt}\left[\frac{x^2+z^2}{a^2}+\left(r_b^2/8a^2\right)\ln\left(\frac{r_o+x}{r_o}\right)\right]\right.$$

$$\left. -\left(1/\gamma^2\right)\frac{d}{dt}\left[\frac{x^2+z^2}{2a^2}-\frac{1}{2}\ln\frac{a}{r_b}\ln\frac{(r_o+x)}{r_o}\right]\right|$$

INTEGRATION (1ST CONSTANT OF THE MOTION)

$$\gamma + 2\nu\left[\frac{1}{2}+\ln\frac{a}{r_b}-\frac{x^2+z^2}{a^2}-\frac{r_b^2}{8a^2}\frac{x}{(r_o+x)}\right]$$

$$-\frac{\nu}{\gamma^2}\left[\frac{1}{2}+\ln\frac{a}{r_b}-\frac{x^2+z^2}{a^2}+\ln\frac{a}{r_b}\ln\frac{(r_o+x)}{r_o}\right]=\gamma_o,$$

$$\nu = N_l\frac{|e|^2}{mc^2} = \frac{I_b(kA)}{17\beta_\theta}$$

WHERE $\gamma_c$ IS A CONSTANT THAT IS DETERMINED FROM THE INJECTION CONDITIONS.

## 2ND CONSTANT OF THE MOTION

## (AVERAGED CANONICAL MOMENTUM)

$$\frac{\langle P_\theta \rangle}{mc} = r\left\{\beta_\theta\left[\gamma + 2\nu\left(\frac{1}{2} + \ell n\,\frac{a}{r_b} + \ell n\left(1 - \frac{X^2 + Z^2}{a^2}\right) - \frac{r_b^2}{8a^2}\,\frac{X}{r}\right)\right]\right.$$

$$- \frac{\Omega_{zo}\, r_o}{c}\left[\frac{1}{2-n}\left(\frac{r_o}{r}\right)^{n-1} + \frac{1-n}{2-n}\,\frac{r_o}{r} + \frac{n}{2}\,\frac{r_o}{r}\left(\frac{z}{r_o}\right)^2\right]$$

$$\left. + \frac{1}{2}\left(\frac{r}{r_o}\right)^2 \frac{\left(\varepsilon_t \Omega_s^{ex}\right)^2}{\omega_{wo}}\left[\frac{I_1^{\,2}(2\alpha R)}{D_1} - \frac{I_3^{\,2}(2\alpha R)}{D_2}\right]\right\}, \qquad (1)$$

WHERE

$R^2 = X^2 + Z^2$, $\nu$ = BUDKER PARAMETER

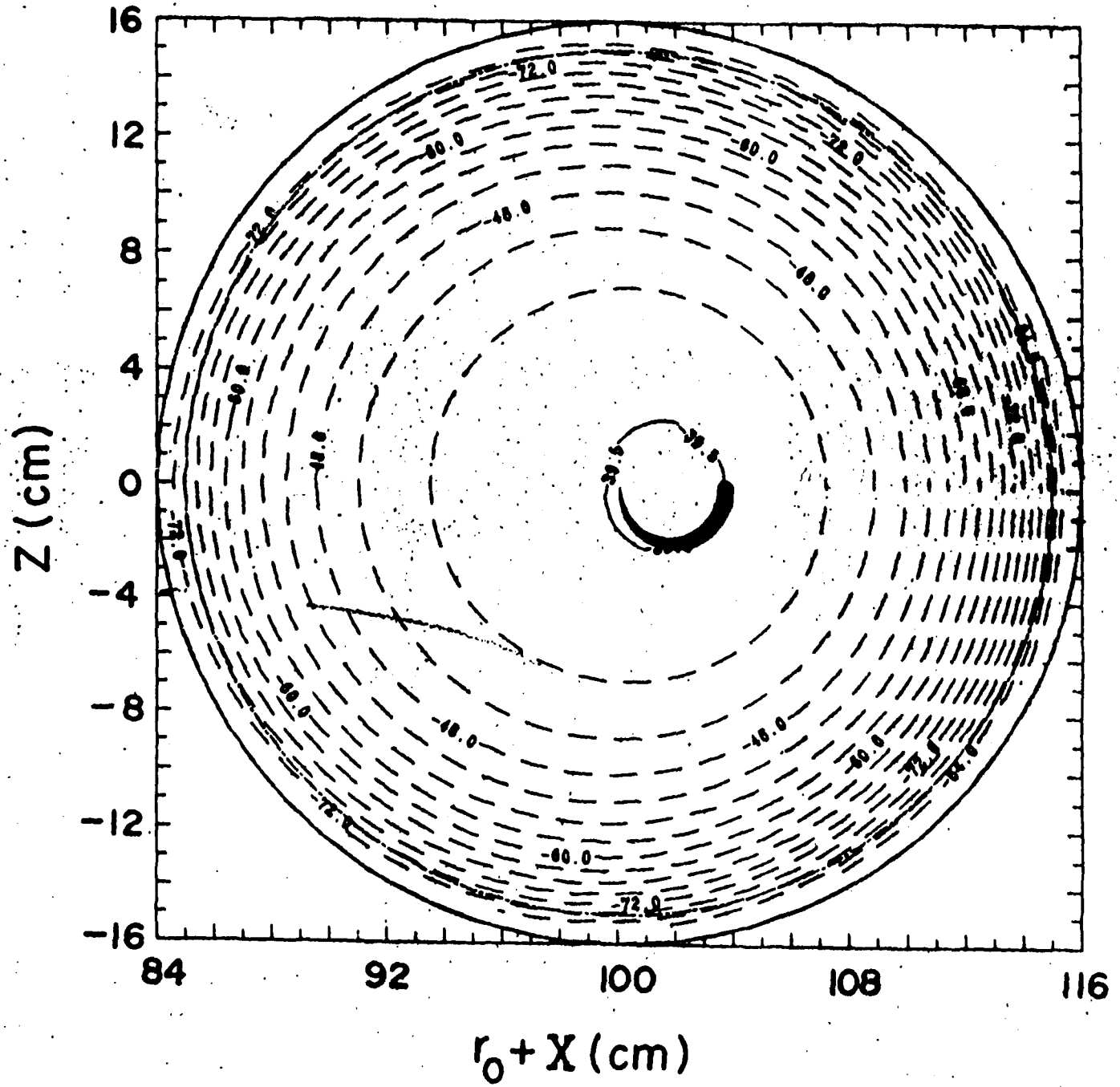
$r = r_o + X$,

$\omega_{wo} = 2\alpha c$,

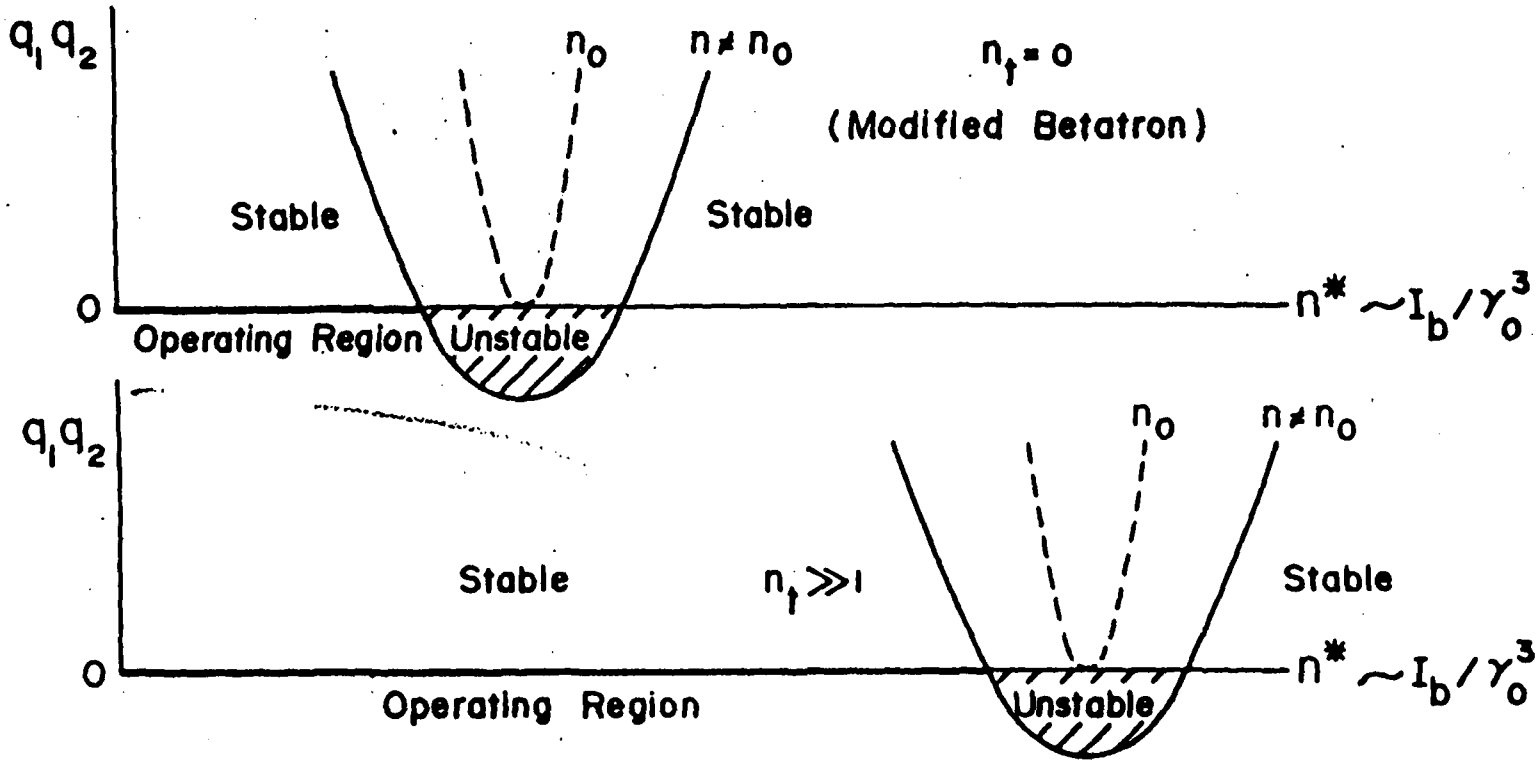
$D_1 = \Omega_{\theta o}^{ex} - \Omega_o - \beta_\theta \gamma \omega_{wo} = \hat{\Omega}_{\theta o} - \beta_\theta \gamma \omega_{wo}$

$D_2 = \Omega_{\theta o}^{ex} - \Omega_o + \beta_\theta \gamma \omega_{wo} = \hat{\Omega}_{\theta o} + \beta_\theta \gamma \omega_{wo}$

$\langle P_\theta \rangle$ = AVERAGE (OVER THE FAST MOTION) CANONICAL ANGULAR MOMENTUM


16
12
8
4
0
-4
-8
-12
-16
Z (cm)
84
92
100
108
116
$r_0 + X$ (cm)

IMPROVING THE CURRENT-CARRYING CAPABILITY
OF THE MODIFIED BETATRON WITH STRONG
FOCUSING. (FOR EXAMPLE, TORSATRON WINDINGS).



# MAXIMUM CURRENT

FOR $n>n_o$ THE MAXIMUM CURRENT IS DETERMINED FROM THE CONDITION $q_1 = 0$

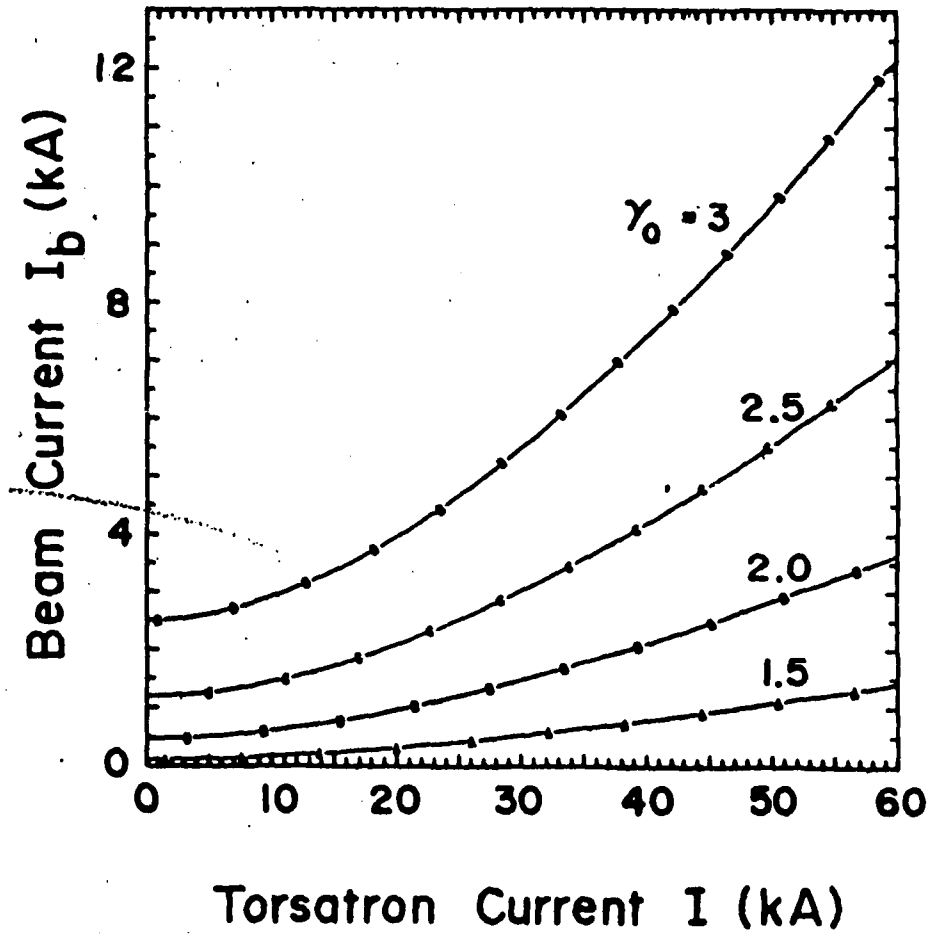
$$\frac{I_b(kA)}{17.045} = \frac{(\gamma_o^2 - 1)^{1/2} + \dfrac{46.93\ \varepsilon_1^2 a^3 r_o^2\ I^2(kA)}{[400\cdot a I^2(kA) - B_{\theta o} + b_w](1-n)}}{\dfrac{2}{(1-n)\ (\gamma_o^2 - 1)}\left[\left(\dfrac{r_o}{a}\right)^2 + \ell n\ \dfrac{a}{r_b}\right] - 1 - \left(2 + \dfrac{1}{\gamma_o^2 - 1}\right)\ell n\ \dfrac{a}{r_b}}\ ,$$

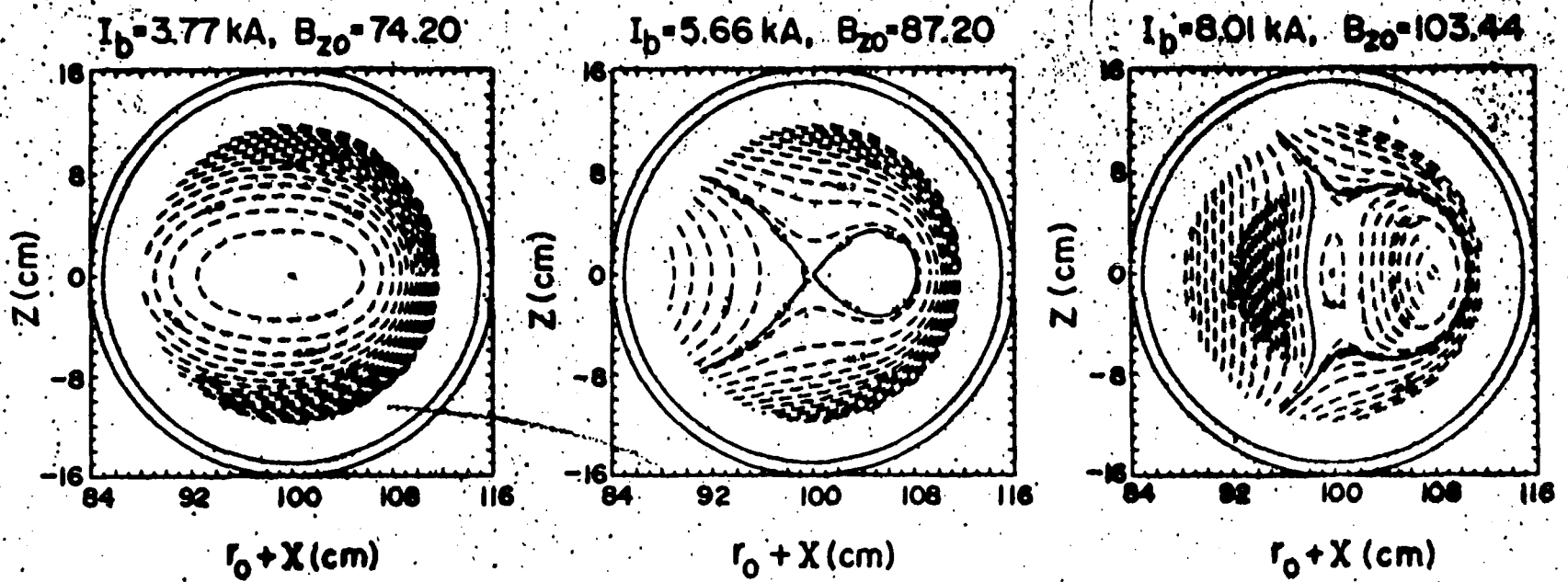
WHERE $b_w = \dfrac{2ac\beta_{\theta o}\gamma_o}{1.76\times10^7}$ , $\varepsilon_1 = 2a\rho_o K_2\ (2a\rho_o)$ AND $n_o = 1/2 + \langle P_\theta \rangle / m r_o^2\ \Omega_{zo}$

(CAUSSIAN UNITS ARE USED EXCEPT FOR THE CURRENT)

ELECTRON RING CURRENT IN A MODIFIED BETATRON

VS. CURRENT IN THE TORSATRON WINGINGS




$I_b$=3.77 kA, $B_{z0}$=74.20
$I_b$=5.66 kA, $B_{z0}$=87.20
$I_b$=8.01 kA, $B_{z0}$=103.44
Z (cm)
16
8
0
-8
-16
84
92
100
108
116
$r_0$+X (cm)
(a)
(b)
(c)

## (II) REDUCTION IN ORBIT DISPLACEMENT RESULTING FROM ENERGY MISMATCH

$$K_o^* = (1-n-n_s r_b^2/a^2 + n_t)\left[\frac{X}{r_o} - \frac{\delta P_\theta / \frac{\Omega_{zo} r_o}{c}(mcr_o)}{(1-n-n_s r_b^2/a^2 + n_t)}\right]^2 + (n-n_s r_b^2/a^2 + n_t)\frac{z^2}{r_o^2}$$

$$\frac{\Delta X}{r_o} = \frac{\delta P_\theta / mcr_o}{\frac{\Omega_{zo} r_o}{c}(1-n-n_s \frac{r_b}{a^2} + n_t)} \quad \text{(ORBIT DISPLACEMENT)}$$

WHEN $n_t >> 1$, $\frac{\Delta X}{r_o}$ IS REDUCED.

BENEFITS

- DESIGN OF THE ACCELERATOR IS SIMPLIFIED.
- WEIGHT OF THE ACCELERATOR IS REDUCED (NO BUS WORK, LENIENT STIFFNESS REQUIREMENTS)
- CONSTRAINTS ON INJECTOR ACCELERATOR ARE RELAXED.

## SUMMARY AND CONCLUSIONS

- FOR $\omega_w < (\Omega_\theta/\gamma)$, WE HAVE DERIVED TWO EQUATIONS THAT DESCRIBE THE NONLINEAR TRANSVERSE MOTION OF THE BEAM GUIDING CENTER IN A MODIFIED BETATRON WITH TORSATRON WINDINGS.

- BY ANALYTICALLY INTEGRATING THE GUIDING CENTER EQUATIONS, WE OBTAINED A CONSTANT OF THE MOTION THAT PREDICTS ACCURATELY THE RING MACROSCOPIC MOTION.

THE ANALYTICAL AND NUMERICAL RESULTS PREDICT THAT ADDING TORSATRON WINDINGS IN THE MODIFIED BETATRON,

- WILL IMPROVE ITS CURRENT-CARRYING CAPABILITY.

- WILL ALLEVIATE THE DIFFICULTY ASSOCIATED WITH THE ORBIT DISPLACEMENT.

- WILL ALLEVIATE THE BEAM DISPLACEMENT ASSOCIATED WITH THE DIFFUSION OF SELF MAGNETIC FIELD.

- WILL REDUCE THE SIZE AND WEIGHT OF FUTURE ACCELERATORS (SIMPLER BUS WORK, LENIENT STIFFNESS REQUIREMENTS, CONSTRAINTS ON INJECTOR ARE RELAXED).

# APPENDIX SS

## Improving the Current Carrying Capability of the Modified Betatron

Nuclear Instruments and Methods in Physics Research B24/25 (1987) 805–809
North-Holland, Amsterdam



# IMPROVING THE CURRENT CARRYING CAPABILITY OF THE MODIFIED BETATRON *

C.A. KAPETANAKOS, D. DIALETIS ** and S.J. MARSH ***

*Plasma Physics Division, Naval Research Laboratory, Washington, DC 20375-5000, USA*

Stability analysis of the macroscopic beam orbits indicates that the current-carrying capability of the modified betatron is substantially improved by adding torsatron windings that carry modest current. An analytic expression has been derived that gives the maximum beam current in a modified betatron as a function of the current in the torsatron windings and other relevant parameters.

## 1. Introduction

High energy physics experiments require electron beams with energy in the TeV range at relative low average current. In contrast most industrial and defense related applications demand high average beam current in the energy range from a few MeV to approximately 1 GeV. In addition, while the compactness of the accelerator is critical in most commercial and defense applications, it plays only a secondary role in the high energy physics experiments.

The development of the modified betatron accelerator at NRL is motivated by its compact size and its potential to generate high current beams of several hundred MeV energy. Extensive theoretical studies [2–9] over the last few years have shown that the modified betatron accelerator has current carrying capability substantially higher than the conventional betatron. The improved current carrying capability of the modified betatron is due to the toroidal magnetic field that controls the minor radius of the circulating electron ring.

The current carrying capability of the modified betatron can be further improved by adding a strong focusing field. This additional field can be conveniently generated by a set of $l = 2$ torsatron windings, i.e., two twisted wires that carry current in the same direction as shown in fig. 1.

In addition to improve the current carrying capability of the device, the strong focusing [10,11] reduces the orbit displacement that results from the energy mismatch. Such a mismatch occurs whenever the energy of the electron beam is not precisely matched to the vertical or betatron magnetic field. Under such conditions the center of the beam gyration in the plane transverse to the minor axis is shifted radially and thus the beam has an enhanced probability to strike the wall of the surrounding vacuum chamber.

By reducing the orbit sensitivity to the energy mismatch, the strong focusing makes the electron ring more tolerable to field errors and thus the stringent constraints on the bus-work and the accelerator support structure are relaxed [11]. Finally, for the same reason, the beam displacement associated with the diffusion of the self magnetic field is reduced and thus the need for compensating windings is eliminated.

## 2. The model

The beam dynamics in a modified betatron with torsatron windings has been recently studied [11] in detail. Assuming that the toroidal velocity $v_\theta$ remains constant and using the lowest nonlinear terms in the expressions for the torsatron fields and keeping only linear terms in the betatron, toroidal and self fields, we derived the guiding center equations for the reference electron that is located at the centroid of an

* Supported by ONR.
** Science Applications Int. Corp. McLean, VA 22102, USA.
*** Sachs/Freeman Associates, Bowie, MD 20715, USA.

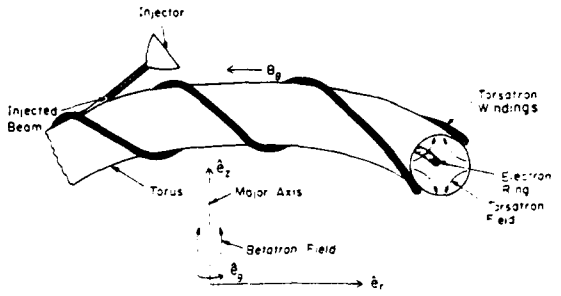



Fig. 1. Schematic of a modified betatron with torsatron windings.

intense electron ring by time averaging out its fast motion. These "slow" equations, together with the energy rate equation, were integrated approximately analytically to obtain two constants of the motion that describe the ring motion in the vertical plane. Recently, the calculation was repeated without assuming $v_\theta$ is constant and using nonlinear expressions for the betatron and toroidal fields. The first, more general constant of the motion, now becomes

$$\frac{\langle P_\theta \rangle}{mc} = r\left\{\beta_\theta\left[\gamma + 2\nu\left(\frac{1}{2} + \ln\frac{a}{r_b} + \ln\left(1 - \frac{X^2+Z^2}{a^2}\right) - \frac{r_b^2}{8a^2}\frac{X}{r}\right)\right]\right.$$
$$- \frac{\Omega_{z0} r_0}{c}\left[\frac{1}{2-n}\left(\frac{r_0}{r}\right)^{n-1} + \frac{1-n}{2-n}\frac{r_0}{r} + \frac{n}{2}\frac{r_0}{r}\left(\frac{Z}{r_0}\right)^2\right]$$
$$\left. + \frac{1}{2}\left(\frac{r}{r_0}\right)^2 \frac{(\epsilon_t \Omega_s^{ex})^2}{\omega_{w0}}\left[\frac{I_1^2(2\alpha R)}{D_1} - \frac{I_3^2(2\alpha R)}{D_2}\right]\right\}, \tag{1}$$

where

$$R^2 = X^2 + Z^2, \qquad r = r_0 + X, \qquad \omega_{w0} = 2\alpha c,$$
$$D_1 = \Omega_{\theta 0}^{ex} - \Omega_0 - \beta_\theta \gamma \omega_{w0} = \hat{\Omega}_{\theta 0} - \beta_\theta \gamma \omega_{w0},$$
$$D_2 = \Omega_{\theta 0}^{ex} - \Omega_0 + \beta_\theta \gamma \omega_{w0} = \hat{\Omega}_{\theta 0} + \beta_\theta \gamma \omega_{w0}.$$

In these equations $\langle P_\theta \rangle$ is the average (over the fast motion) canonical angular momentum, $\beta_\theta = v_\theta/c$, $\gamma$ is the relativistic factor, $\nu$ is the Budker parameter, $r_b$ is the minor radius of the ring, $a$ is the minor radius of the torus, $X$ and $Z$ are the radial and vertical displacements of the guiding center of the beam centroid from the minor axis, $B_s^{ex}\epsilon_t = 2\alpha B_0 \rho_0 K_2'(2\alpha\rho_0)$, $\rho_0$ is the minor radius of the torsatron windings, $K_n$ and $I_n$ are the modified Bessel functions, $\alpha = 2\pi/L$, $L$ is the period of the torsatron windings, $B_0 = \pi I/cL$, $I$ is the current in the torsatron windings, $\Omega_{z0} = |e| B_{z0}/(mc)$, $B_{z0}$ is the betatron field on the minor axis, $n$ is the external field index,

$$\Omega_s^{ex} = |e| B_s^{ex}/mc = -(|e| B_{\theta 0}^{ex}/mc)(r_0/r)$$

and $B_{\theta 0}^{ex} - B_0$ is the total toroidal magnetic field on the minor axis.

As expected, the exact canonical momentum is not a constant of the motion. However, the average over the fast motion canonical momentum of the reference electron is approximately conserved.

An additional constant of the motion can be obtained by integrating the energy rate equation that describes the variation of $\gamma$ as the ring moves along its orbit. Assuming that $\gamma_\theta \approx \gamma$, where $\gamma_\theta = (1-\beta_\theta^2)^{-1/2}$, and omitting a small term that is proportional to $\nu/\gamma^2$, we obtain

$$\gamma + 2\nu\left[\frac{1}{2} + \ln\frac{a}{r_b} + \ln\left(1 - \frac{X^2+Z^2}{a^2}\right) - \frac{r_b^2}{8a^2}\frac{X}{(r_0+X)}\right] - \frac{\nu}{\gamma^2}\left[\frac{1}{2} + \ln\frac{a}{r_b} + \ln\left(1 - \frac{X^2+Z^2}{a^2}\right)\right.$$
$$\left. + \ln\frac{a}{r_b}\ln\frac{(r_0+X)}{r_0}\right] = \gamma_c, \tag{2}$$

where $\gamma_c$ is a constant that is determined from the injection conditions.

Eqs. (1) and (2) describe the slow orbits of the beam centroid in the plane transverse to the minor axis. It has been shown [11] that the approximate constants of the motion predict accurately the guiding center motion of the beam centroid.

Near the minor axis, i.e., when $2\alpha R \ll 1$ and $X/r_0 \ll 1$, eq. (1) can be linearized and the resulting expression, when the small term that contains $I_3$ and the $\beta_\theta \gamma \omega_{w0}$ term are omitted, is

$$\left[\frac{\Omega_{z0} r_0}{2c}(1-n) - \frac{(\Omega_s^{ex}\epsilon_t)^2 \alpha r_0^2}{4cD_{10}} - \frac{\nu r_0^2}{\gamma_0^2 a^2 \beta_{\theta 0}} + \frac{\langle P_\theta \rangle}{mcr_0}\right]\left(\frac{X}{r_0}\right)^2$$
$$+\left[\frac{\Omega_{z0} r_0}{2c} n - \frac{(\Omega_s^{ex}\epsilon_t)^2 \alpha r_0^2}{4cD_{10}} - \frac{\nu r_0^2}{\gamma_0^2 a^2 \beta_{\theta 0}}\right]\left(\frac{Z}{r_0}\right)^2 - \left[\frac{\langle P_\theta \rangle}{mcr_0} + \frac{\nu}{2\gamma_0^2 \beta_{\theta 0}}\left(2 \ln \frac{a}{r_b} + \frac{r_b^2}{2a^2}\right)\right]\left(\frac{X}{r_0}\right)$$
$$= -\frac{\delta P_\theta}{mcr_0}, \tag{3}$$

where $D_{10} = \hat{\Omega}_{\theta 0} - \beta_{\theta 0}\gamma_0 \omega_{w0}$, and

$$\frac{\delta P_\theta}{mcr_0} = \frac{\langle P_\theta \rangle}{mcr_0} - \frac{\langle P_\theta \rangle_{00}}{mcr_0} = \frac{\langle P_\theta \rangle}{mcr_0} + \frac{\nu}{\gamma_0^2 \beta_{\theta 0}} \ln \frac{a}{r_b}.$$

The linearized constant of the motion of eq. (3) is identical to that derived previously [11] under the assumption that $v_\theta$ is constant and for linear betatron and toroidal fields.

Omitting the very small term $(r_b/a)^2$, (eq. (3)) can be written

$$K_0 = q_1\left(\frac{X}{r_0}\right)^2 + q_2\left(\frac{Z}{r_0}\right)^2 - \frac{2\delta P_\theta}{mr_0^2 \Omega_{z0}}\left(\frac{X}{r_0}\right), \tag{4}$$

where

$$q_1 = 1 - n + n_t - n^* + 2\langle P_\theta \rangle / mr_0^2 \Omega_{z0},$$
$$q_2 = n + n_t - n^*,$$
$$K_0 = -2\delta P_\theta / mr_0^2 \Omega_{z0},$$
$$n_t = (\Omega_{s0}^{ex}\epsilon_t)^2 r_0 \alpha / 2\Omega_{z0}(-\hat{\Omega}_{\theta 0} + \beta_{\theta 0}\gamma_0 \omega_{w0})$$

is the torsatron field index,

$$n^* = 2\nu r_0 c/(\gamma_0^2 a^2 \beta_{\theta 0} \Omega_{z0}) \quad \text{and} \quad \hat{\Omega}_{\theta 0} < 0$$

is the combined toroidal field at $r_0$.

According to eq. (4), the macroscopic beam orbits are stable provided $q_1 q_2 > 0$. Fig. 2 shows the product $q_1 q_2$ as a function of $n^*$ for $n_t = 0$ (modified betatron) and $n_t \neq 0$, i.e., a modified betatron with torsatron windings. Since $n^* \sim I_b/\gamma_0^3$ the parameter $n^*$ decreases rapidly during acceleration. Therefore, in order to avoid crossing the instability gap when $\gamma_0$ increases, it is necessary to select the beam parameters during injection so that $n^*$ is located in the left stable region (operating region) of the figure. It is apparent that when $n_t \gg 1$, the operating region can be very wide and thus the maximum ring current that can be stably confined can be considerably higher than when $n_t = 0$.

When $q_1 = q_2$ the orbits are always stable. This occurs when $n = n_0 = \frac{1}{2} + \langle P_\theta \rangle / mr_0^2 \Omega_{z0}$. For $n > n_0$ the maximum current is determined from the condition $q_1 = 0$ and is given by

$$\frac{I_b[\text{kA}]}{17.045} = \frac{(\gamma_0^2 - 1)^{1/2} + \dfrac{46.93\,\epsilon_1^2 \alpha^3 r_0^2 I^2[\text{kA}]}{[400\,\alpha I^2[\text{kA}] - \beta_{\theta 0} + b_w](1-n)}}{\dfrac{2}{(1-n)(\gamma_0^2 - 1)}\left[\left(\dfrac{r_0}{a}\right)^2 + \ln \dfrac{a}{r_b}\right] - 1 - \left(2 + \dfrac{1}{\gamma_0^2 - 1}\right)\ln \dfrac{a}{r_b}}. \tag{5}$$

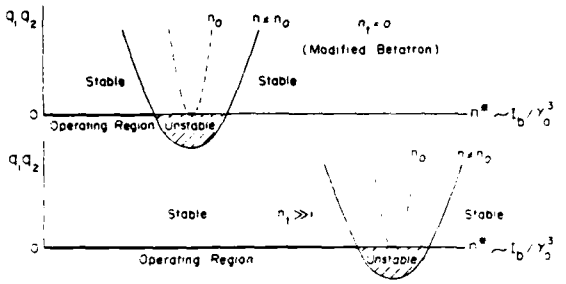



Fig. 2. Stability diagram for the electron ring centroid. Shown is the product $q_1q_2$ vs $n^*$ for $n_1 = 0$ (modified betatron) and $n_1 \gg 1$ (modified betatron with strong focusing). The orbits are closed (stable) when $q_1q_2 > 0$.

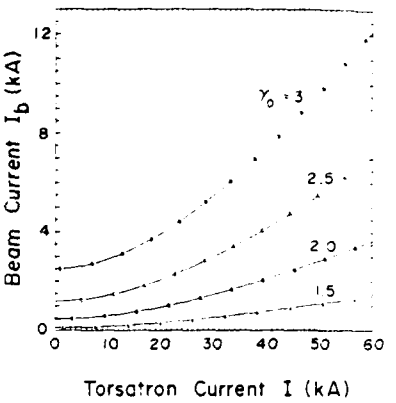



Fig. 3. Maximum beam current $I_b$ (upper limit of the operating region) as a function of the current $I$ in the torsatron windings for $n = 0.6$ and four values of $\gamma_0$. The rest of the parameters are listed in table 1.

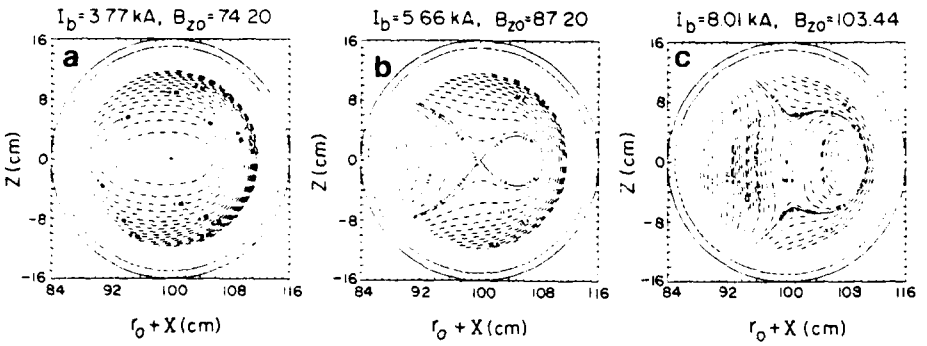



Fig. 4. Macroscopic beam orbits in the transverse plane for $\gamma_0 = 3$ and (a) $I_b = 3.77$ kA, (b) $I_b = 5.66$ kA and (c) $I_b = 8.01$ kA. The rest of the parameters are listed in table 1. In (a) and (c) the orbits are closed near the minor axis.

where $b_w = 2\alpha c\beta_{\theta 0}\gamma_0/(1.76 \times 10^7)$, $\epsilon_1 = 2\alpha\rho_0 K_2(2\alpha\rho_0)$ and Gaussian units are used except for the current. For $n < n_0$, the maximum current is determined by a similar expression, which can be found from eq. (5) by replacing $1 - n$ by $n$ and omitting the $\ln a/r_b$ term that appears inside the square bracket in the denominator of eq. (5).

Fig. 3 shows the maximum beam current $I_b$ as a function of the current in the torsatron windings for $n = 0.6$ and four values of $\gamma_0$. The rest of the parameters are listed in table 1. As shown in fig. 3, for $\gamma_0 = 3$ the maximum beam current increases from 2.5 to 12 kA by increasing the torsatron current from 0 to 60 kA.

Table 1
Values of the various parameters used in eq. (5) to make the plots in fig. 3. The same values are also used in eqs. (1) and (2) to make the plots that are shown in fig. 4.

| | |
|---|---|
| Major radius of the torus | $r_0 = 100$ cm |
| Minor radius of the torus | $a = 16$ cm |
| Beam minor radius | $r_b = 1$ cm |
| External field index | $n = 0.6$ |
| External toroidal field | $B_{\theta 0} = -3$ kG |
| | $\epsilon_1 = -0.1283$ |
| Radius of torsatron windings | $\rho_0 = 18$ cm |
| | $\alpha = 0.1$ cm$^{-1}$ |

For $I = 20$ kA the maximum current in the operating region is 3.9 kA. When $3.9 < I_b < 7.08$ kA the beam is unstable but becomes again stable when $I_b \geqq 7.08$ kA. Fig. 4 shows the beam orbits in the transverse plane for $\gamma_0 = 3$ and $I_b = 3.77$, 5.66 and 8.01 kA. As expected, the orbits near the minor axis are closed for 3.77 and 8.01 kA and open for 5.66 kA.

## References

[1] C.A. Kapetanakos and P. Sprangle, Physics Today (February 1985).
[2] P. Sprangle and C.A. Kapetanakos, J. Appl. Phys. 49 (1978) 1.
[3] C.A. Kapetanakos, P. Sprangle, D.P. Chernin, S.J. Marsh and I. Haber, Phys. Fluids 26 (1983) 1634.
[4] D. Chernin and P. Sprangle, Part. Accel. 12 (1982) 85.
[5] W. Manheimer and J. Finn, Part. Accel. 14 (1983) 29.
[6] C.A. Kapetanakos and S.J. Marsh, Phys. Fluids 28 (1985) 2263.
[7] J.M. Grossman, T.M. Finn and W. Manheimer, Phys. Fluids 29 (1985) 695.
[8] G. Barok and N. Rostoker, Phys. Fluids 26 (1983) 856.
[9] H.S. Uhm, R.C. Davidson and J. Petilo, Phys. Fluids, in press.
[10] C.W. Roberson, A. Mondelli and D. Chernin, Phys. Rev. Lett. 50 (1983) 507.
[11] C.A. Kapetanakos, D. Dialetis and S.J. Marsh, Part Accel., in press; NRL Memo Report No. 5619 (1985).

# APPENDIX TT

## Beam "Self-Trapping" in the NRL Modified Betratron Accelerator

From: HIGH-BRIGHTNESS ACCELERATORS
Edited by Anthony K. Hyder, M. Franklin Rose,
and Arthur H. Guenther
(Plenum Publishing Corporation, 1988)

3

# BEAM "SELF-TRAPPING" IN THE NRL MODIFIED BETATRON ACCELERATOR*

F. Mako, J. Golden, D. Dialetis**, L. Floyd, N. King,***
and C. A. Kapetanakos

Plasma Physics Division
Naval Research Laboratory
Washington, DC 20375 USA

## ABSTRACT

The electron beam in the NRL Modified Betatron is observed to "self-trap" within a narrow range of parameters. It appears that the cause of the "self-trapping" is the localized magnetic field generated by the residual diode stalk current. In this paper, the experimental observations on the "self-trapping" of the beam are briefly summarized, and a model is presented that accurately predicts the experimental results.

## INTRODUCTION

The modified betatron (Sprangle, 1978; Kapetanakos, 1978), (Rostoker, 1980), (Kapetanakos, 1983; Sprangle, 1983; Chernin, 1983; Marsh, 1983; Haber, 1983) is a toroidal induction accelerator that has the potential to generate high current beams. Its field configuration includes a strong toroidal magnetic field in addition to the time varying betatron magnetic field which is responsible for the acceleration. The toroidal magnetic field substantially improves the stability of the circulating electron ring. Preliminary results obtained, so far, from the NRL modified betatron have demonstrated some important aspects of the concept (Mako, 1985; Golden, 1985; Floyd, 1985; McDonald, 1985; Smith, 1985; Kapetanakos, 1985), (Golden, 1986; Mako, 1986; Floyd, 1986; McDonald, 1986; Smith, 1986; Marsh, 1986; Dialetis, 1986; Kapetanakos, 1986), including: (1) the beneficial effect of the toroidal magnetic

---

* work supported by ONR.
** SAIC, McLean, VA, USA
*** Sachs-Freeman Associates, Landover, MD, USA

field on the expansion of the ring's minor radius, (2) the pronounced effect of image forces on the ring equilibrium, (3) the drift (bounce) motion of the ring in the poloidal direction and (4) "self trapping" of the multi-kiloampere beam with efficiency as high as 80%. In this paper, we briefly summarize the experimental observation of "self trapping" of the beam and also present a model that explains its origins.

## EXPERIMENTAL SET-UP AND OBSERVATION

A schematic plan view of the NRL Modified Betatron (Golden, 1983) is shown in Fig. 1. The support structure is an equilateral triangle. Twelve rectangular toroidal field (TF) coils are equally spaced azimuthally about the major axis (perpendicular to the page). Eighteen circular vertical (i.e., betatron) field (VF) coils are located within the TF coils and generate the betatron field that accelerates the electrons. A toroidal vacuum chamber (major radius $r_o$ = 1 m, minor radius a = 15.3 cm) is contained within the coil system. The electron beam is generated in a diode located inside the vacuum chamber. Typically a 0.8 MeV, 1.5-4 kA electron beam is injected tangential to the toroidal field, on the midplane, at a radius of 109 cm.

As theoretically predicted (Kapetanakos, 1982; Sprangle, 1982; Marsh, 1982), when the betatron field ($B_z$) is a particular value $B_{zm}$ ~ 48 G) the beam returns to the injection position after one revolution around the major axis. For lower values of $B_z$, the beam drifts poloidally on a nearly circular trajectory and returns to the injector after a poloidal period (typically 200-500 nsec).

The poloidal trajectory is observed by open shutter photography of the light produced when the beam passes through a thin polycarbonate film that spans the minor cross section of the vacuum chamber. The film target is 2 μm thick and is coated with 2-3 μm of carbon to reduce electrostatic charging.

"Self trapping" is observed for a narrow range of $B_{zo}$ (~ 29 G). In this case, as the beam approaches the injector, it is deflected away from the diode and subsequently performs additional oscillations (see Fig. 2a). At higher betatron magnetic fields the deflection is insufficient, and the beam strikes the injector. At lower $B_{zo}$, the beam drifts into the wall during the first poloidal bounce.

The "self trapping" results from the localized magnetic field associated with the injection diode. Both electric and magnetic fields are associated with the diode because of the applied potential and the current flowing in the cathode stalk (see Fig. 3). However, during the main injection pulse, the fringing electric forces and the magnetic

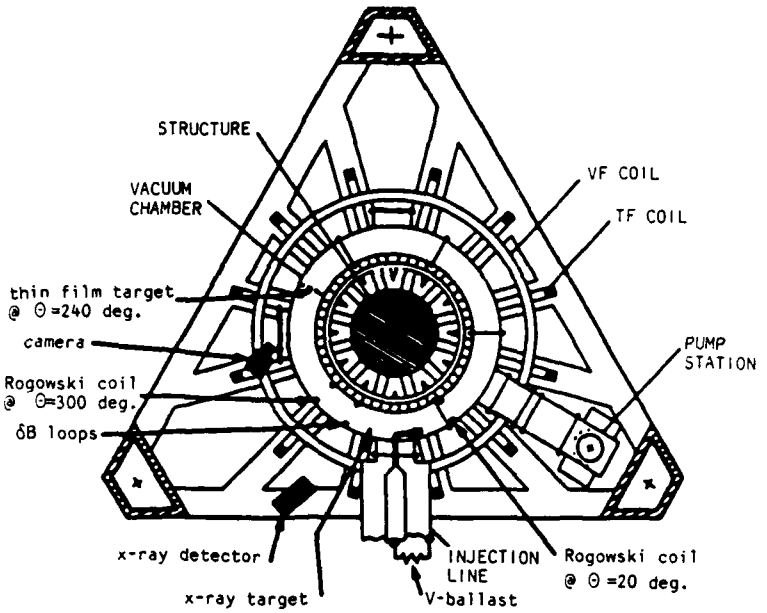



Fig. 1. Schematic plan view of the NRL modified betatron.

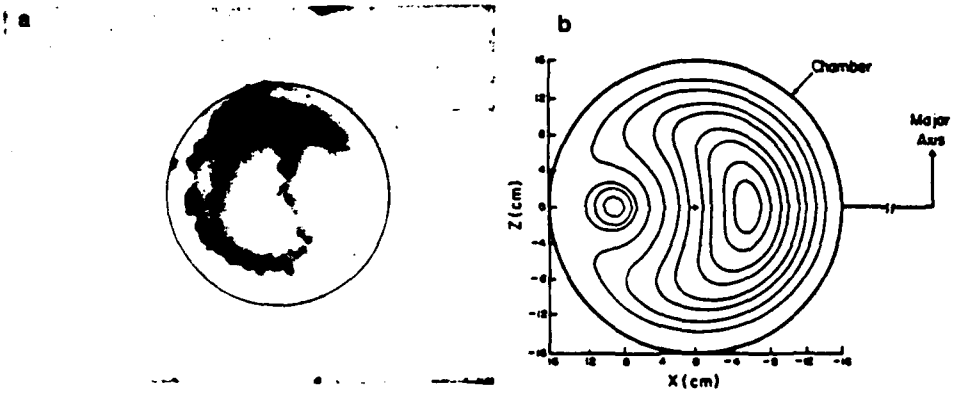



Fig. 2. Experimentally observed (a) and theoretically predicted (b) poloidal motion of the beam.

forces from the 15 cm long azimuthal segment of the cathode stalk nearly cancel. A second pulse (dashed portion of the traces in Fig. 3) follows the main applied voltage pulse by 200 nsec and has an ~ 150 kV peak and a 150 nsec duration. During the afterpulse, the diode impedance is reduced by plasma closure and a 1-4 kA current flows in the stalk. In this case, the magnetic forces are larger than the electric forces and the net component produces a radial inward drift of the beam. This explanation is supported by the observation that when a diverter sparkgap that is in parallel with the diode fires at the end of the flat portion of the main

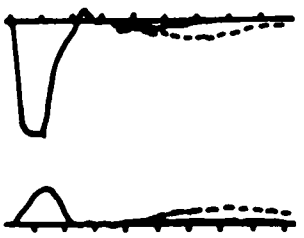


Fig. 3. Potential applied to the injection diode (upper, 850 kV peak, 50 nsec/div), and diode current (lower, 6kA peak, 50 nsec/div). When a diverter switch in parallel with the diode fires at the end of the main pulse, the second pulse (dashed curves) is greatly reduced.

pulse, the second pulse is greatly reduced (solid traces, Fig. 3) and only a small deformation of the drift trajectory is observed. Further evidence is that the radial shift depends on the length of the cathode stalk. A 2-3 cm cathode stalk produces only a slight distortion of the poloidal orbit. A 30 cm long cathode stalk produces a gross distortion of the poloidal orbit.

## THE THEORETICAL MODEL

A simple understanding of the conditions under which the beam can be trapped in the modified betatron in the presence of the diode stalk can be provided by the slow equation (Kapetanakos, 1986; Dialetis, 1986; Marsh, 1986) of the centroid of the beam. For the sake of simplicity, cylindrical geometry is used, i.e., the toroidal corrections of the fields induced by the beam are neglected as well as those of the diode stalk. Also, the beam energy is assumed to have a small variation as the beam moves so that, for all practical purposes, it remains constant. finally, the diode stalk is assumed to be of infinite length. Under these assumptions, the slow equations of motion can be integrated and an expression for the orbits of the beam centroid can be obtained, namely,

$$\left[\frac{\beta\Omega_{zo}r_o}{c}\right]\left[\frac{n}{2}\left(\frac{x}{r_o}\right)^2 - \frac{x}{r_o} - \frac{n}{2}\left(\frac{z}{r_o}\right)^2\right] + \left[\beta^2\gamma\right]\ell n\left(1+\frac{x}{r_o}\right)$$

$$- \left[\frac{\nu}{\gamma^2}\right]\ell n\left(1 - \frac{x^2+z^2}{a^2}\right) - \frac{1}{4\pi}\frac{|e|}{mc^2}\left(V_{ds}-120\pi\beta I_{ds}\right)\left\{\ell n\left[\left(\frac{x-\Delta}{a}\right)^2 + \left(\frac{z}{a}\right)^2\right]\right.$$

$$\left. - \ell n\left[\left(\frac{x\Delta}{a^2}-1\right)^2 + \left(\frac{z\Delta}{a^2}\right)^2\right]\right\} = K. \qquad (1)$$

Rationalized MKS units are used. Here, (x,z) is the position of the beam centroid, $\nu$ Budker's parameter, $\beta$ the beam velocity normalized to the velocity of light c, and $\gamma$ is the relativistic factor of the beam. Also, $r_o$ and a are the major and minor radii of the toroidal chamber while n and $B_{zo}$ are the field index and the betatron magnetic field on the minor axis ($\Omega_{zo} = |e|B_{zo}/m$, where e and m are the electron charge and mass). Finally, $\Delta$ is the distance of the diode stalk from the minor axis, $V_{ds}$ and $I_{ds}$ are the stalk voltage and stalk current. The integration constant K is determined by the initial position of the beam. The various terms in Eq. (1) can be easily identified. Thus, the first and second terms are due to the betatron field and the centrifugal force, while the third term originates from the induced charge and currently by the beam on the chamber walls. The fourth term comes from the fields of the diode stalk and its image due to the conducting walls. When all four terms are comparable to each other, then the possibility arises for the beam to be trapped as Fig. (2b) demonstrates.

Excellent agreement is seen in the comparison of theory and experiment shown in Fig. 2. The experimental parameters have been used in the theoretical model to predict the poloidal orbits. In this case, $\gamma = 1.64$, $r_o = 100$ cm, $I_{ds} = 1$ kA, $\Delta = 9$ cm, a = 16 cm, n = 0.5, the beam current is 1 kA, and the toroidal field is 2 kGauss. Because the model does not include toroidal effects, the model is evaluated with $B_{zo} = 22.16$ G which is equivalent to 29 G in the experiment.

REFERENCES


Golden, J., Mako, F., Floyd, L., McDonald, K., Smith, T., Marsh, S. J., Dialetis, D., and Kapetanakos, C. A., 1986, Beams '86, Proc. of Laser Society of Japan.

Golden, J. et al., 1983, IEEE Trans. Nucl. Sci., NS-30, 2114.

Kapetanakos, C. A., Dialetis, D., and Marsh, S. J., 1986, "Beam Trapping in a Modified Betatron with Torsatron Windings," NRL Memo Report 5619, Washington, DC (to be published in Particle Acceleration).

Kapetanakos, C. A., Sprangle, P., Chernin, D. P., Marsh, S. J., Haber, I., 1983, Phys. Fluids, 26, 1634.

Kapetanakos, C. A., Sprangle, P., and Marsh, S. J., 1982, Phys. Rev. Lett., 49, 741.

Mako, F., Golden, J., Floyd, L., McDonald, K., Smith, T., and Kapetanakos, C. A., 1985, IEEE Trans. Nucl. Sci., NS-32, 3027.

Rostoker, N., 1980, Comments Plasma Phys., 6, 91.

Sprangle, P. and Kapetanakos, C. A., 1978, J. Appl. Phys., 49, 1.

# APPENIDX UU

## A Novel Trapping Scheme in the Modified Betatron Accelerator

Published in 1987 IEEE Particle Accelerator Conference, March 16-19, 1987, Vol 2.

# A NOVEL TRAPPING SCHEME IN THE MODIFIED BETATRON ACCELERATOR*

J. GOLDEN, F. MAKO, L. FLOYD, T. SMITH,
D. DIALETIS†, S. J. MARSH**, and C. A. KAPETANAKOS

Plasma Physics Division

Naval Research Laboratory, Washington DC

## Summary

The previously reported 'self-trapping' of an electron ring in the modified betatron results from current flowing in the diode during a secondary pulse that follows the main pulse.[1,2] A similar shift is produced by a current carrying conductor that is oriented along the toroidal magnetic field $B_\theta$. Because 'self-trapping' is not very versatile, a new trapping scheme is being developed. In this scheme, an induction electric field is applied to a gap in the torus. Preliminary experimental results show that the equilibrium radius of the ring $r_{eq}$ can be shifted by several centimeters.

## Introduction

Following the successful experiments with multikiloampere electron beams injected into the NRL modified betatron,[3] the research effort has focused on efficient trapping and confinement of the ring as a prelude to acceleration. In these studies, a 0.5-1.0 MeV, 1-4 kA beam is injected along the 1-3 kG applied toroidal magnetic field $B_\theta$ from a diode located inside the 1.026 m major radius torus. The observations have confirmed the importance of $B_\theta$ in controlling the minor radius of the beam and are in agreement with the theoretical predictions concerning high current equilibria in the modifed betatron.[4,5]

The dynamics of high current equilibria in the modified betatron are dominated by the forces due to the self-field images of the beam. At the matching value of the betatron magnetic field $B_z$, the forces due to the images, the Lorentz force $ev_\theta \times B_z$ (where e is the charge on the electron and $v_\theta$ is the toroidal velocity) and the centrifugal force are in balance, and the beam does not drift poloidally. After one revolution around the major axis, the beam returns to the injector and strikes the back of the cathode. However, in the high current regime, if the betatron field is less than the matching value, the equilibrium position $r_{eq}$ shifts radially inward, and the beam drifts poloidally about the equilibrium position. The poloidal displacement can easily be adjusted to be sufficient so that the beam does not strike the injector after one turn. For a wide range of parameters, the poloidal drift trajectory is closed, and the beam returns to the injector after a poloidal oscillation (bounce) period. This drift motion has been observed and confirmed with several different diagnostic techniques and is in very good agreement with theory. To achieve trapping, the equilibrium position must be shifted radially inward during the poloidal bounce period so that the beam does not strike the injector.[6]

Within a narrow range of parameters, 'self-trapping' is observed with $\approx$ 80% efficiency. 'Self-trapped' rings with circulating current of 2-3 kA remain for $\approx 4\mu sec$ ($\approx$ 200 revolutions around the major axis). Confinement for 10 $\mu sec$ is observed at 1 kA.

'Self trapping' results from the localized magnetic field associated with current flowing in the cathode stalk during a second pulse that follows $\approx 200nsec$ after the main injection pulse.[2] This afterpulse occurs because the diode is not matched to the pulse forming line of the injector. Because plasma closure has reduced the diode impedance at the afterpulse, a 1-4 kA current may flow although the applied potential is only $\approx 150kV$. Thus, the magnetic forces are larger than the electric forces and the net component produces a radial inward shift of the beam.

This explanation is supported by experiments with a current carrying conductor,i.e. a kicker coil, that is oriented along $B_\theta$. When a short cathode stalk is used and the kicker is not energized, the afterpulse does not significantly affect the beam. However, when the kicker is energized, the shift is similar to that produced by a long cathode stalk with afterpulse. The observed poloidal drift trajectories agree well with calculated orbits.[2]

The use of a kicker coil for trapping avoids the disadvantage of 'self trapping', namely that the conditions for trapping cannot be adjusted independently from the injection conditions. However, such a coil is unattractive. It must be driven with a sufficiently long pulse so that the radius of the poloidal drift trajectory can be reduced by acceleration, and the coil represents another obstacle that the beam must avoid. Therefore, a new trapping scheme is being developed. In this scheme, an induction electric field is applied to a gap in the torus. During the poloidal bounce following injection, the beam is accelerated by this applied field and $r_{eq}$ is shifted. A preliminary experiment to test this scheme has been performed.

## Theory

Trapping by rapidly accelerating the beam with an inductive electric field applied to a gap in the torus is non-invasive. The scheme makes use of the dependence of $r_{eq}$ on $\gamma$. Linear theory predicts that a change in the in the ring energy $\delta\gamma$, will produce a shift in the ring equilibrium position $\delta r$ given by

$$\frac{\delta r}{r_o} = \frac{\delta\gamma/\gamma_o}{1 - n - n_s[r_b^2/a^2]}, \qquad (1)$$

where $\delta r = r_{eq} - r_o$, $B_{zo}$ is the betatron field at the minor axis, $n_s$ is the self-field index, $r_b$ is the beam minor radius, and $r_o$(a) is the chamber major (minor) radius. This expression is valid near the minor axis. However, away from the minor axis, non-linear expressions for the external fields and self-field images must be used. The non-linear equations yield the curves plotted in Fig. 1. These show the energy parameter at the diode $\gamma_D$ versus $r_{eq}$ when $B_{zo} = 30G$. The various curves correspond to different currents and are labelled in units of $I/\beta$ where I is the beam current in kA. It is seen that when $I \approx 1k\mathring{A}$ and $r_{eq} \approx 105cm$, a change in $\gamma$ by 0.1 will produce a shift of $\approx$ 7 centimeters.

CH2387-9/87/0000-0936 $1.00 © IEEE

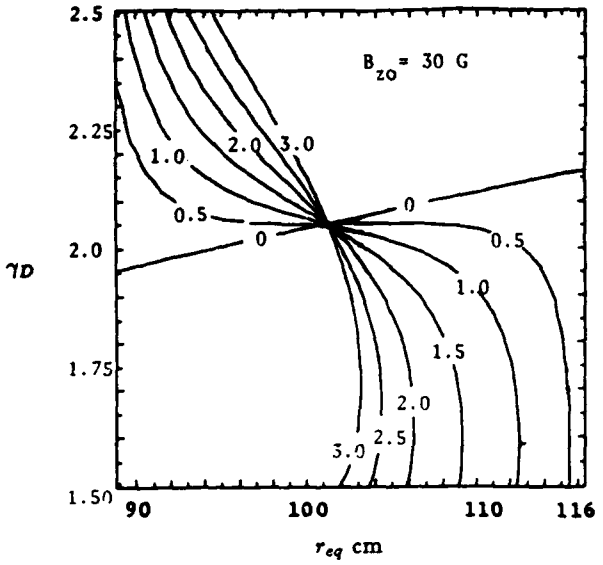



Fig. 1. $\gamma_D$ versus $r_{eq}$ for various values of $I/\beta$ where I is in kA.

The normalized energy of the ring $\gamma$ is less than $\gamma_D$ because energy must be provided to establish the self-fields of the ring. The change in $\gamma$ that occurs during injection of the beam is [7]

$$\langle\gamma\rangle - \gamma_D = \Delta\gamma = -\left(2\nu - \frac{\nu}{\gamma_c^2}\right)\left[\frac{1}{4} + ln\frac{a}{r_b} - \left(\frac{\Delta}{a}\right)^2\right], \quad (2)$$

where $\nu$ is Budker's parameter $= I/17\beta$ (I in kA), $\langle\gamma\rangle$ is the average gamma of the ring, and $\Delta$ is the displacement of the ring centroid from the minor axis.

When the accelerating potential is applied to the gap, $\gamma$ increases, but there is also a significant increase in velocity and current because $\beta$ is less than unity. Thus, the self field flux $\Phi^s$ increases and produces a diamagnetic back-emf at the gap. The rate of change of $\gamma$ that is associated with the change of accelerating flux $d\Phi^{acc}/dt$ and the change in the self field flux $d\Phi^s/dt$, for a fixed position in the transverse plane, is given by

$$m_o c^2 \frac{d\gamma}{dt} = ec\beta\frac{\partial A}{\partial t} = \frac{ec\beta}{2\pi r_o}\left(\frac{d\Phi^{acc}}{dt} - \frac{d\Phi^s}{dt}\right)$$

$$= \frac{ec\beta}{2\pi r_o}\left[V_{gap} - \frac{d[LI]}{dt}\right], \quad (3)$$

where $L \approx \mu_o r_o[ln(8r_o/r_b) - 1.75]$ is the beam inductance, and the change in $\Phi^s$ is proportional to a change in velocity $\delta\Phi^s = LI(\delta\beta/\beta) = LI(\delta\gamma/[\gamma(\gamma^2-1)])$.

Integrating and assuming $\delta\gamma << \gamma$ and $V_{gap} = V_g sin(\pi t/\tau)$ where $\tau$ = trapping pulse duration, one obtains

$$\delta\gamma = \frac{2}{\pi}\frac{\tau}{\tau_o}\frac{eV_g}{m_o c^2}\left[1 + \frac{2L\nu}{\mu_o r_o \gamma^3}\right]^{-1}, \quad (4)$$

where $\tau_o = 2\pi r_o/\beta c$. When $\gamma_D \approx 2.1$, $I \approx 1.5kA$, a=15.3 cm, and $r_b \approx 1cm$, $\gamma \approx 1.6$ and $2L\nu/(\mu_o r_o \gamma^3) \approx 0.3$, i.e., $\delta\gamma$ is reduced by $\approx 25\%$ by the beam diamagnetism. It is seen that a penalty results for 'low' energy injection.

## Experiment

The NRL modified betatron has been described in detail previously.[8] For the present experiments, the principal parameters are listed in Table 1. The betatron field is 'crowbarred' prior to injection and decays with an 'L/R' time constant of several msec so that $B_z$ is quasi-static during the times of interest. Circulating current is measured by Rogowski coils located at two azimuthal positions. The transverse motion of the beam is monitored by three diagnostics: magnetic probes monitoring the poloidal self field of the beam, x-rays emitted when the beam hits a Ta target, and open-shutter photography of the beam interacting with a thin polycarbonate film target that spans the minor cross section of the torus. The film target is 2 microns thick and is coated with carbon to reduce electrostatic charging.

Table 1. Experimental Parameters

| | |
|---|---|
| Injection energy | 0.5-1.0 MeV |
| Injection current | 0.4-3.0 kA |
| Major radius | 1.026 meter |
| Minor radius | 15.3 cm |
| Injection radius | 1.10 m |
| Toroidal field | 3 kG |
| Betatron field | 20 - 80 G |
| vacuum field index | 0.35-0.55 |
| pressure | $4 \times 10^{-6}$ Torr |

To accelerate the electron ring, the flux linked by the ring orbit must increase. This can be accomplished by driving a current around the torus or by changing the flux in a pulse forming line (PFL) that is coaxial with the toroidal chamber. Such a PFL is under development and is shown in Fig. 2. In the mean time, a preliminary test of the trapping scheme has been performed using a planar Blumlein PFL that has been connected to the chamber. This PFL has an impedance of 5Ω/section, a capacitance of 36 nF/section, can be charged up to 18 kV, and produces a pulse of 0.25 $\mu sec$ duration. A typical waveform is shown in Fig. 3.

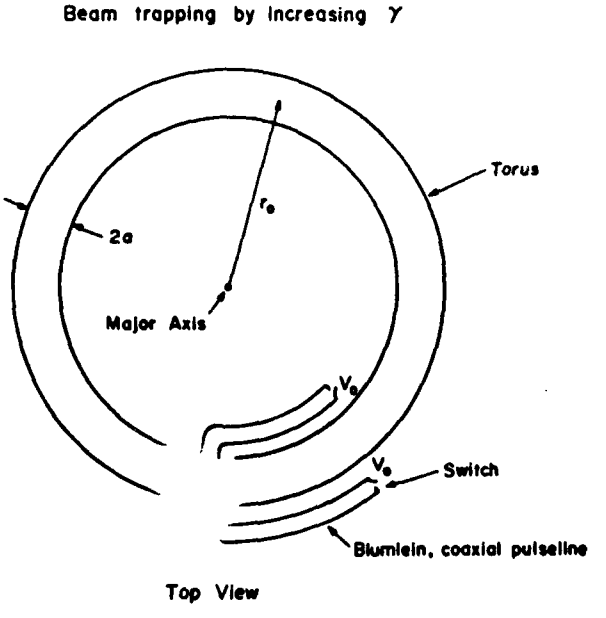



Fig. 2. Schematic of a pulse forming line that is coaxial with the torus.

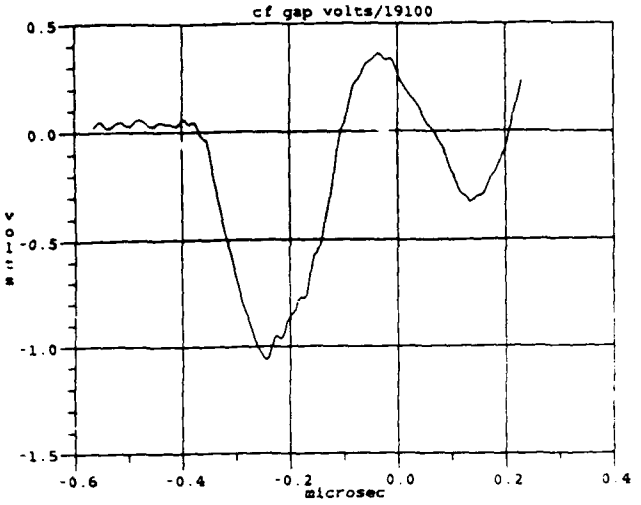



Fig. 3. Typical voltage waveform applied to the gap in the torus (time origin is arbitrary).

To test the trapping scheme, shots were fired with zero and 14 kV applied to the gap. Results are shown in Figs. 4 and 5. The circulating current at two azimuthal positions are shown in each frame of Fig. 4. It is apparent that the duration of the current is substantially longer in the presence of the accelerating voltage (right frame). The poloidal trajectory of the beam obtained by the open-shutter camera technique is displayed in Fig. 5. The injection position is indicated by the arrow, and the major radius is situated to the right of each picture. The results show that the trapping scheme effectively shifts the beam away from the injector.

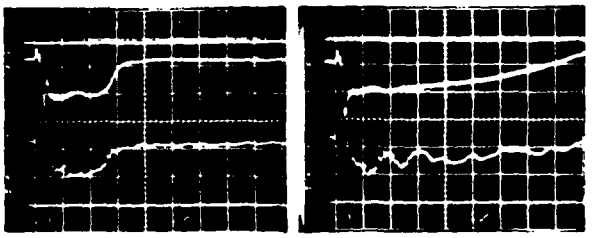


Fig. 4. The circulating ring current at two azimuthal positions versus time (200 nsec/div); left: without gap voltage, right: with 14 kV gap voltage.

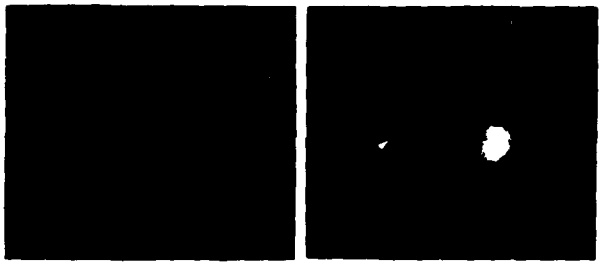


Fig. 5. The poloidal trajectory of the beam. Circle outlines the cross section of the torus; the major axis is to the right. Left: without gap voltage, right: with 14 kV gap voltage.

The displacement of the beam is sensitive to the timing and amplitude of the applied gap potential. Therefore, this scheme offers a way to trap the beam that is independent of the injector and is non-invasive. Following refinement of the apparatus by installing a coaxial Blumlein PFL, experiments to improve the confinement time and accelerate the beam will commence.

* This work is supported by ONR.
† SAIC, McLean VA.
** Sachs-Freeman Associates, Landover MD.

## References

[1] J. Golden, et al., Proc. BEAMS 86 Conf.(1986).
[2] F. Mako, et al., Proc. NATO ASI on High Brightness Beams (1986).
[3] F. Mako, et al., IEEE Trans on Nucl Sci **NS-32** 3027 (1985).
[4] C. A. Kapetanakos, et al., Phys. Fl. **26** 1634 (1983).
[5] C. A. Kapetanakos and S. J. Marsh, Phys. Fl. **28** 2263 (1985).
[6] C. A. Kapetanakos, P. Sprangle, and S. J. Marsh, Phys Rev. Lett **49** 741 (1982).
[7] S. J. Marsh and C. A. Kapetanakos, Memo Report **5933** NRL, Washington DC (1987).
[8] J. Golden, et al., IEEE Trans Nucl Sci **NS-30** 2114 (1983).

# APPENDIX VV

## Beam Extraction from the Modified Betatron

## Development of a Beam Extraction Scheme for the NRL Modified Betatron

## Beam Extraction Scheme From the NRL Modified Betatron Accelerator

# BEAM EXTRACTION FROM THE MODIFIED BETATRON

D. DIALETIS , S.J. MARSH ,
AND C.A. KAPETANAKOS

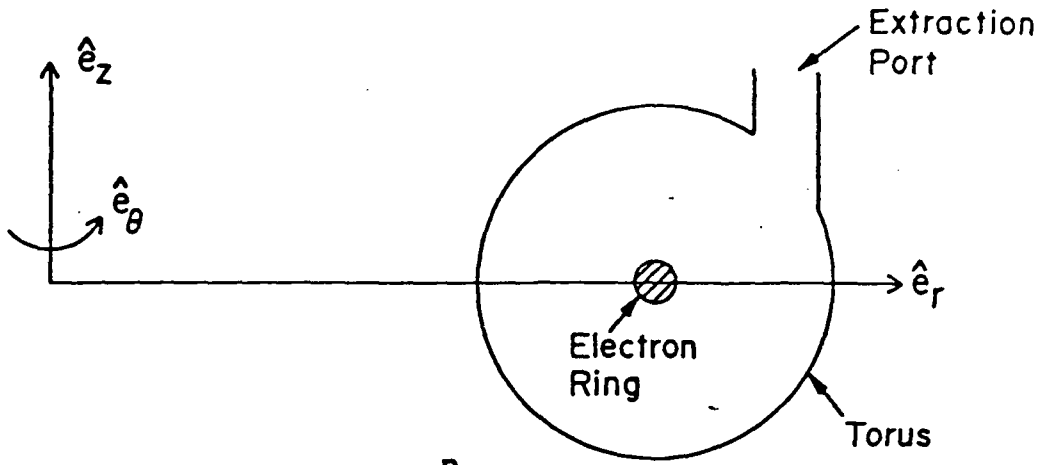
PLASMA PHYSICS DIVISION
NAVAL RESEARCH LABORATORY
WASHINGTON , D.C. 20375

SUPPORTED BY ONR

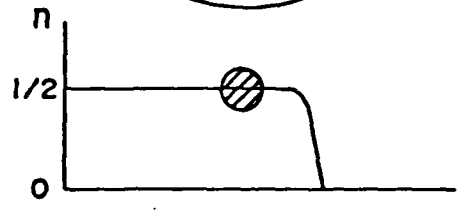
# ABSTRACT

Beam Extraction from the Modified Betatron. D. DIALETIS, S. J. MARSH, C. A. KAPETANAKOS, Naval Researh Laboratory-- A multi-turn beam extraction scheme has been devised that can lead to the unwinding of an electron ring into a straight beam of considerably longer duration than the period of ring's revolution around the major axis of the torus. At the end of the acceleration, the ring centroid is shifted into a region of zero field index by mismatching the beam. Due to the absence of vertical confinement in this region, the ring centroid moves vertically while the beam envelope expands in the same direction. After the electron ring has shifted far from the mid-plane, it enters into a localized ferromagnetic container that has an azimuthal length several times longer than its opening. In the region surrounded by the ferromagnetic material, the magnetic fields are zero and, therefore, the ring unwinds into a straight beam. Analytical and numerical results based on the scheme described above will be presented.
* Supported by ONR

# Modified Betatron
## Multi-turn Extraction Approach(MEA)



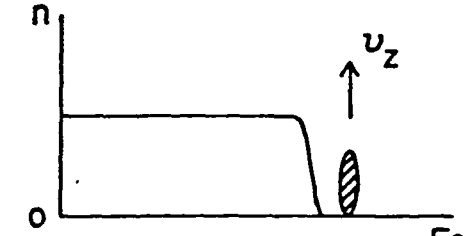

During Acceleration

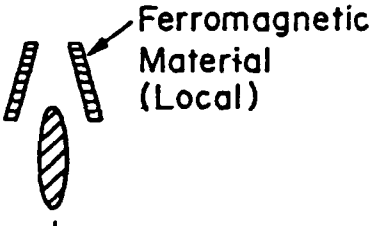



Equ. Position

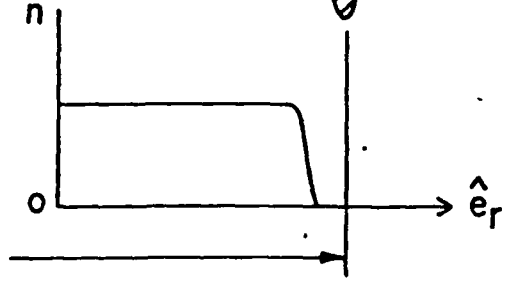
$$r_o = \frac{v_\theta \gamma_o}{\Omega_{zo}}$$

Post-Acceleration

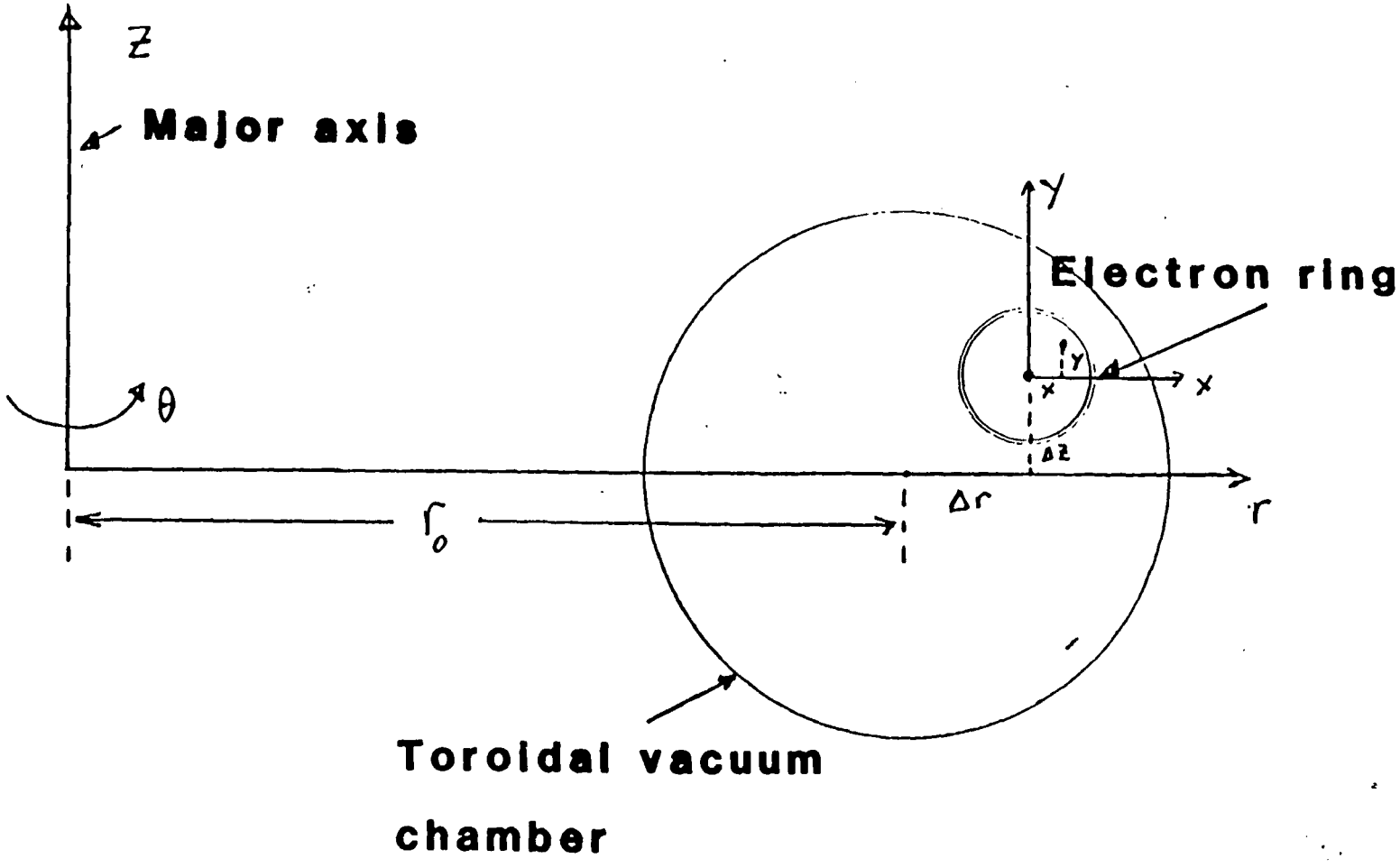



Multi-turn Extraction

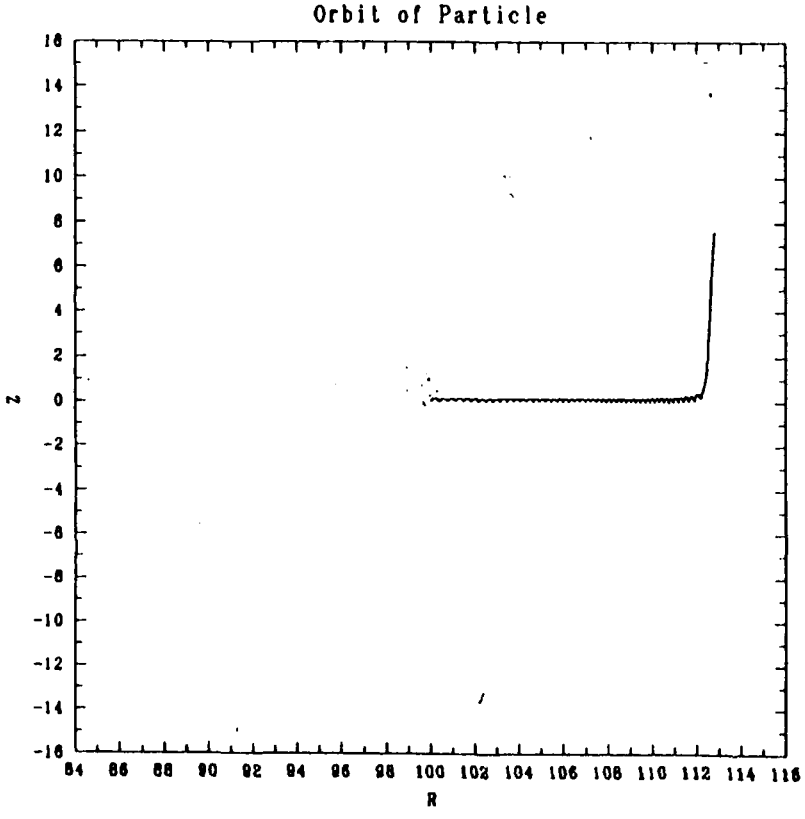


# SYSTEM OF COORDINATES



# RING EXTRACTION

## RING CENTROID MOTION AS $B_z$ IS REDUCED




$$B_z^T = B_z^{st}(R,z) + B_{z_0}^{ex}\, e^{-t/\tau}$$

$\tau =$ 3.5 μsec

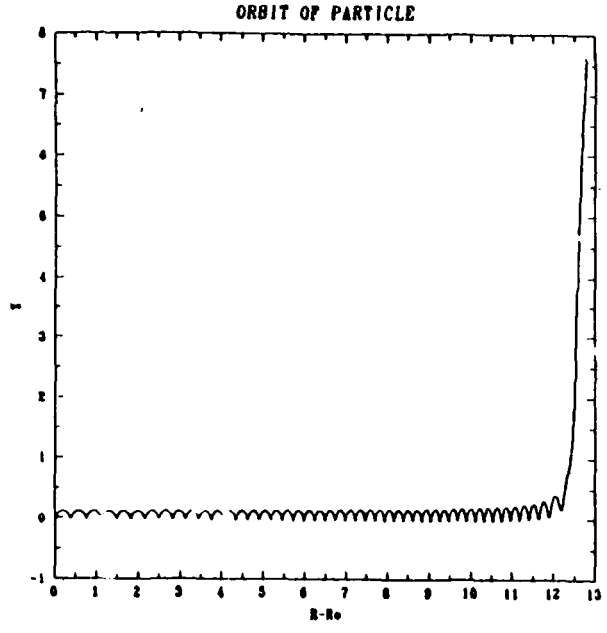
$\gamma =$ 100

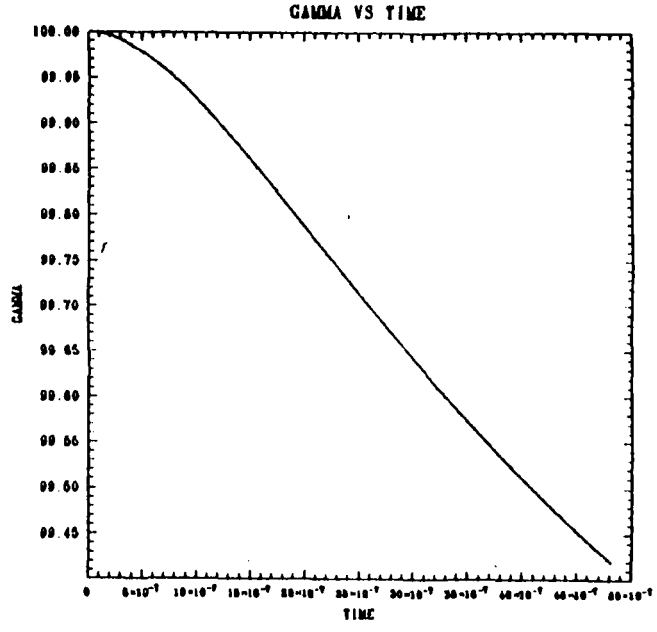
$B_{\theta 0} =$ -2.0 kG

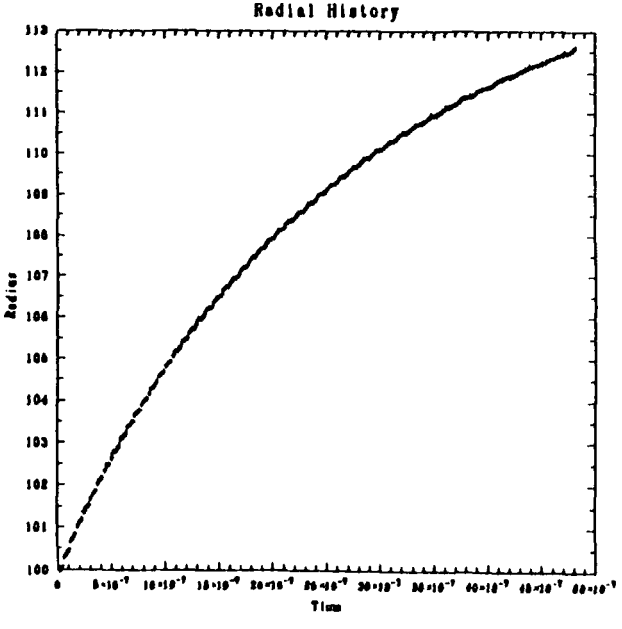
$B_{z_0}^{ex} =$ 204 G

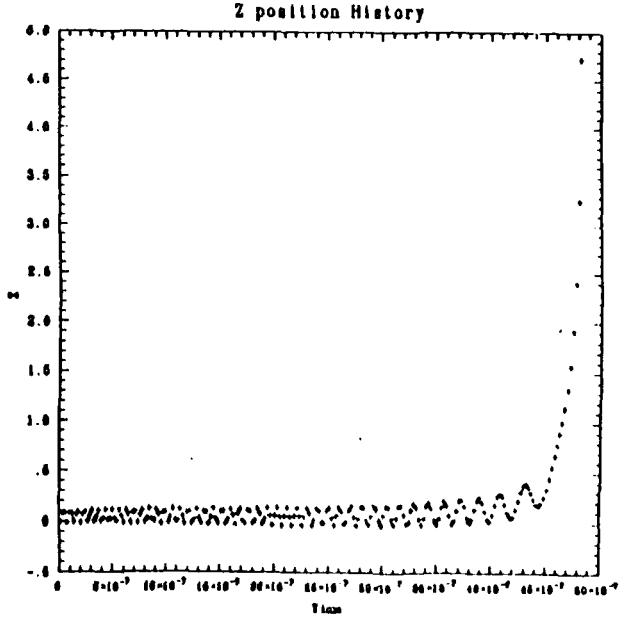
$B_{z_0}^T (t=0) =$ 1.704 kG

**n becomes zero at 12.5 cm**


ORBIT OF PARTICLE
Z
R-Ro


GAMMA VS TIME
GAMMA
TIME


Radial History
Radius
Time


Z position History
Z
Time

# QUADRATIC BETATRON FIELDS

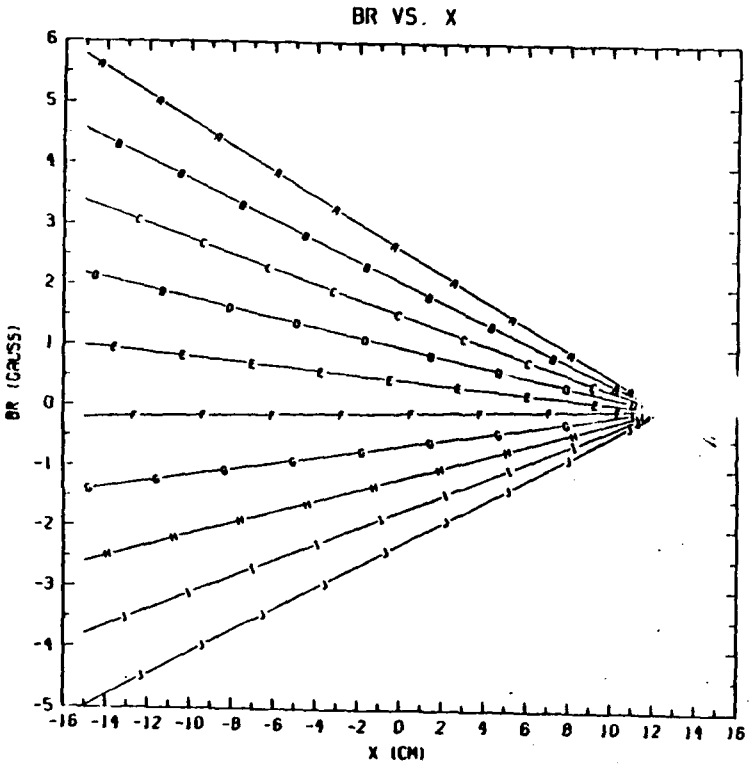
$$n = n_0 \left(1 - \frac{x}{x_0}\right)$$

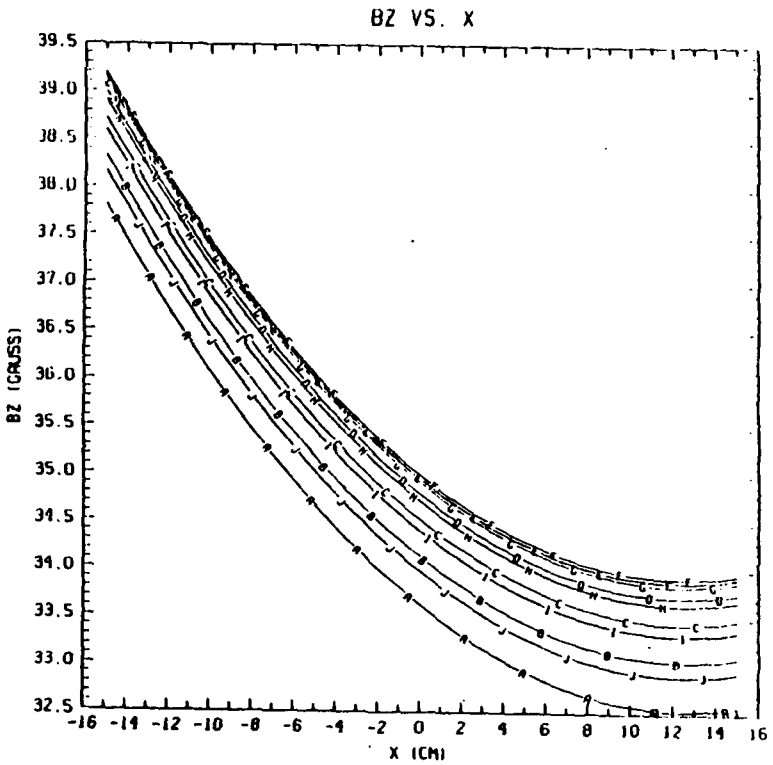
$$B_r = -B_{z0}\left[n_0 - \tilde{n}_0 \frac{x}{\tilde{r}_0}\right]\frac{z}{\tilde{r}_0}$$

$$B_z = B_{z0}\left[1 - n_0 \frac{x}{\tilde{r}_0} + \frac{1}{2}\tilde{n}_0\left(\frac{x}{\tilde{r}_0}\right)^2 + \frac{1}{2}\left(n_0 - \tilde{n}_0\right)\left(\frac{z}{\tilde{r}_0}\right)^2\right]$$

$$\tilde{n}_0 = n_0 \frac{\tilde{r}_0}{x_0}$$

# QUADRATIC BETATRON FIELDS




$r_o = 100$ cm $\quad n_o = 0.5$

$x_o = 12.5$ cm $\quad \tilde{n}_o = 4.0$

$B_{z_o} = 35$ G

# Ring Extraction from the Modified Betatron

## The n = 0 region

### Ring centroid vertical motion

Since vertical confinement is lost, the beam centroid moves vertically. Neglecting again space charge effects ($\gamma$ is large) the slow equations of motion become for n = 0

$$\dot{\Delta z} = -\frac{v_\theta^2}{\hat{\Omega}_\theta/\gamma\,(r_0 + \Delta r)} + \frac{v_\theta(\Omega_{z0}/\gamma)}{\hat{\Omega}_\theta/\gamma} = \frac{v_\theta}{\hat{\Omega}_\theta/\gamma}\left[\left(\frac{\Omega_{z0}}{\gamma}\right) - \frac{v_\theta}{r_0 + \Delta r}\right]$$

$$\dot{\Delta r} = 0$$

Therefore, vertical motion can be controlled mainly by selecting the ratio

$$\frac{(\Omega_{z0}/\gamma) - v_\theta/(r_0 + \Delta r)}{(\hat{\Omega}_\theta/\gamma)}$$

# Beam Extraction From the Modified Betatron

## n = 0 REGION

$\gamma \sim 100$

In this case the toroidal field cannot be neglected. Particle motion is described by the equations

$$\ddot{x} + \omega_x^2 x = -\frac{\Omega_\theta}{\gamma}\dot{y} + k$$

$$\ddot{y} + \omega_y^2 y = \frac{\Omega_\theta}{\gamma}\dot{x}$$

Since $\omega_y^2 = \left(\frac{\Omega_z}{\gamma}\right)^2 n = 0$, these equations can be solved analytically. The dynamics of the beam envelope is determined by taking averages over initial positions and velocities.

**Beam does not rotate as moves vertically**

# Beam Extraction From the Modified Betatron

## n = 0 Region

In the special case that $\langle \dot{x}_o \rangle = \langle \dot{y}_o \rangle = \langle x_o \rangle = \langle y_o \rangle = \langle x_o y_o \rangle = k = 0$ and $\sqrt{\omega_x^2 + \left(\frac{\Omega_\theta}{\gamma}\right)^2}\, t >> 1.$

$$b^2 \equiv \langle y^2 \rangle = \left[\frac{(\Omega_\theta/\gamma)_t}{\omega_x^2 + (\Omega_\theta/\gamma)^2}\right]^2 \langle x_o^2 \rangle\, \omega_x^4 + \langle y_o^2 \rangle$$

and the speed of vertical expansion is

$$\frac{db}{dt} = (\Omega_\theta/\gamma)\, \frac{\omega_x^2\, r_{bo}}{\omega_x^2 + (\Omega_\theta/\gamma)^2}$$

For $B_\theta = 3$ KG, $B = 1.7$ KG, $\gamma = 100 \Longrightarrow \frac{db}{dt} \sim 1.3\ r_{bo}$ mm/nsec.

## CONCLUSION

Numerical solution of equations of motion show that when the energy mismatch increases slowly in relation to the bounce period, the ring follows its equilibrium potition while its radius of rotation around the equilibrium position remains very small.

In the region where the field index becomes equal to zero, since vertical confinement is lost, the beam centroid moves vertically.

# DEVELOPMENT OF A BEAM EXTRACTION SCHEME FOR THE NRL MODIFIED BETATRON.*

D. DIALETIS, S. J. MARSH, R. FAEHL, C. A. KAPETANAKOS, Naval Research Laboratory. In relation to the ICARE (Ion Channel Assisted Radial Extraction) extraction scheme that is presently under development at NRL, a study has been made of the electron ring radial outward motion when the vertical magnetic field is mismatched to the electron energy. Using derived analytic expressions for the vertical magnetic field that give a field index on the midplane that varies from 1/2 close to the minor axis of the torus to 1 near the extractor, we have studied the evolution of the ring envelope as well as its phase space and the time profile of its normalized emittance with the NRL particle-in-cell computer code MOBE. During the approximate 2 $\mu$sec extraction time, the ring moved from the minor axis that is located at 100 cm to the field annihilator extractor that is located at 128 cm with only a factor of two expansion of its radial minor axis and with a factor of two reduction of its minor vertical axis. The vertical displacement of the ring centroid was less than 0.6 cm, while the average electron emittance remained constant over the entire extraction time.

*Supported by SPAWAR and ONR.

APS-DPD Conference San Diego

(6)

# DEVELOPMENT OF A BEAM EXTRACTION SCHEME FOR THE NRL MODIFIED BETATRON

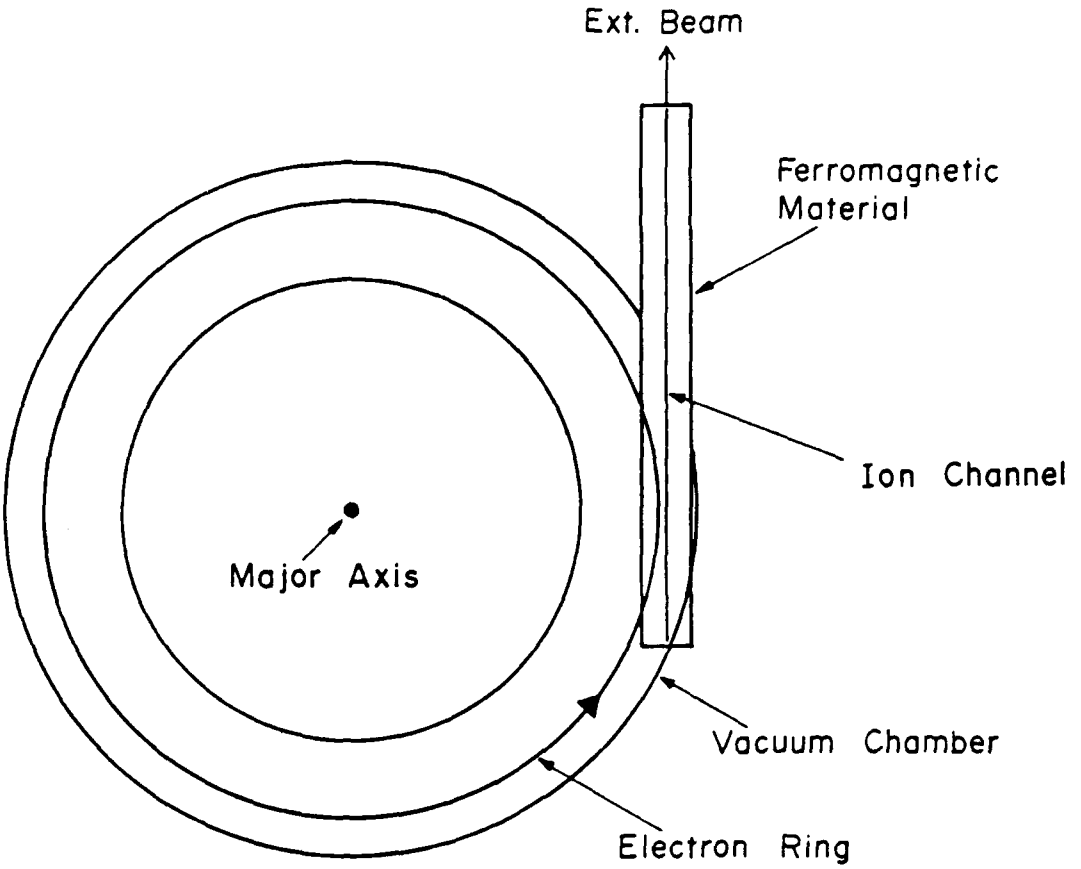
D. DIALETIS , S.J. MARSH ,
AND C.A. KAPETANAKOS

PLASMA PHYSICS DIVISION
NAVAL RESEARCH LABORATORY
WASHINGTON , D.C. 20375

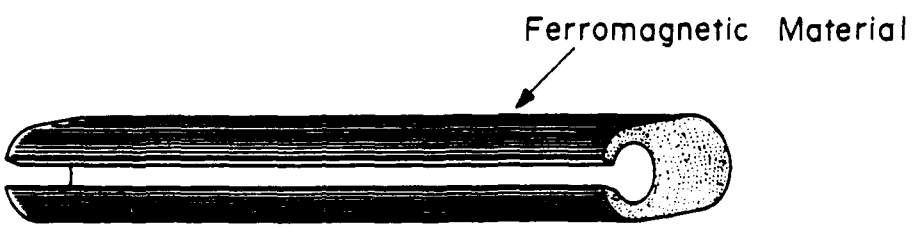
SUPPORTED BY SPAWAR AND ONR

Copy available to DTIC does not permit fully legible reproduction

# I C A R E
## Ion Channel Assisted Radial Extraction from The Modified Betatron

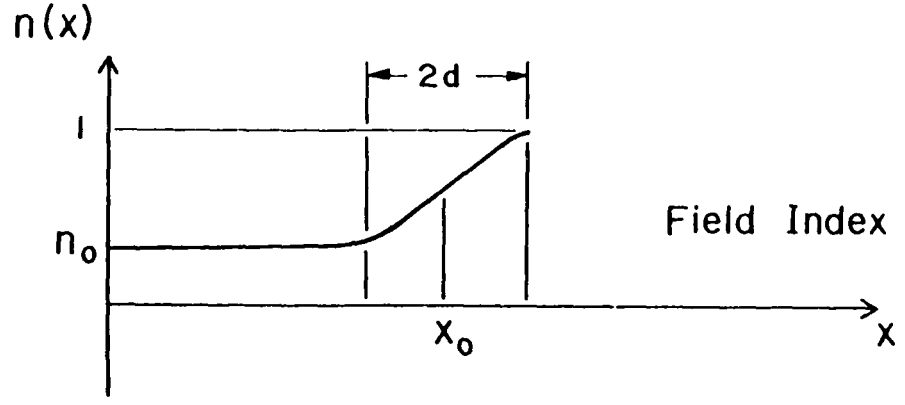


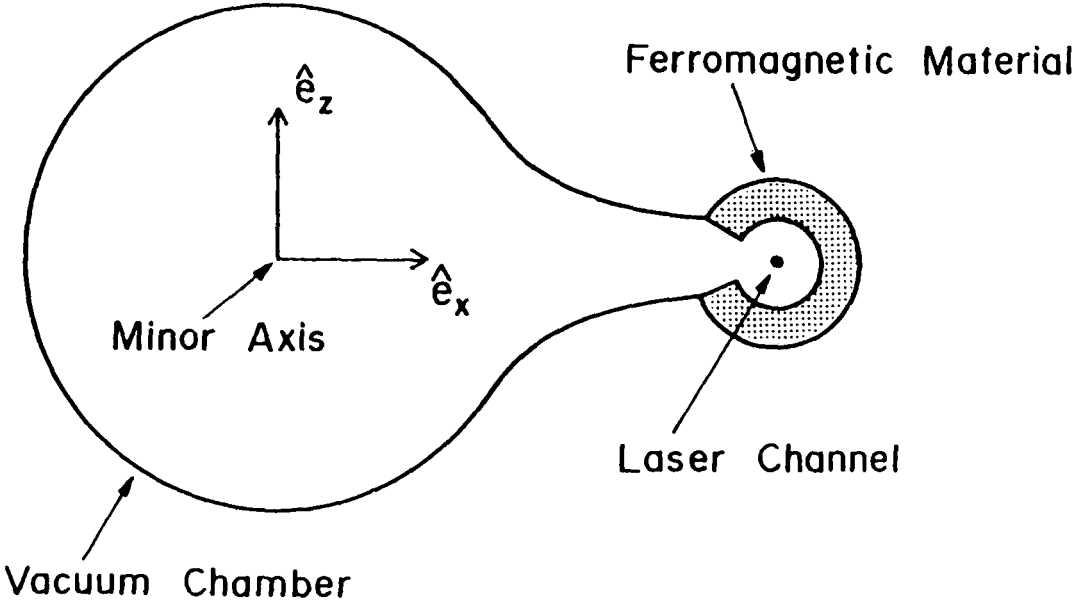

TOP VIEW



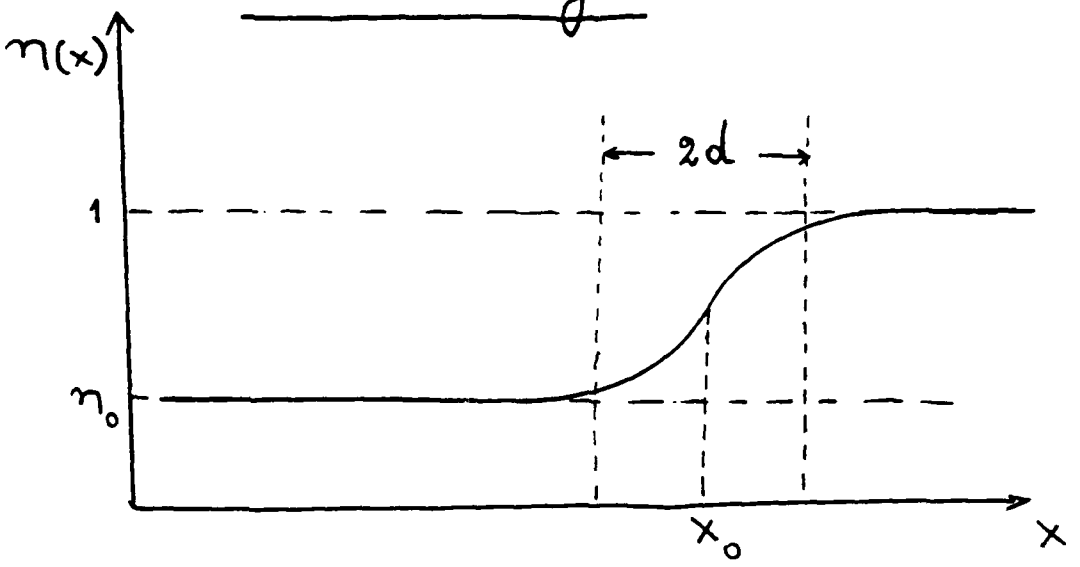

SIDE VIEW

# NRL Modified Betatron
## Single Turn Extraction



# Theory




The field index $n(x)$ at the midplane is equal to

$$n(x) = A\left[B + f^{(0)}(x)\right]$$

where

$$A = \frac{1 - n_0}{1 + \tanh \frac{x_0}{d}}$$

$$B = \frac{n_0 + \tanh \frac{x_0}{d}}{1 - n_0}$$

$$f^{(0)}(x) = \tanh \frac{x - x_0}{d}$$

The magnetic field, correct to first order in toroidal corrections, is equal to

$$B_r(r,z) = -B_z(r,0)\,A\,\frac{z}{r} * \\ * \left[ B + f^{(0)}(x) + \sum_{m=1}^{\infty} b_m(r) \left(\frac{z}{d}\right)^{2m} \right]$$

$$B_z(r,z) = B_z(r,0) * \\ * \left[ 1 - A\,\frac{z}{r} \sum_{m=1}^{\infty} a_m(r) \left(\frac{z}{d}\right)^{2m-1} \right]$$

where

$$x = r - r_0 \quad (r_0 = \text{major radius})$$

$$B_z(r,0) = B_{z0}\left[ 1 - \frac{F_1(r)}{r} \right]$$

$$F_1(r) \equiv \int_{r_0}^{r} n(r')\,dr'$$

$$= A\left[ B\,x + d \ln \frac{\cosh \frac{x-x_0}{d}}{\cosh \frac{x_0}{d}} \right]$$

COMPUTER SIMULATION

Ring Envelope During Extraction

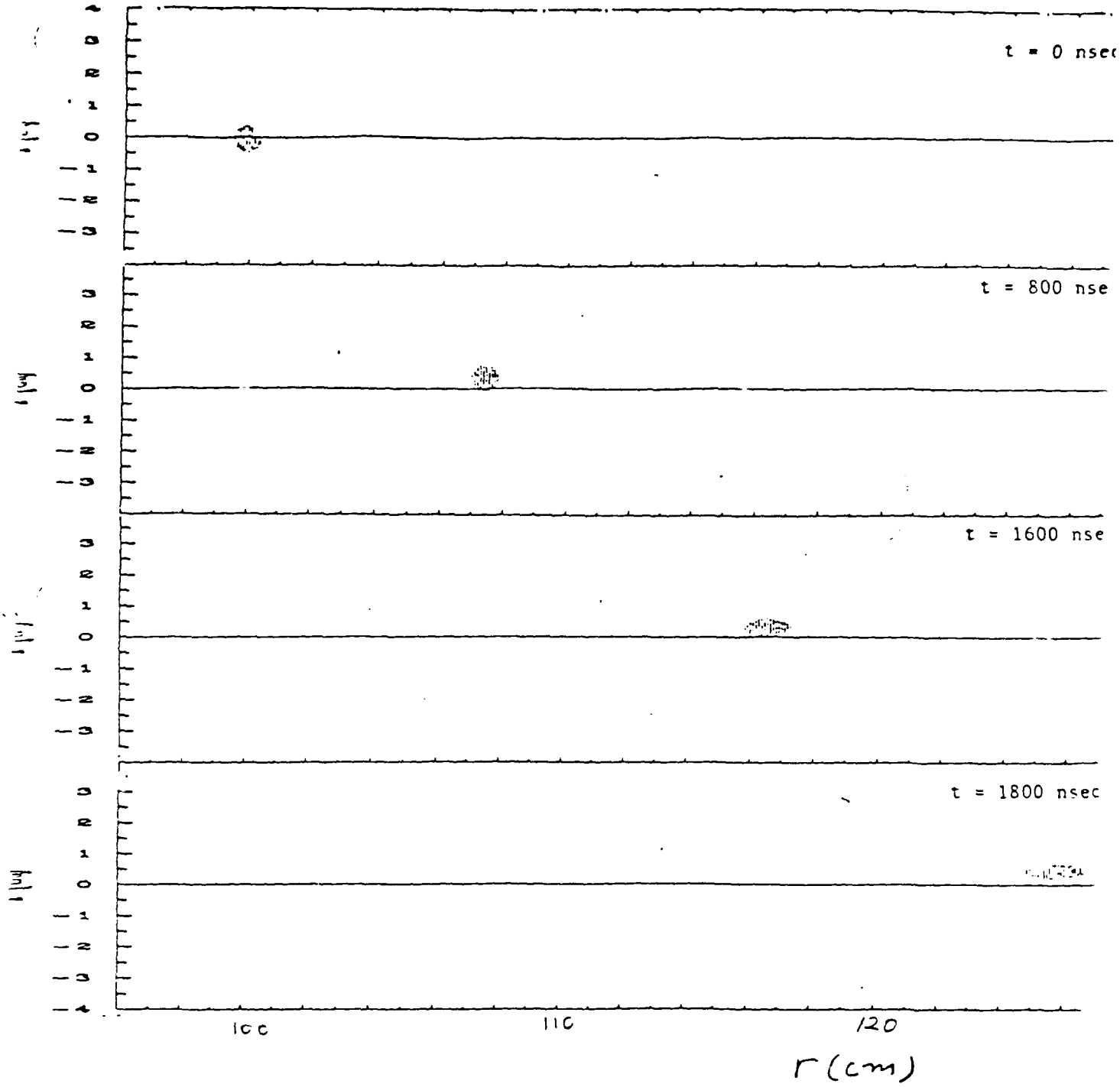
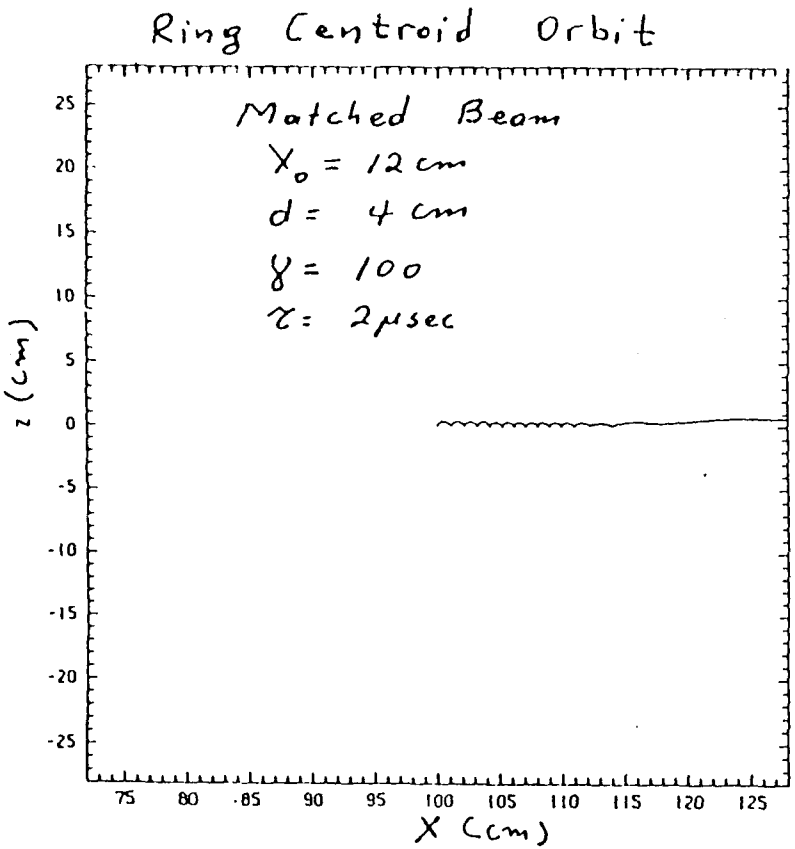
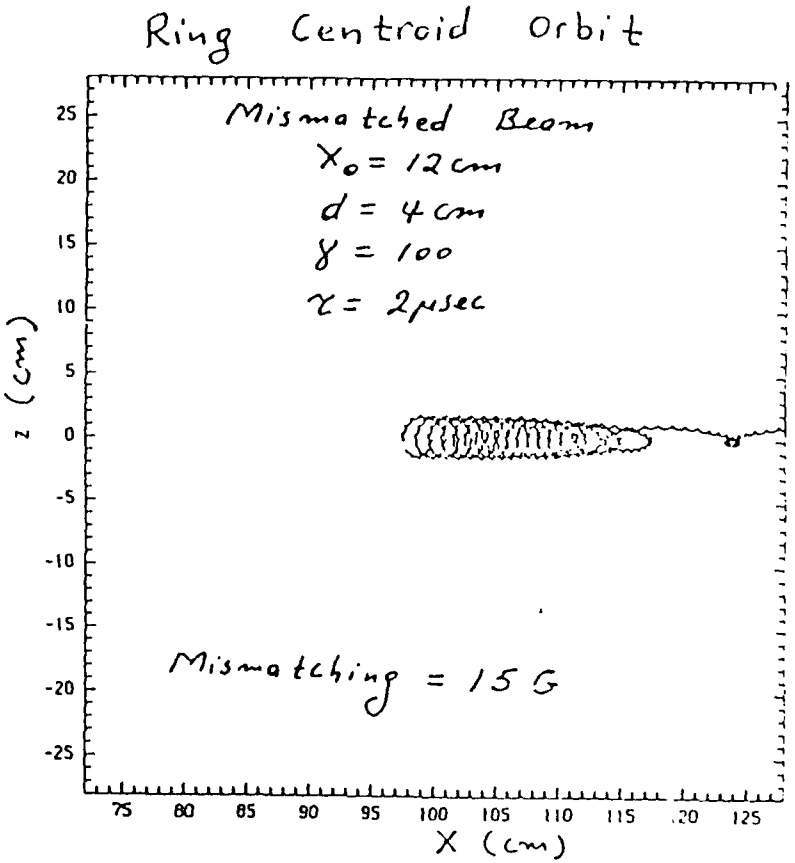



Fig. 1


Ring Centroid Orbit
Matched Beam
$X_0$ = 12 cm
d = 4 cm
$\gamma$ = 100
$\tau$ = 2 μsec
z (cm)
X (cm)

(a)


Ring Centroid Orbit
Mismatched Beam
$X_0$ = 12 cm
d = 4 cm
$\gamma$ = 100
$\tau$ = 2 μsec
Mismatching = 15 G
z (cm)
X (cm)

(b)

Fig. 2

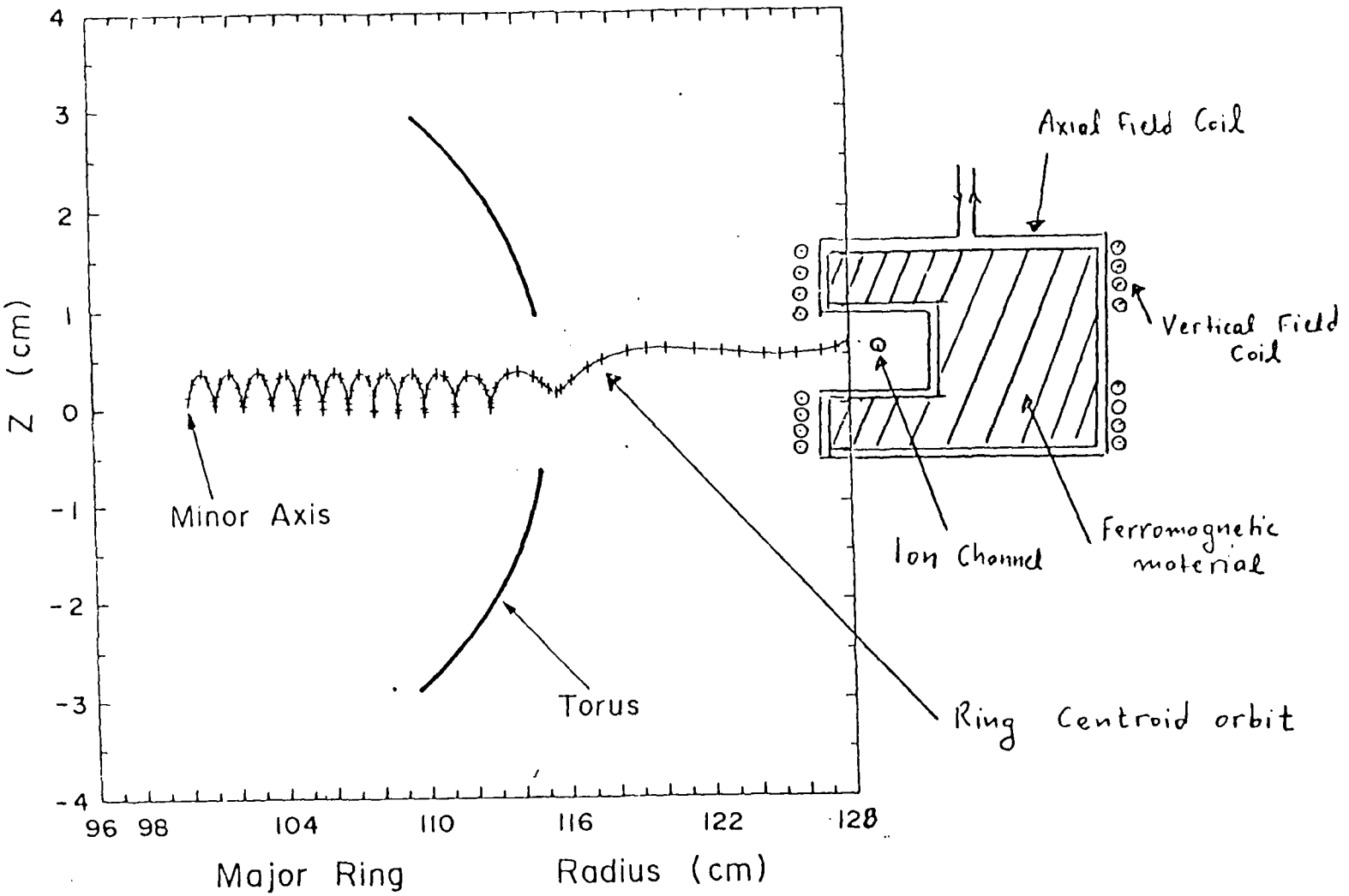

4
3
2
1
0
-1
-2
-3
-4
Z (cm)
96 98
104
110
116
122
128
Major Ring
Radius (cm)
Minor Axis
Torus
Axial Field Coil
Vertical Field Coil
Ion Channel
Ferromagnetic material
Ring Centroid orbit

FIG. 3
Fig. 3

Ring Centroid orbit

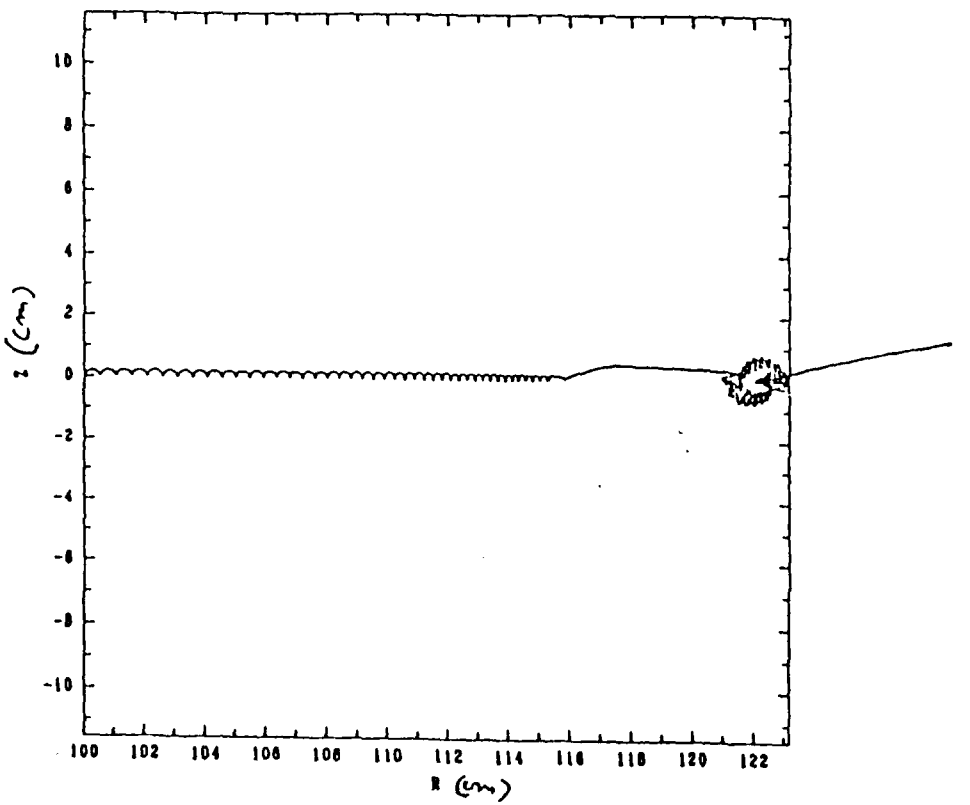
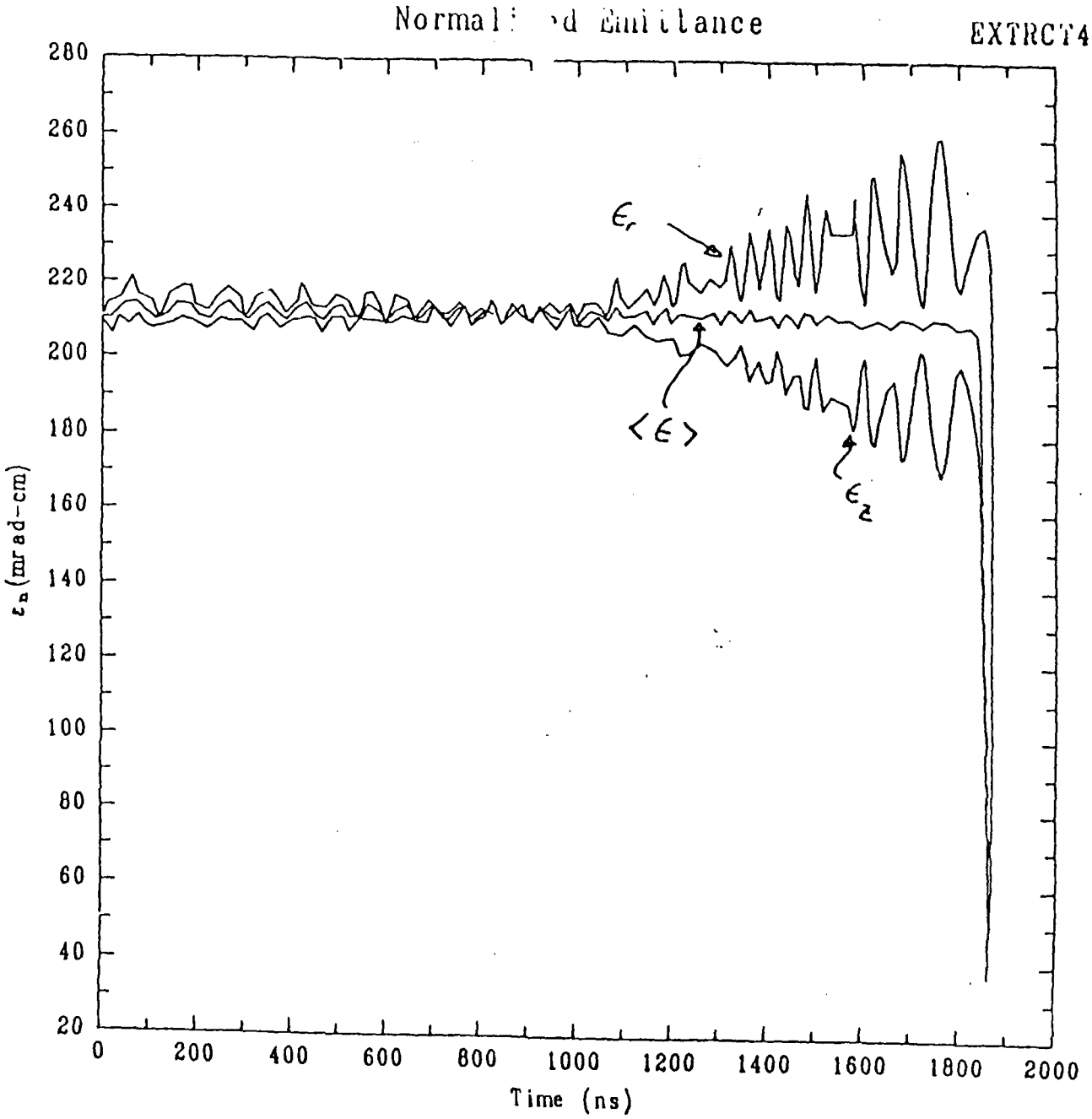



Fig. 4


Normal: d Emittance
EXTRCT4
280
260
240
220
200
180
160
140
120
100
80
60
40
20
$\epsilon_n$ (mrad-cm)
0
200
400
600
800
1000
1200
1400
1600
1800
2000
Time (ns)
$\epsilon_r$
$\langle\epsilon\rangle$
$\epsilon_z$

$$b_m(r) = (-1)^m f^{(2m)}(r)$$

$$a_m(r) = (-1)^m f^{(2m-1)}(r)$$

$m = 1, 2, 3, \ldots$

$$f^{(0)}(r) = \tanh \frac{x - x_0}{d}$$

$$f^{(1)}(r) = \frac{1}{2} \frac{1}{\cosh^2 \frac{x - x_0}{d}}$$

$$f^{(m)}(r) = -2 \sum_{k=0}^{m-2} \frac{(k+1)(m-1-k)(m-k)}{(m-1)\,m\,(m+1)} f^{(k)}(r) f^{(m-1-k)}(r)$$

$m = 2, 3, 4, \ldots$

Here:

$$|z| < d$$

$$|x| << r_0$$

The vector potential, correct to first order in toroidal corrections, is equal to:

$$A_\theta(r,z) = A_\theta(r,0) + B_z(r,0)\, A \frac{d^2}{r} * \left[ \left( B + f^{(0)}(r) \right) \frac{1}{2} \left( \frac{z}{d} \right)^2 + \sum_{m=2}^{\infty} \frac{1}{2m} b_{m-1}(r) \left( \frac{z}{d} \right)^{2m} \right]$$

where

$$A_\theta(r,0) = B_{z0} \left[ \frac{1}{2} \left( r + \frac{r_0^2}{r} \right) - \frac{1}{r} F_2(r) \right]$$

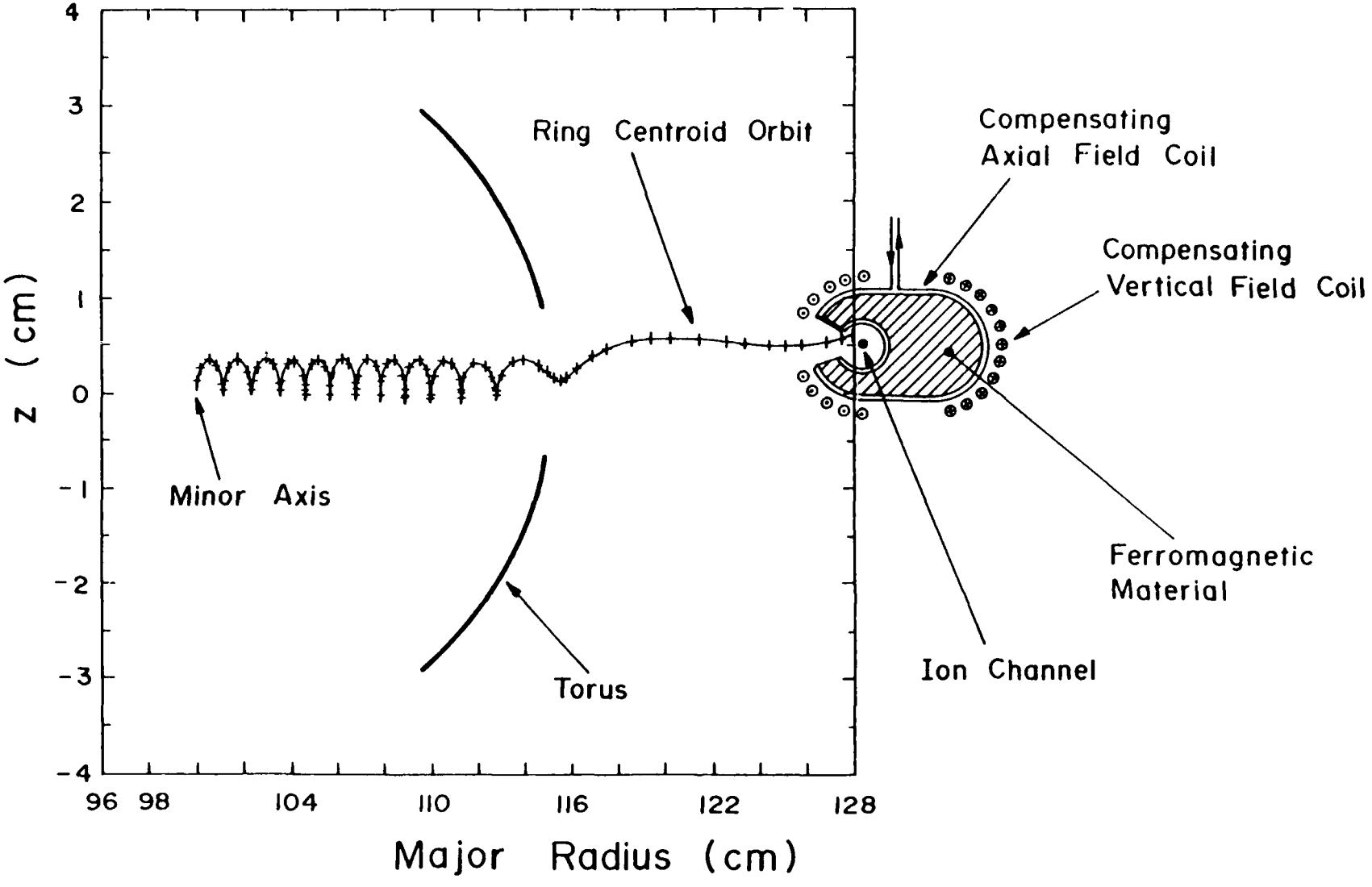
$$B_z(r,0) = B_{z0} \left[ 1 - \frac{F_1(r)}{r} \right]$$

$$F_1(r) = \int_{r_0}^{r} n(r')\, dr'$$

$$F_2(r) = \int_{r_0}^{r} F_1(r')\, dr'$$

# ICARE

## Ion Channel Assisted Radial Extraction from The Modified Betatron



# Computer Simulation

Radial ring displacement by decreasing the vertical field

**Parameters**

$\gamma = 100$

$r_b = 4.2$ mm

$B_{\theta o} = -4$ kg

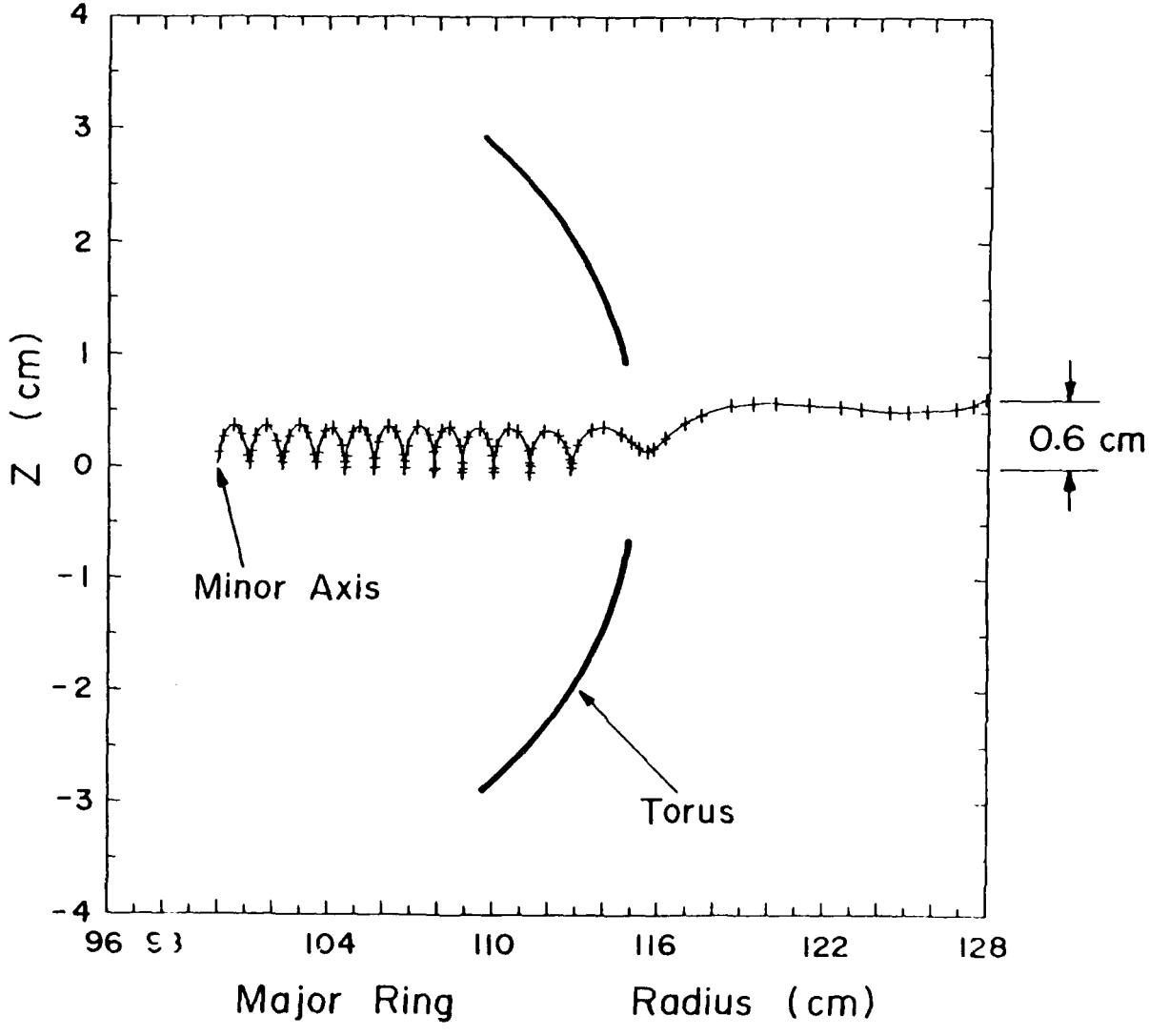
$B_{zo} = 1704.5$ G

$\xi_n = 280$ mrad - cm

$n = 0.5 - 1.0$

$\tau = 4$ $\mu$sec

Exp. decay



COMPUTER SIMULATION (MOBE - PIC)

RUN PARAMETERS

Initial beam energy $\gamma_o$ = 100 [99.98]

Major radius $r_o$ (cm) = 100

Initial beam minor radius $r_b$ (cm) = 4.2 mm

Initial beam center position $r_i$ (cm) = 100

Betatron magn. field at $r_o$, z = o, $B_{oz}$ (G) = 1500 + 204.5 = 1704.5

Toroidal magn. field at $r_o$, z = o, $B_{o\theta}$ (KG) = -4kG

Initial emittance $\varepsilon$ (rad - cm) = 280 mradcm - normalized emittance

External field index n = 0.5 → 1 (tanh variation)

Wall diffusion time $\tau_D$ (nsec) = $\infty$

Time step (nsec) = 200 ps

No. of particles = 128

Trapping field $B_z^{Trap}$ = 204.5 G

Time constant $\tau$ = 4 μsec

$x_o$ = 12 cm

d = 4 cm

# CONCLUSION

Computer simulations of the electron ring outward motion, in a vertical magnetic field that is mismatched to the electron energy, have shown that:

- there is no drastic deformation of the beam cross section
- the vertical displacement of the beam centroid is less than 0.6 cm
- the electron emittance remains constant over the entire extraction time

# BEAM EXTRACTION SCHEME FROM THE NRL MODIFIED BETATRON ACCELERATOR*

D. Dialetis, S.J. Marsh, P. Loschialpo

and C.A. Kapetanakos

Plasma Physics Division

Naval Research Laboratory

Washington, DC 20375

*Supported by SPAWAR

# Beam Extraction Scheme from the Modified Betatron Accelerator*

D. Dialetis†, S. J. Marsh‡, P. Loschialpo and C. A. Kapetanakos, Naval Research Laboratory—A technique is proposed for extracting the electron ring from the modified betatron accelerator. Basically, this technique is based on the transformation of the circulating electron ring into a stationary helix, in the toroidal direction, by exciting the resonance that naturally exists for some specific values of the ratio of the vertical to toroidal magnetic field. Transformation of the ring into a helix is achieved with a localized vertical magnetic field disturbance that is generated by an agitator coil. As the minor radius of the helix increases with each passage through the gap of the agitator coil, the electrons eventually reach the extractor and the electron ring unwinds into a straight beam.

*Supported by SPAWAR.

‡Sachs/Freeman Associates; †SAIC.

# Ring Extraction

## The NRL extraction technique

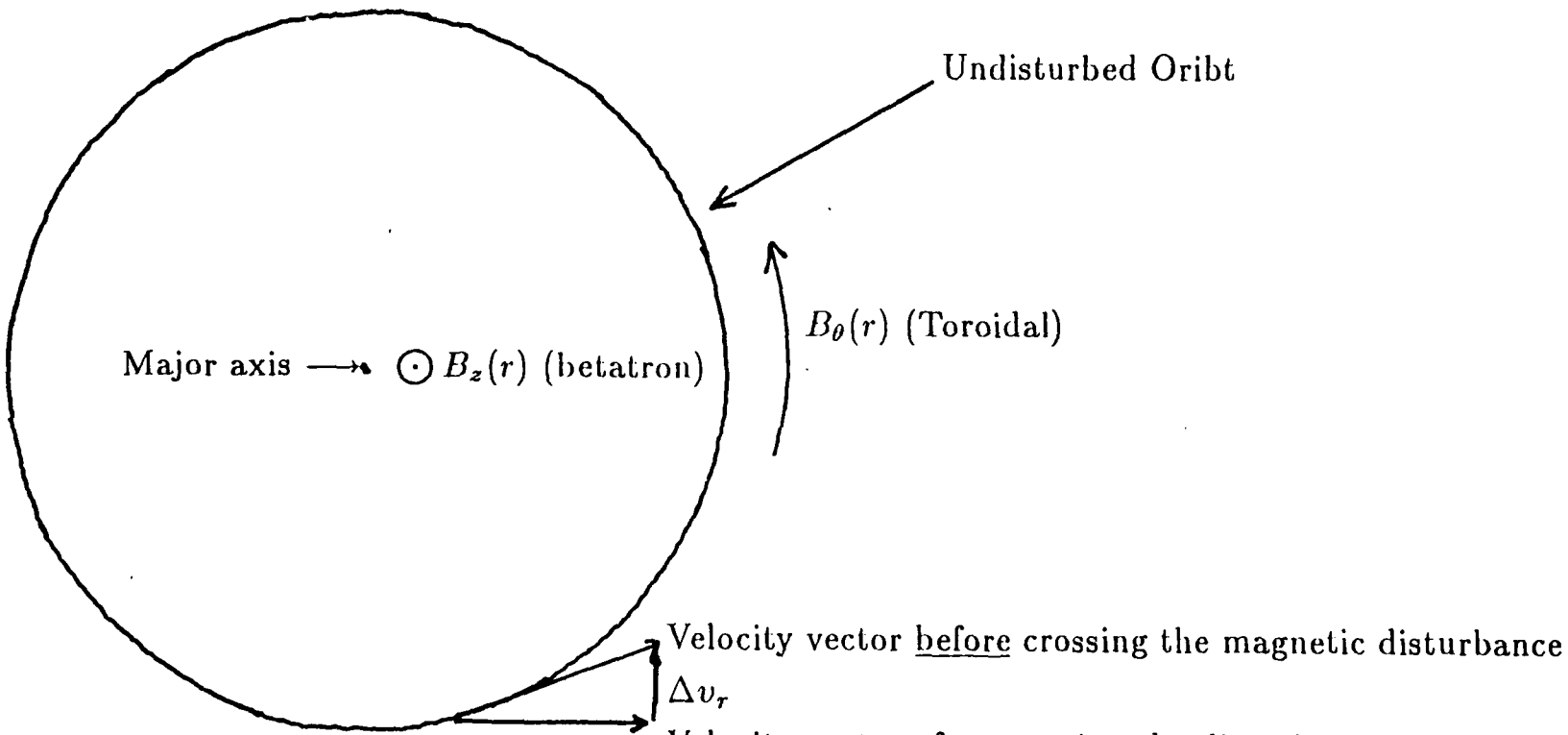
Basically, this technique consists of transforming the circulating electron ring into a stationary helix, in the toroidal direction, by exciting the resonance that naturally exists for some specific values of the ratio of the vertical to toroidal magnetic field.

Transformation of the ring into a helix is achieved with a localized vertical magnetic field disturbance that is generated by an agitator coil.

Two modes of operation:

- Pulsed
- Static

The Resonance Extraction Technique
Physical Mechanism




$$\Delta v_r = -2(\Delta\Omega_z^a/\gamma) r_a \Delta\theta$$

$\Delta\theta$ = Toroidal half width of magnetic disturbance

## Resonance Extraction Technique

As a result of the acquired radial velocity, the electrons start to gyrate in the toroidal magnetic field with radius

$$\rho = 2(N^*/\ell)(\Delta\Omega_z^a)r_a\Delta\theta$$

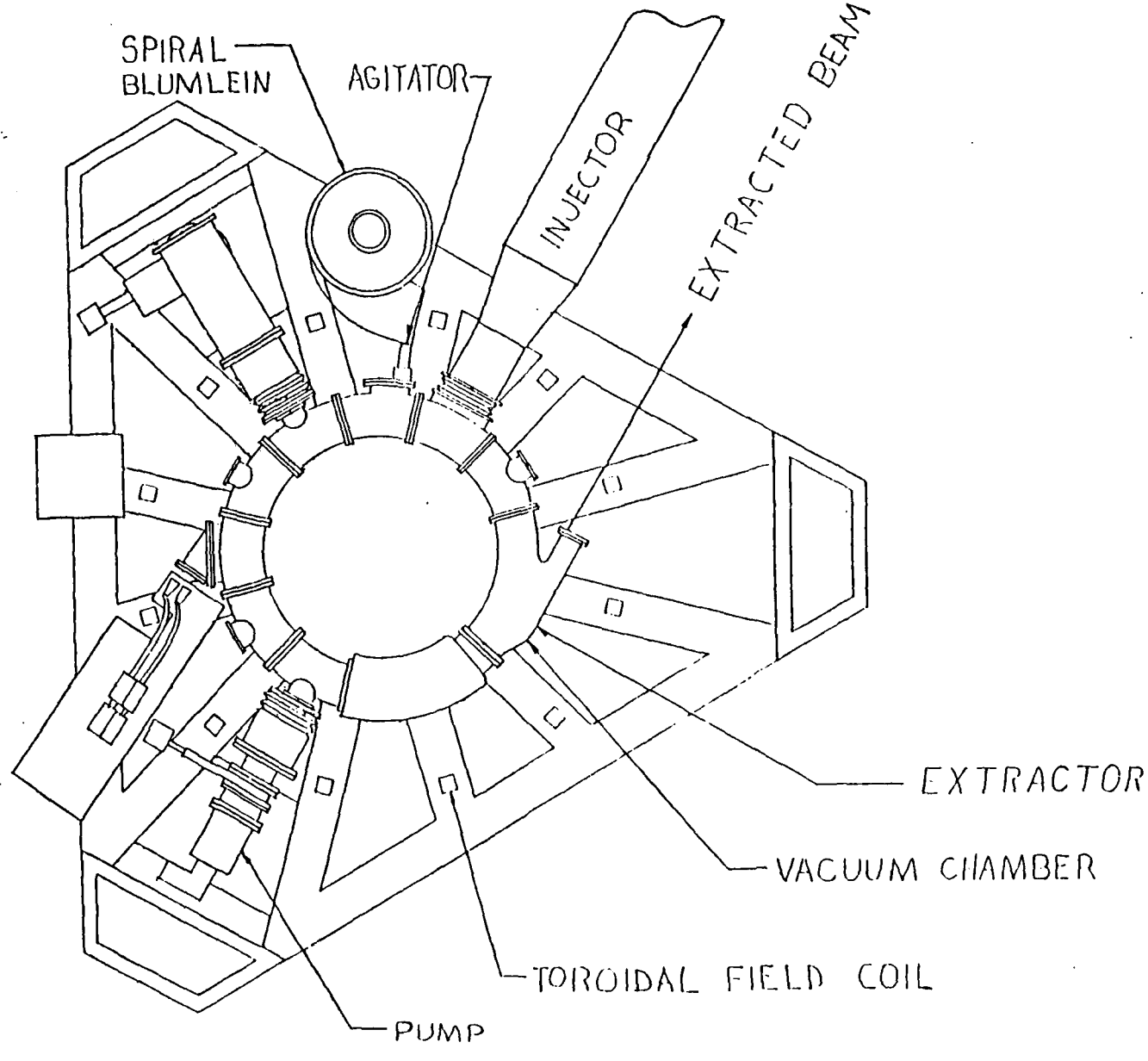
When the ratio $B_z/B_\theta$ at $r = r_a$ satisfies the condition

$$B_z/B_z = 2\ell/(2\ell^2 - 1), \ell = 1, 2, 3...(\text{Resonance condition})$$

Then

- N* = N = number of passes through the disturbance
- All the electrons in the rings execute identical orbits (Coherent motion)

# NRL MODIFIED BETATRON
# WITH EXTRACTION COMPONENTS



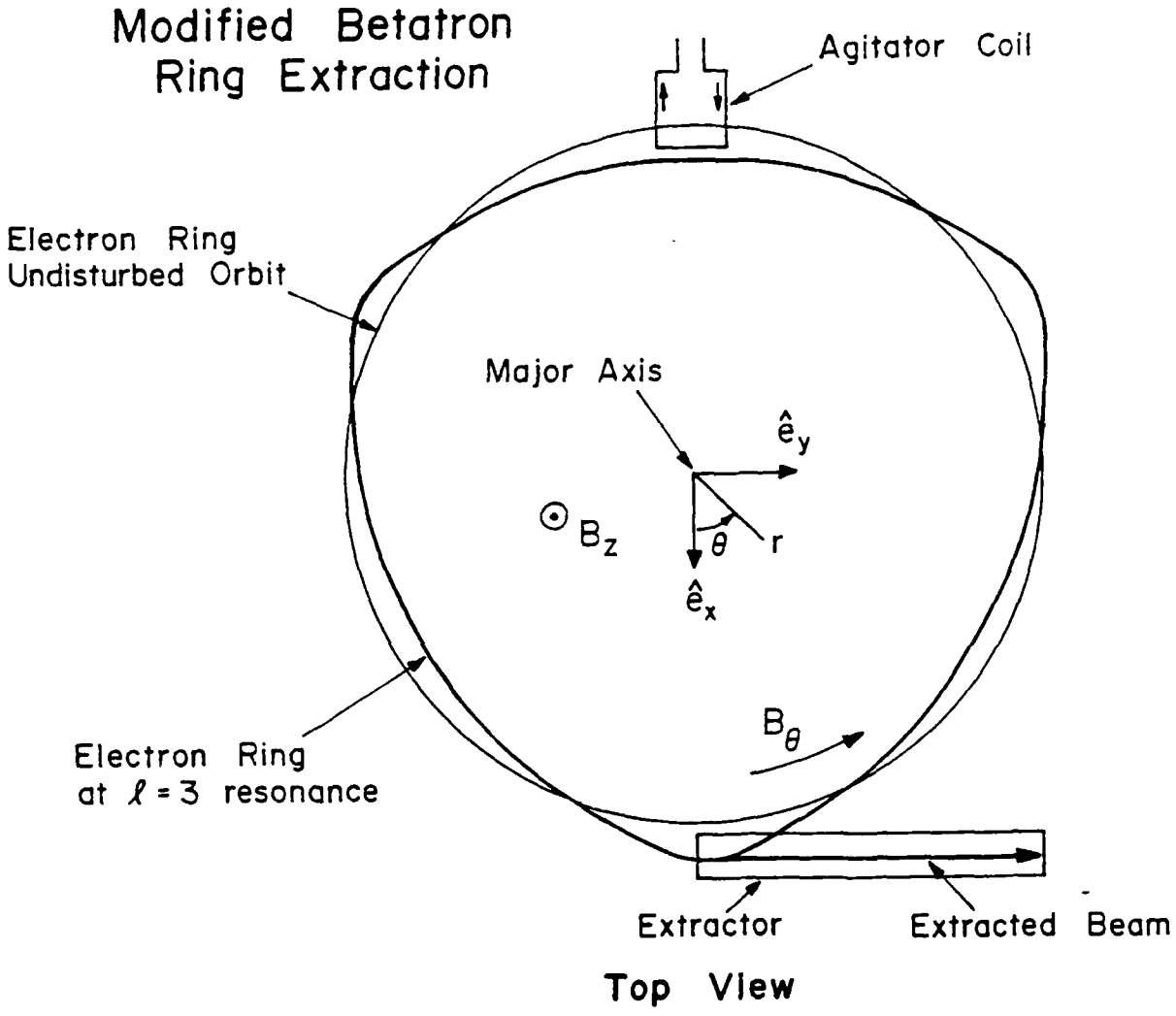



Fig. 1. Schematic of the proposed extraction scheme.

## Agitator

### Required Features

- Its field should be localized in order not to disturb the ring equilibrium orbit
- It should be magnetically transparent to external fields but opaque to its own field
- In the static mode, the radial gradient of the magnetic disturbance should be extremely high (small knee), to avoid the excitation of the fast mode before the ring reaches the main disturbance
- In the pulsed mode, its inductance should be very small, in order for the current rise time to be a small fraction of the period around the major axis.

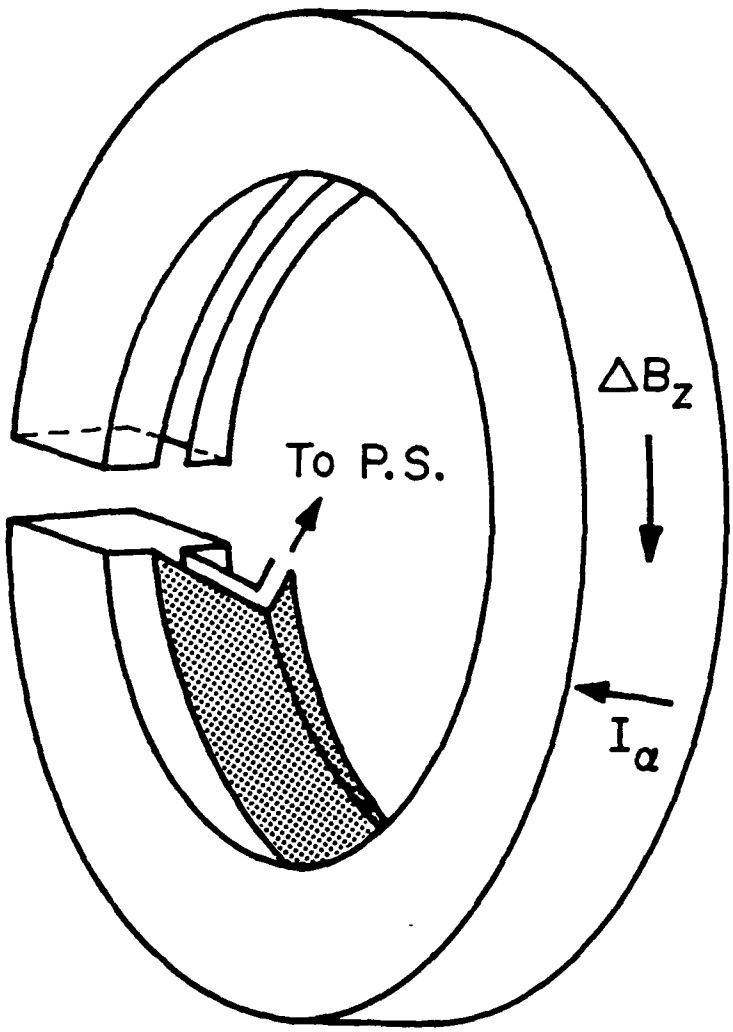



Fig. 2. Agitator coil that generates the localized disturbance. It is powered by a coaxial transmission line.

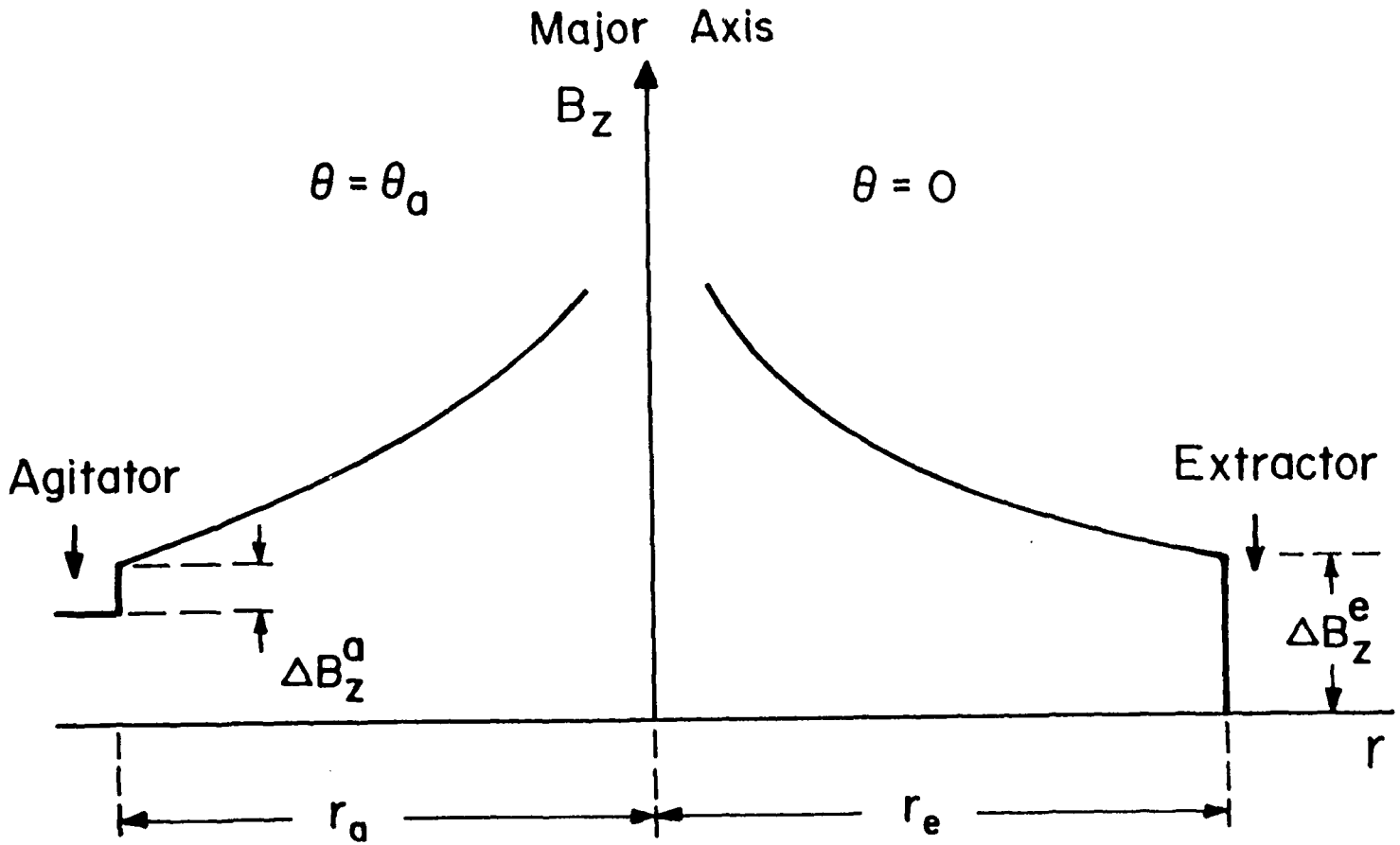



Fig. 3. Radial profile of the vertical magnetic field.

# TABLE

**List of various parameters for the runs # 266 and 270**

| RUN # | 266 | 270 |
|---|---|---|
| Agitator's mode | Static | Static |
| Relativistic factor $\gamma$ | 40 | 400 |
| Major radius $r_o$ (cm) | 100 | 100 |
| Vertical field at $r_o$ (G) | 649.9 | 6501 |
| Toroidal field at $r_o$ (G) | -1971 | -19310 |
| Field index n | 0.5 | 0.5 |
| Resonance integer 1 | 3 | 3 |
| Amplitude of mismatching field (G) | 60 | 600 |
| Time constant of mismatching field ($\mu$sec) | 10 | 10 |
| Agitator's toroidal position | $1.26\pi$ | $1.26\pi$ |
| Agitator's toroidal width $2\Delta\theta$ (rad) | 0.066 | 0.066 |
| Agitator's inner radius (cm) | 120 | 120 |
| Agitator's outer radius (cm) | 124 | 124 |
| Agitator's opening (cm) | 2 | 2.0 |
| Agitator's linear current density (kA/cm) | 0.375 | 3.75 |
| Agitator's field $\Delta B_z^a$ (G) | -450 | -4500 |
| Extractor's opening toroidal position | 0 | 0 |
| Extractor's minimum inner radius (cm) | 120.5 | 120.5 |
| Extractor's minimum outer radius (cm) | 124.5 | 124.5 |
| Extractor's field $\Delta B_z^e$ (G) | -590 | -5900 |

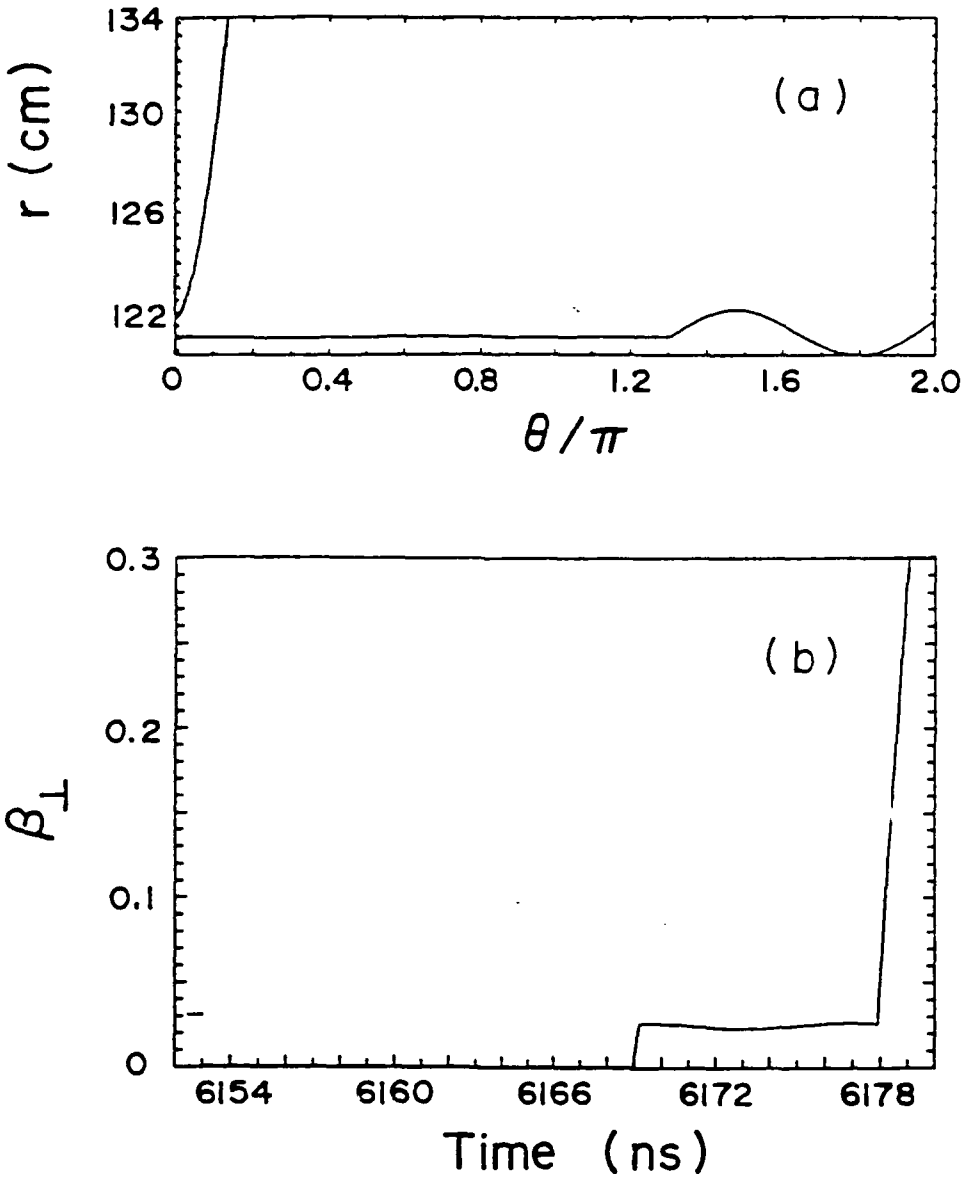



Fig. 4. Radial excursions of a typical electron (1) and its corresponding normalized transverse velocity (b) for the run 267.

# Ring Orbits for $\gamma = 40$

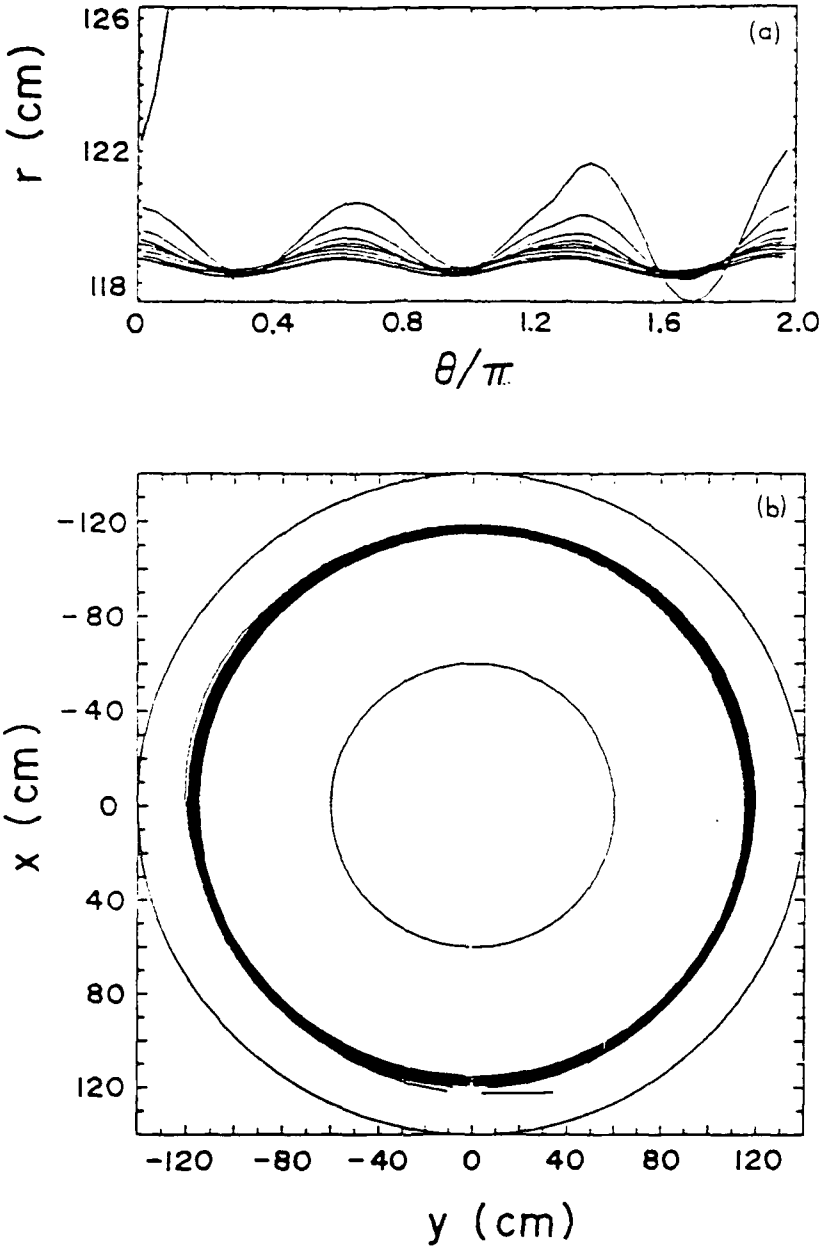



Fig. 5. Radial excursions of a typical electron (a) and top view of its trajectory in the x,y plane for the run 266.

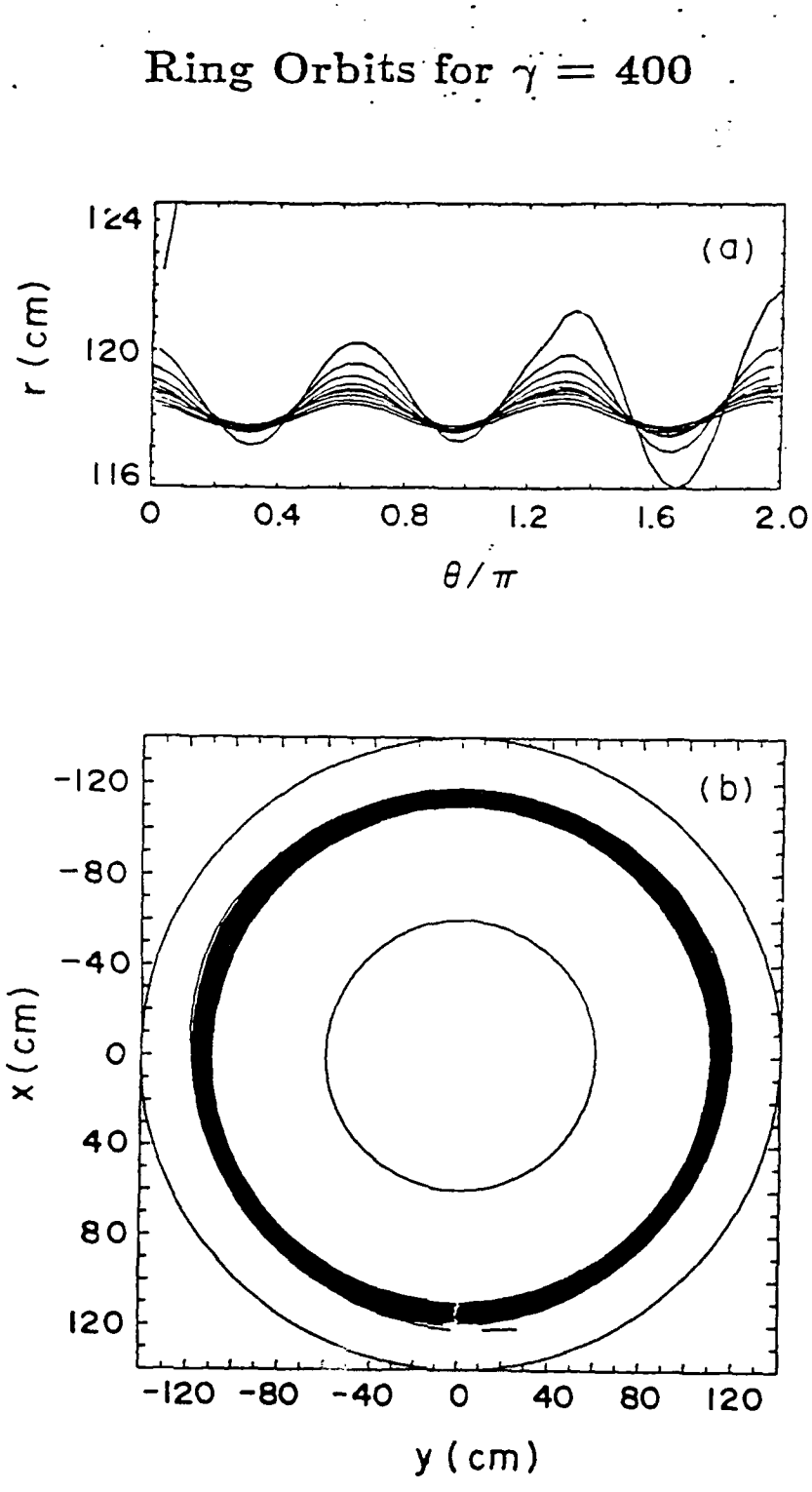



Fig. 7. Radial excursion of a typical electron (a) and top view of its trajectory in the x,y plane for the run 270.

TABLE I. List of various parameters for the runs.

| Parameter \ Run No. | 267 |
|---|---|
| Agitator's mode | Pulsed |
| Relativistic factor $\gamma$ | 40 |
| Major radius $r_0$ (cm) | 100 |
| Vertical field at $r_0$ (G) | 649.9 |
| Toroidal field at $r_0$ (G) | −1921 |
| Field index $n$ | 0.5 |
| Resonance integer $l$ | 3 |
| Amplitude of mismatching field (G) | ... |
| Time constant of mismatching field ($\mu$sec) | ... |
| *Agitator* | |
| Toroidal position | $1.3\pi$ |
| Toroidal width $2\Delta\theta$ (rad) | 0.05 |
| Inner radius (cm) | 120 |
| Outer radius (cm) | 122 |
| Opening (cm) | 1.0 |
| Linear current density (kA/cm) | 0.25 |
| Field $\Delta B_z^a$ (G) | −300 |
| Extractor | |
| Opening toroidal position | 0 |
| Minimum inner radius (cm) | 121.5 |
| Minimum outer radius (cm) | 125.5 |
| Field $\Delta B_z^e$ (G) | −590.0 |

TABLE I

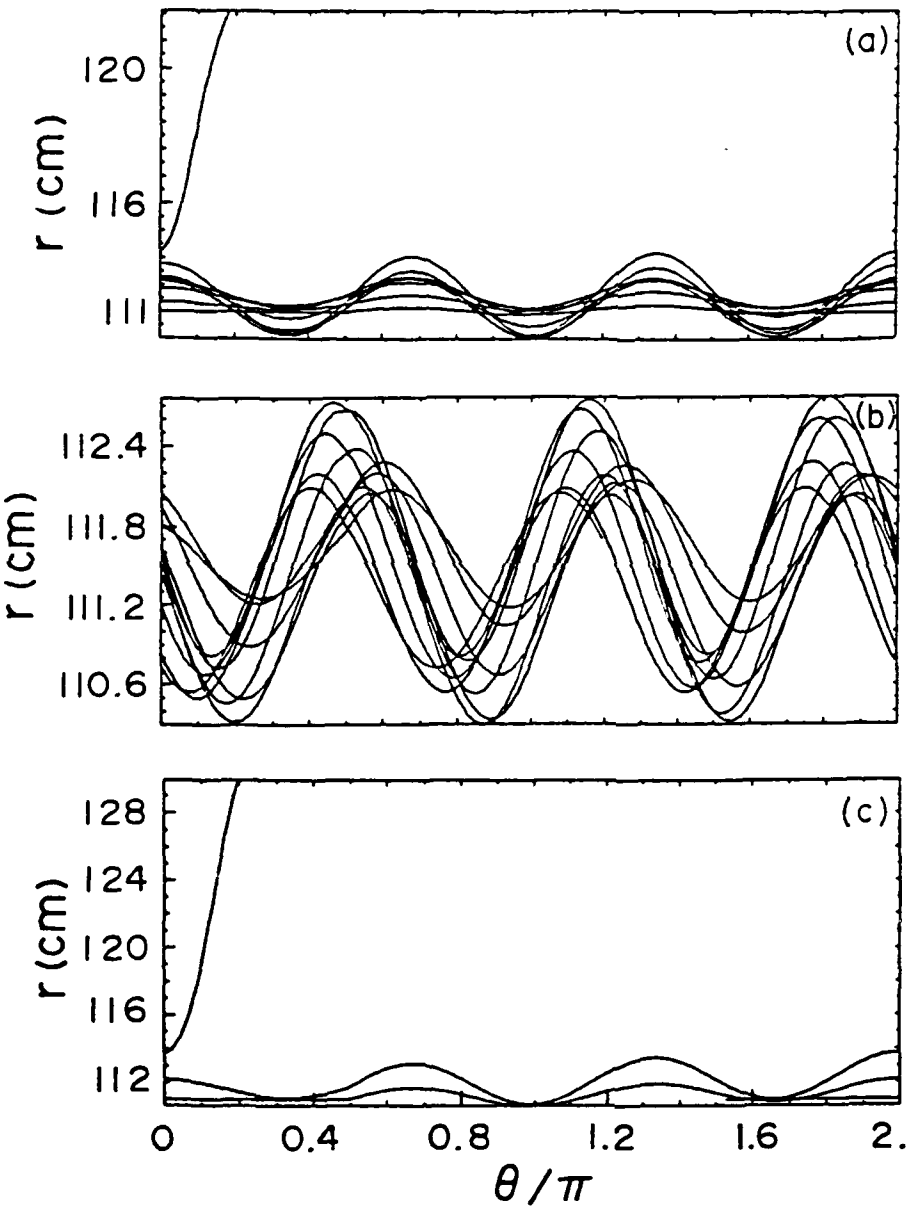
List of various parameters for the runs # 379-381

| RUN # | 379 | 380 | 381 |
|---|---|---|---|
| Agitator's mode | Pulsed | Pulsed | Pulsed |
| Relativistic factor $\gamma$ | 39.9 | 39.9 | 39.9 |
| Major radius $r_o$ (cm) | 100 | 100 | 100 |
| Vertical field at $r_o$ (G) | 681 | 681 | 681 |
| Toroidal field at $r_o$ (G) | -1,920 | -1970 | -1,925 |
| Field index n | 0.5 | 0.5 | 0.5 |
| Resonance integer $\ell$ | 3 | off | 3 |
| Agitator's toroidal position(rad) | 0.493 $\pi$ | 0.493 $\pi$ | 0.493 $\pi$ |
| Agitator's toroidal width $2\Delta\theta$ (rad) | 0.026 | 0.026 | 0.026 |
| Agitator's inner radius (cm) | 110.5 | 110.5 | 110.5 |
| Agitator's outer radius (cm) | 113.5 | 113.5 | 113.5 |
| Agitator's opening (cm) | 2.0 | 2.0 | 2.0 |
| Agitator's linear current density (kA/cm) | 0.1 | 0.1 | 0.4 |
| Agitator's field $\Delta B_z^a$ (G) | -78 | -78 | -350 |
| Extractor's opening toroidal position | 0 | 0 | 0 |
| Extractor's minimum inner radius (cm) | 113.0 | 113.0 | 113.0 |
| Extractor's minimum outer radius (cm) | 116.0 | 116.0 | 116.0 |

# Ring Orbit in the r, $\theta$ Plane

## $\gamma = 40$

## Pulsed Mode




$I_\ell = 100$ A/cm

$I_\ell = 100$ A/cm
(off-resonance)

$I_\ell = 400$ A/cm

## Conclusions

- An extraction technique has been conceptually developed for the modified betatron that is easily realizable and has the potential to lead to very high efficiency, since all the electrons of the ring perform coherent motion
- The design of the various components of the extraction experiment are near completion
- Fabrication, installation and testing of these components is expected to be completed in FY-89

# APPENIDX WW

## Beam Extraction Scheme from the Modified Betatron Accelerator

# Beam Extraction Scheme from the Modified Betatron Accelerator

C. A. Kapetanakos, S. J. Marsh,[a] and D. Dialetis[b]
*Plasma Physics Division, Naval Research Laboratory, Washington, D.C. 20375*
(Received 10 March 1988)

A technique is proposed for extraction of the electron ring from the modified betatron accelerator. Basically, this technique consists of exciting the resonance that naturally exists for some specific values of the ratio of the vertical to toroidal magnetic field.

PACS numbers: 52.75.Di, 29.20.Fj, 41.80.Ee

The modified betatron accelerator[1,2] is one among the several compact, high-current accelerator concepts currently under development in various laboratories. In this device a strong toroidal magnetic field $B_\theta$ has been added to the conventional betatron[3] magnetic field configuration. Although $B_\theta$ substantially improves the stability of the conventional betatron, the beam injection and capture and the electron ring extraction after the completion of acceleration are substantially more involved as a result of the toroidal field.

In this Letter, we report on an extraction scheme that is easily realizable and has the potential to lead to very high extraction efficiency. Briefly, the proposed extraction scheme is based on the transformation of the circulating electron ring into a stationary helix, in the toroidal direction, by excitation of the resonance that naturally exists for some specific values of the ratio of the vertical to toroidal magnetic field. Transformation of the ring into a helix is achieved with a localized vertical magnetic field disturbance that is generated by an agitator coil. As the minor radius of the helix increases with each passage through the gap of the agitator coil, the electrons eventually reach the extractor, which has the property that all the magnetic field components transverse to its axis are equal to zero. Thus, the electron ring upwinds into a straight beam.

Although the proposed scheme is related to the standard techniques[4,5] used for extraction of the beam from existing circular accelerators, several of its key features are different because of the presence of the toroidal magnetic field.

*Extraction scheme.*—After the completion of acceleration, i.e., when the desired electron beam energy has been achieved, the electron ring centroid is displaced radially by the intentional mismatch of the magnetic flux and the betatron magnetic field. In the results that will be shown in the next section, this mismatch has been achieved by superimposition of a low-amplitude vertical magnetic field that varies exponentially with time on the betatron field. It has been shown theoretically and verified by extensive numerical results that during the radial displacement of the ring centroid the amplitude of the slow mode[1] remains very small, i.e., a few millimeters, provided that the mismatching field varies slowly with respect to the ring bounce (poloidal) period. Furthermore, computer simulations with the U.S. Naval Research Laboratory MOBE particle-in-cell computer code have shown that during the radial displacement, that lasts several microseconds, the minor cross section of the ring preserves its integrity and the ring emittance remains constant.

As the major radius of the ring centroid increases slowly with time, the gyrating electrons reach the localized magnetic disturbance generated by the agitator coil. At this radial position the ratio of the vertical magnetic field $B_z$ to the torodial magnetic field $B_\theta$ has been selected to satisfy the condition

$$B_z/B_\theta = 2l/(2l^2-1), \tag{1}$$

where $l = 1,2,3\ldots$.

Equation (1) implies that the frequency of the fast mode[1] is $l$ times the frequency of gyration around the major axis. When $B_\theta \gg B_z$, Eq. (1) is reduced to $\Omega_\theta = l\Omega_z$, where $\Omega_\theta = eB_\theta/m$ and $\Omega_z = eB_z/m$.

The purpose of the magnetic disturbance is to excite the resonance.[6,7] As an electron enters the lower magnetic field region of the disturbance, its velocity vector, which initially is directed in the toroidal direction, rotates slightly in the radial direction, i.e., the electron obtains a radial velocity component. It can be shown from the equations of motion that this radial velocity is given by

$$\Delta v_r \approx -2(\Delta\Omega_z^a/\gamma) r_a \Delta\theta, \tag{2}$$

where $\Delta\Omega_z^a$ is the cyclotron frequency that corresponds to the field of the disturbance generated by the agitator coil, $\gamma$ is the relativistic factor, $r_a$ is the radial distance of the agitator coil, and $\Delta\theta$ is the toroidal half width of the magnetic disturbance.

As a result of the acquired radial velocity, the electrons start to gyrate in the torodial magnetic field with a radius

$$\rho = 2(N/l)(\Delta\Omega_z^a/\Omega_z) r_a \Delta\theta, \tag{3}$$

where $N$ is the number of passes through the disturbance. If condition (1) is not satisfied, $\rho$ grows as $N^{1/2}$ instead of proportionally to $N$.

Work of the U. S. Government
Not subject to U. S. copyright

Since $\gamma$ is very large, self-fields can be ignored. However, because of the gradient of $B_z$ the slow mode[1] (bounce motion) is still excited and the orbits of electrons in the transverse $(r,z)$ plane precess very slowly. Therefore, for times short in comparison with the bounce period, i.e., for a few revolutions around the major axis, all the electrons of the ring perform coherent motion and a stationary helix, in the toroidal direction, is formed. A top view of the helix is shown in Fig. 1, for $l=3$.

Ideally, the radial gradient of the magnetic disturbance should be extremely high, because otherwise the fast mode[1] is excited before the ring reaches the disturbance. In the computer runs of the next section, a disturbance with a satisfactorily sharp radial gradient is obtained by the single-turn agitator coil shown in Fig. 2. The radial gradient of the disturbance is further improved with two single-turn loops that are located at the edges of the gap. In the computer runs, the magnetic field of the disturbance has been obtained from exact analytical expressions that are too long to be given here.

With successive passes through the disturbance of the agitator the radial excursion of the orbit increases until the gyrating electrons reach the extractor, which is located at $\theta=0$ and at a slightly greater radial distance than the agitator coil. The results of the next section were obtained with a simple extractor consisting of two parallel plates with current flowing in opposite directions. These two plates have infinite extent in the $z$ and semi-infinite extent in the $y$ directions. The linear current density of the plates is adjusted to make the total $B_z$ between the plates at $\theta=0$ equal to zero. The side of the extractor at $\theta=0$ is completely enclosed. As a result the fringing fields are absent. The electrons enter the extractor through a thin conducting foil. At the entrance of the extractor the vertical displacement of the electrons and their radial velocity are almost zero. However, they have a small vertical velocity.

In practice, this extractor can be realized by our bending the two plates to form a torus. In order for the field to be uniform over a finite vertical distance, the cross section of each plate, after bending, should be D shaped. In the results of the next section, the orbit of the extracted beam is terminated after it propagates tens of centimeters inside the extractor. The reason is that $\Delta B_z^s$ is independent of $y$ while the betatron field decreases with $y$. Thus, cancellation of the fields is not achieved over the entire length of the extractor. In practice exact cancellation of the two fields can be obtained by an increase in the separation of the two plates as $y$ increases.

In the previous discussions, we have assumed that the magnetic disturbance generated by the agitator coil is static. An alternative mode of operation is to expand the ring until it reaches the gap of the agitator coil and then to pulse the coil rapidly. Since the inductance of the agitator is typically only a few nanohenries, short rise times, of the order of a few nanoseconds, can be achieved with modest voltages. In the pulsed mode of operation the fraction of the ring that will be lost is approximately equal to the ratio of coil rise time to period of gyration around the major axis.

Finally, it should be noticed that an ion channel[8] formed by a laser beam along the axis of the extractor may improve the extraction process and eliminate the need for an additional coil to cancel the component of $B_\theta$ that is transverse to the axis of the extractor or the need to cancel completely the $B_z$ inside the extractor.

*Results.*—We have studied the proposed extraction scheme in both the static and pulsed modes for a range of parameters that are compatible with the U.S. Naval Research Laboratory modified betatron accelerator. In this Letter, we present results from three runs: one in the pulsed mode for $\gamma=40$ and two in the static mode for $\gamma=40$ and 400. The various parameters of these three runs are listed in Table I. Since $\gamma \gg 1$, self-fields and im-

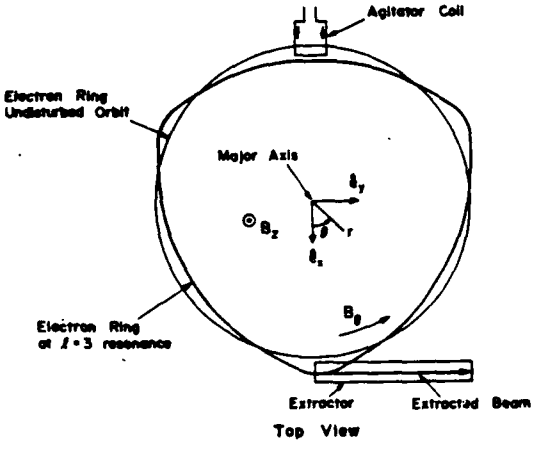



FIG. 1. Schematic of the proposed extraction scheme.

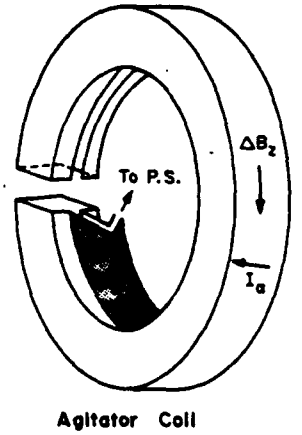



FIG. 2. Agitator coil that generates the localized disturbance. It is powered by a coaxial transmission line.

TABLE I. List of various parameters for the runs shown in Figs. 3 to 5.

| Parameter \ Run No. | 267 | 266 | 268 |
|---|---|---|---|
| Agitator's mode | Pulsed | Static | Static |
| Relativistic factor $\gamma$ | 40 | 40 | 400 |
| Major radius $r_0$ (cm) | 100 | 100 | 100 |
| Vertical field at $r_0$ (G) | 649.9 | 649.9 | 6501 |
| Toroidal field at $r_0$ (G) | −1921 | −1971 | −19700 |
| Field index $n$ | 0.5 | 0.5 | 0.5 |
| Resonance integer $l$ | 3 | 3 | 3 |
| Amplitude of mismatching field (G) | ... | 60 | 600 |
| Time constant of mismatching field ($\mu$sec) | ... | 10 | 10 |
| Agitator | | | |
| Toroidal position | $1.3\pi$ | $1.26\pi$ | $1.26\pi$ |
| Toroidal width $2\Delta\theta$ (rad) | 0.05 | 0.066 | 0.066 |
| Inner radius (cm) | 120 | 120 | 120 |
| Outer radius (cm) | 122 | 124 | 124 |
| Opening (cm) | 1.0 | 2 | 2 |
| Linear current density (kA/cm) | 0.25 | 0.375 | 3.750 |
| Field $\Delta B_r^a$ (G) | −300 | −450 | −4500 |
| Extractor | | | |
| Opening toroidal position | 0 | 0 | 0 |
| Minimum inner radius (cm) | 121.5 | 120.5 | 120.5 |
| Minimum outer radius (cm) | 125.5 | 124.5 | 124.5 |
| Field $\Delta B_r^e$ (G) | −590.0 | −590 | −5900 |

age fields have been ignored and therefore the ring current is not a relevant parameter. Also at this high $\gamma$ the beam minor diameter is expected to be only a few millimeters.

In run 267, the pulsed agitator was turned on after the ring's major radius became 121 cm. Figure 3(a) shows the radial excursion of a typical electron that was located at $\theta=0$ at the turning on of the agitator. After a single pass through the agitator the electron obtains enough radial excursion to enter the extractor and is extracted. Figure 3(b) shows that the electron at the disturbance obtains a transverse velocity approximately $2.8\times10^{-2}c$. Equation (2) predicts a $\Delta v_r=2.7\times10^{-2}c$. In addition, the numerical results show that the electron gyrates around $B_\theta$ with a 1-cm radius, which is also the radius predicted by Eq. (3).

In run 266, the electron started at $r=110$ cm and was moved radially by the mismatching field. The elapsed time from the minor axis to the agitator is $\simeq4.5$ $\mu$sec, that corresponds to an average radial velocity of $\simeq2.2\times10^6$ cm/sec. The amplitude of the slow mode is less than 2 mm. Figure 4(a) shows the radial excursions of a typical electron in the $r,\theta$ plane and Fig. 4(b) shows a top view of its orbit. The electrons reach the extractor with a vertical displacement from the midplane that is only a few millimeters. For the reason given in the previous section, the run was terminated after the electron propagated $\simeq30$ cm inside the extractor.

In run 268, $\gamma$ was increased to 400 with a corresponding increase in the value of magnetic fields. Figure 5(a) shows the radial excursions of the electron and Fig. 5(b) is a top view of the orbit. The coherence of the radial excursions is remarkable. We have found that this coherence is preserved even when Eq. (1) is not satisfied

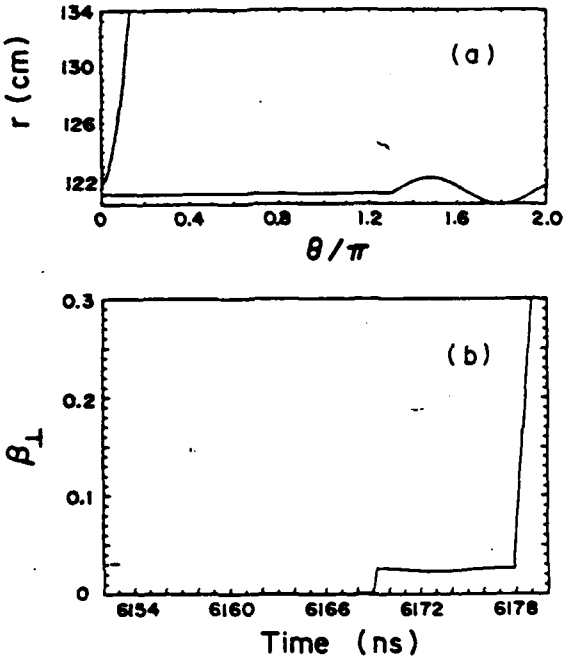



FIG. 3. (a) Radial excursions of a typical electron and (b) its corresponding normalized transverse velocity for the run 267.

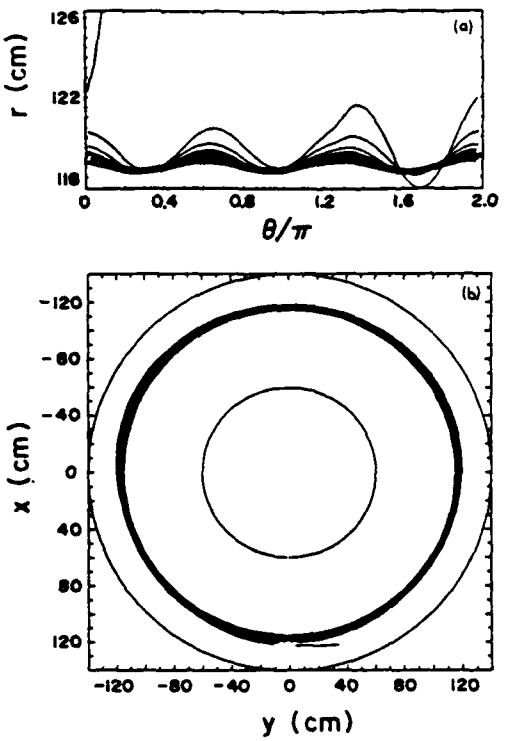



FIG. 4. (a) Radial excursions of a typical electron and (b) top view of its trajectory in the $x,y$ plane for run 266.

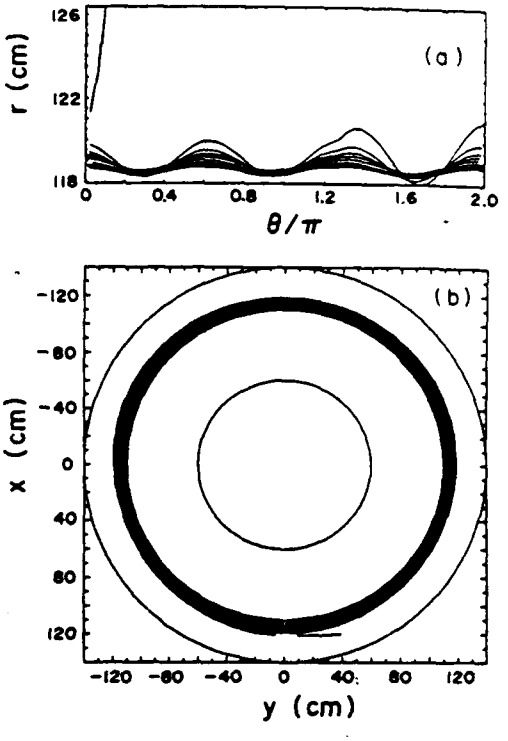



FIG. 5 (a) Radial excursion of a typical electron and (b) top view of its trajectory in the $x,y$ plane for run 268.

exactly, i.e., when the value of field $B_\theta$ is off by tens of gauss. Finally, by operation at $l=1$ or 2 instead of at $l=3$, the value of $B_\theta$ can be substantially reduced.

Several successive runs with $\gamma=400$ electrons that are located at different positions on the minor cross section of a 3-mm-diam ring show that all these electrons arrive at the entrance of the extractor with less than 1 nsec time difference. In addition, the results show that although the vertical width of the ring has been slightly reduced, its corresponding radial width has been increased by approximately a factor of 3. This spread of the beam is probably associated with the slightly different value of $\Delta B_z$ experienced by the different electrons as a result of the finite gradient of the agitator.

In conclusion, we have developed a new extraction scheme that is practical and has the potential, since all the electrons of the ring perform coherent motion, to lead to a very high extraction efficiency.

The authors are grateful to Professor D. Kerst and Dr. J. Golden, Dr. P. Sprangle, and Dr. R. Faehl for many illuminating discussions. This work was supported by the Space and Naval Warfare Systems Command and the U.S. Office of Naval Research.

---

[a]Permanent address: Sachs/Freeman Associates, Inc., Landover, MD 20785.

[b]Permanent address: Science Applications, Inc., McLean, VA 22102.

[1]C. A. Kapetanakos, P. Sprangle, D. P. Chernin, S. J. Marsh, and I. Haber, Phys. Fluids **26**, 1634 (1983).

[2]H. Ishizuka, G. Lindley, B. Mandelbaum, A. Fisher, and N. Rostoker, Phys. Rev. Lett. **53**, 266 (1984).

[3]D. W. Kerst, Nature (London) **157**, 90 (1940).

[4]L. C. Teng, in *Physics of High Energy Particle Accelerators*, edited by R. A. Carrigan, F. R. Huson, and M. Month, AIP Conference Proceedings No. 87 (American Institute of Physics, New York, 1982), p. 62.

[5]E. J. N. Wilson, in CERN Report No. 77-13, 1987 (unpublished), p. 111.

[6]D. Chernin and P. Sprangle, Part. Accel. **12**, 101 (1982).

[7]D. Dialetis, S. J. Marsh, and C. A. Kapetanakos, Part. Accel. **21**, 227 (1987).

[8]B. Hui and Y. Y. Lau, Phys. Rev. Lett. **53**, 2024 (1984).

# APPENDIX XX

## Studies of a Multi-Kiloampere Electron Ring Confined in a Modified Betatron Accelerator

Published in the Proceedings of 'Beams 88'

# STUDIES OF A MULTI-KILOAMPERE ELECTRON RING CONFINED IN A MODIFIED BETATRON ACCELERATOR*

J. Golden, L. K. Len[a], A. V. Deniz[b], J. Mathew[c], T. J. Smith,
P. Loschialpo, J. H. Chang, D. Dialetis[b],
S. J. Marsh[c], and C. A. Kapetanakos
Plasma Physics Division
Naval Research Laboratory, Washington DC, U.S.A.

## ABSTRACT

This paper briefly summarizes recent experimental results on the dynamics of a multi-kiloampere electron ring, confined in a modified betatron magnetic field configuration and discusses the cause of its premature loss from the confining fields. In addition, it outlines a ring extraction scheme that is easily realizable and has the potential to lead to high extraction efficiency.

## INTRODUCTION

The objective of the NRL modified betatron project is to study the critical physics issues associated with high current, toroidal accelerators.[1-6] The most important of these issues are injection and capture, space charge and wall effects, ring equilibrium and stability, acceleration and finally extraction.

As previously reported,[1,2] the circulating current of the electron ring is in the range 0.4-3kA and the electron energy between 0.5-1.0 MeV. Ring lifetimes as long as 10 $\mu$sec, corresponding to approximately 500 revolutions around the major axis have been obtained. The experiments have confirmed the major theoretical predictions.[7,8]

## ELECTRON RING DYNAMICS

Linear analytical and computational studies of transverse dynamics over the last several years have shown that the centroid of an electron ring confined in a modified betatron magnetic field configuration has two characteristic frequencies, one fast and one slow.[7] The fast frequency becomes approximately equal to the toroidal cyclotron frequency when the ratio of the toroidal $B_\theta$ to the vertical betatron magnetic field $B_z$ is much greater than unity. The slow or bounce frequency $\omega_B$ is due to the image fields and the gradient of $B_z$.

When the electron ring $I_b$ current is high, the image forces dominate, and the ring bounce motion in the transverse plane is diamagnetic. The orbitally stable electron ring current range associated with the diamagnetic motion of the beam is named the high current regime. In contrast, when the gradient of $B_z$ dominates, the ring motion is paramagnetic and the ring current range that exceeds the maximum current that can be stably confined in a conventional betatron[9] is named the low current regime. In both the high and low current regimes the ring orbits, in the transverse plane, are closed. However, when the field index n is different than 0.5 the two regimes are separated by a region, the centroid instability gap, in which the orbits are open.

Figure 1 shows the orbital stability diagram of an electron ring confined in a modified betatron magnetic field configuration. The parameter in the horizontal axis

$$N_s \equiv n_s r_b^2/a^2 = (2\nu/\gamma_o^3\beta_{\theta o}^2)(r_o/a)^2, \qquad (1)$$

is proportional to the circulating ring current, since the Budker parameter $\nu = I_b(kA)/17\beta_\theta$. In Eq. (1) $n_s$ is the self field index, $\beta_\theta = v_\theta/c, v_\theta$ is the electron toroidal velocity, $\gamma_o$ is the relativistic factor and $r_b$ and a are the minor radii of the ring and the torus.

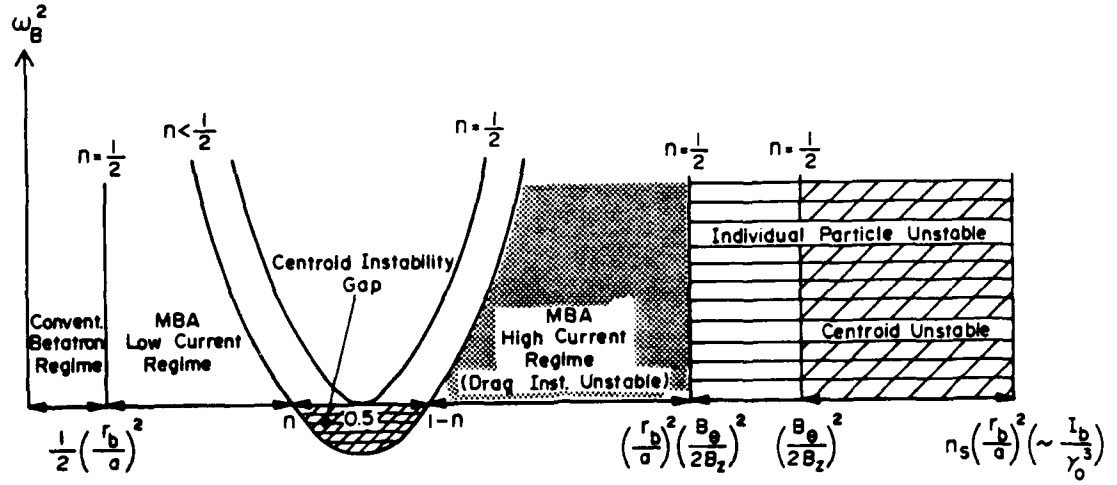



Fig. 1. Orbital stability diagram for an electron ring in a modified betatron configuration.

In the region $(r_b/a)^2(B_\theta/2B_z)^2 < N_s < (B_\theta/2B_z)^2$, the ring centroid is stable, but the individual electrons are unstable,[10] therefore, the circulating ring current is expected to continuously decrease until $N_s$ becomes less than $(r_b/a)^2(B_\theta/2B_z)^2$. In addition, the high current regime is not very useful because during acceleration $\gamma_o$ increases and the ring centroid has to cross the instability gap. Furthermore, the region to the right of the instability gap is unstable to the drag instability, a potent collective mode that has its origin in the finite resistivity of the vacuum chamber.

We have studied experimentally the region to the right of the centroid instability gap, i.e., when $N_s > 1 - n$, for $n \leq 0.5$. The experimental results have confirmed the basic predictions of the theory. Specifically, when $N_s > (r_b/a)^2(B_\theta/2B_z)^2 \simeq 2.5$, or when $I_b > 2.5$ kA the ring current decreases continuously with time, as shown in Fig. 2a. Underneath the current trace there is an open shutter photograph of the light that is emitted as the ring passes through a thin polycarbonate film, which is graphite coated on the upstream side to avoid electrostatic charging. In the high current regime, i.e., when $0.6 \leq N_s \leq 2.5$, we do not, in general, observe current loss. The ring is lost suddenly either by striking the injector, after the completion of a bounce period (when the capture field is not energized), or by striking the wall before the completion of a bounce period. Typical results are shown in Fig. 2b and 2c. Parametric studies of the ring confinement time as a function of ring current and $B_\theta$ indicate that the ring loss is most likely due to drag instability.

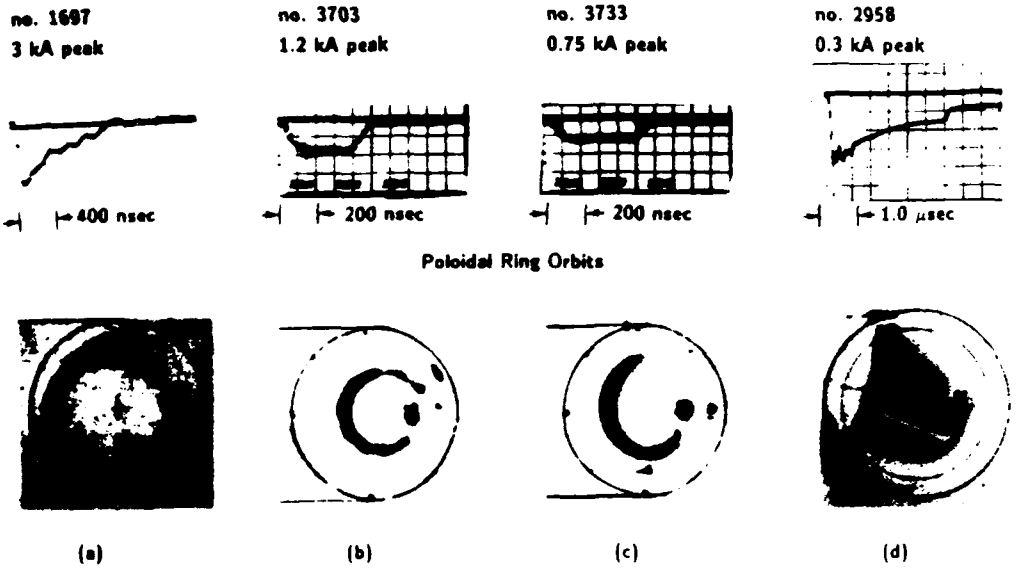



Fig. 2. Circulating current and ring orbits in the transverse plane for different values of $N_e$: (a) $N_e >$ the individual particle stability limit, (b) and (c) in the high current regime and (d) at the instability gap. The circle indicates the minor cross section of the torus, and the mark x indicates the injection position.

The drag instability results from the poloidal phase shift between the electric and magnetic field images that is caused by the finite resistivity of the vacuum chamber wall surrounding the ring. The phase shift between the two images produces a poloidal field component which drives the ring toward the wall in the high current regime and toward the minor axis in the low current regime. Linearized theory[6] shows that, when

$$\left[\frac{b}{(b-a)}\right]^{\frac{1}{2}} > \frac{\delta}{(b-a)} > 1, \tag{2}$$

the growth rate of the drag instability $\Gamma$ is given by

$$\frac{2\pi\Gamma}{\omega_B} = \frac{2\gamma_o\eta\Omega_{\theta o}r_b^2}{a}\frac{x}{(1-x)^2}, \tag{3}$$

where $\delta = c\sqrt{\rho/(2\pi|\omega_B|)}$, $\rho$ is the wall resistivity, $\eta = \rho/(b-a)$, a is the inner radius and b the outer radius of the chamber, $\Omega_{\theta o} = \mid e \mid B_{\theta o}/mc$, $x = I_b/I_{bcrit}$ and $I_{bcrit}$ is the ring current that corresponds to the instability gap, and the subscript o denotes values on the minor axis.

For the results shown in Fig. 2b and 2c, $\Gamma \approx 3 \times 10^6 sec^{-1}$, which implies that the radius of the ring's poloidal orbit will double, and therefore the ring will strike the wall, in about 200 nsec. In addition, the experimental results show that when $x \rightarrow 1$, the growth rate becomes very large, in agreement with Eq. (3).

When the capture field[12] is turned on during the first bounce period, we often observe the ring to drift toward the minor axis and $I_b$ decays slowly with time, as shown in Fig. 2d. Finally, after confinement time of a few $\mu$sec the ring suddenly strikes the wall. The open

shutter photograph underneath the current trace clearly shows that $\omega_B$ changes sign and its motion become paramagnetic. In these shots the ring loss is attributed to the crossing of the instability gap.

Recently, by reducing the injected beam current and increasing the energy of the injected electrons to approximately one MeV, the operating point was shifted to the low current regime. In this regime, avoidance of the injector after a period around the major axis is achieved with a pulsed radial magnetic field $B_r$. This field is generated by two sets of conductors that are located symmetrically about the midplane and carry current in opposite directions as shown in Fig. 3a. Radial shifts approximately 6 cm are observed, when the current in the kicking coil is approximately 350A. Typical results are shown in Fig. 3b. Additional results on the low current regime will be reported in a future communication.

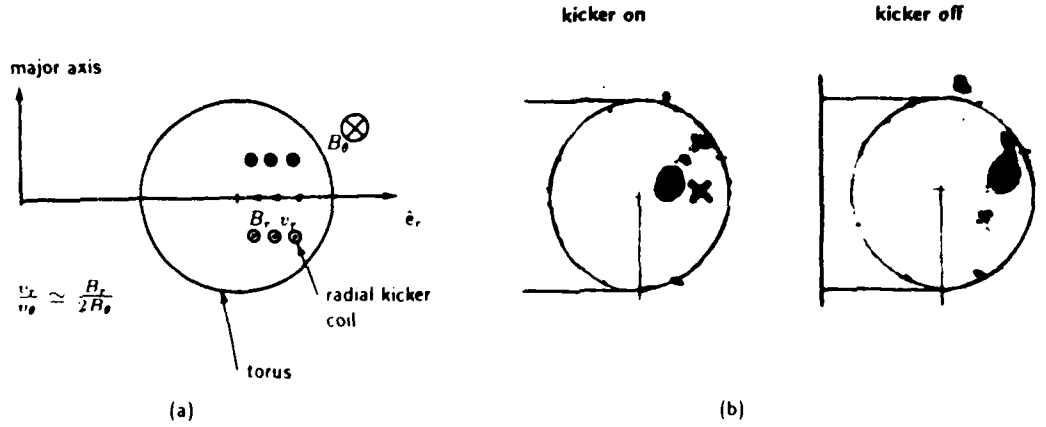



Fig. 3. Beam trapping in the low current regime: (a) fast pulsed coil inside the vacuum chamber and (b) ring orbits in the transverse plane with and without $B_r$.

## RING EXTRACTION FROM THE MODIFIED BETATRON

Frequently in the past, the usefulness of the modified betatron has been challenged on the grounds that the extraction of the electron ring from the device after the completion of acceleration will be very difficult, if not impossible. Recently,[13] we have developed an extraction technique that is easily realizable and has the potential to lead to very high efficiency.

Briefly, the proposed extraction scheme is based on the transformation of the circulating electron ring into a stationary helix, in the toroidal direction, by exciting the resonance that naturally exists for some specific values of the ratio of the vertical to toroidal magnetic field. Transformation of the ring into a helix is achieved with a localized vertical magnetic field disturbance that is generated by an agitator coil. As the minor radius of the helix increases with each passage through the gap of the agitator coil, the electrons eventually reach the extractor, which has the property that all the magnetic field components transverse to its axis are equal to zero. Thus, the electron ring unwinds into a straight beam.

A key feature of our extraction scheme is that for time short in comparison with the bounce period, i.e., for several revolutions around the major axis, all the electrons of the ring perform coherent motion and a stationary helix, in the toroidal direction, is formed. A top view of the helix is shown in Fig. 4 for $\ell = 3$, where $\ell$ satisfies the relation

$$B_z/B_\theta = 2\ell/(2\ell^2 - 1). \tag{4}$$

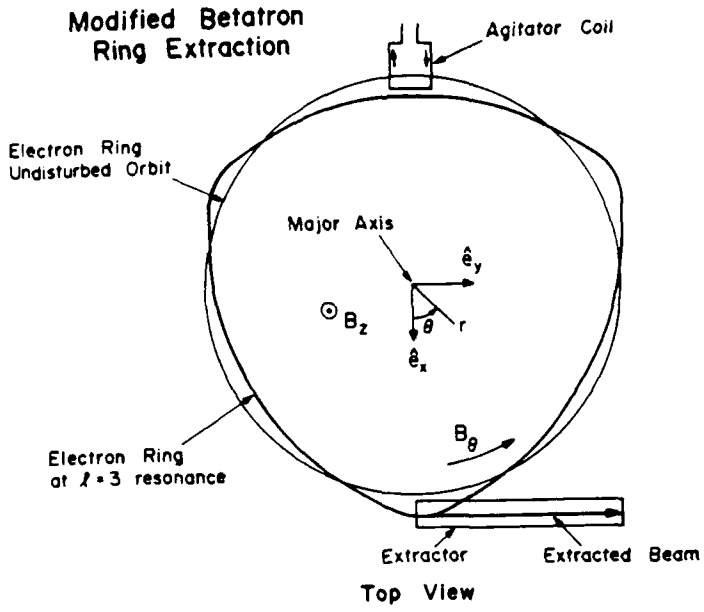



Fig. 4. Schematic of the extraction scheme.

We have studied the resonance extraction scheme in both the static and pulsed mode for a range of parameters that are compatible with the NRL modified betatron. Typical results are shown in Fig. 5, for the parameters listed in Table I.

A typical electron started at r = 110 cm and was moved radially by a mismatching field. Figure 5a shows the radial excursions of a typical electron in the r, $\theta$ plane and Fig. 5b shows a top view of the orbit. The electrons reach the extractor with a vertical displacement from the midplane that is only a few mm. The run was terminated after the electron beam propagated ~ 30 cm along the extractor. The coherence of the radial excursions is remarkable. We have found that this coherence is preserved even when Eq. (4) is not satisfied exactly, i.e., when the value of $B_\theta$ is off by tens of Gauss. Finally, by operating at $\ell = 1$ or 2 instead of at $\ell = 3$, the value of $B_\theta$ can be substantially reduced.

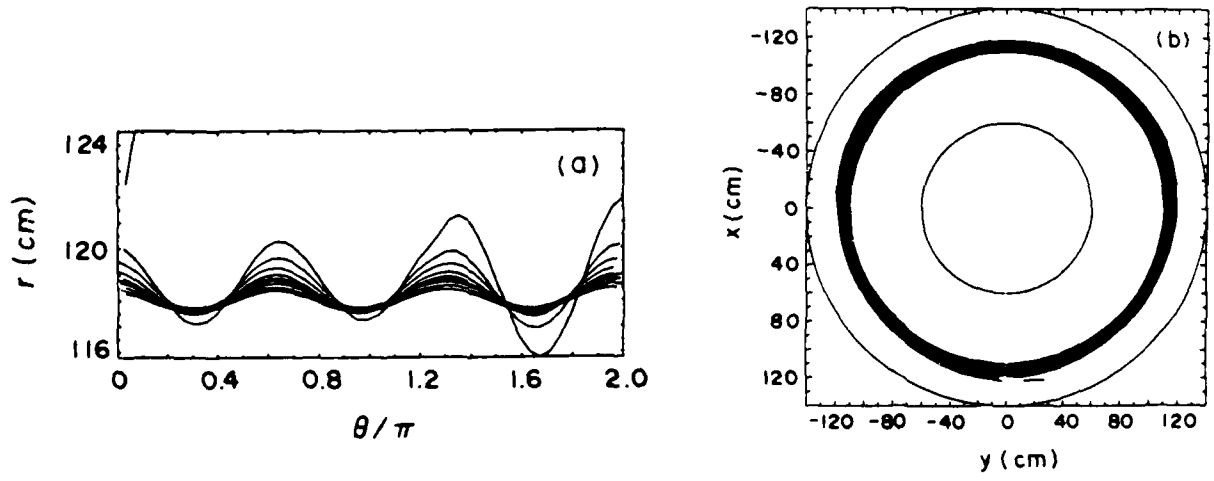



Fig. 5. Radial excursions of a typical electron vs. toroidal angle (a) and top view of its trajectory in the x,y plane (b).

TABLE I

List of various parameters for the run shown in Fig. 5

| | | | |
|---|---|---|---|
| | | Agitator Parameters: | |
| Agitator's mode | Static | Toroidal width $2\Delta\theta$ (rad) | 0.066 |
| Relativistic factor $\gamma$ | 400 | Inner radius (cm) | 120 |
| Major radius $r_o$ (cm) | 100 | Outer radius (cm) | 124 |
| Vertical field at $r_o$ (G) | 6501 | Gap opening (cm) | 2.0 |
| Toroidal field at $r_o$ (G) | -19310 | Linear current density (kA/cm) | 3.75 |
| Field index n | 0.5 | Field $\Delta B_z^a$ (G) | -4500 |
| Resonance integer $\ell$ | 3 | Extractor Parameters: | |
| Mismatching field $B_m$ (G) | 600 | Entrance toroidal position | 0 |
| Time constant of $B_m$ ($\mu$sec) | 10 | Minimum inner radius (cm) | 120.5 |
| Agitator's toroidal position | $1.26\pi$ | Minimum outer radius (cm) | 124.5 |
| | | Field $\Delta B_z^e$ (G) | -5900 |

* This work is supported by ONR and SPAWARS.

a FM Technologies, Fairfax Station VA.

b SAIC, McLean VA.

c Sachs-Freeman Associates, Landover MD.

REFERENCES

[1] J. Golden, et al., Proc. BEAMS 86 Conf. (1986).

[2] F. Mako, et al., IEEE Trans on Nucl Sci **NS-32**, 3027 (1985).

[3] H. Ishizuka, *et al.*, Phys. Rev. Letts. **53**, 266 (1984).

[4] S. Humphries, Jr. and L.K. Len, Proc. of 1987 IEEE art. Accel. Conf., 914 (1987).

[5] V. Bailey, *et al.*, Proc. of 1987 IEEE Part. Accel. Conf., 920 (1987).

[6] W. K. Tucker, *et al.*, Proc. of 1987 IEEE Part. Accel. Conf., 957 (1987).

[7] C. A. Kapetanakos, et al., Phys. Fl. **26**, 1634 (1983).

[8] C. A. Kapetanakos and S. J. Marsh, Phys. Fl. **28**, 2263 (1985).

[9] D.W. Kerst, Nature **157**, 90 (1940).

[10] P. Sprangle and C. A. Kapetanakos, J. Appl. Phys. **49**, 1 (1978).

[11] P. Sprangle and C.A. Kapetanakos, Part. Accel. **14**, 15 (1983).

[12] J. Golden, *et al.*, Proc. of the 1987 IEEE Part. Accel. Conf. **2**, 936 (1987).

[13] C. A. Kapetanakos, *et al.*, NRL Memo Report 6214 (1988).

# APPENDIX YY

## On the Relationship Between Neutron Yield and Plasma Current in the Dense Z-Pinch

# On the Relationship Between Neutron Yield and Plasma Current in the Dense Z-Pinch

William Grossmann
Science Applications International Corporation
342 Madison Avenue
New York City, NY 10012

and

William R. Ellis
Naval Research Laboratory
4555 Overlook Avenue, SW
Washington, DC 20375-5000

January 17, 1989

## 1. Introduction

Recent z-pinch experiments[1,2] employing frozen deuterium fibers have provided a number of very challenging questions regarding the interpretation and understanding of the results. These questions pertain to the experimentally observed stability characteristics and the total neutron yield. According to classical ideal MHD theory,[3-5] a linear z-pinch plasma carrying a longitudinal current, I, is linearly unstable to $m = 0$, finite $k_z$ perturbations ($m$ refers to the azimuthal wavenumber and $k_z$ refers the longitudinal wavenumbers; *i.e.*, $exp\ i(m\theta + k_z z)$) with a growth rate equal to a fraction of an Alf'ven transit time and proportional to the total plasma current, I. Early experiments with z-pinch devices[5-7] have confirmed the ideal MHD predictions over a wide range of experimental parameters. Indeed, the classical z-pinch plasma has been shown to be one of natures most unstable configurations. In the case of a dense z-pinch where the plasma radius is of the order of 100 microns, the instabilities can theoretically disrupt the plasma in an extremely short time. For the parameters of the NRL dense z-pinch (DZP), this growth time translates to a theoretical plasma disruption time via the $m = 0$ instability of several nanoseconds. The Naval Research Laboratory (NRL) DZP experimental results[1] are, however, that the plasma column remains stable for a time which is approximately 1-2 orders of magnitude longer than the theoretical disruption time. Further, the experimental results show that this stable behavior is observed as long as the time rate of change of total pinch current remains positive definite (dI/dt>0) and, becomes lost to an $m = 0$ perturbation when $dI/dt \approx 0$. Several (5-10) $m = 0$ neck regions are discernable photographically after the instability sets in. Neutrons are observed immediately after initiation of the $m = 0$ instability with peak neutron yield occurring close to the time when $dI/dt = 0$. The neutrons continue to be produced after peak production for a time at least one order of magnitude longer than the theoretical disruption time. The rise time for peak neutron yield in the DZP experiment is consistent with the theoretical disruption time. The total time integrated neutron yield has been shown to scale with the total plasma current as $I^{\alpha}$ with $\alpha \approx 10$. The NRL DZP has achieved $10^9$ neutrons with a plasma current of 600 kiloamperes;

a doubling of the current would result in $\sim 10^{13}$ neutrons assuming the scaling holds. Such neutron yields lead to the consideration of relatively simple high neutron flux materials test facility designs[8] as well as to fusion energy reactors.[9,10]

Thus, the forementioned puzzles of why the DZP plasma appears to be so stable, and what mechanism is responsible for the neutron production and scaling law, require answers prior to future practical application of the DZP devices. The purpose of this research paper is to offer a mechanism and analysis which purports to explain the observed neutron scaling. We will show that the $m = 0$ instability is accompanied by strong electric fields and may promote high energy directed deuteron beams (discussed often in previous works) which upon interaction with cold target deuterons yield the required neutrons and scaling. Our analysis allows a prediction of expected scaling for neutron yield in future DZP experiments.

Although the main emphasis of the present work concerns neutron yield scaling, some remarks concerning the plasma column stability will also be presented.

The plan of the paper is as follows. First we give a historical perspective of the z-pinch and relate known details of stability and neutron production to the NRL experiment. Next, the details of the observed $m = 0$ column collapse are abstracted for our purposes. The neutron production rate via the beam-plasma interaction is then analyzed and the scaling with total current is extracted from the neutron production rate integral. Finally we conclude with a summary and recommendations for further work.

## 2. Historical Perspective

In this section we consider some aspects of z-pinch folklore which relate to the NRL DZP experiment. A z-pinch is a plasma configuration containing only a longitudinal current with an accompanying azimuthal magnetic field. Z-pinch plasmas have been well studied in the past[6] and have been proposed and studied[9,10] for potential application to net energy producing fusion power reactors. The main reason for abandoning the quest for fusion via pure z-pinches is the inherent instability of the plasma configuration. With the exception of the recent DZP plasmas, practically all other experimental z-pinches exhibit instability characteristics which can be predicted and explained by MHD theory. In most cases ideal MHD theory is valid. Depending on the details of the mathematical-physical model used to analyze the stability[11] (*e.g.*, thin skin or surface current model, constant or distributed current density model) the ideal MHD growth rate, $\gamma_o$, for the $m = 0$, finite $k_z$ mode can be written as $\gamma_o = Iaf(k_z)/\sqrt{N_p}$, where $a$ is the effective plasma radius for the plasma line density $N_p$ and $f(k_z)$ is a monotonically increasing function of $k_z$ and is weakly dependent on the plasma current distribution. The NRL DZP forms its plasma from an initially frozen solid deuterium fiber $\approx 100$ microns in diameter suspended in vacuum between two electrodes 5 cm apart. As stated earlier, the NRL DZP experimental parameters translate $\gamma_o^{-1}$ into several nanoseconds. The NRL results indicate stability against the $m = 0$ mode for a period of time roughly 50-100 times longer than $\gamma_o^{-1}$ until such time when $dI/dt$ vanishes. The data further show that, simultaneously with the vanishing of $dI/dt$, $m = 0$ sausage modes appear resulting in column collapse at the $m = 0$ neck regions and an intense burst of neutrons which are known to originate from a deuteron-deuteron reaction.

Attempts to explain the column stability over the observed stable time period have included: a) reliance on profile effects to either reduce the growth rate or eliminate the instability altogether,[3] b) resistive and viscous effects[12] to decrease the growth rates, c) finiteness of the ablation time required to vaporize the solid deuterium core.[13] The actual cause of the prolonged plasma stability more than likely involves a combination of these effects. Indeed one can construct a plausible scenario as follows: at time zero

when the deuterium fiber is initially subjected to the imposed voltage, a current path is formed on the exterior surface of the column. Joule heating and radiation constructively work to vaporize the fiber and convert the frozen deuterium into plasma. During the vaporization phase, the bulk of the current flows along the outer surface in a thin channel. This vaporization phase has been numerically simulated[13] for conditions close to the NRL experiment, with the result that the conversion of the fiber to plasma requires a time which is consistent with the length of the observed stable phase. Thus, the plasma column, upon completion of the vaporization phase, would exist in a state with an outer concentric current channel at low temperature. Depending on how narrow the current channel is, and invoking non-ideal effects including the full Braginskii stress tensor, resistivity, Hall effect and axial plasma flow, the growth rate for the $m = 0$ mode can be shown[12] to be significantly reduced from that of ideal MHD. The column, however, will diffuse naturally into a relaxed state with a distributed current channel. The relaxation of arbitrary initial states of a z-pinch plasma to a unique self-similar state has been studied in some detail recently.[14] Unless certain conditions are met leading to radiative collapse (related to the Pease current[15] condition) the relaxed state should be accessible from a wide range of initial distributions, including thin annular surface current distributions. The relaxed state is considerably more unstable to the $m = 0$ mode. In addition to the natural diffusion processes, it is possible that the consequences of $dI/dt$ vanishing enhance the redistribution of the current channel. Thus the plasma column now exists with a broad current distribution; if the ion temperature is sufficiently high, the $m = 0$ instability can turn on. The growth rate, as mentioned, will be characteristically large.

The disruption time defined above can be estimated using ideal MHD once the current density distribution is known. Again, for the NRL DZP experimental parameters, the disruption time can be shown to be on the order of several nanoseconds. There is some uncertainty in the experimentally obtained value of $k_z$ prohibiting us from obtaining a sharp comparison between the theoretically and experimentally determined growth rate.

It is interesting to note that many of the stability characteristics of the NRL DZP experiment are similar to those observed in earlier exploding wire experiments.[16-18] Exploding wires pass through a vaporizing phase before becoming plasmas and in many cases $m = 0$ instabilities have been observed when $dI/dt$ vanishes. Furthermore, there are observations of neutron production coincident with $dI/dt$ vanishing in exploding wire experiments[19] with deuterated polyethelene fibers. There has been, so far, no serious attempt to understand the similarities of the various z-pinch results; this is left for future work.

Neutrons have been observed in z-pinches in various plasma media as well as in plasma focus devices;[20] the collapsed collimated phase of a plasma focus has been considered by many experimenters to be a z-pinch and the interpretation of focus results has relied heavily on basic z-pinch phenomena.[21] For example, an extensive investigation of the neutron production in a focus device has concentrated on simulating the plasma in the collapsed state with one and two-dimensional MHD models, including viscosity, resistivity and heat conductivity; the calculated time evolution of density and temperature profiles were used in a separate calculation of neutron yield assuming deuterium plasma and thermonuclear production.[22] The calculated total neutron yields are roughly one order of magnitude less than experimentally observed and were predicted to scale with total current as $I^7$.

More recently a point model system analysis of the DZP as an intense neutron source[8] has shown that, under the assumption of stable plasma profiles, a D-T thermonuclear z-pinch will produce $10^{14}$ neutrons with the yield scaling as $I^{8-9}$. Thus the scaling of z-pinch neutron yield with total current $I^\alpha$, $7 \leq \alpha \leq 9$, has been known for some time.

Finally, we mention a recent work[23] which also discusses z-pinch neutron yield current scaling and interprets the NRL DZP results as a consequence of beam-target interaction caused by an $m = 0$ instability.

## 3. The m = 0 Instability and Deuteron Acceleration

In this section we present a discussion of the $m = 0$ instability leading to the generation of axial electric fields. We then assume that deuterons are accelerated by these fields and give estimates of the possible energy range of the high energy deuterons. The accelerated deuterons are further assumed to form a beam which interacts with cold or target deuterons producing neutrons; this process is discussed later.

The electric fields required for the beam deuteron acceleration are created during the z-pinch c mn collapse as the $m = 0$ instability proceeds. The geometry associated with this process is shown in Figure 1. In the figure $r_o$ is the undisturbed plasma radius in which the total plasma current, $I$, flows. The current density distribution is assumed to be uniform over the column; this assumption is not necessary but allows the following computations to be carried out simply. The magnetic field is in the positive $\theta$ direction. The column becomes unstable to the $m = 0$ sausage mode with the distortion of the surface occurring at a finite number of axial positions separated by wavelength $\lambda$. Experiments show that the number of unstable wavelengths may be between 5 and 10. The surface distortion proceeds with some velocity $v_r$ as sketched in the figure. The region in front of the collapsing surface distortion experiences an increase in $B_\theta$ with time thus producing an electric field in the z-direction. An idealization of this region useful for the following computations is shown in Figure 2. In the following we restrict our attention to the indented zone of length $\ell$ and obtain an order of magnitude estimate of the electric field in $0 \leq r \leq r_0$. Assuming uniform current density distribution in the region $r \leq r_1$ we can approximate the solution for $B_\theta$ in $0 \leq r \leq r_o$ as shown in Figure 3. In the figure, $r_1^i, i = 0, 1...n$ represent the sequence of m = 0 neck radii during unstable collapse. Also shown is the increase in magnetic field as $r_1$ decreases and the region $r \geq r_o$ shows no change in $B_\theta$ with time. The instantaneous $B_\theta$ profiles can be given immediately as:

$$\frac{\mu_o I}{2\pi}\left(\frac{r}{r_1^2}\right),\ r \le r_1 \tag{1}$$

$$B_\theta = \Bigg\{$$

$$\frac{\mu_o I}{2\pi r_1}\left(\frac{r_1}{r}\right),\ r > r_1 \tag{2}$$

We compute the time rate of change of $B_\theta$ in the region $r \le r_1$ as

$$\begin{aligned}\frac{\partial B_\theta}{\partial t} &= \frac{\mu_o I r}{2\pi}\frac{\partial}{\partial t}\left(\frac{1}{r_1^2}\right),\ r_1 = r_1(t) \\ &= -\frac{\mu_o I r}{2\pi}\left(\frac{2}{r_1^3}\ \dot{r}_1\right).\end{aligned} \tag{3}$$

For the region $r \ge r_1$ the field profile follows the form given by (2). In the above we have assumed that $I$ is constant in time consistent with the experimental observations that $dI/dt = 0$ during the unstable phase.

We assume the time evolution of the unstable perturbation to be given by the following expression:

$$r_1 = r_o\,(1 - \delta\ e^{\gamma_o t}), \tag{4}$$

where $\delta < 1$ is a small number, and $\gamma_o$ is the $m = 0$ growth rate. A measure of $\delta$ can be found from the required time, $t = t_c$, for the column to collapse to zero radius,

$$\delta = e^{-\gamma_o\ t_c}. \tag{5}$$

Using (4) in (3) gives

$$\frac{\partial B_\theta}{\partial \tau} = \frac{\mu_o I r}{\pi}\left(\frac{r_o \gamma_o \delta}{r_1^3}\right) e^{\gamma_o t},\ \ r \le r_1. \tag{6}$$

The electric field consistent with $B_\theta$ given by (6) is found from

$$\nabla \times \mathbf{E} = -\frac{\partial}{\partial t}\,\mathbf{B}, \tag{7}$$

and, from the geometry shown in Figure (2) yields

$$\frac{\partial E_z}{\partial r} = -\frac{\mu_o I r}{\pi}\left(\frac{r_o \gamma_o \delta}{r_1^3}\right) e^{\gamma_o t}, \tag{8}$$

which has the following solution:

$$E_z^{<} = -\frac{\mu_o I r^2}{2\pi}\left(\frac{r_o \gamma_o \delta}{r_1^3}\right) e^{\gamma_o t} \tag{9}$$

where the symbol $E_z^{<}$ indicates $E_z$ for $r < r_1$.

The spatial distribution of $E_z$ in the region $r_i \leq r \leq r_o$, can be obtained similarly. Neglecting fringing effects due to the finiteness of the region $E_z^{>}$ can be taken to be constant and upon matching with $E_z^{>}$ at $r = r_1$ gives:

$$E_z^{>} = -\frac{\mu_o I}{2\pi}\left(\frac{r_o \gamma_o \delta}{r_1}\right) e^{\gamma_o t} \tag{10}$$

or using (4) gives

$$E_z^{>} = -\frac{\mu_o I \gamma_o \delta}{2\pi}\,\frac{e^{\gamma_o t}}{1 - \delta\, e^{\gamma_o t}}. \tag{11}$$

and using (5) gives

$$E_z^{>} = -\frac{\mu_o I \gamma_o}{2\pi}\,\frac{e^{\gamma_o (t - t_c)}}{1 - e^{\gamma_o (t - t_c)}}. \tag{12}$$

Equations (9) and (12) give the electric field strengths for the regions $r \leq r_1$ and $r_1 \leq r \leq r_o$ respectively. The maximum value of $E_z$ according to the above is obtained at $r = r_1$. If we assume $\gamma_o t_c \sim 1$, which is close to the experimental situation, then (12)

can be plotted as a function of time as seen in Figure 4 where $f(\tau) = e^{(\tau-1)}/(1-e^{(\tau-1)})$, and $\tau = t/t_c$.

The magnitude of electric field strength reached during pinch collapse can be estimated from the experimental data:

$$I_o = 5 \times 10^5 \text{Amperes},$$

$$\gamma_o = \frac{1}{\tau_c},\ \tau_c = 3\text{ns},$$

$$\mid E_z \mid = \frac{1}{3} \times 10^8\ f(\tau), \tag{13}$$

where $\mid E_z \mid$ is in volts per meter. An $\mid E_z \mid$ of $10^8$ requires $f(\tau) = 3$ and this occurs at $\tau = 0.7$. The model for the time evolution of $r_1(t)$ is based on the assumption that the linear phase of the $m = 0$ instability persists; this assumption may not be valid for late times into the instability. Our result for the time evolution of the electric field can be compared with that of a similar analysis which computes the change of inductance using the non-linear plasma column compression via an $m = 0$ mode.[24] This comparison is shown in Figure 4 where we observe that the late time evolutions of the electric fields are nearly identical (in the figure the circles denote the $f(\tau)$ values from equation 12 and the squares are from an analysis based on the change of inductance).

Ignoring for the moment any ion larmor orbit effects due to the magnetic field, the maximum energy a deuterium ion can attain, $\mathcal{E}_d$, before collision, is given by $\mathcal{E}_d = |E_z|\ell$. For example, if $\ell$ is of the order of the fiber diameter (200 $\mu m$), then $\mathcal{E} \sim 20KeV$ for $\tau = 0.7$ and $\sim 130KeV$ when $\tau = 0.95$. The exact nature of the ion acceleration is complicated and dependant on the details of the plasma region considered. Experimental data obtained in the NRL DZP show evidence of deuteron energies up to 72 KeV.

We conclude this section with the following observation. If the accelerated ions constitute a deuteron beam then the beam velocity distribution will be centered around some mean beam velocity, $V_d$, which we assume can be given by:

$$V_d = [2e\ \mathcal{E}_d/m_d]^{1/2} \tag{14}$$

where $e$ and $m_d$ are the electron charge and deuteron mass respectively. We have previously shown that $\mathcal{E}_d$ is proportional to $\gamma_o I$ and that $\gamma_o$is also proportional to I resulting in the following relation for $V_d$:

$$V_d = \beta(t) I, \tag{15}$$

where $\beta(t)$ is time varying function. The validity of the physics implied by Eq. 15, as already stated, depends on many complicating factors, including collision frequency and magnetic field strength, to name two. We assume its validity for the analysis in the following section.

## 4. Beam Target Neutrons

We have argued above that a beam of deuteron ions has been accelerated by the electric field to a mean velocity $V_d$. Let us further assume that this beam is formed with a beam-like distribution function, centered around the mean beam velocity and containing a thermal spread equal to the background level which we will take to be the Bennett temperature, $T_o$. This is a reasonable assumption since we have implicitly assumed that the plasma column reaches an equilibrium prior to onset of instability. For the beam distribution function let us choose the following Maxwellian $f_d(V)$ about $V = V_d$:

$$f_d(V) = \mathrm{A} \ \exp\Big\{\frac{-(V - V_d)^2}{\kappa T_o}\Big\}. \tag{16}$$

In the last section we developed an expression for $V_d$ as a function of the total current $I, V_d = \beta I$. From the Bennet pinch relation[25] we also know that $T_o$ can be written as $T_o = \beta_1 I^2$, where $\beta_1$ depends only on the background or equilibrium line density; this background line density is the source of target deuterons. Using this information we can rewrite Eq. 16 as:

$$f_d(x) = \mathrm{A} \ \exp\Big\{\frac{-(x-1)^2}{\bar{\beta}_1}\Big\}, \tag{17}$$

where $x = V/V_d = V/(I\beta_1)$ and $\bar{\beta}_1 = \kappa\beta_1/\beta^2$.

We can now write the expression for the neutron reaction integral, $R$, as:

$$R = \int_{V_d}\int_{V_B} d\mathbf{V}_B \ d\mathbf{V}_d \ f_B \ f_d \ |V|\sigma_{dd}(|\mathbf{V}|), \tag{18}$$

where $d\mathbf{V}_B$ refers to the velocity integration for the background target (cold) deuterons, $f_B$ is the background deuteron distribution function, $|\mathbf{V}|$ is the relative velocity between the target deuterons and the beam deuterons, and $\sigma_{dd}$ is the deuteron-deuteron collision cross-section expressed as a function of the relative velocity $|V|$. We take the target

deuterons to be cold, e.g. they have zero or small velocity. The relative velocity is therefore $V_d$ allowing $R$ to be written as:

$$R = N_B \int dv_d f_d(v_d) v_d \sigma_{dd}(v_d) \quad , \tag{19}$$

where $N_B$ is the background line density. Upon integration, Eq. 19 gives the usual form for the reaction rate $R = N_B N_d < \sigma|\mathbf{V}| >$, useful in computing the total neutron yield assuming certain quantities, discussed shortly, are known. Instead, we analyze the integral in Eq. 19 in a manner which makes the scaling of the neutron production rate more transparent. First, we note the cross section $\sigma_{dd}(V_d)$ is a monotone increasing function of $V_d$ up to some value $V_d^{MAX}$ where $\sigma_{dd}$ reaches a maximum. $\sigma_{dd}$ $(V_d)$ is given by:[26]

$$\sigma_{dd}(V_d) = \frac{482\left[(1.177 - 3.08 \times 10^{-4}\mathcal{E})^2 + 1\right]^{-1}}{\mathcal{E}\left[\exp\left(\frac{47.88}{\mathcal{E}^{1/2}}\right) - 1\right]} \quad , \tag{20}$$

where $\mathcal{E} \sim V_d^2$. $\mathcal{E}$ in Eq. 20 is in KeV and $\sigma_{dd}$ is in barns. If the temperature $T_o$ in Eq. 16 is low enough, then the distribution function $f_d$ will be localized in $\mathcal{E}$ and will appear as a sharp spike when compared with $\sigma_{dd}$. This is shown schematically in Fig. 5.

Since the background target plasma temperature is no larger than 100 ev in the NRL DZP experiment, the distribution function $f_d$ will appear very sharply peaked and localized about $V_d$. If we then assume that $\sigma_{dd}$ can be represented by a simple polynomial function about $V_d$, the integral in Eq. 19 can be written in the following form:

$$R = \bar{A}\left(\int_o^\infty \exp\left[\frac{-(x-1)^2}{\bar{\beta}_1}\right] x^{2\nu+3} dx\right) I^{2\nu+4} \quad , \tag{21}$$

where $\bar{A}$ is a constant and $\nu$ is defined by the polynomial approximation of $\sigma_{dd}(V_d) \sim \mathcal{E}^\nu \sim (V_d^2)^\nu$ over an interval in $\mathcal{E}$ sufficiently broad to contain the dominant part of $f_d$ and narrow enough such that the approximation for $\sigma_{dd}$ valid. Denoting the term in parentheses in Eq. 21 by $f(\bar{\beta}_1, \nu)$, we have

$$R = \bar{A} f(\bar{\beta}_1,\ \nu) I^{2\nu+4} \quad . \tag{22}$$

Using the approximation for $\sigma_{dd}$ we find that for $V_d$ between 20 and 60 KeV, $\nu$ satisfies $3.8 \geq \nu \geq 2.3$. Substituting this into Eq. 22 we discover

$$R \sim I^{\alpha} \quad , \tag{23}$$

where $11.6 \geq \alpha \geq 8.6$.

The result given by Eq. 23 depends directly on the assumption of an accelerated beam of deuterons. It remains to be seen if this beam in fact does form. The experiments with the NRL DZP have shown that high energy deuterons are present but there is no indication where they are formed or how many ions are accelerated. We discuss later a companion work aimed at simulating the beam formation process in the DZP.

It is straightforward to use the result obtained for the reaction rate $R$ to estimate the total integrated neutron yield. There are a number of assumptions required which, if properly made, allow one to obtain precisely the yields observed in the experiment. For example, the number density for the background and beam particles can be chosen independently. It is also necessary to know the interaction cross-sectional area as well as the number of interaction zones. Although we can make reasonable estimates for these quantities, at present we do not have a method for self-consistently obtaining them. We address this issue in our conclusions. Furthermore, we also need to know the slowing down trajectory of the beam deuterons during collisions with targets and with background electrons. The slowing down time for the beam can be estimated using classical formulas but the characteristically large magnetic fields must play an important role in this process. Indeed, simulations have already shown that the magnetic fields significantly distort the ion orbits into a more vortex-like pattern.[27] This effect would lead to an enhancement in neutron production since it would tend to keep the high energy beam particles in the target zone for longer times. In short, plausible estimates of the required quantities show that $10^9$ 2.5 MeV total neutrons are well within the range of parameter variations relevant to the experiment in question.

It was mentioned that our analysis allows a prediction of the neutron yield scaling with total current in future DZP experiments. For example, for a frozen deuterium-tritium fiber, a similar exercise utilizing the $\sigma_{dt}$ cross-section instead of the $\sigma_{dd}$ cross-section reveals the scaling; but the neutron yield estimate so obtained requires even more assumptions than the present case. The difficulty here arises in knowing whether deuterons or tritons or both are accelerated and how many of each. If one assumes they are accelerated equally, for example, a scaling of $I^{\alpha}, 12 \geq \alpha \geq 9$ is obtained which would yield approximately $10^{12}$ 14 MeV neutrons under the conditions of the NRL experiment.

Finally, we remark that it is difficult to predict the range of total plasma currents for which the predicted scaling should hold. The reason is that the deuteron energy may not reach its full potential because of magnetic field effects and collisions. Ignoring these, and assuming a value of deuteron mean energy for a given fiber and total current, the scaling for beam energy with current shows that doubling the current will result in a beam energy well past the peak in the collision cross-section. For example, assuming 20 KeV for I = 500 KAmps means that doubling I yields 80 KeV, past the cross-section peak. Thus, the total neutrons and scaling should decrease noticeably. It is necessary to understand the deuteron dynamics in order to clarify this question of scaling range. Particle simulation codes are a viable tool for obtaining the required deuteron dynamics.

## 5. Discussion and Conclusions

The main result of the present work is contained in Eq. 23. The total neutron yield for the DZP, assuming frozen deuterium fibers as the plasma source, should scale as $I^{\alpha}$ where $11.6 \geq \alpha \geq 8.6$. This result is consistent with the experimental observations. The physics behind the result requires a deuteron beam to be produced during the unstable phase of the z-pinch discharge, producing neutrons from a beam-target interaction. Although no analysis has been offered to substantiate the existence of the accelerated deuterium beam, the experimental data contains evidence of deuteron energies up to at least 72 KeV. The beam acceleration and beam-target interaction have been invoked in previous studies of z-pinch dynamics without sufficient emphasis being placed on examining the conditions leading to beam production. For this reason we have initiated a computer study whose goal is to analyze and simulate the beam formation in a deuterium z-pinch plasma. Results from this study will be reported later.

The ramification of the beam-target analysis presented here is that the basic plasma configuration is unstable. This status leads, for the device, towards a possible application for intense neutron sources for material breeding such as tritium or neutron irradiation test facilities. Another possibility of the combined experimental-theoretical study of DZP devices is that a route toward stable operation of the pinch may be found and, if this is the case, this would renew interest in DZP devices for fusion energy applications.

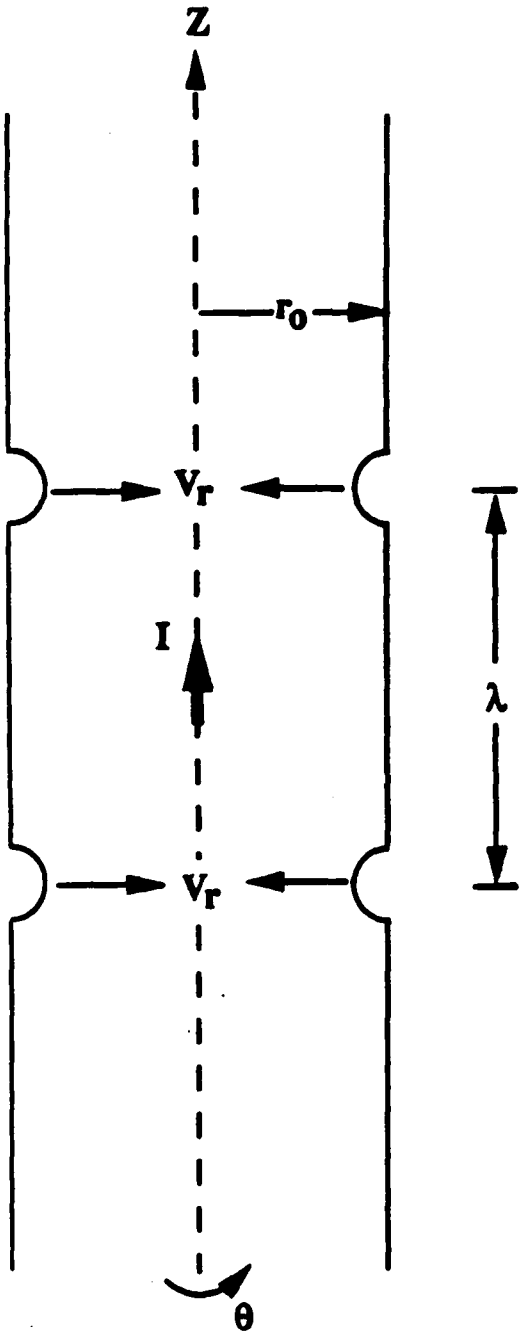



**Figure 1**

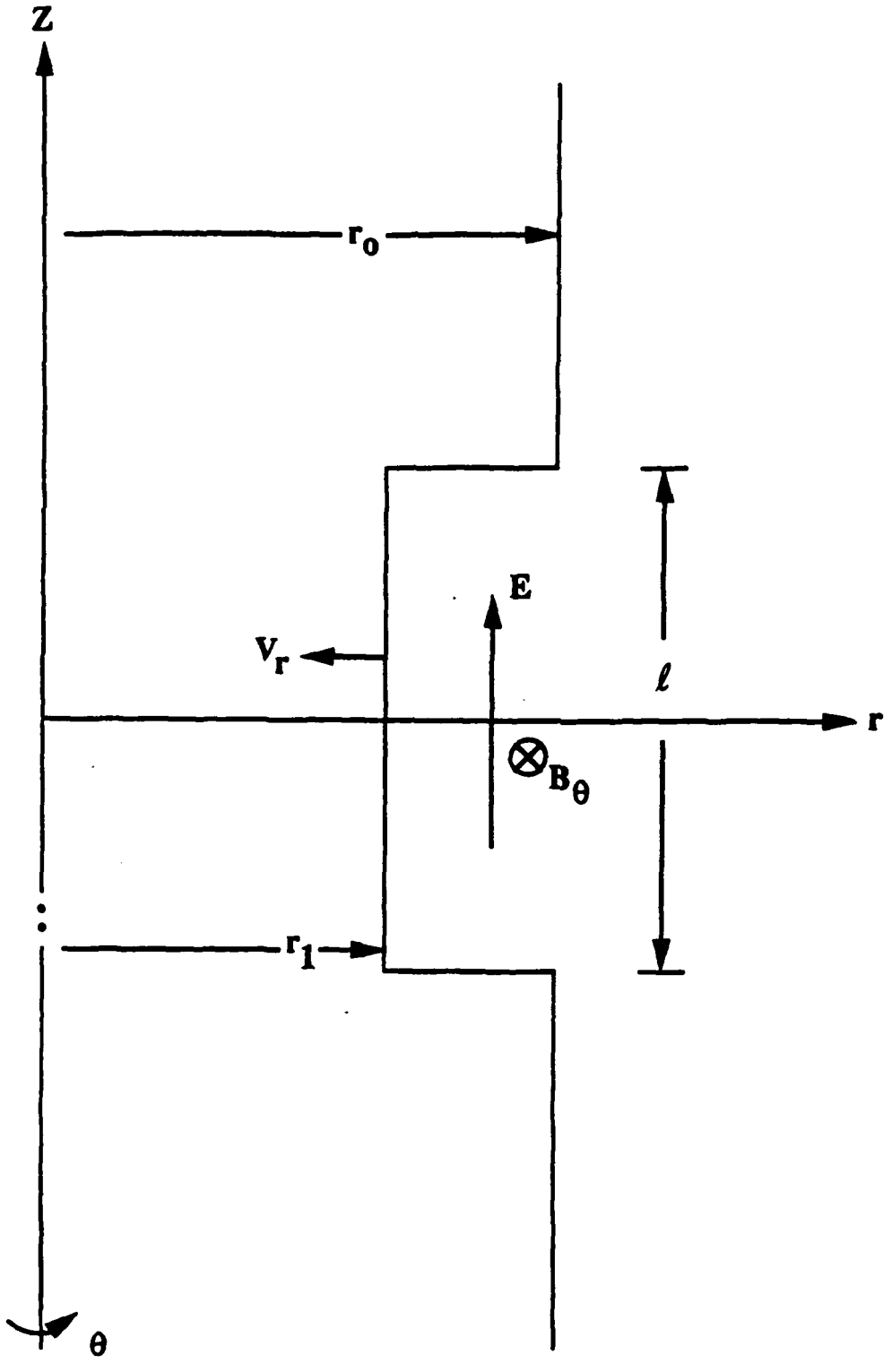



**Figure 2**

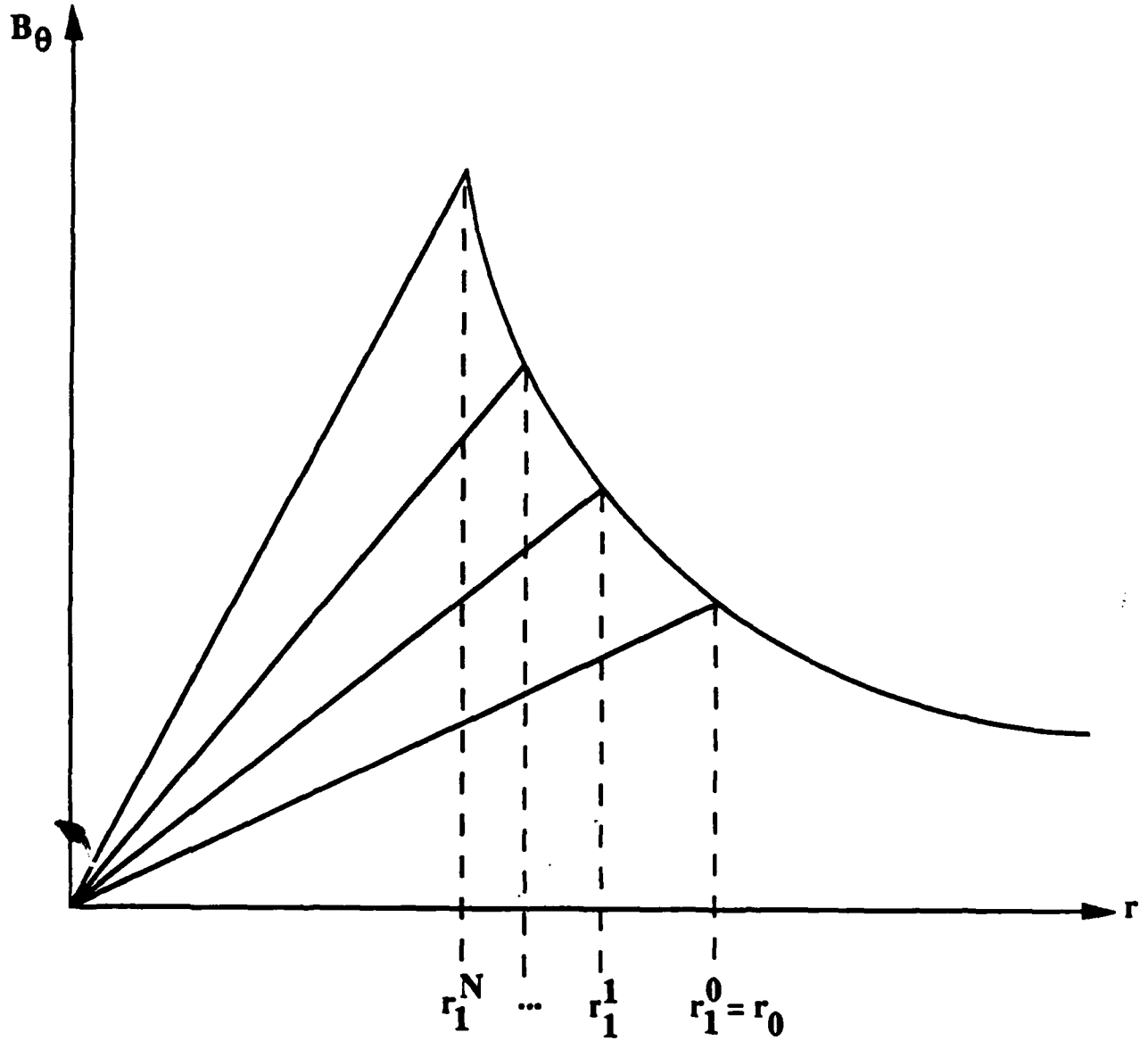



**Figure 3**

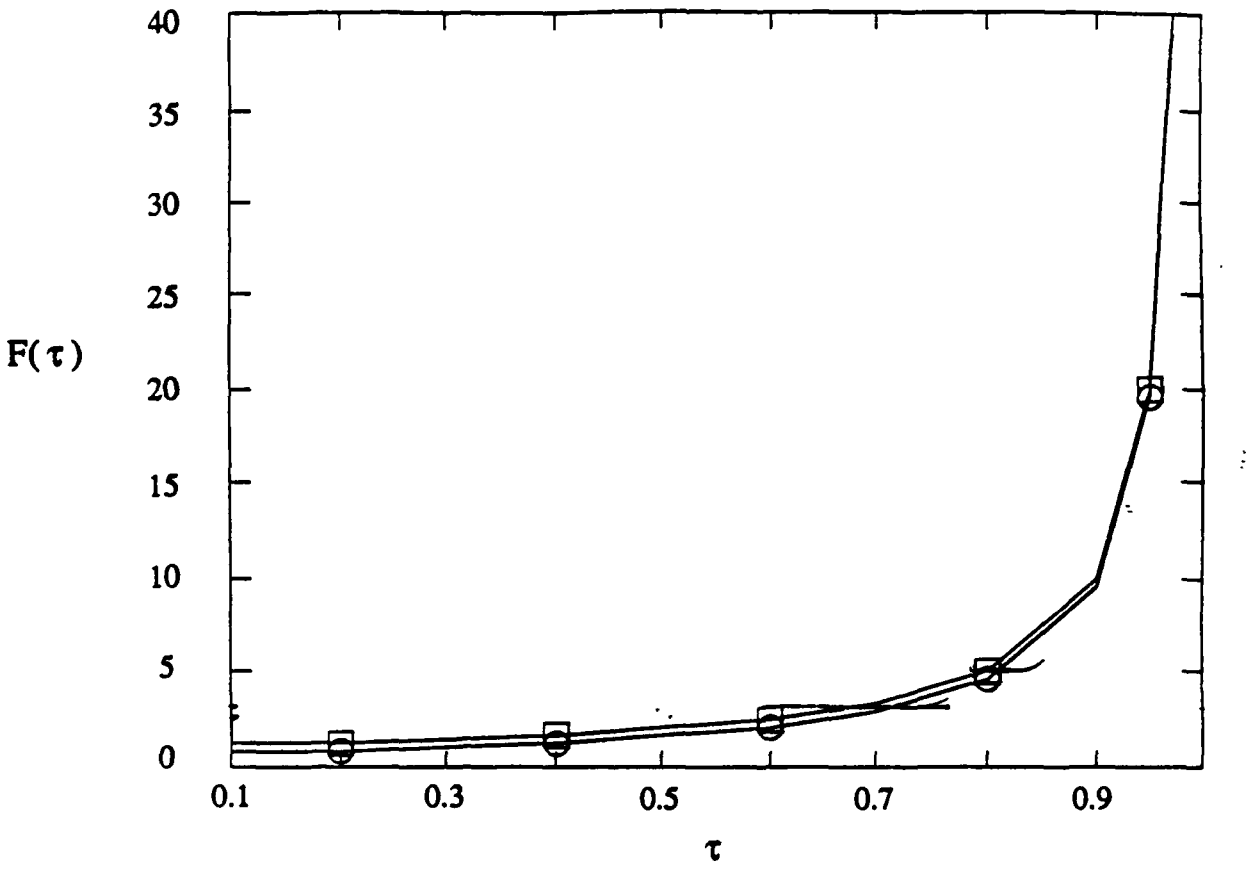



**Figure 4**

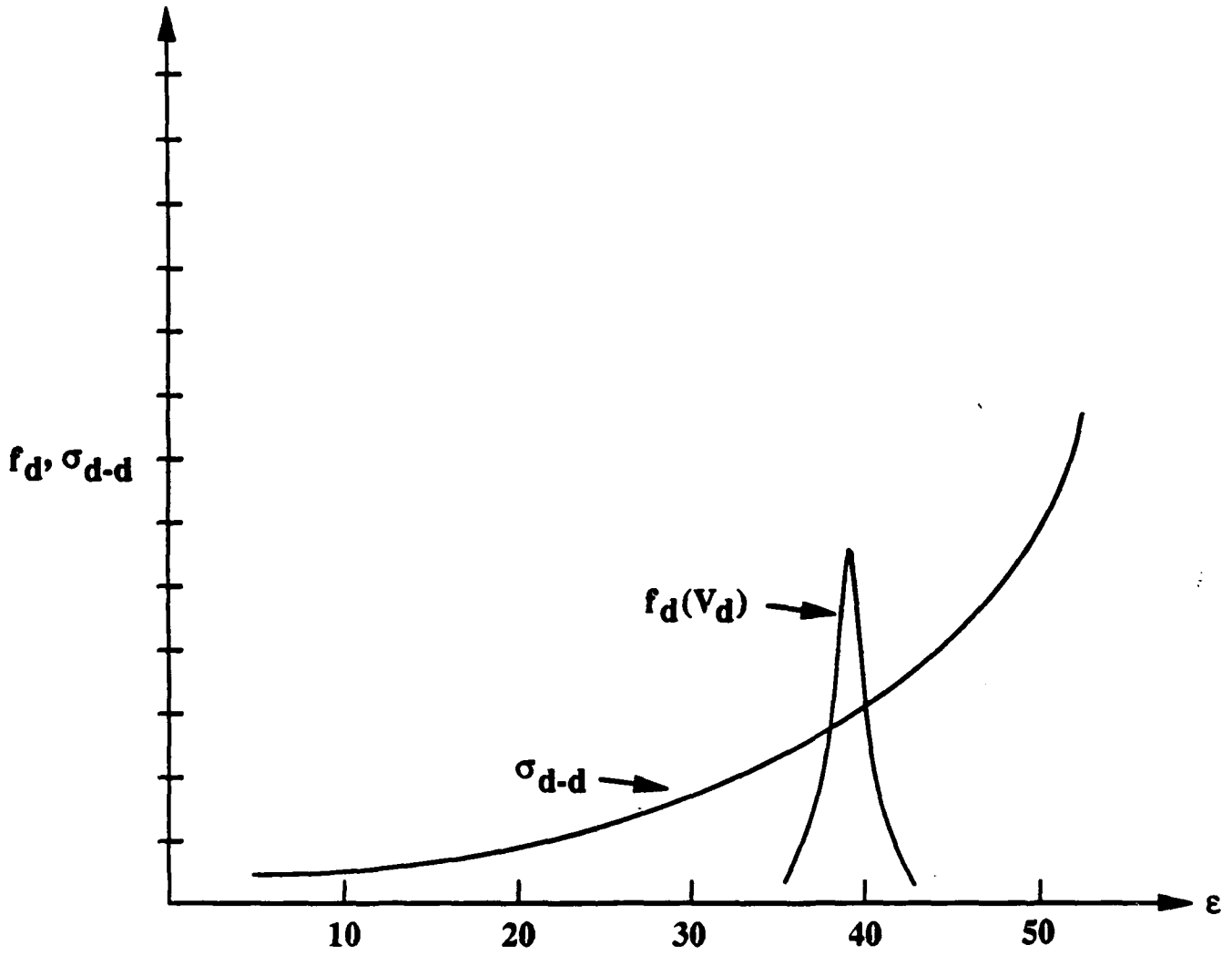



**Figure 5**

## References


1. Sethian, J.D., A. E. Robson, K. A. Gerber, and A. W. DeSilva, Phys. Rev. Lett. **59**, 892 (1987); **59**, 1790(E) (1987).

2. Hammel, J.E., D. W. Scudder, and J. S. Schlachter, in *Proceeding of the First International Conference of Dense Z-Pinches for Fusion*, edited by J. D. Sethian and K. A. Gerber (Naval Research Laboratory, Washington, D.C., 1984), p. 13.

3. Kadomtsev, B., "Hydromagnetic Stability," Rev. of Plas. Phys. **2**, 153 (1966).

4. Suydam, B. R., Los Alamos National Laboratory Report LA- 7809-MS (1979).

5. Pereira, N.R., N. Rostoker, J. S. Pearlman, J. Appl. Phys. **55** (3), 704 (1984).

6. Anderson, O. A., W. R. Baker, S. A. Colgate, J. Ise, Jr., R. V. Pyle, Phys. Rev., **110** (6), 1375 (1968).

7. Shiloh, J., A. Fisher, E. Bat-Avraham, Appl. Phys. Lett. **35** (5), 390 (1979).

8. Hagenson, R., J. Hammel, R. Krakowski, R. Miller, R. Nebel, D. Scudder, K. Werley, "The High Density Z-Pinch (HDZP) as a Fusion Neutron Source," *Proceedings at 12th Symposium on Fusion Engineering.*

9. Hagenson, R. L., A. S. Tai, R. A. Krakowski, R. W. Moses, Nucl. Fusion **21** (11), 1351 (1981).

10. Walker, S. P., M. Javadi, A. E. Robson, *Proceedings 14th Symposium on Fusion Technology*, Avignon **2**, 1875 (Sept. 8- 12, 1986).

11. Freidberg, J. P., "Ideal Magnetohydrodynamics," Plenum Press, NYC, 1987.

12. Sheehey, P. W., R. A. Nebel, I. Lindemuth, Bulletin of Am. Phys. Soc., **33** (9), 1908 (1988).

13. Lindemuth, J., R. Nebil, *ibid.*

14. Rosenau, P., R. A. Nebel, H. R. Lewis, to be published.

15. Pease, R. S., *Proc. Phys. Soc. B*, **70**, 11 (1957).

16. Chang, T. S., M. L. Chang, "Initial Behavior of an Exploding Wire," Exploding Wires, vol. 3 *Proceedings of the 3rd Conf. on the Exploding Wire Phenomenon*, held Boston, MA March 10-12, 1964, Ed. W. G. Chace, H. K. Moore, Plenum Press, NYC. 1964.

17. Ross, D. P., O. H. Zinke, "High Temperature Plasmas Produced by Exploding Wires," *ibid.*

18. Vitkovitsky, J. H., "Similarities in Spark and Exploding Wire Discharges," *ibid.*

19. Stephanakis, S. J., L. S. Levine, D. Mosher, I. M. Vitkovitsky, F. Young, Phys. Rev. Lett. **29** (9), (1972).

20. Decker, G., R. Deutsch, W. Kies, J. Rybach, Plas. Phys. Contr. Fusion **27**, 609 (1985).

21. Deutsch, R., W. Kies, Plas. Phys. Contr. Fusion **30**, 921 (1988).

22. D'Yachenko, V. F., V. S. Imshennik, Reviews of Plas. Phys. **5**, Consultants Bureau, New York (1970).

23. Lindemuth, I., G. McCall, R. Nebel, Phys. Rev. Lett. **62** (3), 264 (1989).

24. McCall, G. H., To be published.

25. Bennett, W. H., Phys. Rev. **45**, 890 (1934).

26. Book, D. L., NRL Plasma Formulary, (Naval Research Laboratory, 1987) p. 44.

27. Imshennik, V. S., N. M. Zueva, O. V. Lokutsieskij, M. S. Mikhajlova, in Plasma Physics and Controlled Nuclear Fusion Research, Vol. 2, 10th Conference proceedings, London, 12-19 Sept. 1984, paper IAEA-CN-44/D-III-6-1.

# APPENDIX ZZ

## Laser-Plasma Experiments and Laser Development at the Naval Research Laboratory

INTERNATIONAL ATOMIC ENERGY AGENCY

TWELFTH INTERNATIONAL CONFERENCE ON PLASMA PHYSICS AND CONTROLLED NUCLEAR FUSION RESEARCH

Nice, France, 12-19 October 1988

IAEA-CN-50/B-II-3

# LASER-PLASMA EXPERIMENTS AND LASER DEVELOPMENT AT THE NAVAL RESEARCH LABORATORY

S. BODNER, S. OBENSCHAIN, R. LEHMBERG, J. GARDNER, K. KEARNEY, C. MANKA, A. MOSTOVYCH, C. PAWLEY, T. PEYSER, M. PRONKO, A. SCHMITT, AND J. STAMPER
Naval Research Laboratory,
Washington, D.C.

J. GOLDHAR,
University of Maryland,
College Park, MD

J. SHIPMAN,
Sachs-Freeman Assoc.,
Landover, MD

United States of America

Copy available to DTIC does not permit fully legible reproduction

This is a preprint of a paper intended for presentation at a scientific meeting. Because of the provisional nature of its content and since changes of substance or detail may have to be made before publication, the preprint is made available on the understanding that it will not be cited in the literature or in any way be reproduced in its present form. The views expressed and the statements made remain the responsibility of the named authors; the views do not necessarily reflect those of the government of the designating Member State(s). In particular, neither the IAEA nor any other organization or body sponsoring this conference can be held responsible for any material reproduced in this preprint which is the property of another organization.

# LASER-PLASMA EXPERIMENTS AND LASER DEVELOPMENT AT THE NAVAL RESEARCH LABORATORY


## Abstract

Using our Pharos III Nd:glass laser facility, we have found that the induced spatial incoherence technique reduces the stimulated convective Raman instability by orders of magnitude as compared to an ordinary laser beam -- even with the use of infrared laser light and a low-Z target. The threshold for the instability is also in relatively good agreement with analytic theory, in contrast with other experiments with an ordinary laser that have had thresholds an order of magnitude lower that theory. We have also begun building a new KrF laser, called Nike (named after the goddess of victory) to test the hydrodynamic stability of accelerating thin targets. This laser has been designed to include the echelon-free ISI optical smoothing technique.


## 1. NIKE KrF LASER FACILITY

The direct-drive approach to laser fusion places two requirements on the laser driver: the use of induced spatial incoherence (ISI) for optical smoothing of the laser beam [1,2,3], and the use of an ultraviolet laser wavelength for high efficiency and for control both plasma and fluid instabilities. KrF lasers can satisfy these requirements, with a 1/4 μm wavelength and with the broad bandwidth necessary for ISI. The Naval Research Laboratory has also begun building a new KrF laser, called Nike (named after the goddess of victory), to complete the laser-target physics data base that is required before one could commit to an ignition-sized facility. This laser has been designed to include the echelon-free ISI optical smoothing technique that should produce very uniform illumination on a target [4].

The overall milestone for the Nike facility will be to accelerate a thin, dense foil (approximately a millimeter in diameter) to fusion-like velocities with a flatness of ±1%, as a demonstration that thin targets can be symmetrically and stably imploded. The successful acceleration of flat targets is at least as difficult, and as scientifically useful, as the acceleration of hydrodynamically-equivalent small pellets, with the advantage that foils have much better diagnostic access. Operation of Nike for laser-target experiments is planned for 1992-3, depending on the rate of funding and on possible surprises in laser technology. Our existing Nd:glass laser will not be used for laser fusion research after 1990.

In addition to the overall milestone, Nike will be used in four physics and technology areas: (1) to demonstrate the practicality of high-power KrF lasers; (2) to demonstrate that the optical technique of echelon-free ISI can produce uniform illumination; (3) to measure the growth rate of the Rayleigh-Taylor instability and show that it is low enough for thin-shell pellet implosions; (4) to measure the effective thresholds of the plasma instabilities and show that these thresholds are high enough to avoid preheat in thin pellet shells.

The Nike laser has been designed for 4 kJ on target, with initial operation at 2 kJ using half of the laser beams. The pulse length will be compressed from 240 nsec to 5 nsec using optical multiplexing. Nike will also have what is so far a unique feature: the use of echelon-free ISI for optical smoothing. Use of this optical technique requires that the laser be designed with a broad bandwidth and with low chromatic aberration and low off-axis aberration. Except for optical imperfections and amplifier distortion, the beams have been

designed to be twice diffraction-limit, an order-of-magnitude improvement over other multiplexed systems. The improvement is based upon the use of mirrors instead of lenses to relay the laser beams. So far, Nike is the only KrF laser to be designed with the capability for broad bandwidth, low aberration, and ISI. Figure 1a shows the overall dimensions of the Nike facility, with 24 of the 48 beam lines.

The echelon-free ISI concept is shown in Fig. 1b, in simplified form. The oscillator has a broad bandwidth and many spatial modes -- the opposite of the usual approach to laser design. The laser beam is then focused and apertured to produce the intensity profile that is desired on the target. This intensity profile has the characteristics of ISI: temporal incoherence and a short transverse spatial coherence. The aperture is at the focus of a second lens; the beam then propagates through an amplifier system (and a multiplexing system that is not shown here), and focused onto the target. The intensity profile at the target will then be the same as the profile at the aperture, provided that the KrF amplifier system does not introduce excessive linear and nonlinear distortion. When an object is placed at the focus of a lens, the light at the opposite focal point is essentially a fourier transform. Therefore the information on the shape of the intensity profile at the aperture is contained in small beamlets (similar to the usual ISI) that propagate through the amplifier system. As long as the aberration in the amplifier system has a transverse scale that is large compared to the beamlets, the information in the beamlets is preserved. The focusing lens inverts the fourier transform, reproducing at the target plane the intensity profile created at the aperture. Detailed computational studies have shown that this technique can work -- but only with a laser such as KrF that has small nonlinear distortion [4].

## 2. Suppression of stimulated Raman Scatter using ISI Optics

We are now using our existing Nd:glass laser facility to investigate the effect of ISI upon plasma instabilities, and for further measurements of the growth rate of the Rayleigh-Taylor fluid instability. Here we would like to report some of our studies of the effect of ISI upon stimulated Raman backscatter (SRS), using a low-Z target with one-micron laser light. We have found that ISI reduces the Raman backscatter by orders of magnitude, and that the onset of the instability follows the predictions of a convective gain model. Our results are in contrast with earlier experiments using an ordinary laser beam where the SRS instability occured at much lower laser intensity than predicted by the convective gain model.

Until this experiment, the threshold for the stimulated Raman instability had also been in conflict with the designs for high-gain direct-drive pellet [5-9]. It has been shown that SRS efficiently generates fast electrons that can produce fuel preheat. It has also been shown that if one uses both a short laser wavelength and a high-Z target, then there is a major reduction in SRS [9]. But with the low-Z targets that are used in direct-drive, experimental thresholds have typically been 1/10 of the predictions of a convective-gain theoretical model with a monotonic density profile. This has been troublesome since high-gain, direct-drive laser fusion targets have been designed to be near the theoretical threshold (thin pellet shells) or above the theoretical threshold (thick pellet shells).

Several mechanisms have been proposed to explain the low SRS threshold, including: (a) hot spots in the incident laser beam can filament and the resulting higher laser intensity can then drive SRS; (b) temporal modulations in the laser profile can produce flat regions in the density profile which enhance SRS; (c) there could be density cavities or mode coupling that cause the instability to become absolute [10]; (d) the observed scatter may be Thompson scattering rather than the Raman mode [11]. Until now, the only practical means to control the SRS instability used a combination of short laser wavelength and a high-Z target to provide collisional damping.

Our experiments used two beams of the NRL Pharos III laser, one with and one without ISI echelons, focused onto thick CH targets. The beams could be operated with either a broad bandwidth (2 psec coherence) or a narrow bandwidth (2 nsec coherence). The ordinary (non-ISI) beam had a top-hat intensity profile with hot spots a factor of 2-3 above the average. The focal-spot diameter of the ordinary beam was chosen so that the average intensity across the top matched the average FWHM of the ISI beam.

Figure 2a shows the peak Raman backscatter in the 1350-1750 nm range for three cases, using germanium detectors with a 0.6 nsec time resolution. The SRS emission with an ordinary beam, and with narrowband ISI, are orders of magnitude higher than that obtained with broadband ISI. Variations of the bandwidth of the ordinary beam (not shown here) had little effect on the Raman emission. The SRS with ISI was suppressed for a coherence time as long as 10 psec. The time duration of the broadband ISI emission was much longer than the laser pulse, and consisted of just thermal radiation from the hot target. The signals from the other two cases had pulse widths shorter than the incident laser pulse, consistent with an instability.

Any explanation of these results must consider the following: the bandwidth had little effect on the SRS from the ordinary beam, and the broader-bandwidth ISI experiment still had $\Delta\gamma < \omega$ if one uses the laser intensity of the instantaneous peaks of the ISI beam. We conclude that the suppression with broadband ISI must involve some type of hydrodynamic phenomena that occurs on a relatively long time scale, such as filamentation or density profile modification. Our 2D and 3D computer simulations indicate that, under our experimental conditions, the ordinary beam and the narrowband ISI beam are susceptible to strong ponderomotive filamentation, while the broadband ISI beam is resistant to filamentation [12]. The suppression of Raman by Brillouin that has been observed in other experiments [13] could not occur here, because SBS is also strongly suppressed by ISI [14].

### 3. Comparison of SRS Theory and Experiment

In another set of experiments, shown in fig. 2b, we were able to obtain SRS signals with broadband ISI by focusing the beam onto a preplasma that preceded the ISI beam by 2 nsec. Presumably the preplasma increased the SRS because of the longer scalelength. The theoretical expression [15] for convective Raman growth is given by $I_R = I_n e^{GLI}$, where $I_n$ is the noise level, G = 1.6x10-13 cm/W for a 1 mm laser near n=0.1 $n_c$, and L is the plasma size. If one uses the time-averaged ISI intensity in this formula, the prediction is still less than the experiment. But the ISI beam is not constant in time, and the instantaneous peaks will have a growth rate . Therefore we modified the standard convective theory by assuming that these hot spots will drive the SRS. The instantaneous electric field at the target satisfies a gaussian probability distribution, corresponding to an intensity distribution $P(I) = 1/I_0 \exp(-I/I_0)$. Integrating over P(I), one obtains the expression:

$$I_R = I_n \int_0^{I_s} e^{GLI} P(I)\, dI + \alpha \int_{I_s}^{\infty} I\, P(I)\, dI$$

Here $I_s$ is the incident intensity that saturates the Raman scatter, and $\alpha$ is a saturation coefficient that satisfies $I_n \exp(GLI_s) = \alpha I_s$ . Provided that $\alpha$ is not too small, Eq. 1 is a function that is relatively flat for small $I_0$, with a rapid increase for $I_0 > (GL)^{-1}$. We chose the value of $\alpha$, ($10^{-5}$ $nm^{-1}$), to match the experimental slope of the SRS above threshold. The threshold value (the break in the curve) is insensitive to the choice of $\alpha$. The optimum value of L = 0.08 cm is larger than the experimental value of 0.06 cm that was obtained by

direct interferometry measurements. This remaining slight disagreement between theory and experiment may reflect several factors: Io and L are only known to ±15%, and there may be a slight remaining filamentation with broadband ISI.

In summary, our experiments show that ISI has a strong stabilizing influence on the convective SRS instability as compared to an ordinary beam or narrowband ISI ( the latter simulating the random phase screen with high F# optics), and the backscatter intensity is in relatively good agreement with an analytic theory that includes the probabilistic intensity distribution of ISI and a saturation term. These results suggest that direct-drive high-gain laser fusion pellets may not have problems with fast electron preheat from SRS -- if one uses a thin pellet shell. In more recent experiments with ISI using green light (527 nm), there was some evidence of additional suppression of SRS by a broader bandwidth. This effect could allow usage of the somewhat thicker pellet shells (with less pellet gain) that are preferred by some groups.

Acknowledgement: Supported by the U.S. Department of Energy

## REFERENCES

[1] LEHMBERG, R. H. and OBENSCHAIN, S. P., Opt. Comm. 46 (1983) 27
[2] LEHMBERG, R. H., SCHMITT, A. J., and BODNER, S. E., Theory of induced spatial incoherence, J. Appl. Phys. 62 (1987) 2680
[3] OBENSCHAIN, S. P. et al., Phys. Rev. Lett. 56 (1986) 2807
[4] LEHMBERG, R. H. and GOLDHAR, J. Use of incoherence to produce smooth and controllable irradiation profiles with KrF fusion lasers, Fusion Tech. 11 (1987) 532
[5] TANAKA, K. et al., Phys. Rev. Lett. 48 (1082) 1179
[6] SHEPARD, C. L. et al., Phys. Fluids 29 (1986) 583
[7] SEKA, W. K. et al., Phys. Fluids 27 (1984) 2181
[8] DRAKE, R.P. et al., Phys. Rev. Lett. 60 (1988) 1018
[9] TURNER, R. E. et al., Phys. Rev. Lett. 54 (1985) 189
[10] BARR, H. C. et al., Phys. Rev. Lett., 60 (1988) 1950
[11] SIMON, A. and SHORT, R. W., Phys. Rev. Lett. 53 (1988) 1912
[12] SCHMITT, A. J., Phys. Fluids 31 (1988)
[13] VILLENEUEVE et al., Phys. Rev. Lett., 59 (1987) 1585
[14] MOSTOVYCH, A. N. et al., Phys. Rev. Lett., 59 (1987) 1193
[15] LIU, C. S., ROSENBLUTH, M. N., and WHITE, R. B., Phys. Fluids 17 (1974) 1211

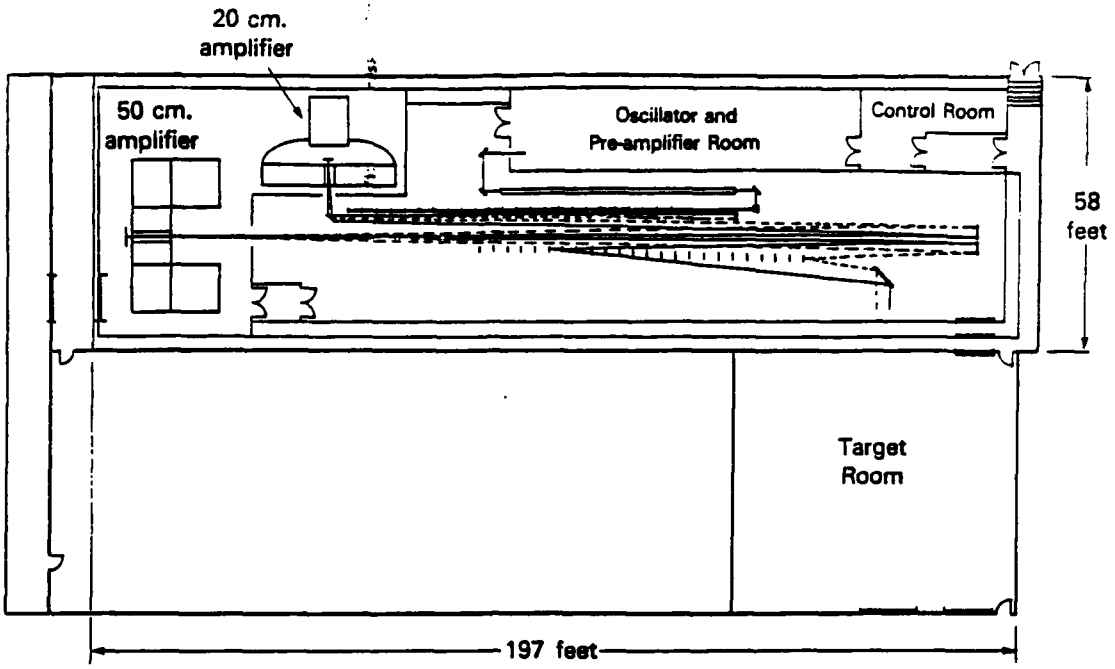
## FIGURE CAPTIONS

FIG. 1: (a) Floor plan for the Nike KrF laser now being built at NRL. There are two e-beam pumped amplifiers, 20x20x80 $cm^3$, and 50x50x200 $cm^3$. The optical multiplexing will use primarily mirrors instead of lenses. The targets will be flat foils. (b) With the echelon-free ISI concept, the desired intensity profile is imaged onto the target through the laser chain, using partially-coherent light. Good fidelity is obtained if nonlinear effects and chromatic aberration are minimized.

FIG. 2: (a) The peak Raman emission in the band 1350-1750 nm. The intensities are the average across the FWHM of the ISI focal profile, and the average across the "flat top" region of the ordinary beam. (b) Energy per nm in the Raman band near 1600 nm with broadband ISI, with and without a preplasma. Data is plotted as a function of the time-averaged intensity at the peak of the focal distribution; this is 1.4 times larger than the intensities in (a). Theoretical curves use the equation in the text, with a correction for the emission from the preplasma.

**(a)**

NIKE LASER




**(b)**

ECHELON-FREE ISI

**Desired intensity profile is imaged onto the target through the laser chain, using partially-coherent light. Good fidelity is obtained if nolinear effects and chromatic aberration are minimized.**

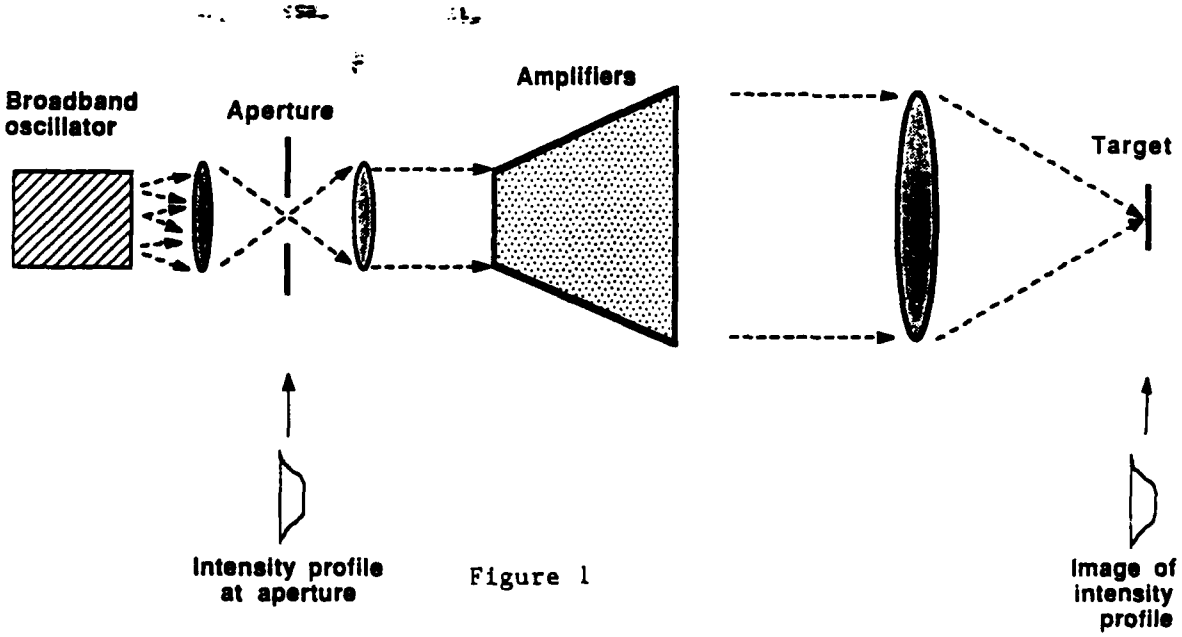
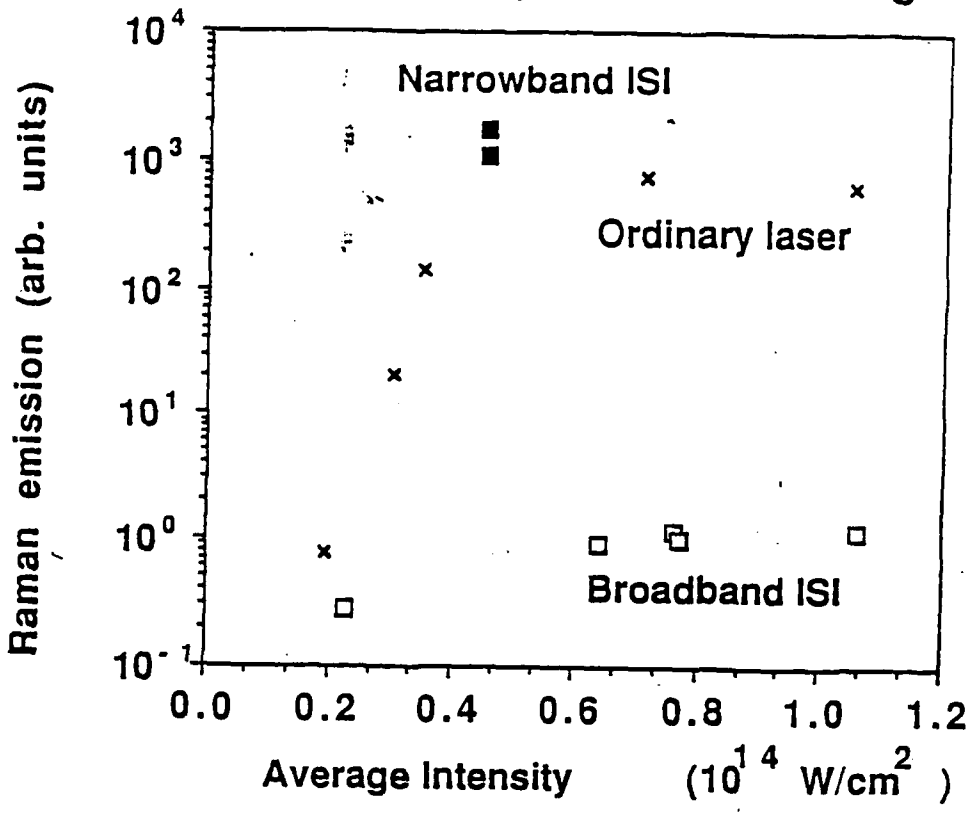



Figure 1

(a)

ISI reduces SRS by orders of magnitude




(b)

Comparison of experiment & theory, SRS with ISI

(one micron light, CH target)

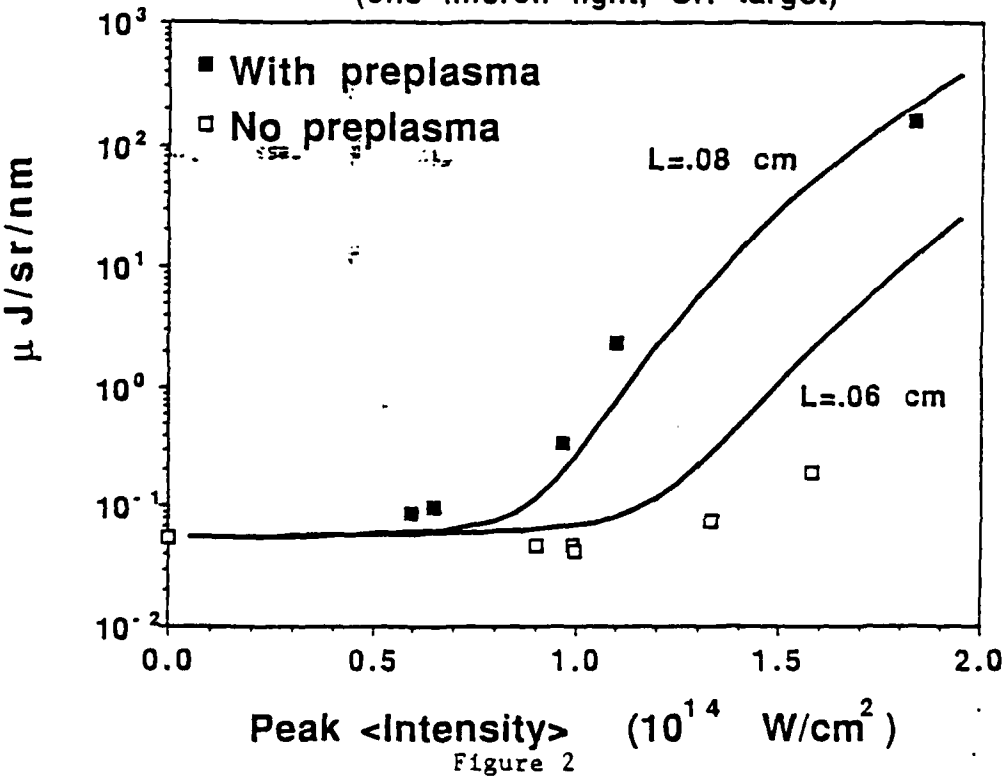
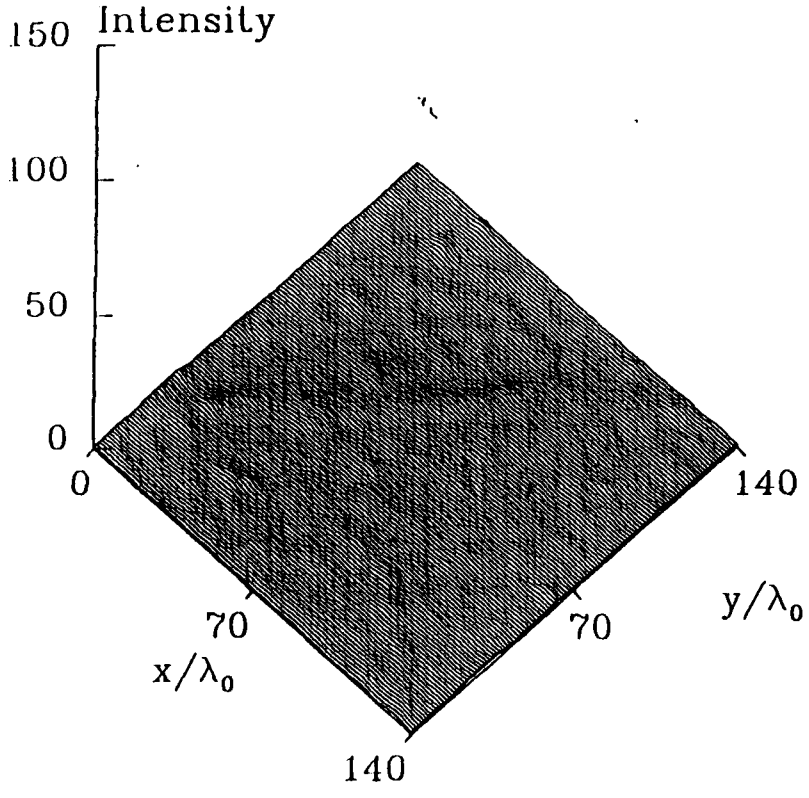



Figure 2

# 3D simulations show that ISI quenches the filamentation that occurs with ordinary laser beams.

one micron light, 2x1014 W/cm2, F/10 optics
Plasma corona is 1000 mm from 0.01 nc to nc
Plots are at 0.5 nc

ISI: $100t_c$ time average




NO ISI: $\sigma_{RMS_0}$=0.25

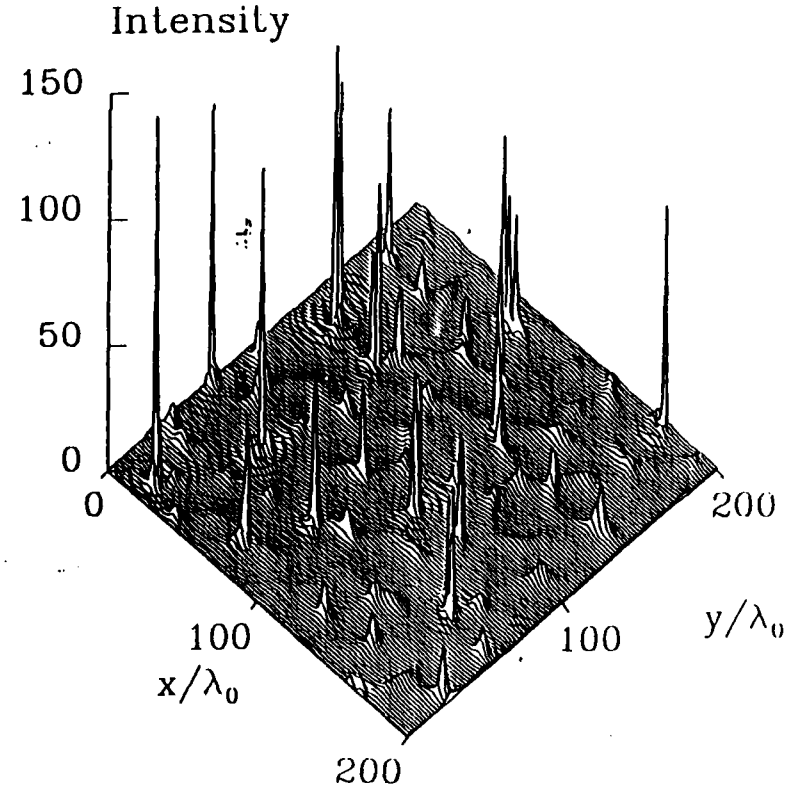



Figure 3

# APPENDIX AAA

## Nanosecond Framing Photography for Laser-Produced Interstreaming Plasmas

To be published in the Proceeding of the SPIE 32nd Annual International Technical Symposium on Optical & Optoelectronic Applied Science & Engineering. 14-19 August 1988, San Diego, CA.

# Nanosecond Framing Photography for Laser-Produced Interstreaming Plasmas

E.A. McLean, B.H. Ripin, J.A. Stamper, and C.K. Manka
Naval Research Laboratory, Washington, D.C. 20375-5000

and

T.A. Peyser
Science Applications International Corporation
Mclean, VA 22102

## ABSTRACT

Using a fast-gated (120 psec-5 nsec) microchannel-plate optical camera (Gated Optical Imager), framing photographs have been taken of the rapidly streaming, laser plasma (~5 x $10^7$ cm/sec) passing through a vacuum or a background gas, with and without a magnetic field. Observations of Large-Larmor-Radius Interchange Instabilities are presented.

## 1. INTRODUCTION

When a pulsed laser beam strikes a solid target an energetic plasma is produced, and ions and electrons stream away from the target with velocities often greater than $10^7$ cm/sec. If these plasmas expand into an ambient plasma or into a magnetic field, various instabilities can develop that can cause spatial nonuniformities to develop in the plasma.[1,2] These instabilities include Rayleigh-Taylor instability or interchange instability, counterstreaming plasma instability, and several other instabilities. There is considerable interest in observing these instabilities using fast cameras, such as streak cameras and framing cameras which give time-resolution of better than a nanosecond and spatial resolution ranging down to a few microns. A framing camera has the additional advantage of giving a two dimensional view of the plasma structure.

In this article, we will describe experiments done with a Gated Optical Imager, which is a microchannel plate intensified, gated single-frame camera with a 18-mm diameter cathode and an exposure time ranging from 120 psec to 5 nanoseconds. We will show examples of the laser produced plasma both with and without a magnetic field and in a vacuum as well as in presence of a background gas. The development of a strong plasma-magnetic-field interchange Rayleigh-Taylor instability in the limit of large ion Larmor radius will be described.

## 2. EXPERIMENT

### 2.1 Camera

The camera used in these experiments, as shown in Fig. 1, is a Grant Applied Physics, Inc., Gated Optical Imager[3] (GOI) which gives a single frame with a minimum exposure time of 120 psec FWHM over a full 18-mm diameter cathode aperture. The super-fast, gating speeds are obtained with a solid-state electronic pulser which has a jitter of less than 50 psec and a trigger delay of ~14 nsec. The exposure time can easily be varied by the interchange of plug-in modules. The camera has three modes of operation: 1) D.C. on, 2) slow-gated (300 $\mu$sec), and 3) fast-gated (120 psec to 5 nsec). The resolution is typically 10 lp/mm. A fiber optics output allows convenient coupling to photographic film or to a CCD readout. A Polaroid camera back is part of the camera, and Polaroid Type 667 film was used in this experiment. Either fiber

optics or a quartz window can be used on the input side, depending on use in the ultraviolet. An S25 photocathode responding out to 850 nm, allows calibration with a laser diode. A further description of the operation of the camera is given in Ref. 3.

### 2.2 Plasma Source and Chamber

The hot plasma is produced by focusing one beam of the NRL Pharos III Nd-laser (1.05 $\mu$m wavelength) onto small aluminum foil targets (1 mm in diameter and 2 $\mu$m thick, as shown in Fig. 2. The focal spot diameter is ~250 $\mu$m in diameter. These targets are located in a chamber either evacuated to pressures of ~4 x $10^{-4}$ Torr, or filled with a low pressure, background gas (a few Torr or less of $H_2$). Typically, the laser pulse has an irradiance of $10^{13}$ W/cm$^2$, 30 Joules of energy, and a 3-nsec (FWHM) time duration.

A magnetic field, produced with a pair of Helmholtz coils and ranging from 1 to 10 kG, is applied prior to the laser pulse. The field is aligned perpendicular to the laser axis and parallel to the optic axis of the GOI camera. The direction of the magnetic field is towards the GOI camera. To allow photographs to be taken of low light level filaments on the periphery of the plasma, the very high emitted intensity region near the target was blocked with a small mask located about 1 cm from the target, between the target and the GOI camera. Since a wide range of intensities were observed, attenuating optical filters were placed in front of the GOI. Using a f/5, 10- inch focal length lens, the plasma image was optically reduced by a factor of 6.7 at the GOI photocathode. Previous spectroscopic studies showed that there are many aluminum ions (AlI) to AlIV) that emit radiation in the bandwidth accepted by the GOI, so there is ample light to observe the plasma shape and motion.

## 3. PHOTOGRAPHS OF THE INSTABILITY

### 3.1 Variations of Magnetic Field

Using this camera, the photographs of the effect of the magnetic field on the laser-plasma are shown in Fig. 3. To get this sequence of photographs, the phenomena must be assumed to be reproducible; which in a separate experiment, proved to be the case. The conditions for this sequence were: background pressure was ~3 x $10^{-4}$ Torr, laser energy was ~27 J for a 2.8-nsec pulse, the time of observation was 115 nsec after the laser struck the target, and the camera exposure time was 2 nsec.

Figure 3(a) shows the nature of the ion emission with no magnetic field. The vertical line on the left side is the target stalk and the 2 bright lines at the center are magnetic field probes that are hit by the ions. Also, the bright ring and the bright blobs near the top of the photograph are diagnostic probes that are behind the plasma and reflect light into the cameras. The outermost extent of the light on the right side of the photograph shows the distance the ions have traveled in 115 nsec. Figure 3(b) shows the same conditions except that a magnetic field of 1 kG is present. Now a series of short spikes (flutes) have developed around the edge of the plasma. The spikes have extended to approximately the same distance as the zero-field plasma, but the main front does not go out as far. There has been a definite interaction of the plasma with the magnetic field. Then in Fig. 3(c), one can see the effect of a much larger magnetic field, namely, 9 kG. Here small spikes have now become larger spikes which are not only fatter but also longer. The overall light intensity of the plasma is higher than the case for lower

magnetic fields. The main front of the plasma is not as far from the target for the 9-kG case; however, the tip of the flutes are still almost the same distance from the target as for the 1-kG case.

### 3.2 Temporal variation

By holding the magnetic field constant at 10 kG, a variation of the time at which the photograph was taken shows how these flutes develop in time. Figure 4 shows the plasma at 3 times: (a) 44 nsec, (b) 115 nsec, and (c) 205 nsec. At 44 nsec, the flutes are not present. (Again, the ring-shaped image and the blobs at the top of the photograph are reflections from diagnostic probes in the chamber and should be ignored.) However, at 115 nsec the flutes are well developed, and further are curved due to the presence of the magnetic field. (A reversal of the direction of the magnetic field caused the flutes to curve in the opposite direction.) At 205 nsec the flutes are much more diffuse and appear to be dissipating, probably in part due to the plasma cooling and the conductivity decreasing. The expansion of the plasma has stopped by this time.

### 3.3 Pressure variation

In the next series, hydrogen gas was added to the chamber prior to the shot. The $H_2$ pressure was varied while the magnetic field was held constant at 1 kG and the time was held constant to 150 nsec. In Fig. 5, three different hydrogen pressures are shown: (a) 9 mTorr, (b) 100 mTorr, and (c) 2 Torr. In Fig. 5(a) the 9 mTorr of hydrogen background gas shows the same general characteristics as the case for a vacuum ($2 \times 10^{-4}$ Torr of air), namely, the short spikes on the edge of the plasma; however, the distance the plasma has propagated is greater. This could be due to the velocity of the ions being greater in hydrogen than air, even with the higher pressure of $H_2$. As the hydrogen pressure is increased to 100 mTorr, a leaky blast wave begins to form as shown in Fig. 5(b). Then with a further increase of pressure to 2 Torr $H_2$, a well-formed blast wave develops as shown in Fig. 5(c). The blast-wave behavior appears to be insensitive to the presence of the applied magnetic fields. Details of the possible effects of the magnetic field on the shock structure are currently being investigated.

## 4. INTERPRETATION AND CONCLUSION

In the presence of an external magnetic field, the bulk plasma decelerates as it excludes magnetic field energy. Without instabilities, the plasma would stop near the magnetic confinement radius, where the excluded field energy equals the original plasma energy. It is shown with the photographs presented here that an instability sets in and the plasma breaks up into free-streaming flute tips. A comparison of these results with a modified MHD theory of A.B. Hassam and J.D. Huba, which will not be discussed here, but is presented in Ref. (4). showed that many features seen in the experiment are similar to those predicted by the theory; also, these features are similar to the structures seen in a barium-release space experiment with the Active Magnetospheric Particle Tracer Explorer satellite.[5]

With a background gas the laser produced plasma interacts with the preionized gas and shock waves or blast waves are formed. This luminous front will steepen and grow much brighter as the blast wave moves out from the target. In the higher pressure regime, P~1-5 Torr, the structure instability is mostly damped out as more and more collisions occur.

In conclusion, the Grant Applied Physics Gated Optical Imager camera was able to view these rapidly changing plasmas, which are often only weakly luminous, with sufficient time- and space-resolution and also with sufficient amplification to give adequate images that allow a detailed comparison with theory.

## 5. ACKNOWLEDGEMENTS

The authors would like to acknowledge the useful advice of Jonathan Hares of the Kentech Instruments, Limited of England, who designed this camera; and the support and encouragement of S.E. Bodner. Also, we would like to acknowledge the advice and assistance of our scientific colleagues, H.R. Griem, S.P. Obenschain, M. Pronko, A.N. Mostovych, K. Kearney, J. Grun, T.N. Lee, C. Pawley, A.B. Hassam, and J. Huba. The technical assistance of N. Nocerino, J. Ford, L. Daniels, L. Shirey, and M. Kirby is also appreciated. This work has been supported by the Defense Nuclear Agency.

## 6. REFERENCES

1. B.H. Ripin, A.W. Ali, H.R. Griem, J. Grun, S.T. Kacenjar, C.K. Manka, E.A. McLean, A.N. Mostovych, S.P. Obenschain, and J.A. Stamper, "Physics of Laser-Produced Interstreaming Plasmas," in Laser Interaction and Related Plasma Phenomena, edited by H. Hora and G.H. Miley, Vol. 7, pp. 857-877 [Plenum, New York, (1986)].

2. B.H. Ripin, E.A. McLean, C.K. Manka, C. Pawley, J.A. Stamper, T.A. Peyser, A.N. Mostovych, J. Grun, A.B. Hassam, and J. Huba, "Large-Larmor-Radius Interchange Instability," Phys. Rev. Lett. 59, 2299-2302 (1987).

3. J.D. Hares, "Advances in Sub-nanosecond Shutter Tube Technology and Applications in Plasma Physics," SPIE, Vol. 831, pp. 165-170 (1987).

4. J.D. Huba, J.G. Lyon and A.B. Hassam, "Theory and Simulation of the Rayleigh-Taylor Instability in the Limit of Large Larmor Radius," Phys. Rev. Lett. 59, 2971-2974 (1987).

5. A.B. Hassam and J.D. Huba, "Structuring of the AMPTE Magnetotoil Barium Release," Geophys. Res. Lett. 14, 60-63 (1987).

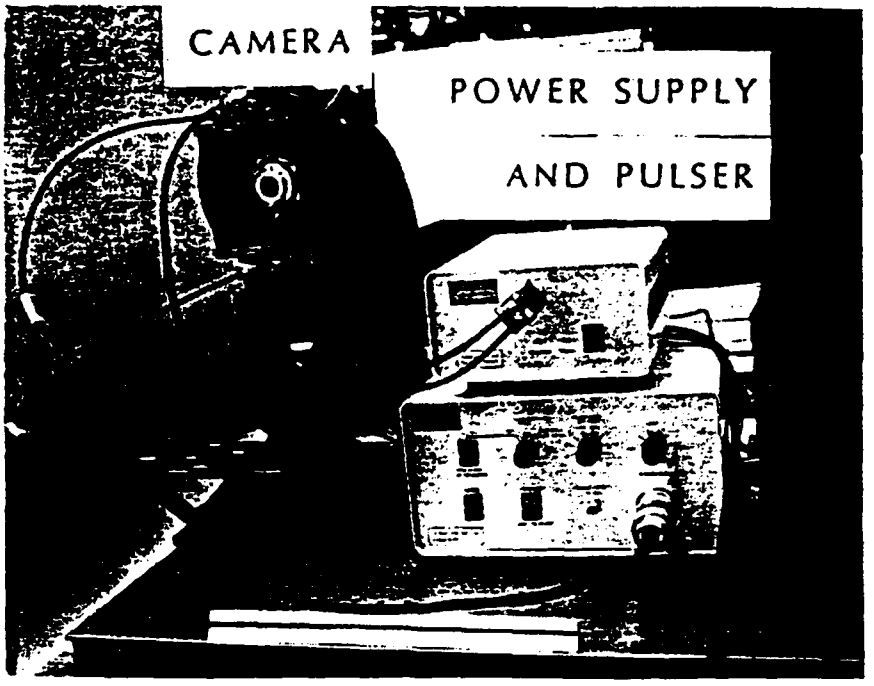



Figure 1. Photograph of Gated Optical Imager, showing the back of the camera with the film pack removed.

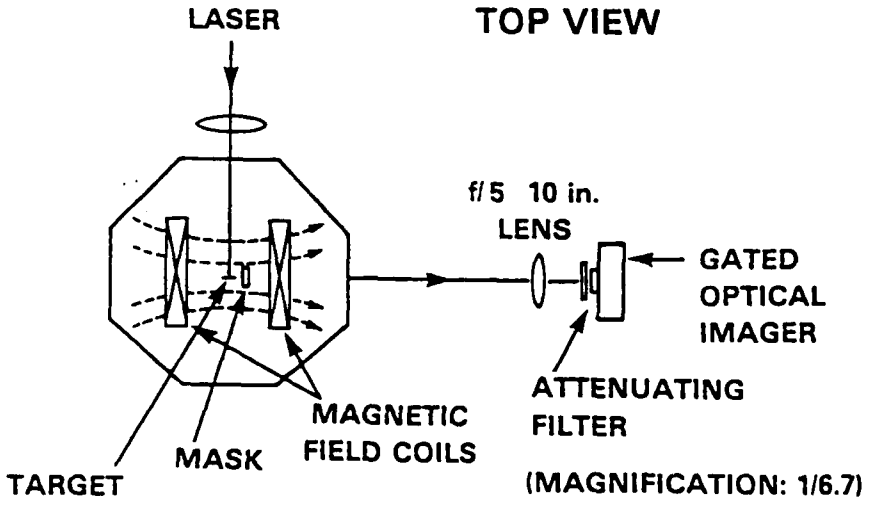



Figure 2. Experimental arrangement.

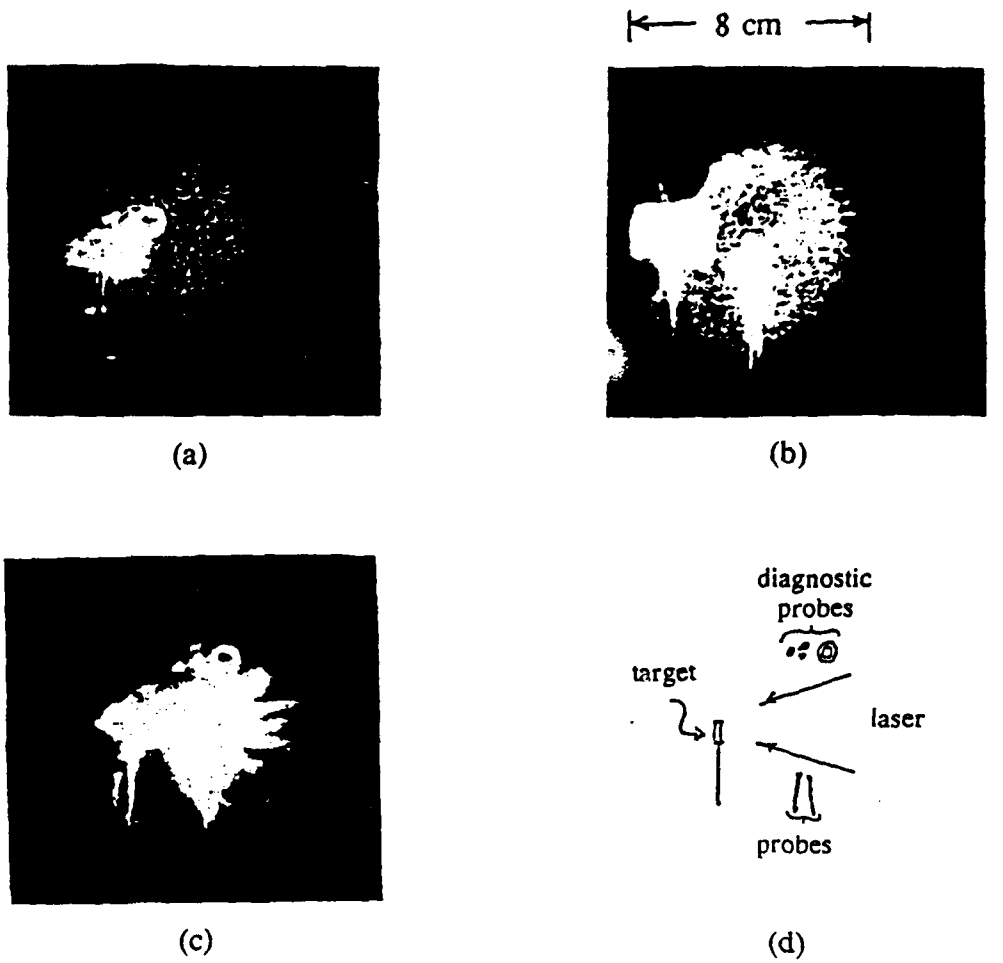
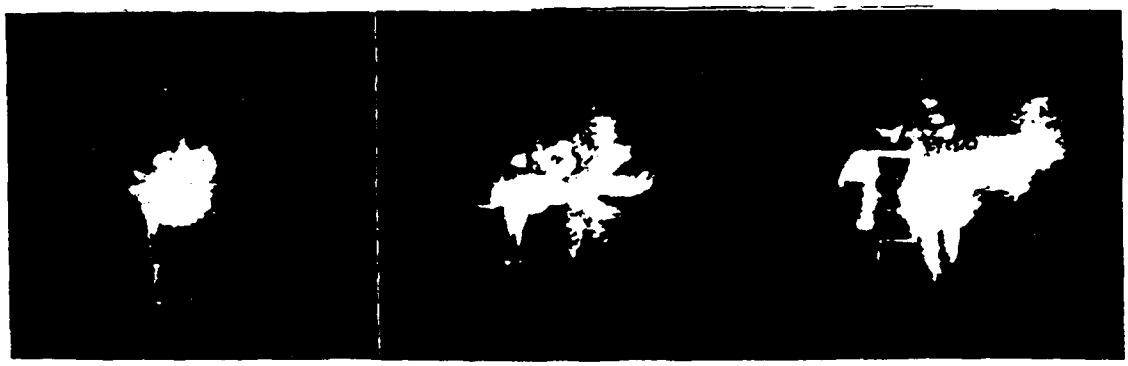



Figure 3. Photographs of the laser plasma taken 115 nsec after the laser strikes the target in a vacuum of ~2 x $10^{-4}$ Torr showing the variation of the magnetic field (a) 0 kG, (b) 1 kG, and (c) 9 kG. A sketch showing the experimental arrangement is shown in (d). The exposure time is 2 nsec.



(a) (b) (c)

Figure 4. Photographs of a plasma in a vacuum in the presence of a magnetic field of 10 kG showing various times after the laser strikes the target; (a) 44 nsec, (b) 115 nsec, and (c) 205 nsec. The exposure time 2 nsec.



(a) (b) (c)

Figure 5. Photographs of a plasma in a magnetic field of 1 kG at 150 nsec after the laser struck the target showing the variation of the background gas pressure (a) 9 x $10^{-3}$ Torr $H_2$, (b) 100 x $10^{-3}$ Torr $H_2$, and (c) 2 Torr $H_2$. The exposure time is 2 nsec.

# APPENDIX BBB

## Large-Larmor-Radius Interchange Instability

# Large-Larmor-Radius Interchange Instability

B. H. Ripin, E. A. McLean, C. K. Manka, C. Pawley,[a] J. A. Stamper, T. A. Peyser,[a] A. N. Mostovych, J. Grun, A. B. Hassam,[a] and J. Huba

*Naval Research Laboratory, Washington, D.C. 20375*

(Received 15 June 1987)

We observe linear and nonlinear features of a strong plasma-magnetic-field interchange Rayleigh-Taylor instability in the limit of large ion Larmor radius. The instability undergoes rapid linear growth culminating in free-streaming flute tips.

PACS numbers: 52.35.Gz, 52.35.Py, 52.50.Lp, 52.55.Lf

Plasma expanding into a magnetic field can undergo Rayleigh-Taylor or interchange instability as the heavy fluid (plasma) is decelerated by the light fluid (magnetic field).[1,2] Direct observations of this instability have been made in the limit of small ion Larmor radius (compared to density gradients and wavelengths),[3] where conventional MHD theory applies. When the ion Larmor radius becomes finite the instability is predicted to stabilize.[4] However, when the ion Larmor radius becomes large compared to other characteristic plasma dimensions, i.e., when the ions are effectively unmagnetized but the electrons are effectively magnetized, a related instability is predicted with an even higher growth rate than that of the original MHD instability.[5] The recent barium-release space experiment with the Active Magnetospheric Particle Tracer Explorer satellite, which showed substantial structure, was in such a regime.[6] A previous laser-plasma experiment in a regime of moderate-sized ion Larmor radius also measured instability growth.[7]

In this paper, we observe a robust interchangelike instability in the limit of very large ion Larmor radius. The instability exhibits a rapid linear phase with subsequent nonlinear free-streaming flutes and examples of density clumping, flute-tip bifurcation, and interesting late-time spirallike structures.

Our experiment is comprised of an energetic laser-produced plasma expanding radially outward into a uniform magnetic field $B$ formed by a pair of Helmholtz coils,[8] as depicted in Fig. 1. Steady-state (on the time scale of the experiment) vacuum $B$ fields from 0 to 1 T are used. Plasma bursts are created by our focusing a beam of the Pharos III neodymium laser onto small Al (2 $\mu$m thick, 1 mm diam) disk targets. Unless noted otherwise, the nominal laser pulse has an irradiance of about $10^{13}$ W/cm$^2$, 30 J of energy, and 3-ns duration (FWHM). The principal diagnostic used to measure the plasma and instability development is a Grant Applied Physics fast-gated microchannel-plate optical camera focused onto the target midplane antiparallel (usually) to the magnetic field lines. Shutter speeds of 1 or 2 ns are used. In addition to the gated camera, we also used ion time-of-flight detectors to measure the plasma ion velocity distribution, several small (230 $\mu$m diam, two turn) magnetic induction probes to obtain magnetic field dynamics, small Langmuir and capacitive probes to measure density gradients and fluctuations, open-shutter photography and witness plates to see persistent structure, and fiber-optic spectroscopy to estimate density profiles during the plasma/magnetic field interaction.

The velocity distribution of the expanding plasma, measured for $B=0$ with an ion time-of-flight detector, peaks at $V_0=5.4\times10^7$ cm/s with a FWHM spread of $\pm1.8\times10^7$ cm/s. The total plasma mass is about $m_0=0.2$ $\mu$g (half of which is directed into the front $\pm45°$ expansion cone), the initial electron temperature is about 500 eV, and the initial aluminum ionization state is approximately 10.[9] Thus, the ion Larmor radii are large, over 1.4 cm for 1.0 T and over 14 cm for $B=0.1$ T (on the assumption that $Z$ is 10 or less). The electrons, on the other hand, are effectively magnetized with Larmor radii below 1 mm. Most of the experiments were performed under good vacuum ($<0.1$ mTorr) so that the magnetic field rather than residual collisions dominates the plasma expansion. The plasma expansion speed is very sub-Alfvénic, being more than 1 order of magnitude slower than the maximum possible Alfvén velocity in the residual background air.

In the absence of a magnetic field, the plasma expands

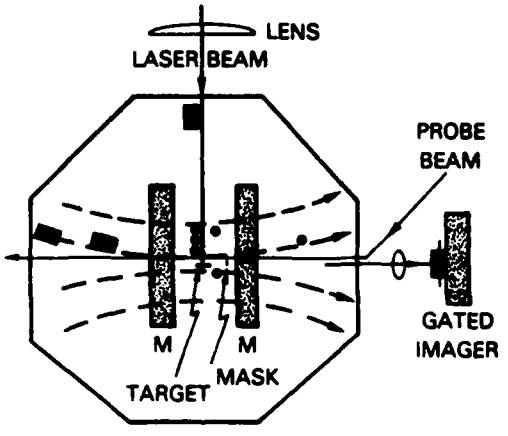



FIG. 1. Experimental arrangement for instability experiments. A schematic of the equipment is shown; ion detectors are denoted by rectangles and magnetic probes by circles.

© 1987 The American Physical Society

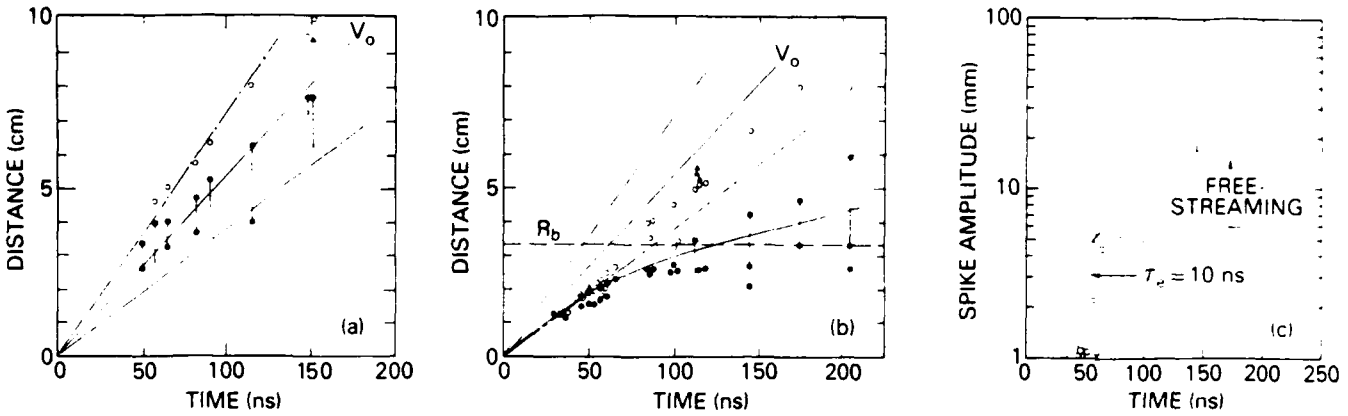



FIG. 2. Development of the instability. Locations of the instability spike tips (open circles) and main plasma boundaries (closed circles) with time for (a) the low-field (0.1 T) case and (b) the high-field (1.0 T) case. Shots denoted by triangles are plasma boundaries with zero applied magnetic field (free-streaming plasma). (c) Spike-to-bubble amplitudes vs time for 1.0 T (circles) and for 0.1 T (squares). $E_1 = 25$–$30$ J, $V_0 = 5.4 \times 10^7$ cm/s, and $P < 0.1$ mTorr for all cases.

radially outward from the focal region with a velocity and spread consistent with the time-of-flight ion distribution. In such expansions, most of the energy ends up in directed ion motion, with a relatively low plasma temperature (a few electronvolts).[8] When an external field is applied, the bulk plasma decelerates as it excludes magnetic field energy. Ideally, a symmetrical plasma expansion would stop near the "magnetic confinement" radius, $R_b$, where the excluded field energy equals the original plasma energy. For the typical 30-J shot in our experiment, $R_b$ is 3.3 cm for $B = 1$ T and 15 cm for $B = 0.1$ T. The plasma has a deceleration of about $5 \times 10^{14}$ cm/s$^2$ at $R = 3$ cm for $B = 1$ T [Fig. 2(b)]. The deceleration is less apparent in the 0.1-T experiments since we observe it for $R < R_b$. At intermediate magnetic field values the observed magnetic confinement distance follows the expected $B^{2/3}$ dependency within the data error bars ($\pm 20\%$). The plasma continues to cross the magnetic field beyond $R_b$, but at reduced speed, which is a consequence, perhaps, of our lack of a totally symmetric expansion.

The density scale lengths of the plasma fronts in a magnetic field at about 3 cm from the target fall in the range $L_n = 10 \pm 3$ mm. These estimates were obtained from the emission profiles of the time-resolved optical images, the rise times of the Langmuir and potential probe signals, and the rise time of spatially and temporally resolved $Al^{+2}$ line (361.2 nm) emission

The array of magnetic field probes located at 1, 2, 3, 4, and 5 cm from the target show a very small (few percent at most) magnetic compression ahead of the plasma front followed by a greater than 30% diminished field within the plasma front. This field behavior is generally consistent with sub-Alfvénic plasma expansion with, perhaps, a higher than classical resistivity, e.g., $L_b \approx c/\omega_{pi}$.

Before the plasma reaches $R_b$, structure develops in the plasma leading (outer) edge. Distinct plasma flutes or spikes project out from the main plasma body into the magnetic field. The initial development of the instability can be seen in the low-field (0.1 T) case shown in Fig. 3(a). During the first 50 ns ($R < R_b/5$) the plasma expands with speeds near $V_0$ and no sign of instability is

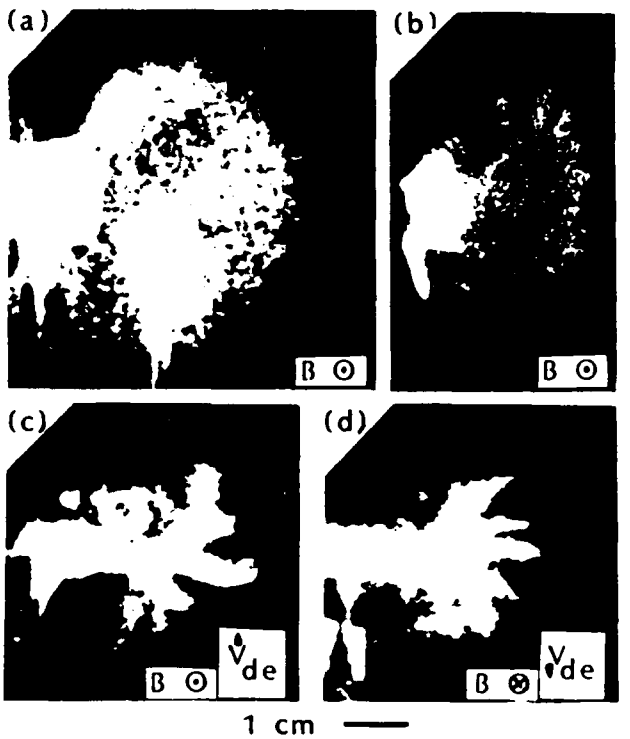



FIG. 3. Examples of the instability development. (a) 0.1-T case observed at time 115 ns. (b) Example of density clumps in the early time phase development with $B = 1.0$ T at time 59 ns. (c) Example of curved spike structure with 1.0-T field (field points out of paper) at 115 ns. (d) Same as (c) except field points into paper and $t = 100$ ns; note reversal of curvature sense. $E_1 = 25$–$30$ J and $P < 0.1$ mTorr for these shots.

discernible; suddenly, near $R=3$ cm, radial plasma projections appear with amplitudes comparable to their wavelengths (5–10 mm). It is clear from Fig. 2 that these plasma tips then continue to execute free streaming outward into the magnetic field. Since $R \ll R_b$, the bulk plasma is also still expanding almost uniformly. Curiously, despite a much stronger deceleration in the 1-T case ($g \propto B^2$), the instability also begins to develop at about the same distance and time as in the lower-field case. This onset behavior is consistent with the instability criterion[10] $g/L_n > \Omega_i^2/4$ which is independent of the magnetic field; $\Omega_i$ is the ion cyclotron frequency. The instability wavelengths also do not appear to be a strong function of the magnetic field strength in contrast to Ref. 7. The flute amplitude grows rapidly after onset with a linear growth rate of about $10^8\ s^{-1}$ as seen in Fig. 2(c).[7] Unfortunately, the accuracy of the growth rate measurement (a factor of 2) is limited by the shot-to-shot reproducibility of the onset time. For comparison, the conventional (small ion Larmor radius) MHD Rayleigh-Taylor growth rate [$\gamma=(g/L_n)^{1/2}$ for $kL_n > 1$] for our parameters ($B=1$ T) is about $2\times10^7\ s^{-1}$, whereas the large-Larmor-radius instability theory[5] predicts a 6 times faster growth rate for the observed wavelengths, which is consistent with our experimental result. At times the plasma structure initially appears as density clumps in the leading edge of the expansion plasma. This clumpinglike behavior, shown in Fig. 3(b), is a predicted characteristic of this instability.[5,10] Subsequent to the rapid linear phase of the instability the flute tips perform free streaming with speeds near $V_0$.

The wavelengths of the predominant flute modes (measured at the base of the flutes) are typically in the 6- to 10-mm range and are insensitive to most parameter changes. As time goes on, the instability wavelength tends to remain in this range even though the plasma continues to expand radially. Some indication of how this can occur was obtained by our placing witness plates (black Polaroid film) perpendicular to the magnetic field a few centimeters to one side of the target. These recorded time-integrated patterns of the plasma running down the field lines. Long spikes are seen in the exposures with curvature toward the midplane and additional projections formed towards the sides of the pattern with increasing distance from the source. The fact that the patterns on the witness plate are not washed out indicated that the plasma structure, once formed, does not undergo much azimuthal motion. Several examples of spike-tip bifurcation are also seen. The combination of these two effects tends to maintain constant wavelength and increase the instability mode number, $m=2\pi R/\lambda$, with distance. Sydora *et al.*[11] suggest that the azimuthal mode number of the most unstable mode would increase with decreasing charge separation between the unmagnetized ions and the plasma electrons; perhaps this is what is occurring in the experiment. It will be interesting to see if this increasing-mode-number–type behavior persists when more spherically symmetric expansions are examined.

The dominant instability wavelength, $\lambda=8\pm2$ mm, may be determined by the bulk plasma-density scale length, $L_n=10\pm3$ mm, or possibly by the magnetic diffusion length into the plasma. The collisionless skin ($c/\omega_{pe}$) depth is only a fraction of a millimeter, but possible anomalous resistivity associated with this or another instability could push the diffusion length into the centimeter ($c/\omega_{pi}$) range.

For some shots, the magnetic field was rotated 90° so that the instability development could be viewed perpendicular to the field lines. The plasma projections, which have the appearance of slim spikes in the end-on view, actually run smoothly along the field lines like flutes.

The free-streaming flutes exhibit some interesting features at later times. One common characteristic in the high-field experiments is the curvature and spurlike appearance of the instability fingers seen in Figs. 3(c) and 3(d). The curvature is in the electron cyclotron or electron $\mathbf{E}\times\mathbf{B}$ drift sense and reverses with magnetic field direction. It is not yet known whether the curvature arises from the spike tips moving upward or the bubble downward. But the distinct structure seen on the witness plates precludes large-scale azimuthal motion. Two possibilities are that curved flutes are caused either by $\mathbf{E}\times\mathbf{B}$-induced azimuthal electron velocity shear,[11] or as a response of large–Larmor-radius plasma to Alfvénic magnetic stresses: The theory of Hassam and Huba[5] predicts that a localized spike expanding into a magnetic field curves in the electron gyrodirection, consistent with experiment.

A number of other parameter variations were performed during the course of this investigation. The background pressure was increased up to 2 Torr of $H_2$ to test the effects of increasing collisionality and decreasing Alfvén speed on the instability. For the 0.1-T case viewed at 150 ns, free-streaming structure persisted up to 100-mTorr $H_2$ pressure at which point signatures of collisional effects were seen.[8]

In another series of shots, a 7.6-cm-diam, 3-mm-thick copper disk was placed 4 to 5 cm to one side of the target, perpendicular to the field lines, to short out the dynamic motion of the magnetic field lines. The gross feature of the instability persisted independent of whether the copper plate was grounded, ungrounded, insulated, or bare.

Finally, several shots were taken with much larger incident laser energy (400 J) but comparable irradiance at a variety of magnetic fields and pressures. The major effect of higher laser energy is to increase the plasma mass proportionally and, hence, to increase the magnetic confinement radius by $R_b \propto E_l^{1/3}$.

Another interesting observation in these experiments was the presence of a strong high-frequency (> 250

MHz) signal seen in all electrical and magnetic probes whenever the Rayleigh-Taylor instability occurred. This noise is in the ion plasma or lower hybrid frequency range. The relationship of this noise to the magnetic instability is not yet clear, but may be related to the growth of very short-wavelength Rayleigh-Taylor modes, which cannot be seen in the framing pictures, or to the generation of microinstabilities in the plasma shell.[12,13]

In summary, we have experimentally demonstrated linear and nonlinear properties of a robust instability in the important regime of large ion Larmor radius and sub-Alfvénic expansion speed. The instability has many features recently predicted by a modified MHD theory[5] and computer simulation,[10] and is similar to structure in the barium-release space experiment with the Active Magnetospheric Particle Tracer Explorer satellite.[5] However, it is possible that a number of closely related instabilities, such as the lower-hybrid–drift[12,13] and Kelvin-Helmholtz[11] instabilities, may be playing a role here also.

The authors are please to acknowledge useful discussions with W. White, R. Kilb, D. Winske, and H. Dickinson. The technical assistance of J. Ford, L. Daniels, N. Nocerino, and M. Kirby is likewise appreciated. This work was supported by the Defense Nuclear Agency.

[a]Present address: Science Applications International Corp., McLean, VA 22102.

[1]M. Kruskal and M. Schwarzschild, Proc. Roy. Soc. London A **223**, 348 (1954).

[2]M. N. Rosenbluth and C. L. Longmire, Ann. Phys. (N.Y.) **1**, 120 (1957).

[3]H. Dickinson, W. H. Bostick, J. N. DiMarco, and S. Koslov, Phys. Fluids **5**, 1048 (1962).

[4]M. N. Rosenbluth, N. A. Krall, and N. Rostoker, Nucl. Fusion Suppl. Pt. 1, 143 (1967).

[5]A. B. Hassam and J. D. Huba, Geophys. Res. Lett. **14**, 60 (1987), and to be published.

[6]P. A. Bernhardt *et al.*, J. Geophys. Res. **92**, 5777 (1987).

[7]S. Okada, K. Sato, and T. Sekiguchi, Jpn. J. Appl. Phys. **20**, 157 (1981).

[8]B. H. Ripin *et al.*, in *Laser Interaction and Related Plasma Phenomena*, edited by H. Hora and G. H. Miley (Plenum, New York, 1986), Vol. 7, pp. 857–877.

[9]B. H. Ripin *et al.*, Phys. Fluids **26**, 588 (1983).

[10]J. D. Huba, J. G. Lyon, and A. B. Hassam, to be published.

[11]R. D. Sydora, J. S. Wagner, L. C. Lee, E. M. Wescott, and T. Tajima, Phys. Fluids **26**, 2986 (1983).

[12]N. A. Krall and P. C. Liewer, Phys. Rev. A **4**, 2094 (1971); D. Winske, private communication.

[13]Yu. P. Zakharov, A. M. Orishich, A. G. Ponomarenko, and V. G. Posukh, Fiz. Plasmy **12**, 1170 (1986) [Sov. J. Plasma Phys. **12**, 674 (1986)].

# APPENDIX CCC

## Structuring Processes in Expanding Laser-Produced Plasmas

Naval Research Laboratory

Washington, DC 20375-5000

NRL Memorandum Report 6154

# Structuring Processes in Expanding Laser-Produced Plasmas

B. H. RIPIN, J. GRUN, T. N. LEE, C. K. MANKA,
E. A. MCLEAN, A. N. MOSTOVYCH, C. PAWLEY,
T. A. PEYSER AND J. A. STAMPER

*Plasma Physics Division*

March 30, 1988

Approved for public release; distribution unlimited.

## CONTENTS


INTRODUCTION ..... 1

EXPERIMENTAL ARRANGEMENT ..... 2

LARGE LARMOR RADIUS INTERCHANGE INSTABILITY ..... 2

CROSS-FIELD JETTING ..... 9

STRUCTURE ASSOCIATED WITH COLLISIONAL PLASMAS ..... 11

CONCLUSIONS ..... 16

REFERENCES ..... 17

DISTRIBUTION ..... 19

# STRUCTURING PROCESSES IN EXPANDING LASER-PRODUCED PLASMAS

## INTRODUCTION

A plasma expanding into a magnetic field and/or another plasma can undergo several processes which will cause spatial nonuniformities and large-scale structure to develop. Structure forming instabilities include various forms of the Rayleigh-Taylor instability or interchange instability, Kelvin-Helmholtz instability, universal instabilities, and streaming instabilities. In addition, geometric and plasma production factors can affect expansion uniformity.

In this article, we describe experiments in which plasma nonuniformities arise when laser-produced plasmas expand into other ambient plasmas and/or magnetic field regions. Several types of density structure appear, depending upon the operational regime.[1] *Dramatic large-scale flutes* grow when the laser-plasma expands into a vacuum magnetic field or a low-density magnetized plasma. The mechanism has been identified as a type of Rayleigh-Taylor or interchange instability occurring in a relatively unexplored regime where the ion Larmor radii are large.[2,3] Plasma jetting across magnetic fields has been studied. This is caused by polarization drifts arising when gross asymmetry is present.[4,5] When the laser-produced plasma expands into a high pressure background-plasma or gas, collisional blast-waves are formed. Several structure-forming mechanisms occur here also. Aneurisms,[1,6] which are protrusions from the otherwise smooth blast-fronts, often appear; several mechanisms are responsible for these unusual projections, among them effects associated with the incoming laser-beam deposition[6] and material jetting normal to the target.[7] Finally, it has recently been shown that ablatively accelerated foils undergo Rayleigh-Taylor (R-T) instability during laser irradiation.[8] These R-T unstable accelerated thin-foils continue to develop gross turbulence as they expand into a vacuum or background gas. The measured turbulence has been Fourier analyzed to yield power spectra at successive times in the expansion phase.[9]

Manuscript approved December 22, 1987.

In the remainder of this article, we will describe these structuring processes in more detail. These phenomena are, for the most part, not unique to laser-produced plasmas and should be applicable to a broad range of disciplines. Our results are related to problems in space physics, magnetic confinement/fusion, laser-guided particle beams, ICF reactor design, and basic plasma physics.

## EXPERIMENTAL ARRANGEMENT

The experiment consists of an energetic laser-produced plasma expanding into a vacuum and/or a photoionized gas as depicted in Fig. 1. Details of the basic experimental arrangement and earlier results have been published elsewhere.[1] The energetic laser-produced plasma is formed by placing a small target, typically a 1 mm or less diameter and 2 $\mu$m thick aluminum disk, at the focus of one or two beams of the PHAROS III Nd-glass laser. Laser pulse durations of 3 to 5 ns, energies up to 400 J/beam, irradiances of $10^{12}$ to $10^{14}$ W/cm$^2$, and spot diameters between 0.25 and 1 mm are used in the present studies. Laser-produced ablation plasmas having initial temperatures of 500 to 1000 eV are formed; these expand radially away from the focal region and reach asymptotic speeds of 5 to 8 x $10^7$ cm/s within a millimeter to two. If a background gas is introduced, it is partially photoionized by the X-ray and UV emissions of the laser-plasma interaction. A magnetic field up to 11 kG is often impressed on the entire system by means of a pulsed set of 25 cm diameter Helmholtz coils; the magnetic field is effectively steady-state during the relevant part of the experiment.

A large array of instruments are used to measure the plasma properties and dynamics. Diagnostics include ion time-of-flight detectors, magnetic-field induction probes, diamagnetic loops, multi-time dark-field optical shadowgraphy, interferometry, Langmuir and capacitance probes, x-ray detector arrays, fiber-optic/OMA spectroscopy systems, and more. Most of these diagnostics are described in detail in Ref. 1. There are two notable additions. A fast-gated (120 ps < $\Delta$t < 5 ns) Grant Applied Physics microchannel plate S-25 optical camera (dubbed a GOI, gated optical imager) is used to obtain high-resolution time-resolved images of low-density plasma interactions. This instrument is used to image the plasma structure in low density situations, such as those encountered in the next section. The other new diagnostic is a resonant laser probe, which is also useful in low density plasmas. The resonant probe beam comes from a dye laser, pumped with a 5-ns duration frequency-doubled Nd-laser, which is tuned to either the wing or center of a plasma ion-resonance line. Index of refraction enhancements of 1000 over the usual electron contribution are possible using this technique. One form of plasma jets, to be discussed later, was found using this technique.

## LARGE LARMOR RADIUS INTERCHANGE INSTABILITY

Plasma expanding into a magnetic field can undergo Rayleigh-Taylor or interchange instability as the heavy fluid (plasma) is decelerated by the light fluid (magnetic

field).[10,11] This instability has been observed in experiments where MHD theory is valid, namely, where the ion Larmor radius is small with respect to density gradients and instability wavelengths.[12-14] When the ion Larmor radius becomes larger, i.e., comparable to density gradient scale-lengths, the instability is predicted to stablize,[15] although no experimental verification of this has yet been made. Recently, however, it has been predicted that when the ion Larmor radii are very large (i.e., the ions are effectively unmagnetized, but the electrons remain magnetized) the instability not only reappears, but exhibits a much faster growth and different character than the ordinary MHD Rayleigh-Taylor version.[2,16] The recent AMPTE Barium release space experiment, which also showed structuring, was in such a regime.[17]

We observe a robust interchange-like instability in the very large ion Larmor radius limit.[3] The instability exhibits a rapid linear phase with subsequent nonlinear freestreaming flutes and examples of density clumping, flute-tip bifurcation, and interesting late-time spiral-like structures.

Our experiment[3] is comprised of an energetic laser-produced plasma expanding radially outward into the uniform magnetic field, as depicted in Fig. 1. Vacuum B-fields from zero to one Tesla are used. Plasma bursts are created by focusing one or two beams of the PHAROS III Nd-laser onto small Al (2 $\mu$m thick, 1 mm diameter) disk targets. Unless noted otherwise, the nominal laser pulse has an irradiance of about $10^{13}$ W/cm$^2$, 30 J of energy, and 3 ns duration (FWHM). The principle diagnostic used to measure the plasma and instability development is the previously described GOI microchannel plate camera focused onto the target mid-plane antiparallel (usually) to the magnetic field lines. Shutter speeds of 1 or 2 ns are used. In addition to the gated camera, we also used: ion time-of-flight detectors to measure the plasma ion velocity distribution; several small (230 $\mu$m dia., two-turn) magnetic induction probes to obtain magnetic field dynamics; small Langmuir and capacitive probes to measure density gradients and fluctuations; open-shutter photography and witness plates to see persistent structure; and fiber-optic spectroscopy used to estimate density profiles during the plasma/magnetic field interaction.

The velocity distribution of the expanding plasma, measured with zero magnetic field, peaks at $V_o = 5.4 \times 10^7$ cm/s with a FWHM spread of $\pm$ 1.8 x $10^7$ cm/s. The total plasma mass is about $m_o = 0.2$ $\mu$gm (half of which is directed into the front $\pm$ 45° expansion cone), the initial electron temperature is about 500 eV, and the aluminium ionization state is approximately 10. Thus, the ion Larmor radii are large, over 1.6 cm for 1.0 Tesla and over 16 cm for B=0.1 Tesla (assuming Z is ten or less). The electrons, on the other hand are effectively magnetized with Larmor radii below one millimeter. Most of the experiments were performed with ambient pressures below 0.1 mTorr so that the magnetic field dominates the plasma expansion. The plasma

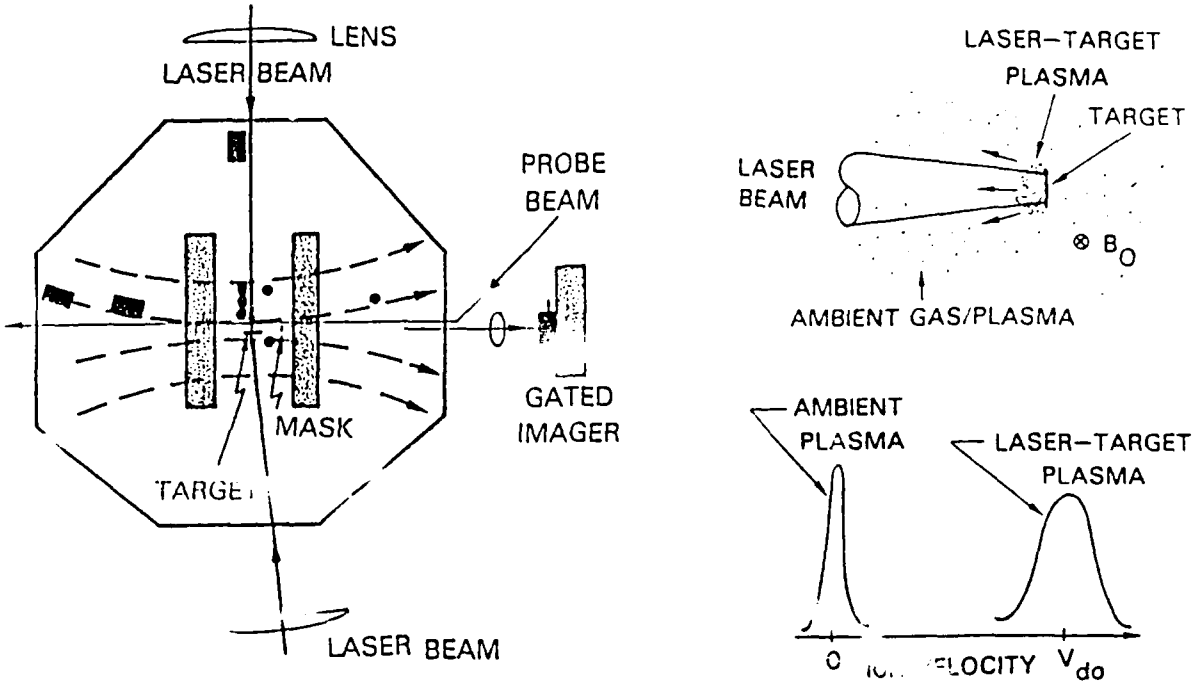



Figure 1. Arrangement for laser-plasma structure experiments.

expansion speed is very subAlfvenic, being more than one order-of-magnitude slower than the maximum possible Alfven velocity in the residual background air.

In an external magnetic field, the expanding plasma decelerates as it excludes magnetic field energy. Ideally, a symmetric plasma expansion would stop near the "magnetic confinement" radius, $R_b$, where the excluded field energy equals the original plasma energy. For the typical 30 J shot in our experiment, $R_b$ is 3.3 cm for B=1 Tesla and 15 cm for B=0.1 Tesla. The plasma decelerates with $g \approx -5 \times 10^{14}$ cm/s$^2$ at R=3 cm for B=1 Tesla, as seen in Fig. 2b. The deceleration is less apparent in the 0.1 Tesla experiments, Fig. 2a, since we observe it for $R < R_b$. At intermediate magnetic field values the observed magnetic confinement distance follows the expected $B^{2/3}$ dependency within the data error bars ($\pm$20%).[18,19] The plasma continues to diffuse across the magnetic field beyond $R_b$, but at reduced speed, a consequence, perhaps, of our lack of a totally symmetric expansion.

The density scale-lengths of the plasma fronts in a magnetic field at about 3 cm from the target fall in the range $L_n = 10 \pm 3$ millimeters. These estimates were obtained from the emission profiles of the time-resolved optical images, the risetimes of the Langmuir and potential probe signals, and the risetime of spatially and temporally resolved $Al^{+2}$ line (361.2 nm) emission.[20,21]

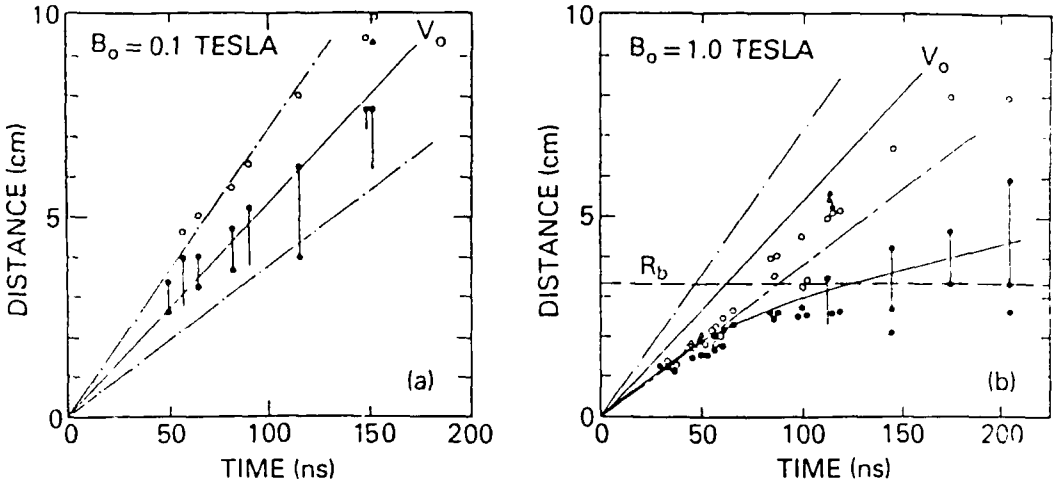



Figure 2. Development of the plasma expansion and instability. Locations of the instability spike tips (o) and main plasma boundaries (•) with time for the low (0.1 Tesla) field case (a) and the high (1.0 Tesla) field case (b). Shots denoted by a Δ are plasma boundaries with zero applied magnetic field (freestreaming plasma). $E_1$ = 25-30 J, $V_o$ = 5.4 x $10^7$ cm/s, and P<0.1 mT for all cases.

An array of magnetic field probes located at 1, 2, 3, 4, and 5 cm from the target show a very small (few percent at most) magnetic compression ahead of the plasma front followed by a greater than 30% diminished field within the plasma front. This field behavior is generally consistent with subAlfvenic plasma expansion with, perhaps, a higher than classical resistivity leading to a magnetic diffusion length, $L_b \approx c/\omega_{pi}$.

Before the plasma reaches $R_b$, structure develops in the plasma leading (outer) edge. Distinct plasma flutes project out from the main plasma body into the magnetic field, as shown in Fig. 3. The initial development of the instability can be seen in the low (0.1 Tesla) case shown in Fig. 2a. During the first 50 ns ($R < R_b/5$), the plasma expands with speeds near $V_o$ and no sign of instability is discernible; suddenly, near R = 3 cm, radial plasma projections appear with amplitudes comparable to their wavelengths 5±1 mm. It is clear from the distance versus time plot, that these plasma tips then continue to freestream outward into the magnetic field. Since $R << R_b$ the bulk plasma is also still expanding close to its intial speed. Curiously, despite a much stronger deceleration in the 1 Tesla case ($g \propto B^2$), the instability also begins to develop at about the same distance and time as in the lower field case (see Fig. 4). This onset behavior is consistent with the instability criterion[16] $g/L_n > \Omega_i^2/4$, which is independent of the magnetic field; $\Omega_i$ is the ion cyclotron frequency. The instability wavelengths turn out to be also independent of the magnetic field strength. The flute amplitude grows rapidly after onset with a linear growth rate above $10^8$ $s^{-1}$,

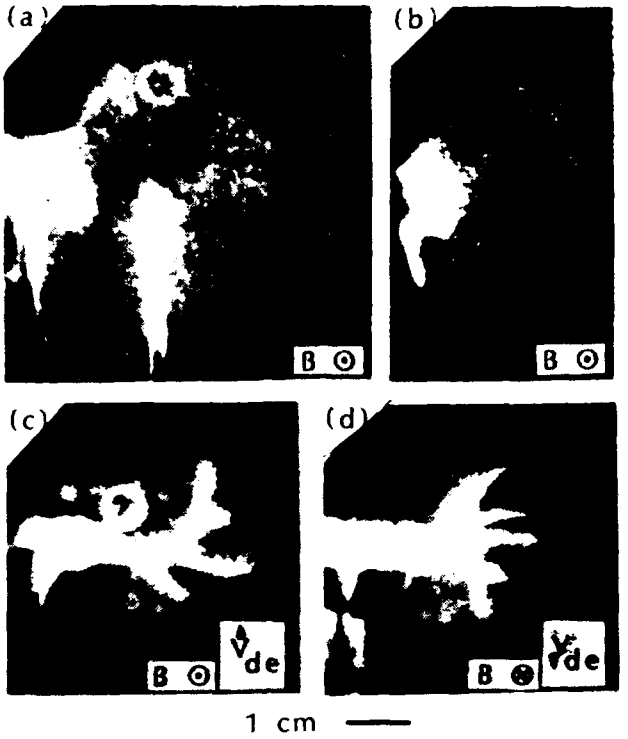



Figure 3. Examples of the instability development. (a) 0.1 Tesla case observed at time 115 ns. (b) Example of density clumps in the early-time phase development with B = 1.0 Tesla at time 59 ns. (c) Example of curved spike structure with with 1.0 Tesla field (field points out of paper) at 115 ns. (d) Same as (c) except field points into paper and t = 100 ns; note reversal of curvature sense. $E_1$ = 25-30 J and P< 0.1 mT for these shots.

as seen in Fig. 4. Unfortunately, the accuracy of the growth rate measurement (factor of two) is limited by the shot-to-shot reproducibility of the onset time. For comparison, the conventional (small ion Larmor radius) MHD Rayleigh-Taylor growth rate ($\gamma = (g/L_n)^{1/2}$ for $kL_n > 1$) for our parameters (B = 1 T) is only about $2 \times 10^7$ $s^{-1}$, whereas the large Larmor radius instability theory[2] predicts a six times faster growth rate for the observed wavelengths, consistent with our experimental result. At times, the plasma structure initially appears as density clumps in the leading edge of the expansion plasma. This clumping-like behavior, shown in Fig. 3b, is a predicted characteristic of this instability.[2,16] Subsequent to the rapid linear phase of the instability the flute tips freestream with speeds near $V_o$.

The wavelengths of the predominant flute modes (measured at the base of the flutes) are typically about 5 mm and are also insensitve to most parameter changes. As time goes, on the instability wavelength tends to remain constant even though the plasma continues to expand radially. Thus, the

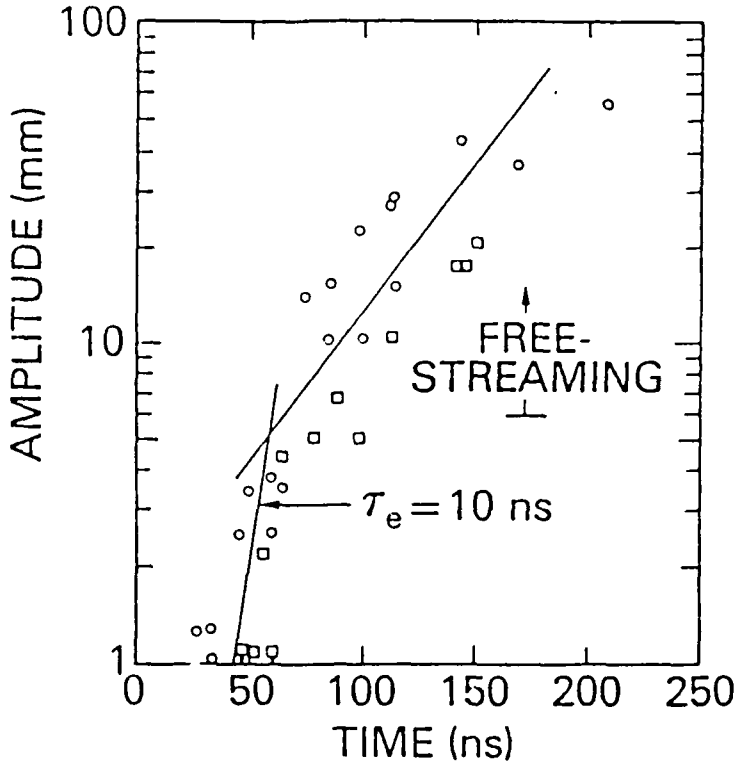



Figure 4. Onset and growth of instability flutes. Flute-tip-to-bubble amplitudes versus time for the 1.0 Tesla ( o ) and 0.1 Tesla ( □ ) data of Fig. 2. Note that the onset time for both field values occurs near 50 ns and the linear growth e-fold time for the B=1 T data is about $10^{-8}$s.

effective mode-number increases with radius. Some indication of how this can occur was obtained by placing witness plates (black Polaroid film) perpendicular to the magnetic field a few centimeters to one side of the target. These recorded time-integrated patterns of the plasma running down the field lines. Long spikes are seen in the exposures with curvature toward the midplane and additional projections formed towards the sides of the pattern with increasing distance from the source. The fact that the patterns on the witness plate are not washed out indicates that the plasma structure, once formed, does not undergo much azimuthal motion. Several examples of flute-tip bifurcation are also seen in the time-resolved GOI images,[18,19] such as shown in Fig. 5. The combination of these two effects tends to maintain constant wavelength and increase the instability mode number, $m = 2\pi R/\lambda$, with distance.

The dominant instability wavelength may be determined by the bulk plasma density scalelength, $L_n = 10 \pm 3$ mm, or possibly by the magnetic diffusion length into the plasma front, $L_b = 10$ mm. The collisionless skin ($c/\omega_{pe}$) depth is only a fraction of a millimeter, but possible anomalous resistivity associated with this or another instability could push the diffusion length into the centimeter ($c/\omega_{pi}$) range.

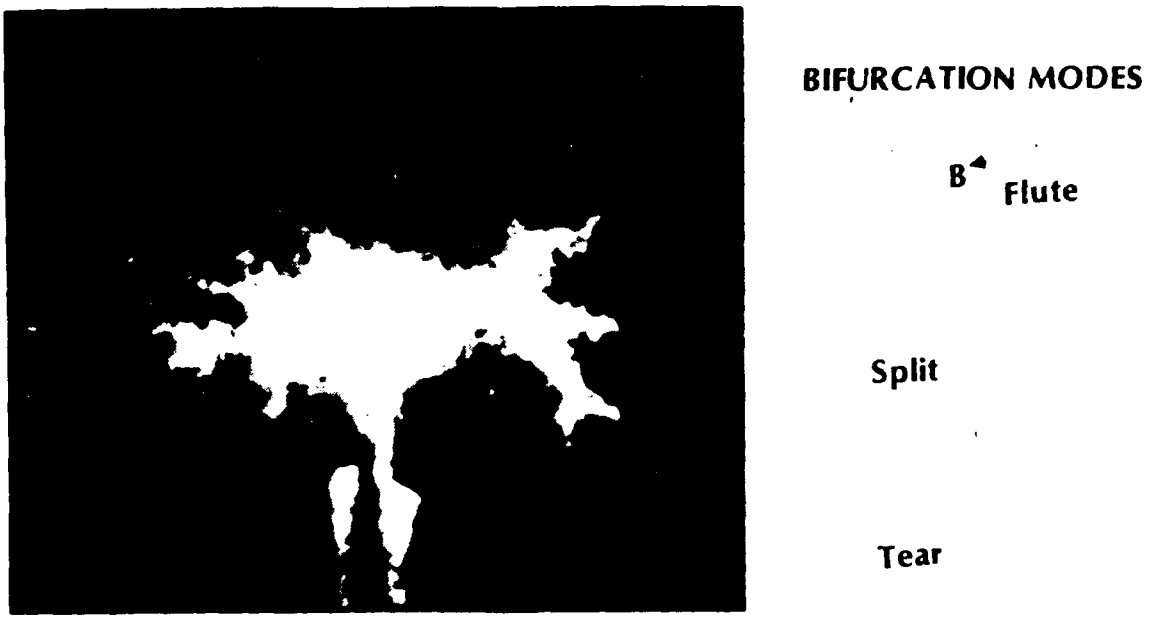



Figure 5. Example of LLR-instablity flutes undergoing bifurcation observed at t=100 ns, B=1 T, with the GOI.

For some shots, the magnetic field was rotated 90° so that the instability development could be viewed perpendicular to the field lines. The plasma projections, which have the appearance of slim spikes in the end-on view, actually run smoothly along the field lines, confirming the flute-like geometry of the instability.

The freestreaming flutes exhibit some interesting features at later times. One common characteristic in the high field experiments is the curvature and spur-like appearance of the instability fingers seen in Figs. 3 and 5. The flute curvature is in the electron cyclotron or electron E x B drift sense and reverses with magnetic field direction. It is not yet known whether the curvature arises from the spike tips moving upward or the bubble downward. Two possibilities are that curved flutes are caused either by E x B or $\nabla$ B x B induced electron velocity shear.[18,19]

A number of other parameter variations were performed during the course of this investigation. The background pressure was increased up to 2 Torr of $H_2$ to test the effects of increasing collisionality and decreasing Alfven speed on the instability. For the 0.1 Tesla case, viewed at 150 ns, freestreaming structure persisted up to 100 mTorr $H_2$ pressure at which point signatures of collisional effects were seen.[1]

In another series of shots, a 7.6 cm diameter, 3 mm thick copper disk was placed 4 to 5 cm to one side of the target, perpendicular to the field lines, to short out the dynamic motion of the magnetic field lines. The gross features of the instability persisted independent of whether the copper plate was grounded, ungrounded, insulated or bare.

Finally, several shots were taken with much larger incident laser energy (400 J) but comparable irradiance at a variety of magnetic fields and pressures. The major effect of higher laser energy is to proportionally increase the plasma mass and, hence, increase the magnetic confinement radius by $R_b \propto E_l^{1/3}$.

Another interesting observation in these experiments was the presence of a strong high-frequency (>250 MHz) signal seen in the plasma front by electrical and magnetic probes whenever the Rayleigh-Taylor instability occurred. This noise is in the ion-plasma or lower-hybrid frequency range. The relationship of this noise to the magnetic instability is not yet clear, but may be due to the growth of very short wavelength Rayleigh-Taylor modes, which cannot be seen in the framing pictures, or to the generation of microinstabilities in the plasma shell.[14,21,22]

## CROSS-FIELD JETTING

If a blob of plasma is projected across a magnetic field with velocity V, then charge can accumulate on its boundaries due to polarization forces within the plasma. The polarization arises from the V x B forces on the electron and ion distributions as shown in Fig. 6. The charge separation in turn sets up a polarization electric field E which then allows the bulk of the plasma mass to E x B drift across the magnetic field near the original speed V. There are, of course, necessary conditions for this to occur; for one, the charges at the boundary need to be replenished, as they are peeled off and left behind the main plasma by the fringe polarization electric fields. Also, since energy is dissipated by the internal currents, the plasma jet will eventually stop. A good discussion of these criteria is given in Borovsky.[23] The plasma jet tends to form a sharp wedge when viewed end-on to the magnetic field, due to electric field gradients and curvature. A wedge-shaped plasma jet was previously noted by Jellison and Parson.[5] On the other hand, the plasma should fan out in the plane containing the magnetic field lines.

Fig. 6 also shows an excellent example of a Barium plasma jet viewed in absorption with our resonant probe diagnostic. This shadowgram was taken with the dye laser tuned to near the center of the 450 mm BaII ion line at a time of about 750 ns.[4] The jet is moving across the 10 kG field at its initial speed of $10^6$ cm/s. The expected characteristic wedge-shape phenomena view and along B is very prominant. However, the view across the magnetic field is surprising indeed! The plasma is fanned out as expected, but remarkable fishbone-like structure is observed along the field lines.[4] A more detailed account can be found in Ref. 4.

Plasma jets have been formed several other ways in our experiment by creating asymmetric expansions. Fig. 7 shows two examples of such jets. The left side of Fig. 7 shows two jets resulting from plasma expansions of the type described in the last section. To induce jets, rather than the large Larmor radius instability, we put a cylindrical shield with a radius of about 1 cm about the target with slots cut in it to only allow two thin plasma sheets to pass through. In the example on the right side of Fig. 7, high-

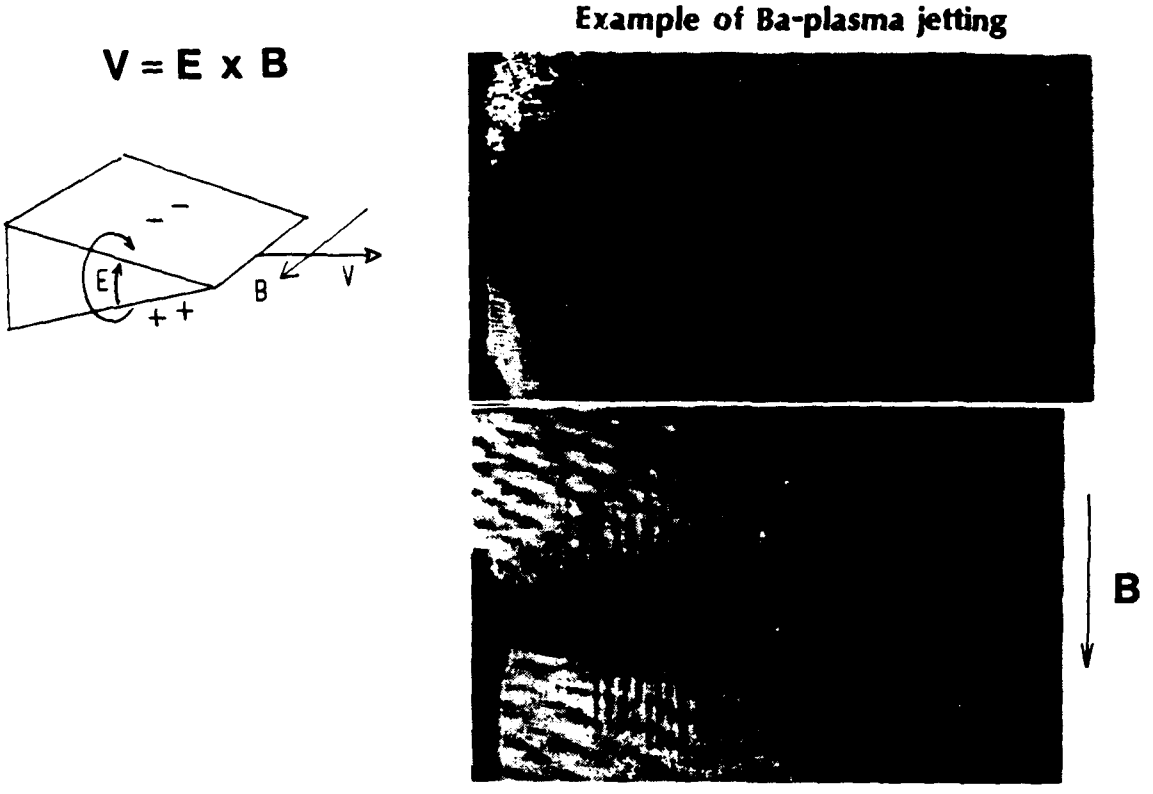



Figure 6. Cross-field jetting model and a laboratory example. The change separation and E x B drift models are illustrated to the left. On the right, an example of Ba-plasma jetting in a 1-T field is seen. The characteristic wedge shape (top) and "fish bone" instability (bottom) are seen.

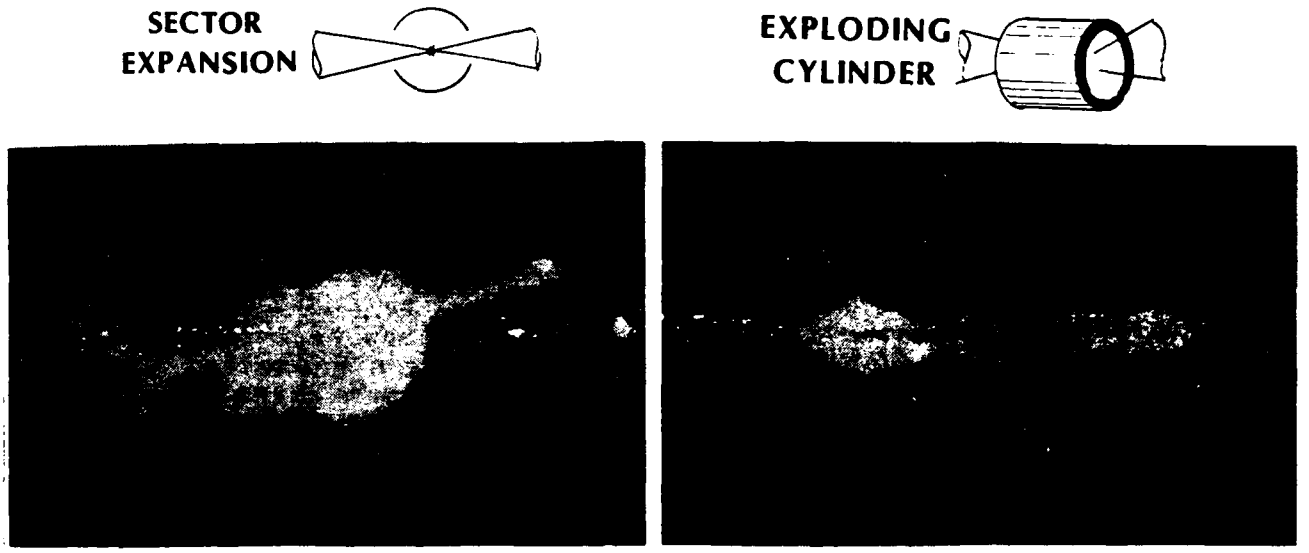



Figure 7. Two examples of laboratory jetting induced by geometric asymmetry. (left) A 30 J/beam two-beam expansion with a cylinderical shield [t=90 ns]. (right) A 100 J/beam two-beam shot into a cylinderical glass target [t=1 $\mu$s].

density, low-temperature jets are formed in an entirely different way.[24] Two oppositely-directed laser beams were focused into the ends of a glass cylindrical target (1 mm diameter, 2 mm long and with 50 $\mu$m wall thickness) causing dense plasma plumes to squirt out the cylinder ends across the applied magnetic field (10 kG in this case). Note that the observation time here is 1 $\mu$s after the laser pulse. Highly directed jets are seen crossing the field in both directions followed by masses of slower ($V = 3 \times 10^6$ cm/s) plasma.[24] Curiously, the slower plasma blobs seem to be fluting in a similar manner to the large Larmor radius instability as they move across the field.

A more detailed discussion of the important subject of cross-field jetting and these experiments will appear elsewhere. Jetting phenomena are important wherever plasma masses are projected across magnetic field regions such as in several astrophysical situations.[25]

## STRUCTURE ASSOCIATED WITH COLLISIONAL PLASMAS

When a background gas is introduced around the laser-produced plasma, interactions between the expanding plasma and the stationary background plasma and gas are possible. At low gas pressure (below 100 mTorr), these interactions are collisionless beam/beam type instabilities.[1] Above about 1-Torr pressure, the interactions are collisionally dominated. A transition occurs between these two regimes. Fig. 8 shows a typical high-pressure dark-field shadowgram. Thin steep blast-waves are the dominant feature.[1] Several additional phenomena are also evident, such as aneurisms, large-scale turbulence regions behind the target, and a

turbulent region inside the blast front. We have recently established the mechanism causing on-axis aneurisms to be laser channel heating,[6] and this will be discussed below. The nature of the gross turbulence appearing behind the target will be discussed in the following section.

## Aneurisms

Aneurism-like protrusions have been seen in several different laser-plasma experiments.[1,26] They frequently appear along the incident beam axis and near the target surface normal, although they are also seen at other angles as well.[1] A number of mechanisms have been suggested to explain these aneurisms including laser beam channel heating of the ambient gas,[27] jetting material from the target,[28] Rayleigh-Taylor instability of the blast front,[1] and magnetic field/thermal ablation process of the blast-wave interior.[29] We have recently discovered that several of these processes do occur, causing similar appearing, but different type, aneurisms.

Aneurisms aligned with the incident laser beam, such as shown in Figs. 8 and 9, are usually caused by laser heating of a channel in the ambient gas.[6] This phenomena would be of importance in proposed ICF reactors[30] in which a buffer gas is used to protect the first-wall against prompt x-ray and debris heating. Laser or particle beams would also create heated channels in the gas which could cause material in the aneurisms to be aimed at the last focusing optic, an undesirable effect.

The channel and resulting aneurism is formed as follows.[6] The UV and X rays from the laser-plasma interaction at the solid target photoionize the nearby gas. Fractional ionizations of a few percent are typical 1 cm from the target for 100 J incident energies and 5 Torr nitrogen gas pressures; the radial dependence of the ionization goes as approximately $1/r^2$. A very small fraction (0.4%) of the incident beam is absorbed in this low density plasma via inverse bremsstrahlung. The plasma in the laser channel quickly heats up to about 100 eV out to beyond 1 cm; this hot plasma expands radially in a cylindrical blast-wave causing a reduced density channel along the laser-beam axis. Later, the material swept up into the spherical blast-wave from the expanding target material is slowed less in the low density channel than off-axis and causes the aneurism protrusion.

We have established this mechanism experimentally by tilting the target 30% to separate the laser axis from the target normal and noting that aneurisms usually form along the laser-beam axis for higher energy ($E_L$ > 10 J) shots at multi-Torr pressures. Additionally, we have found that target thickness and diameter, different laser focal-spot diameters, hot-spots, or ultra-smooth ISI focal spots[31] do not affect these on-axis aneurisms. We have observed the cylindrical shock formed by the superheated channel soon after the incident laser pulse is over; from its motion we infer that about 1% of the incident laser beam energy is

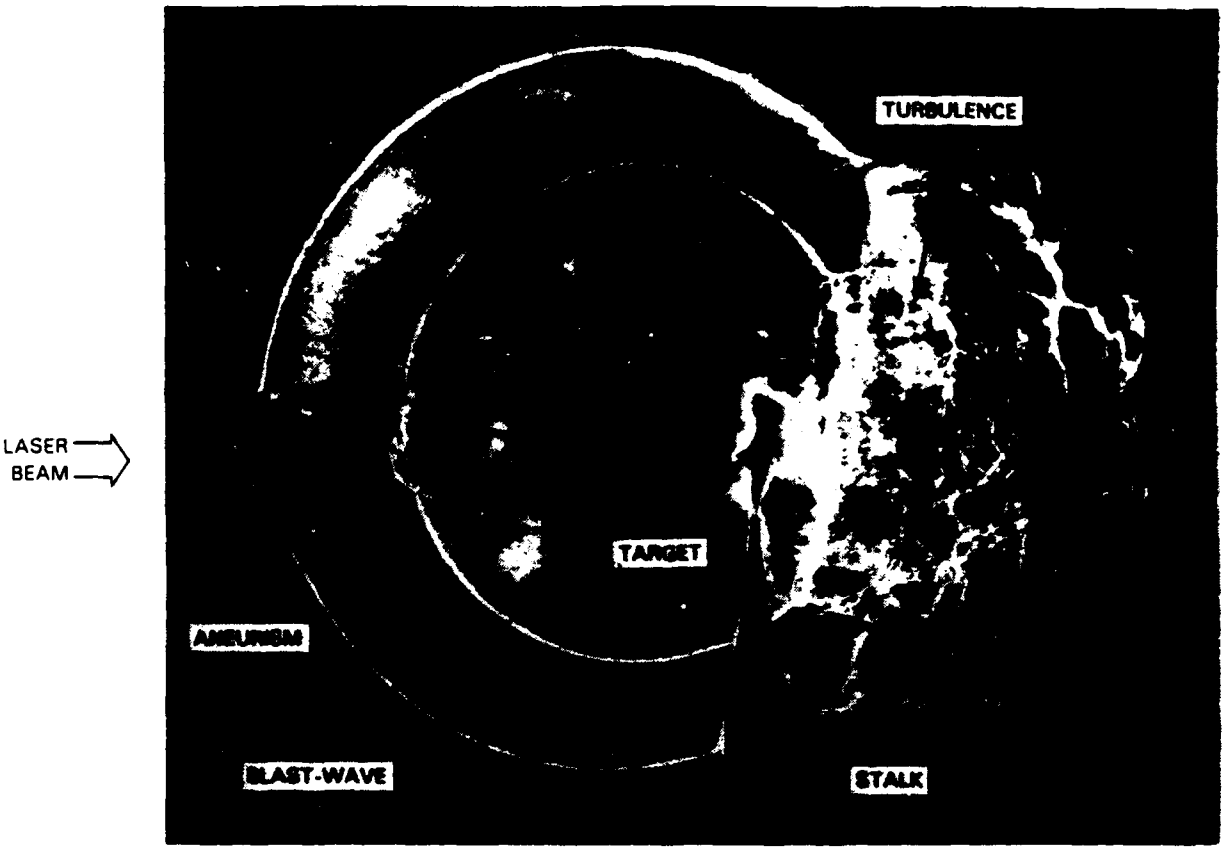



Figure 8. Blast-wave associated structure seen in dual-time shock-front shadowgrams (55 and 160 ns) of a 5 T $N_2$ ambient pressure shot. (36 J on a stalk mounted Al target).

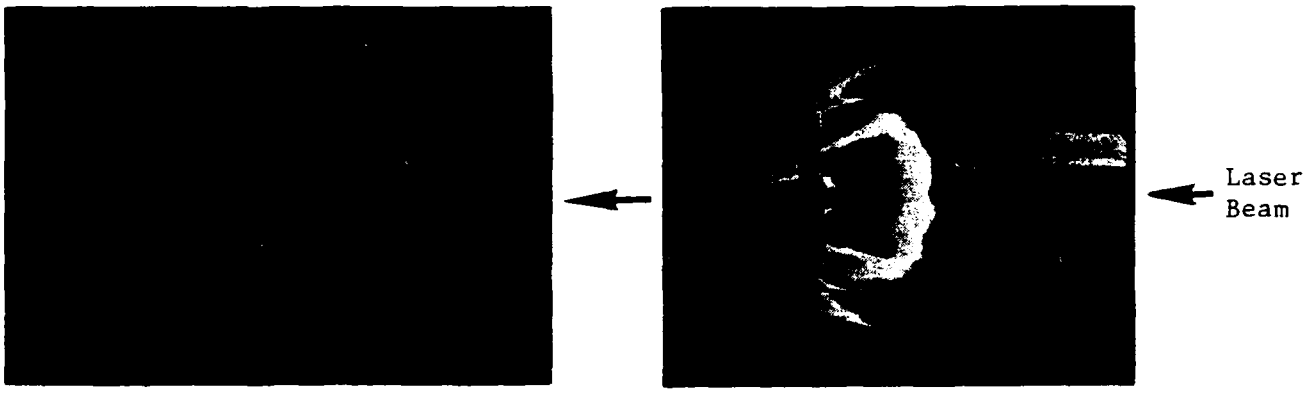



Figure 9. Example of pronounced on-axis beam-heated aneurism (5 T $N_2$, 109 J, t=71, 146 ns) (left) and cylinderical blast-wave (5 T $N_2$, 245 J) (right) formed by expansion of the beam-heated plasma at early time (14 ns).

invested in the channel formation, in agreement with theory and 2D computer simulations.[6] Quantitative agreement has been obtained between most aspects of the experiment and the corresponding theory/computer simulation; the reader is directed to Ref. 6 for more details.

Fig. 10 shows other examples of aneurisms where mechanisms other than beam channel heating must be operating. Aneurisms formed at lower incident energy near the normal to the target surface, as in Fig. 10a, appear to be caused primarly by target material jetting. Slow masses of target material, perhaps ejected after the incident laser pulse is over or from the region surrounding the focal region, catch up to the decelerating blast-front and punch out an aneurism. Evidence for jetting comes from framing camera pictures of the blast-wave system, taken with interference filters at specific Al II and Al III emission lines. These pictures show directed jets of Al target material inside the blast-front pushing out an off-axis aneurism.

Occasionally, turbulent appearing aneurisms are observed, such as shown in Fig. 10b. A cause of these aneurisms could be Rayleigh-Taylor instability of the blast-front.[1] Ordinarily, blast-waves are thought to be stable against hydrodynamic instability. But, if the blast-wave density profile is modified by radiation cooling or thermal conduction effects, adverse density gradients (oppositely directed density gradient and deceleration vectors could result. Classic Rayleigh-Taylor growth rates of about 10 ns [$(kg)^{1/2}$] are sufficient to explain the observed structure.[1]

Aneurisms also appear at angles other than the target normal and incident beam directions, such as shown in Fig. 10c. These aneurisms may be caused by ejection phenomena

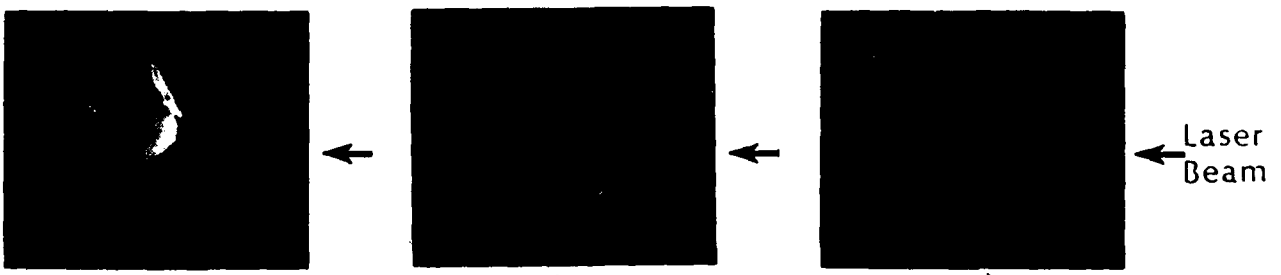



Figure 10. Examples of aneurisms not formed by the on-axis beam-heating mechanism. (a) Example of an aneurism probably directed about the target normal (30° from the laser axis) which is probably formed by plasma jetting. (35 J, 5 T, $N_2$ t=59 ns) (b) Turbulent appearing aneurism, perhaps caused by blast-wave Rayleigh-Taylor instability. [20 J, B=600 G, 7=1.5 Torr (90% $N_2$ + 10% $H_2$, t=52, 169 ns] (c) Odd-angle aneurism, perhaps caused by mechanism postulated by Giuliani, ref. 29. [38 J, B=0, 5 Torr, (90% $N_2$ + 10% $H_2$), t=52, 16 ns].

or, alternatively, by the thermal conduction model of Giuliani.[29] This model depends upon there being a hot plasma inside the blast-front. Imbedded in the blast-front are azimuthal magnetic fields, of order 1 kG, which originate either in the initial laser-plasma interaction[32] or are created in the expanding shock $\nabla n \times \nabla T$ gradients.[33] The magnetic fields inhibit the heat conduction to the blast-front except near the axial null of the azimuthal fields. The enchanced ablation in this region will both thin and accelerate this portion of the blast-wave to form an aneurism. Quantitatively, this process is consistent with all known experimental parameters,[29] but no direct verification has yet been made of its validity.

Dense Target Disassembly

The turbulence formed by the target material expanding away from the laser beam direction is especially striking as seen in Fig. 8. This material is dense target foil material which has been accelerated in reaction to the ablation plasma created on the laser side of the target.[34-36] It has been demonstrated that ablatively accelerated foils, such as used in these experiments, undergo Rayleigh-Taylor (RT) instability by the target acceleration g (of order $10^{15}$ $cm/s^2$) during the laser pulse duration.[8] Growth rates of about 60% of the classical $[(kg)^{1/2}]$ rate have been measured in detail by Grun et al.[37] An interesting question is whether the turbulence which is seen long after the laser pulse has ended is dominated by the RT created during the laser pulse? To answer this question, we create a dominant RT mode by using a grooved target and compare the resulting structure to flat targets as successively later times after the laser pulse.

Fig. 11 shows a compilation of such a sequence. The top row shows shadowgrams at various times when a 100 $\mu$m grooved target was accelerated. The bottom row is the same as the top row except that the target is a smooth flat foil of the same thickness. The 100 $\mu$m perturbed targets undergo RT growth during the laser pulse. Although, some residual remnants of the original 100 $\mu$m perturbation may be present after 80 ns, it is clear that the dominant structure is of much higher mode number and is largely independent of whether the target had an initial perturbation or not. Turbulent regions of the shadowgrams have been digitized and Fourier analyzed showing that they have similar spectral properties.[9] It has been suggested by Stamper that the dense target may undergo a Benard-type hydrodynamic instability causing the short-wavelength turbulence. The Benard instability would occur between a hot surface (laser side of the target is several hundred eV in temperature) and a cold surface (rear of target is known to be only a few eV) when an adverse acceleration direction is present. However, definitive demonstration of the cause of this turbulence, its long term time dependence, and the possible interaction with the background plasma/gas still needs to be determined.

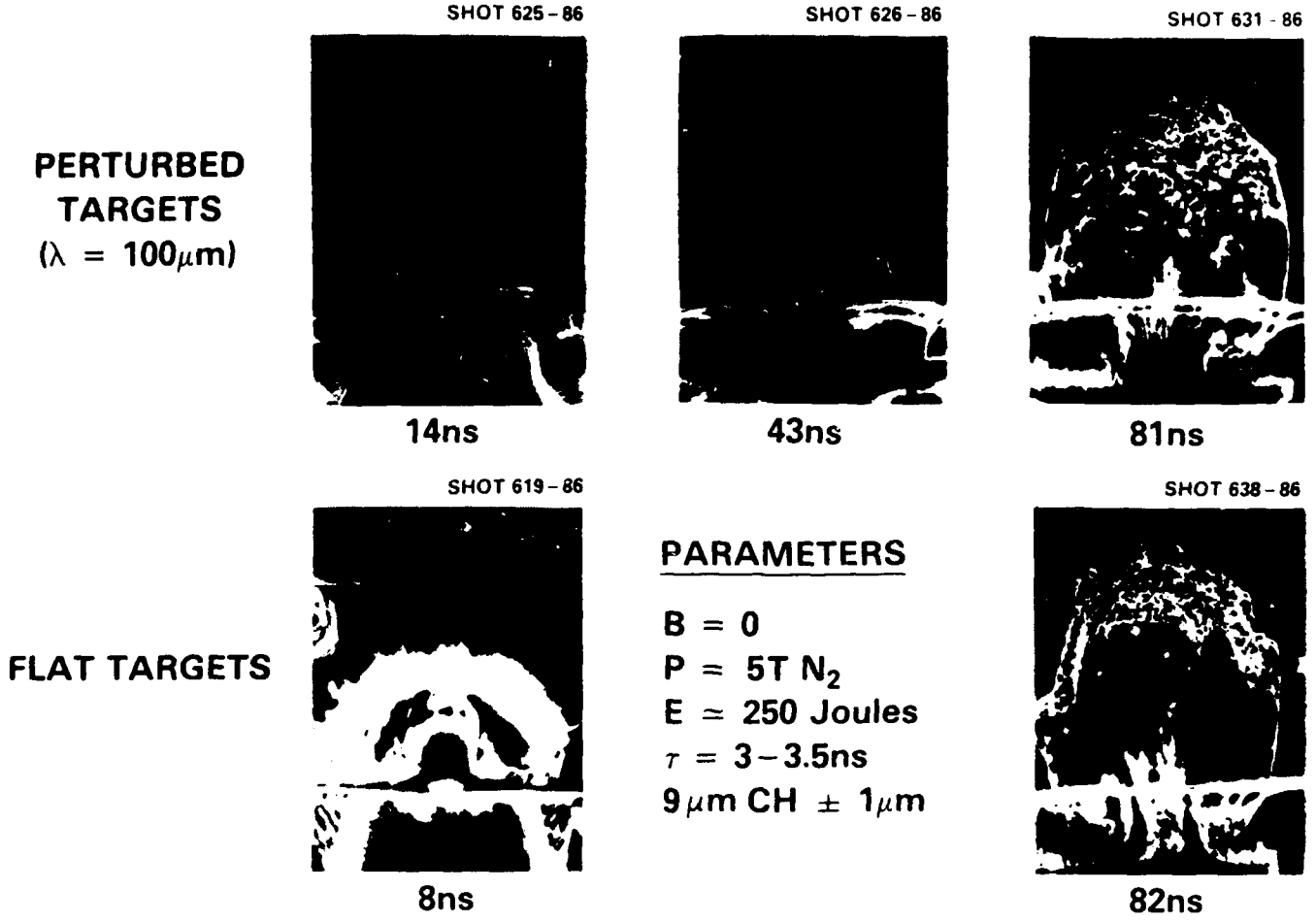



Figure 11. Sequences of turbulence formed as an accelerated perturbed target (top) and smooth target (bottom) expand behind the original target location.

## CONCLUSIONS

It is clear that a wide variety of density structure is generated when a plasma expands into a magnetic field, another plasma, or both. The evolution of the structure, whether generated by instability, geometry, or by the laser beam itself impacts a wide variety of disciplines. The robust instability that occurs when a large ion Larmor radius plasma expands into a magnetic field has applicability to space physics situations, magnetic fusion confinement devices, as well as basic nonlinear plasma theory. We described a numbe- of unusual phenomena that occur that should challenge the ingenuity of theorists. Aneurisms, which appear simple, are actually caused by several mechanisms. One mechanism studied in detail is laser-beam channel heating. This phenomena could be important in ICF reactors that use an ambient gas to reduce the first-wall impulse loading, as well as for laser beam guided particle beam schemes. The turbulence formed as dense highly-accelerated targets disassemble and expand is particularly striking. The dominant turbulent structure

appears to be independent of the Rayleigh-Taylor instability that has been observed during the laser-ablation acceleration process. Fourier analysis of the resulting turbulence, perhaps initiated by the Benard instability, shows a statistically well-developed large-amplitude turbulent plasma. This plasma may then become very useful as a test-bed to study fully developed turbulence theory.

This work was supported by the Defense Nuclear Agency.

REFERENCES

° Present address: Science Applications International Corporation, McLean, Virgina 22105.

1. B.H. Ripin, A.W. Ali, H.R. Griem, J. Grun, S.T. Kacenjar, C.K. Manka, E.A. McLean, A.N. Mostovych, S.P. Obenschain, and J.A. Stamper in: "Laser Plasma Interactions and Related Plasma Interactions, Vol 7" pgs 857-877, G. Miley and H. Hora, ed., Plenum Press, NY (1986).
2. A.B. Hassam and J.D. Huba, Geophys. Res. Letters 14, 60 (1987).
3. B.H. Ripin, E.A. McLean, C.K. Manka, C. Pawley, J.A.Stamper, T.A. Peyser, A.N. Mostovych, J. Grun, A.B. Hassam and J. Huba, Phys. Rev. Letters 59, 2299 (1987).
4. A.N. Mostovych, B.H. Ripin, and J.A. Stamper Bull. Am. Phys. Soc. 32, 1909 (1987); see also: Phys. Rev. Letters (1988).
5. G. Jellison and C. Parsons, Phys. Fluids 24, 1787 (1981).
6. J.A. Stamper, B.H. Ripin, R. Peterkin, Jr., R. F. Stellingwerf, (submitted to Phys. Fluids, 1987).
7. E.A. McLean, B.H. Ripin, and J.A. Stamper (to be published).
8. J. Grun, M.H. Emery, S.Kacenjar, C.B. Opal, E.A. McLean, S.P. Obenschian, B.H. Ripin, and A. Schmitt, Phys. Rev. Letters 53, 1352 (1984).
9. J. Grun, J.A. Stamper, and B.H. Ripin (to be published).
10. M. Kruskal and M. Schwarzchild, Proc. Roy. Soc. (London) A223, 348 (1954).
11. M.N. Rosenbluth and C.L. Longmire, Ann. Phys. (NY) 1 120 (1957).
12. H. Dickinson, W.H. Bostick, J.N. DiMarco, and S. Koslov, Phys. Fluids 5, 1048 (1962).
13. S. Okada, K. Sato, and T. Sekiguchi, Jap. J. App. Phys 20, 157 (1981).
14. Yu. P. Zakharov, A.M. Orishich, A.G. Ponomarenko, and V.G. Posukh, Sov. J. Plasma Phys. 12, 674 (1986).
15. M.N. Rosenbluth, N.A. Krall, and N. Rostoker, Nucl. Fusion Supplement Part 1, 143 (1967).
16. J.D. Huba, J.G. Lyon, and A.B. Hassam, Submitted to Phys. Rev. Letters (1987).
17. P.A. Bernhardt, R. Roussel-Dupre, M.B. Pongritz, G. Haerendel, A. Valenzuela, D.A. Gurnett, and R.R. Anderson, J. Geophys. Resh. 92, 5777 (1987).

18. B.H. Ripin, Bull. Am. Phys. Soc. 32, 1876 (1987).
19. B.H. Ripin, et al, (submitted to Phys. Fluids 1987).
20. C.K. Manka, C.J. Pawley, E.A. McLean, B.H. Ripin, T.A. Peyser, and J.A. Stamper, Bull. Am. Phys. Soc. 32 190 (1987).
21. N.A. Krall and P. C. Liewer, Phys. Rev. A 4, 2094 (1971)
22. D. Winske, (submitted to Phys. Fluids (1987).
23. J. Borovsky, Phys. Fluids 30, 2518 (1987).
24. C.K. Manka, T.A. Peyser, and B.H. Ripin (to be published).
25. M.C. Begelman, R.D. Blandford and M.J. Rees, Rev. Mod. Phys. 56, 255 (1984).
26. See for example: H. Azechi, Y. Sakagami, T. Yamanaka, C. Yamanaka, Appl. Phys. Letter 30 187 (1977); G.V. Sklizkov, in: "Laser Interaction and Related Plasma Phenomena, Vol 2" p 235-257, H.J. Schwarz and H. Hora, ed., Plenum Press, NY (1972).
27. J.G. Lyon, NRL Memo Report 5491 (1985).
28. C. Longmire, private communications.
29. J.L. Giuliani, NRL Memo Report 5420 (1985).
30. R.R. Peterson, and G. Moses, Nucl. Tech. and Fusion 4, 860 (1983).
31. R.H. Lehmberg, and S.P. Obenschain, Opt. Commun. 46, 27 (1983).
32. J.A. Stamper and B.H. Ripin, Phys. Rev. Letters 34, 138 (1975).
33. R.S. Bird, L.L. McKee, F. Schwirzke, and A.W. Cooper, Phys Rev A7, 1328 (1973); D.F. Edwards, V.V. Korobkin, S.L. Motilyov, and R.V. Serov, Phys Rev A16, 2437 (1977).
34. B.H. Ripin, R. DeCoste, S.P. Obenschain, S.E. Bodner, E.A. McLean, F.C. Young, R.R. Whitlock, C.M. Armstrong, J. Grun, J.A. Stamper, S.H. Gold, D.J. Nagel, R.H. Lehmberg, and J.M. McMahon, Phys Fluids 23 1012 (1979); 24 990 (E) (1981).
35. J. Grun, S.P. Obenschain, B.H. Ripin, R.R. Whitlock, E.A. McLean, J. Gardner, M.J. Herbst, and J.A. Stamper, Phys Fluids 26 588 (1983).
36. M. Rosen, R.H. Price, E.M. Campbell, D.W. Phillion, K.G. Esterbrook, B.F. Lasinski, J.M. Anerbach, S.P. Obenschain, E.A. McLean, R.R. Whitlock, and B.H. Ripin Phys Rev A 36, 347 (1987).
37. J. Grun, M.H. Emery, C.K. Manka, T.N. Lee, E.A. McLean, A. Mostovych, J. Stamper, S. Bodner, S.P. Obenschain, and B.H. Ripin Phys. Rev. Letters 58, 2672 (1987).

# APPENDIX DDD

## Laboratory Laser-Produced Astrophysical-Like Plasmas

For: Proceedings of the 19th European Conference
on Laser Interaction with Matter, Madrid
October 3-7, 1988

# LABORATORY LASER-PRODUCED ASTROPHYSICAL-LIKE PLASMAS

B. H. Ripin, C. K. Manka, T. A. Peyser[a], E. A. McLean, J. A. Stamper, A. N. Mostovych, J. Grun, K. Kearney, J. R. Crawford[b] and J. D. Huba

Plasma Physics Division
Naval Research Laboratory
Washington, DC 20375-5000
USA

ABSTRACT

Laser-produced plasmas have many properties similar, or can be scaled, to those encountered in space and astro-physical plasmas, and in magnetospheric chemical releases. We describe several such experiments performed with the PHAROS III Nd-laser facility at NRL.

INTRODUCTION

Laser-produced plasmas provide unique laboratory test beds to investigate many space or astrophysical relevant processes. Parameters of laser-produced plasmas span the ranges of: very high-energy densities ($10^9$ J/cc) to strongly coupled plasmas (kinetic energy < potential energy), very low plasma-$\beta$ (<<1) to high $\beta$ (>100), temperatures of 1 eV to >1 keV, and directed velocities exceeding $10^8$ cm/s. These conditions can be generally achieved with good control, reproducibility, and diagnosibility.

Because of the great versatility of laser-produced plasmas, many ionospheric, magnetospheric, space and astrophysical related problems can be studied. In this paper we discuss experiments which are related to space physics phenomena which hopefully will bring some insight to these processes. In this article we briefly discuss: sub-Alfvenic plasma expansions across magnetic fields (such as the large Larmor radius instability), blast-waves, cross-field plasma jetting and plasmoid formation, MHD turbulence, and strong coupled plasma production.

PLASMA PROPERTIES

Lasers can generate several types of plasmas useful for space or astrophysical studies; these plasma components include:

- o Ablation plasma
- o Ambient plasma
- o Highly-accelerated target foils
- o Shocked target plasma
- o Strong coupled plasma.

Schematics of the origins of these different plasma components are shown in Figure 1.

Ablation plasma is generated directly in the laser-solid target interaction. Laser energy is absorbed in the plasma on the front of the target near the critical density (plasma frequency equals the laser frequency, $10^{21}$ e/cc for 1.06 $\mu$m Nd-laser light). This high initial energy density plasma (~$10^9$ J/cc) subsequently streams away from the focal region with velocities ranging from $10^6$ to over $10^8$ cm/s, depending upon irradiation conditions.[1,2] These ablation plasmas become wind-like,[3] in which most energy resides in a relatively cold (few-eV), but energetic (multi-keV) ion component after expanding a few millimeters from the focal spot. Ablation plasma has characteristics very much like the solar wind[4] (streaming velocities of several hundred km/s and temperatures of a few eV) excepting that it has much higher density and is much smaller in size. The ablation plasma energy-density and velocity can also be raised to values approaching supernova conditions (1000 to 10,000 km/s).

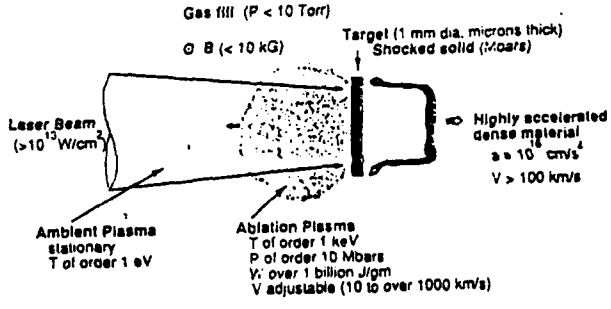



Figure 1. Schematics of laser-target-plasma interactions. Regions of formation of ablation, ambient, accelerated, and shocked plasma components are indicated.

a) Science Applications Int. Corp., McLean, VA.
b) SW Texas State University, San Marcos, TX USA.

Ambient plasma can be formed simultaneously with the energetic ablation component by bleeding gas into the chamber at pressures up to 10 Torr; the gas becomes photoionized by laser-target interaction radiation in the vicinity of the target[5] or, over a larger volume, by means of a preionizer device. A magnetic field can be applied using a set of coils (22 cm dia, Helmholtz pair in our case) so that magnetized plasma up to 10 kG can be obtained. Ambient plasma is typically cold (about 1 eV) with no net velocity. The fast ablation plasma streams into the ambient media and causes interactions that emulate many space and astrophysical processes. In this way, interesting phenomena occurring when the solar wind impinges on the magnetospheric and ionospheric plasmas and with obstacles such as comets, moons and planets can be emulated in the laboratory. Similarly, interstreaming plasma conditions, such as blast-waves,[6] can also be generated which have supernova shock-like behavior.

The laser-target ablation plasma puts tremendous pressure (tens of Megabars) on the remaining target material as it streams away acting much like a rocket exhaust. These high pressures can accelerate the remaining nearly solid-density target-foil to speeds over 100 km/s.[7] Targets can undergo accelerations of $10^{16}$ cm/s$^2$ or more at high density and are susceptible to hydrodynamic instabilities, such as Rayleigh-Taylor.[8] This dense plasma/target component has been very useful in generating and studying MHD turbulence, which is similar in appearance to that found in supernova remnants.

Shock waves set up in the target interior by the high-pressure laser/plasma impulse can create a slower plasma component which expands towards the laser like the ablation plasma, but more slowly (V~$10^6$ cm/s). This plasma component can be eliminated by using thin targets or accentuated by using special target shapes, such as cylinders. This type of plasma has be especially useful in our study of moderate-$\beta$ plasma jets. Plasma jets are plasma blobs which can travel many gyro-radii across magnetic fields; they may be involved in astrophysical jetting, solar disrupted plasma transport, and bipolar stars.

An especially low energy density plasma (strong-coupled) can also be made using lasers. Strong coupled plasmas have the property that the particle kinetic energy is less than the interparticle potentials. The basic method we use to produce strong coupled plasmas is described in reference 9. Strong coupled plasmas exist in solar interiors, white dwarfs, and Jupiter.

## SCALING FROM SPACE TO LABORATORY

There are obvious differences in length, time, and density scales between space and laboratory plasmas. First, it should be emphasized that there is no known *universal* scaling law that will reproduce all details of a space plasma in the laboratory; scaling must be specific to the phenomenon under investigation. For collisional or collisionless dominated plasma effects, scaling laws are obtained by casting the appropriate governing equations (eg., MHD, Vlasov equations) in dimensionless form; these dimensionless variables define the scaling relation. However, it is usually difficult to satisfy all of the scaling laws simultaneously and an educated mixture is often more appropriate. The dominant parameters for the phenomenon are picked for accurate scaling and the less crucial variables allowed to deviate. Other rationals for scaling include: unusual plasma regimes (strong coupled, degenerate....); magnetic pressure or Larmor scaling; plasma thermal, directed or total $\beta$; turbulence parameters; radiation loss or time scales; choice of fixed parameters (velocities, instability growth periods,...); sound or Alfvenic Mach numbers; and others.

## LARGE LARMOR RADIUS INSTABILITY

The large Larmor radius (LLR) instability is an good example of a space phenomena that can be scaled to the laboratory. This instability was first seen in the March 1985 AMPTE barium release experiment in the tail of the magnetosphere (about 10 earth radii away).[10] Marked striations appeared before the barium plasma expanded to its maximum radius (radius at which the excluded magnetic field equaled the plasma kinetic energy) even though the barium ion Larmor radius was very large (about equal to the magnetic confinement diameter). Huba and Hassam developed a MHD-like theory[11] for sub-Alfvenic expansions in the large Larmor radius (LLR) limit. The LLR instability is the analog to the conventional MHD Rayleigh-Taylor (interchange) instability but has a much faster growth rate, ie.,

$$\gamma_{LLR} = k L_n \gamma_{MHD} , \qquad (1)$$

where the MHD growth rate is $\gamma_{MHD} = [g/L_n]^{1/2}$, k is the instability wave number, and $L_n$ is the density gradient length in the expanding plasma leading edge. Dominant unstable wavelengths are slightly less than $L_n$ yielding LLR instability




Figure 2. Two examples of the LLR instability seen in the NRL experiment. Left side shows instability near the end ot its linear stage (10 kG, 376 J, 99 ns). The right side shows some facinating bifurcation-like structure appearing in the nonlinear stage (10 kG, 30 J, 90 ns).

growth rates factors 6 or more than $\gamma_{MHD}$. A laser-plasma experiment was launched to verify the existence and properties of this new instability using the ablation plasma expanding into across a magnetic field (up to 10 kG).[12] Figure 2 shows two examples of the unstable plasma structure: the left photo is an example of structure near the end of the linear phase showing the well-developed flute structure, and the right photo is an example of the very unusual structure seen a later, nonlinear stage. The nonlinear structure does not really saturate, but rather it continues to expand outward at approximately the original plasma velocity even though it is well beyond the magnetic stopping distance. In addition, the flutes take on an erratic structure and even appear to bifurcate. It seems like each flute tip is acting like an independent plasma jet. Further details of the linear growth and nonlinear development of this experiment can be found in references12 and 13.

## HIGH MACH NUMBER SHOCKS

When an ambient plasma is introduced, the Mach number of the ablation plasma goes from sub-sonic (or sub-Alfvenic when B > 0) to super-sonic. Mach numbers of hundreds are easily produced. Additionally, when the ambient gas pressure is above 0.5 Torr (for $V_d = 5 \times 10^7$ cm/s) collisional blast-waves are formed. A good example of the variety of phenomena that can appear under these circumstances is shown in the dual-time, dark-field shadowgram (backlit with laser pulses at the indicated times) shown in Figure 3. Very strong, thin, energy and momentum conserving shocks are seen in the laser side of the target as the ablation plasma sweeps up the ambient media.[6] These shocks behave much like ideal VonNeumann-Sedov shocks[14] but do exhibit many deviations from the simple theory. Supernova structure, such as found in the Crab Nebula (1054 AD), result from similar shocks blowing through ($V_{sn} \sim 1000$ km/s) the outer layers of the collapsing star. Note the small scale-length turbulence formed behind these shocks (hazy region just inside the bubbles) and the gross large scale-length turbulence formed behind the target. The 'aneurism' features results from a cylindrical shock caused by laser beam warming of a channel[15] or by jetting target material.

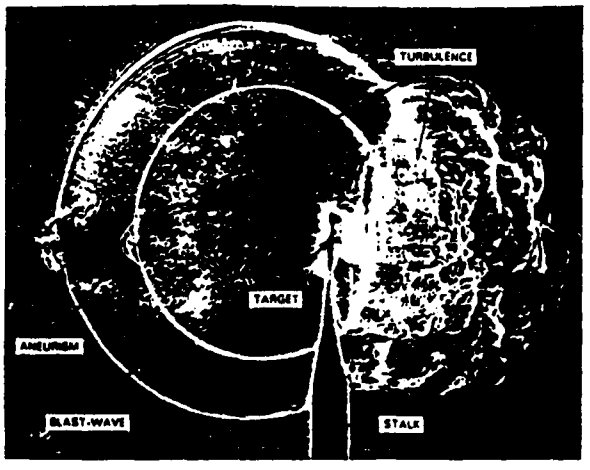



Figure 3. Features of a laser-plasma ambient media interaction in the collisional regime. Note the sharp blast-fronts, regions of turbulence, and the aneurism. The laser is incident from the left. (36J, 5 Torr $N_2$, Al 1.5 μm thick target, B = 800 G, t = 55 ns and 155 ns)

## TURBULENCE

In this Section the nature of the large scale turbulence that appears behind the target (eg., Fig. 3) is explored. Turbulence (or turbulent appearing structure) is seen in a wide variety of space and astrophysical situations ranging from the solar wind behind the bow-shock, within supernova remnants, and several other astrophysical objects.

The turbulent structure is best seen in the laboratory when optical diagnostics sensitive to small light deflections, such as dark-field shadowgraphy, are used for detection. Structure is also observed in the natural optical emission image of the turbulent region, but the shorter wavelength components tend to wash out.

The turbulent plasma is generated when the highly accelerated target foil ($a \sim 10^{16}$ cm/s$^2$) pushes into the ambient background gas/plasma. The accelerated material has high Mach number ($M \sim 100$, $V_t \sim 100$ km/s) with respect to the ambient media. Turbulence is not observed when the target foil is accelerated under high vacuum conditions, nor when the gas density is low (collisionless conditions). Even though the accelerated foil is known to undergo Rayleigh-Taylor hydrodynamic instability during acceleration,[8] the turbulence seen at late times (>100 ns) is not correlated with the target Rayleigh-Taylor structure. This was demonstrated by comparing results from smooth and pregrooved accelerated targets. Observations, such as seen in Figure 3, can be densitometered, digitized, corrected for film response and Fourier analyzed to obtain the turbulence power spectral density function. Kolmogorov turbulence [big eddys decaying into smaller eddys] is characterized by a $k^{-5/3}$ power-law spectrum between an inner and an outer scale length. We have done a preliminary analysis on several cases and can fit either a power law or an exponential spectral shape to the data. Eventually, we hope to completely characterize the nature and cause of this turbulence and apply the findings to relevant space situations.

## PLASMA CROSS-FIELD JETTING

Plasma jets and blobs have been observed to propagate large distances across magnetic fields, distances much greater than ion gyro-radii, in many space and laboratory situations. This isn't possible for isolated charged particles, but units of plasmas can act collectively to overcome the externally applied magnetic field force. Generally, what happens is the $V_o \times B_o$

force on a plasma moving across magnetic field $B_o$ with speed $V_o$ causes a polarization electric field $E_p$ to form inside the plasma. $E_p \times B_o = V_o$, hence the plasma continues forward at its original velocity. Of course, charge is depleted at the boundaries and the process eventually will quit.[16]

Figure 4 shows examples of cross-field jetting observed in our experiments. The top picture shows a high-β jet produced simply by aperaturing the ablation plasma with a cylindrical mask to allow plasma sectors to flow across the magnetic field. The middle picture shows a moderate-β jet produced by firing the laser into the ends of a small glass cylinder and allowing an asymmetric plasma to squirt out its ends across the magnetic field. [See: Manka, Peyser, and Ripin; these proceedings] Finally, the bottom photo shows a low-β barium plasma jet squirting across the B-field.[17]

There are several notable features of our laboratory jets: 1) They occur if the plasma is asymmetric. 2) They propagate great distances across the magnetic field at nearly their initial speed. 3) They tend to pinch down at their leading edge, probably due to curvature of the internal polarization electric field. 4) They often form field-aligned structure on their boundaries, presumably results of instability.

## SUMMARY AND CONCLUSIONS

Laser-produced plasmas can be made with parameters of space and astrophysical interest. Aspects of the solar wind, magnetosphere, ionosphere, supernova shocks, and some jet-like features can be emulated in the laboratory. The interactions of these plasmas with magnetic fields and other plasma components produce many phenomena which resemble those observed in space. Although it is naive to believe that our experiments are miniature simulations of space phenomena, laboratory investigations may aid in their understanding.


## ACKNOKLEDGEMENTS

We thank the following persons for their assistance in this work: L. Daniels, J. Ford, N. Nocerino, M. Pronko, C. Pawley, T. Lee, and S. Obenschain. This work has been supported by the US DNA.

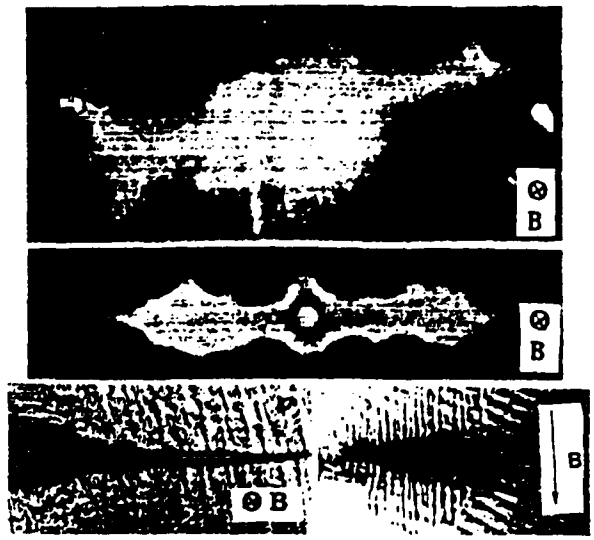




Figure 4. Three examples of cross-field plasma jetting.

## REFERENCES


1) Ripin, B. H., et al, "Laser-Plasma Interaction and Ablative Acceleration of Thin Foils at $10^{12}$- $10^{15}$ W/cm$^2$," Phys. Fluids, 23, 1012 (1980).
2) Grun, J., et al., "Ablative Acceleration of Planar Targets to High Velocities," Phys. Fluids, 26, 588 (1983).
3) Grun, J., R. Stellingwerf, and B. H. Ripin, "Control of Ion-Velocity Distributions in Laser-Target Interaction Experiments," Phys. Fluids, 29, 3390 (1986).
4) Brandt, J. C., Introduction to the Solar Wind, (Freeman, San Francisco, 1970).
5) Ripin, B.H., et al.,"Structuring Processes in Expanding Laser-Produced Plasmas," NRL Memo Rept. 6154 (1988).
6) Ripin, B.H., et al., "Physics of Laser-Produced Interstreaming Plasmas,Laser Interaction and Related Plasma Phenomena, Vol 7 (Plenum, NY,1986), ed. H. Hora and G. Miley.
7) Obenschain, S.E., et al., "Uniform Ablative Acceleration of Targets by Laser Irradiation at $10^{14}$ W/cm$^2$," Phys. Rev. Lett., 50, 44 (1983).
8) Grun, J., et al., "Rayleigh-Taylor Instability Growth Rates in Targets Accelerated with a Laser Beam Smoothed by Induced Spatial Incoherence," Phys. Rev. Lett., 58, 2672 (1987).
9) Mostovych, A.N. and B. H. Ripin, private communications (1987).
10) Bernhardt, et al., "Observations and Theory of the AMPTE Barium Releases," J. Geophys. Res., 92, 5777 (1987).
11) Hassam, A.B., and J.D. Huba,"Structuring of the AMPTE Magnetotail Barium Release," Geophys. Res. Lett., 14, 60 (1987).
12) Ripin, B. H., et al., "Large Larmor Radius Inter-change Instability, "Phys. Rev. Lett., 59, 2299 (1987).
13) Ripin , B. H. , et al., "Large Larmor Radius Instability, " to be published (1988).
14) Sedov, L. I., Similarity and Dimensional Methods in Mechanics, (Academic Press, NY, 1959).
15) Stamper , J.A. , et al., "Aneurisms in Laser-Driven Blast-Waves, " Phys. Fluids, Nov. (1988).
16) Schmidt, G., Phys. Fluids, 3, 961 (1960); and Borovsky , J., "Limits on the Cross-Field Propaga-tion of Streams of Cold Plasma," Phys. Fluids, 30, 2518 (1987).
17) Mostovych , A. N., B. H. Ripin, and J. A. Stamper, "Resonant Diagnostics of Laser-Produced Barium Plasmas," Rev. Sci. Insts. (1988).

# APPENDIX EEE

## Jets in Laser-Produced Plasmas

For: Proceedings of the 19th European Conference
on Laser Interaction with Matter, Madrid
October 3-7, 1988

# JETS IN LASER-PRODUCED PLASMAS

C.K. Manka, T.A. Peyser, B.H. Ripin,
J.A. Stamper, J. Grun, J. Crawford,
A. Hassam, and J.D. Huba

Laser Plasma Branch, Plasma Physics
Division, Naval Research Laboratory,
Washington, D.C. USA

## ABSTRACT

Plasma jets have been produced by the focusing the NRL PHAROS III laser on the inside of small cylindrical targets. Large well defined jets are produced and persist over long distances and for surprisingly long times when strong magnetic fields are applied. The jets travel across several ion Larmor radii and are photographed in emission by a fast framing camera, dark field shadowgraphy and other diagnostics. Jet properties and parameters are presented and their relation to astrophysical plasmas is discussed.

## INTRODUCTION

Plasma jetting across magnetic field lines has been the subject of many investigations both theoretical and experimental. The jetting is usually attributed to the establishing of a *polarization E-field* which just compensates for the Larmor force from the B-field. The bulk plasma then travels essentially force free across the field lines. The purpose of the work reported here was to produce a highly directional plasma expansion that was symmetrical along an axis perpendicular to an applied magnetic field and to observe in detail the formation of jets and their subsequent evolution in both space and time.

## EXPERIMENT

The arrangement of the experiment and diagnostics is shown in Figure 1. The NRL PHAROS III laser was operated at a wavelength of 1.053 micron with energy in the range of 30 to 300 joules, pulse lengths of 2 to 4 ns FWHM and focal spot diameters of approximately 400 microns.

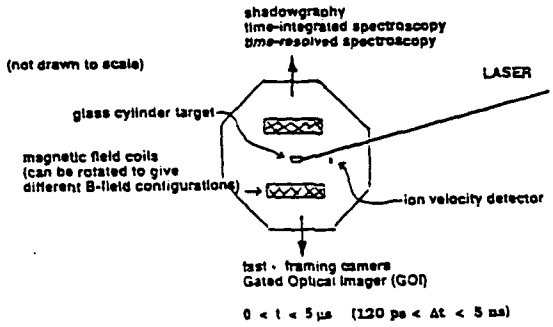



Figure 1. Schematic of the experiment arrangement and diagnostics for the jet studies.

An external magnetic field of up to 10 kG is applied by current pulsed through two coils in a Helmholtz configuration. The pulse is slow enough that the magnetic field does not change appreciably during the time that the plasma is observed.

The laser targets were glass cylinders 2 - 4 mm in length with 1 mm outer diameter and 40 micron thick walls. Inner and outer diameters were uniform to within 1 micron and the cylinders were mounted on very thin stalks. The laser was focused on the inside of one end of the cylinder at an angle of about 15 deg to the axis of the cylinder. The fast ablation plasma ($v = 10^7$ cm/s) travels across the cylinder in a time which is small compared to the time required for the disintegration of the relatively massive cylinder. Plasma expansion is symmetrical out the ends of the cylinder with the axial velocity higher than the transverse velocity.

The principle diagnostic is a fast Gated Optical Imager (GOI) framing camera which has framing (exposure) times selectable from 5 ns to 120 ps and the time at which the exposure was made could be delayed up to 10 us after the jets were produced. The GOI is sensitive to light of 350 -900 nm wavelength. Photographs were obtained on both Polaroid high speed positive film and on the new high dynamic range KODAK TX3200 negative film. Spatially resolved spectra were obtained using an optical multichannel analyzer and silicon linear arrays in both the time-integrated and 10 ns-gated mode. Time-of-flight ion detectors were also deployed.

## RESULTS

The time evolution the plasma jets is illustrated in Figure 2 for an applied magnetic field of 10 kG, Figure 3 for 6 kG and Figure 4 for 3 kG. The formation of long narrow jets is clearly evident, especially in the higher field cases in which the effect of the magnetic field constraining the plasma expansion is otherwise the largest. The long narrow jets have a characteristic velocity of 6 $x10^6$ cm/s only slightly less than the fast ablation plasma velocity. The jets are followed by slower plasma with a mean velocity of 2 x $10^6$ cm/s. It is this slower plasma which displays such dramatic structuring at later times. The "bumps and wiggles" observed on this bulk plasma over a range of magnetic field strengths appear similar to instabilities observed on astrophysical jets which are widely regarded as streams of collimated plasma originating in galactic nuclei.[1]

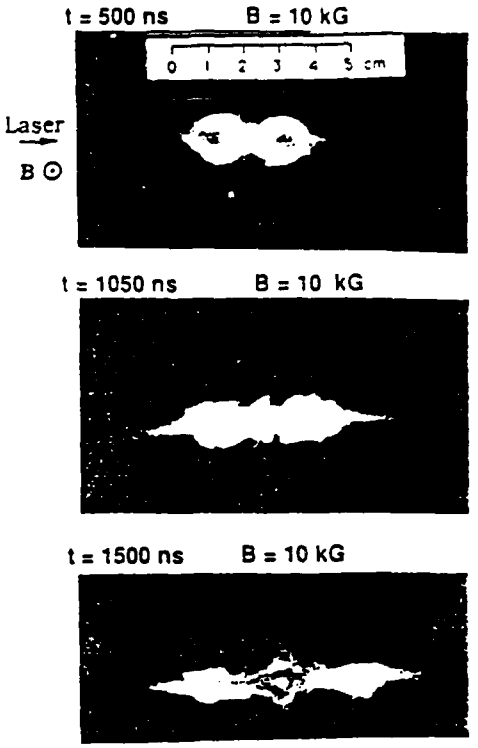



Figure 2. Time evolution of plasma jets at 10 kG. Long narrow jets are well defined.

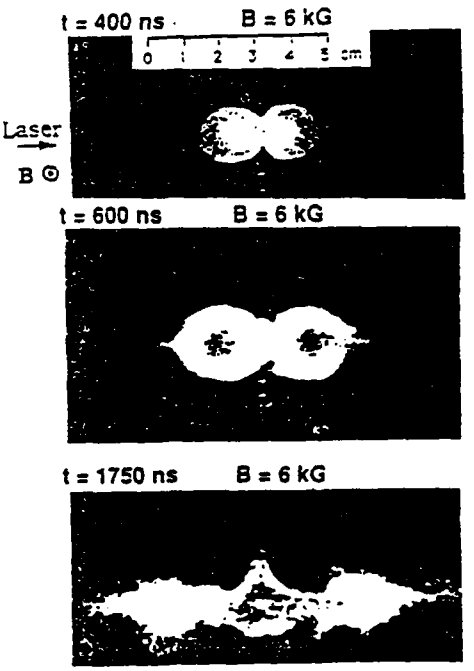



Figure 3. Time evolution of plasma jets at 6 kG. Jet formation is comparable to higher field example.

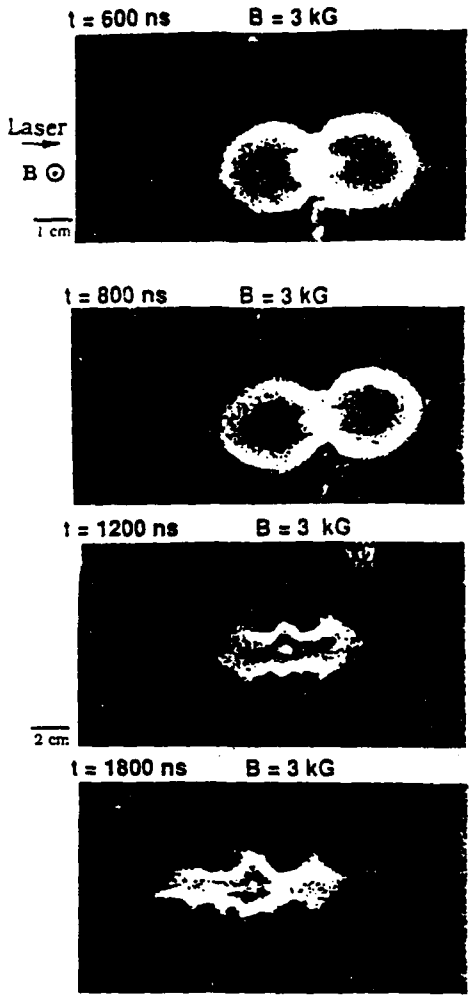



Figure 4. Time evolution of plasma jets at 3 kG. Jet formation is delayed as is onset of instability compared to higher field examples.

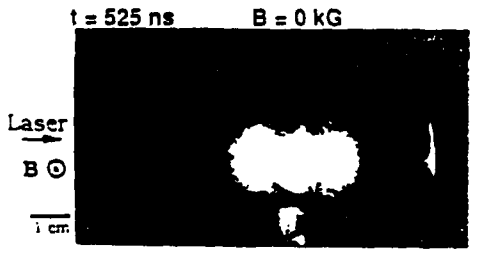



Figure 5. The plasma expansion at early time and zero magnetic field applied.

Jet formation and the onset of instabilities at fields of 1 kG and below was not observed. This may simply be that we have not observed sufficiently late in time to observe their development. Figure 5 presents the plasma expansion at zero field for comparison. The jets are not cylindrical in shape but rather expand along the magnetic field lines much more rapidly than transverse so that the jets are more fan shape. This is shown in Figure 6.

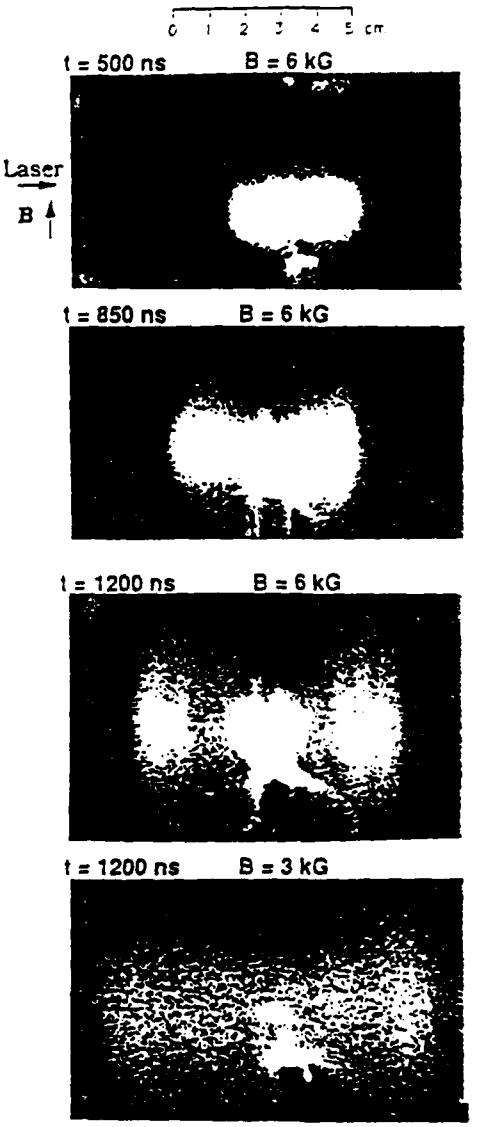



Figure 6. Plasma expansion along the field lines. The striations parallel to the applied field are spatially correlated with the structuring seen side-on due to plasma instabilities.

The expansion plasma parameters can be changed by plugging one end of the cylinder. Both the expansion velocity and plasma density out the one open cylinder end are thereby increased with the result that the structuring observed in the bulk plasma is greatly enhanced as shown in Figure 7.

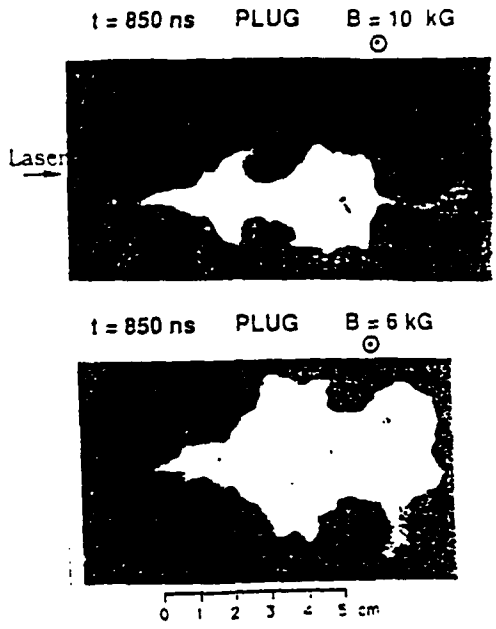



Figure 7. Increase in plasma structuring at two magnetic field strengths obtained by plugging one of the glass cylinder (right hand side).

## CONCLUSIONS

We have demonstrated a new technique for producing cross-field plasma jets which display dramatic structuring due to a number of possible plasma instabilities. Two possible plasma instabilities that may be relevant to the observed structuring are Kelvin-Helmholtz driven by velocity shear and Rayleigh-Taylor driven by magnetic field decleration of the plasma. Preliminary calculations sugggest that the Kelvin-Helmholtz instability may have a growth rate on the scale observed in the present experiment. Similar estimates of Rayleigh-Taylor growth rates also give values close to the experimental observations, however the framing photographs suggest the instability has more of the vortex roll-up character of classical Kelvin-Helmholtz as opposed to the spike and bubble morphology of Rayleigh-Taylor. While E X B drift explains the overall jetting, a more detailed picture must be developed to explain the onset of instabilities and their characteristic shapes.

## ACKNOWLEDGEMENTS

We would like to thank the following persons for their support and assistance: S. Obenschain, M. Pronko, J. Ford, L. Daniels, N. Nocerino, and L. Shirey. This work was supported by the US DNA.

[1] M.C. Begelman, R.D. Blandford and M.J. Rees, "Theory of extragalactic radio sources", *Reviews of Modern Physics*, **56**, 256 (1984).

# APPENDIX FFF

## Equilibrium of Solar Coronal Arcades

**Naval Research Laboratory**
Washington, DC 20375-5000




NRL Memorandum Report 6402

# Equilibrium of Solar Coronal Arcades

JOHN M. FINN* AND JAMES CHEN

*Geophysical and Plasma Dynamics Branch*
*Plasma Physics Division*

**Science Applications International Corporation*
*McLean, VA 22102*

**University of Maryland*
*College Park, MD 20742*

March 27, 1989

Approved for public release; distribution unlimited.

## CONTENTS


| | | |
|---|---|---|
| I. | INTRODUCTION | 1 |
| II. | LINEAR ARCADE EQUILIBRIA | 6 |
| III. | COMPUTATIONAL METHOD | 15 |
| IV. | DISCUSSION | 26 |
| V. | SUMMARY | 31 |
| | ACKNOWLEDGMENTS | 32 |
| | REFERENCES | 33 |
| | APPENDIX A | 35 |
| | APPENDIX B | 37 |
| | DISTRIBUTION LIST | 63 |

# EQUILIBRIUM OF SOLAR CORONAL ARCADES

## I. Introduction

Numerous fundamental issues remain unresolved concerning important energetic phenomena in the solar corona. For example, the possible mechanisms of solar flares, coronal mass ejections and various eruptive processes are not well understood. In these energetic events, energy release is manifested in the form of heating, radiation and/or mass motion in the coronal plasma. In addition, the corona evidently undergoes continual and pervasive (but perhaps less explosive) heating. Various theories have been proposed to explain these observed phenomena (for an overview, see, for example, Sturrock 1980). A substantial number of them assume that magnetic fields are the ultimate source of energy. This underlying assumption is strengthened by the recent observations (e.g., the Skylab mission, 1973) showing that the corona is a highly complicated system with magnetic fields and currents presumed to control the structuring and dynamics of coronal plasmas. As a result, it is important to understand the equilibrium and dynamical properties of magnetic structures in the corona.

In studying coronal magnetic fields, two dimensional magnetohydrodynamic (MHD) equilibrium models have received considerable theoretical attention. Such models are important both because of their relative simplicity and because many fundamental issues that arise in 2D may also exist in three dimensional systems. For example, linear arcades may be relevant to magnetic structures associated with neutral lines, where the normal component of the magnetic field $\mathbf{B}$ is zero. Such structures have been inferred from observations. An arcade may have a considerable amount of magnetic shear but typically varies weakly in the direction along the neutral line. As another example, cylindrically symmetric geometry has been used to model sunspot fields (Barnes and Sturrock 1972; Yang, Sturrock, and Antiochos 1986).

One frequently invoked scenario in which the magnetic energy of a structure in the corona is thought to be built up and stored is the following; as coronal magnetic field lines anchored in the photosphere are sheared, the structure evolves through a sequence of quasi-equilibrium configurations, stressing the field lines and building up magnetic energy. As the twist of field lines in the corona is increased, equilibrium limits may be exceeded, resulting in catastrophic loss of equilibrium and sudden

Manuscript approved January 26, 1989.

release of magnetic energy. This scenario is an appealing one because of the ubiquity of coronal magnetic fields. A similar scenario in which loss of equilibrium occurs as a result of increasing the pressure, a measure of the internal energy of the plasma, has also been suggested. The issues addressed in this paper pertain to sequences of equilibria and loss of equilibrium. We believe that these issues are relevant in both two- and three-dimensional structures.

In this paper we specialize to straight arcade equilibria such that $\partial/\partial z = 0$ for all variables. Figure 1 shows a schematic drawing of a linear arcade field line configuration. Such arcades have been studied in the context of quasistatic evolution of equilibria (Barnes and Sturrock 1972; Low 1977,1982; Jockers 1978; Birn, Goldstein, and Schindler 1978; Heyvaerts et al. 1982; Yang, Sturrock, and Antiochos 1986; Zwingmann 1987; Priest 1988; Klimchuk, Sturrock, and Yang 1988) as well as dynamical evolution (Wu, Bao, and Tandberg-Hanssen 1987; Mikic, Barnes, and Schnack 1988.) Figure 1 shows schematically the coordinate system and a representative field line. The field lines are labelled by the flux $\psi = A_z(x,y)$. The footpoints are displaced in z by an amount $d(\psi)$ in the photosphere S. We adopt the usual ideal MHD line-tying condition in the photosphere. Then, the footpoint displacement can be specified by plasma motion in the photosphere. Arcade equilibrium studies have been previously performed with the idea that magnetic energy $W = \int dV B^2/8\pi$ increases as the shear is increased and that because of this increase, MHD instability or loss of equilibrium is possible. A standard method for obtaining equilibrium solutions is to solve the Grad-Shafranov equation. The most natural approach to solving this equation for a linear arcade is to specify the axial component of the magnetic field $B_z(\psi)$ and/or the pressure $p(\psi)$. [In the following, when we write $p = p(\psi)$, we assume that the relevant length scales in the corona are smaller than the gravitational scale height in the corona.] Thus, in many of the earlier papers, loss of equilibrium, or bifurcation, has been studied in the context of arcade equilibria with $B_z$ specified (for an overview, see, for example, Birn and Schindler 1981). Another approach is to treat the equilibrium problem as a time dependent one involving Clebsch variables and introduce artificial viscosity or drag (Chodura and Schluter 1981; Yang, Sturrock and Antiochos 1986; Klimchuck, Sturrock and Yang 1988). This

"magneto-frictional" method allows the system to find a stable equilibrium for specified footpoint displacement.

By solving the Grad-Shafranov equation with prescribed axial field $B_z$, bifurcations have been found in the two-dimensional force-free limit (Jockers 1978). Having found multiple solutions, Jockers then pointed out that it may be more physically significant to specify the footpoint displacement rather than $B_z$ and that bifurcations may not exist with respect to specification of footpoint displacement $d(\psi)$. The reason is that, in the idealized limit of perfectly conducting photosphere and corona, the specified footpoint displacement can be conserved as the system adjusts to find its equilibrium, while the coronal plasma posseses no physical mechanism which can hold $B_z$ (or equivalently the transverse current perpendicular to z) fixed during this process. It also depends upon the assumption that inertia dominates magnetic forces in the photosphere ($\rho v^2/2 \gg B^2/8\pi$) and therefore the actual fields obtained in the arcade equilibrium do not influence the footpoint motion. In a recent comprehensive and detailed study, Zwingmann (1987) obtained sequences of arcade equilibria by varying footpoint displacement and pressure. The conclusion of this work is that no multiple solutions (i.e., bifurcations) exist if footpoint displacement is prescribed, confirming the suggestion of Jockers (1978), but that multiple solutions do exist if pressure $p(\psi)$ is prescribed. Thus, it was argued that the onset conditions for solar eruptive processes might be determined by bifucations with respect to increasing the pressure. In this work, Zwingmann used an iteration method developed by Keller (1977). Priest (1988) has also suggested that if the pressure is increased beyond a certain critical point, eruptive motion (e.g., coronal mass ejections) may result due to loss of equilibrium. Recently, Klimchuck, Sturrock and Yang (1988) also found that the magnetic energy of a linear dipole field increased indefinitely with increasing footpoint shear.

Clearly, it is important to distinguish between specifying $B_z(\psi)$ and specifying footpoint displacement $d(\psi)$ because the bifurcation properties are completely different. An analogous distinction exists between specifying the pressure $p(\psi)$ and specifying the entropy $s(\psi)$, both quantities being measures of internal energy of the plasma. The entropy can be defined in terms of the heat contained between flux surfaces (Sec. II).

In the limit of adiabatic coronal plasma, the entropy is a conserved quantity. In the corona, we expect perpendicular thermal conduction to be smaller than parallel conductivity and different flux surfaces are effectively thermally isolated. If, in addition, the parallel heat flux between the corona and the photosphere is small enough, then the corona is thermally isolated along the field lines from the photosphere. If these conditions are satisfied, then the adiabatic limit may be approximately valid and the entropy $s(\psi)$, like the footpoint displacement, is conserved as the system adjusts to find its equilibrium. Here, it is implicitly assumed that the Alfven speed or magnetosonic speed is sufficiently fast that radiation and thermal conduction to the photosphere are negligible on the time scale of relaxation to equilibrium. We also discuss in Sec. II an alternative limit of an isothermal model, corresponding to clamping of temperature by radiative processes or by parallel thermal conduction. This limit has essentially the same mathematical form as the adiabatic limit, but with adiabatic index of unity. In contrast, it appears that there is no such limiting case, arising from a reasonable energy equation for the coronal plasma, in which the pressure $p(\psi)$ is conserved as the flux surfaces adjust themselves to find an equilibrium.

In the present paper, we present a method to solve the Grad-Shafranov equation for linear arcades with prescribed footpoint displacement $d(\psi)$ or entropy $s(\psi)$. Using this technique, we consider the bifurcation properties of equilibrium arcades. We find that no multiple solutions exist if $d(\psi)$ is increased, in agreement with Zwingmann (1987). However, we find that there are no multiple solutions if the entropy $s(\psi)$, rather than the pressure, is specified. In situations where the entropy rather than the pressure is to be specified, the bifurcations with respect to the pressure are of mathematical rather than physical significance.

We also consider questions regarding the formation of sheet current in "open field configurations" which have been postulated as the limit of infinite footpoint displacement (Barnes and Sturrock 1972; Yang, Sturrock, and Antiochos 1986; Aly 1984, 1985). This configuration is a potential field ($\mathbf{j} = 0$) except along the current sheet. The development of sheet currents ("tangential discontinuities" of the magnetic field) has been an active area of investigation since it was suggested by Parker (1972, 1983) as a possible source of coronal heating. See also van Ballegooijen (1985),

Zweibel and Li (1987), Low and Wolfson (1988) and Antiochos (1988). We find that as $d(\psi)$ is increased, the current density $j_z$ does become more peaked but that the maximum value of $j_z$ increases only slowly, if at all, with footpoint displacement, and that, relative to the total current $I_z$, a decreasing fraction of current is carried by the current peak. We conclude that the field does not approach the postulated open field configuration. By the same token, if the entropy $s(\psi)$ is increased, the current density $j_z$ becomes increasingly peaked but a decreasing fraction of current is carried by the peak relative to the total current $I_z$.

In Sec. II we formulate the MHD equilibrium problem for a straight arcade with pressure and gravity. We discuss the specification of footpoint displacement and entropy and relate the former to the familiar Clebsch representation for fields. In Sec. III, we discuss the computational method used to obtain the equilibria when footpoint displacement or entropy is prescribed. We then show results obtained by this method for various profiles of photospheric flux, footpoint displacement, and entropy. We compare these results with some simple analytic cases and show estimates based upon scaling for large footpoint displacement or entropy. The relevance to the formation of a sheet current as $d \to \infty$ or $s \to \infty$ is discussed. Sec. IV contains discussions of the results and their significance to coronal observations. The salient results are summarized in Sec. V.

## II. Linear Arcade Equilibria

### a) Basic Equations

The geometry considered in this paper is that of a linear arcade with a straight neutral line. We choose coordinates as shown in Fig. 1, with $\hat{e}_y$ the unit vector normal to the surface S(y = 0) corresponding to the photosphere and x labelling the non-ignorable direction in S. We adopt the usual assumption that the corona has infinite electrical conductivity (on the time scales of interest) and that the photosphere is infinitely conducting and massive. Then, the field line footpoints are line-tied in the surface S. In such a geometry where z is the ignorable direction, the magnetic field can be represented by

$$\mathbf{B} = \nabla\psi \times \hat{e}_z + B_z\hat{e}_z \ , \tag{1a}$$

where the flux function $\psi(x,y)$ is the z-component of the vector potential. The current density $\mathbf{j} = \nabla \times \mathbf{B}$ (in normalized units $c/4\pi = 1$) is then given by

$$\mathbf{j} = \nabla B_z \times \hat{e}_z - \nabla^2\psi\hat{e}_z \ . \tag{1b}$$

Including the effects of pressure p and gravity, the equation of motion is

$$\mathbf{j} \times \mathbf{B} - \nabla p - mgn\hat{e}_y = 0, \tag{2}$$

where n is the ion (or electron) density and m is the ion mass. The component of eq. (2) in the z-direction gives $\mathbf{B}\cdot\nabla B_z = 0$ which implies

$$B_z = B_z(\psi). \tag{3}$$

The quantity $B_z(\psi)$ can be related in a simple manner to the transverse current per unit length in the z direction. Consider a closed path around a rectangle defined by $\psi_1 < \psi < \psi_2$, $0 < z < L$ on the photospheric surface (S). Ampere's law $\oint \underline{B} \cdot d\underline{l} = I$ then yields $[B_z(\psi_1) - B_z(\psi_2)]$ as the transverse current per unit length in z flowing between the flux surfaces $\psi = \psi_1$ and $\psi = \psi_2$. Writing the pressure, temperature and density as functions of the nonorthogonal coordinates $\psi$ and y, we find that the component of eq. (2) parallel to $\underline{B}$ leads to

$$\frac{\partial}{\partial y} p(\psi,y) = - \frac{mgp(\psi,y)}{2kT(\psi,y)} \tag{4a}$$

where k is Boltzmann constant, T is the electron temperature and m is the ion mass. This equation can be solved to give

$$p(\psi,y) = p(\psi,0)\exp\left(- \frac{mg}{2k}\int_0^y \frac{dy'}{T(\psi,y')}\right) . \tag{4b}$$

For the special case $T = T(\psi)$, we find

$$n(\psi,y) = n_o(\psi)\exp[- mgy/2kT(\psi)]. \tag{4c}$$

Here, $p(\psi,0)$, $n(\psi,0)$ are the pressure and density on S. Equation (4a) simply states that the plasma is in hydrostatic equilibrium along the field lines. Substituting eqs. (3) and (4b) in the $\nabla\psi$ component of eq. (2) leads to the Grad-Shafrarov (G-S) equation

$$\nabla^2\psi = - \lambda(\psi)B_z(\psi) - \frac{\partial p}{\partial \psi} , \tag{5a}$$

where

$$\lambda(\psi) \equiv \frac{dB_z}{d\psi} ,$$

and

$$p(\psi,y) = 2n(\psi,y)kT(\psi,y). \qquad (5b)$$

In the remainder of this work, we adopt the assumption that y is much smaller than the gravitational scale height in the corona h = 2kT/mg so that force balance along the field lines is achieved by having pressure constant along the field lines in the corona, giving $p = p(\psi)$. We will also assume that paralle thermal conduction dominates in the corona (but not in the transition zone, chromosphere, or the photosphere) so that $T = T(\psi)$. It follows from eq. (5b) that density is also constant along field lines, $n = n_0(\psi)$. An important special case occurs if the plasma beta $\beta = 2p/B^2$ is small, giving the force free condition $p = 0$.

The boundary conditions which we specify on eq. (5) are that the flux $\psi(x,0)$ is given on the surface S and is assumed to be constant (zero, without loss of generality) for $(x,y) \to \infty$. This, of course, determines the component $B_y = -\partial\psi(x,0)/\partial x$ normal to S. In practice, these conditions are replaced by those specifying $\psi(x,0)$ for a finite interval $0 < x < a$ on S and by requiring $\psi$ to be zero on the surfaces $x = 0$, $x = a$ and $y = L$. See Figure 2. We will return to the implications of these boundary conditions on a box of finite size (in x,y) in Sec. III. Mathematically, the G-S equation (5) is usually posed as a nonlinear boundary value problem by specifying the nonlinear functions $B_z(\psi)$ and $p(\psi)$. This specification can lead to multiple solutions (bifurcations). However, it was suggested by Jockers (1978) that $B_z$ is not a physically specifiable quantity in the corona and that bifurcations may not exist if the footpoint displacement is specified. This point was recently demonstrated by Zwingmann (1987), who also found bifurcations with respect to specifying the pressure $p(\psi)$.

b) Specifiability of Physical Quantities

In this section, we discuss the specifiability of a number of physical quantities. For this purpose, it is helpful to use an imaginary two-step process. Consider a system in equilibrium (e.g., $\underline{j} \times \underline{B} = 0$). Suppose a physical quantity (e.g., footpoint displacement) is changed holding all other quantities fixed (first step). Then the system is no longer in equilibrium and it must relax to a new equilibrium (second step). If the

physical quantity in question is a conserved quantity during the relaxation process, then it retains the given value after reaching the new equilibrium. Such a conserved quantity can be specified. If, on the other hand, the quantity is not a conserved quantity, then it also changes during the relaxation process so that it cannot be held fixed. In this case, a specified value need not be attainable.

For example, if the footpoint displacement is increased from that of an initial equilibrium, then it is a constant of the motion in the subsequent relaxation motion of the plasma in the limit where the photosphere is assumed to be infinitely conducting and infinitely massive. It is mathematically allowable to compute equilibria by specifying $B_z(\psi)$. However, if $B_z$ is increased from that of an equilibrium, the coronal plasma cannot hold it fixed during relaxation to a new equilibrium. It is not a constant of the motion under ideal MHD motion. That is, a specified value of $B_z$ need not be attainable from the initial equilibrium. If one is to study quasi-static response to a slow photospheric motion, slow enough so that the coronal inertia is negligible, then the footpoint displacement, rather than $B_z$, must be specified.

The internal energy of a volume of plasma can be represented by the pressure p or entropy s (to be defined below). If the entropy of an initial equilibrium is increased, then it is conserved in the relaxation process in the limit where the plasma is assumed to be adiabatic on the relaxation time scale. That is, there exists a limit in which the plasma can be described by an equation conserving the entropy (eq. [6d]). However, no conservation law based on a reasonable energy equation has been identified in which the pressure is conserved and which is suitable for the coronal environment. A third limit which may be relevant to the corona is the isothermal limit.

In reality, coronal plasmas need not correspond strictly to any of the limiting cases, in which case none of the physical quantities discussed would be specifiable rigorously. Specification of a quantity is physically meaningful only in a suitable limit in which the quantity is a conserved constant of the motion. Nevertheless, it may still be useful to adopt one or more of the limiting assumptions and explore theoretical issues. In the next section, we discuss the limiting conditions under

which the above quantities are conserved. Additional physical implications of specifiability are discussed in Sec. IV.

c) Footpoint Displacement and Entropy

By integrating the z-component of the field line equations $d\underline{x}/ds = \underline{B}/B$ (ds measures arc length along the magnetic field) from footpoint 1 to footpoint 2, we find

$$d(\psi) = B_z(\psi)V'(\psi), \tag{6a}$$

where

$$V'(\psi) \equiv \int_1^2 ds/B \tag{6b}$$

Here, $V(\psi) = \int dxdy = \int ds_p d\psi/|\nabla\psi| = \int ds d\psi/B$, where $ds_p$ measures arc length in the transverse plane. The quantity $V(\psi)$ is proportional to the area in the x-y plane enclosed by the flux surface labelled by $\psi$ and $V'(\psi) = dV/d\psi$, so that $V'(\psi)d\psi$ is the volume per unit length in the z direction between the flux surfaces labelled $\psi$ and $\psi + d\psi$. Also, if we define $\Phi(\psi) = \int dxdy B_z$ to be the axial flux bounded by the flux surface labelled by $\psi$ and the photosphere, then we find from eq. (6a)

$$d(\psi) = \frac{d\Phi}{d\psi} .$$

During the process of increasing $d(\psi)$ with respect to time, the velocity $v_z$ produces a tangential electric field $E_x = v_z B_y$ on S, which is responsible for the change of $\Phi$ in time. Thus, the footpoint displacement is directly specifiable through the boundary conditions and is a constant of motion in any process in which the plasma relaxes to equilibrium on a time scale faster than the time scale for the change in footpoint displacement. We point out that Clebsch variables have also been used in specifying footpoint displacement (e.g., Yang, Sturrock, and Antiochos 1986; Klimchuck, Sturrock, and Yang 1988). See Appendix A.

If we assume that the coronal gas is an ideal gas, then the entropy $\sigma'(\psi)d\psi \equiv (d\sigma/d\psi)d\psi$ of this volume is such that

$$\sigma'(\psi) = Q\ln(pV'^{\gamma})$$

where the contribution $\gamma Q\ln(d\psi)$ has been dropped because only the difference in entropy is significant. Here, $\gamma = 5/3$ is the adiabatic index. For convenience, we will refer to the following quantity $s(\psi)$ as "entropy" in this paper but the above relationship is understood;

$$s(\psi) = p(\psi)[V'(\psi)]^{\gamma} . \tag{6c}$$

Then $s(\psi) = \exp[\sigma'(\psi)/Q]$.

In our formulation, the entropy $s(\psi)$ replaces the pressure $p(\psi)$ as the specified quantity. It can be shown that the entropy is conserved in MHD directly without resorting to thermodynamic considerations. Specifically, the entropy is conserved by adiabatic motions satisfying the adiabatic law

$$\frac{\partial p}{\partial t} + \underset{\sim}{v}\cdot\nabla p + \gamma p\nabla\cdot\underset{\sim}{v} = 0. \tag{6d}$$

This is easily seen by noting that $p^{1/\gamma}$ satisfies the same continuity equation as the density $\partial n/\partial t + \nabla\cdot(n\underset{\sim}{v}) = 0$. Then, the quantity $S \equiv \int p^{1/\gamma}dV$ is conserved if there is no transport of plasma across the flux surfaces. This condition holds if the plasma satisfies ideal MHD so that the flux surfaces move the the fluid. Here, the integral is over the volume between any two flux surfaces. If we take a small volume $\delta V$ between two closely spaced flux surfaces at $\psi$ and $\psi + \delta\psi$, then $\delta V$ is proportional to $V'(\psi)\delta\psi$. Therefore, S is equal to $p(\psi)^{1/\gamma}V'(\psi)\delta\psi$. Since $\delta\psi$ is conserved for ideal MHD motions, the entropy $s(\psi) \equiv S^{\gamma}/\delta\psi^{\gamma}$ is conserved for an adiabatic process. Grad, Hu, and Stevens (1975) have developed algorithms to specify

entropy in toroidal systems. In the arcade geometry treated here, an additional assumption of negligible heat flux to the photosphere is required. As in the justification for specifying footpoint displacement, the entropy is the directly specifiable response to varying the internal energy of the plasma in the adiabatic limit. Note that pressure is not conserved in adiabatic processes. In the following discussion, we will adopt the scenario in which the internal energy of the plasma is specified by specifying the entropy $s(\psi)$.

In the isothermal limit, the temperature remains fixed (perhaps by some radiative proces) during the relaxation to equilibrium. An isothermal plasma obeys a relationship similar to eq. (6c). If the mass $M(\psi)$ contained under each flux surface is conserved (no photospheric sources), then $M'(\psi) = mn(\psi)V'(\psi)$ may be specified, where

$$M(\psi) = m\int n(\psi)\frac{d\psi ds}{B} .$$

Mathematically, it is simple to see (Appendix B) by comparing eqs. (6a) and (6c) that $p(\psi)$ can be identified with $(1/2)B_z(\psi)^2$ and $s(\psi)$ with $(1/2)d(\psi)^2$, having $\gamma = 2$ and $\gamma = 5/3$, respectively, a rather insignificant difference. For the isothermal case, $s(\psi)$ is replaced by $M'(\psi)$ with $\gamma = 1$.

d) Simple Analytic Equilibria

We now illustrate some basic physical features of equilibrium solutions of eq. (5) using force-free examples. A particularly simple example can be given by the form $B_z(\psi) = \lambda_0\psi$ where $\lambda_0$ is a constant. Then, the G-S equation (eq. [5a]) reduces to the Helmholtz equation

$$\nabla^2\psi + \lambda_0^2\psi = 0. \qquad (7)$$

Solutions confined to $0 < x < a$ with $\psi(0,y) = \psi(a,y) = 0$ but extending to $y = \infty$ $(0 < y < \infty)$ have the form

$$\psi = \psi_o \sin\left(\frac{n\pi x}{a}\right) e^{-k_n y}, \tag{8}$$

with $k_n = [(n\pi/a)^2 - \lambda_o^2]^{1/2}$. This equilibrium is the two-dimensional, linear arcade analogue of the Lundquist (1951) solution (one-dimensional, cylindrical geometry) and has been used by Heyvaerts and Priest (1984) in a model for coronal heating. If the flux on the surface S is taken to be $\psi(x,0) = \sin(\pi x/a)$, then only $n = 1$ occurs. In this case, the imposed $\lambda_o$ must satisfy $k_1^2 > 0$ or $\lambda_o < \lambda_c \equiv \pi/a$. That is, if it were physically reasonable to specify $\lambda_o$ [$B_z(\psi) = \lambda_o \psi$], then one might expect to encounter a violent loss of equilibrium as $\lambda_o$ is increased past $\lambda_c = \pi/a$.

Using eq. (6a), we obtain

$$d(\psi) = B_z(\psi) \int_{x_1}^{x_2} \frac{dx}{B_x} \tag{9a}$$

$$= -\frac{2\lambda_o}{k_1}(x - x_o), \tag{9b}$$

where $x_o = a/2$ is the point where $\psi$ is maximum ($\psi = \psi_o$) on S with $B_y = 0$, and $x = x(\psi)$ is the inverse of $\psi = \psi(x,0)$. Also, $x_1$ and $x_2$ are the x values where the flux surface labelled by $\psi$ crosses the photosphere. The footpoint displacement d is linear in x and the maximum in magnitude of d occurs at $x = 0$, $x = a$ and equals

$$d_{max} = \frac{\lambda_o a}{\left[(\pi/a)^2 - \lambda_o^2\right]^{1/2}} \tag{10a}$$

Since the <u>form</u> of $d(\psi)$ is unchanged by $\lambda_o$, we can consider $d_{max}$ to be specified and $\lambda_o$ to be computed after the fact:

$$\lambda_o = \left(\frac{d_{max}}{a}\right) \frac{\pi}{\left(a^2 + d_{max}^2\right)^{1/2}} . \tag{10b}$$

Since the maximum of $B_z$, $(B_z)_{max}$, equals $\lambda_o\psi_o$, we can consider eq. (9) to be a computation of $d(\psi)$ when $B_z(\psi)$ is specified and eq. (10b) to be a computation of $B_z(\psi)$ when $d(\psi)$ is specified. In the latter case, no equilibrium catastrophe is reached; as $d_{max} \to \infty$, $\lambda_o$ merely increases, approaching the limiting value $\lambda_c = \pi/a$. This model is illustrative, especially since it also shows the relationship between $d_{max} \to \infty$ and vertical flux surface expansion, which is equivalent to $k_1 \to 0$ (see eq. [8]). However, it has two special properties that do not hold in general; (i) $\lambda_o$, or equivalently $(B_z)_{max}$, monotonically increases with $d_{max}$ and (ii) the form of $B_z(\psi)$ does not change as $d_{max}$ changes with the form of $d(\psi)$ fixed.

## III. Linear Arcade Equilibria

### a) Some General Properties

In this section, some general properties of force-free configurations are discussed. First, we point out that an arcade equilibrium on the half space $-\infty < x < \infty$, $y > 0$ with flux $\psi$ and footpoint displacement $d(\psi)$ specified on the x-axis, must have a surrounding region of potential field with $\lambda(\psi) = dB_z/d\psi = 0$ or at least with $B_z$ and $dB_z/d\psi$ approaching zero sufficiently fast as $(x, y) \to \infty$. The footpoint displacement in the our model is such that $d \to 0$ as $x \to \pm\infty$, representing an arcade whose footpoint shear is confined to a finite extent in x in the photosphere. For this type of arcades, $\lambda(\psi)$ cannot be constant everywhere or asymptotically approach a non-zero constant. This can be seen by the following consideration. Here, we specialize to the case in which $\psi(x,0)$ is an even function about $x = 0$, monotonically decreasing for $x > 0$. Without loss of generality, we may demand that $\psi(x,0) \to 0$ as $x \to \pm\infty$. As a concrete example, assume $B_z(\psi) = \lambda_0\psi + B_0$, where $B_0$ is the $B_z$ field at infinity. Suppose $\lambda_0 \neq 0$ so that $dB_z/d\psi \neq 0$ for all x. Now, suppose, for contradiction, that $B_0 \neq 0$. Then, $V'(\psi)$ becomes infinite for $\psi \to 0$ as $(x, y) \to \infty$. This implies (eq. [6a]) that, if $B_0 \neq 0$, then an infinite footpoint displacement $d(\psi)$ must result as $x \to \pm\infty$ and $\psi \to 0$. Therefore, the outermost flux surfaces must have $B_z = B_0 = 0$ at $x = \pm\infty$ if $d(\psi)$ is to vanish. Thus, we set $B_0 = 0$. Then, eq. (5a) leads to $\nabla^2\psi + \lambda_0^2\psi = 0$. If $\phi(k)$ is the Fourier transform of $\psi(x,0)$, the solution takes the form

$$\psi(x,y) = \int_{-\infty}^{\infty} dk\phi(k)\cos(kx)e^{-\mu(k)y} \tag{11}$$

where $\mu(k) = (k^2 - \lambda_0^2)^{1/2}$. Note that

$$\int_{-\infty}^{\infty} dx\psi(x,0)\cos(kx) = 2\pi\phi(k).$$

Since $\psi(x,0)\cos(kx)$ is even in x, $\phi(k)$ is nonzero in general. In particular, $\phi(k)$ is nonzero for $k < \lambda_0$. The solution must then be oscillatory. This physically unacceptable behavior occurs because of the

supposition $\lambda_0 \neq 0$. For a more general case with arbitrary $B_z(\psi)$, the above argument shows that $\lambda(\psi) = dB_z/d\psi$ must approach zero as $\psi \to 0$. If, say $\lambda(\psi)$ is assumed to be a constant $\lambda_0 \neq 0$ in some region $y > y_c$, then the above argument applies to the region $-\infty < x < \infty$, $y > y_c$, again with the result that $\psi$ cannot be well behaved for $y \to \infty$. This is a generalization to the half-space with line-tying of the well known virial theorem that a plasma cannot be confined by its own fields. As another example of virial theorem application, we note that if there is no potential field surrounding the localized $j \neq 0$ region, then the structure cannot be force-free and the pressure must be lower in that region than in the surrounding region. This has been shown for a three-dimensional "toroidal" solar current loop structure (Xue and Chen 1990). Note that an earlier example of a force-free field without a surrounding potential field (Low 1977) is a configuration in which the footpoint displacement has an infinite extent in the photosphere and asymptotically approaches a finite maximum at $x = \pm\infty$.

b) Effects of Finite Computational Domains

As mentioned earlier, the boundary conditions are that $\psi(x,0)$ is specified for $0 < x < a$ on S, and $\psi = 0$ on the remaining three surfaces; the two side walls at $x = 0$, $x = a$, and the top wall at $y = b$. The flux $\psi(x,0)$ is chosen to be even about $x = a/2$ so that the maximum value $\psi_0$ occurs at $x = a/2$ and $\psi$ decreases monotonically to zero at $x = 0$ and $x = a$. We consider a current-carrying plasma confined away from the side and top walls. Let the outermost flux surface of the current-carrying region be $\psi = \psi_v$. This surface intersects the surface S at $x = x_v$ and $x = a-x_v$ where $x_v = x(\psi_v)$. The flux surfaces outside this region ($\psi < \psi_v$) are then potential flux surfaces. Based on the arguments of the preceding section, we specify $d(\psi)$ to be zero (thus $B_z = 0$) on the potential flux surfaces. For $\psi_v = 0$, the current fills the entire box. Then a force-free configuration is supported by the walls and the form of $B_z(\psi)$ for specified $d(\psi)$ will be seriously modified. For larger $\psi_v$, a force-free structure is supported by the surrounding potential flux, which in turn is supported by the walls. If $\psi_v$ is sufficiently large, then the interface surface $\psi = \psi_v$ is sufficiently far from the walls and its shape is determined by the

actual force balance requirement. In this section, we will discuss the generic effects of the finiteness of the computational domain on the solution. Hereafter, we use dimensionless variables with x,y, $d(\psi)$ scaled to a ($0 < x < 1$). The flux function $\psi$ is scaled to its maximum $\psi_o$, $B_z$ is scaled to $\psi_o/a$, and p is scaled to $\psi_o^2/a^2$.

We expect the general form of $d(\psi)$ to be linear in x near the neutral line at $x = a/2$ [as it is in eq. (9b)] and vanish as the potential region is approached. Clearly, $d(\psi)$ must vanish at $x = a/2$ because the field line has zero length there. Furthermore, if the magnetic field is regular in that vicinity, then d is linear in x unless $B_z$ is finite and <u>both</u> components $B_x$ and $B_y$ vanish at $x = a/2$, $y = 0$. Otherwise, an 0-point rises above the boundary surface S. This is inconsistent with specifying $d(\psi)$; if an 0-point forms, then d must have a step function discontinuity.

As a first example, we have computed force-free equilibria with d(x) of the form

$$d(x) = d_o\left(x - \frac{a}{2}\right) \tanh\left[\frac{(x - x_v)}{W(a/2 - x_v)}\right] \qquad \begin{matrix} x_v < x < a/2 \\ (\psi > \psi_v), \end{matrix} \tag{12a}$$

$$= 0 \qquad \begin{matrix} x < x_v \\ (\psi < \psi_v) \end{matrix} \tag{12b}$$

and anti-symmetric about $x = a/2$. The G-S equation is solved iteratively for specified $d(\psi)$. The computational method is described in Appendix B. In Figure 2a, we show the flux surfaces for a representative equilibrium. We have used $\psi(x,0) = \psi_o \sin(\pi x/a)$ with $\psi_o = 1$, the height of the integration box $b/a = 2$, and $\psi_v = 0.195$, for which $x_v = 0.0625$. The maximum footpoint displacement is specified to be $d_{max} = 1.85$ and we have chosen $W = 0.1$. The coefficient $d_o$ is adjusted so that the specified value of $d_{max}$ is obtained. The short-dashed contour corresponds to $\psi = \psi_v$ where $j_z = 0$ and $d = 0$. All the current is contained inside ($\psi > \psi_v$) the $\psi = \psi_v$ surface. Thus, the outer boundary surface of the $\mathbf{j} \neq 0$ region is removed from the computational box by a moderate amount. The long-dashed contour corresponds to the flux surface $\psi = \psi_w$, defined to be the flux surface such that $d(\psi_w) = d_{max}/2$. (For this example, we have $d(\psi_w) = 0.92$, $x_w = 0.08$, and $\psi_w = 0.25$.) The bulk of the current is actually enclosed by this surface, farther away from the walls than the $\psi_v$ surface. Figure 2(b)

shows the footpoint displacement profile. (This figure shows d only for $0 < x < 0.5$. The overall sign is reversed from that of eq. [12a] for convenience.) The above form has the general feature that the anti-symmetric footpoint displacement is zero for $0 < x < x_v$ with most of the footpoint displacement shear concentrated in $x_v < x < x_m$ where $x_m \simeq x_v + W(a/2 - x_v)$ is where the maximum footpoint displacement $d_{max} = d(x_m)$ occurs. In $x_m \lesssim x \lesssim (a - x_m)$, $d(x)$ is essentially linear so that field lines on different flux surfaces are parallel and unsheared. For larger values of W, the footpoint displacement shear is less concentrated.

In Fig. 2(c), we have plotted $B_z(\psi)$ versus $\psi$ for $0 < \psi < 1$. (Recall that on the surface S, $\psi = 0$ for $x = 0$ and $x = 1$, and $\psi(x=0.5, y=0) = \psi_o = 1$.) We see that $B_z(\psi)$ is linear in $\psi$ near $\psi_o$ and deviates from linearity in the region of maximum shear in the footpoint displacement. In Fig. 2(d), we show $\lambda(\psi) = dB_z/d\psi$ as a function of $\psi$. As expected, $\lambda(\psi)$ has its maximum variation in the region of maximum shear in $d(\psi)$.

In Fig. 3, the quantity $(B_z)_{max} \equiv B_z(x=0.5,y=0)$ is plotted as a function of $d_{max}$ for a number of model equilibria. Curve 1 is a plot of eq. (10b), a linear force-free configuration confined horizontally to $0 \lesssim x \lesssim 1$ but extending vertically to $y = \infty$. For this system, $(B_z)_{max}$ (thus $\lambda_o$) is linear in $d_{max}$ for small $d_{max}$ and asymptotically approaches $\pi/a$ as $d_{max} \to \infty$. For small $d_{max}$, $V'(\psi)$ is, to lowest order, the value for the potential field ($d_{max} = 0$) and $(B_z)_{max}$ is proportional to $d_{max}$ (see eq. [6a]). For $d_{max} \to \infty$, on the other hand, the increase in $d_{max}$ causes an expansion of flux surfaces, i.e. an increase in $V'(\psi)$, with $(B_z)_{max}$ approaching a constant. Curve 2 of Fig. 3 is for the solution of eq. (7) for a finite height b, where the boundary condition is $\psi(x, y=b) = 0$. The equilibrium can be described analytically by

$$\psi(x,y) = \sin\left(\frac{\pi x}{a}\right)\sinh k_1(b-y)/\sinh k_1 b, \qquad (13)$$

where $k_1 = [(\pi/a)^2 - \lambda_o^2]^{1/2}$ for $\pi/a > \lambda_o$. For $\lambda_o > \pi/a$, eq. (13) is replaced by

$$\psi(x,y) = \sin\left(\frac{\pi x}{a}\right)\sin k_1(b - y)/\sin k_1 b, \qquad (14)$$

where $k_1 = [\lambda_o^2 - (\pi/a)^2]^{1/2}$. For this equilibrium of finite height, the

functional form of $d(\psi)$ (not merely the amplitude $d_{max}$) changes with $\lambda_o$ so that, unlike the infinite height equilibrium given by eq. (8) or eq. (10b) (curve 1), specifying $\lambda_o$ or $(B_z)_{max}$ is not essentially equivalent to specifying $d_{max}$. For the infinite height case, eq. (9b), the profile of d remains linear in x and that of $B_z$ linear in $\psi$ for all values of $\lambda_o$, or equivalently, for all values of $d_{max}$. Nevertheless, the curves 1 and 2 are similar. Curve 2, however, shows that $(B_z)_{max}$ (or $\lambda_o$) can increase beyond the limit $\lambda_o \to \pi/a$, in contrast with curve 1. For curve 2, the finite height (b) of the box prevents the flux surfaces from expanding freely as $d_{max} \to \infty$. In this case, $V'(\psi)$ cannot increase without bounds and $d_{max}$ can increase only through an increase in $(B_z)_{max}$ (see eq. [6a]). However, for this equilibrium, the flux function $\psi$ takes the form of eq. (14) for $\lambda > \pi/4$ and an O-point appears at $x = a/2$ above the surface S ($y > 0$) if $k_1 b > \pi/2$, or $\lambda_o > (\pi/a)(1 + a^2/4b^2)^{1/2}$. For $b/a = 2$, the parameter used in curves 2 and 3, this gives $\lambda = 3.24$. We have not attempted to extend $d_{max}$ past this point. Curve 3 is the equilibrium for a footpoint displacement profile given by eq. (12a) with $\psi_v = 0.195$ and $W = 0.1$, the equilibrium shown in Fig. 2a. This equilibrium is numerically computed in the same finite box as for curve 2. As in curve 2, $(B_z)_{max}$ increases past $\pi/a$ as $d_{max}$ increases, albeit slowly, because of the finite size of the computational domain. Presumably, $(B_z)_{max}$ continues to increase, at a faster rate with respect to $d_{max}$, as $d_{max}$ increases further. However, the non-zero current region (inside the short-dashed flux surface in Fig. 2a) is detached from the side walls (and the region $\psi_v < \psi < \psi_w$ has less current than in Fig. 2a). Thus there is relatively more room to expand than in the configuration described by curve 2. This flexibility for the flux surfaces to expand against the potential flux surfaces is responsible for the smaller values of $(B_z)_{max}$ for large $d_{max}$. The difference in the slopes of curve 3 and curve 1 (or curve 2) is not physically significant, but is related to the fact that $d_{max}$ itself has a different meaning for the two very different profiles of $d(\psi)$, given by eq. (9b) and eq. (12). Curve 3 shows that the numerically computed equilibrium solutions whose current-carrying regions are only slightly removed from the walls are similar to the analytic solutions in which the current-carrying plasmas fills the finite box. The main effect of the walls is to cause $(B_z)_{max}$ to increase past the asymptotic limit $\lambda_o = \pi/a$ of eq. (10b) as $d_{max} \to \infty$.

c) Equilibrium Solutions with Horizontal Expansion

The flux surfaces in Fig. 2a have expanded upward to a large degree with fairly large $d_{max} = 1.85$. In order to investigate equilibria with the walls farther away, allowing more room to expand horizontally as well as vertically in response to increasing $d_{max}$, we consider a more general class of equilibria with

$$\psi(x, 0) = \sin^{\nu}(\pi x/a) \tag{15}$$

with $\nu > 1$. For purposes of illustration we again consider solution of eq. (7), satisfying the boundary condition (19). Then,

$$\psi(x,y) = \sum_{n=1}^{\infty} A_n \sin\left(\frac{n\pi x}{a}\right) \frac{\sinh[k_n(b - y)]}{\sinh k_n b} \tag{16}$$

where $k_n = [(n\pi/a)^2 - \lambda_o^2]^{1/2}$. If $k_n^2 < 0$, hyperbolic sine is replaced by sine. Here, $A_n$ are the Fourier sine coefficients of eq. (15). In Fig. 4, $(B_z)_{max}$, which is equal to $\lambda_o$ (from $B_z = \lambda_o\psi$ and $\psi_o = 1$), is shown as a function of $d_{max}$ for $\nu = 7$. We see that $(B_z)_{max}$ increases past $\pi/a$ for $d_{max} \gtrsim 2$ but with a much smaller slope than for $d_{max} \lesssim 2$. Also plotted in Fig. 4 is the total current in the z-direction, $I_z = \int dxdy j_z = \int dxdy B_z(\psi) dB_z/d\psi$. This component of current is seen to increase quadratically for small $d_{max}$ ($I_z \propto \lambda_o^2$) and to continue to increase for larger $d_{max}$. This behavior appears to be general for straight two-dimensional arcade equilibria, as will be shown with more general examples. For the equilibrium given by eq. (8) with $n = 1$, $I_z$ is proportional to $\lambda_o^2/k_1 = \lambda_o^2/(\pi^2/a^2 - \lambda_o^2)^{1/2}$.

In Fig 5(a), we show the flux surfaces for an equilibrium with $\nu = 7$,

$$d(x) = d_o(x - a/2) \tanh^2\left[\frac{(x - x_v)}{W(a/2 - x_v)}\right] \qquad x_v < x < a/2 \tag{17a}$$

$$= 0 \qquad x < x_v \tag{17b}$$

(and again antisymmetric about x=a/2) having $x_v = 0.31$ ($\psi_v = 0.25$), $d_{max} =$

0.36, and W = 0.40. For this example, $\psi_w$ = 0.40 which intersects the surface S at x = 0.34. The change in form between eqs. (12) and (17) [providing continuous derivative d'(x) at $x_v$], and the larger value of W, serve to make the solutions less sensitive to behavior near $\psi = \psi_v$. The corresponding profiles of $d(\psi)$, $B_z(\psi)$, and $\lambda(\psi)$ are shown in Figs. 5(b)-5(d). The equilibria shown in Figs. 6 and 7 have larger footpoint displacements $d_{max}$ = 0.61 and 1.35, respectively. It is easily seen that the flux surfaces expand upward and outward as $d_{max}$ increases.

In the example of eqs. (8), (13) and (16), and in the numerical results shown in Figs. 3 and 4, $(B_z)_{max}$ continues to increase with $d_{max}$ approaching a limiting value or increasing depending upon whether the upward expansion of flux surfaces, and therefore further increase of $V'(\psi)$, is limited by a wall at y = b. For the examples shown in Figs. 5-7, the flux surfaces are allowed to expand horizontally as well as vertically. The effect of allowing horizontal spreading of the flux surfaces manifests itself in the graph on $(B_z)_{max}$ versus $d_{max}$ in Fig. 8. For equilibria of the series (B) shown in Figs. 5-7, for which $x_v$ = 0.31 and W = 0.40, there is a peak in $(B_z)_{max}$ at $d_{max}$ = 0.35. For another related series (A) of equilibria, having $x_v$ = 0.17 ($\psi_v = 9 \times 10^{-3}$) and W = 0.45, the peak is broader and is located near $d_{max}$ = 0.5. The observed decrease in $(B_z)_{max}$ is related to horizontal spreading for the following reason: if no horizontal spreading occurs, as in eqs. (8), (13) and (16), $B_z$ increases very slowly for large $d_{max}$, and in the case of eq. (8), has an asymptote $(B_z)_{max} \to \pi/a$. As we have discussed, this behavior is due to the fact that vertical spreading in flux surfaces, i.e. the increase in the $V'(\psi)$ term in eq. (6a), can provide the increase in $d_{max}$ with little change in $(B_z)_{max}$. When horizontal spreading is allowed by having the photospheric flux concentrated as in eq. (15), $V'(\psi)$ can increase at a rate faster than $d_{max}$, giving a decrease in $(B_z)_{max}$. For the case of Fig. 4 described by eqs. (15) and (16), this effect cannot occur. Mathematically, this is simply traced to the fact that if $\lambda_o = (B_z)_{max}$ is prescribed in eq. (7), then the solutions are unique, and therefore only one value of $d_{max}$ is possible for each $\lambda_o$. Physically, this appears to arise from the fact that for $\psi_v = 0$, the outer surfaces spread out horizontally even for very small $d_{max}$, when $(B_z)_{max}$ is increasing rapidly. Thus, it appears that, in order for $(B_z)_{max}$ to attain a peak and decrease thereafter, a certain amount of potential

flux, or at least a profile having $\lambda(\psi) \to 0$ as the wall is approached, is required to separate the current-carrying region and the fixed walls so that the flux surfaces can spread out against a "soft" wall when the displacement is large. Nevertheless, for even larger $d_{max}$, $(B_z)_{max}$ must again begin to increase, when the expansion of flux surfaces is arrested by the walls. This effect may be beginning to occur for $d_{max} \gtrsim 1$ in Fig. 8. However, this effect is due to the unphysical boundaries. We expect that $(B_z)_{max}$ will continue to decrease in the absence of such boundaries.

In our iteration scheme to solve the G-S equation for specified $d_{max}$ (Appendix B), the outer iteration loop described by eq. (12) converges very rapidly near the peak in $(B_z)_{max}$ and beyond, because the solutions ha a relatively weak dependence upon $d_{max}$. However, the inner loop given by . (B1) does not noverge for solution near and past this in $(B_z)_{max}$. This is because $B_z(\psi)$ is specified in the inner loop as an intermediate step and the peak corresponds to a bifurcation in this case. Although such bifurcations are not physical as discussed in Secs. I and IIb, they have mathematical and numerical significance for our iteration scheme. In general, an iteration as in eq. (B1) is expected to converge for one class of solutions (with smaller $d_{max}$) and diverge for the other class (with larger $d_{max}$). We overcome the divergence problem by renormalizing $B_z(\psi)$ in the inner loop iterations [that is, changing $(B_z)_{max}$ with no change in the profile $B_z(\psi)/(B_z)_{max}$] in order to conserve the total z-current $I_z = \int dxdy B_z dB_z/d\psi$. This is a simple operation because $I_z$ scales as $(B_z^2)_{max}$. From Fig. 4, we see that $I_z$ increases much more rapidly with $d_{max}$ than $(B_z)_{max}$ for the solution given by eq. (16). In fact, it is found that $I_z$ increases for all solutions even when $(B_z)_{max}$ decreases. With this prescription in which $I_z$ rather than $(B_z)_{max}$ is held fixed during the iteration process, there is no bifurcation. When this method is employed, the inner loop iterations are always found to converge.

For $d_{max} = 0.36$ (Figs. 5a - 5d), the region of strong shear in footpoint displacement is $0.31 < x < 0.34$, or equivalently $0.26 < \psi < 0.40$. In this region, $B_z(\psi)$ [Fig 5(c)] deviates significantly from linearity. Note that $\lambda(\psi) = dB_z/d\psi$ is not constant (Fig. 5d), decreasing to zero as $\psi$ decreases. This behavior is consistent with the general properties discussed in Sec. IIIa. Closer to the center, $x > 0.34$ and $\psi > 0.40$, $B_z$ is fairly linear in $\psi$, although $\lambda$ shows a slight peaking at the center. Since $\mathbf{j} = \lambda(\psi)\mathbf{B}$ for these equilibria, this indicates a peaking of the current

density relative to the solutions of the form eqs. (8), (13) and (16). In Fig. 6, for a larger footpoint displacement with $d_{max}$ =0.61, this tendency appears to be somewhat more pronounced. Although not evident in Fig. 6(b), Figure 6c shows a sharp drop-off in $\lambda$ in the shear region $0.26 < \psi < 0.40$, a further peaking near the center ($\psi > 0.8$) and a plateau in between. For a still larger footpoint displacement $d_{max} = 1.35$ (Fig. 7c), this tendency is even more pronounced, with $\lambda(\psi)$ having a rather narrow peak for $\psi > 0.9$, sharp drop-off in the shear region $0.26 < \psi < 0.40$, and a valley around $\psi = 0.7$. The current density $j_z = B_z dB_z/d\psi = \lambda B_z$ is quite peaked; its value at the center $x = a/2$, $y = 0$ ($\psi = 1$) is 65 (in normalized units), compared to a considerably lower value of 10 at $\psi = 0.7$. That is, in a sense, solutions with increasing $d_{max}$ exhibit a considerable amount of peaking in the current density. Nevertheless, we will show below that the peaking in $j_z$ at the center with increasing $d_{max}$ does not lead to formation of current sheets. Moreover, the current density perpendicular to the photosphere $j_y = \lambda B_y = -\lambda \partial\psi/\partial x$ is proportional to $\sin^6(\pi x/a)\cos(\pi x/a)\lambda(\psi)$. Because $B_y$ is small near $x = a/2$ ($\psi = 1$), the peak in $\lambda$ also does not correspond to a large peaking of $j_y$.

In Fig. 9, $\lambda_{max}$, the maximum value of $\lambda(\psi)$, is shown as a function of $d_{max}$. This maximum occurs at $\psi = \psi_o$ for all cases. Recall that $\lambda_{max} = \lambda_o$ is identical to $(B_z)_{max}$ for solutions eqs. (8), (13), and (16). For the equilibria of Fig. 9, however, there are qualitative differences. Note that $\lambda_{max}$ begins to flatten for increasing $d_{max}$, at $d_{max} \simeq 0.2$ for series B and at $d_{max} \simeq 0.4$ for series A while $(B_z)_{max}$ peaks at $x \simeq 0.35$ and $x \simeq 0.5$, respectively. However, in both cases $\lambda_{max}$ continues to increase, unlike $(B_z)_{max}$. It seems likely that $\lambda_{max}$ may have a peak with respect to $d_{max}$ for larger values of $x_v$ and/or W. However, for the present parameters, the proximity of the wall causes the slow increase in $\lambda_{max}$ for $d_{max} \gtrsim 0.4$. This behavior shows further the lack of any physical meaning to the "bifurcations" in Fig. 8.

We now consider the peaking in $\lambda(\psi)$ and $j_z(\psi)$ in more detail. In Fig. 10, we show the maximum current density $j_z$ as a function of $d_{max}$. For solutions of eq. (7) (for example, eqs. [8], [13], and [16]), $j_z$ is proportional to $\lambda_o^2$ [$j_z = \lambda_o^2\psi$; see eq.(7)]. We see that for series A and B, $j_z$ and $\lambda$ are seen to have similar behavior; $j_z$ increases rapidly for $d_{max} \lesssim$

0.35 (series B) and for $d_{max} \lesssim 0.50$ (series A), the same regions for rapid increase in Figs. 8 and 9. Also, $j_z$ continues to increase, but much more slowly, for larger values of $d_{max}$. The slow increase of $j_z$ for $d_{max} \gtrsim 0.5$ appears to be due to the proximity of the wall. We also expect that $(j_z)_{max}$ might decrease with $d_{max}$ for larger $x_v$ and/or W. At the same time, the profile of $j_z = \lambda B_z$ continues to narrow so that the total $j_z$ current in the peak region decreases. In Fig. 11, we show the total z-current $I_z$ is shown for series A and B. It is observed to increase quadratically for $d_{max} \lesssim 0.1$ and monotonically for all $d_{max}$ (as noted above.) However, $I_z$ does not increase as rapidly for large $d_{max}$ as in Fig. 4. The important points to note are (i) that the peak current density $j_z$ is always found to increase at a very slow rate with respect to $d_{max}$, giving a decrease in the total $j_z$ current in the peak region. Concurrently, (ii) the total current $I_z$ increases rapidly with $d_{max}$, so that the fraction of the total current $I_z$ carried by the peak decreases very rapidly with $d_{max}$.

We point out that the single-valuedness of the graphs in Figs. 8-11 is due to the fact that a single solution is found when $d(\psi)$ is specified. We take this as empirical evidence that these solutions are unique. Therefore, any other physical quantity such as the total magnetic energy will also be single-valued. It has also been found that the total magnetic energy of a linear dipole field can be well fitted with a logarithmic dependence on footpoint shear (Klimchuk, Sturrock, and Yang 1988).

As we have discussed in Sec. IIc and Appendix B, finite $\beta$ equilibria with entropy prescribed can be computed in essentially the same manner. In Fig. 12 we show results with $d_{max} = 0$ (i.e. $B_z = 0$) as a function of the maximum entropy $s_{max}$. As suggested by the analogy between eqs. (B4) and (B5), the form of $s(\psi)$ is chosen to be $[d(\psi)]^{1/2}$, where $d(\psi)$ is the footpoint displacement form factor of eq. (17). Fig. 12a, we show the dependence of $p_{max}$ versus $s_{max}$ for $x_v = 0.31$ and $W = 0.40$, the same choices as in curve B in Fig. 8. We have used zero footpoint displacement since the results of Zwingmann (1987) show that this is the case with the strongest degree of bifurcation when pressure is specified. We see that $p_{max}$ is a well-behaved, single-valued function of $s_{max}$. For very small $s_{max}$, increasing $s_{max}$, i.e., the internal energy content, predominantly leads to a linear increase in $p_{max}$. This curve has a broad maximum around

$s_{max} \simeq 0.3$; increasing $s_{max}$ in this region leads to expansion of the structure in such a way that $p_{max}$ remains nearly unchanged. For $s_{max} \gtrsim 0.4$, increasing $s_{max}$ is predominantly accomplished by expansion of the structure and the pressure in fact decreases. This behavior is similar to that of $(B_z)_{max}$ versus $d_{max}$ (see Fig. 8). The flux surfaces are similar to those shown in Figs. 5a, 6a, 7a. The overall behavior of equilibria with respect to variation of $s_{max}$ is generally similar to that with respect to $d_{max}$ with no remarkable differences. We note that Fig. 7 of Zwingmann (1987), which corresponds to a solution on the upper branch of the W (energy) versus $\lambda_p$ (a measure of pressure) curve, shows apparent formation of an O-point. Such an equilibrium cannot evolve from configurations without O-points via ideal MHD motions. Mathematically, such O-points will not occur when $d(\psi)$ or $s(\psi)$ is prescribed because these quantities are specified only on the range $0 < \psi < \psi_0$ and the occurence of an O-point indicates the existence of surfaces with $\psi > \psi_0$, the maximum flux value specified on S. The occurence of O-points when $B_z(\psi)$ is specified has also been found by Birn, Goldstein, and Schindler (1978).

In Fig. 12b, we show the total axial current $I_z$ and the peak current density $j_z(x=a/2, y=0)$. As the entropy increases, the current density $j_z = dp/d\psi$ becomes peaked at the center, as in the case of increasing the footpoint displacement. However, the total current again increases at a faster rate with respect to $s_{max}$ than the current in the peak region ($x = a/2$), so that the fraction of the current associated with the peak decreases relative to $I_z$ as $s_{max}$ increases. No remarkable differences appear to exist between specifying $d_{max}$ and specifying $s_{max}$, consistent with the mathematical similarity apparent in the formulations in eqs. (6a) and (6c). Note that $p_{max}$ and $I_z$ are well-behaved, single-valued functions of $s_{max}$. Thus, the total energy, which is the sum of the magnetic energy and internal energy ($\propto p$) integrated over the volume, is single-valued, exhibiting no bifurcations.

## IV. Discussion

The basic physical mechanism behind the expansion of the flux surfaces as $d_{max}$ or $s_{max}$ is increased is relatively simple. The force-free equilibrium condition $\underline{j} \times \underline{B} = 0$ can be written as $(j_p B_z - j_z B_p) = 0$, where $j_p$ is the transverse (x,y) component. For a force free equilibrium, $j_p B_z \sim dB_z^2/d\psi$ is an upward force if $B_z$ monotonically increases in $\psi$. In an imaginary two-step process (Sec. IIb), if the footpoint displacement is increased, at first with no change in the flux surfaces [no change in $\psi(x,y)$, $B_p$ or $j_z$], $B_z$ must increase. However, the plasma will be out of equilibrium and will expand upward under $j_p B_z$ until force balance is achieved again. This expansion will occur with $d_{max}$ conserved in the limit of infinitely conducting photosphere, which means that the $B_z$ flux between any two flux surfaces will be conserved. This expansion process will then necessarily decrease $B_z$. In the new equilibrium, $B_z$ may be greater than or less than that of the initial equilibrium, depending on whether the initial increase of $B_z$ dominates the subsequent decrease of $B_z$. There is a simple circuit analogy to this process. As we have seen in the discussion following eq. (6), $d(\psi)$ is proportional to the axial flux between two nearby flux surfaces. Also, $B_z(\psi)$ is essentially the total transverse current between the flux surface labelled by $\psi$ and that labelled by $\psi_v$ (see the discussion after eq. [3]). By eq. (6a), $V'(\psi)$ (which is a property only of the geometry of the flux surfaces) can therefore be identified as the inductance relating transverse current to axial flux. In the first step of the imaginary two-step process above, when the photospheric motion takes place ($d_{max}$ is increased) with the geometry held fixed, we have $LdI/dt = V_o$. The voltage $V_o$ is proportional to the tangential electric field on the photospheric surface $E_x = v_z B_y$. In the second step, the geometry and current change, conserving flux $d(LI)/dt = 0$. For small $d_{max}$, the process is completed primarily by increasing the current with little change in inductance; for large $d_{max}$, the inductance increases by an amount sufficiently large that the current must decrease.

A similar argument applies to the pressure. In thermal equilibrium, the thermal input and radiative loss between any two flux surfaces, say, $\psi_1$ and $\psi_2$, are balanced. If, for example, the heating rate increases, the pressure "initially" (i.e., before relaxation to equilibrium) increases.

Then, in approaching equilibrium, the flux surfaces $\psi_1$ and $\psi_2$ will both expand under $\nabla p$ in such a way as to decrease the pressure, by adiabatic decompression (assuming that MHD time scales are shorter than radiative or thermal time scales). During this process, if expansion dominates, then the new equilibrium pressure will be lower than that of the initial equilibrium. The imaginary two-step process described in Sec. IIb and above is helpful not only for conceptualization but for predicting the response of the coronal plasma to a source of heat that occurs on a faster time scale than the nominal heating and radiative loss mechanisms.

The scenario for which entropy rather than pressure should be specified assumes that the photosphere does not act as a source of material or energy. This can achieved if thermal conduction along the field lines between the corona and the photospheric or subphotospheric regions is negligible on the MHD time scale for relaxation to equilibrium, or equivalently, if the magnetic field in the arcade is large enough and the coronal density small enough that the Alfven time scale is much shorter than the time scale for parallel thermal conduction in the photosphere. This argument also assumes that radiation is negligible on the Alfven time scale. On the other hand, if the radiation is dominant, and the plasma is isothermal, the mathematical formulation is essentially identical to the adiabatic case (but with adiabatic index $\gamma = 1$.) In our computation, we have also assumed that the arcade length scales are short compared with the coronal gravitational scale height $2kT_c/mg$, so that $p = p(\psi)$ in the corona. This is only for convenience, and is not critical, especially if $\beta = 2p/B^2$ is small. (The photospheric scale height $2kT_p/mg$, on the other hand, is assumed to be small. This is important in order to be able to specify footpoint displacement. This is consistent with $T_p$ being much less than $T_c$.) On the other hand, suppose one attempts a justification for specifying coronal pressure based on the dominance of photospheric processes by specifying the photospheric pressure $p(\psi,0)$. Accordingly, assume that an increased photospheric pressure is imposed with no changes in the flux surfaces, as in the imagined two-step process discussed above. At this step in the process, the increased coronal pressure is given by eq. (4b). Then, the pressure $p(\psi,y)$ will subsequently decrease as the system relaxes to equilibrium. There does not seem to be a reasonable conservation law, one based upon an energy equation for the plasma, in

which the pressure in the corona $p(\psi,y)$ given by eq. (4b) can be specified. Using this interpretation, we conclude that bifurcations with respect to prescribing pressure do not correspond to a physical loss of equilibrium.

The effect of expansion of the flux surfaces and the effect upon the curves in Figs. 8 and 12a can be understood better by the following scaling argument. First, consider the force free case $s(\psi) = p(\psi) = 0$. For arcades that are free to expand upward but are constrained in the horizontal direction (e.g., eqs. [8] and [13]; also Fig. 2a), the Grad-Shafranov equation (5a) implies in the large $d_{max}$ limit that $B_z \sim \psi/a$, independent of the height h of the flux surfaces. From eq. (6a), we have $d = B_z V'$ so that, for large h, $V' \sim ah/\psi$, $d \sim (\psi/a)(ah/\psi)$ and $h \sim d$. On the other hand, if the plasma is free to expand in both directions, its width will be of the same order as its height h for large h and the G-S equation gives $B_z \sim \psi/h$. Using $V' \sim h^2/\psi$, we again obtain $d \sim (\psi/h)(h^2/\psi) \sim h$. This in turn implies $B_z \sim \psi/d$ for large d. This exact scaling is not observed in the results of Fig. 8 for two reasons. First, the effect of the proximity of the wall is probably non-negligible for $d_{max} \gtrsim 1.0$ in Fig. 8. Second, such a scaling argument cannot include the effects of profile changes, e.g., the peaking in the $\lambda$ profile seen in Fig. 7c. Nevertheless, this scaling does illustrate the general features of the results observed.

A similar scaling law can be obtained if entropy is specified with $d(\psi) = B_z(\psi) = 0$. If only vertical expansion is allowed, then $p \sim \psi^2/a^2$ (from the G-S equation) and, using $s = pV'^{\gamma}$, we obtain $s \sim (\psi^2/a^2)(ah/\psi)^{\gamma}$ for large h, or $s \sim h^{\gamma}$. For two-dimensional expansion, we obtain $p \sim \psi^2/h^2$ and $s \sim (\psi^2/h^2)(h^2/\psi)^{\gamma} \sim h^{2(\gamma-1)}$. We then find the scaling $p \sim s^{-1/(\gamma-1)} \sim s^{-3/2}$. Expressing these results in terms of an equivalent footpoint displacement $\delta \equiv (2s)^{1/2}$ and an equivalent $B_z' \equiv (2p)^{1/2}$ as suggested by eqs. (14a) and (14b), we find $B_z' \sim \delta^{-3/2}$. Again, these scalings are in qualitative agreement with the results of Fig. 12a.

The results presented in Figs. 5-11 and Fig. 12b have a bearing on the development of a so-called "open field configuration". This open field configuration is defined as the potential solution having the same boundary condition on the flux $\psi(x,o)$ but necessarily having a sheet current along $\psi = \psi_o$. It has been stated (Barnes and Sturrock 1972; Yang, Sturrock, and Antiochos 1986; Aly 1984,1985) that the field approaches such a

configuration as the footpoint displacement increases. The current is conjectured to become entirely concentrated into the sheet. As noted in the discussion of Fig. 7c, the transverse components of the current density do not become peaked in space as $d_{max}$ increases. Also the magnitude of the transverse current density $j_p$ scales as $\lambda_{max}$ with increasing $d_{max}$ and thus increases slowly for large $d_{max}$. Furthermore, the total transverse current is proportional to $(B_z)_{max}$ and is found to decrease as $d_{max}$ is increased. The other component of current density $j_z = B_z dB_z/d\psi$ becomes peaked near $\psi = \psi_o$ (see the discussion of Fig. 7c). However, the peak of $j_z$ at $x = a/2$ increases slowly for large $d_{max}$ (Fig. 10). (The slow increase in the peak value of $j_z$ for $d_{max} \gtrsim 0.5$ is again attributable to the influence of the walls.) Furthermore, the total $j_z$ current in the peak region decreases. On the other hand, the total z-current $I_z$ increases at a considerably faster rate than the peak current density. We conclude that the peak in $j_z$ near $\psi = \psi_o$ contributes a rapidly <u>decreasing</u> fraction of the total current $I_z$ as $d_{max}$ increases, and therefore sheet currents with progressively narrower current profiles carrying the bulk of the current do not occur. The increase in $I_z$ appears to be due to the same cause as the increase of $I_z$ for eq. (8) for which $I_z \propto \lambda_o^2/(\pi^2/a^2 - \lambda_o^2)^{1/2}$, namely that the equilibrium continues to expand, with nearly uniform current density filling the space. We conclude that increasing the footpoint displacement does indeed cause the flux surfaces to expand but that the resulting equilibrium approaches a configuration with finite current density ($j_z$) and increasing total current $I_z$ but no concentration of the current into sheets.

In the present paper, we have adopted the conventional approach that the footpoints of magnetic field lines are tied to the infinitely conducting and massive photosphere and have found no bifurcations (i.e., no loss of equilibrium) with respect to physically specifiable quantities. In this scenario, all the flux associated with the arcade is contained in the corona. If the photosphere is assumed to have finite conductivity and finite mass, then the fluxes can extend below. In a recent paper, Chen (1989) studied the behavior of "toroidal" current loops in which the current was assumed to be closed in or below the photosphere. In this work, a circuit parameter $\varepsilon \equiv \Phi_p/\Phi_T = L_p/L_T$ was found to play a role in determining the stability behavior of a loop, where $\Phi_p$ ($L_p$) is the flux

(inductance) in the corona enclosed by the loop and $\Phi_T$ ($L_T$) is the total flux (inductance) including the flux structure below the photosphere associated with the loop. Thus, the quantity $\varepsilon$ parametrizes the subphotospheric flux/current structure relative to what is above the photosphere. In this model, the infinitely conducting and massive photosphere assumption corresponds to the $\varepsilon = 1$ limit. In this limit, loops are found to be stable. If, on the other hand, the subphotospheric flux is large enough ($\varepsilon$ less than some critical value $\varepsilon_{cr}$), then a loop can be unstable to major radial expansion, leading to a wide range of motion and magnetic energy dissipation. In the present linear arcade model, too, it is possible that if the fluxes are allowed to extend below the photosphere, loss of equilibrium or instabilities may occur.

## V. Summary

A study of two-dimensional MHD equilibrium of linear coronal arcades has been presented. An iterative method has been used to solve the Grad-Shafranov equation with prescribed footpoint displacement $d(\psi)$ or entropy $s(\psi)$. This method involves, as an intermediate mathematical step, the prescription of $B_z$ and $p(\psi)$. A modification of the method has been developed to compute equilibria through purely mathematical bifurcation points which can occur when axial field $B_z$ and pressure are prescribed in the intermediate steps. Sequences of equilibria have been computed with $d(\psi)$ or $s(\psi)$ specified. No multiple solutions exist if $d(\psi)$ is specified, consistent with the suggestion of Jockers (1978) and in agreement with the recent result of Zwingmann (1987). We have also shown that no multiple solutions exist if the entropy $s(\psi)$ is specified. The entropy, like the pressure, is a measure of the internal energy of the plasma. Generally, if the entropy is specified, then the pressure cannot be specified and vice versa. In the limit in which the arcade plasma can be assumed to be adiabatic, then the entropy rather than the pressure is physically specifiable. In this case, the pressure-based bifurcations do not indicate the possibility of an eruptive process. We have described physical conditions under which the entropy may be specified, and discussed the difficulty in posing a physically meaningful situation in which the pressure is specifiable. Our results indicate that increasing footpoint displacement and entropy increases the magnetic energy of an arcade but not the magnetic free-energy to drive eruptive processes in the corona.

We have also investigated the formation of the so-called open field configuration and formation of sheet current (e.g., Barnes and Sturrock 1972; Aly 1984,1985; Yang, Sturrock and Antiochos 1986) and found that the profile of the current density $j_z$ indeed becomes more peaked with increasing footpoint displacement but that the total $j_z$ current in the peak region decreases as the total current $I_z$ increases, so that a rapidly decreasing fraction of current is carried by the current peak at the center ($x = a/2$). Based on our solutions, especially Figs. 10,11 and 12(b), we expect no sheet current formation (i.e., concentration of current at $x = a/2$) to takes place as a result of increasing footpoint displacement.

## ACKNOWLEDGMENTS

We wish to thank P. Sturrock, S. Antiochos and E. Zweibel for stimulating discussions. This work was supported by the Office of Naval Research.

## REFERENCES


Aly, J.J., 1984 Ap. J., 283, 349.

Aly, J.J., 1985 Astron. Astrophys., 193, 19.

Antiochos, S. K. 1989, in "Solar and Stellar Flares: Poster Papers", eds. B. M. Haisch and M. Rodono, publ. Oss. Astrfis. Catania, No. ____, (in press).

Barnes, C. and Sturrock, P. 1972, Ap. J., 174, 659.

Birn, J., Goldstein, H., and Schindler, K. 1978, Solar Phys., 57, 81.

Birn, J. and Schindler, K., 1981, in Solar Flare Magnetohydrodynamics, ed. E. Priest, Gordon and Breach, N.Y.

Chen, J. 1989, Ap. J., March, (in press).

Chodura, R. and Schluter, A. 1981, J. Comput. Phys.,41,68.

Drake, J. F., Hassam, A. B., and G. Van Hoven 1988, Plasma Preprint UMLPR #88-044, University of Maryland.

Grad, H., Hu, P. N., and Stevens, D. C. 1975, Proc. Nat. Acad. Sci USA,72,3789.

Heyvaerts, J., Lasry, J. M., Schatzman, M., and Witomsky, P. 1982, Astr. Ap., 111, 104.

Heyvaerts, J. and Priest, E. R. 1984, Astr. Ap., 137, 63.

Jockers, K. 1978, Solar Phys., 56, 37.

Keller, H. B. 1977, in P. Rabinowitz (ed.), Applications of Bifurcation Theory, New York: Academic Press.

Klimchuk, J., Sturrock, P. and Yang, W. H. 1988, Center for Space Science and Astrophysics Report CSSA-ASTRO-87-17 (submitted to Ap. J.).

Low, B. C. 1977, Ap. J., 212, 234.

Low, B. C. 1982, Ap. J., 263, 952.

Low, B. C. and Wolfson, R. 1988, Ap. J., 324, 574.

Lundquist, S. 1951, Phys. Rev., 83, 307.

Mikic, Z., Barnes, D.C., and Schnack, D.C. 1988, Ap. J., 328, 830.

Parker, E. N. 1972, Ap. J., 174, 499.

——— 1983, Ap. J., 264, 642.

Priest, E. R. 1988, Ap. J., 328, 848.

Sturrock, P. A., ed. 1980, Solar Flares, Boulder: Colorado Associated University Press.

van Ballegooijen, A. A. 1985, Ap. J., 298, 421.

Wu, S.T., Bao, J.J., Tandberg-Hanssen, E., 1987, Space Science Laboratory Preprint Series No. 87-147.

Xue, M. L. and Chen, J. 1983, Solar Phys., 84, 119.

Yang, W.H., Sturrock, P.A., and Antiochos, S.K. 1986 Ap. J., 309, 383.

Zweibel, E. and Li, H.-S. 1987, Ap. J., 312, 423.

Zwingmann, W., 1987, Solar Phys, 111, 309 .

## Appendix A

As an aside, we note that Clebsch variables have been used by other authors in specifying footpoint displacements. That is, the total field is written as

$$\underline{B} = \nabla\alpha \times \nabla\beta,$$

where $\alpha = \psi$ and $\beta = z - f(x,y)$. Writing $f(x,y) = \Theta(x,y)d_o(\psi)$ and using eq. (1a), we find

$$\underline{B}\cdot\nabla\Theta = B_z(\psi)/d_o(\psi)$$

$$\Theta = \frac{B_z(\psi)}{d_o(\psi)} \int \frac{ds}{B},$$

with an indefinite integral along the field line. If $\Theta$ is required to increase by unity in integrating from one footpoint to the other, we obtain, from eq. (6a), that $d_o(\psi) = d(\psi)$. Therefore, specification of $f(x,0)$ at one footpoint (e.g. where $B_n > 0$) is equivalent to specifying $d(\psi)$.

## Appendix B

The computational method we employ is to start with a trial $B_z(\psi)$. For brevity, we begin with the case $p = 0$. We iterate eq. (5a) by solving

$$L\psi_{k+1} \equiv \nabla^2\psi_{k+1} = R(\psi_k), \tag{B1}$$

where $R(\psi) = - B_z(\psi)dB_z/d\psi$. Given $\psi_k$, a standard Poisson solver is used to solve eq. (B1) for $\psi_{k+1}$. Formally, this can be expressed as $\psi_{k+1} = L^{-1}[R(\psi_k)]$. It is helpful to introduce a relaxation parameter r and iterate according to $\psi_{k+1} = rL^{-1}[R(\psi_k)] + (1-r)\psi_k$. The convergence properties of the inner loop iteration $\psi_k(\underline{x}) \rightarrow \psi_{k+1}(\underline{x})$ depend on the bifurcation properties of eq. (5a) with the trial function $B_z(\psi)$. In order to carry out the iteration past the mathematical bifurcation points arising from specifying $B_z$ as an intermediate step, it is necessary to take the further step of renormalizing $B_z(\psi)$ such that the total axial current $I_z$ remains fixed during successive iterations.

For a given footpoint displacement $d(\psi)$, we integrate along the field lines to compute $V'(\psi)$, defined in eq. (6b). We then compute $B_z(\psi)$ from eq. (6a) with a relaxation parameter $\rho$ such that

$$B_z^{new}(\psi) = \rho d(\psi)/V'(\psi) + (1 - \rho)B_z{}^{old}(\psi). \tag{B2}$$

The method of inner-outer loop iteration is best summarized in a flow chart as follow. First, we specify the footpoint displacement $d(\psi)$. We then

1) guess a solution to eq. (B1) by giving $B_z(\psi)$ and $\psi(x,y)$, and compute the total axial current $I_z$;

2) iterate eq. (B1) with a (inner-loop) relaxation parameter r. If $d_{max}$ is on the right side of the mathematical bifurcations (e.g., for $d_{max} >$ 0.35 for the B-series equilibria of Fig. 8), renormalize $B_z(\psi)$ at each

iteration so that $I_z$ remains unchanged for the series of "inner loop" iterations. There is no bifurcation with respect to $I_z$;

3) compute $V'(\psi)$ (eq. [6b]) for these solutions to eq. (5);

4) update $B_z(\psi)$ by eq. (B2) with a second (outer-loop) relaxation parameter $\rho$, and return to step 2.

For small footpoint displacement, $V'(\psi)$ is insensitive to changes in footpoint displacement because $\psi$ is the potential solution to lowest order. In this case, the outer loop iteration (B2) (with relaxation parameter $\rho$ = 1) converges rapidly. For larger footpoint displacement, $V'(\psi)$ becomes quite sensitive, but in practice it is found that the iteration oscillates if it diverges, and therefore a positive relaxation parameter $\rho$ (with $\rho$ decreasing with $d_{max}$) guarantees convergence, provided the iteration process is properly chosen if mathematical bifurcation with $B_z$ specified occurs as described above. This is discussed further in Sec. IIc for specific examples. This method of inner and outer loop iterations generally converges very rapidly if the correct relaxation parameters are chosen. However, it often requires an accurate first guess for $\psi(x,y)$ if footpoint displacement is large. Therefore, we generally find solutions by varying parameters from one run to the next, starting with small footpoint displacement.

A similar scheme is used to include pressure when the entropy $s(\psi)$ is prescribed. The analogue to eq. (B1) is $R(\psi) = -dp/d\psi$ and $p(\psi)$ is renormalized to keep $I_z$ fixed during inner loop iterations, as discussed in Sec. IV. Using eq. (6c), the analog to eq. (B2) is

$$p^{new}(\psi) = \rho' s(\psi)/V'(\psi)^{\gamma} + (1 - \rho')p^{old}(\psi). \qquad (B3)$$

Since the right hand side of the G-S equation (5a) is $-(d/d\psi)[p(\psi) + B_z(\psi)^2/2]$, the prescriptions for computing $B_z(\psi)$ and $p(\psi)$, and their effects on the final solutions, are quite similar. This is most easily seen if we rewrite eqs. (6a) and (6c) as

$$\frac{1}{2} B_z(\psi)^2 = \frac{1}{2} d^2(\psi)/V'(\psi)^2 \qquad (B4)$$

and

$$p(\psi) = s(\psi)/V'(\psi)^\gamma. \qquad (B5)$$

In fact, if it were not for the rather insignificant difference between $\gamma = 5/3$ and 2, there would be a formal identification $(1/2)B_z(\psi)^2 \leftrightarrow p(\psi)$ and $(1/2)d(\psi)^2 \leftrightarrow s(\psi)$. [Similar statements hold for the isothermal plasma, in which the analogue of eq. (B5) is $\gamma = 1$ with $s(\psi)$ replaced by $M'(\psi)$.] Because of this similarity, the iteration scheme eq. (B3) has essentially identical properties as eq. (B2), but with somewhat different optimum relaxation parameters in the outer loop.

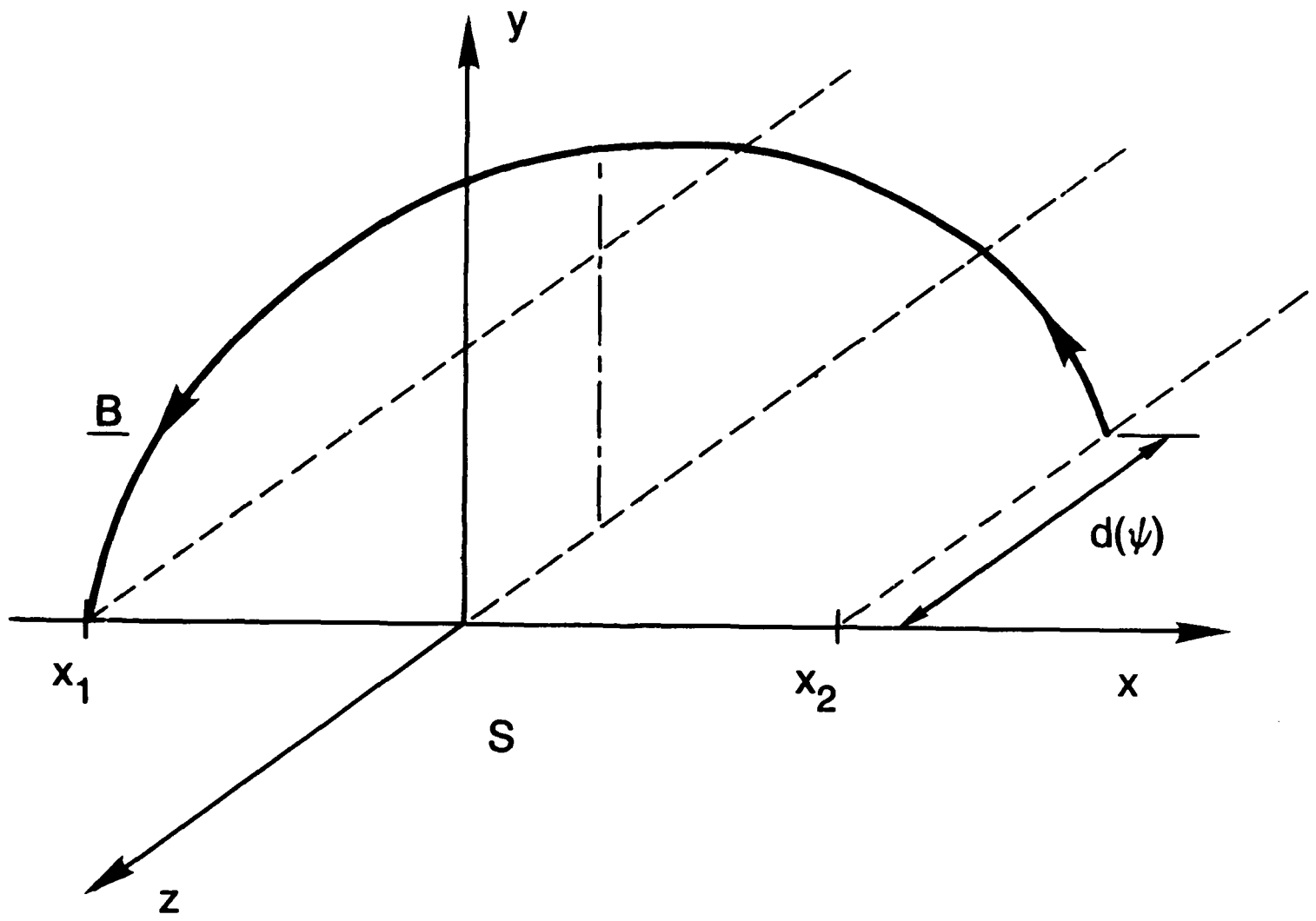



Fig. 1 — Schematic diagram of an arcade geometry. A representative magnetic field line labelled by $\psi$ is shown with the footpoints displaced by $d(\psi)$. A field line has an "axial" component along the z-direction and a "transverse" perpendicular to z.

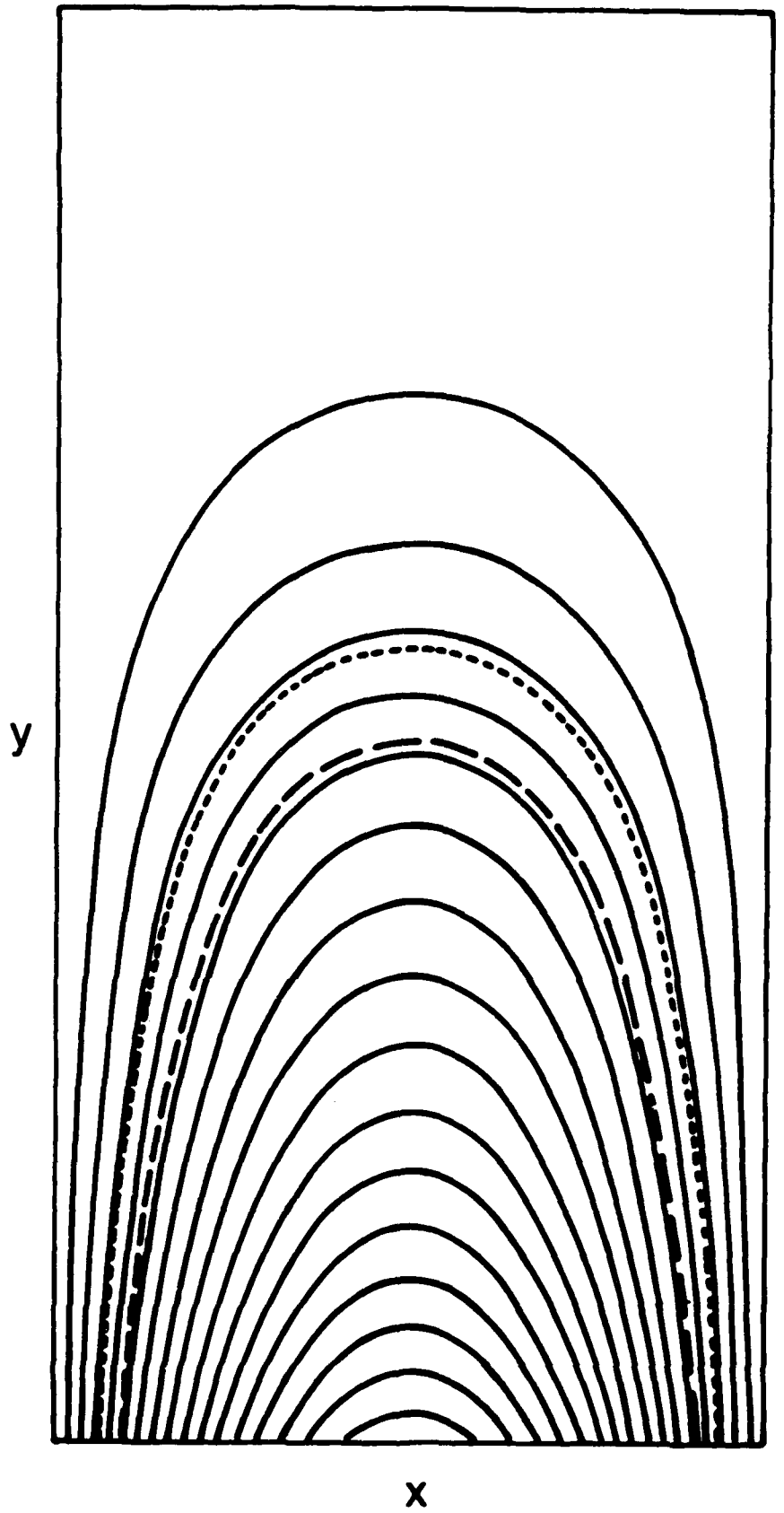



Fig. 2 — A force-free arcade for $d(\psi)$ given by Eq. (16) and $\psi\,(x,0) = \sin(\pi x/a)$. A relatively small amount of potential flux $\psi_v = 0.195$ surrounds the current-carrying plasma. (a) Flux ($\psi$) surfaces. (b) Footpoint displacement versus $x$. (c) $B_z$ versus $\psi$. (d) $\lambda = dB_z/d\,\psi$

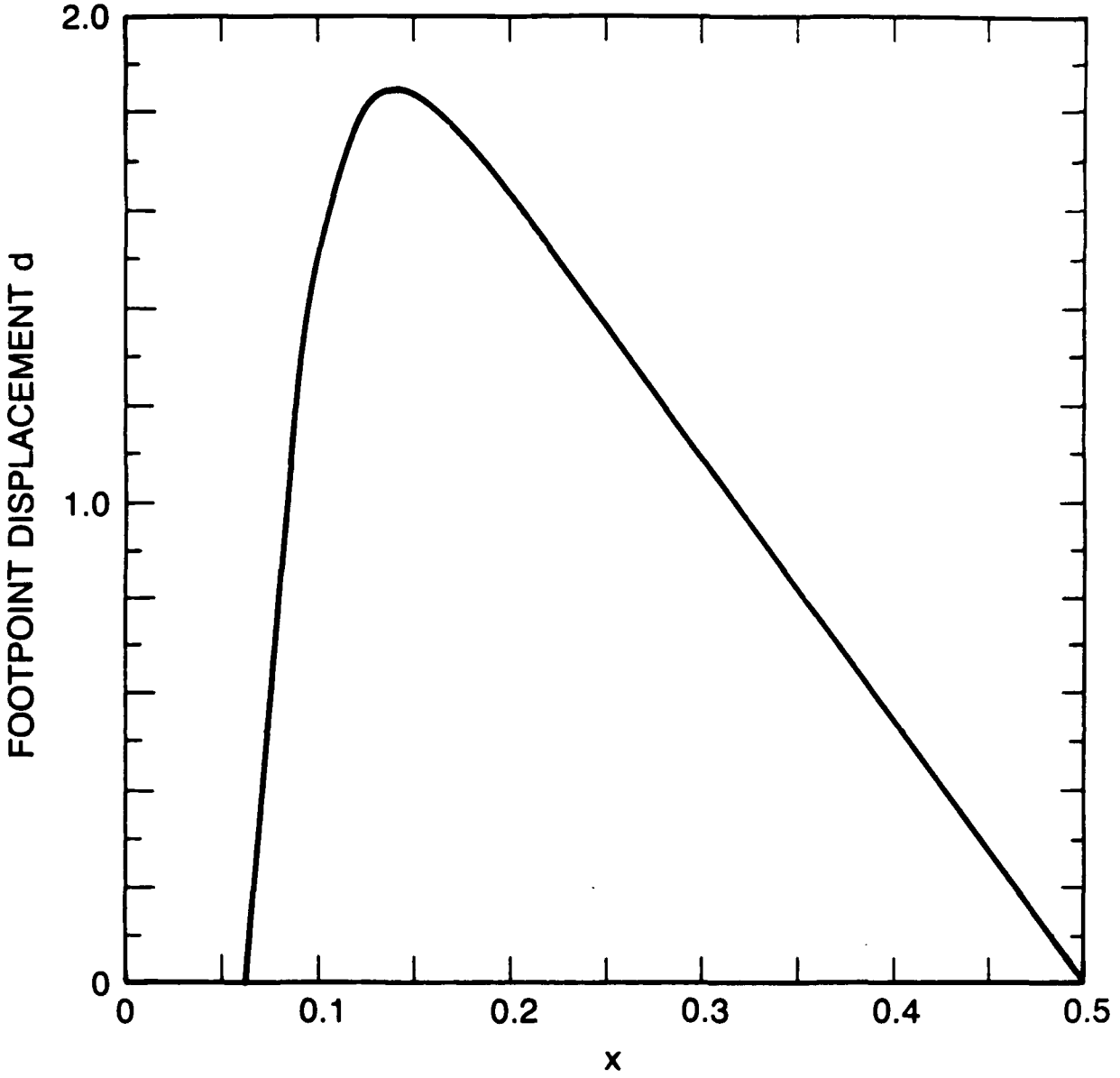



Fig. 2 (Continued) — A force-free arcade for $d(\psi)$ given by Eq. (16) and $\psi(x,0) = \sin(\pi x/a)$. A relatively small amount of potential flux $\psi_v = 0.195$ surrounds the current-carrying plasma. (a) Flux ($\psi$) surfaces. (b) Footpoint displacement versus $x$. (c) $B_z$ versus $\psi$. (d) $\lambda = dB_z/d\psi$

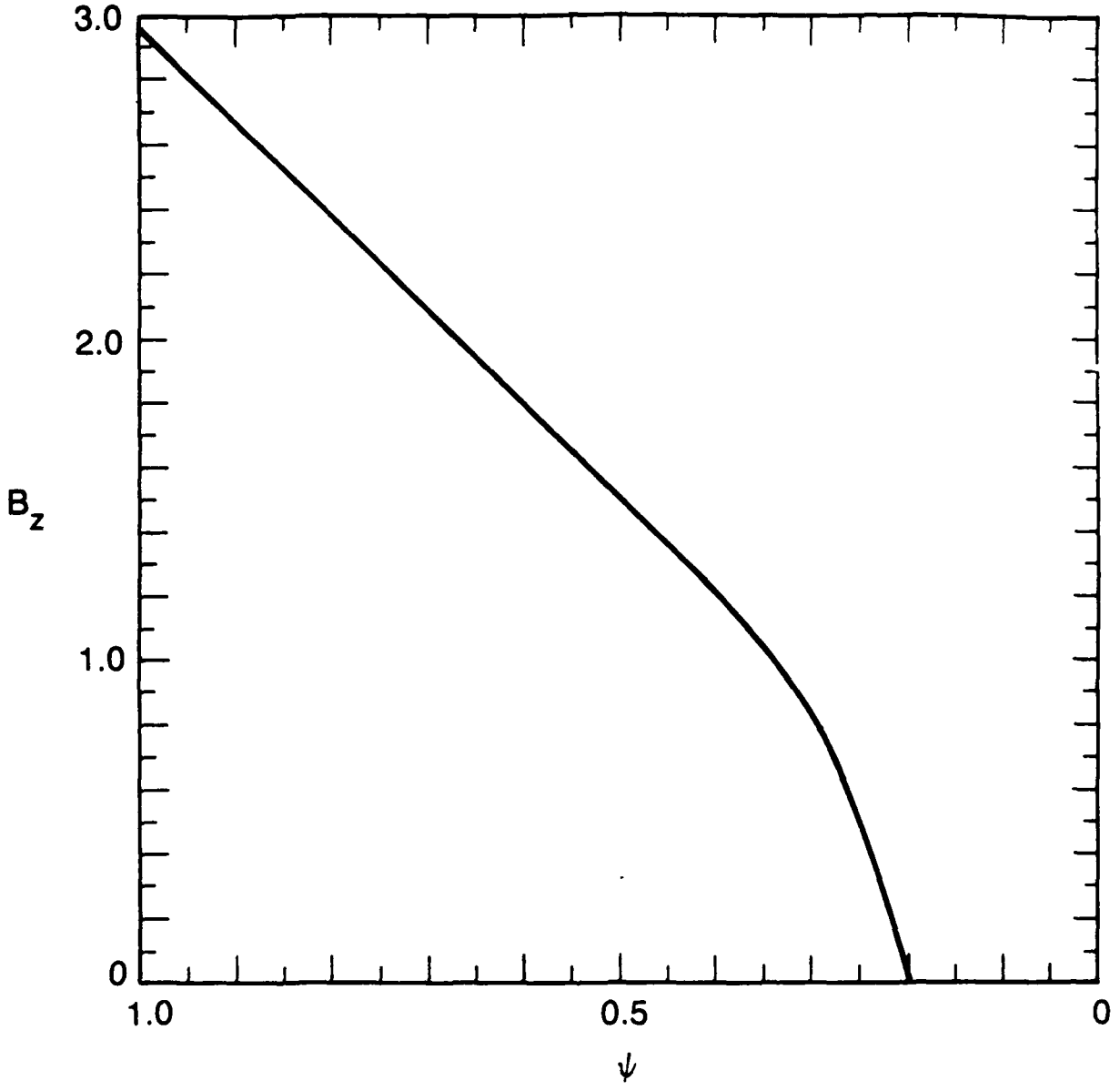



Fig. 2 (Continued) — A force-free arcade for $d(\psi)$ given by Eq. (16) and $\psi(x,0) = \sin(\pi x/a)$. A relatively small amount of potential flux $\psi_v = 0.195$ surrounds the current-carrying plasma. (a) Flux ($\psi$) surfaces. (b) Footpoint displacement versus $x$. (c) $B_z$ versus $\psi$. (d) $\lambda = dB_z/d\psi$

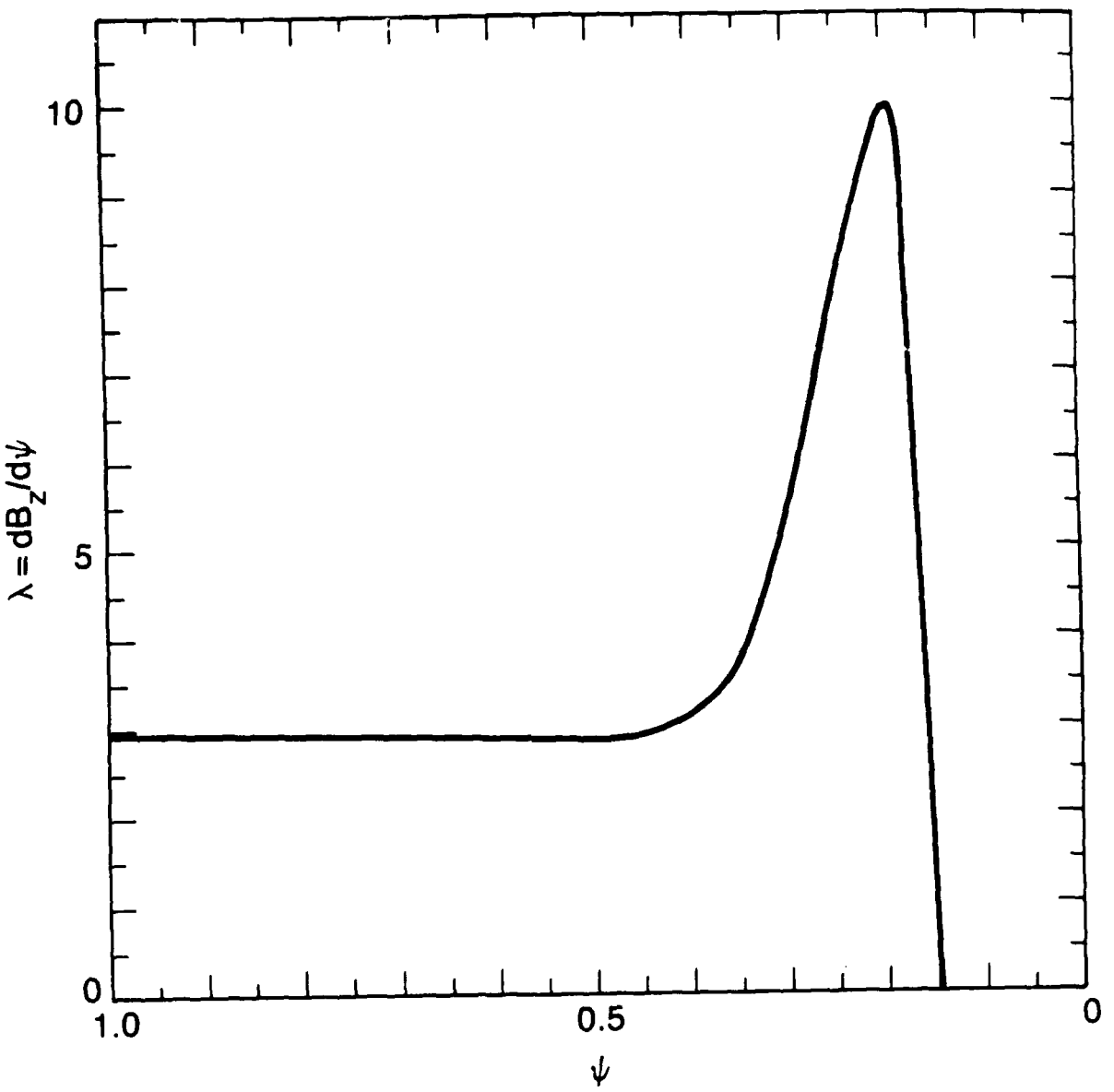



Fig. 2 (Continued) — A force-free arcade for $d(\psi)$ given by Eq. (16) and $\psi(x,0) = \sin(\pi x/a)$. A relatively small amount of potential flux $\psi_v = 0.195$ surrounds the current-carrying plasma. (a) Flux ($\psi$) surfaces. (b) Footpoint displacement versus $x$. (c) $B_z$ versus $\psi$. (d) $\lambda = dB_z/d\psi$

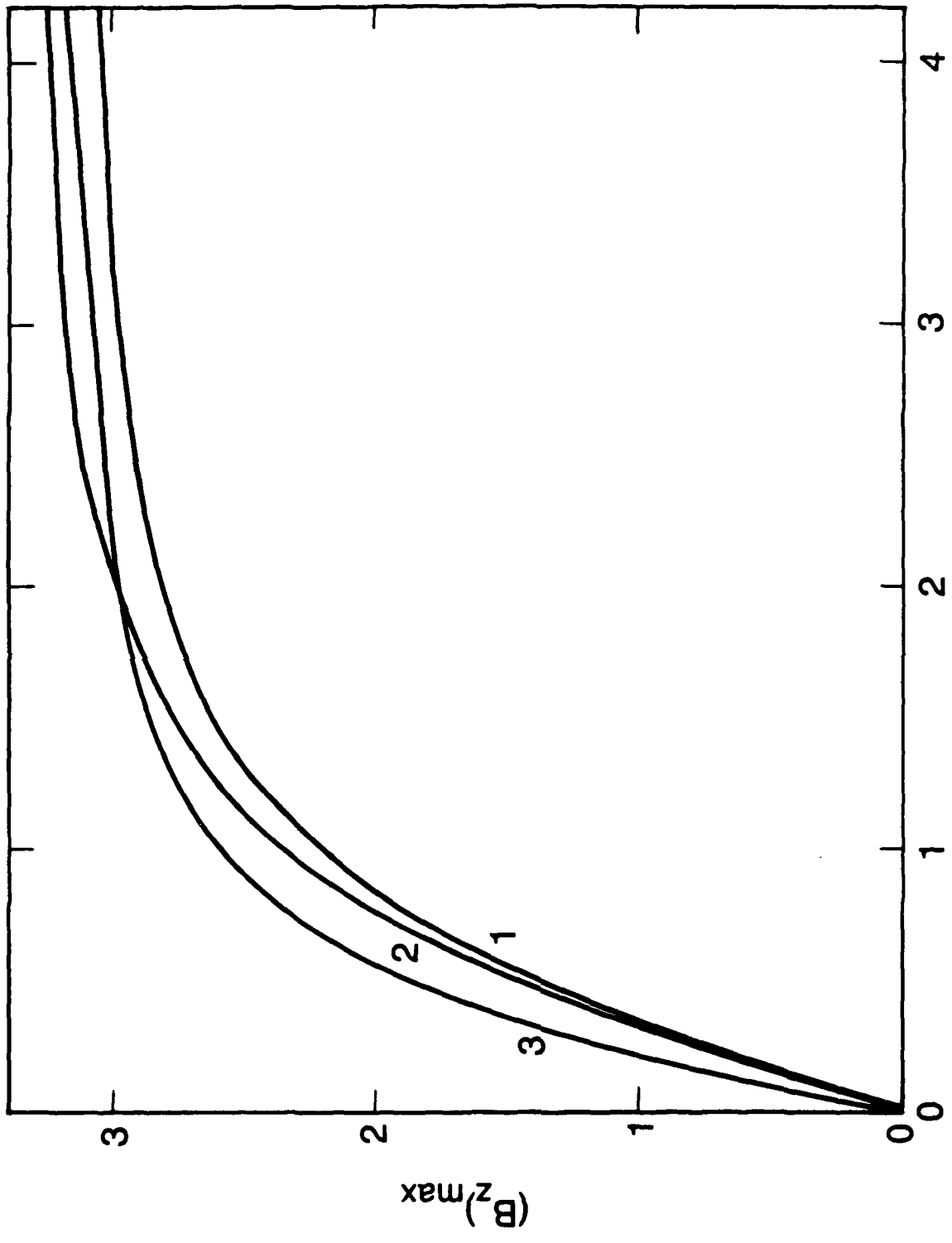



Fig. 3 — $(B_z)_{max}$ versus $d_{max}$. Curve 1 corresponds to equilibrium given by Eq. (8) and curve 2 to equilibrium given by Eqs. (17) and (18). Curve 3 describes the numerical equilibrium with parameters given as in Fig. 2.

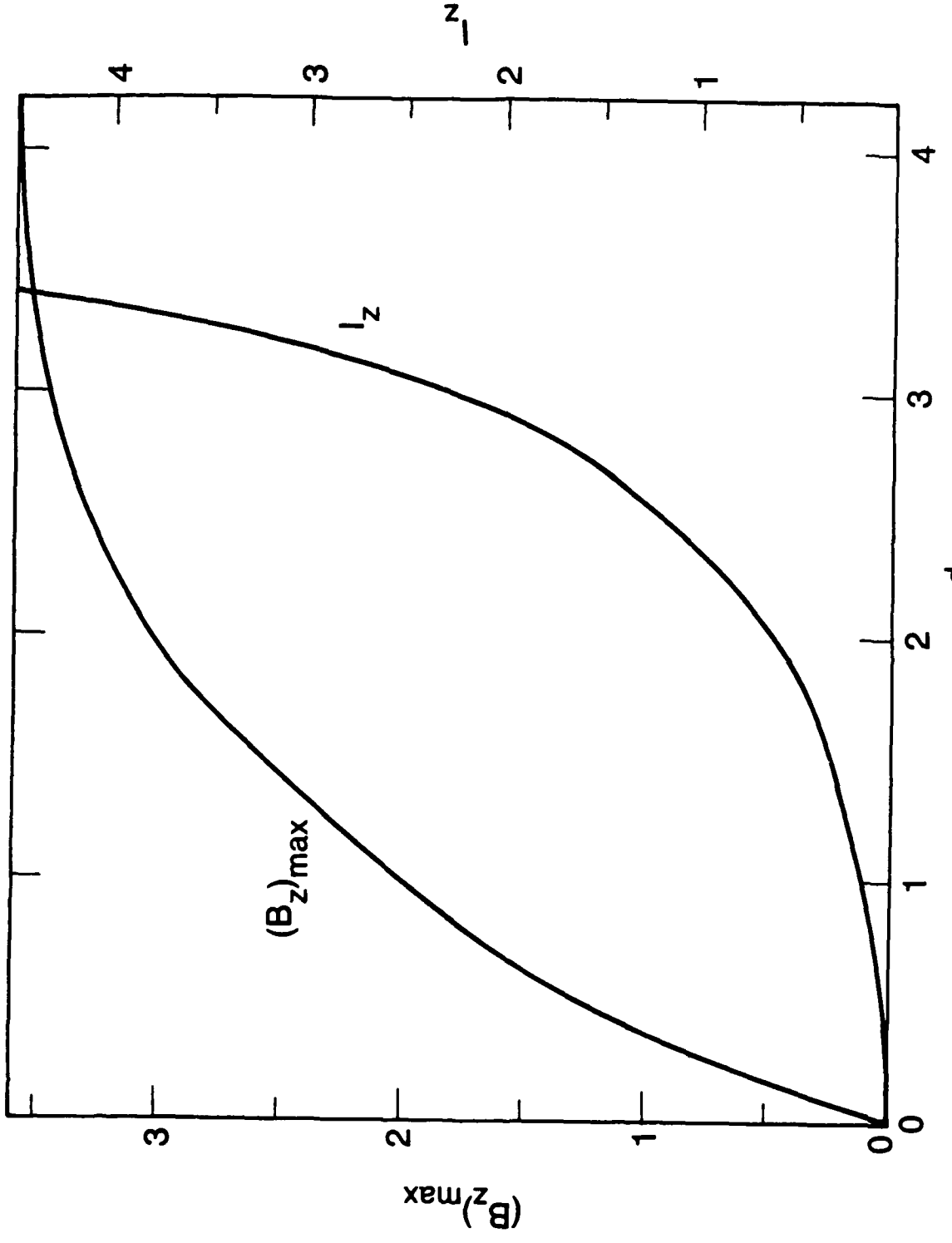



Fig. 4 — $(B_z)_{max}$ and the total current $I_z$ as functions of $d_{max}$ for the equilibrium analytically given in Eqs. (19) and (20) with $\nu = 7$.

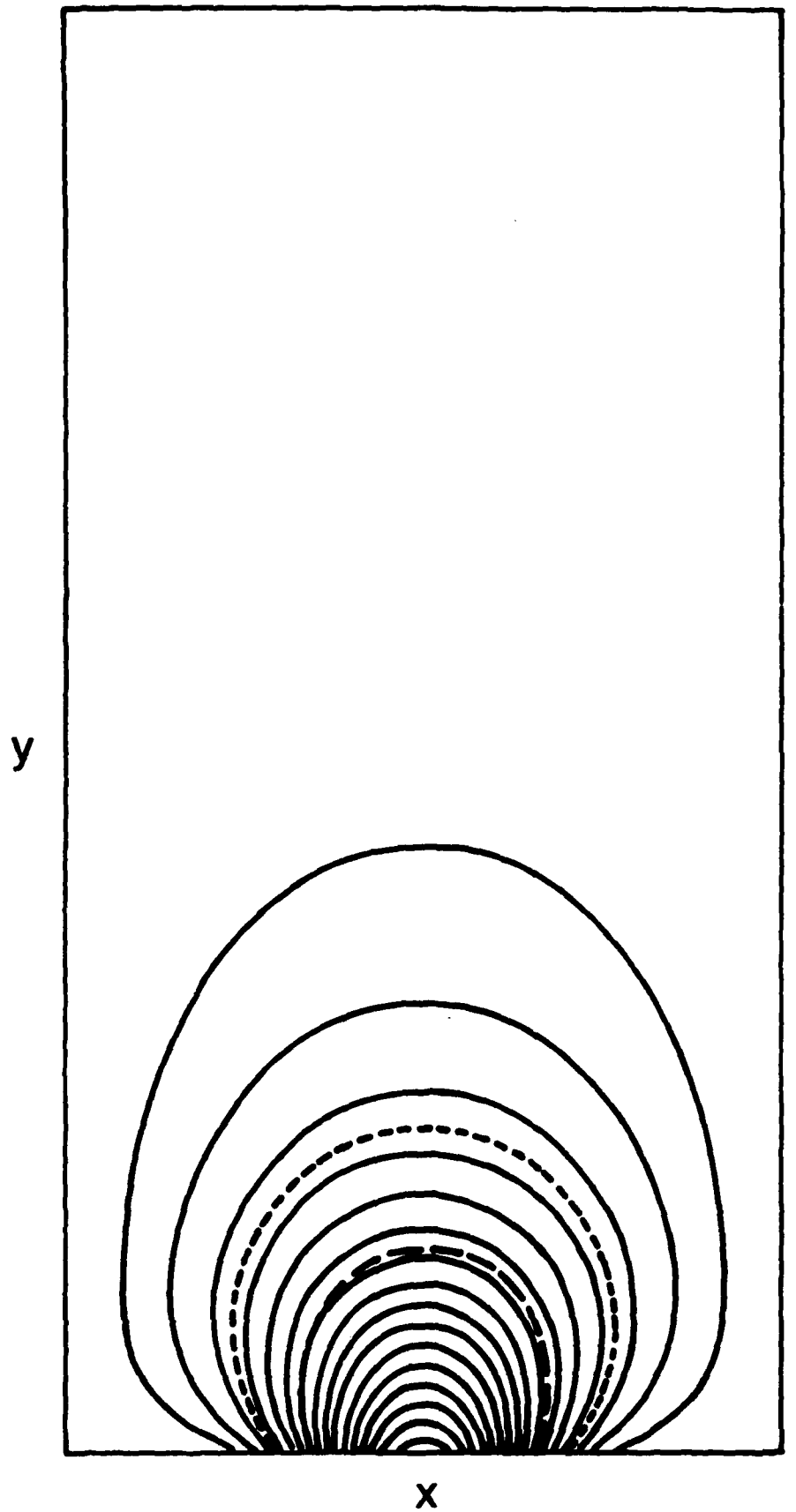



Fig. 5 — Numerical equilibrium with boundary condition given by Eq. (19) for $\nu = 7$ and with footpoint displacement given by Eq. (21). The current-carrying region is surrounded by a relatively large amount of flux $\psi_v = 0.25$ ($x_v = 0.31$), $W = 0.40$, and $d_{max} = 0.36$. (a) Flux surfaces. (b) Footpoint displacement versus $x$. (c) $B_z$ versus $\psi$. (d) $\lambda$ versus $\psi$.

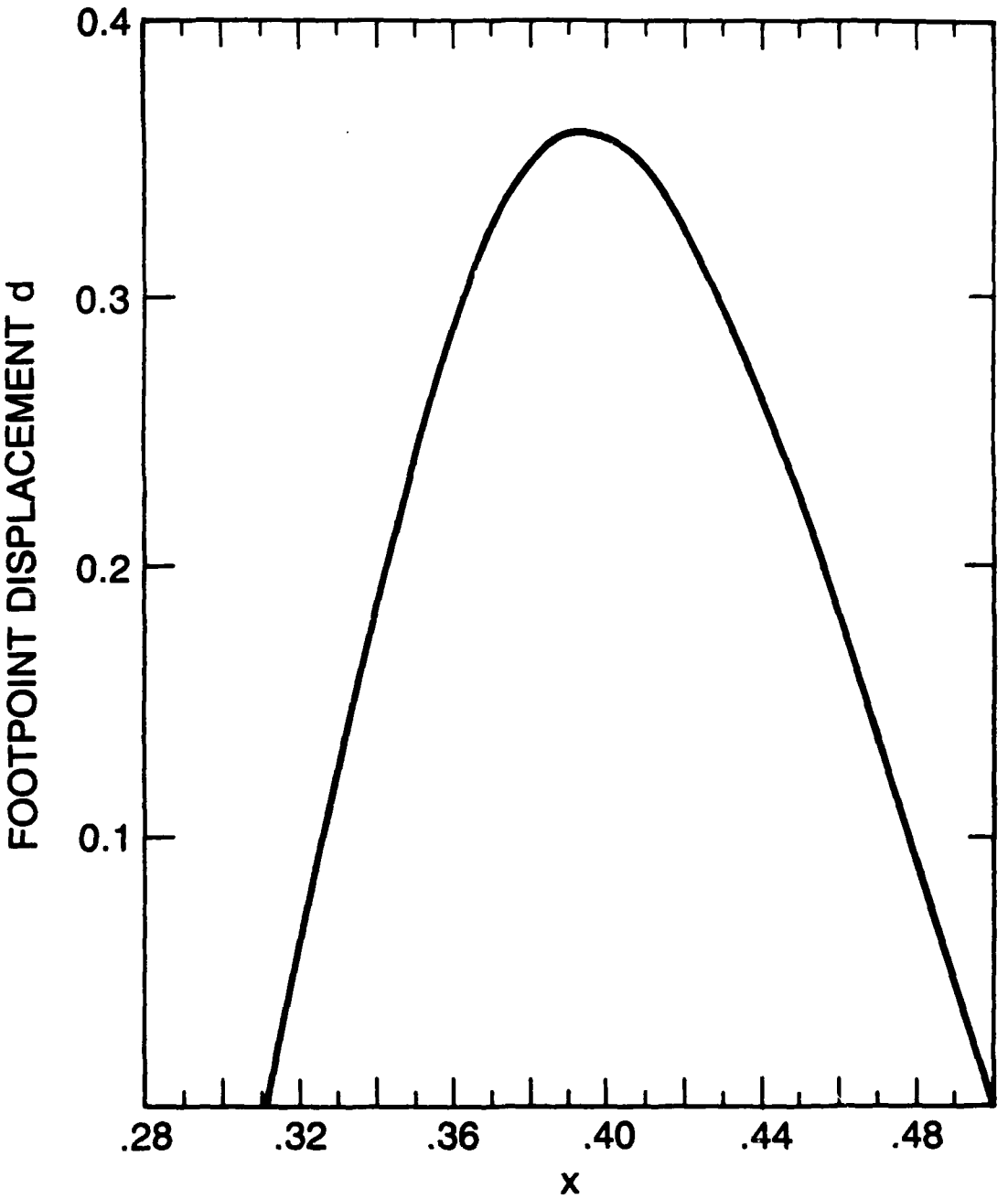



Fig. 5 (Continued) — Numerical equilibrium with boundary condition given by Eq. (19) for $\nu = 7$ and with footpoint displacement given by Eq. (21). The current-carrying region is surrounded by a relatively large amount of flux $\psi_v = 0.25$ ($x_v = 0.31$), W = 0.40, and $d_{max} = 0.36$. (a) Flux surfaces. (b) Footpoint displacement versus x. (c) $B_z$ versus $\psi$. (d) $\lambda$ versus $\psi$.

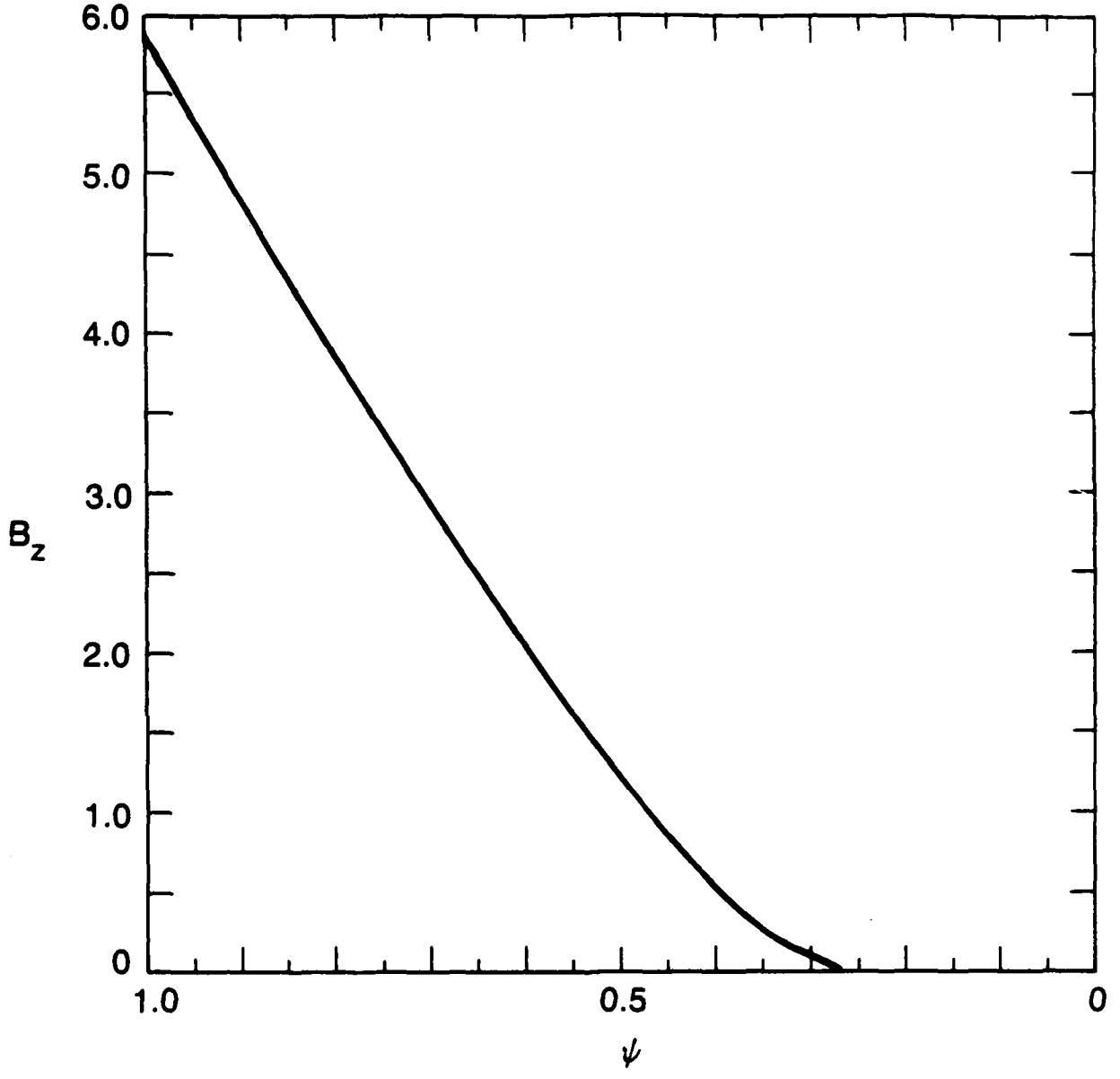



Fig. 5 (Continued) — Numerical equilibrium with boundary condition given by Eq. (19) for $\nu = 7$ and with footpoint displacement given by Eq. (21). The current-carrying region is surrounded by a relatively large amount of flux $\psi_v = 0.25$ ($x_v = 0.31$), W = 0.40, and $d_{max} = 0.36$. (a) Flux surfaces. (b) Footpoint displacement versus x. (c) $B_z$ versus $\psi$. (d) $\lambda$ versus $\psi$.

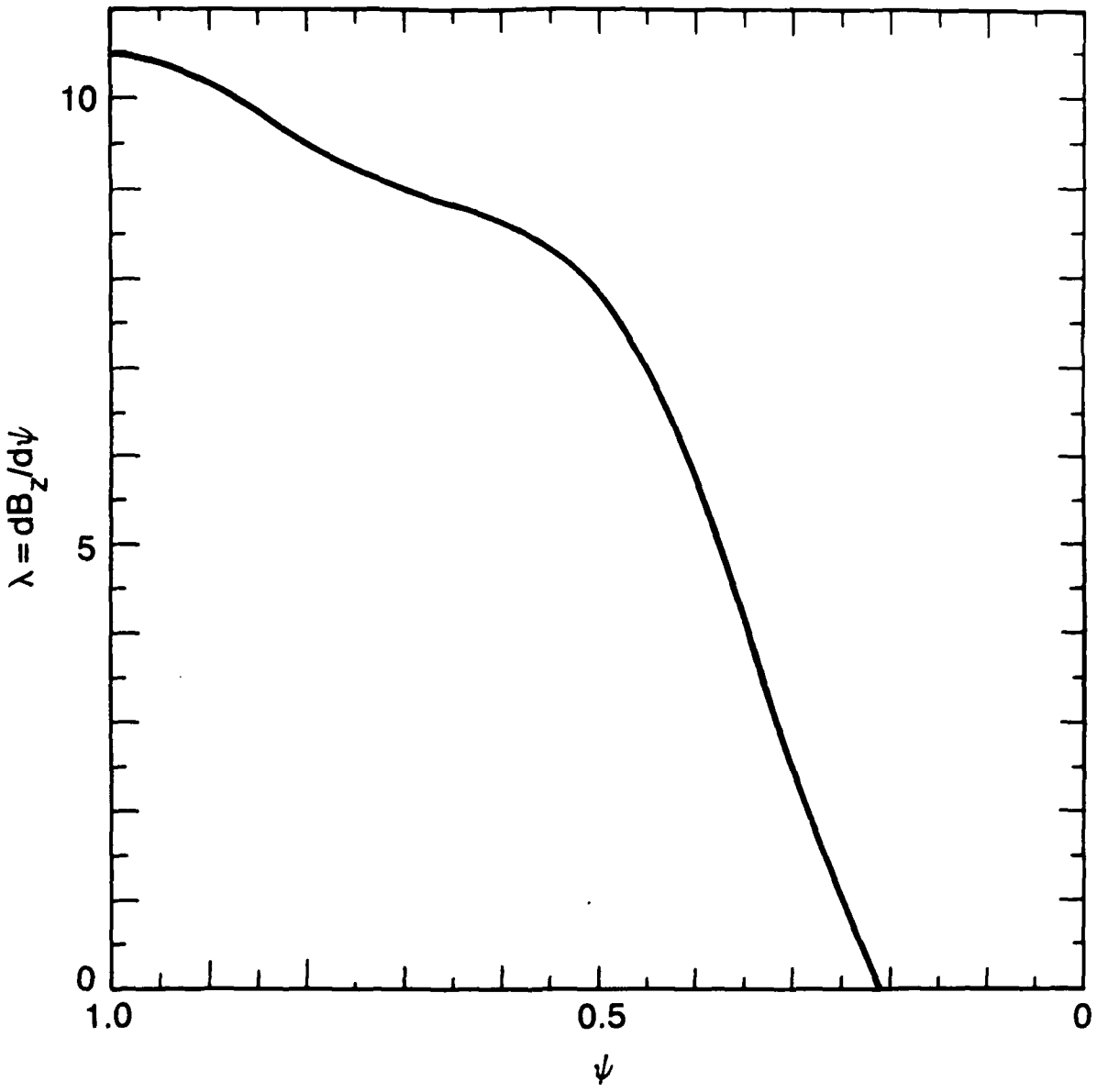



Fig. 5 (Continued) — Numerical equilibrium with boundary condition given by Eq. (19) for $\nu = 7$ and with footpoint displacement given by Eq. (21). The current-carrying region is surrounded by a relatively large amount of flux $\psi_v = 0.25$ ($x_v = 0.31$), W = 0.40, and $d_{max} = 0.36$. (a) Flux surfaces. (b) Footpoint displacement versus x. (c) $B_z$ versus $\psi$. (d) $\lambda$ versus $\psi$.

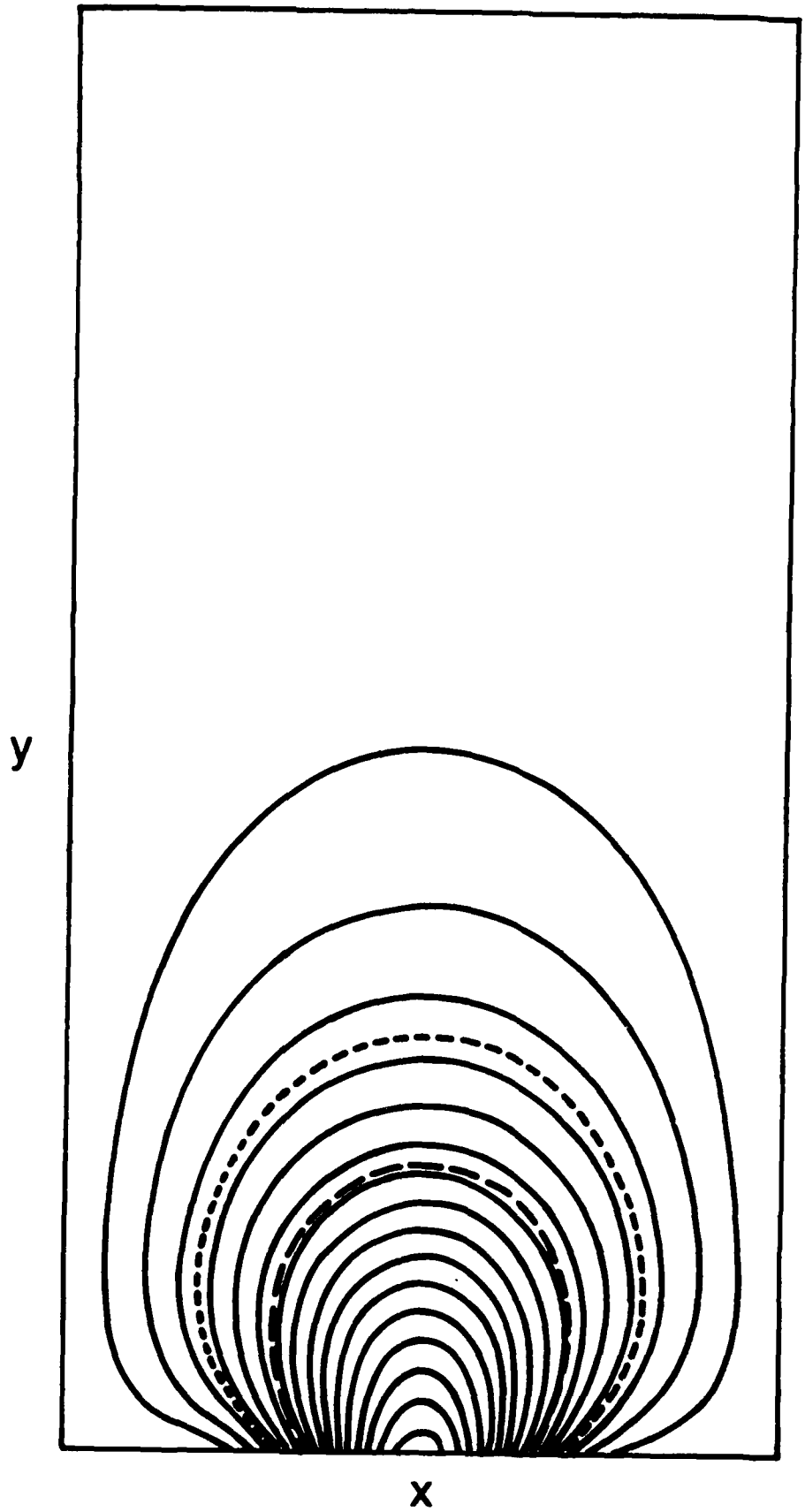



Fig. 6 — Equilibrium with parameters as in Fig. 5 except $d_{max} = 0.61$.

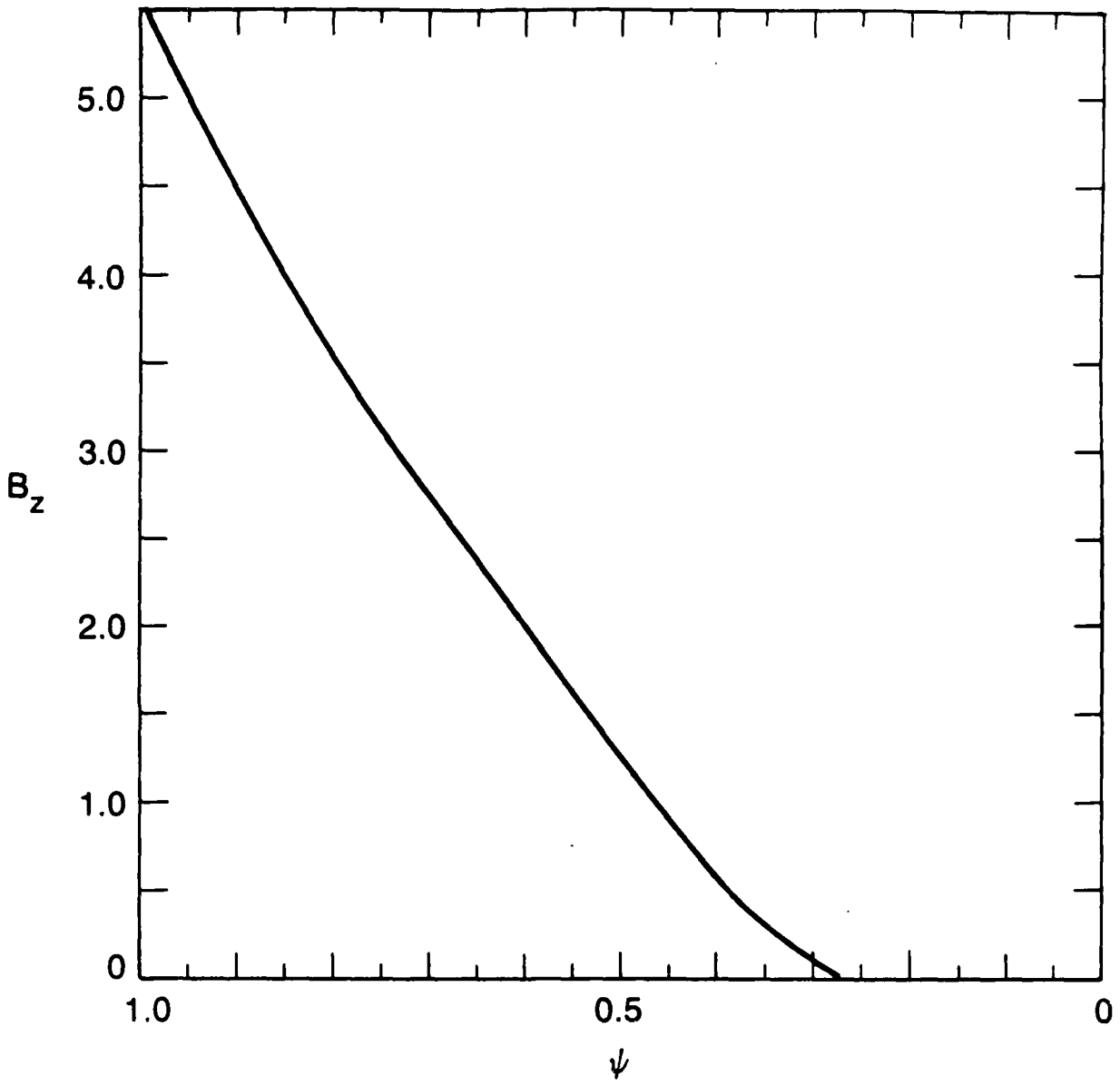



Fig. 6 (Continued) — Equilibrium with parameters as in Fig. 5 except $d_{max} = 0.61$.

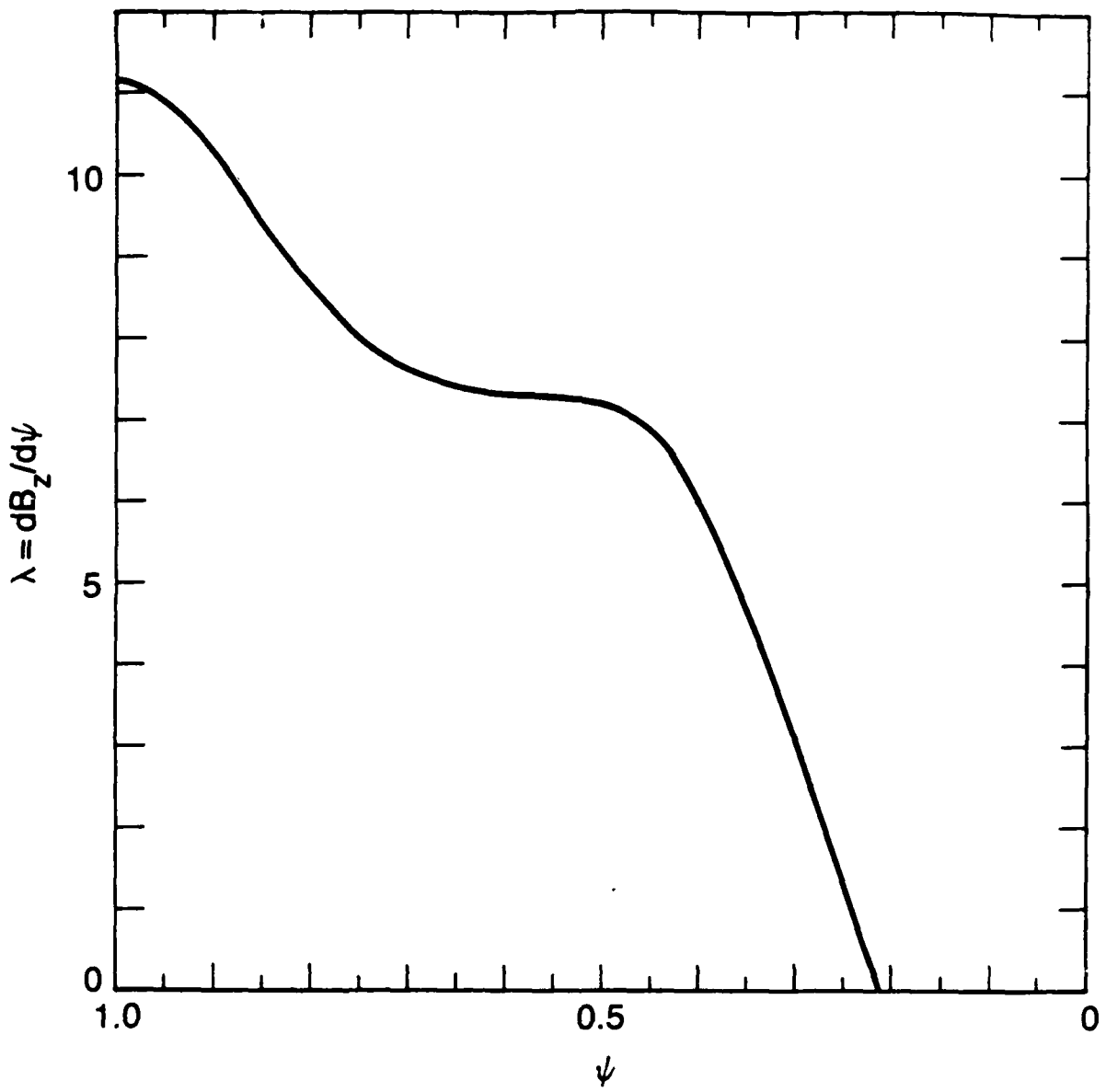



Fig. 6 (Continued) — Equilibrium with parameters as in Fig. 5 except $d_{max} = 0.61$.

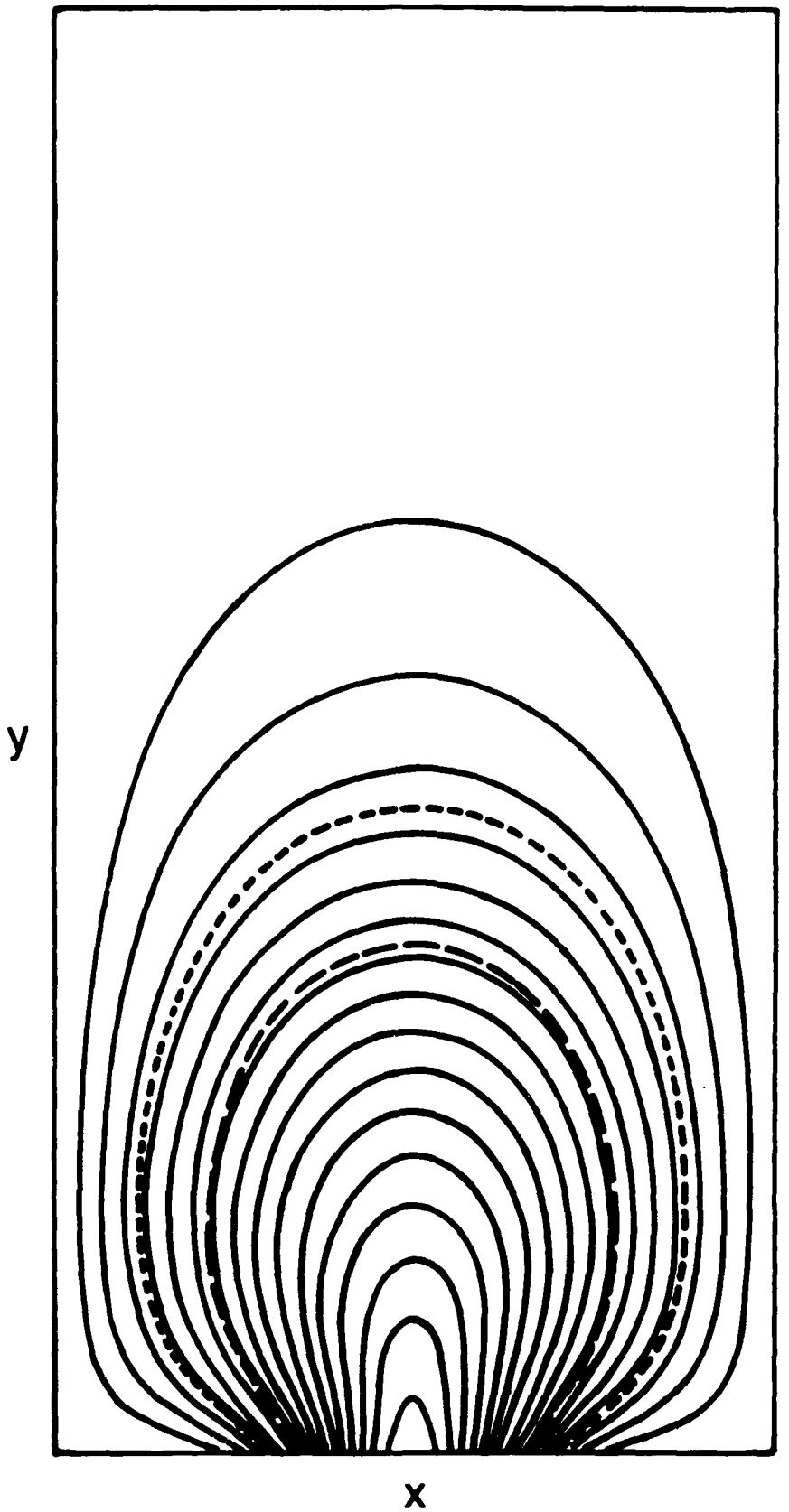



Fig. 7 — Equilibrium with parameters as in Fig. 5 except $d_{max} = 1.35$.

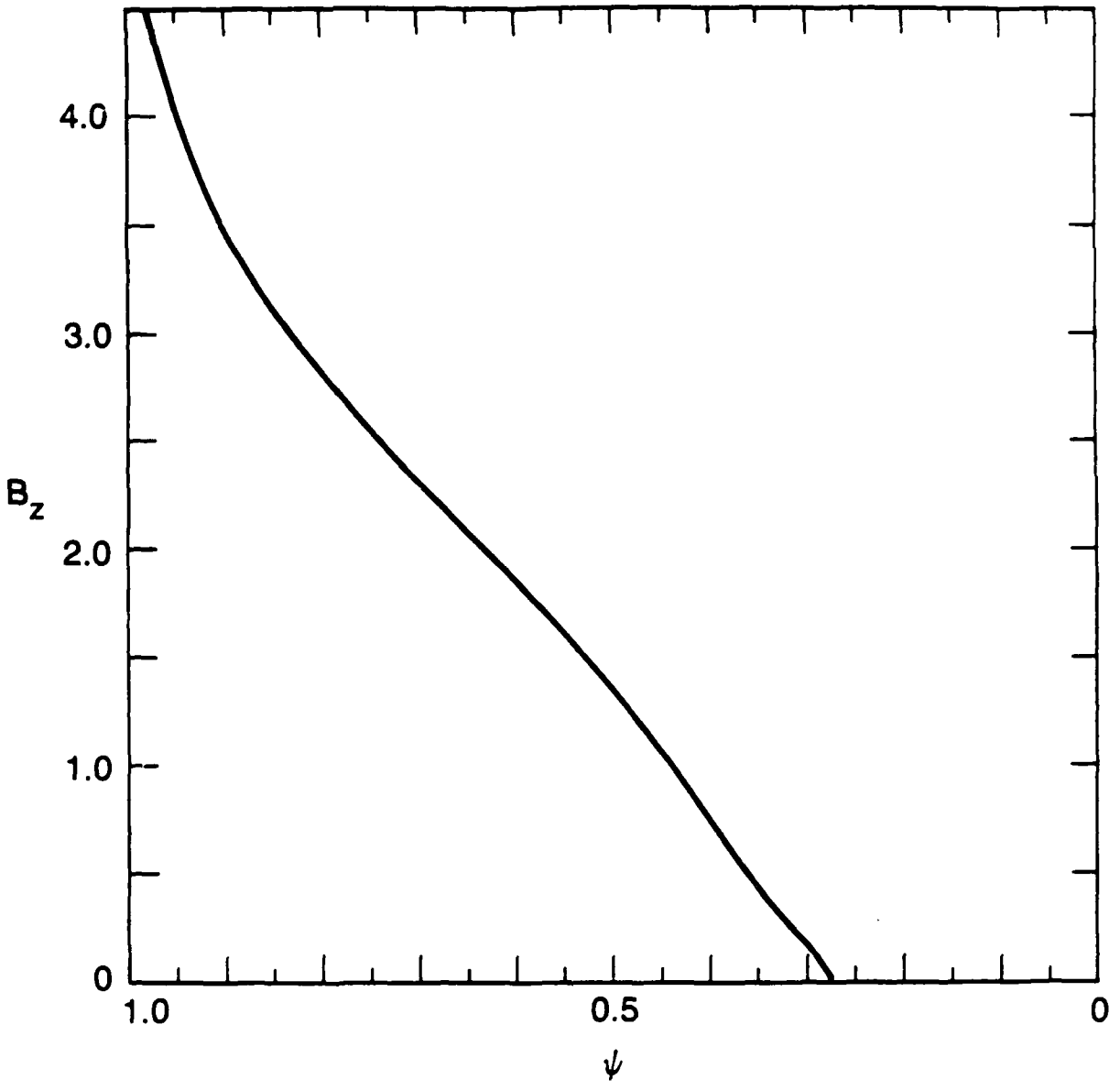



Fig. 7 (Continued) — Equilibrium with parameters as in Fig. 5 except $d_{max} = 1.35$.

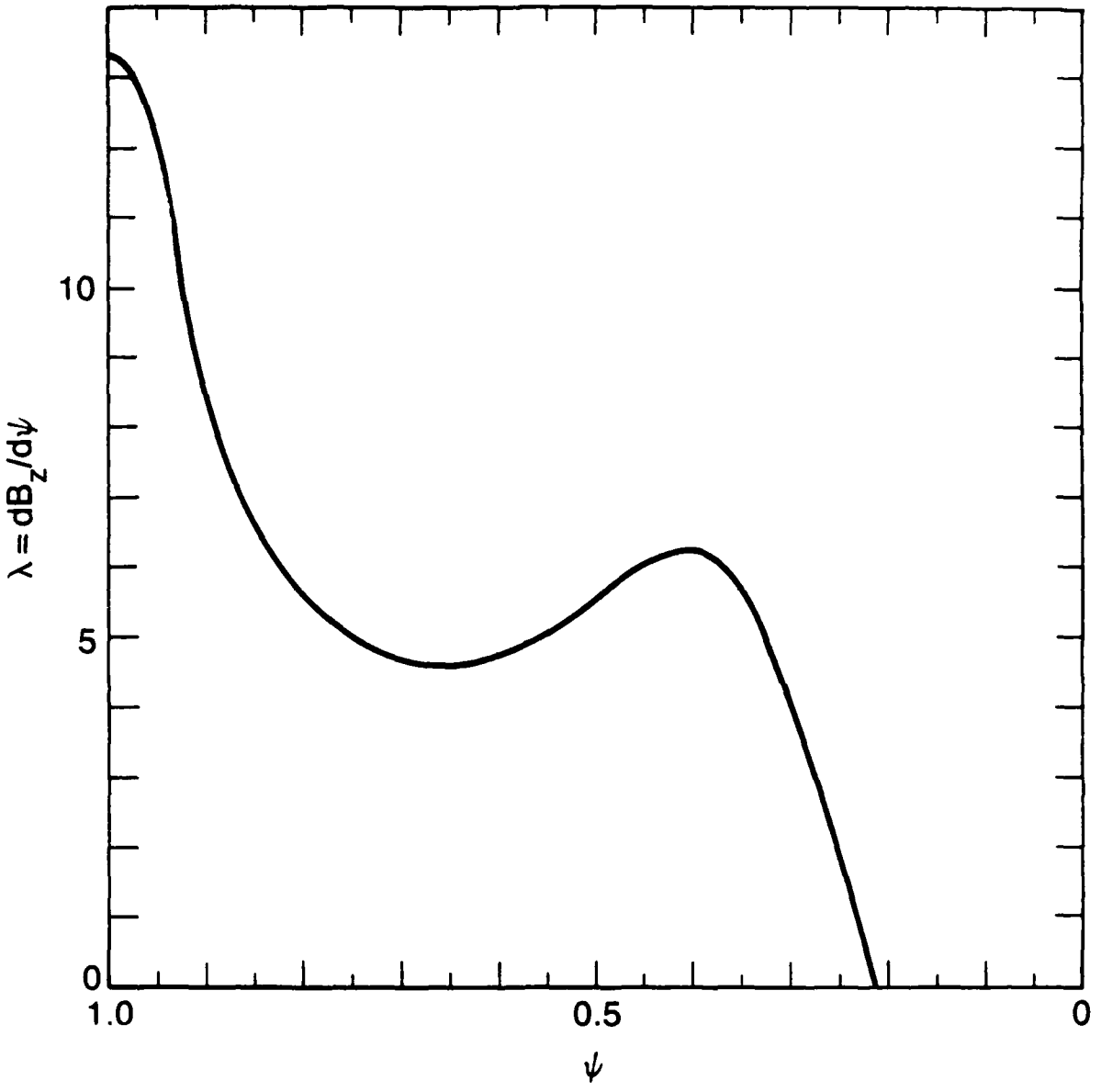



Fig. 7 (Continued) — Equilibrium with parameters as in Fig. 5 except $d_{max}$ = 1.35.

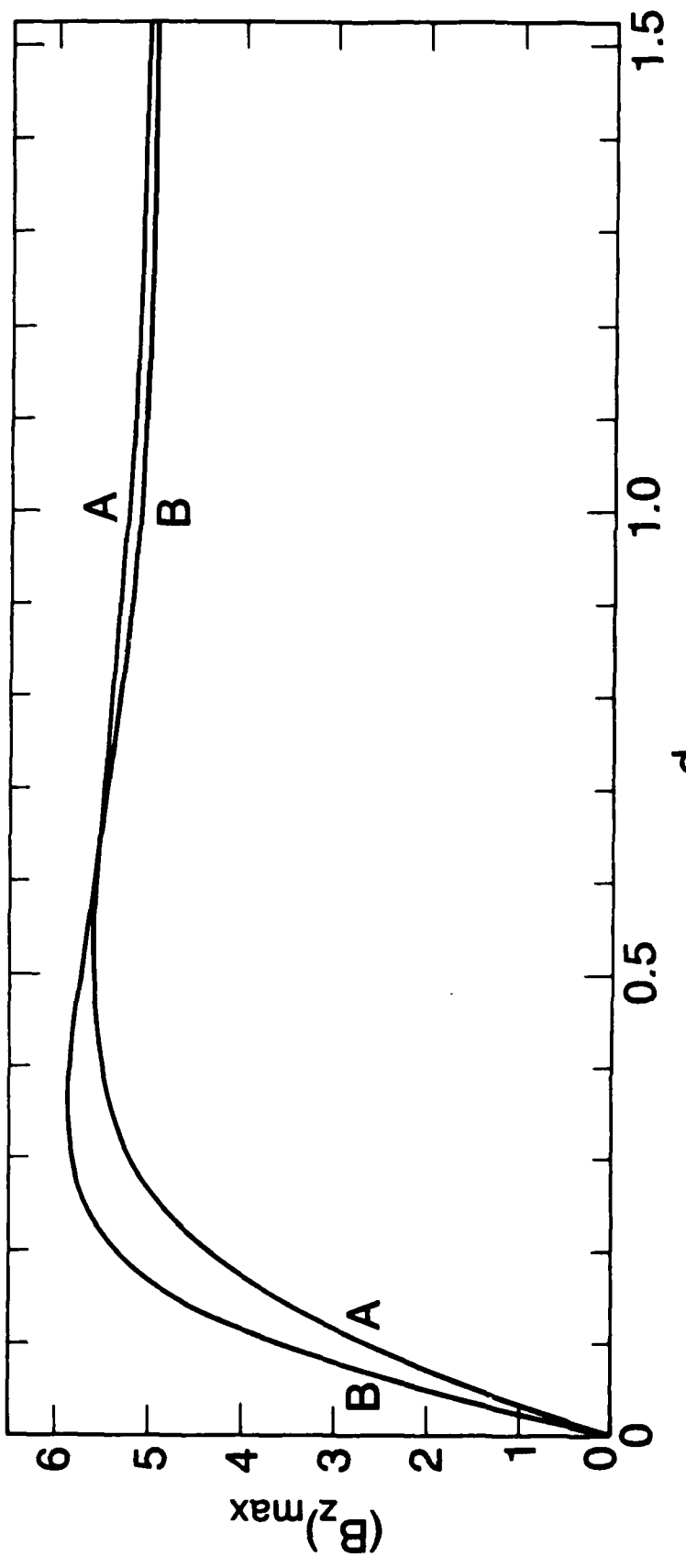



Fig. 8 — $(B_z)$max versus $d_{max}$ for two series of equilibria. Series B has parameters as in Figs. 5 — 7. Series A has the same parameters, except $\psi_v = 9 \times 10^{-3}$ ($x_v = 0.17$) and W = 0.45.

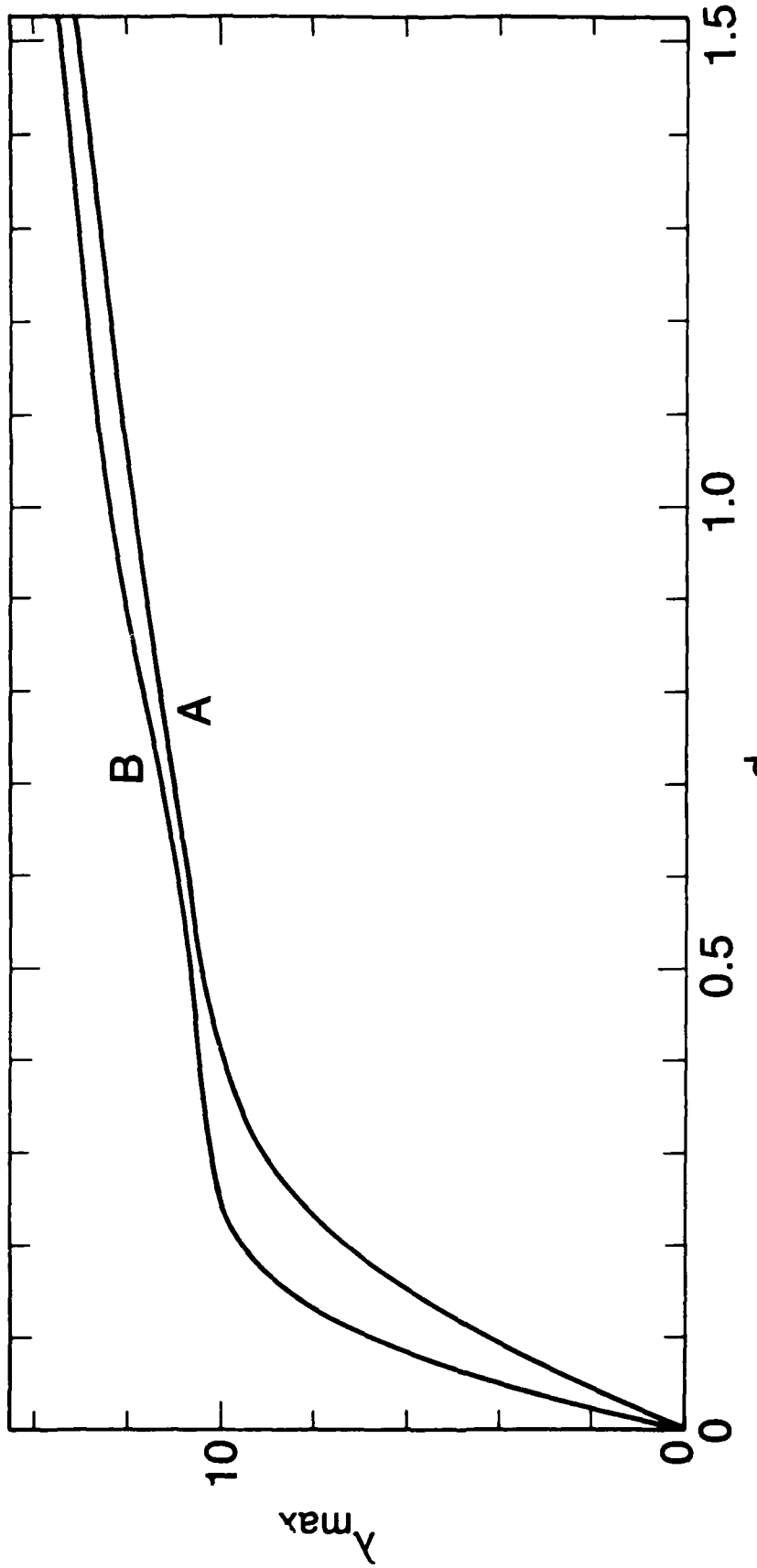



Fig. 9 — The maximum of $\lambda$ ($\psi$), $\lambda_{max}$ versus $d_{max}$ for the equilibria of Fig. 8.

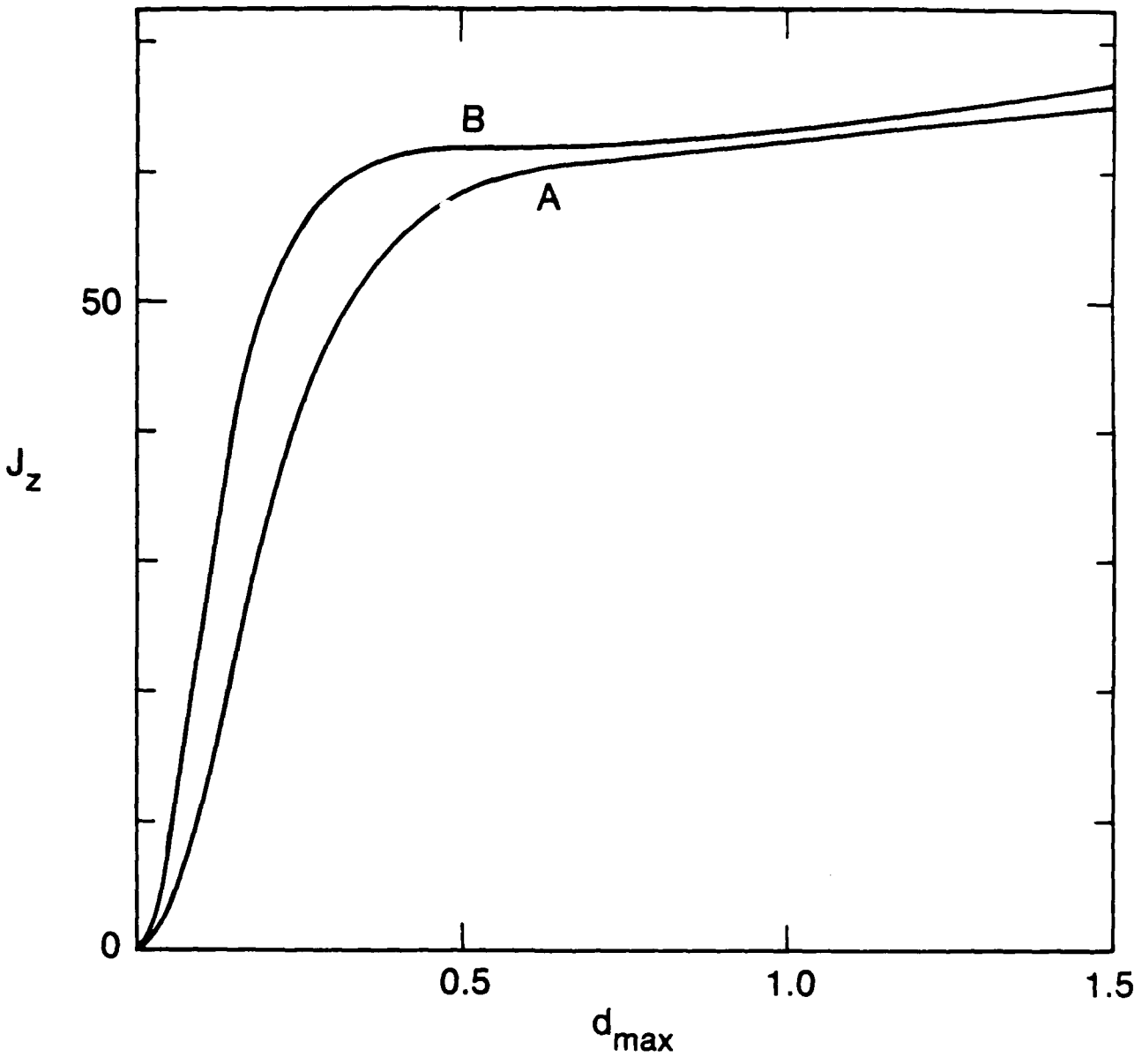



Fig. 10 — Maximum current density $j_z l$ versus $d_{max}$ for the equilibria of Fig. 8.

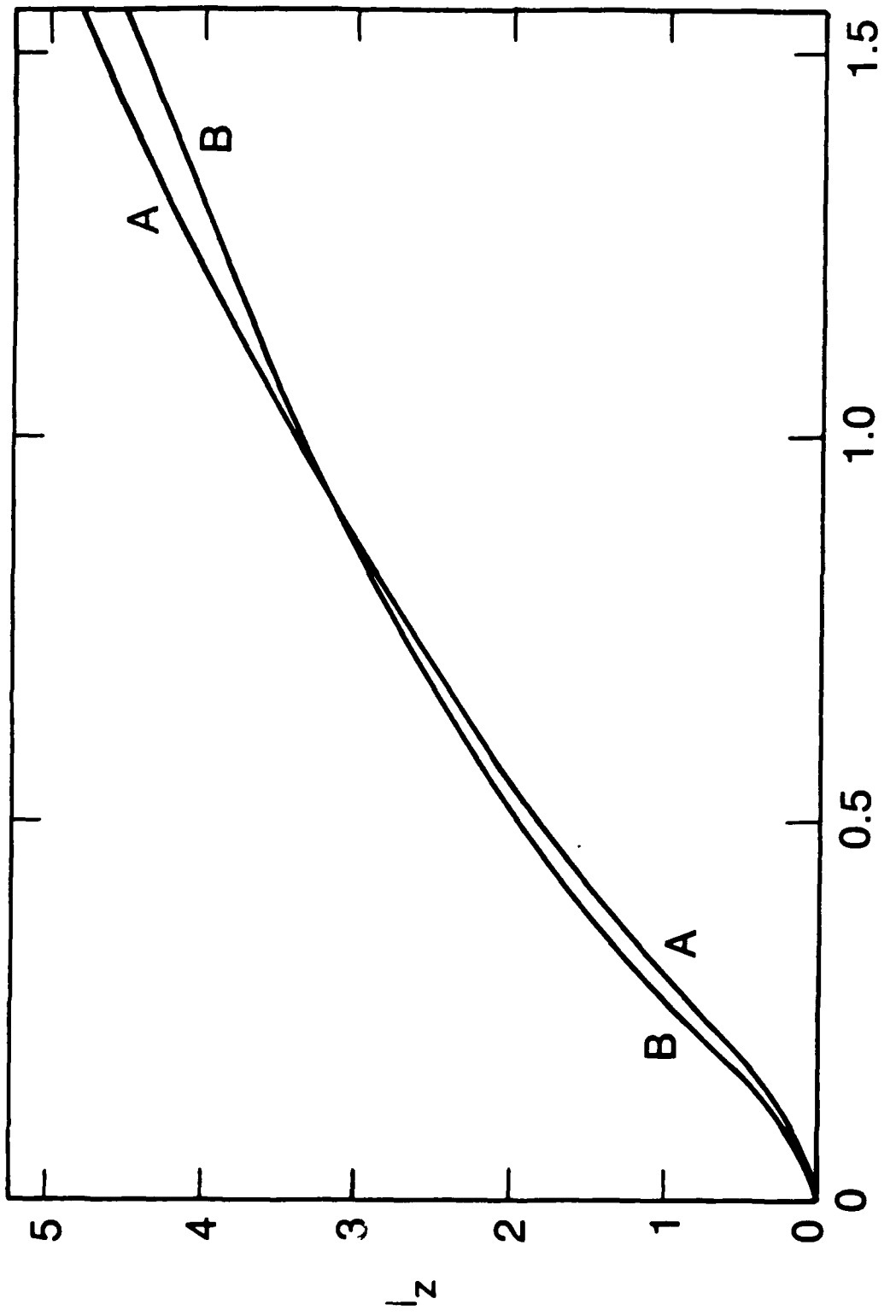



Fig. 11 — Total current $I_z$ versus $d_{max}$ for the equilibria of Fig. 8.

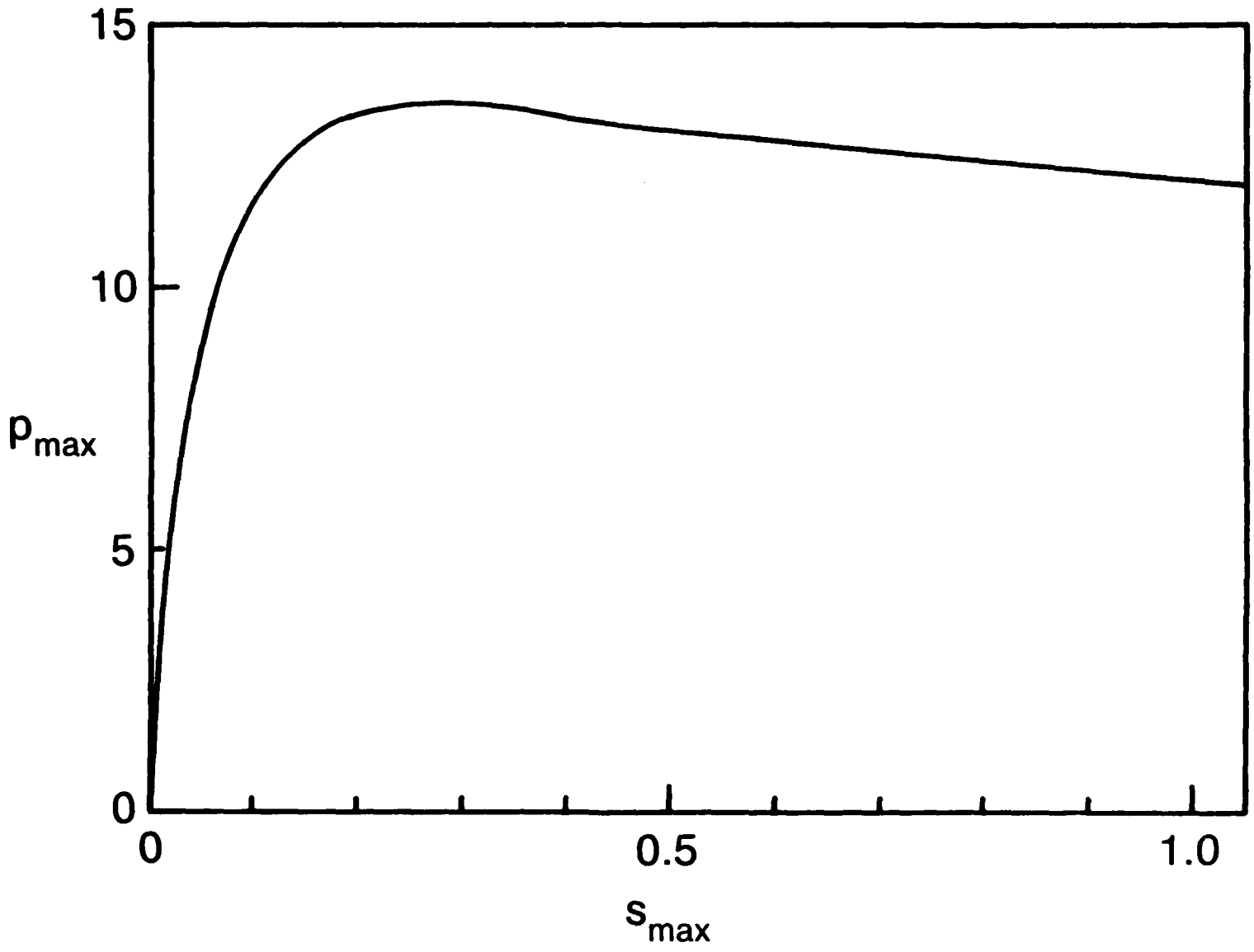



Fig. 12 — Sequence of equilibria with respect to specification of entropy. (a) Maximum pressure $p_{max}$ versus maximum entropy $s_{max}$ for a class of finite $\beta$ equilibria with $d_{max} = 0$. The form of $s(\psi)$ is given by $[d(\psi)]^{1/2}$, where $d(\psi)$ is the form factor in Eq. (21). The other parameters are those of Figs. 5 — 7 and series B of Fig. 8. (b) Total current $I_z$ and maximum current density $j_z$ versus $s_{max}$.

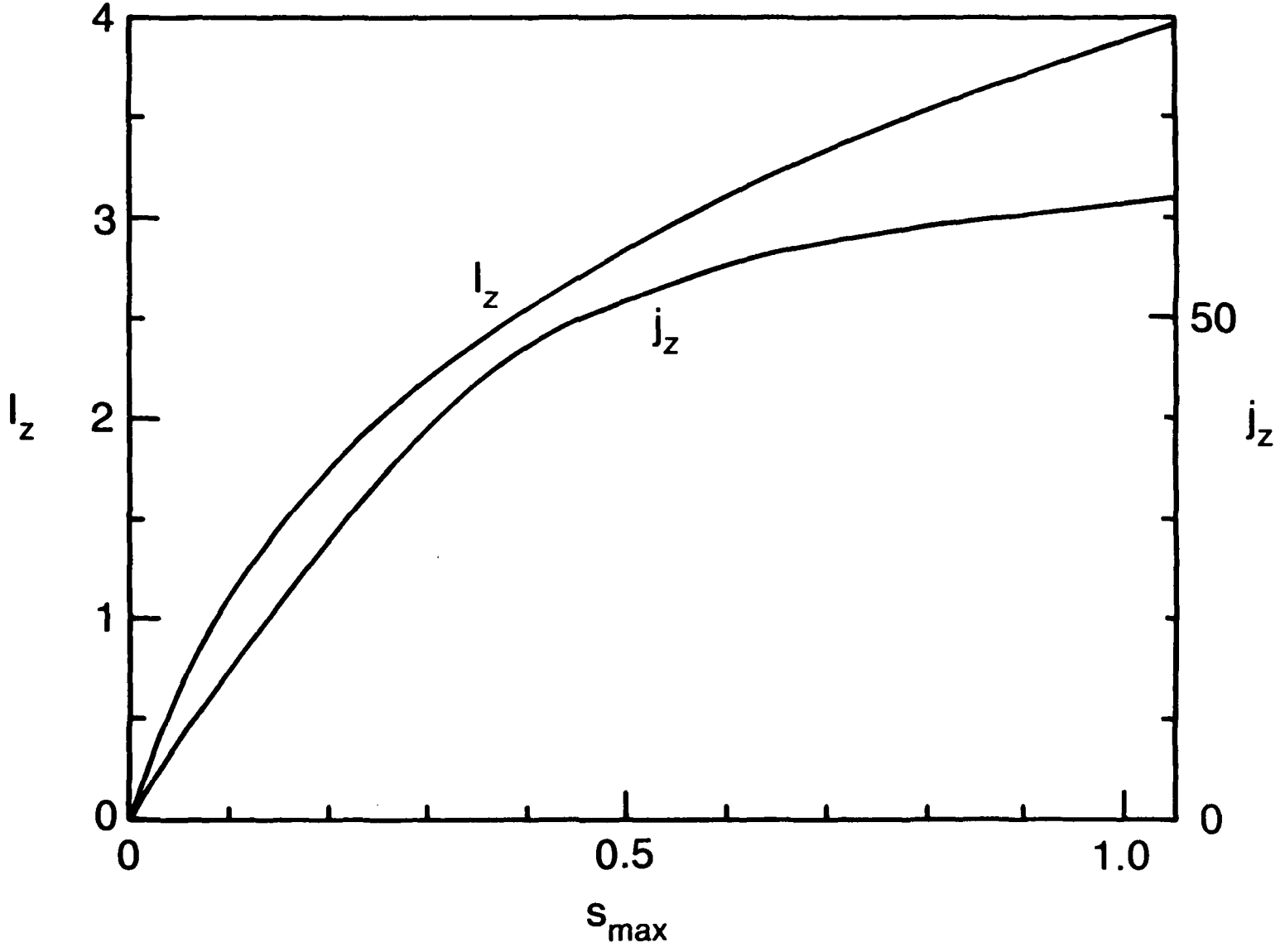



Fig. 12 (Continued) — Sequence of equilibria with respect to specification of entropy. (a) Maximum pressure $p_{max}$ versus maximum entropy $s_{max}$ for a class of finite $\beta$ equilibria with $d_{max} = 0$. The form of $s(\psi)$ is given by $[d(\psi)]^{1/2}$, where $d(\psi)$ is the form factor in Eq. (21). The other parameters are those of Figs. 5 — 7 and series B of Fig. 8. (b) Total current $I_z$ and maximum current density $j_z$ versus $s_{max}$.